Université du Québec
Institut National de la Recherche Scientifique
Centre Eau Terre Environnement

GEOLOGY OF THE BANDED IRON FORMATION-HOSTED MUSSELWHITE GOLD DEPOSIT, SUPERIOR PROVINCE, ONTARIO, CANADA

Géologie du gisement aurifère encaissé dans des formations de fer Musselwhite, Province du Supérieur, Ontario, Canada

par William Oswald, Ingénieur Géologue

Thèse présentée pour l'obtention du grade de
Philosophiæ doctor (Ph.D.) en sciences de la Terre

Jury d'évaluation

Président du jury et examinateur interne	Patrick Mercier-Langevin, Ph.D. Commission géologique du Canada
Examinateur externe	Richard Goldfarb, Ph.D. Colorado School of Mines, USA Goldfarb Global Gold
Examinateur externe	Michel Gauthier, Ph.D. Université du Québec à Montréal, Canada Gardin Inc.
Directeur de recherche	Sébastien Castonguay, Ph.D. Commission géologique du Canada
Codirecteur de recherche	Benoît Dubé, Ph.D. Commission géologique du Canada
Codirecteur de recherche	Michel Malo, Ph.D. INRS-ETE

© Droits réservés de William Oswald, 2018

ACKNOWLEDGEMENTS

Bien moins que pour certains, mais plus que pour d'autres, ce projet a été une épreuve de longue haleine et à ce titre de nombreuses personnes doivent être remerciées pour leur contribution à la production de cette thèse.

Tout d'abord, mes plus sincères remerciements à mes superviseurs Sébastien Castonguay, Benoît Dubé et Michel Malo, pour m'avoir offert l'opportunité de travailler sur un sujet qui continue de me passionner aujourd'hui, m'avoir fait bénéficier de leur expertise autant sur le terrain qu'au bureau, et m'avoir constamment motivé à m'améliorer. Ce projet a bénéficié des contributions scientifiques de Patrick Mercier-Langevin, Vicki McNicoll, Simon Jackson, Ingrid Kjarsgaard, Wouter Bleeker, Thomas Skulski et Robert Creaser.

I want to give a special thanks to John Biczok, without whom this project would not have been possible. His involvement, knowledge, and past experiences have been greatly helpful; and his mentorship was inspiring.

I also want to thank the Goldcorp Inc. staff at Musselwhite for their help, time, and efforts in the various tasks I undertook while on site. Geology aside, I also learned a lot during my time at Musselwhite and I am very grateful to all the people that contributed to this personal enrichment.

I am thankful to the organizations that financially supported this project, including the Natural Sciences and Engineering Research Council (NSERC), Goldcorp Inc., the Fonds québécois de recherche sur la nature et les technologies (FQRNT), the Geological Survey of Canada (GSC), and the Institut National de la Recherche Scientifique (INRS).

Je voudrais saisir cette opportunité pour remercier ma sœur Déborah pour cette petite suggestion qu'elle fit il y a plus de dix ans, concernant « cette école qui proposait un cursus en géologie à laquelle je devrais postuler ». Sans cela, bon nombre de choses auraient été différentes. Plus largement je suis profondément reconnaissant envers ma famille et le soutien dont j'ai bénéficié malgré la distance. À ce titre, mon frère Arnold mérite un remerciement supplémentaire pour avoir diminué cette distance l'espace de deux ans et ainsi atténué le sentiment d'isolement familial.

Je tiens également à remercier mon entourage amical. Parmi les amis de longues dates, Adrian, Cyril et Rémi méritent particulièrement ma reconnaissance. Chacun à sa façon a été une source de soutien, d'enrichissement personnel, et d'inspiration des plus précieuses, plus que je saurai l'exprimer ici.

Les années passées à Québec ont aussi apporté leur lot de nouvelles amitiés dont certaines ont particulièrement compté. Un grand merci à Boris, Maelle, Alex, Catherine, Maxime, Antoine, Julie,

Mahamed, Arnaud, Pierre, Marion, Marc, Aurélie, et toute autre personne avec qui j'ai eu le plaisir de partager du temps et, souvent, du café.

Un dernier remerciement, et non des moindres, doit aller à Julia, pour son soutien de chaque jour et particulièrement durant la dernière phase de réalisation de cette thèse. Sans elle, cette dernière marche de l'ascension aurait été bien plus pénible à gravir.

Many other people have had a contribution to this project. Whether it was a scientific or personal contribution, thank you to all who helped make these few years a more enriching and enjoyable experience.

RÉSUMÉ

La mine Musselwhite se situe près du lac Opapimiskan dans le nord-ouest de l'Ontario, à 475 km au nord de la ville de Thunder Bay. En exploitation depuis 1997, plus de 4 Moz d'or y ont été produites. Le gisement d'or de classe mondiale Musselwhite est encaissé dans les formations de fer rubanées (FFR) polydéformées au faciès métamorphique des amphibolites de la ceinture de roches vertes mésoarchéenne (3.0-2.7 Ga) de North Caribou (CNC), dans le nord-ouest de la Province du Supérieur. Ce type de gisement est relativement rare et peu d'études se sont penchées sur la genèse et les contrôles régissant les mineralisations aurifères dans les FFR. Elles peuvent cependant former des gisements colossaux, comme l'illustre celui de Homestake de 40 Moz d'or, aux USA. Le présent projet constitue une étude multidisciplinaire de la géologie et de la métallogénie du gisement d'or Musselwhite, caractérisé à l'aide de données géologiques, structurales, pétrographiques et géochimiques.

La NCG est majoritairement composée de basalte et komatiite tholéiitiques datés entre 3,05 et 2,91 Ga, recouvert de greywackes syn-orogéniques (<2,85 Ga). De larges batholithes de type TTG datés entre ca. 2,85 et ca. 2,73 Ga entourent la CNC. Trois phases principales de déformation ont affecté les roches de la CNC qui sont métamorphisées au faciès des amphibolites, daté à ca. 2660 Ma.

Les étroites enveloppes sub-verticales de minerai sont encaissées dans la FFR à grunérite-grenat affectée par des zones de forte déformation D_2 associées à des plis fermés à isoclinaux. La minéralisation aurifère épigénétique s'est formée sous des conditions métamorphiques de la zone à grenat, via un remplacement à pyrrhotite et une silicification de la FFR par des fluides issus de la dévolatilisation métamorphique des roches sous-jacentes. Elle est accompagnée d'une altération distale potassique (biotite) et proximale calcique (hornblende) remplaçant la grunérite dans la FFR. La teneur en or a une corrélation positive avec celles de l'Ag, du Cu, Se et Te. La minéralisation aurifère à Musselwhite est synchrone à la déformation D_2 et au métamorphisme M_2, et s'est mise en place entre 2720 et 2660 Ma.

Le gisement Musselwhite comporte des éléments communs à d'autres gisements tels que Lupin (TNO, Canada), Homestake (USA), Nevoria (Australia), notamment le contrôle lithologique de la FFR silicatée sur l'or. Un tel horizon clé, un contexte structural complexe et de forts gradients de déformation sont des vecteurs d'explorations importants au sein de la CNC, du nord-ouest de la Province du Supérieur, et dans d'autres terrains métamorphisés précambriens.

Mots-clés : Archéen ; Province du Supérieur ; North Caribou ; or encaissé dans formations de fer rubanées ; or épigénétique ; gradient de déformation ; métamorphisme amphibolite ; Ontario.

ABSTRACT

The Musselwhite mine is located near Opapimiskan Lake in northwestern Ontario, 475 km north of Thunder Bay. Over 4 Moz of gold have been produced since the start of operation in 1997. The world-class Musselwhite gold deposit is hosted by polydeformed, amphibolite-grade banded iron formations (BIF) in the Mesoarchean (3.0-2.7 Ga) North Caribou greenstone belt (NCG), in northwestern Superior Province. This deposit type is quite rare and few studies focused on their genesis and gold ore-forming processes. However, they can form large deposits, such as the Homestake mine (40 Moz of gold, USA). This project constitutes a multidisciplinary study of the geology and metallogeny of the Musselwhite gold deposit, using geological, structural, petrographic, and geochemical data.

The NCG is mainly composed of tholeiitic basalts and komattites dated between 3.05 and 2.91 Ga, overlain by syn-orogenic greywackes (<2.85 Ga). Large TTG-type batholiths dated between 2.85 and 2.73 Ga surround the NCG. Three major phases of deformation affected rocks of the NCG, which were metamorphosed to amphibolite facies around 2660 Ma.

Narrow sub-vertical ore zones are hosted by garnet-grunerite BIF in D2 high-strain zones associated with close to isoclinal folds. Epigenetic gold mineralization formed under garnet zone metamorphic conditions through pyrrhotite-replacement and silicification of the BIF by fluids stemming from metamorphic devolatilization of underlying rocks. It is accompanied by potassic (biotite) alteration and proximal calcic (hornblende) alteration of grunerite in the BIF. Gold grade is positively correlated with Ag, Cu, Se and Te. Gold mineralization at Musselwhite is synchronous to D_2 deformation and M_2 metamorphism, and was emplaced between 2720 and 2660 Ma.

The Musselwhite deposit shows features common with other deposits such as Lupin (NWT, Canada), Homestake (USA), and Nevoria (Asutralia), notably the lithological control of silicate BIF on gold. Marker horizons, complex structural context, and strong deformation gradient are key exploration vectors in the NCG, the northwestern Superior Province, and other Precambrian terranes.

Key words: Archean; Superior Province; North Caribou; BIF-hosted gold; epigenetic gold; deformation gradient; amphibolite metamorphism; Ontario.

SOMMAIRE RÉCAPITULATIF

Chapitre 1 : Introduction

La mine Musselwhite se situe près du lac Opapimiskan, dans le district minier Patricia au nord-ouest de l'Ontario, à 475 km au nord de la ville de Thunder Bay (Figure 1). La découverte des premières traces d'or dans cette région remonte aux années 1960. Des travaux d'exploration dans les années 1970 et 1980 ont mené à des découvertes successives et permirent la définition de zones minéralisées économiques. La production menée par la Musselwhite Joint-Venture commença en 1997. Depuis 2006, la mine est gérée par Goldcorp Inc. Elle a produit plus de 4,5 Moz d'or et, au 1er décembre 2016, dispose de réserves prouvées et probables de 1,85 Moz.

Musselwhite est un gisement d'or de type orogénique encaissé dans une formation de fer rubanée (FFR) poly-déformée, métamorphisée au faciès des amphibolites et comprise dans une séquence principalement volcanique de la ceinture de roches vertes archéenne de North Caribou, dans la Province du Supérieur occidentale du Bouclier canadien (Fig. 1). Le minerai aurifère à Musselwhite est majoritairement formé par le remplacement du faciès silicaté de la FFR par de la pyrrhotite localement associée à de la silicification.

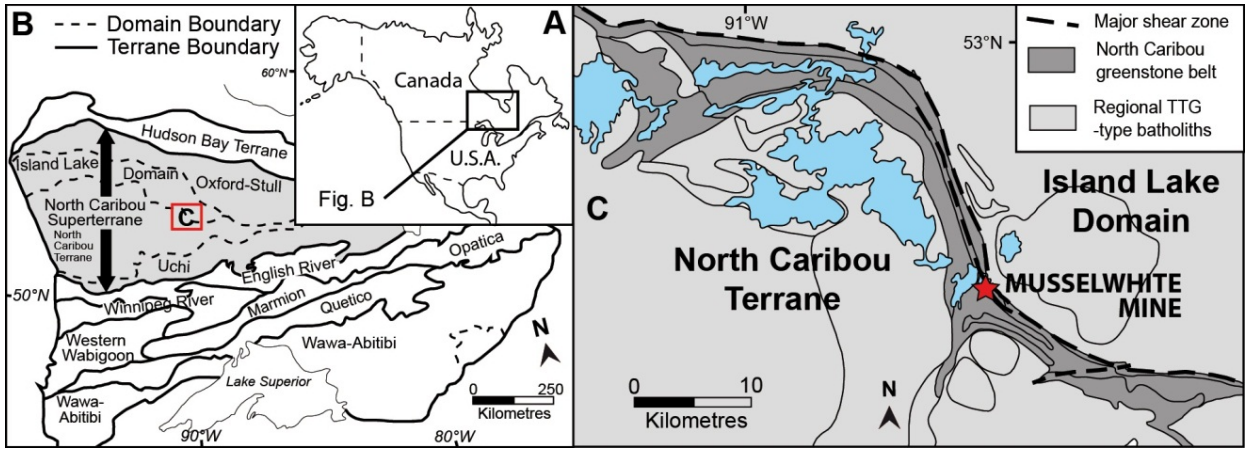

Figure 1 : (A) Localisation géographique de la mine Musselwhite et de la zone d'étude , (B) carte des terranes et domaines lithotectoniques de la Province du Supérieur, et (C) Localisation de la mine Musselwhite au sien de la ceinture de roches vertes de North Caribou (A et B, modifiée de Rayner et Stott, 2005, et Stott et al., 2010 ; C, modifiée de Thurston et al., 1991).

La production et les ressources en or du Canada sont largement associées aux districts miniers situés dans les terrains archéens de la Province du Supérieur, notamment dans la ceinture de roches vertes de l'Abitibi (Gosselin et Dubé, 2005 ; Percival, 2007). Les gisements d'or orogéniques à veines de quartz-carbonates sont principalement encaissés au sein de roches volcaniques et d'intrusions, les FFR ne formant qu'une partie mineure des lithologies hôtes. Le spectre des gisements d'or orogéniques encaissés dans des FFR semblent se répartir entre deux pôles (Dubé et al., 2011) : un gisement en apparence isolé de grande taille qui sont quasi-uniquement encaissés dans les FFR, tel que les mines de Musselwhite (ON) et de Meadowbank (NU ; Janvier, 2016) ; et ceux qui ne sont que partiellement encaissés dans les FFR, formant souvent un district associé à des zones de faille majeures, comme ceux de Méliadine (NU ; Lawley et al., 2015) ou Geraldton (ON ; Toth et al., 2015). Les gisements d'or orogéniques encaissés dans

des FFR peuvent constituer des gisements de classe mondiale, comme celui de Homestake et ses 40 Moz d'or (Caddey et al., 1991), et représentent des cibles d'exploration importantes.

La présente étude de la mine Musselwhite fait partie du projet or de la phase 4 de l'Initiative Géoscientifique Ciblée menée par Ressources Naturelles Canada (Dubé et al., 2011). Elle s'inscrit dans une logique visant à améliorer les connaissances géologiques à disposition des compagnies d'exploration minière au Canada, dans un contexte de diminution du taux de découvertes de gisements (Villeneuve et al., 2011), afin d'aboutir à des modèles et des pratiques d'exploration plus efficaces. Les objectifs de la présente étude sont les suivants : 1) améliorer la compréhension du contexte géologique local et subrégional du gisement Musselwhite, 2) documenter les paramètres contrôlant la formation, la distribution et la géométrie des zones minéralisées aurifères, 3) documenter les caractéristiques géochimiques de celles-ci et de l'empreinte de l'altération hydrothermale associée, 4) documenter les relations chronologiques entre l'introduction de l'or et les différents événements tectonométamorphiques, et 5) définir des vecteurs pour l'exploration locale, régionale et dans d'autres terrains archéens.

Pour y parvenir, une collecte de données géologiques et structurales a été accomplie grâce à de la cartographie d'affleurements décapés et de galeries souterraines. Des échantillons ont été prélevés à des fins d'analyses géochronologiques U-Pb sur zircon et U-Th-Pb sur monazite, effectuées en collaboration avec V. McNicoll de la Commission géologique du Canada à Ottawa. Des carottes de forage ont été examinées et échantillonnées afin d'obtenir des données pétrographiques, de chimie minérale et de lithogéochimie roche-totale. Finalement, de la cartographie élémentaire sur grenat et sulfures a été réalisée par LA-ICP-MS sur des échantillons clés.

Chapitre 2 : Contexte géologique régional

La Province du Supérieur est un craton archéen couvrant une large portion du Québec et la quasi-intégralité de l'Ontario (Wheeler et al., 1996). Sa portion occidentale est composée de terrains principalement juvéniles âgés de 3,0-2,9 Ga incluant des roches plutoniques de ca. 2,85 et ca. 2,72 Ga (Percival, 2007). La Province s'est formée par l'accrétion successive vers le sud de terrains orientés est-ouest. Les processus impliqués dans cette formation restent sujet à débat (Percival, 2007 ; Bédard et Harris, 2014).

La ceinture de roches vertes de North Caribou (CNC) se situe sur la bordure nord du terrain de North Caribou, où il jouxte le domaine de l'Island Lake (Figure 2). Elle est formée des assemblages à dominance volcanique, South Rim (SRA), Agutua Arm et Keeyask (AAV, KLA), Opapimiskan-Markop (OMA), Forester Lake (FLV) et North Rim (NRA), et des assemblages à dominance sédimentaire du lac Eyapamikama (ELS) et de Zeemel-Heaton (ZHA) (Breaks et al., 2001 et références incluses). À l'exception du NRA daté autour de. 2,87 Ga, les assemblages volcaniques se forment entre 3,0 et 2,9 Ga, tandis que les assemblages sédimentaires se déposent entre 2,85 et 2,7 Ga. Les séquences volcaniques sont interprétées comme le produit de l'interaction entre une plume mantellique et une croûte continentale mafique plus ancienne (Hollings et Kerrich, 1999), dont les interruptions du volcanisme permirent le dépôt de FFR de type Algoma grâce aux apports chimiques de systèmes hydrothermaux et d'une sédimentation détritique (Breaks et al., 1985 ; Moran, 2008).

Trois phases déformation majeures affectent les roches de la CNC ; la principale étant la D_2 (Figure 3 ; Hall et Rigg, 1986 ; Breaks et al., 1986 ; Breaks et al., 2001). La première est caractérisée par des plis

isoclinaux à vergence nord-est dotés d'une foliation S_1 pénétrative. La déformation D_2 a produit des plis droit ouverts à isoclinaux plongeant faiblement vers le nord-ouest, caractérisée par une fabrique S_2 de plan axial variant d'un clivage espacé à une schistosité pénétrative. L'interférence des plis P_1 et P_2 produit un patron d'interférence de type 3 (Ramsay et Huber, 1987). Des zones de cisaillement sub-verticales D_2 sont hôtes de la minéralisation aurifère où elles recoupent la FFR. Les zones de failles majeures régionales se développent durant la D_2. Les effets de la D_3 sont distribués de façon hétérogène, augmentant vers le sud-est et se traduisent par des plis en Z à vergence sud plongeant modérément vers l'ouest. La phase de déformation D_2 est associée à un métamorphisme régional (M_2) allant du faciès des schistes verts inférieur à celui des amphibolites (Figure 4).

La CNC comporte un peu plus d'une dizaine d'occurrences aurifères notables sur l'ensemble de son étendue, mais aucune de taille comparable à celle de la mine Musselwhite. Elles se trouvent principalement dans la partie nord de la ceinture, à proximité de limites entre assemblages lithostratigraphiques.

Chapitre 3 : Géologie, pétrographie et géochimie des roches hôtes du gisement Musselwhite

Dans la région de la mine Musselwhite, les assemblages du South Rim, Opapimiskan-Markop et Zeemel-Heaton sont affectés par un duo de plis régionaux formé par le West antiform et du East Bay synform (Figure 5). La mine se trouve au sein du synforme, où la minéralisation aurifère est encaissée dans une séquence de FFR nommée Northern iron formation (NIF). Celle-ci est le produit de sédimentations détritique et chimique simultanées (Boström, 1973 ; Kamber et al., 2005 ; Lawrence et Kamber, 2006 ; Moran, 2008 ; Baldwin, 2011 ; Oswald et al., 2015b). La caractérisation des roches de la zone d'étude est focalisée sur les unités présentes dans la séquence du gisement en commençant par les roches volcaniques puis sédimentaires, et puise dans les données géologiques, pétrographiques et lithogéochimiques récoltées.

Des analyses géochronologiques U-Pb sur zircon ont montré que la séquence de la mine est inversée (McNicoll et al., 2016). L'unité Avol, au sommet structural, fait partie du SRA. Elle contient à sa base une portion mineure de coulées andésitiques et dacitiques en coussins, recouvertes par des rhyodacites fragmentaires polymictiques et quelques horizons de tufs felsiques (Figure 3-7, 3-8 ; Wynchester et Floyd, 1977 ; MacLean et Barrett, 1993). Les échantillons prélevés dans la zone de la mine montrent une roche typiquement composée de quartz (50 %vol.), de micas (jusqu'à 30 %vol.) et de feldspath (de 5 à 15 %vol.). Sa composition chimique traduit une affinité calco-alcaline (Ross et Bédard, 2009) et son profil d'éléments des terres rares étendu normalisés au manteau primitif (PM-n ; Sun et McDonough, 1989) présente un fort enrichissement en LREE et de fortes anomalies négatives en Ti, Nb et Ta.

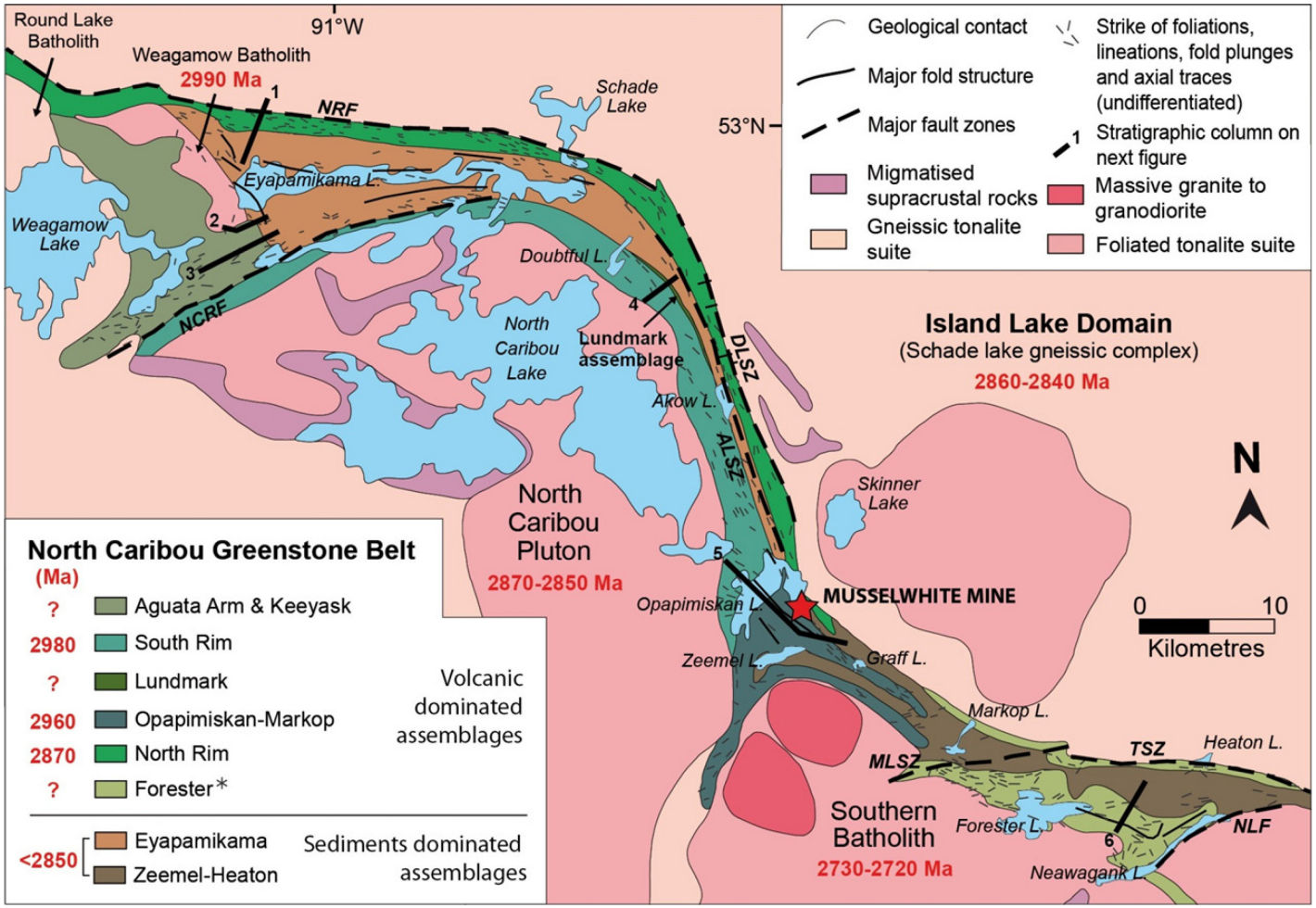

Figure 2 : Carte tectonostratigraphique simplifiée de la ceinture de North Caribou (modifiée de McNicoll et al., 2016, après Biczok et al., 2012). Données géochronologiques de Breaks et al., 2001, McNicoll et al (2013, 2016), et Van Lankvelt (2013). Données structurales d'après Breaks et al. (2001) et McNicoll et al. (2016). NRF: zone de faille North Rim, NCRF: zone de faille de la rivière North Caribou, DLSZ: zone de cisaillement du lac Dinnick, ALSZ: zone de cisaillement du lac Akow, MLSZ: zone de cisaillement du lac Markop, TSZ: zone de cisaillement Totogan, NLF: zone de faille du lac Neawagank.

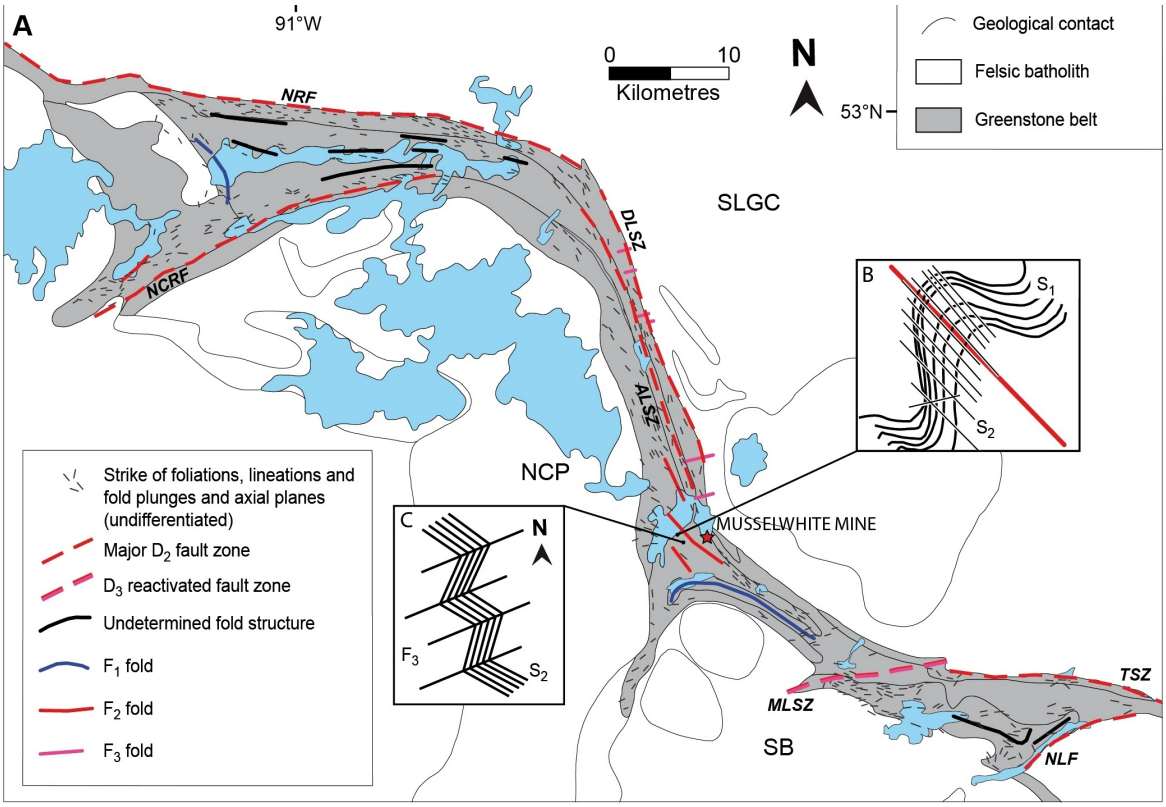

Figure 3 : A. Carte structurale simplifiée de la NCG (modifiée de McNicoll et al., 2016, après Biczok et al., 2012) Acronymes des zones de failles, voir figure 4. B. et C. Relations de recoupement entre les foliations S_1-S_2 et S_2-S_3 dans la zone du lac Opapimiskan.

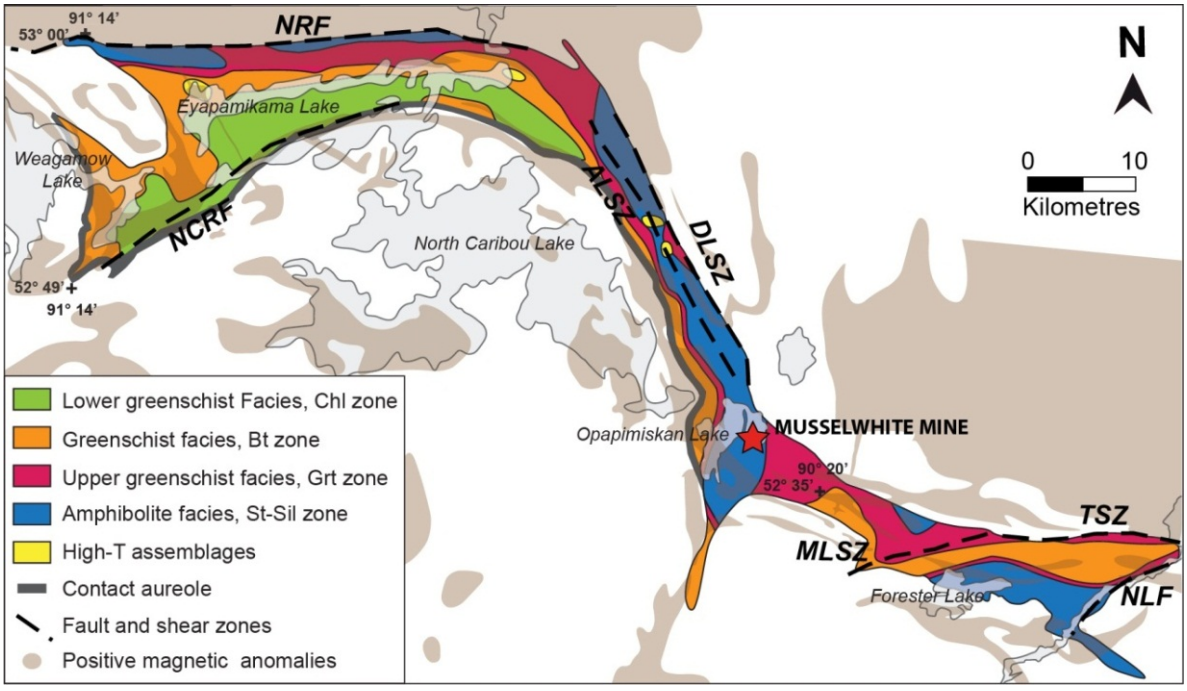

Figure 4 : Cartes des zones métamorphiques de la NCG (modifiée d'après Gagnon et al., 2015, après Breaks et al., 2001, et Kelly et al., 2013).

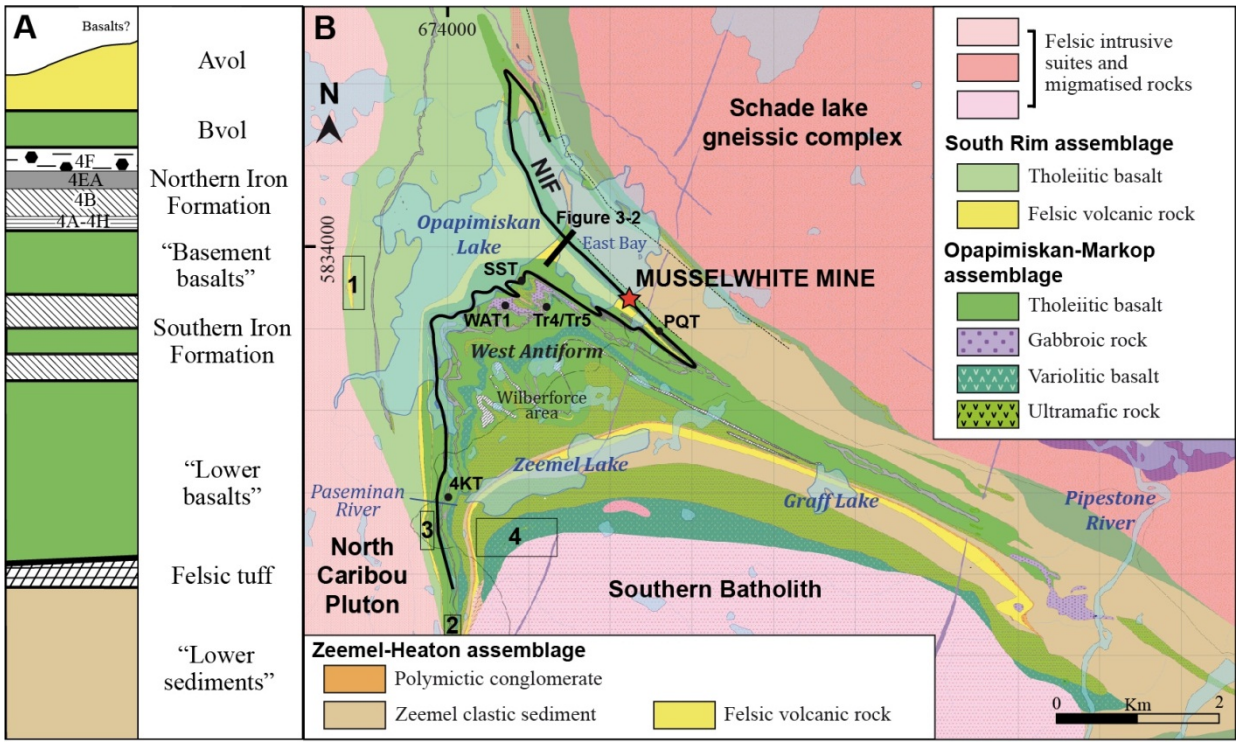

Figure 5 : A. Colonne lithologique schématique de la zone d'étude (stratigraphie inversée ; nomenclature locale des unités ; échelle verticale non respectée ; modifiée d'après Biczok et al., 2012). B. Carte géologique de la zone du lac Opapimiskan. Trait gras noir : trace de la séquence NIF. Points noirs et codes correspondent à la localisation des tranchées cartographiées. Les rectangles numérotés 1 à 4 renvoient aux études de Smyk (2013), Chadwick (2014), Pisani (inédit), et Quinn (2014), respectivement.

L'unité Bvol, sous-jacente, forme la base stratigraphique de l'OMA et précède la NIF, hôte de la minéralisation aurifère. Elle consiste principalement en coulées massives et en coussins de basalte et de basalte andésitique tholéiitiques (Figures 3-9 et 3-10). L'assemblage minéralogique typique comprend de la hornblende (50-80 %vol.), du feldspath plagioclase (5-20 %vol.) et du quartz (5-10 %vol.). Les profils d'éléments traces normalisés au Manteau Primitif sont majoritairement plats ; un groupe se distingue par un enrichissement modéré en LREE. Entre les coulées s'intercalent des lentilles « intra-formationnelles » d'amphibolite à grenat (unité 4E) et de schiste à biotite-grenat (unité 4F), décrites ci-après. Celles-ci sont interprétées comme des accumulations locales de sédiments épiclastiques et détritiques mafiques.

L'unité « Basement basalts » se trouve entre les séquences des FFR NIF et SIF. Sa base stratigraphique est marquée par une coulée d'andésite en coussins d'affinité calco-alcaline, recouverte d'intercalations de basalte et basalte komatiitique tholéiitiques à transitionnels dont la minéralogie est très proche de celle de l'unité Bvol, exceptée la présence d'actinolite. Les profils PM-n de cette unité montrent fréquemment un enrichissement en LREE et une anomalie négative en Nb-Ta.

L'unité « Lower basalts » inclut toute la séquence volcanique sous la SIF. Peu représentée dans la zone de la mine, elle couvre une large portion de la zone du West antiform au sud-ouest. Coulées de basalte, basalte komatiitique et komatiite en coussins, brèches de sommet de coulées et intrusions gabbroïques sont présentes (Figure 3-15).

Les roches sédimentaires détritiques-chimiques dans la séquence de la mine sont représentées tout d'abord par les unités 4E, 4F et 6 (sections 3.6, 3.7 et 3.8). Ces trois unités sont à dominante détritique, mafique pour les deux premières, felsique pour la troisième. L'unité 4E est constituée d'une matrice de hornblende contenant des porphyroblastes de grenat millimétriques à centimétriques, et contient 50 % pds. de SiO_2, 10 % pds. d'Al_2O_3 et 30 % pds. de fer total. L'unité 4F, formant la base de la NIF, est faite d'une matrice de biotite-quartz à porphyroblastes de grenat, localement de staurolite, pouvant atteindre 30 %vol. Elle inclut localement des bandes de chert. Elle contient 50 à 55 % pds. de SiO_2, 15 à 20 % d'Al_2O_3 et environ 20 % de fer total. L'unité 6, enfin, est marquée par une minéralogie de feldspath plagioclase et potassique (30-50 %vol.), de micas (20-30 %vol.) et de quartz (10-20 %vol.). Elle contient environ 60 % pds. de SiO_2, 18 % pds. d'Al_2O_3 et 10 % pds. de fer total. Ces unités montrent des évidences de sédimentation chimique (e.g., anomalie positive en Eu*), mais sont principalement issues d'apports détritiques.

L'unité 4EA est le faciès silicaté riche en aluminium de la NIF et hôte majeur de la minéralisation aurifère. Elle se caractérise par un assemblage de grenat (25 %vol.)-grunérite (55 %vol.)-chert (20 %vol. ; Figure 3-26). Elle contient environ 48 % pds. de SiO_2, 8 % pds. d'Al_2O_3 et 38 % pds. de fer total. Elle représente le début de la prépondérance de la sédimentation chimique sur la sédimentation détritique.

L'unité 4B est un faciès à oxydes classique d'une FFR, montrant une alternance de bandes de chert et de magnétite ± grunérite. Elle est présente dans la séquence de la NIF et de la SIF. Elle contient un faciès clastique 4Bc incluant des bandes à grenat-amphiboles. Tous deux contiennent environ 48 % pds. de SiO_2 mais le faciès clastique contient 6 % pds. d'Al_2O_3 et 38 % pds. de fer total en moyenne tandis que l'autre en comporte autour de 3 % pds. et 43 % pds., respectivement. L'anomalie positive en Eu* plus forte atteste du plus grand apport hydrothermal lors de la sédimentation de cette unité.

L'unité 4A, également présente dans la NIF et SIF, est un faciès silicaté pauvre en aluminium caractérisé par une alternance de chert et de grunérite. Dans la SIF, où elle est la plus pure, elle contient typiquement 75 % pds. de SiO_2, 0,5 % pds. d'Al_2O_3 et 20 % pds. de fer total. Elle est interprétée comme marquant la fin du système hydrothermal.

L'unité 4H, horizon d'argilite à pyrrhotite présent dans la NIF et la SIF, marque le retour de la domination de l'apport détritique dans la sédimentation et la fin de la séquence de FFR. La matrice est composée de 10 à 20 %vol. de pyrrhotite, d'environ 30 %vol. de quartz, de 10-15 %vol. de feldspath, jusqu'à 20 %vol. d'actinolite et de biotite, et environ 10 %vol. de graphite. De la tourmaline de type dravite peut atteindre 3 à 5 %vol. Les proportions en SiO_2, Al_2O_3 et fer total sont affectées par la teneur en soufre, mais sont communément aux alentours de 50, 5-10 et 23 % pds., respectivement.

La séquence de la mine est recoupée par plusieurs dykes ultramafiques. Ceux-ci sont composés de 75 à 85 %vol. d'actinolite et d'hornblende actinolitique, et fortement déformés. Présents à proximité de certaines zones minéralisées, ils sont fortement serpentinisés, mais ne contiennent pas d'or. Ils sont interprétés comme des structures d'alimentation des formations ultramafiques situées plus haut dans la stratigraphie (unité « Lower basalts »).

À l'est de la mine, ainsi que plus au sud-est et au sud de la zone d'étude, les roches sédimentaires du ZHA sont abondantes. À proximité de la mine, elles comprennent majoritairement des greywackes. Plus au sud, elles incluent localement des horizons d'argilite ainsi qu'un conglomérat basal. Au sud-est, des brèches et des conglomérats mal triés sont présents (Figure 3-44), ainsi que d'épaisses séquences de grès conglomératiques à laminations entrecroisées (Figure 3-45), indiquant un environnement de dépôt

fluviatile ou deltaïque. Dans la région au nord-ouest du lac Markop, un affleurement présente une discordance interne au ZHA (Figure 3-46). Une unité de rhyolite massive est intercalée au sein de ces roches. Plus à l'est, les roches sédimentaires du ZHA incluent d'épaisses séquences, relativement homogènes de grès et de grauwacke (Duff, 2014).

Chapitre 4 : Géochronologie U-Pb

Malgré plusieurs données géochronologiques sur les assemblages lithostratigraphiques de la NCG (e.g., de Kemp, 1987 ; Davis et Stott, 2001 ; Biczok et al., 2012 ; Duff, 2014), l'âge des séquences du SRA, OMA et du ZHA demeure imprécise. Afin d'améliorer les contraintes temporelles sur la stratigraphie de la NCG et la chronologie des événements géologiques dans la zone d'étude, une sélection d'échantillons géochronologiques U-Pb sur zircon ont été analysées, dont une partie a déjà été publiée (Figure 6 ; McNicoll et al., 2016). Les analyses ont recouru à la technique de spectrométrie de masse à dilution isotopique et ionisation thermique (ID-TIMS), ou à l'aide de la microsonde ionique à haute résolution (SHRIMP II ; section 1.2.7) pour deux échantillons de roches sédimentaires.

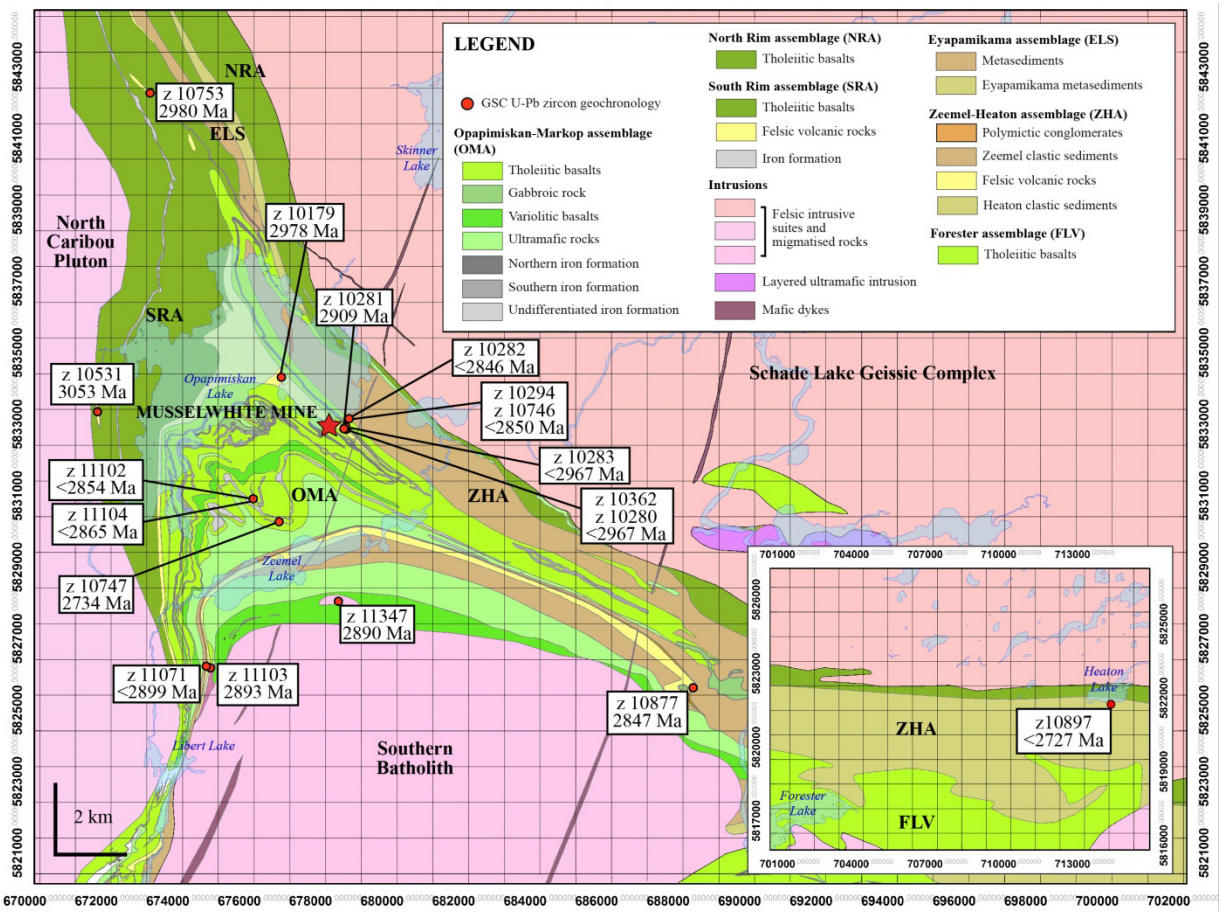

Figure 6 : Localisation des échantillons et résultats des analyses de géochronologie U-Pb sur zircon de cette étude (incluant les données de McNicoll et al., 2016). L'encart montre la portion la plus au sud-est de la ceinture, à 30 km de la zone d'étude principale. Au sein du SRA (Figure 4-2), une unité de rhyolite à l'ouest du lac Opapimiskan a été datée à 3053 Ma, un échantillon de rhyodacite pris au nord de la zone d'étude a été daté à 2980 Ma, et un échantillon de l'unité Avol a produit une analyse à 2978 Ma.

Dans le OMA (Figures 4-3 et 4-4), les roches pélitiques structuralement au-dessus de la FFR ont un âge maximum de <2967 Ma (McNicoll et al., 2016). Cet âge, combiné avec celui à 2909 Ma d'un dyke felsique recoupant la séquence de la mine (McNicoll et al., 2016), permet de contraindre la période de dépôt de celle-ci. Deux unités felsiques intrusives à feldspath porphyriques, affleurant au sud de la zone d'étude, ont été datées durant cette étude à 2893 Ma et 2890 Ma. Tandis que trois autres, interceptées en forage entre les lacs Opapimiskan et Zeemel, ont des âges maxima de <2854 et <2865 Ma et un âge de 2734 Ma (cette étude).

Dans le ZHA enfin (Figure 4-5), une nouvelle chronologie des dépôts successifs peut ainsi être dressée (Figure 4-6) : un conglomérat basal s'est déposé après 2899 Ma ; suivi par des sédiments moins grossiers de type grauwackes contraints à <2850 et <2846 Ma, tandis qu'une rhyolite au sud-est de la zone d'étude est datée à 2847 Ma. Enfin, une unité volcanoclastique intermédiaire de la portion la plus orientale de la ceinture est quant à elle plus jeune que 2727 Ma.

Chapitre 5 : Géologie structurale

L'architecture structurale des unités rocheuses de la zone d'étude est le résultat de trois phases de déformation successives (Breaks et al., 1986 ; Hall et Rigg, 1986). La phase de déformation D_2 est la plus importante et est caractérisée par un gradient de déformation augmentant vers le nord-est et culminant à bordure avec le complexe gneissique du lac Schade (Figure 7). Le contexte tectonométamorphique ainsi que la rhéologie, la forte anisotropie planaire et les contrastes de compétence internes des FFR influence la réponse des roches aux contraintes exercées. Ces caractéristiques des FFR sont susceptibles de jouer un rôle dans la mise en place d'une minéralisation aurifère orogénique, pour laquelle la déformation est un aspect essentiel (Dubé et Gosselin, 2005 ; Robert et al., 2005 ; Goldfarb et al., 2005).

Les fabriques associées à la première phase de déformation, D_1, sont mieux préservées dans la zone du West antiform, où l'intensité de déformation D_2 est la plus faible. Trois tranchées ont été cartographiées en détails (Fig. 5-6, 5-7, 5-8). La fabrique S_1 consiste en schistosité préservée dans les charnières de plis P_2 dans les FFR et sous la forme d'une foliation pénétrative dans les roches volcaniques. Dans la FFR, des plis P_1 produisent avec les plis P_2 une figure d'interférence de type 3 (Fig. 5-9 ; Ramsay et Huber, 1987). Leur géométrie indique que les plis P_1 avaient initialement une orientation NO-SE et une vergence nord, et suggère une position structurale sur le flanc inverse d'un synclinal mégascopique P_1. Cette hypothèse est soutenue par des indicateurs de polarité stratigraphique (e.g., basalte en coussins), ainsi qu'un rajeunissement des contraintes géochronologiques des unités en profondeur et vers le sud. (chapitre 4) Ces éléments mènent à interpréter la présence d'un synclinal P_1 kilométrique dont le plan axial longe le lac Zeemel (Fig. 7).

L'intensité des fabriques associées à la phase D_2 peut être divisée en deux domaines: le West antiform et la zone de la mine centrée sur le East Bay synformc (Figure 5). Dans le premier, les plis P_2 sont généralement ouverts, à plan axial subvertical et une plongée modérée vers le NO (Figure 5-15). La fabrique S_2 associée varie d'un clivage espacé à une schistosité pénétrative. Avec l'augmentation du gradient de déformation vers le NE, le domaine de la mine se distingue par des plis serrés à isoclinaux à faible plongée (entre 10 et 35°) vers le nord-ouest. Des failles et des zones de cisaillement de plan axial aux plis P_2 sont particulièrement visibles dans les roches volcaniques mafiques où elles sont accompagnées d'une forte altération à biotite (à distance) et à calcite (au cœur ; Figure 5-30). Dans la FFR, la transposition du rubanement compositionnel dans ces zones est extrême. Le boudinage est surtout

marqué dans la FFR, où la rotation antithétique des boudins indique une composante horizontale de cisaillement dextre et une composante verticale inverse vers le SO (Figure 5-27). L'intensité de l'aplatissement associée à la phase D_2 est aussi mise en évidence par l'inversion du flanc est du synforme de la mine, phénomène typique d'une déformation prolongée (Figure 5-33 ; Bleeker, 2015), et par le développement de zones de mylonites dans les roches volcaniques mafiques adjacentes de la FFR (Figure 5-29) et des roches sédimentaires à l'est de la mine à l'approche de la zone de faille majeure qui sépare la ceinture de roches vertes du complexe gneissique du lac Schade (Figure 7).

La déformation D_3 est exprimée de façon hétérogène par les roches de la zone d'étude. Les roches les plus anisotropes y développent des plis en Z, dont le plan axial est fortement incliné vers le nord-ouest et plonge modérément vers l'ouest-sud-ouest. Localement, un jeu de plis conjugués orientés nord-sud se développe. La fabrique de plan axial, S_3 crénule la foliation S_2. L'intensité de D_3 augmente vers le sud-est et culmine le long de la zone de cisaillement du lac Markop (Figure 5-45). Cette phase ne semble avoir que peu d'impact sur la distribution et la géométrie des zones minéralisées aurifères.

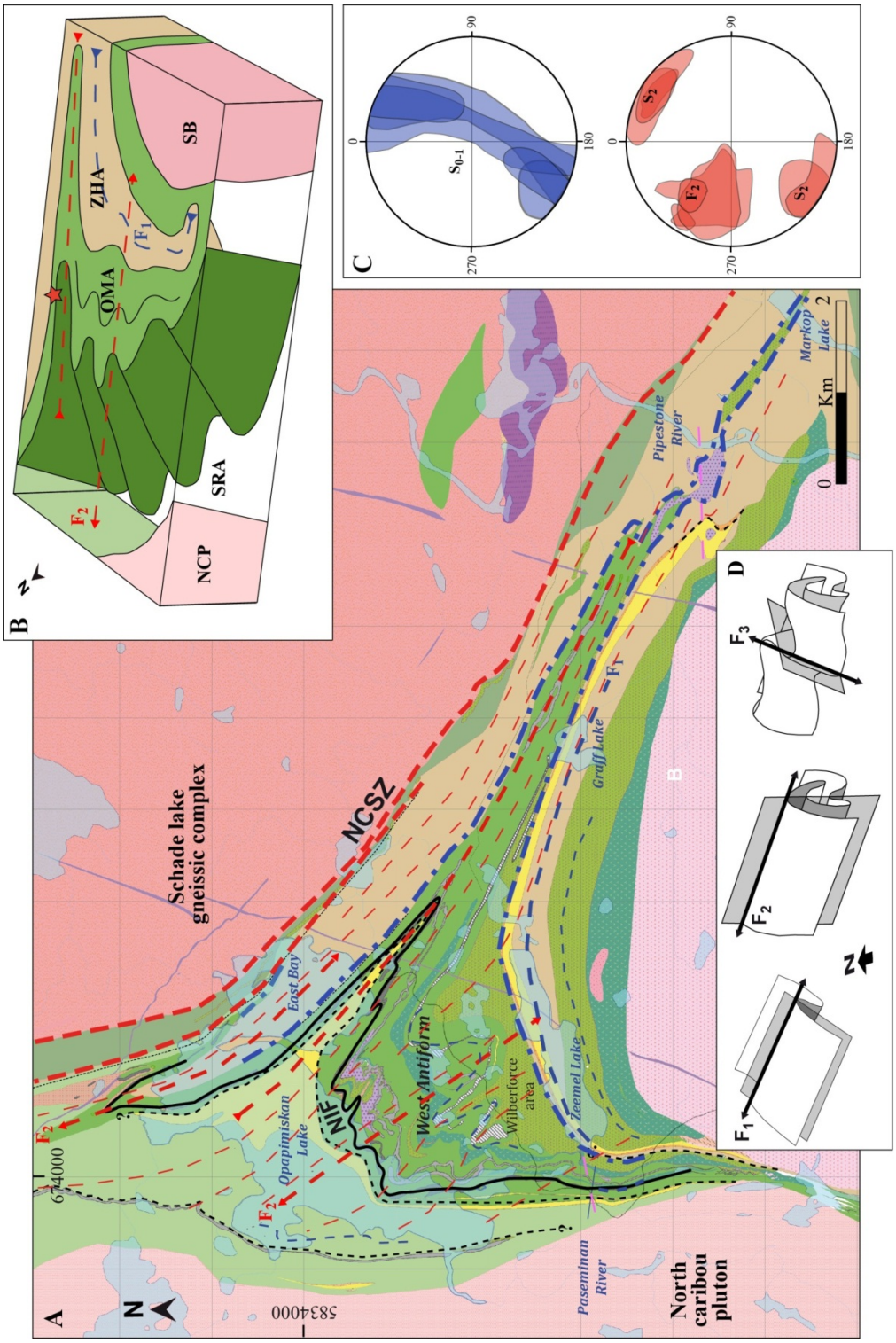

Figure 7 : A. Carte géologique et structurale de la zone d'étude montrant l'orientation générale des fabriques S_1, S_2 et S_3, la zone de faille D_1 et la structure D_2 de 1er ordre (NCSZ). B. Bloc diagramme schématique de la zone. C. Projections stéréographiques des mesures compilées de S_{0-1}, F_2 et S_2 des tranchées. D. Diagrammes schématiques des figures d'interférence de plis P_1, P_2 et P_3.

Chapitre 6 : Métamorphisme

Les assemblages de minéraux métamorphiques des roches de la zone d'étude et leur relation avec les fabriques tectoniques attestent que le grade métamorphique a atteint le faciès des schistes verts supérieur (M_1) suite à la phase de déformation D_1 (e.g., staurolite anté-S_2, unité 4F ; Figure 6-2) et qu'il culmina au faciès des amphibolites (M_2) pendant la déformation D_2 (Figure 6-4). Cette interprétation est soutenue notamment par la distribution des inclusions en « S » dans les cœurs des porphyroblastes de grenat qui imprègnent et préservent un fabrique ancienne, probablement la fabrique S_1, et une fabrique S_2 marquant les bordures des grenat et la matrice. Ces relations se retrouvent dans les assemblages à grenat-grunérite de l'unité 4EA de la FFR. Des occurrences d'hedenbergite faiblement déformé dans l'unité 4A de la FFR attestent également de l'intensité du métamorphisme M_2 (Haase, 1982 ; Klein, 1983, 2005).

Des estimations de température calculées avec le géothermomètre grenat-biotite (Holdaway, 2000) sur des analyses d'échantillons du schiste à biotite-grenat (unité 4F) indiquent une température moyenne de 624° ± 25°C (Figure 6-17). Des analyses géochronologiques in situ de microsonde ionique à haute résolution (SHRIMP) de grains de monazite de l'unité 4F ont révélé une population unique dont le traitement indique un âge de 2660 Ma, interprété comme datant le pic du métamorphisme M_2 (Figure 6-20). Les données pétrographiques permettent d'interpréter cette donnée comme l'âge minimum de l'introduction de l'or à Musselwhite.

Chapitre 7 : Caractéristiques et distribution des roches minéralisées en or

Le minerai aurifère à Musselwhite est présent au sein d'enveloppes atteignant 100 à 250 m de hauteur, 5 à 15 m d'épaisseur et s'étendant sur de 200 à 1000 m de long. Les zones minéralisées sont concentrées dans la NIF à l'intersection de zones de forte déformation D_2 de plan axial à des charnière épaissies de plis majeurs P_2 (e.g., T-antiform, zone PQD ; Figures 8 et 9), de plis P_2 parasitiques (e.g., zones Esker et Jets, zones Red Wing-Thunder Wolves, zone WEL), ou le long de flancs atténués de plis P_2 (e.g., zone Lynx).

Il y a deux styles de minéralisation aurifère : Un remplacement par pyrrhotite, ponctuellement accompagnée de silicification et des veines de quartz-pyrrhotite. Le style par remplacement est de loin le plus abondant et productif au sein des unités de FFR à grenat-grunérite-chert (unité 4EA), grunérite-chert (unité 4A) et chert-magnétite clastique (faciès 4Bc). La majorité (~90%) de la production provient du remplacement dans l'unité 4EA. Le style à veines de quartz est surtout présent dans le schiste à biotite-grenat (unité 4F) et le faciès « pur » à chert-magnétite de la FFR (unité 4B).

Les principaux minéraux de gangue de l'unité 4EA minéralisée sont la hornblende/ferro-tschermakite verte, le grenat almandin rouge, la biotite brune et le quartz gris (Figure 10). La pyrrhotite, le minéral métallique principal (~95%), est distribué le long des plans de foliation et accumulé dans les zones de faible pression telles que les espaces inter-boudins et les ombres de pression des grenats. Elle est systématiquement accompagnée de chalcopyrite (~5%), ainsi que de traces de pentlandite, galène et arsénopyrite/löllingite. Des analyses statistiques montrent que la teneur en or dans le 4EA est positivement corrélée au contenu en S, CaO, CO_2, Cu, Ag, Se, Te et dans une mesure moindre, Pb et Ga.

Le minerai de l'unité 4EA est localement formé de zones de silicification où celui-ci est presque exclusivement formé de quartz, pyrrhotite, grenat et hornblende (Figure 7-23) ; et de zones où la FFR a été complètement remplacée par une matrice de hornblende/tschermakite contenant localement des

grenats centimétriques ou des amas de hédenbergite-quartz-calcite, et entourant des zones de pyrrhotite semi-massive (Figures 7-24 et 7-25).

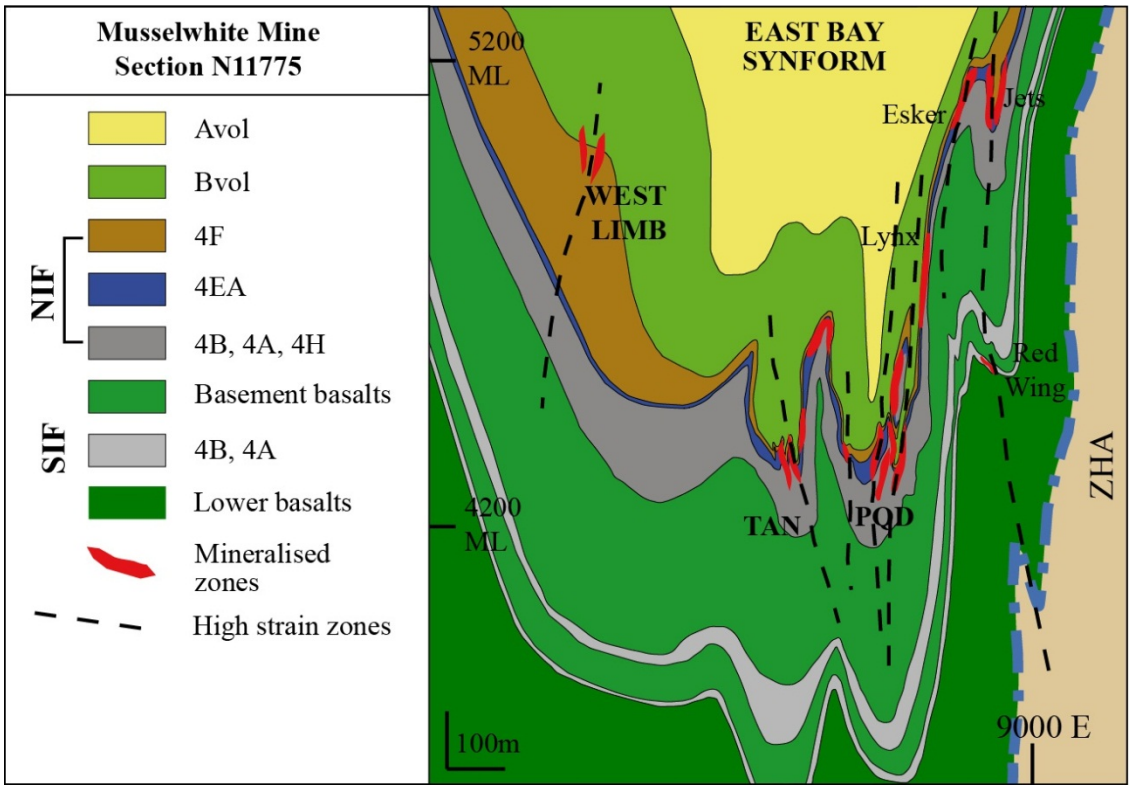

Figure 8 : Section géologique simplifiée de la mine à 11775 N montrant la projection des principales zones de minerai. Voir figures 7-2, 7-3,7-4 pour le nom des zones et leur contexte détaillé.

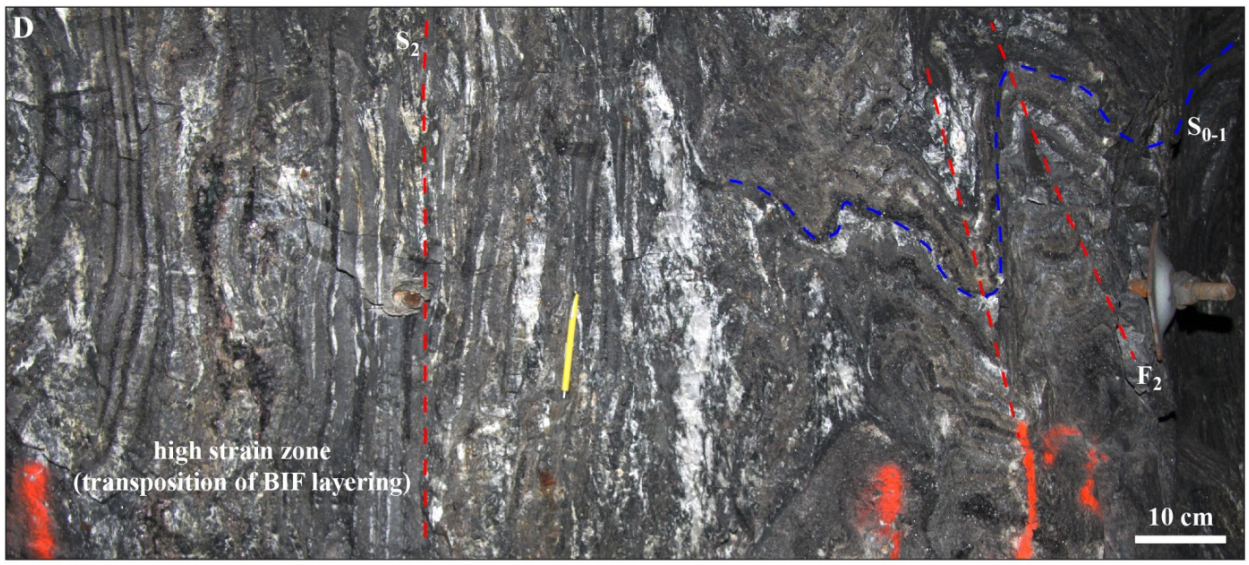

Figure 9 : Paroi souterraine exposant une zone de forte déformation traversant le faciès silicaté 4EA de la FFR. Notez l'intensité du gradient de déformation D_2, où des plis ouverts P_2 côtoient une zone de transposition totale du rubanement dans l'orientation du S_2 sub-vertical, niveau 770, section 11780 N (photo B. Dubé).

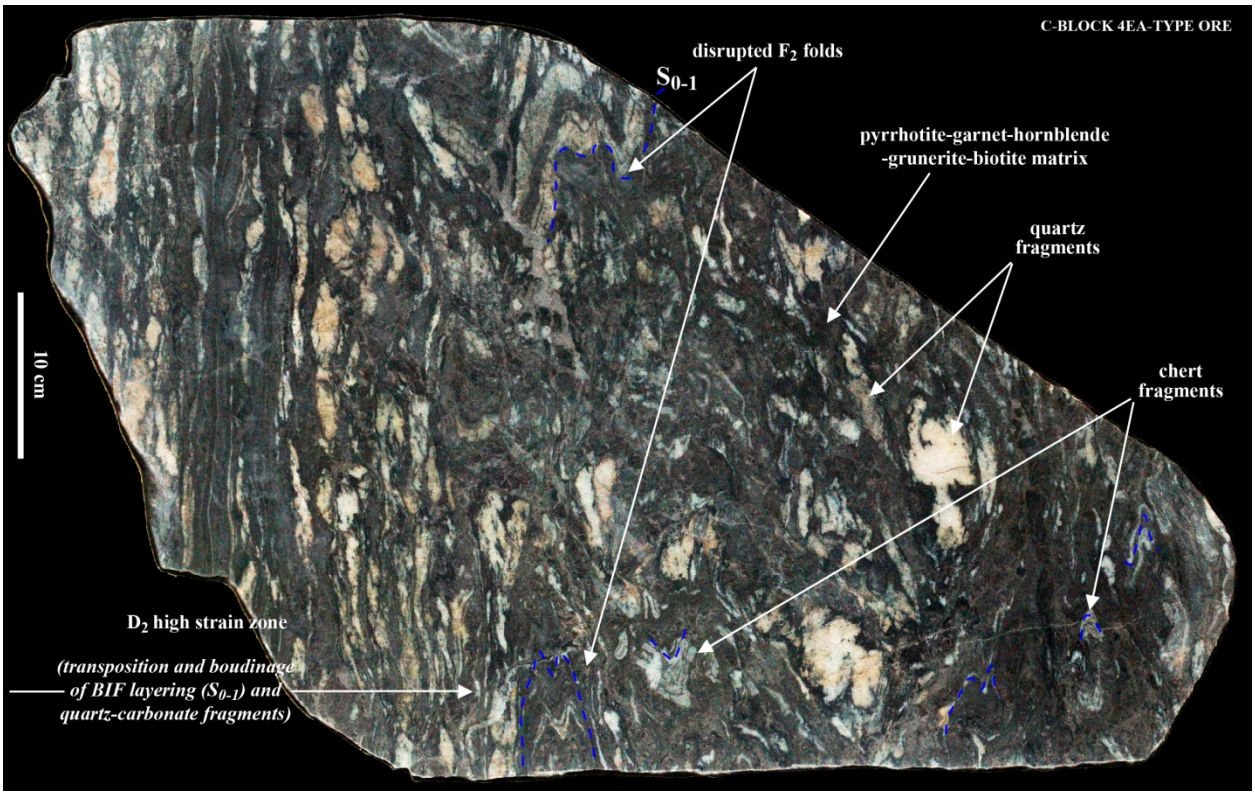

Figure 10 : Tranche polie de minerai de FFR silicaté à haute teneur de la zone C-block, niveau 770, section 11730 N, zone PQD. L'intensité de la déformation D_2 augmente à gauche vers la zone de forte déformation hôte de la minéralisation aurifère qui transpose le rubanement de la FFR. À droite, des boudins de veines de quartz sont entourés d'une matrice de pyrrhotite-grenat-tschermakite/hornblende-biotite.

Le grenat est un élément essentiel de la paragenèse métamorphique et de la minéralisation du faciès silicaté 4EA. Sa structure interne est complexe et doublée d'une zonation chimique montrant notamment un enrichissement en Ca syn-cinématique. Couplée à la présence de grenats grossiers pauvres en inclusions, mais contenant des inclusions de pyrrhotite-or tout en étant marqué de fractures remplies de pyrrhotite-or, elle démontre le caractère syn-D_2 de la minéralisation aurifère, ainsi que de son caractère syn-métamorphisme M_2 grâce aux relations observées entre grenat et monazite (chapitre 6).

La minéralisation par remplacement dans les unités 4E, 4A et 4Bc présente des variations principalement reflétées dans l'assemblage minéralogique qu'elle produit. L'unité 4E aurifère est marquée d'un assemblage de bandes à grenat-grunérite-pyrrhotite, à hornblende-actinolite-hédenbergite et à quartz-hornblende. L'unité 4A aurifère contient un assemblage de pyrrhotite- hédenbergite-hornblende-grunérite-quartz. Enfin, le faciès 4Bc aurifère est constitué d'un assemblage de grunérite-biotite-hornblende-magnétite où cette dernière est remplacée par la pyrrhotite. L'interprétation des données lithogéochimiques et les traitements statistiques dont elles ont fait l'objet montrent globalement des caractéristiques similaires à l'unité 4EA. Chaque lithologie présente toutefois quelques distinctions : l'enrichissement en CaO de l'unité 4E est plus prononcé (6 % pds.) ; l'unité 4A est enrichie en CaO (4 à 10 % pds.) et CO_2 (3 à 10 % pds.).

Le style des veines de quartz aurifères varie selon les contrastes de compétences entre les lithologies. Les veines dans la FFR à chert-magnétite sont interprétées comme des évidences de déformation localement

cassante durant le développement des plis de cette lithologie et la minéralisation. Les veines du schiste à biotite-grenat, accompagnée d'un halo d'altération calcique à hornblende-hédenbergite, apparaissent plus tardives (e.g., dans la zone WEL), notamment du fait de veinules déformées recoupant en partie la fabrique S_2.

Chapitre 8 : Altération hydrothermale

Au faciès métamorphique des amphibolites, une minéralisation aurifère épigénétique par remplacement à sulfures est communément accompagnée de : 1) une altération distale potassique à biotite, 2) une altération proximale calcique/à carbonates, et 3) une sulfuration de la FFR (Phillips et al., 1984 ; Mueller et Groves, 1991 ; Bullis et al., 1994 ; Mueller, 1997 ; Eilu et al., 1999 ; Goldfarb et al., 2005).

La distribution de l'altération associée au gisement Musselwhite fut examinée en ayant recours aux données de lithogéochimie de roche totale provenant des forages. La composition moyenne des échantillons les moins altérés (sélection sur critères macroscopique, microscopique et géochimiques) de chaque lithologie furent utilisée pour normaliser les valeurs de chaque échantillon le long d'un profil de forage (Figure 11). Ainsi, les enrichissements en K_2O, CaO, CO_2 et S ont été mis en valeur (Figures 8-3 à 8-9). Toutefois, hormis dans les roches mafiques dont la zonation des altérations est classique, les altérations distale et proximale de la FFR se sont développées de façons asymétriques.

Le faciès à oxyde de la FFR est très peu réactif à l'altération potassique qui s'exprime par la cristallisation de grunérite secondaire. L'altération proximale y est par contre bien marquée par la calcite et l'ankérite. Dans le faciès silicaté, l'altération distale produit un faible enrichissement en K_2O se traduisant par une faible cristallisation de biotite et une modification de la texture minéralogique avec l'augmentation de la taille des cristaux de grenat. L'altération proximale calcique provoque le remplacement de la grunérite par de la hornblende. Enfin, au cœur des zones altérées, la FFR réagit très fortement avec le soufre formant de la pyrrhotite et provoquant la précipitation de l'or, provenant très probablement de complexes sulfurées de type $Au(HS^-)_2$ (Stefansson et Seward, 2004 ; Tomkins, 2010).

L'altération du schiste à biotite-grenat est centrée sur les veines de quartz. L'altération distale produit une recristallisation de la matrice biotite-quartz-feldspath en biotite massive et grenat. L'altération proximale est calcique et se traduit par la présence de hornblende et d'hédenbergite. Une silicification de l'unité est fréquente à proximité des zones aurifères (Figure 8-25).

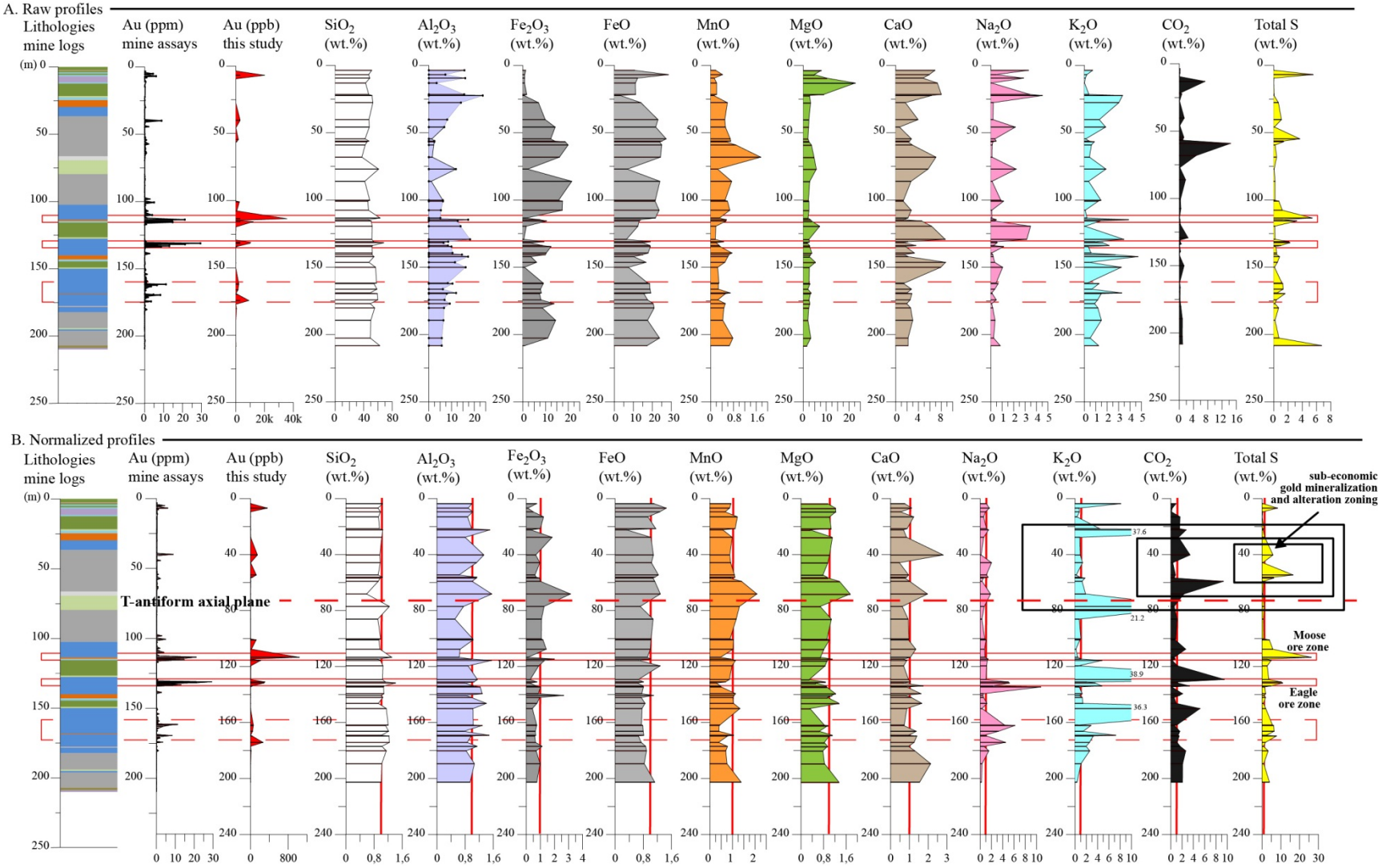
A. Raw profiles
Lithologies mine logs
Au (ppm) mine assays
Au (ppb) this study
SiO2 (wt.%)
Al2O3 (wt.%)
Fe2O3 (wt.%)
FeO (wt.%)
MnO (wt.%)
MgO (wt.%)
CaO (wt.%)
Na2O (wt.%)
K2O (wt.%)
CO2 (wt.%)
Total S (wt.%)
B. Normalized profiles
T-antiform axial plane
sub-economic gold mineralization and alteration zoning
Moose ore zone
Eagle ore zone

Figure 11 : Profils de l'or et éléments majeurs du forage 09-TAN-014, flanc ouest du T-antiform, section 11775 N. A. Profils des données brutes de chaque élément. Les variations reflètent principalement la lithologie. B. Profils utilisant les données normalisées avec la valeur moyenne des échantillons les moins altérés de chaque lithologie. L'axe des X correspond au facteur « y » de l'opération $X_A = y (X_{LA})$ reliant la valeur de l'échantillon altéré à la moyenne des moins altérés.

Chapitre 9 : Source des fluides et métaux

L'examen des carottes de forage des roches volcaniques situées sous la mine révèle que la fabrique S_2 a une intensité variable. Les zones où elle est la plus pénétrative sont marquées par un intense lessivage des minéraux ferromagnésiens qui atteste de l'altération (Figure 12). Ceci confirme que des fluides, possiblement minéralisateurs, ont ont en partie atteint la NIF en traversant migré verticalement à travers les roches sous-jacentes au gisement. En plus de constituer une voie de passage de fluides minéralisateurs, ces roches volcaniques et les horizons de FFR interstratifiés peuvent avoir contribué à l'apport en or et métaux du gisement Musselwhite, tel que prédit par les modèles comme celui de Phillips et Powell (2009, 2010 et références incluses). Toutefois, cette contribution est considérée comme généralement mineure (e.g., Tomkins, 2010). Plusieurs études s'intéressent au potentiel de source aurifère des sédiments, fréquemment riche en nodules de pyrite, qui sont associés spatialement aux gisements d'or orogéniques (Pitcairn et al., 2006 ; Large et al., 2011, 2012 ; Lisitsin et Pitcairn, 2016 ; Steadman et Large, 2016).

Dans la zone d'étude, la composition élémentaire des nodules de pyrite des horizons d'argilite (unité 4H) de la zone Wilberforce, ainsi que celle des sulfures des sédiments du ZHA à l'est de la mine (Figures 13 ; 9-6, 9-7, 9-8) ont été cartographiées par LA-ICP-MS. Les premiers de fortes teneurs en Au, Ag, As, Sb, Te, Pb et Bi qui s'amenuisent vers l'extérieur, avec une pyrite environnante distinctement enrichies en Co et une pyrrhotite adjacente se démarquant par des valeurs faibles dans ces éléments et fortes en Se et Ni. La texture, les teneurs en As et Co et la distribution de l'Ag, de l'Sb, du Bi, du Te et du Pb autour de la pyrite du ZHA suggèrent que cette pyrite est d'origine métamorphique. La conversion de la pyrite en pyrrhotite et la distribution des éléments traces associée montrent que les horizons d'argilite ont pu contribuer au stock de métal présent dans le gisement mais leur faible volume en fait des sources très mineures.

Figure 12 : Carotte de roche volcanique mafique, unité « Basement basalts », forage 10-SIF-003, 136,5-139 m.

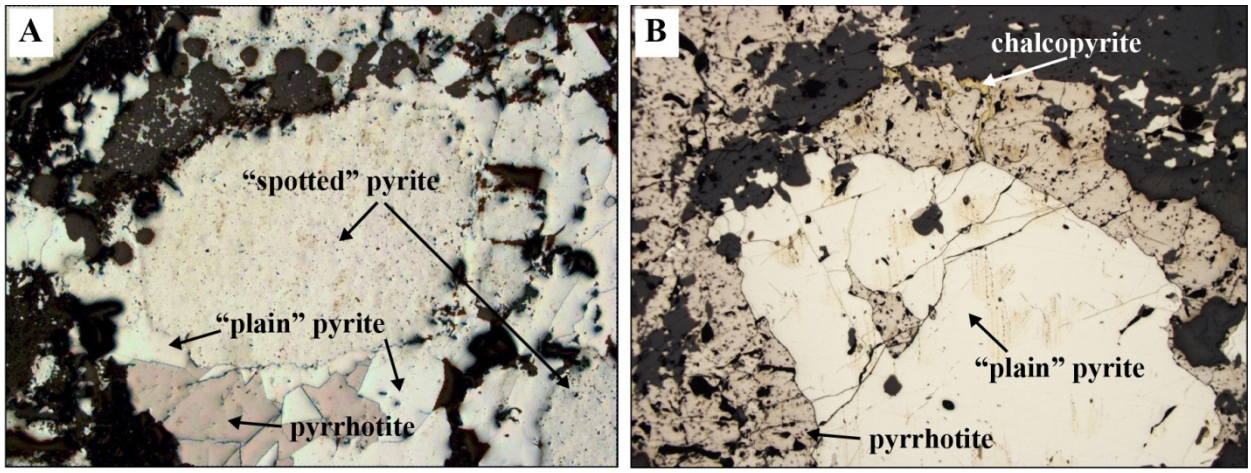

Figure 13 : A. Microphotographie en lumière réfléchie du nodule de pyrite 1, échantillon MW-12-092-1. Deux phases de pyrite y sont distinguées : une « tachetée » formant le nodule, et une phase « lisse » autour. B. Microphotographie en lumière réfléchie d'un grain de pyrite lisse entouré de pyrrhotite dans une matrice silicatée, échantillon MW-13-460.

Chapitre 10 : discussions & conclusions

L'analyse et l'interprétation des données récoltées dans le cadre de cette étude permettent d'améliorer les connaissances sur la stratigraphie et l'évolution tectonométamorphique de la ceinture de roches vertes de North Caribou (Figures 14 et 10-5) afin de proposer un nouveau modèle d'évolution géologique de la région du lac Opapimiskan (Figure 15). Ces données ont également permis de mieux contraindre les contrôles structuraux et lithologiques de la minéralisation aurifère, ainsi que les relations spatio-temporelles avec les épisodes de déformation et métamorphismes. Cela abouti à une nouvelle proposition de modèle génétique pour le gisement aurifère Musselwhite. La comparaison avec d'autres gisements similaires permet de dégager des éléments visant à améliorer l'efficacité des guides d'exploration minière pour ce type de minéralisation aurifère.

Les assemblages lithostratigraphiques du SRA, OMA et FLV ont été formés entre 3060Ma et 2910Ma par le volcanisme majoritairement mafique et ultramafique issu de l'interaction entre une plume mantellique et une croûte continentale ancienne. Des interruptions de l'activité volcanique ont mené au dépôt de séquences de FFR de type Algoma, dont une est hôte principale de la minéralisation aurifère à Musselwhite. À partir de 2890Ma des intrusions felsiques mineures se mettent en place, suivi, entre 2880 et 2830Ma, d'une phase majeure de croissance crustale par la mise en place de batholithes de type TTG et par du volcanisme mafique des séquences volcaniques du NRA (Figure 14). Cet épisode semble déstabiliser la ceinture de roches vertes et mener au développement d'un grand bassin sédimentaire (ELS, ZHA). Une période de convergence liée à la collision du domaine Oxford-Stull contre celui d'Island Lake au nord, induit un raccourcissement durant D_1 au sein de la ceinture et la formation de plis et chevauchement (Figure 15A, B). Une phase de plutonisme (2730-2710Ma) conduit à l'emplacement du Southern batholith. La phase D_2 est associées à une déformation ductile intense et un métamorphisme régional au faciès des amphibolites résulte de l'épaississement crustal provoqué par la collision du domaine d'Island Lake contre le terrain de North Caribou vers 2700Ma (Figure 15C, D, E). Des zones de cisaillement majeures se forment en réponse à un régime transpressif (Gagnon et al., 2016). Plus tard la

partie sud de la ceinture est affectée par un cisaillement dextre est-ouest (D_3 ; zone de cisaillement de Markop Lake).

La minéralisation aurifère du gisement Musselwhite est interprétée comme épigénétique et mise en place durant la déformation D_2 (Hall et Rigg, 1986). La majorité des études soutient cette interprétation (Zhang, 1997 ; Otto, 2002 ; Blower et Kiernan, 2003 ; Snow, 2004 inédit ; Hill et al., 2006 ; Isaac, 2008 ; Moran, 2008 ; Kolb, 2010 ; Stott et Biczok, 2010 ; Biczok et al., 2012). Plusieurs modèles géologiques sur les contrôles structuraux de la minéralisation aurifère ont été proposés allant d'une la mise en place contrôlée par les charnières de plis, par les failles cassantes, ou par des zones de cisaillement. Certains auteurs ont proposé un modèle de minéralisation syngénétique (Couture, 1995 ; Kerswill, 1996).

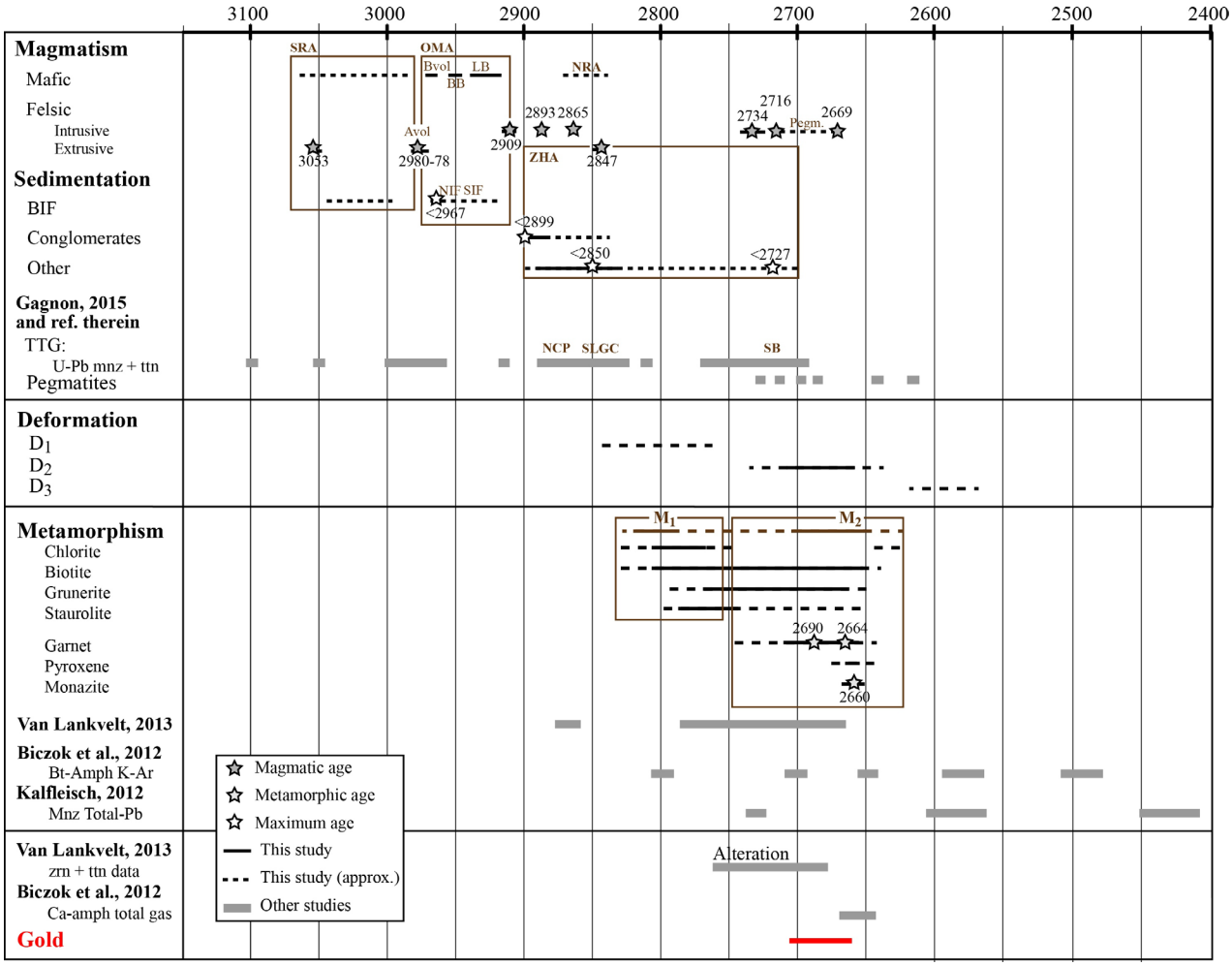

Figure 14 : Synthèse de l'évolution tectonométamorphique de la ceinture de roches vertes de North Caribou dans la zone du lac Opapimiskan.

Cette étude a documenté le contrôle sur la minéralisation aurifère de zones de forte déformation en position subparallèle au plan axial P_2, notamment présente à proximité des charnières de plis épaissies de la FFR. Ces zones transposent le rubanement de la FFR silicatée et concentrent la pyrrhotite et l'or associé, tandis que le processus d'altération et minéralisation change sa minéralogie et composition chimique. La géométrie des zones minéralisées, leur distribution et les structures qu'elles contiennent (p.ex., plis isolés/sans racines) suggèrent une mise en place de la minéralisation lors d'une phase de

déformation progressive. La FFR silicatée minéralisée est caractérisée par un assemblage minéral de pyrrhotite-grenat-hornblende-grunerite-biotite-hedenbergite-quartz dont les composants montrent des évidences texturales de cristallisation durant la phase de déformation D_2. La concentration locale de pyrrhotite en une veine semi-massive dotée d'un halo d'altération à matrice amphibolitique (p.ex., zone C-block), la structure et les relations texturales du grenat soulignent également une chronologie de la minéralisation syn-D_2/M_2. Localement, les amphiboles calciques sont remplacées par un assemblage d'hédenbergite-calcite-quartz ± grenat indiquant que l'assemblage minéral d'altération est métamorphisé. Les analyses géochronologiques sur grenat (Maas, 2006, inédit), amphiboles (Biczok et al., 2012) et monazite (cette étude) permettent de contraindre la mise en place de la minéralisation aurifère à la période 2700-2660 Ma.

La distribution de l'or à Musselwhite est contrastée de trois façons : 1) entre les roches volcaniques mafiques et les séquences de FFR, 2) entre la FFR silicatée (unité 4EA) et la FFR à oxyde (unité 4B), et 3) entre la NIF et la SIF (Figure 8). Ceux-ci sont liés à la rhéologie des roches, leur caractère anisotrope ou relativement homogène et à leur réactivité avec les fluides minéralisateurs. Les roches volcaniques constituent un matériau relativement homogène et rigide, au sein duquel les zones de forte déformation se développent progressivement durant le raccourcissement D_2. La FFR est fortement anisotrope et compétente, formant des plis dont la charnière est fortement épaissie (Figure 16A, B). Cela résulte en la formation de multiples zones de forte déformation qui focalisent la circulation des fluides. En outre, le contenu en fer total très élevé de la FFR lui confère une réactivité plus élevée que les roches mafiques qui l'entourent, faisant d'elle un piège chimique efficace.

La minéralisation a lieu préférentiellement dans le faciès silicaté de la FFR plutôt que dans celui à oxyde (Figure 16). Ceci est attribué à une différence majeure de style de déformation des deux faciès liée à leur minéralogie et à leur perméabilité secondaire (Cox et al., 2001). Le faciès à oxyde, constitué de bandes quasi monominérales de quartz et magnétite, se déforme en plis similaires et de façon plastique relativement homogène. À l'inverse, le faciès silicaté est constitué de bandes poly-minérales dont les constituants sont des phases rigides présentant un caractère cassant à des températures supérieures à celle du quartz (Gagnon et al., 2016 ; Baratoux et al., 2005) et une granulométrie variable, ce qui résulte en un milieu où la répartition hétérogène des contraintes induit une perméabilité secondaire élevée (Cox et al., 2001). Les fluides minéralisateurs circulent alors préférentiellement au sein de cette lithologie et interagissent peu avec la FFR à oxyde sous-jacent (Figure 16C, D), aboutissant au contraste de contenu en or observé. Le contraste observé entre les séquences de FFR NIF et SIF relève en partie du même mécanisme, à ceci près que l'unité 4EA est absente de la SIF et que c'est l'unité 4A, qui ne contient pas de grenat, qui est l'hôte principal de la minéralisation. La différence d'épaisseur entre la NIF et la SIF (60 vs. 10 m) est aussi considérée comme un paramètre important de cette différence de contenu en or.

Les éléments de chronologie relative (minéralisation syn-D_2, entre 2710 et 2660 Ma) et absolue (intrusions majeures entre 2870 et 2840 Ma, et 2730-2710 Ma) montrent qu'il n'y a pas de lien temporel direct entre magmatisme et minéralisation aurifère (section 10.5.1.4). Les fluides minéralisateurs sont donc interprétés comme issus de la dévolatilisation métamorphiques des roches (Colvine, 1989 ; Powell et al., 1991 ; Groves et al., 1995 ; Goldfarb et al., 2005 ; Phillips et Powell, 2010). Ceux-ci ont une composition chimique assez homogène, principalement aqueuse et riche en CO_2, avec une faible salinité, et transportant l'or sous forme de complexes bi-sulphures (McCuaig et Kerrich, 1998 ; Mikucki, 1998 ; Hagemann et Cassidy, 2000 ; Goldfarb et al., 2005 ; Ridley et al., 2009 ; Goldfarb et Groves, 2015). A Musselwhite, les roches sources de ces fluides sont les roches volcaniques et sédimentaires situées plus en

profondeur sous la mine. Les zones de forte déformation sub-verticales sont les principales voies de migration. L'or et les métaux associés ont été lessivés par les fluides hydrothermaux lors de leur ascension à travers les roches sous le gisement.

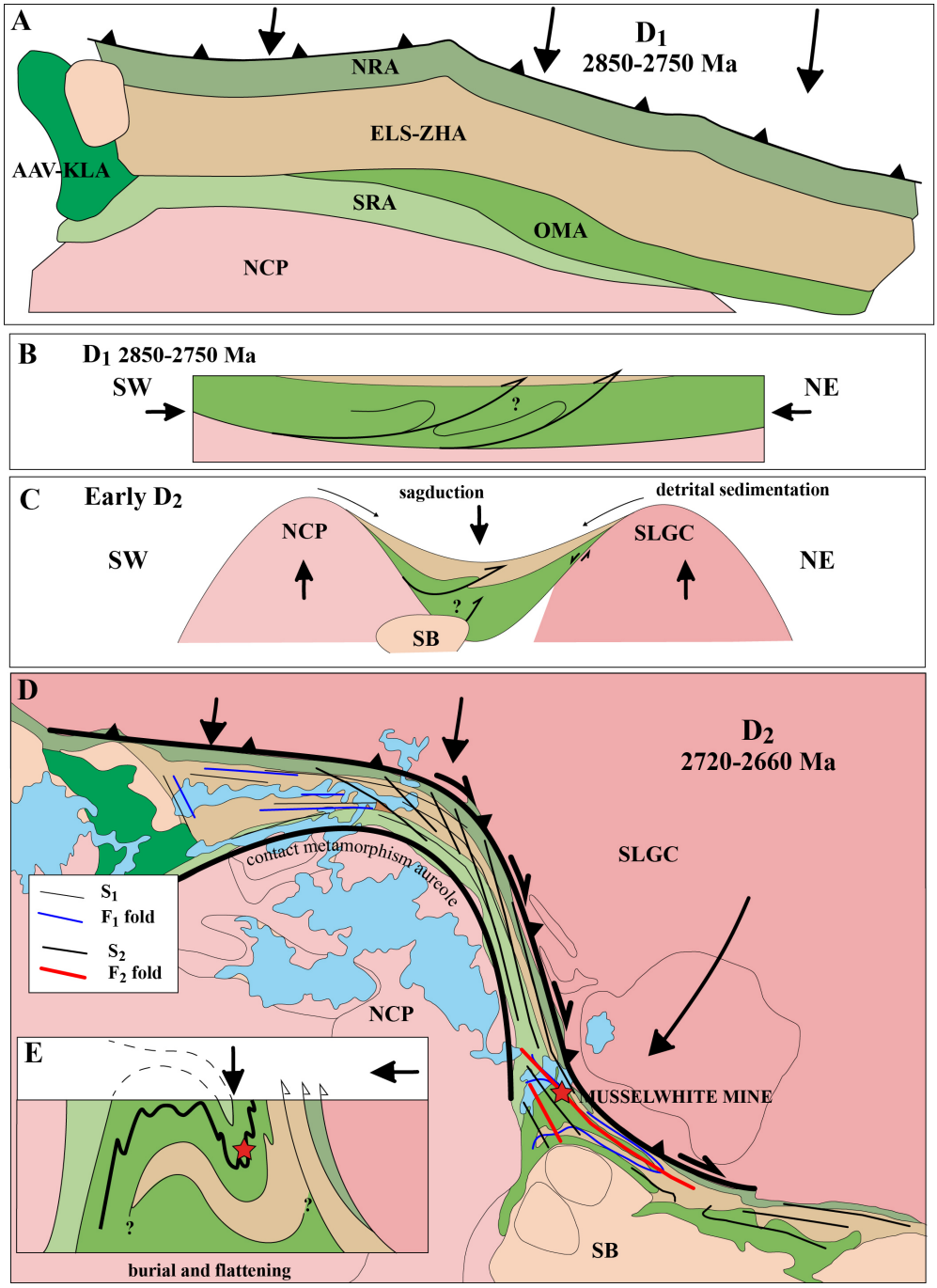

Figure 15 : Synthèse schématique des événements tectonométamorphiques dans la NCG. A. Vue en plan de la déformation D_1. B. Section schématique NS-SO montrant les plis et chevauchements associés à la déformation D_1. C. Evolution au début de la déformation D_2 avec sagduction et sédimentation détritique, ainsi que le début du chevauchement du complexe gneissique du lac Schade sur la NCG. D. Vue en plan de l'aplatissement et du cisaillement horizontal de la déformation D_2. E. Section schématique de l'aplatissement et enfouissement D_2 dans la zone de la mine Musselwhite.

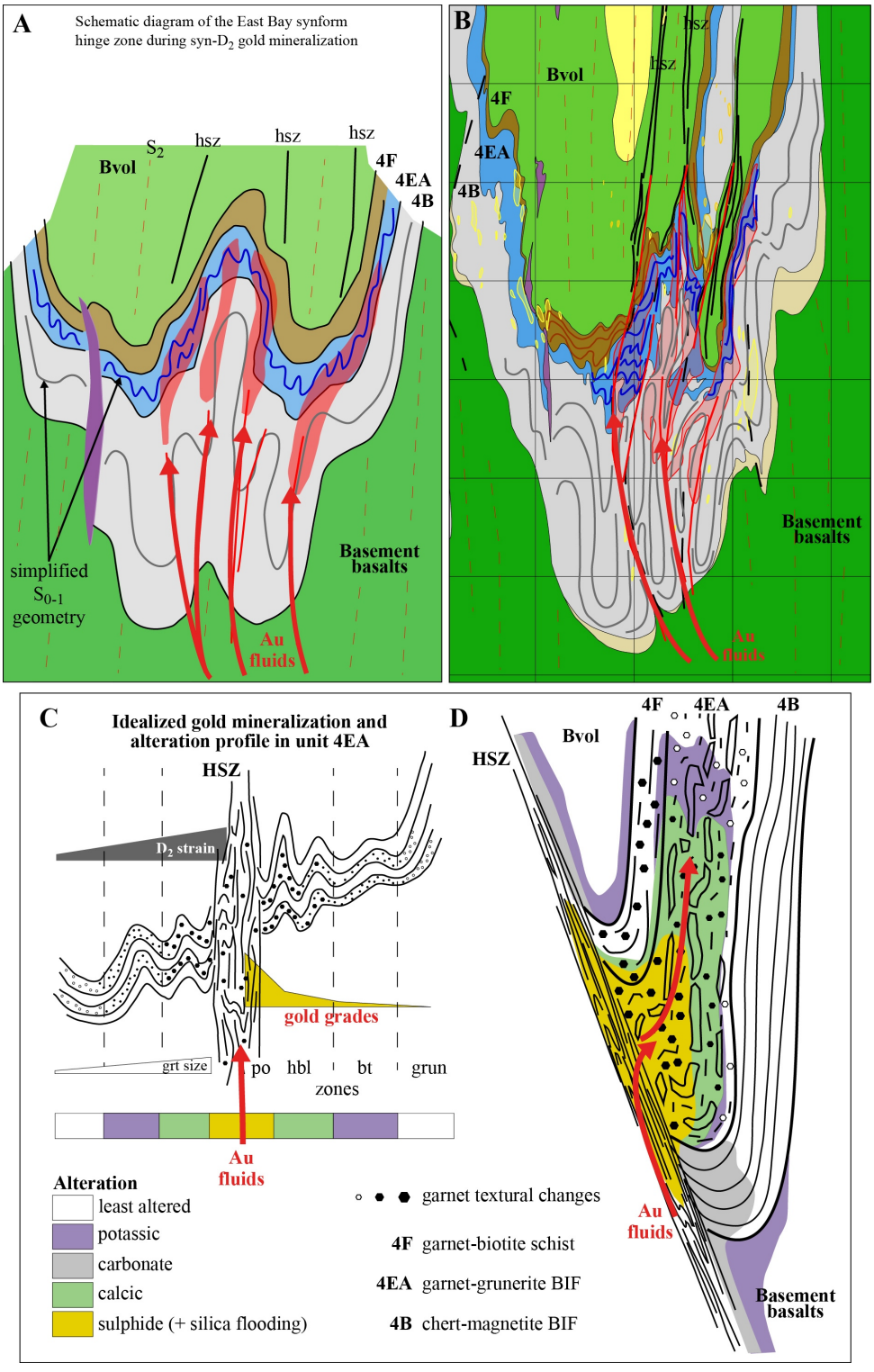

Figure 16 : A. et B. Diagrammes **schématiques de l'évolution géométrique de la charnière du synforme de East Bay pendant la déformation D_2 et la minéralisation aurifère (basés sur la section 11775 N). C. et D. Modèle schématisé du développement de la minéralisation aurifère et de l'altération hydrothermale qui y est associée dans les lithologies adjacentes. Les zones de forte déformation (HSZ) contrôle la circulation des fluides. Les zones libellées po, hbl, bt et grun représentent la zonation de l'altération (po = pyrrhotite, hbl = hornblende, bt = biotite, grun = grunérite).**

Globalement, le modèle génétique du gisement Musselwhite le plus robuste est celui d'une minéralisation aurifère épigénétique orogénique hypozonale liée à des fluides métamorphiques et une mise en place durant l'épisode tectonométamorphique D_2/M_2, et dont le pic de température est daté à 2660 Ma. La phase préalable D_1/M_1 joua un rôle préparateur en affectant la distribution des horizons de FFR et en modifiant leur minéralogie par le développement d'une paragenèse métamorphique.

Des gisements tels que ceux de Lupin (Slave Province, Territoires du Nord-Ouest ; Lhotka et Nesbitt 1989 et références incluses), Mineral Hill (Wyoming craton, USA ; Smith, 1996), Homestake (Black Hills, USA ; Caddey et al., 1991) et Nevoria (Yilgarn craton, Western Australia ; Mueller, 1997) permettent de comparer les éléments de chronologie relative de la minéralisation aurifère et des épisodes tectonométamorphiques à Musselwhite avec des minéralisations aurifères similaires dans des contextes géologiques différents (section 10.6).

Cette analyse comparative permet de mettre en avant l'importance de l'intersection de structures de second et troisième ordre avec des horizons de faciès silicaté de FFR étroitement plissés comme cibles d'exploration principales. Les zones de changement d'orientation des ceintures de roches vertes et les structures de premier ordre qui s'y trouvent sont des zones très prospectives pour de telles cibles.

Les terrains archéens et protérozoïques métamorphisés au faciès des schistes verts supérieur et des amphibolites sont le plus susceptibles de contenir des minéralisations aurifères similaires à Musselwhite. Les halos d'altérations associés à ces gisements présentent deux zones, l'une distale potassique et l'autre proximale calcique. La présence de sulfures est un élément clé : pyrrhotite et arsénopyrite dans les terrains à dominante sédimentaire, pyrrhotite seulement dans les terrains à dominante volcanique mafique.

Les relations de chronologie entre les phases de déformation, de métamorphisme, et magmatiques sont critiques pour déterminer le rôle potentiel de ces dernières dans la genèse de zones minéralisées. Elles peuvent n'avoir qu'un rôle mécanique dans l'évolution de la ceinture (p.ex., Musselwhite), ou bien contribuer au flux de chaleur du métamorphisme régional (p.ex., Lupin), ou être directement impliquées dans la genèse de la minéralisation (p.ex., Nevoria).

Cette étude multi-disciplinaire a généré des données abondantes qui ont encore du potential pour la recherche, notamment pour des questions concernant :

- La compréhension de la lithostratigraphie de la zone du lac Opapimiskan et ses implications pour l'histoire de la ceinture de roches vertes du North Caribou;
- Les contraintes du métamorphisme en utilisant la géochronologie Lu-Hf sur grenat ainsi que la géothermobarométrie;
- Les raisons de l'absence d'As associé à la minéralisation aurifère;
- L'étude des caractéristiques isotopiques des sulphures de la minéralisation aurifère (e.g., Cu, Pb).

TABLE OF CONTENTS

ACKNOWLEDGEMENTS iii
RÉSUMÉ v
ABSTRACT vii
SOMMAIRE RÉCAPITULATIF ix
TABLE OF CONTENTS xxxiii
LIST OF FIGURES xxxix
LIST OF TABLES xlvii
1 INTRODUCTION 1
1.1 Problematic and Objectives 2
1.2 Methodology 3
1.2.1 Surface mapping 4
1.2.2 Underground mapping 6
1.2.3 Drill core description 6
1.2.4 Lithogeochemistry 7
1.2.5 Petrography 8
1.2.6 Mineral chemistry 8
1.2.7 Geochronology 9
1.2.8 2D elemental mapping by LA-ICP-MS 10
1.3 Banded Iron Formations 11
1.3.1 Introduction 11
1.3.2 Definition 11
1.3.3 Classification 12
1.3.4 Space-Time distribution 13
1.3.5 Significance of iron formations 15
1.4 General characteristics of Algoma-type iron formations 16
1.4.1 Depositional environment 16
1.4.2 Chemical sediment precursor and lateral facies variations 16
1.4.3 Mineralogy and metamorphism 19
1.4.4 Geochemistry of banded iron formations 20
1.5 Metallogenic Context 23
1.5.1 Introduction 23
1.5.2 Greenstone-hosted vein Au deposits 26
1.5.3 Banded-iron-formation-hosted Au deposits 28
2 REGIONAL GEOLOGICAL SETTING 33
2.1 Western Superior province and North Caribou terrane 33
2.2 North Caribou greenstone belt 34
2.2.1 Supracrustal rocks 35
2.2.2 Intrusive phases 44
2.2.3 Structural geology 47
2.2.4 Metamorphism 49
2.2.5 Economic geology 53

3 PETROGRAPHY AND GEOCHEMISTRY OF ROCK UNITS IN THE MUSSELWHITE MINE AREA 56
3.1 Introduction 56
3.1.1 Geochemistry of volcanic units 59
3.1.2 Geochemistry of sedimentary units 62
3.2 Unit “Avol” 68
3.3 Unit “Bvol” 71
3.4 Unit “Basement basalts” 75
3.5 Unit “Lower basalts” 79
3.6 Unit 4E 83
3.7 Unit 4F 87
3.8 Unit 6 93
3.9 Unit 4EA 96
3.10 Unit 4B and facies 4Bc 100
3.11 Unit 4A 106
3.12 Unit 4H 109
3.13 Other banded iron formations 112
3.14 Ultramafic dykes 112
3.15 Other intrusive units 115
3.15.1 Mafic intrusions 115
3.15.2 Felsic intrusive phases 115
3.16 Zeemel-Heaton assemblages 116
3.16.1 Zeemel assemblage 117
3.16.2 Heaton assemblage 127
4 U-PB GEOCHRONOLOGY 129
4.1 South Rim assemblage 129
4.1.1 Felsic volcanic rock – western Opapimiskan Lake area 129
4.1.2 Felsic volcanic rock – northern Opapimiskan Lake area 130
4.1.3 Unit “Avol” – Musselwhite mine area 131
4.2 Opapimiskan-Markop assemblage 132
4.2.1 Unit 4F and 6 – Musselwhite mine area 132
4.2.2 Felsic dyke – Musselwhite mine area 132
4.2.3 Feldspar porphyry – Zeemel-Libertt lakes area 132
4.2.4 Feldspar porphyry – southern Zeemel lake area, ... 133
4.2.5 Felsic rocks – Wilberforce zone 133
4.3 Zeemel-Heaton assemblage 134
4.3.1 Conglomerate – southwestern Zeemel Lake area 134
4.3.2 “Lower Felsic Volcanics” – Musselwhite mine area 134
4.3.3 Felsic volcanic rocks – Pipestone River area 134
4.3.4 “Lower Sediments” – Musselwhite mine area 135
4.3.5 Intermediate volcaniclastic rock – Heaton Lake area 135
4.4 Summary and implications of data 135
4.4.1 Stratigraphy of the SRA 135

4.4.2 Stratigraphy of the OMA 136
4.4.3 Stratigraphy of the ZHA 138
5 STRUCTURAL GEOLOGY 139
5.1 Introduction 139
5.1.1 Replication of structural patterns at various scales 140
5.1.2 Rheology of banded iron formation 141
5.2 D_1 deformation 146
5.2.1 F_1 folds 146
5.2.2 S_1 foliation 152
5.2.3 Interpreted D_1 fault zone 154
5.2.4 Kilometre-scale F_1 fold(s) 154
5.3 D_2 deformation in the West antiform domain 157
5.3.1 F_2 folds 157
5.3.2 S_2 foliation 163
5.4 D_2 deformation in the mine area structural domain 163
5.4.1 F_2 folds 163
5.4.2 S_2 foliation 171
5.4.3 Fault and shear zones 176
5.4.4 Evidence of high D_2 deformation intensity 180
5.4.5 First-order structure 185
5.5 D_3 deformation 187
5.5.1 F_3 folds 187
5.5.2 S_3 foliation 188
5.5.3 L_3 lineation 188
5.5.4 Fault and shear zones 194
5.6 Synthesis of the structural geology of the Opapimiskan Lake area: West antiform and Mine structural domains 198
5.6.1 D_1 deformation 198
5.6.2 D_2 deformation 198
5.6.3 D_3 deformation 199
6 METAMORPHISM 201
6.1 Metamorphic paragenesis of ultramafic and mafic volcanic rocks 201
6.2 Metamorphic paragenesis of pelitic rocks 203
6.3 Metamorphic paragenesis of banded iron formations 211
6.3.1 Unit 4EA 211
6.3.2 Unit 4B 218
6.3.3 Unit 4A 221
6.4 Thermobarometric and geochronological constraints of M_2 metamorphism 222
6.4.1 Thermobarometry of M2 metamorphism 223
6.4.2 Geochronology of M_2 metamorphism 228
6.5 Summary and implications 230
7 CHARACTERISTICS AND DISTRIBUTION OF GOLD-MINERALIZED ROCKS 235
7.1 Distribution and geometry of mineralized zones 235
7.2 Main pyrrhotite-replacement mineralization style 243

7.2.1 Mineralogical and petrographic characteristics of 4EA-hosted ore 243
7.2.2 LA-ICP-MS 2D elemental mapping 258
7.2.3 Whole-rock geochemistry of 4EA-hosted ore 263
7.3 Variations of replacement-style mineralization 274
7.3.1 4EA – silica-flooding end-member 274
7.3.1 4EA – Pyrrhotite-rich end-member 274
7.3.2 Unit 4E “intraformational” 278
7.3.3 Unit 4A 282
7.3.4 Clastic 4B and typical 4B mineralized rocks 286
7.4 Main quartz-vein mineralization style 293
7.5 Other quartz-vein mineralization styles 300
7.5.1 Auriferous quartz veins in mafic volcanic rocks 300
7.5.2 Visible gold occurrences 304
7.6 Summary on gold mineralization 307
7.6.1 Main characteristics of gold-mineralized rocks 307
7.6.2 Preliminary interpretations for the timing of gold mineralization 307
8 HYDROTHERMAL ALTERATION 309
8.1 Introduction 309
8.2 Spatial distribution of hydrothermal alteration 312
8.2.1 Methodology 312
8.2.2 Results 313
8.3 Alteration characteristics of mafic volcanic rocks (unit Bvol) 325
8.3.1 Alteration mineral assemblages 325
8.3.2 Geochemical variations 329
8.4 Alteration characteristics of unit 4EA 333
8.4.1 Alteration mineral assemblages 333
8.4.2 Geochemical variations 338
8.5 Alteration characteristics of unit 4F 347
8.5.1 Alteration mineral assemblages 347
8.5.2 Geochemical variations 350
8.6 Alteration characteristics of unit 4B 350
8.6.1 Alteration mineral assemblages 352
8.6.2 Geochemical variations 354
8.7 Na-bearing alteration mineral assemblages 357
8.8 Summary 358
9 FLUIDS PATHWAYS AND METAL SOURCES 361
9.1 Potential fluid pathways 361
9.1.1 “Basement basalts” unit 363
9.1.2 Southern iron formation (SIF) 364
9.1.3 Preliminary interpretations 364
9.2 Potential gold and metals sources 366
9.2.1 Argillite horizons of the Wilberforce area 366
9.2.2 Pyrite-rich sedimentary rocks of the ZHA 373
9.2.3 Summary 376

10 SYNTHESIS, DISCUSSION, AND CONCLUSIONS 379
10.1 Synthesis of observations in the study area 380
10.1.1 Regional geological context and geology of the Opapimiskan Lake area 380
10.1.2 Structure and metamorphism 385
10.1.3 Mineralization and alteration 386
10.1.4 Fluid and metal sources 387
10.2 Revised tectonostratigraphy of the North Caribou greenstone belt 388
10.2.1 Early volcanism and sedimentation (3.1-2.97 Ga) 388
10.2.2 Mantle plume-related volcanism and iron formation deposition (2.97-2.91 Ga) 389
10.2.3 Voluminous magmatism and crustal growth (2.90-2.82 Ga and 2.73-2.71 Ga) 393
10.2.4 Detrital sedimentation (2.90-2.72 Ga) 394
10.3 Revised tectonometamorphic evolution of the NCG 396
10.3.1 D_1-M_1 event 396
10.3.2 D_2-M_2 event 399
10.3.3 D_3-M_3 event 401
10.4 Geological evolution of the NCG 402
10.5 Discussion 403
10.5.1 Distribution, controls, and timing of gold mineralization at Musselwhite 403
10.5.2 Alteration zonation and gold precipitation mechanisms 410
10.5.3 Potential influence of dykes on gold mineralization 418
10.5.4 Origin of fluids and metals, and migration routes 419
10.5.5 New genetic model for the Musselwhite gold deposit 422
10.6 Comparisons with other BIF-hosted gold deposits 425
10.6.1 Contwoyto-Point lakes area: the Lupin gold mine and regional gold occurrences 425
10.6.2 Mineral Hill, Jardine, Montana, USA 427
10.6.3 Homestake mine, South Dakota, USA 428
10.6.4 Nevoria mine, Southern Cross belt, Yilgarn craton, Western Australia 429
10.6.5 Lac Lilois prospect, Ashuanipi complex, northeastern Superior province, Canada 430
10.6.6 Summary 431
10.7 Implications for exploration 431
10.7.1 Exploration in the North Caribou greenstone belt 431
10.7.2 Exploration in other Precambrian terranes 434
10.8 Conclusions 435
10.8.1 Main contributions 435
10.8.2 Outstanding questions 436
REFERENCES 439
APPENDICES 463

LIST OF FIGURES

Figure 1-1: Geographic location of the Musselwhite mine and study area. 2
Figure 1-2: Simplified map of the Opapimiskan Lake area. 5
Figure 1-3: Tectonic environments of iron formations in shelf, ridge and back-arc settings. 13
Figure 1-4: Global map showing the distribution of Precambrian cratons and successions containing iron formations. 14
Figure 1-5: BIFs through time.. 15
Figure 1-6: Algoma-type IF depositional environment and processes. 18
Figure 1-7: Model for deposition of iron formation in deep-shelf environments in association with shallow-shelf to deepwater platform carbonates. 19
Figure 1-8: Relative stabilities of minerals in metamorphosed iron formations as a function of metamorphic zones. 20
Figure 1-9: Diagram of Fe/Ti vs. Al/(Al + Fe + Mn) ratios for iron-formation and chlorite tuff samples from the Heath Steele belt. 22
Figure 1-10: Upper continental crust (UCC)-normalized REE+Y patterns 24
Figure 1-11: A. Annual gold production and B. Canadian gold production, for the period 2012-2014. 24
Figure 1-12: Simplified geological map of Canada showing geological domains by supercontinent cycle and the distribution of non-ferrous metalliferous and kimberlite diamond deposits. 25
Figure 1-13: Schematic crustal section showing inferred levels of gold deposition for the different clans of lode gold deposits. 26
Figure 1-14: Summary of features of the continuum model. 27
Figure 1-15: Grade and tonnage of major BIF-hosted gold deposits in the world. 29
Figure 1-16: Examples of sulphidation of Algoma-type BIF. 31
Figure 2-1: Terrane boundaries in the western Superior province. 34
Figure 2-2: Simplified tectonostratigraphic map of the North Caribou greenstone belt and surrounding area. 36
Figure 2-3: Terminology and schematic stratigraphic columns of the lithostratigraphic assemblages of the North Caribou greenstone belt. 37
Figure 2-4: A. Schematic Musselwhite mine stratigraphy column. B. Geological map of the Opapimiskan Lake area. 43
Figure 2-5: Simplified structural map of the North Caribou greenstone belt and surrounding area. 48
Figure 2-6: Metamorphic facies of the NCG. 50
Figure 2-7: Location of major mineral occurrences in the North Caribou greenstone belt. 54
Figure 3-1: Geological setting of the Musselwhite mine. 57
Figure 3-2: Geological section of Musselwhite mine.. 58
Figure 3-3: MgO vs. Al_2O_3 binary plot of least altered mafic to ultramafic rock samples. 62
Figure 3-4: Zr-Hf plot of all volcanic rock samples from this study. 62
Figure 3-5: A. Binary plot of Fe/Ti vs. Al/(Al + Fe + Mn) ratios for least altered samples of the NIF sequence. B. Ternary plot showing the detrital/terrigenous (Al_2O_3 / (Al_2O_3 + Fe III Total + MnO)), ferrous (Fe III Total), and volatile (CO_2 + total S + LOI) components of the siliciclastic and BIF facies of the NIF sequence. 67
Figure 3-6: Binary plot of MUQ-n Eu and Y anomalies for sedimentary units of the OMA. 68

Figure 3-7: Mine Unit Avol 70
Figure 3-8: Unit Avol. 71
Figure 3-9: Mine Unit Bvol. 73
Figure 3-10: Unit Bvol. 74
Figure 3-11: Unit Bvol 75
Figure 3-12: “Basement basalts” unit. 78
Figure 3-13: “Basement basalts” unit. 78
Figure 3-14: “Basement basalts” unit. 79
Figure 3-15: “Lower basalts” unit. 81
Figure 3-16: “Lower basalts” unit. 82
Figure 3-17: “Lower basalts” unit. 83
Figure 3-18: Unit 4E. 85
Figure 3-19: Unit 4E. 86
Figure 3-20: Unit 4E. 87
Figure 3-21: Unit 4F. 90
Figure 3-22: Unit 4F. 91
Figure 3-23: Unit 4F. 92
Figure 3-24: Unit 6. 94
Figure 3-25: Unit 6. 95
Figure 3-26: Unit 4EA. 97
Figure 3-27: Unit 4EA. 98
Figure 3-28: Unit 4EA. 99
Figure 3-29: Unit 4B. 101
Figure 3-30: Unit 4B. 103
Figure 3-31: Facies 4Bc. 104
Figure 3-32: Unit 4B. 105
Figure 3-33: Unit 4A. 107
Figure 3-34: Unit 4A. 108
Figure 3-35: Unit 4H. 110
Figure 3-36: Unit 4H. 111
Figure 3-37: Ultramafic dykes. 113
Figure 3-38: Ultramafic dykes 114
Figure 3-39: Geological map of the southern NCG 116
Figure 3-40: Zeemel sedimentary rocks in the Paseminan river area. 118
Figure 3-41: Sedimentary rocks of the Zeemel assemblage SE from Graff Lake 119
Figure 3-42: Rock units of the Zeemel assemblage in the mine area. 120
Figure 3-43: ZHA Pyrite-bearing sedimentary rocks. 121
Figure 3-44: Breccias of the Zeemel assemblage. 123
Figure 3-45: Sandstones of the Zeemel assemblage. 124
Figure 3-46: Unconformity within the Zeemel assemblage. 125
Figure 3-47: Zeemel felsic rocks. 126

Figure 3-48: Clastic rocks of the Heaton assemblage 127
Figure 4-1: Location and results of U-Pb zircon geochronological data from this study 130
Figure 4-2: Synthetic diagram of the magmatic and sedimentary evolution of the NCB in the Opapimiskan Lake area. 136
Figure 4-3: Synthetic lithological column of the NCG in the study area 137
Figure 5-1: Structural domains of the Opapimiskan Lake area and general orientation of the S_1, S_2, and S_3 fabrics. 140
Figure 5-2: Replication of structures at various scales. 141
Figure 5-3: BIF rheology. 143
Figure 5-4: BIF rheology. 144
Figure 5-5: Preserved soft-sediment deformation structures in BIF. 145
Figure 5-6: Geological map of West Antiform Trench 1 147
Figure 5-7: Geological map of South shore trench (SST) exposure. 148
Figure 5-8: Geological map of Trench 4 149
Figure 5-9: Refolded F_1 folds in the West antiform area. 151
Figure 5-10: S_1 foliation in volcanic rocks. 152
Figure 5-11: S_{0-1} foliation in garnet-biotite schist. 153
Figure 5-12: OMA-ZHA boundary in the mine area. 155
Figure 5-13: D_1 thrust fault, juxtaposing the SRA and OMA over the ZHA. 156
Figure 5-14: Geological map of the Opapimiskan Lake area and 3D schematic block diagram. 157
Figure 5-15: West antiform structural domain – stereographic projections of D_2 structures from surface stripped outcrops (equal angle, lower hemisphere). 159
Figure 5-16: F_2 folds in the West antiform area. 160
Figure 5-17: Faults associated to F_2 folds. 161
Figure 5-18: Evidence of ductile deformation. 162
Figure 5-19: S_2 foliation in the WASD. 164
Figure 5-20: PQ trench detailed map. 165
Figure 5-21: Geological and structural interpretation of mine section 11775 N, looking north. 166
Figure 5-22: Geological and structural interpretation of mine section 12000 N, looking north. 167
Figure 5-23: Geological and structural interpretation of mine section 12675 N, looking north. 168
Figure 5-24: Inclined plan view of Musselwhite mine between mine levels 920 and 1145. 169
Figure 5-25: F_2 folds in the MASD. 172
Figure 5-26: F_2 folds in the MASD. 173
Figure 5-27: Photographs of boudinaged bed of unit 4B, PQ trench. 174
Figure 5-28: L_2 mineral lineation and L_{2-3} intersection lineation on S_2 plane 175
Figure 5-29a: S_2 foliation in the MASD. 176
Figure 5-30: Carbaonte-altered HSZ in the mine 178
Figure 5-31: Carbaonte-altered HSZ in the mine. 179
Figure 5-32: Geometry of the NIF Duplication Structure. 181
Figure 5-33: Fold limb inversion and shear bands. 183
Figure 5-34: Detachment structures in the BIF 185
Figure 5-35: Akow Lake and Dinnick Lake shear zones.. 186

Figure 5-36: NCSZ. 187
Figure 5-37: F_3 folds. 189
Figure 5-38: F_2-F_3 fold interference in BIF, Trench 4 exposure, West antiform area. 190
Figure 5-39: F_3 folds. 191
Figure 5-40: S_3 foliation. 192
Figure 5-41: S_3 crenulation in oxide-BIF. 193
Figure 5-42: S_3 crenulation in oxide BIF. 194
Figure 5-43: D_3 shear zone. 195
Figure 5-44: 4-km BIF trench geological map. 196
Figure 5-45: Markop Lake shear zone (MLSZ). 197
Figure 5-46: Synthetic chart of the geological and structural evolution of the Opapimiskan Lake area. . 199
Figure 6-1: Actinolite (ac) -cummingtonite (cm) -Mg-chlorite (chl) -ilmenite (ilm) mineral assemblage in ultramafic rocks of the OMA 202
Figure 6-2: Microphotograph of poikilitic staurolite porphyroblasts in biotite-feldspar-sericite-quartz matrix. 204
Figure 6-3: Microphotograph of altered andalusite with staurolite remnants and fibrous sillimanite intergrown with biotite. 204
Figure 6-4: Microphotograph of euhedral almandine garnet with poikilitic core and inclusions of poikilitic staurolite, in unit 4F sample. 205
Figure 6-5: Garnet porphyroblasts. 209
Figure 6-6: Garnet microprobe elemental mapping, unit 4F. 210
Figure 6-7: Typical garnet-grunerite-chert assemblage of unit 4EA. 213
Figure 6-8: Garnet porphyroblast in garnet-quartz-biotite matrix. 214
Figure 6-9: Grunerite and garnet in relation to structural fabrics. 215
Figure 6-10: Grunerite and garnet in relation with structural fabrics. 216
Figure 6-11: Primary vs secondary grunerite. 217
Figure 6-12: Typical chert-magnetite-grunerite layering in oxide-BIF. 219
Figure 6-13: Typical grunerite-magnetite-chert assemblage in unit 4B. 220
Figure 6-14: Pyroxene occurrence in unit 4B. 221
Figure 6-15: Metamorphic minerals in unit 4A. 222
Figure 6-16: Microphotographs with locations of garnet and biotite spot analyses in barren (A, C, and D) and auriferous (B) garnet-biotite schist samples. 226
Figure 6-17: Garnet-biotite temperature calculations from Holdaway (2000). 227
Figure 6-18: Comparison of temperature calculations from Holdaway (2000) and Ferry and Spear (1978). 228
Figure 6-19: Petrographic and textural context of monazite grains. 232
Figure 6-20: Synthetic diagram of the magmatic, sedimentary, structural and metamorphic evolution of the NCB in the Opapimiskan Lake area. 233
Figure 7-1: Simplified geological section of the mine at 11775 N,. 236
Figure 7-2: Geological and structural interpretation of mine section 11775 N. 239
Figure 7-3: Geological and structural interpretation of mine section 12000 N. 240
Figure 7-4: Geological and structural interpretation of mine section 12675 N. 241

Figure 7-5: Typical pyrrhotite-replacement ore in garnet-grunerite BIF (unit 4EA). 246
Figure 7-6: Polished slab of high-grade silicate-BIF ore 246
Figure 7-7: Mineral paragenesis of 4EA-hosted ore. 247
Figure 7-8: Garnet porphyroblasts in 4EA ore. 250
Figure 7-9: Garnet porphyroblasts in 4EA-hosted ore. 251
Figure 7-10: Biotite in 4EA ore. 252
Figure 7-11: Chlorite in 4EA ore. 254
Figure 7-12: Gold in 4EA ore. 256
Figure 7-13: Gold in 4EA ore. 257
Figure 7-14: 2D LA-ICP-MS elemental maps of garnets associated with high-grade gold-mineralized unit 4EA sample. 259
Figure 7-15: 2D LA-ICP-MS elemental maps of garnets associated with high-grade gold-mineralized unit 4EA sample 260
Figure 7-16: 2D LA-ICP-MS elemental map of garnet associated with low-grade gold-mineralized unit 4EA sample. 261
Figure 7-17: 2D LA-ICP-MS elemental map of sulphides associated with high-grade gold-mineralized unit 4EA sample. 262
Figure 7-18: Box plot of major elements composition for 4EA samples with gold grade over 1000 ppb. 266
Figure 7-19: Binary plot of gold content and total sulphur content (CLR data) for least altered (blue squares) and altered to gold-mineralized (light blue diamonds) 4EA samples. 268
Figure 7-20: Binary plot showing the variance of components F1 to F20 (blue line) and cumulative variance (red line) associated with the Principal Component Analysis of geochemical data from 4EA samples 271
Figure 7-21: Pearson correlation coefficients of trace metals with gold associated with the Principal Component Analysis of geochemical data from 4EA samples 272
Figure 7-22: Principal Component Analysis of geochemical data from 4EA samples. 273
Figure 7-23: Silica-rich replacement 4EA-hosted ore. 275
Figure 7-24: Massive pyrrhotite lens in C-block ore zone 276
Figure 7-25: Polished slabs of pyrrhotite-rich ore samples from mine level 970, section 12630 N. 278
Figure 7-26: Gold-mineralized unit 4E. 279
Figure 7-27: Mineral paragenesis of gold-mineralized unit 4E. 281
Figure 7-28: Major element whole-rock composition for samples with over 1 ppm Au of unit 4E (n = 32). 281
Figure 7-29: F1-F2 and F1-F3 projections of PCA on CLR data, major elements, unit 4E samples with over 1 ppm Au. 282
Figure 7-30: Gold-mineralized samples of unit 4A. 283
Figure 7-31: Mineral paragenesis of gold-bearing 4A. 284
Figure 7-32: Major element whole-rock composition for samples with over 1 ppm Au of unit 4A (n = 27). 285
Figure 7-33: F1-F2 and F1-F3 projections of PCA on CLR data, major elements, unit 4A samples with over 1 ppm Au (n = 27). 286
Figure 7-34: Gold-mineralized clastic 4B unit. 288
Figure 7-35: Gold-mineralized clastic-rich unit 4B. 289

Figure 7-36: Mineral paragenesis of gold-bearing 4Bc. 290
Figure 7-37: Petrography of gold-mineralized unit 4B. 291
Figure 7-38: Major element whole-rock composition for samples with over 1 ppm Au of A. unit 4Bc and B. unit 4B. 292
Figure 7-39: F1-F2 and F1-F3 projections of PCA on CLR data, major elements, all oxide-dominant BIF samples. 293
Figure 7-40: Gold-mineralized samples of garnet-biotite schist (unit 4F). 295
Figure 7-41: Mineral paragenesis of gold-mineralized 4F 296
Figure 7-42: Petrography of gold-mineralized unit 4F. 297
Figure 7-43: Garnet-biotite-chlorite assemblage in auriferous unit 4F. 298
Figure 7-44: Major element whole-rock composition for samples with over 1 ppm Au of unit 4F (n = 35). 299
Figure 7-45: F1-F2 and F1-F3 projections of PCA on CLR data, major elements, all garnet-biotite schist samples. 299
Figure 7-46: Auriferous quartz-calcite vein in unit Bvol. 301
Figure 7-47: Quartz-pyrrhotite and calcite-rich veining in mafic volcanic rocks (unit Bvol). 302
Figure 7-48: Gold in mafic rocks, sample MW-11-015, DDH 10-PQE-054. 303
Figure 7-49: Visible gold occurrence in the selvage of a D_2-deformed quartz vein hosted by mafic volcanic rock. 304
Figure 7-50: Visible gold occurrence associated with a quartz-pyrrhotite-arsenopyrite vein 305
Figure 7-51: Visible gold occurrence in an F_2-folded quartz vein hosted by mafic volcanic rock 306
Figure 8-1: Variations in D_2 strain and gold mineralization gradients. 311
Figure 8-2: Sections of DDH profiles presented in this chapter. 316
Figure 8-3: Gold and major elements profiles of drill hole 10-PQE-056, East limb area, section 12675 N. A.. 317
Figure 8-4: Gold and major elements profiles of drill hole 10-PQE-066, East limb area, section 12675 N. A. 318
Figure 8-5: Gold and major elements profiles of drill hole 06-PQE-013, PQD area, section 11775 N.... 319
Figure 8-6: Gold and major elements profiles of drill hole 06-PQE-095, PQD area, section 11775 N.... 320
Figure 8-7: Gold and major elements profiles of drill hole 06-PQE-083, PQD area, section 11775 N.... 321
Figure 8-8: Gold and major elements profiles of drill hole 09-TAN-014, T-antiform west limb, section 11775 N.. 322
Figure 8-9: Gold and major elements profiles of drill hole 09-TAN-029, T-antiform west limb, section 11775 N.. 323
Figure 8-10: Distribution of alteration zones over the PQD area. 324
Figure 8-11: Biotite and carbonate alteration in unit Bvol 327
Figure 8-12: Altered mafic volcanic rocks. 328
Figure 8-13: Geochemical footprint of alteration in unit Bvol. 331
Figure 8-14: Isocon diagram between “least altered” and moderate alteration (altered group 1) average compositions (Table 8-2). Isocons were traced using Al_2O_3, TiO_2, and Zr ratios. 332
Figure 8-15: Isocon diagram between “least altered” and strong alteration (altered group 2) average compositions (Table 8-2). Isocons were traced using Al_2O_3, TiO_2, and Zr ratios. 332
Figure 8-16: Garnet-grunerite-biotite-quartz mineral assemblage in unit 4EA. 336

Figure 8-17: Secondary grunerite in unit 4EA. 336
Figure 8-18: Proximal, Ca-amphibole-bearing alteration in unit 4EA. 337
Figure 8-19: Garnet-grunerite-hornblende-quartz assemblage in unit 4EA. 338
Figure 8-20: SiO_2-Al_2O_3-X ternary diagrams of major elements in unit 4EA. 340
Figure 8-21: SiO_2-Al_2O_3-X ternary diagrams of major elements in unit 4EA. 341
Figure 8-22: SiO_2-Al_2O_3-X ternary diagrams of trace elements in unit 4EA. 343
Figure 8-23: Major and trace element average values of 4EA unit, per gold assays value classes. 346
Figure 8-24: Drill core sections of altered unit 4F. 348
Figure 8-25: Alteration of unit 4F. 349
Figure 8-26: SiO_2-Al_2O_3-X Ternary diagrams for major elements in unit 4F. 351
Figure 8-27: Average major and trace element content in unit 4F for sample groups of increasing gold content. 352
Figure 8-28: Alterated clastic facies of unit 4B. 353
Figure 8-29: Carbonate alteration of unit 4B. 354
Figure 8-30: Relationships between primary Al_2O_3, K_2O, and CO_2 contents in least altered unit 4B. 355
Figure 8-31: SiO_2-Al_2O_3-X ternary diagrams for unit 4B. 356
Figure 8-32: Average major and trace element content in unit 4B for sample groups of increasing gold content. 357
Figure 8-33: Na_2O content of all altered and gold-rich samples in units 4EA (n = 291) and 4F (n = 133). 358
Figure 9-1: Alteration in “Basement basalts” unit. 362
Figure 9-2: K_2O vs. Na_2O in units Bvol (A) and “Basement basalts” (B). 363
Figure 9-3: SIF. 365
Figure 9-4: Wilberforce unit 4H. 367
Figure 9-5: Pyrite nodules in argillaceous rock, Wilberforce area 368
Figure 9-6: LA-ICP-MS 2D elemental maps of pyrite nodule #1 in sample MW-12-092-1. 370
Figure 9-7: LA-ICP-MS 2D elemental maps of pyrite nodule #2 in sample MW-12-092-1. 372
Figure 9-8: Drill core segment of sedimentary rock of the ZHA. 374
Figure 9-9: LA-ICP-MS 2D elemental maps of pyrite grain in sample MW-13-460A. 375
Figure 9-10: Wilberforce and ZHA pyrite. 376
Figure 10-1: Simplified tectonostratigraphic map of the North Caribou greenstone belt and surrounding area. B. Geological map of the Opapimiskan Lake area. 381
Figure 10-2: Synthetic lithological column of the NCG in the study area. 383
Figure 10-3: Synthetic chart of the tectonometamorphic evolution of the NCG in the Opapimiskan Lake area. 384
Figure 10-4: Th/Yb vs. Nb/Yb plot of “least altered” volcanic rocks from the Musselwhite mine stratigraphy. 393
Figure 10-5: Structural map of the Opapimiskan Lake area 398
Figure 10-6: Schematic synthesis of tectonometamorphic events in the NCG. 404
Figure 10-7: Evolution of the geological model for the Musselwhite deposit. 406
Figure 10-8: Summary of alteration mineralogical reactions in unit 4EA. 412
Figure 10-9: Gold mineralization and alteration in the iron formation. 412

Figure 10-10: Rheological contrasts and gold endowment. 414
Figure 10-11: Schematic diagrams of the geometrical evolution of the East Bay synform hinge zone during syn-D_2 gold mineralization. 415
Figure 10-12: Summary of alteration mineralogical reactions in units 4A and 4B. 418
Figure 10-13: Schematic representation of possible fluid migration pathways at sub-regional scale in the study area. 422
Figure 10-14: Metamorphic facies of the NCG with location of major mineral occurrences in the North Caribou greenstone belt. 433

LIST OF TABLES

Table 1-1: Relative stabilities of predominant constituent minerals in metamorphosed iron formations... 21
Table 1-2: Some mineralogical reactions during low- to high-grade metamorphism in iron formations... 22
Table 1-3: Some criteria to distinguish between syngenetic and epigenetic origin of BIF-hosted gold mineralization. ... 30
Table 2-1: Types of gold mineralization associated with supracrustal assemblages of the North Caribou Lake belt. ... 55
Table 3-1: Average major element composition of Geological Survey of Canada internal standards and of the main volcanic units of the OMA in the Musselwhite mine area ... 60
Table 3-2: Average trace element composition and standard deviation of Geological Survey of Canada internal standards and of the main volcanic units of the OMA in the Musselwhite mine area. 61
Table 3-3: Threshold values used to define “least altered” sample groups for each unit of the Northern iron formation. ... 63
Table 3-4: Average major element composition and standard deviation for sedimentary units of the OMA. ... 64
Table 3-5: Average trace element composition and standard deviation for sedimentary units of the OMA. ... 65
Table 4-1: Summary of U-Pb zircon geochronological samples and results from this study. ... 131
Table 6-1 : Garnet and biotite mineral chemistry data and corresponding calculated temperatures from Holdaway (2000). ... 225
Table 6-2: Location of garnet-biotite schist samples with gold content and monazite occurrence. ... 229
Table 6-3: Morphologic and petrographic characteristics of analyzed monazite grains. ... 230
Table 7-1: List of the mine areas and the ore/mineralized zones, main host rock, and dominant mineralization style.. ... 237
Table 7-2: Average chemical composition and standard deviation of major minerals in unit 4EA ore. .. 248
Table 7-3: Average chemical composition and standard deviation of sulphide minerals and electrum in unit 4EA ore. ... 255
Table 7-4: Average major and trace element composition of gold-mineralized samples of the various BIF units. ... 264
Table 7-5: Pearson and Spearman correlation coefficients for major elements of 4EA samples ... 269
Table 8-1: Average major element composition and standard deviation for units 4F, 4EA, 4B, and 4A. 313
Table 8-2: Average major element composition and standard deviation of least altered and altered samples of unit Bvol. ... 330
Table 8-3: Pearson correlation coefficients of major and trace elements of unit 4EA altered and mineralized samples. ... 344
Table 9-1: Trace element content of pyrite-rich sediment of the ZHA. ... 374

1 INTRODUCTION

Canada's gold production and resources are mainly related to mining districts located within the Archean terranes of the Superior province, notably the Abitibi sub-province, where gold deposits are largely hosted by greenstones (Gosselin and Dubé, 2005, 2007; Percival, 2007; section 1.5). Gold can be concentrated and deposited in a variety of geological settings including: volcanogenic massive sulphides, intrusion-related, orogenic greenstone-hosted deposits, etc. (Poulsen et al., 2000; Golfarb et al., 2005; Robert et al., 2005; Dubé and Gosselin, 2007). In granite-greenstone terranes, orogenic quartz-carbonate-vein-type gold deposits are mainly hosted by mafic volcanic rocks and intrusions, banded-iron formation (BIF) only making for a minor portion of host lithologies. There are two end-member types of BIF-hosted gold deposits (Dubé et al., 2011; Dubé and Mercier-Langevin, 2015): those almost entirely BIF-hosted that commonly form large, apparently "isolated" deposits (e.g., Musselwhite and Meadowbank mines) and those partially hosted in BIF, which are commonly part of a district associated with major fault zones (e.g., Meliadine (NU) and Geraldton (ON) districts). BIF-hosted gold deposits have the potential to form world-class gold deposits (e.g., Homestake deposit, South Dakota, 40 Moz Au; Caddey et al., 1991) and represent important exploration targets in several greenstone belts especially in the northern part of the Canadian Shield.

Musselwhite is a lode gold deposit hosted by poly-deformed, amphibolite-grade iron formations comprised in the volcanic-dominated sequence of the Archean North Caribou greenstone belt in the western Superior province of the Canadian Shield (Figure 1-1; chapter 2). Gold ore at Musselwhite is mainly characterized by pyrrhotite-rich replacement and/or silica flooding of silicate facies iron formation with local gold-bearing quartz veins in the oxide-dominant facies.

The present study of the Musselwhite mine is part of the "Lode Gold" project of Natural Resources Canada's fourth phase of the Targeted Geoscience Initiative program (TGI-4) (Dubé et al., 2011; Dubé and Mercier-Langevin, 2015). The Musselwhite Gold Mine is located on the southern shore of Opapimiskan Lake in the Patricia Mining District of Northwestern Ontario, 475 km north of the city of Thunder Bay (Figure 1-1; NTS 53 B/9, Lat. 52°36'50" N, Long. 90°21'43" W).

The Musselwhite gold deposit was found by the Musselwhite brothers (Harold and Alan) through prospection during the 1960's (Appendix I). Gold panning in the Opapaimiskan Lake area led to the discovery of auriferous quartz veins near the northern shores and abundant gold grains in the regolith along the southern shores ("Western Anticline" area). Ten companies were involved in the Musselwhite Prospection grubstake by 1973. From 1973 to 1984, exploration campaigns resulted in the discovery of significant gold mineralization in the "West Anticline" area. Additional drilling and discoveries (e.g., Hall

and Rigg, 1986) led to a prefeasibility study, in 1987. In 1989, the three remaining members of the 1983 Musselwhite Joint Venture (Placer Dome, Inco Gold and Corona) initiated a full feasibility study. Further exploration, including underground drifting led to full mine operation in 1997. Since then, successive discoveries have allowed replacement of ore reserves and economic sustainability of the operation. The mine has been operated by Goldcorp Inc. since 2006. It has produced over 4.5 Moz of gold and has total proven and probable additional reserves of 1.85 Moz as of December 31, 2016 (www.goldcorp.com).

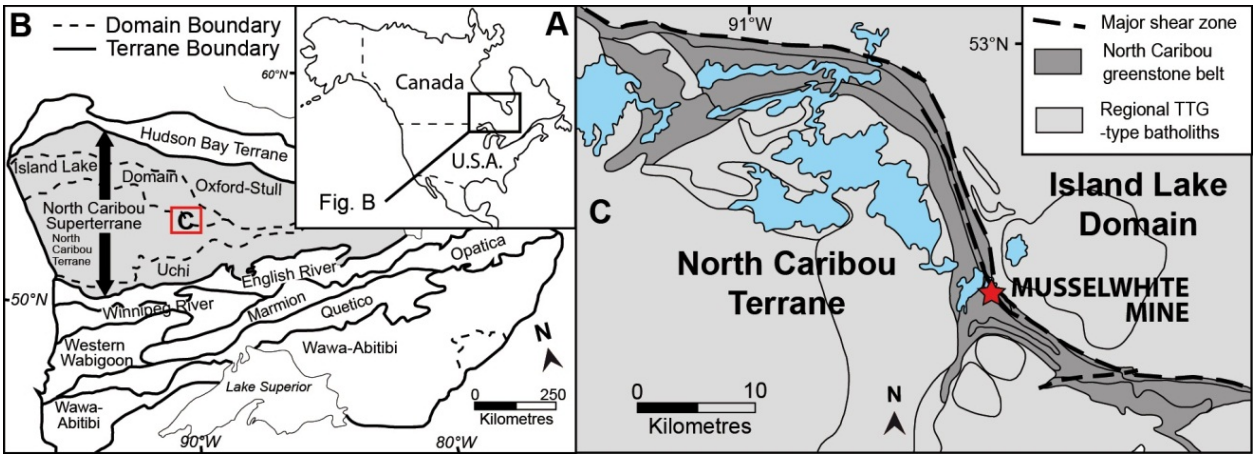

Figure 1-1: Geographic location of the Musselwhite mine and study area in: (A) North America, (B) the western Superior province, and (C) the North Caribou greenstone belt (A and B, modified from Rayner and Stott, 2005, and Stott et al., 2010; C, modified from Thurston et al., 1991).

1.1 Problematic and Objectives

The intrinsic complexity of deformed and metamorphosed terranes makes exploration a highly challenging task. Practices have greatly evolved over the recent decades. Grassroot exploration complemented by increasingly sophisticated techniques, helped by a more profound understanding of ore-forming systems, has resulted in new discoveries (e.g., Agnico-Eagle's Amaruq, NU). Nevertheless, discovery rate has declined during the past twenty years (Villeneuve et al., 2011), following the discovery of more easily accessible, surface and sub-surface deposits. To overcome the numerous obstacles lying in the way of new discoveries, especially deeply-seated deposits ("blind deposits"), new and efficient exploration parameters are required. Such exploration parameters stem from a greater understanding of the geological setting and mineralization processes.

Several research aspects related to BIF-hosted Precambrian gold deposits have been identified in the TGI-4 Lode Gold project. (1) First and foremost, the geological controls on the formation and distribution of BIF-hosted Au mineralization. (2) The timing of the gold mineralization event(s) with respect to deformation episodes and metamorphism. (3) The nature and chronology of hydrothermal alteration, in

distal and proximal settings to the deposit, and the geochemical signature distinguishing the metamorphosed protoliths from the altered and metamorphosed host rocks. And (4), ultimately, the nature of the main metallotects needed to design more efficient exploration models for similar deposit types in the North Caribou greenstone belt and elsewhere in Precambrian terranes (Dubé et al., 2011; Dubé and Mercier-Langevin, 2015). The Musselwhite mine is one of the few BIF-hosted gold deposits currently in production, and as such, provides extensive surface and underground exposure as well as abundant drill core and other geological datasets. It represents a highly suitable site to address the key points that control the formation of this type of gold deposits.

Nonetheless, uncertainties remain in the definition and correlation of some lithostratigraphic assemblages of the North Caribou greenstone belt. Various intrusive phases and sedimentary units occur in the vicinity of the Musselwhite deposit and their significance in relation to the formation and location of ore zones is also uncertain. In addition, the timing and relationship of metamorphism and associated deformation with respect to the ore-forming hydrothermal event is yet to be fully understood. Consequently, the objectives of the Musselwhite deposit study are to:

(1) Improve the understanding of the local and sub-regional lithostratigraphic setting and structural setting of the Opapimiskan Lake area;

(2) Document the lithological and structural controls on the formation, distribution and geometry of gold mineralization;

(3) Document the geochemical characteristics of gold host rock and the alteration footprint of the auriferous hydrothermal system;

(4) Improve absolute and relative constraints on the timing of gold mineralization and the various tectono-metamorphic events including the timing of gold introduction in the main host unit, the Northern iron formation;

(5) Define exploration criteria for future exploration in the deposit area as well as the North Caribou greenstone belt and in other Archean terranes.

1.2 Methodology

The project started in the fall of 2011 and was designed as a field-based study including three full summers of geological and structural mapping of surface exposures and underground workings, as well as extensive drill core logging and sampling for whole-rock geochemistry and petrography. Targeted U-Pb

geochronology was also carried out in collaboration with V. McNicoll of the Geological Survey of Canada in Ottawa (GSC-O).

1.2.1 Surface mapping

Two components of surface geological mapping were undertaken: sub-regional reconnaissance and exploration-oriented geological and structural mapping in the Opapimiskan Lake area in collaboration with Goldcorp Musselwhite exploration geologists; and detailed mapping of a set of selected stripped outcrops. This activity provides data primarily to improve the understanding of Musselwhite's geological and structural settings (objective 1) and document the relative chronology between gold mineralization and tectono-metamorphic events (objective 4). It also bears some impact on documenting the parameters that controlled the formation and distribution of gold mineralization (objective 2) and defining exploration criteria in the North Caribou greenstone belt (objective 5).

1.2.1.1 Sub-regional

Sub-regional mapping helped build the geological setting of the deposit and link the new generated data with previous studies, especially regarding lithostratigraphic correlations and structural trends (objective 1). Taking advantage of increased rock exposure due to a forest fire in 2011, lithological and structural data were gathered throughout the Opapimiskan Lake area, as well as further to the SW up to Cigar Lake, to the SE near Graff Lake and up to the Pipestone River, with a focus on gathering information and knowledge throughout the West Antiform area (also referred to as "West Anticline"; Figure 1-2).

1.2.1.1 Stripped outcrops

Using previous mapping (Breaks et al., 2001; Goldcorp Inc., unpublished data), stripped outcrops (also referred to as "trenches") were selected based on their structural setting and location with respect to the West antiform and East Bay synform, the main fold structures of the mine area (Figure 1-2). Some trenches were selected in lower strain areas in order to document the early structures, which are otherwise strongly overprinted by the main fabrics (West antiform trench 1 – WAT1, South shore trench – SST, Trench 4). Others were selected in high strain zones, associated to the main deformation event (PQ trench, 4KM BIF trench – 4KT).

Tools and data processing – The main challenge of mapping magnetic banded iron formations is the ensuing impossibility to use a standard compass for structural measurements. A classic solution to

overcome this issue is the use of a sun compass, where measurements are taken relative to the sun orientation and which requires careful documentation of time and geographic location of the measurement to subsequently use reference tables to convert measurements into standard structural data (susdesign.com). With the development of global positioning system (GPS) technology, high-resolution GPS consisting of a base unit acting as a reference and a mobile unit for data acquisition is now available for detailed mapping. The GPS unit used in this study is an AshTech Promark 800, operating with the Fast Survey software. It provides a measurement x-y precision close to 1 cm (5 cm along the z-axis). Precision and accuracy are influenced by the stability and speed of the mobile GPS unit during data acquisition. This tool enables increased data collection speed as well as faster transfer to a GIS software, such as ESRI's ArcGIS 10.0.

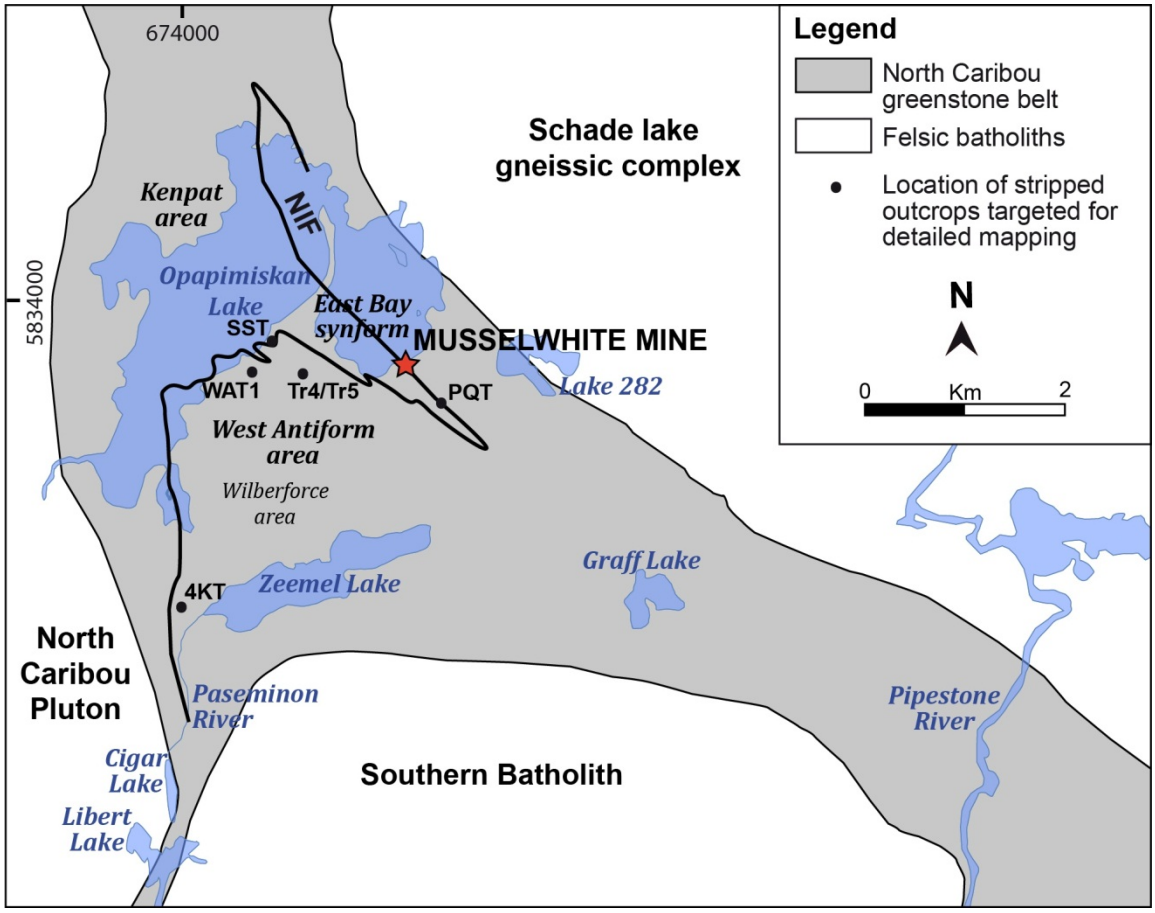

Figure 1-2: Simplified map of the Opapimiskan Lake area with hydrographic names, studied stripped-outcrop locations and local area names. NIF = Northern iron formation. This BIF sequence is the major host rock for ore at the Musselwhite Gold Mine.

Structural measurement method – Azimuths are obtained by collecting 3-5 location points along the geologic features (contacts, fabrics and structures), at a 10-20 cm spacing, depending on size/scale. Additional information such as dip or plunge is measured with a clinometer and entered in the description

part of the data points. Data points are subsequently extracted as a text file, imported and projected in ArcGIS. Then a manual linear regression is done to draw a line over the data points and the measurement strike is calculated from the coordinates of the line extremities.

1.2.2 Underground mapping

The mine extends over 4 kilometres and ore zones are distributed between multiple areas: the T-antiform (TAN), the PQ (Shallows and Deeps), and the East limb. Underground mapping of drifts was undertaken to complement data acquired from studied drill core sections (sections 1.2.2, 1.2.3), to produce section maps and a composite geological map of a representative part of the deposit. This allows the documentation of parameters that control the formation and distribution of gold mineralization (objective 2) and of its relative timing relationships with other geological events (objective 4). Underground mapping is hindered by limited access to underground (UG) workings, which heavily depends on mining activities and inherent safety policies. Nevertheless, UG mapping of certain levels has allowed documentation of geological features and structures in ore zones and surrounding host rocks, and also description of specific geological features of the mine (e.g., the "Conveyor Shear").

Tools and data processing – Mapping is done using the mine grid, surveyed underground maps of galleries and a measuring tape to locate observations, measurements and samples. Orientations of contacts and structural features are collected using a degree ruler with azimuth measured with respect to the gallery-face orientations. Face orientation is subsequently converted from mine grid reference to true North, measurements are recalculated to true North and plotted using stereographic projection softwares (e.g., Stereonet©, Allmendinger et al., 2013; Cardozo and Allmendinger, 2013; Stereo32).

Inclined plan view – Compiled mine data and new geological and structural features documented through underground mapping and drill hole descriptions were plotted on an inclined view of the mine between 11800 northing and 13100 northing. This plan, a pseudo-down-plunge projection, covers mine levels 920 to 1120 and was produced using 3D modelling software, Vulcan (www.maptek.com/vulcan9.1/) and Leapfrog3D (www.leapfrog3d.com).

1.2.3 Drill core description

Drill core description is a key component of the study. Three sections across the deposit were selected (11775 N, 12000 N, and 12675 N) to describe geological, mineralogical and structural features of the host rocks (objective 1), document the geometry and characteristics of every major ore zone (objective 2; PQ blocks, Lynx, TAN zones), and examine macroscopic, distal to proximal, textural and mineralogical

changes in host lithologies with respect to the ore zones (objective 3; chapter 3). Secondary mineralized zones (Esker, Red Wing-Thunder Wolves, WEL-A and WEL-C) were also examined with specific drill hole intersects.

1.2.4 Lithogeochemistry

During drill core description, samples were taken to document petrographic and geochemical characteristics of the various lithologies and their spatial variations (Oswald et al., in prep.). Samples of banded iron formations, which have centimetre- to decimetre-scale compositional variations (sections 1.3, 1.4) were a minimum of 30 cm in length to obtain an averaged composition. In distal settings relative to Au-mineralization (i.e., hundreds of metres away from mineralized intervals), samples were taken at several metres to a few tens of metres spacing according to the lithologies thicknesses and succession. In the vicinity of the mineralized intervals (≤10 metres), sample spacing is reduced to as small as a few tens of centimetres. Sample spacing was strongly guided by macroscopic variations of lithologies, deformation intensity, alteration mineral assemblages, or sulphide abundance.

Analytical procedure – Pulverized samples were analyzed at Activation Laboratories in Ancaster, Ontario. Major oxides, Ba, Be, Sc and Sr were determined by lithium metaborate / lithium tetraborate fusion followed by dissolution and inductively coupled plasma optical emission spectrometry (FUS-ICPOES). Silver, As, Bi, Ce, Co, Cr, Cs, Cu, Dy, Er, Eu, Ga, Gd, Ge, Hf, Ho, In, La, Lu, Mo, Nb, Nd, Ni, Pb, Pr, Rb, Sb, Sm, Sn, Ta, Tb, Th, Tl, Tm, U, W, Y, Yb, and Zr were analyzed by lithium metaborate / lithium tetraborate fusion followed by dissolution and inductively coupled plasma mass spectrometry (FUS-ICPMS). Silver, Cd, Co, Cr, Cu, In, Li, Mn, Mo, Ni, Pb, and Zn were also analyzed by 4-acid total dissolution followed by ICP mass spectrometry (TD-ICPMS). Arsenic, Bi, Sb, Se, and Te were analyzed by hydride generation and ICPMS (NP-MS). Hg was analyzed by flow injection mercury system (Hg-FIMS) for the first sample batch and subsequently removed from the analysis package due to inconsistent data. CO_2 and S were analyzed by infrared detection (IR) during combustion. LOI (loss on ignition) was measured during combustion. FeO was analyzed by titration. B was analyzed by prompt gamma neutron analysis (PGNAA). Gold was measured by fire assay with an atomic absorption finish (FA-AA). Gold and Ag were also measured by fire assay – gravimetric (FA-GRA). In cases of elements that were analyzed by more than one method, the analysis with the lowest detection limit was preferred.

Note, when analyzing for FeO, Fe_2O_3 and LOI on Fe-rich samples, oxidation of FeO to Fe_2O_3 during combustion results in a mass gain that must be accounted for (Dahéron et al., 2015). As a result, negative

LOI values can be obtained and Activation Laboratories provided a "LOI2" correction of LOI, along with a Total1 and Total2 for major elements.

1.2.5 Petrography

Petrographic studies at the micro-scale provide critical insight on the characteristics of the ore (objective 2), its associated hydrothermal alteration (objective 3) and to document timing relationships of tectono-metamorphic events (objective 4). They also provide general data regarding the nature of lithologies, metamorphism, and structures.

Polished thin/thick sections – A polished thin (30 µm) section was made from each lithogeochemistry sample. Thick (200 µm) sections were also done for samples used for LA-ICP-MS 2D elemental mapping (section 1.2.8). The sections were done by Vancouver Petrography Ltd. in Langley, British Columbia. Section size was the standard 26 by 46 mm. Thin sections were examined at the INRS-ETE using a standard metallogenic microscope with transmitted and reflected light.

1.2.6 Mineral chemistry

Mineral chemistry can provide key information to characterize: the composition of the mineral assemblages hosting the ore zones (objective 2), the nature and chemistry of the hydrothermal mineral assemblages associated to the mineralization vs. the metamorphic assemblages (objective 3), and their relative chronology with other events (objective 4). Mineral chemistry may also serve as a tool for exploration vectoring (objective 5). Mineral growth history occurs over variable periods of time and can include several growth stages. In a context where the regional metamorphic paragenesis and ore-associated alteration mineralogy comprise similar mineral species, spatial mineral chemical variations can represent a key tool to distinguish them and hopefully to provide exploration vectors. Consequently, several sets of thin sections were selected to document the composition of specific minerals.

Quantitative analyses were carried out with an automated five-spectrometer Cameca SX-100 electron microprobe by wavelength dispersive X-ray analysis (WDX) at the Laboratoire de Microanalyse du Département de Géologie et de Génie géologique of Laval University in Quebec City. Background positions were carefully selected to avoid peak overlap. Most background measurements were made at 50% peak counting time on each side of the analyzed peak. Raw X-ray data were converted to elemental wt.% by the Cameca PAP matrix correction program. A series of well-characterized natural and synthetic minerals and compounds were used for calibration. All mineral phases were analyzed using a 15-kV accelerating voltage, 20-nA beam current, 5-mm electron beam with a counting time of 20 s.

1.2.7 Geochronology

The geochronological component of this study was designed to improve the general understanding of the local and sub-regional geological and structural settings (objective 1) by increasing the amount of age constraints available in the North Caribou belt lithostratigraphic sequence. Zircon U-Pb geochronological analyses were done on 18 samples of intermediate to felsic lithologies from various localities as identified on the geological map (Breaks et al., 2001). The chronology of geological and metallogenic events (objective 4) was also addressed through zircon U-Pb dating of key geological units, as well as *in situ* monazite U-Th-Pb dating to establish the timing of metamorphism (Appendix II; Zhu et al., 1997; Zhu and O'Nions, 1999). Dating of lamprophyre dykes was also attempted, but no zircon was found (Appendix III).

1.2.7.1 U-Pb analyses on zircon

U-Pb analyses were carried out by V. McNicoll and colleagues at the geochronological laboratory of the GSC in Ottawa. Analytical techniques follow that of McNicoll et al. (2016, and references therein), as described below.

Heavy minerals were concentrated from the samples using standard crushing, grinding, and separation on a Wilfley table and by heavy liquid techniques. Mineral separates were sorted by magnetic susceptibility using a Frantz^{TM} isodynamic separator and hand-picked using a binocular microscope. All analyses were done on single zircon grains that were either chemically abraded following the techniques of Mattinson (2005) or strongly air abraded (Krogh, 1982). The former were annealed for 48 hours at 1000°C prior to leaching with HF at 180°C for varying lengths of time.

U-Pb isotope dilution thermal ionization mass spectrometry (ID-TIMS) techniques utilized in this study are modified after Parrish et al. (1987). Treatment of analytical errors follows Roddick (1987), with regression analysis modified after York (1969). Procedural blank levels were generally on the order of 0.5-1.0 pg for Pb. Age uncertainties are presented at the 2σ level.

1.2.7.2 In situ U-Th-Pb analyses on monazite

In situ U-Th-Pb analyses on monazite were done using the GSC's sensitive high-resolution ion microprobe (SHRIMP) (Stern, 1997). Thin sections of a favourable lithology (i.e., garnet-biotite schist) that had been previously described were selected and imaged under a Zeiss Evo scanning electron microscope (SEM) to locate monazite grains. Back-scattered electron (BSE) images were generated for

each monazite grain, to identify internal compositional domains if present, and to guide analytical spot placement. After careful examination and ranking of monazite grains based on their shape, size, and textural petrographic setting, they were cored (3-mm diameter) from thin sections and mounted in epoxy together with pre-polished laboratory standard monazites (GSC medium-Th monazite from paragneiss z3345; $^{207}Pb/^{206}Pb$ TIMS age = 1821.0 ± 0.6 Ma (2σ); GSC low-Th monazite from granite z2908, $^{207}Pb/^{206}Pb$ TIMS age = 1795 ± 2 Ma (2σ); GSC bimodal monazite z8153; $^{206}Pb/^{238}U$ = 513 Ma; Stern and Berman, 2000). Sample preparation followed requirements of Rayner and Stern (2002), and analytical protocols for monazite are described in detail by Stern and Sanborn (1998) as well as Stern and Berman (2000). Analyses were conducted using a 16O- primary beam, with an elliptical spot size of 7 x 9 µm. Ten masses were sequentially measured over 6 scans with a single electron multiplier and a pulse counting system with deadtime of 24 ns. Off-line data processing was accomplished using customized in-house software. Isoplot v. 4.15 (Ludwig, 2003) was used to generate the concordia plot and calculate weighted means. Error ellipses on the concordia diagram and the weighted mean error are reported at 2σ.

1.2.7.3 Re-Os analyses on arsenopyrite

Re-Os geochronology was attempted through collaboration with R. Creaser (University of Alberta). The analysis of 2 samples unfortunately did not yield interpretable data.

1.2.8 2D elemental mapping by LA-ICP-MS

Recent developments in analytical techniques and data processing software have enabled the characterization of mineral phases by elemental mapping (Jackson et al., 2009). While primarily focused on sulphide minerals in ore (Cabri and Jackson, 2011; Jackson et al., 2013), these techniques can be applied on other minerals, such as silicates. To document some geochemical characteristics of gold mineralization at Musselwhite (objective 3), a selection of garnet porphyroblasts from the matrix of high-grade gold ore, was mapped. This activity was conducted in collaboration with S. Jackson from the GSC-O, who handled the analytical part following the methodology of Cabri and Jackson (2011).

1.3 Banded Iron Formations

1.3.1 Introduction

Banded iron formations are a central element of this study as they host most (≥90%) of the ore at Musselwhite. A review of the literature concerning their genesis, primary characteristics, and evolution through geological times is presented below. Such information has influenced the approach and methodology used to reach the objectives of the project, especially those regarding the petrography and lithogeochemistry of the various iron formation facies and their relationships with gold mineralization. Such review does not aim at resolving ongoing debates regarding the processes of iron formation deposition and genesis, but rather at giving an overview of current knowledge to provide a background for interpretations and discussions.

1.3.2 Definition

Iron formations (IF) are a distinct rock type that results from the lithification of "*chemical sediment, typically thin-bedded or laminated, containing 15 percent or more iron of sedimentary origin, commonly but not necessarily containing layers of chert*", as defined by James (1954). Although very general, this definition avoids the exclusion of rocks referred to as iron formations such as "Itabirites" in Brazil (James, 1954), yet includes rock types such as sulphide-rich argillite that have facies relationships with more classical iron formations. Trendall (1983) suggested refining the definition by replacing the mention of the "15 percent or more iron" for a more inclusive "*an anomalously high content of iron*", as some ferruginous rocks could be excluded by James' (1954) initial definition. For consistency, in this study the term banded iron formation (BIF) is used to designate all lithologies falling under the aforementioned definitions, including their few non-banded occurrences.

Most iron formations are Precambrian in age (Trendall, 1968). They are the product of a wide range of processes involving numerous parameters (Bekker et al., 2010), which will be briefly reviewed hereafter (section 1.4). This complexity in iron formations deposition and genesis and the ensuing diversity in chemical composition and textures spark recurring discussions over a more detailed classification (Klein, 2005).

1.3.3 Classification

Three major types of BIF have been distinguished, mainly on the bases of the inferred tectonic environments of the host stratigraphic sequence (Figure 1-3; Gross, 2009): Algoma, Superior and Rapitan types.

1.3.3.1 Algoma-type BIF

Named after the BIF of the Helen mine, in the Wawa area of the Algoma District in Ontario (Goodwin, 1962; Gross, 1965), Algoma-type BIF is characterized by a host sequence dominated by volcanic rocks. The latter are ultramafic to felsic in composition and associated with variable proportions of sedimentary units of greywacke, shales, or volcaniclastic rocks (Gross, 1996; Jébrak and Marcoux, 2008). These iron formations are linked to strong hydrothermal activity in tectonic environments, such as volcanic arcs, spreading ridges, rift graben, or volcanic centers (Figure 1-3). They occur in major abundance and thicknesses during the Archean eon (Beukes and Gutzmer, 2008; Klein, 2005; Bekker et al., 2010) and can be as old as 3.8-3.7 Ga (Isua, Greenland; Katsuta et al., 2012).

1.3.3.2 Superior-type BIF

Superior-type BIF has been defined from the study of iron formations distributed between Lake Superior and Lake Michigan (Gross, 1965, 1980, 2009). They are characterized by a host sequence dominated by sedimentary rocks such as conglomerates, arenites, greywackes, shales, and carbonate rocks deposited on a platform, along a passive margin of a continent or craton (Figure 1-3). Most Superior-type BIFs are Paleoproterozoic in age (Klein, 2005). The Hamersley basin BIF in Western Australia is one of the most famous examples.

1.3.3.3 Rapitan-type BIF

Rapitan BIFs are a minor younger type, specifically associated with glacial sedimentary deposits, usually formed of sandstone and conglomerate (Klein and Beukes, 1993). They commonly have a much more restricted extent compared to that of their host sequences (Bekker et al., 2010), which are mostly Cryogenian in age (e.g., Neoproterozoic; Klein, 2005).

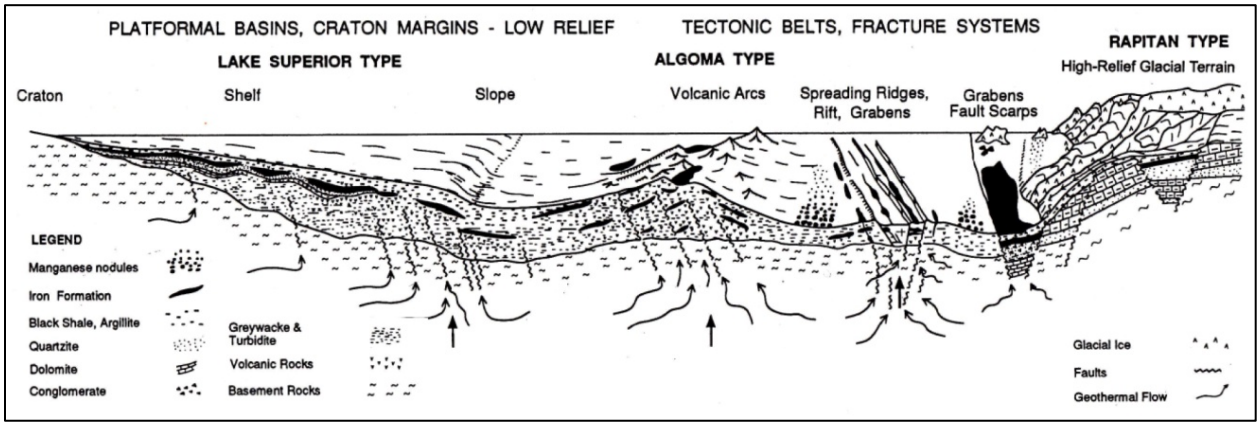

Figure 1-3: Tectonic environments of iron formations in shelf, ridge and back-arc settings (from Gross, 2009).

1.3.4 Space-Time distribution

Precambrian iron formations are frequently deformed and metamorphosed, which often make their classification difficult (Bekker et al., 2010). Algoma- and Superior-type BIF are present around the world, concentrated within cratonic basement (e.g., Yilgarn craton, Superior province; Figure 1-4). BIF deposition occurred over a large time span. Algoma-type BIFs tend to be Archean in age, whereas Superior-type BIFs formed mostly during the Proterozoic (Figure 1-5). Algoma-type BIFs are more common and tend to be thin and small in volume, while Superior-type BIFs are fewer, but much thicker, laterally extensive, and continuous (Figure 1-5B). There is a notable drop in the deposition of BIF after 1.8 Ga, which has been linked to a major change in redox conditions in the atmosphere and oceans (Bekker et al., 2010); an event also referred to as the *Great Oxidation Event*.

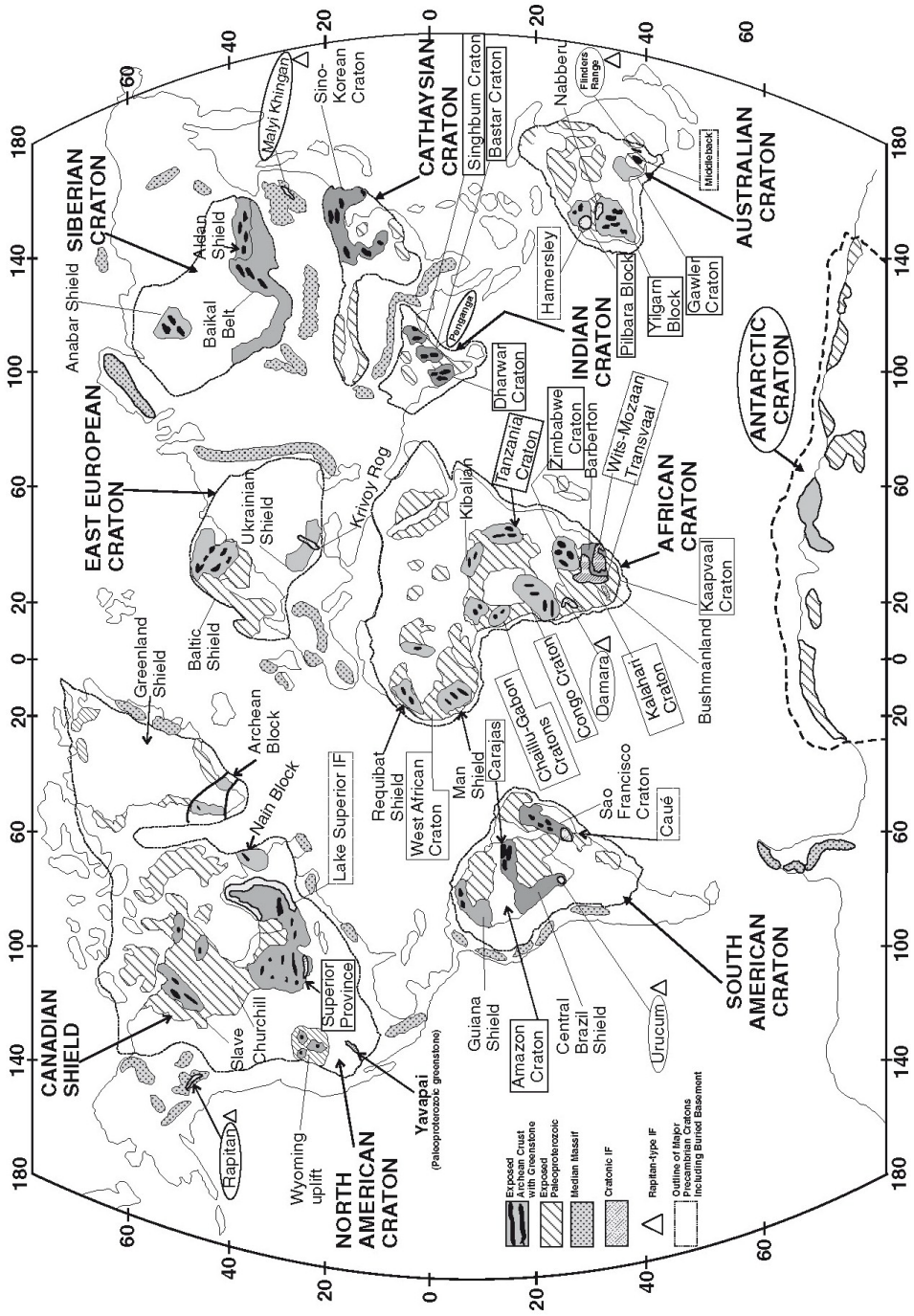

Figure 1-4: Global map showing the distribution of Precambrian cratons and successions containing iron formations. The distribution of greenstone belts is schematic (from Beukes and Gutzmer, 2008, modified after Goodwin, 2000).

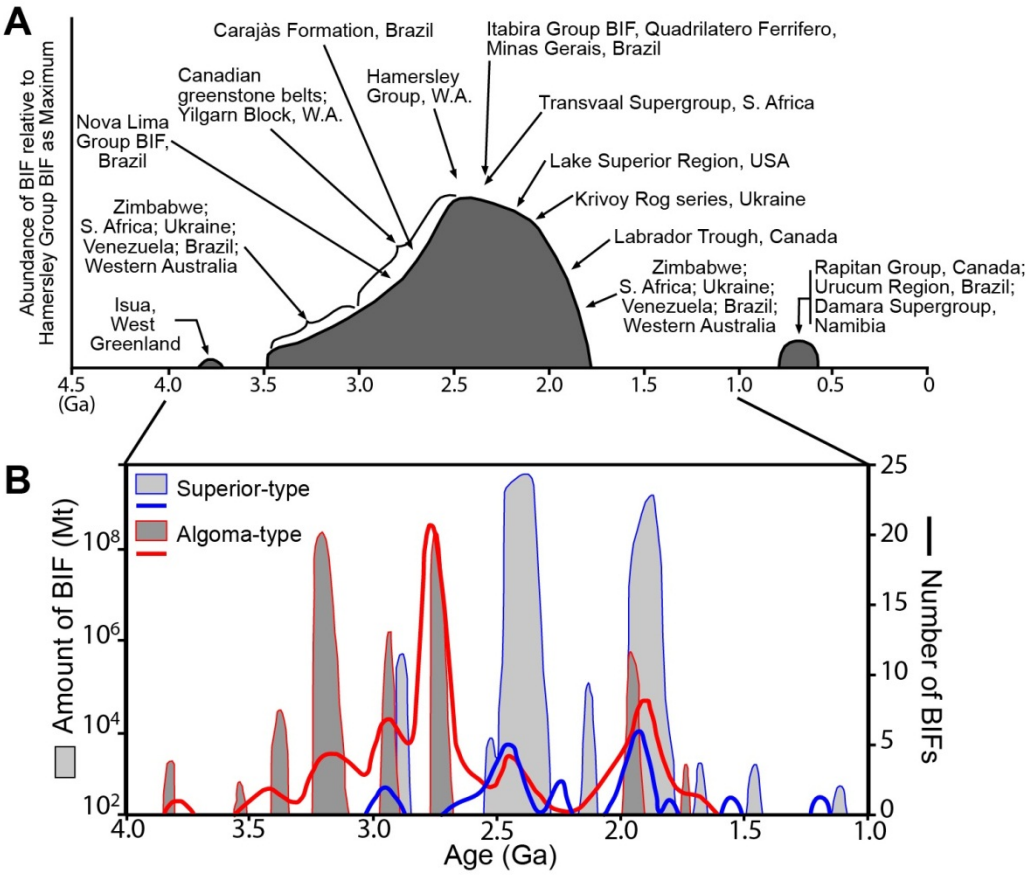

Figure 1-5: BIFs through time. A. Schematic diagram showing the relative abundance of Precambrian BIFs vs. time, with several of the major BIFs or major BIF regions identified (from Klein, 2005). Estimated abundances are relative to the Hamersley Group BIF volume taken as a maximum (adapted from Gole and Klein, 1981a; also based on compilation of BIF dates in Walker et al., 1983). Recent age evaluations for the Hamersley Basin (2.8 to 2.2 Ga) are available from Trendall et al. (2004); for the Labrador Trough BIFs (1.88 Ga) from Findlay et al. (1995), and for the BIFs in the Frere Formation, Western Australia (1.9 to 1.8 Ga) from Williams et al. (2004).; B. Temporal distribution of Algoma- and Superior-type iron formations according to amount (plain curves) and numbers (empty curves), between 4.0 Ga to the end of the Mesoproterozoic (from Beukes and Gutzmer, 2008, based on Huston and Logan, 2004).

1.3.5 Significance of iron formations

Iron formations are the product of a complex interplay of factors, including oceanic and atmospheric conditions, hydrothermal activity, detrital input, and biogenic contribution (Bekker et al., 2010). Superior-type BIFs can be well preserved and some are very weakly metamorphosed, whereas Algoma-type BIFs are commonly poly-deformed and poly-metamorphosed up to amphibolite or granulite facies. For that reason, most of the research on deposition processes and elaboration of genetic models of BIFs mainly originates from studies of Superior-type BIF (Klein, 2005; Beukes and Gutzmer, 2008; Bekker et al., 2010). They are also useful to document Precambrian environmental or paleoecological conditions

(Trendall, 1973; Beukes and Gutzmer, 2008; Bekker et al., 2010) or for paleocontinent reconstructions (e.g., Vaalbara paleocontinent; Beukes and Gutzmer, 2008).

Because they contain unusual amounts of iron, BIFs have been a primary target for iron ore as some have been subjected to epigenetic processes that upgraded their iron content to up to ca. 65 wt% Fe (Clout and Simonson, 2005). China, Australia, and Brazil dominate the global market for iron ore and also have major reserves associated with large deposits in Superior-type iron formations (Clout and Simonson, 2005). Iron formations are also host to significant epigenetic gold mineralization (Phillips et al., 1984). They are not as common as orogenic quartz-carbonate veins hosted in mafic volcanic and intrusions (Dubé et al., 2011; Dubé and Mercier-Langevin, 2015), yet they have the potential to form world-class size deposits. Consequently, BIF-associated gold mineralization constitutes an important exploration target in Precambrian terranes.

1.4 General characteristics of Algoma-type iron formations

1.4.1 Depositional environment

Algoma-type BIFs (Gross, 1959, 1965, 1983) are mostly found in association with volcanic rocks in Archean greenstone belts. Their geodynamic depositional environments have been related to rift settings, oceanic spreading ridges, or active volcanic centers (Gross, 1980). These tectonically dynamic environments are associated with important magmatic and hydrothermal activity as well as highly variable detrital inputs related to irregular and instable basin topography. The chemical sediment, precursor to the iron formation, is thus the combination of elements derived from hydrothermal, detrital and ambient seawater sources, and the resulting facies and mineralogy reflect the variations of those diverse inputs (Figure 1-6A, B).

1.4.2 Chemical sediment precursor and lateral facies variations

The Red Sea (Bölstrom, 1973) or the Atlantic mid-ocean ridge (Rudnicki, 1995) have been used to study the characteristics of iron formation genesis, as well as volcanogenic massive sulphide (VMS) formation, and the use of BIF for mineral exploration of VMS (Figure 1-6B; Spry et al., 2000; Gibson et al., 2015; Peter, 2003). In these environments, the thermal influx in the crust generates hydrothermal cells where cold seawater percolating through the oceanic crust is heated and circulates toward a discharge point (Skirrow and Franklin, 1994), or hydrothermal vent. During their ascent, fluids interact with the host rocks and, upon discharge into the seawater, have acquired drastically different characteristics (e.g.,

higher temperature, lower pH, high metal content, different rare earth element profiles and isotopic signatures; Skirrow and Franklin, 1994). In some cases, contamination by magmatic fluids can also contribute to these changes (Franklin et al., 2005).

A number of processes take place when the buoyant hydrothermal plume rises and interacts with the cold ambient seawater, which has very different physico-chemical characteristics (Figure 1-6C). The sudden drop in temperature has a huge effect on the solubility of many elements (Gibson et al., 2015): in the immediate vicinity (<50 m) with respect to the high-temperature (350-400°C) hydrothermal vent, the first minerals to precipitate are sulphides containing Cu, Pb, Zn, Ag, Fe (Figure 1-6B, C; Lydon, 1984), and in some cases, Au (Dubé et al., 2007). In proximal settings (tens to hundreds of metres) from the main hydrothermal vent or in low temperature hydrothermal systems (i.e., 150-200°C), "white smokers" precipitate sulfates, such as barite (Lydon, 1984). Following sulfur precipitation, carbonate particles precipitate and as the hydrothermal plume rises and expands, iron may oxidize, depending on the redox conditions of surrounding seawater (Figure 1-6D; Parr and Plimer, 1993; Peter, 2003). Recycling of some of the particles occurs at the base of the plume (Figure 1-6C), and is prolonged in the case of non-buoyant hydrothermal plume (Rudnicki, 1995), allowing for further interaction of particles with seawater and scavenging of various elements (incl. P, V, Cr, As, REE). This scavenging also occurs as the hydrothermal plume is dispersed, potentially in presence of oceanic bottom currents (Figure 1-6B, C).

Precambrian oceans are characterized by chemoclines of redox conditions (Figure 1-7; Klein and Beukes, 1989; Klein, 2005; Beukes and Gutzmer, 2008; Bekker et al., 2010), which had an important impact on the circulation of elements in solution and their precipitation and are widely presented in genetic models of BIF. Many additional factors, such as atmospheric conditions, influenced transfers between atmosphere and oceanic waters and impacted the nature of the material coming from emerged landmasses (Kamber, 2010). The photic zone depth also controlled biogenic contribution in the BIF final isotopic signatures. For shallow hydrothermal activity, the wave base depth also influenced physico-chemical conditions (50-100 m, occasionally 200 m; Beukes and Gutzmer, 2008).

The hydrothermal activity leading to VMS and/or Algoma-type iron formation deposition depends on the temporal evolution of thermal input and the frequency of volcanic episodes (Peter, 2003). Such variability may result in the formation of a unique or multiple BIF and/or VMS horizon(s) with complex lateral facies changes (Figure 1-6D).

BIF deposition is characterized by the production of compositional banding at various scales: sub-millimetres to millimetres (microbands), centimetres (mesobands), and metres to several tens of metres (macrobands; Trendall and Blockley, 1970). The cause of this compositional banding could relate to annual cycles (Trendall and Blockley, 1970), solar and tidal cycles (Trendall, 1973; Walker and Zahnle,

1986; Williams, 2000; Müller et al., 2005), Milankovitch cycles during the Precambrian (Simonson and Hassler, 1996; Pickard et al., 2004), or biological activity at shallow depth (Hashizume et al., 2016). In the case of chert layers, syn-deposition mechanisms are considered (Clout and Simonson, 2005): biogenic fixation in the water column (LaBerge et al., 1987), concentration of silica by evaporation and co-precipitation (Ewers, 1983), or silica aggregation in response to electrolytic changes (Morris, 1993). Post-sedimentation processes are also possible, such as early-diagenetic separation of silica from iron compounds leading to the formation of a separate layer (Trendall and Blockley, 1970; Slack et al., 2007; Fischer and Knoll, 2009), although a study of metamorphosed BIF in the Yellowknife greenstone belt suggests it is unlikely (Katsuta et al., 2012).

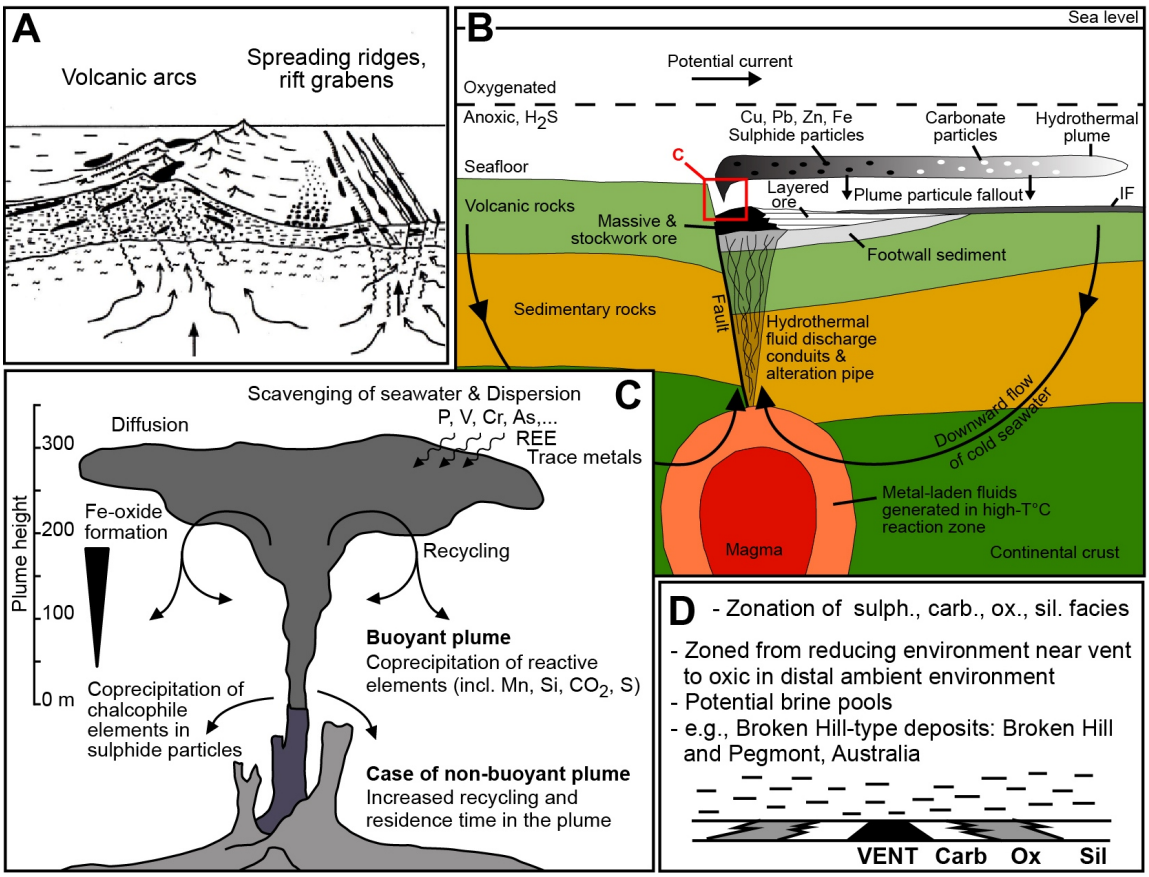

Figure 1-6: Algoma-type IF depositional environment and processes A. Schematic geodynamic settings for Algoma-type iron formation deposition (inset of Figure 1-3); B. Schematic cross sections depicting the hydrothermal plume end-member model for formation of iron formation (IF) that is spatially and temporally associated with VMS mineralization (modified after Spry et al., 2000); C. Chemical and physical processes in the TAG hydrothermal plume, Mid-Atlantic Ridge (modified after Rudnicki, 1995); D. Schematic representation of lateral facies changes in Algoma-type iron formation (modified after Peter, 2003).

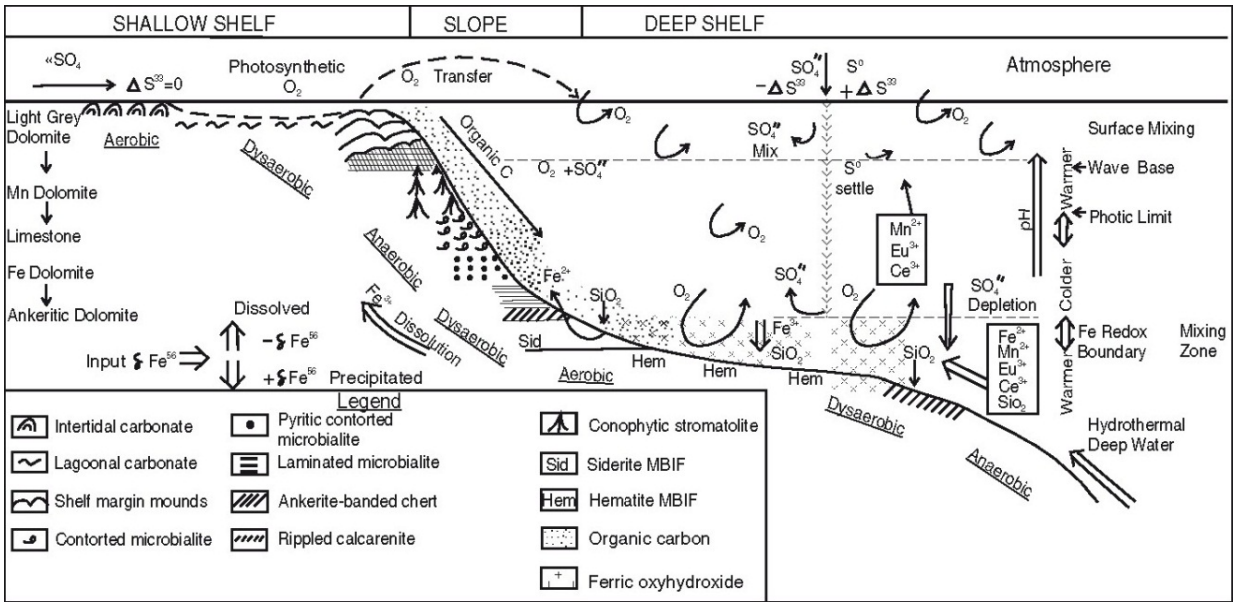

Figure 1-7: Model for deposition of iron formation in deep-shelf environments in association with shallow-shelf to deepwater platform carbonates, from Beukes and Gutzmer (2008). The model is largely based on stratigraphic relationships observed in the Gamohaan-Kuruman succession and has significant differences with the earlier model of Klein and Beukes (1989).

1.4.3 Mineralogy and metamorphism

After precipitation and the first diagenetic processes (i.e., compaction, lithification, etc.) and possibly very low metamorphism, the mineralogy of the silica-rich gel invariably produces chert layers, while iron-rich beds mineralogy is distributed between four groups that define the iron formation facies: sulphides, carbonates, silicates, and oxides (Table 1-1). As metamorphic grade increases, mineralogical changes occur and induce devolatilization (French, 1968, 1973; Haase, 1982; Klein, 1983, 2005), and element redistributions (Katsuta et al., 2012). These changes occur through oxidation-reduction and/or hydration-decarbonation equilibria (Haase, 1982); processes that may be difficult to distinguish based on mineral textural relationships (Frost, 1979a, b). The main metamorphic reactions occurring in iron formations depend on the composition of the facies in which they occur (i.e., the relative proportions of carbonate, oxide, and silicate minerals) and will produce varying proportions of H_2O and CO_2 (Haase, 1982; Klein, 2005). Oxide and carbonate minerals have stability fields extending through most of low- (Haase, 1982), medium- and high-grade metamorphism (Klein, 2005). However, minerals of both types can be involved in metamorphic reactions of silicate minerals, such as the transition of greenalite to minnesotaite + magnetite (French, 1968), the conversion of stilpnomelane + ankerite to grunerite (Haase, 1982), or the reaction of magnetite + quartz + H_2O to produce grunerite (Klein, 2005). The silicate mineralogy of the iron formation is its most evolving component (Figure 1-8), with serpentine-like material (greenalite)

converted to iron-rich talc (minnesotaite) and aluminous talc-like minerals (stilpnomelane), which in turn produce chlorite (chamosite) or amphiboles (e.g., grunerite) and, under higher metamorphic conditions, pyroxenes and olivine (Table 1-2).

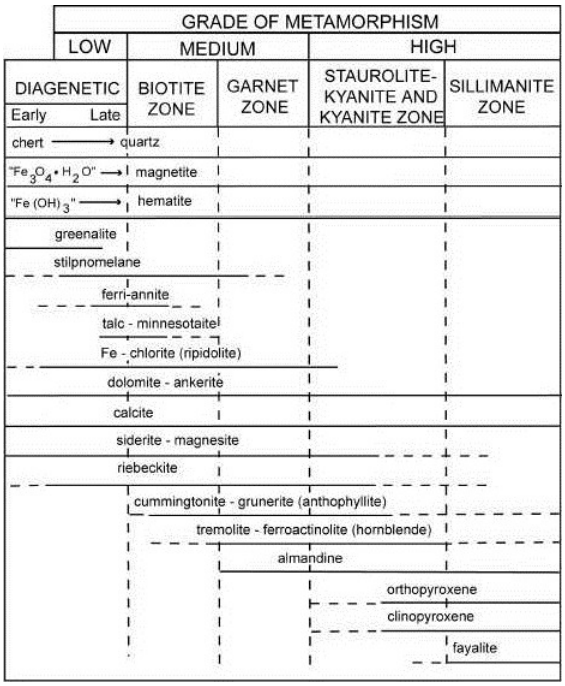

Figure 1-8: Relative stabilities of minerals in metamorphosed iron formations as a function of metamorphic zones, from Klein (1983).

1.4.4 Geochemistry of banded iron formations

SiO_2 and total Fe_2O_3 (Fe_2O_3 (T)) dominate the bulk composition of BIF, constituting up to 70 wt% of the rock. Generally they range between 34-56 wt% and 20-40 wt%, respectively (Klein, 2005). The Fe_2O_3/FeO ratio shows variations controlled by the main mineral assemblage of the BIF facies (e.g., higher in oxide-dominant). Al_2O_3 is present in highly variable proportions, from virtually absent (Klein, 2005) to slightly over 20 wt% (Klein and Fink, 1976; Peter, 2003). K_2O, TiO_2, and Na_2O also constitute a fairly small portion of the BIF and are associated to Al_2O_3 in the detrital part (Peter, 2003). CaO, MgO, MnO, and P_2O_5 – in decreasing respective amounts – are minor components, and MnO and P_2O_5 can be close to absent. Along with other features such as REE abundance (Bau and Dulski, 1996), Al_2O_3 can be used as a proxy for detrital input in the iron formation sequence (Boström, 1973; Klein, 2005; Beukes and Gutzmer, 2008). The quantification of detrital contamination was first attempted by Boström (1973), using modern seafloor hydrothermal systems and sediments as analogs (Figure 1-9).

Table 1-1: Relative stabilities of predominant constituent minerals in metamorphosed iron formations (modified after Peter, 2003, and Spry et al., 2000). Based on data from French (1968, 1973), Immega and Klein (1976), Frost (1979a), Haase (1982), Klein (1983), and Miyano and Klein (1986). Abbreviations (brackets denote possible presence or presence in lesser amounts): Act actinolite; Agt aegerine-augite; Alm almandine; Ank ankerite; Ann annite; Ath anthophyllite; Aspy arsenopyrite; Bd berthierine; Bt biotite; Cc calcite; Cb cubanite; Cpy chalcopyrite; Chm chamosite; Cln clinochlore; Cum cummingtonite; Dol dolomite; Fa fayalite; Fe-Ann ferro-annite; Ged gedrite; Gn galena; Gnl greenalite; Gru grunerite; Hbl hornblende; Hem hematite; Hd hedenbergite; Mt magnetite; Mgs magnesite; Mn minnesotaite; Nn nontronite; Po pyrrhotite; Py pyrite; Qtz quartz; Rbk riebekite; Sd siderite; Sp sphalerite; Sps spessartine; Stp stilpnomelane; Tlc talc; Tr tremolite; Wtz wurtzite; Zrn zircon.

General Mineral type	Precursor mineral	Low-grade metamorphism	Intermediate-grade metamorphism	High-grade metamorphism
Temperature range		200-350°C	350-550°C	>550°C
Sulphides				
Fe sulphides	Py, Po, Aspy	Py, Po, Aspy	Py, Po, Aspy	Py, Po, Aspy
Pb sulphides	Gn	Gn	Gn	Gn
Zn sulphides	Sp, Wtz	Sp, Wtz	Sp	Sp
Cu-Fe sulphides	Ccp, Cb	Ccp, Cb	Ccp, Cb	Ccp, Cb
Carbonates				
Fe carbonate	Sd	Sd	Sd	Sd
Ca-Fe carbonate	Ank	Ank	Ank	Ank
Mg carbonate			Mgs	
Ca-Mg carbonate	Dol	Dol	Dol	Dol
Ca carbonate	Cc	Cc	Cc	(Cc)
Oxides				
Hydrated Fe oxides	Hydrated Fe oxides	Hem, Mt	Hem, Mt	Hem, Mt
Gahnite		(Gah)	Gah	Gah
Silicates				
Quartz	Amorphous silica	Chert/Qz	Chert/Qz	Chert/Qz
Serpentine-like	Amorphous Gnl, Brt	Gnl, Brt	Gnl, Brt	
Talc-like structure	Nn, amorphous Fe oxide	Stp, Fe-Ann, Bt	(Stp), Fe-Ann, Bt	
Fe-talc	Nn	Mn, Tlc	(Mn)	
Fe-Mg chlorite	Chm, Cln	Chm, Cln	(Chm, Cln)	
Na-rich amphibole		Rbk		
Mg-Fe amphiboles		Gru	Gru-Cum, Ath, Ged	Gru-Cum, Ath, Ged
Ca-Fe-Mg amphiboles		Act-Tr, Hbl	Act-Tr, Hbl	
Mn-Fe-Al rich	Chm?	(Sps)	Alm, Sps	Alm, Sps
Orthopyroxene			(Fs)	Fs
Clinopyroxenes		(Agt)	Agt, Hd	Agt, Hd
Fe olivine			(Fa)	Fa
Zircon	Zrn	Zrn	Zrn	Zrn
Phosphates				
Apatite		Ap	Ap	Ap

Table 1-2: Some mineralogical reactions during low- to high-grade metamorphism in iron formations, from French (1968), Frost (1979a), Haase (1982), Klein (2005), and references therein.

Reactants									→	Products					Volatiles			
		greenalite	+	O2					→	magnetite			+	qz		+	H2O	
siderite									→	magnetite					+	CO2		
ferro-dolomite			+	O2					→	magnetite			+	ankerite	+	CO2		
		greenalite	+	qz					→	minnesotaite						+	H2O	
		greenalite							→	minnesotaite	+	magnetite				+	H2O	
		chlorite/chamosite	+	qz					→	stilpnomelane						+	H2O	
		stilpnomelane	+	excess Fe					→	minnesotaite	+	Al, trace Na, K				+	H2O	
		stilpnomelane	+		+	H2O			→	minnesotaite	+	chlorite	+	qz				
siderite			+	qz	+	H2O			→	minnesotaite					+	CO2		
ankerite			+	qz	+	H2O			→	grunerite			+	calcite	+	CO2		
		magnetite	+	qz	+	H2O			→	grunerite								
		minnesotaite							→	grunerite			+	qz		+	H2O	
ankerite	+	stilpnomelane							→	grunerite	+	hornblende			+	CO2	+	H2O
Siderite									→	magnetite					+	CO2		
siderite			+	qz					→	grunerite					+	CO2		
Fe-dolomite			+	qz					→	grunerite	+	tremolite	+	calcite	+	CO2		
calcite	+	grunerite							→			actinolite			+	CO2	+	H2O
ankerite	+	grunerite							→			actinolite			+	CO2	+	H2O
ankerite	+	chlorite/chamosite	+	qz					→	grunerite	+	garnet			+	CO2	+	H2O
siderite		chlorite/chamosite	+	qz					→	grunerite	+	garnet			+	CO2	+	H2O
		chlorite/chamosite	+	qz					→	grunerite	+	garnet					+	H2O
ankerite			+	qz					→	clinopyroxene					+	CO2		
calcite	+	grunerite	+	qz					→	clinopyroxene					+	CO2	+	H2O
siderite			+	qz					→	orthopyroxene					+	CO2		
		grunerite							→	orthopyroxene			+	qz			+	H2O
		grunerite							→	olivine							+	H2O

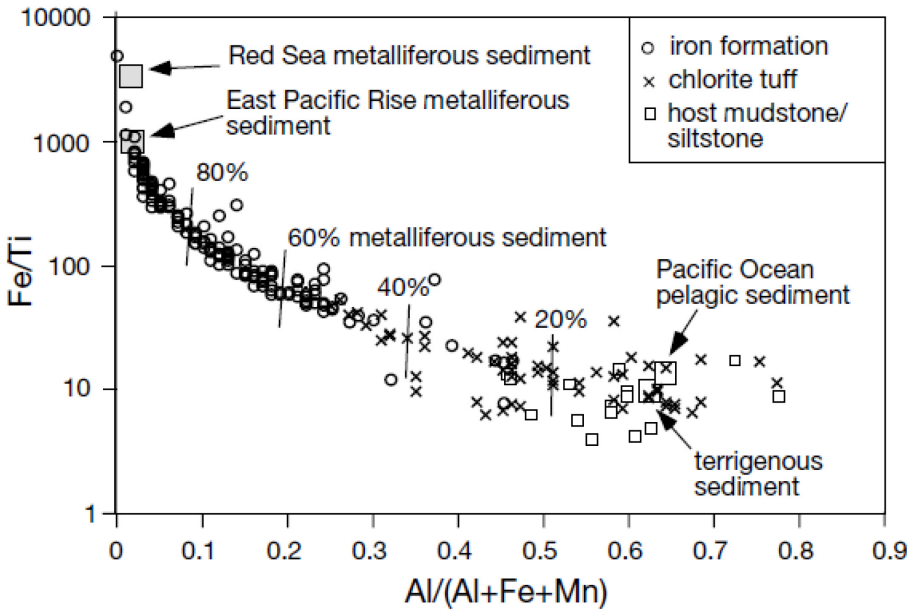

Figure 1-9: Diagram of Fe/Ti vs. Al/(Al + Fe + Mn) ratios for iron-formation and chlorite tuff samples from the Heath Steele belt (n = 218; after Boström, 1973) from Peter et al. (2003). This plot is used to estimate the hydrothermal contribution to sediments. Host mudstone-siltstones from the Heath Steele belt are also shown, as well as the average pelagic Pacific Ocean sediment, terrigenous sediment, and East Pacific Rise metalliferous sediment (Boström, 1973).

Statistical analyses such as multidimensional scaling (Kruskal, 1978) and cluster analysis (Hartigan, 1975) have been used to differentiate the main sources for trace metals and REE in BIF (Peter, 2003; Moran, 2008). Be, Ce, Co, Cr, Ga, Hf, La, Lu, Nb, Ni, Rb, Se, Ta, Th, U, V, Y, Yb, and Zr seem to be related to detrital input (Pearson Product Moment inter-element correlations, in Peter, 2003), and sub-groups can be related to aluminosilicates or feldspar. Fe_2O_{3T} and CaO, CO_2, P_2O_5, Sr, S, Ag, As, Au, Bi, Cd, Cu, Eu, Eu/Eu*, Hg, In, Mo, Pb, Sb, Se, Tl, and Zn are more closely related to hydrothermal products (oxides, carbonates, silicates, and sulphides).

REE profiles are used to identify fluids inputs (Figure 1-10A, C) and distinguish different signatures in the BIF (Figure 1-10B). They are normalized to several standards depending on the geological setting of the BIF and the objectives of the study (Peter and Goodfellow, 1996; Klein, 2005; Moran, 2008; Planavsky et al., 2010; Baldwin, 2011; Haugaard et al., 2013). The chondrite standard (C1, Sun and McDonough, 1995) is commonly used, and other standards include: the North American Shale Composite (NASC; Haskin and Haskin, 1966; Gromet et al., 1984), the Post-Archean Australian Shale (PAAS; Nance and Taylor, 1976; Taylor and McLennan, 1985), and the Mudstone of Queensland (MUQ; Kamber et al., 2005). Key parameters include the Eu/Eu* anomaly intensity as a proxy for hydrothermal input (Alexander et al., 2008), the Y/Y* anomaly as a function of seawater input (Bau and Dulski, 1996), or the Ce/Ce* ratio anomaly for oxidation conditions (Bolhar et al., 2004).

1.5 Metallogenic Context

1.5.1 Introduction

Gold is found in a wide variety of mineral systems and geological contexts throughout geological times (Hagemann and Brown, 2000; Goldfarb et al., 2001, 2005; Groves et al., 2005; Goldfarb et al., 2010). Canada, an important producer, was in 5th position in 2015 with 160 t produced (Figure 1-11A). Three quarters of this gold is extracted in Ontario and Québec (Figure 1-11B; MAC), where fertile Archean terranes occur (Figure 1-12; Dubé and Gosselin, 2007; Lydon, 2007), notably from the outstandingly well-endowed Abitibi sub-province (Gosselin and Dubé, 2005; Robert et al., 2005; Dubé and Gosselin, 2007; Percival, 2007).

A classification scheme for lode gold deposits in Canada was proposed in the early 2000s (Figure 1-13). They are divided into the epithermal, intrusion-related, and greenstone vein clans. The following discussion will focus on the general attributes of greenstone vein clan and BIF-hosted gold deposits in order to provide a suitable background for the present study.

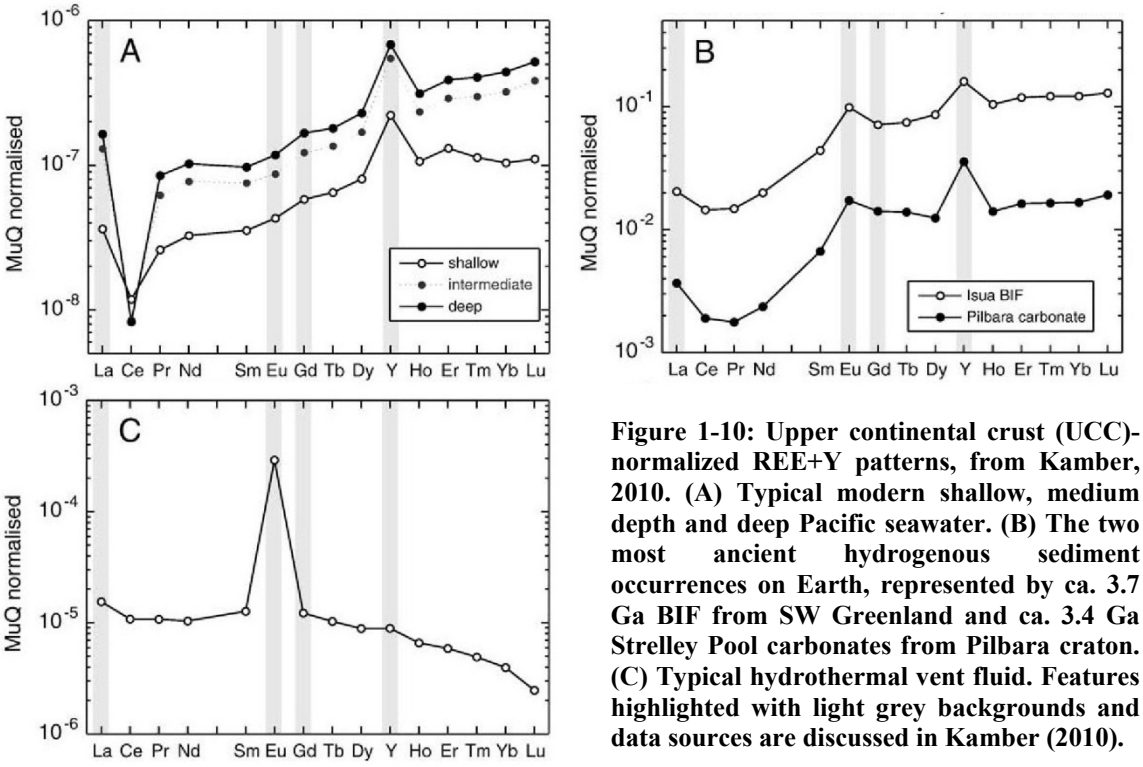

Figure 1-10: Upper continental crust (UCC)-normalized REE+Y patterns, from Kamber, 2010. (A) Typical modern shallow, medium depth and deep Pacific seawater. (B) The two most ancient hydrogenous sediment occurrences on Earth, represented by ca. 3.7 Ga BIF from SW Greenland and ca. 3.4 Ga Strelley Pool carbonates from Pilbara craton. (C) Typical hydrothermal vent fluid. Features highlighted with light grey backgrounds and data sources are discussed in Kamber (2010).

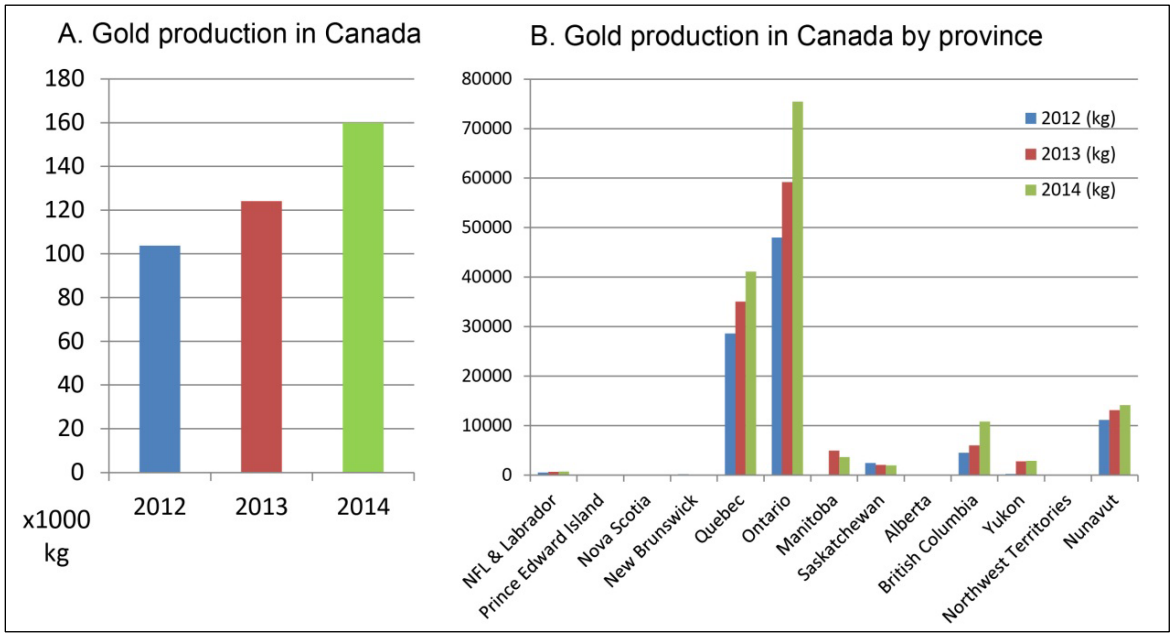

Figure 1-11: A. Annual gold production and B. Canadian gold production, for the period 2012-2014. Data from "Facts and figures, 2015", Mining Association of Canada.

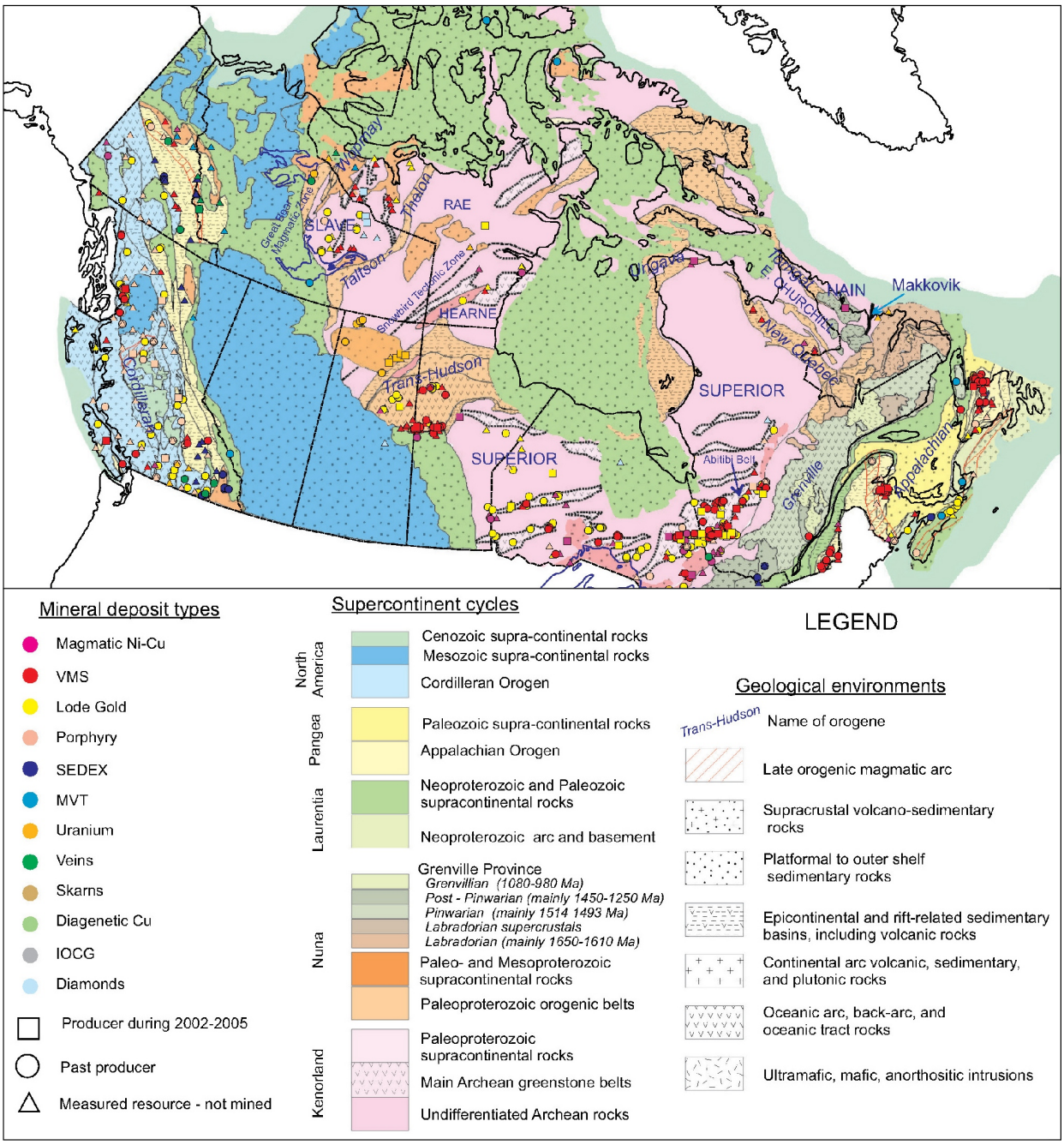

Figure 1-12: Simplified geological map of Canada showing geological domains by supercontinent cycle and the distribution of non-ferrous metalliferous and kimberlite diamond deposits. Deposits are colour-coded by mineral deposit types and shapes of symbol reflect production status. Only deposits for which a mineral resource has been measured are plotted (from Lydon, 2007).

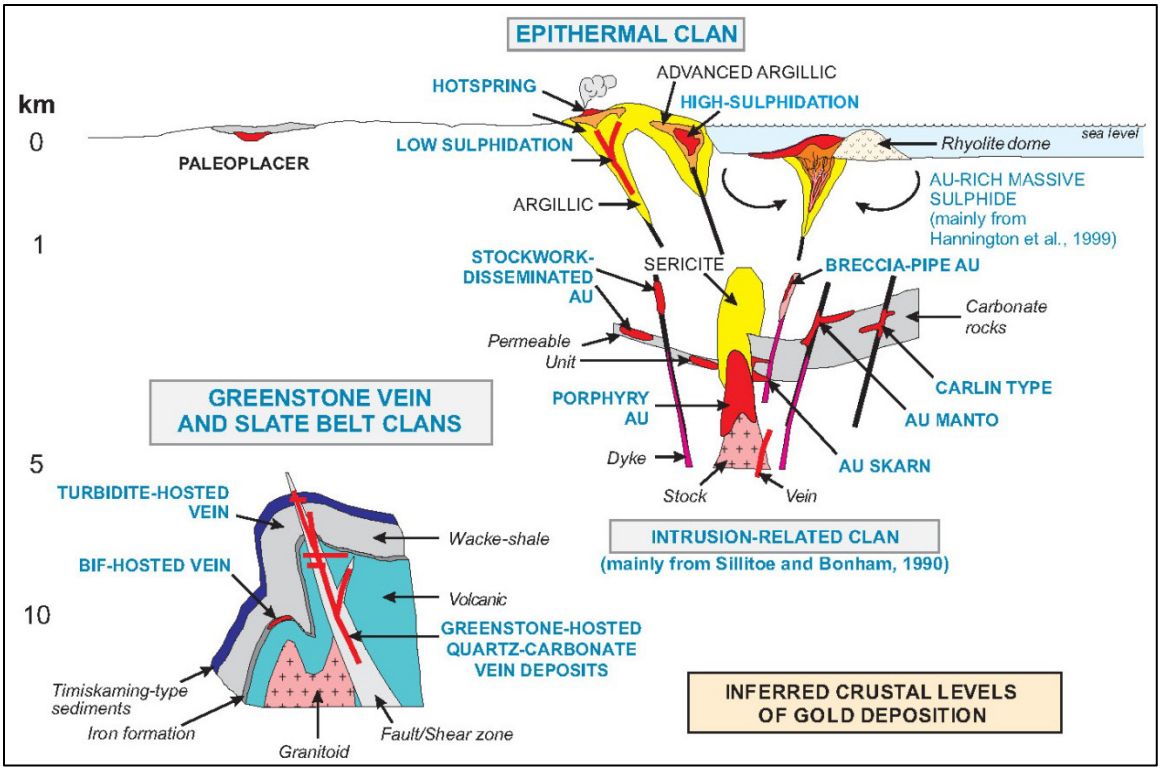

Figure 1-13: Schematic crustal section showing inferred levels of gold deposition for the different clans of lode gold deposits (Dubé et al., 2011, modified from Poulsen et al., 2000, and Dubé and Gosselin, 2007).

1.5.2 Greenstone-hosted vein Au deposits

Greenstone-hosted quartz-carbonate-vein gold deposits are epigenetic and structurally controlled. On a regional scale, as in the Abitibi sub-province or the Goldfields of Western Australia (Robert et al., 2005), their distributions show a close spatial association with major compressional to trans-tensional crustal-scale fault zones (Robert, 1990; Hodgson, 1993; Goldfarb et al., 2005; Dubé and Gosselin, 2007). These fault zones are often major boundaries between lithostratigraphic assemblages of deformed terranes and act as pathways for metamorphic fluids (Goldfarb et al., 2005). They are the result of compressional tectonics, though interpreted by some to be originating from the reactivation of pre-existing major extensional structures (Cox et al., 2001; Bleeker, 2015).

Quartz-carbonate vein gold deposits are associated with second-order structures or splays, and located in dilation zones of regional-scale fault zones (Robert, 1990; Hodgson, 1993; Sibson, 2001). They are hosted by very diverse lithologies: from ultramafic volcanic rocks to granitoid intrusions, with frequent district-specific metallotects. The style variations of gold-bearing vein networks are controlled by specific lithologies constituting structural and/or chemical traps for fluids (Bateman and Hagemann, 2004; Dubé

and Gosselin, 2007, and references therein). The relative timing of mineralization emplacement in relation to the tectono-metamorphic evolution depends on crustal depths (Groves, 1993; Figure 1-14).

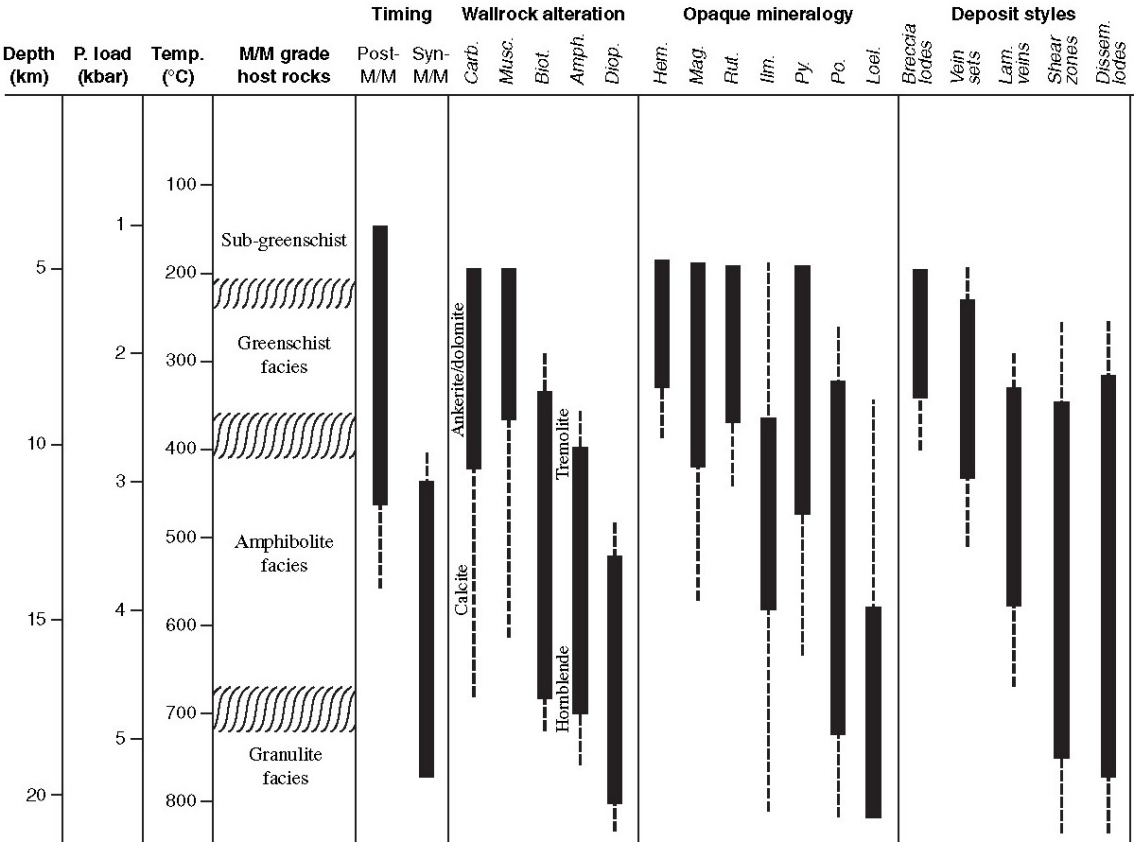

Figure 1-14: Summary of features of the continuum model after Groves, 1993, in Goldfarb et al., 2005. Abbreviations: Amph = amphibole, Biot = biotite, Carb = carbonate, Diop = diopside, Dissem = disseminated, Hem = hematite, Lam = laminated, Lim = limonite, Loel = loellingite, Mag = magnetite, M/M = metamorphic, Musc = muscovite, Po = pyrrhotite, Py = pyrite, Rut = rutile.

A recurrent vein pattern has been documented (e.g., Robert, 1990; Hodgson, 1993; Robert et al., 1994; Robert and Poulsen, 2001, and references therein), consisting of moderately to steeply dipping laminated fault-fill veins lying at low angle to the main foliation, frequently associated with fringing shallow-dipping extension or oblique-extension veins oriented at high angle to the main foliation and elongation lineation. In greenstone-hosted quartz-carbonate-vein gold deposits, the mineralization event is accompanied by widespread hydrothermal fluid flow that produces a geochemical footprint (Goldfarb et al., 2005). In greenschist-facies rock units, major elements variations, distal to proximal to the ore, consist in progressive K_2O, CO_2, and S enrichment, and in leaching of Na_2O, which result in a mineral zonation comprising of a distal chlorite-calcite alteration, grading into an iron(-bearing) carbonates-sericite-sulphides alteration (Phillips et al., 1984; Roberts, 1987; Colvine et al., 1988; Dubé and Gosselin, 2007). The abundance and nature of the carbonates are controlled by the host rock reactivity to H_2O-CO_2-rich

fluids (e.g., Fe-rich tholeiitic rocks, BIF; Groves, 1993). At higher metamorphic grades, amphiboles and biotite are formed before phases such as garnet or pyroxene, while sulphide species evolve into more stable phases (e.g., arsenopyrite to löllingite, pyrite to pyrrhotite; Mueller and Groves, 1991; Witt, 1991; Hagemann and Cassidy, 2000).

1.5.3 Banded-iron-formation-hosted Au deposits

1.5.3.1 Introduction

Banded iron formations (notably the oxide-dominant facies) have higher iron content than most rock types hosting quartz-carbonate gold deposits in greenstone belts, even mafic volcanic rocks (commonly 35-40 wt% vs. 10 wt%). This makes them more reactive to sulfur-bearing fluids and thus an ideal chemical trap – and host – for gold mineralization (Phillips et al., 1984). Because of their rheology and layered anisotropy, BIF units are known to accommodate more strain than their neighbouring volcanic rocks, which increases the likelihood of BIF acting as a physical trap for gold. Although these characteristics are counterbalanced by a relative scarcity, BIFs are hosts to major gold deposits (e.g., Kolar Gold fields in India, Kolb et al., 2012; Geita in Tanzania, Borg, 1993, Vos, et al., 2009; Cuiabá and Morro Velho in Brazil, Ribeiro-Rodrigues et al., 2007, Vial et al., 2007; Homestake in the U.S.A., Klein and Day, 1994; Figure 1-15). Ore minerals in iron-formation-hosted gold deposits are largely the same as those hosted by mafic volcanic rocks (i.e., pyrite, pyrrhotite, arsenopyrite, etc.; Phillips et al., 1984; Eilu et al., 1999).

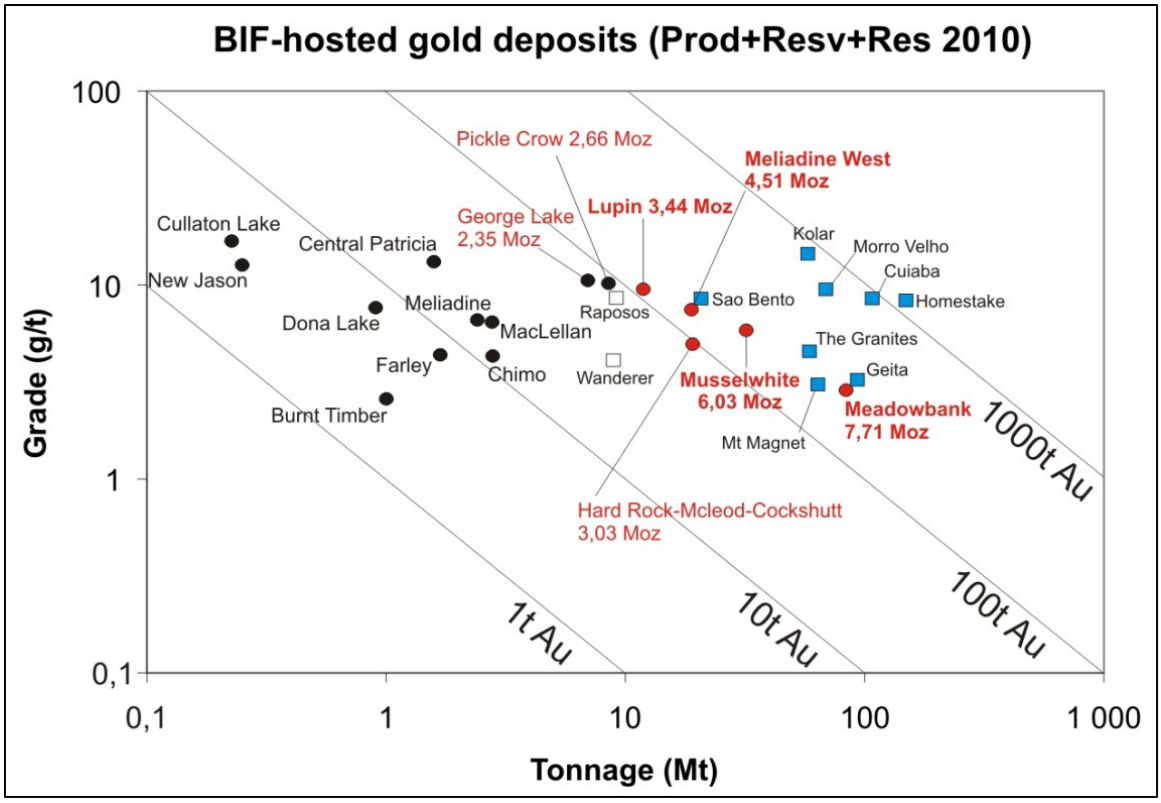

Figure 1-15: Grade and tonnage of major BIF-hosted gold deposits in the world (round = Canada, square = world), from Dubé and Bécu, unpublished data.

1.5.3.2 Syngenetic versus epigenetic models

BIF-hosted gold mineralization is characterized by stratabound sulphide-replacement of the iron formation, usually its oxide component, the genesis of which has led to some debate (Phillips et al., 1984; Oberthür et al., 1990; Kerswill, 1996). Early workers argued that structural control was evidence for epigenetic emplacement (Goldberg, 1964; Lewis, 1965). Others have suggested syngenetic gold mineralization (Ridler, 1970; Hutchinson et al., 1971; Hutchinson, 1976; Fripp, 1976), drawing on analogies with volcanogenic-massive sulphide deposits.

Phillips et al. (1984) investigated the possibility of epigenetic origin for BIF-hosted gold through comparison with volcanic-rock-hosted gold-mineralized bodies in several districts, such as Mt Magnet, Western Australia, and Barberton, South Africa. They established criteria that should be met to classify a BIF-hosted gold deposit as syngenetic or epigenetic in origin (Table 1-3); recognizing, however, that post-mineralization and metamorphism may obliterate some of the evidence needed to make this distinction.

Table 1-3: Some criteria to distinguish between syngenetic and epigenetic origin of BIF-hosted gold mineralization, modified from Phillips et al. (1984).

Syngenetic model	Epigenetic model
1. The sulphides (and gold) participated in all deformation and metamorphic events recorded in the adjacent and laterally-equivalent rocks;	1. Sulfide (and gold) mineralization postdates earlier deformation or metamorphic events recorded in the oxide-facies banded iron-formation;
2. On the macroscopic scale, mineralization should not be restricted to specific faults structure or zones of more intense fracturing;	2. On the macroscopic scale, the control of mineralization by folds or fault structures or zones of intense fracturing;
3. Gold grades should not be related to transgressive features such as fractures and faults;	3. Gold grades are related to transgressive features and/or sulphides are transgressive to layering;
4. Boundaries between sulphide-facies ans oxide-facies and/or carbonate-facies BIF should be gradational and may be reflected by facies change in associated sediments (if any);	4a. Boundaries between sulphides and oxide-facies BIF are sharp and related to transgressive features; 4b. There is evidence for replacement of Fe oxide (or carbonate) on a mesoscopic scale;
5. Associated alteration, if present, is restricted to the stratigraphic footwall of the iron formation;	5. Associated wall-rock alteration is present and transgressive to the stratigraphy;
6. The elemental composition of the ore and/or fluid inclusions should reflect at least partial involvement of Cl-rich brines: high base metal content, low Au/Ag ratio	6a. The ore fluid as deduced from fluid inclusion data is similar to that responsible of the volcanic-hosted gold deposits (H2O-CO2-H2S-rich, low-salinity fluids); 6b. The elemental composition of the ores is similar to that of demonstrably epigenetic deposits in the same terrain, reflecting a similar fluid source: high Au enrichment (±Sb, Bi, Hg, W, B) relative to base metals, High Au/Ag ratio.

Equivocal distinction between syngenetic and epigenetic may thus be difficult to achieve. The Lupin deposit in Canada is a good example (Poulsen et al., 2000). Kerswill et al. (1996) favoured a syngenetic model, while Lhotka and Nesbitt (1989), Bullis (1990) and Bullis et al. (1994) argued for an epigenetic model, also favoured by Geusebroek and Duke (2004). Often, gold deposits in BIF previously interpreted as syngenetic in origin, such as Homestake and Mineral Hill, U.S.A., and Morro Velho, Brazil (Kerswill, 1996), have since been reinterpreted as epigenetic (Morelli et al., 2010; Smith, 1996; Vial et al., 2007, respectively). Sulphide-bearing mineral deposits in BIF that have a demonstrably syngenetic origin, such as Broken Hill and Pegmont, generally lack economical gold grades and are mined for base metals like Pb or Zn (Parr and Plimer, 1993; Peter, 2003).

The sulphides-facies iron formation is an important feature to account for syngenetic or epigenetic origin of gold mineralization. A primary sulphide-dominant facies, when present in Algoma-type BIF, has an extensive lateral continuity and a gradational transition to carbonate- or oxide-dominant BIF (Peter, 2003). Contrastingly, the transition from sulphide- to oxide-dominant (carbonate- or silicate-) in epigenetic gold mineralization is characterized by replacement of the iron oxide(s) by sulphide(s), tends to be very sharp and to occur over a short distance (Figure 1-16). For Superior-type BIF, studies in the Dales Gorge member of the Hamersley Group in Western Australia (Miyano and Miyano, 1982; Miyano and Klein, 1983) or in the Labrador Trough (Klein, 1973, 2005) indicate a lack of a sulphide-dominant

facies in that type of iron formation. On the basis of being able to restrict a BIF to the Superior type, any sulphide mineralization present would have to be epigenetic.

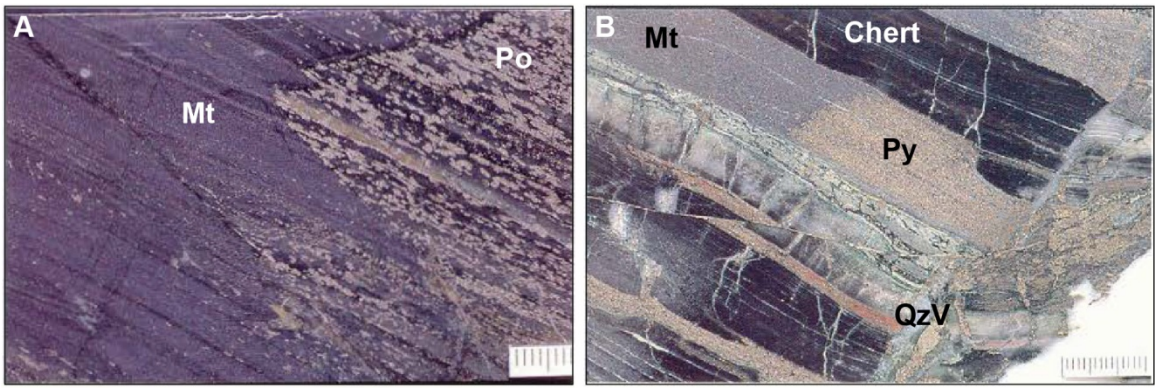

Figure 1-16: Examples of sulphidation of Algoma-type BIF (modified from Eilu et al., 1999) with A. Pyrrhotite replacing magnetite in a sample from a gold deposit in the Flin Flon-Snow Lake belt, Manitoba, and B. Pyrite replacing magnetite in a sample from Water Tank Hill mine, Mt Magnet, Australia. Centimetre scale located in lower right corner of the photographs.

A variant of both models has also been proposed (Ford and Duke, 1993), where the BIF has high initial metal contents (i.e., tens to hundreds ppb) and gold is subsequently remobilized and concentrated during metamorphism and deformation. In their study, Ford and Duke (1993) note that several occurrences of BIF in the Slave province, Canada, have higher background gold values than those reported for Algoma-type BIF (Gross, 1988). Yet, the studied occurrences have a well-identified, sulphide-dominant BIF unit interpreted to be primary in origin, which may not be the case in other regions or could not be unequivocally demonstrated.

1.5.3.3 Epigenetic gold: alteration zones and metamorphism

The strong structural control of epigenetic gold deposits implies that alteration haloes surrounding the mineralized zone(s) have very variable extents (Eilu et al., 1999). It is also a function of the secondary permeability of the host rocks and intensity and life-span of the hydrothermal system, especially in terms of width: the signature of the distal alteration can be anywhere from 1 m to 2 km-wide, the intermediate zone may cover 1 m to 100 m width, and the proximal alteration may be up to 50 m-wide (Eilu et al., 1999). This variability is increased in BIF-hosted gold deposits because of their rheology, permeability, and reactivity to sulfur-bearing fluids (Phillips et al., 1984). Alteration-related minerals of BIF-hosted gold mineralization depend on the pre-existing mineral assemblage resulting from the BIF-facies primary composition and metamorphic grade during the alteration processes (Colvine, 1989; Klein, 2005; section 1.5.3). Although three alteration zones can be described in volcanic rocks (i.e., distal, intermediate, and

proximal to the mineralized zone), the intermediate alteration zone frequently cannot be delineated in the BIF (Woad, 1981; Thompson et al., 1990; Newton, 1991; Vielreicher, 1994). Under greenschist metamorphic conditions, BIF-hosted gold mineralization tends to be hosted by the oxide-dominant facies, whereas under amphibolite-grade metamorphic conditions the silicate facies of the BIF is favoured as a host for gold (Kerswill, 1996; Robert et al., 2007).

At greenschist facies, distal alteration commonly comprises magnetite-quartz-chlorite ± hematite, Fe-amphiboles, stilpnomelane, calcite, and pyrite (Eilu et al., 1999). Proximal alteration is evidenced by the intense sulphidation – and an associated reaction front – of the BIF's iron-rich layers in the vicinity of quartz-dominated veins (Phillips et al., 1984; Mueller and Groves, 1991; Bullis et al., 1994): it consists of an assemblage of quartz-pyrite ± dolomite/ankerite, siderite, chlorite, magnetite, and arsenopyrite (Figure 1-16). During the transition to the amphibolite facies, certain changes occur in the alteration mineral assemblages (Eilu et al., 1999): 1) pyrrhotite replaces pyrite as the dominant sulphide; 2) biotite replaces sericite as the main K-bearing mineral; 3) calcite dominates over other carbonates; and 4) grunerite accompanies and/or replaces chlorite. Increasing metamorphic grade is also marked by the presence of Ca-amphiboles (tschermakite, actinolite, and hornblende) replacing grunerite commonly at the selvage of quartz-carbonate veins (Smith, 1996), within apparently less extensive alteration haloes. If present, titanium oxides change from rutile to ilmenite. The lateral extent of the alteration haloes also seems to diminish under higher metamorphic conditions (e.g., distal alteration width down to 1-200 m instead of 1-2000 m; Bloem, 1994; Knight, 1994; Eilu and Mikucki, 1996), likely in relation with changes in fluid flow regime during deformation (Ord and Oliver, 1997). At mid-amphibolite facies and higher metamorphic grade, the distal alteration mineral assemblage greatly resembles the regional metamorphic paragenesis (Eilu et al., 1999). In BIF, it is reflected by grunerite-quartz-magnetite-Ca-amphibole ± pyrrhotite-almandine. Proximal alteration is characterized by a strong sulphidation, associated with calc-silicate minerals such as clinopyroxene (diopside, hedenbergite), increased amphibole content, and Fe-rich garnet (usually almandine). Fayalite (olivine) can be present at higher metamorphic conditions.

2 REGIONAL GEOLOGICAL SETTING

2.1 Western Superior province and North Caribou terrane

The Superior province is an Archean craton that occupies a large portion of eastern Canada and constitutes the basement of the eastern part of Manitoba, most of Ontario, as well as the western half of Québec (Wheeler et al., 1996). It is naturally divided into the western and northeastern Superior province by the Hudson and James bays as well as the Phanerozoic sedimentary cover. The northeastern Superior province comprises 2.78-2.69 Ga plutonic rocks that intrude 3.8-2.83 Ga crust (Percival, 2007; Percival et al., 2012). This crust is dominantly constituted by rocks characteristic of continental arc context with a component of juvenile magmatic rocks (Figure 2-1). Comparatively, the western Superior province is formed by terranes 3.0 to 2.69 Ga in age, including major juvenile components. The western Superior province was constructed by successive, southward accretion and amalgamation of multiple terranes with a dominant east-west orientation (Figure 2-1; Percival et al., 2006; Percival, 2007).

The accretion process is thought to have started with the collision of the Oxford-Stull and Island Lake domains with the North Caribou core. At ca. 2720 Ma, during the Northern Superior orogeny (Percival et al., 2012), the Hudson Bay terrane collided with the North Caribou terrane. The Oxford-Stull domain comprises 2.88-2.73 Ga rocks reflecting a juvenile continental margin, and the Island Lake domain is largely composed of plutonic rocks. South of the North Caribou terrane, the various terranes (Winnipeg River, Marmion, Wabigoon, Wawa-Abitibi) and belts (English River, Quetico) were accreted over a complex history including three main orogenic phases (Percival et al., 2012): the Uchian orogeny (2720-2700 Ma), the Central Superior orogeny (ca. 2700 Ma), and the Shebandowanian orogeny (ca. 2690 Ma).

This study uses the terrane terminology (and boundaries) of Stott et al. (2010) with the exception of the North Caribou core (Figure 2-1), which, for consistency with the literature of the study area and work of Percival et al. (2012), is termed the North Caribou terrane (NCT). The NCT has been heavily intruded by large tonalite-trondhjemite-granodiorite (TTG)-type batholiths (Thurston et al., 1991), which record abundant magmatism at 2.87-2.85 Ga. They contain sporadic relics of 3.0 Ga tonalitic bodies and are intruded by younger 2.75-2.69 Ga TTG-type intrusions, synchronous to the main compressional events (Corfu and Stone, 1998; Percival, 2007). Adjacent greenstone belts (e.g., Sandy Lake, North Spirit Lake, Horseshoe Lake, and North Caribou greenstone belts; Thurston et al., 1991) attest of widespread volcanism at ca. 3.0-2.97 Ga, as is suggested by U-Pb geochronology on zircon in felsic volcanic rocks and age population clusters in sedimentary rocks (Thurston et al., 1991; Davis and Stott, 2001; Percival, 2007). Volcanic sequences include thick assemblages of tholeiitic basalts, komatiitic basalts and

komatiites that appear to have locally preserved evidence of interaction between mantle plume and continental crust (Hollings and Kerrich, 1999).

Many gold occurrences have been documented in the NCT and in terranes to the north but, currently, Musselwhite mine is the only major gold deposit in production. This contrasts with the gold endowment of the English River-Uchi terranes (e.g., Red Lake gold district) as well as other terranes to the south (MNDM Database May 2015), which comprise a higher proportion of greenstone belts compared to the North Caribou terrane, Island Lake, Oxford-Stull and Hudson Bay domains, where granitoid batholiths dominate (Stott et al., 2010).

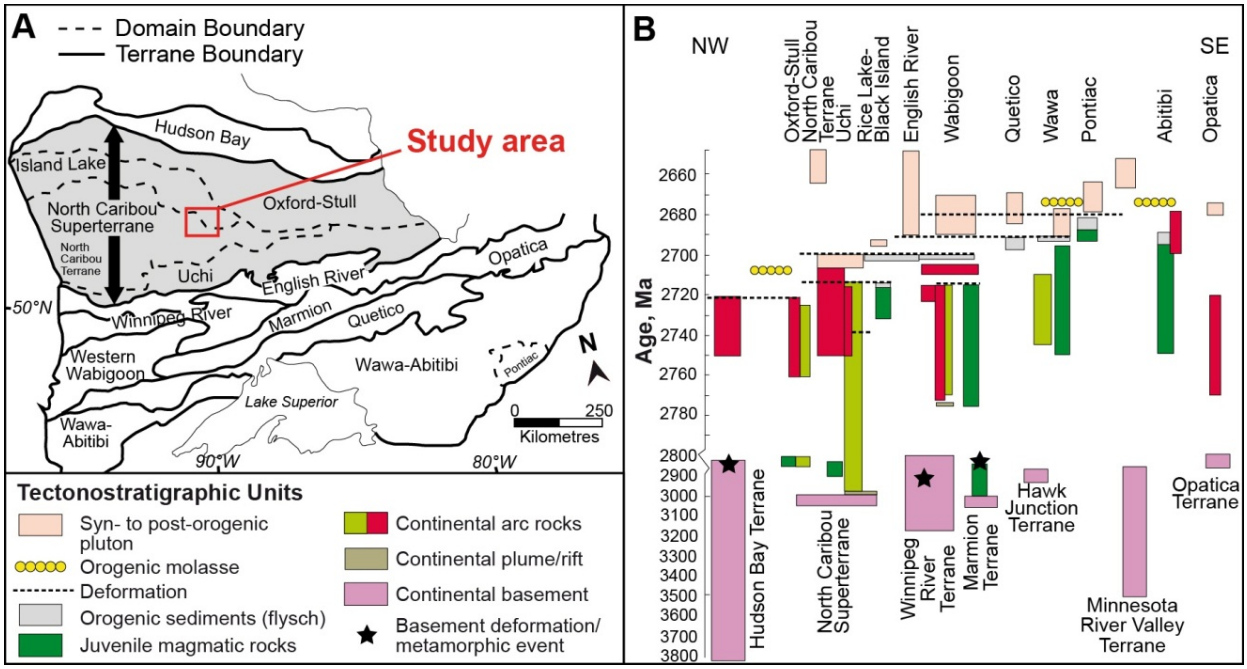

Figure 2-1: A. Terrane boundaries in the western Superior province (modified from Rayner and Stott, 2005, and Stott et al., 2010). B. Tectonometamorphic chart of terranes of the western Superior province (from Percival, 2007).

2.2 North Caribou greenstone belt

The North Caribou greenstone belt (NCG) is located on the northern edge of the North Caribou terrane, south of the Island Lake domain (Figure 2-1 andFigure 2-2; Breaks et al., 1985). It comprises various volcanic-dominated assemblages formed during two major magmatic phases dated at ca. 2980 and ca. 2870 Ma (Figure 2-2; Breaks et al., 2001). Sedimentary-dominated assemblages lie in the core of the NCG. They are interpreted to have been deposited after 2980 Ma in the northern NCG, and after 2850 Ma in the southeastern NCG (Davis and Stott, 2001). The greenstones are intruded by several batholiths emplaced during the two magmatic phases at ca. 2870-2850 Ma and ca. 2750-2690 Ma (Corfu and Stone,

1998; Davis and Stott, 2001; Percival, 2007). Regional-scale mapping programs and studies have defined multiple lithostratigraphic assemblages (Figures 2-2 and 2-3; Satterly, 1941; Breaks et al., 1985, 1991, 2001; de Kemp, 1987; Piroshco et al., 1989; Breaks and Bartlett, 1991; Thurston et al., 1991), which have been used in a variety of combinations in literature (Hollings and Kerrich, 1999; Isaac, 2008; Moran, 2008; Wyman et al., 2011; Kalbfleisch, 2012; Kolb, 2010; Smyk, 2013; Van Lankvelt, 2013; Chadwick, 2014; Duff, 2014; Gagnon 2015; Figure 2-3). Stratigraphic correlations between assemblages of the NCG are based on the nature of their contacts, geochronological constraints, and geological and geochemical characteristics of their respective sequence (Figure 2-3; Breaks et al., 2001). To simplify writing, the three segments of the greenstone belt will be designated from north to south, respectively: the "northern NCG", the "central NCG", and the "southeastern NCG". Given that all rock units of the study area have been metamorphosed, the prefix meta- is implied and omitted where referring to protoliths.

2.2.1 Supracrustal rocks

2.2.1.1 Agutua Arm assemblage

The Agutua Arm assemblage (AAV) is located at the western end of the northern NCG (Figure 2-2). It comprises massive, fine-grained mafic volcanic flows, rare pillowed flows and fragmental rocks of normal to slightly magnesium-rich tholeiitic composition (Piroshco and Shields, 1985; de Kemp, 1987; Breaks et al., 2001). Frequent intermediate to felsic rocks are present between Weagamow Lake and the contact with the Keeyask assemblage. Due to the paucity of outcrops, the sequence is poorly defined, but it includes thickly bedded pyroclastic rocks such as fragment-supported felsic tuff (Breaks et al., 2001). U-Pb geochronological analyses of zircon in felsic fragmental rocks yielded an age of 2981 ± 1.8 Ma (de Kemp, 1987). Rare stratigraphic top indicators suggest that the sequence is SW- to SE-facing (Breaks and Bartlett, 1991).

The AAV is intruded to the northeast by the Weagamow batholith and to the west by the Round Lake batholith. To the south, the AAV is in fault contact with the South Rim assemblage (Breaks et al., 2001), and to the east, the Keeyask assemblage unconformably overlies the AAV (de Kemp, 1987). Rocks of the AAV are moderately to strongly deformed and have rarely preserved primary features.

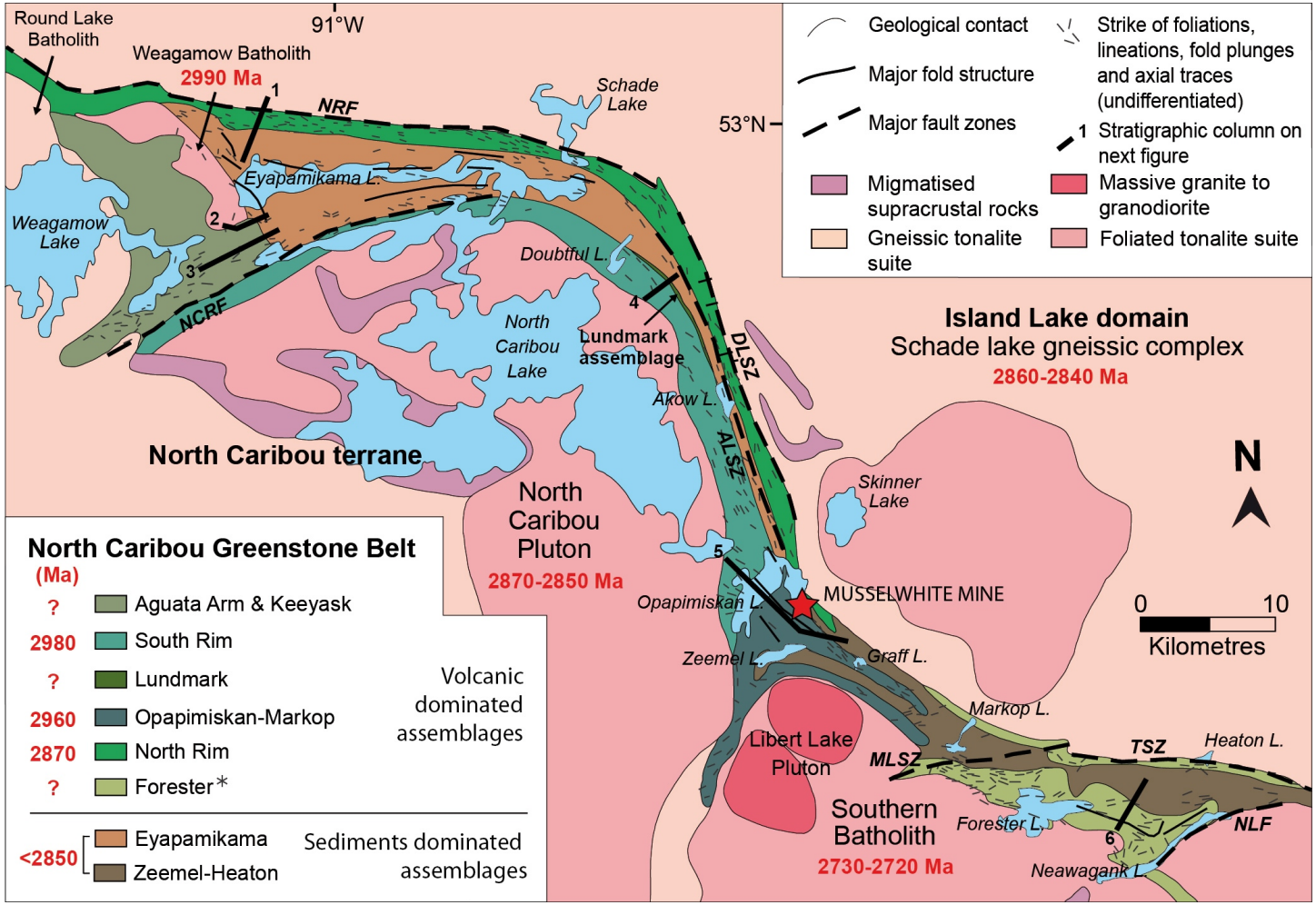

Figure 2-2: Simplified tectonostratigraphic map of the North Caribou greenstone belt and surrounding area (modified from McNicoll et al., 2016, after Biczok et al., 2012); geochronological data from Breaks et al. (2001), McNicoll et al. (2013, 2016), and Van Lankvelt (2013). (*) The thin band of volcanic rocks on the northern edge of the southeastern NCG is herein grouped with the Forester assemblage following Thurston et al. (1991). Breaks et al. (2001) provide no account of this package; Biczok et al. (2012) consider it as part of the Opapimiskan-Markop assemblage. Major folds and structural items orientation are from Breaks et al. (2001). Major fault zones from Breaks et al. (2001) and Gagnon et al. (2016): NRF: North Rim Fault, NCRF: North Caribou River Fault, DLSZ: Dinnick Lake Shear Zone, ALSZ: Akow Lake Shear Zone, MLSZ: Markop Lake Shear Zone, TSZ: Totogan Shear Zone, NLF: Neawagank Lake Fault.

Early terminlogy (Breaks et al., 2001 and references therein)		Revised terminology (Thurston et al., 1991)	This study	
Agutua Arm metavolcanic assemblage	AAV	Agutua Arm assemblage	Agutua Arm assemblage	AAV
Keeyask Lake metasedimentary assembl	KLS	Keeyask assemblage	Keeyask assemblage	KLA
Keeyask Lake metavolcanic assemblage	KLV		South Rim assemblage	SRA
South Rim metavolcanic assemblage	SRV	South Rim unit	North Rim assemblage	NRA
North Rim metavolcanic assemblage	NRV	North Rim unit	Eyapamikama assemblage	ELS
Opapimiskan Lake metavolcanic assembl	OLV	Opapimiskan unit	Opapimiskan-Markop assembage	OMA
Forester Lake metavolcanic assemblage	FLV	Forester unit	Forester assemblage	FLV
Eyapamikama Lake metasedimentary assemblage	ELS	Eyapamikama assemblage (north of Opapimiskan Lake)	Zeemel-Heaton assemblage	ZHA
		Zeemel-Heaton assemblage (south of Opapimiskan Lake)	Lundmark assemblage	LLV
Lundmark Lake metavolcanic assemblage	LLV	Lundmark Lake metavolcanic formation	Schade Lake gneissic complex	SLGC
Schade Lake gneissic complex		Schade gneissic complex	North Caribou pluton	NCP
North Caribou Lake batholith		North Caribou batholith	Southern batholith	SB

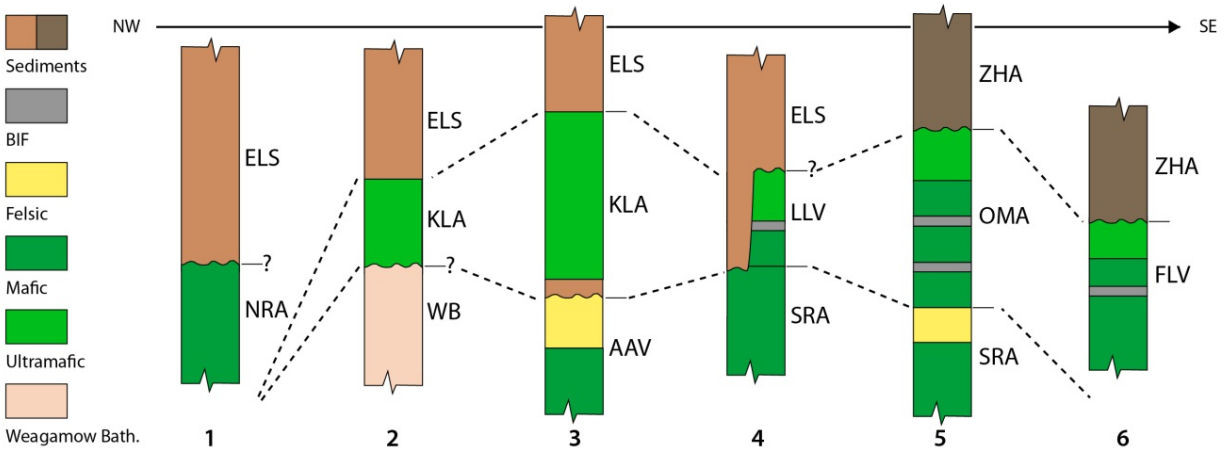

Figure 2-3: Terminology and schematic stratigraphic columns of the lithostratigraphic assemblages of the North Caribou greenstone belt. The vertical scale does not represent true thickness of the assemblages. Columns 1 to 6 are in order from the northwestern to the southeastern parts of the belt. Question marks indicate where the nature of the contact is uncertain. Dash lines represent probable correlation across the NCG.

2.2.1.2 Keeyask assemblage

The Keeyask assemblage (KLA) comprises two packages (de Kemp, 1987): the lower KLA is constituted by a thin (≈20 m) sequence of metasedimentary rocks, while the upper portion consists of 50 to 1700 m of ultramafic to mafic volcanic rocks. The assemblage is oriented NNW-SSE and is consistently facing to the east. U-Pb ages on detrital zircon indicate that the sediments are younger than 2978.1 ± 3 Ma (de Kemp, 1987). The komatiites overlying these sediments are intruded by the Keeyask Lake porphyry that has an age of 2863 ± 1 Ma (Davis and Stott, 2001).

The sedimentary sequence starts with 10-30 cm thick lenses of basal conglomerate and mature quartz arenite unconformably overlying the AAV (Breaks et al., 2001). They are followed up-section by mudstone and siltstone units, some of which contain stromatolites of high paleoenvironmental

significance (Arias, 1986; Beukes and Gutzmer, 2008). The top of the Keeyask metasedimentary sequence is marked by a chert-magnetite BIF, up to 5 m thick, which includes angular breccia and laminated chert. The BIF unit laterally transitions northward into a very thinly bedded to laminated, dolomite-rich calcarenite (de Kemp, 1987). The volcanic rocks of the upper KLA are dominantly spinifex-textured ultramafic flows. Above, interlayered basaltic komatiites and komatiitic rocks are progressively more frequent. The uppermost part of the volcanic sequence consists of pillowed basaltic komatiites, *in situ* broken pillow breccias and variolitic massive flows.

The eastern contact of the Keeyask assemblage with the sedimentary rocks of the Eyapamikama assemblage changes from well-defined, sharp and conformable, to unconformable with a gradational transition where conglomeratic beds incorporate clasts of the underlying lithologies. Contact with the SRA to the south is tectonic in nature (de Kemp, 1987).

2.2.1.3 South Rim assemblage

The South Rim assemblage (SRA) extends along the southern margin of the upper and central NCG (Figure 2-2). It is dominated by mafic pillowed and massive flows with minor intermediate to felsic volcanic rocks and subordinate ultramafic rocks and sedimentary units (Breaks et al., 1991). U-Pb zircon geochronology on felsic tuff samples yielded ages of 2981.9 ± 0.8 Ma, 2973.7 ± 2.2 Ma and 2972.4 ± 1.6 Ma (respectively, Davis and Stott, 2001; Klipfel, 2002; Biczok et al., 2012). Recent U-Pb zircon age dating on a rhyolite unit yielded a result of 3053.2 ± 0.8 Ma (McNicoll et al., 2016), and thus represents the oldest (known) volcanic unit in the North Caribou greenstone belt.

The geochemistry of the basalt flows shows normal and magnesium-rich tholeiitic affinity (Breaks et al., 1991). Pillows present a large diversity of morphologies (i.e., size and length to width ratio) and contain 55 to 90% hornblende with plagioclase aggregates. Intermediate to felsic volcanic rocks occur locally as flows and pyroclastic units (e.g., tuff, lapilli tuff, heterolithic tuff breccia; Breaks et al., 2001). Sedimentary rocks are present as thin units including quartz-plagioclase, garnet-biotite-quartz-feldspar or biotite-sericite-quartz schists (Breaks et al., 1991). Geophysical anomalies in the vicinity of Doubtful Lake also suggest BIF occurrences (Breaks et al., 2001).

A linear electromagnetic anomaly, identified on a 2002 survey, occurs a few hundreds of metres to the east of the 3053 Ma rhyolite (Goldcorp Musselwhite Ltd.). Exploration drilling in the northwestern Opapimiskan Lake area has intersected chert-magnetite iron formation, and to the south, an exposure of argillitic rock was mapped and sampled (Goldcorp Musselwhite Ltd.). A felsic tuff occurring to the east, on the western shore of Opapimiskan Lake, is dated at 2981.9 ± 0.8 Ma (Davis and Stott, 2001). A

number of intermediate units are also present to the north of Opapimiskan Lake. The 70-Ma time gap between felsic units suggests that the aforementioned BIF and argillitic unit represent a previously unrecognized unconformity separating two sequences of contrasting age within the SRA.

In the western 3.05 Ga sequence, rhyolitic units display calc-alkaline magmatic affinity, LREE and LILE enrichment, Ti and V negative anomalies, and ε_{Nd} ranging -2.79 to -0.89 (Smyk, 2013). Surrounding mafic rocks have a basaltic composition forming two groups: one with flat PM-n extended trace element profiles and no significant anomaly; the second with moderately-enriched LREE and negative Nb anomaly (Smyk, 2013). The 2.98 Ga sequence, between the unconformity and the top of the SRA, consists mainly in mafic volcanic flows and intrusions interlayered with intermediate units and felsic units, including unit Avol, which is dated at 2978.7±1.0 Ma (McNicoll et al., 2016) and 2972.4±1.6 Ma (Biczok et al., 2012). South-west of the mine, near the Paseminan River, detail mapping of unit Avol conducted during this study shows a transition from mafic to intermediate to felsic volcanic rocks, suggesting a progressive differentiation of magmas. Geochemical data from mafic rocks of the SRA shows they have a flat PM-n extended trace element profiles and negligible Nb-Ta, Ti and Sc anomalies (Hollings and Kerrich, 1999). Contrastingly, unit Avol consistently displays a clear calc-alkaline magmatic affinity with strong LREE enrichment, weakly fractionated HREE, as well as strongly negative Nb-Ta, Ti and Sc anomalies on PM-n extended trace element profiles (Hollings and Kerrich, 1999). Lastly, pelitic sediments and slivers of sulphide-rich argillite overlying unit Avol have been repeatedly documented (Goldcorp Musselwhtie Ltd.). This suggests a period of quiescence before deposition of the OMA.

Collectively, geological, geochemical, and geochronological data suggests the SRA is the product of a mantle plume-type source, as first proposed by Hollings and Kerrich (1999), similar to ocean plateau basalts (Sun and McDonough, 1989). Smyk (2013) interprets that initial mafic magmas were locally contaminated by pre-existing crust during ascent (Perring et al., 1996; Shervais, 2001; Dickin, 2005). This process occurred over the 3054 to 2972 Ma period in two main phases of underwater volcanism, between which detrital and chemical sedimentation could take place to produce chert-magnetite iron formation and argillites.

From the northern NCG to the study area, the SRA consistently underlies the ELS. Geochronology results are close to the 2980 Ma age obtained on felsic rocks of the AAV (de Kemp, 1987) suggesting contemporaneity. However, the AAV/SRA contact is of tectonic nature (Breaks and Bartlett, 1991) and de Kemp's zircon age is from a single zircon fraction, so stratigraphic correlation is speculative. Units of the South Rim assemblage are progressively more deformed and metamorphosed in the central NCG than

in the northern NCG. Strain is heterogeneously distributed and is frequently focused in hyaloclastites-rich zones of pillowed flows (Breaks et al., 2001). In the study area, the SRA underlies the OMA.

2.2.1.4 Lundmark assemblage

The Lundmark assemblage is a narrow assemblage located in the northern half of the central NCG, between Doubtful Lake and Akow Lake (Figure 2-2). It occurs as a <0.2 km-thick, 13 km-long, steeply ENE-dipping lense of mafic to ultramafic volcanic rocks and interlayered banded iron formation (Breaks et al., 1991).

Volcanic rocks are dominantly pillowed, basaltic komatiite flows. Where pillows are homogeneous, actinolite-rich and lack visible varioles, amygdules or phenocrysts. A few occurrences of monolithic, clast-supported, ultramafic breccia have been documented (Breaks et al., 1991). Pillowed basalt flows of normal tholeiitic affinity are intercalated with massive, fine- to medium-grained ultramafic flows. The banded iron formation greatly varies in thickness (11 to 50 m). It comprises fine- to locally coarse-grained and garnet-bearing thinly bedded silicate and oxide facies layers (Breaks et al., 2001). Chert layers typically make up 40-50% of the lithology, locally down to 10% or up to 90%. Iron-rich bands are mostly constituted by magnetite and grunerite.

Rocks of the LLV are moderately to strongly deformed and dip steeply to the ENE (Breaks et al., 2001). The banded iron formation is less competent than volcanic units due to its anisotropy, and beds are intensely folded and boudinaged. Based on the geochemistry of volcanic rocks and occurrence of BIF, LLV could be the along-strike equivalent of the KLV and OMA (Breaks et al., 2001).

2.2.1.5 North Rim assemblage

The North Rim assemblage occurs along the northern edge of the upper and central NCG, from Weagamow Lake to Opapimiskan Lake (Figure 2-2; de Kemp, 1987; Breaks et al., 1991). It is mostly constituted of mafic volcanic flows but locally also includes ultramafic, rare felsic to intermediate volcanic rocks, silicate-facies BIF, dolomitic and clastic sedimentary rocks. A U-Pb zircon geochronological analysis of a rhyolite sample yielded an age of 2870 ± 2 Ma (Davis and Stott, 2001).

In mafic flows, pillows are ubiquitous and massive flows scarce. They generally contain hornblende and plagioclase with up to 10% quartz-carbonate amygdules (Breaks et al., 2001). Rocks commonly display discontinuous gneissic layering suggesting medium-grade metamorphism, with epidote-, diopside-, and/or hornblende-rich bands that alternate with fine- to medium-grained hornblende-plagioclase amphibolite

bands. The BIF units occur within six lenses of complex, plastically-deformed mélange (Breaks et al., 2001). Chert-grunerite BIF is found in contact with feldspar-rich arenite and garnet-bearing mafic schist. Carbonate-rich sedimentary units have been documented in several occurrences in the NRA of the northern NCG (Breaks et al., 1991) and contain layers of carbonates intercalated with arsenopyrite-bearing garnet-biotite schist. The overall carbonate-silicate assemblage suggests occurrence of the metamorphic reaction "dolomite + quartz + water = calcite + tremolite + CO_2" (Breaks and Bartlett, 1991).

Rocks of the NRA are much younger than the SRA (i.e., ~100 Ma; Davis and Stott, 2001). The contact with the sedimentary rocks of the Eyapamikama Lake assemblage appears as a gradational interlayering of mafic volcanic rocks of the NRA with sediments. Rocks in this area have undergone intense ductile deformation (flattened pillows with L-W ratios of up to 50:1; Breaks et al., 1991) and the lack of reliable top indicators prevents from determining the stratigraphic relationship between the NRA and Eyapamikama Lake assemblage (Breaks et al., 2001).

2.2.1.6 Eyapamikama Lake assemblage

In contrast to the other lithostratigraphic assemblages of the NCG, the Eyapamikama Lake assemblage (ELS) is dominated by sedimentary rocks (Breaks et al., 2001). The cartographic width of the ELS approaches 15 km along the contact with the Weagamow batholith and the Keeyask assemblage, and tapers southward to a few hundred metres north of Opapimiskan Lake (Figure 2-2). A maximum age of <2850 Ma has been determined for rocks of the ELS, using detrital U-Pb zircon geochronology (Davis in de Kemp, 1987; Davis and Stott, 2001).

In the northern NCG, sedimentary facies vary from coarse, clast-supported, polymictic alluvial conglomerates to fine-grained, turbidite greywacke and slate beds (de Kemp, 1987; Breaks and Bartlett, 1991). Conglomerate clasts comprise a wide range of lithologies that are similar to those of the adjacent assemblages (e.g., BIF clasts similar to the KLA iron formation; Breaks et al., 2001). Wackes are divided into two groups: one with a matrix constituted of chlorite, muscovite, biotite, carbonate, quartz, and plagioclase; the other with a quartz-dominated matrix (55 to 60%). In the central NCG, fine-grained facies such as thickly-bedded, biotite-chlorite pelites and minor quartz-feldspar wackes prevail, reflecting an overall sedimentary transition from proximal to distal facies (Breaks et al., 1991). Also, aluminosilicate porphyroblasts such as garnet, andalusite, cordierite, and staurolite are more common to the south (section 2.2.4), individually or as coexisting phases (Breaks et al., 1991; Gagnon et al., 2016).

Detrital zircon ages obtained from conglomerate and sandstone of the ELS include two main populations, ca. 2980 Ma and ca. 2850 Ma (Davis in de Kemp, 1987; Davis and Stott, 2001), corresponding to the age of rocks of the adjacent AAV, KLA, SRA, and NRA. For Davis and Stott (2001), the lack of the 2750-2700 Ma detrital zircon population, a major period of magmatism in the Superior province (Figure 2-1; Percival, 2007), suggests the ELS was deposited before this event. However, features such as the lack of outcropping rocks of this age range in the drainage basin can be responsible for this.

2.2.1.7 Opapimiskan-Markop assemblage

The Opapimiskan-Markop assemblage (OMA) occurs from Markop Lake to Opapimiskan Lake, in the southeastern NCG (Figure 2-2). It is largely dominated by mafic to ultramafic volcanic rocks interlayered with significant units of BIF, including one that is continuous for over 30 km (Figure 2-4; Breaks et al., 1985; Breaks et al., 2001; Biczok et al., 2012).

The volcanic sequence comprises pillowed and massive lava flows, pillow breccia and flow top breccia. Massive flows commonly grade into monolithic flow top breccia (Breaks et al., 2001). Varioles are found in both pillowed and massive flows. Komatiites are common, but mafic units dominate most of the stratigraphy. Both usually have normal-tholeiite MgO/Al_2O_3 ratio. Spinifex textures and hyaloclastites are uncommon. Sedimentary rocks of the OMA comprise three units characterized by variable clastic-chemical sedimentary inputs (Biczok et al., 2012): the Northern iron formation (NIF) sequence consists of garnet-biotite schist, and silicate- and oxide-facies iron formations, *sensu stricto*; the Southern iron formation (SIF) comprises several horizons of oxide-facies BIF with local lenses of sulphide-rich argillite; and an unnamed and unexposed iron formation, which is only intersected in drill holes in the area ~1 km NW of Zeemel Lake (Guest, 2013; Figure 2-4). Three main volcanic packages have been distinguished based on their position relative to the NIF and SIF (Biczok et al., 2012): the "Bvol", structurally on top; the "Basement basalts", between the NIF and SIF; and the "Lower basalts", underlying the SIF and including the minor, unnamed BIF (Figure 2-4).

Breaks et al. (2001) have suggested that the OMA is correlative to the KLA, LLV and FLV, based on similar volcanic rock types and abundance, lithogeochemistry, and presence of BIF units. The OMA sequence, and notably the Northern iron formation sequence, hosts the world-class Musselwhite Au mine (Figure 2-4). Consequently some attention was given to the study of the BIF facies using petrography and lithogeochemistry (Moran, 2008). The stratigraphy of the assemblage was carefully studied during this project and is presented in detail in chapter 3.

2.2.1.8 Zeemel-Heaton assemblage

The Zeemel-Heaton assemblage (ZHA) occupies the center of the southeastern NCG (Figure 2-2). It is dominated by sedimentary units, from which zircon U-Pb geochronology indicates deposition after 2853 ± 1 Ma (Davis and Stott, 2001) and possibly, in part, as young as 2723 ± 23 Ma and 2674 ± 29 Ma (Duff, 2014).

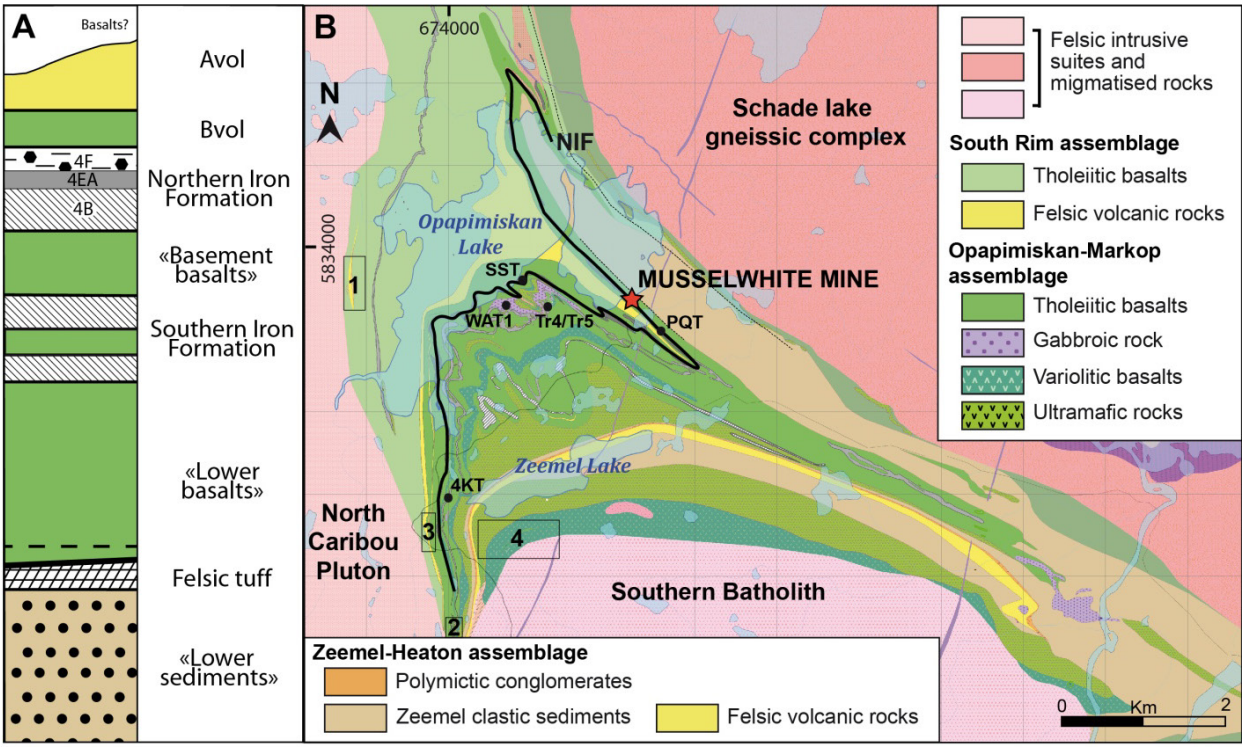

Figure 2-4: A. Schematic Musselwhite mine stratigraphy column as defined by Biczok et al., 2012. Unit names are local. B. Geological map of the Opapimiskan Lake area (modified from Goldcorp Inc., unpublished data). Bold black line: Northern iron formation sequence. Black dots and codes refer to detail trench locations (see text hereafter). Numbers 1 to 4 refer to Smyk (2013), Chadwick (2014), Quinn (2014), and Pisani (unpublished).

The ZHA is dominated by quartz wackes and quartz arenites with minor, poorly sorted conglomerates and mudstones (Breaks et al., 2001). Conglomerate clasts include quartz arenite and wacke indicating reworking of older sedimentary units, and minor proportions of BIF, felsic volcanic rocks, quartz veins, and foliated tonalite.

Although in apparent continuity with the ELS north of Opapimiskan Lake, the ZHA contains younger zircon age populations and could represent (Duff, 2014): 1) a lateral extension of the basin in which the ELS was deposited; 2) a separate, contemporaneous basin of that of the ELS; 3) a separate basin where sedimentation occurred after a significant hiatus (~100 Ma). The youngest age constraint of ca. 2674 Ma

has been used to suggest the ZHA could represent, in part, a Timiskaming-like, syn-orogenic sedimentary unit (Duff et al., 2013). Also, the large span of detrital ages within the ZHA and apparent concentration of young ages to the Heaton Lake area led to the suggestion that the ZHA may be sub-divided into the Zeemel assemblage, west of Markop Lake, and the Heaton assemblage to the east (McNicoll et al., 2016).

2.2.1.9 Forester assemblage

The Forester assemblage (FLV) is located in the southeastern NCG (Figure 2-2). It is dominantly constituted of mafic volcanic rocks and dispersed iron formation, especially to the east near Neawagank Lake (Breaks et al., 1986). There is no published geochronological data for the FLV.

Volcanic units consist of pillowed and massive, mafic and ultramafic flows, mainly of komatiitic composition and lesser tholeiitic units (Breaks et al., 2001). These volcanic rocks are metamorphosed mostly to amphibolite facies and commonly contain calc-silicate aggregates of fine-grained diopside-epidote-plagioclase ± quartz ± garnet. Two occurrences of felsic metavolcanic units have been documented: one quartz-rich fragmental unit and a sub-volcanic unit intercalated in pillowed mafic flows. BIFs of the FLV are composed of ~15 m-thick layers of laminated to thinly bedded magnetite-chert facies. Similar to those of the OMA in the Musselwhite mine area, BIFs locally include garnet-actinolite-chlorite layers indicative of some clastic input (Breaks et al., 1985).

The FLV may be stratigraphically correlated with the OMA based on similar proportions and compositions of mafic and ultramafic volcanic rocks, as well as presence of BIFs (Breaks et al., 2001). The nature and correlation of the volcanic rocks located along the northern edge of the southeastern NCG (Figure 2-2) is equivocal, partly due to the lack of absolute geochronological constraint. Thurston et al. (1991) initially attributed this unit to the FLV. It was later referred to as the "Heaton Lake metasedimentary rocks" (Breaks et al., 2001), before being considered as part of the OMA (Biczok et al., 2012) or the NRA (Duff, 2014).

2.2.2 Intrusive phases

Initial regional-scale geological mapping accompanied by limited geochemical and geochronological sampling was carried out during Ontario Geological Survey mapping programs (de Kemp, 1987; Breaks et al., 2001, and reference therein). Subsequently, additional geochronological and geochemical data was collected for studies by Stott and Biczok (2010), Wyman et al. (2011), Biczok et al. (2012), and Van Lankvelt (2013). Geochronological constraints from these studies on the various intrusions around the

NCG define magmatic phases that are consistent with magmatic events in the Superior province as defined by Thurston et al. (1991), Corfu and Stone (1998), and Percival (2007) (section 2.1).

2.2.2.1 Weagamow batholith

The Weagamow batholith is a 2990 ± 1.8 Ma, predominantly trondhjemitic intrusion occurring in the western part of the northern NCG (Figure 2-2; de Kemp, 1987). It is typically composed of 50 ± 5% plagioclase, 30-40% quartz, <9% K-feldspar, up to 9% biotite and accessory minerals (Breaks and Bartlett, 1991). Although the oldest, large felsic intrusion of the NCG, it is only weakly deformed along its margins where biotite defines a subtle foliation (Breaks and Bartlett, 1991).

2.2.2.2 North Caribou pluton

The North Caribou pluton (NCP) forms a crescent-shaped tonalite-trondhjemite-granodiorite (TTG)-complex at the southern boundary of the northern and central NCG. It includes massive, medium-grained granitic units and moderately foliated, recrystallized biotite trondhjemite and granodiorite with enclaves of supracrustal rocks (Breaks et al., 2001). It is commonly composed of 30-35% quartz, 55% plagioclase, and 5-10% biotite (Breaks and Bartlett, 1991). The contact with the South Rim assemblage demonstrates the intrusive character of the NCP, with numerous xenoliths and an aureole of contact metamorphism (Breaks and Bartlett, 1991). Multiple intrusive phases are documented and dated from ca. 2870 Ma to 2850-2830 Ma (de Kemp, 1987; Davis in Thurston et al., 1991; Biczok et al., 2012; Van Lankvelt, 2013), with emplacement depth-pressure increasing from 5 to 8 kbar (Van Lankvelt, 2013). U-Pb zircon ages on a sample from the southernmost part of the batholith show clusters at ca. 3.0 Ga and ca. 2728 Ma (Van Lankvelt, 2013). The former indicates inheritance from an older crustal component, in agreement with other terrane-scale studies (Percival et al., 2006; Percival, 2007). The latter indicates a younger phase of magmatism (Biczok et al., 2012), also in agreement with syn-tectonic magmatism reported by Percival (2007). It has been suggested that the emplacement of the NCP was, at least in part, the drive of regional deformation and metamorphism, and possibly of gold mineralization at Musselwhite (Stott and Biczok, 2010).

2.2.2.3 Schade Lake gneissic complex

The Schade Lake gneissic complex (SLGC) is a metamorphosed TTG-type intrusion (Breaks et al., 1991). It lies in the Island lake domain and extends all along the northern margin of the NCG (Figures 2-1, 2-2;

Davis and Stott, 2001; Wyman et al., 2011). It is composed of numerous phases of tonalite, trondhjemite, granite, and diorite commonly showing gneissic texture (Breaks et al., 1986, 1991, 2001; Van Lankvelt, 2013). Geochronological data suggest that this phase of emplacement occurred at 2857.3 ± 1.4 Ma (de Kemp, 1987; Biczok et al., 2012). A recent geochronological study suggests a more protracted emplacement history that could range from 2880 to 2830 Ma (Van Lankvelt, 2013). Thermobarometric data suggests the SLGC represents a lower crustal level than the NCP and NCG (Van Lankvelt, 2013).

The SLGC-NCG boundary is marked by a well-developed ductile fault zone with protomylonitic to mylonitic texture (Breaks et al., 2001). North of Musselwhite mine, the dominant fabric in the SLGC is shallowly dipping to the east and steepens toward the contact with the NCG, where a sub-horizontal to shallow south-plunging mineral lineation is present (Gagnon et al., 2016). The magnetic susceptibility map of the SLGC (Ontario Geological Survey, 2003) shows curvilinear features that are dragged dextrally along the central NCG, compatible with models of regional structural evolution including transpressional events (Gagnon et al., 2016).

2.2.2.4 Skinner Lake complex

The Skinner Lake complex is a subordinate intrusion within the SLGC, located north-northwest of the southeastern NCG (Figure 2-2). It is mainly composed of foliated tonalitic rocks (Wyman et al., 2011; Van Lankvelt, 2013). U-Pb ages of magmatic zircons cluster ca. 2870 and ca. 2830 Ma. Some zircon rims are dated at ca. 2735 ± 7 Ma and interpreted as the result of hydrothermal activity possibly linked to gold mineralization (Van Lankvelt, 2013; Van Lankvelt et al., 2016).

2.2.2.5 Southern batholith

The Southern batholith (SB) lies south of the Opapimiskan Lake area (Figure 2-2) and extends along the southern boundary of the southeastern NCG. It is predominantly constituted of granodioritic to granitic phases (Biczok et al., 2012), and includes a secondary phase of tonalitic composition referred to as the Libert Lake pluton (Wyman et al., 2011; Van Lankvelt, 2013). Zircon U-Pb geochronology indicates that the batholith was emplaced ca. 2730-2710 Ma, which is significantly younger than the NCP and SLGC (Biczok et al., 2012; Van Lankvelt, 2013).

2.2.2.6 Minor intrusive bodies

Other minor intrusive bodies include peraluminous rocks ranging from medium-grained to pegmatitic muscovite and biotite-muscovite trondhjemite to granite and pegmatitic granodiorite (Breaks et al., 2001). Crosscutting relationships suggest that these bodies were emplaced during late-D_2 deformation (Breaks et al., 2001), and U-Pb geochronological analyses on zircon and monazite range from ca. 2725 to 2668 Ma (Biczok et al., 2012). This type of intrusion occurs throughout much of the NCG and is spatially associated with clastic sedimentary packages. This association and a recent geochemistry study (Fry, 2013) suggest that their petrogenesis is linked to partial melting of the sediments.

2.2.3 Structural geology

2.2.3.1 Regional structural patterns

The envelope of the main structural fabric and fold structures is roughly parallel to the contact of the narrow, elongate, two-arc shape of the North Caribou belt (Figure 2-2; Breaks et al., 2001). Three major phases of ductile to brittle-ductile deformation have been documented (D_1, D_2, D_3), in addition to minor late structures related to brittle deformation ("D_4"). Several regional fault zones separate lithostratigraphic assemblages (Figures 2-2, 2-5; Breaks et al., 2001, and reference therein). The dominant regional structural pattern and main tectonometamorphic phase is related to D_2.

2.2.3.2 D_1 deformation event

Evidence of the D_1 deformation is better preserved in the northern NCG (Breaks and Bartlett, 1991). Sedimentary rocks of the ELS are affected by mesoscopic tight to isoclinal F_1 folds, and regional stratigraphic polarity indicators and rock types distribution suggest sub-regional-scale folds are present (Figure 2-5A; de Kemp, 1987; Breaks and Bartlett, 1991). Vertical to steeply dipping S_1 foliations are commonly sub-parallel to the NCG boundaries. With the exception of preserved F_1 hinge zones, S_1 is sub-parallel to S_0. Folds axes dominantly plunge to the east and are coaxial with documented L_1 mineral stretching lineations (Breaks and Bartlett, 1991).

In the central and southeastern NCG, D_2 overprint is strong (Breaks et al., 2001). However, in areas of low D_2 deformation intensity such as the southern Opapimiskan Lake area, S_1 foliation is preserved and penetrative (Hall and Rigg, 1986; Breaks et al., 1986; Smyk, 2013). Volcanic rocks have better recorded S_1 comparatively to banded iron formations. In contrast, BIF units contain numerous occurrences of F_1-F_2

fold interference pattern (Hall and Rigg, 1986; Breaks et al., 1986). Presence of L_1 mineral stretching lineations has not been documented in the southern half of the NCG.

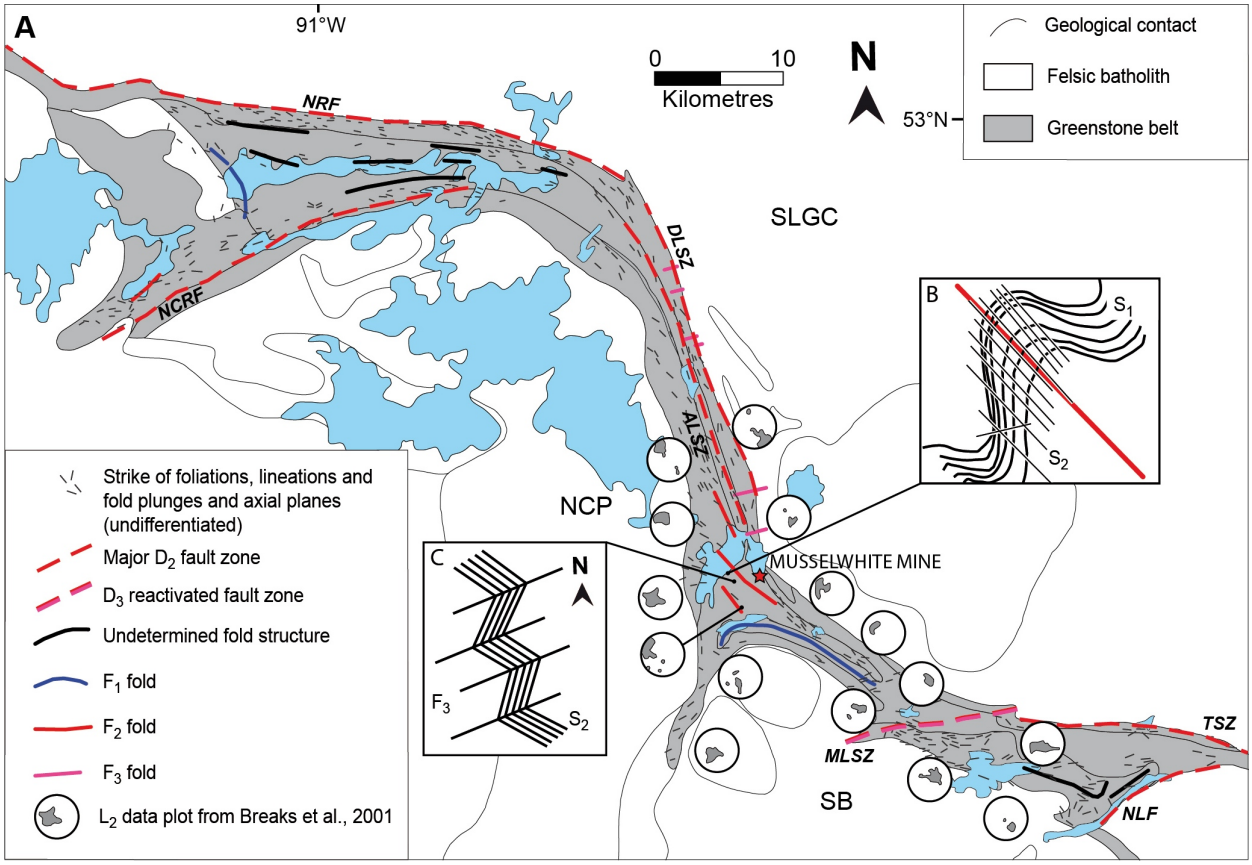

Figure 2-5: A. Simplified structural map of the North Caribou greenstone belt and surrounding area (modified from McNicoll et al., 2016, after Biczok et al., 2012); see Figure 2-2 for geological units. Major folds and traces of fabrics and stereonets are from Breaks et al. (2001). Major fault zones from Breaks et al. (2001) and Gagnon et al. (2016): NRF: North Rim Fault, NCRF: North Caribou River Fault, DLSZ: Dinnick Lake Shear Zone, ALSZ: Akow Lake Shear Zone, MLSZ: Markop Lake Shear Zone, TSZ: Totogan Shear Zone, NLF: Neawagank Lake Fault. B. Crosscutting relationship between S_1 and S_2 foliations in the Opapimiskan Lake area. C. Crosscutting relationship between S_2 and S_3 foliations in the Opapimiskan Lake area.

2.2.3.3 D_2 deformation event

The regional D_2 deformation produced open to isoclinal, shallowly NW-plunging F_2 folds in the Opapimiskan Lake area(Hall and Rigg, 1986; Breaks et al., 1986). Asymmetric folds are common (Breaks et al., 1986; Breaks and Bartlett, 1991), and have a typical 70-100° interlimb angle. In BIFs, fold limbs are commonly attenuated and boudinaged (Breaks et al., 1986). The axial-planar S_2 foliation is steeply dipping and moderately to strongly developed. In moderately deformed volcanic rocks, S_2 is present as a spaced cleavage crosscutting the well-developed S_1 (Figure 2-5B). Occurrences of "Dome and Basin" and canoe-shaped F_1-F_2 fold interference pattern have been documented (Hall and Rigg, 1986). Variations in

F_2 plunge directions across the greenstone belt could be inherited from the geometry and orientation of D_1 structures (Breaks et al., 2001). Regional ductile D_2 shear zones of variable orientations, apparent motion, and stratigraphic implications occur throughout the NCB (Figures 2-2, 2-5A; Breaks et al., 2001). Microstructural evidence suggest some later reactivation (Kalbfleisch, 2012; Gagnon et al., 2016).

2.2.3.4 D_3 deformation event

Strain related to the D_3 deformation is unevenly distributed. It translates into a crenulation of the S_2 fabric, commonly associated with open to gentle, upright, west- to south-west-plunging chevron F_3 folds (Breaks et al., 2001). In the central NCG, large-scale F_3 folds have been interpreted based on reversal of L_2 lineations (Breaks et al., 2001). In the Opapimiskan Lake area, F_3 asymmetric folds are generally Z-shaped (Figure 2-5C; Hall and Rigg, 1986). Intensity and style of D_3 deformation depend on the competency and anisotropy of the deformed rocks. For instance, the S_3 crenulation is better developed in intensely foliated komatiitic basalts and pelitic bands of iron formations. Data from field and microstructural studies (Kalbfleisch, 2012; Gagnon et al., 2016), along with *in situ* U-Th-Pb monazite age dating, is interpreted to show the Markop Lake shear zone was reactivated during D_3 (Figure 2-5).

2.2.3.5 "D_4" deformation event

Minor post-D_3 deformation features generally consist in mesoscopic brittle structures such as strike-slip faults locally including fault breccia or pseudotachylite (Breaks et al., 2001). These faults commonly have offsets of less than one metre. In the West antiform area, Hall and Rigg (1986) reported their occurrence of northwest-striking, subvertical, chloritized shear zones, cored by lamprophyre dykes, which crosscut all previous fabrics.

2.2.4 Metamorphism

2.2.4.1 Regional metamorphism

The metamorphic facies of supracrustal rocks of the North Caribou greenstone belt increases northward (Breaks and Bartlett, 1991) and eastward (Breaks et al., 1986; Figure 2-6).

In the northern NCG, the area covered by the lower greenschist-chlorite zone extends south of Eyapamikama Lake. It comprises rocks of the SRA and a portion of the ELS, where chlorite and muscovite are ubiquitous in sedimentary rocks (Breaks and Bartlett, 1991). Both metamorphic minerals

define the S_1 foliation. The greenschist-biotite zone surrounds the chlorite zone and includes the AAV and KLA, as well as the northern ELS (Figure 2-6; Breaks and Bartlett, 1991). Two generations of biotite have been documented in pelitic rocks: a fine-grained biotite defining the regional S_1 fabric, and a coarser, poikiloblastic biotite defining the S_2 crenulation cleavage (Breaks and Bartlett, 1991). Volcanic rocks of the AAV contain little to no biotite. The sedimentary rocks of the northernmost ELS attain the upper greenschist metamorphic facies, marked by the appearance of garnet. The garnet zone also extends into the NRA. Garnet overgrows the S_1 foliation and appears unaffected by D_2 strain (Breaks and Bartlett, 1991). Several occurrences of higher temperature mineral assemblages have been documented ("High-T assemblages" on Figure 2-6; Satterly, 1941; Breaks and Bartlett, 1991; Kelly et al., 2013; Gagnon, 2015), including garnet-biotite-staurolite-andalusite (garnet zone), garnet-biotite-staurolite ± sillimanite (staurolite and sillimanite zone), and garnet-biotite-andalusite ± cordierite. One occurrence of kyanite was also documented in pelitic rocks, attesting for amphibolite grade metamorphism in the northern NCG (Breaks and Bartlett, 1991).

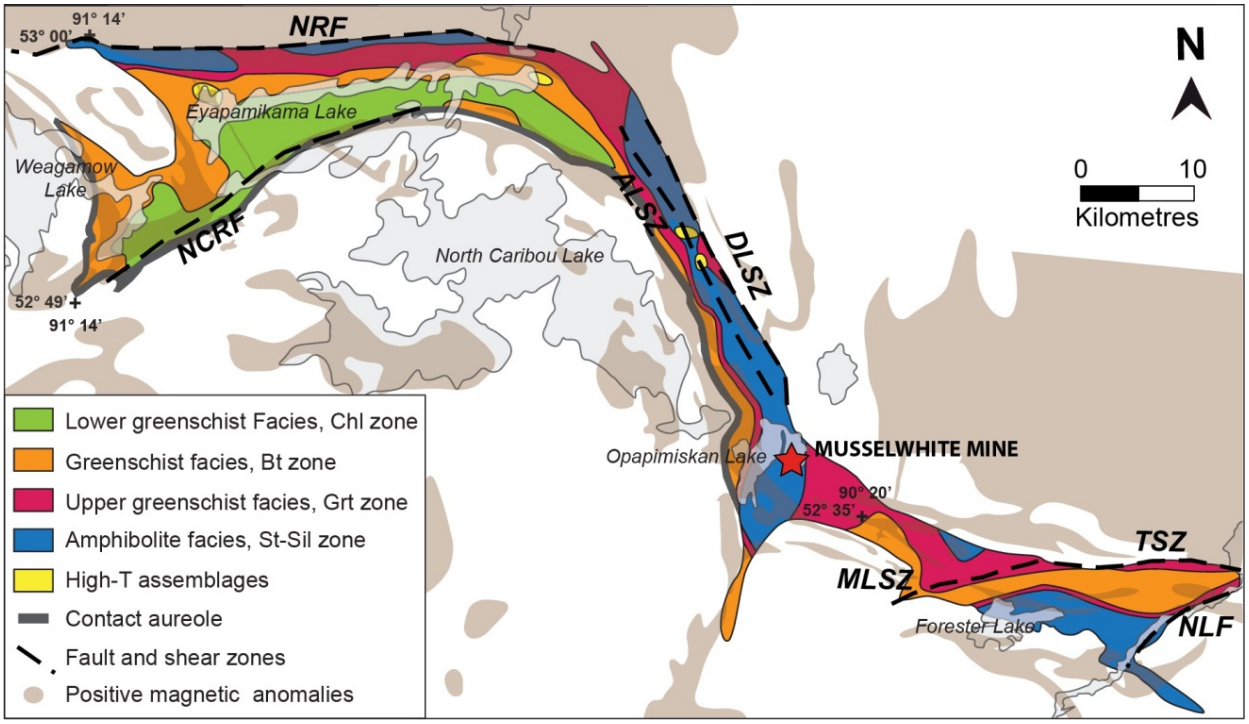

Figure 2-6: Metamorphic facies of the NCG (modified from Gagnon et al., 2015, after Breaks et al., 2001, and Kelly et al., 2013). NRF: North Rim fault zone, NCR: North Caribou River fault zone, DLSZ: Dinnick Lake shear zone, ALSZ: Akow Lake shear zone, MLSZ: Markop Lake shear zone, TSZ: Totogan shear zone, NLF: Neawagank Lake fault zone.

In the central NCG, the chlorite zone is absent (Figure 2-6). The biotite zone extends over the western half of this section of the NCG (Breaks et al., 1991). There, low-K_2O mafic and ultramafic rocks consist in green hornblende and plagioclase feldspar. The garnet and staurolite-sillimanite zones extend over the

eastern half of the central NCG (Breaks et al., 1991; Gagnon et al., 2015). Similarly to the northern NCG, pelitic rocks of the central NCG display mineral assemblages that suggest M_1 metamorphism produced a first generation of matrix biotite and hornblende and porphyroblasts such as andalusite, staurolite, and cordierite (Breaks et al., 1991). Also, garnet porphyroblasts appear to be related to M_2 and are affected by some of D_2 deformation. For instance, some garnet-rich layers in BIF show D_2-related boudinage (Breaks et al., 1991). M_2 biotite and subordinate chlorite define the S_2 foliation and are overprinted by late-D_2 hornblende poikiloblasts (Breaks et al., 1991). Volcanic lithologies of the LLV are Mg-rich rocks mainly composed of actinolite, and may contain some Mg-chlorite despite being within the garnet isograd (Breaks et al., 1991).

Recent research (Gagnon, 2015, and reference therein) has improved the interpretation of metamorphic patterns in the southeastern NCG. The garnet ± staurolite zone is thought to extend over most of the southeastern NCG, with the exception of a narrow biotite zone along the MLSZ and Totogan SZ (Figure 2-6). Mafic rocks of the FLV generally comprise hornblende and plagioclase (Breaks et al., 1986).

Pressure-temperature conditions for regional metamorphism have been estimated in the northern NCG using staurolite-bearing rocks and critical reaction curves (Breaks et al., 2001, and reference therein). Thermobarometric data ranges between 400-500°C and 3 kbar (0.3 Gpa) pressure. In pelitic rocks containing the staurolite-garnet assemblage in the southeastern NCG (Forester lake area; Figure 2-6), estimates are around 550°C and 3-4 kbar (Breaks et al., 1986). Garnet-biotite geothermometry was conducted on pelitic bands within barren and gold-mineralized iron formation along the southern shore of Opapimiskan Lake (using Ferry and Spear, 1978 calibration; Hall and Rigg, 1986). Calculations were performed with 3 kbar pressure corrections according to Carmichael (1984, unpublished) petrogenetic grid and indicate temperature estimates of 500-550°C (Hall and Rigg, 1986). Arsenopyrite geothermometry was also carried out, following indications from Sharp et al. (1985), and provided temperature estimates of 530-570°C for arsenopyrite crystallization (Hall and Rigg, 1986). Geobarometric calculations on samples of barren garnet-biotite schist and garnet-amphibole iron formation from the Musselwhite mine area suggest pressures of 5 to 7 kbar (Otto, 2002). Corresponding geothermometric calculations obtained temperatures between 540 and 600°C. While Otto's (2002) pressure estimates are significantly higher than the ones of Hall and Rigg (1986), temperatures are within similar ranges.

Minor retrograde metamorphism in the Opapimiskan Lake area is evidenced by chlorite overprinting higher temperature assemblages (Breaks et al., 2001). Thermometric calculations on a chlorite-bearing ore sample from Musselwhite mine suggest this occurred under temperatures ca. 210-250°C (Otto, 2002).

2.2.4.2 Contact metamorphism

A contact metamorphism aureole, 100 m to 1 km wide, around the ca. 2728 Ma (Van Lankvelt, 2013) North Caribou pluton (NCP) has been documented in the northern NCG (Figure 2-6; Breaks and Bartlett, 1991). It is characterized by a hornblende-plagioclase assemblage in mafic volcanic rocks of the SRA. The pattern of regional metamorphic isograds increases away from the NCP suggesting it did not contribute to regional metamorphism (Breaks et al., 1991). It is unclear, however, whether the contact metamorphism aureole overprints or is overprinted by the regional metamorphic paragenesis. In contrast, no contact aureole is associated with the SLGC. Metamorphic minerals affected by structural fabrics advocate that regional, upper greenschist-amphibolite grade metamorphism and D_1 and D_2 deformations post-date the emplacement of these batholiths (Kalbfleisch, 2012). Thus, it is likely that the SLGC contact aureole has been obliterated by subsequent geological events. Despite poor exposure of the Southern Batholith (SB) at the boundary with the greenstone belt, Breaks et al. (1986) report a hornblende-plagioclase assemblage in volcanic rocks and suggest it may represent the contact aureole of the SB.

In the upper and central NCG, multiple, well-defined, cordierite-rich zones have been mapped in pelites of the ELS (Breaks and Bartlett, 1991; Breaks et al., 1991; Gagnon, 2015, and reference therein). They form elliptical shapes of a few hundred metres to a few kilometres (Figure 2-6). Locally, the highest metamorphic grade is identified by the cordierite-sillimanite association. Sillimanite tends to grow as randomly oriented fibrous aggregates (Breaks and Bartlett, 1991). These cordierite-rich zones within sedimentary units coincide with local positive magnetic susceptibility anomalies (Ontario Geological Survey 2003), suggesting they could represent surface expression of the contact aureole of unexposed small intrusive bodies generated by partial melting of sediments (Biczok et al., 2012).

2.2.4.3 Timing constraints on metamorphism

The northward-increasing regional metamorphic gradient observed in the northern NCG and contact aureole, surrounding the NCP, suggest that its emplacement may have modified a pre-existing metamorphic pattern (Breaks et al., 2001). This would imply that some metamorphism occurred prior to the 2870-2830 Ma period and prior to the Kenoran orogeny constrained between 2750 and 2500 Ma, with culmination of tectonism between 2720 and 2660 Ma (Thurston et al., 1991). However, most of the metamorphic history of the NCG and the Superior province is thought to relate to the Kenoran orogeny (Thurston et al., 1991, Stott, 1997; Percival et al., 2006).

2.2.5 Economic geology

Since the early days of prospection by the Musselwhite brothers in the early ’70s, exploration in the NCG has focused on gold mineralization, which occurs in seven of the NCG supracrustal assemblages (Piroshco et al., 1989; Breaks et al., 2001; Figure 2-7; Table 2-1). Other commodities include Ag-Zn-Pb-Cu in shear-hosted, sulphide-rich, quartz-calcite veins (Breaks and Bartlett, 1991), Zn-Cu-Pb in massive sulphides (Janes et al., 1990), or Pt-Pd in magmatic sulphides (Breaks et al., 1986).

Most gold occurrences are of the auriferous quartz-veins type (section 1.5.2; Breaks et al., 2001). They are hosted by biotite- to carbonate-altered, mafic to ultramafic, metavolcanic rocks and in oxide- and silicate-facies iron formations (Piroshco et al., 1989). Gold grades show a strong spatial association with sulphide species. For instance, at the Wesley Lake occurrence gold is found with massive to disseminated arsenopyrite-pyrite-pyrrhotite veinlets hosted by sheared dioritic rocks. Gold is also frequently spatially associated with D_2-related structures (Piroshco et al., 1989). This is notably the case of gold occurrences around Opapimiskan Lake and at Musselwhite mine, where vein- and replacement-type, sulphide-bearing, gold mineralization is found at the intersection of D_2 structures with the BIF horizons (Hall and Rigg, 1986).

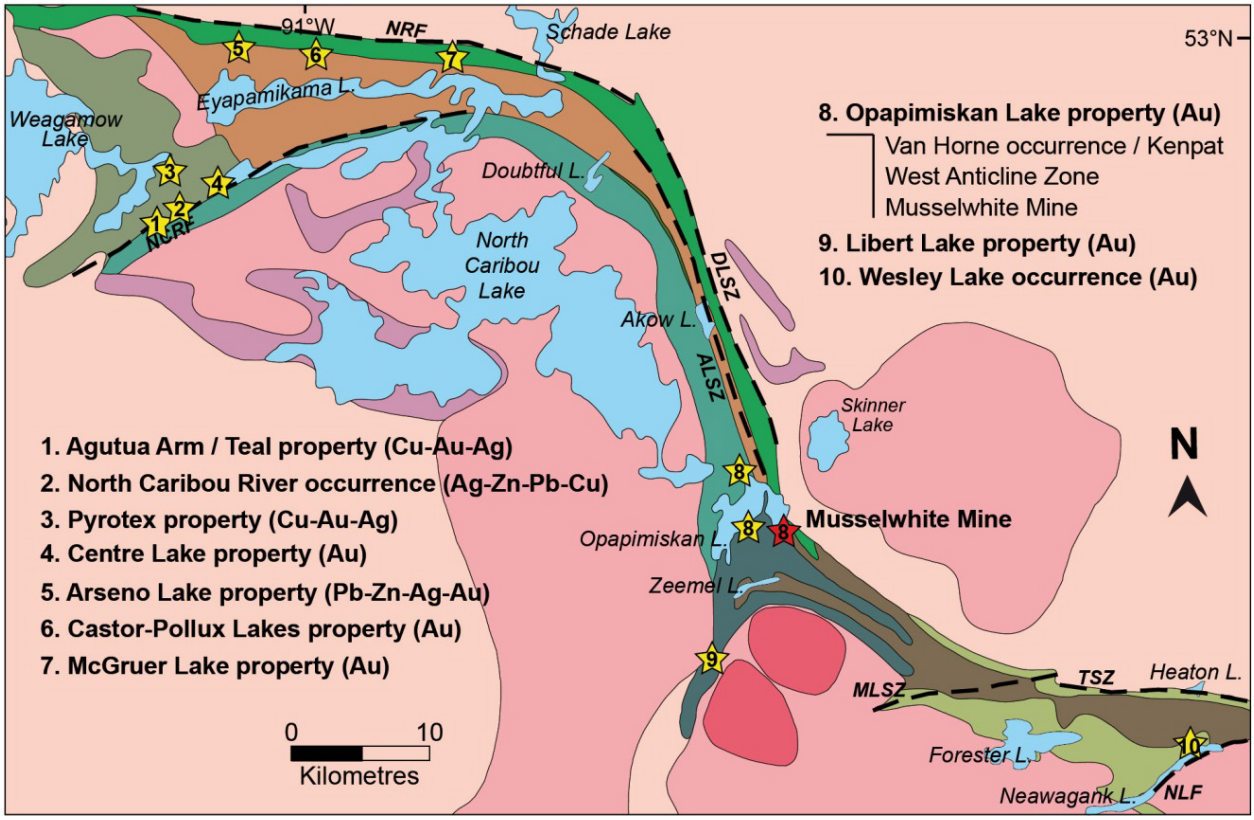

Figure 2-7: Location of major mineral occurrences in the North Caribou greenstone belt. Data from Breaks et al. (2001) and reference therein. Legend: see Figure 2-2.

The Teal and Pyrotex occurrences in the Agutua Arm assemblage (Figure 2-7; Piroshco and Shields, 1985) are notable as they contain anomalous values of Cu-Au-Ag and mineral assemblages such as tetrahedrite, native silver, and Ag-Sb phases, which are interpreted by Breaks et al. (2001) as suggesting epithermal-style metallic association. In light of the Musselwhite deposit and of the multiple showings in the SRA, LLV, and NRA, north of Opapimiskan Lake, BIF-hosted gold mineralization is a key target for exploration in the NCG (Breaks et al., 2001). Molybdenite-fluorite occurrences are apparently associated with the late-D_2 peraluminous intrusions located on both ends of Eyapamikama Lake (Breaks and Bartlett, 1991). Also, anomalous gold values were reported in association with albite-rich dykes at Musselwhite n°1 showing (West Anticline Zone; Piroshco et al., 1989).

Table 2-1: Types of gold mineralization associated with supracrustal assemblages of the North Caribou Lake belt, modified from Breaks et al. (2001).

Supracrustal assemblage	Mineralization type	Gold	Silver/ Lead/ Zinc	Examples
AAV	Ankerite-sulphide quartz veins in carbonatized D2 shear zones	2.4-1115 ppm	32.2-3011 ppm	Teal Cu-Ag-Au occrrence
		530-4200 ppb	72-100 ppm	North Caribou River occurrence
	Arsenopyrite-chalcopyrite-pyrite quartz veins in carbonatized mafic metavolcanic rocks	5-72 600 ppb	<2-36 ppm	Pyrotex Cu-Au-Ag occurrence
KLV	Pyrite-arsenopyrite carbonatized ultramafic rocks	380-470 ppb		Centre Lake Au occurrence
ELS	Arsenopyrite-bearing interbanded metapelite and dolomitic marble	1.4 ppm		Castor Lake
NRA	Grunerite + magnetite BIF, local arsenopyrite, pyrrhotite	1.4-7.2 ppm		Castor lake
	Arsenopyrite-tourmaline;	10.7 ppm (grab)		McGruer Lake Au occurrence
	Quartz vein in BIF	1.7 m @ 5.1 ppm		
	Grunerite + magnetite BIF with arsenopyrite, sphalerite, galena	274 ppm, 1.4 ppm	4.9% Pb, 3.6% Zn	Arseno lake Pb-Zn-Ag-Au occurrence
OMA	Grunerite - magnetite BIF associated with mafic metavolcanic rocks	3.2 Mt averaging 5.8 3.3 m @ 3 ppm to 15 cm @1444 ppm 3.6 m @ 4.4 ppm		Musselwhite deposit, Opapimiskan Lake Van Horne Resources Au occurrence, North Opapimiskan Lake Paseminon River occurrence
SRA	Arsenopyrite-pyrite-bearing shear zone in mafic metavolcanic rocks	605-4630 ppb		Seeseep Channel occurrence
	Tourmaline-sulphide-carbonate quartz vein in mafic metavolcanic rocks	6.1 m @ 8.2 ppm		Kenpat N°1 Vein, Opapimiskan Lake
FLV	Arsenopyrite-pyrite shear zone in metagabbro	2.5-14.4 ppm		Wesley Lake occurrence

3 PETROGRAPHY AND GEOCHEMISTRY OF ROCK UNITS IN THE MUSSELWHITE MINE AREA

3.1 Introduction

This chapter provides the geological, petrographic and petrologic characterization of rocks units of the Musselwhite deposit area, based on macroscopic and microscopic descriptions, and lithogeochemical data. Geochronological data of key igneous and sedimentary units, providing the latest stratigraphic constraints on the NCGB in the study area, is presented in chapter 4. The tectonostratigraphy of the Musselwhite deposit comprises the uppermost part of the South Rim assemblage (SRA), the Opapimiskan-Markop assemblage (OMA), and part of the Zeemel-Heaton assemblages (ZHA), and is affected by a major F_2 fold ("East Bay synform" or "mine synform"; Figures 3-1, 3-2; Biczok et al., 2012; Oswald et al., 2015b). Data collected through geological mapping, structural analysis (chapter 5), and geochronological analyses (chapter 4; McNicoll et al., 2016) show that the Musselwhite mine sequence is overturned, probably resulting from D_1-D_2 polyphase folding (chapter 5): the oldest rocks (unit Avol) occur in the core of the East Bay synform (Figure 3-2), and structurally underlying rocks are younger. Consequently, units will be described below from the oldest to youngest, or from the structural top to bottom (Figure 3-1), with volcanic units first, then sedimentary units and intrusive units. Unit names correspond to the mine's lithological nomenclature. Despite the poorly defined stratigraphy of the ZHA, targeted geological mapping and geochronology have yielded data with significant implications for the regional geological evolution and genetic model of the Musselwhite deposit. Description of this assemblage is thus presented in a specific section at the end of this chapter.

The overall OMA stratigraphy established by sub-regional geological mapping in the Opapimiskan Lake area (Breaks et al., 2001; Biczok et al., 2012) was refined by underground mapping and trench mapping. Underground mapping and drill core description allowed thorough examination of part of the OMA extending from the felsic rocks of the SRA, in the core of the mine synform, to the volcanic rocks structurally underlying the Northern iron formation (NIF) (Figure 3-1). Although drill holes locally extend down to the Southern iron formation (SIF), the latter is mostly accessible from surface exposures. The PQ and South Shore trenches expose the NIF and volcanic rocks immediately above and below (Oswald et al., 2014b; Oswald et al., 2015a). West antiform trench 1, 4, and 5 as well as 4 km BIF trench expose the SIF and surrounding volcanic rocks (Figure 3-1; Oswald et al., 2015a). Insights on the geochemical composition of the rock sequence of Musselwhite mine were gained through sampling of drill cores (section 1.2.4).

Rocks of the Musselwhite mine area have been subjected to a highly variable degree of hydrothermal alteration (chapter 2). Macroscopic observations give a first-order appraisal of the level of alteration, although it may be cryptic. Lithogeochemical data provides a powerful means to characterize igneous and sedimentary rocks (this chapter) and to study the changes induced by the gold-bearing hydrothermal system (chapter 7). The following sub-sections therefore present the procedure used to establish groups of "least altered" samples considered suitable to represent the protoliths of the Musselwhite mine rock sequence, and give an overview of their lithogeochemistry.

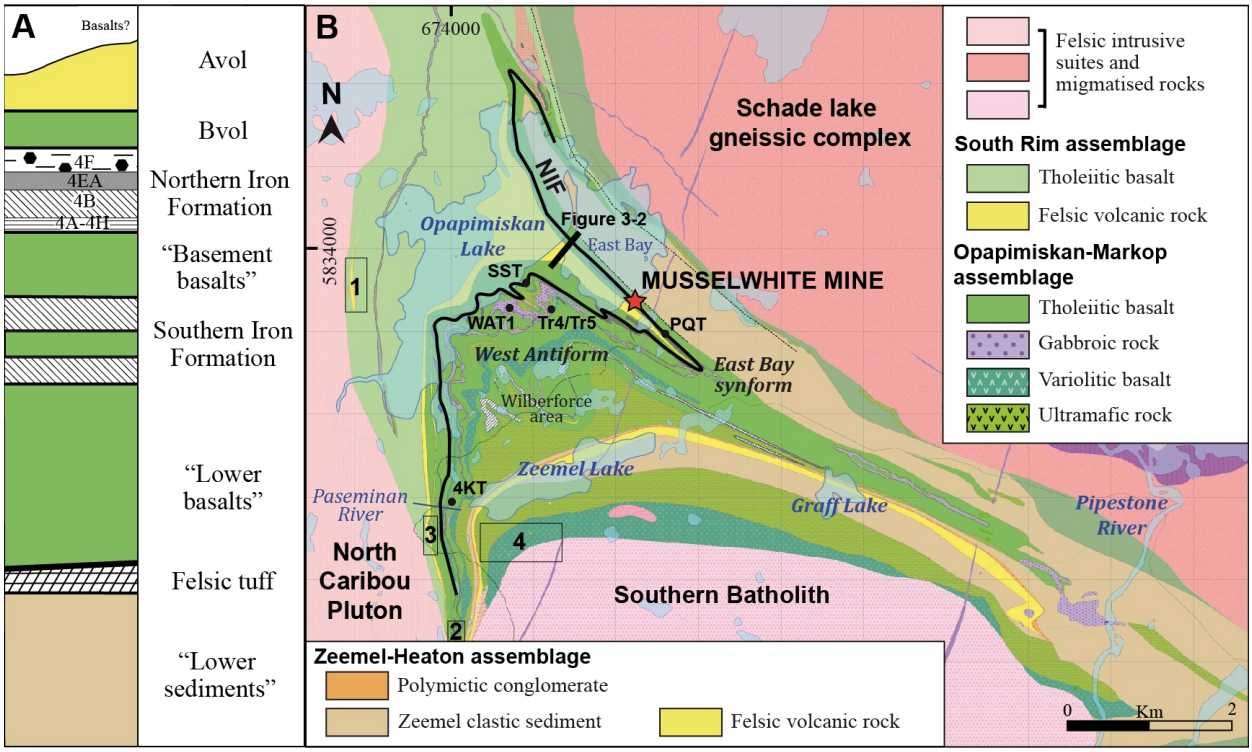

Figure 3-1: Geological setting of the Musselwhite mine. A. Schematic lithological column (local unit nomenclature; thicknesses not to scale) of the Musselwhite deposit area (modified from Biczok et al., 2012). B. Geological map of the Opapimiskan Lake area. Bold black line: Northern iron formation sequence. Black dots and codes refer to detail trench locations (WAT1 = West antiform trench 1, SST = South Shore trench, Tr4/Tr5 = Trench 4 and Trench 5, PQT = PQ trench, 4KT = 4 km BIF trench). Areas labeled 1 to 4 refer to study locations of Smyk (2013), Chadwick (2014), Pisani (unpublished), and Quinn (2014), respectively.

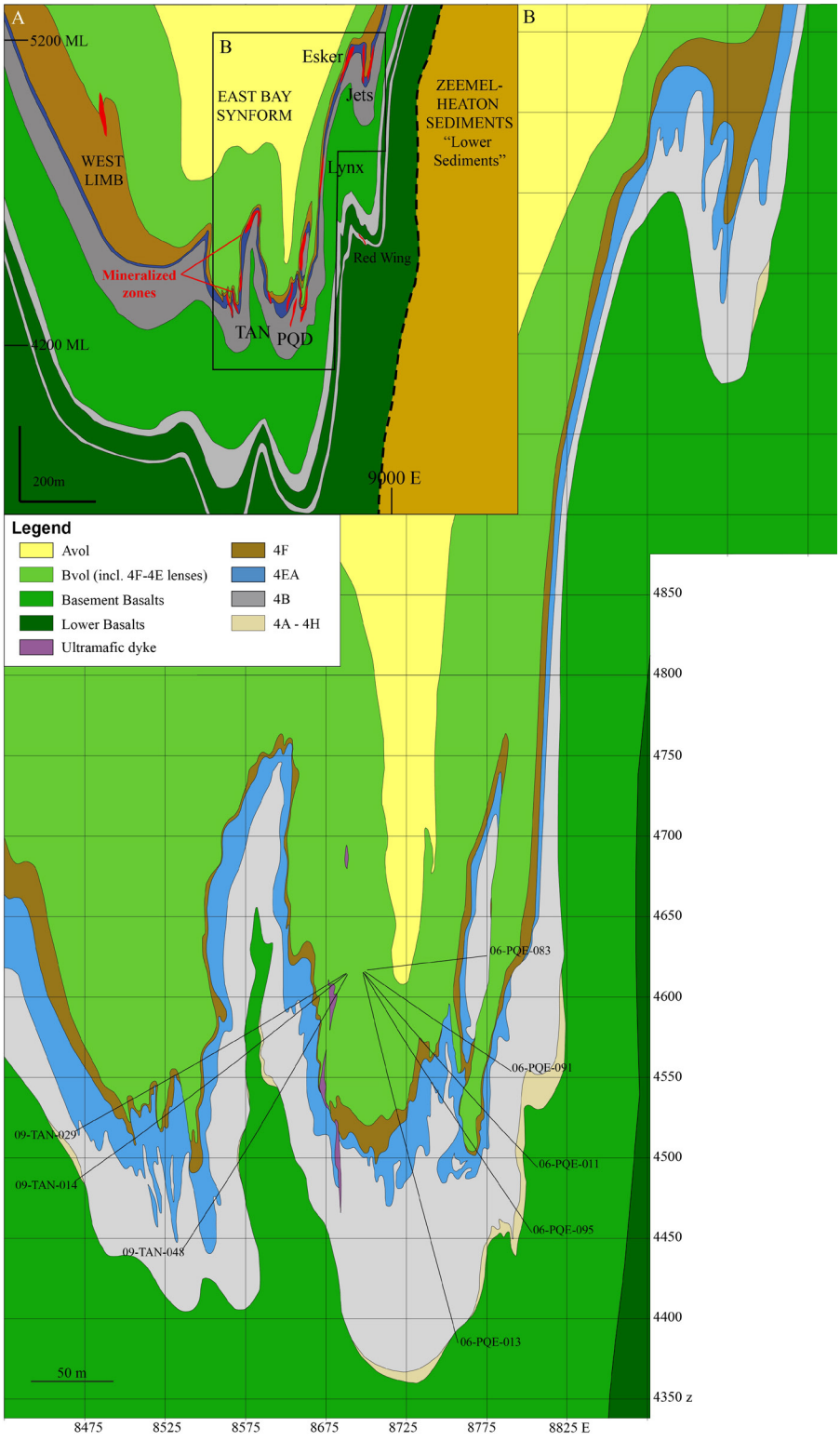

Figure 3-2: Geological section of Musselwhite mine. A. Schematic geological section of the East Bay synform on mine grid northing 11775 showing the structural position of the various mine ore bodies (red shapes), modified from Oswald et al. (2015a). Most sedimentary units of the Musselwhite mine sequence are comprised in the OMA. The OMA-ZHA boundary may not be linear, see chapter 5. B. Close-up of A, interpreted geological section of Musselwhite mine 11775 N with location of sampled drill holes (black lines).

3.1.1 Geochemistry of volcanic units

The selection of the "least altered" samples and the best "protolith" for units Avol and Bvol, the "Basement basalts" and the "Lower basalts" included an initial appraisal of the alteration intensity based on macroscopic criteria (i.e., presence of known alteration minerals, such as carbonates or sulphides; section 1.5), and further assessed with geochemical data and petrographic observations. Rock samples with abnormal major element signatures (compared to unaltered rocks) were discarded. Values of unaltered volcanic rocks were taken from GSC internal standards and available literature (Table 3-1 and Klein, 2004), with some margin so as to ensure that each group of "protoliths" or least altered rocks contains at least 10 to 20 samples and thus have better statistical significance (e.g., samples with K_2O content around 0.5 wt.% were kept despite GSC internal standards having K_2O content of 0.04 wt.%). The result shows that in terms of major element composition, unit Avol is typical of intermediate to near-felsic volcanic rocks (Table 3-1 and Table 3-2). Bvol, "Basement basalts", and "Lower basalts" have common ultramafic and mafic compositions ranging from komatiitic to normal and Mg-rich tholeiite (Figure 3-3), consistent with previous work (Breaks et al., 2001).

Some elements have relatively low reactivity with typical hydrothermal fluids of ore-forming systems (e.g., VMS, orogenic gold; MacLean and Barrett, 1993; Rollinson, 1994; Gifkins et al., 2005) and are considered immobile. These include major elements Al and Ti, as well as trace elements such as high-field-strength elements (HFSE; Ta, Nb, Y, Zr and Hf), and Rare Earth Elements (REE). Examination of ratio variations is helpful to assess the quality of analytical results and to understand the effect of alteration when characterizing volcanic rocks (Figure 3-4; MacLean and Barrett, 1993).

Volcanic units is mainly characterized hereafter in this chapter using immobile-element diagrams, which include: 1) a TiO_2-Zr fractionation trend (MacLean and Barrett, 1993), 2) a Nb/Y-Zr/Ti classification (Wynchester and Floyd, 1977), 3) a Zr/Y-Th/Yb magmatic affinity (Ross and Bédard, 2009), and 4) extended REE-profiles normalized to the primitive mantle (PM-n; Sun and McDonough, 1989).

Table 3-1: Average major element composition of Geological Survey of Canada internal standards and of the main volcanic units of the OMA in the Musselwhite mine area (data from the present study). n = number of samples used for each group.

(wt.%)	SiO_2	Al_2O_3	Fe_2O_3	FeO	Total Fe_2O_3	MnO	MgO	CaO	Na_2O	K_2O	TiO_2	P_2O_5	CO_2	LOI	Total S	n =
GSC Felsic standard																2
AVERAGE	75.39	12.77	0.35	0.85	1.29	0.032	0.535	1.415	3.435	2.13	0.199	0.045	1.00	2.05	0.06	
SD	0.70	0.14	0.41	0.35	0.02	0.001	0.007	0.021	0.007	0.01	0.001	0.007	0.01	0.07	0.00	
GSC Mafic standard																5
AVERAGE	46.75	16.28	2.41	7.66	10.93	0.169	8.88	11.16	1.85	0.042	0.85	0.06	0.125	3.22	0.098	
SD	0.52	0.17	0.13	0.15	0.13	0.001	0.19	0.12	0.02	0.004	0.01	0.01	0.068	0.13	0.041	
Avol																11
AVERAGE	70.69	14.73	0.68	2.58	3.55	0.09	0.62	2.75	2.90	2.67	0.45	0.15	0.50	1.08	0.29	
SD	1.24	0.43	0.44	0.71	0.78	0.036	0.22	0.44	0.99	0.51	0.016	0.02	0.25	0.34	0.19	
Bvol																35
AVERAGE	48.85	15.76	1.58	9.97	12.67	0.19	8.31	8.50	2.94	0.53	0.79	0.06	0.85	0.97	0.06	
SD	1.09	0.47	0.69	0.99	0.94	0.02	0.67	1.22	0.45	0.35	0.13	0.01	0.80	0.33	0.03	
Basement Basalts (mafic)																14
AVERAGE	53.57	12.98	1.18	8.77	10.94	0.19	9.03	7.82	2.47	1.07	0.60	0.06	0.36	1.27	0.08	
SD	3.79	1.41	0.34	0.89	0.87	0.01	2.44	2.05	0.67	0.80	0.08	0.015	0.25	0.49	0.06	

SD = standard deviation

Table 3-2: Average trace element composition and standard deviation of Geological Survey of Canada internal standards and of the main volcanic units of the OMA in the Musselwhite mine area (data from the present study). Number of samples of each group is the same as Table 3-1.

ppm	B	Be	Cr	Co	Ni	Sc	Mn	V	Cu	Pb	Zn	Ag	Au (ppb)	As	Ge	Sb	Se	Te	Tl	Bi	Cd	In	Sn	W	Mo
	Halogens		Transition metals									Prec. met.		Other trace metals						Granitoids					
GSC Felsic standard																									
AVERAGE	43.00	1.00	32.50	1.15	2.00	3.00	218.50	14.50	12.60	7.50	28.40	0.53	8.00	27.00	2.45	0.01	0.50	0.01	0.08	0.15	0.10	0.05	0.50	4.83	0.50
SD	7.07	0.00	19.09	0.07	0.00	0.00	19.09	2.12	2.55	2.12	2.12	0.39	2.83	16.97	0.92	0.00	0.00	0.00	0.07	0.08	0.00	0.00	0.00	6.47	0.00
GSC Mafic standard																									
AVERAGE	4.90	0.50	183.60	51.22	188.80	38.80	1246.00	265.00	126.80	1.00	69.52	0.25	4.30	78.18	2.02	0.04	0.41	0.05	0.03	0.05	0.10	0.06	0.50	0.39	0.50
SD	4.64	0.00	50.95	5.78	15.43	0.45	150.93	3.67	10.03	0.00	5.13	0.00	2.56	169.84	0.28	0.05	0.20	0.07	0.00	0.04	0.00	0.02	0.00	0.19	0.00
Avol																									
AVERAGE	36.80	0.80	28.90	9.79	20.30	8.40	598.20	62.60	27.15	8.40	58.39	2.42	15.65	6.71	1.42	0.03	0.34	0.03	0.47	0.04	-	-	-	2.25	0.55
SD	18.00	0.26	6.38	2.14	5.17	0.70	237.76	3.86	9.07	0.70	20.97	4.64	21.84	6.68	0.18	0.06	0.46	0.04	0.14	0.02	-	-	-	2.28	0.16
Bvol																									
AVERAGE	4.75	0.51	185.66	51.26	158.69	39.26	1412.59	269.77	150.66	1.77	93.43	0.28	12.18	29.62	2.05	0.08	0.12	0.05	0.05	0.04	-	-	-	1.29	0.54
SD	4.28	0.03	43.95	2.18	22.64	2.28	198.46	26.78	25.80	0.79	12.55	0.05	6.78	19.91	0.29	0.13	0.12	0.04	0.04	0.02	-	-	-	1.04	0.08
Basement Basalts (mafic)																									
AVERAGE	3.07	0.89	386.57	48.58	191.43	33.14	1398.57	197.29	82.05	6.71	95.95	0.47	10.71	27.22	2.07	0.19	0.71	0.19	0.10	0.03	-	-	-	1.64	0.71
SD	2.66	0.51	173.18	10.34	107.39	8.41	141.22	48.67	26.87	5.02	12.46	0.25	8.59	26.21	0.23	0.16	0.60	0.16	0.09	0.02	-	-	-	1.39	0.31

ppm	Li	Ga	Cs	Ba	Rb	Sr	Ta	Nb	Y	Zr	Hf	Th	U	La	Ce	Pr	Nd	Sm	Eu	Gd	Tb	Dy	Ho	Er	Tm	Yb	Lu
	Low Fields						High Fields							Rare Earth elements													
GSC Felsic standard																											
AVERAGE	11.00	12.50	2.15	525.00	72.00	147.50	0.99	11.00	15.95	114.50	2.80	10.90	2.67	42.20	72.75	7.49	24.60	3.75	0.69	2.74	0.40	2.54	0.52	1.74	0.30	2.06	0.36
SD	1.41	0.71	0.07	1.41	2.83	2.12	0.13	0.28	0.21	2.12	0.00	0.14	0.06	0.42	0.49	0.01	0.28	0.02	0.02	0.10	0.02	0.05	0.02	0.03	0.00	0.06	0.05
GSC Mafic standard																											
AVERAGE	14.60	15.40	0.16	15.40	0.50	114.40	0.11	1.10	12.44	30.40	0.80	0.13	0.03	2.11	5.51	0.86	4.40	1.45	0.61	1.83	0.34	2.25	0.48	1.40	0.22	1.42	0.21
SD	1.52	0.89	0.05	0.55	0.00	1.52	0.07	0.63	0.46	1.82	0.10	0.03	0.01	0.25	0.53	0.06	0.23	0.09	0.04	0.12	0.02	0.10	0.02	0.06	0.01	0.05	0.01
Avol																											
AVERAGE	18.20	17.20	3.12	283.30	68.30	105.90	0.73	7.49	13.14	163.00	3.78	7.26	1.86	26.54	49.30	5.42	19.32	3.51	0.87	2.92	0.44	2.47	0.48	1.38	0.21	1.34	0.22
SD	3.85	1.03	0.59	25.99	11.59	17.30	0.06	0.72	1.44	7.51	0.20	0.57	0.37	2.98	4.92	0.53	1.68	0.34	0.07	0.22	0.03	0.19	0.04	0.11	0.02	0.14	0.03
Bvol																											
AVERAGE	38.32	15.77	0.50	47.17	11.99	123.94	0.13	1.78	15.76	39.89	1.08	0.28	0.06	3.35	7.80	1.15	5.62	1.79	0.67	2.30	0.43	2.76	0.58	1.77	0.27	1.83	0.29
SD	13.75	1.33	0.39	43.01	11.15	28.45	0.04	0.65	2.46	7.78	0.23	0.09	0.02	1.31	2.30	0.26	1.12	0.31	0.10	0.41	0.07	0.43	0.09	0.28	0.05	0.30	0.04
Basement Basalts (mafic)																											
AVERAGE	23.14286	14.00	0.65	174.64	32.00	92.21	0.35	3.61	14.93	73.64	1.76	3.55	1.18	10.31	20.14	2.40	9.81	2.33	0.67	2.50	0.44	2.70	0.55	1.67	0.25	1.67	0.25
SD	7.142857	2.00	0.59	135.21	28.43	31.50	0.32	2.91	3.16	48.20	1.18	3.67	1.26	8.65	15.83	1.74	6.40	1.15	0.21	1.01	0.15	0.81	0.15	0.39	0.05	0.33	0.04

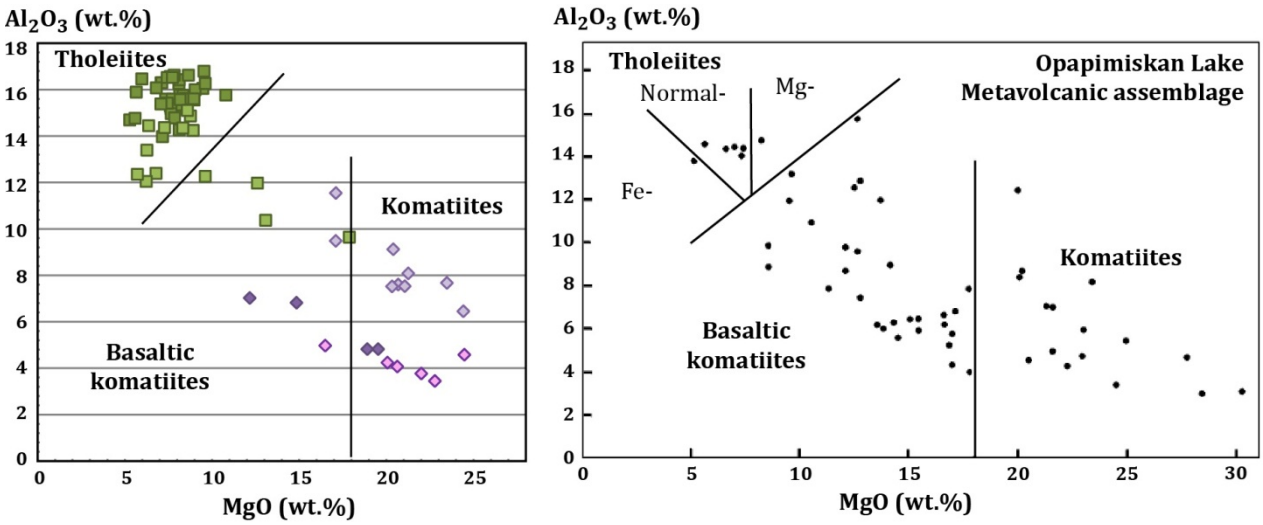

Figure 3-3: A. MgO vs. Al_2O_3 binary plot of least altered mafic to ultramafic rock samples from this study (dark green squares = unit Bvol; medium green squares = "Basement basalts" mafic rock samples; light purple diamonds = "Basement basalts" ultramafic rock samples; dark purple diamonds = "Lower basalts" unit; pink diamonds = ultramafic dyke samples). B. Surface rock samples from Breaks et al. (2001).

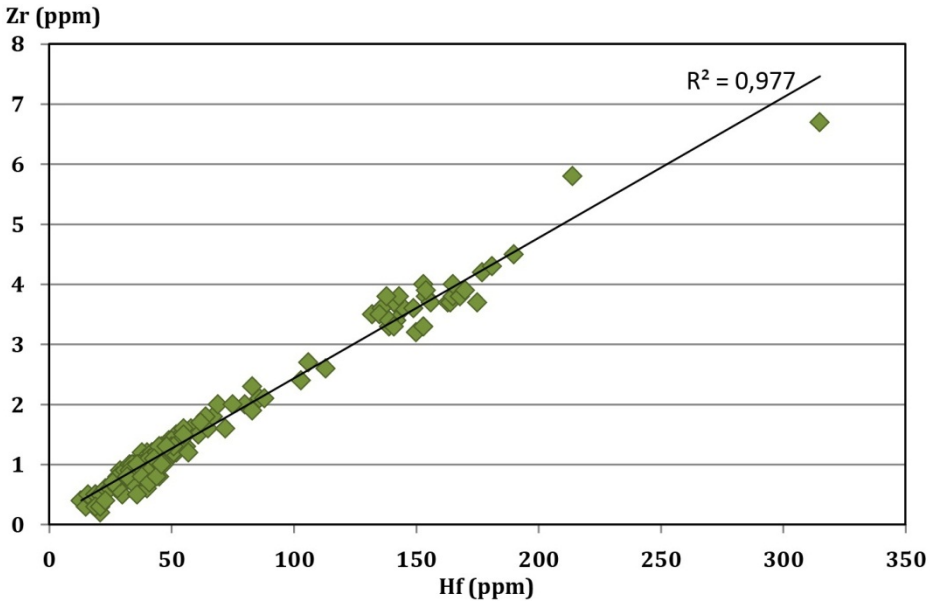

Figure 3-4: Zr-Hf plot of all volcanic rock samples from this study. The high linear correlation coefficient of these immobile elements, across sample batches, shows the good quality of geochemical analyses.

3.1.2 Geochemistry of sedimentary units

Most sedimentary units of the Musselwhite mine sequence are comprised in the OMA (Figure 3-2; Oswald et al., 2015b) and consist of mixed detrital-chemical sediments found as pelitic lenses at the base of and throughout unit Bvol (also referred to as "Intraformationals" – ITF), and as continuous BIF

horizons (NIF, SIF). The NIF consists of a single horizon separated into six facies that are exposed in underground mine workings and at the PQ trench. The SIF comprises four horizons including three facies, which are exposed at surface in the West antiform area.

Geochemical data from sedimentary samples was sorted using gold content (mostly <50 ppb) and major element oxides, with threshold values determined through literature review (Table 3-3; section 1.4; Govindaraju, 1994). BIF units are assessed in terms of major element oxides composition (Table 3-4) as well as trace element content (Table 3-5), notably Rare Earth Elements and yttrium (REE+Y) profiles. REE+Y profiles are normalized to the Mudstone of Queensland standard (MUQ; Kamber et al., 2005; Baldwin, 2011).

Table 3-3: Threshold values used to define "least altered" sample groups for each unit of the Northern iron formation. Threshold for gold was taken as low as possible and kept at 100 ppb when it would have reduced the number of samples kept too significantly. n = number of samples.

	Au (ppb)	**Na_2O**	**K_2O**	**CO_2**	**Total S**	**LOI**	**n =**
Unit 6	50	3.00	4.50	0.50	0.50	1.50	5
Unit 4E	100	0.35	1.00	1.15	1.00	1.00	8
Unit 4F	40	0.35	5.00	0.10	1.00	1.00	19
Unit 4EA	65	0.30	1.00	0.35	0.50	1.00	18
Unit 4B (c)	100	1.00	1.00	1.00	0.35	1.00	31
Unit 4B	70	0.25	0.50	4.00	0.50	3.00	31
Unit 4A	100	0.05	0.30	3.00	0.50	3.50	24
Unit 4H	100	2.50	3.50	-	-	-	10

In contrast with igneous rocks, sedimentary rocks do not have consistent contents of "immobile" elements to reliably define "protoliths". Instead, values typically fall within a given range, so that various ratios or combinations thereof have to be used to characterize the different facies (Figure 3-5). These elements (e.g., Al, Ti) are proxies for detrital input, in combination with iron content, which represents the contribution of chemical sedimentation (Figure 3-5A; Boström, 1973). Pelitic units are richer in "immobile" elements than BIF units (Figure 3-5A; Klein, 2005; chapter 1), as is reflected by our data from units 6 and 4F. Whereas, their $Al_2O_3/(Al_2O_3$+Total Fe III+MnO) ratios reflect an elevated detrital contribution, while silicate- and oxide-BIF facies (units 4EA, 4Bc, 4B, 4A) contain >60% of chemically-derived input. Unit 4E has a composition with roughly equivalent detrital and chemical contributions (Figure 3-5B). Ternary plots of aluminum-iron with volatile (CO_2, total S, and LOI) also contribute distinguishing the most chemically-derived facies (i.e., unit 4B, 4A; Figure 3-5B). Such distinctions can also be made using MUQ-n Eu and Y anomalies as proxies for hydrothermal and hydrogenous contributions (Figure 3-6; Lawrence and Kamber, 2006; Oswald et al., 2015b).

Table 3-4: Average major element composition and standard deviation for sedimentary units of the OMA (data from this study). Negative LOI is due to iron oxidation during ignition (section 1.2.4; Dahéron et al., 2015). n = number of samples.

	SiO_2	Al_2O_3	Fe_2O_3	FeO	Total Fe_2O_3	MnO	MgO	CaO	Na_2O	K_2O	TiO_2	P_2O_5	CO_2	Total S	LOI	Au (ppb)	n =
Unit 6																	5
Average	62.73	16.63	0.72	5.6	6.95	0.12	2.14	3.92	1.93	3.69	0.43	0.097	0.18	0.045	0.26	5.80	
SD	1.85	0.34	0.39	1.09	1.51	0.04	0.52	0.76	0.76	0.32	0.03	0.01	0.19	0.05	0.38	4.97	
Unit 4E																	8
Average	51.39	8.21	8.03	19.63	29.86	0.48	3.92	5.27	0.28	0.29	0.35	0.13	0.71	0.67	-2.61	55.87	
SD	3.31	3.4	1.85	3.92	4.4	0.16	0.65	1.62	0.15	0.27	0.16	0.03	0.34	0.23	0.77	23.51	
Unit 4F																	19
Average	51.82	17.9	4.07	13.38	18.94	0.62	2.8	1.93	0.32	3.72	0.96	0.09	0.05	0.46	-1.09	22.15	
SD	2.62	2.07	1.91	2.34	2.57	0.38	0.56	1.02	0.43	0.56	0.13	0.02	0.06	0.19	0.41	15.72	
Unit 4EA																	18
Average	48.3	8.11	12.24	23.59	38.47	0.66	3.04	2.03	0.1	0.45	0.38	0.14	0.16	0.21	-4.5	34.17	
SD	3.59	1.08	2.22	2.56	3.46	0.25	0.39	0.4	0.06	0.26	0.07	0.02	0.08	0.07	0.48	19.18	
Unit 4Bc																	26
Average	48.72	5.94	15.04	21.2	38.61	0.58	2.4	1.4	1.11	1.43	0.3	0.13	0.42	0.18	-3.17	20.02	
SD	2.16	0.97	2.67	1.39	2.48	0.16	0.21	0.5	0.63	0.67	0.06	0.02	0.24	0.06	0.45	21.89	
Unit 4B																	36
Average	46.00	1.81	19.78	22.25	44.53	0.67	2.69	3.14	0.175	0.35	0.087	0.16	1.79	0.24	-2.11	25.39	
SD	2.15	1.07	3.81	1.71	2.86	0.23	0.56	0.95	0.14	0.23	0.06	0.02	0.77	0.1	0.92	26.90	
Unit 4A																	25
Average	63.53	1.002	5.13	18.92	26.17	0.84	2.69	3.60	0.054	0.236	0.038	0.123	2.05	0.98	-0.662	29.23	
SD	11.06	1.02	3.23	4.88	7.14	0.45	1.08	1.59	0.04	0.28	0.04	0.05	1.15	1.44	0.96	25.22	
Unit 4H																	10
Average	47.02	8.86	4.05	20.33	26.66	0.34	2.61	5.07	1.1	1.83	0.4	0.08	1.16	9.2	3.23	55.90	
SD	7.75	3.97	5.52	8.02	9.2	0.4	1.02	3.68	0.85	1.26	0.22	0.07	1.04	3.77	2.57	18.14	

SD = standard deviation

Table 3-5: Average trace element composition and standard deviation for sedimentary units of the OMA (data from this study). See Table 3-4 for number of samples used.

ppm	B	Be	Cr	Co	Ni	Sc	Mn	V	Cu	Pb	Zn	Ag	Au ppb	As	Ge	Sb	Se	Te
Unit 6																		
Average	36.40	1.40	70.20	24.94	71.20	18.40	919.40	134.40	67.32	9.40	67.64	0.54	11.00	52.26	2.14	0.19	0.39	0.12
SD	26.91	0.55	47.96	24.33	81.62	14.94	296.28	108.67	91.60	3.36	10.94	0.29	12.50	96.69	0.55	0.35	0.19	0.19
Unit 4E																		
Average	9.13	1.31	76.88	20.76	51.75	12.88	3338.75	101.13	83.65	3.25	140.78	0.29	55.88	17.26	3.96	0.07	1.15	0.28
SD	11.68	0.75	45.52	10.26	27.44	7.06	1257.54	49.30	46.61	1.83	76.33	0.12	23.51	20.64	1.22	0.15	0.63	0.17
Unit 4F																		
Average	55.12	1.44	232.37	49.79	139.32	39.05	3880.56	291.42	170.02	5.53	165.21	0.59	22.34	78.36	2.97	0.05	0.91	0.24
SD	27.77	0.73	54.05	10.21	27.51	6.28	2215.58	48.51	57.18	2.72	90.66	0.23	14.92	63.38	0.93	0.06	0.47	0.20
Unit 4EA																		
Average	1.03	1.72	96.56	19.71	53.67	14.56	4587.06	113.44	60.20	3.03	83.63	0.30	34.17	26.92	4.98	0.12	0.77	0.17
SD	1.23	0.55	20.88	3.70	11.69	2.85	1556.96	19.63	22.78	1.36	19.03	0.13	19.18	26.83	1.01	0.23	0.40	0.14
Unit 4Bc																		
Average	3.69	1.94	76.96	15.84	41.77	11.04	3996.54	90.23	59.54	3.00	56.40	0.39	20.48	12.66	6.27	0.20	0.76	0.18
SD	5.07	0.29	19.35	3.25	10.12	1.99	983.30	17.77	16.32	0.89	13.67	0.52	21.78	15.72	1.63	0.32	0.45	0.13
Unit 4B																		
Average	2.89	2.07	46.44	7.28	17.92	4.04	4793.80	34.53	25.61	2.31	35.51	0.28	24.31	17.06	6.10	0.49	0.80	0.20
SD	3.43	0.59	28.20	4.22	11.96	3.12	2086.26	26.03	17.89	1.01	14.12	0.11	26.43	24.54	2.39	0.58	0.50	0.17
Unit 4A																		
Average	7.18	1.56	42.48	5.84	19.00	1.76	5135.22	16.00	22.37	4.60	57.21	0.25	28.50	51.86	1.94	0.29	1.24	0.30
SD	17.65	0.74	44.73	5.79	19.79	2.31	2466.07	16.55	23.90	4.41	61.64	0.00	24.96	67.64	0.82	0.36	1.75	0.43
Unit 4H																		
Average	244.35	1.45	126.60	82.69	317.10	15.40	2452.70	116.90	338.60	65.10	1071.40	0.34	55.90	199.30	1.25	0.17	3.44	1.58
SD	470.91	0.76	85.93	45.95	248.66	10.74	3101.75	60.91	190.81	51.95	907.78	0.20	18.14	462.12	0.38	0.33	0.69	0.71

Table 3-5 (cont'd): Average trace element composition and standard deviation for sedimentary units of the OMA (data from this study). See Table 3-4 for number of samples used.

ppm	Tl	Bi	Cd	In	Sn	W	Mo	Li	Ga	Cs	Ba	Rb	Sr	Ta	Nb	Y	Zr	Ti
Unit 6																		
Average	0.23	0.07	0.14	0.05	0.60	3.69	0.50	35.00	18.20	2.32	300.40	103.80	98.60	0.52	4.72	9.74	123.00	3352.32
SD	0.06	0.04	0.09	0.00	0.22	6.23	0.00	14.21	1.79	0.61	66.63	25.67	38.38	0.23	2.02	1.14	40.01	1691.10
Unit 4E																		
Average	0.05	0.06	0.23	0.06	0.50	1.13	1.25	18.88	9.75	0.48	38.88	8.13	36.50	0.24	2.04	15.08	46.75	2110.93
SD	0.04	0.02	0.12	0.02	0.00	0.91	1.22	12.08	4.17	0.44	30.37	7.23	5.29	0.08	1.01	5.25	21.35	985.70
Unit 4F																		
Average	0.35	0.08	0.32	0.05	0.69	2.03	1.21	64.65	19.53	3.24	281.16	104.53	31.63	0.30	3.53	20.61	84.42	5684.27
SD	0.13	0.04	0.27	0.01	0.49	1.30	0.79	53.31	1.90	0.82	68.52	16.64	13.01	0.09	0.80	2.30	11.13	763.55
Unit 4EA																		
Average	0.07	0.05	0.15	0.08	0.50	1.06	0.94	16.47	9.50	1.71	138.22	22.47	31.28	0.18	1.84	17.94	46.44	2302.01
SD	0.06	0.03	0.09	0.03	0.00	1.27	0.54	7.21	1.65	1.39	142.12	13.54	11.96	0.07	0.71	3.62	6.54	404.18
Unit 4Bc																		
Average	0.29	0.04	0.10	0.06	0.50	1.57	0.81	11.19	7.35	16.52	197.46	74.62	54.77	0.15	1.24	14.62	34.81	1859.32
SD	0.18	0.02	0.02	0.02	0.00	2.81	0.72	5.76	1.23	11.85	48.86	32.00	22.54	0.15	0.62	2.10	6.40	362.11
Unit 4B																		
Average	0.10	0.03	0.10	0.06	0.50	2.09	1.13	4.00	3.44	5.86	76.56	27.32	39.58	0.06	0.51	11.54	14.43	668.59
SD	0.11	0.03	0.00	0.02	0.00	3.96	0.90	2.69	1.93	8.03	65.27	26.74	15.57	0.08	0.50	2.03	8.96	533.22
Unit 4A																		
Average	0.09	0.07	0.18	0.06	0.50	0.83	1.62	2.84	2.48	0.36	43.76	14.38	22.08	0.05	0.44	8.98	11.78	316.29
SD	0.12	0.05	0.20	0.02	0.00	1.06	1.13	3.27	2.55	0.35	99.60	18.83	16.89	0.13	1.11	3.71	18.96	508.85
Unit 4H																		
Average	0.63	0.72	3.37	0.08	1.50	2.89	4.50	13.00	15.20	1.54	312.60	55.70	56.40	0.32	3.12	16.22	63.30	2370.36
SD	0.70	0.39	2.68	0.03	1.13	2.03	1.90	9.10	6.68	3.02	254.61	35.11	42.67	0.14	1.62	2.98	26.17	1302.63

ppm	Hf	Th	U	La	Ce	Pr	Nd	Sm	Eu	Gd	Tb	Dy	Ho	Er	Tm	Yb	Lu
Unit 6																	
Average	2.92	4.37	1.30	19.55	33.77	3.58	12.79	2.45	0.83	2.17	0.33	1.90	0.36	1.05	0.15	1.03	0.16
SD	0.88	2.38	0.70	10.30	16.59	1.61	4.96	0.68	0.13	0.28	0.03	0.23	0.06	0.16	0.03	0.17	0.02
Unit 4E																	
Average	1.19	1.80	0.55	9.18	16.46	1.90	7.69	1.66	0.69	1.99	0.34	2.10	0.45	1.39	0.21	1.35	0.21
SD	0.55	0.70	0.23	3.13	5.27	0.62	2.42	0.57	0.24	0.67	0.11	0.71	0.16	0.46	0.07	0.42	0.07
Unit 4F																	
Average	2.07	2.07	0.66	10.04	20.38	2.56	10.78	2.69	0.97	3.22	0.57	3.59	0.75	2.27	0.35	2.34	0.36
SD	0.38	0.65	0.20	2.27	4.50	0.49	1.68	0.39	0.15	0.49	0.08	0.48	0.10	0.28	0.04	0.27	0.05
Unit 4EA																	
Average	1.12	1.53	0.45	8.97	16.10	1.91	7.56	1.72	0.77	2.12	0.36	2.32	0.50	1.54	0.24	1.55	0.25
SD	0.20	0.31	0.08	1.23	2.41	0.28	0.99	0.23	0.10	0.24	0.04	0.22	0.05	0.14	0.02	0.16	0.03
Unit 4Bc																	
Average	0.86	1.17	0.34	8.31	13.78	1.59	6.43	1.40	0.59	1.70	0.29	1.84	0.40	1.22	0.19	1.21	0.19
SD	0.15	0.18	0.06	1.97	3.25	0.35	1.33	0.29	0.10	0.33	0.05	0.32	0.07	0.21	0.03	0.20	0.03
Unit 4B																	
Average	0.34	0.53	0.15	5.39	8.84	1.04	4.22	0.92	0.55	1.19	0.20	1.31	0.29	0.92	0.14	0.93	0.15
SD	0.23	0.31	0.09	1.60	2.99	0.36	1.45	0.32	0.18	0.34	0.06	0.36	0.08	0.24	0.04	0.24	0.04
Unit 4A																	
Average	0.27	0.75	0.23	5.56	10.16	1.21	4.84	1.06	0.64	1.19	0.20	1.29	0.28	0.87	0.13	0.88	0.14
SD	0.50	1.30	0.39	4.15	7.73	0.88	3.51	0.75	0.29	0.69	0.11	0.69	0.14	0.41	0.06	0.42	0.07
Unit 4H																	
Average	1.54	4.50	1.41	15.57	29.97	3.50	13.67	3.03	1.18	2.78	0.46	2.89	0.60	1.81	0.28	1.95	0.33
SD	0.67	2.51	0.76	6.07	11.25	1.23	4.35	0.80	0.14	0.46	0.07	0.42	0.09	0.27	0.04	0.31	0.06

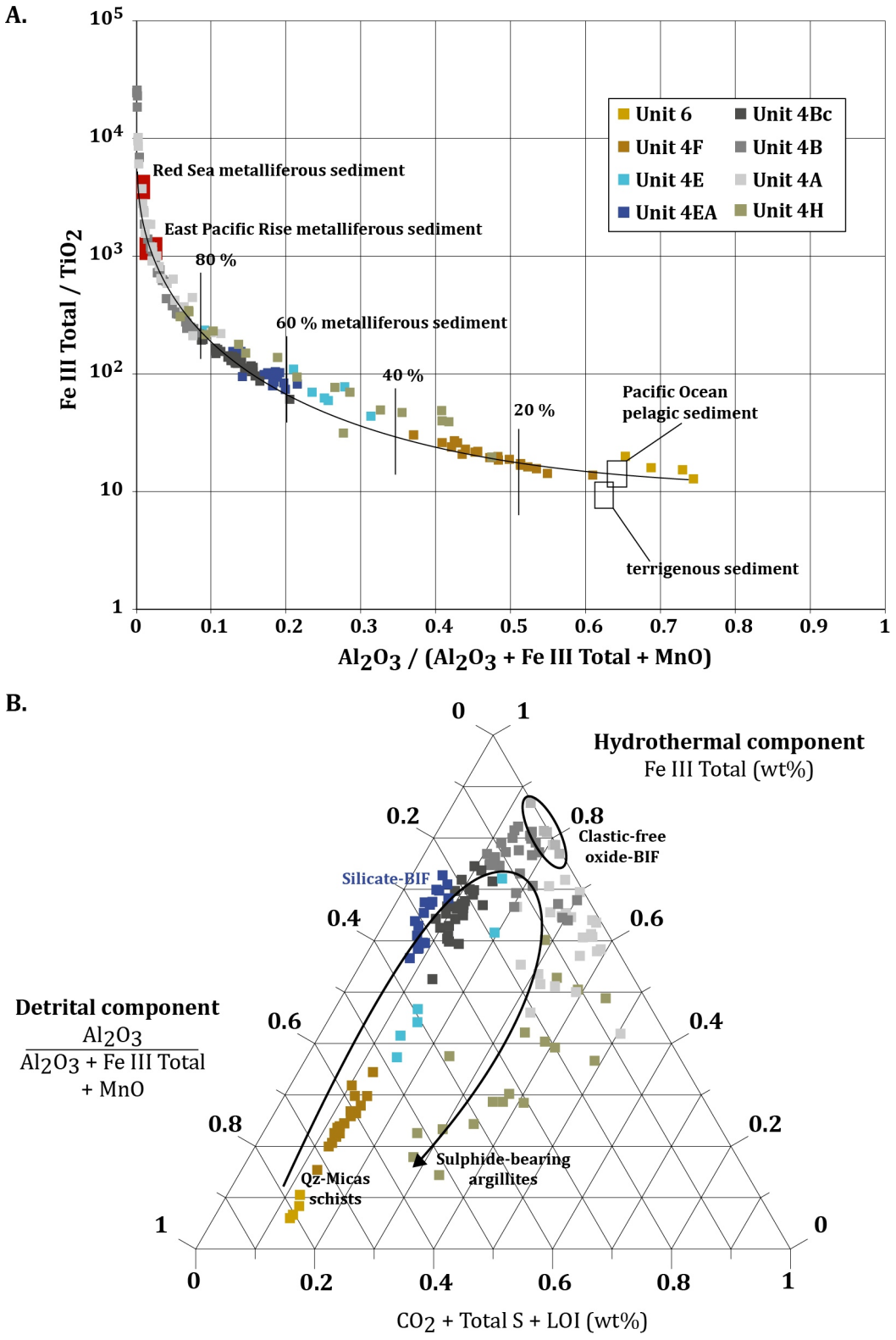

Figure 3-5: A. Binary plot of Fe/Ti vs. Al/(Al + Fe + Mn) ratios for least altered samples of the NIF sequence. Average fields of values for pelagic Pacific Ocean sediment, terrigenous sediment, and Red Sea and East Pacific Rise metalliferous sediment are from Boström (1973). B. Ternary plot showing the detrital/terrigenous

(Al_2O_3 / (Al_2O_3 + Fe III Total + MnO)), ferrous (Fe III Total), and volatile (CO_2 + total S + LOI) components of the siliciclastic and BIF facies of the NIF sequence. The black arrow represents the stratigraphic progression from unit 4F to unit 4H: detrital inputs dominates in the beginning, then the relative proportion of hydrothermal input increases with a minor hydrogenous component, and detrital input dominates again at the end.

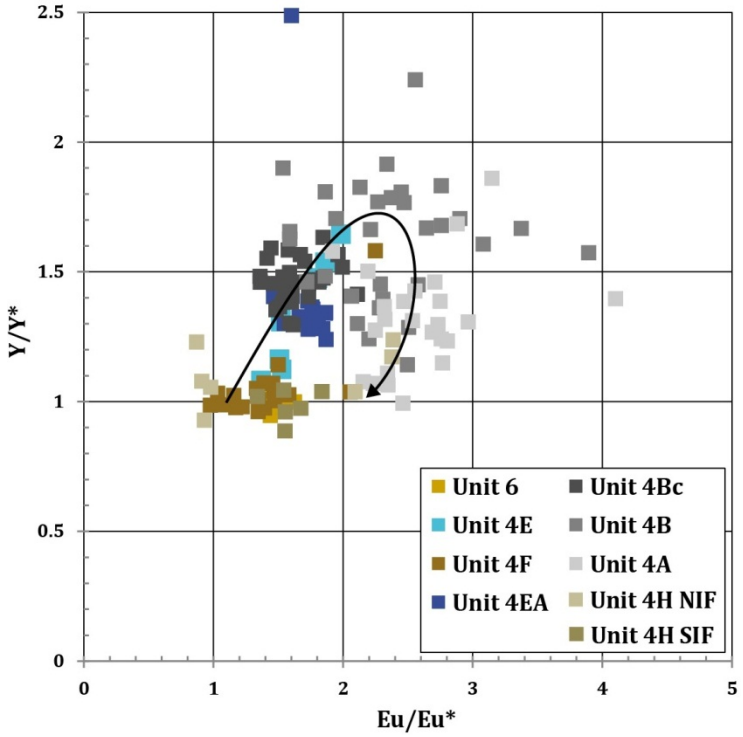

Figure 3-6: Binary plot of MUQ-n Eu and Y anomalies for sedimentary units of the OMA. Eu* = square-root of (Sm x Gd); Y* = square root of (Dy x Ho); The black arrow represents the stratigraphic progression from unit 4F to unit 4H.

3.2 Unit "Avol"

Unit Avol is the uppermost unit of the South Rim assemblage (SRA). The extent of the Avol has mainly been defined by drilling as it mostly lies underneath Opapimiskan Lake (Figure 3-1). It occurs as a 10-50 m band in the core of the East Bay synform, under the mine site, and wraps around the West antiform southwestward, where it is exposed in a series of outcrops southwest of Zeemel Lake (UTM 673500/5827500). These outcrops provide a section from west to east, starting in strongly bleached, pillowed basalt overlain by a metre-thick, chert-amphibole-garnet ± magnetite unit, and then across the Avol intermediate to felsic volcanic succession.

Unit Avol starts with minor, pillowed, andesitic to dacitic flows (Figure 3-7A). They are overlain by multiple, 1 to 15 m thick, dacitic massive flows and matrix-supported, polymictic fragmental rocks (Figure 3-7B to E). A decimetre-thin, fine-grained, felsic tuff overlies the fragmental rocks. Fragmental

lithologies comprise plagioclase-rich mafic clasts, plagioclase-phyric intermediate clasts, and fine-grained felsic clasts, the latter of which dominates in the upper part of the section. The contact between unit Avol and the structurally underlying unit Bvol often comprises a sedimentary garnet-biotite-quartz horizon, which locally includes thin, discontinuous, slivers of sulphide-rich argillite (mine unit 4H, section 3.12).

Unit Avol shows mineralogical composition variations. A typical sample from the dacitic units (Figure 3-7F), however, comprises 50 vol.% quartz, up to 30 vol.% micas (sericite and/or biotite), 5-15 vol.% feldspar (mainly plagioclase with minor K-feldspar), and trace amounts of tourmaline, apatite, ilmenite, calcite, and sulphides. Quartz grains are generally fine-grained (<50 μm), granoblastic (i.e., anhedral and equi-granular), and polygonal in shape (Figure 3-7G, H). Plagioclase feldspar is also fine-grained and granoblastic, intergrown with quartz and locally altered to sericite + albite. Micas are fine-grained, homogeneously distributed, and aligned along the main fabric. Biotite crystals are medium to dark brown, whereas sericite is colourless to pale brown.

Lithogeochemical data of Avol samples have TiO_2 and Zr average values of 0.4 wt.% and 160 ppm, respectively (Figure 3-8A), and classify in the dacite to rhyodacite field of composition (Figure 3-8B) with Zr/Ti and Nb/Y ratio values of around 0.06 and 0.5-0.8, respectively. Avol samples show a calc-alkaline magmatic affinity (Figure 3-8C) with Zr/Y values of 10.5 and Th/Yb values around 5-6. Primitive Mantle-normalized (PM-n) trace elements profiles show slightly concave HREE curves with steep MREE and LREE profiles (Figure 3-8D; PM values from Sun and McDonough, 1989) and strong negative Ti-, Ta- and Nb-anomalies.

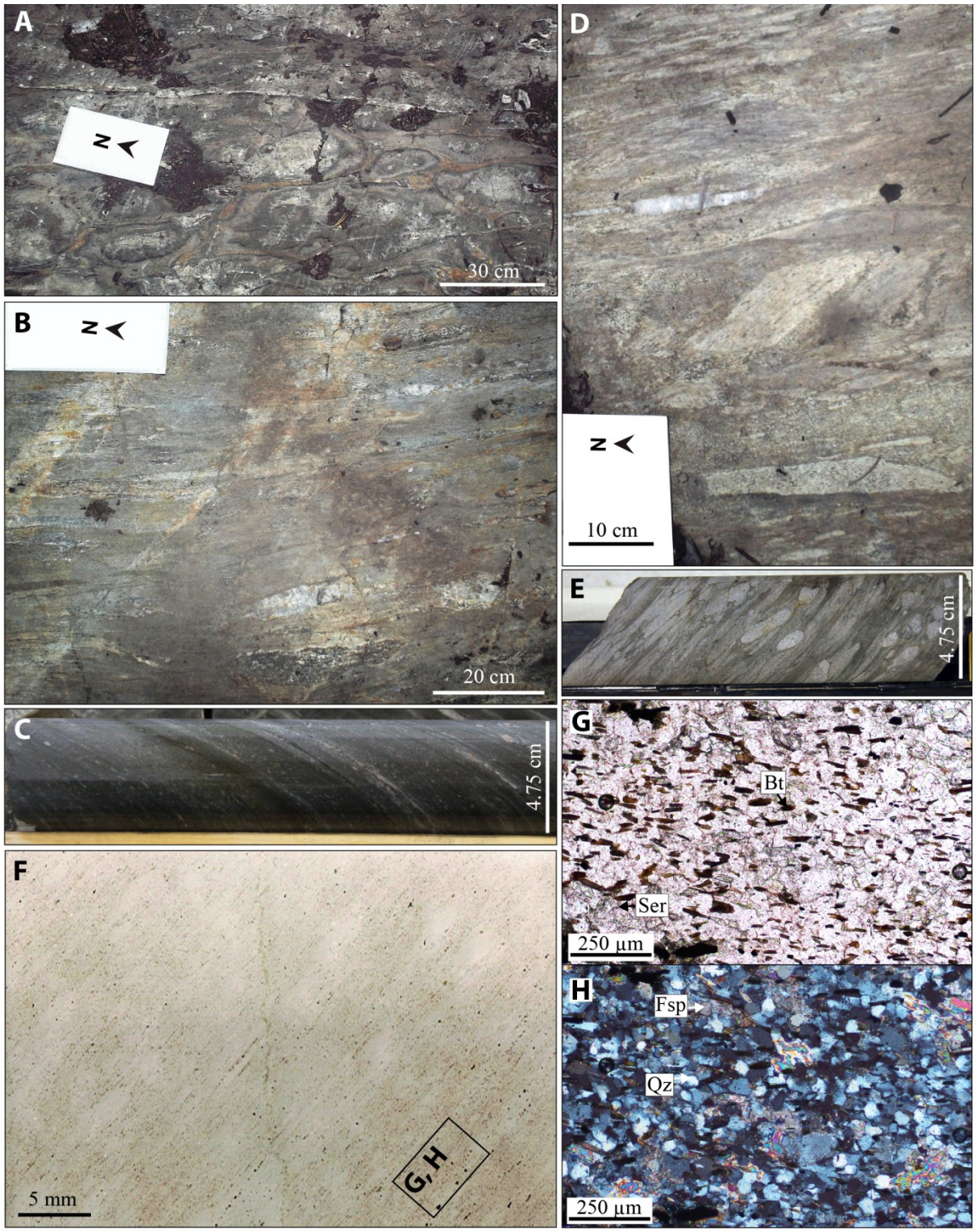

Figure 3-7: Mine Unit Avol, surface exposure photographs (A, B, D) are from study area 4, SW of the mine (Figure 3-1). Drill core photographs (C, E) are from the mine area. A. Pillowed, andesitic to dacitic flow underlying the Avol. B. Matrix-rich fragmental rocks and equivalent in drill core (C). D. Clast-rich fragmental rocks and its equivalent in drill core (E). F. Scan of a thin section of felsic rock, note the faint

shape of clasts in the greenish-brownish matrix (sample MW-11-225). Photomicrographs of the latter sample, in polarized light (G) and in cross-polarized light (H).

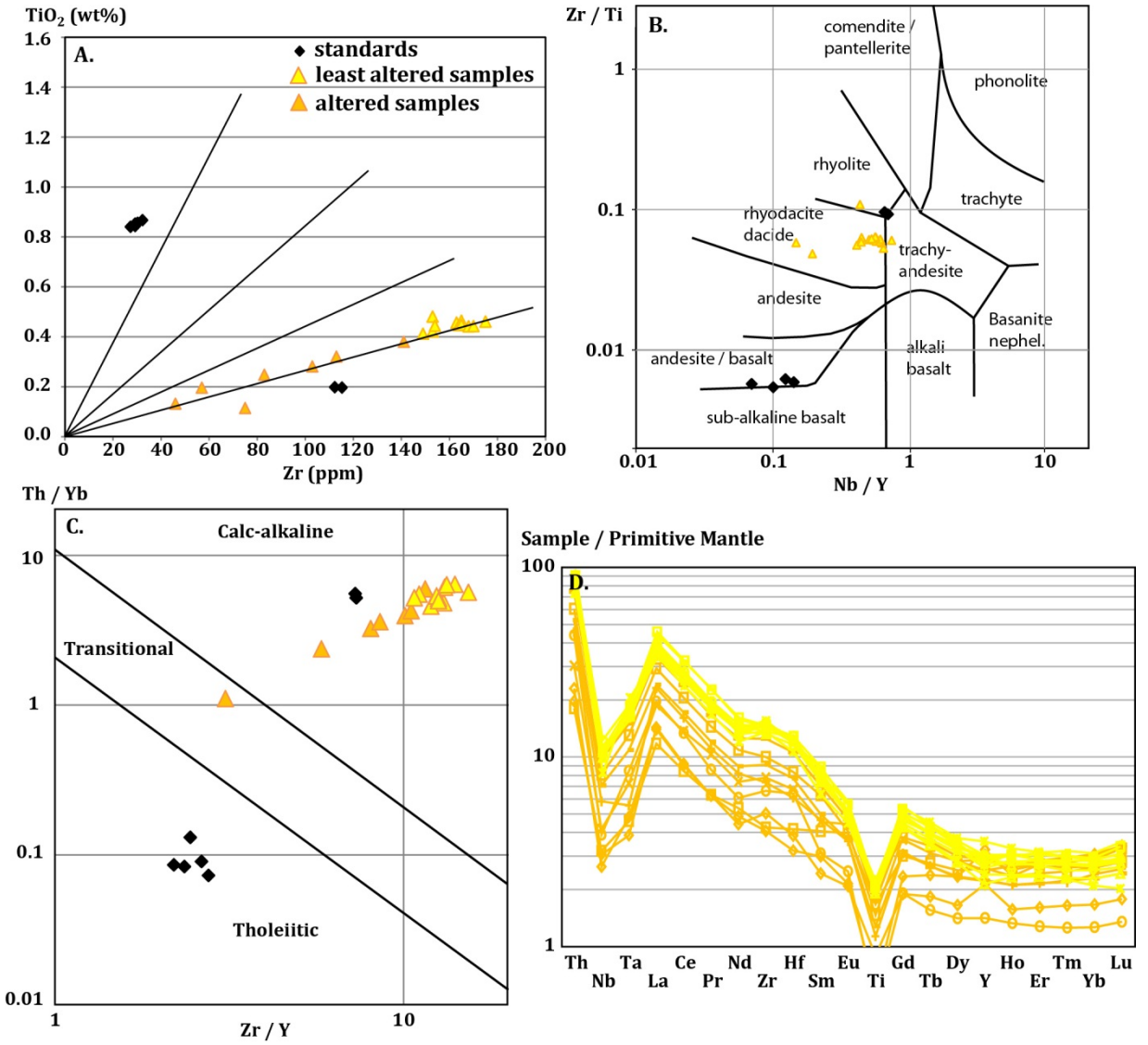

Figure 3-8: Unit Avol. A. Zr vs. TiO_2 binary plot (after MacLean and Barrett, 1993); yellow triangles = least altered samples, orange triangles = moderately to strongly altered samples; black diamonds are mafic and felsic volcanic rock standards; black lines show the main trends of this study's dataset. B. Nb/Y vs. Zr/Ti classification diagram from Wynchester and Floyd (1977). C. Zr/Y vs. Th/Yb binary plot for magmatic affinity from Ross and Bédard (2009). D. Trace elements profiles of Avol samples normalized to Primitive Mantle (PM) values from Sun and McDonough (1989). Bright yellow lines = least altered Avol samples, orange lines = moderately to strongly altered Avol samples.

3.3 Unit "Bvol"

Unit Bvol comprises mafic volcanic rocks that lie between unit Avol and the Northern iron formation (NIF; Figure 3-1). Although it constitutes the bedrock of the area between northern Opapimiskan Lake

area and Cigar Lake (Figure 3-1), only a limited number of outcrops have been uncovered. Extensive surface and underground drilling at Musselwhite mine provides abundant core material to study this volcanic package. Thickness of unit Bvol varies from 50 m on the eastern limb of the East Bay synform (Figure 3-2) to over 150 m in the West antiform area. Lenses of garnet-biotite, staurolite-biotite and garnet-amphibole schist occur within the unit and are referred to as “intraformationals” (sections 3.6 and 3.7).

Unit Bvol includes pillowed to massive basalt (Figure 3-9A, B), with local gabbroic units. The basalt is mainly composed of hornblende, with minor proportions of plagioclase and biotite. Gabbroic units are coarser-grained and have higher plagioclase content. In drill core, Bvol rocks generally have a green to greyish green colour, with local bleaching or brown tint, marking zones of alteration (Figure 3-9C).

Typical Bvol rocks contain 50 to 80 vol.% green to brownish hornblende and actinolitic hornblende in the matrix, intergrown with 5 to 10 vol.% quartz and 5 to 20 vol.% plagioclase feldspar (Figure 3-9D, E, F). Biotite and minor sericite can make up to 20 vol.% of the matrix. Trace minerals include ilmenite and apatite. The main fabric is weakly to strongly developed, which influences the size and shape of mineral grains. Fine-grained, pale green pleochroic, amphibole grains are equi-granular to elongate and locally slightly poikilitic. Quartz and plagioclase feldspar are fine-grained, intergrown granoblastic grains. Where present, biotite is fine-grained, aligned along foliation planes and unevenly distributed.

Lithogeochemical data of Bvol samples have TiO_2 values between 0.6 and 1.1 wt.% and Zr values ranging from 25 to 60 ppm (Figure 3-10A; MacLean and Barrett, 1993). They fall within the basalt to andesitic basalt field of composition (Figure 3-10B), with Zr/Ti values mainly under 0.01 and Nb/Y values from 0.04 to 0.3. Bvol data indicate a clear tholeiitic magmatic affinity (Figure 3-10C) with Zr/Y and Th/Yb ratio values of 2-4 and 0.08-0.5, respectively. A small number of mainly altered samples cluster within the transitional field.

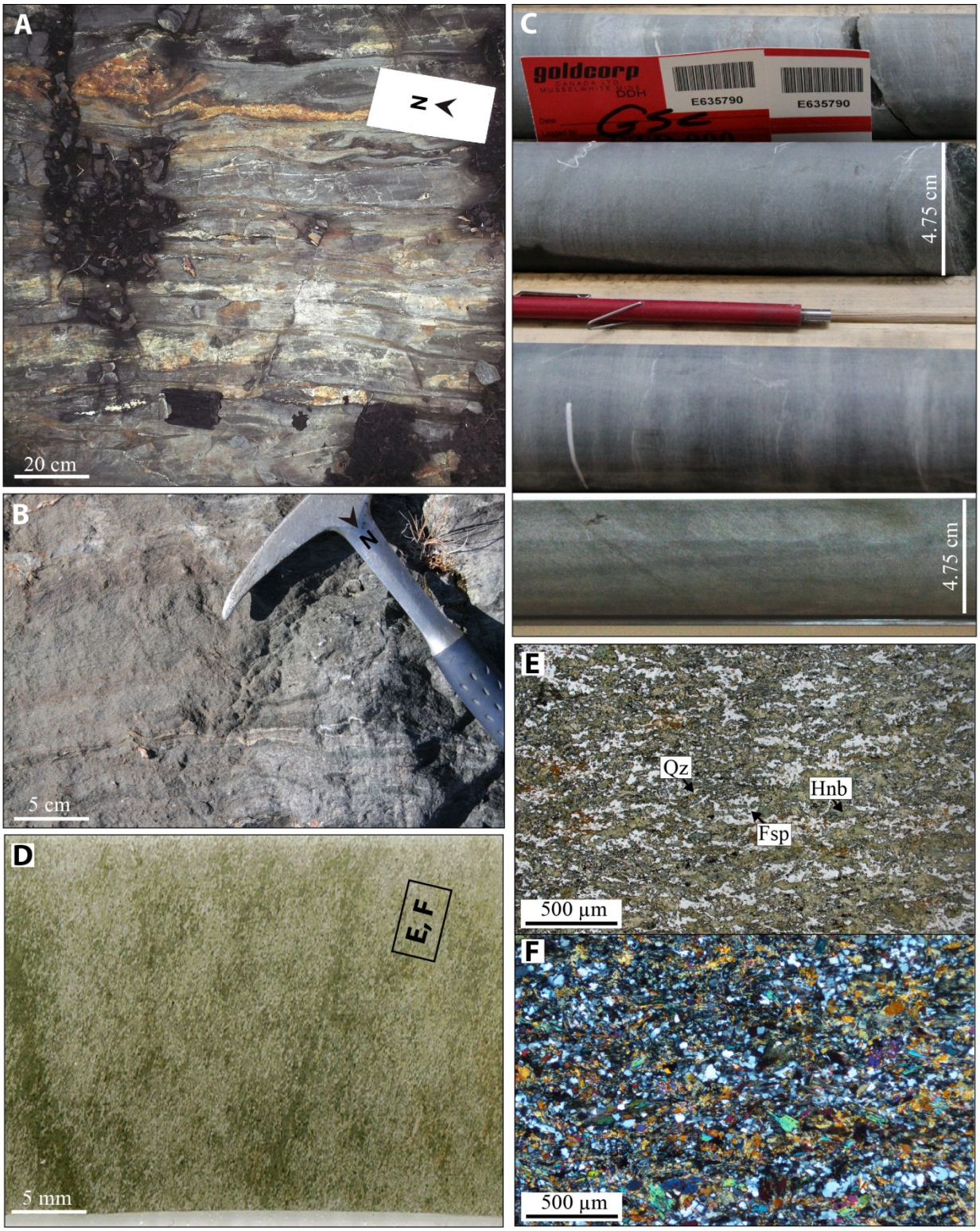

Figure 3-9: Mine Unit Bvol, surface exposure photographs (A, B) are from B. Pisani (unpublished) study area, SW of the mine and PQ trench (Figure 3-1). Drill core photographs (C) are from the mine area. A. Flattened pillowed basaltic flow. B. Massive basalt showing strong S_2 foliation and biotite alteration with

trace iron carbonates. C. Drill core section of grey (top) and green (bottom) Bvol basalt. D. Thin section scan of sample MW-12-390, with typical mineralogy in polarized light (E) and in cross-polarized light (F).

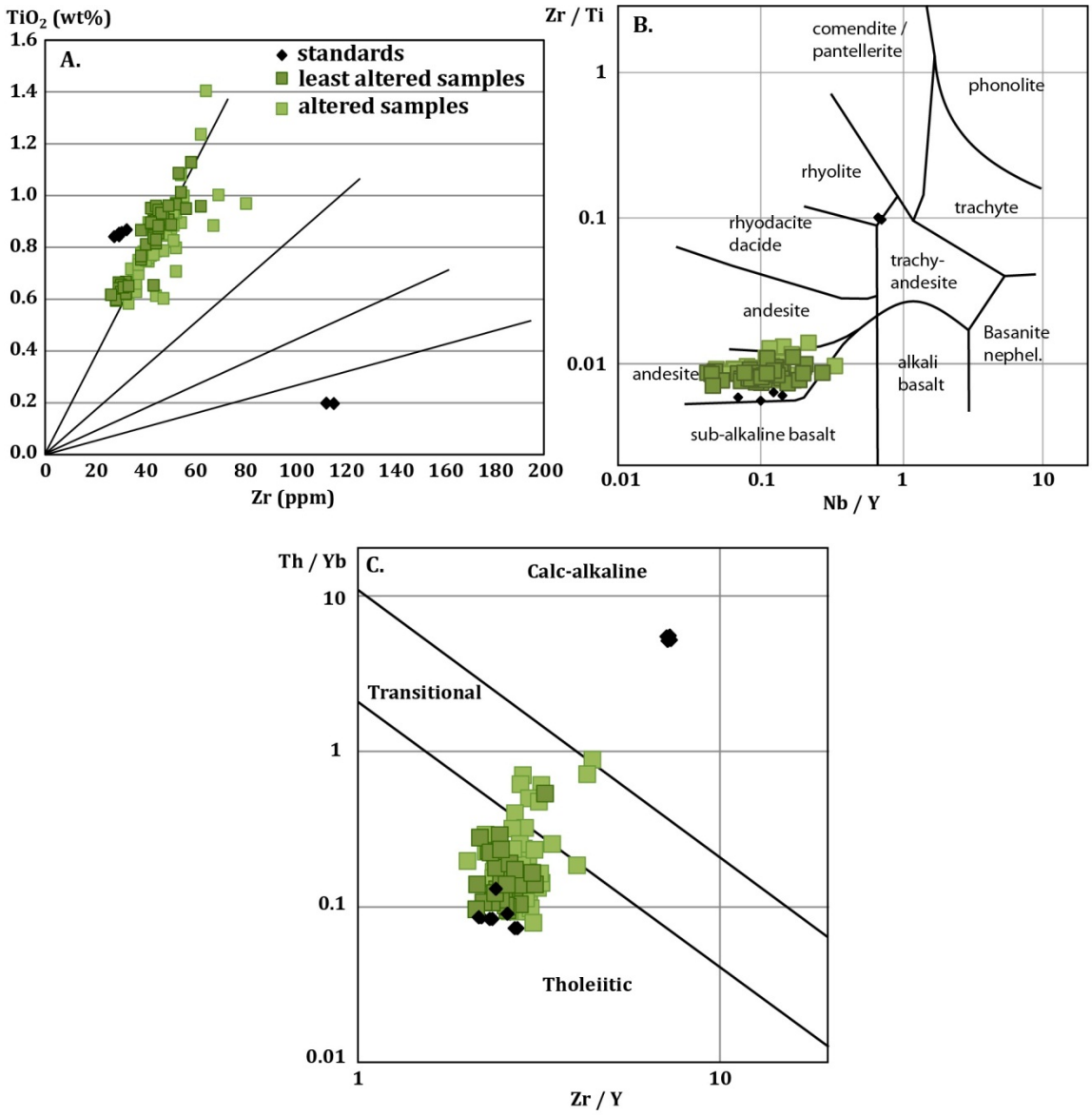

Figure 3-10: Unit Bvol. A. Zr vs. TiO_2 binary plot (after MacLean and Barrett, 1993); dark green squares = least altered samples, light green squares = moderately to strongly altered samples; black diamonds are mafic and felsic volcanic rock standards; black lines represent the main trends of this study's dataset. B. Nb/Y vs. Zr/Ti classification diagram from Wynchester and Floyd (1977). C. Zr/Y vs. Th/Yb binary plot for magmatic affinity from Ross and Bédard (2009).

Primitive Mantle-normalized (PM-n) trace elements profiles of Bvol samples can be roughly subdivided into four groups (Figure 3-11). Groups 1 to 3 show a progressive trace element enrichment compared to PM values, clustering around 3, 3.5-4 and 4-5 times PM values, respectively. Group 1 shows fairly flat profiles. Groups 2 and 3 in contrast, show weakly negative Y, Ti and Hf anomalies. Group 4 samples are distinguished by a clear LREE enrichment, along with moderate negative Hf-Zr anomaly, and small

negative Ti and Y anomalies. Samples from group 4 are spatially restricted to an area a few metres off of the contact between units Bvol and Avol, in the structurally higher levels of unit Bvol, suggesting they belong to a possible subdivision of unit Bvol (Figure 3-2).

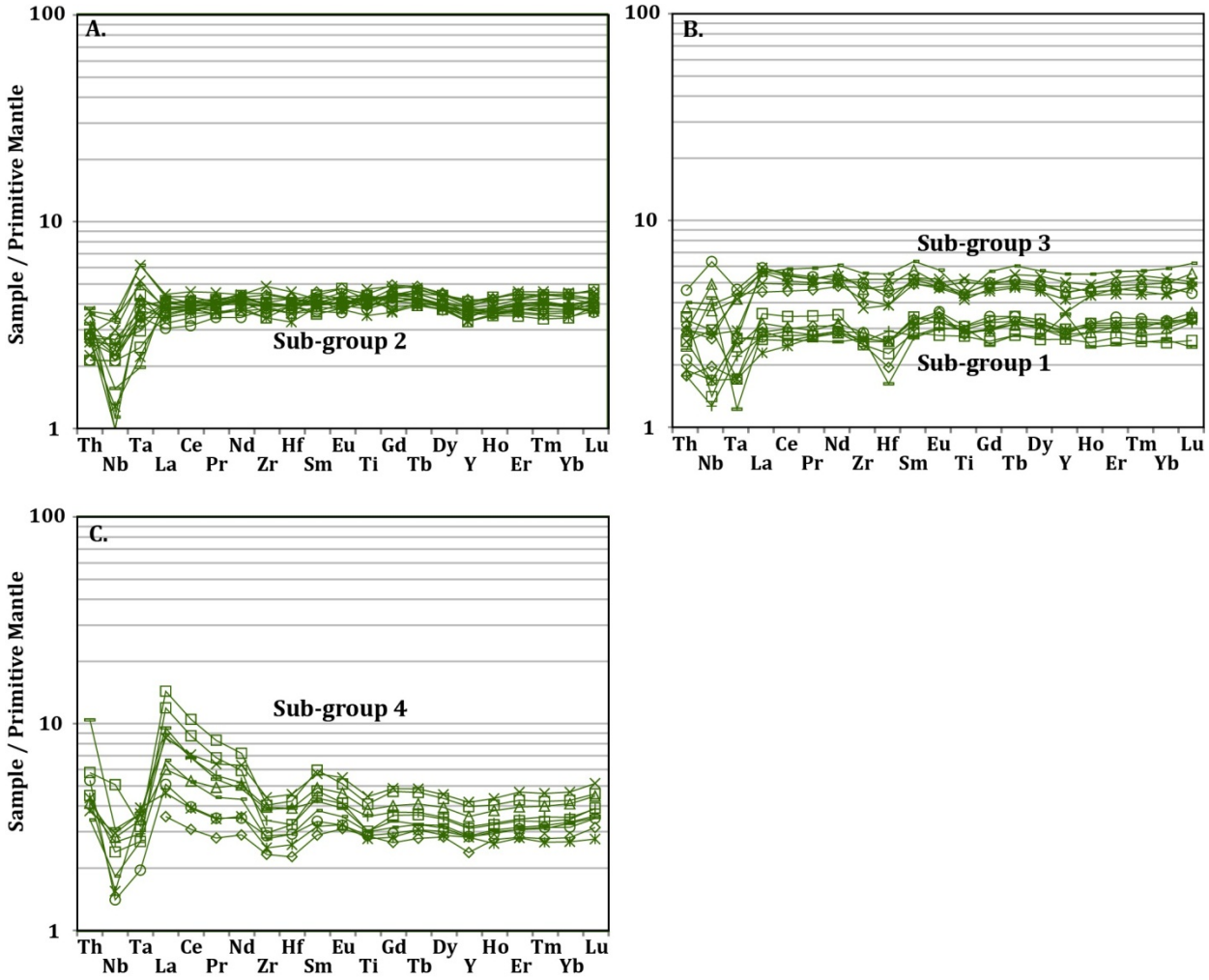

Figure 3-11: Unit Bvol PM-normalized trace element profiles of least altered samples, divided into groups based on trace elements enrichment over PM values, LREE enrichment and Y, Ti, and Hf anomalies. (PM values from Sun and McDonough, 1989) A. Group 2. B. Group 1 and 3. C. Group 4.

3.4 Unit "Basement basalts"

"Basement basalts" designates the ultramafic and mafic volcanic package found in between the NIF and the SIF. It has an extent similar to that of unit Bvol, but more abundant surface exposures, especially in the West antiform area where it is thickened in fold hinge zones (Figure 3-1). Along regional-scale fold limbs, the "Basement basalts" unit is approximately 50 m thick.

The “Basement basalts” unit comprises ultramafic flows, dykes and sills, pillowed to massive mafic flows, and gabbros (Figures 3-1, 3-12A). These rock types are well exposed on the eastern side of PQ trench (Figure 3-12A, B). Mafic rocks have a green to greyish green colour and, similarly to Bvol mafic rocks, are mainly constituted of hornblende, with variable plagioclase and biotite contents (Figure 3-12C). Ultramafic rocks are distinguished by their pale green colour, softness and very fine-grained texture (Figure 3-12D).

The common proto-mylonitic texture of “Basement basalts” lithologies in the mine area is visible at microscopic scale (Figure 3-12E, F, G). Mafic rocks show segregation between quartz-rich and amphibole-rich bands (Figure 3-12E). Matrix typically contains 60 to 80 vol.% weakly pleochroic, pale green actinolite with 5 to 10 vol.% very fine-grained quartz and 5 to 10 vol.% feldspar. Micas are locally present and trace minerals include ilmenite and apatite. Ultramafic rocks are constituted of up to 50 vol.% Mg-rich chlorite and 45 vol.% actinolite. Minor amount (5%) of cummingtonite is common and trace minerals include ilmenite and chalcopyrite.

The “Basement basalts” unit includes both mafic and ultramafic rocks (section 3.4). Three fractionation trends are delineated on a Zr/TiO_2 binary plot (Figure 3-13A; MacLean and Barrett, 1993): one similar to that of unit Bvol samples (0.4-0.7 wt.% TiO_2, 25 to 40 ppm Zr), one with lower TiO_2 values and slightly higher Zr (0.3-0.5 wt.% and 35-60 ppm), and a third with distinctively high Zr values (130-150 ppm). Ultramafic samples fall at the lower end of the first two trends. Samples also cluster within three separate fields on Wynchester and Floyd (1977)’s classification diagram: andesitic basalt, andesite, and dacite/rhyodacite (Figure 3-13B). Andesitic basalt samples show a tholeiitic to transitional affinity while andesite samples plot just above the transitional to calc-alkaline boundary (Figure 3-13C). Dacitic samples tightly cluster in the calc-alkaline field near the felsic rock standards. Ultramafic samples are distributed among mafic sample clusters, except for two that lay distinctively below mafic rock standards, in the tholeiitic field. Those two samples come from the structurally lowermost part of the “Basement basalts” unit.

Andesitic basalt and andesite samples of the “Basement basalts” unit form a fairly homogeneous group of PM-n trace elements profiles (Figure 3-14A). They have moderate LREE enrichment, moderate negative Nb-Ta anomaly, weakly negative Ti anomaly and a small negative to no Hf anomaly. Dacitic samples form a very tight group with strong LREE enrichment, moderate negative Nb-Ta anomaly and negative Ti anomaly, and a weak negative Y anomaly. It is worth noting that all dacitic samples have been collected within a few metres of the contact with the NIF (Figure 3-2).

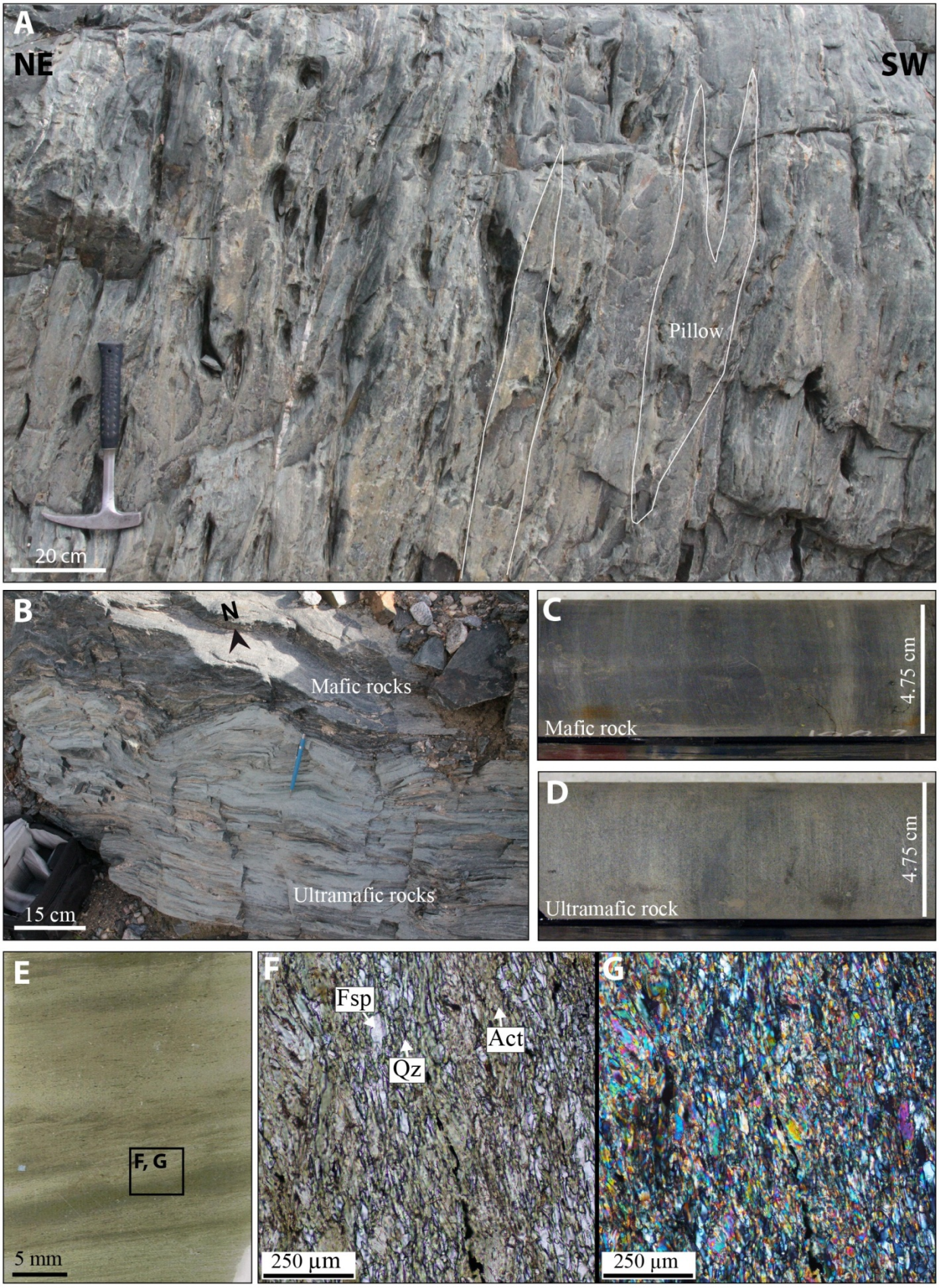
A
NE
SW
Pillow
20 cm
B
N
Mafic rocks
Ultramafic rocks
15 cm
C
4.75 cm
Mafic rock
D
4.75 cm
Ultramafic rock
E
F, G
5 mm
F
Fsp
Act
Qz
250 µm
G
250 µm

Figure 3-12: "Basement basalts" unit. Surface exposure photographs (A, B) are from PQ trench (Figure 3-1). A. NE-SW section of a pillowed basalt flow. B. Steeply-inclined exposure of both mafic and ultramafic lithologies of the Basement basalts unit. C. Drill core segment of the mafic lithology. D. Drill core segment of the ultramafic lithology. E. Thin section scan of ultramafic rock sample NW-11-135, with typical mineralogy in F. polarized light and G. cross-polarized light. Note: This unit is more intensely deformed and displays proto-mylonitic texture.

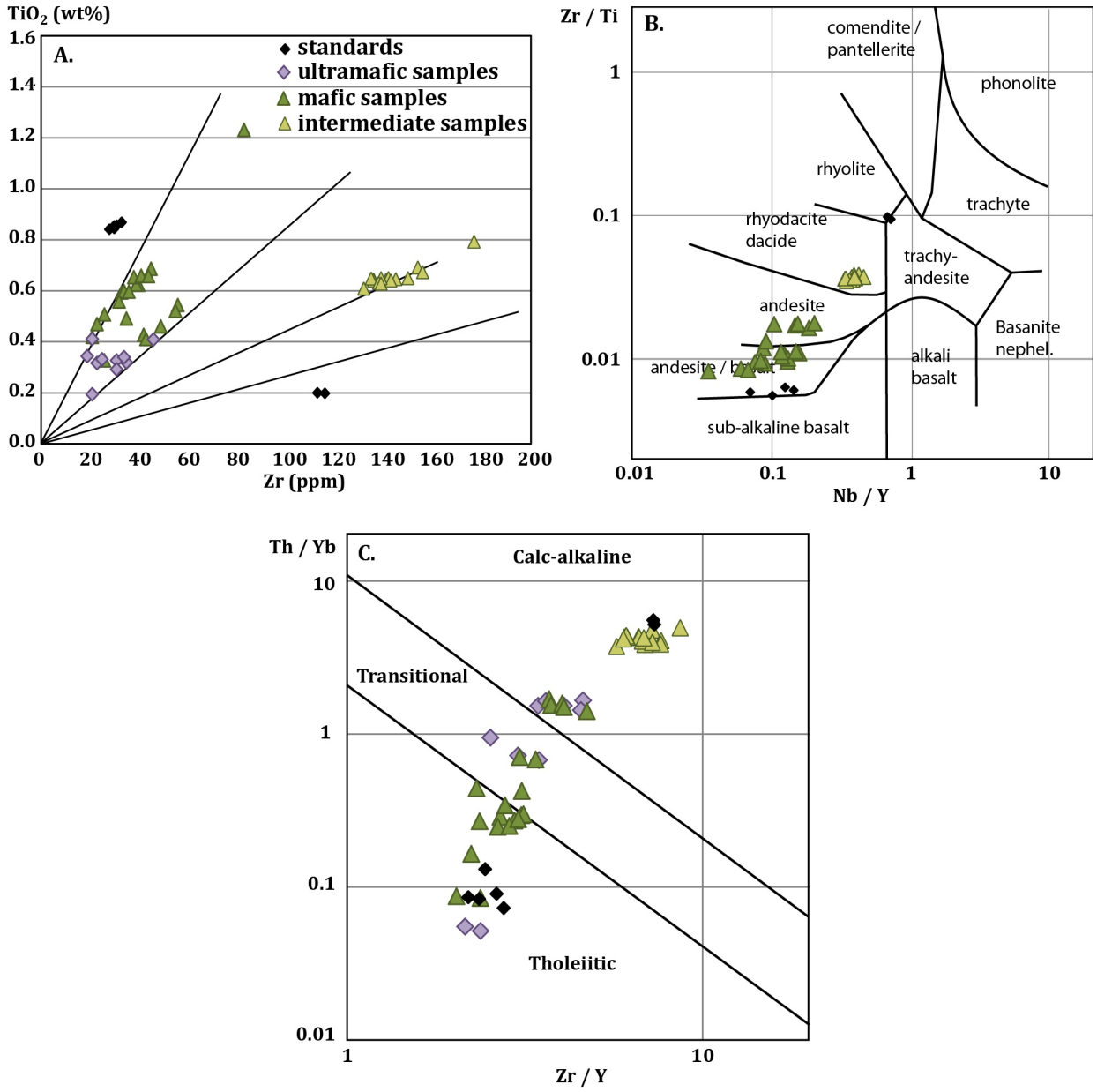

Figure 3-13: "Basement basalts" A. Zr vs. TiO_2 binary plot (after MacLean and Barrett, 1993); light purple diamonds = ultramafic samples, green triangles = mafic samples, light green triangles = intermediate samples, black diamonds = mafic and felsic volcanic rock standards; black lines = main trends within this study's dataset. B. Nb/Y vs. Zr/Ti classification diagram from Wynchester and Floyd (1977). C. Zr/Y vs. Th/Yb binary plot for magmatic affinity from Ross and Bédard (2009).

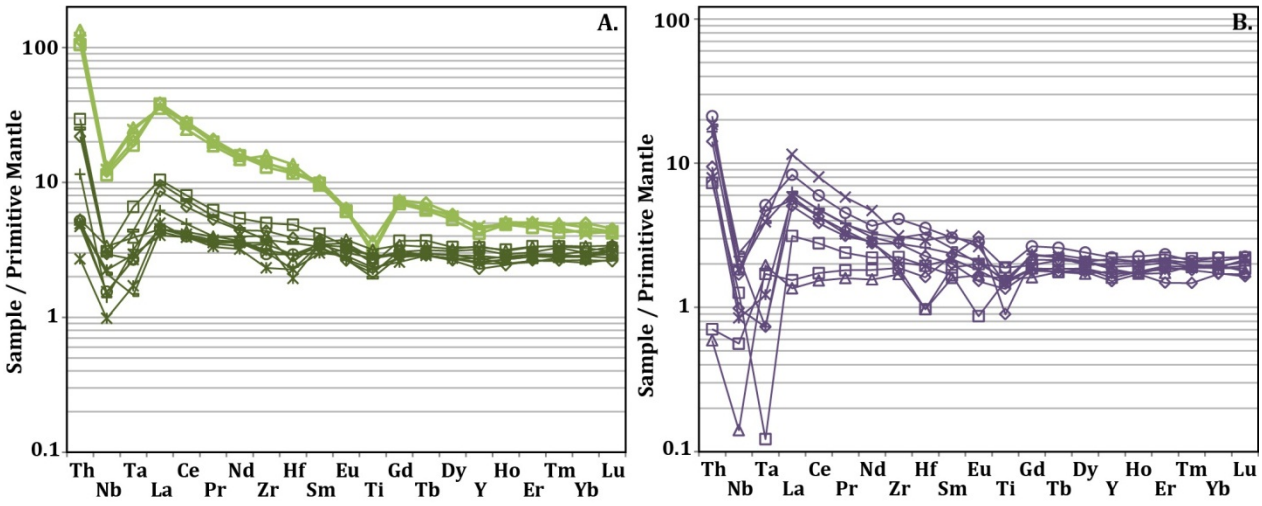

Figure 3-14: "Basement basalts" unit. A. PM-n trace element profiles of mafic (dark green) and intermediate (light green) rock samples. B. PM-n trace element profiles of ultramafic rock samples (PM values from Sun and McDonough, 1989).

3.5 Unit "Lower basalts"

The "Lower basalts" unit comprise all volcanic rocks structurally below the SIF sequence (Figure 3-2). This package is thickest in the West antiform area and thinnest along the east limb of the East Bay synform (around 60 m). The lower and central portions of the unit have only been examined through surface mapping in the West antiform area. Drill core descriptions in the mine area complement surface mapping of the upper portion. The "Lower basalts" unit encompasses four major lithologies: pillowed to massive basalt, gabbro, high-Mg mafic and ultramafic rocks (Figure 3-1). Between Graff Lake and the Wilberforce area several rather thin (<10 m) BIF horizons have been intersected in drill holes (Figure 3-1; Guest, 2013). Stratigraphic top indicators, mainly derived from pillowed basalt, generally face to the south.

The stratigraphic base of the "Lower basalts" unit is exposed in the West antiform area and comprises pillowed and massive basalt with a local, matrix-supported breccia (Figure 3-15A, B). The matrix is chlorite-rich and clasts are monolithic, rounded to angular. This breccia is interpreted as either a pillow breccia or auto-breccia (McPhie, 1993). The central portion of the "Lower basalts" unit consists of pillowed and massive basalt and a fairly continuous layer of high-Mg basalt (Figure 3-1; Goldcorp Inc., unpublished data). The stratigraphic upper portion, exposed north of Zeemel Lake, comprises mostly pillowed and massive komatiitic basalt with local, monolithic, matrix-supported, pebbly epiclastic sediments (Figure 3-15C, D, E). Despite an intense attenuation in the thickness of volcanic sequences along the east limb of the East Bay synform, these mafic to ultramafic lithologies have been mapped

along the OMA-ZHA boundary southeastward into the Pipestone River area (Figure 3-1). Slivers of ultramafic rocks are intersected in drill core in the mine area, at the contact with the ZHA (Figure 3-15F, G) and likely represent the continuation of the rocks exposed north of Zeemel Lake.

The “Lower basalts” have solely been sampled in the mine area where strain intensity is high. Mafic rock samples (MW-12-370 and -371) show evidence of grain-size reduction (mylonitisation; Figure 3-16A, B, C). It is composed of 70 to 85 vol.% pale green to locally brown hornblende and actinolitic hornblende, 5 to 10 vol.% very fine-grained quartz, and up to 5 vol.% fine-grained plagioclase feldspar. Biotite (a few vol.%) is locally present, and trace minerals include ilmenite and pyrrhotite. In ultramafic rock samples (MW-12-368 and -369), mylonitisation is much more intense (Figure 3-16D, E). Hornblende-rich, actinolite-rich, biotite-rich, and quartz-rich bands can be distinguished (Figure 3-16D).

Only four samples of this unit have been collected close to the contact with the ZHA, east of the mine. Although their analyses may not be statistically representative of the whole unit, obtained data provide a useful complement to surface mapping information (section 3.5). All samples plot on the same fractionation trend (Figure 3-17A). Mafic samples fall within the andesitic basalt field of Wynchester and Floyd (1977), and all samples have a tholeiitic, close to transitional, magmatic affinity (Figure 3-17B, C). PM-n trace element profiles are sub-parallel, with ultramafic and mafic samples showing values equal to 1.5-2 and 2-3 times PM values, respectively (Figure 3-17D). They show moderate positive Ta and negative Nb anomalies, and weak negative Hf-Zr and Ti anomalies.

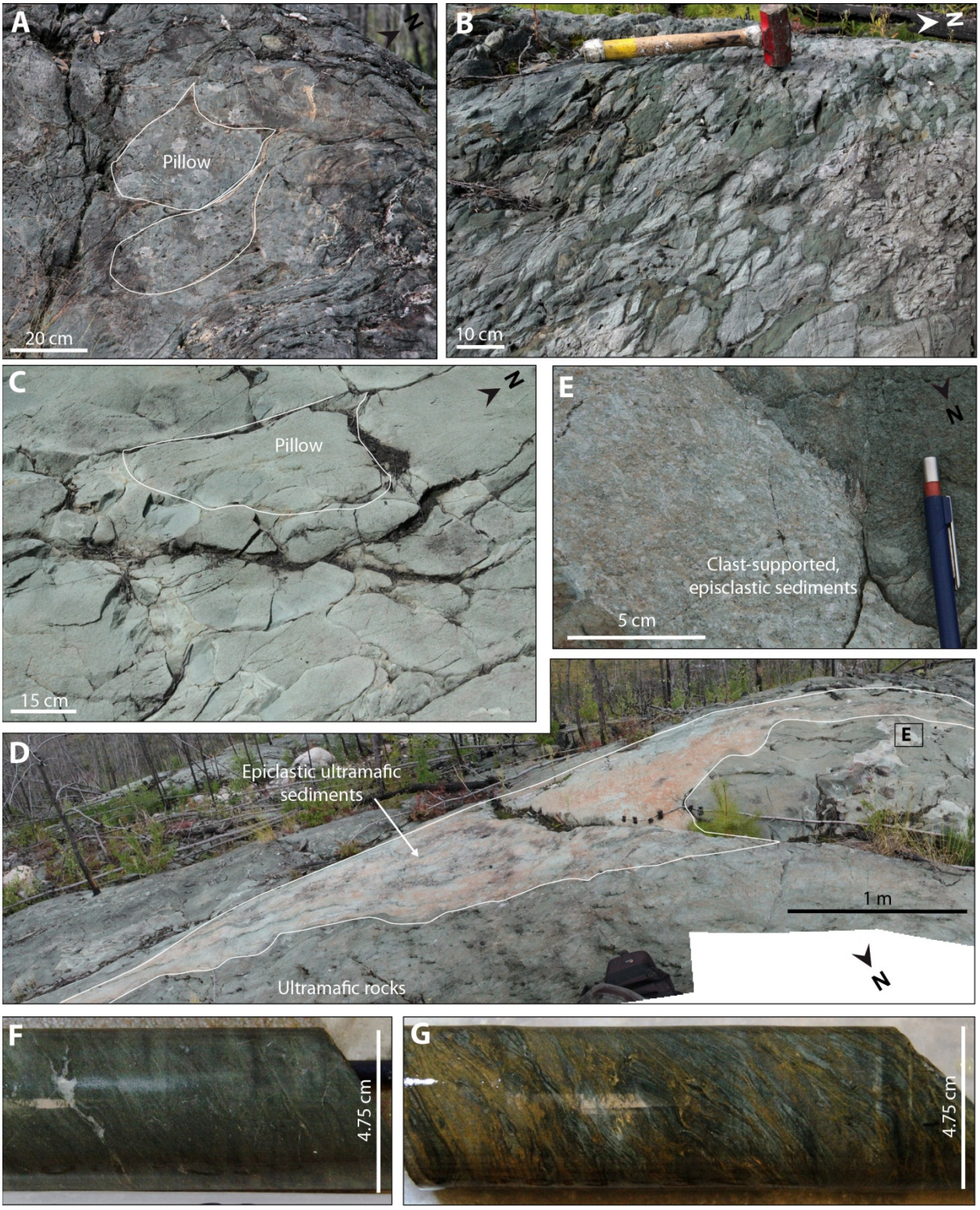

Figure 3-15: "Lower basalts" unit. A. SE-facing pillow in basalt flow from a surface exposure in the West antiform area (UTM 676015/5832075). B. Possible flow top breccia from the same outcrop. C. SSE-facing pillow in komatiitic basalt flow from a surface exposure north of Zeemel Lake (UTM 675417/5828813). D. Decametre-scale depression filled with clast-supported, pebble-rich, epiclastic, ultramafic sediments; with top facing SSE (UTM 676000/5829200). E. Close-up of epiclastic sediments in D. F. Drill core segment of a typical

mafic lithology in the "Lower basalts", sample MW-12-370. G. Strongly carbonate-altered and deformed ultramafic lithology, sample MW-12-368, from the OMA-ZHA contact zone, east of Musselwhite mine.

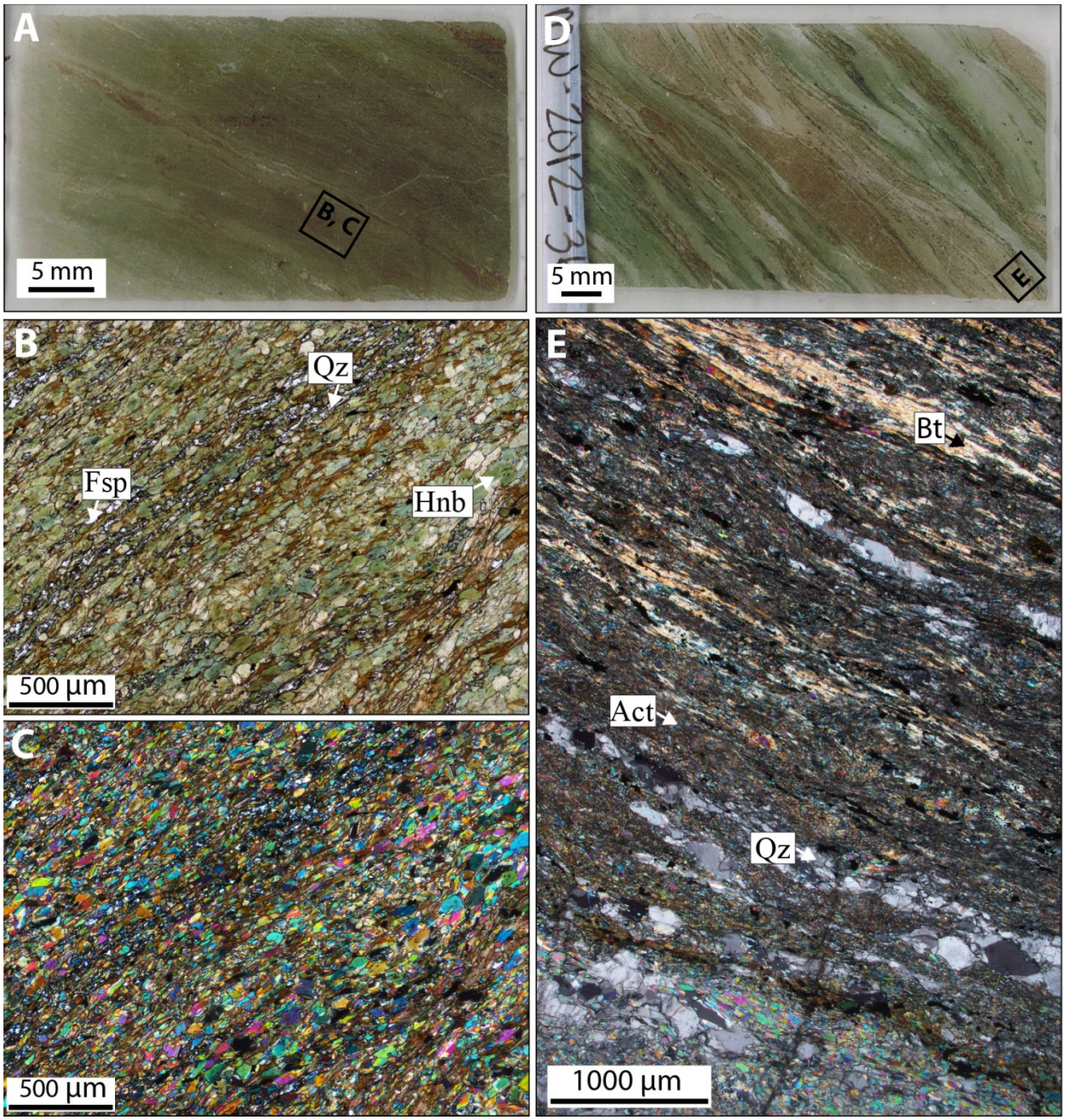

Figure 3-16: "Lower basalts" unit. A. Thin section scan of mafic rock sample MW-12-370 with typical, hornblende-feldspar matrix in B. polarized light, and C. cross-polarized light. D. Thin section scan of ultramafic rock sample MW-12-368 with mylonitic, actinolite-biotite ± quartz matrix in E. cross-polarized light.

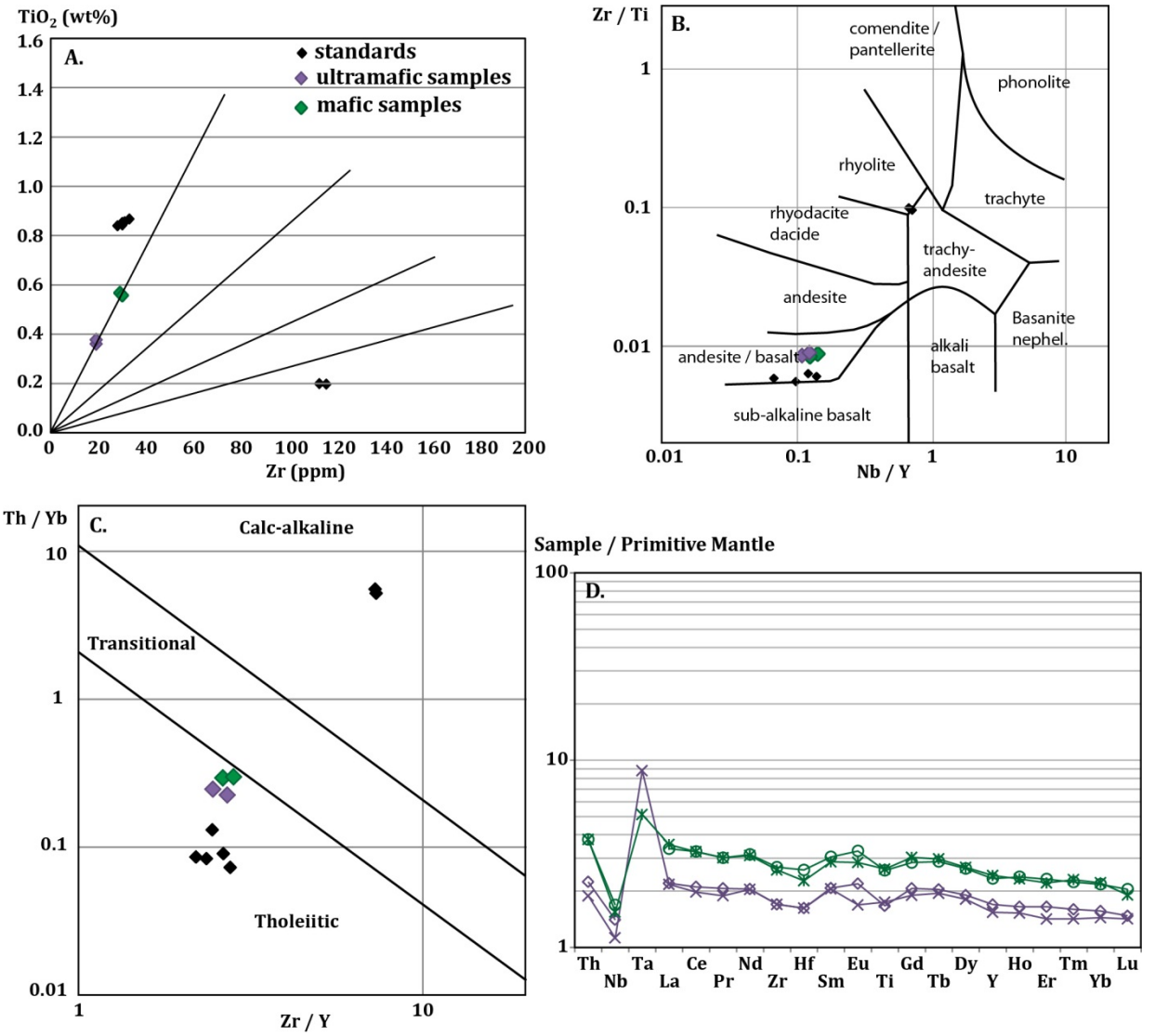

Figure 3-17: "Lower basalts" unit A. Zr vs. TiO_2 binary plot (after MacLean and Barrett, 1993); purple diamonds = ultramafic samples, green diamonds = mafic samples, black diamonds = mafic and felsic volcanic rock standards; black lines = main trends within this study's dataset. B. Nb/Y vs. Zr/Ti classification diagram from Wynchester and Floyd (1977). C. Zr/Y vs. Th/Yb binary plot for magmatic affinity from Ross and Bédard (2009). D. PM-n trace element profiles of rock samples (PM values from Sun and McDonough, 1989).

3.6 Unit 4E

Unit 4E ("4E") is a garnet amphibolite occurring as intraformational lenses within unit Bvol, and as a thin unit at the base of the NIF sequence from the northern Opapimiskan Lake area to the Paseminan River area, west of Zeemel Lake (Figure 3-1). Its thickness is commonly a metre or less; locally up to 3-4 m. Lenses of 4E within unit Bvol are often situated at the interface between volcanic flows, and show some mineralogical heterogeneity.

Unit 4E is dark to light green and mainly constituted of a massive, fine-grained, hornblende-rich matrix with ~20 vol.% garnet (pink almandine) porphyroblasts (Figure 3-18A, B). Chert layers may locally constitute ~30 vol.% of the rock but chert-free 4E beds are common (Figure 3-18C, D, E). Garnets show a wide variation in grain size and shape. They are mainly 1-5 mm in size, although centimetre-scale crystals are common (Figure 3-18B, D, E).

The typical mineral assemblage of the matrix of unit 4E is fine-grained and composed of: 30 to 70 vol.% subhedral, green hornblende crystals, 20 to 50 vol.% subhedral, beige grunerite-cummingtonite crystals, up to 5 vol.% anhedral quartz, trace to 15 vol.% anhedral magnetite and trace plagioclase feldspar (Figure 3-19). Other trace mineral phases include: albite, ilmenite, calcite, siderite, apatite, pyrrhotite, and chalcopyrite. Garnet porphyroblasts are notably poikilitic and subhedral (Figure 3-19A, B). They are deformed by the main fabric and usually surrounded and partly replaced by a halo of grunerite (Figure 3-19A). Inclusions in garnet are commonly composed of subhedral to euhedral, randomly oriented grunerite crystals (Figure 3-19B). The significance of garnet growth and internal structure is further examined and discussed in 0.

The garnet amphibolite unit 4E (8 “least altered” samples) contains on average 50 wt.% SiO_2, 10 wt.% Al_2O_3 and 30 wt.% total iron (FeO/Fe_2O_3 ratio of 2; Figure 3-20A). Most other major oxides each make up less than 1 wt.%, except for MgO (4 wt.%) and CaO (5-6 wt.%). MnO is close to 0.5 wt.%. Significant variations in CaO and Fe_2O_3 correlate negatively to variations SiO_2 (presence or absence of chert).

MUQ-normalized REE+Y profiles of 4E samples show a slightly positive slope and a small light REE depletion relative to heavy REE (Figure 3-20B). La, EU and Y have notable positive anomalies (1.24, 1.64, and 1.34, respectively).

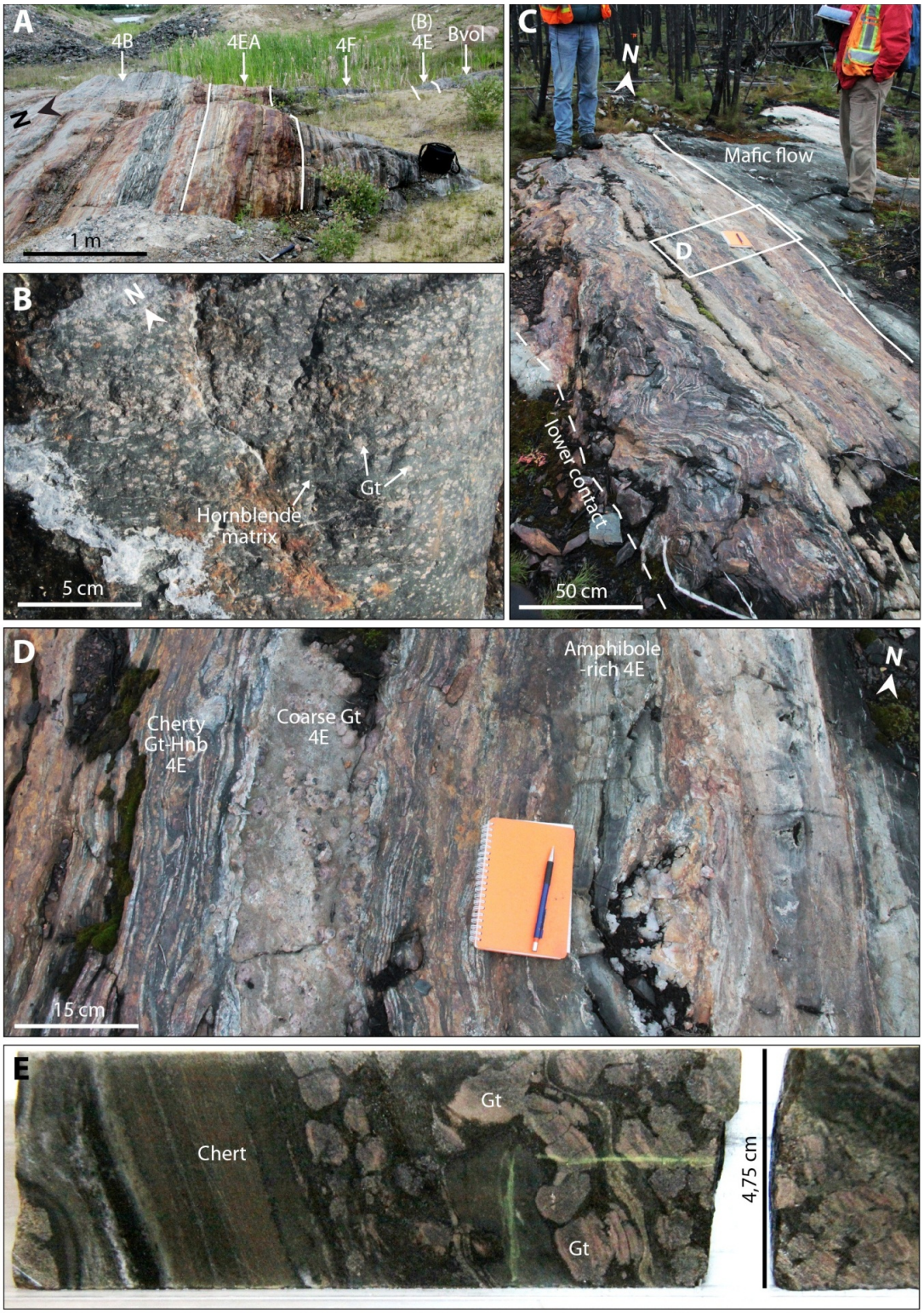

Figure 3-18: Unit 4E. A. Surface exposure of unit 4E at PQ trench. It is the first facies of the NIF sequence, following unit Bvol. B. Close-up of unit 4E at PQ trench. C. Surface exposure of the "intraformational" unit 4E, occurring between mafic volcanic flows. D. Close-up of C, note the variations of layering composition and thickness, and porphyroblast size over a short interval. E. Drill core of "intraformational" unit 4E sample MW-12-222.

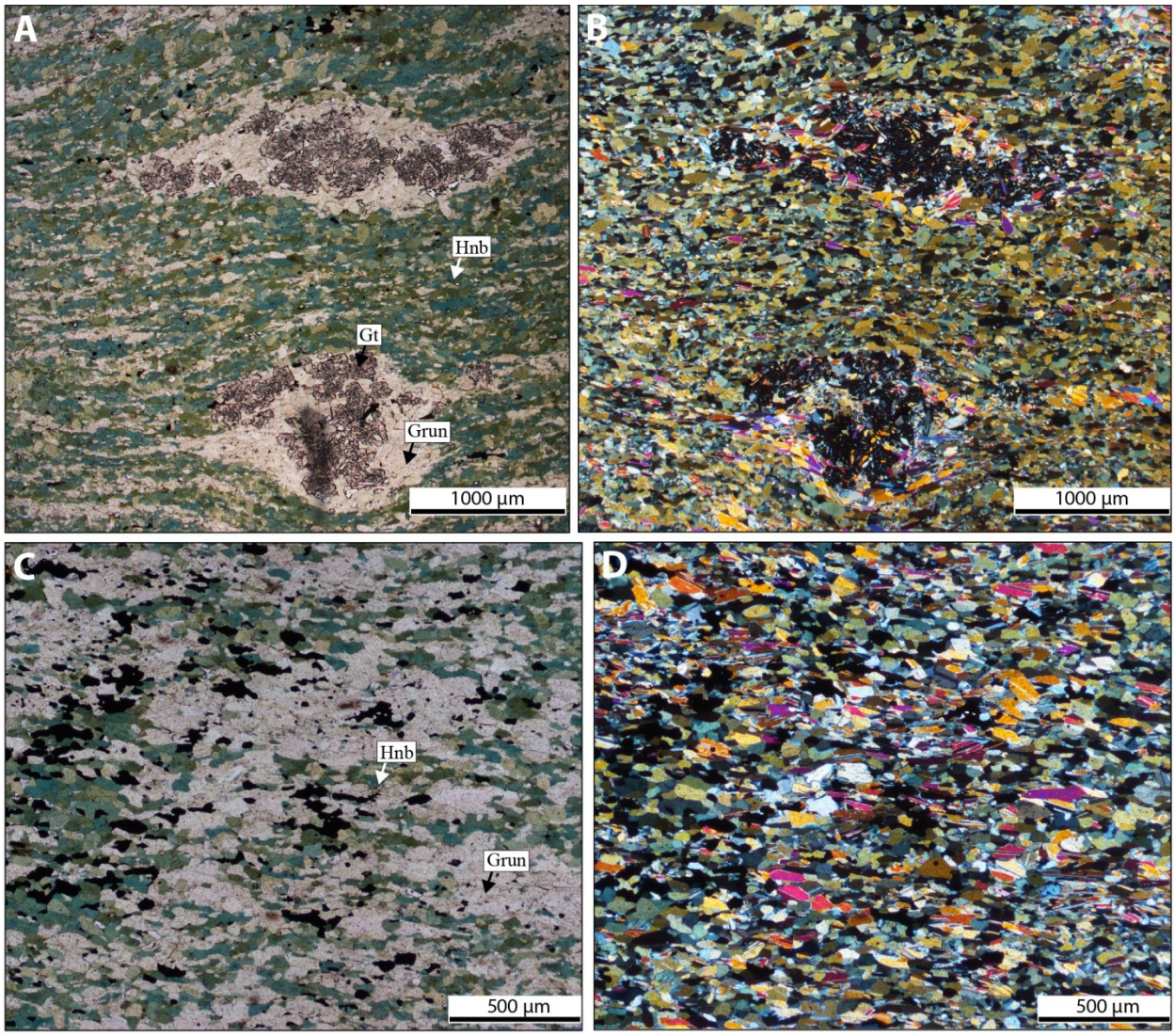

Figure 3-19: Photomicrographs of unit 4E. A. Garnet porphyroblasts partly replaced by grunerite, in strongly foliated, hornblende-grunerite matrix (polarized light, zoom x25). This type of garnet is the most frequent one in unit 4E at the base of the NIF sequence, as illustrated in Figure 3-18B. B. Same as A. in cross-polarized light. C. Typical hornblende-grunerite-magnetite matrix (polarized light, zoom x50). D. Same as C. in cross-polarized light.

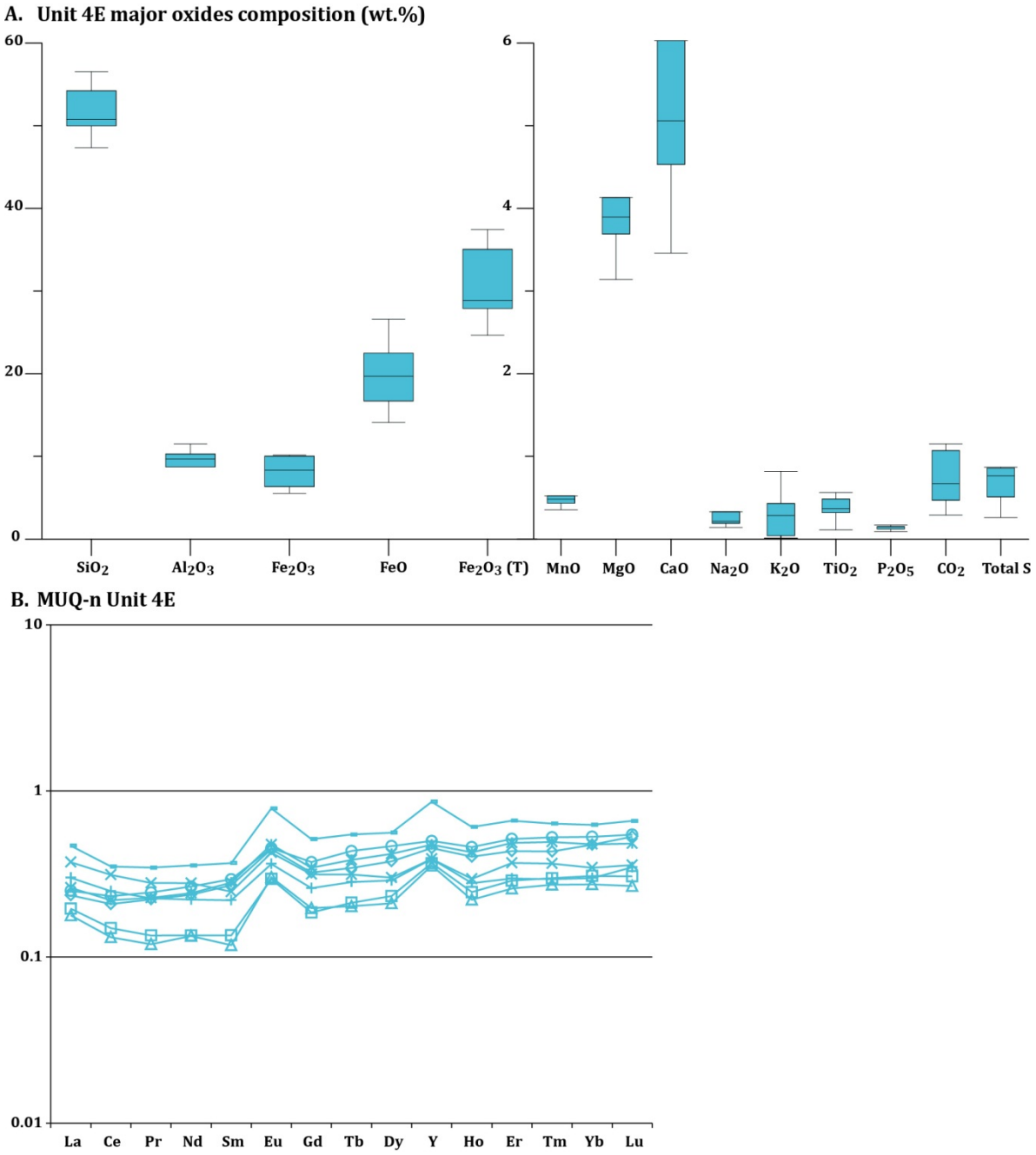

Figure 3-20: Unit 4E. A. Box plot of major oxides composition, 8 samples. Box = first to third quartile, black line = median, whiskers = interquartile range (IQR)*1.5 (Upton and Cook, 1996). B. REE+Y profiles of least altered 4E samples normalized to the MUQ standard (Kamber et al., 2005).

3.7 Unit 4F

Unit 4F ("4F") is a garnet-biotite schist interpreted as a metamorphosed metapelitic rock. It is interlayered within unit Bvol and occurs in the NIF sequence from the northern Opapimiskan Lake area to the

Paseminan River area, west of Zeemel Lake (Figure 3-1 and 3-21A). Unit 4F is a very incompetent lithology that tends to be tectonically strongly deformed and attenuated along fold limbs and thickened in hinge zones; it varies from a few metres to 20-25 m in thickness in the mine area. Unit 4F comprises three facies: (1) a staurolite-biotite ± garnet schist; (2) a cherty garnet-biotite schist; and (3) a massive garnet-biotite schist. Beds of 4E (amphibole-rich) are also found interlayered within unit 4F (Figure 3-21B).

Unit 4F is dark brown and surface weathering highlights pink garnet-rich layers, green amphibole-rich layers or purplish brown biotite-rich layers (Figure 3-21A, B, C). The staurolite-bearing facies is preferentially located at the base of unit Bvol. The transition to the dominant garnet-biotite facies is progressive. Staurolite forms disseminated, fine-grained, beige-to-orange, subhedral porphyroblastic crystals (Figures 3-21D; 3-22A, D). Garnet porphyroblasts are typically millimetric to locally centimetric, greyish violet to pinkish, subhedral to euhedral (Figure 3-22A). Porphyroblast distribution tends to be homogeneous in chert-free 4F and heterogeneous in chert-rich bands. Where both Al-silicates are present, garnet overgrows staurolite.

While chert bands attest of the chemical component of unit 4F, its detrital component and variations in mineral proportions are best observed in thin sections. The matrix of unit 4F usually includes 20 to 60 vol.% fine-grained, elongated, brown biotite and 10 to 25 vol.% fine-grained quartz (Figure 3-22B, C). Plagioclase feldspar typically makes up 3-5 vol.% of the matrix, to locally up to 30 vol.%, with trace potassic feldspar. Sericite ranges from trace to 10 vol.%; it typically occurs as fine-grained, needle-shaped grains aligned along the main fabric. Trace minerals include tourmaline, allanite, apatite, calcite, ilmenite, graphite, pyrite, pyrrhotite and chalcopyrite. Tourmaline, commonly schörl, is locally concentrated in bands, overgrowing biotite. Porphyroblasts make up 15 to 40 vol.% of the rock and mainly include pink to reddish pink, subhedral to euhedral garnet and yellow, subhedral staurolite, and locally, altered, poikilitic andalusite (Figure 3-22B, D, E). An internal foliation is defined by quartz inclusions in poikilitic staurolite grains. Garnet crystals typically show a strongly poikilitic core with an internal fabric and subhedral to euhedral inclusion-poor to inclusion-free rim (Figure 3-22B, E). Inclusions in porphyroblasts comprise quartz, biotite, hornblende, chlorite, and opaque minerals such as ilmenite ± magnetite.

The garnet-staurolite-biotite schist is the most aluminous unit of the OMA. It roughly contains the same amount of SiO_2 than unit 4E (50-55 wt.%; Figure 3-23A), but twice as much Al_2O_3 (18-20 wt.%). Total iron content is around 20 wt.% (with FeO/Fe_2O_3 ratio of 3), and secondary oxides include 3-4 wt.% K_2O, 3 wt.% MgO, and 2 wt.% CaO. MnO is close to 0.5 wt.%.

MUQ-normalized REE+Y profiles of 4F samples show a more pronounced LREE depletion relative to HREE (Figure 3-23B). The positive Eu anomaly is lower than in unit 4E (average of 1.32). There is little to no Y anomaly (average 1.07) and positive La anomaly is around 1.24, similar to unit 4E.

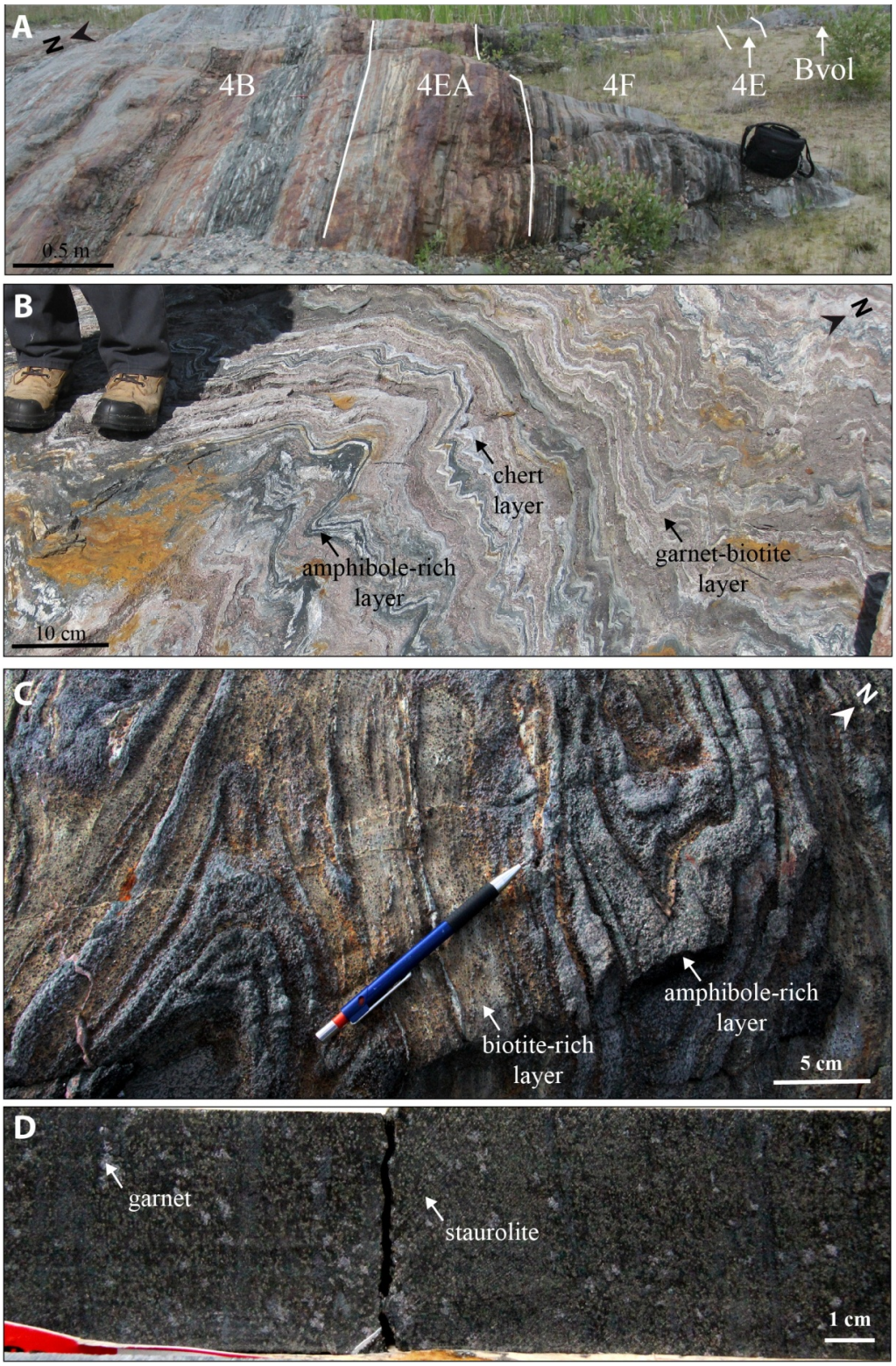

Figure 3-21: Unit 4F. A. Surface exposure of the NIF sequence at PQ trench; unit 4F is a massive garnet-biotite schist at the base of the NIF. B. Chert-rich facies of unit 4F at the South Shore Exposure. C. Surface exposure of the garnet-biotite ± hornblende facies of unit 4F, in the West antiform area, UTM 675925/5832680. D. Drill core of staurolite-bearing facies of unit 4F, sample MW-12-410.

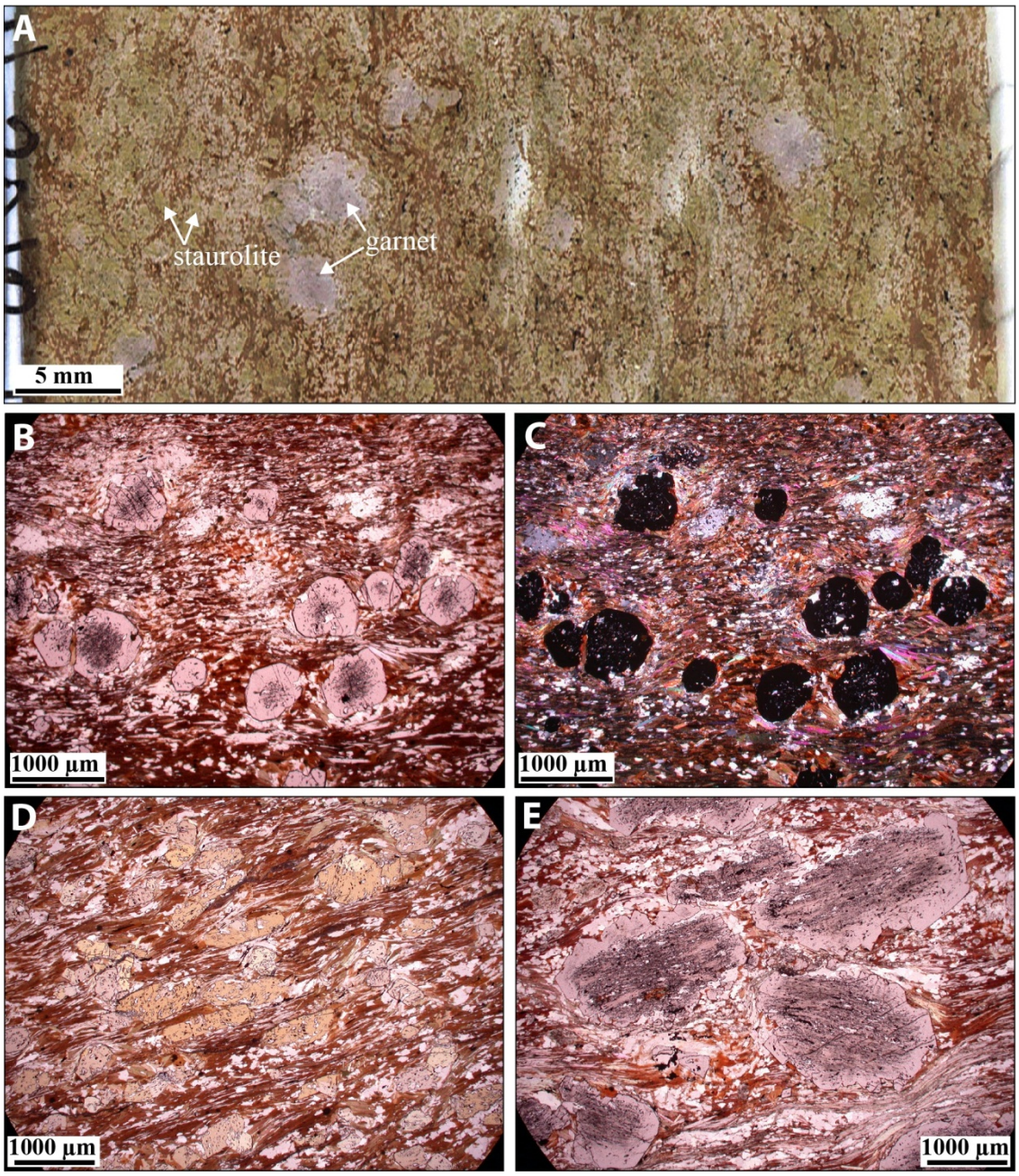

Figure 3-22: Unit 4F. A. Thin section scan of sample MW-12-410, staurolite-garnet 4F facies. B. Photomicrograph (polarized light) of typical fine-grained garnet porphyroblasts in a biotite-sericite-quartz matrix (sample MW-12-432). C. Same as B. in cross-polarized light. D. Photomicrograph (polarized light) of the typical habitus of staurolite porphyroblasts (sample MW-11-162). E. Photomicrograph (polarized light) of medium-grained garnet porphyroblasts showing large, strongly poikilitic cores and thin, inclusion-poor rims (sample MW-11-091).

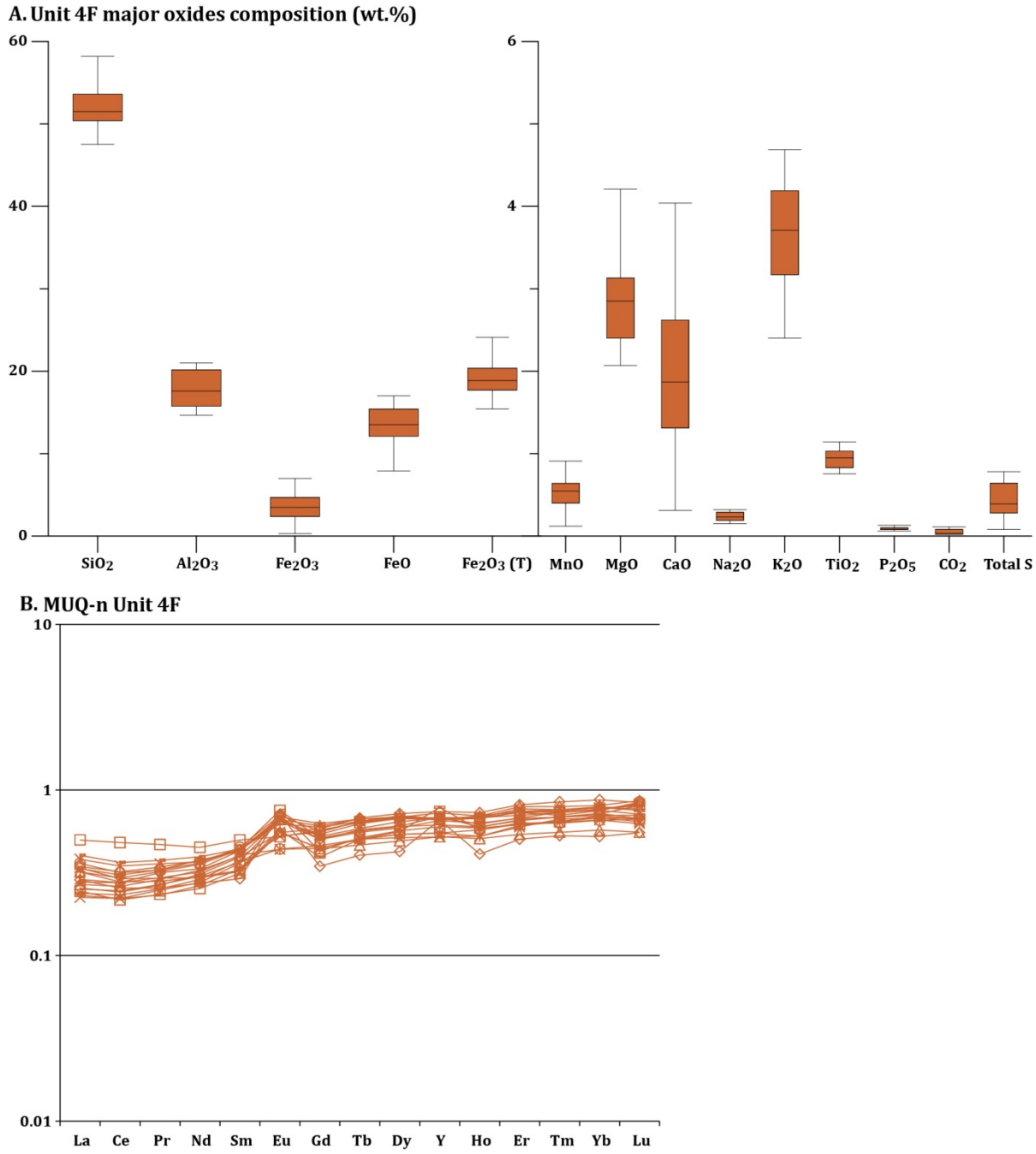

Figure 3-23: Unit 4F. A. Box plot of major oxides composition, 19 samples. Box = first to third quartile, black line = median, whiskers = interquartile range (IQR)*1.5 (Upton and Cook, 1996). B. REE+Y profiles of least altered 4F samples normalized to the MUQ standard (Kamber et al., 2005).

3.8 Unit 6

Unit 6 is a biotite-quartz-feldspar schist with occasional millimetre-scale anhedral garnets (Figure 3-24A). It mostly occurs as a discontinuous, 0.5-4 m-thick horizon within unit 4F. The discontinuous character of unit 6 may largely be attributed to its incompetent nature, relative to the surrounding garnet-biotite schist (Figure 3-24B).

Unit 6 is more quartzo-feldspathic than unit 4F (Figure 3-24C, D, E). Its foliated, fine-grained matrix comprises 20 to 30 vol.% equi-granular plagioclase feldspar, intergrown with 10 to 20 vol.% granoblastic quartz, 10-20 vol.% potassic feldspar (e.g., microcline), and 20 to 30 vol.% micas, with fine-grained biotite much more abundant (>2 to 1 ratio) than medium-grained, poikiloblastic muscovite. Minor and trace mineral phases include green to brownish hornblende, pyroxene, tourmaline (schörl), calcite, allanite, apatite, ilmenite, pyrrhotite, pyrite-troilite, and chalcopyrite. This unit has been interpreted as a volcaniclastic sedimentary rock (McNicoll et al., 2016), or as a sandstone (Moran, 2008).

Unit 6 has a different Al_2O_3/TiO_2 ratio than unit 4F (Figure 3-5A), suggesting a different, likely more felsic, source rock as illustrated by its quartzo-feldspathic matrix. It is also more siliceous (~62 wt.%) and has only up to 10 wt.% total Fe_2O_3 (Figure 3-25A). Secondary oxides include 4 wt.% K_2O and CaO, and a little over 2 wt.% MgO and Na_2O.

MUQ-normalized REE+Y profiles of unit 6 samples display a negative La-Lu slope (Figure 3-25B). A minor positive La anomaly (1.16) and a positive Eu anomaly (average of 1.53) are noted, but there is no Y anomaly.

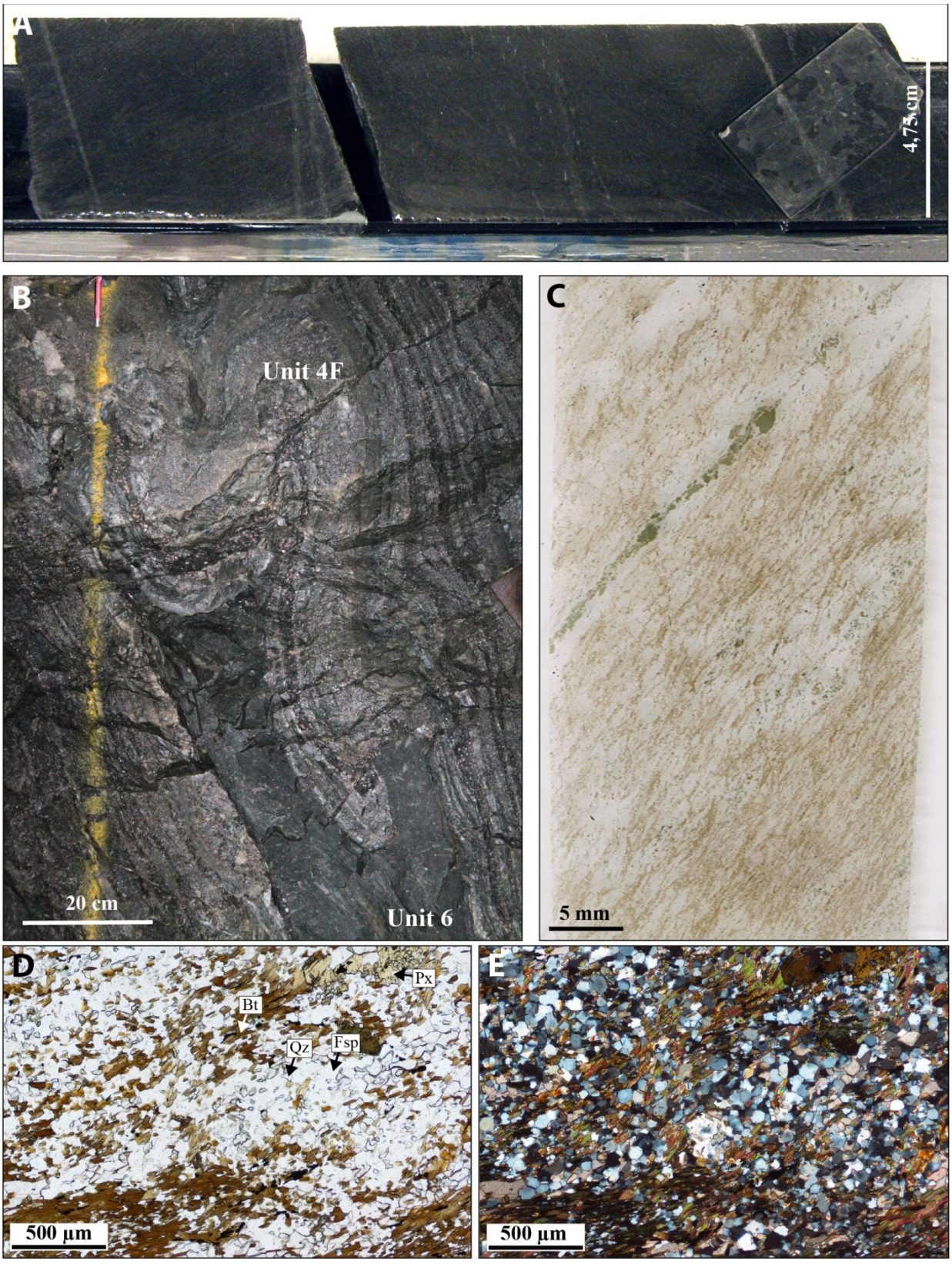

Figure 3-24: Unit 6. A. Drill core of unit 6 (sample MW-11-100). B. Underground exposure of pinched unit 6 interfolded with unit 4F (level 1070, section 12900 N, North face). C. Thin section scan of unit 6 sample MW-

13-006. D. Photomicrographs in polarized light and in cross-polarized light (E) showing the typical quartz-feldspar-biotite ± pyroxene matrix.

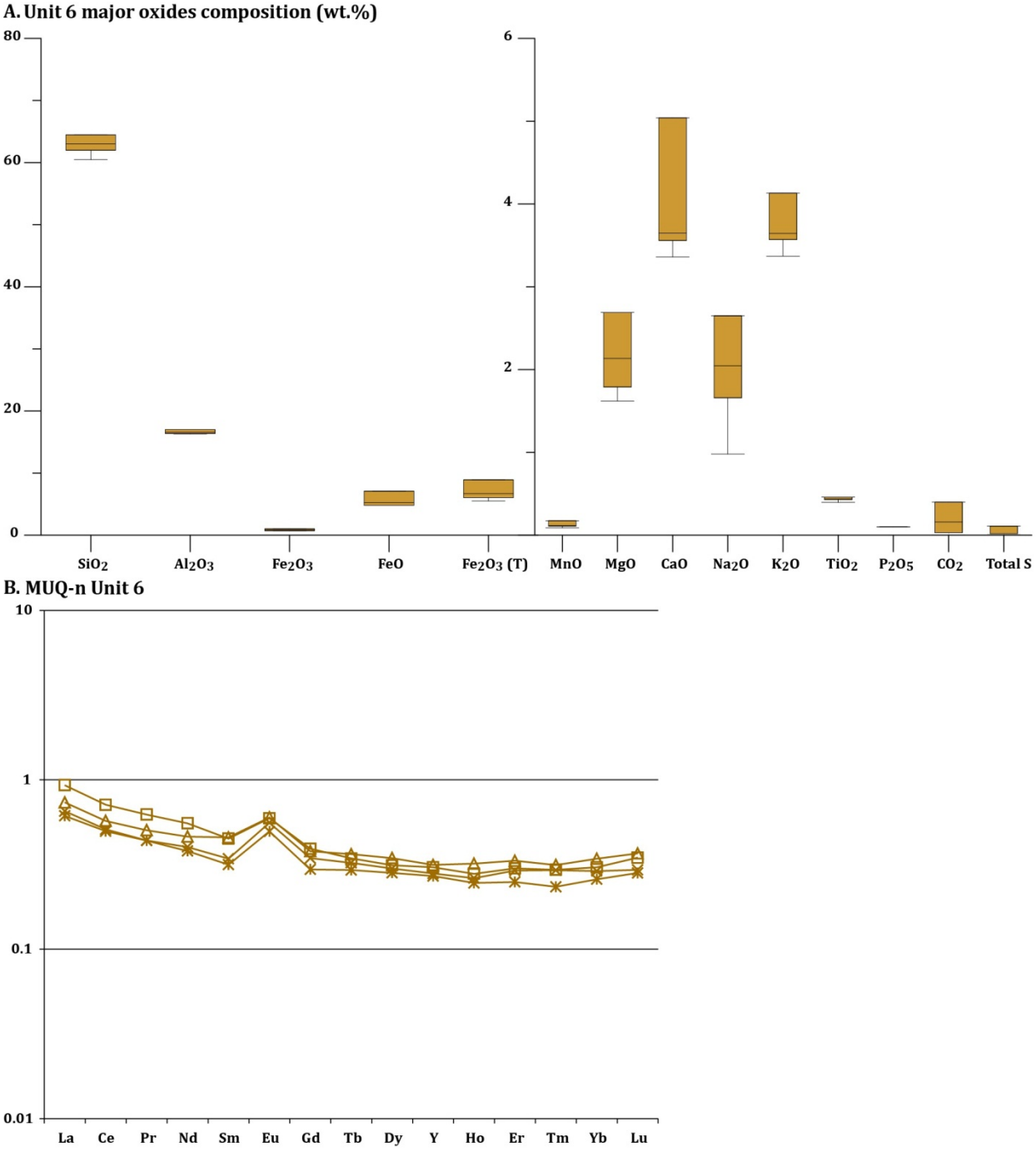

Figure 3-25: Unit 6. A. Box plot of major oxides composition, 5 samples. Box = first to third quartile, black line = median, whiskers = interquartile range (IQR)*1.5 (Upton and Cook, 1996). B. REE+Y profiles of least altered unit 6 samples normalized to the MUQ standard (Kamber et al., 2005).

3.9 Unit 4EA

Unit 4EA, the main silicate-dominated facies of the NIF, is characterized by alternating chert and garnet-grunerite-rich bands. It structurally underlies unit 4F and overlies unit 4B. It mainly occurs in the eastern Opapimiskan Lake area (Figure 3-1) and is exposed at PQ trench (Figure 3-26A). Its thickness varies from about 0.5 m up to 30-40 m in thickened hinge zones (Figure 3-2). Along the west limb of the East Bay synform and in the West antiform area, unit 4EA is generally thin and frequently interlayered with bands of the 4F facies. It is also reported to thin out in the northern Opapimiskan Lake area (Biczok J. – personal communication). Unit 4EA is the main host rock for gold mineralization (Figure 3-2; chapter 7).

Typically, unit 4EA is composed of centimetre-scale bands of chert and 40/60 vol.% almandine-grunerite assemblage. Garnet porphyroblasts are generally millimetric, pink to red, subhedral occurring in a beige, grunerite-rich matrix (Figure 3-26B, C). Minor amounts of green amphibole can be present. Garnet-biotite-rich layers are also common near the contact with unit 4F.

At microscopic scale, chert bands include fine-grained magnetite and grunerite laminas (Figure 3-27A, B). In silicate-dominated bands, fine-grained, lozenge-shaped grunerite grains form 70-90 vol.% of the matrix, along with subordinate magnetite and anhedral quartz, and trace green chlorite, brown biotite and sulphides (Figure 3-27B, C). Anhedral to euhedral almandine garnet crystals make up 20 to 50 vol.% of the rock. They have well-defined poikilitic cores with abundant inclusions of quartz, chlorite, magnetite, ilmenite, and trace of biotite and rims with few to no inclusions (Figure 3-27B, C, D). Garnet porphyroblasts are frequently tabular.

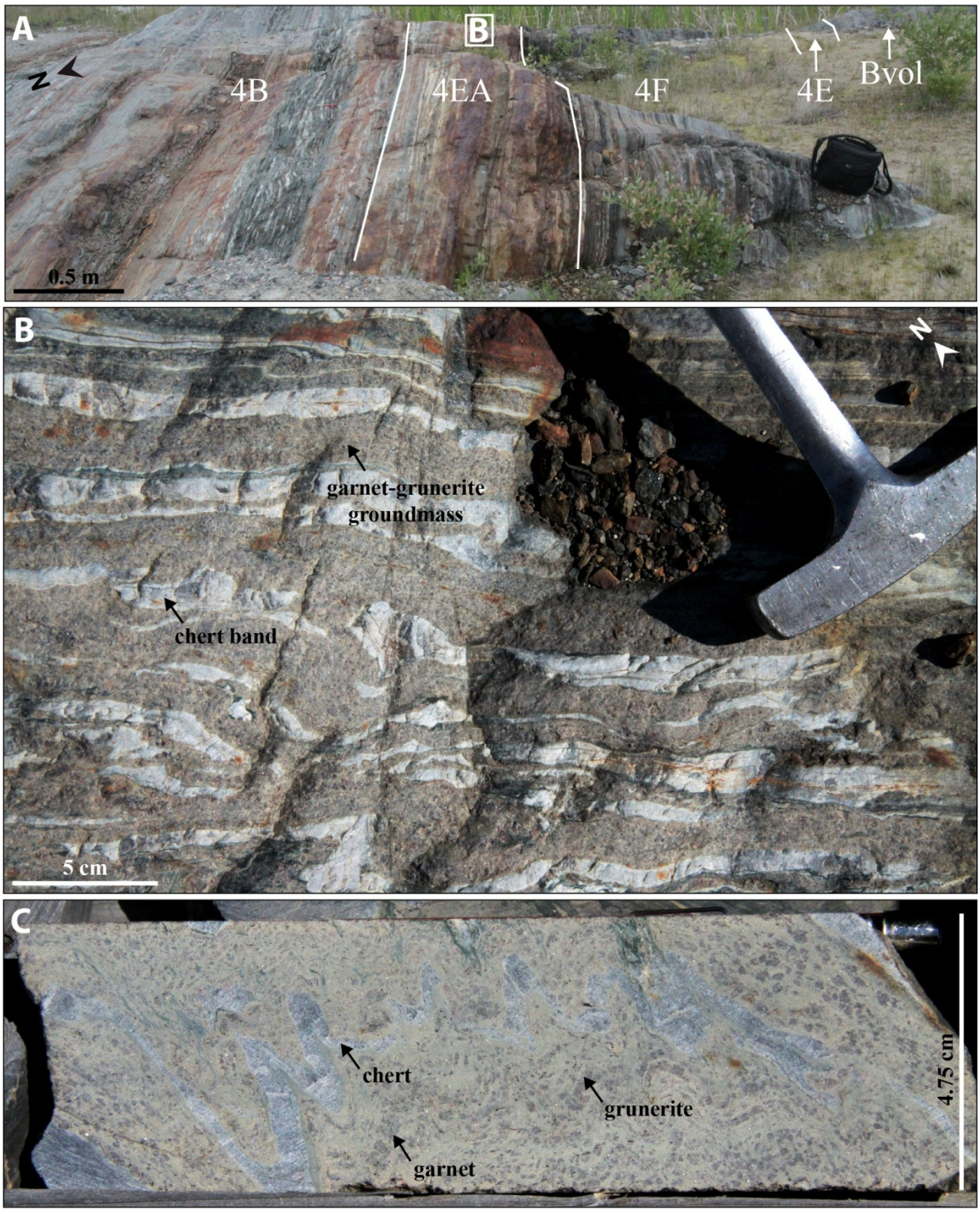

Figure 3-26: Unit 4EA. A. Surface exposure of the NIF sequence at PQ trench, mine area. Unit 4EA is located between unit 4F (garnet-biotite schist) and unit 4B (oxide-dominated BIF). B. Close-up of the compositional layering of unit 4EA at PQ trench (see A for location). C. Drill core of unit 4EA from DDH 06-PQU-001.

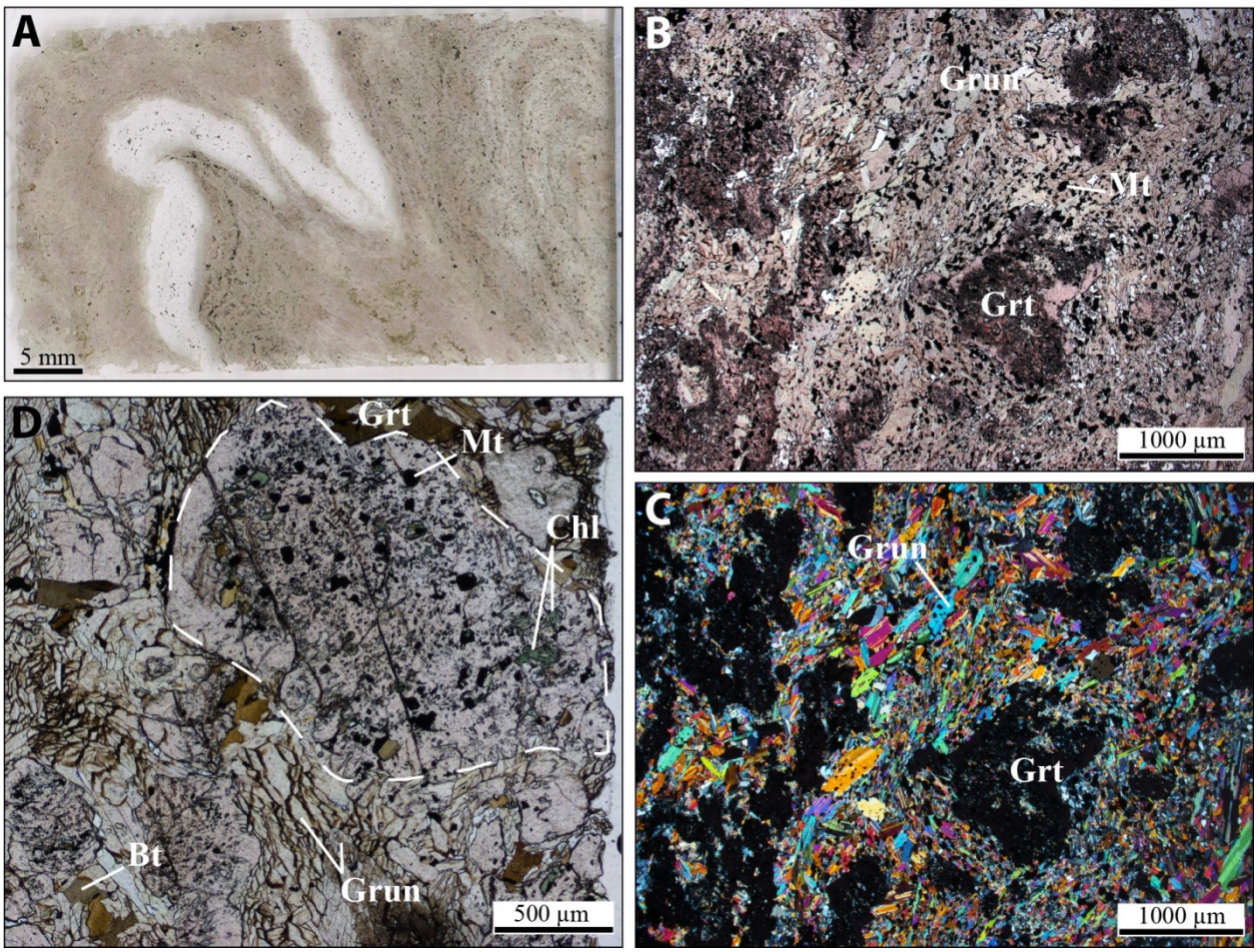

Figure 3-27: Unit 4EA. A. Thin section scan showing a folded quartz veinlet in the garnet-grunerite-magnetite matrix (sample MW-14-017A). B. Photomicrographs (polarized light) showing garnet porphyroblasts in the grunerite matrix. C. Same as B. in cross-polarized light. D. Close-up in polarized light of a garnet porphyroblast with magnetite, chlorite, and biotite inclusions.

The silicate-BIF unit (18 "least altered" samples) has a fairly constrained major oxides composition (Table 3-4; Figure 3-28A): 45-50 wt.% SiO_2, 8 wt.% Al_2O_3, 35 wt.% total iron (2 to 1 FeO-Fe_2O_3 ratio), 3 wt.% MgO, and 2 wt.% CaO. Other major oxides are present at or under 0.5 wt.%.

MUQ-n REE+Y profiles of unit 4EA are similar to those of unit 4E (Figure 3-28B). They show a strong positive Eu anomaly (average of 1.71) and moderate to high positive Y anomaly (average of 1.40). La is also weakly anomalous at 1.27 MUQ value.

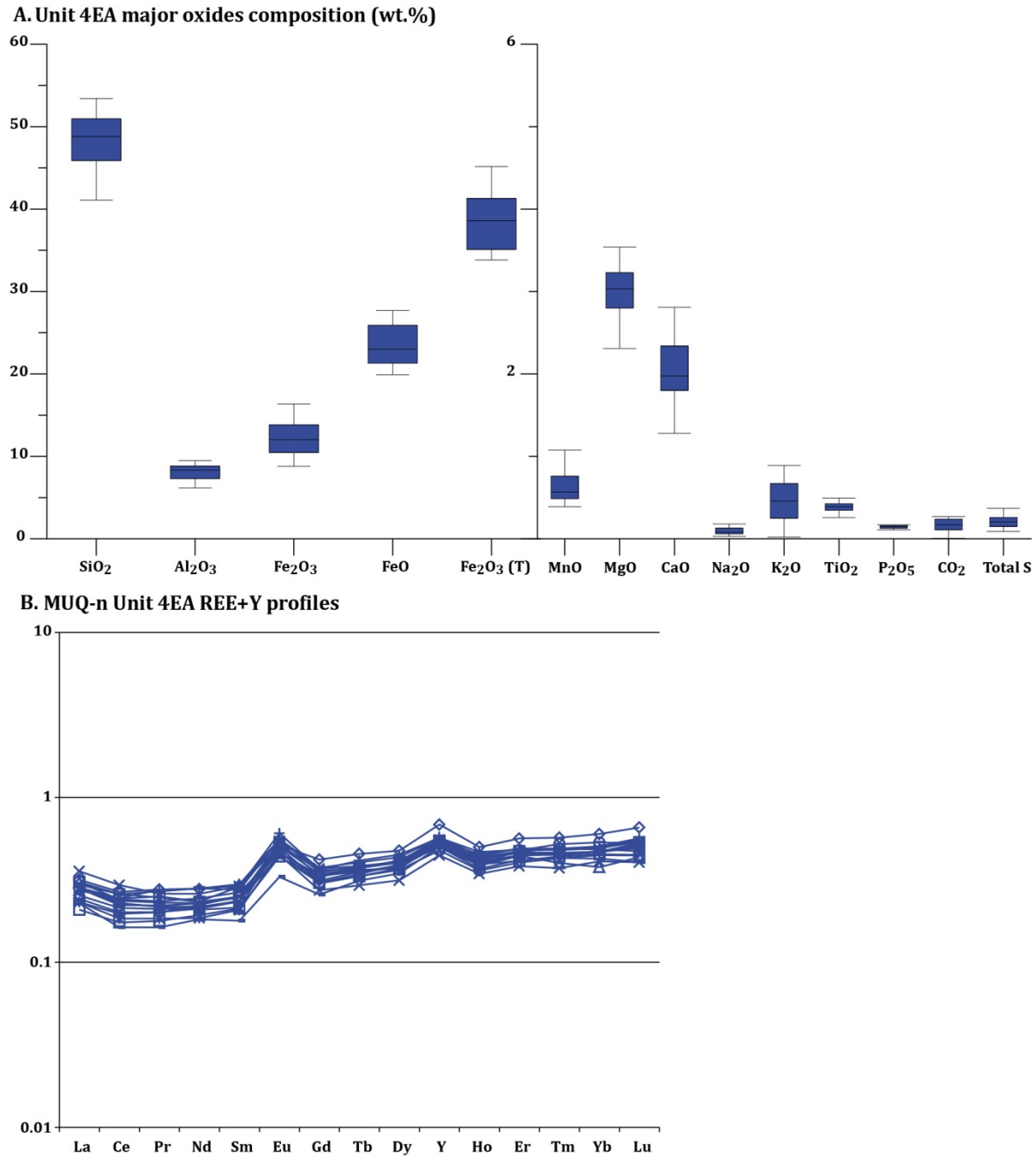

Figure 3-28: Unit 4EA. A. Box plot of major oxides composition, 18 samples. Box = first to third quartile, black line = median, whiskers = interquartile range (IQR)*1.5 (Upton and Cook, 1996). B. REE+Y profiles of least altered 4EA samples normalized to the MUQ standard (Kamber et al., 2005).

3.10 Unit 4B and facies 4Bc

Unit 4B is the oxide-dominated and most abundant facies of the NIF and SIF. In the NIF, it is 10-80 m-thick and constitutes most of the structurally lower half of the sequence (Figures 3-1A, 3-29A). In the SIF, it is 1 to 15 m-thick and forms the structurally upper portion of its multiple horizons. In contrast to the NIF, the SIF is extensively exposed in the West antiform area and, to a certain extent, in the area west of Zeemel Lake (Figure 3-1).

As typical of oxide-dominated BIF, unit 4B is constituted by alternating chert and magnetite layers (section 1.4; Figure 3-29B, C). In the NIF, facies of unit 4B evolve from its upper contact with unit 4EA to its lower contact with unit 4A from: 1) 1-2 cm-thick chert-magnetite bands, and 30-40 vol.% garnet-amphibole-rich bands (referred to as "clastic 4B" – 4Bc; Figures 3-29D, E; 3-30A) to, 2) millimetre-scale chert-magnetite bands with disseminated green amphibole (Figure 3-29F, G), and to 3) centimetre-scale chert-magnetite bands, frequently including iron carbonates. The latter lithology is similar to the dominant facies of unit 4B in the SIF (Figure 3-29B, C).

Thin sections of the 4B facies show magnetite-rich bands comprising up to 30 vol.% fine-grained, elongate, beige grunerite intergrown with opaque minerals, largely dominated by magnetite (~90 vol.%), with minor pyrrhotite and trace of chalcopyrite, arsenopyrite and graphite (Figure 3-30A, B, C). In clastic 4B facies, magnetite-poor bands include garnet porphyroblasts in a fine-grained matrix mainly composed of elongate, green to olive hornblende with minor brown biotite, colourless to pale beige grunerite and interstitial quartz (Figure 3-30B, C). Garnet has two main habitus (Figure 3-30A): 1) strongly poikilitic, pale pink, tabular, anhedral to subhedral, millimetre-scale crystals, next to chert or silica-rich bands; or 2) poikilitic to inclusion-poor, pink, rounded, subhedral, 1-5-mm crystals, in amphibole-rich bands. It occasionally occurs as inclusion-free anhedral grains in association with hedenbergite and carbonate (mostly calcite). The internal structure and metamorphic significance of garnet is further discussed in 0.

Chert bands vary in thickness and frequency across the different facies of unit 4B. They commonly contain over 80-90 vol.% quartz and trails of very fine-grained, disseminated hornblende, grunerite, biotite and magnetite (Figure 3-30A, D). Thin horizons of semi-massive grunerite are frequent at the boundary between magnetite-rich bands and chert bands, with occasional hedenbergite crystals. Grunerite in this habitus tends to be coarser than in the matrix.

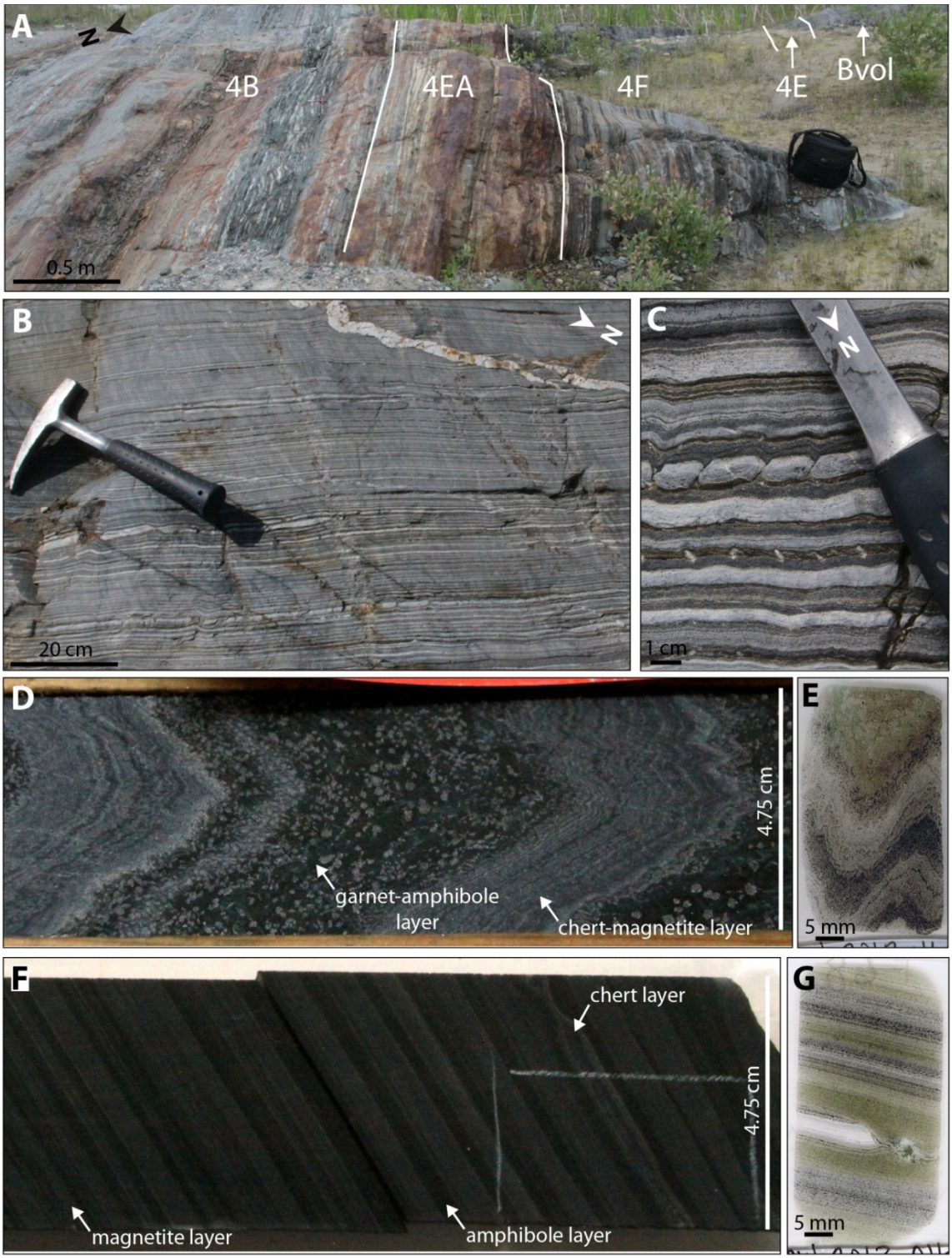

Figure 3-29: Unit 4B. A. Surface exposure of the NIF sequence at PQ trench, mine area. Unit 4B contains progressively less clastic input (garnet-amphibole layers) away from the 4EA contact. B. Surface exposure of the SIF sequence at "Zebra trench", West antiform area, showing typical chert-magnetite BIF (4B). C. Close-up view of the 4B facies at "Zebra trench". D. and E. Drill core and thin section scan of clastic-rich 4B (sample MW-12-460). F. and G. Drill core segment and thin section scan of typical 4B (sample MW-13-016).

Lithogeochemical data of unit 4B/4Bc is consistent with the progressive decrease of detrital content from the contact with unit 4EA, as 4Bc samples contain ≈ 48 wt.% SiO_2 and 6 ± 2 wt.% Al_2O_3 (Figure 3-31A). The Al-rich detrital content of facies 4Bc is restricted to well-defined garnet-hornblende bands, which contrast with the more diffuse distribution of detrital content in the garnet-grunerite bands of unit 4EA. Total Fe_2O_3 approaches 40 wt.%, more than half of which consists of FeO. MgO makes up roughly 2.5 wt.% and CaO, Na_2O and K_2O are at 1 to 1.5 wt.%. Average MnO value is close to 0.5 wt.%, similar to other units. Typical 4B contains the same amount of silica than the 4Bc but only 0.5 to 4 wt.% Al_2O_3 (average 1.82%; Figure 3-32A). In the SIF, Al_2O_3 content of the 4B is lower than 0.5 wt.% (Figure 3-32B). Unit 4B is the most iron-rich BIF facies, with up to 45 wt.% total Fe_2O_3 (close to 1 to 1 FeO-Fe_2O_3 ratio), and also includes 3-4 wt.% CaO and 2-3 wt.% MgO. It contains more CO_2 (1-2 wt.%) than unit 4EA.

MUQ-n REE+Y profiles of 4Bc and 4B are fairly similar, with a slight depletion of LREE over HREE (Figures 3-31B, 3-32C). The chemically-derived component of 4B translates into strong positive La, Eu and Y anomalies (Eu: 2.36 over 1.64; Y: 1.62 over 1.46, and La: 1.39 over 1.35).

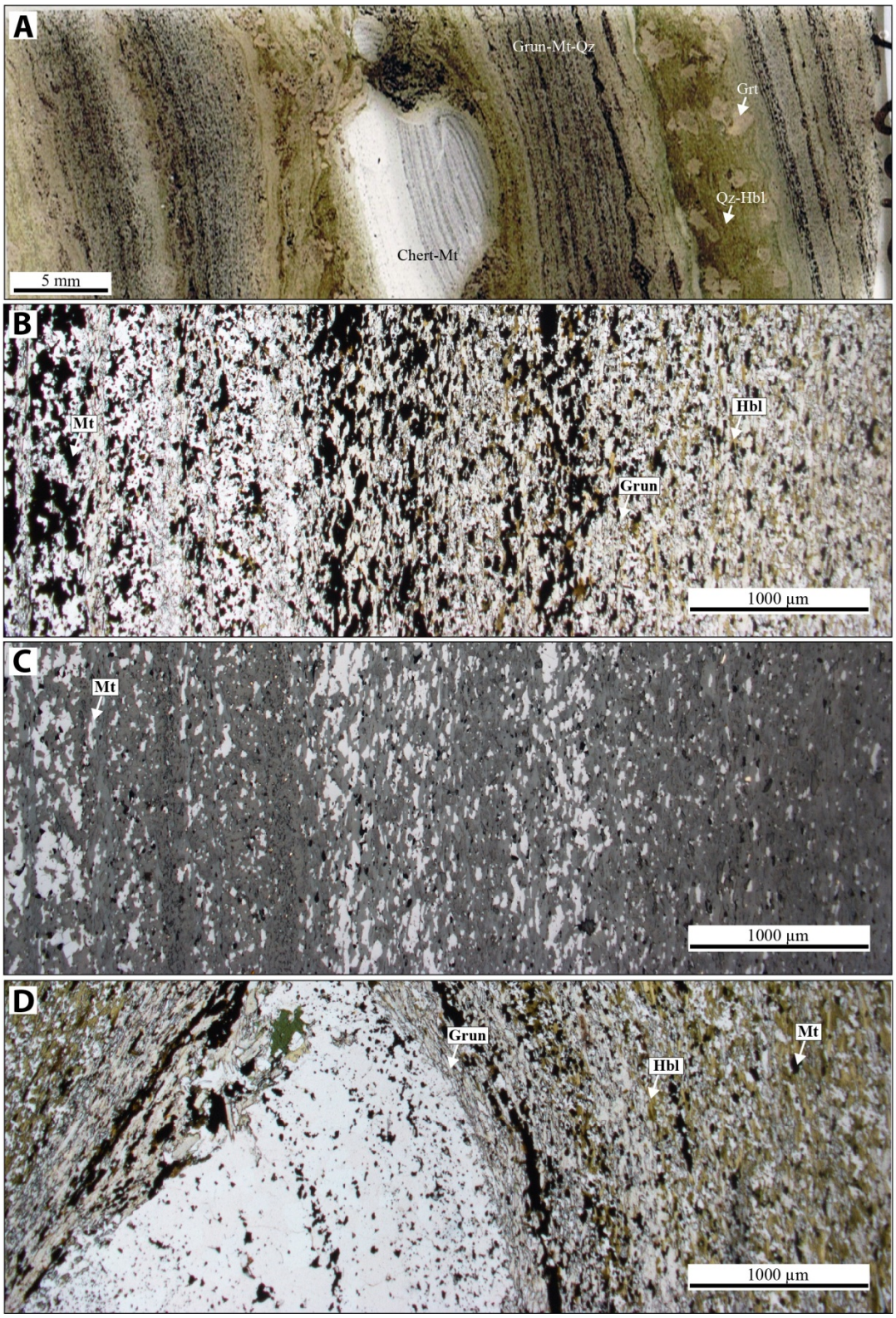

Figure 3-30: Unit 4B. A. Thin section scan of clastic 4B sample MW-13-023 showing garnet-amphibole bands and the various habitus of garnet. Note the preserved primary structure in boudinaged chert layer. B. Photomicrograph (transmitted light) showing composition variation in the matrix in magnetite-rich bands

(sample MW-13-016; Figure 3-29G). C. Same as B. in reflected light. D. Photomicrograph (transmitted light) showing a boudinaged chert band (sample MW-13-016) that has preserved primary bedding, and surrounding grunerite-magnetite layers.

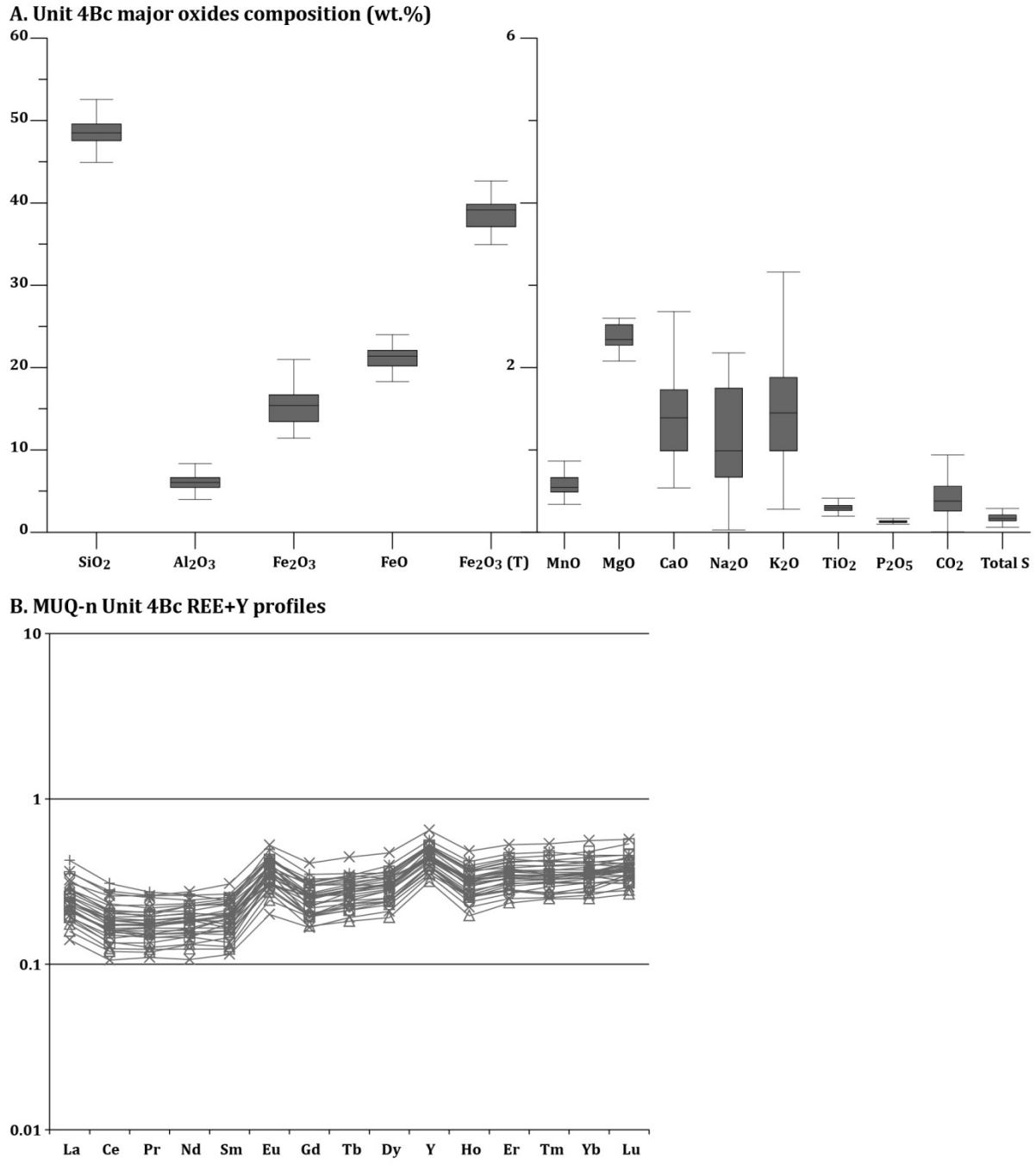

Figure 3-31: Facies 4Bc. A. Box plot of major oxides composition, 26 samples. Box = first to third quartile, black line = median, whiskers = interquartile range (IQR)*1.5 (Upton and Cook, 1996). B. REE+Y profiles of least altered 4Bc samples normalized to the MUQ standard (Kamber et al., 2005).

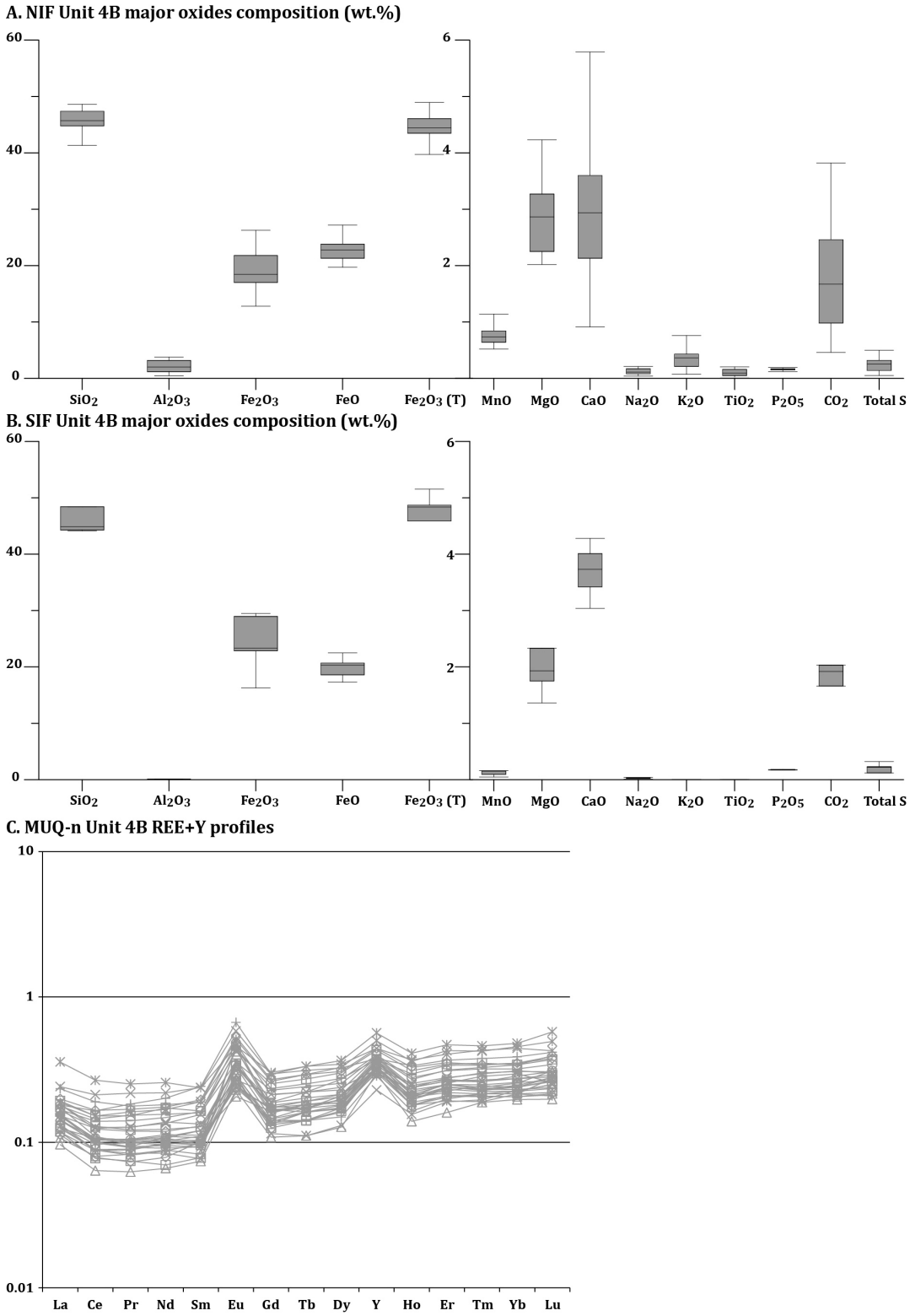

Figure 3-32: Unit 4B, 36 samples. A. and B. Box plot of major oxides composition of least altered 4B samples in the NIF and SIF, respectively. Box = first to third quartile, black line = median, whiskers = interquartile range (IQR)*1.5 (Upton and Cook, 1996). C. REE+Y profiles of least altered 4B samples normalized to the Mudstone of Queensland standard (Kamber et al., 2005).

3.11 Unit 4A

Unit 4A is a secondary silicate-facies of the NIF and SIF. In the NIF, it is 1 to 5 m-thick and marks the stratigraphical top of the sequence (Figure 3-33A). In the SIF, it is 1 to 15 m-thick and structurally underlies the 4B facies. It is the main host rock for gold mineralization in SIF mineralized zones (e.g., Red Wing-Thunder Wolves zones; Figure 3-2A; chapter 7). The unit consists of alternating chert and silicates bands, and includes some to frequent magnetite and/or detrital-rich bands (i.e., garnet-biotite) in the NIF (Figure 3-33B, C). Band thickness ranges between 0.5 and 3 cm, but may be tectonically thinned to 1-3 mm in the mine area. Silicates bands typically comprise beige grunerite, and some light green amphibole and pyroxene.

At microscopic scale, chert bands are composed of >90 vol.% quartz and very fine-grained, anhedral grunerite and trace amounts of calcite and magnetite (Figure 3-33D, E, F). Silicate bands are almost exclusively composed of colourless, fine-grained, subhedral to euhedral grunerite (Figure 3-33D, E), with up to 30 vol.% fine-grained, anhedral magnetite. Locally, pleochroic, medium green hornblende is intergrown with grunerite and traces of calcite. Contact between chert bands and grunerite bands may contain up to 15-20 vol.% pale green, anhedral pyroxene (orthopyroxene: ferrosilite, clinopyroxene: hedenbergite; Figure 3-33E), but it typically contains only a few percent of disseminated magnetite (Figure 3-33F). Trace minerals include potassic feldspar, biotite, graphite, and ankerite.

Unit 4A is the most siliceous competent unit with around 65 wt.% SiO_2 in the NIF (Figure 3-34A) and up to 75 wt.% in the SIF (Figure 3-34B). Detrital component is nearly absent, with very low Al_2O_3, TiO_2 and K_2O contents. Iron content is roughly 25 wt.% with $4/5^{th}$ FeO. MgO and CaO contents are slightly higher in the NIF than the SIF (3-4% vs. around 2 wt.%), as are CO_2 and sulphur contents 2-3% vs. 1 wt.% and 0.5-1% vs. <0.5 wt.%, respectively. Unit 4A in the NIF shows more variability in minor oxide compositions (Figure 3-34A). MUQ-n REE+Y profiles are similar to unit 4B (Figure 3-34C) with weak LREE depletion over HREE and strongly positive Eu anomaly (average of 2.60). However, Y and La positive anomalies are weaker than unit 4B, at 1.32 and 1.26, respectively.

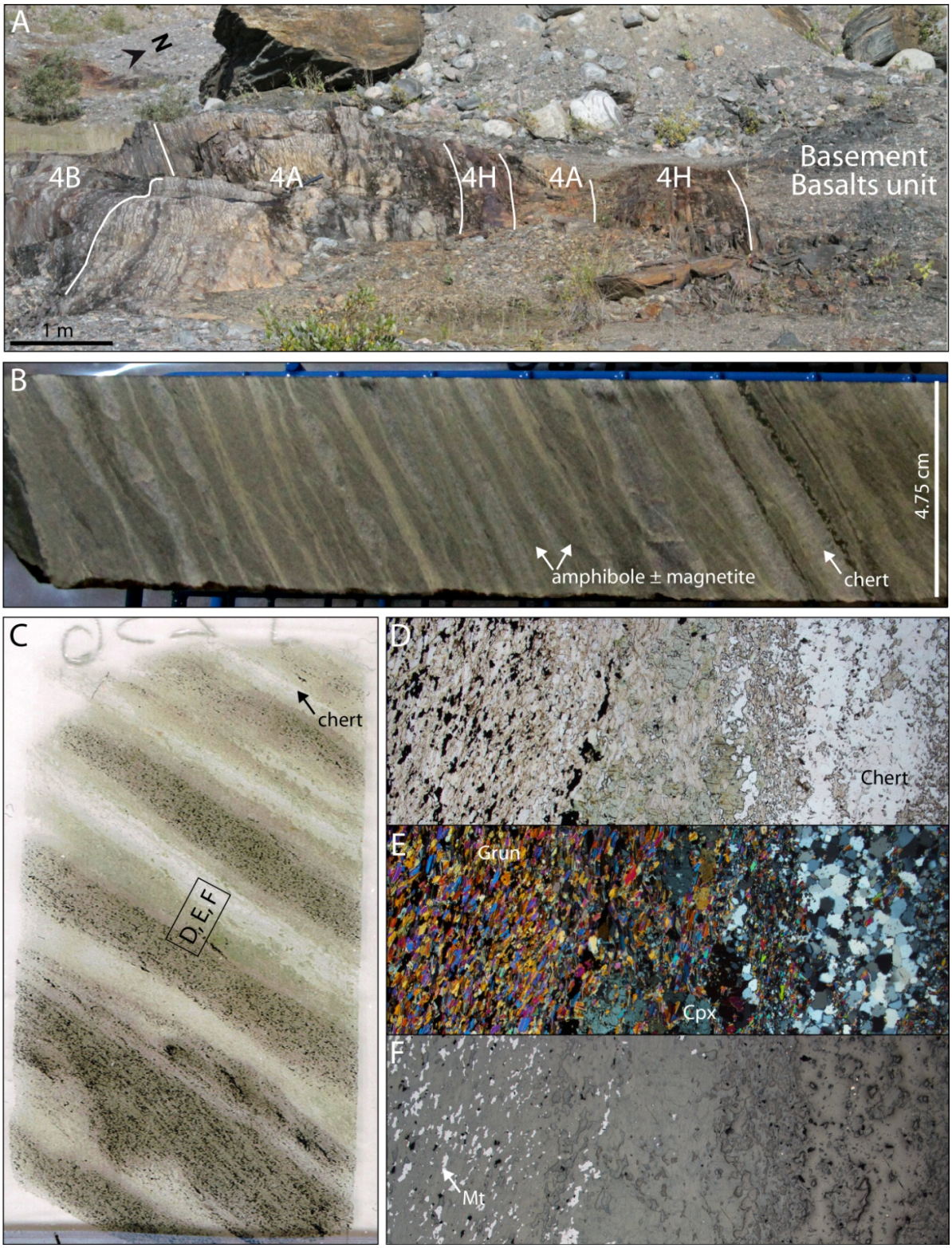

Figure 3-33: Unit 4A. A. Progressive transition between unit 4A and 4B at PQ trench. B. Drill core of typical 4A facies (sample MW-12-335). C. Thin section scan of the same sample. Note the mineral zonation between chert bands and magnetite-bearing bands. D., E., and F. Photomicrographs of C. in polarized light, cross-polarized light, and reflected light, respectively.

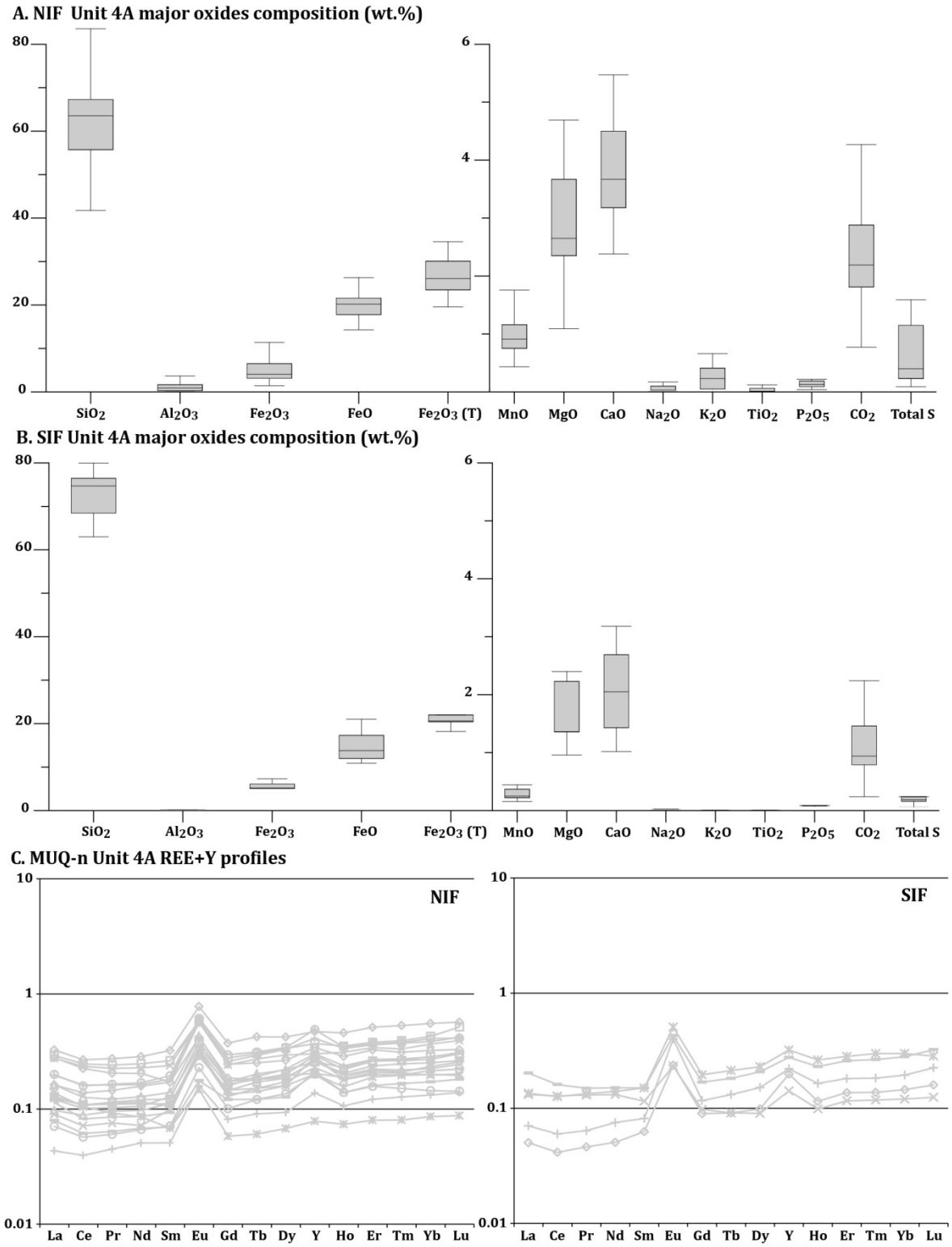

Figure 3-34: Unit 4A, 25 samples. A. and B. Box plot of major oxides composition of least altered 4A samples in the NIF and SIF, respectively. Box = first to third quartile, black line = median, whiskers = interquartile range (IQR)*1.5 (Upton and Cook, 1996). C. REE+Y profiles of least altered 4A samples normalized to the MUQ standard (Kamber et al., 2005).

3.12 Unit 4H

Unit 4H is a pyrrhotite-rich meta-argillite present in both the NIF and SIF. At the structural base of the NIF, it occurs as 10-50 cm-thick lenses, and as interlayers within the 4B and 4A facies of the SIF.

At PQ trench (see map, chapter 5), sulphides of unit 4H are strongly weathered, producing an intense rusty stain (Figure 3-35A). Unit 4H typically contains 10-20% pyrrhotite with occasionally 1-3% arsenopyrite in a very fine-grained argillaceous matrix (Figure 3-35B). In the NIF, unit 4H frequently contains some 4A, and chert layers that can make up to 5% of the unit (Figure 3-35B, C).

At microscopic scale, the matrix of the 4H facies is a mixture of net-textured pyrrhotite (with local magnetite) and very fine-grained quartz-actinolite-feldspar-graphite ± biotite (Figure 3-35C, D, E). Granoblastic quartz and feldspars (plagioclase and potassic) make up around 30 vol.% and 10 to 15 vol.% of the matrix, respectively. Intergrown fine-grained, actinolite and biotite contribute up to 20 vol.%. Graphite is very fine-grained, opaque and with low relief, and makes up to 10 vol.% of the matrix. Disseminated poikiloblastic tourmaline (dravite) usually occurs in trace amount, but locally can reach 3-5 vol.% of silicate bands (Figure 3-35D). Trace minerals include titanite, calcite, sphalerite, galena and arsenopyrite.

The 4H facies of the NIF frequently includes minor chert-grunerite or amphibole and is more heterogeneous than other BIF units. Consequently, content of some major oxides are quite variable (Figure 3-36A). SiO_2 content ranges 45-60 wt.%; CaO ranges 3-10 wt.%, and the total sulphur content constitutes 6 to 10 wt.%. Iron is mostly present as FeO and makes up ≈ 28 wt.% of the rock, and Al_2O_3 content ≈ 4 wt.%. Other oxides remain in the same range than in previous BIF units.

In the SIF, aluminum content of the 4H is higher (approximately 10 wt.%; Figure 3-36B). SiO_2 and total iron content are slightly lower (45 and 25 wt.%, respectively), with a more variable FeO-Fe_2O_3 ratio. Subordinate major oxides are all slightly more abundant; total sulphur content is around 10 wt.%.

MUQ-n profiles of 4H samples from the SIF differ from those of the NIF by their slight LREE enrichment, instead of the LREE depletion observed in other lithologies (Figure 3-36C). In addition, HREE such as Tm, Yb and Lu seem to be slightly enriched in the 4H samples of the SIF. Recurrent anomalies are still present but weaker than in previous units. The positive Eu anomaly has an average value of 2.06 and 1.59 (in the NIF and SIF, respectively). Only a few samples from the NIF have a positive Y anomaly, around 1.20. The positive La anomaly is more consistent in both NIF and SIF samples (1.17 and 1.19).

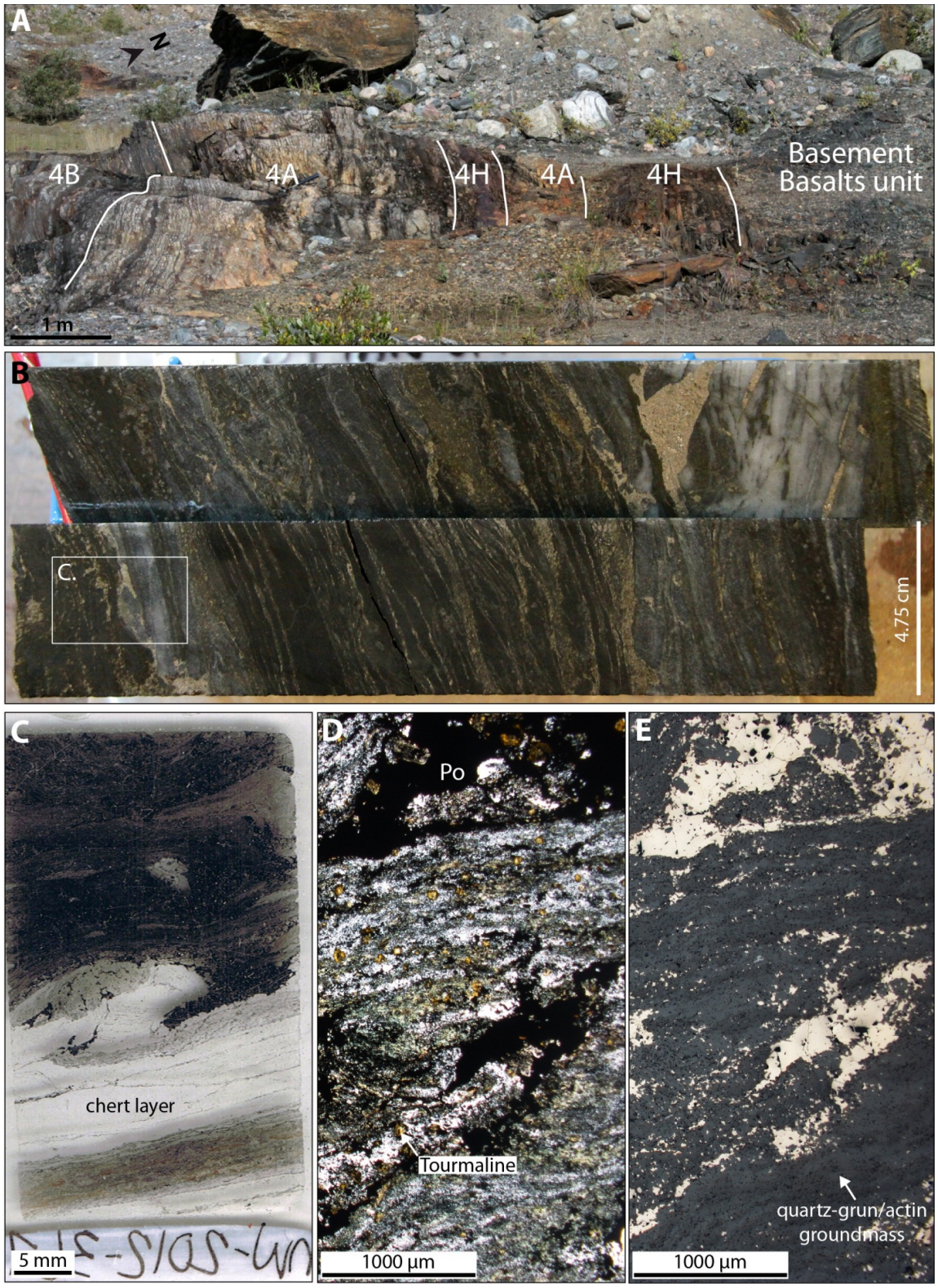

Figure 3-35: Unit 4H, 10 samples. A. PQ trench exposures of the NIF sequence. Unit 4H is distinctly rusty-weathered. Duplication is probably due to local asymmetric Z-fold. B. Drill core of typical 4H (sample MW-12-367). C. Thin section scan of the same sample. D. and E. Photomicrographs of typical argillaceous matrix with sulphide under polarized light and cross-polarized light.

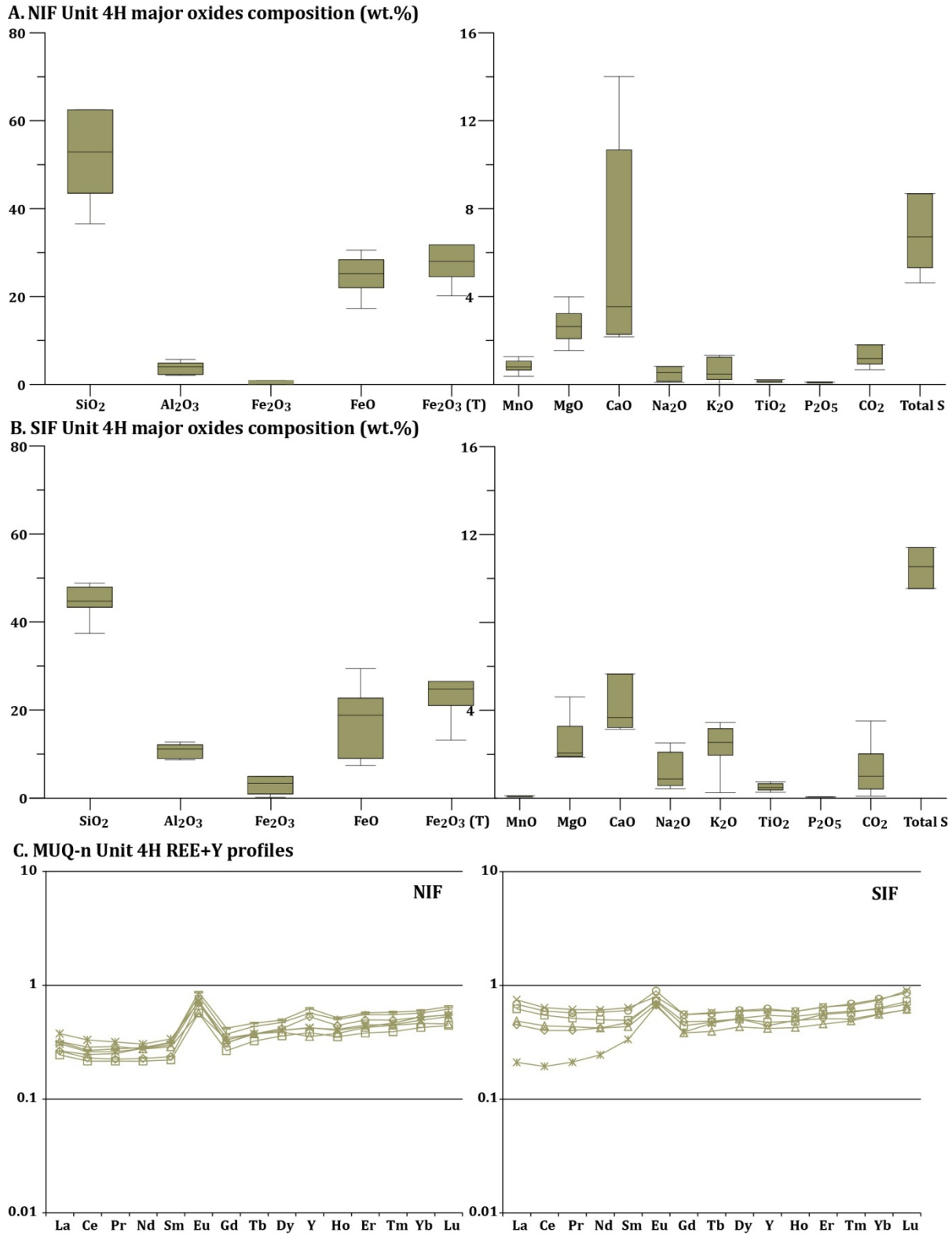

Figure 3-36: Unit 4H – A. and B. Box plot of major oxides composition of least altered 4H samples in the NIF and SIF. Box = first to third quartile, black line = median, whiskers = interquartile range (IQR)*1.5 (Upton and Cook, 1996). C. REE+Y profiles of least altered 4H samples normalized to the MUQ standard (Kamber et al., 2005).

3.13 Other banded iron formations

The aeromagnetic map of the Opapimiskan Lake area outlines a series of strong anomalies in the central West antiform area, as well as between the Zeemel and Graff lakes. These anomalies are located close to the boundary between the part of the "Lower basalts" dominated by tholeiite and the one dominated by komatiitic basalt and komatiite (Figure 3-1). Exploration drilling intersected BIF horizons associated with pyrite-pyrrhotite massive sulphide and pyrite-nodule-bearing carbonaceous argillite (Wilberforce area), or classic chert-magnetite BIF (Zeemel and Graff lakes area). The pyrite nodule-bearing carbonaceous argillite was sampled to investigate their precious and base metals content and potential as metal source using 2D LA-ICP-MS elemental mapping (section 1.2.8; chapter 9).

3.14 Ultramafic dykes

Several ultramafic dykes are intersected by drilling in the mine area, both within unit Bvol and NIF (Figure 3-37A, B). A boudinaged and folded (F_2) ultramafic dyke is located along the eastern limb of the T-antiform where it cuts the NIF (mapped underground at mine level 1020; Figures 3-2; 3-37B, C). The dyke is composed of fine-grained, strongly foliated amphiboles (Figure 3-37D, E). The matrix is composed of 75 to 85 vol.%, colourless to pale green, actinolite and actinolitic hornblende and 5-10 vol.% quartz (Figure 3-37E, F, G). Trace minerals include plagioclase feldspar, magnetite and pyrrhotite.

Samples of ultramafic dykes have been collected where they intrude unit Bvol (Figure 3-2). Data from underground mapping and drill core examination suggests these dykes are pre-tectonic and possibly syn-volcanic, related to extrusive ultramafic units of the OMA.

Geochemical data shows mostly komatiitic MgO-Al_2O_3 composition (Figure 3-3A), supported by Zr values between 15 and 20 ppm and approximately 0.35 wt.% TiO_2 (Figure 3-38A; MacLean and Barrett, 1993), similar to other ultramafic rocks of the Opapimiskan Lake area. They display a tholeiitic magmatic affinity (Figure 3-38B; Ross and Bédard, 2009). Their PM-n trace element profiles have very weakly negative La to Lu slopes, which include a weak to moderate negative Hf anomaly and a weak negative Y anomaly (Figure 3-38C). HREE values are close to PM values.

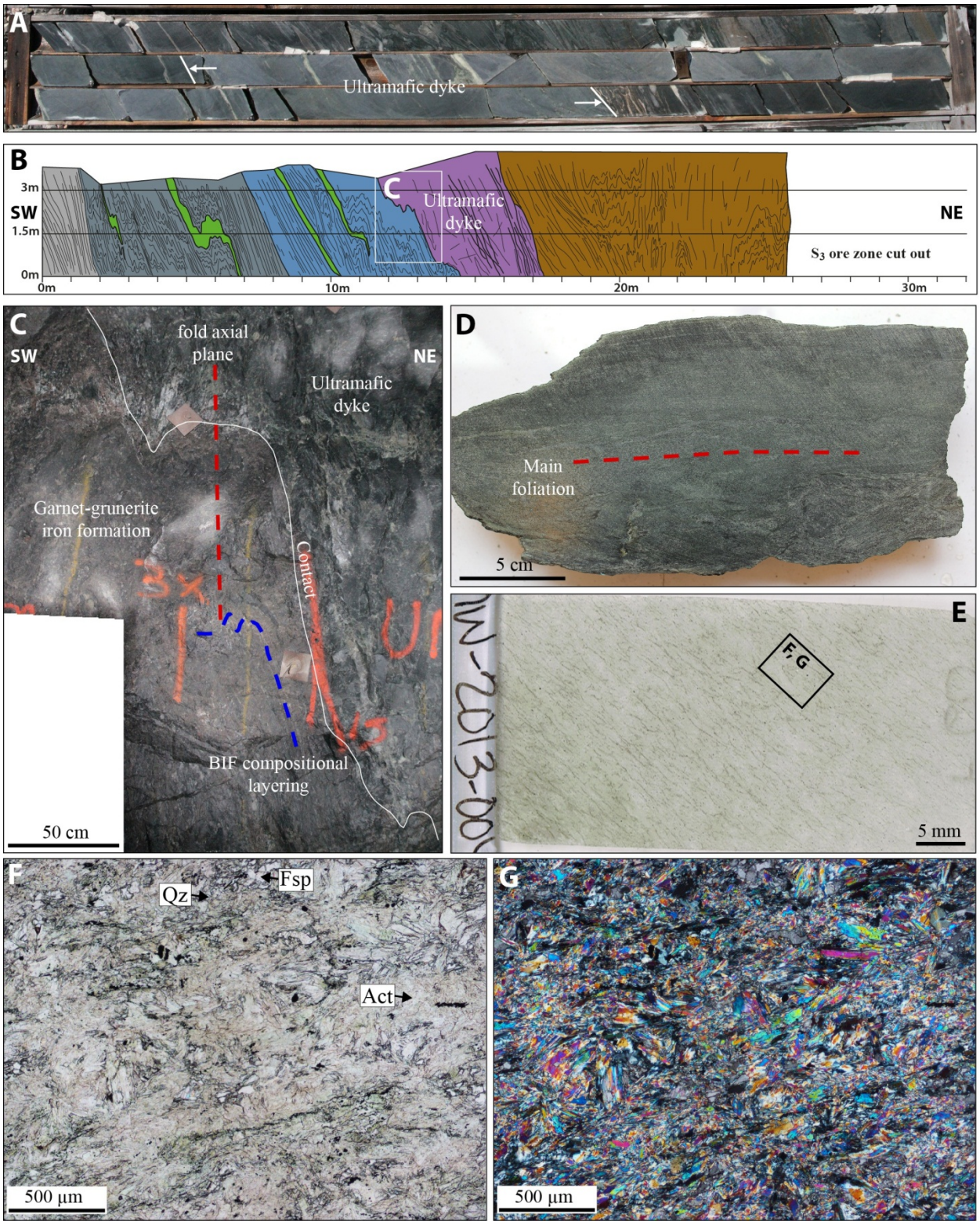

Figure 3-37: Ultramafic dykes. A. Drill core segment from drill hole 09-TAN-029 where the ultramafic dyke crosscuts unit Bvol above the NIF. B. Underground face map of mine level 1020, Main Ramp access, showing the NIF sequence cut by the ultramafic dyke. Smaller mafic dykes are shown in green. (Colour legend is the same as Figure 3-2B) C. Photograph of the folded, NIF-dyke contact as seen in B. D. Grab sample slab of the

dyke. E. Thin section scan of sample MW-13-004, taken from the drill core segment shown in A., with typical mineralogy in F. polarized light and G. cross-polarized light.

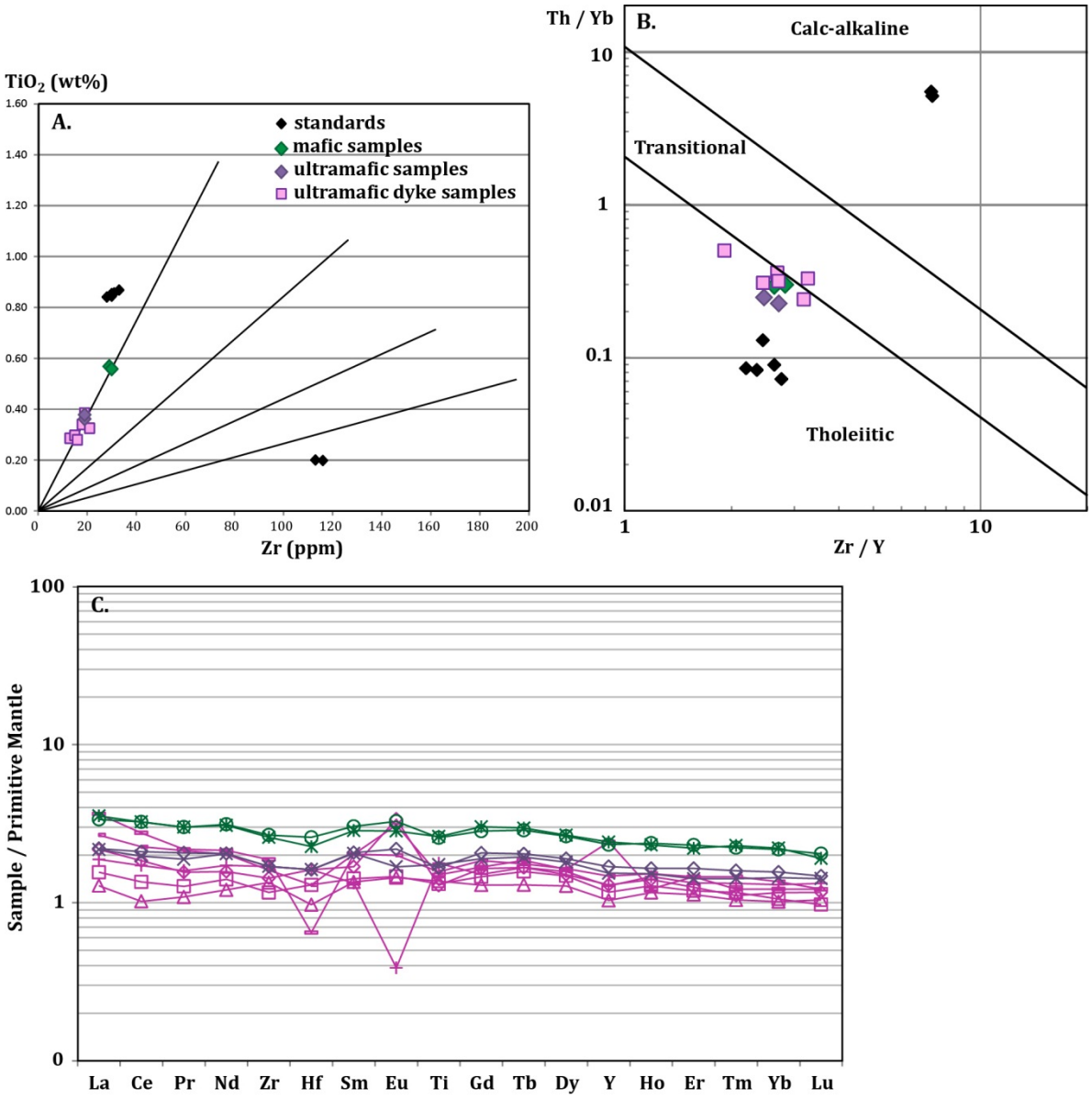

Figure 3-38: Ultramafic dykes A. Zr vs. TiO_2 binary plot, "Lower basalts" (LB) samples are shown for comparison (after MacLean and Barrett, 1993); pink squares = ultramafic dyke samples, purple diamonds = LB ultramafic samples, green diamonds = LB mafic samples, black diamonds = mafic and felsic volcanic rock standards; black lines = main trends of this study's dataset. B. Zr/Y vs. Th/Yb binary plot for magmatic affinity from Ross and Bédard (2009). C. PM-n trace element profiles (PM values from Sun and McDonough, 1989). Pink lines represent ultramafic dyke samples, purple and green lines symbolize LB samples for comparison.

3.15 Other intrusive units

3.15.1 Mafic intrusions

Mafic intrusions are common in all facies of the NIF. They constitute up 10-20 cm-thick intersection in drill holes and are readily visible on underground faces (Figure 3-37B). They consist of foliated, fine-grained amphibolitic rock with local disseminated garnets. They generally crosscut the BIF compositional layering but are frequently sub-parallel to it and deformed by F_2 folds. No sulphide or gold mineralization is associated with these dykes (Goldcorp Inc. Musselwhite mine data). Consequently, they have not been investigated in detail in the course of this study.

3.15.2 Felsic intrusive phases

Ultramafic and mafic volcanic rocks and sedimentary rocks of the OMA are also cut by felsic intrusions that can be divided in three groups: 1) fine to medium-grained, quartz-feldspar-phyric dykes, 2) medium-grained, quartz-feldspar-phyric intrusions, and 3) pegmatitic muscovite-bearing, granitic dykes.

The first type of dykes was sampled during this study for U-Pb zircon geochronology to improve the constraints on the age of the iron formation sequences (McNicoll et al., 2016; chapter 4). These fine- to medium-grained, quartz-feldspar-phyric dykes are thought to be related to the felsic volcanism of the OMA. The quartz-feldspar-phyric intrusions have been documented in three zones: the Wilberforce area, south of Zeemel Lake, and in the Paseminan area (Figure 3-1). Samples for geochronology were taken at each occurrence (chapter 4). Finally, pegmatitic dykes are interpreted as the product of partial melting of sedimentary rock types associated with late stages of the regional tectono-metamorphic evolution (Biczok et al., 2012; Fry, 2013). They are especially present in the intensely deformed rocks of the ZHA, east of Musselwhite mine (DDH 11-282-001 to -003).

While there are reports of anomalous gold values associated with albite pegmatite dykes in the West antiform area (Hall and Rigg, 1986), such occurrence has not been encountered by Placer Dome Inc. or Goldcorp Inc. exploration (Biczok J., personal communication; Goldcorp Inc. Musselwhite mine data). Consequently, these dykes have not been studied during this study.

3.16 Zeemel-Heaton assemblages

This section presents geological data collected mainly during reconnaissance mapping and targeted geochronology sampling over the southern NCG. Although the ZHA is not part of the deposit host sequence, data from this assemblage has implications on the regional geological evolution of the NCG, as well as on the genesis of the Musselwhite gold deposit (chapter 10).

The scarce information published on the ZHA prior to this study (e.g., Breaks et al., 2001; Davis and Stott, 2001) shows a complex and highly diversified sedimentary-volcanic rock assemblage (chapter 2). It has been proposed that the western and eastern portions of the ZHA constitute two separate rock packages, the Zeemel and Heaton assemblages, respectively (Figure 3-39; Goldcorp Inc., unpublished data; McNicoll et al., 2016). Recent research (e.g., Duff, 2014; Bath et al., 2015) and part of the present study have contributed to a better understanding of the ZHA stratigraphic framework (Figure 3-39; chapter 4). This work has established that ZHA occurring northwest of the Markop Lake Shear Zone (Zeemel assemblage) comprises a great diversity of sedimentary facies yielding the oldest maximum age constraints (Figure 4-1), while ZHA rocks laying to the south-east of the shear zone (Heaton assemblage) show a more mature type of sedimentation (i.e., well-sorted sandstones) with maximum age constraints as young as 2723 ± 23 Ma (Duff, 2014; Bath et al., 2015). These assemblages are described separately below.

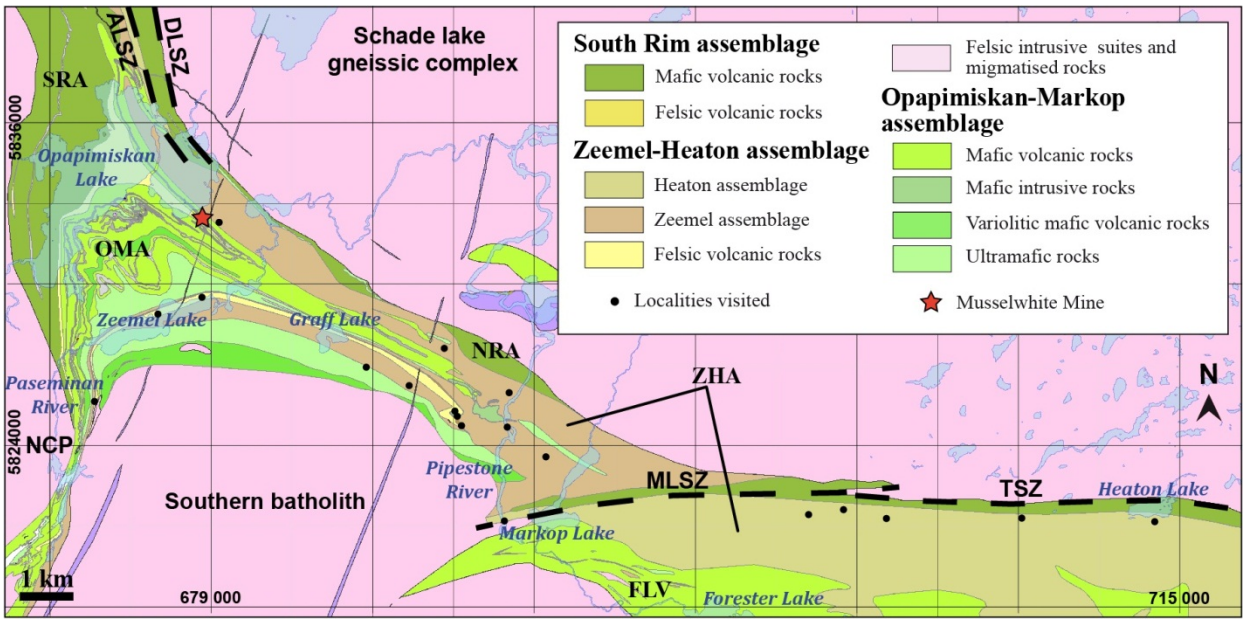

Figure 3-39: Geological map of the southern NCG (modified from Breaks et al., 2001, and Goldcorp Musselwhite Ltd.) with location of visited localities. Refer to Figures 2-2 and 2-3 for acronym definitions.

3.16.1 Zeemel assemblage

3.16.1.1 Zeemel assemblage near the OMA

This subsection describes rocks of the Zeemel assemblage that have been mapped within a hundred metres from the OMA contact, which is largely covered by quaternary overburden (Figure 3-39). In the Paseminan River area, parts of the ZHA (Figure 3-39) consist of a strongly deformed, polymictic, matrix-supported conglomerate (Figure 3-40A). Clast types are largely dominated by neighbouring felsic and mafic lithologies (Figure 3-40B, C). Some chert clasts have also been documented. Other outcrops roughly 100-200 m to the southeast show a strongly-lineated, feldspar-phyric felsic rock and a feldspar-phyric mafic rock, with steep stretching lineation (L_2), that are interpreted to belong to the OMA.

A different sedimentary facies occurs to the SE of Graff Lake, along the contact with the OMA (Figure 3-39). There, volcanic rocks of the OMA are in contact with a sequence of coarse-grained to medium-grained greywackes including a cherty fine-grained schist horizon with some sulphide staining (Figure 3-41A, B). The alternation of fine- and medium-grained beds and occurrence of graded-bedding are suggestive of a NE-younging turbiditic sequence.

In the immediate mine area (Figure 3-39), drill holes intersect the contact between the OMA and ZHA, which appears to be tectonic (section 5.2.4). DDH 11-282-003 (section 8500 N) provides access to hundreds of metres of quartz-feldspar-biotite schist, locally including sulphides (pyrite 80%, pyrrhotite 20%; Figure 3-42A). The schist shows a strong, eastward-increasing strain gradient illustrated by the progressive development of a mylonitic fabric, the development of a mineral segregation, and an increase in the proportion of the boudinage and transposition of quartz veins (Figure 3-42B, C). Mylonitic quartz-feldspar bands alternate with biotite-rich bands containing quartz vein fragments.

Pyrite-rich sedimentary rocks were sampled to investigate the composition of sulphides using LA-ICP-MS elemental mapping (chapter 9). Whole-rock geochemical data from these samples show an average SiO_2 content of 42 wt.%, 8.1 wt.% Al_2O_3, 30 wt.% total Fe_2O_3, and 19 wt.% total S (Figure 3-43A). Chondrite (C1)-normalised extended REE profiles show LREE-enriched slopes and flat HREE (Figure 3-43B). There is consistent moderate negative Ti-anomaly, strong negative Nb-Ta anomalies, and weak to moderate positive Zr-Hf anomalies. This suggests a sedimentary source dominated by calc-alkaline, intermediate to felsic rocks such as those mapped in the SRA (unit Avol, section 3.2; felsic rocks in western Opapimiskan Lake area, chapter 4; Smyk, 2013).

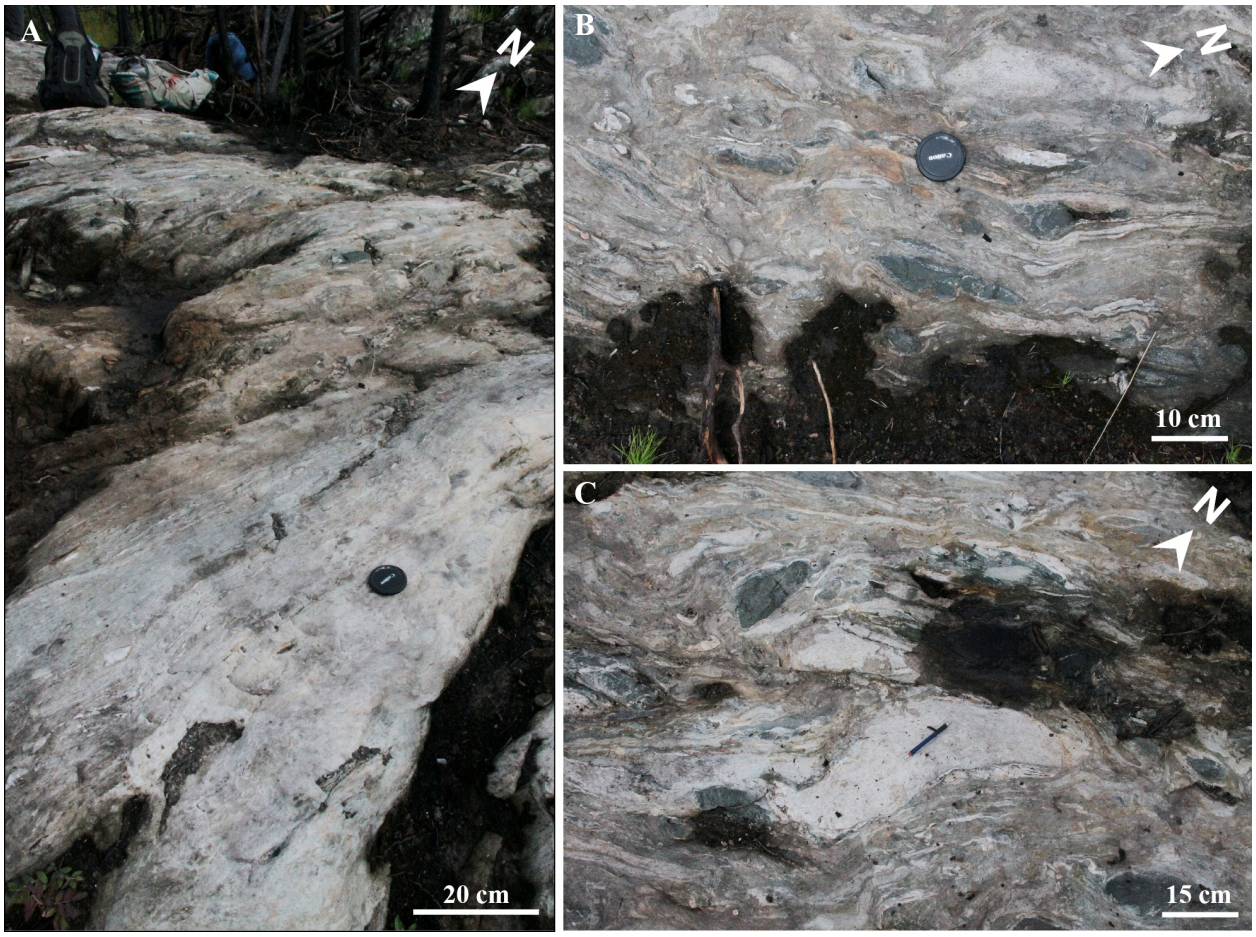

Figure 3-40: Zeemel sedimentary rocks in the Paseminan river area. A. Photograph of the overall exposure of conglomerate near UTM 674750/5825760. B. and C. Close-up photographs of clasts in the conglomerate showing two major types of clasts (i.e., mafic and felsic) , the flattening of the clasts and the strong NNE-trending foliation overprinted by asymmetric folds.

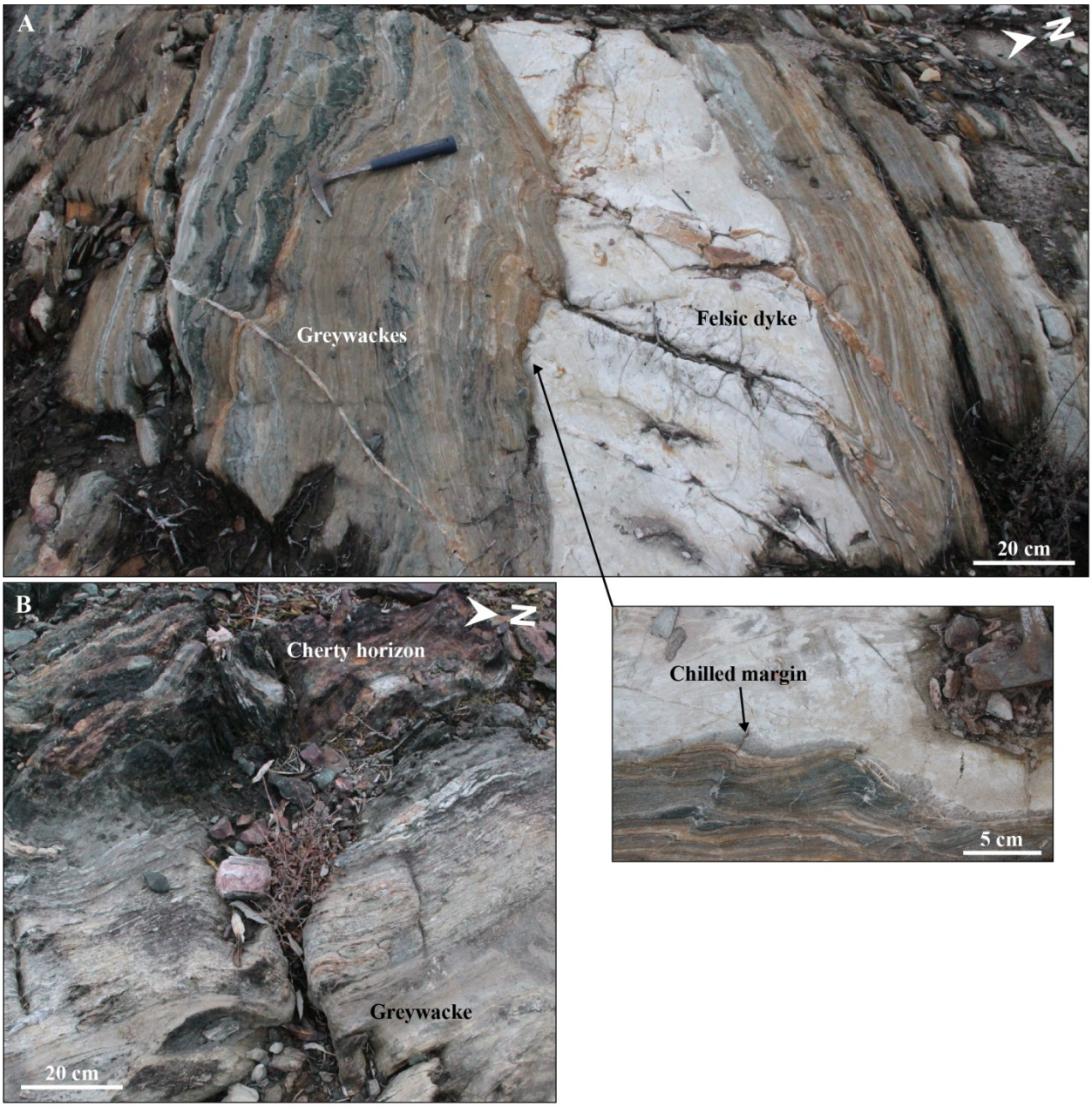

Figure 3-41: Sedimentary rocks of the Zeemel assemblage SE from Graff Lake (exposure near UTM 684285/5826621). A. Fine-grained, thinly bedded sedimentary rock cut by a felsic dyke. Inset: close-up photography of the dyke's chilled margin. Asymmetric folds are related to D_3 deformation (chapter 5). B. Cherty, fine-grained, clastic sedimentary rock intercalated in medium-grained, greywacke-type sedimentary rock.

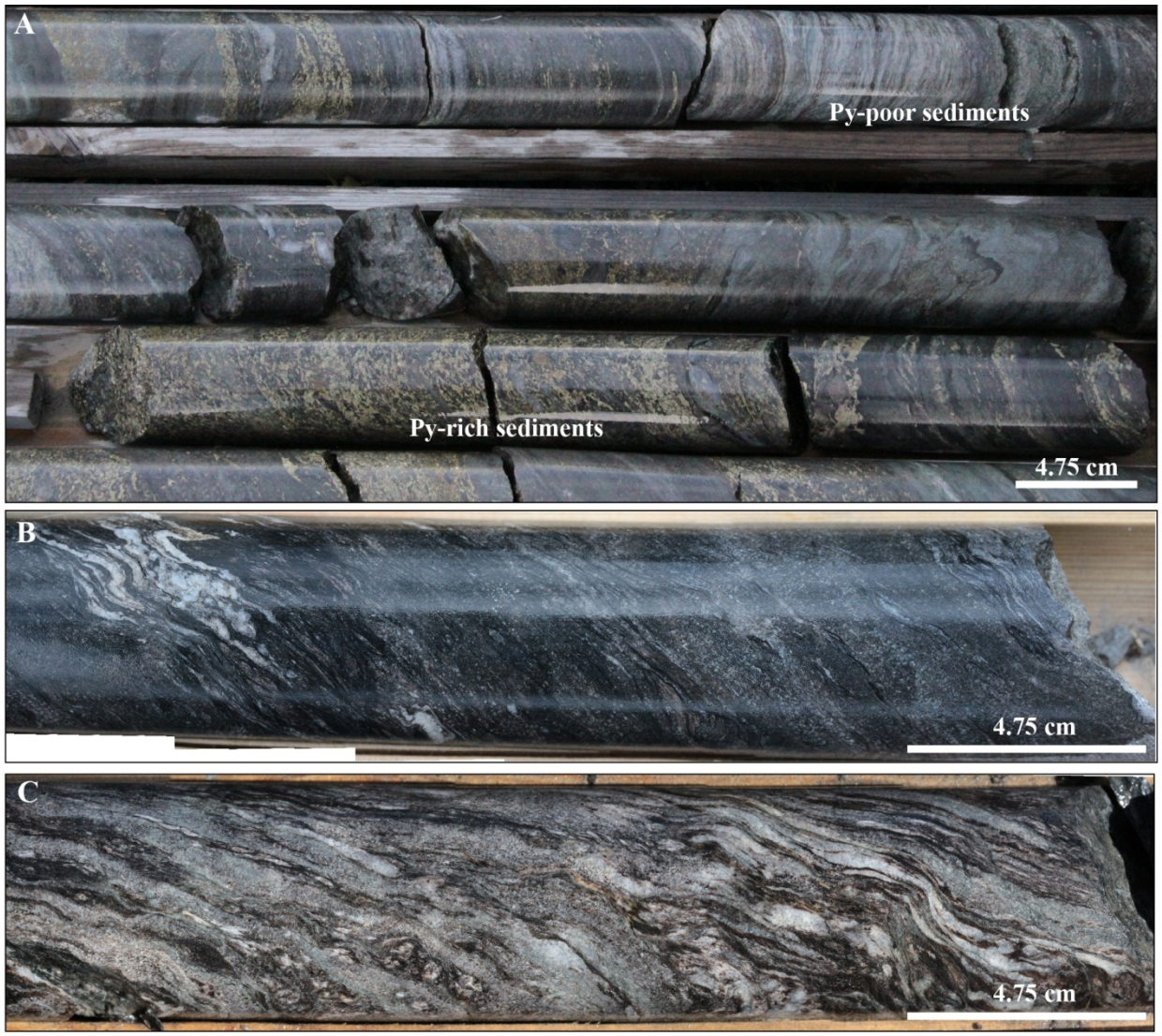

Figure 3-42: Rock units of the Zeemel assemblage in the mine area. A. Drill core segments from DDH 05-PQE-110 (ca. 140 m) of a strongly foliated, Py-poor and Py-rich sedimentary rock. B. Drill core segment from 11-282-003 (@242.3 m) of a strongly sheared quartz-feldspar-biotite sedimentary rock. C. Drill core segment from 11-282-003 (@701.2 m) of a strongly sheared quartz-feldspar-biotite sedimentary rock. Note the mineral segregation and mylonitic texture of quartz-rich bands.

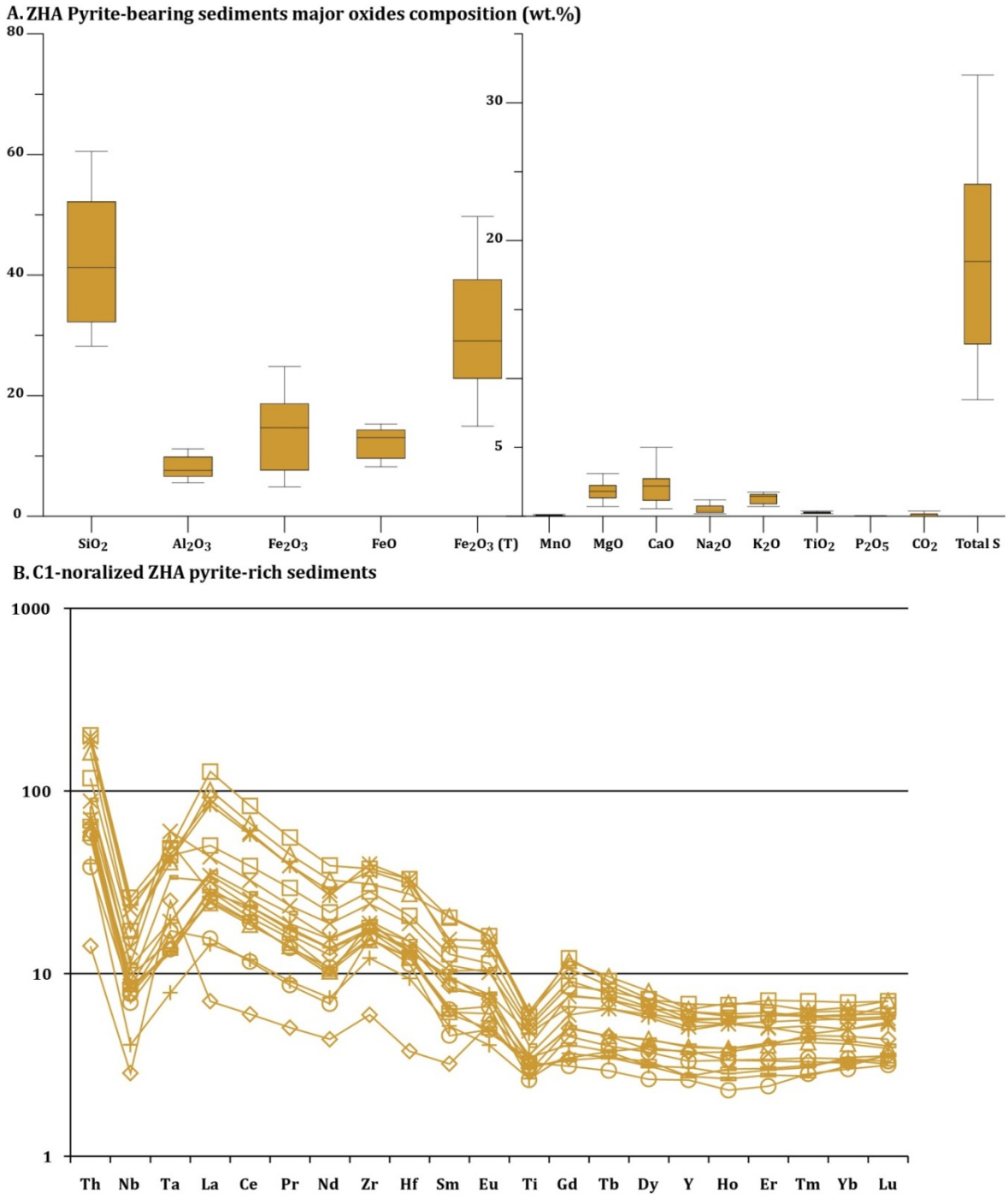

Figure 3-43: ZHA Pyrite-bearing sedimentary rocks - A. Box plot of major oxides composition, 14 samples. Box = first to third quartile, black line = median, whiskers = interquartile range (IQR)*1.5 (Upton and Cook, 1996). B. Extended REE profiles of ZHA pyrite-bearing sedimentary rock samples normalized to the C1 chondrite standard (Sun and McDonough, 1995).

3.16.1.2 Zeemel assemblage distant from the OMA

A large portion of the Zeemel clastic assemblage includes thick sequences of coarse- to medium-grained, quartz-rich detrital rocks, such as sedimentary breccias and sandstones. The former mainly consist of poorly-sorted, polymictic to monomictic breccias with strongly angular to well-rounded clasts and variable clast-to-matrix ratios (Figure 3-44). The latter include numerous polymictic conglomeratic beds with greenstone and iron formation clasts, interlayered with more homogeneous cross-bedded sandstones that are several tens of metres in thickness (Figure 3-45B). The complexity and protracted history of sedimentation and deformation is highlighted by an exposure of poorly-sorted breccias unconformably overlying greywackes (Figure 3-46). The latter displays a penetrative, NW-SE-trending early fabric that is overprinted by a younger NE-SW fabric that also affects the sedimentary breccias.

3.16.1.3 Felsic units

The Zeemel assemblage includes foliated massive, dacitic to rhyolitic rocks occurring along the northern shore of Zeemel Lake (Figures 3-39, 3-47A) and west of the Pipestone River (near UTM 688285/5825202; Figure 3-47B), where massive quartz-feldspar phyric felsic rocks are interlayered with a monogenic, clast-supported felsic breccia. This package, which is tentatively interpreted as a rhyolite dome, was sampled for U-Pb geochronological analysis (chapter 4). It is plausible that this package is temporally correlated to the felsic rocks exposed along the northern shore of Zeemel Lake. Extrusive volcanic rocks also include a coarse-grained, matrix-supported fragmental unit documented SE of Graff Lake (near UTM 684285/5826621). There, and further to the south-east (UTM 686415/5826228), sedimentary rocks are intruded by felsic dykes (Figure 3-41A). Chilled margins and sharp contacts suggest sediments were already consolidated during emplacement of the dykes. These are apparently unaffected by an older fabric present in the sedimentary host rocks (chapter 5).

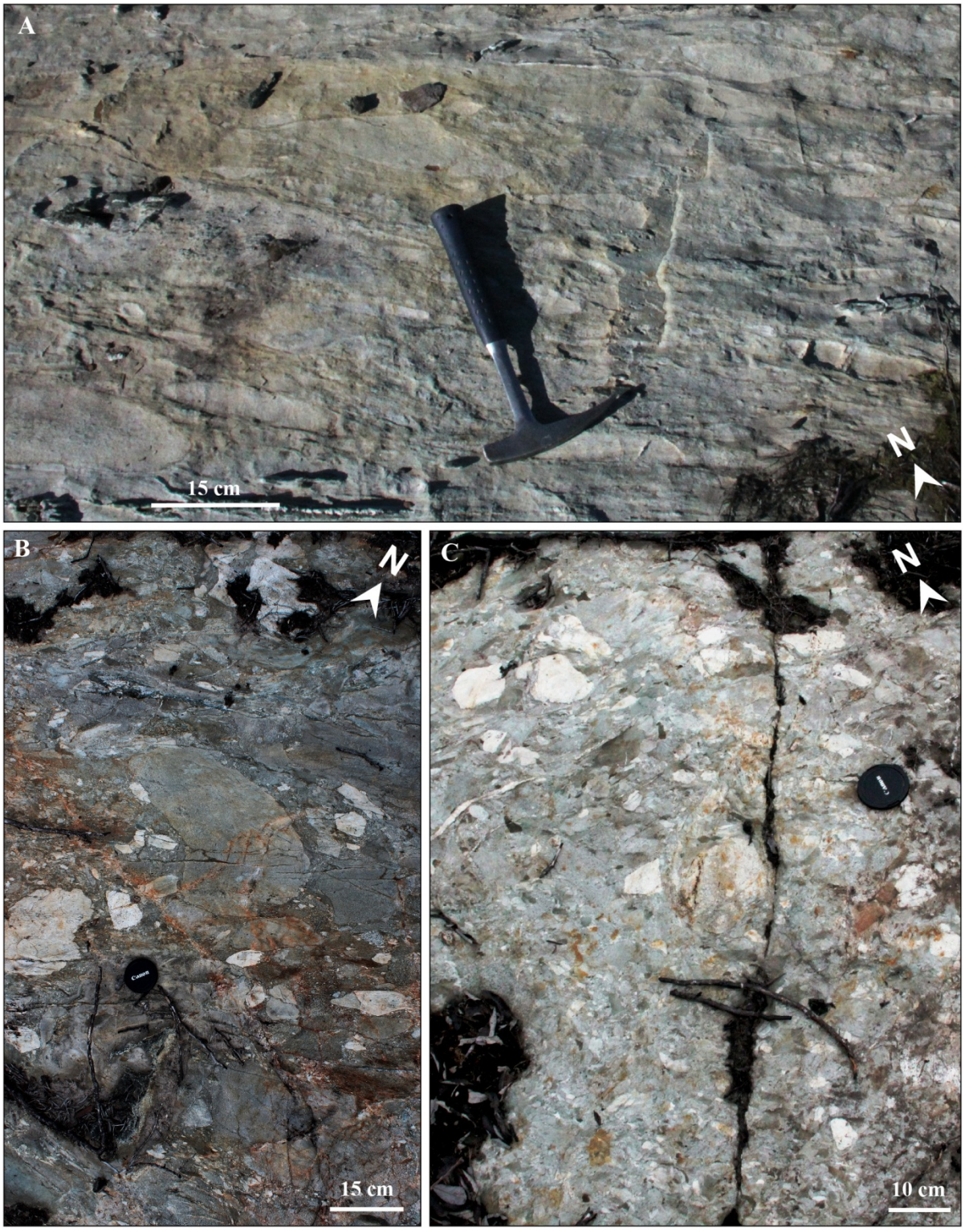

Figure 3-44: Breccias of the Zeemel assemblage. A. Exposures of poorly-sorted, matrix-supported, monogenic breccia exposed SE of Graff Lake, near UTM 686415/5826228. B. and C. Exposures of poorly-sorted polymictic sedimentary breccias near UTM 688000/5824500.

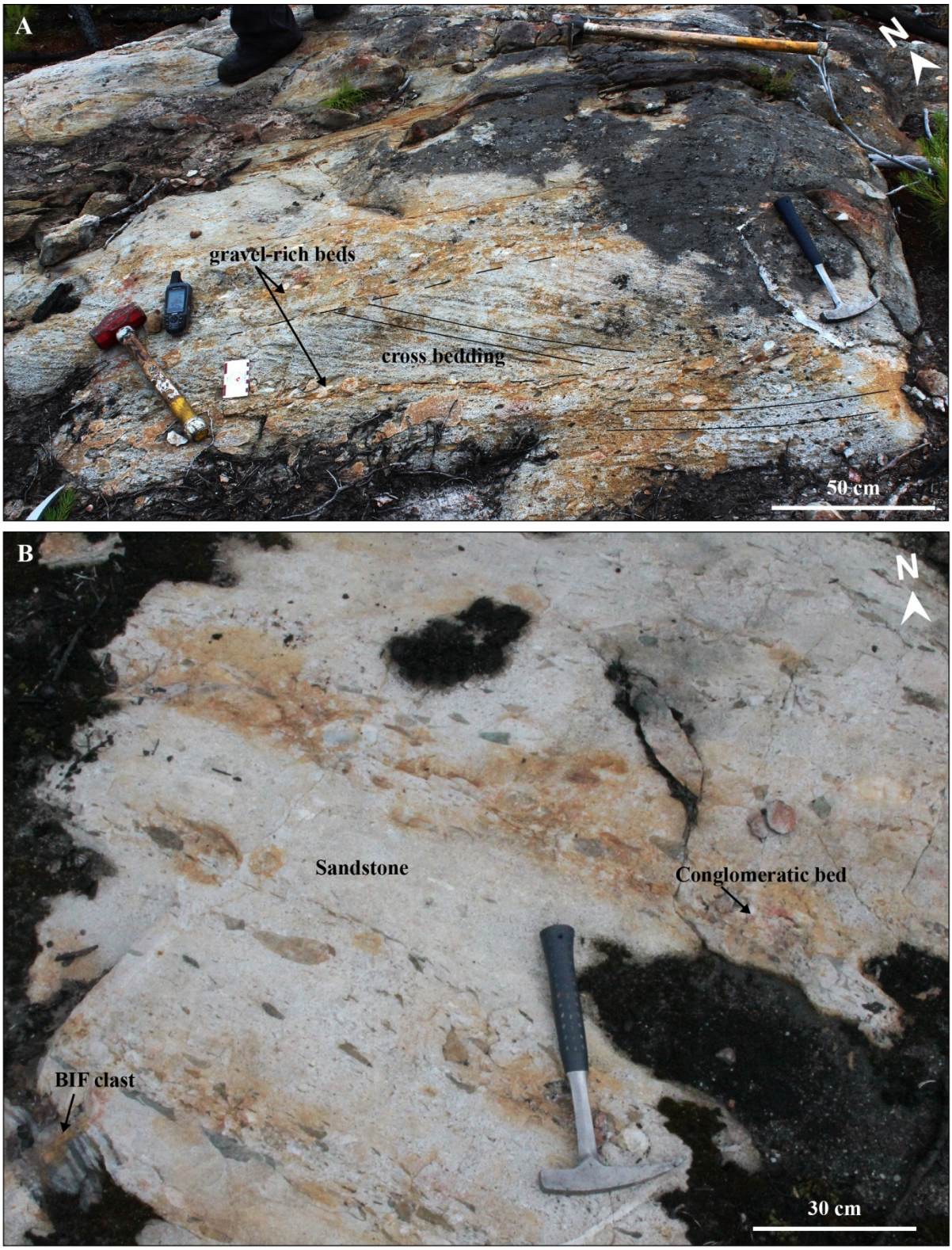

Figure 3-45: Sandstones of the Zeemel assemblage. A. Conglomeratic cross-bedded sandstone exposed west of the Pipestone River (near UTM 688000/5824500). B. Conglomeratic sandstone with mafic and iron formation clasts exposed east of the Pipestone River and north of Markop Lake (near UTM 691490/5823520).

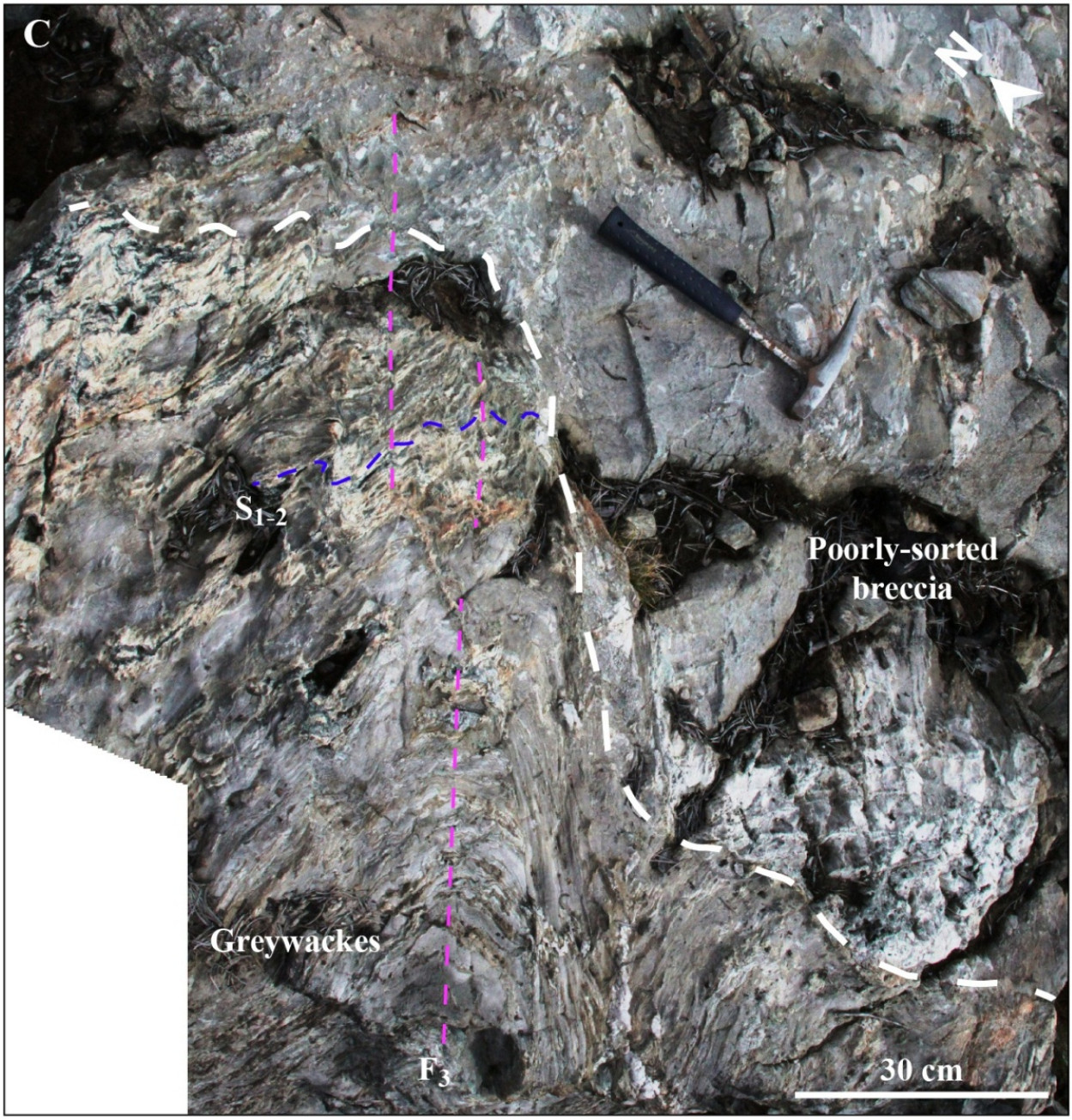

Figure 3-46: Unconformity within the Zeemel assemblage. Greywackes with a penetrative, NW-SE-trending fabric overprinted by a NE-SW fabric and folds are apparently overlain by moderately deformed, poorly-sorted sedimentary breccia, near UTM 688000/5824500.

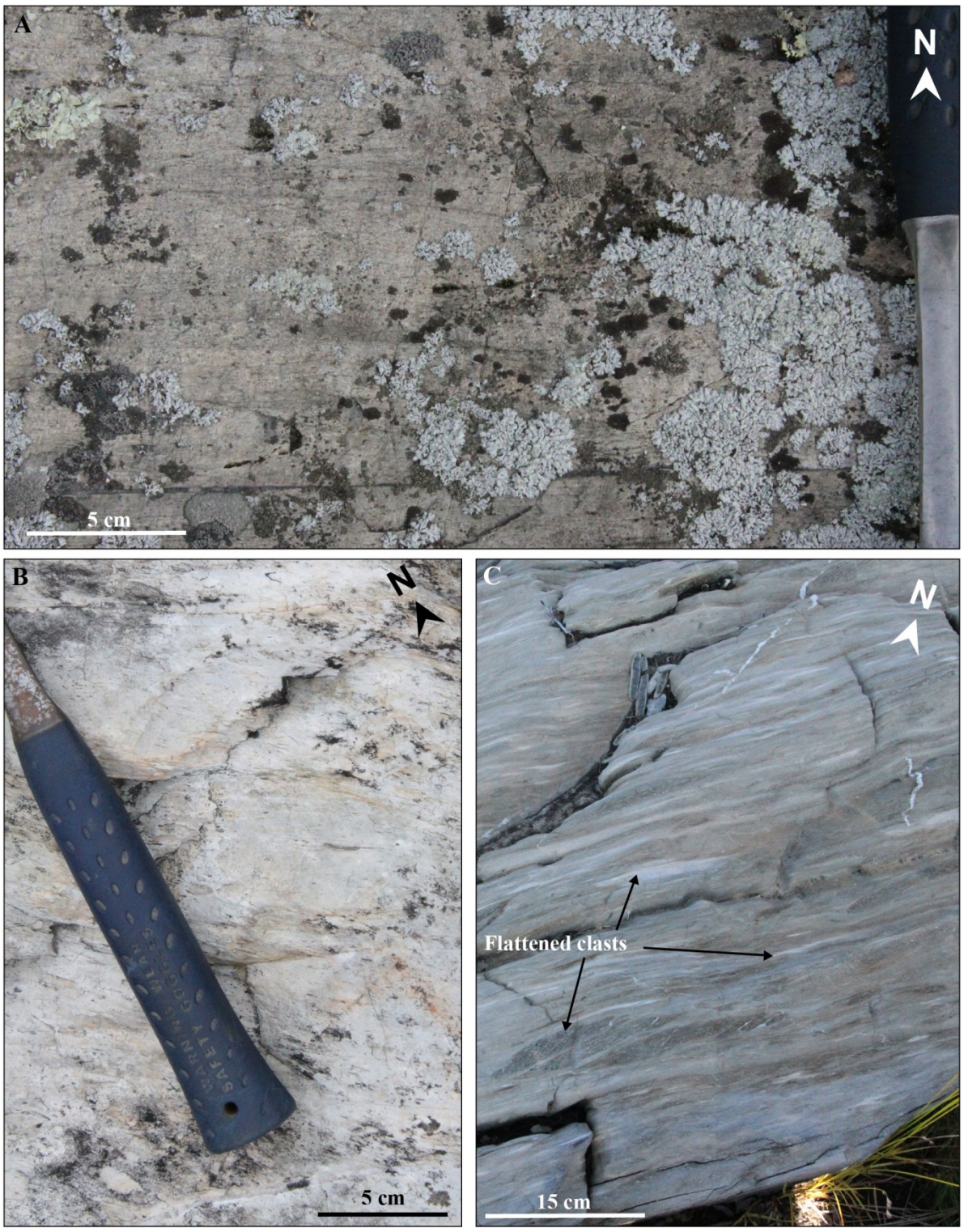

Figure 3-47: Zeemel felsic rocks. A. Well-foliated, massive felsic rock exposed on the northern shore of Zeemel Lake (near UTM 678742/5829553). B. Well-foliated, massive felsic rock (near UTM 688285/5825202). C. Highly flattened, matrix-supported, coarse-grained fragmental felsic rock exposed SE of Graff Lake (684285/5826621).

3.16.2 Heaton assemblage

Only a few localities were visited east of the Markop Lake Shear Zone (Figure 3-39). They are all located a few hundreds of metres south of the Totogan Shear Zone. There, rocks of the Heaton assemblage are highly strained and consist of moderately to strongly foliated schists (Figure 3-48) comprising a fine-, locally medium-grained matrix of quartz-feldspar-biotite ± muscovite with rare garnet porphyroblasts. Other workers have reported metasedimentary rocks with inferred protoliths such as sandstone, wacke and psammite (Duff, 2014; Bath, 2014, unpublished; Bath et al., 2015).

Figure 3-48: Clastic rocks of the Heaton assemblage A. quartz-feldspar-mica schist with strong, E-W fabric, near UTM 704841/5821210. B. quartz-rich sedimentary rock with strong, E-W fabric, near UTM 709034/5821300.

4 U-PB GEOCHRONOLOGY

The U-Pb geochronological analysis of zircon is a powerful tool to improve timing constraints on geological events, such as phases of intrusive/extrusive magmatism, sedimentation and metamorphism (Parrish and Noble, 2003). Geochronological studies have defined the age of the main assemblages of the North Caribou greenstone belt (2; Davis and Stott, 2001; Biczok et al., 2012; Duff, 2014; McNicoll et al., 2016), yet uncertainties remained concerning the age and stratigraphy of the South Rim assemblage and Opapimiskan-Markop assemblage, but also of the Zeemel-Heaton assemblage, part of which have been dated as young as 2681 Ma (U-Pb zircon data; Duff, 2014).

To improve our knowledge of the stratigraphy of the North Caribou greenstone belt and the chronology of events in the Musselwhite mine area, a series of rock samples were selected for U-Pb geochronology of zircon. Sampled localities and rocks types were selected based on previous reports (Breaks et al., 2001, and reference therein), suggestions from Goldcorp's Musselwhite mine and exploration staff and questions raised in the course of this study. Some of the data have been published in McNicoll et al. (2016), along with detailed sample and analytical descriptions.

This chapter provides a description of the samples selected, the results and their interpretation (Figure 4-1; Table 4-1). Most analyses used the Isotope Dilution Thermally Ionization Mass Spectrometry (ID-TIMS) technique, except for two sedimentary samples analysed by Sensitive High Resolution Ion Microprobe (SHRIMP II). The analytical procedures and methodology are presented in chapter 1 (section 1.2.7). Samples were taken from of the Opapimiskan-Markop assemblage (OMA) in the immediate mine area, but also from the South Rim assemblage (SRA) and Zeemel-Heaton assemblage (ZHA). The significance and implications of these results on the timing of events in the Musselwhite deposit area and on the geological evolution of the NCG are discussed in chapter 10.

4.1 South Rim assemblage

4.1.1 Felsic volcanic rock – western Opapimiskan Lake area

A rhyolite (z10531) was sampled from the SRA at a locality situated 1 km west of Opapimiskan Lake and 200 m east of the contact with North Caribou pluton (Figure 4-1). This locality has been studied by Smyk (2013). The 3 m thick rhyolitic unit is interlayered with a series of fine-grained clastic rocks, which are surrounded and intruded by mafic plutonic rocks (Smyk, 2013). The sample consists of very fine-grained, white-weathered, moderately- to strongly-foliated rhyolite. Four zircon grains were analyzed and yielded

a weighted average $^{207}Pb/^{206}Pb$ age of 3053.2 ± 0.8 Ma (MSWD= 0.92), which is interpreted as the crystallization age of the rhyolite (McNicoll et al., 2016).

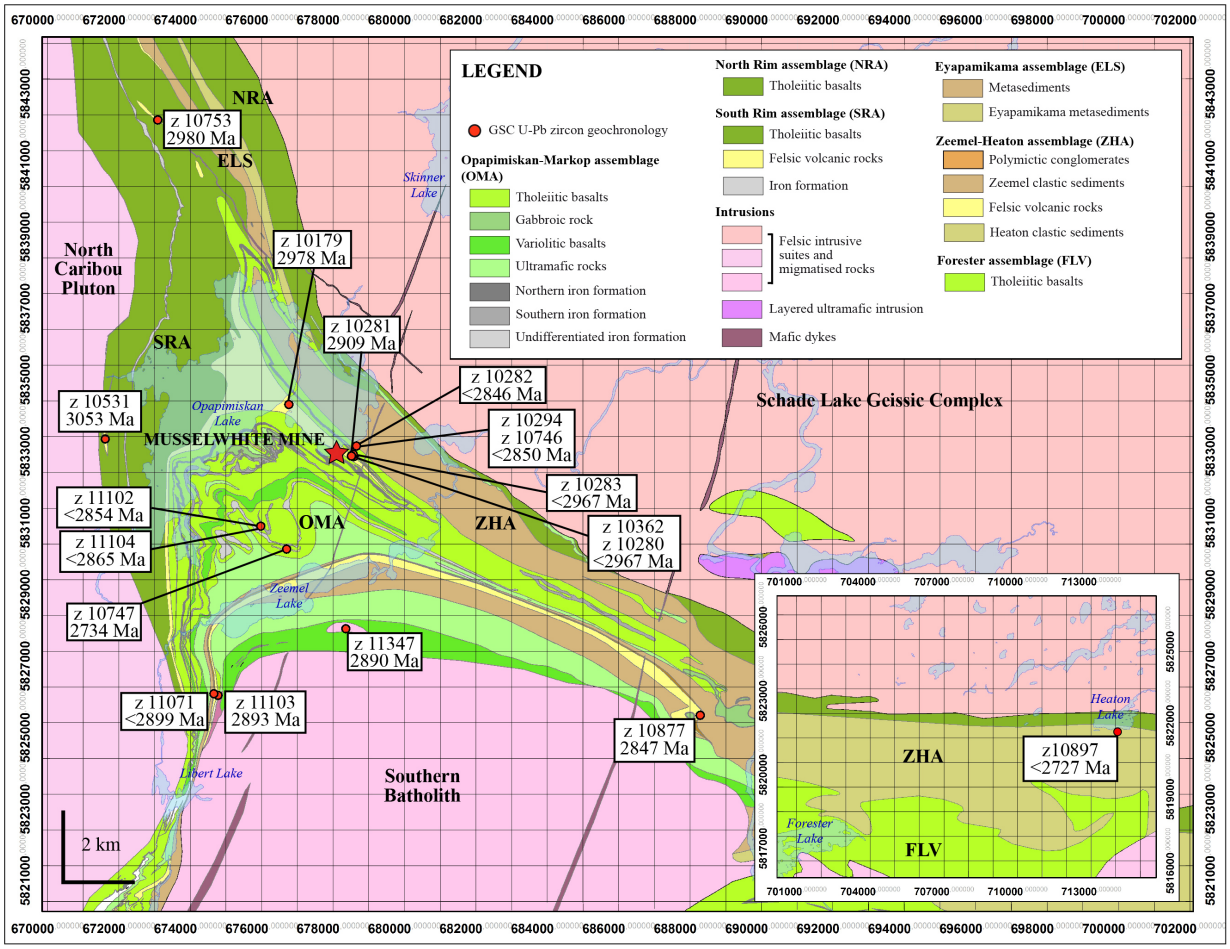

Figure 4-1: Location and results of U-Pb zircon geochronological data from this study (including data from McNicoll et al., 2016). The inset shows the easternmost portion of the NCG, 30 km east of the area covered by the main map.

4.1.2 Felsic volcanic rock – northern Opapimiskan Lake area

A felsic rock (z10753) of the SRA was collected from a lakeshore exposure, roughly 5 km NNW of Opapimiskan Lake (Figure 4-1). The unit is a 7 to 10 m-wide, fine-grained, foliated dacitic to rhyodacitic rock with quartz eyes and disseminated biotite in sharp, foliation-parallel, contacts with basaltic rocks. Five zircon grains were analyzed and gave a weighted average $^{207}Pb/^{206}Pb$ age of 2980 Ma, which is interpreted as the crystallization age of the unit.

Table 4-1: Summary of U-Pb zircon geochronological samples and results from this study.

Sample #	UTM NAD83 Zone 15	Assem-blage	Lithology	Interpreted age (Ma)	Analytical technique	Reference
z 10531	671619 E 5832928 N	SRA	Rhyolite	3053	ID-TIMS	McNicoll et al., 2016
z 10753	673094 E 5841848 N	SRA	Intermediate volcanic rocks	2980	ID-TIMS	this thesis
z 10279	678520 E 5832451 N	SRA	Unit Avol - Rhyodacite	2978	ID-TIMS	McNicoll et al., 2016
z 10283	678567 E 5832497 N	OMA	Unit 4F - Gt-Bt schist	< 2967	ID-TIMS	McNicoll et al., 2016
z 10362 z 10280	678585 E 5832438 N	OMA	Unit 6 - Qz-Fsp schist	< 2967	ID-TIMS	McNicoll et al., 2016
z 10281	676662 E 5832943 N	OMA	Felsic dyke	2909	ID-TIMS	McNicoll et al., 2016
z 11347	678360 E 5827618 N	OMA	Feldspar porphyry	2890	ID-TIMS	this study, to be published
z 11104	675978 E 5830489 N	OMA	felsic igneous rock	≤ 2865	ID-TIMS	this study, to be published
z 11102	675978E 5830489 N	OMA	felsic igneous rock	≤ 2854	ID-TIMS	this study, to be published
z 10747	676703 E 5829850 N	OMA	Qz-Fdp-phyric rhyolite	2734	ID-TIMS	this study, to be published
z 11071	674777 E 5825760 N	ZHA	Polymictic conglomerate	< 2899	SHRIMP II	this study, to be published
z 11103	674662 E 5825807 N	ZHA	Feldspar porphyry	2893	ID-TIMS	this study, to be published
z 10294 z 10746	678659 E 5832731 N	ZHA	Mine sed tuff	< 2850	ID-TIMS	McNicoll et al., 2016
z 10877	688285 E 5825202 N	ZHA	Rhyolite	2847	ID-TIMS	this study, to be published
z 10282	678659 E 5832731 N	ZHA	Bt-Qz-Fdp sediments	< 2846	ID-TIMS	McNicoll et al., 2016
z 10897	* 307004 E 5820416 N	ZHA	Felsic volcanicastic rock	≤ 2727	ID-TIMS & SHRIMP II	this study, to be published

* Sample location in UTM NAD83 Zone 16

4.1.3 Unit "Avol" – Musselwhite mine area

A sample of unit Avol (z10279), part of the SRA, was collected from a drill hole on section 9500 N, and structurally located in the core of the East Bay synform (Figure 4-1). The rock consists of a moderately foliated, light grey, fine-grained, feldspar-phyric, felsic ash tuff. It contained small (50–100 μm), euhedral, and prismatic zircon grains. Analyses define a single population and a linear regression including all of the analyses has a lower intercept at 577 Ma and an upper intercept at 2978.7±1.0 Ma (MSWD= 1.4). The latter data is interpreted as the crystallization age of the tuff (McNicoll et al., 2016).

4.2 Opapimiskan-Markop assemblage

4.2.1 Unit 4F and 6 – Musselwhite mine area

In the NIF sequence, unit 6 (quartz-feldspar-biotite schist) is interlayered with unit 4F (garnet-biotite±staurolite schist) with sharp or gradational contacts (Biczok et al., 2012). Samples of both lithologies were selected from drill hole 05-PQU-44, which cuts the eastern limb of the East Bay synform (z10380, z10362, z10283; Figure 4-1). All samples contained pale brown to colourless, euhedral, stubby prismatic to elongate zircon grains. Analyses from both units reveal the presence of >3 Ga inherited grains and produces clusters of points at ca. 2980 Ma, possibly reflecting inheritance from eroded felsic volcanic rocks of the SRA. The youngest population of concordant to near-concordant data of both samples reach an age of 2967 Ma. The ages of the garnet-biotite schist (unit 4F) and quartz-feldspar-biotite schist (unit 6) from the base of the NIF sequence are thus both constrained to be <2967 Ma (McNicoll et al., 2016). This is younger than the structurally overlying unit Avol, and the SRA.

4.2.2 Felsic dyke – Musselwhite mine area

A felsic dyke (z10281) was sampled from drill hole 10-SIF-002, structurally located in the hinge zone of the East Bay synform (Figure 4-1). This dyke cuts the NIF, as well as the structurally underlying "Basement basalts", SIF, and "Lower basalts" units (Figure 3-2). The sample consists of a white, fine- to medium-grained, feldspar-phyric, moderately foliated felsic rock. Analysed 100–150 μm-long zircon grains were mainly euhedral, stubby prismatic to prismatic crystals and yielded a single age population with no evidence of inheritance. The weighted average of the $^{207}Pb/^{206}Pb$ ages is 2909.4 ± 0.7Ma (MSWD= 0.88), which is interpreted to represent the crystallization age of the dyke (McNicoll et al., 2016).

4.2.3 Feldspar porphyry – Zeemel-Libertt lakes area

A felsic rock was sampled SSW of the mine area, between Zeemel Lake and Libertt Lake (Figure 4-1). The sample (z11103) consists in a foliated porphyritic unit comprising 30 vol.% feldspar phenocrysts within a quartz-sericite matrix. Data from five analyses shows no evidence of inheritance. Four are near-concordant to concordant and a single one is discordant. The weighted average of the $^{207}Pb/^{206}Pb$ ages is 2893 ±0.6 Ma, which is interpreted to represent the crystallization age of the unit.

4.2.4 Feldspar porphyry – southern Zeemel lake area,

The mafic volcanic rocks occurring along the northern margin of the Southern Batholith are interpreted to be part of the OMA (Figure 4-1). This package also comprises thick interlayers of felsic rock, which was sampled for analysis (z11347). The sample consists of a foliated porphyritic rock made of a quartz-sericite matrix with 30 vol.% feldspar phenocrysts. The four analysed zircon grains yielded near-concordant results, with a weighted average of $^{207}Pb/^{206}Pb$ ages of 2890 Ma. This data is interpreted as the crystallization age of this unit, which may represent a sub-volcanic intrusion within the OMA.

4.2.5 Felsic rocks – Wilberforce zone

The Wilberforce zone is central to the West antiform area, NW of Zeemel Lake (Figure 4-1). A series of drill holes that targeted aeromagnetic anomalies have intercepted felsic rocks interlayered with BIFs, argillites, and Py-Po massive sulphides (Guest, 2013).

Sample z11102 was taken in DDH 12-WIL-001, from 152.5 to 155.5 m. It consists in a fine-grained, medium grey felsic volcanic unit, with local biotite and sulphide alteration. Contacts with adjacent units are moderately to strongly sheared. Data from sample z11102 shows multiple concordant to near-concordant points. The age of the youngest grain is ≤2854 Ma with inherited grain populations at ca. 2970 and 2865 Ma.

A second sample (z11104) was taken from 21.5-23.0 m and 24.3-27.2 m. It consists in light - medium grey, homogeneous felsic volcanic with blue quartz eyes. Data from sample z11104 shows similar distribution with the youngest age population of ca. ≤2865 Ma and inherited grains of ca. 2982, 2910 and 2900 Ma.

In DDH 01-010, sample z10747 was taken from 70.3-70.7 m, 75.1-76.2 m, and 76.2-77.6 m. It consists in a medium grey, quartz-feldspar phyric rock with 1% quartz and 2% feldspar phenocrysts, and disseminated sericite on foliation planes. Quartz eyes and feldspar phenocrysts are homogeneously distributed and contacts with adjacent units are sharp, suggesting that this unit as a felsic intrusion. Data from sample z10747 yields a single cluster of points at ca. 2734 Ma, which represents a much younger age than the aforementioned Wilberforce samples.

4.3 Zeemel-Heaton assemblage

4.3.1 Conglomerate – southwestern Zeemel Lake area

A sample (z11071) of the ZHA in the SSW part of the study area, just 125 m west of the felsic unit sample z11103 (Figure 4-1), roughly 450 m from the contact with the Southern Batholith. The exposed bedrock consists of a strongly foliated, polymictic conglomerate with clast of fine-grained, homogeneous felsic rock; feldspar-phyric felsic rock; fine-grained mafic rock; medium-grained, feldspar-phyric mafic rock; BIF, and quartz fragments. The sampled material mainly consists of the matrix of the conglomerate. Results from SHRIMP II analyses of 70 zircon grains show a single peak distribution at 2899 Ma, which provides the maximum deposition age of the conglomerate.

4.3.2 "Lower Felsic Volcanics" – Musselwhite mine area

A sample (z10282) of felsic ash tuff of the ZHA was collected east of Musselwhite mine (Figure 4-1). It was collected from drill hole 05-PQU-110 in an interval located structurally below the Opapimiskan-Markop assemblage, approximately 125 m below the SIF (Figure 3-2). The light grey, fine-grained, foliated felsic ash tuff comprises colourless to light brown, stubby prismatic to elongate zircon grains ranging in length from 100 to 200 µm. Analyses yielded a cluster of concordant to near-concordant data at ca. 2982 Ma. This age may reflect inheritance from neighbouring volcanic rocks of the SRA. However, a scatter of younger zircon ages, including two concordant analyses at ca. 2870 Ma and a one at 2850 Ma, suggests that the tuff was deposited after 2850 Ma (McNicoll et al., 2016).

4.3.3 Felsic volcanic rocks – Pipestone River area

A sample (z10877) was collected from a rhyolitic unit of the ZHA from a large natural outcrop located 1.6 km west of the Pipestone River and 1100 m northeast of the Southern Batholith contact. It consists in a quartz-feldspar phyric felsic volcanic rock. Four zircon grains were analysed and yielded a single age population with no evidence of inheritance. The weighted average of all $^{207}Pb/^{206}Pb$ ages is ca. 2847 Ma, which is interpreted to represent the crystallization age of the rhyolite.

4.3.4 "Lower Sediments" – Musselwhite mine area

Two samples (z10294, z10746) of fine-grained siliciclastic sedimentary rock of the ZHA were collected east of Musselwhite mine (Figure 4-1), from the drill hole 05-PQU-110. The samples were taken structurally below rocks of the OMA, from an interval situated approximately 125 m below the SIF (Figure 3-2); they both consist of a fine-grained, biotite-quartz-feldspar sedimentary rock. Detrital zircon grains include small (50–100 μm), euhedral, stubby prismatic to prismatic crystals and grain fragments. Analyses provided ages ranging from >2880 Ma to a cluster of ca. 2846 Ma. This latter population provides the maximum age of the unit (McNicoll et al., 2016).

4.3.5 Intermediate volcaniclastic rock – Heaton Lake area

A sample (z10897) was collected from a small surface exposure, 200 m south of Heaton Lake (Figure 4-1). The sample is a strongly foliated, fine- to medium-grained intermediate volcaniclastic rock tentatively interpreted to belong to the uppermost portion of the ZHA. A probability plot of 29 zircon SHRIMP analyses yield a dominant age population around 2728 Ma and a minor one at 2830 Ma. Complementary ID-TIMS analyses confine the deposition age to <2727 Ma.

4.4 Summary and implications of data

4.4.1 Stratigraphy of the SRA

Geochronological data from this study have improved the stratigraphic framework of the SRA in the western Opapimiskan Lake area and the timing of geological events (section 3.6; Figure 4-2 and 4-3). Results show that the western part of the SRA is significantly older than the eastern part in the mine area (e.g., 3053 Ma from McNicoll et al., 2016, vs. 2980 Ma from Davis and Stott, 2001) and that a possible unconformity or structural discontinuity may be present along the western shore of Opapimiskan Lake (Figure 4-1). The 2978 Ma age data of unit Avol has been critical to interpret that the stratigraphic polarity of the SRA is inverted in the Musselwhite mine area, implicating the occurrence of a cryptic, early, megascopic folding event (cf Chapter 6; McNicoll et al., 2016).

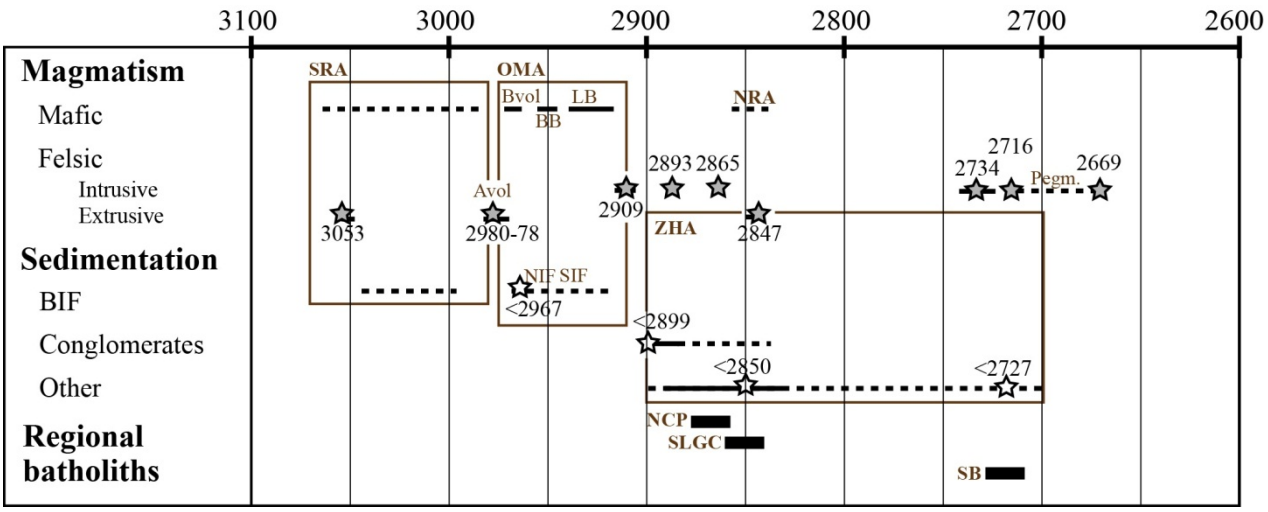

Figure 4-2: Synthetic diagram of the magmatic and sedimentary evolution of the NCB in the Opapimiskan Lake area. Geochronological data (in Ma) is from Biczok et al. (2012), McNicoll et al. (2016), and this study. Dash line: tentative constraints.

4.4.2 Stratigraphy of the OMA

The stratigraphic polarity of the OMA in the immediate mine area is interpreted to be SE- and downward-younging (Oswald et al., 2015b; McNicoll et al., 2016). Most of the OMA was deposited between 2978 Ma and 2909 Ma, as constrained by the age of unit Avol (section 4.1.3), data from unit 4F and unit 6 at <2967 Ma (section 4.2.1), and of the felsic dyke that cuts the units (section 4.2.2; Figure 4-2).

Unit Bvol was deposited prior to 2967 Ma, as constrained by unit 6 and unit 4F. The interval of pyrrhotite-rich meta-argillite (4H unit), documented in drill cores at the contact between units Avol and Bvol, represents a period of slow, fine-grained, clastic sedimentation, and suggests a period of volcanic quiescence, which could have lasted up to 11 Ma.

The age constraints of the OMA sequence cover the various inherited population observed in the data from the Wilberforce samples, which have yielded zircon ages at least 44 to 55 Ma and 175 Ma younger than their host sequence. Although the nature of the lithological contacts between the OMA and Wilberforce units is not systematically well-defined, Wilberforce felsic rocks are interpreted to be intrusive. The youngest zircon ages are thought to date the crystallization age of these intrusive units. The 2890 Ma and 2893 Ma feldspar-phyric units located south-west and south of Zeemel Lake, respectively, intrude units of the OMA.

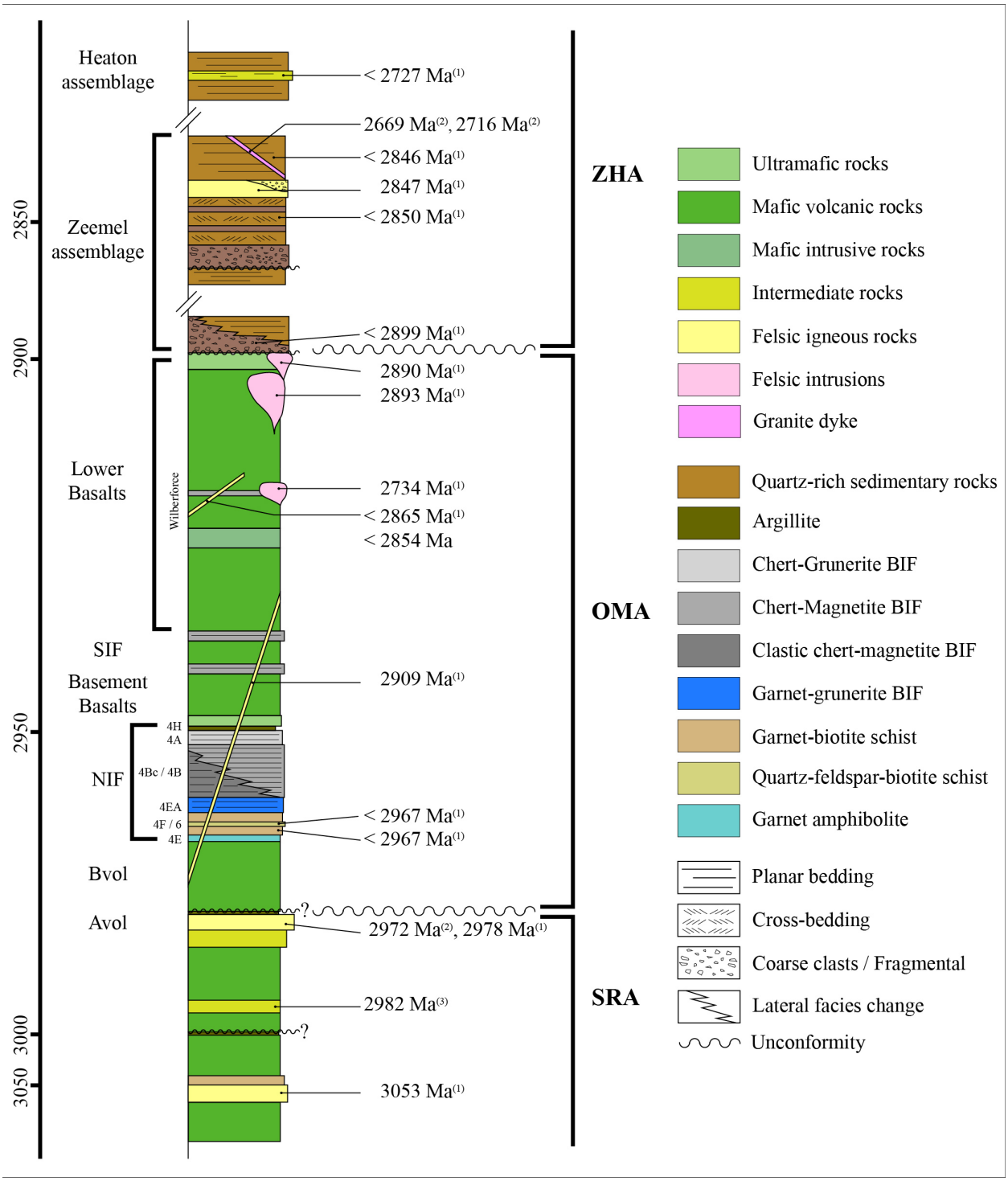

Figure 4-3: Synthetic lithological column of the NCG in the study area (not to scale; idealized stratigraphic relationships). Geochronological data from (1) this study, McNicoll et al. (2016); (2) Biczok et al. (2012); and (3) Davis and Stott (2001).

4.4.3 Stratigraphy of the ZHA

Geochronological data complements geological mapping (chapter 3) and exemplify the complex and prolonged history of the Zeemel-Heaton assemblage. In the Paseminan River area, conglomerates show that clastic sedimentation started as early as 2899 Ma. The greywacke overlying ultramafic rocks of the OMA, SE of Graff Lake, may represent a distal equivalent of these conglomerates (Figure 3-22). It is possible that clastic sedimentation of the ZHA was sourced by products of ca. 2890 Ma and ca. 2860 Ma volcanism, as suggested by the dated intrusive units of Zeemel Lake and in the Wilberforce area. The massive rhyolite and tuffs dated at 2847 Ma attest for felsic volcanism during the deposition of the ZHA. The unconformity documented west of the Pipestone River (chapter 3) and the <2727 Ma intermediate volcaniclastic rock of the Heaton Lake area (and data from Duff, 2014, and Bath et al., 2015) indicate that the ZHA comprises at least two cycles of sedimentation.

5 STRUCTURAL GEOLOGY

5.1 Introduction

The distribution and geometry of rock units in the Opapimiskan Lake area is the result of three major deformation phases (e.g., Breaks et al., 2001; Hall and Rigg, 1986; 2). The associated metamorphism has reached amphibolite facies (6), which has affected the rheology of lithologies and influenced their responses to strain. In the context of gold deposits in Archean greenstone belts, it is essential to understand the structural setting of the host rocks in order to establish the chronology of the gold mineralization relative to the different generations of structures.

This chapter presents the analysis of structural data gathered through sub-regional-scale and detailed trench-scale surface mapping, as well as from underground face mapping and drill core description. In the Musselwhite mine area, three structural domains are distinguished on the basis of the intensity of D_2 deformation and position relative to major F_2 folds (Figure 5-1):

- Mine area (MASD),
- West antiform (WASD),
- South West Zone (SWSD).

The MASD corresponds to the East Bay synform (3; Figure 3-2) and comprises rocks showing the strongest D_2 strain intensity and transposition. The WASD covers the hinge zone of a regional-scale F_2 fold, where D_2 strain is moderate and D_1 structures are preserved. Last, the SWSD includes the western limb of the West Antiform where, according to previous studies (Breaks et al., 2001), D_1 and D_2 structures are mainly coplanar.

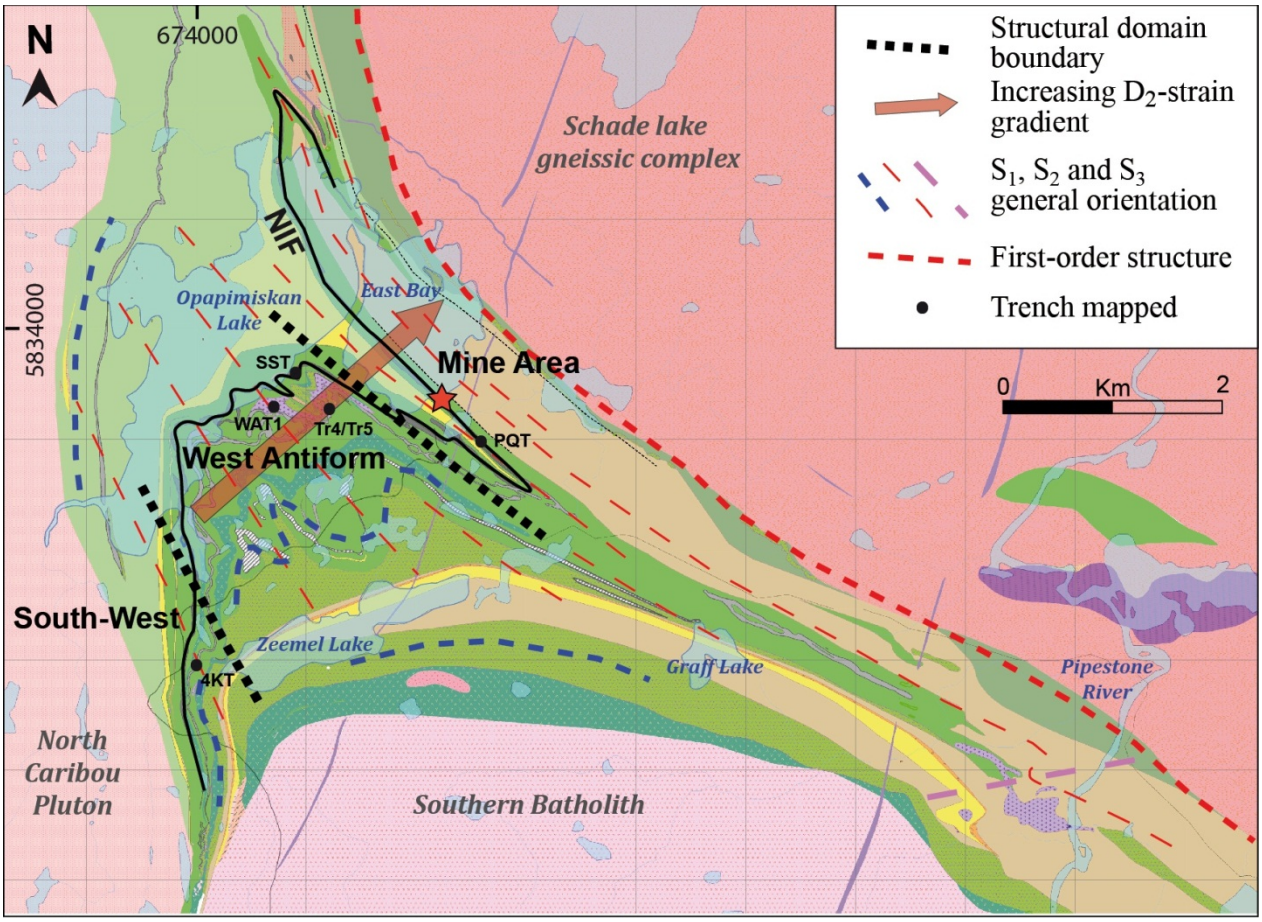

Figure 5-1: Structural domains of the Opapimiskan Lake area and general orientation of the S_1, S_2, and S_3 fabrics (chapter 2; Breaks et al., 2001; Goldcorp Inc.; Smyk, 2013) and trenches. Refer to Figure 3-1 for geological map legend.

5.1.1 Replication of structural patterns at various scales

Similar structural patterns are commonly present at various scales (i.e., self-similarity) a property that is the basis for analogic modeling (Fossen, 2010). Such phenomenon can prove to be a useful tool for geological interpretations. In the study area, the sub-regional-scale pattern reproduces outcrop-scale fold pattern (Figure 5-2A, B), and mine geology sections display structures that are also present in grab samples (Figure 5-2C, D).

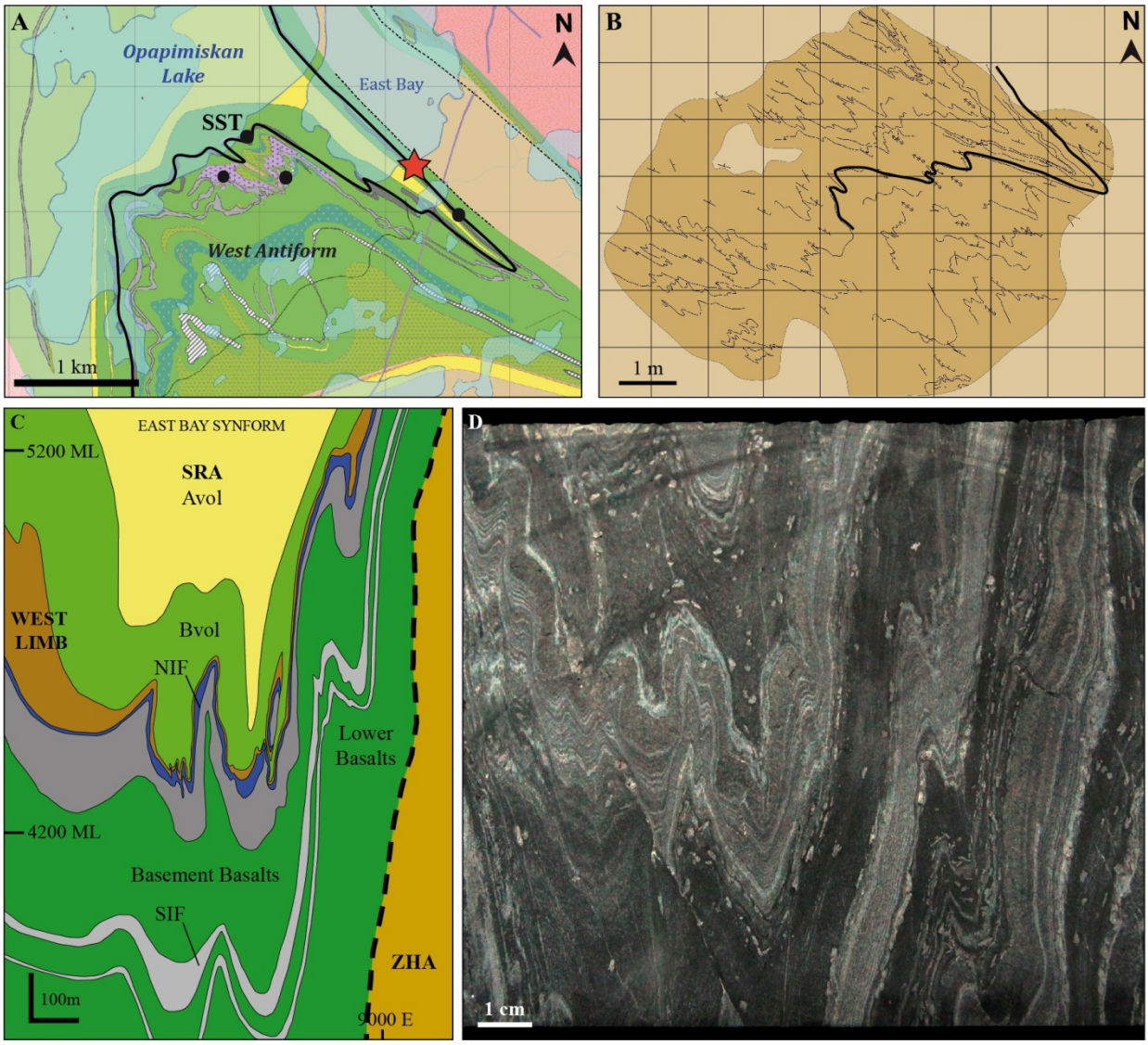

Figure 5-2: A. Geological map of the Opapimiskan Lake area. Black dots are stripped outcrops mapped in detail for this study. Red star is Musselwhite mine portal location. Black line is the NIF sequence, highlighting a wide antiform and tight synform ("West antiform" and "East Bay synform"). B. Geological map of the South shore trench with outline of the compositional layering (blue lines). Bold black line highlights the antiform-synform pattern similar to A. C. Sketch of a geological section of Musselwhite mine at 11775 N. D. Slab of unit 4Bc sample from mine level 920, Moose ore zone, showing fold geometry and structures similar to C.

5.1.2 Rheology of banded iron formation

Rheology is a branch of physics that studies the deformation and the flow of matter, which in geology translates to the study of the mechanical properties of rocks and their response to external constraints applied during deformation (Fossen, 2010). The response of a rock to deformation depends on its chemical and mineralogical composition, on thermobarometric conditions, and on strain rates (Fossen,

2010). Thermobarometric conditions, in particular, influence a large number of processes involved in the occurrence of orogenic gold mineralization, such as the location of the transition between brittle and ductile deformation regimes (Colvine et al., 1988; Witt, 1993; Sibson, 2001).

In BIF, the primary chemical layering creates strong planar anisotropy and competence contrasts (sections 1.3 and 5.1.2). The contrasts arise from the various lithological facies present within the BIF and from those of the surrounding rock types of the host sequence, such as thicker and more rigid mafic volcanic rocks (chapter 3). Competence contrasts result in heterogeneous strain distribution and can produce a wide diversity of structures with varied styles and orientations (Figure 5-3A). In the study area, this specificity of BIF is illustrated in several manners: (1) structural variations including tighter folds and more penetrative fabrics than those of other adjacent rock types (Oswald et al., 2015a; Figure 5-3B); (2) intense strain partitioning may induce rotation and boudinage of some beds or other deformed elements, while surrounding beds or units show little evidence of deformation (Figure 5-3C, D); (3) sustained strain and deformation can obliterate primary bedding/features (e.g., boudinaged chert band) and older fabrics/structures (Figure 5-4A, B); and (4) heterogeneous strain partitioning can lead to the local preservation of syn-sedimentary or lithification structures (e.g., soft-sediment deformation and dewatering features; Figure 5-5). Those characteristics are important to consider for structural analysis and to establish the timing and controls on gold mineralization.

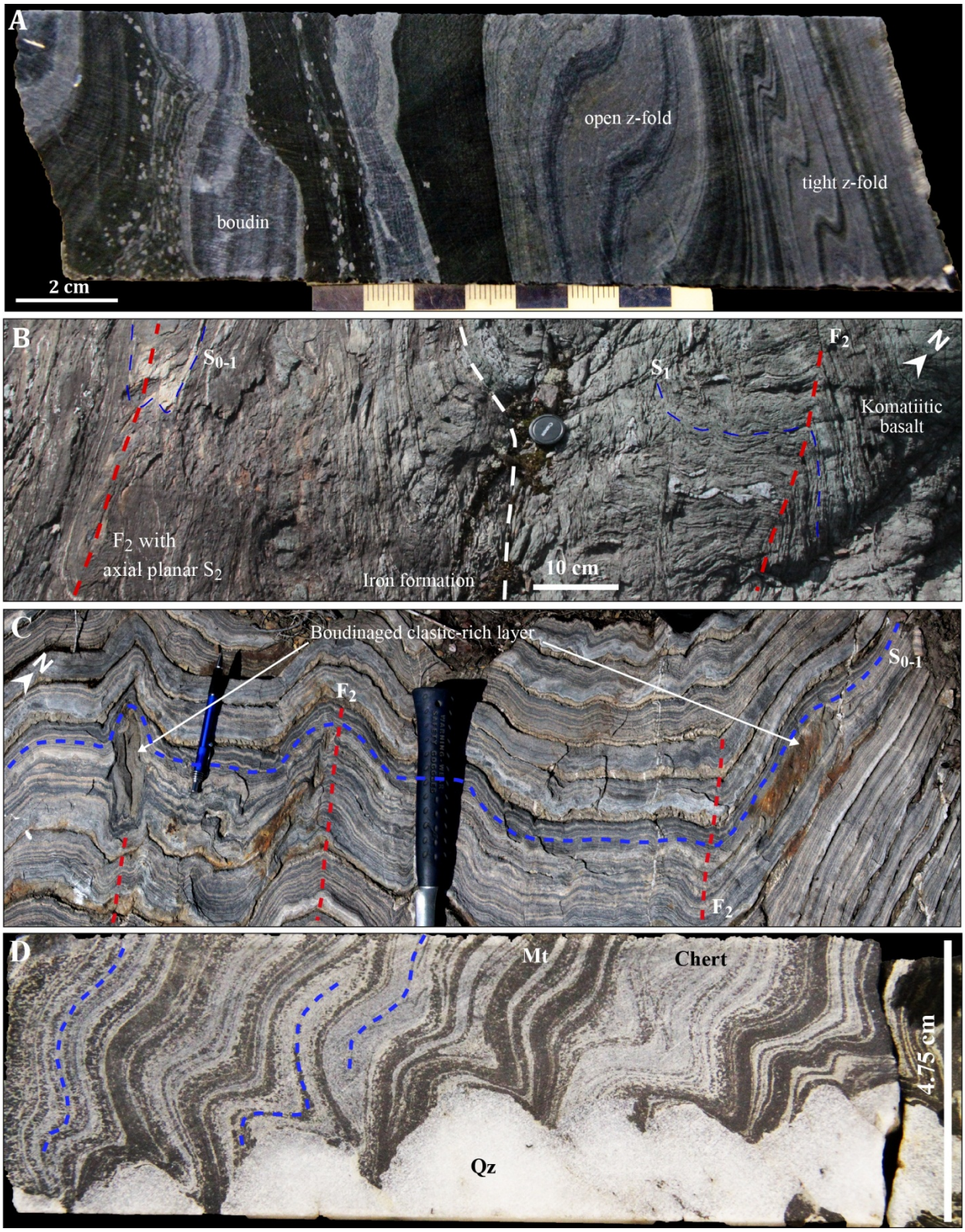

Figure 5-3: BIF rheology A. NQ drill core segment of oxide-BIF showing the diversity of deformation features (e.g., tight folds, open folds, boudins, etc.) of a highly anisotropic material with varied layer thickness. DDH: 12-BIN-001, @132.7 m, sample width is 4.76 cm. B. Contrast in deformation accommodation between BIF

and volcanic rocks, West antiform trench 1 exposure: in the former, the S_{0-1} compositional layering forms tight F_2 folds; in the latter, the S_1 foliation is affected by open, F_2 S-fold. C. Surface exposure of oxide-BIF on "Zebra trench". Red dash lines: fold axial traces, blue dash lines: compositional layering. Note the isolated boudins of a clastic-rich layer, where one has been rotated parallel to the fold axial plane. D. Drill core section of folded oxide-BIF (blue dash line: axial trace) and a crosscutting, deformed quartz vein. The BIF deforms plastically around the quartz dominoes. DDH: 03-CMP-053, @229.8 m.

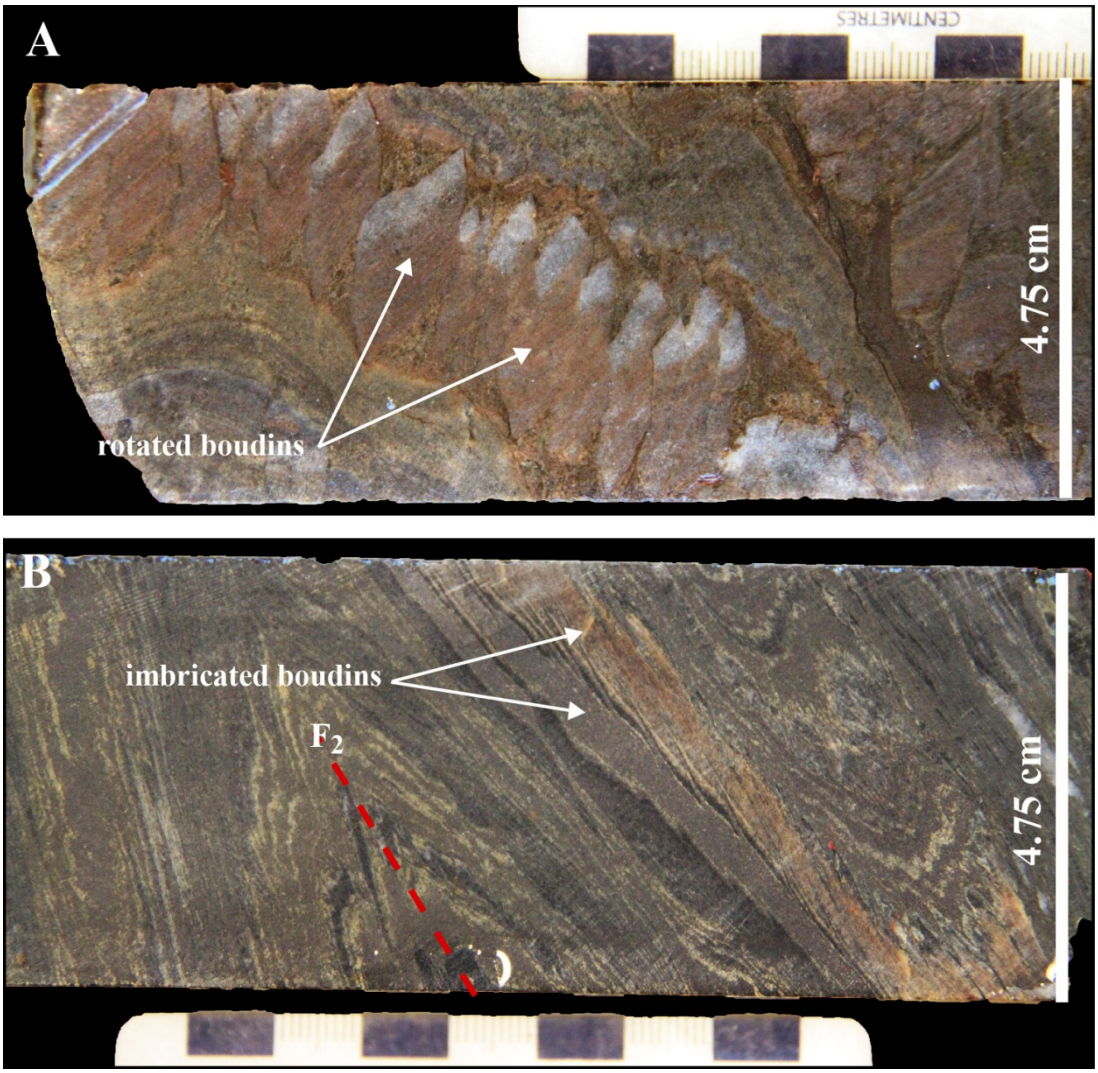

Figure 5-4: BIF rheology A. Drill core section of oxide-BIF showing strongly rotated boudins of a chert layer. B. Drill core section of intensely deformed oxide-BIF. Red dash line: fold axial trace; DDH: 04-PQD-003. Note the nearly complete transposition of boudinaged magnetite and chert bands.

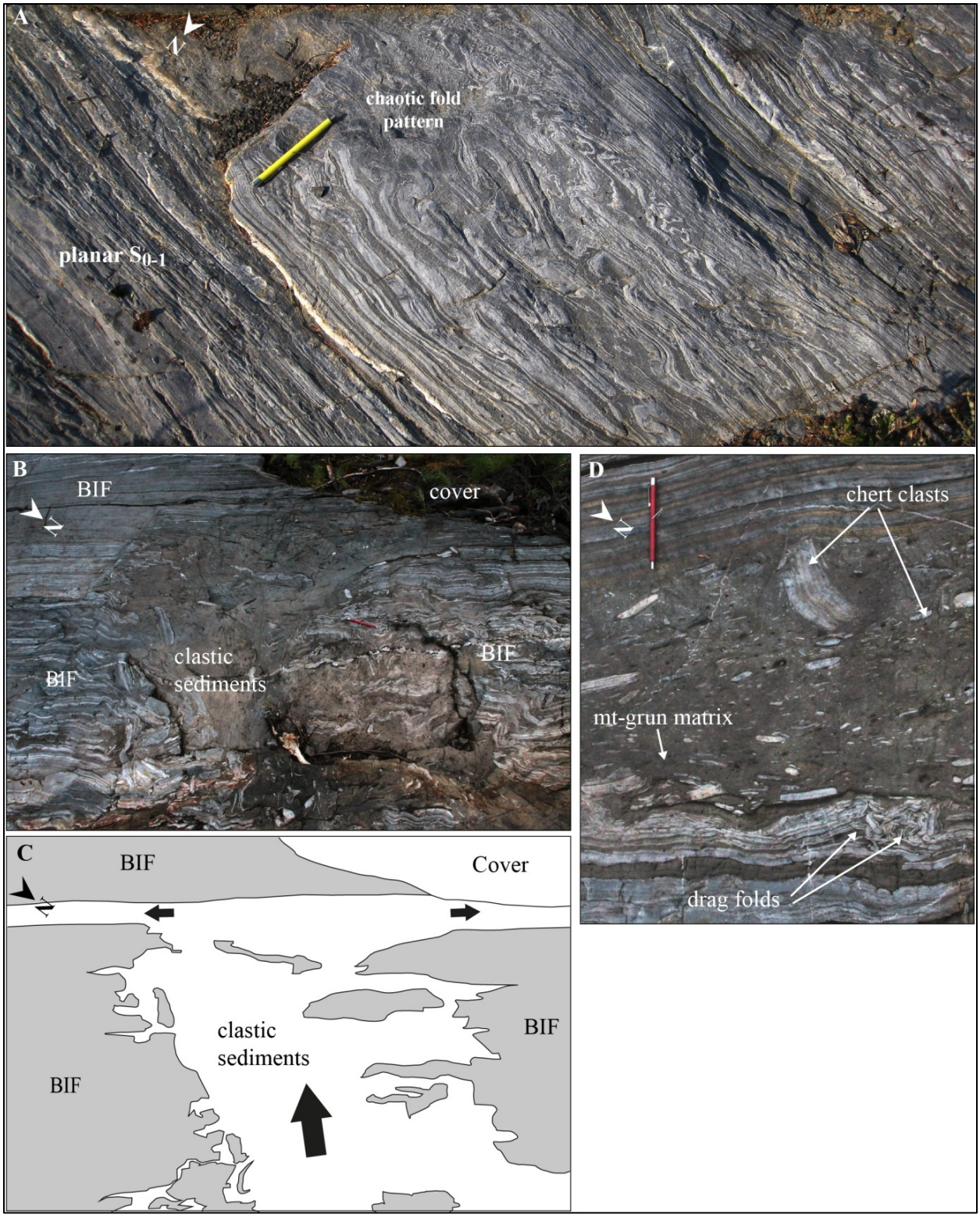

Figure 5-5: Preserved soft-sediment deformation structures in BIF. A. 50 cm-thick bed marked by chaotic, locally ptygmatic folds and delimited by weakly folded, planar chert-magnetite beds. Exposure located 200 m west of Trench 4, West antiform area. B. Dewatering structure in BIF: during deposition of early chemical sediments and compaction of underlying clastic-rich layers, the pressure exerted causes the water contained

in clastic sediments to burst through the overlying oxide-rich and silica-rich bands. It then spreads laterally in all directions, probably as a plume. The presence of drag folds on the depositional surface, a few metres from the eruption point, suggests the plume settled down quickly. C. Sketch of photo B. D. Clasts and boudinaged beds of chert in a grunerite-magnetite-quartz matrix and sedimentary drag folds at the base of the unit. Location: South-West Zone, 4.2 km BIF trench.

5.2 D_1 deformation

Structural features of the D_1 deformation are best preserved in the WASD, where D_2 deformation overprint is moderate (Figure 5-1). In addition to reconnaissance geological mapping in the West antiform area, three trenches were mapped in detail using a high resolution differential GPS (section 1.5.1.1; Figure 5-6 Figure 5-8). D_1 structural features such as isoclinal folds (abundant in sedimentary rocks) and penetrative axial planar foliation (locally conspicuous in volcanic rocks) are well preserved.

5.2.1 F_1 folds

Centimetre- to decimetre-scale F_1 folds are mapped in the cherty garnet-biotite schist of the NIF (Figure 5-9A, B) and within chert-magnetite sequences of the SIF (Figure 5-9C, D). A metre-scale F_1 fold outlined by a thin horizon of BIF within komatiitic basalts is visible on the WAT1 exposure (Figure 5-9E). Several occurrences of decimetre- to metre-scale F_1 folds that affect volcanic rocks and iron formation were also mapped.

F_1 folds are mostly isoclinal, locally rootless. They are overprinted by F_2 folds in a manner similar to the type 3 interference pattern of Ramsay and Huber (1987). Such a pattern suggests that F_1 folds were originally NE-verging, oriented at high angle with the F_2 axial planes. The shallow NW plunge of F_2 folds may be due to F_1 being reclined with axial planes shallowly dipping to the NW (Turner and Weiss, 1963; Hobbs et al., 1976). This is consistent with observations on the orientation of S_1 in volcanic rocks (5.2.2).

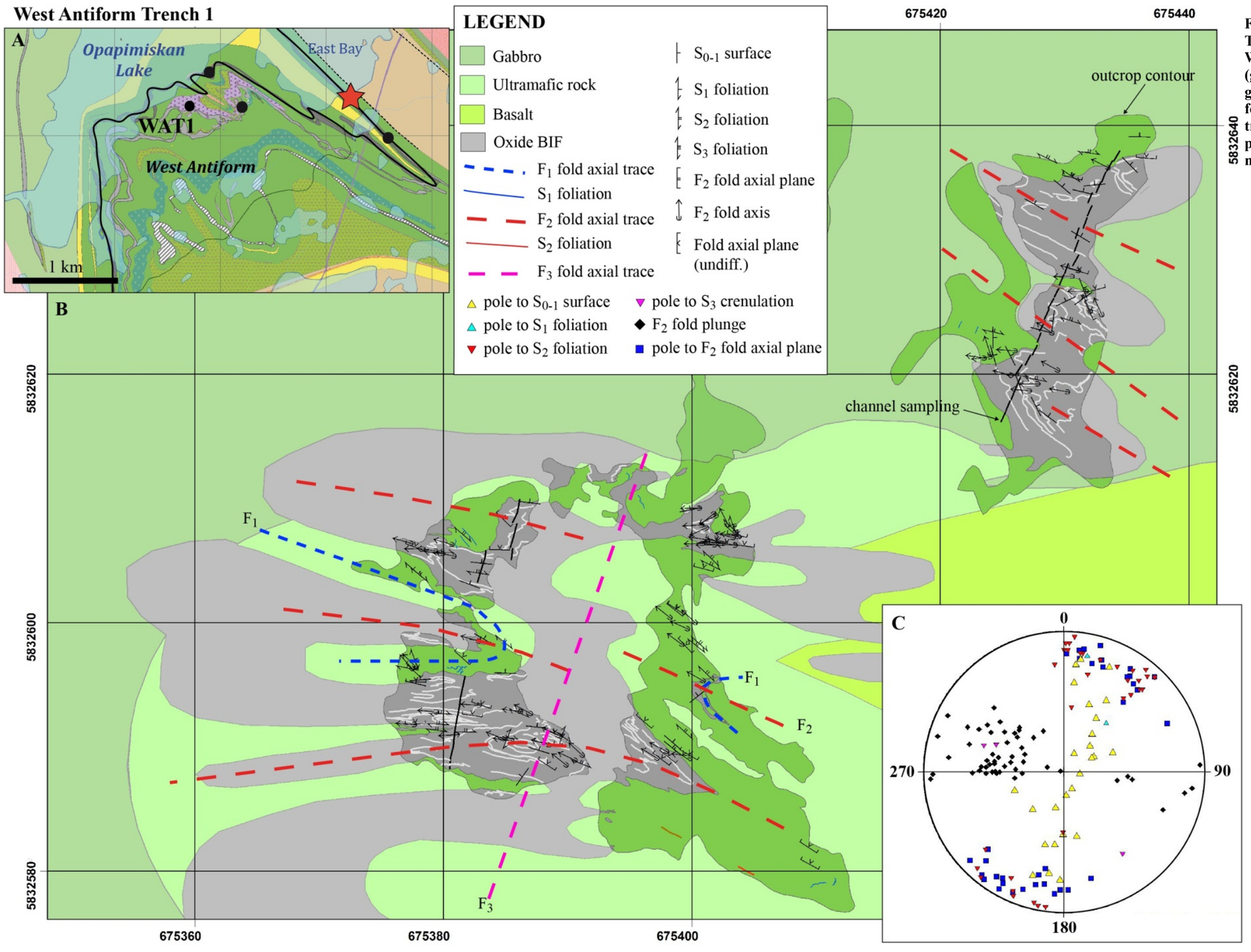

Figure 5-6: Geological map of West Antiform Trench 1, West antiform area. A. Location of the WAT1 exposure in the West antiform area (geology from Figure 3-1). B. WAT1 detail geological map with measured structural features. Dashed lines represent approximate trace of the various fabrics. C. Stereographic projection (equal angle, lower hemisphere) of measured fabrics.

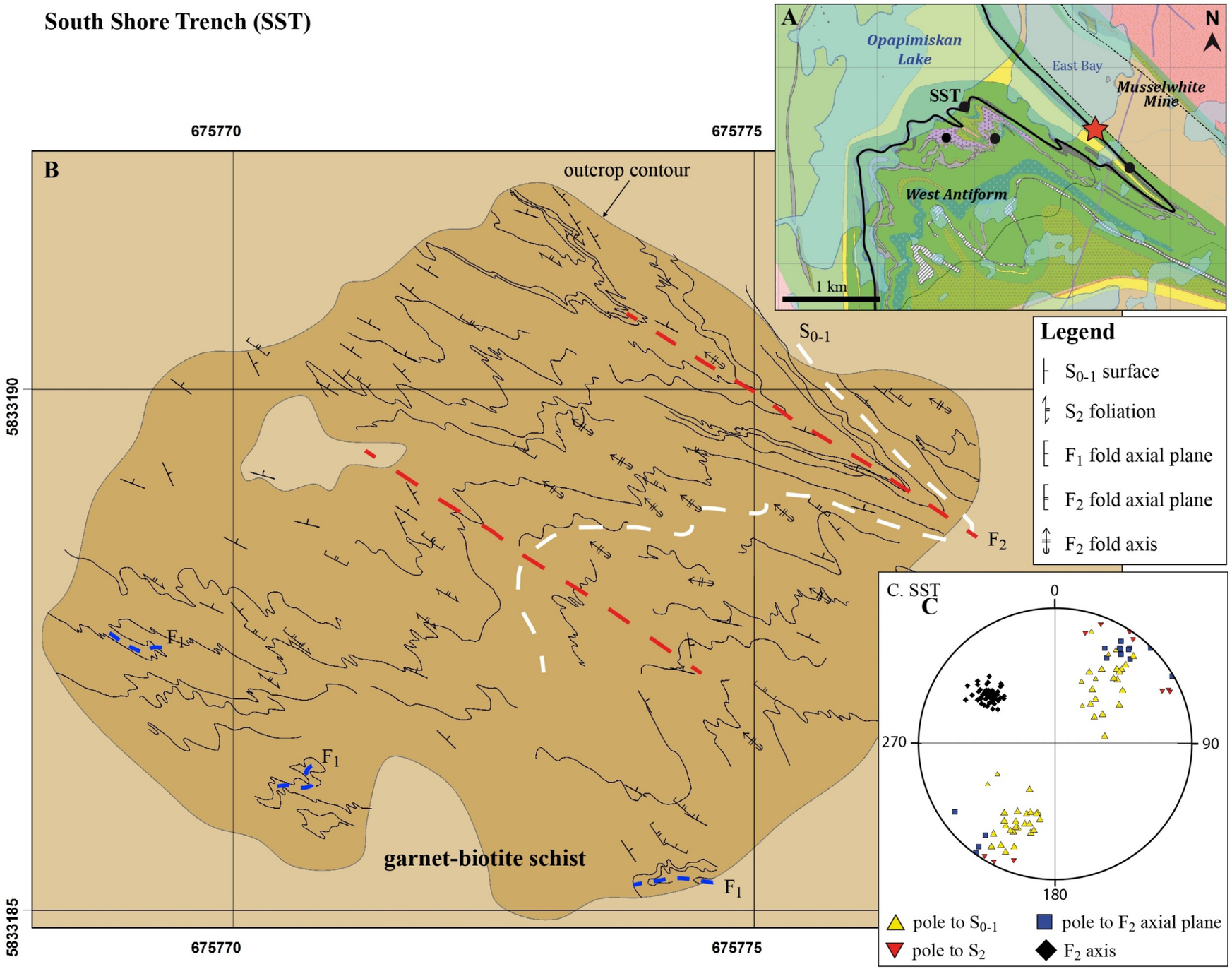

Figure 5-7: Geological map of South shore trench (SST) exposure. A. Location of the SST exposure in the West antiform area (Geology from Figure 3-1). B. SST detailed geological map with measured structural features. C. Stereographic projection (equal angle, lower hemisphere) of the SST exposure.

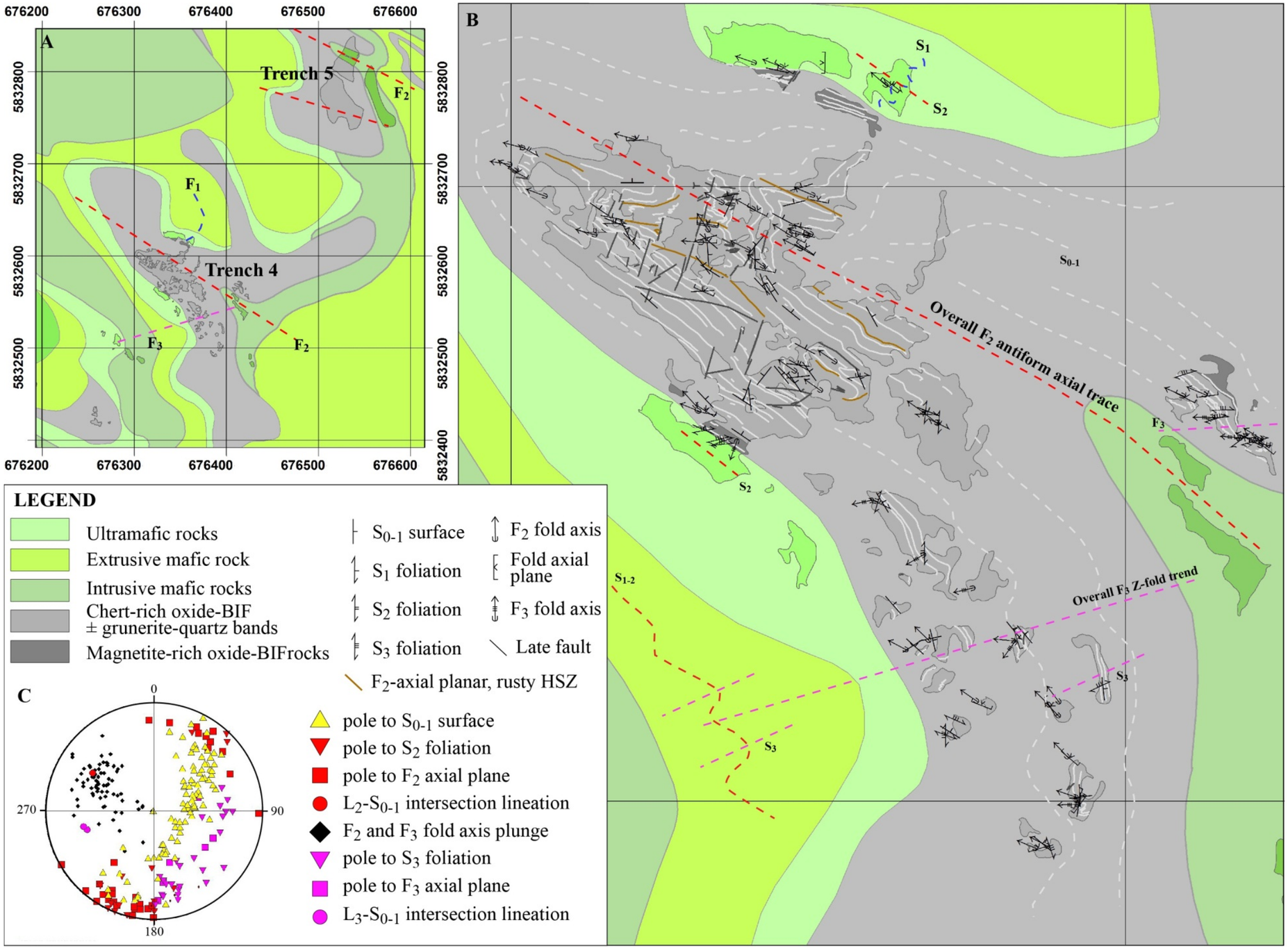

Figure 5-8: Geological map of Trench 4, West antiform area. A. General location of outcrops of Trench 4 and Trench 5 exposures and main structural features. B. Trench 4 detailed geological map with measured structural features. Dashed lines represent approximate trace of the various fabrics. C. Stereographic projection (equal angle, lower hemisphere) of measurements from Trench 4 and Trench 5.

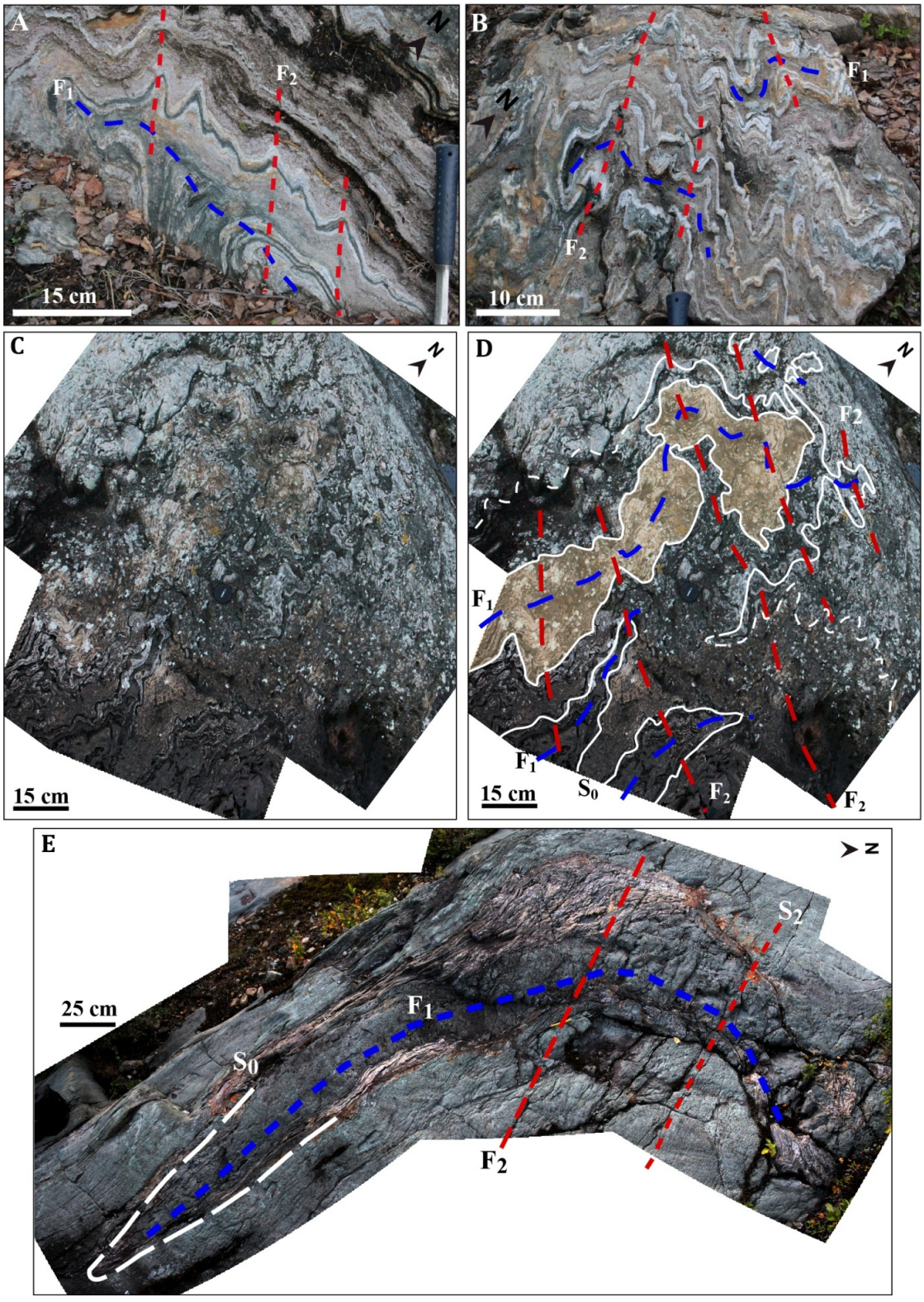

Figure 5-9: Refolded F_1 folds in the West antiform area. A. and B. F_1-F_2 folds from the SST exposure, UTM 675774/5833188. C. and D. Type 3 F_1-F_2 fold interference pattern on Grunerite Island (local name), UTM 673920/5832055. Breaks et al. (2001) had interpreted a type 1 fold interference pattern (dome and basin). E. F_1-F_2 folds from the WAT1 exposure, UTM 673922/5832055.

5.2.2 S_1 foliation

S_1 is generally a penetrative fabric that is best preserved in the "Basement basalts" and "Lower basalts", and in intrusions such as in the WASD (Figure 5-10A). It is best differentiated along the hinge of F_2, in massive volcanic rocks and gabbro, in which D_2 transposition is limited (Figure 5-10B, C, D). There, S_1 is delineated by metamorphic minerals such as magnesian chlorite and amphiboles. Angular relationships with D_2 fabrics suggest that S_1 was initially NE-SW trending and shallowly dipping to the NW. S_1 is best preserved in the hinge zone of F_2 folds, near chert bands in silicate-dominant BIF (unit 4EA) and garnet-biotite schist (unit 4F; Figure 5-11). It is usually poorly-developed in the oxide-dominant facies of BIF lithologies, as chert bands tend to fracture and boudinage, while magnetite bands deform plastically and fill openings.

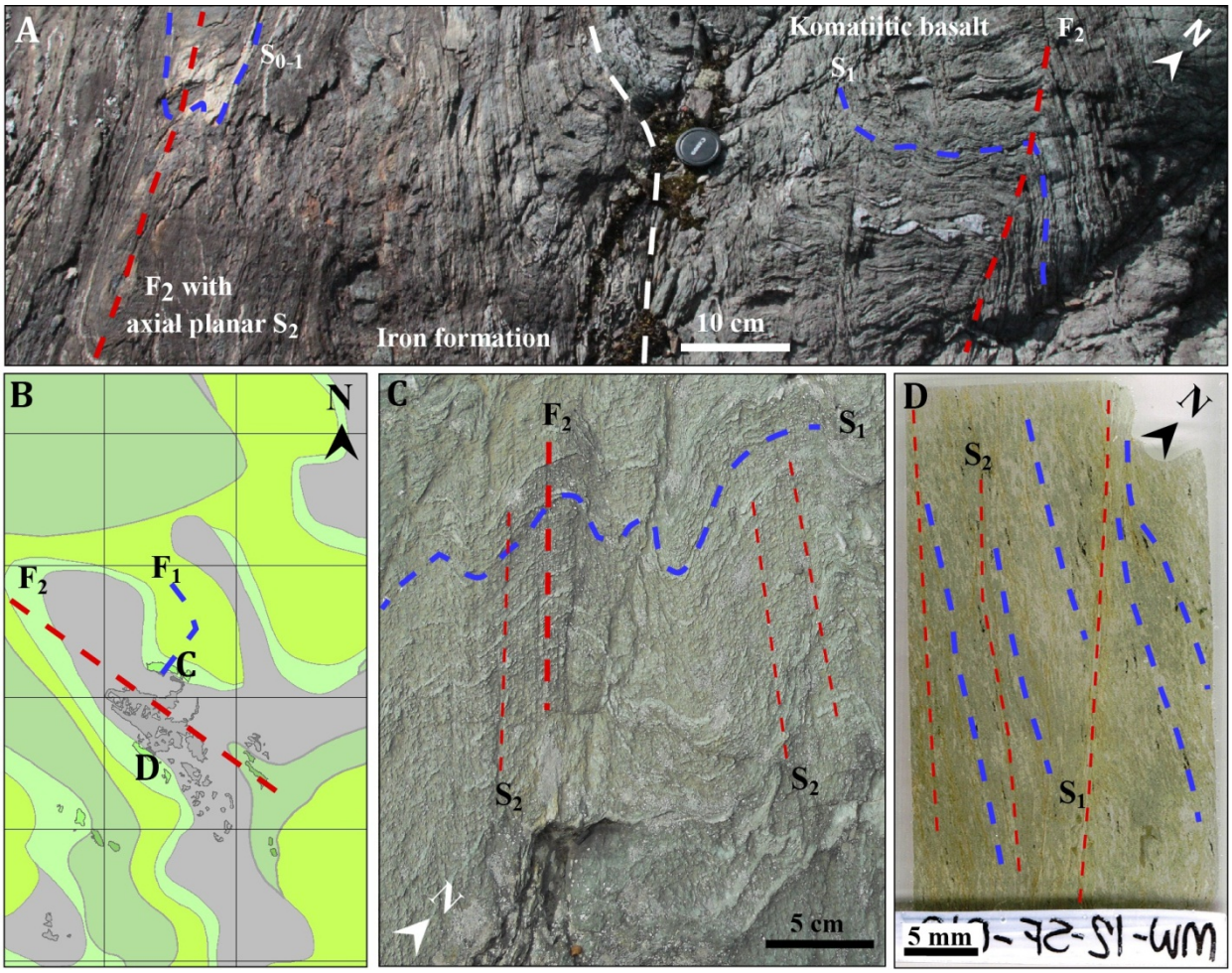

Figure 5-10: S_1 foliation in volcanic rocks. A. S_1 foliation affected by F_2 S-fold in komatiitic basalt, West antiform trench 1 exposure. B. Simplified map of the Trench 4 exposure and surroundings with location of F_1-F_2 relationship observations: C. High angle crosscutting relationship of penetrative S_1 foliation and S_2

cleavage in volcanic rock; and D. Low angle S_1-S_2 crosscutting relationship along the flank of the outcrop-scale F_2 fold, as shown in A.

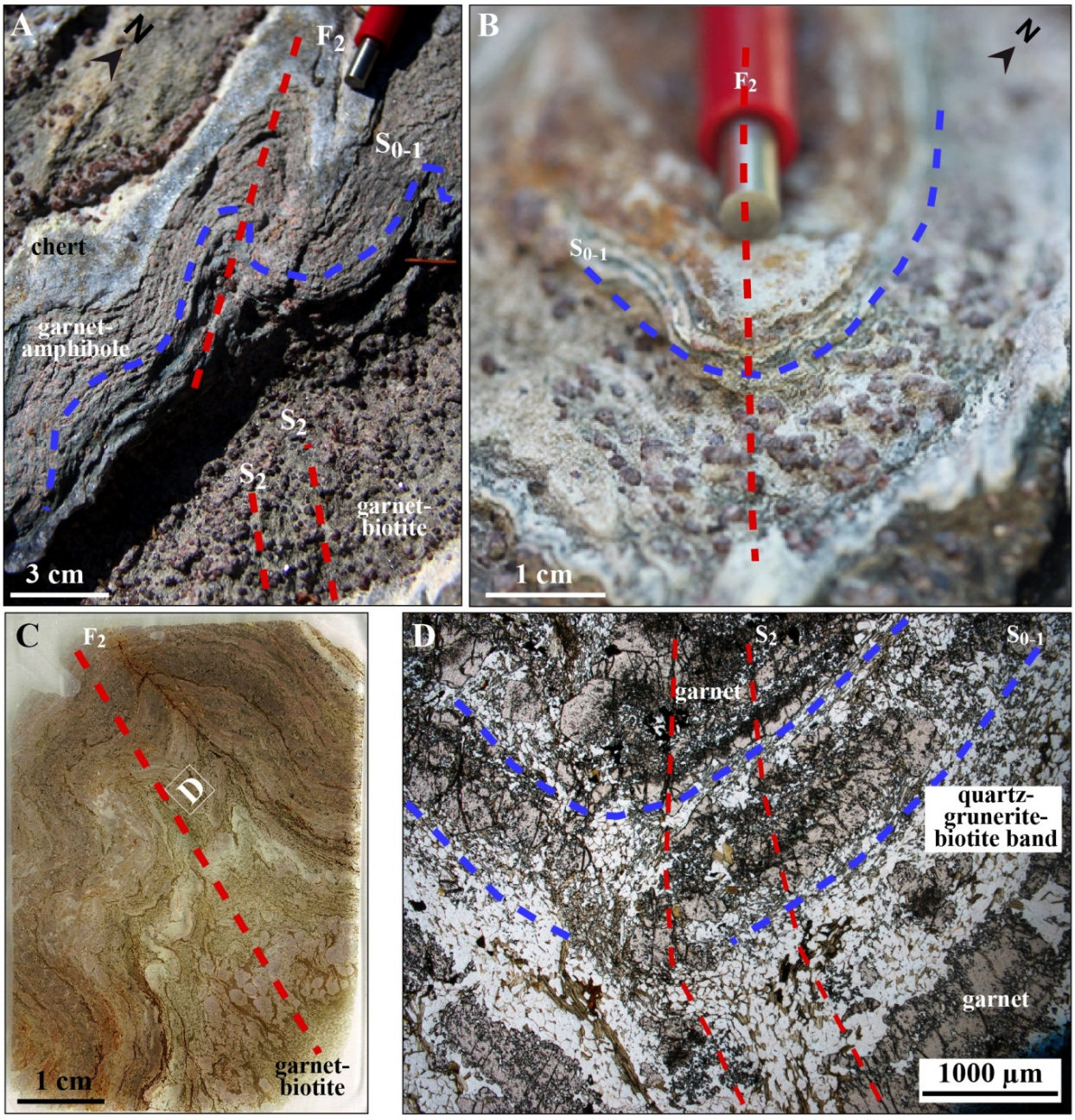

Figure 5-11: S_{0-1} foliation in garnet-biotite schist. A. Preserved S_{0-1} in garnet-amphibole band near a chert band, South shore trench, West antiform area. Note the obliteration of S_{0-1} in the underlying garnet-biotite band. B. Close-up view of the S_{0-1} foliation in a garnet-biotite band along a F_2 fold hinge, same location as A. C. Oriented thin section across an F_2 fold from the South shore trench, West antiform area, with location of D. microphotograph of the S_{0-1}-S_2 crosscutting relationship in the hinge of an F_2 synform. Note the tabular shape of poikilitic garnet porphyroblasts and the S_2-parallel fracture they exhibit.

5.2.3 Interpreted D_1 fault zone

Geochronological data from the OMA and the ZHA in the mine area shows that there is a 10 to 65 Ma age difference between these assemblages (section 3.6). In contrast to outcrops from the Paseminan River area (Figure 3-1; chapter 3), drill cores of the ZHA sedimentary rocks from the mine area reveal no evidence of a conglomerate at the contact with the OMA (Figure 5-12A, B). In the mine area, especially along the east limb, D_2 strain is intense and can be considered as globally homogeneous. Yet, drill cores of the OMA ("Lower basalts" unit) display a distinct, eastward-increasing strain gradient that culminates at the contact between the OMA and the ZHA and is not significantly present in adjacent sedimentary rocks (Figure 5-12C). The OMA-ZHA contact is interpreted to be tectonic in nature, likely related to D_1 thrusting of the OMA over the ZHA (Figure 5-13). This timing is supported by the fact that the OMA-ZHA contact is folded by a major F_2 antiform north of Opapimiskan Lake (Figure 5-1). Drill holes through the contact zone uncover one, locally two, intercalation(s) of units of the ZHA and OMA (Figure 5-12A). Such distribution may represent a tectonic sliver and/or an F_2 fold; the second interpretation is favoured.

5.2.4 Kilometre-scale F_1 fold(s)

The presence of mesoscopic, refolded, NE-verging F_1 folds and the potential fault at the boundary between the OMA and ZHA are indicative of regional-scale D_1 fold-and-thrust or nappe-style deformation. They also suggest that regional-scale folds may occur in the study area. A compilation of stratigraphic top directions measured from pillowed flows of the "Basement basalts" and "Lower basalts" units of the OMA (chapter 3) shows that the stratigraphy north of Zeemel Lake is overturned and younging southward. Contrastingly, top indicators in rocks south of Zeemel Lake point to the north. This suggests that a major fold axial trace probably occurs through the ZHA rocks in the Zeemel Lake area (Figure 5-14). Geochronological data confirms that the OMA stratigraphy between Opapimiskan and Zeemel lakes is inverted, and shows that parts of the ZHA are markedly younger than the OMA (chapter 4). These elements strongly support the interpretation of a major, ENE-WSW, gently inclined, SSE-verging F_1 syncline (Figure 5-14; Oswald et al., 2015a, 2015b).

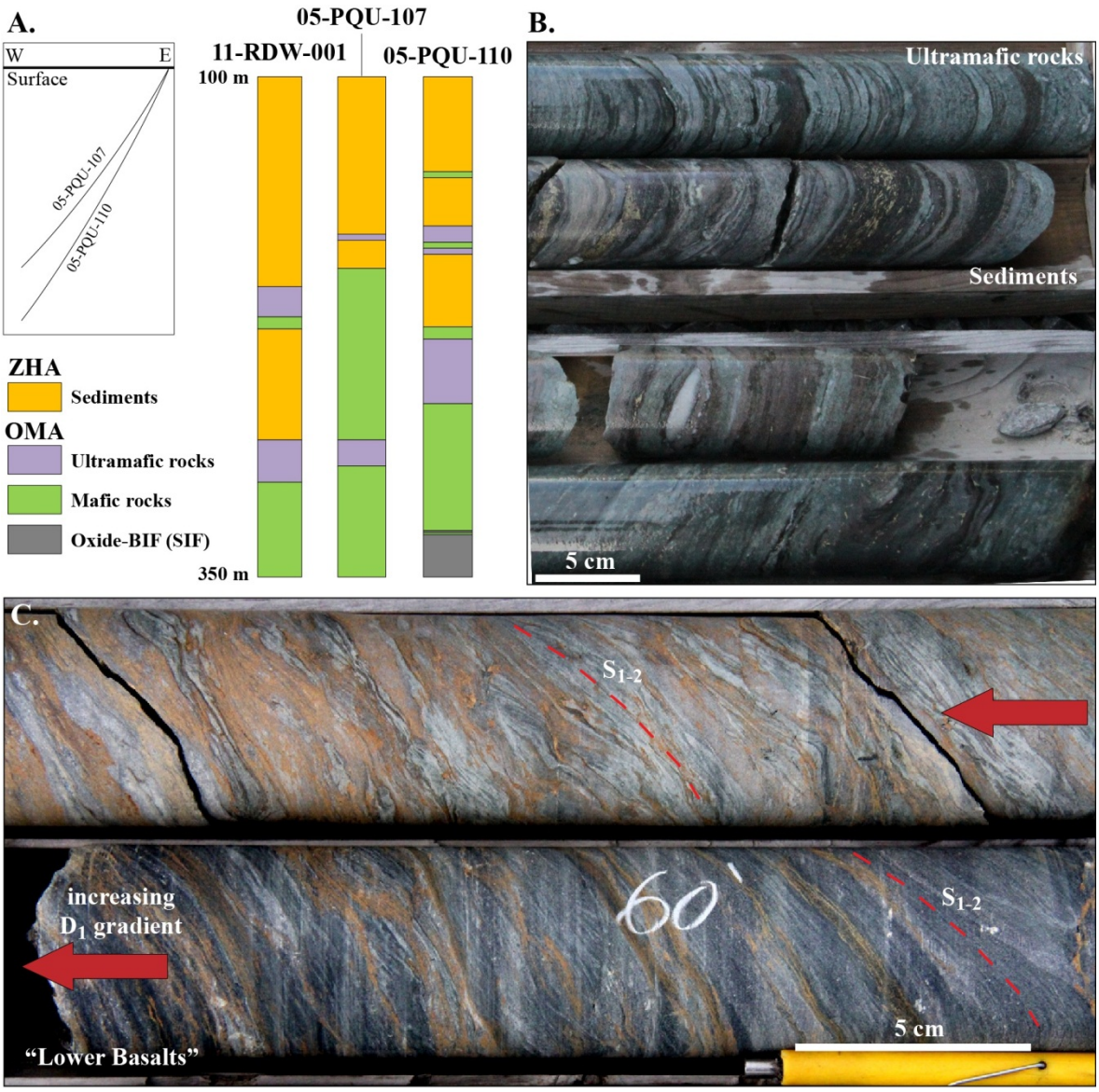

Figure 5-12: A: Lithological sequence (to scale) of three drill holes through the OMA-ZHA boundary in the mine area. B. Photograph of drill core from DDH 05-PQU-110 showing the typical sedimentary and ultramafic to mafic volcanic rocks. C. Photograph of drill core from DDH 05-PQU-110 showing the strain gradient in mafic and ultramafic rocks near the OMA-ZHA boundary (photo B. Dubé).

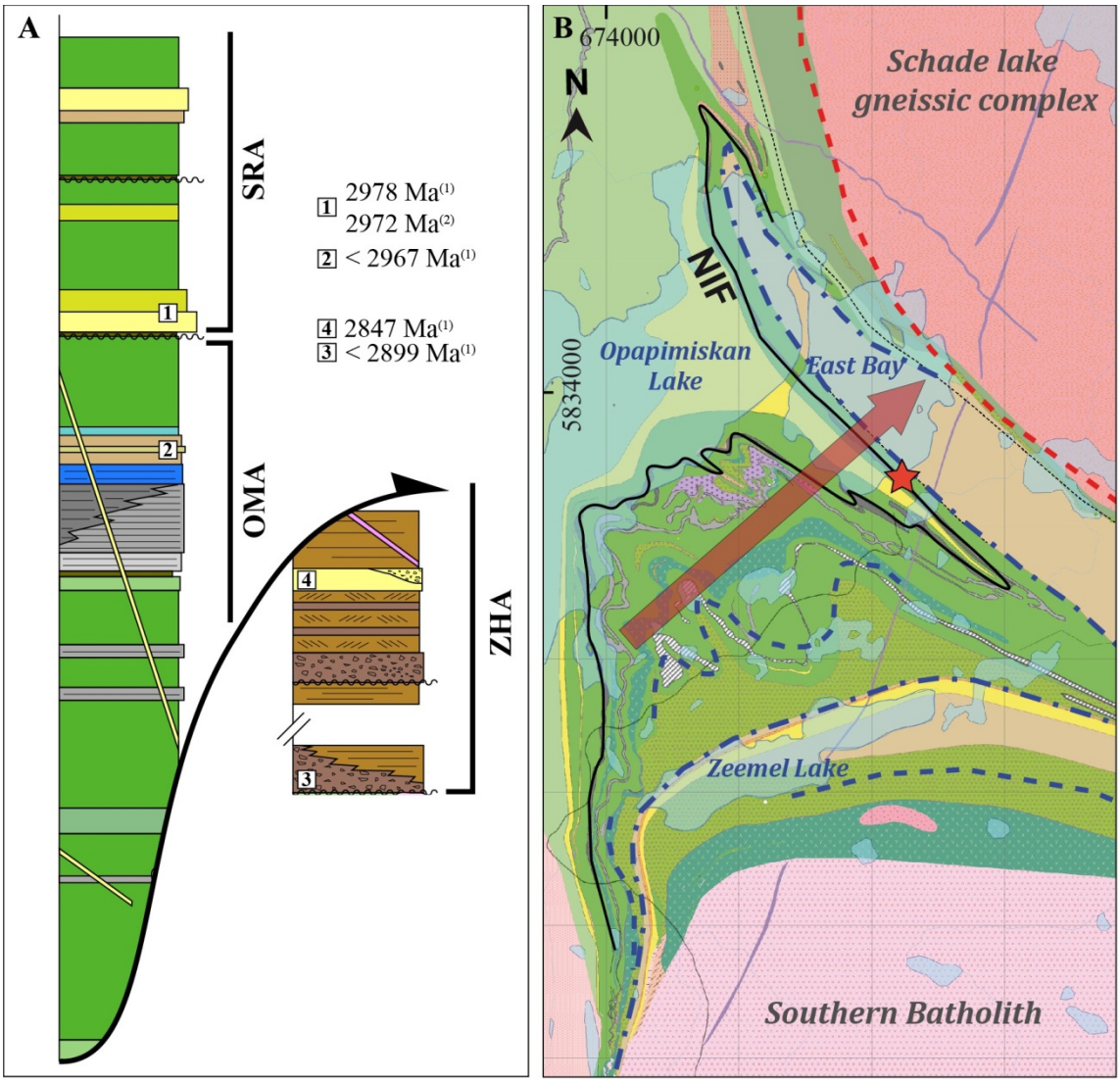

Figure 5-13: A. Schematic representation of the D_1 thrust fault, juxtaposing the SRA and OMA over the ZHA. See Figure 4-3 for geochronological data sources. B. Simplified geological map of the Opapimiskan Lake area outlining the folded fault contact between the OMA and the ZHA. Refer to Figure 3-1 and 5-1 for geological map and structural features legends.

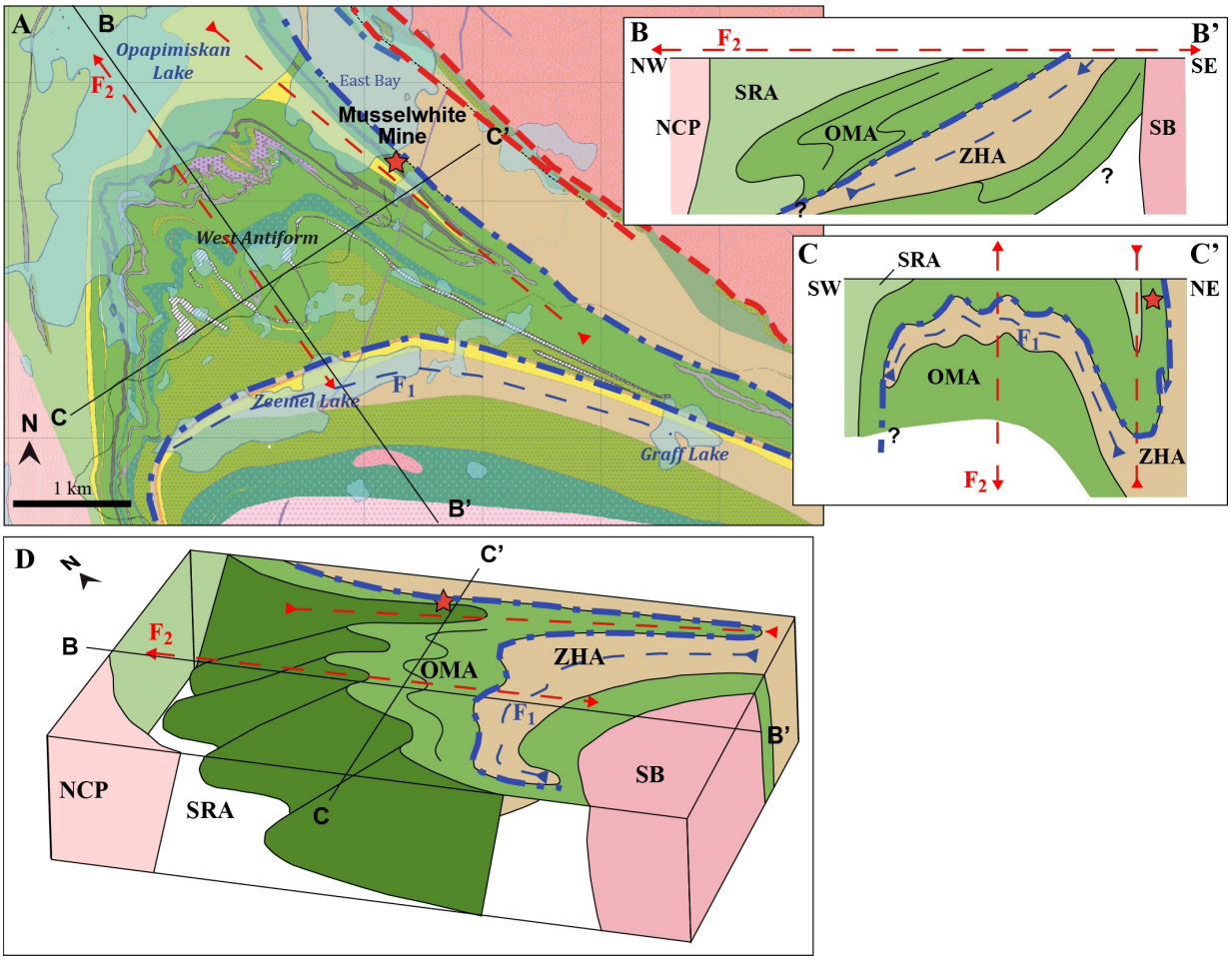

Figure 5-14: A. Geological map of the Opapimiskan Lake area outlining the main structural features and location of B-B' and C-C' NW-SE and NE-SW schematic sections. D. 3D schematic block diagram.

5.3 D_2 deformation in the West antiform domain

D_2 is the main phase of deformation in the Opapimiskan Lake area (Breaks et al., 2001; Hall and Rigg, 1986; chapter 2), where it is associated with a strong, northeastward-increasing, ductile strain gradient. Accordingly, descriptions of D_2 fabrics and structures are given below from west to east, from the WASD, using trench maps (Figures 5-6, 5-7, 5-8), to the MASD (section 5.4), based on surface (PQ trench) and underground mapping, and drill section interpretations.

5.3.1 F_2 folds

Typically, and at all scales, F_2 folds are open to tight and have moderately to shallowly NW-plunging axes (Figure 5-2 andFigure 5-15). Northwest-trending axial planes are dominantly sub-vertical to steeply-

dipping to the east. On a stereographic projection, measurements of S_{0-1} from Trench 4 are distributed on a plane, the pole of which plunges roughly 25° toward approximately 300°, which is consistent with measured F_2 fold axes. Measurements from the SST are consistent with those of Trench 4 and 5: F_2 axes form a tight cluster averaging at N305°-30°. Measurements in the iron formation from the WAT1 show S_{0-1} orientations that define a great circle with a pole plunging 20° towards N285°, compatible with orientation of measured F_2 folds axes. The greater dispersion of F_2 fold axes (including some east-plunging folds; Figure 5-15C) and axial planes on the WAT1 may be caused by overprinting D_3 deformation, as is the case for structures of the 4KT exposure (section 5.4).

The geometry of F_2 folds greatly varies depending on rock type, strain intensity, and, specifically for BIFs, on mineralogy and thickness of the compositional layering. In volcanic rocks, close, locally chevron-style upright F_2 folds affect the S_1 foliation (Figure 5-16A; McClay, 1987). In the garnet-biotite schist, folds are typically open and symmetrical (Figure 5-16B), but can be isoclinal in higher strain areas (Figure 5-16C). Contrastingly, folds in oxide-BIF are open to tight, generally asymmetrical and similar, with sharp hinge to limb transition, locally chevron-like (Figure 5-16D, E). Fold limbs are often faulted and boudinaged along chert bands. In clastic-rich oxide-BIF (4Bc) and silicate-BIF (4EA), F_2 folds display strongly thickened hinges and attenuated limbs. Within asymmetrical fold structures, short limbs more frequently include parasitic Z- and S-type folds.

A number of secondary structures are associated with F_2 folds, due to strain partitioning, notably in the oxide-BIF. These structures mostly consist of faults and shear zones along the limbs, documented both in drill core (Figure 5-17A) and outcrops (Figure 5-17B). These high-strain zones are typically parallel to F_2 axial planes, but are locally refracted where crosscutting thick rigid units (Figure 5-2D). Breccia locally occur in rigid, chert-rich BIF (Figure 5-17B). In magnetite-rich BIF, some high-strain zones display well-defined shear bands, sub-parallel to F_2 axial planes and NW-plunging asymmetric folds (Figure 5-18).

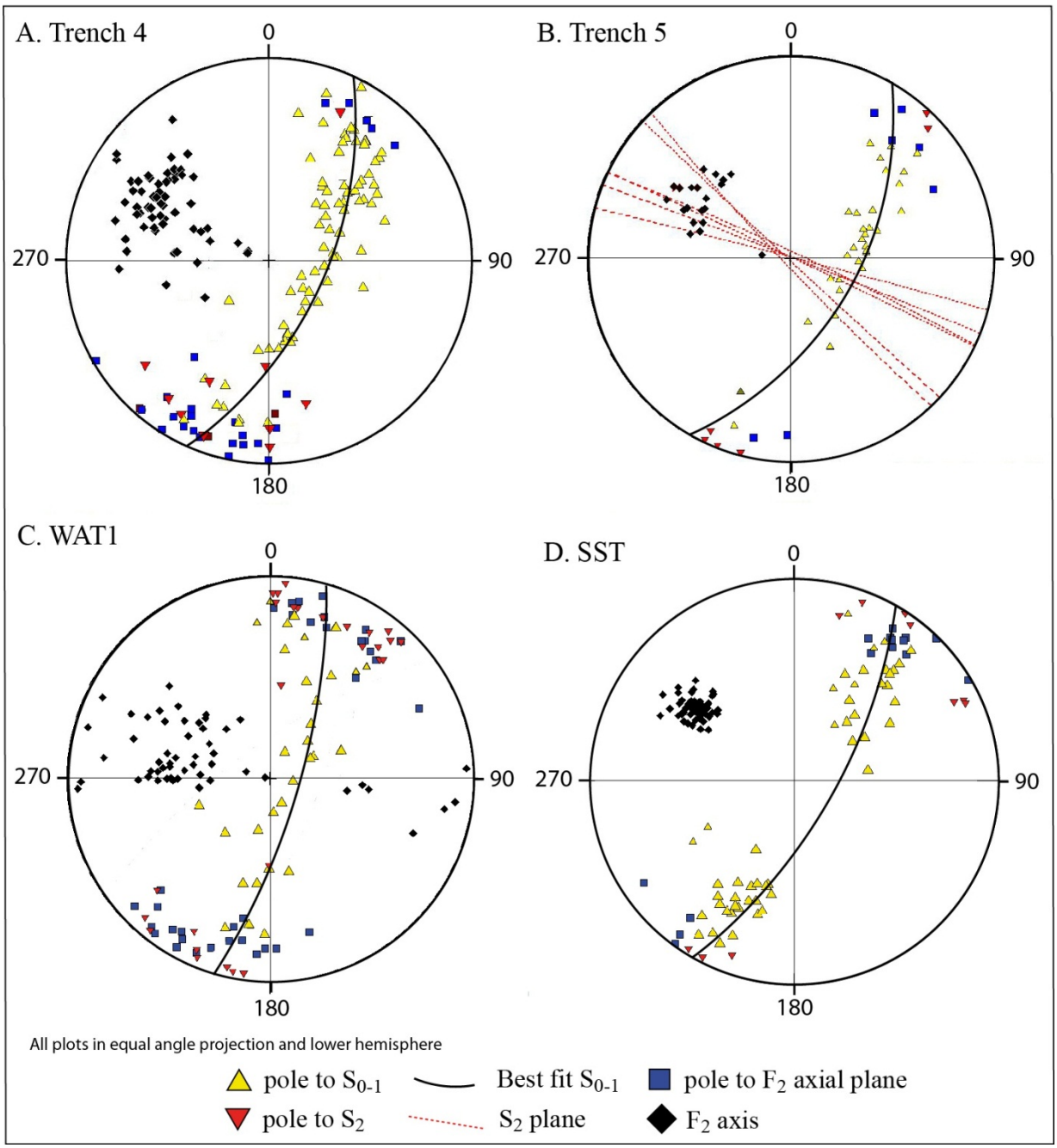

Figure 5-15: West antiform structural domain – stereographic projections of D_2 structures from surface stripped outcrops (equal angle, lower hemisphere). A. Trench 4; B. Trench 5; C. West antiform trench 1; D. South shore trench.

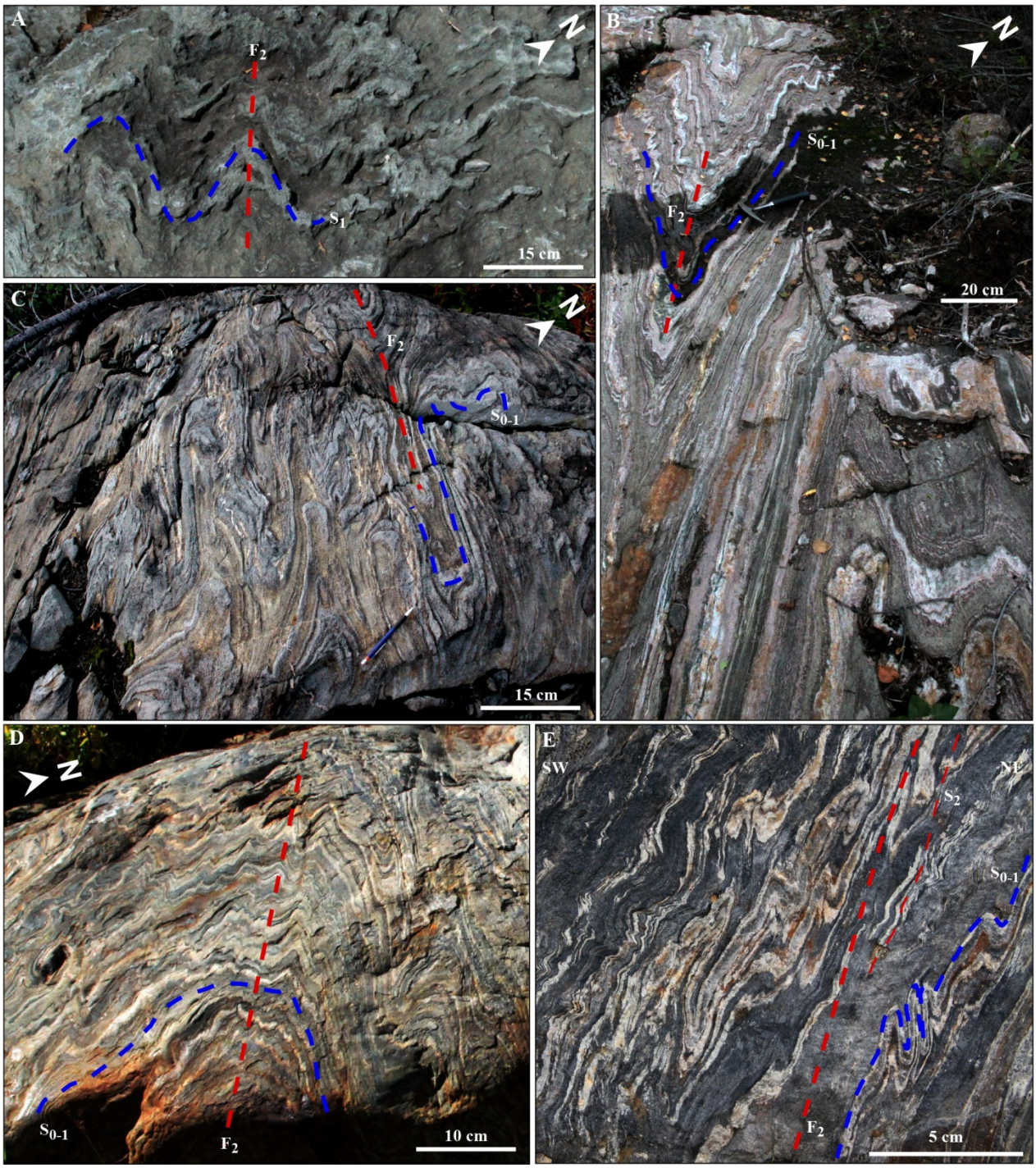

Figure 5-16: F_2 folds in the West antiform area. A. Semi-chevron-type folds affecting the S_1 fabric in volcanic rocks, WAT1 exposure. B. Close F_2 folds in the chert-rich facies of unit 4F, South shore trench. C. Tight to isoclinal F_2 folds in the garnet-biotite ± hornblende facies of unit 4F, West antiform area, near UTM 675900/5832700. D. Open antiform with M-shaped parasitic folds in chert-magnetite BIF, WAT1 exposure. E. Open to tight, parasitic Z-folds in chert-magnetite BIF, Trench 4.

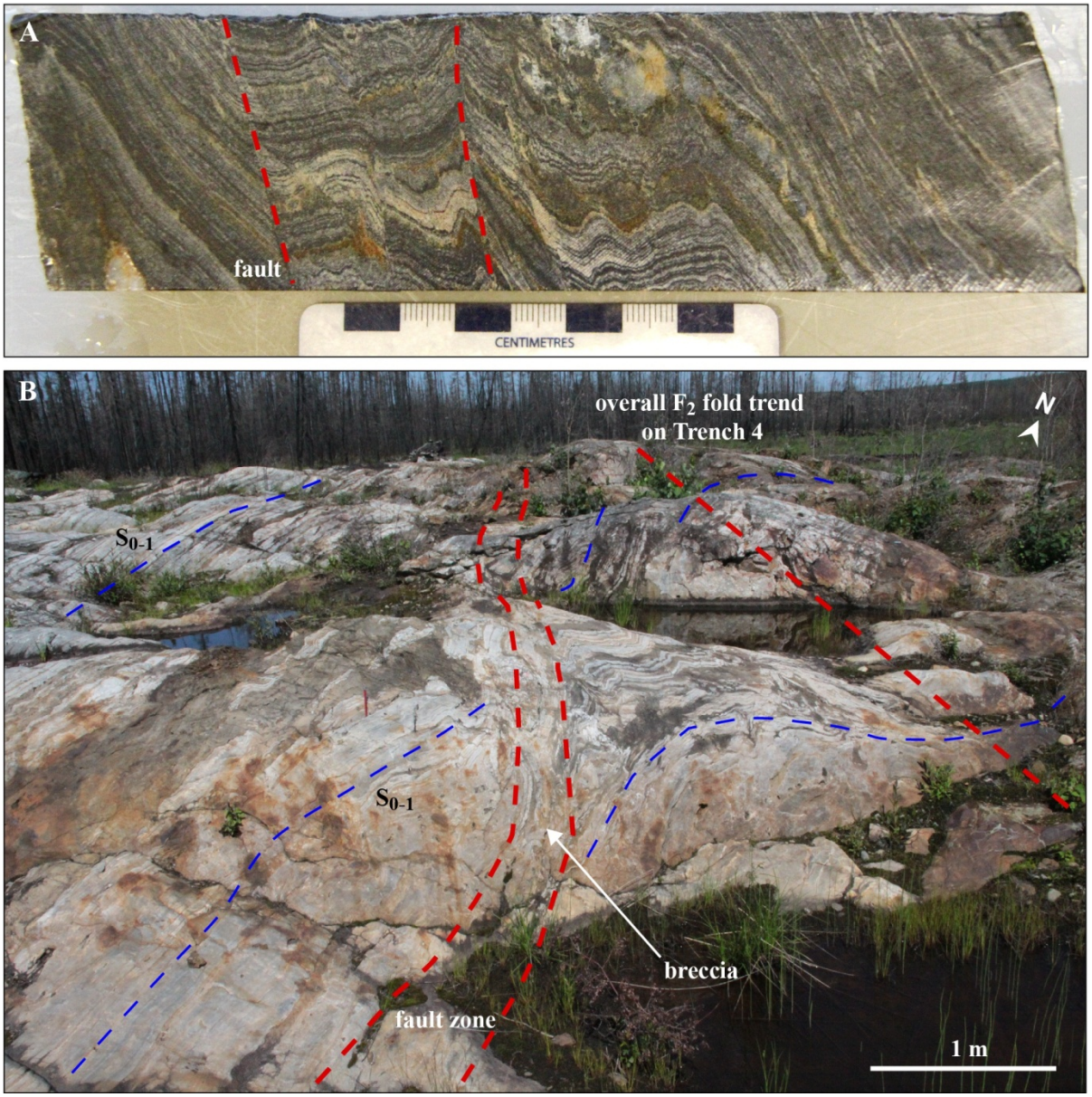

Figure 5-17: Faults associated to F_2 folds. A. Drill core segment of oxide-BIF with faults crosscutting the compositional layering. B. Decimetre-scale fault zone crosscutting the Southern iron formation, Trench 4 exposure, West antiform area (also see Figure 5-8).

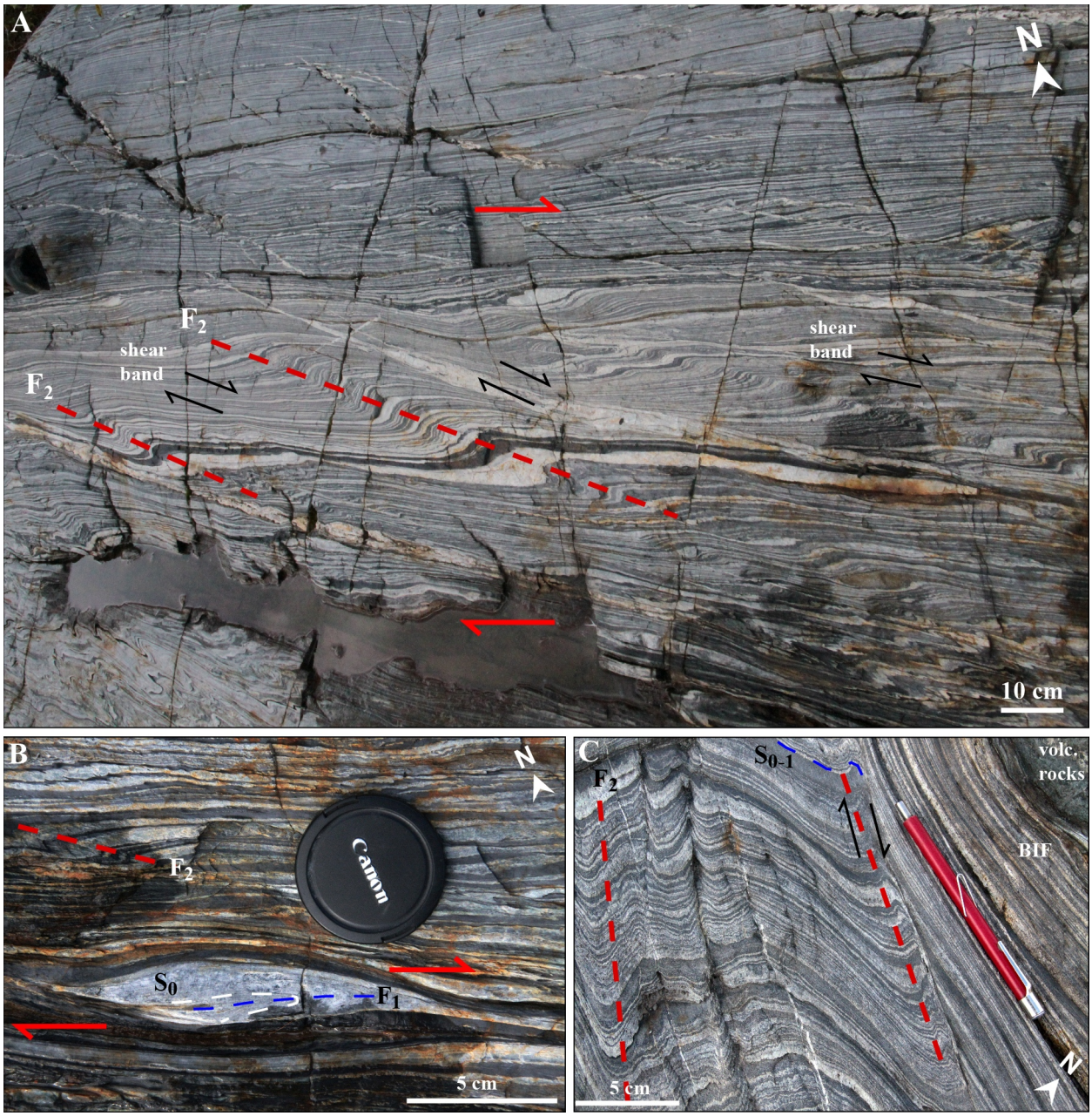

Figure 5-18: Evidence of ductile deformation. A. Development of folds between ductile high-strain zones in chert-magnetite BIF near the contact with volcanic rocks, Trench 4, West antiform area. B. Close-up view of a preserved F_1 fold hinge in an isolated boudin resulting from dextral shearing, same location as A. C. F_2 folds and ductile high-strain zone in chert-magnetite BIF near the contact with volcanic rocks, same location as A.

5.3.2 S_2 foliation

The S_2 fabric is moderately- to strongly-developed, steeply NE- or SW-dipping, and axial planar to F_2 folds (Figure 5-15). Local variations in dip, and to a lesser extent in orientation, are largely due to refraction of the fabric between rock units or beds of contrasting competencies.

In volcanic rocks, S_2 varies from a spaced cleavage (Figure 5-10C) to a penetrative foliation (Figure 5-19A) within fold hinge zones, high-strain zones, and hyaloclastite-rich pillowed basalt units. In sedimentary units, S_2 varies from penetrative, such as in unit 4F (Figure 5-19B), to very weakly-developed, especially in unit 4B, where a faint intersection lineation is present on S_{0-1} planes (Figure 5-19C, D).

5.4 D_2 deformation in the mine area structural domain

D_2 deformation intensity is much higher in the mine area than in the WASD (section 5.3). Structural features presented below are based on surface (PQ trench; Figure 5-20) and underground mapping, and on interpreted drill sections (Figures 5-20, 5-21, 5-22, 5-23, 5-24).

5.4.1 F_2 folds

The geometry of F_2 folds in the MASD is mainly affected by two parameters: lithology and strain intensity. Strong strain gradients have been mapped underground, in the vicinity of gold-mineralized high-strain zones. In oxide-BIF, typical fold geometry progresses from close similar folds in medium-strain zones (Figure 5-25A, C) to isoclinal, locally rootless, asymmetrical folds in high-strain zones (Figure 5-25B, D). The orientation of F_2 axial planes is similar to that of folds in the WASD; however, axes have a slightly shallower plunge (i.e., 18° vs. 30°; Figure 5-25E). Underground measurements show slightly steeper fold plunges than southeastward at surface (e.g., PQ trench; Figure 5-20), which is consistent with regional-scale variations documented by Breaks et al. (2001). In other BIF facies and pelitic rocks, F_2 are close to tight in medium strain zones, and locally asymmetrical, such as the T-antiform west limb or in the hinge zone of larger folds (Figure 5-26). In high-strain zones, folds tend to be isoclinal in garnet-biotite schist or are frequently rootless in silicate-BIF and clastic-rich oxide-BIF.

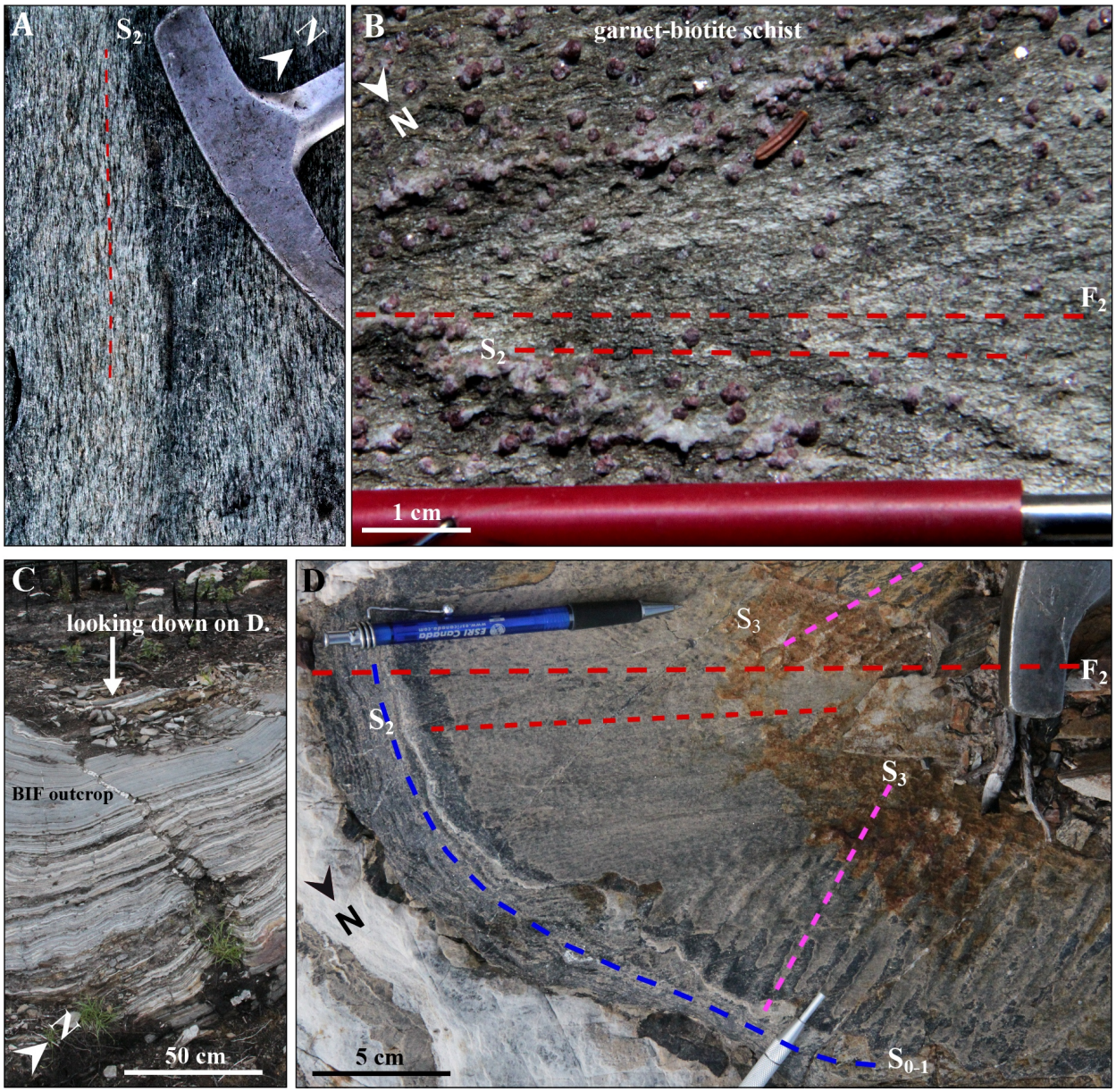

Figure 5-19: S_2 foliation in the WASD. A. S_2 penetrative foliation, Trench 4. B. S_2 foliation in garnet-biotite schist, SST exposure. C. Oxide-BIF exposure with location of photograph presented in D. S_2 foliation in open F_2 fold in chert-magnetite BIF, Trench 4, and resulting L_{1-2} intersection lineation on S_{0-1} surface. The crenulation of S_2 by S_3 and L_3 intersection lineation is also present.

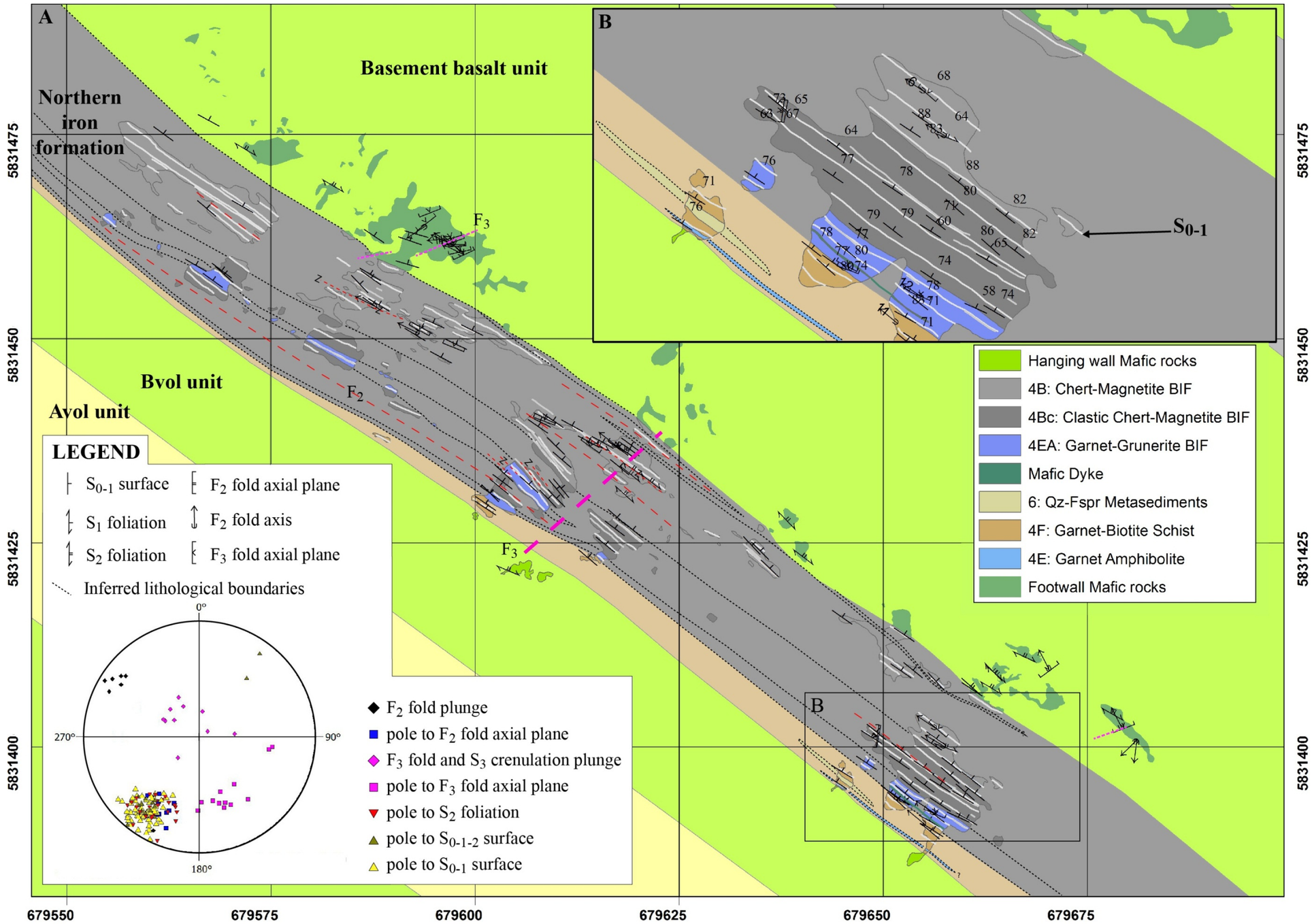

Figure 5-20: PQ trench detailed map. A. Geological map of the exposure with measured structural items and interpreted F_2 and F_3 fold axial traces. The main F_3 fold trace is evidenced in the field by sharp changes in BIF layering orientation and presence of decimetre-scale D_3 features in volcanic rocks and BIF. B. Southeastern portion of the exposure showing a nearly continuous section through the NIF sequence. C. Stereographic projection in equal angle, lower hemisphere, of structural measurements from PQ trench.

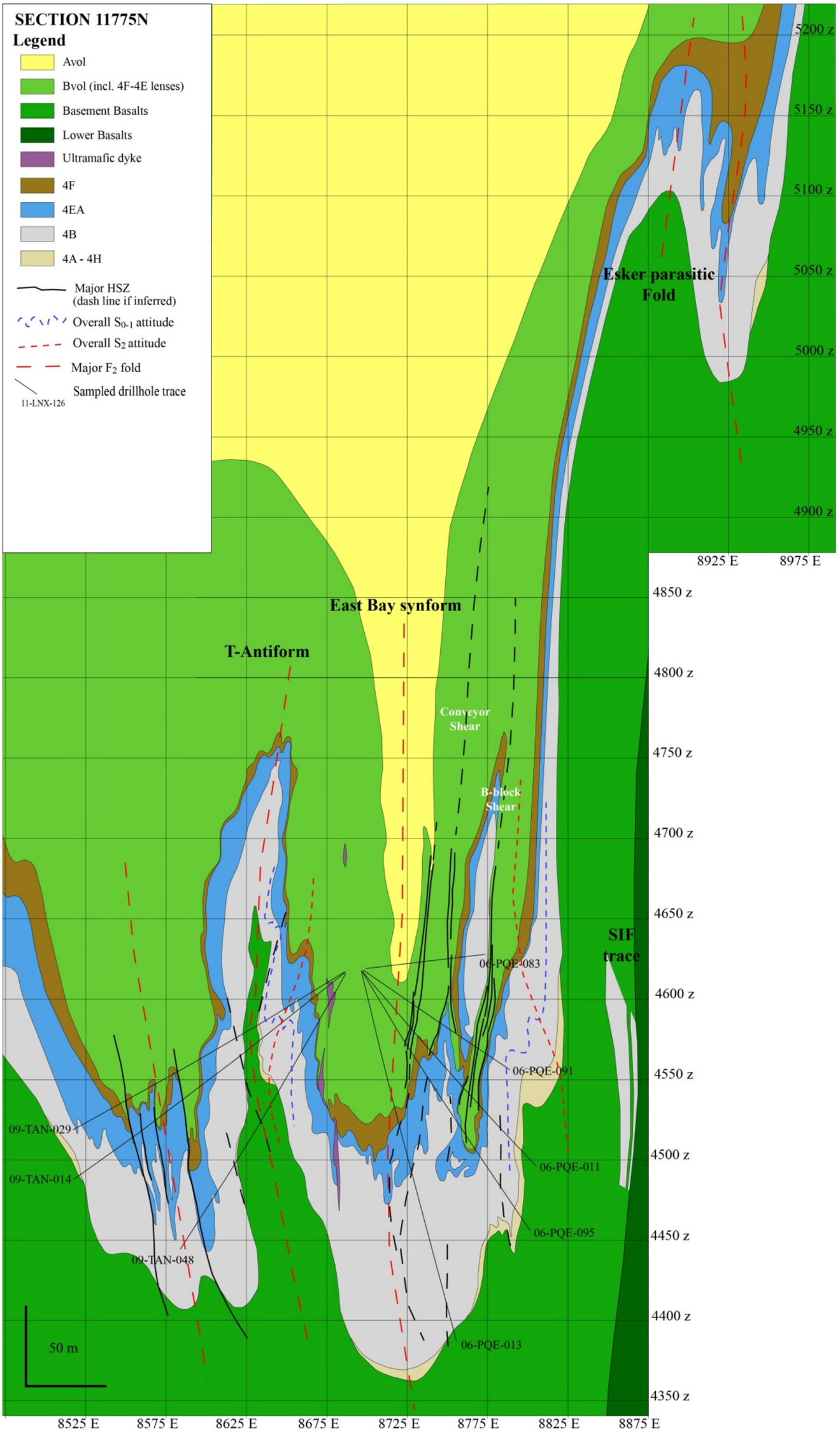

Figure 5-21: Geological and structural interpretation of mine section 11775 N, looking north.

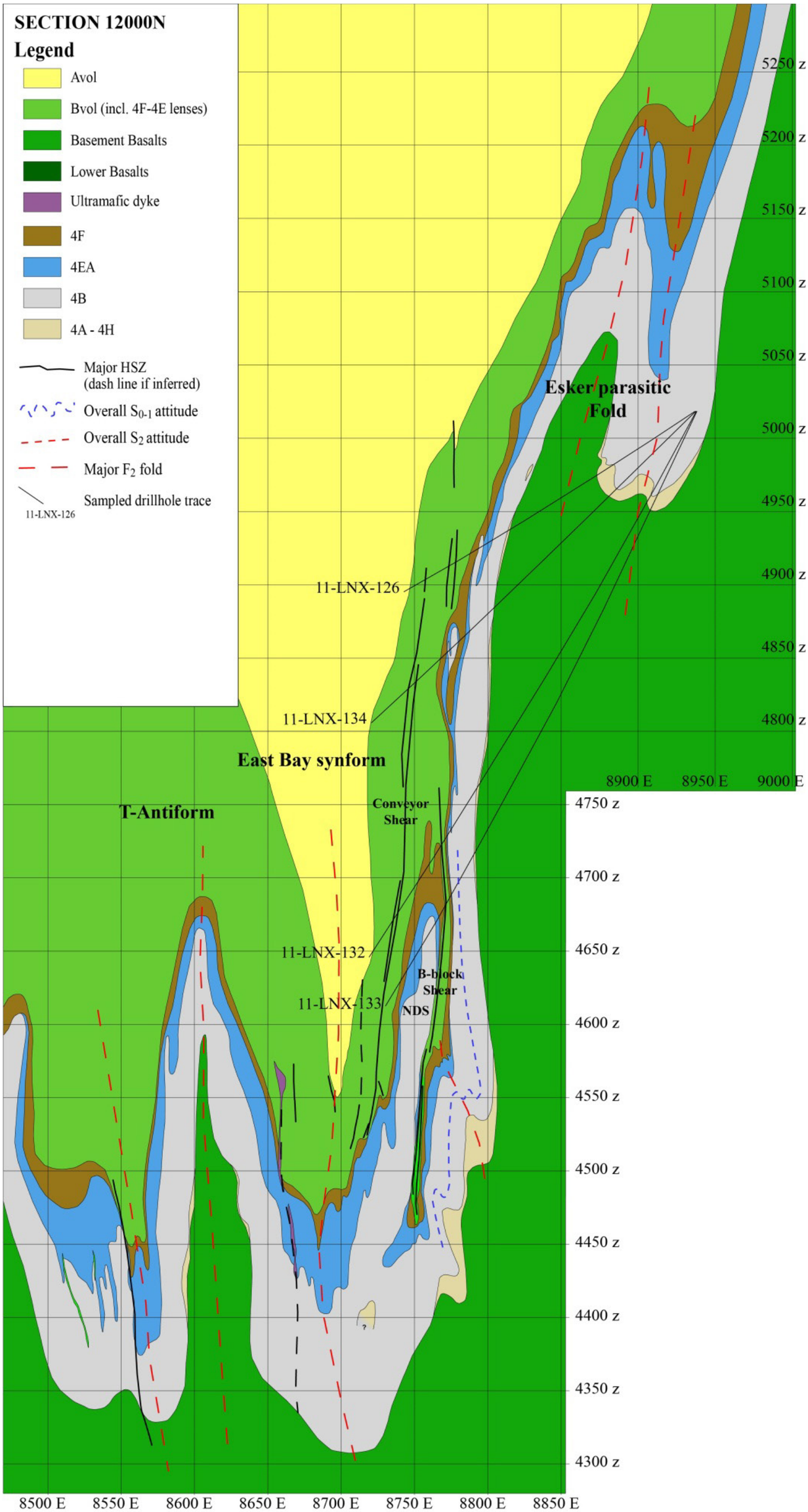

Figure 5-22: Geological and structural interpretation of mine section 12000 N, looking north.

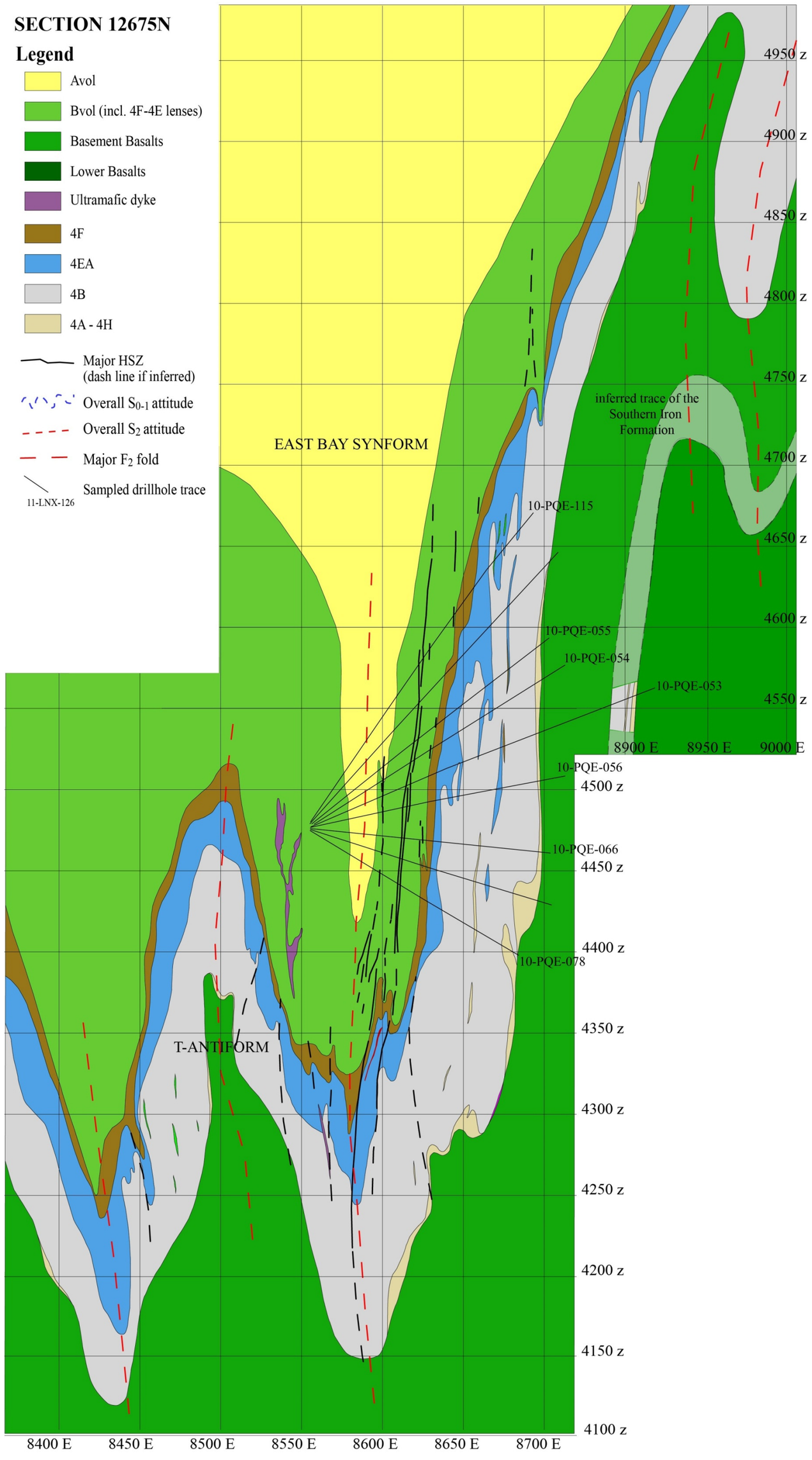

Figure 5-23: Geological and structural interpretation of mine section 12675 N, looking north.

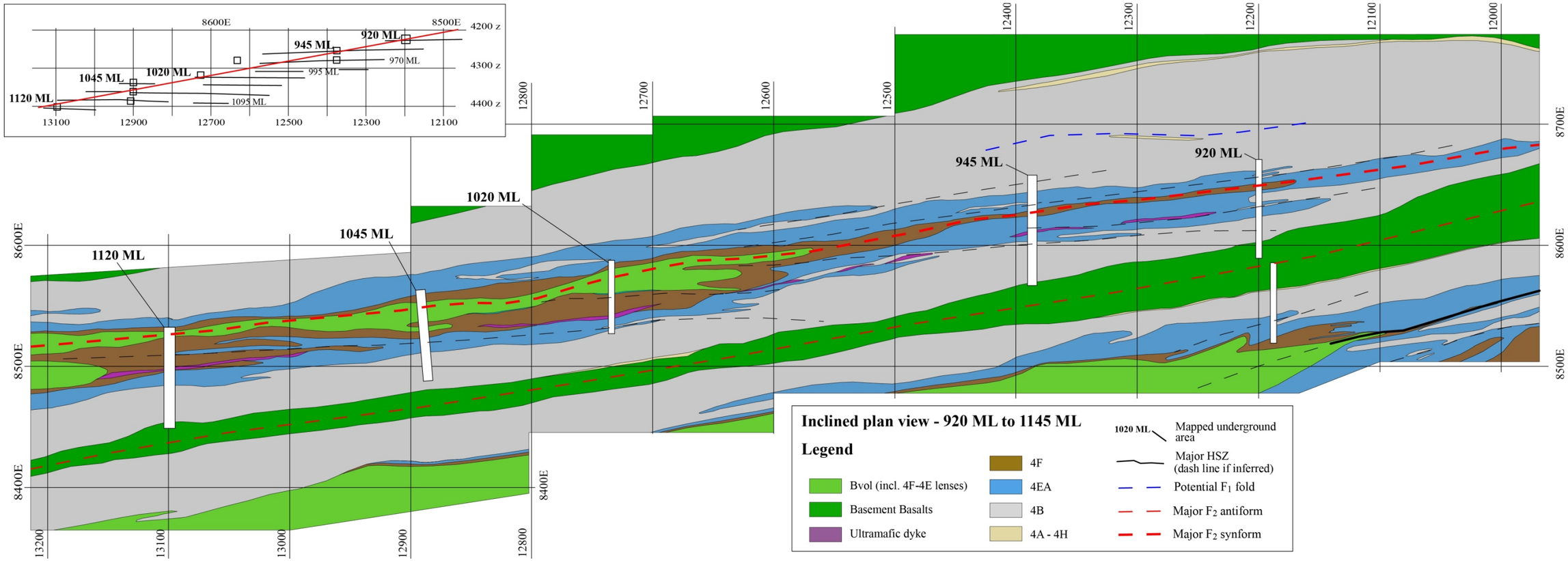

Figure 5-24: Inclined plan view of Musselwhite mine between mine levels 920 and 1145, with position of the plan with respect to the location of the studied mine workings (red line, upper left corner).

Limbs of tight F_2 folds are locally boudinaged. This is especially the case in the oxide-BIF (unit 4B) due to the competency contrast between chert bands and magnetite-rich bands. On PQ trench, boudins are developed both in plan and section views (Figure 5-27A, B). Beds of unit 4A and 4EA also stretched, albeit less extensively along the east limb of the mine synform. Back-rotated boudins suggest an apparent east-side-up vertical shear motion (Figure 5-27A) and apparent dextral kinematics on plane view (Figures 5-27B, C; 3-2). The long axis of boudins in oxide-BIF have two main orientations (Figure 5-27D): the well-defined $L_{1\text{-}2A}$, parallel to the axis of boudins, and the weakly-defined $L_{1\text{-}2B}$, which may reflect "chocolate tablet" style boudinage, reflecting two directions of stretching.

$S_{0\text{-}1\text{-}2}$ planes along limbs of tight to isoclinal F_2 locally display a shallowly northwest-plunging mineral lineation. It was documented exclusively in the garnet-biotite schist (unit 4F). This lineation is formed by the long axis of garnet porphyroblasts and their pressure shadow/recrystallization tails in the biotite matrix (Figure 5-28). This lineation tends to be absent in hinge zones.

5.4.2 S_2 foliation

In the mine area, S_2 is a penetrative foliation striking north-west and steeply dipping to the northeast or the southwest, which is axial planar to F_2 folds, (Figures 5-25E, 5-26E). In mafic volcanic rocks, S_2 is defined by amphibole and biotite (Figure 5-29A). In lithologies of the NIF, S_2 is generally weakly to moderately-developed due to the abundance of chert and garnet-amphibole or magnetite bands (Figure 3-26). S_2 is penetrative in massive (i.e., chert-free) garnet-biotite schist and in rare amphibole/biotite-rich beds of chert-rich oxide-BIF (Figure 5-29B).

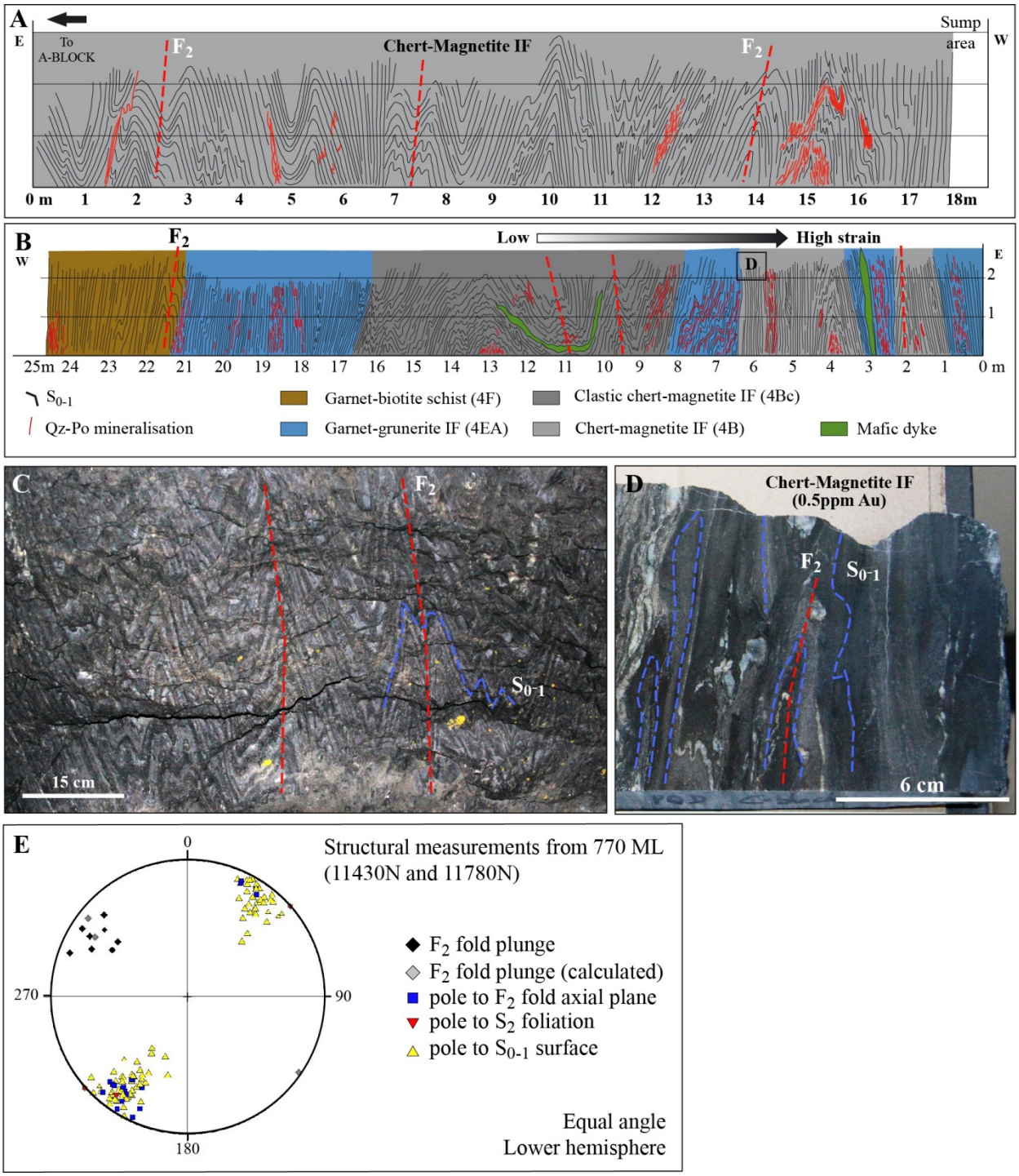

Figure 5-25: F_2 folds in the MASD. A. Face map of the mine level 770 at 11430 N section, facing south, showing typical similar folds in chert-magnetite BIF. B. Face map of the mine level 770 at 11780 N section, facing north, showing the strong strain gradient near a gold-mineralized high-strain zone (C-block ore zone; modified from Oswald et al., 2015a). C. Asymmetrical folds in unit 4B, north facing underground face at mine level 1020. D. Close-up view of a polished sample (see B for location) showing rootless and isoclinal F_2 folds in highly strained chert-magnetite BIF. E. Stereograph of structural measurements on mine level 770, equal angle and lower hemisphere. Calculated fold plunges come from S_{0-1} measurements.

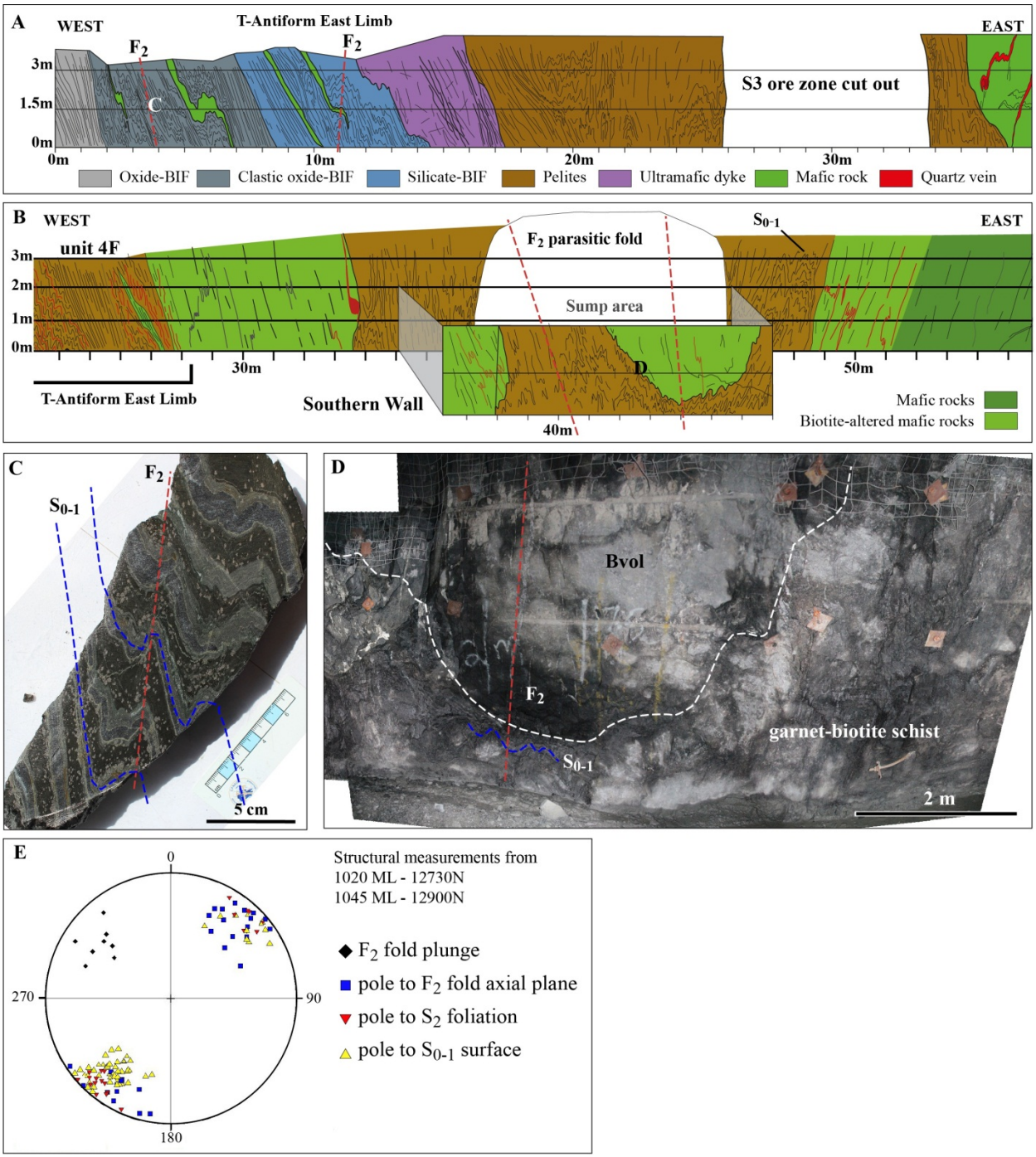

Figure 5-26: F_2 folds in the MASD. A. Mine level 1020 face map crosscutting the east limb of the T-antiform (Figure 5-21) and showing the distribution of F_2 folds in the various facies of the NIF. B. Mine level 1045 face map crosscutting a parasitic F_2 fold at the Bvol/NIF contact, near the east limb of the T-Antiform. C. Underground sample of clastic-rich oxide-BIF from mine level 1020 showing typical asymmetrical F_2 folds. D. Photograph of a south-facing wall on mine level 1045 showing the hinge zone of a shallowly NW-plunging F_2 fold at the Bvol/NIF contact. E. Stereograph of structural measurements from mine levels 1020 and 1045.

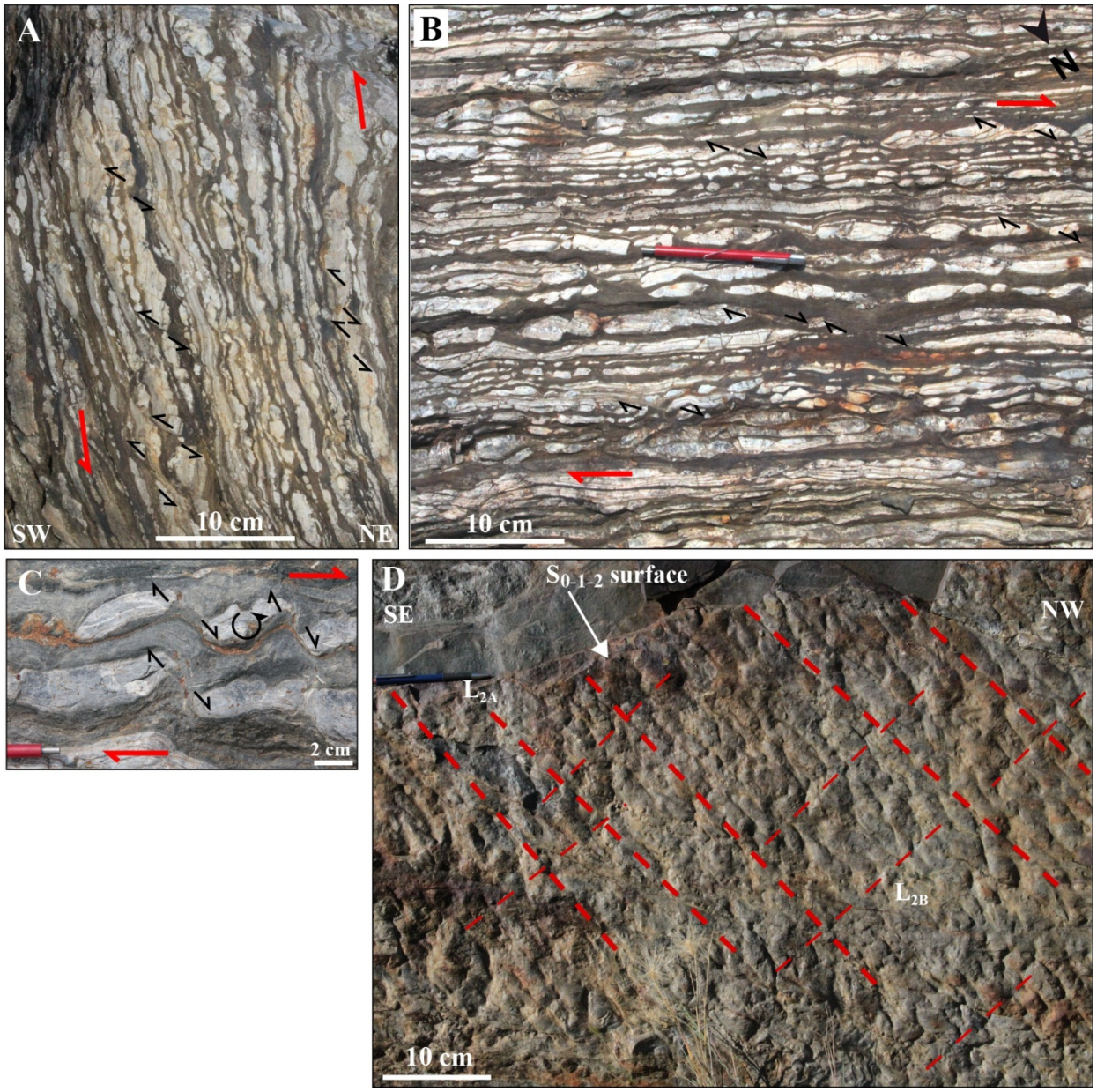

Figure 5-27: Photographs of boudinaged bed of unit 4B, PQ trench. A. Section view facing NW. B. Plan view facing south. C. Close-up on individual back-rotated boudins with relative motion and overall shear sense. D. Vertical view facing SW of a S_{0-1-2} surface.

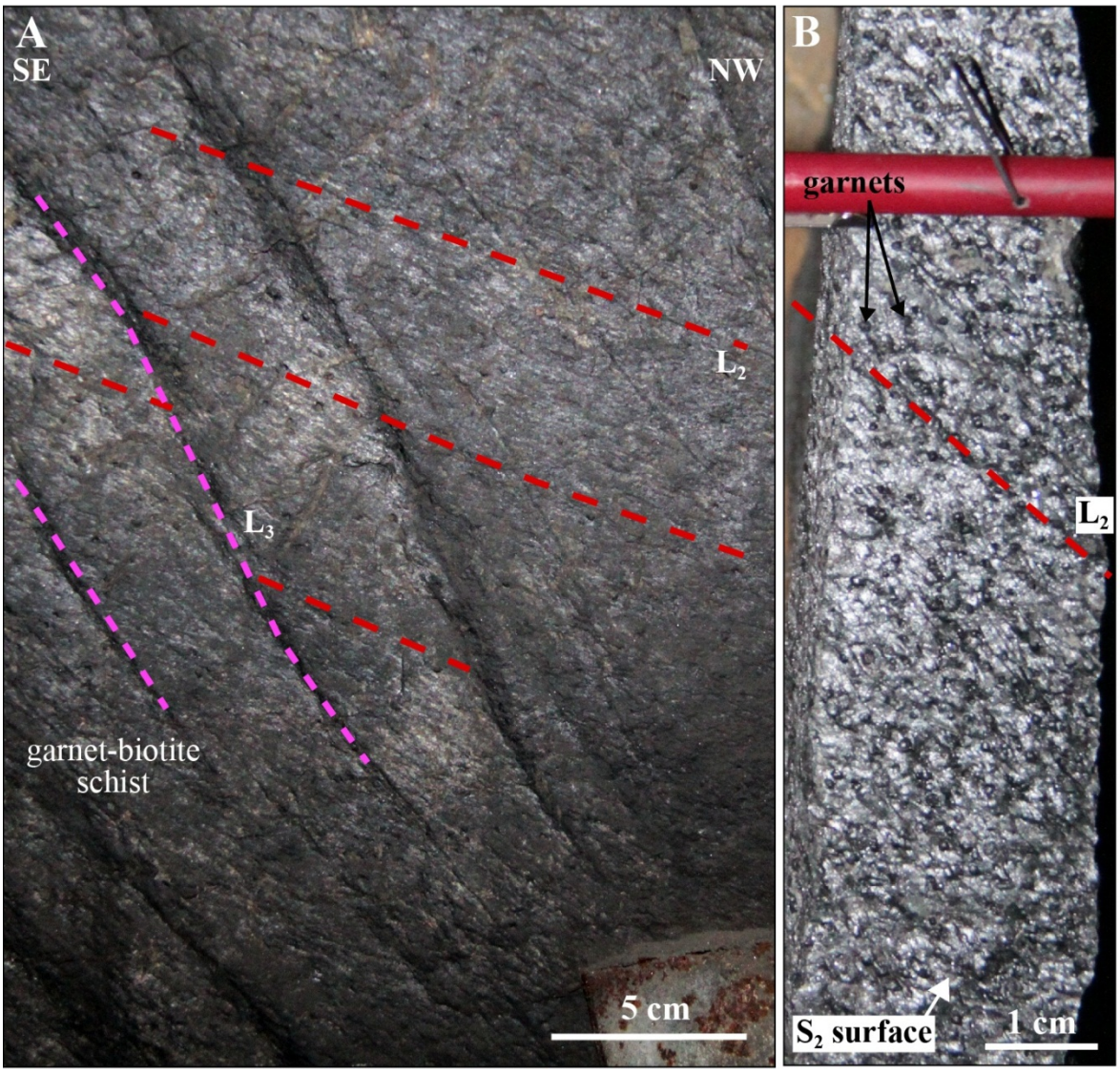

Figure 5-28: A. Underground exposure of garnet-biotite schist displaying L_2 mineral lineation and L_{2-3} intersection lineation on S_2 plane, mine level 720 "backdoor", section 11830 N. B. Close-up on the rough L_2 mineral lineation defined by garnet porphyroblasts, underground sample from mine level 720 "backdoor", section 11830 N.

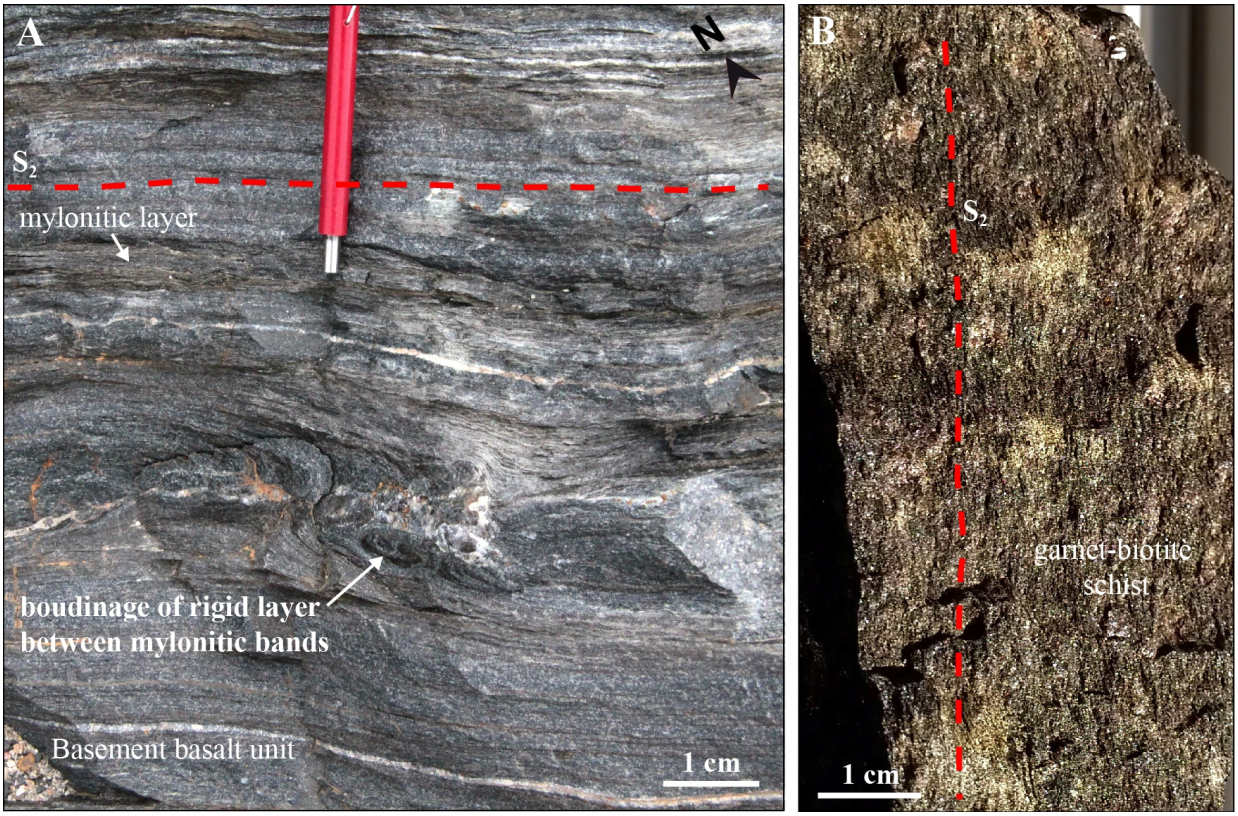

Figure 5-29a: S_2 foliation in the MASD. A. Penetrative S_2 in mafic rocks of the "Basement basalts" unit, PQ trench. B. Penetrative S_2 in garnet-biotite schist, sample from mine level 1020, section 12730 N, 8600 E.

5.4.3 Fault and shear zones

The higher strain intensity in the MASD, relative to the WASD, is not only evidenced by tighter F_2 folds and a penetrative S_2 fabric, but also illustrated by the development of high-strain zones. Those high-strain zones represent fault/shear zones and have a set of common characteristics that are best summarized by describing the "conveyor shear" (local name).

The conveyor shear is situated along the east limb of the East Bay synform (Figure 5-30A). It is a sub-vertical, northwest-trending, 1-4 metre-thick, strongly carbonatized (10-40% calcite) zone of sheared, biotite-altered mafic rocks (Figure 5-30C, D), which occurs along the entire extent of the mine (Figures 5-21, 5-22, 5-23). Within the strongly carbonatized zone, calcite largely dominates over other carbonates. Calcite is frequently intergrown with hornblende/actinolite and diopside, replacing the biotite-feldspar-quartz ± garnet assemblage (Figures 5-30C, D; 5-31A, B). The conveyor shear is not accessible in the upper part of the mine; however, a similar carbonate-altered shear zone occurs to the west (Figure 5-30A) and affects units Avol and Bvol (Figure 5-31C). At depth above the NIF, the "conveyor shear" comprises a series of thinner, more diffuse carbonate-altered high-strain zones (Figure 5-23). In the NIF below, BIF

units are marked by zones of intense folding to complete transposition of the compositional layering (Figure 5-31D). Gold mineralization is frequently spatially associated to these high-strain zones (chapter 7). The kinematic and displacement along the conveyor shear are unknown. Plan views of the high-strain zone show little evidence of asymmetrical features or kinematic indicators (Figure 5-30D). Section views from drill core intersections and underground faces show abundant asymmetrical features, such as quartz-carbonate sigmoids, and suggest a dip-slip component, with a tentative west-side-down sense of motion.

The "B-block shear" (local name) is a similar, intensely carbonate-altered high-strain zone that is located east of the conveyor shear (Figure 5-30A). It is mapped from section 11400 N to section 12400 N and affects the Bvol and faulted limb of an isoclinal antiform-synform pair outlined by the NIF (Figure 5-30A, B; Figure 5-32). Goldcorp's maps and sections do not show evidence of intense strain in the underlying BIF, which would indicate that the B-block shear does not extend down-section. As for the conveyor shear, the sense of motion and displacement along the B-block shear zone is unconstrained.

Overall, observations suggest that the conveyor shear and parallel similar high-strain zones played a significant role in accommodating deformation, presumably during the late stage of D_2 deformation. The carbonate alteration is likely related to the gold-bearing hydrothermal alteration event (chapter 7). Alternatively, a portion of this large-scale carbonate-replacement may also be due to CO_2 devolatilisation during late metamorphism of the underlying BIF (chapter 6).

A lenticular slice of the NIF hosting ore zones (B-block; chapter 7) is delineated by the conveyor and B-block shear zones along the eastern limb of the East Bay synform. Its nature and significance are unequivocal, but may have implications for exploration. Goldcorp's geologists have previously interpreted this structure either as a sheath fold or as the result of late brittle sinistral strike-slip faulting.

The geometry of the lenticular slice evolves from south to north as portrayed on selected mine sections (Figure 5-32): On section 11430 N (Figure 5-32A), it occurs as a lens of unit 4F surrounded by unit Bvol, gradually thickens and lengthens northward along-strike to include other facies of the NIF (Figure 5-32B to D). This slice progressively merges with the main NIF horizon near section 11750 N to become a second-order isoclinal antiform of the East Bay synform. Concurrently, mafic rocks of unit Bvol laying east of this portion of the NIF thin out to the north and ultimately disappear on section 12600 N, where the slice merges with the NIF of the eastern limb of the East Bay synform.

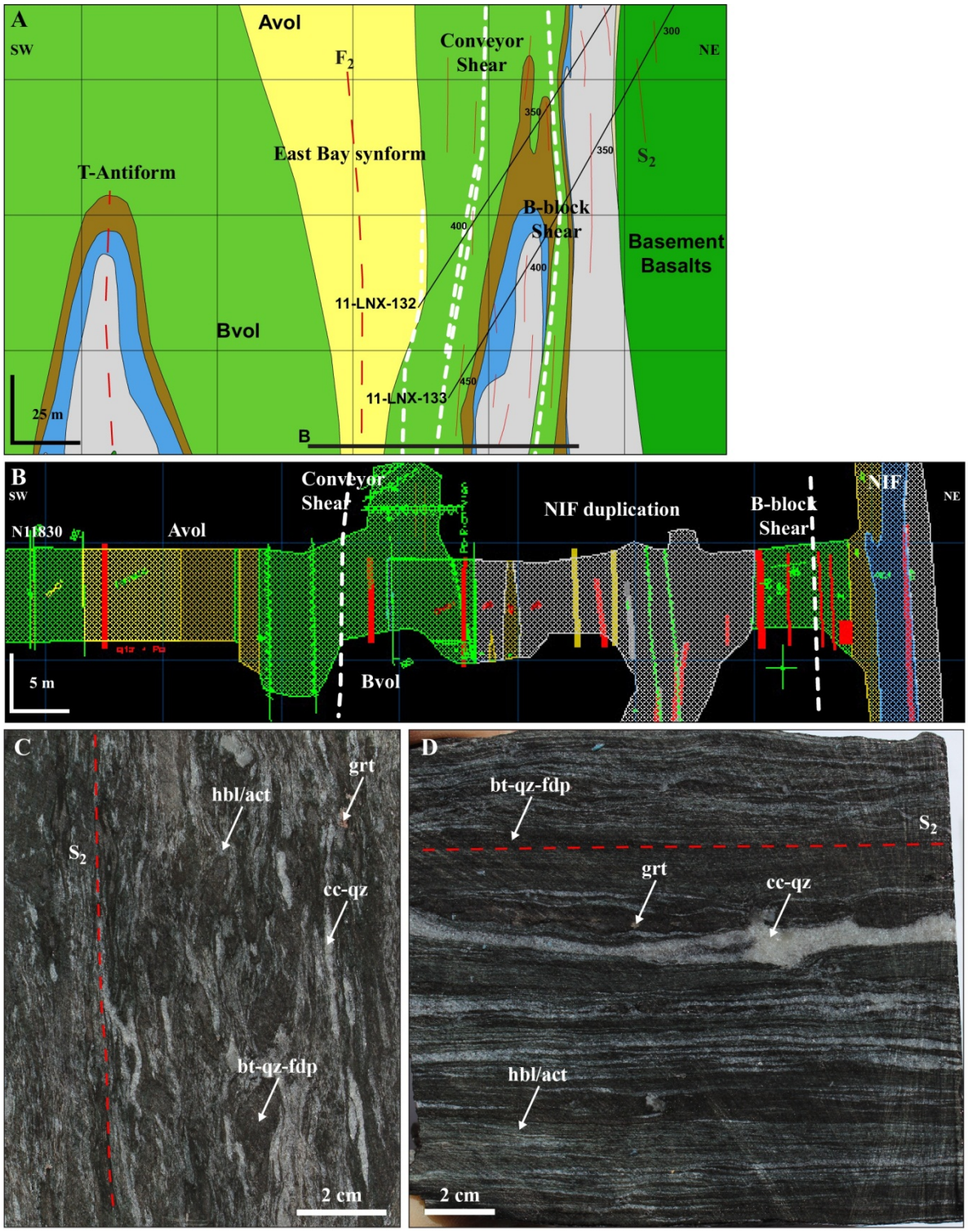

Figure 5-30: Carbaonte-altered HSZ in the mine A. Close-up of the 12000 N mine section showing the position of the conveyor and B-block shear zones, and the relative position of mine level 720 (B). B. Geological map of the mine level 720 "backdoor" crosscut to A-block and B-block on section 11830 N. C. Polished slab (vertical section perpendicular to S_2) of an underground sample showing carbonate-altered mafic rocks within the conveyor shear, mine level 570. D. Polished slab (horizontal section perpendicular to S_2) of an underground sample of carbonate-altered mafic rocks within the conveyor shear, mine level 620.

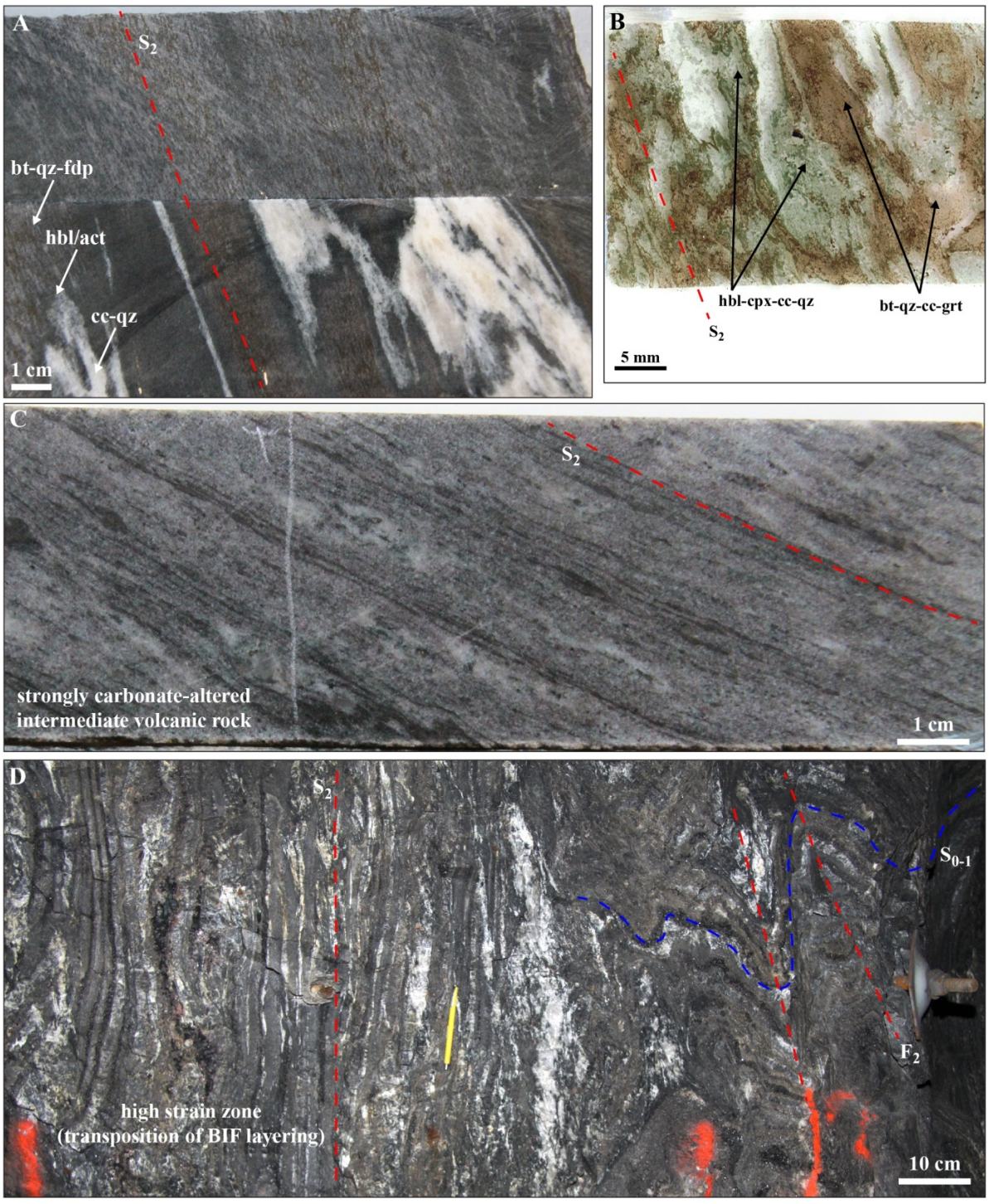

Figure 5-31: Carbaonte-altered HSZ in the mine A. Drill core segments showing the overprint of carbonate alteration and veinlets on biotite-altered mafic rocks in the vicinity of high-strain zones (sample MW-13-028, DDH 09-TAN-029, @128.5 m, section 11775 N). B. Thin section of mafic rock sample MW-12-164 (DDH 06-PQE-091, @87.75-88 m, section 11775 N) showing the hornblende-clinopyroxene assemblage overprinting the biotite-garnet-calcite assemblage in the B-block shear zone. C. Drill core segment of a strongly carbonate-altered intermediate volcanic rock of unit Avol (sample MW-13-287, DDH 11-LNX-132, @431 m). D. Underground exposure of a high-strain zone in facies 4EA. Note the strong transposition of the layering, parallel to the sub-vertical S_2, mine level 770, 11780 N crosscut (photo B. Dubé).

Besides the previously invoked models, there are alternative interpretations for this complex but economically important structure (chapter 7): One is that it results from the interplay of dip-slip motions along the adjacent coalescent shear zones oriented at an angle oblique to that of F_2 axial planes. A similar explanation involving strike-slip motion appears unlikely as no horizontal kinematic indicators have been documented so far. Another option involves a pre-existing F_1 fold(s), potentially associated with a fault zone, subsequently refolded by the East Bay synform. This hypothesis is supported by the presence of slivers of unit 4A within unit 4B, near the hinge zone of the East Bay synform, which may represent the nose of synclinal F_1 folds refolded by an F_2 fold; similar neighbouring 4EA slivers may then correspond to F_1 anticlinal fold noses (Figures 5-24; 5-32C, D).

5.4.4 Evidence of high D_2 deformation intensity

The development of carbonate-altered high strain zones in mafic volcanic rocks structurally above the NIF is symptomatic of the high intensity of D_2 deformation (Figure 5-32). It is also illustrated by the extreme tightness of the East Bay synform, the attenuation of its eastern limb, and associated thickening of the fold hinge zone (Figure 5-21 to Figure 5-24). Furthermore, folds limbs are locally affected by ductile fault zones that tend to fan around the axial plane of the main fold (Figure 5-33A, B). These zones affect the NIF sequence in a similar way than mesoscopic shear bands affecting the $S_{0\text{-}1}$ in oxide-BIF (unit 4B; Figure 5-33C).

As deformation intensity increases, thickened fold hinge zones comprising competent layers form more rigid features, inducing strain to concentrate along fold limbs, which progressively pinch and become inverted between hinge zones. This is documented at band-scale in oxide-BIF (Figure 5-33D) and at mine-scale on PQ trench, where the east limb steeply dips to the east (Figure 5-20).

BIF tend to accommodate more strain compared to the surrounding volcanic rocks (Figure 5-10A and 5-34A). The high intensity of D_2 strain leads to strongly disrupted and transposed compositional layering in the BIF. This is notably illustrated on mine level 280, Esker area, located in the upper part of the east limb, where a section of the NIF is exposed. Centimetre-scale F_2 folds are isolated by the development of detachment surfaces (Figure 5-34B, C), and boudinage is well-developed (Figure 5-34D), similarly to that of PQ trench (Figure 5-27).

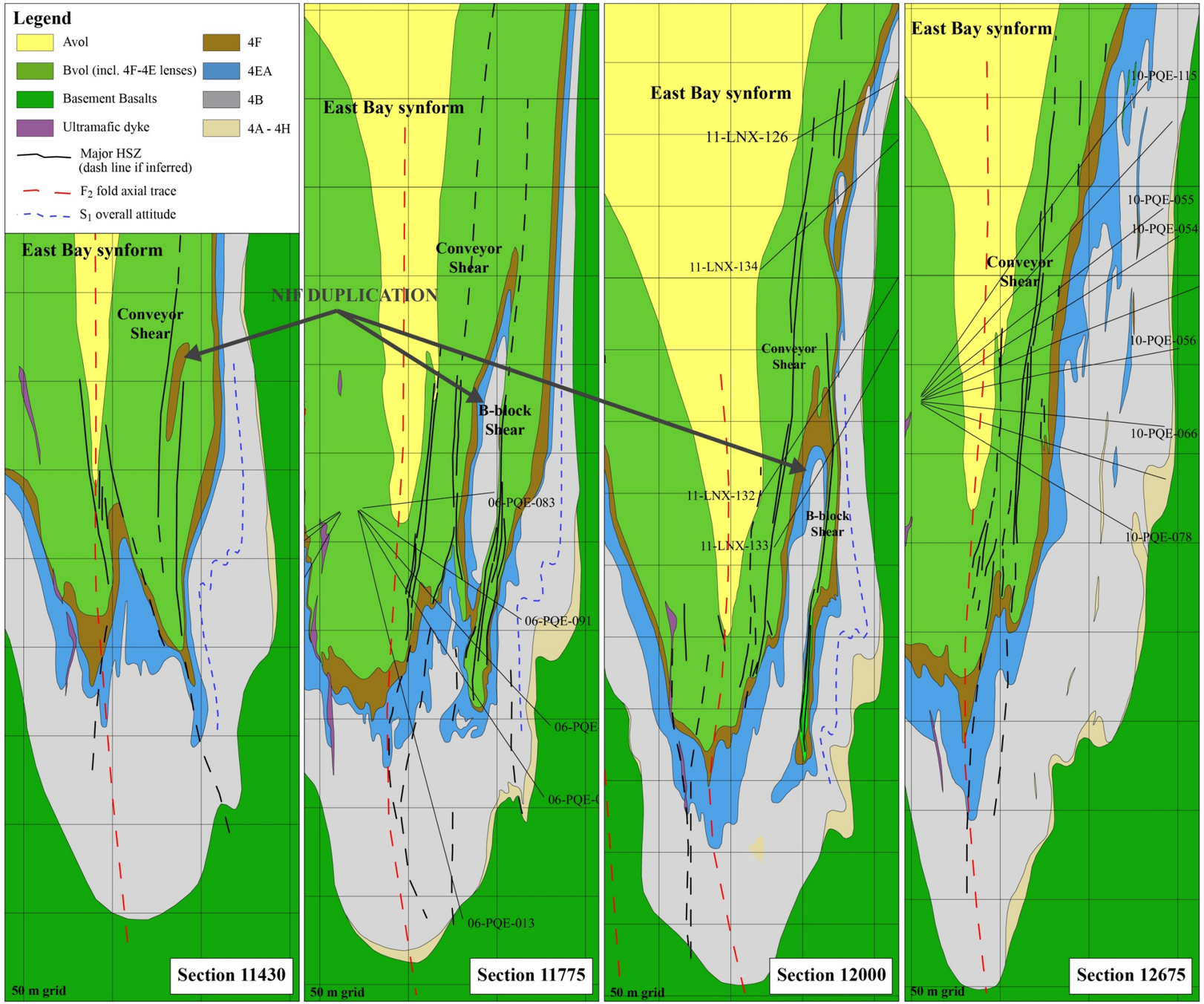

Figure 5-32: Geometry of the NIF Duplication Structure. A. Section 11430 N. B. Section 12775 N (335 m north of A). C. Section 12000 N (225 m north of B). D. Section 12675 N (675 m north of C).

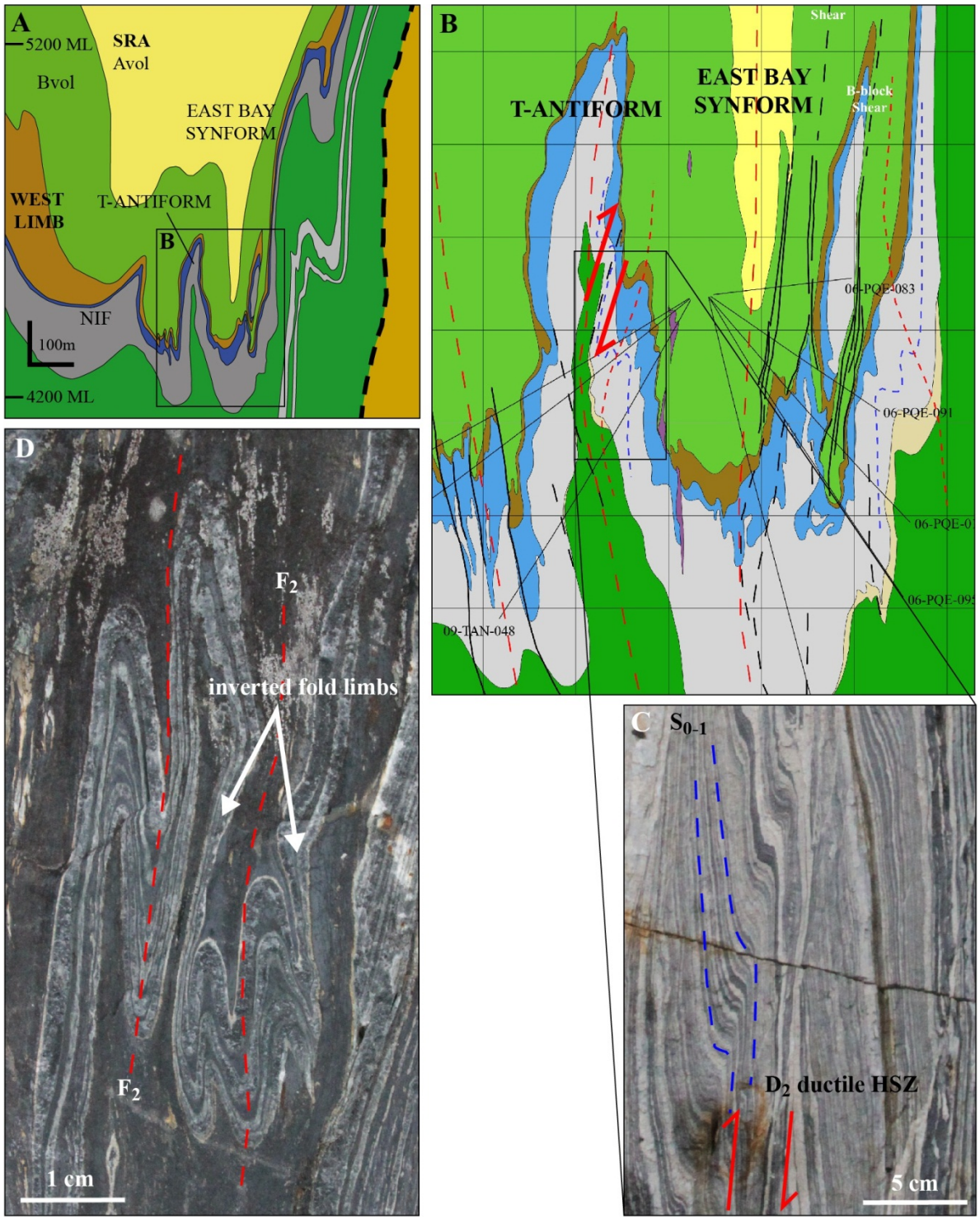

Figure 5-33: Fold limb inversion and shear bands A. Simplified geological section of Musselwhite mine at 11775 N. B. Geological interpretation of the T-antiform and the East Bay synform on section 11775 N. The geometry of the NIF envelope shows thickening and attenuation zones suggestive of the presence of ductile high-strain zones. C. Mesoscopic ductile high-strain zone documented in oxide-BIF from the Trench 4 exposure, West antiform area. The BIF compositional layering has an envelope comparable to that of the NIF on B. D. Mesoscopic F_2 fold limb inversion in oxide-BIF, Trench 4, West antiform area. This is similar to mapping done in the PQ trench and interpreted mine sections.

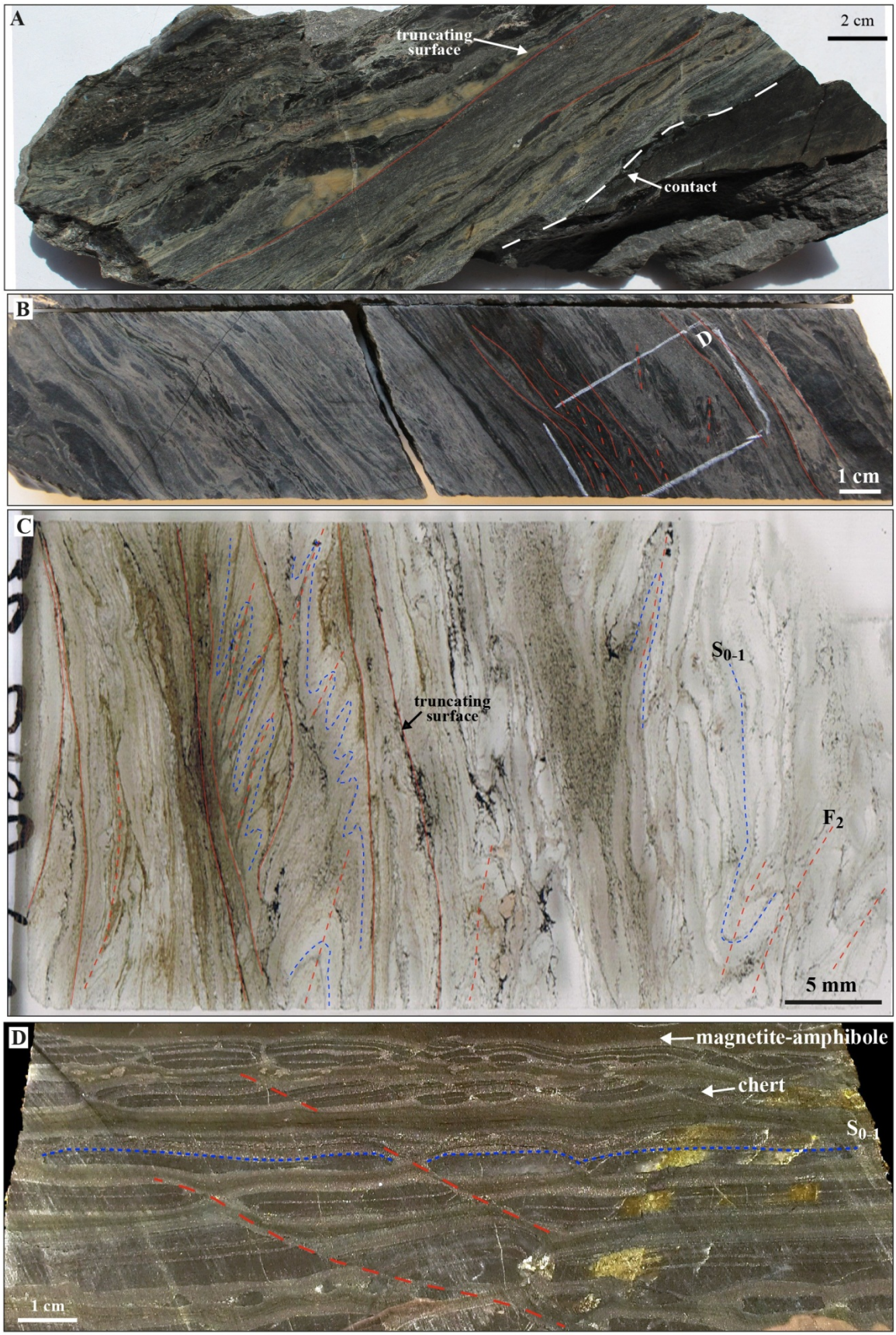
A
truncating surface
2 cm
contact
B
D
1 cm
C
truncating surface
S_{0-1}
F_2
5 mm
D
magnetite-amphibole
chert
S_{0-1}
1 cm

Figure 5-34: Detachment structures in the BIF A. Grab sample of intensely deformed chert-grunerite BIF (unit 4A) in contact with foliated and biotite-altered mafic rocks of the "Basement basalts", mine level 280, Esker area. B. Drill core segment of chert-grunerite BIF showing the intense disruption of BIF layering through folding, boudinage, and faulting (sample MW-13-351, DDH 12-PIL-001, mine level 280, Esker area). C. Thin section from sample MW-13-351 showing the development of detachment surfaces in the BIF. D. Slab of strongly boudinaged chert-magnetite BIF (unit 4B), mine level 280, Esker area.

5.4.5 First-order structure

The northeastern contact between the NCG and the Schade Lake gneissic complex is marked by a series of ductile fault zones, which are termed the "North Rim fault" (NRF; Breaks et al., 2001), in the Eyapamikama Lake area, the Dinnick Lake shear zone north of Opapimiskan Lake (DLSZ; Gagnon et al., 2016), and the Totogan shear zone (TSZ; chapter 2) in the eastern part of the NCG. Although these fault segments may have different kinematics and timing, they likely form the same first-order structure.

Reconnaissance geological mapping north of the Opapimiskan Lake area consisted in traverses across the DLSZ and Akow Lake shear zone (ALSZ), which occurs west and parallel to the DLSZ (Figure 5-1). The ALSZ juxtaposes the ELS against the NRA along a zone of moderately to strongly deformed, locally mylonitic mafic rocks. A east to west section across the DLSZ shows that the main fabric in rocks of the Schade Lake Gneissic Complex evolves from a moderately (37°) east-dipping to a sub-vertical intense foliation at the contact with the NCG (Figure 5-35B). This steepening appears to be accompanied by a shift in azimuth from N350° to N334°. Across the main contact within rocks of the NRA, the main fabric shows local orientation variations (N130° to N170°) but remains very steep to sub-vertical. Asymmetric z-shaped F_2 folds with shallow to moderate SSE- and NNW-plunging axis and back-rotated quartz vein boudins suggest dextral transpression (Figure 5-35A). These observations are consistent with previous studies (Breaks et al., 2001; Van Lankvelt, 2013; Gagnon et al., 2016). Implications on the regional evolution of the NCG are discussed in chapter 10.

The possible southward extension of the ALSZ and DLSZ was investigated by studying cores of a SW-dipping exploration drill hole (11-282-003; Figure 3-26), collared east of Musselwhite mine. Around 700 m down-hole, drill core segments include schists of the ZHA with a strong, eastward increasing strain gradient. It is evidenced by the progressive development of a steeply NNE-dipping mylonitic fabric and strong mineral recrystallization/segregation (e.g., quartz-feldspar bands alternating with biotite-rich bands; Figure 5-36A), and an increase in the proportion of sheared quartz vein boudins. Kinematic indicators are globally scarce, but the vergence of microscopic folds in mylonitised metasedimentary rock of the ZHA suggests an east-side-up component of motion (Figure 5-36B).

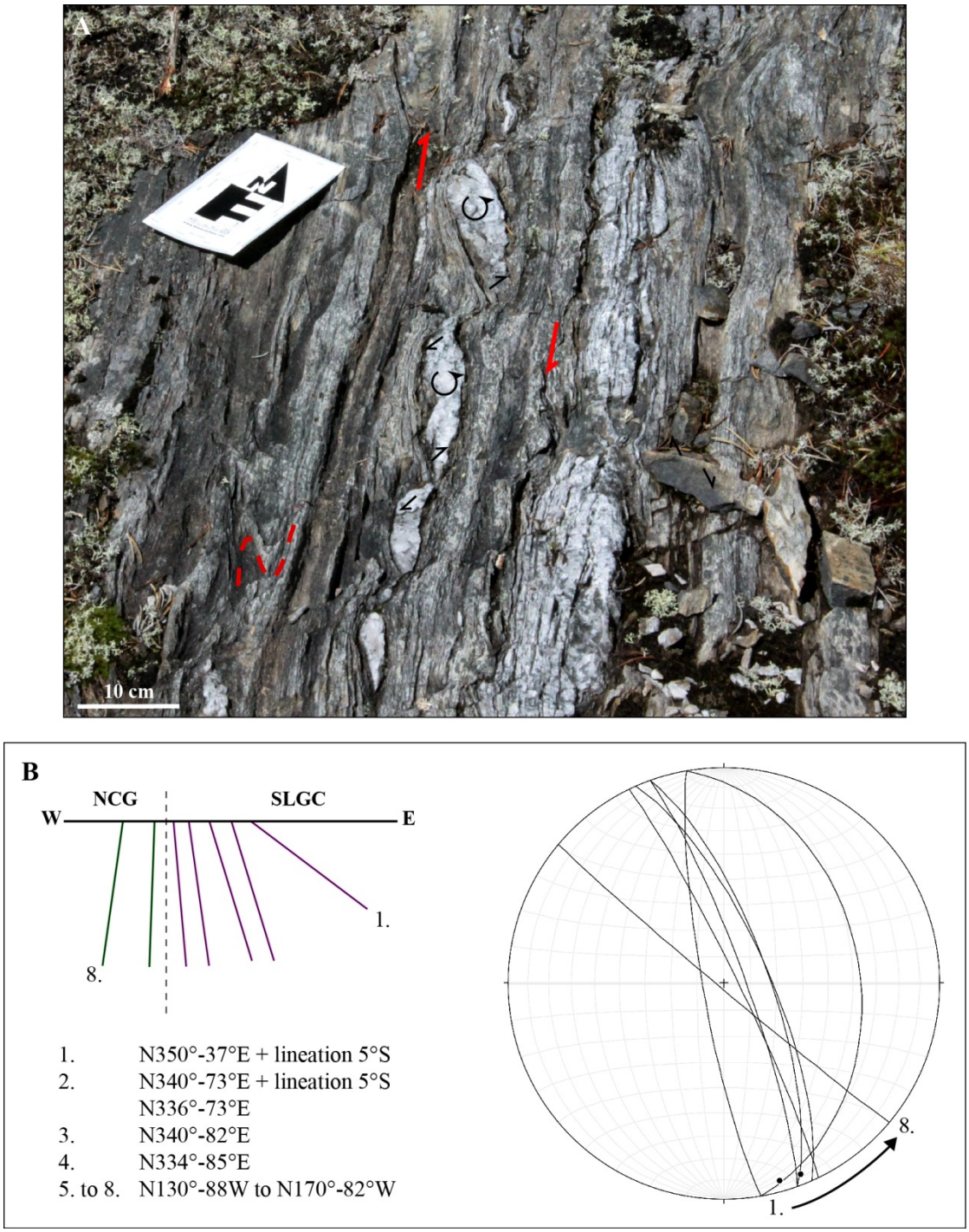

Figure 5-35: Akow Lake and Dinnick Lake shear zones. A. Strongly foliated mafic rocks with asymmetric folds and back-rotated quartz vein boudins. B. Schematic section across the Dinnick Lake shear zone (not to scale) showing the variations in orientation of the main fabric, with stereograph (equal angle, lower hemisphere).

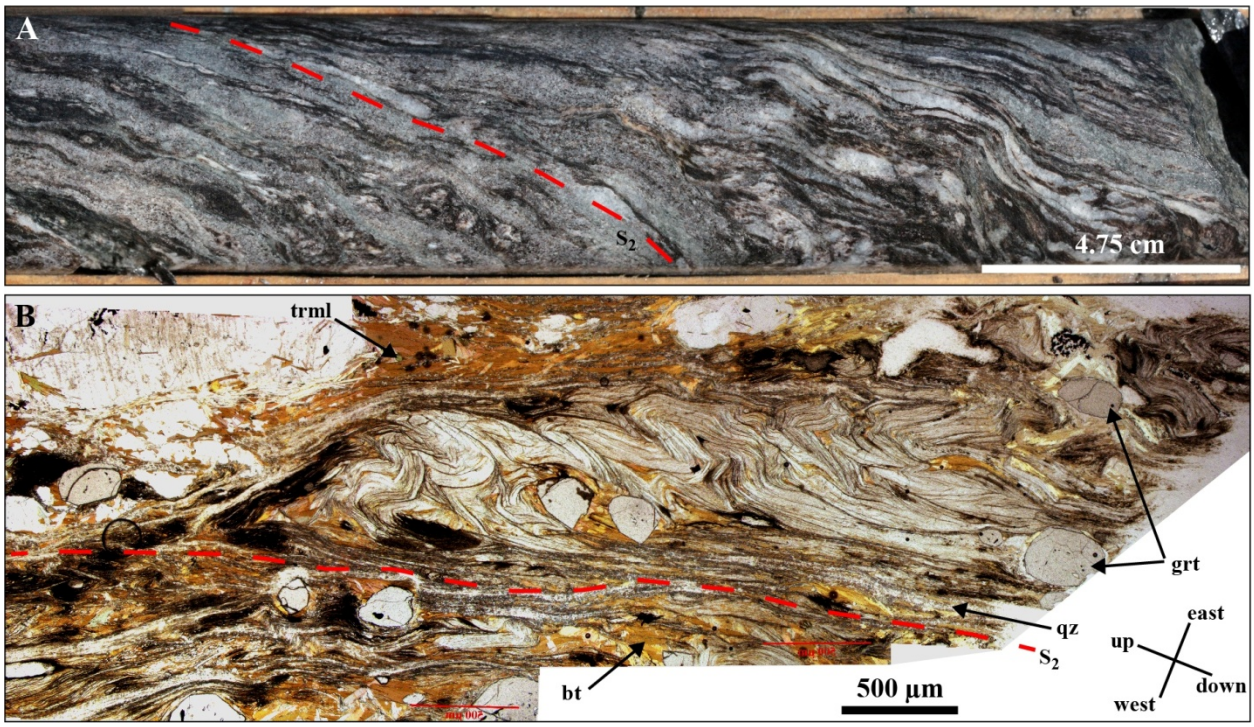

Figure 5-36: NCSZ. A. Mylonitised metasedimentary rock of the ZHA. B. Microphotograph of a strongly deformed quartz-biotite-muscovite matrix, sample MW-13-328, DDH 11-282-003, @700 m depth.

5.5 D_3 deformation

The D_3 deformation phase postdates the main regional metamorphic event in the Opapimiskan Lake area (Breaks et al., 2001; Hall and Rigg, 1986). D_3 deformation is present in all structural domains, yet discreet and unevenly distributed. Orientations of D_3 fabrics slightly vary due to the nature and pre-existing structural complexity of the bedrock. The intensity of D_3 structural features increases to the southeast, culminating at the Markop Lake shear zone (chapter 2).

5.5.1 F_3 folds

F_3 folds are open to close, Z-shaped and plunge moderately to the WSW (Figure 5-37A). A second, possibly conjugate, set of folds occurs in the WASD, locally producing polyclinal, box-type F_3 folds (Figure 5-37B; McClay, 1987). F_3 folds are generally best developed in strongly anisotropic rocks, such as mylonitic volcanic rocks or BIF (Figure 5-37B, C, D).

In BIF, F_3 Z-folds are present as weak to well-developed distortion of F_2 folds and $S_{0\text{-}1}$ layering (Figure 5-38A). F_3 are frequently associated with diverse subordinate structures, including localized faults and shear zones, slip surfaces, and drag folds (Figure 5-38B). In rigid lithologies, such as felsic rocks, F_3 folds

include axial planar quartz veins (Figure 5-39). They are interpreted as tension gashes resulting from differential strain partitioning. Locally, decametre-scale F_3 folds are implied by the occurrence of doubly-plunging F_2 folds, as documented on the WAT1 exposure, where it produced a canoe-shaped fold interference pattern (Figure 5-6Figure 5-15C). At hectometre- to kilometre-scale, the thick packages of volcanic rocks hosting the BIF sequences prevent the development of sub-regional-scale F_3 folds. As illustrated on PQ trench, they only form 100-m wavelength undulations (Figure 5-20).

5.5.2 S_3 foliation

The axial-planar S_3 foliation varies from a spaced-cleavage to a penetrative crenulation, which affects S_{0-1} and S_2, forming millimetre- to centimetre-scale kink bands and chevron-style folds. The main S_3 strikes in average at 250° N and dips 60-70° to the NW. A less common, conjugate sub-set (S_3') trends at 180-190° N and dips 60° to the W (Figure 5-37A). The latter set is best developed in protomylonitic to mylonitic ultramafic and mafic rocks (Figure 5-40A), such as those on PQ trench (Figure 5-20), in the finely laminated chert-magnetite facies of BIF (Figures 5-40B, C; 5-41A), and in clastic-rich beds (Figure 5-41B). S_3 affects and locally kinks the previous paragenesis, but it is not associated with a significant metamorphic assemblage or recrystallization (Figure 5-42).

5.5.3 L_3 lineation

No mineral or stretching lineation is associated with D_3. Locally, the intersection trace of S_3 on S_{0-1} or S_2 planes forms a crenulation lineation, which is collinear with the axes of F_3 (25 to 60° toward 250°N). Best examples are documented in laminated chert-magnetite BIF in the West antiform area (Figure 5-19C; WAT1, Trench 4) and underground in unit 4F (garnet-biotite schist; Figure 5-28A).

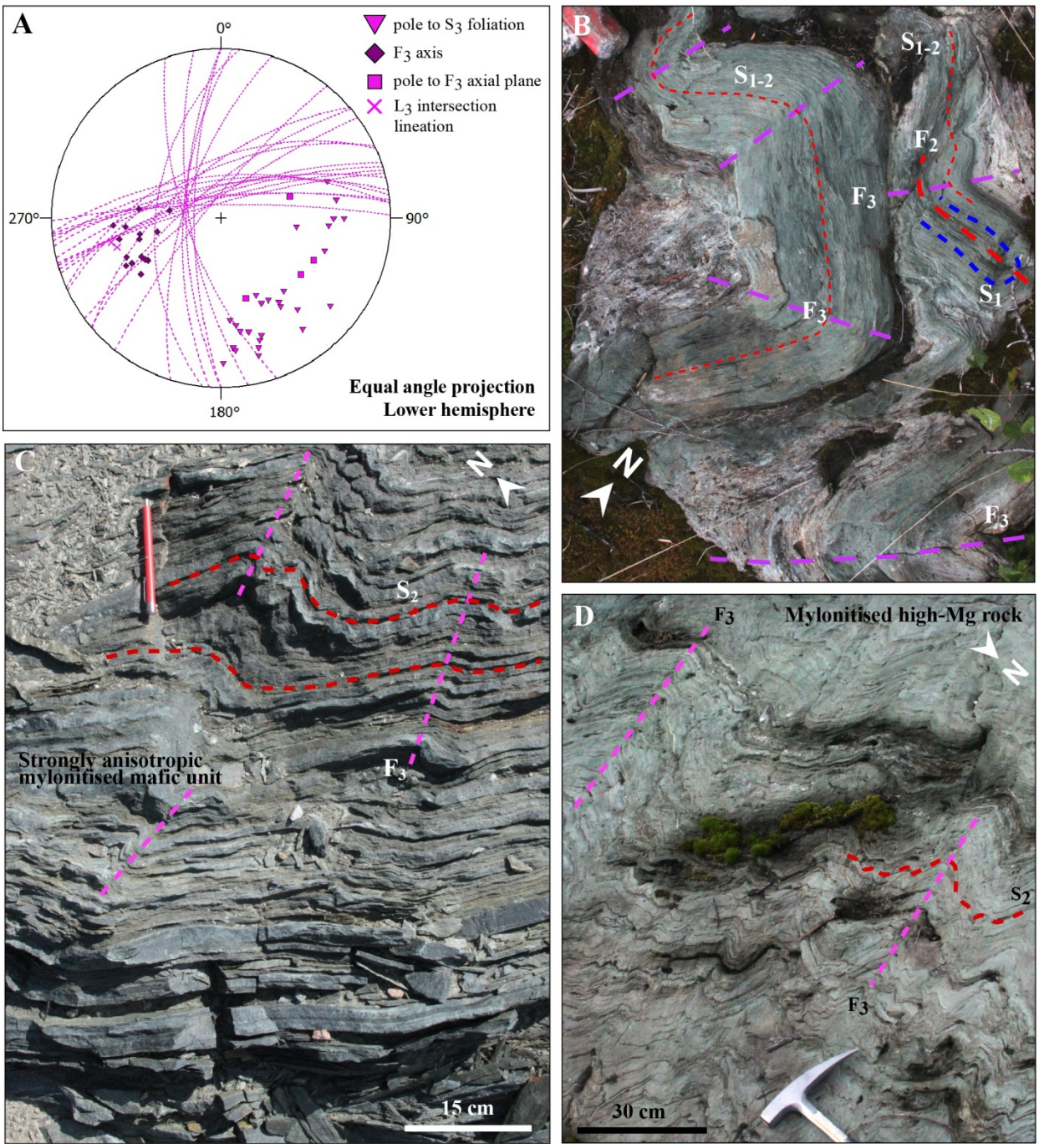

Figure 5-37: F_3 folds. A. Stereographic projection of D_3 fabrics. Most folds plunge WSW with an axial planar foliation; however, a S-trending foliation subset is also documented. B. Polyclinic F_3 fold in strongly foliated ultramafic rocks, northwestern shore of Zeemel Lake, West antiform area. C. Asymmetric F_3 folds in mylonitised pillowed tholeiites of the "Basement basalts" unit on PQ trench, MASD. D. F_3 folds and penetrative S_3 in mylonitised high-Mg rocks of the "Lower basalts" unit, unnamed exposure, West antiform area, UTM 674563/5828631.

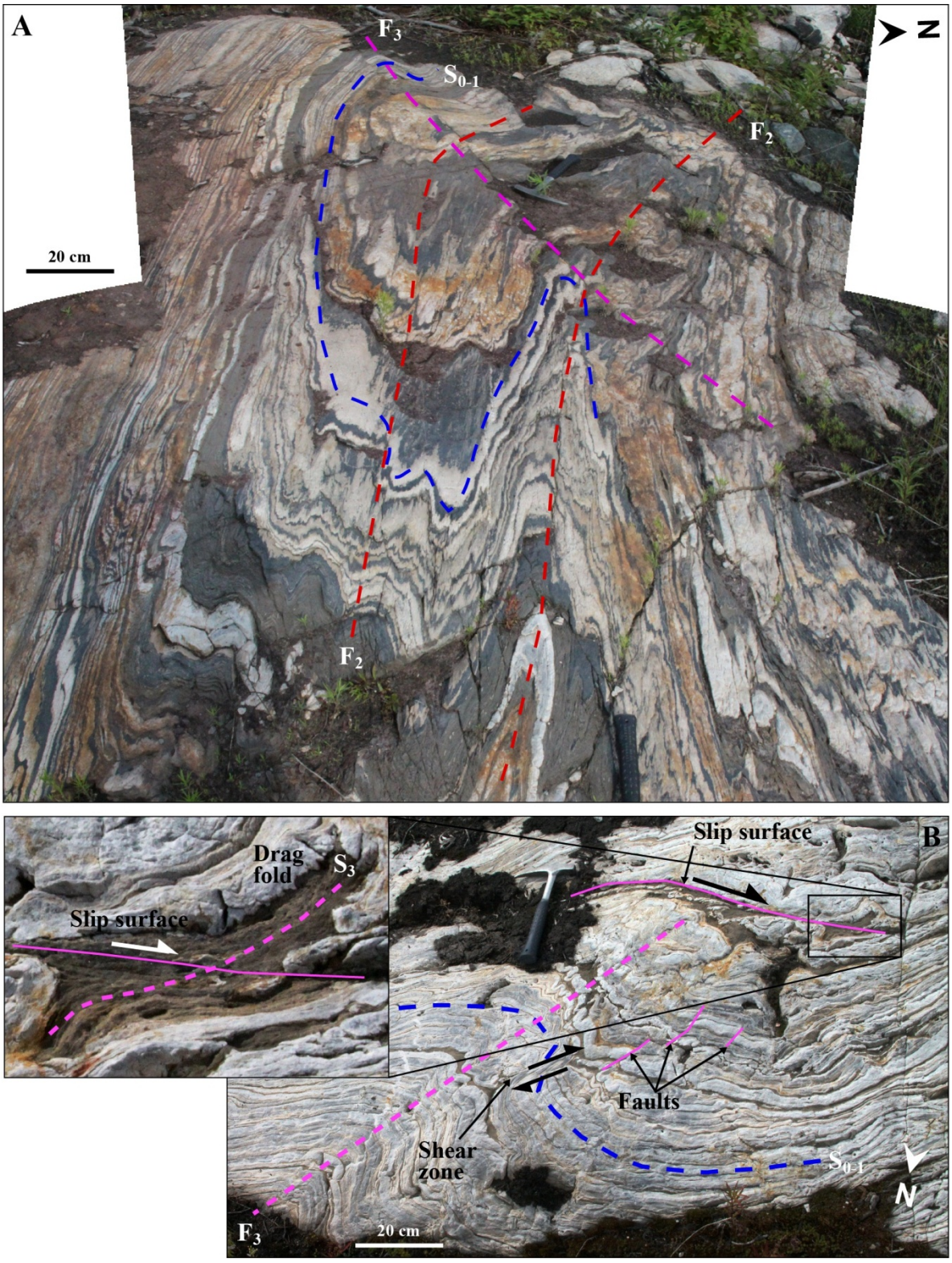

Figure 5-38: A. F_2-F_3 fold interference in BIF, Trench 4 exposure, West antiform area. See Figure 5-41A for structural fabric relationships. B. F_3 and secondary structural features in chert-rich BIF along an F_2 limb, unnamed exposure 350 m SW of Trench 4, West antiform area, UTM 676130/5832295.

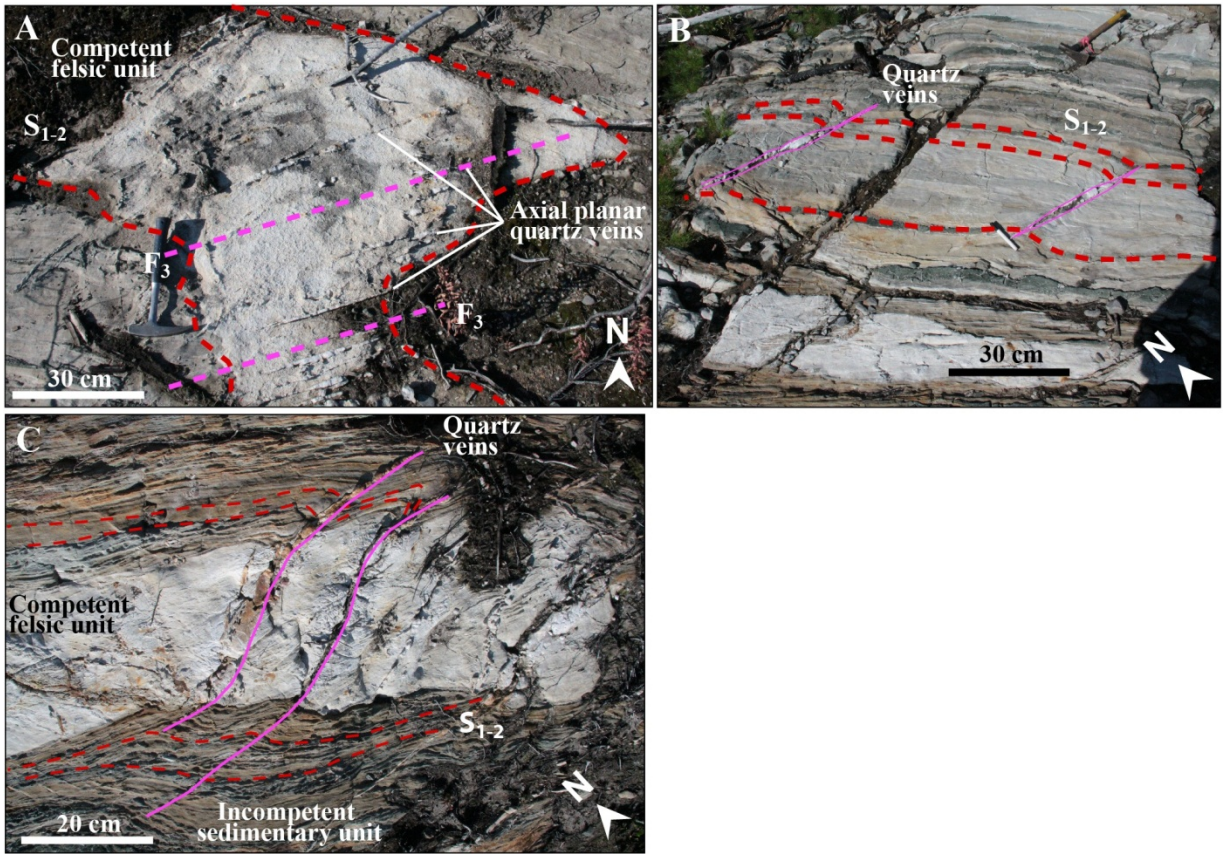

Figure 5-39: A. Folded felsic unit in ZHA sediments displaying axial planar quartz veins, surface exposure near UTM 686418/5826235. B. West-trending quartz veins filling inter-boudin spaces in quartz-rich beds of ZHA sedimentary rock, surface exposure near Graff Lake (UTM 684200/5827200). C. West-trending quartz veins formed in a competent felsic unit and axial-planar to open F_3 folds in fine-grained ZHA sedimentary rock, same exposure as B.

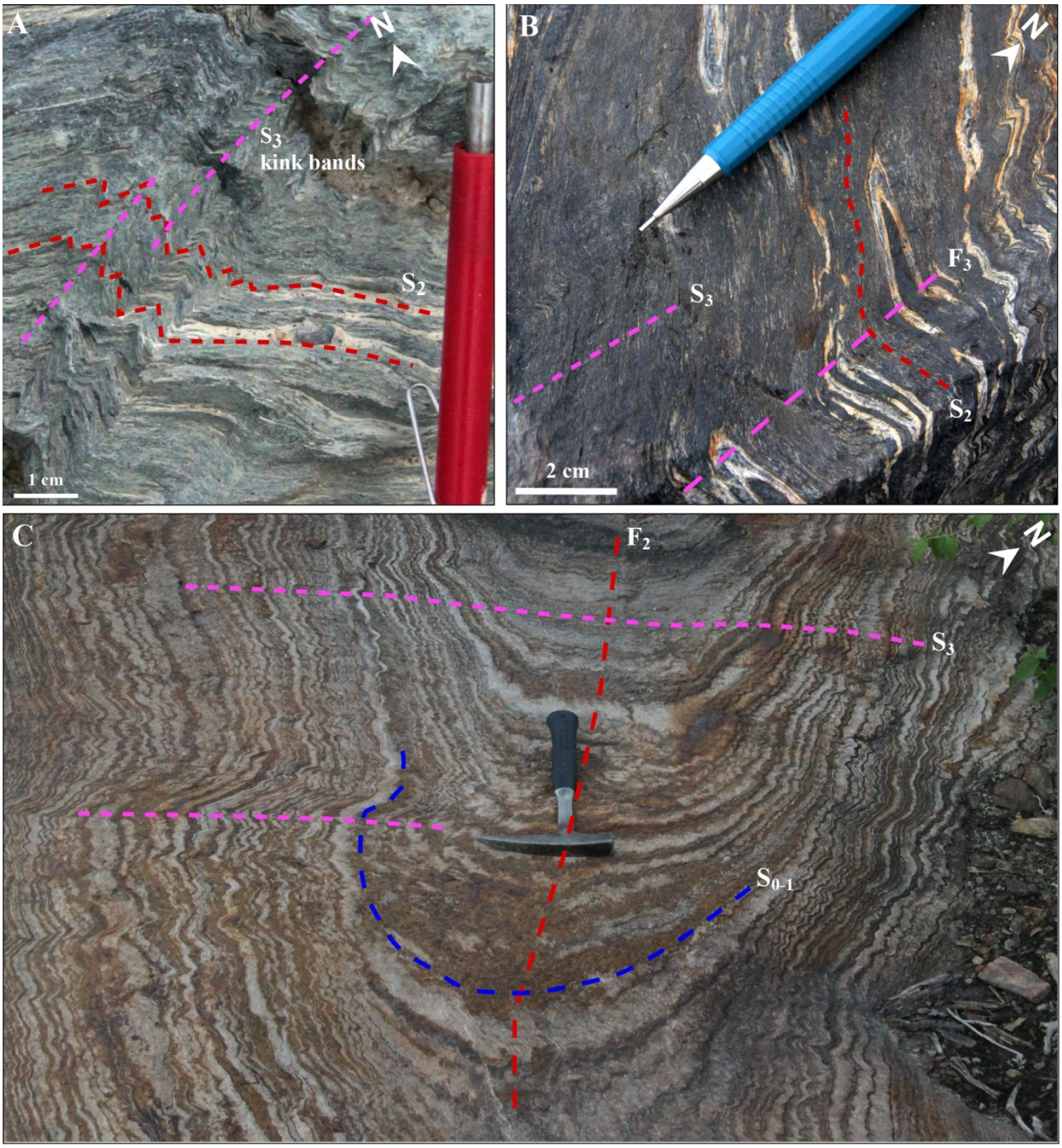

Figure 5-40: S_3 foliation at Trench 4, West antiform area. A. S_3 kink bands in mylonitised tholeiites of the "Basement basalts" unit on PQ trench, MASD. B. SSW-trending S_3 crenulation in magnetite-rich oxide-BIF. C. S_3 crenulation and F_3 folds overprinting the F_2-folded S_{0-1} compositional layering, Trench 5, West antiform area.

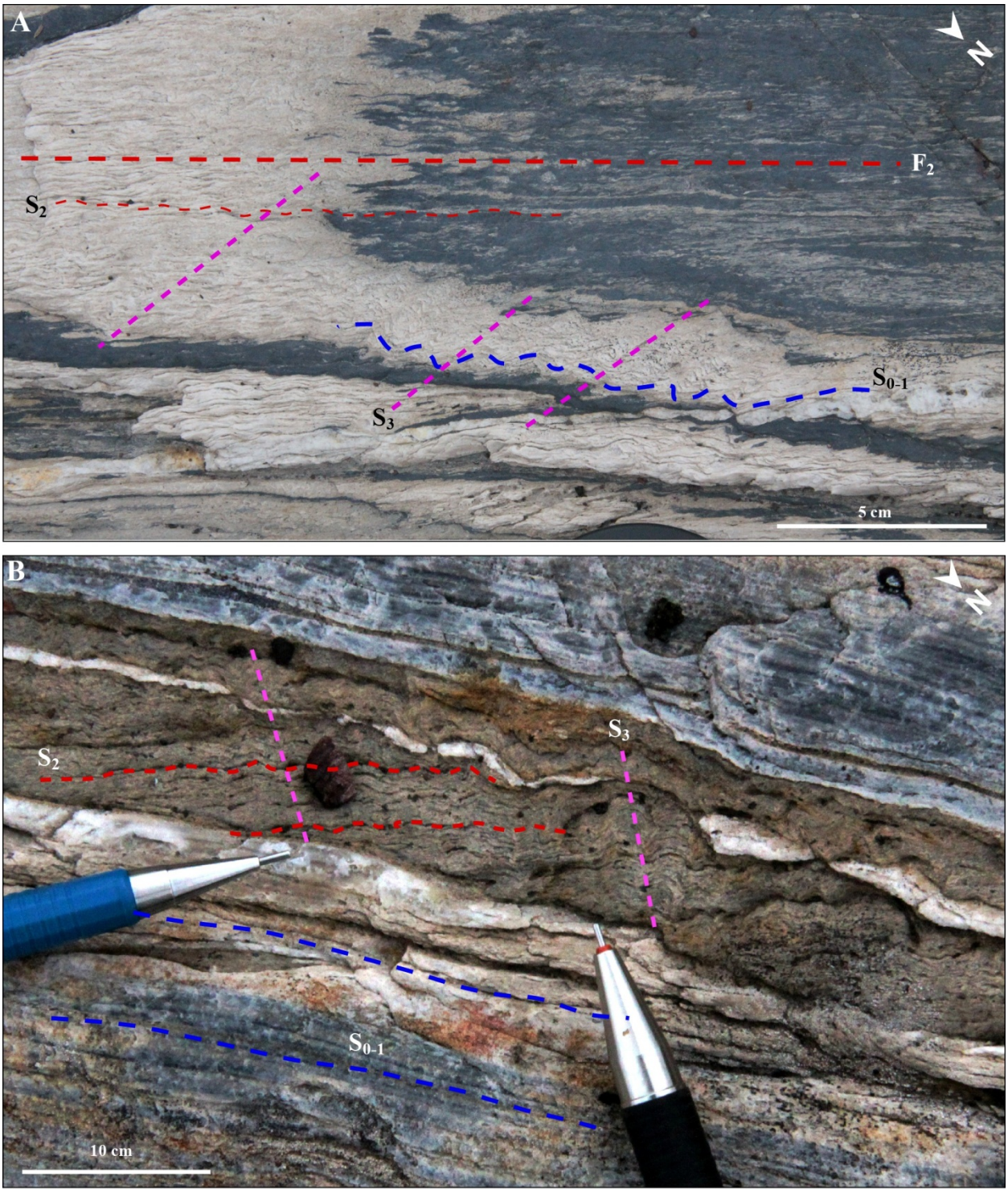

Figure 5-41: A. WSW-trending S_3 crenulation in oxide-BIF, Trench 4, West antiform area. B. SSW-trending S_3 crenulation in a silicate-rich band, Trench 4, West antiform.

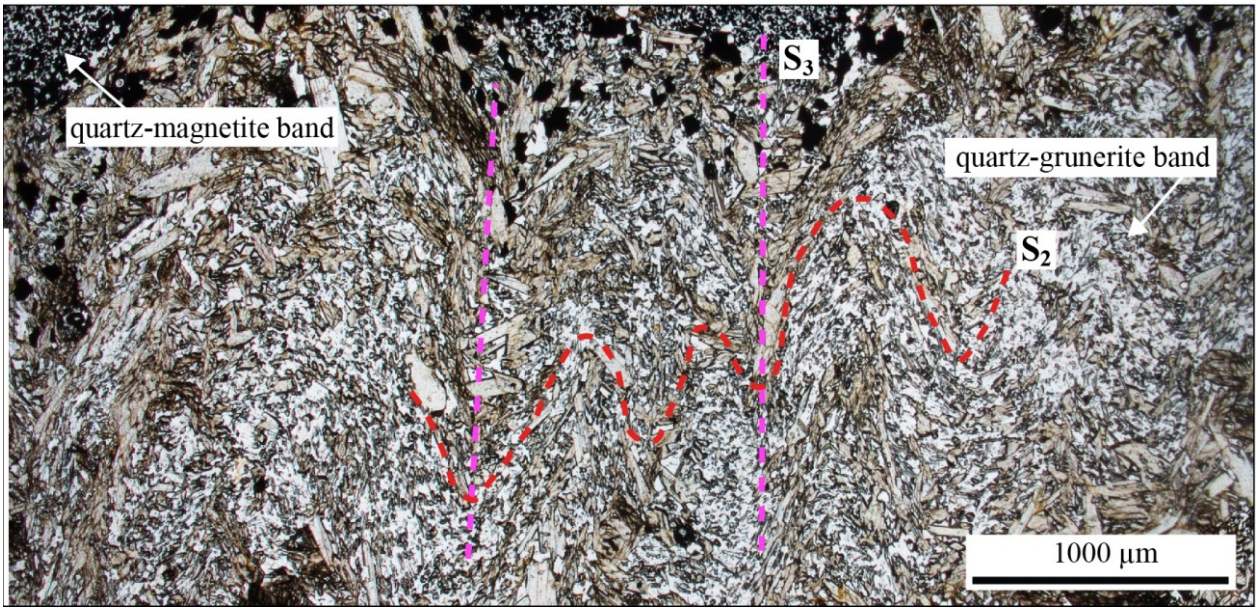

Figure 5-42: S_3 crenulating the S_2 fabric in a chert-grunerite band of oxide-BIF, sample from the Trench 4, West antiform area.

5.5.4 Fault and shear zones

Mesoscopic shear zones crosscutting F_2 folds and the S_2 foliation are mostly present in strongly anisotropic rocks, especially BIFs, in which they develop along the short limbs of Z-shaped F_3 folds, parallel to axial planes (Figure 5-43A). Such structures are minor; however, they can locally develop into larger shear zones, such as on the 4KT exposure (Figure 5-43B**Erreur ! Source du renvoi introuvable.**B), where a 2 m-wide high-strain zone occurs near the contact between the SIF and surrounding volcanic rocks. In the adjacent BIF, an anastomosed network of faults, marked by quartz vein fragments and sulphide staining, is oriented sub-parallel to F_3 axial planes (**Erreur ! Source du renvoi introuvable.**C). The S_3 orientation and drag folds tentatively suggest an apparent dextral motion.

Reconnaissance mapping in the area of the Markop Lake shear zone (Figure 3-22) has delineated a southeastward-increasing D_3 strain gradient and a mylonitic fabric in granitic rocks of the easternmost part of the Southern Batholith (Figure 5-45A). In medium- to coarse-grained granitic rocks, Z-shaped intrafolial F_3 folds affect a moderately- to strongly-developed S_2 foliation. They suggest an apparent dextral shear motion (Figure 5-45B, C). Incipient C-planes have developed in response to prolonged D_3 strain.

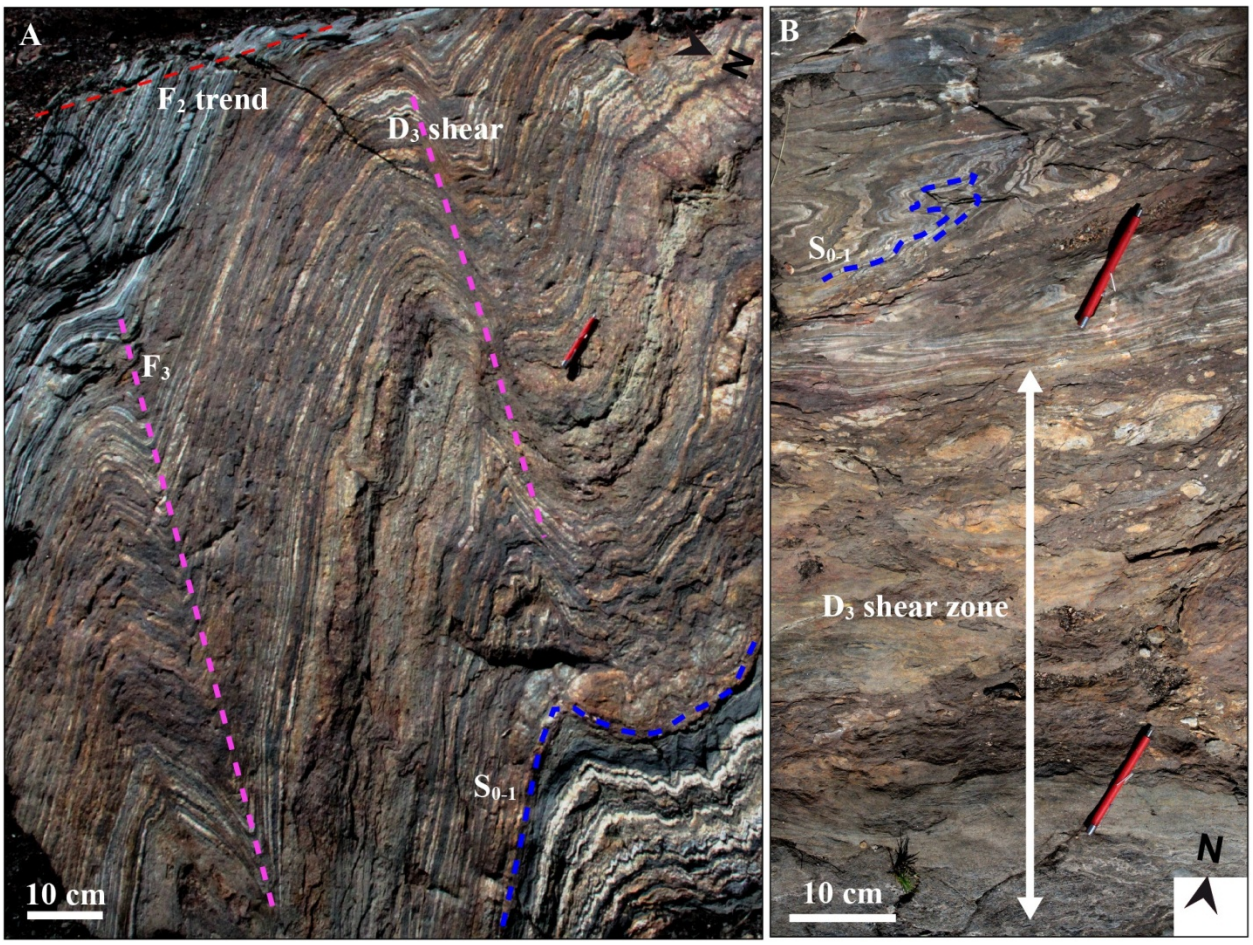

Figure 5-43: A. Localized shearing along the short limb of an asymmetrical F_3 Z-fold in thinly bedded chert-magnetite BIF, Trench 4. B. D_3 shear zone on 4KT. The shear zone is marked by quartz vein fragments and moderate sulphide staining.

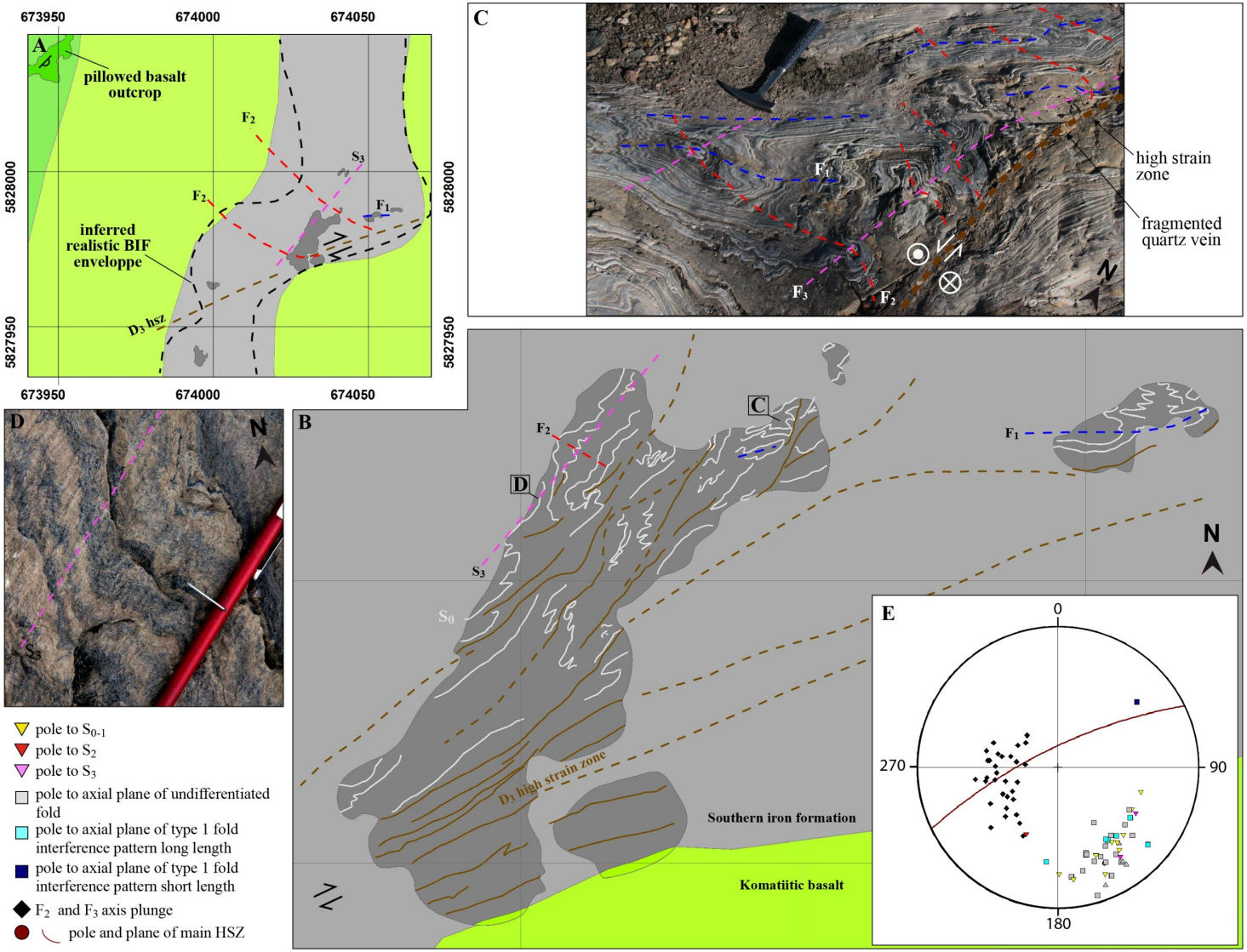

Figure 5-44: 4-km BIF trench geological map. A. Geological context of the exposure (geology from Goldcorp Inc.). B. Geological map of the 4KT showing the pattern and overall orientation of the main fabrics. C. F1-F2-F3 fold interference pattern and D3 high-strain zone. D. S3 crenulation of the S0-1 and S2 fabrics. E. Stereographic projection of structural measurements on the 4KT (equal angle, lower hemisphere).

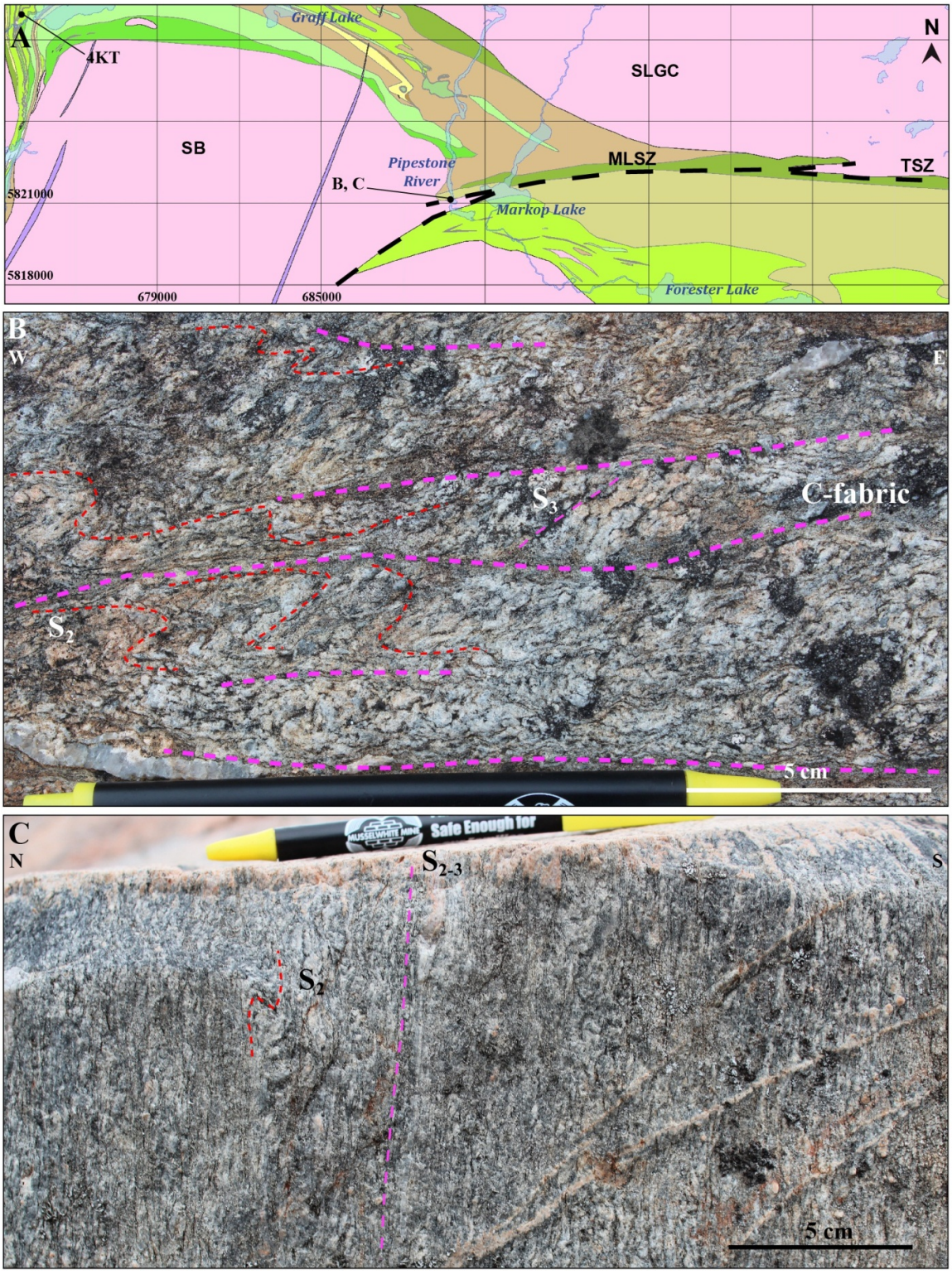

Figure 5-45: Markop Lake shear zone (MLSZ) A. Geological map of the Markop Lake shear zone area (colour legend is similar to Figure 3-22). B. Plan view of the S_2-S_3 fabric relationship in a granodioritic rock of the Southern Batholith, see A for location. C. Vertical section view of the mylonitic S_3 fabric in granodioritic rock of the Southern Batholith, see A for location.

5.6 Synthesis of the structural geology of the Opapimiskan Lake area: West antiform and Mine structural domains

5.6.1 D_1 deformation

D_1 fabrics have been extensively deformed throughout the NCG (e.g., Breaks et al., 2001). In areas of lower relative D_2 deformation, such as in the West antiform area, "type 3" F_1-F_2 interference pattern and preserved S_1 foliation show that D_1 originally produced predominantly NW-SE-trending, shallowly SW-dipping structures, with most likely shallow F_1 fold plunges. Such folds are classified as reclined folds (Hobbs et al., 1976). The overturned character of parts of the OMA sequence, the interpreted kilometre-scale F_1 synform in the Zeemel Lake area, and evidence that OMA and ZHA were juxtaposed by a D_1 fault all suggest that D_1 consisted in a major episode of large-scale folding and interpreted thrusting.

Timing constraints on D_1 are scarce. Evidence of D_1 deformation (especially S_1 foliation) has been mapped throughout the SRA and OMA, and most of the sedimentary rocks of the <2899 Ma ZHA. However, an apparent internal unconformity was mapped in the ZHA in the vicinity of the 2847 Ma felsic volcanic rocks (Figure 3-46). A conglomerate that overlie this unconformity is apparently not affected by the S_1 fabric, providing a tentative minimum age for D_1 deformation. So, the approximate age bracket for D_1 deformation is 2850-2750 Ma (Figure 5-46). This will be further discussed in chapter 10, in combination with the results of other studies on the tectonometamorphic evolution of the NCG.

5.6.2 D_2 deformation

In the Opapimiskan Lake area, F_2 folds are NW-plunging upright folds with thickened hinge zones. The axial planar S_2 foliation ranges from a spaced cleavage in volcanic rocks of the West antiform area to a penetrative schistosity in the mine area, where the D_2 northeastward-increasing strain gradient culminates. Steep, NE-dipping high-strain zones are commonly associated with F_2 folds, along attenuated limbs and within thickened hinge zones.

D_2-deformed 2734 Ma felsic rocks (chapter 4) and 2730-2710 Ma Southern Batholith (chapter 2) provide a maximum age for D_2 (Figure 5-46). U-Th-Pb age dating of M_2 (late D_2) monazite from the Musselwhite mine area (chapter 6) suggests D_2 deformation may have lasted until 2660 Ma.

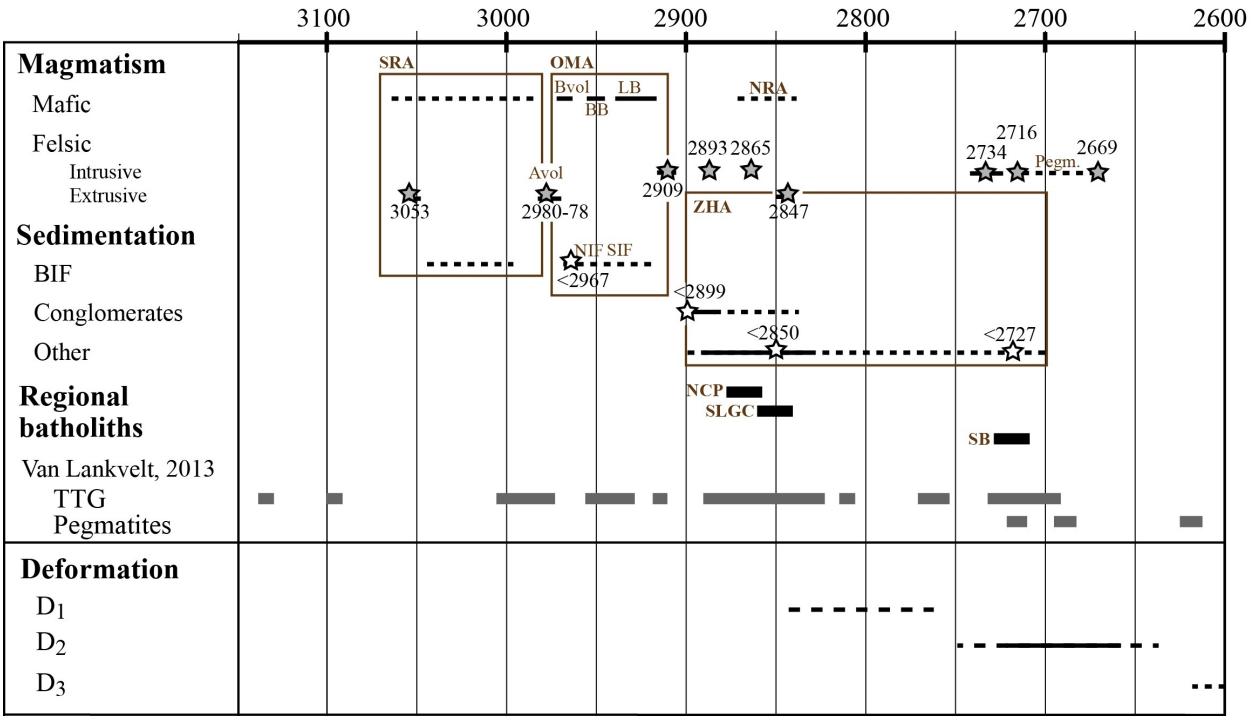

Figure 5-46: Synthetic chart of the geological and structural evolution of the Opapimiskan Lake area. Geochronological data (in Ma) is from Biczok et al. (2012), Kalbfleisch (2012), Van Lankvelt (2013), McNicoll et al. (2016), and this study (chapter 4). Dash line: constraints to be improved.

5.6.3 D_3 deformation

D_3 structures mainly comprise conjugate sets of asymmetrical Z-folds and axial planar crenulation cleavages. F_3 fold development is highly variable, depending on the orientation and anisotropy of affected rocks. D_3 deformation is more common in the western and eastern part of the study and appears to be fairly limited in the Opapimiskan Lake area. Geological and structural mapping farther to the southeast shows an increase in D_3 strain intensity, culminating along the Markop Lake shear zone (2; Figure 5-45). Timing of the D_3 deformation event is unconstrained.

6 METAMORPHISM

Metamorphism is intrinsically linked to tectonic evolution through a variety of processes, often concomitant, including progressive burial due to crustal thickening, and/or heating through igneous activity (e.g., Winter, 2001). Metamorphism induces two main types of change: phase changes, whereby the original minerals are replaced by new metamorphic (paragenetic) minerals; and textural changes, during which minerals are recrystallized to produce new textures such as mineral alignment or coarsening (e.g., Yardley, 1989). The textural and overprinting relationships between the metamorphic paragenesis and structural fabrics give information on the relative timing and evolution of tectonometamorphic events. Metamorphism often has an important role in the formation of orogenic lode gold deposits (e.g., Groves et al., 2003; Phillips and Powell, 2010), providing fluids that leach, transport and subsequently precipitate metals in or near major structures.

As described in chapters 2 and 5, field, petrographic and petrologic data shows that the North Caribou greenstone belt (NCG) underwent two major deformation phases, which are associated with an episode of regional metamorphism that reached upper greenschist to amphibolite facies (Breaks et al., 1986; Hall and Rigg, 1986). Recent work has suggested the differentiation of two major metamorphic events dated at ca. 2.86 Ga and ca. 2.75-2.71 Ga (Kalbfleisch, 2012). Evidence for a number of subsequent, possibly retrograde, metamorphic events has also been identified (Otto, 2002; Biczok et al., 2012; Gagnon, 2015; Kelly and Schneider, 2015).

This chapter presents the petrography, metamorphic paragenesis and textural/structural relationships of the supracrustal rocks in the Musselwhite mine area in order to better understand the tectonometamorphic evolution of the NCG and its links with gold mineralization. The description focuses on non-mineralized units in the mine area. Altered samples of BIF facies are also briefly presented as they provide insights on the relative timing of metamorphism and gold mineralization, however, detailed description and discussion on this topic is covered in the next chapters.

6.1 Metamorphic paragenesis of ultramafic and mafic volcanic rocks

In the Opapimiskan Lake area, mafic volcanic rocks consist of basalts and komatiitic basalts dominantly of tholeiitic affinity. Ultramafic rocks mostly consist of komatiites and local sills with diverse magmatic affinity. Least-altered ultramafic volcanic rocks have a typical metamorphic assemblage including Mg-rich chlorite-actinolite ± cummingtonite, whereas mafic volcanic rocks contain hornblende-plagioclase ± magnetite (chapter 3; Figures 3-9, 3-37 and 6-1). These parageneses are consistent with amphibolite-

facies metamorphic reactions resulting in the progressive breakdown of chlorite and epidote to form amphibole, which also involves gradually more calcic plagioclase feldspar, and can be summarized as (Liou et al., 1974; Winter, 2001):

albite + epidote + chlorite + quartz = oligoclase + tschermakite/hornblende + magnetite + H_2O.

South of Graff Lake, komatiitic units containing euhedral magnetite crystals overgrowing the main fabric (S_{1-2}) were mapped (UTM 684285/5826621; Figure 3-22).

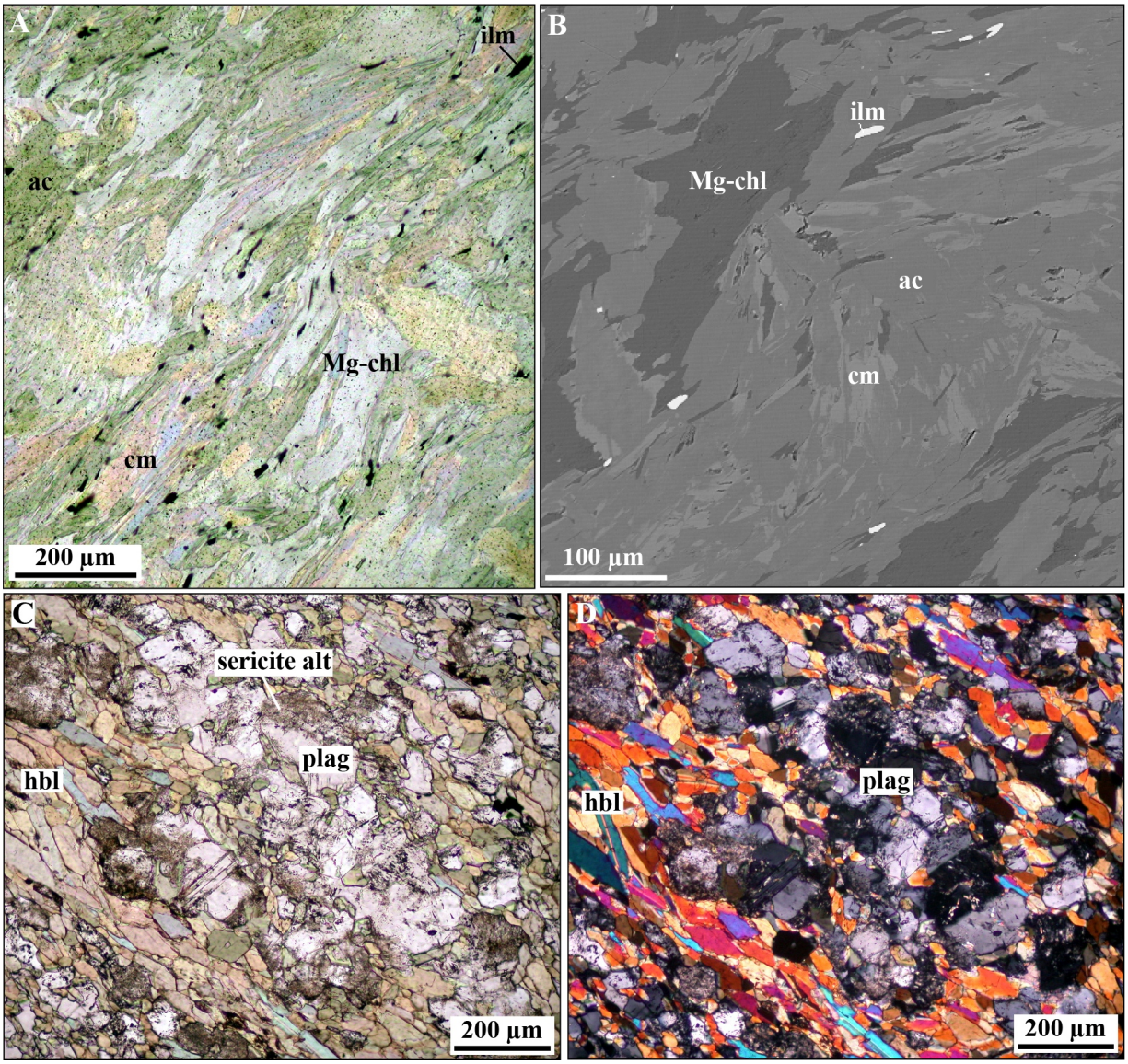

Figure 6-1: A. Actinolite (ac) -cummingtonite (cm) -Mg-chlorite (chl) -ilmenite (ilm) mineral assemblage in ultramafic rocks of the OMA, sample MW-11-134, DDH 10-PQE-054, plain polarized light. B. Same mineral assemblage as A., as a relative density map. C. Hornblende (hbl) -feldspar (plag) mineral assemblage in mafic volcanic rocks of the OMA, sample MW-11-093, DDH 10-PQE-053, plain polarized light. D. Same as C. in cross-polarized light.

In analyzed samples of the present study, plagioclase feldspar composition ranges from andesine to anorthite, but is frequently altered to sericite (Figure 6-1C, D). Amphibole species include cummingtonite (Mg-#, (Mg/Fe+Mg) x 100 = 56) and magnesio- and tschermakitic hornblende (Mg-#67 to 72). Chlorite is Mg-rich (i.e., Mg-#79 in ultramafic rocks, Mg-#64-67 in mafic rocks). This end-member is the more stable form of chlorite during the greenschist to amphibolite transition (Spear, 1993).

Mafic volcanic rocks in the West antiform area show that D_2 folding and axial-planar transposition of S_1 is moderate to locally strong (chapter 5). In the mine area, transposition is intense and textural relationships show that S_2 fabric is delineated by a neo-crystallized hornblende-plagioclase assemblage. This suggests that prograde metamorphism probably reached the greenschist facies after D_1 deformation, and subsequently increased to amphibolite facies during the D_2 deformation event.

6.2 Metamorphic paragenesis of pelitic rocks

The primary sedimentary bulk composition of pelitic rocks of the Opapimiskan Lake area (i.e., unit 4F – garnet-biotite schist) comprise a hydrothermal component in (3). They thus have a slightly different bulk chemical composition than a typical pelite (section 3.7; Figure 3-10; Tinkham et al., 2011; Symmes and Ferry, 1991; Mahar et al., 1997; Atherton and Brotherton, 1982). While Al_2O_3 content is quite similar to reported average contents, SiO_2 content is lower (ca. 50 instead of 60 wt.%) and total iron is twice as high as typical pelitic rocks (average of 19 wt.% in unit 4F). Also, Na_2O content is significantly lower in unit 4F, and MnO content much higher (0.59 wt.% vs. 0.07-0.16). Such differences in bulk composition have influenced the metamorphic paragenesis of unit 4F, which also shows internal compositional variations, with, for example, increases in Al_2O_3 content (i.e., 20-22 wt.%) in lenses near the Avol/Bvol contact.

The metamorphic mineral assemblage of unit 4F consists mainly of garnet-biotite-quartz (Figure 3-9), but also locally of staurolite-biotite-quartz ± sillimanite ± andalusite ± garnet (Figure 6-2). A small part of porphyroblasts consists of altered andalusite. Matrix minerals also locally include fine-grained, acicular sillimanite (Figure 6-3). Finally, parts of unit 4F include alternating hornblende/grunerite-rich bands and chert bands.

In this study, analyzed biotite and staurolite are Fe-rich, with Mg-# of 35 and Fe/(Fe+Mn+Mg) ratio of 0.85, respectively (Appendix IV). Even though staurolite usually crystallizes at higher metamorphic conditions than those of garnet (Spear, 1993), the crystallization of staurolite in iron-rich pelitic rocks is possible at low P/T conditions (biotite zone; Winter, 2001). It likely occurs through the continuous reaction and supported by the abundance of quartz inclusions in staurolite:

$$\text{chloritoid (+ muscovite)} = \text{staurolite + biotite (+ quartz + } H_2O)$$

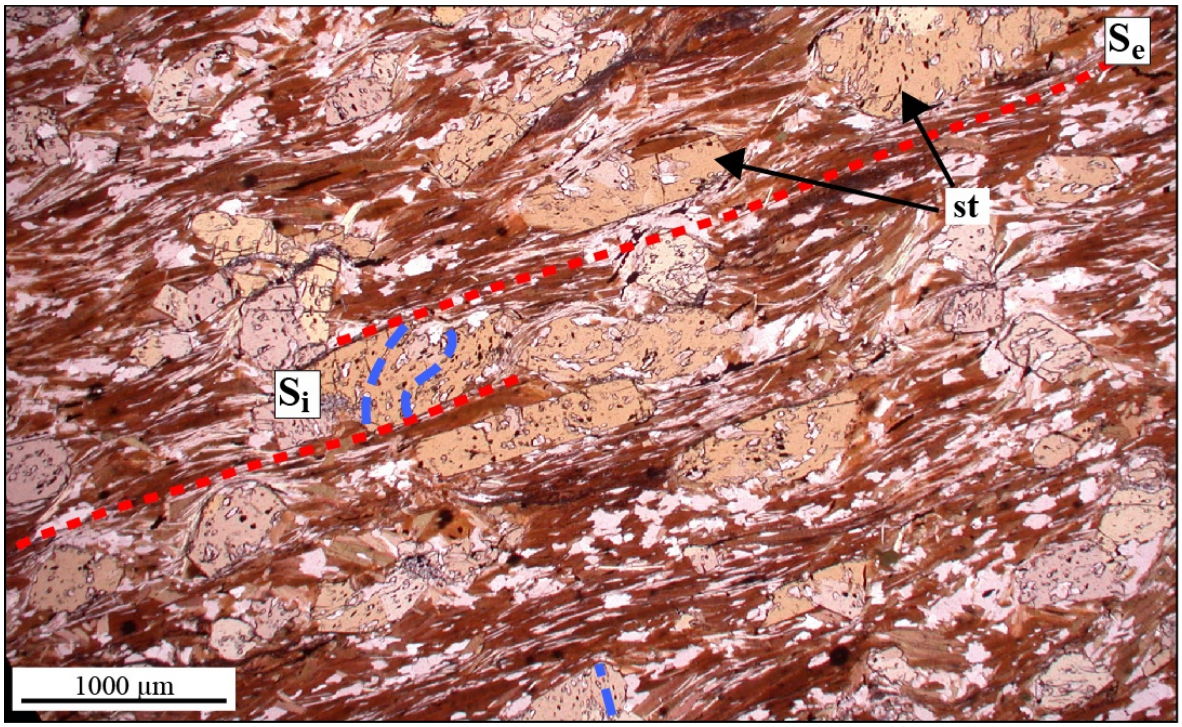

Figure 6-2: Microphotograph of poikilitic staurolite porphyroblasts in biotite-feldspar-sericite-quartz matrix, plain polarized light. Blue dash line = internal fabric (S_i); red dash line = external fabric (S_e); unit 4F sample MW-11-162, DDH 10-PQE-078.

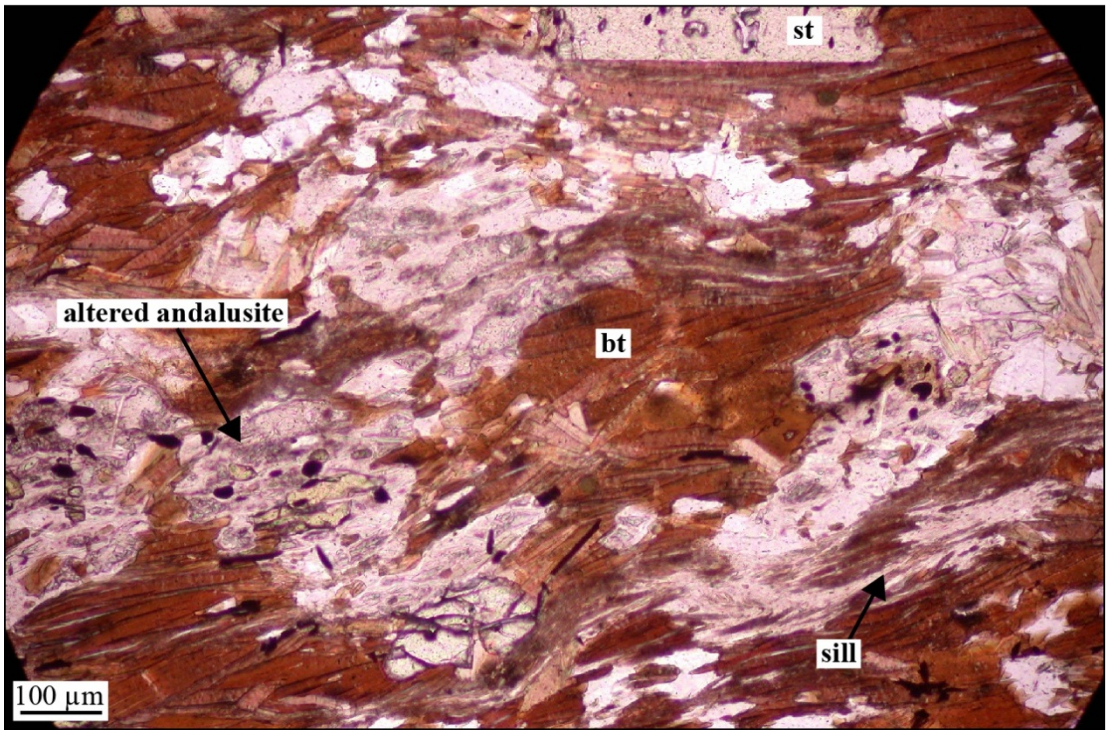

Figure 6-3: Microphotograph of altered andalusite with staurolite remnants and fibrous sillimanite intergrown with biotite, plain polarized light. The external fabric is S_2. Sample MW-11-162A, DDH 10-PQE-078.

Garnet porphyroblasts occur in a variety of textural contexts and show at least two crystallization phases (Figures 3-11B, E; 6-4; 6-5). Cores are systematically poikilitic and typically contain inclusions of quartz and ilmenite, and locally of chlorite and biotite. Rims are subhedral to euhedral and inclusion-free. Where staurolite and garnet porphyroblasts cohabit, garnet contains inclusions of euhedral staurolite (Figure 6-4). The phase boundary between staurolite and garnet is mostly clear and linear, suggesting there was little staurolite breakdown during garnet growth. Crystallization of garnet may have operated through the following reactions (Winter, 2001):

$$\text{Fe-chlorite (+ quartz)} = \text{almandine (+ } H_2O\text{)}$$

or, alternatively,

$$\text{Fe-(low Al)-chlorite (+ muscovite + quartz)} = \text{almandine + annite (+}H_2O\text{)}.$$

Early biotite may be consumed to produce garnet through the reaction:

$$\text{chlorite + biotite (+ quartz)} = \text{garnet (+ muscovite + } H_2O\text{)}$$

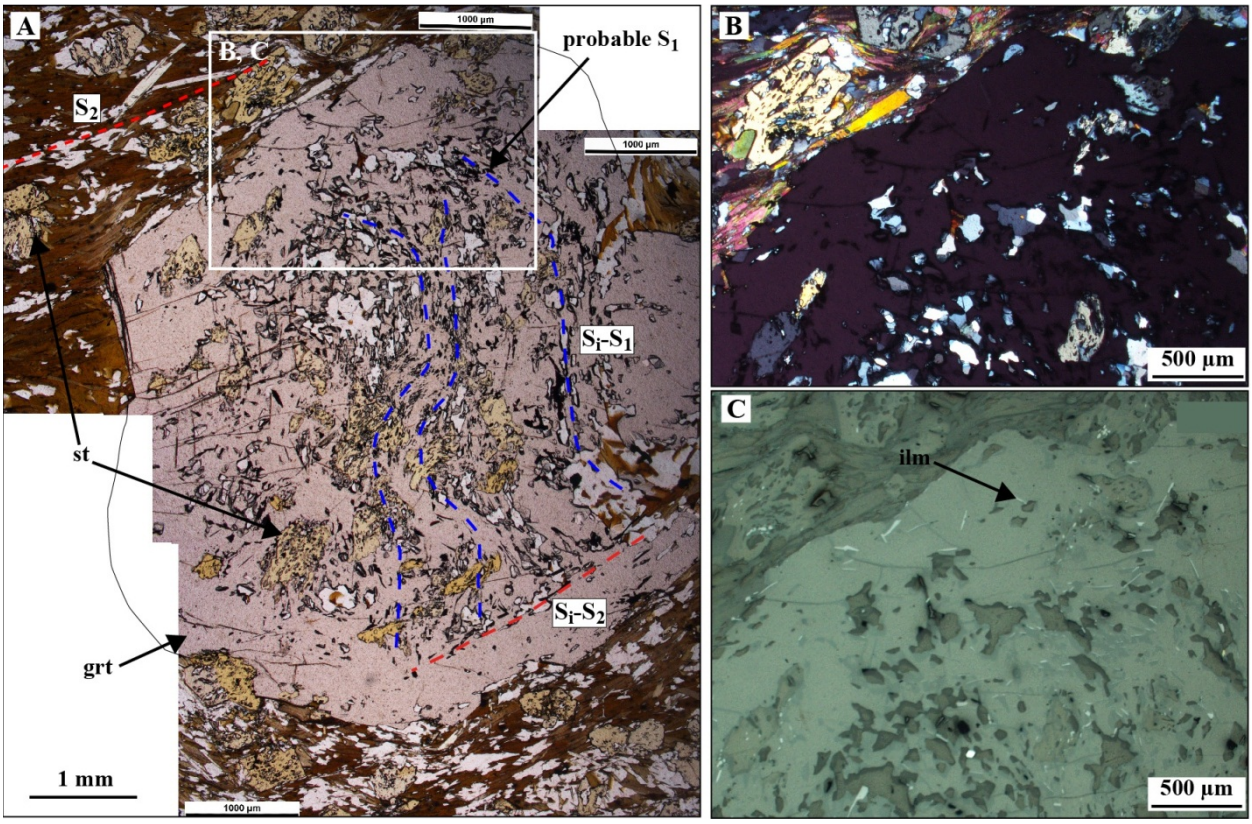

Figure 6-4: A. Microphotograph of euhedral almandine garnet with poikilitic core and inclusions of poikilitic staurolite, in unit 4F sample MW-12-049, DDH 10-PQE-056, plain polarized light. The inclusions of staurolite in garnet and the two distinct fabrics that are at an angle (e.g., lower part of the porphyroblast) suggest that the folded internal fabric is S_1, while the rim of the garnet comprises fractures parallel to the Se and probably related to S_2. B. Close-up of A. in cross-polarized light. C. Same as B. in reflected light.

Mineral chemistry data from this study shows that garnet phases are mostly of almandine composition, and that rims are distinctively poorer in Mn (Mn-# = Mn/(Fe+Mn+Ca+Mg) between 1 and 11.5) compared to cores (Mn-# up to 30). This may be due to depletion of available Mn, or increase in metamorphic conditions favouring incorporation of Fe in garnet. This is consistent with studies showing that Mn-rich almandine garnet crystallizes and is stable at lower metamorphic facies than Fe-rich almandine garnet (Tinkham et al., 2011; White et al., 2014). Microprobe mapping of a garnet porphyroblast (Figure 6-6) shows the progressive core-to-rim decrease in Mn, while Mg content is constant or slightly increases probably to compensate for the loss of Mn. Variations in Ca content reveal a concentric zonation, which correlates with changes in abundance and orientation of inclusion trails. Four zones are defined from core to rim: Inclusions in the Mn- and Ca-rich inner core are patchy and less uniform than in the Ca-poor outer core, where they are extremely fine, continuous, and well-aligned. The boundary between zone 1 and 2 is very irregular and frequently diffuse, suggesting corrosion during discontinuous growth. In zone 3, Mn content decreases to background values while Ca is enriched, and inclusion trails are less dense but display a sharp curvature in the thickest sides of the porphyroblast long axis. In contrast, the narrow zones at the top and bottom of the grain show coarser, more linear quartz inclusions, sub-parallel to matrix S_2, suggesting crystallization of zone 3 took place under dynamic shear strain conditions. The outer rim is nearly inclusion-free and appears to slightly overgrow the external fabric, suggesting late- to post-kinematic growth (Figure 6-6C).

The various textural relationships of minerals and structural fabrics suggest a relative tectonometamorphic evolution. In the staurolite-biotite schist, poikilitic staurolite porphyroblasts contain quartz and ilmenite inclusion trails delineating an internal fabric oriented at high angle to the S_2 foliation in the matrix, which wraps around porphyroblasts (Figure 6-2). This indicates that staurolite porphyroblasts overgrew the S_1 fabric and predated the development of S_2. Chert bands influence the preservation of structural fabrics in unit 4F (Figure 5-11): S_{0-1} is locally preserved, except in biotite-rich bands, where S_2 foliation is pervasive. Garnet porphyroblasts occurring in or near chert bands are consistently tabular (Figure 6-5A, B), which contrasts with the round, euhedral shape in biotite-rich bands. These tabular garnet aggregates are made of fine-grained crystals (Figure 6-5C), which nucleation and growth are controlled by the well-developed compositional (and mineralogical) layering in unit 4F and adjacent iron formation. The linear inclusion trails in tabular garnet aggregates delineate an internal fabric (S_i) that is either sub-parallel to a preserved S_{0-1} in the matrix (Figure 6-5C) and/or at high angle with the surrounding S_2 in the matrix (Figure 6-5D). Fractures sub-parallel to S_2 in garnets suggest they were affected by some of D_2 deformation (Figure 6-5C, D, E). Subhedral garnet crystals in biotite-rich bands are frequently zoned and show diverse curved, S- or Z-shaped inclusion trails (Figure 6-4A andFigure 6-5E). Typically, where the internal fabric (Si) is continuous with and the same as the external fabric (Se), crystal growth of

porphyroblasts is considered as syn-kinematic (Bard, 1980), here syn-D_2. However, in more complex zoned garnets (i.e., Figure 6-6), the internal fabric of garnet zones 1 and 2 is interpreted as S_1 (or composite S_{1-2}), the curved fabric in zone 3 may represent an S_2, whereas euhedral crystallization of zone 4 appears to have partly overgrown the S_2 fabric and would be late- to post-D_2.

Data from pelitic rocks of the OMA in the mine area suggests that peak M_1 metamorphism reached the upper greenschist facies late- to post-D_1 deformation, resulting in the growth of staurolite porphyroblasts. Mn-rich garnet core appears to crystallize during the early stage of D_2 deformation, and almandine-rich phases grew throughout D_2 tectonometamorphism. Inclusion trails developed during the initial stages of syn-D_2 garnet now lie at an angle with the S_e (S_2) due to later progressive deformation. Incipient sillimanite growth (fibrolite) along S_2-parallel biotite suggests M_2 metamorphism clearly reached the amphibolite facies.

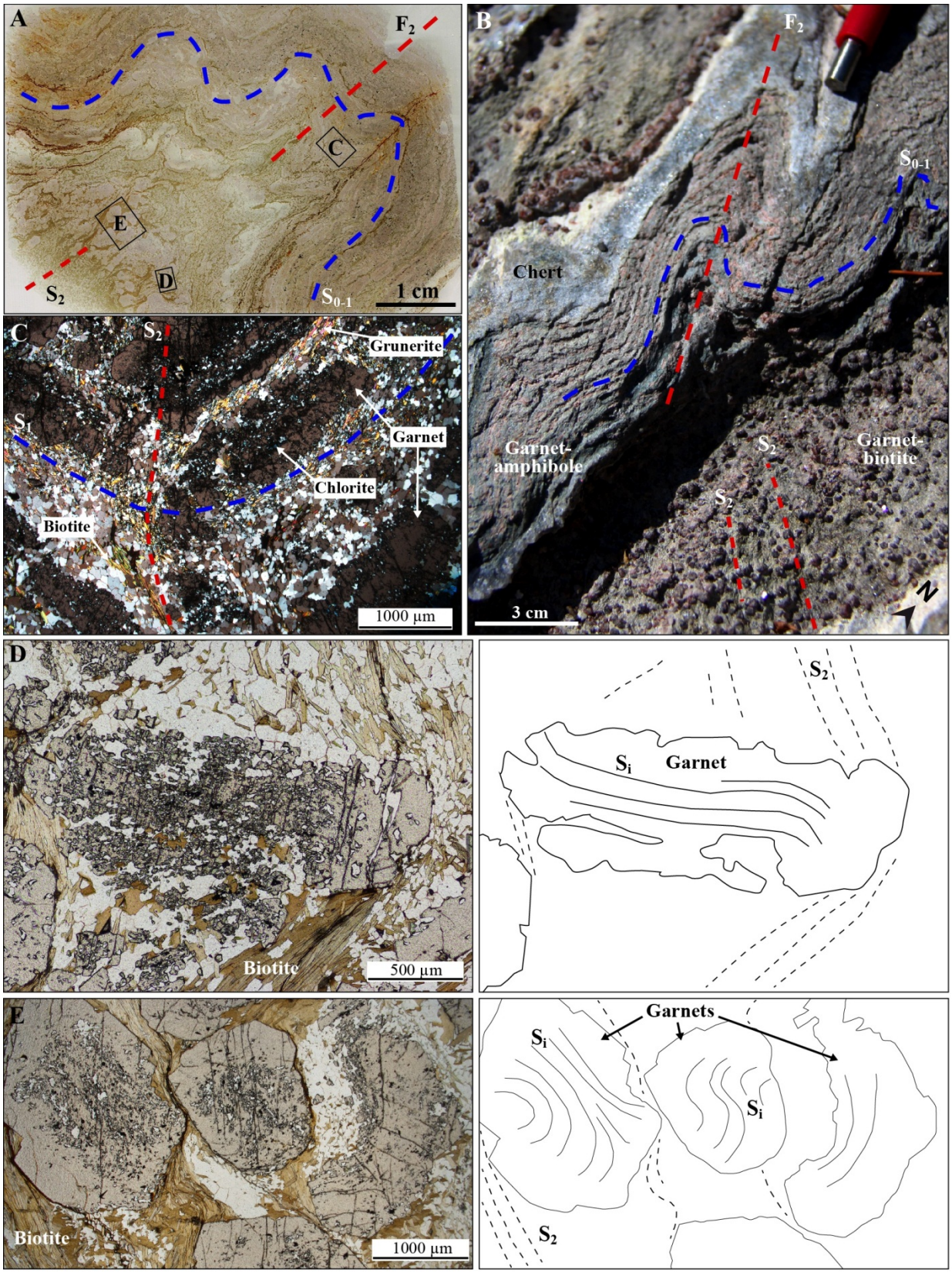
A
F2
C
E
D
S2
S0-1
1 cm
B
F2
S0-1
Chert
Garnet-amphibole
S2
S2
Garnet-biotite
3 cm
C
S2
Grunerite
S1
Garnet
Chlorite
Biotite
1000 µm
D
Biotite
500 µm
S2
Si
Garnet
E
Biotite
1000 µm
Garnets
Si
Si
S2

Figure 6-5: Garnet porphyroblasts A. Thin section of unit 4F, with identification of the main structural fabrics and fold, as well as location of microphotographs C, D, and E. The compositional layering, S_{0-1}, is F_2-folded and overprinted by the axial planar S_2. Oriented sample MW-12-SF-016 from the South shore trench, West antiform area. B. Illustration of similar structural and mineralogical relationships as A. S_1 is preserved near chert bands, while S_2 is weakly to moderately-developed in grt-bt bands. Cherty garnet-biotite schist, South shore trench, West antiform area. C. Microphotograph of tabular garnet aggregates in grunerite-quartz matrix near chert bands. Note the chlorite inclusions and S_2-parallel fractures in garnet. Cross-polarized light, zoom x25. D. Microphotograph and sketch of garnet porphyroblast with internal fabric S_i perpendicular to the S_2 fabric, suggesting S_i is a preserved S_1 or an early-S_2 fabric (plain polarized light, zoom x50). E. Microphotograph and sketch of garnet porphyroblasts showing diverse internal fabric patterns that likely represent a syn-kinematic S_2 (plain polarized light, zoom x25).

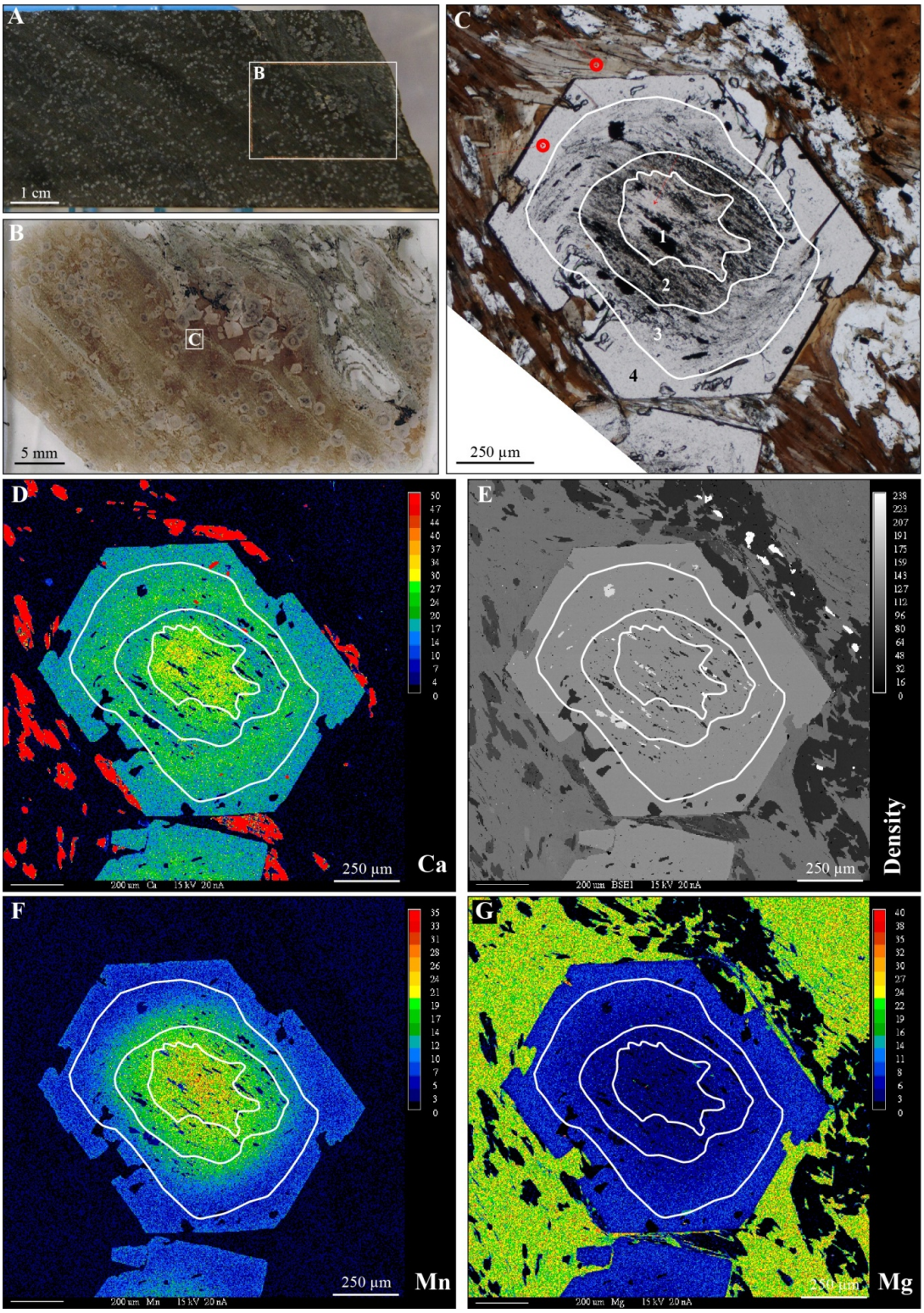

Figure 6-6: Garnet microprobe elemental mapping, unit 4F, sample MW-12-352, DDH 09-TAN-014 A. Drill core photograph. B. Thin section scan. C. Garnet porphyroblast in biotite-quartz matrix, with zonation pattern based on inclusion abundance and pattern (white bold line). Red circles are location of microprobe spot analyses used for geothermometry (section 6.4.1). D. Elemental map for Ca. E. Relative density map. F. Elemental map for Mn. G. Elemental map for Mg.

6.3 Metamorphic paragenesis of banded iron formations

The facies of BIF described in chapter 3 are the product of various metamorphic reactions (section 1.4.3). The composition of the initial compositional layering has a strong influence on the resulting metamorphic paragenesis, notably the Al content, which will in turn influence the BIF's response to deformation and reactivity to fluids. Also, the composition of the BIF protolith will determine the amount of volatiles released during subsequent metamorphism. BIFs of the Opapimiskan-Markop assemblage include an Al-rich (unit 4EA) and Al-poor (unit 4A) silicate facies, as well as an oxide facies (unit 4B) with a decreasing Al content up-stratigraphy (i.e., structurally down-section).

6.3.1 Unit 4EA

"Least altered" unit 4EA typically comprises a garnet-grunerite groundmass interlayered with chert bands (Figure 6-7A). Silicate bands usually include garnet-grunerite ± magnetite ± hornblende ± biotite (3). Garnet porphyroblasts are distributed homogeneously. They are typically zoned and contain inclusions of various mineral phases, sizes and distribution.

Precursor minerals for the crystallization of grunerite include: iron-bearing carbonates, magnetite, quartz and silicate minerals such as greenalite, minnesotaite, stilpnomelane and chamosite (chlorite) (Table 1-2; 1; Haase, 1982; Klein, 2005). By-products of those metamorphic reactions include hornblende, tremolite and biotite, along with significant volumes of CO_2 and H_2O (Klein, 1983, 2005). Garnet growth requires the presence of aluminum, provided by chlorite (Haase, 1982), through any of the three following, unbalanced reactions:

$$\text{ankerite} + \text{chlorite} + \text{quartz} = \text{grunerite} + \text{garnet} + CO_2 + H_2O$$

$$\text{siderite} + \text{chlorite} + \text{quartz} = \text{grunerite} + \text{garnet} + CO_2 + H_2O$$

$$\text{chlorite} + \text{quartz} = \text{grunerite} + \text{garnet} + H_2O$$

The occurrence of such reactions is supported by the frequent presence of chlorite inclusions in garnet porphyroblasts (Figure 6-7B, C). The absence of carbonate inclusions attests that they were either a limiting reactant or initially not present in the parent mineral assemblage of garnet-grunerite.

Garnet porphyroblasts also commonly include magnetite and ilmenite inclusions (Figure 6-7D, E, F). Ilmenite is a Fe-Ti-oxide common in BIF with clastic input of all metamorphic grades (Gole and Klein, 1981b). It likely formed from Ti released by the conversion of Al-bearing minerals to garnet. Magnetite inclusions in garnet may be remnants of primary magnetite after reaction with quartz and H_2O to form

grunerite (Table 1-2; Klein, 1983). The presence of magnetite and absence of quartz in the matrix may be the result of quartz being a limiting reactant to the crystallization of grunerite. While magnetite is mainly the metamorphic product of iron hydroxides and hematite, it can also be produced by breakdown of carbonates (e.g., siderite = magnetite + CO_2; Haase, 1982), or early silicate phases such as greenalite (e.g., greenalite = minnesotaite + magnetite + H_2O; French, 1968; Klein, 2005).

Grunerite inclusions in garnet are generally small, subhedral, and concentrated in the poikilitic core. In some samples, garnet rims may contain euhedral grunerite inclusions with no preferred orientation (Figure 6-8). This suggests the presence of at least two generations of grunerite: an earlier generation that was affected by some deformation (likely D_1) prior to garnet overgrowth; and a later generation of randomly-oriented euhedral crystals, which can predate D_2 or have crystallized during a period of strain quiescence during D_2.

Similarly to garnet in unit 4F, some garnets in unit 4EA are apparently tabular. However, the possibility that this is the result of grains aggregation is more apparent (Figure 6-9A, B, C). In F_2 fold hinge zones, such porphyroblasts contain a moderately-developed linear internal fabric that is at high angle with the external S_2. The orientation of garnets and the apparent continuity of linear fabric in between crystals (Figure 6-9C) seem to define a folded S_1 fabric. In the adjacent fold limb (Figure 6-9A, D, E), the internal fabric of garnet is at high angle with S_2 and the compositional layering. These observations suggest that, in the silicate BIF, the crystallization of garnet porphyroblasts is pre- to early-D_2.

Microscopic observations show that the orientation of matrix grunerite is parallel to S_1 along F_2 fold hinges, especially near chert bands. Away from chert bands, grunerite is mostly parallel to S_2 but appears to have the same timing of crystallization (Figure 6-10). It is unclear how this matrix grunerite relates to grunerite found as inclusions in garnet porphyroblasts (Figures 6-7 and 6-8). A distinct generation of semi-massive, coarse-grained, subhedral grunerite oriented parallel to S_2 locally occurs between silicate bands and chert bands (Figure 6-11). Based on scientific literature on iron formations and gold-bearing hydrothermal systems (sections 1.4.3 and 1.5.3.3) and previous studies in the Opapimiskan Lake area (Hall and Rigg, 1986; Breaks et al., 2001; Blower and Kiernan, 2003), this later phase can be interpreted as the by-product of the interaction of chert and adjacent grunerite-magnetite matrix components (i.e., magnetite + quartz + H_2O = grunerite; Klein, 1983) with fluids, during D_2 deformation. These fluids may have been sourced from metamorphic devolatilization of nearby phases or from regional-scale hydrothermal activity. The implications of this type of grunerite are further examined in chapter 8, in which the hydrothermal alteration associated with gold mineralization is described.

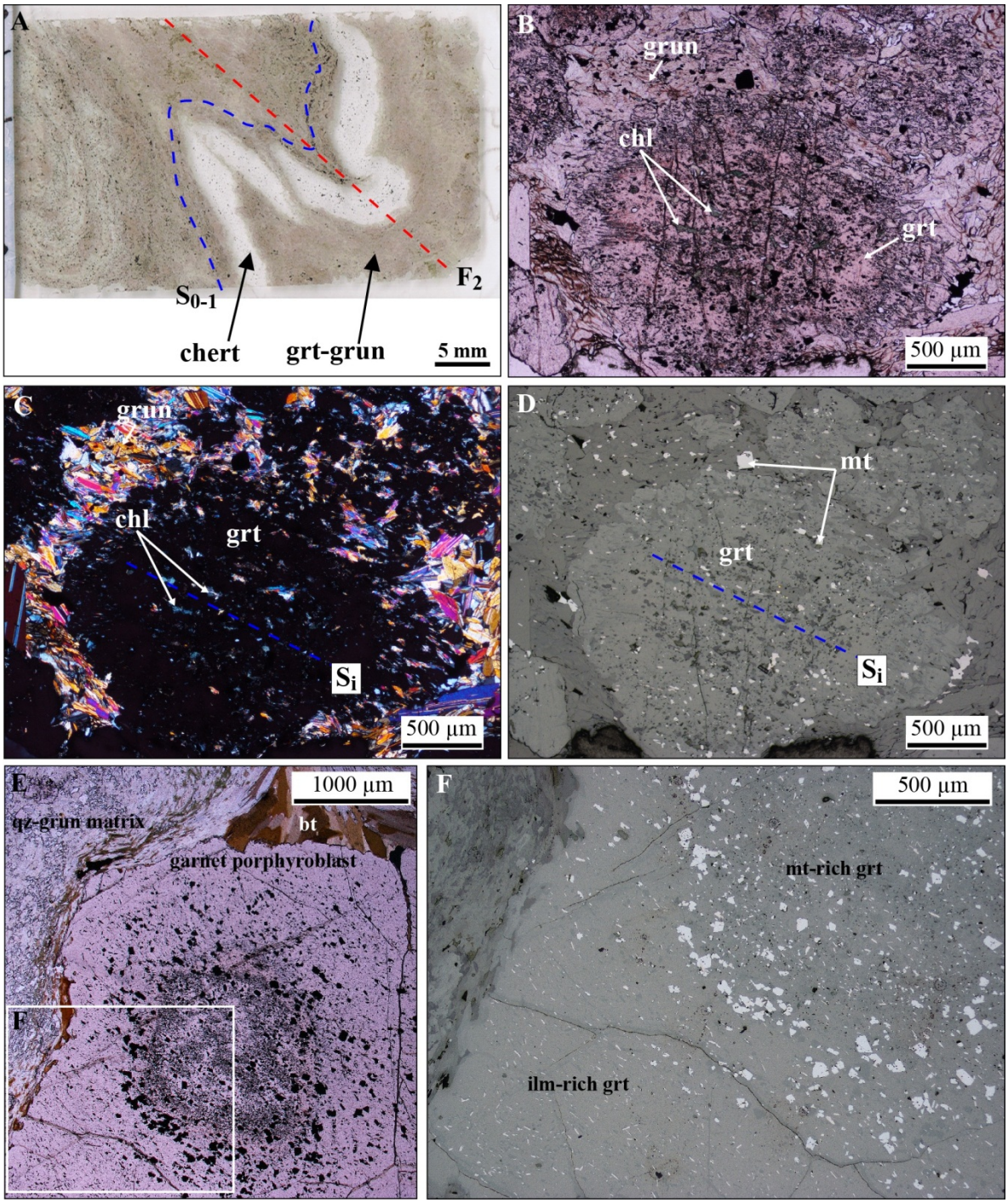

Figure 6-7: A. Typical garnet-grunerite-chert assemblage of unit 4EA. Thin section of sample MW-14-017A, DDH 06-NSD-001. B. Microphotograph of garnet porphyroblast with chlorite, quartz, magnetite, and grunerite inclusions in grunerite-quartz matrix, plain polarized light, sample MW-14-017A. C. and D. Same as B. in cross-polarized light and reflected light, respectively. E. Microphotograph of garnet porphyroblast in grunerite-quartz-biotite matrix, plain polarized light, sample MW-12-422, DDH 12-TAN-031. The garnet porphyroblast has a poikilitic core, dominated by very fine-grained quartz-magnetite inclusions, and surrounded by coarser magnetite inclusions. Margins are dominated by very fine-grained ilmenite inclusions. F. Close-up of E. in reflected light, highlighting the oxide-inclusion zonation.

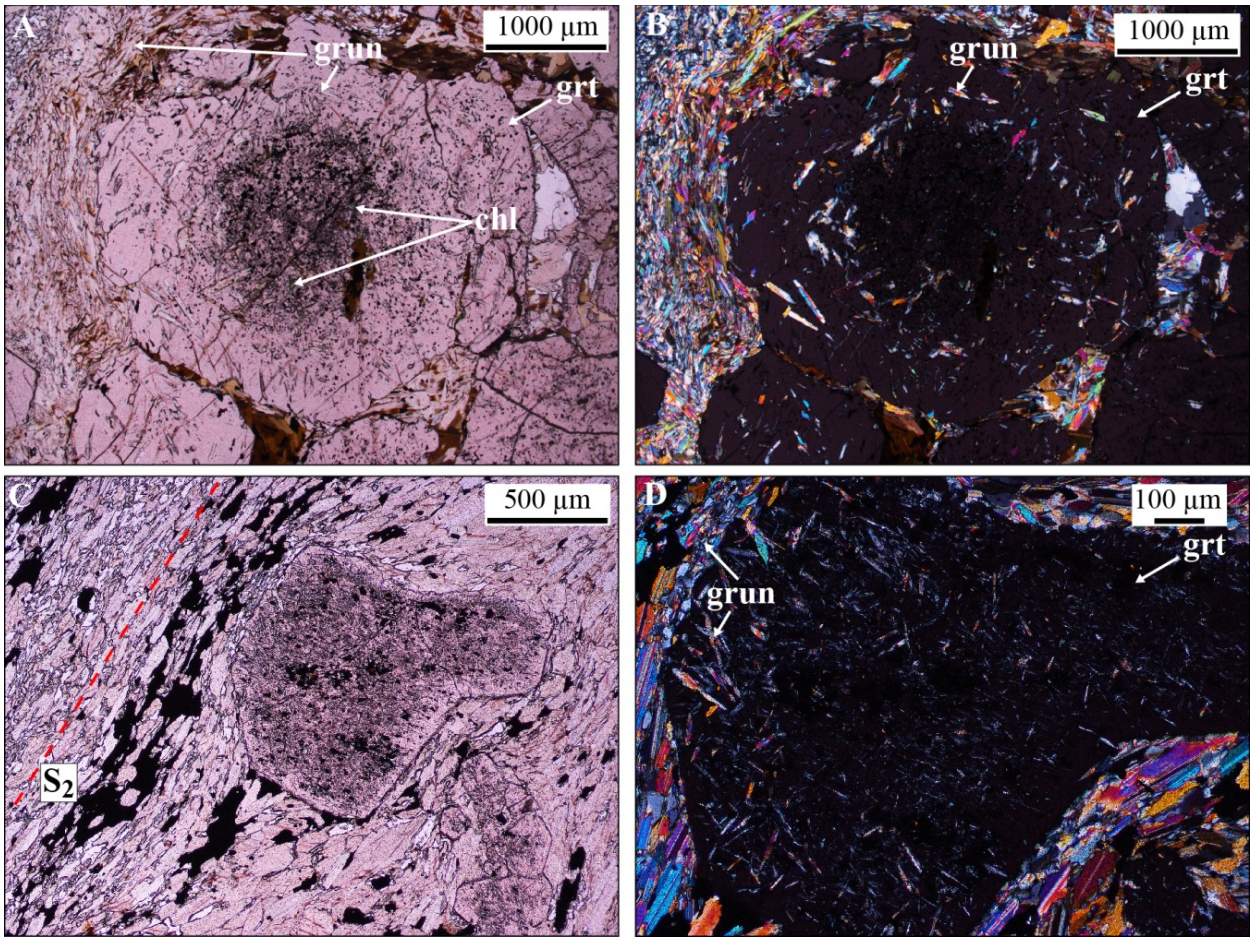

Figure 6-8: A. Garnet porphyroblast in garnet-quartz-biotite matrix, plain polarized light; sample MW-12-492, DDH 10-PQE-016. Poikilitic core contains quartz, grunerite and chlorite inclusions. Rims contain coarse, euhedral, randomly-oriented grunerite inclusions. B. Same as A. in cross-polarized light. C. Euhedral garnet porphyroblast in foliated grunerite-magnetite-quartz matrix, plain polarized light; MW-12-523, DDH 10-PQE-020. D. Close-up of C. in cross-polarized light. The extinction of garnet reveals non-oriented grunerite inclusions in the porphyroblast margin.

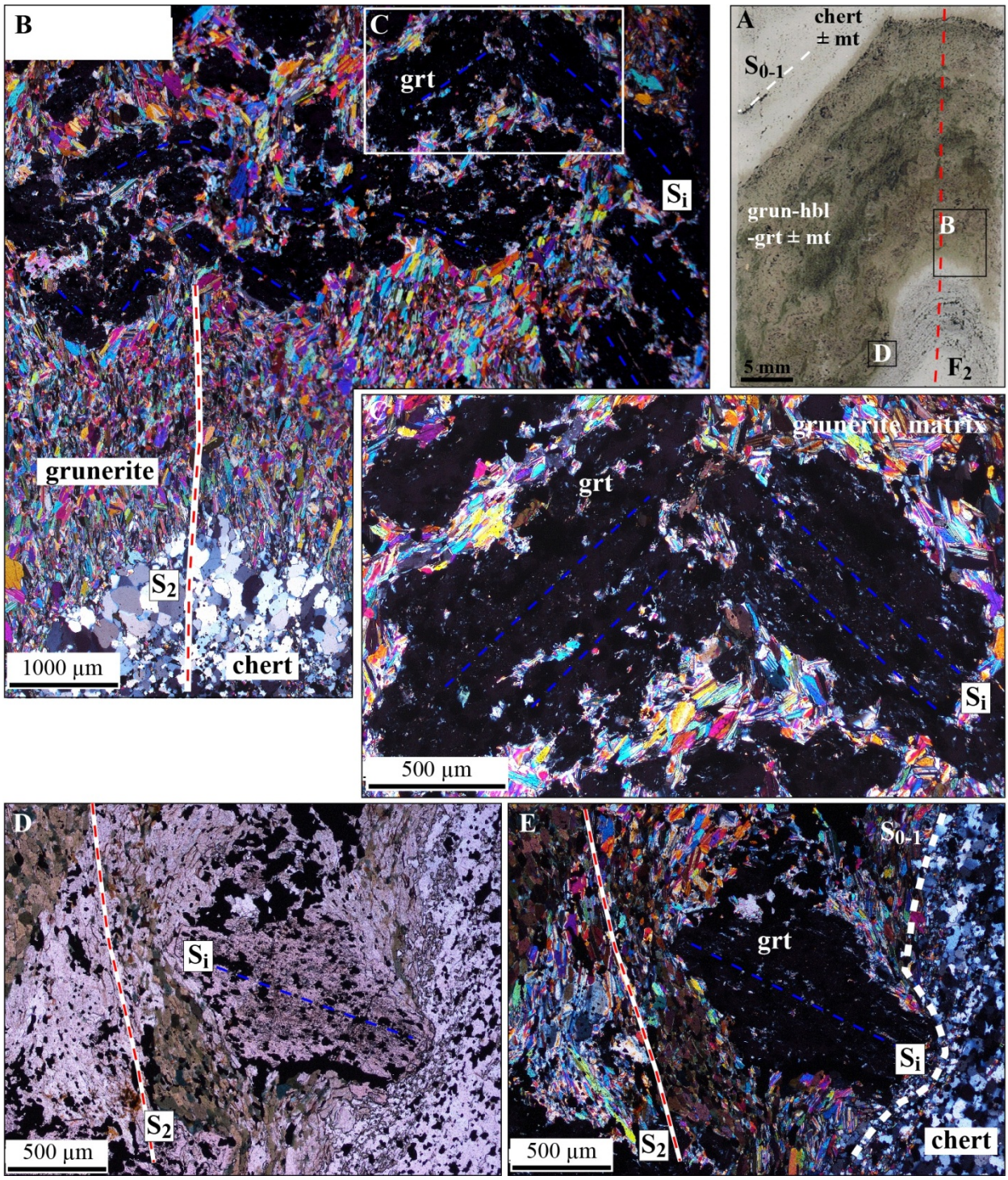

Figure 6-9: Grunerite and garnet in relation to structural fabrics. A. Thin section scan of unit 4EA sample MW-12-284 showing F_2-folded chert-magnetite and garnet-grunerite-hornblende-magnetite bands, with location of microphotographs in B. and D. B. Microphotograph of F_2 hinge zone showing grunerite oriented parallel to S_2 fabric, with C. Close-up of B., showing the linear internal fabric (S_i) in garnet porphyroblasts. Grunerite grains are sub-parallel to the S_i in garnet and show evidence of transposition into the S_2 fabric. Inclusion trails suggest garnets overgrew the S_1 foliation. D. Microphotograph of garnet porphyroblast in foliated grunerite-hornblende-magnetite matrix, plain polarized light. The internal fabric of the

porphyroblast is at high angle with the compositional layering and the external foliation (S_2). E. Same as C. in cross-polarized light.

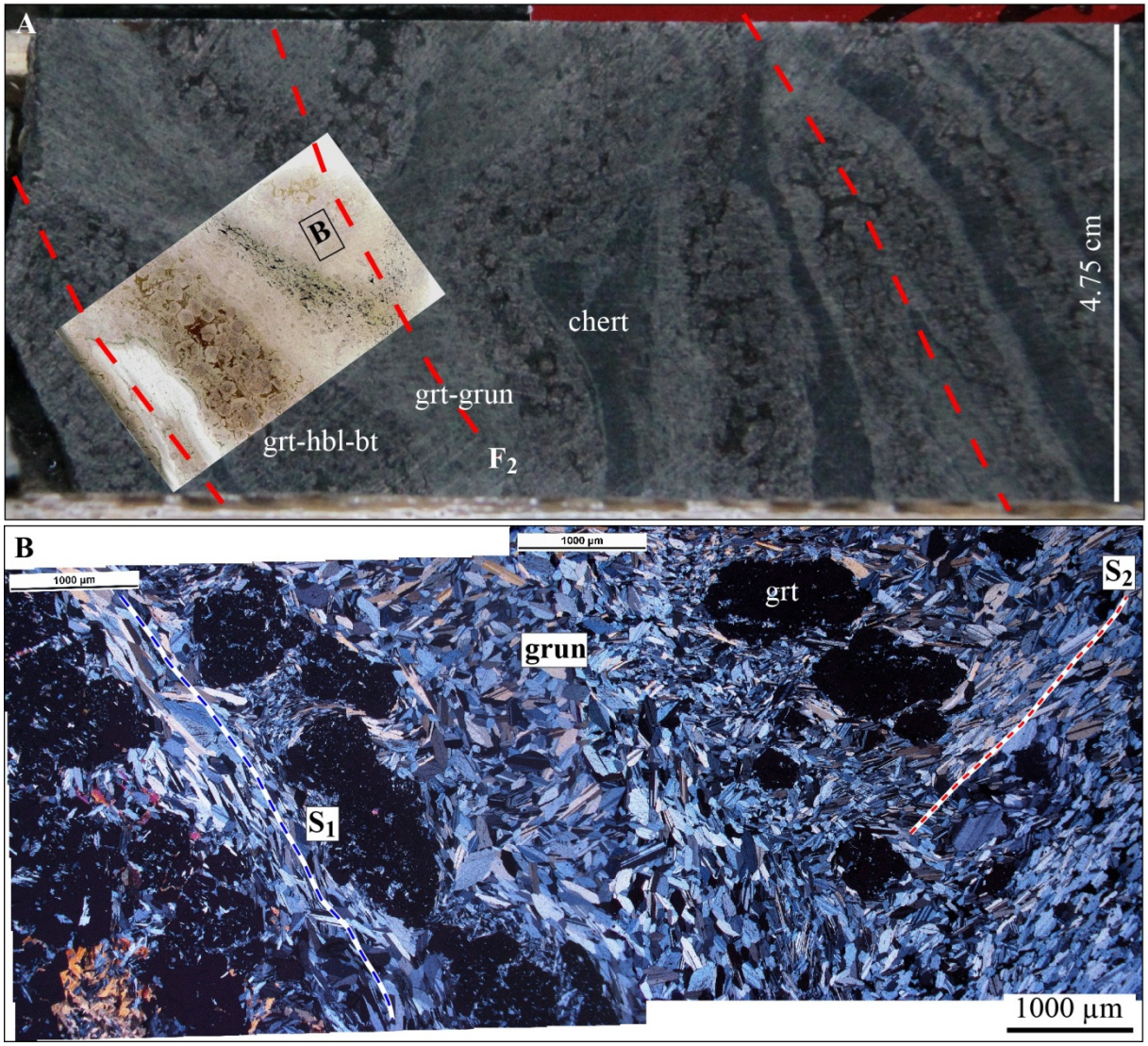

Figure 6-10: Grunerite and garnet in relation with structural fabrics. A. Drill core segment of unit 4EA, sample MW-12-424, DDH 12-TAN-031, showing tight F_2 folds. The thin section scan of the sample is overlain on the drill core photograph for context. B. Microphotograph of garnet porphyroblasts in grunerite matrix in relation with structural fabrics S_1 and S_2.

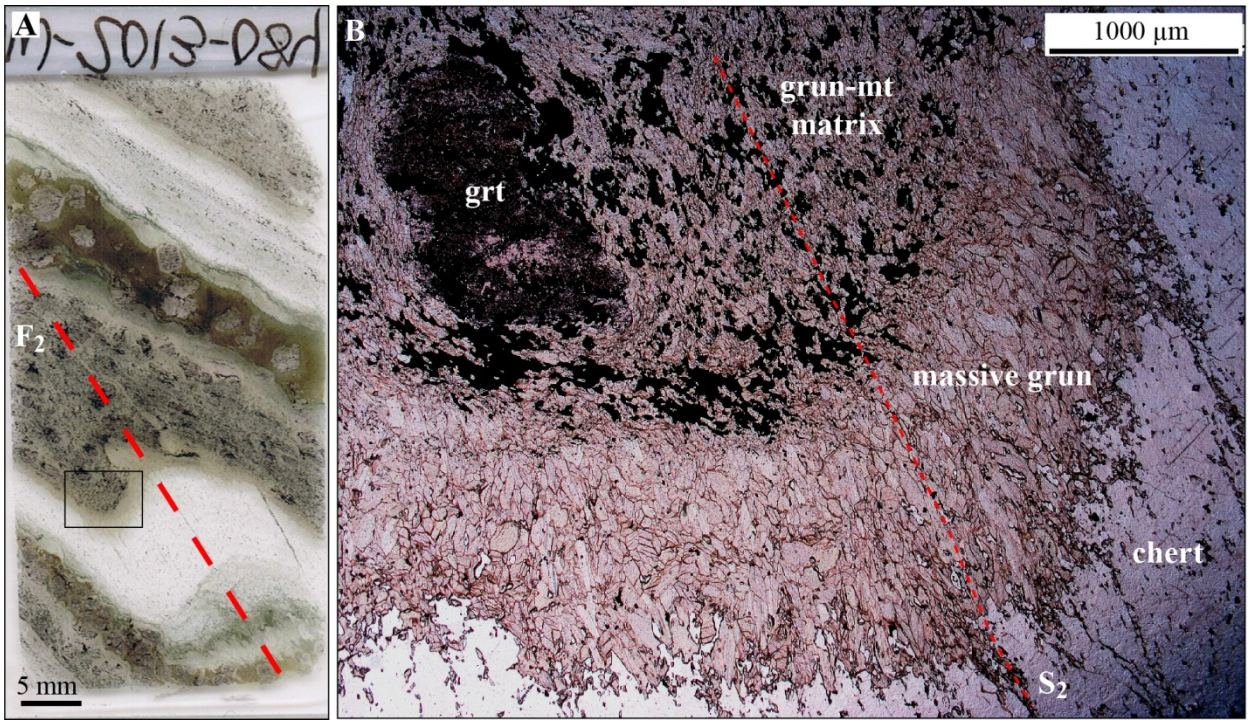

Figure 6-11: Primary vs secondary grunerite A. Thin section of unit 4EA, sample MW-13-084, DDH 09-TAN-048. A chert band is S-folded with the axial planar S_2 foliation. B. Microphotograph of poikilitic garnet porphyroblast in grunerite-magnetite matrix separated from the adjacent chert band by a layer of coarse, euhedral grunerite grains, which are oriented parallel to S_2; plain polarized light.

The metamorphic paragenesis of least-altered unit 4EA samples shows that M_1 metamorphism reached conditions equivalent to the biotite zone in pelitic rocks late during D_1 deformation (i.e., conversion of silicate phases to grunerite and Al-bearing amphiboles). Crystallization of M_2 garnet porphyroblasts shows that the metamorphic facies is comparable to the garnet zone and is interpreted to have occurred syn-D_2 deformation. At higher grade, metamorphic pyroxene is a stable phase of BIF, where carbonates are present (Haase, 1982; Klein, 1983):

$$\text{ankerite} + \text{quartz} = \text{clinopyroxene} + CO_2$$

$$\text{siderite} + \text{quartz} = \text{orthopyroxene} + CO_2$$

$$\text{calcite} + \text{grunerite} + \text{quartz} = \text{clinopyroxene} + CO_2 + H_2O$$

At Musselwhite, unit 4EA locally comprises thin layers of clinopyroxene-calcite-grunerite between chert and garnet-hornblende/tschermakite bands. However, such occurrences of pyroxene appear to be largely confined to hydrothermally altered zones related to gold mineralization (chapters 7 and 8).

6.3.2 Unit 4B

In the NIF sequence, unit 4B evolves from a "pure" facies (chert-magnetite ± amphibole bands, 6 to 0.5 wt.% Al_2O_3) to a more "clastic-rich" facies, termed 4Bc (chert-magnetite bands and garnet-amphibole bands, 6-8 wt.% Al_2O_3; chapter 3). In the SIF sequence, unit 4B is virtually devoid of Al_2O_3, with only 0.05-0.2 wt.%. The cycle of clastic and chemical inputs during the sedimentation of BIF induces a characteristic sequence of metamorphic mineral assemblages in unit 4B (Figure 6-12A): (1) quartz ± grunerite ± hornblende ± magnetite, for chert bands; (2) magnetite-grunerite ± carbonate ± hornblende ± quartz, for oxide-rich bands; and (3) hornblende-grunerite ± biotite ± garnet ± quartz ± magnetite, for clastic-rich bands (present in unit 4Bc; Figure 6-12B).

Chert and magnetite bands are typical diagenetic products of silica-rich gel and iron oxyhydroxides. Magnetite can also be a metamorphic by-product of the breakdown of greenalite (silicate phase) and iron-bearing carbonates (French, 1968). Grunerite occurs mostly in the matrix of oxide-rich bands (Figures 3-29, 3-30) and is formed through any of the following reactions (Table 1-2; French, 1968; Haase, 1982; Klein, 1983):

$$\text{minnesotaite} = \text{grunerite} + \text{quartz} + H_2O$$

$$\text{siderite} + \text{quartz} = \text{grunerite} + CO_2$$

$$\text{ankerite} + \text{quartz} + H_2O = \text{grunerite} + \text{calcite} + CO_2$$

$$\text{ankerite} + \text{stilpnomelane} = \text{grunerite} + \text{hornblende} + CO_2 + H_2O$$

Residual traces of calcite in oxide-rich bands suggest that they initially contained carbonates, which were involved in grunerite crystallization, probably as a limiting reactant. Locally, grunerite crystallizes at the interface of chert and oxide bands through the reaction (Klein, 1983):

$$\text{magnetite} + \text{quartz} + H_2O = \text{grunerite}.$$

The required water may originate from the metamorphic change of subordinate silicate phases present in adjacent oxide-rich bands during conversion to hornblende and grunerite (Table 1-2), or from an external source. Matrix grunerite is generally fine-grained to locally medium-grained. In low-D_2 deformation zones, grunerite crystals are frequently oriented parallel to the BIF compositional layering ($S_{0\text{-}1}$; Figures 3-30, 6-13A). Grunerite present as a layer at the interface of chert and magnetite bands tends to form coarser, euhedral crystals parallel to S_2, as described for unit 4EA (Figure 6-7). Magnetite is mostly anhedral and fills inter-granular space between quartz and amphiboles. Large magnetite aggregates are locally preserved in areas of low D_2 deformation intensity (Figure 6-13B). Some grunerite is oriented parallel to S_1, suggesting that one episode of grunerite crystallization occurred during the D_1 event, and

that M_1 metamorphism reached middle to upper greenschist facies, equivalent to the biotite zone for pelitic rocks (Klein, 2005).

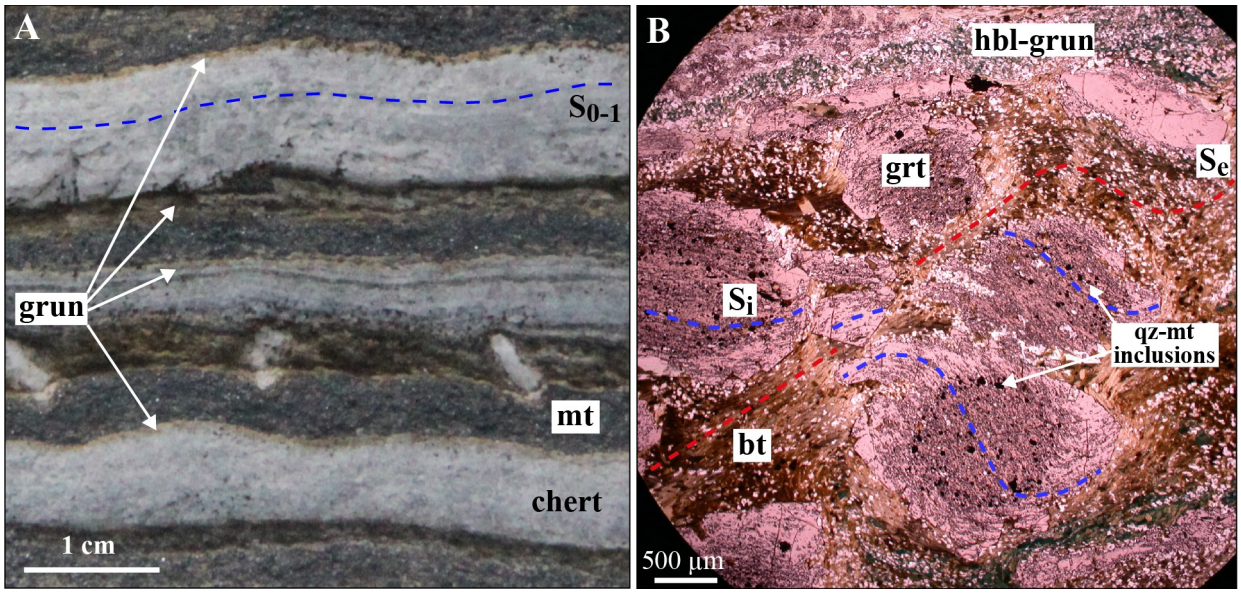

Figure 6-12: A. Typical chert-magnetite-grunerite layering in oxide-BIF, Southern iron formation, "Zebra trench", West antiform area. UTM 675800/5832360. Note the thin grunerite horizon crystallized between chert and magnetite-rich bands. B. Microphotograph of poikilitic garnet porphyroblasts in biotite-rich matrix of a clastic-rich band of facies 4Bc, sample MW-12-459, DDH 12-TAN-060, plain polarized light. Quartz-magnetite inclusion trails in garnet cores form a planar internal fabric (blue dash line). Inclusion trails extend in the subhedral to euhedral garnet rim, locally forming Z-shape pattern extending toward the external fabric (red dash line). This relation between S_i and S_e (S_2) suggests that while Si in the garnet rims is certainly an earlier stage of S_2, the fabric garnet cores can be interpreted either as an early S_2 or a preserved S_1.

In clastic-rich bands, metamorphic reactions leading to the crystallization of amphiboles and garnet in unit 4B are the same as for unit 4EA (section 6.3.1). Garnet porphyroblasts also display a similar internal structure as in unit 4EA, and comprise two garnet phases including strongly poikilitic cores and moderately-developed, inclusion-poor rims (Figure 6-12B). Inclusions mainly consist of quartz, magnetite and grunerite, and magnetite inclusions tend to be larger and much more abundant in unit 4B. Inclusion trails delineate an internal fabric in the rims of garnet porphyroblasts that is continuous and therefore likely correlates to the external S_2 fabric of the matrix. The internal fabric within the cores of garnet is parallel to that of the rims at the core-rim contact, so that it may represent an early S_2 or a composite S_{1-2} (i.e., overgrown S_1 transposed into the early S_2). Inclusion-poor rims are generally thin, less developed than in unit 4EA. These observations suggest that M_2 metamorphism reached the amphibolite facies, equivalent to the garnet zone in pelitic rocks, during D_2 deformation.

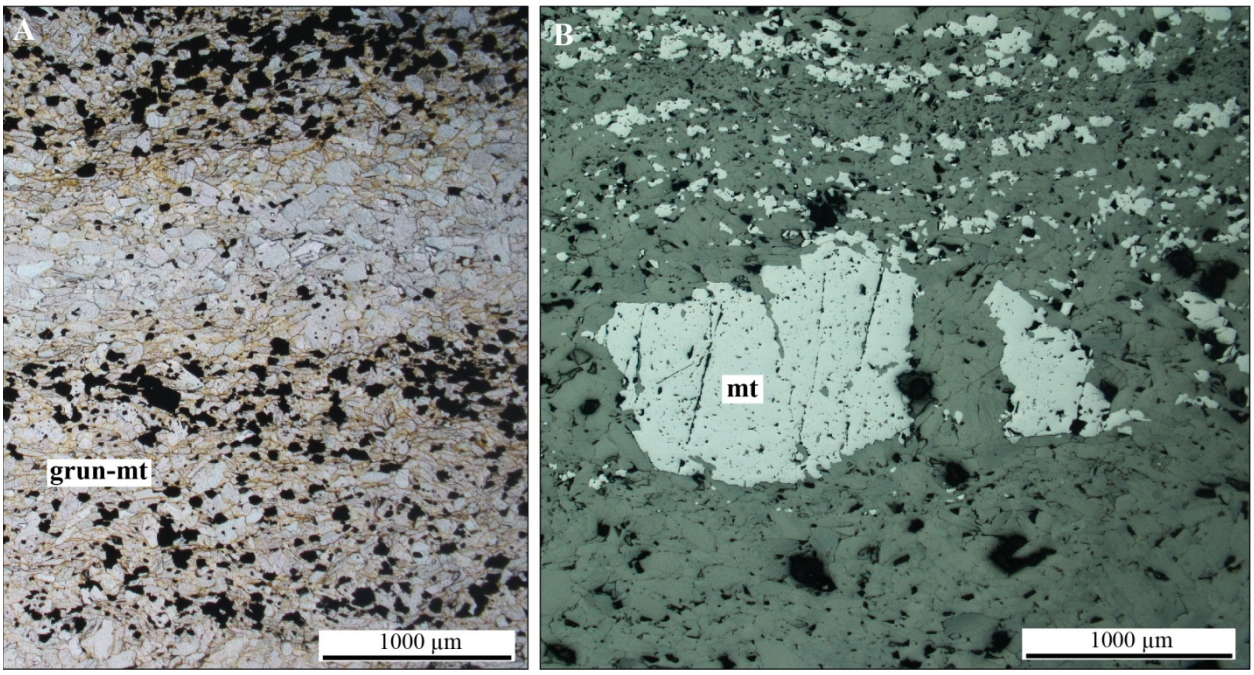

Figure 6-13: A. Microphotograph of fine- to medium-grained grunerite crystals in grunerite-magnetite and grunerite bands, unit 4B, surface sample MW-13-443, Trench 5. Plain polarized light. B. Microphotograph of large magnetite aggregate in grunerite matrix, reflected light, same sample as A.

Amphibole-rich bands frequently contain an assemblage of hedenbergite intergrown with grunerite-quartz-calcite (Figure 6-14A). This iron-rich clinopyroxene can be formed through the following reaction (Haase, 1982):

$$\text{calcite} + \text{grunerite} + \text{quartz} = \text{clinopyroxene} + CO_2 + H_2O.$$

Unit 4B has a higher primary CO_2 content than unit 4EA (i.e., 1.79 vs. 0.16 average wt.% content; chapter 3). Unlike unit 4EA, unit 4B may locally contain enough carbonates to form pyroxene without CO_2 enrichment during metamorphism. Inclusion-poor, red to orange almandine garnet is locally associated with pyroxene, representing a facies equivalent to staurolite-zone to sillimanite-zone in typical pelitic rocks (Klein, 2005). These phases show little evidence of deformation, suggesting late-D_2 crystallization. These metamorphic conditions positively correlate with those locally reported north of Opapimiskan Lake area (2; Kelly et al., 2013; Gagnon et al., 2015).

Locally, hedenbergite is altered to an orange-brown Al-rich oxyhydroxide (Figure 6-14B). This alteration can be spatially associated with aegirine-calcite veinlets, in the vicinity of which hornblende is altered to riebeckite. This is indicative of rehydration (Morfin et al., 2013), possibly linked to Na-metasomatism under high metamorphic conditions, as evidenced by the presence of aegirine, and implications will be discussed in chapters 8 and 10.

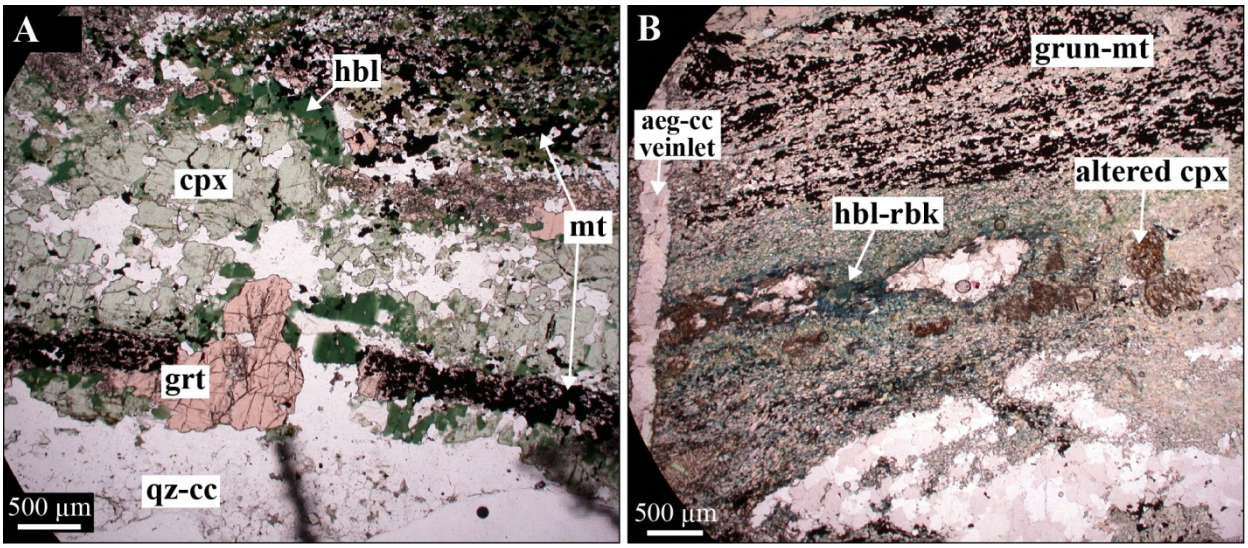

Figure 6-14: A. Microphotograph of pale green clinopyroxene intergrown with deep green hornblende and pink garnet between quartz-calcite and grunerite-hornblende-magnetite-garnet bands. Garnets have extremely poikilitic and magnetite-rich core. Same sample as B., plain polarized light. B. Microphotograph of aegirine-calcite veinlet cutting grunerite-magnetite and grunerite-hornblende-clinopyroxene bands in unit 4B sample. Hornblende is altered to riebeckite, and hedenbergite is altered to an orange-brown Al-oxyhydroxide. Sample MW-11-136, DDH 10-PQE-053, plain polarized light.

6.3.3 Unit 4A

Unit 4A is a secondary silicate-BIF. It consists of quartz-rich chert bands alternating with grunerite-hornblende ± pyroxene ± magnetite bands (3; Figure 3-33E). While present in both NIF and SIF sequences, unit 4A is best developed in the SIF.

Similar to unit 4B, grunerite in unit 4A partially delineates the $S_{0\text{-}1}$ fabric in zones of low D_2 deformation (Figure 6-15A) and is affected by the main S_2 fabric elsewhere. It supports previous observations that M_1 metamorphism reached greenschist facies conditions. Hedenbergite intergrown with grunerite occurs near chert bands (Figure 6-15B). Hedenbergite appears to have experienced little to no D_2 strain. The metamorphic reaction involved is thought to be mainly the same than in unit 4B (i.e., calcite + grunerite + quartz = clinopyroxene + CO_2 + H_2O; Haase, 1982). The absence of calcite suggests it was a limiting factor to the reaction. The presence of Hedenbergite in unit 4A attests of peak M_2 metamorphism conditions equivalent to staurolite-zone to sillimanite-zone in typical pelitic rocks (Klein, 2005).

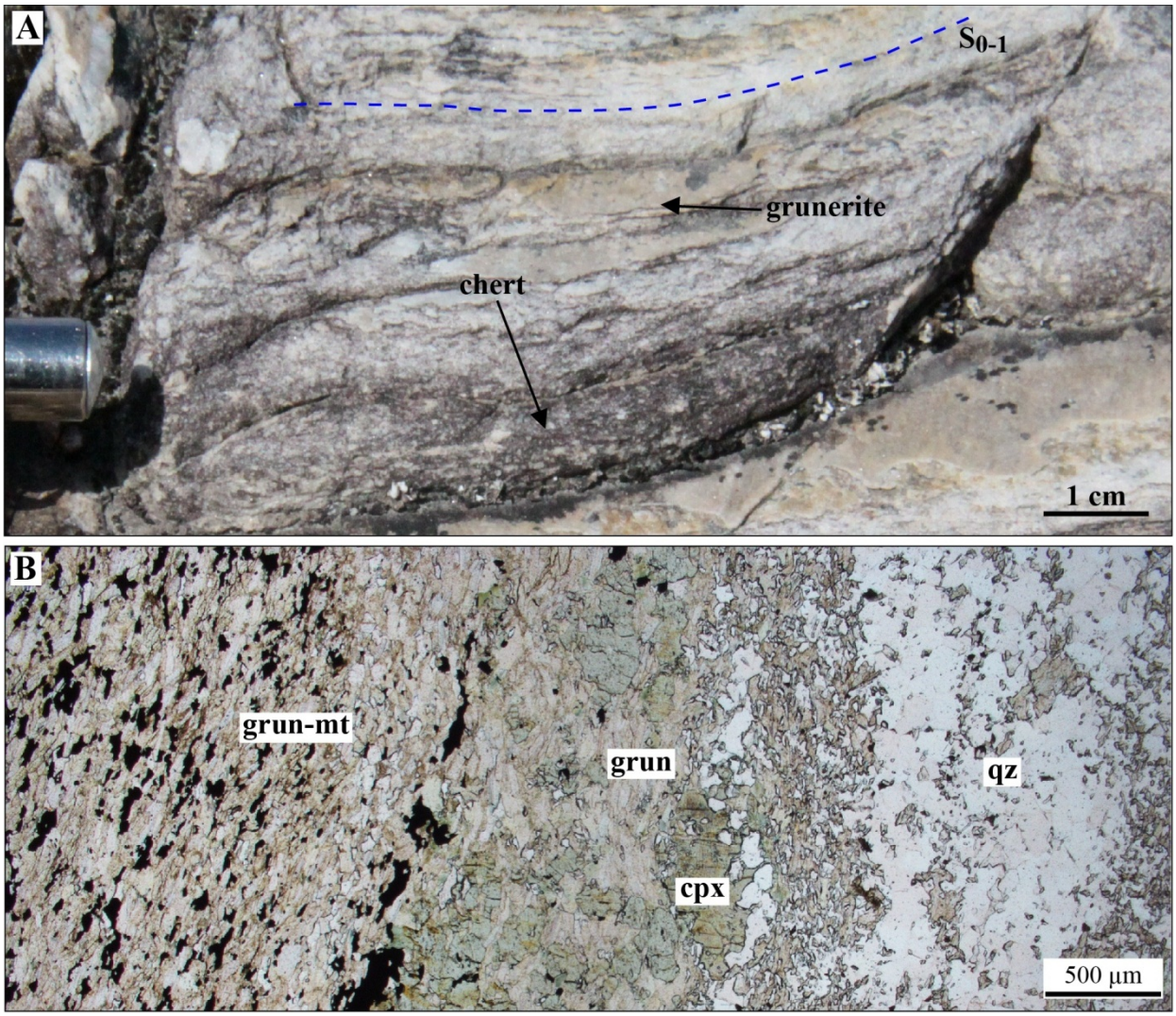

Figure 6-15: A. Chert-rich unit 4A with grunerite delineating the S_{0-1}, Trench 4 exposure, West antiform area. B. Pale green, anhedral to subhedral hedenbergite crystals in grunerite ± magnetite matrix, at the interface with well-foliated, grunerite-magnetite band and quartz band in unit 4A BIF, plain polarized light; qz = quartz, cpx = hedenbergite, grun = grunerite, mt = magnetite. Sample MW-12-335, DDH 09-TAN-014.

6.4 Thermobarometric and geochronological constraints of M_2 metamorphism

The overall paragenesis of the OMA in the Opapimiskan Lake area attests for a regional prograde metamorphism that reached greenschist facies during M_1 phase, and attained lower to middle amphibolite facies during peak M_2 metamorphism. First-order estimates, based on the mineralogical and petrographic data from this study and using petrogenetic diagrams of Winter (2001) and Tinkham et al. (2011), suggest that peak M_2 thermobarometric conditions have reached between 550 and 650°C and below 0.35 GPa. Previous studies (Otto, 2002; Biczok et al., 2012; Kalbfleisch, 2012; Gagnon, 2015; Kelly and Schneider,

2015), augmented by new geothermometric and U-Th-Pb in situ geochronological data presented below, provide updated constraints on peak metamorphism.

6.4.1 Thermobarometry of M2 metamorphism

6.4.1.1 Introduction

Hall and Rigg (1986) have provided the first constraints on the thermobarometric conditions of regional metamorphism. They analyzed unit 4F samples from the West antiform area, 2-3 km west of Musselwhite mine, using the grt-bt Fe-Mg exchange thermometer of Ferry and Spear (1978) and reported peak temperature estimates of around 550°C for pressures of 0.3 GPa. Otto (2002) used the grt-bt Fe-Mg exchange thermometer of Indares and Martignole (1985), the Ti in hornblende thermometer (Colombi, 1988), and the Grt-Hbl continuous net-transfer equilibria thermometer, as described in Graham and Powell (1984). Otto (2002) also studied retrograde chlorite (chlorite thermometer from Walshe, 1986) to investigate the conditions of retrograde metamorphism. Their geobarometry data were estimated from the continuous net-transfer equilibria systems of Kohn and Spear (1990) and Hoisch (1990). Otto (2002) established temperature estimates ranging 550 to 600°C and pressure estimates of 0.6 to 0.7 GPa. This pressure data is unrealistically high given the documented mineralogy (e.g., absence of kyanite).

Geothermometry and geobarometry calculations are extremely complex, as they rely on many chemical, mineralogical, physical, and thermodynamic parameters (Winter, 2001). Published models are usually based on precise data sets and constant value calculations that hinder the direct use of a model to a different data set (e.g., Holdaway, 2000). In this context, we used microprobe data only to obtain tentative grt-bt geothermometric constraints.

6.4.1.2 Methodology

Garnet-biotite experimental calibrations in the Fe-Mg system were first done by Ferry and Spear (1978). This work was followed by numerous studies leading to work by Holdaway (2000, and reference therein), who used garnet and biotite in an Al-Ti-Fe-Mg-Ca-Mn system. In the present study, garnet-biotite geothermometric data was generated using point microprobe analyses of pelitic and BIF samples (Table 6-1). Barren samples were collected tens to hundreds of metres away from gold-mineralized rocks. Auriferous samples come from multiple ore zones (e.g., Lynx, Moose).

Two contexts of mineral assemblages were analyzed: the most common was garnet porphyroblast rim in contact with biotite (Figure 6-6C andFigure 6-16), whereas garnet rim and matrix biotite from distant

areas of the same thin section were used in a few cases. Three different calculations were done: 1) using calibrations of Ferry and Spear (1978) for reference to previous work at Musselwhite (Hall and Rigg, 1986); 2) using calibrations from Holdaway (2000) in the Al-Ti-Fe-Mg-Ca-Mn system; and 3) calibrations from Holdaway (2000) in the Fe-Mg system. Individual data results have ± 25°C uncertainties (Holdaway, 2000).

6.4.1.3 Results

In the Al-Ti-Fe-Mg-Ca-Mn system, grt-bt analyses from barren and gold-mineralized garnet-biotite schists, interpreted as pelitic samples, produce temperature estimates ranging between 605 and 635°C, with the exception of one data point at 680°C and two gold-bearing samples at 650-655°C (y-axis, Figure 6-17). The average temperature estimate from grt-bt analyses in pelitic samples is 624°C. Outlying data can be attributed to the higher Ca content of garnets, which tends to make calculations less reliable (Winter, 2001). Calculations in the Fe-Mg system for the same dataset yield a much wider variation, from 350 to 600°C (x-axis, Figure 6-17).

Table 6-1 : Garnet and biotite mineral chemistry data and corresponding calculated temperatures from Holdaway (2000). P = estimated pressure (in kbar) used to calculate temperature in the Fe-Mg system (last column); lnKD, B, G, B(T), G(T), D and X: parameters calculated from mineral chemistry data (including constant values from Holdaway, 2000). T°C, temperature calculated in the Al-Ti-Fe-Mg-Ca-Mn system.

				Bt								Grt				thermomètre Holdaway								
grt-bt couples	Rock type	Au	P	Fe	Mg	Alvi	Ti	XFe	XMg	XAl	XTi	XMg	XFe	XMn	XCa	lnKD	B	G	B(T)	G(T)	D	X	T°C	T°C non cor
MW-12-352-1	grt-bt schist		3	3,008	1,575	0,903	0,215	0,52763	0,27627	0,15839	0,03771	0,075	0,802	0,063	0,060	*1,719*	*227687*	*10328,4*	*-262,7*	*-0,192*	*16,89*	*251709,6*	*627*	*538*
MW-12-352-2	grt-bt schist		3	3,030	1,570	0,831	0,262	0,53223	0,27578	0,14597	0,04602	0,077	0,791	0,071	0,061	*1,673*	*212474*	*10497,5*	*-245,5*	*-0,018*	*16,51*	*236665,2*	*630*	*556*
MW-12-146-1	grt-bt schist		3	3,246	1,353	0,793	0,301	0,57017	0,23766	0,13929	0,05287	0,074	0,850	0,024	0,052	*1,564*	*203524*	*9230,7*	*-236,1*	*-1,120*	*15,61*	*226448,4*	*623*	*605*
MW-12-146-2	grt-bt schist		3	3,236	1,371	0,827	0,287	0,56564	0,23964	0,14456	0,05017	0,075	0,847	0,024	0,053	*1,561*	*211181*	*9198,3*	*-244,7*	*-1,059*	*15,58*	*234073,5*	*623*	*606*
MW-11-085 (2)	grt-bt schist		3	2,990	1,782	0,538	0,338	0,52941	0,31548	0,09533	0,05979	0,045	0,563	0,143	0,249	*2,009*	*145876*	*16109,0*	*-169,3*	*4,262*	*19,30*	*175678,6*	*680*	*436*
MW-11-091 (3)	grt-bt schist		3	2,908	2,316	0,595	0,160	0,48637	0,38736	0,09951	0,02676	0,074	0,794	0,068	0,063	*2,144*	*152153*	*10585,7*	*-175,0*	*-0,032*	*20,43*	*176432,3*	*630*	*397*
MW-12-406 (3c)	grt-bt schist		3	3,041	1,626	0,802	0,236	0,53304	0,28501	0,14058	0,04137	0,057	0,766	0,102	0,075	*1,972*	*204099*	*12325,5*	*-235,8*	*0,594*	*19,00*	*230118,3*	*632*	*448*
MW-12-406 (3)	grt-bt schist		3	3,265	1,458	0,865	0,154	0,56862	0,25392	0,15064	0,02682	0,036	0,789	0,103	0,073	*2,281*	*213512*	*13166,9*	*-246,9*	*0,385*	*21,57*	*240372,6*	*624*	*362*
MW-12-406 (2)a	grt-bt schist		3	3,278	1,447	0,863	0,163	0,56999	0,25161	0,15006	0,02834	0,044	0,790	0,095	0,071	*2,070*	*213410*	*12593,1*	*-246,9*	*0,275*	*19,81*	*239696,7*	*627*	*418*
MW-12-406 (2)b	grt-bt schist		3	3,278	1,447	0,863	0,163	0,56999	0,25161	0,15006	0,02834	0,057	0,793	0,075	0,075	*1,815*	*213410*	*11637,8*	*-246,9*	*0,181*	*17,69*	*238741,3*	*630*	*501*
MW-12-432 (3)	grt-bt schist		3	3,516	1,382	0,638	0,254	0,60719	0,23875	0,11012	0,04394	0,041	0,896	0,052	0,010	*2,141*	*161760*	*10701,6*	*-188,6*	*-2,463*	*20,40*	*186155,1*	*607*	*398*
MW-12-432 (4)a	grt-bt schist		3	3,502	1,268	0,819	0,194	0,60551	0,21931	0,14155	0,03363	0,055	0,888	0,038	0,018	*1,762*	*202586*	*9828,0*	*-235,2*	*-2,194*	*17,25*	*226108,3*	*615*	*521*
MW-12-432 (4)b	grt-bt schist		3	3,588	1,104	0,740	0,285	0,62763	0,19305	0,12941	0,0499	0,055	0,888	0,038	0,018	*1,599*	*187182*	*9828,0*	*-218,3*	*-2,194*	*15,89*	*210703,9*	*618*	*589*
MW-12-545 (2)	grt-bt schist	*y*	3	3,329	1,751	0,506	0,226	0,57278	0,30127	0,08706	0,03889	0,063	0,728	0,034	0,175	*1,805*	*130102*	*11848,3*	*-151,5*	*1,727*	*17,61*	*155643,8*	*657*	*505*
MW-12-545 (1b)	grt-bt schist	*y*	3	3,306	1,783	0,580	0,215	0,56186	0,30303	0,09857	0,03654	0,063	0,732	0,035	0,171	*1,835*	*147835*	*11844,1*	*-171,6*	*1,670*	*17,86*	*173372,9*	*650*	*494*
MW-12-535 (1)	grt-bt schist	*y*	3	3,493	0,998	0,874	0,259	0,62109	0,17745	0,15541	0,04605	0,039	0,817	0,072	0,072	*1,789*	*218738*	*12243,9*	*-254,3*	*-0,163*	*17,48*	*244675,6*	*627*	*511*
MW-12-535 (2)	grt-bt schist	*y*	3	3,767	1,178	0,694	0,203	0,64481	0,20164	0,11879	0,03475	0,044	0,834	0,054	0,068	*1,780*	*171032*	*11532,3*	*-199,7*	*-0,568*	*17,40*	*196258,5*	*629*	*514*
MW-12-404-1	grt-amphibolite		3	4,307	0,988	0,446	0,224	0,72205	0,16563	0,07477	0,03755	0,031	0,837	0,053	0,080	*1,837*	*108401*	*12228,3*	*-129,2*	*-0,453*	*17,88*	*134323,5*	*637*	*493*
MW-12-404-2	grt-amphibolite		3	4,207	0,940	0,485	0,220	0,7189	0,16063	0,08288	0,03759	0,033	0,776	0,032	0,159	*1,654*	*117948*	*12509,8*	*-140,2*	*1,225*	*16,35*	*144152,0*	*655*	*565*
MW-13-272-2	silicate BIF		3	4,051	0,951	0,509	0,259	0,70208	0,16482	0,08821	0,04489	0,031	0,825	0,047	0,097	*1,847*	*126593*	*12311,9*	*-150,0*	*-0,069*	*17,95*	*152598,9*	*635*	*490*
MW-12-171B (2/3)	oxide-BIF		3	3,583	1,584	0,549	0,154	0,61039	0,26985	0,09353	0,02624	0,023	0,763	0,125	0,089	*2,687*	*135139*	*14417,4*	*-157,7*	*1,091*	*24,94*	*163250,2*	*626*	*276*
MW-11-128 (4)	chert-grun BIF		3	4,003	1,2	0,341	0,240	0,69208	0,20747	0,05896	0,04149	0,022	0,693	0,119	0,166	*2,245*	*85494,6*	*15156,5*	*-102,5*	*2,916*	*21,27*	*114345,0*	*673*	*371*
MW-11-129 (5)	chert-grun BIF		3	3,402	1,588	1,031	0,167	0,54977	0,25663	0,16661	0,02699	0,048	0,711	0,103	0,138	*1,934*	*254822*	*13627,3*	*-293,9*	*2,029*	*18,68*	*282143,7*	*636*	*460*
MW-13-276-2	grt-amphibolite	*y*	3	3,615	1,573	0,576	0,167	0,60951	0,26522	0,09712	0,02816	0,046	0,627	0,053	0,274	*1,781*	*142281*	*13826,2*	*-165,9*	*3,636*	*17,41*	*169800,6*	*672*	*514*
MW-12-372 (6)	silicate BIF	*y*	3	3,416	1,685	0,464	0,224	0,59008	0,29107	0,08015	0,03869	0,078	0,816	0,006	0,100	*1,641*	*119096*	*9463,8*	*-139,2*	*-0,224*	*16,24*	*142253,8*	*641*	*570*
MW-12-193 (3)	silicate BIF	*y*	3	3,458	1,578	0,536	0,230	0,596	0,27198	0,09238	0,03964	0,077	0,754	0,045	0,124	*1,501*	*136496*	*10962,1*	*-159,3*	*0,986*	*15,08*	*161151,8*	*656*	*635*
MW-13-246-5	clastic oxide-BIF	*y*	3	4,060	0,957	0,392	0,330	0,70744	0,16675	0,0683	0,0575	0,029	0,794	0,041	0,136	*1,882*	*101707*	*12678,9*	*-121,8*	*0,824*	*18,25*	*128079,5*	*647*	*477*
MW-13-191-3	clastic oxide-BIF	*y*	3	3,962	1,060	0,482	0,264	0,68689	0,18377	0,08356	0,04577	0,031	0,700	0,061	0,209	*1,814*	*121023*	*13812,0*	*-143,3*	*2,856*	*17,68*	*148528,5*	*666*	*502*
MW-13-191-4	clastic oxide-BIF	*y*	3	4,372	1,085	0,318	0,217	0,72964	0,18107	0,05307	0,03621	0,043	0,783	0,065	0,109	*1,513*	*76734,4*	*12427,5*	*-93,0*	*0,733*	*15,18*	*102855,8*	*684*	*629*
MW-13-190-2	oxide-BIF	*y*	3	4,127	1,145	0,532	0,135	0,6949	0,19279	0,08958	0,02273	0,023	0,773	0,120	0,085	*2,248*	*126159*	*14248,0*	*-148,8*	*0,897*	*21,29*	*154101,0*	*638*	*370*
MW-13-190-3	oxide-BIF	*y*	3	4,103	1,126	0,562	0,117	0,69448	0,19059	0,09513	0,0198	0,025	0,719	0,095	0,161	*2,068*	*132574*	*14406,0*	*-156,1*	*2,437*	*19,79*	*160674,3*	*653*	*419*
MW-11-082 (2)	altered mafic volcanic rock		3	2,861	2,065	0,572	0,241	0,4985	0,35984	0,09966	0,04199	0,069	0,694	0,083	0,155	*1,983*	*150331*	*12719,4*	*-173,5*	*2,072*	*19,09*	*176744,0*	*655*	*444*

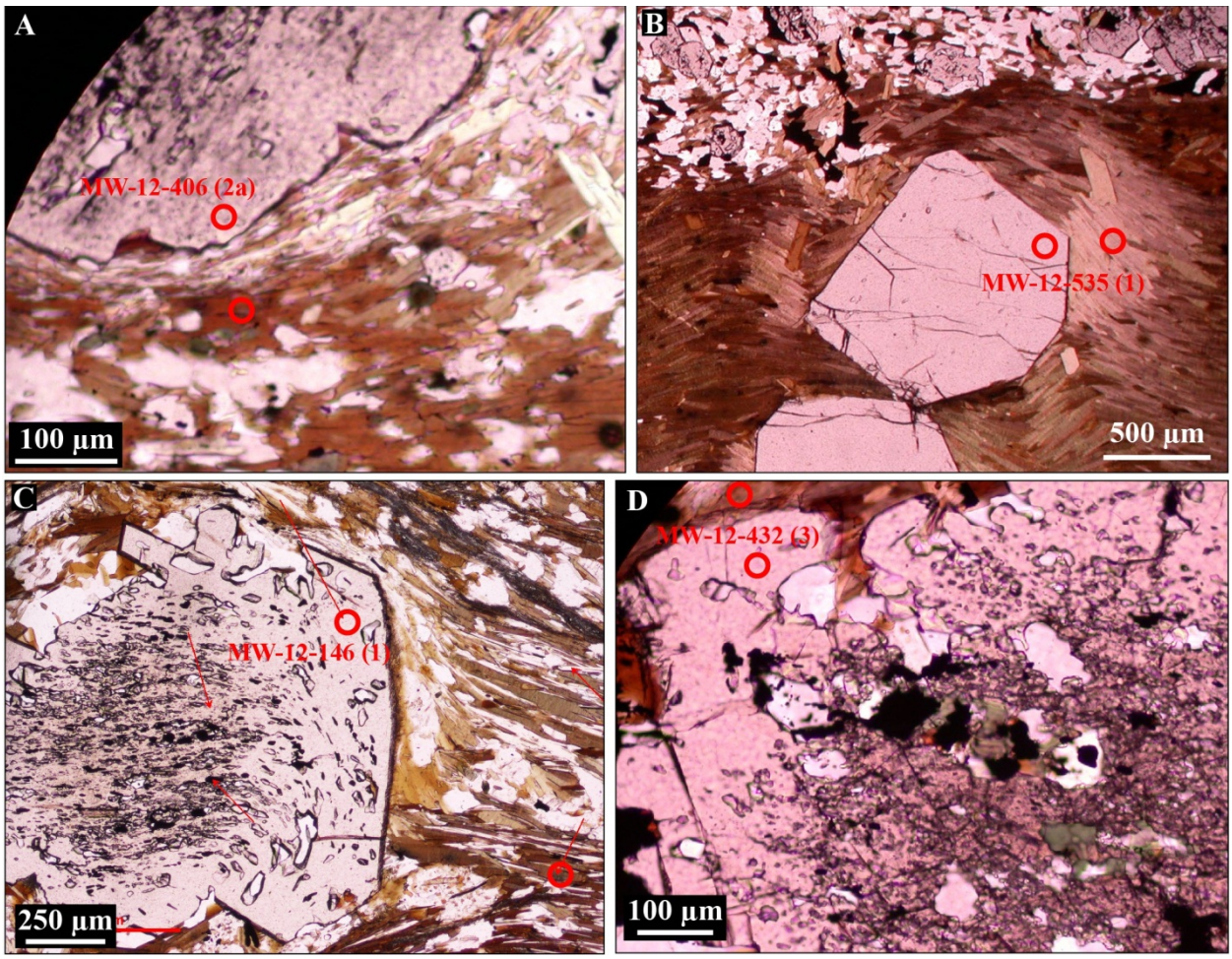

Figure 6-16: Microphotographs with locations of garnet and biotite spot analyses in barren (A, C, and D) and auriferous (B) garnet-biotite schist samples, plain polarized light. A. Sample MW-12-406, circle 2. B. Sample MW-12-535, circle 1. C. Sample MW-12-146, circle 1. D. Sample MW-12-432, circle 3.

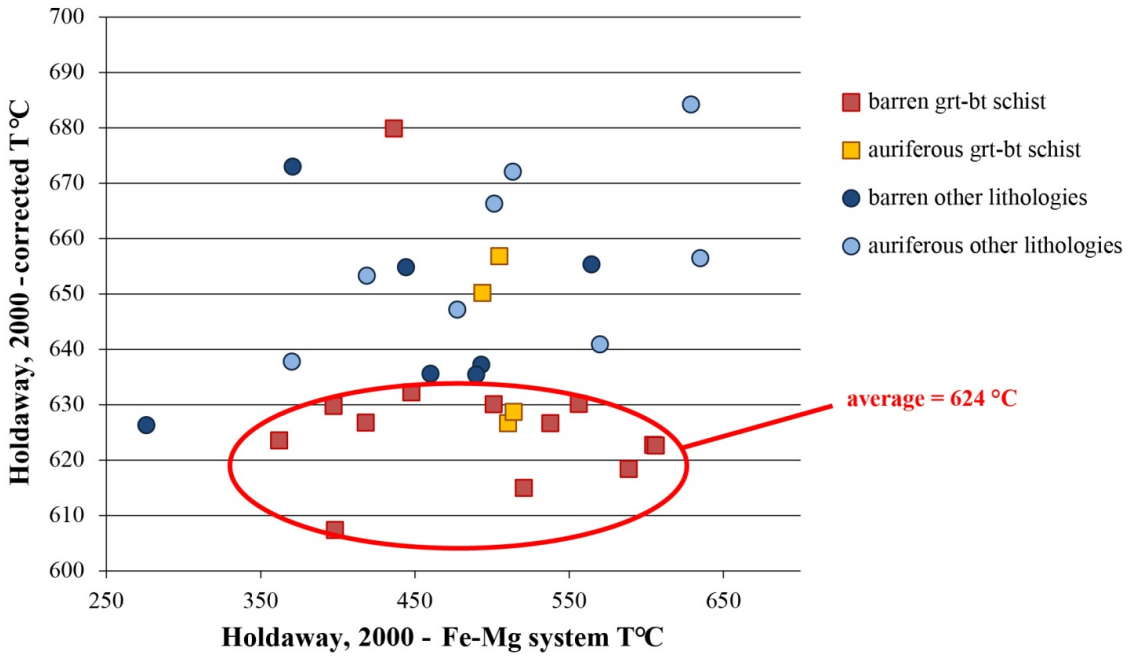

Figure 6-17: Garnet-biotite temperature calculations from Holdaway (2000). X-axis represents temperature calculations in the Fe-Mg system. Y-axis represents temperature calculations corrected for the effects of Al and Ti in biotite as well as Ca and Mn in garnet, which gives more reliable values. Grt-bt schist samples, without the 650°C and 680°C outlying data, provide an average temperature of 624°C. Although the standard deviation on these results is ± 7°C, the uncertainty stemming from the initial model is typically considered to be ± 25°C (Holdaway, 2000).

Almost all calculations from grt-bt couples in barren and auriferous BIF samples are higher than those of pelitic samples (Figure 6-17), which is most probably related to the higher Ca content of garnets in iron formation samples (Table 6-1). There is no apparent distinction between results from barren and auriferous BIF samples.

Temperature calculations using the Fe-Mg system based on Ferry and Spear (1978) produce results similar to those from the Holdaway (2000) method, but with a fairly consistent offset (Figure 6-18), possibly due, in part, to differences in mathematical expression used for calculations. Although considerably higher than previous estimates, these preliminary results correlate quite well with the observed mineral assemblages (Winter, 2001). At least one other study (Paulick and Franz, 2001) pointed out the tendency of Holdaway's geothermometer to give high temperature estimates (i.e., in the 550-850°C range). Paulick and Franz (2001) used calibrations from Kleeman and Reinhardt (1994.

Temperature calculations from three monazite-bearing garnet-biotite schist samples (MW-12-406, 12-432; 12-535) yield homogeneous estimates that average 624 ± 8°C. U-Th-Pb in situ geochronological analysis of these same samples was carried out to determine the timing of peak metamorphism. The results are presented below.

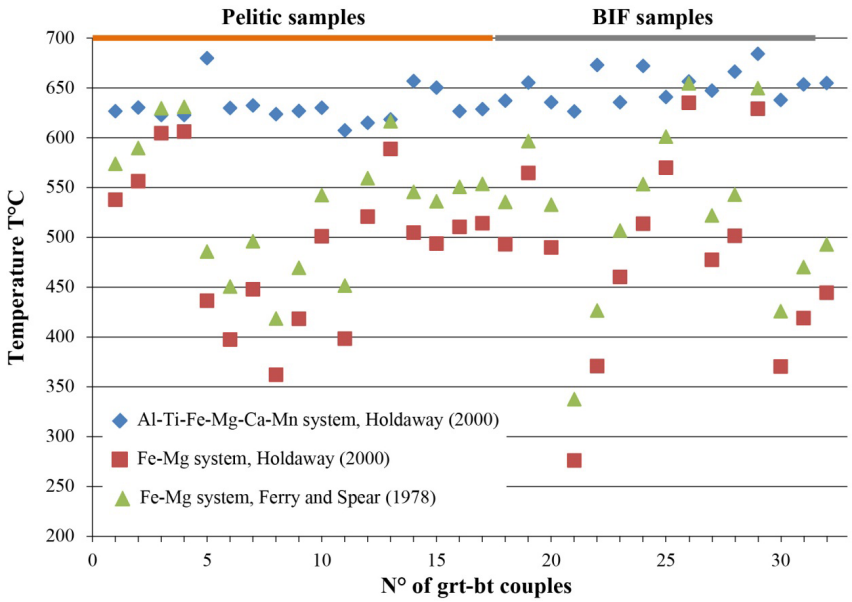

Figure 6-18: Comparison of temperature calculations from Holdaway (2000) corrected (blue diamond), non corrected (red square), and Ferry and Spear (1978) (green triangle).

6.4.2 Geochronology of M_2 metamorphism

In situ monazite U-Th-Pb geochronology has become a common method to establish the age of igneous and metamorphic events, using non-destructive techniques such as electron microprobe or in situ ion microprobe analyses (Parrish, 1990; Catlos et al., 2002). Monazite tends to crystallize under metamorphic conditions of the staurolite or garnet zones in pelitic rocks (Smith and Barreiro, 1990), and remains stable at high temperatures (Montel et al., 2000). In pelitic rocks, monazite forms from precursor minerals such as allanite, apatite and REE/Ti oxides at temperatures above 500°C (Smith and Barreiro, 1990). Some issues in the interpretation of monazite results include (Catlos et al., 2002): 1) analytical uncertainties, 2) spot of analysis overlapping age domains within monazite grains, 3) Pb loss from prolonged high-grade metamorphic conditions, 4) retrograde dissolution or re-precipitation reactions, and 5) episodic monazite growth. Some issues can be linked to bulk chemical composition of the host pelitic rock, which can influence monazite growth and composition (Winter, 2001; Catlos et al., 2002; Fitzsimons et al., 2005).

At Musselwhite, mineral textural relationships and geological observations indicate that peak M_2 metamorphism is syn- to late-D_2 deformation, and that gold-mineralized zones have a strong spatial association with D_2 structures (chapter 5 and chapter 7). Determining the age of M_2 metamorphism using in situ monazite U-Th-Pb geochronology provides better constraints on the timing of gold mineralization at Musselwhite. The following sections summarize the geochronological results; data tables are provided in Appendix II.

6.4.2.1 Methodology

Four samples of garnet-biotite schist (unit 4F) were selected (Table 6-2). Two samples were taken in the T-antiform structure of the mine area, a few hundreds of metres away from any known gold-mineralized zone (MW-12-406 and -432). Two other samples were taken in gold-bearing zones of the PQD area (MW-12-535 and -545). Upon examination of the thin sections under Secondary Electron Microscope (SEM), three contained monazite grains. These samples are mainly composed of 40-60% biotite, 15-25% almandine garnet, and 17-25% quartz (Figure 6-19A, B). Minor to accessory phases include: grunerite, plagioclase, tourmaline, ilmenite and allanite. Complete petrographic description of the samples is provided in Appendix II.

Table 6-2: Location of garnet-biotite schist samples with gold content and monazite occurrence.

Sample #	DDH	From (m)	To (m)	Au content	Monazite
MW-12-432	12-BIN-004	219,0	219.4	Barren	yes
MW-12-406	12-TAN-031	308.5	308.7	Barren	yes
MW-12-535	09-PQE-050	119.1	119.5	4.58 ppm	yes
MW-12-545	09-PQE-075	169,5	169,9	7.5 ppm	no

6.4.2.2 Monazite grains

Monazite grains were individually examined and ranked based on their morphology, size and textural context (Table 6-3). They all show homogeneous texture under SEM, although some are fractured (Appendix II). Monazite grains lay in three main textural contexts (Figure 6-19C): 1) in biotite-dominated matrix, aligned with the main S_2 foliation; 2) in the matrix but in contact with a garnet crystal; or 3) as an inclusion in the outer inclusion-free rim of a garnet crystal. Analyzed monazite grains from this study are particularly small, averaging 174 square µm in surface (Results

Despite diverse contexts and the small size of monazite grains, there are no significant age differences between the three analyzed monazite grains found as inclusions in garnet porphyroblasts and the eight present in the matrix (Table 6-3). There is also no meaningful age difference between monazite grains from the gold-bearing sample (5 grains) and those of the barren samples (6 grains). Data yields a tight cluster (except one) of homogeneous results giving a regression age of 2660 Ma. This indicates that syn-D2- peak M2 metamorphism occurred at 2660 Ma; the implications of such data for regional tectonometamorphic evolution and the timing of gold mineralization at Musselwhite will be discussed in chapter 10.

). Smaller monazite grains are generally less prone to Pb loss, because their surface area to volume ratio is higher than that of larger grains (Catlos et al., 2002). In addition, grains found as inclusions in garnet porphyroblasts are less subjected to Pb loss than monazite of the matrix (Montel et al., 2000).

6.4.2.3 Results

Despite diverse contexts and the small size of monazite grains, there are no significant age differences between the three analyzed monazite grains found as inclusions in garnet porphyroblasts and the eight present in the matrix (Table 6-3). There is also no meaningful age difference between monazite grains from the gold-bearing sample (5 grains) and those of the barren samples (6 grains). Data yields a tight cluster (except one) of homogeneous results giving a regression age of 2660 Ma. This indicates that syn-D_2- peak M_2 metamorphism occurred at 2660 Ma; the implications of such data for regional tectonometamorphic evolution and the timing of gold mineralization at Musselwhite will be discussed in chapter 10.

Table 6-3: Morphologic and petrographic characteristics of analyzed monazite grains.

Sample #	Grain #	Morphology	Area (sq. µm)	Breadth (µm)	Length (µm)	Textural context
MW-12-432	11349-1	equant	104,0	11,0	15,6	in biotite
	11349-4	equant	97,8	10,5	14,4	in garnet
	11349-2	equant	110,1	9,9	16,6	in biotite, touching garnet
MW-12-406	11350-39	elongate	244,6	12,5	31,3	in quartz; near biotite
	11350-40	elongate	165,1	7,6	30,1	in biotite
	11350-11	blocky	177,3	12,4	19,9	in biotite
MW-12-535	11351-14	elongate, corroded	299,6	14,7	33,6	in biotite
	11351-24	elongate	195,7	10,0	27,6	in garnet
	11351-8	equant, slightly corroded	97,8	10,5	16,6	in garnet
	11351-29	slighly elongate	226,2	15,1	26,7	in biotite
	11351-20	slighly elongate	195,7	12,3	25,5	in biotite

6.5 Summary and implications

Evidence of M_1 metamorphism is preserved in garnet that overgrows S_1 marked by chlorite and biotite inclusions. Staurolite porphyroblasts in pelitic rocks formed after S_1 and prior to the development of S_2, indicating that peak M_1 metamorphism post-dates D_1 deformation. Multiple generations of grunerite are present, the earliest of which crystallized during D_1 deformation. Subsequent generation(s) of grunerite

are complexly associated with almandine garnet porphyroblasts, where present. Garnet porphyroblasts typically show an internal zonation that indicates multiple stages of early- to late-D_2 growth (Figure 6-20). Local occurrences of clinopyroxene (hedenbergite in iron formations and pelites, diopside in mafic volcanic rocks) show that M_2 metamorphism has reached amphibolitic metamorphic conditions.

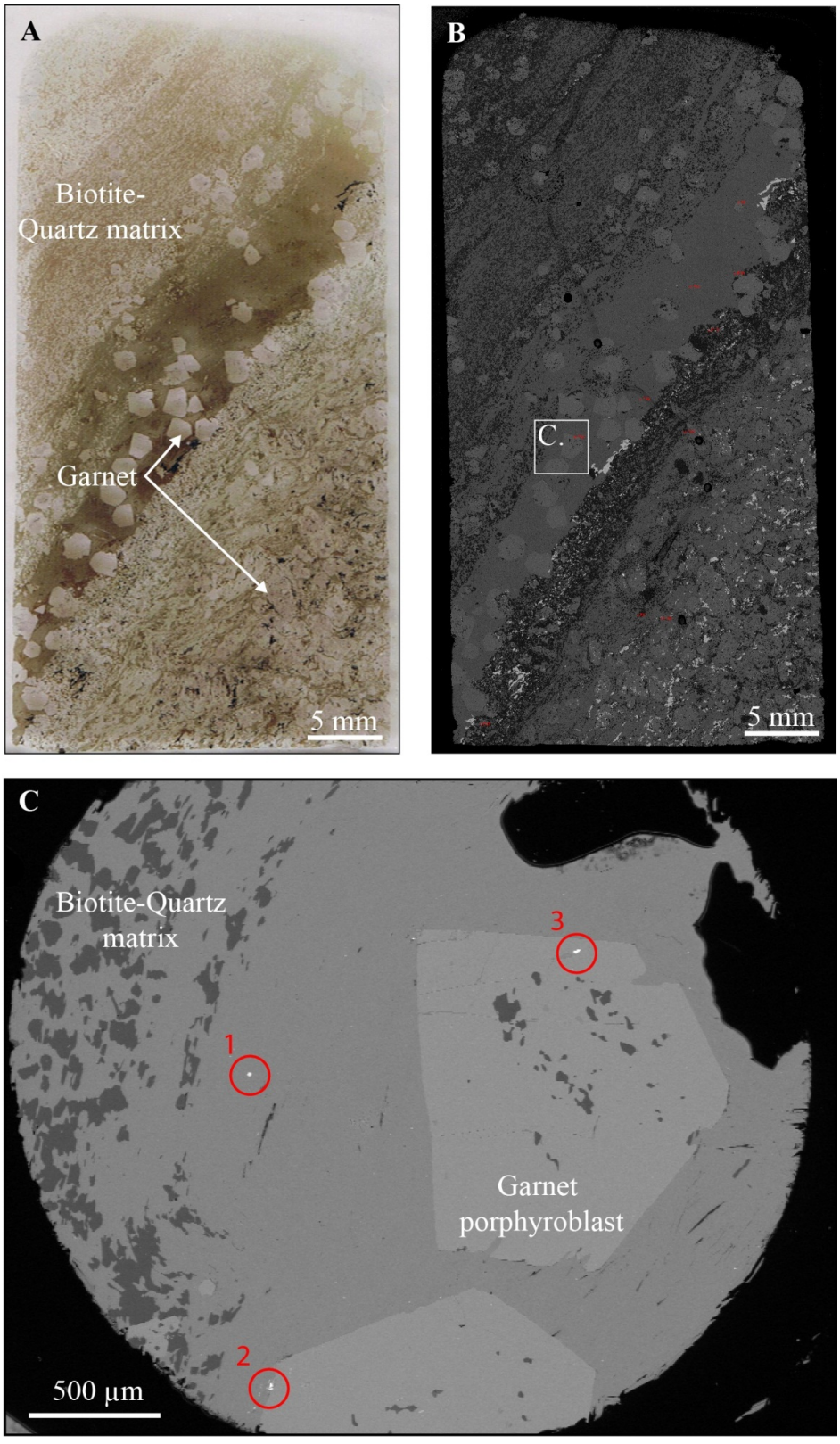

Figure 6-19: Petrographic and textural context of monazite grains (outlined by red dots and circles). A. Scan of the thin section from MW-12-535 sample of garnet-biotite schist. B. SEM image of the same thin section. C. Close-up of the SEM image with location of monazite grains as numbered in the text.

Petrographic observations coupled with the analysis of structural data show that metamorphism in the Opapimiskan Lake area is linked to two major phases of deformation (D_1 and D_2), and likely followed a single prograde path that culminated at the amphibolite facies at 2660 Ma (in situ monazite U-Pb data; Figure 6-20). Biczok et al. (2012) report a Sm-Nd garnet age of 2690 ± 9 Ma; however, the cited source (Maas, 2006, unpublished) also mentions a garnet separate yielding a Sm-Nd age of 2664 ± 19 Ma. This age and associated uncertainty cover and exceed the time range provided by the monazite data, which is in agreement with textural relationships showing that monazite occurs in garnet rims but is absent in cores (Figure 6-19C), indicating that garnet growth predated and outlasted monazite growth.

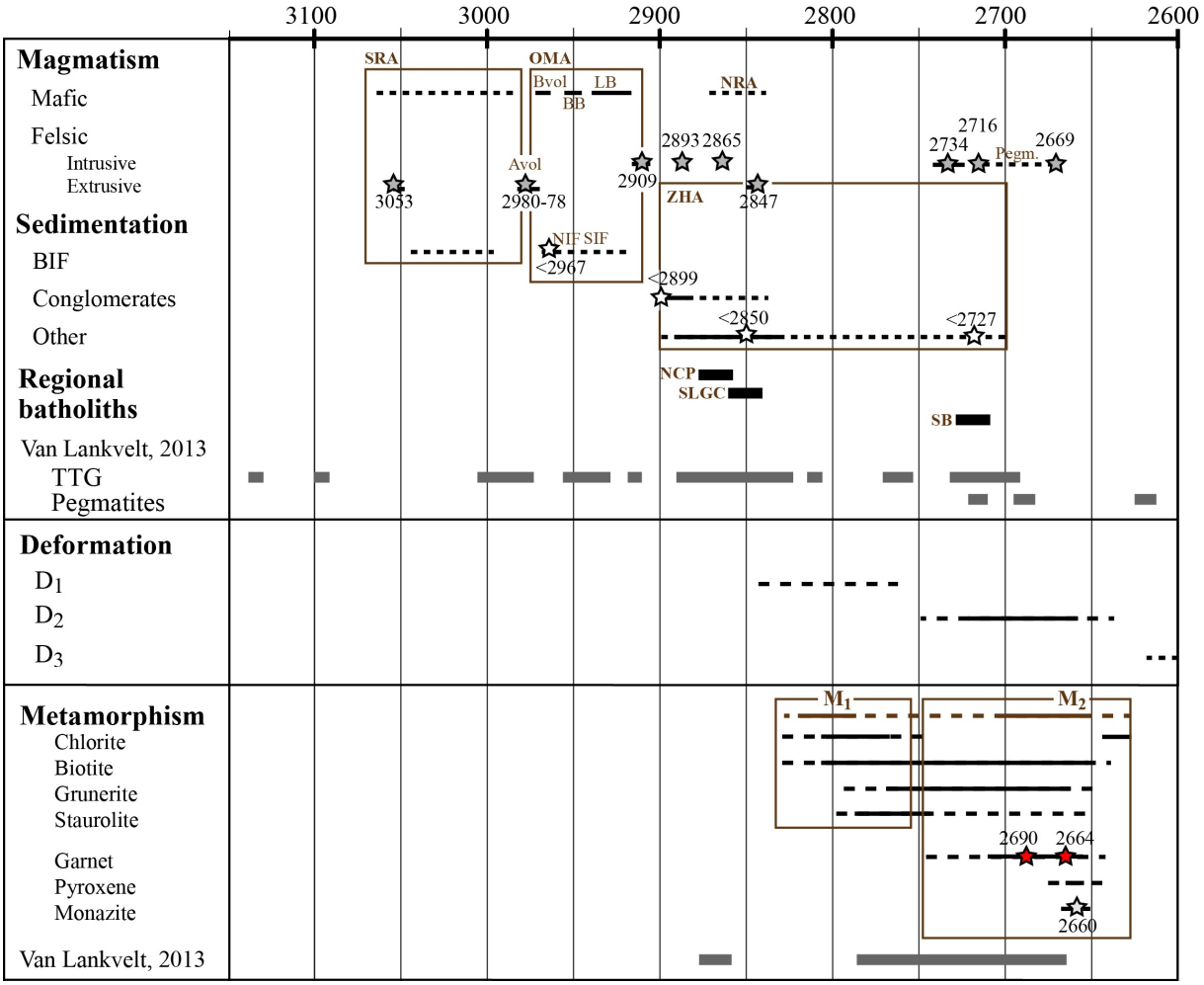

Figure 6-20: Synthetic diagram of the magmatic, sedimentary, structural and metamorphic evolution of the NCB in the Opapimiskan Lake area. Geochronological data (in Ma) is from Biczok et al. (2012), Kalbfeisch (2012), Van Lankvelt (2013), McNicoll et al. (2016), and this study (chapters 4 and6). Dash line: constraints to be improved.

7 CHARACTERISTICS AND DISTRIBUTION OF GOLD-MINERALIZED ROCKS

The study of gold-mineralized zones is critical to understand the genesis of the Musselwhite deposit. Previous studies have noted the spatial association of gold with D_2-related structures (Hall and Rigg, 1986; Breaks et al., 1985), as well as the presence of two major gold mineralization styles, consisting of quartz veining and sulphide-replacement of BIF (Hall and Rigg, 1986; Breaks et al., 2001; Otto, 2002; Blower and Kiernan, 2003; Moran, 2008; Biczok et al., 2012). Musselwhite has been described as an orogenic gold deposit (Otto, 2002), and a genetic relationship with magmatism was also suggested (Isaac, 2008; Stott and Biczok, 2010; Biczok et al., 2012). Previous petrographic studies of Musselwhite ore partly focused on the texture and chemical composition of garnet porphyroblasts to constrain the timing of gold mineralization (Kolb, 2010; Biczok et al., 2012; Duff, 2014).

This chapter presents the macroscopic, microscopic, and geochemical characteristics of gold mineralization at Musselwhite, focusing on the most economically viable host rock (garnet-grunerite BIF, unit 4EA), and depicts the relative timing relationships between gold mineralization and structural and metamorphic events. The replacement-style mineralization is mainly hosted in the garnet-grunerite BIF (unit 4EA), but also occurs with some mineralogical and textural variations in the garnet amphibolite (unit 4E), the grunerite-chert BIF (unit 4A), and the clastic and pure oxide-BIF (unit 4B, including facies 4Bc). Vein-style mineralization is hosted by the garnet-biotite schist (unit 4F), with rare occurrences of mafic volcanic rock-hosted auriferous veins (unit Bvol). Gold mineralization in unit 4B is a hybrid between the two main styles with replacement of magnetite by pyrrhotite and systematic presence of quartz veins.

7.1 Distribution and geometry of mineralized zones

Gold ore zones at Musselwhite are structurally related to F_2 folds (Figures 7-1, 7-2, 7-3, 7-4), regardless of host rock or mineralization style (Table 7-1). Ore zones are spatially associated with axial-planar high strain zones crosscutting hinges of tight F_2 folds (e.g., PQ Deeps, T-antiform, Jets) or along their attenuated limbs (e.g., Lynx, Esker, West limb), and commonly overlap the contact between unit 4B and 4EA (e.g., A-, B-, and C-blocks; Figure 7-2). Ore zones are 100-250 m-high and 5-15 m-thick, and extend over 200-1000 metres in length. In a few occurrences, economic gold mineralization shows a spatial association with a deformed ultramafic dyke. This is the case of the S2 and S3 ore zones (as mapped on mine level 1045, Figure 5-26B), which are located along strike of the dyke mapped on section 11775 N (Figure 7-2; Goldcorp Inc.). In the main part of the mine (PQD, TAN, and East limb areas), the ore zones

are sub-vertical to steeply dipping and sub-parallel to the axial plane of the East Bay synform (F_2). Mineralized zones in the West limb and in the Southern iron formation are slightly oblique to F_2 axial planes. Sub-economical gold mineralization is also documented along strike or beside the main ore zones (Figures 7-2, 7-3, 7-4).

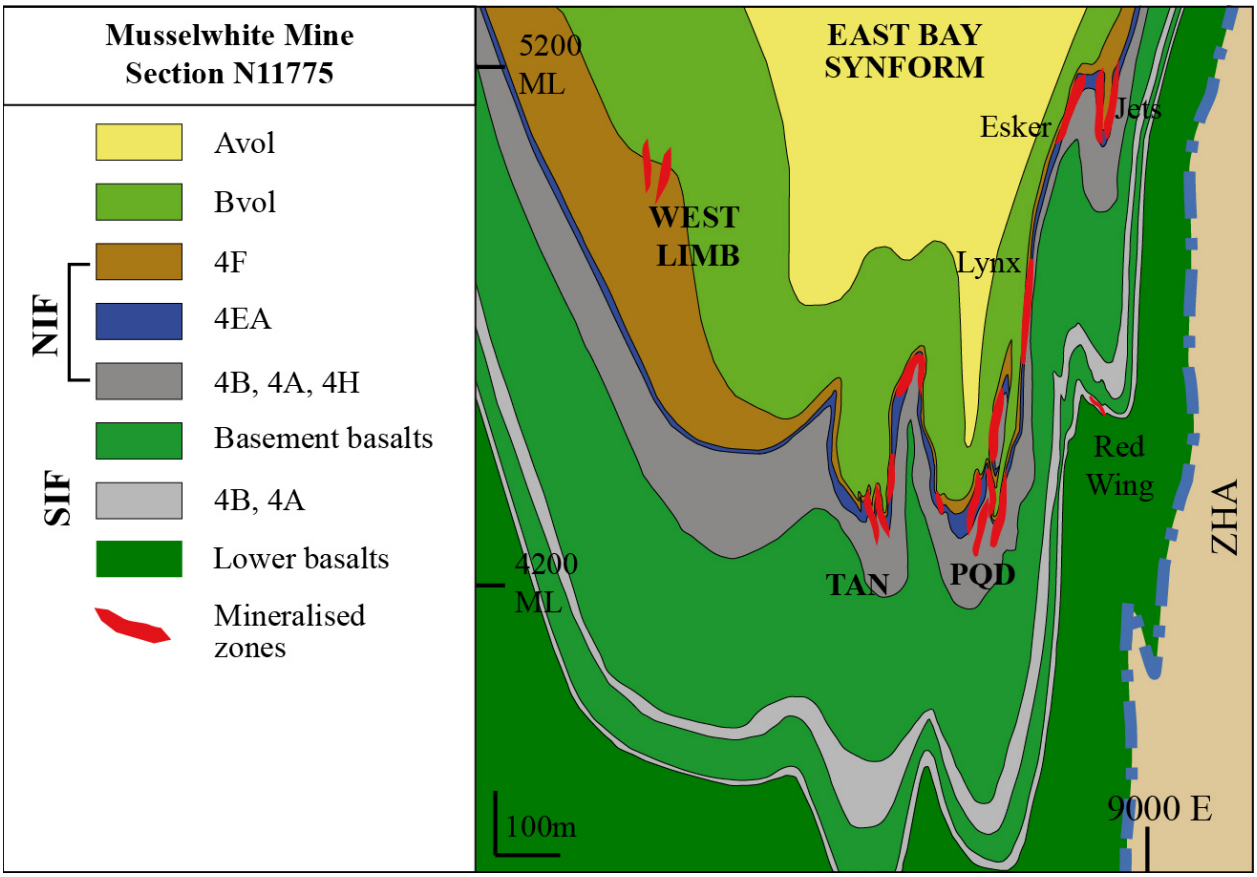

Figure 7-1: Simplified geological section of the mine at 11775 N, showing the locations of the main ore zones projected on a single mine section. See Figures 7-2, 7-3, 7-4 for individual ore zones name and detailed setting.

Table 7-1: List of the mine areas and the ore/mineralized zones, main host rock, and dominant mineralization style. Rock units: 4EA = garnet-grunerite BIF, 4B = oxide BIF, 4A = grunerite BIF, 4F = garnet-biotite schist, 2T = altered mafic volcanic rocks.

Mine area	Ore zone	Mineralized zone	Main host rock	Other host rock	Mineralization style
T-antiform	Moose		4EA		Replacement
	Eagle		4EA		Replacement
	Tan (S, C, T, WA)		4EA		Replacement
	S_1		4EA		Replacement
	S_2		4EA		Replacement
	S_3		4EA		Replacement
PQ Shallows	OP zone		4EA	4B	Mixed
	PQ zone		4EA	4B	Mixed
PQ Deeps	A-block		4EA	4B	Replacement
	B-block		4EA	4B	Mixed
	C-block		4EA		Replacement
	C_{east}-block		4EA		Replacement
	C_2-block		4EA		Replacement
	D-block		4B		Veining
East limb	Esker		4EA		Replacement
	Jets		4EA		Replacement
	Lynx		4EA	4F	Replacement
		Upper Lynx	4EA		Replacement
SIF		Red wing	4A	4B	Replacement
		Thunder wolves	4A	4B	Replacement
		Snoppy	4A	4B	Mixed
		South Snoppy	4A	4B	Mixed
West Limb	Spur		4F	2T	Veining
		Spur East	4F	2T	Veining

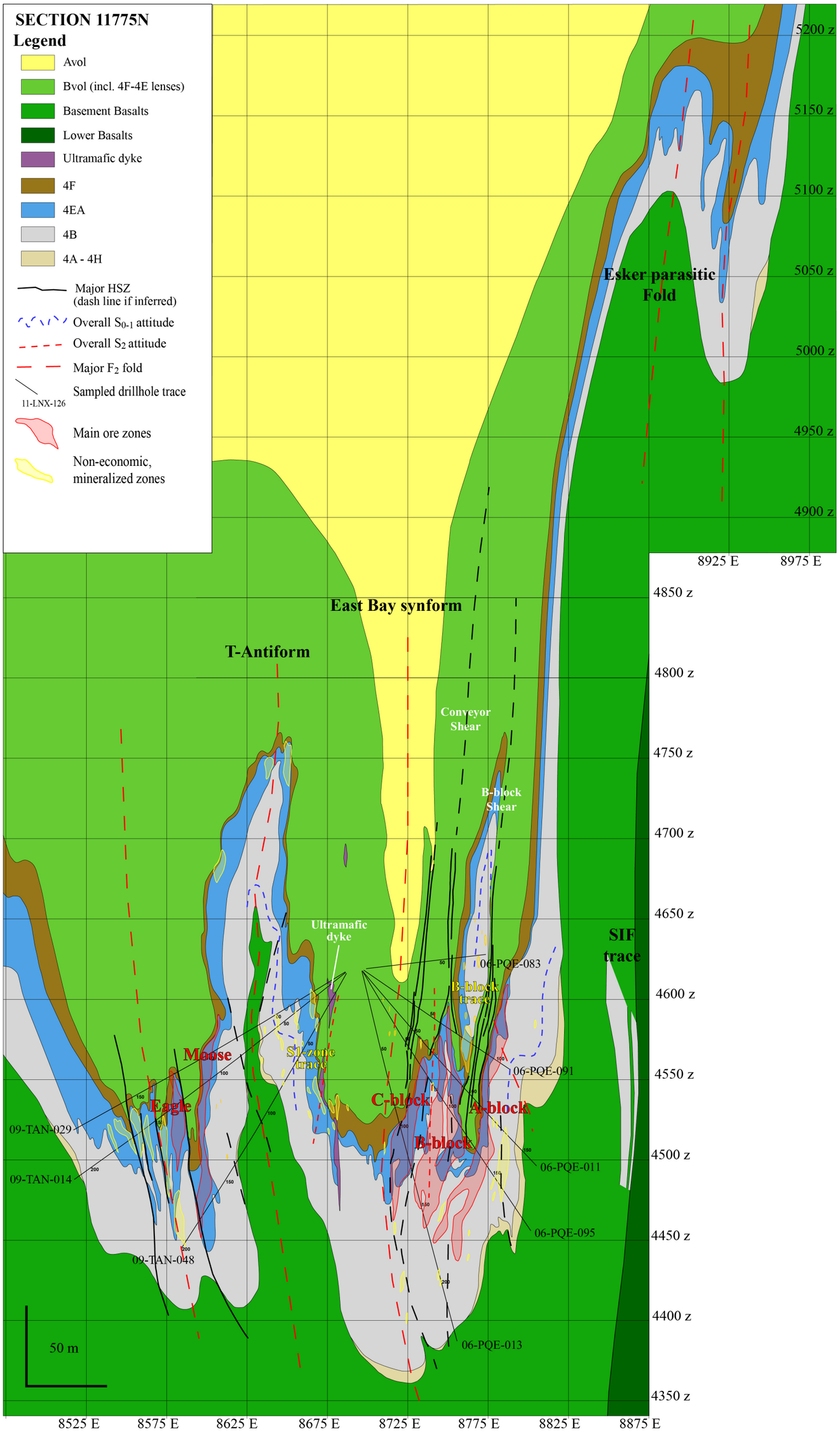

Figure 7-2: Geological and structural interpretation of mine section 11775 N, looking north, with contours of gold-mineralized rocks (yellow and red lines).

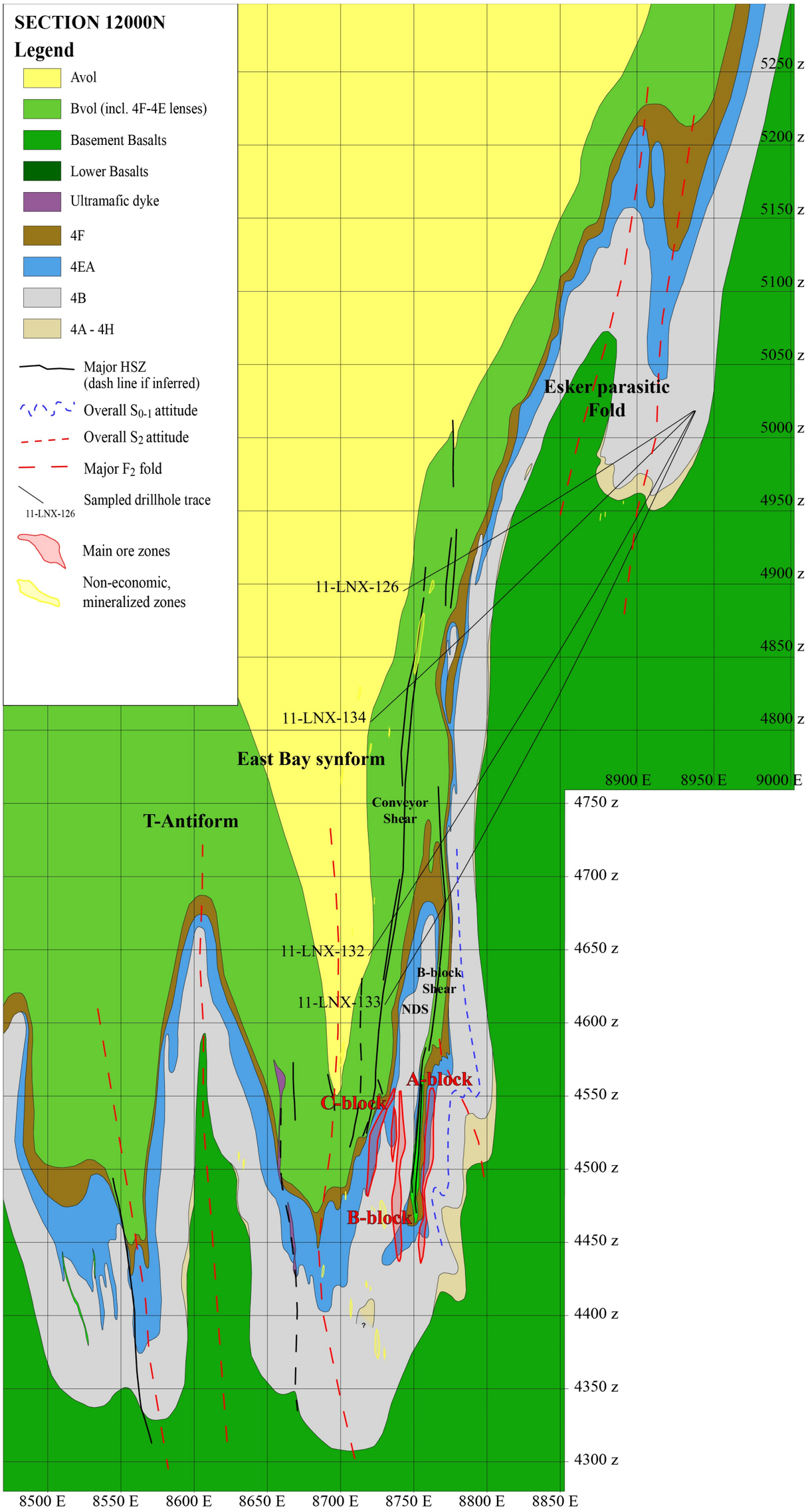

Figure 7-3: Geological and structural interpretation of mine section 12000 N, looking north, with contours of gold-mineralized rocks (yellow and red lines).

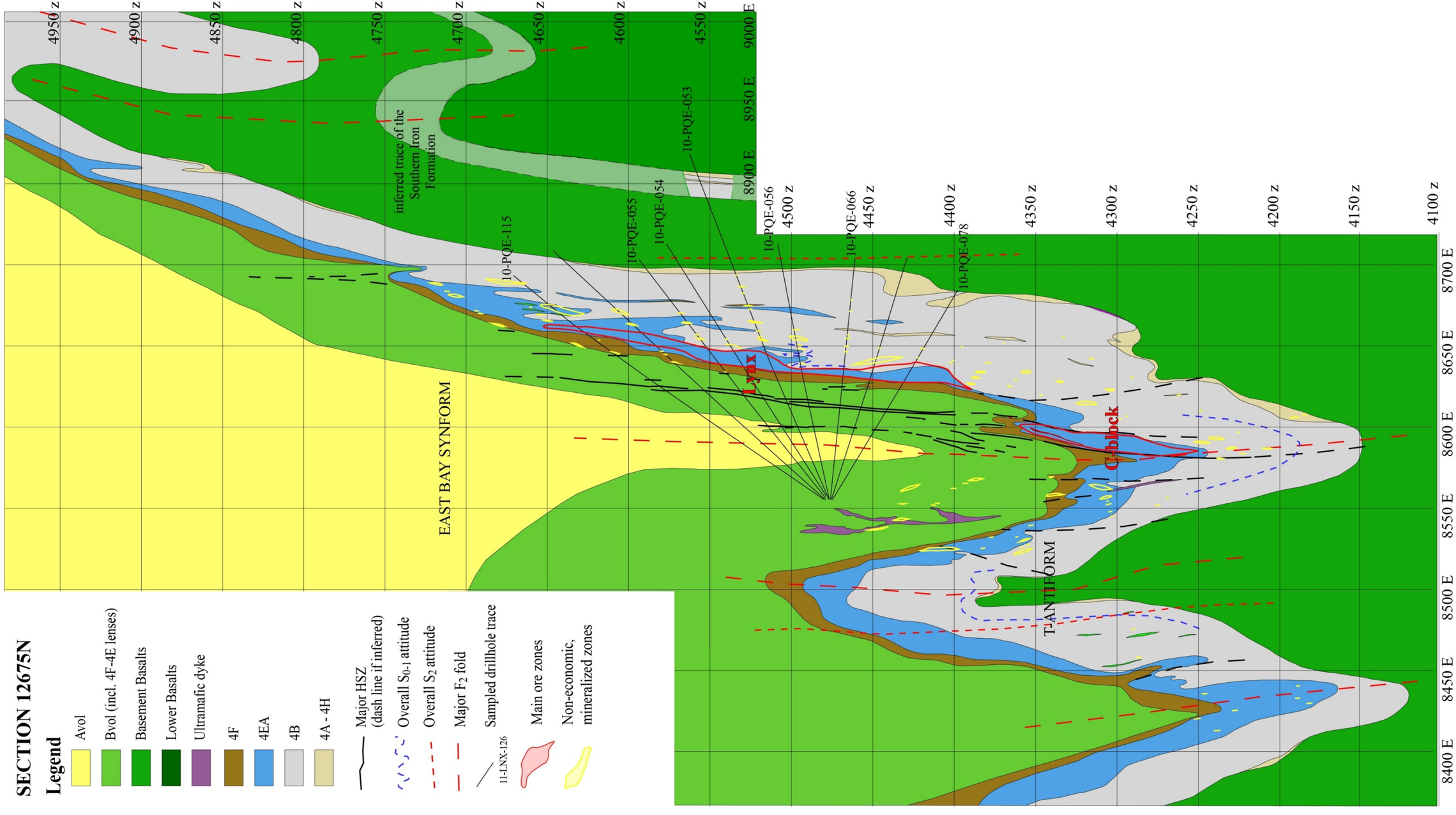

Figure 7-4: Geological and structural interpretation of mine section 12675 N, looking north, with contours of gold-mineralized rocks (yellow and red lines).

7.2 Main pyrrhotite-replacement mineralization style

7.2.1 Mineralogical and petrographic characteristics of 4EA-hosted ore

Gold mineralization in the garnet-grunerite BIF (unit 4EA) consists in pyrrhotite-replacement and silica flooding that are accompanied by the disruption of the BIF compositional layering and strong D_2 transposition (Figures 7-5 and 7-6). Three major mineral assemblages are present: 1) pyrrhotite-garnet-grunerite-biotite ± hornblende, 2) hornblende-tschermakite-garnet-biotite ± pyrrhotite, and 3) quartz-hornblende-biotite ± pyrrhotite. The contact between chert and iron-rich bands (including grunerite and magnetite) appears to be a primary control on mineralizing-fluids infiltration and/or reaction front with the host rocks. Pyrrhotite preferentially occurs along margins of garnet-grunerite bands (Figure 7-5A) and ultimately forms entire bands (Figure 7-5B). Competent chert bands are abruptly disrupted by folds, veins, and faults (Figures 7-5 and 7-6), and this process is accompanied by quartz recrystallization.

Quartz varies between 5 and 50 volume percent (vol.%). It is mostly found as fine- to medium-grained, anhedral, interlocking grains in almost monomineralic bands (Figure 7-7A, B), or intergrown with grunerite and pyrrhotite between garnet porphyroblasts in a texture referred to as “silica flooding”. The term is used with a descriptive function, as silica appears as diffuse masses in the main mineral assemblage. Quartz bands or aggregates may represent recrystallized chert bands or quartz veins. The latter are usually coarser-grained and include trace amounts of plagioclase feldspar, hornblende/grunerite, biotite, and carbonate.

Amphiboles form a major component of the gangue and include the grunerite-cummingtonite, hornblende, tschermakite, and actinolite-tremolite series (Figure 7-7; Table 7-2). Grunerite ($Fe_7Si_8O_{22}(OH)_2$) constitutes 1 to 45 vol.% of the rock mineral assemblage. It occurs as fine- to medium-grained colourless, elongated, bladed crystals intergrown with hornblende, actinolite, biotite, hedenbergite, magnetite, and pyrrhotite. Grunerite, which may occur as its dimorph ferro-anthophyllite, is commonly concentrated near garnet porphyroblasts. Calcium-bearing amphiboles ($Ca_2(Fe,Al)_5Si_8O_{22}(OH)_2$) make up 1 to 40% of the rock and include fine- to medium-grained pale to grassy green hornblende and blue-green actinolite. Both are intergrown with biotite and pyrrhotite, and locally with grunerite and hedenbergite, near garnet. Rare anhedral calcium-bearing amphiboles are present as inclusions in garnet.

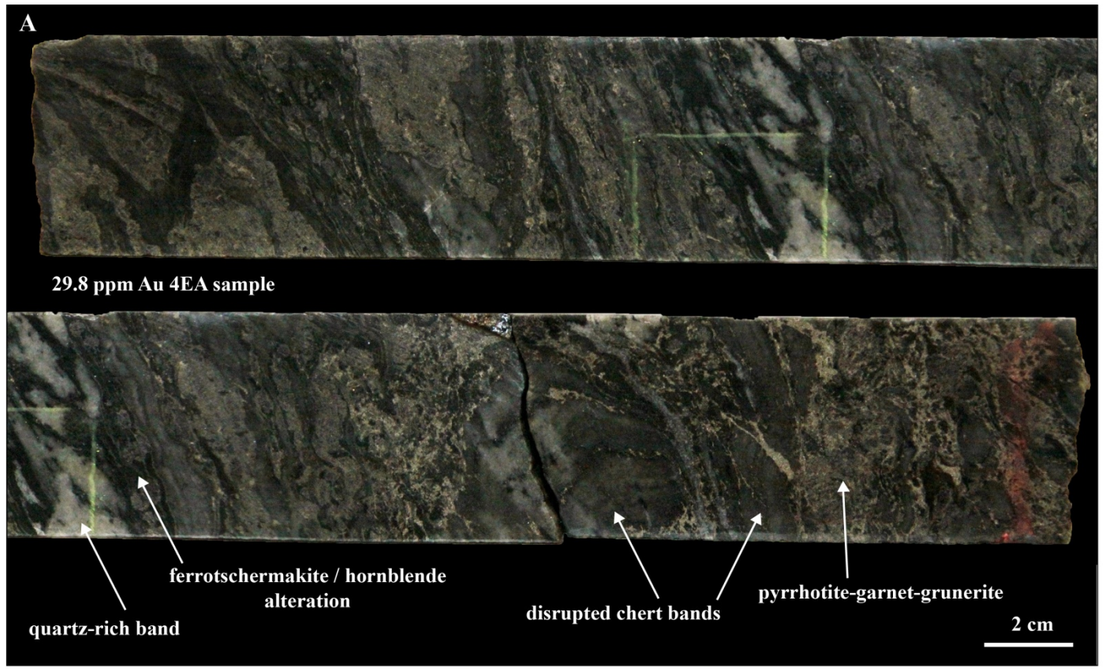
A
29.8 ppm Au 4EA sample
quartz-rich band
ferrotschermakite / hornblende alteration
disrupted chert bands
pyrrhotite-garnet-grunerite
2 cm

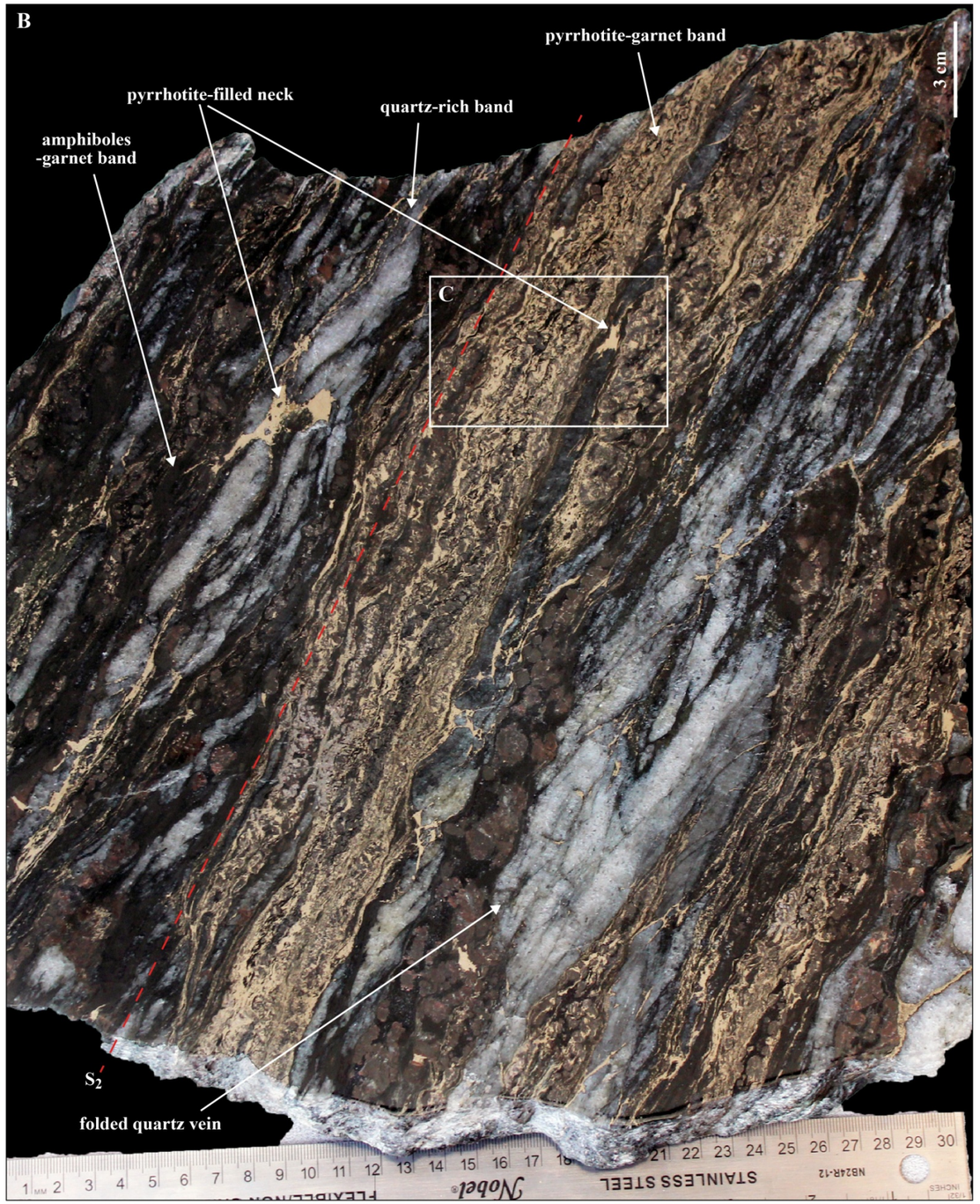
B
pyrrhotite-garnet band
pyrrhotite-filled neck
quartz-rich band
amphiboles -garnet band
3 cm
C
S2
folded quartz vein

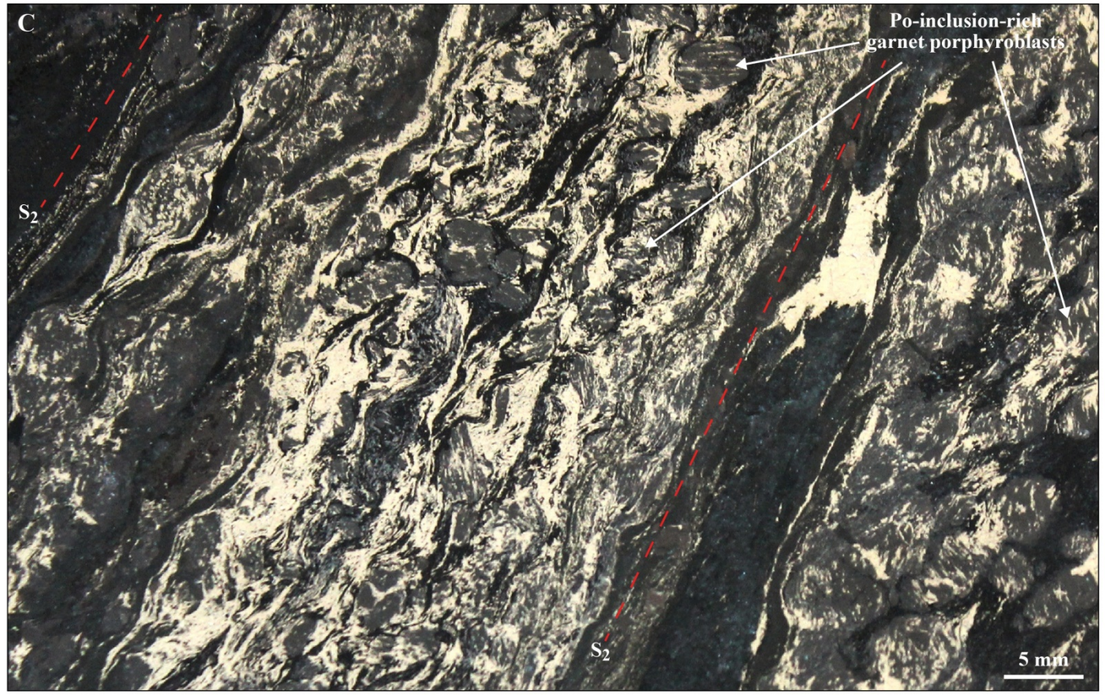
C
Po-inclusion-rich garnet porphyroblasts
S2
S2
5 mm

Figure 7-5: Typical pyrrhotite-replacement ore in garnet-grunerite BIF (unit 4EA). A. Drill core segment of 28.9 ppm Au 4EA ore from the PQD area, sample MW-12-167, DDH 06-PQE-091. It shows the progressive replacement of garnet-grunerite bands by an assemblage of pyrrhotite-garnet-hornblende-biotite. Chert bands are disrupted and progressively recrystallized and/or replaced by free quartz (silica flooding) and minor quartz veins. B. Polished slab of 4EA ore from the C-block ore zone, 1095 mine level showing intense transposition and recrystallization of the BIF leading to a compositional layering consisting of pyrrhotite-garnet-dominated, garnet-hornblende-dominated, and quartz-dominated bands. Local quartz veins are strongly deformed. Quartz-dominated bands are locally boudinaged and pyrrhotite fills in boudin necks, indicating local remobilization of sulphides. Garnets in pyrrhotite-rich replacement zones are generally smaller, anhedral, and richer in inclusions than garnets in pyrrhotite-poor bands, which appear to have crystallized later during D_2. C. Close-up of B. on pyrrhotite-rich bands showing the well-defined internal fabric in garnet porphyroblasts formed by pyrrhotite inclusion trails. These inclusion trails are mostly continuous with the external S_2 fabric, suggesting garnets are syn-D_2. Overall, this sample shows evidence of deformation during and after the gold mineralization event.

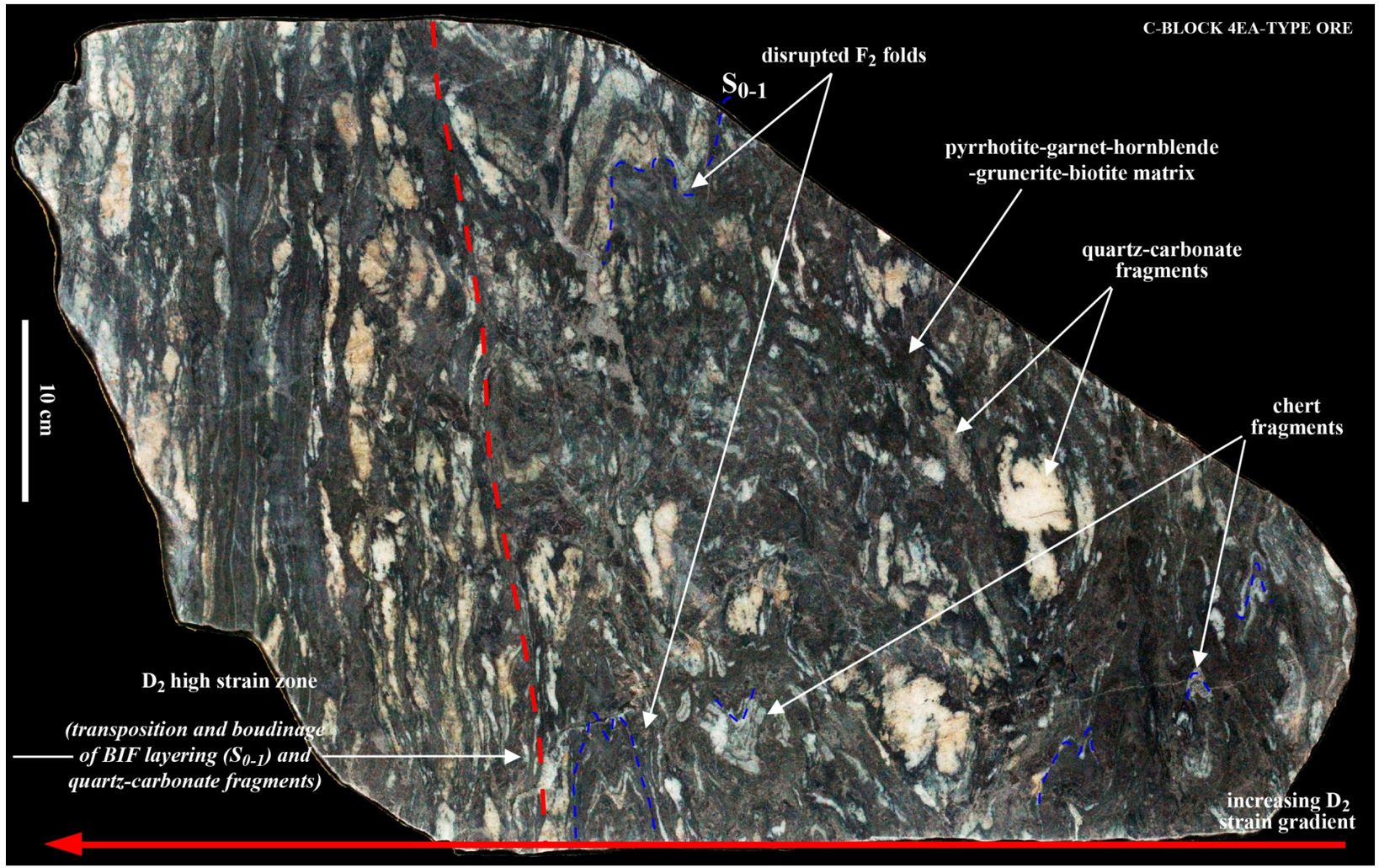

Figure 7-6: Polished slab of high-grade silicate-BIF ore from the C-block zone, mine level 770, section 11730 N, PQD area. The D_2 strain gradient increases toward the high strain zone to which gold mineralization is spatially associated. F_2 folded layering is disrupted by boudinaged quartz-carbonate veins and a mixture of pyrrhotite, garnet, tschermakite/hornblende, and biotite.

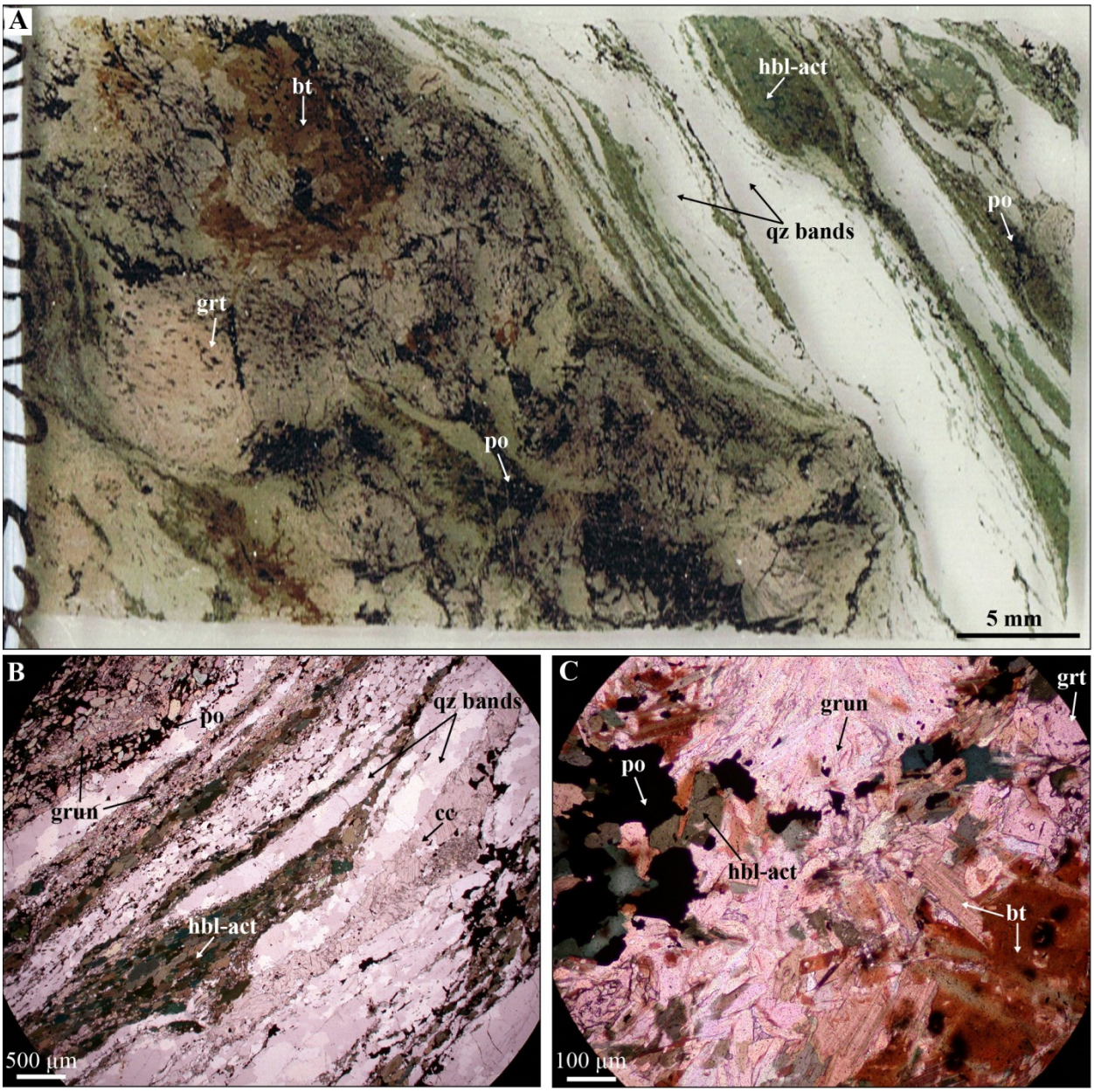

Figure 7-7: Mineral paragenesis of 4EA-hosted ore. A. Thin section scan of sample MW-12-528, DDH 10-PQE-020, 33.5 ppm Au showing the typical band compositions of the ore: garnet-pyrrhotite-grunerite-biotite assemblage (lower left) and quartz-hornblende-actinolite assemblage (upper right). B. Microphotograph in plain polarized light of quartz-amphibole bands, which shows quartz-dominated and hornblende-dominated microbands. Sample MW-12-528. C. Microphotograph in plain polarized light of grunerite intergrown with hornblende, biotite, and pyrrhotite in a garnet-rich band. Sample MW-12-528.

Table 7-2: Average chemical composition and standard deviation of major minerals in unit 4EA ore.

		Mg/(Mg+Fe2)	Si	Al	Ti	Cr	Fe	Mn	Mg	Ni	Ca	Na	K	F	Cl	OH*	n =
Hornblende	avg	27.33	6.41	2.33	0.04	0.00	3.25	0.02	1.03	0.00	1.82	0.32	0.10	-0.01	0.00	1.83	6
	SD	6.20	0.17	0.27	0.02	0.00	0.18	0.01	0.29	0.00	0.06	0.09	0.06	0.03	0.00	0.25	
Grunerite	avg	25.97	7.94	0.11	0.00	0.00	5.03	0.05	1.76	0.00	0.08	0.02	0.00	0.00	0.00	1.73	25
	SD	3.18	0.05	0.06	0.01	0.00	0.21	0.02	0.22	0.00	0.04	0.01	0.00	0.02	0.00	0.36	
Cummingtonite	avg	39.07	7.93	0.16	0.00	0.00	4.12	0.03	2.64	0.00	0.07	0.02	0.00	0.00	0.00	1.89	32
	SD	6.19	0.04	0.07	0.00	0.00	0.43	0.03	0.41	0.00	0.05	0.01	0.00	0.01	0.00	0.20	
Ferro-tschermakite	avg	25.66	6.17	2.80	0.03	0.00	3.15	0.01	0.93	0.00	1.81	0.40	0.09	0.00	0.00	1.76	22
	SD	31.19	0.14	0.33	0.02	0.01	0.47	0.01	0.51	0.00	0.07	0.08	0.04	0.01	0.00	0.35	

		Si	Ti	Al	Cr	Fe total	Mn	Zn	Mg	Ca	Na	pyr	spess	alm	gross	n =
Garnet core	avg	2.98	0.00	1.98	0.00	2.46	0.08	0.00	0.18	0.32	0.00	6.03	2.63	80.82	10.52	105
	SD	0.02	0.00	0.02	0.00	0.16	0.08	0.00	0.05	0.10	0.00	1.73	2.72	5.25	3.42	
Garnet rim	avg	2.98	0.00	1.99	0.00	2.44	0.07	0.00	0.21	0.33	0.00	6.85	2.30	80.03	10.82	28
	SD	0.02	0.00	0.02	0.00	0.16	0.07	0.00	0.07	0.14	0.00	2.13	2.28	5.34	4.44	

		Fe/FeMnMg	Si	Ti	Al	Cr	V	Fe2+	Mn	Ni	Zn	Mg	Ca	Sr	Ba	Na	K	∑	F	Cl	Mg-#	n =
Biotite	avg	0.70	5.44	0.19	3.11	0.00	0.01	3.60	0.01	0.00	0.00	1.49	0.00	0.00	0.01	0.05	1.80	15.72	0.02	0.00	31.38	51
	SD	0.07	0.17	0.08	0.33	0.00	0.01	0.46	0.01	0.00	0.00	0.38	0.01	0.00	0.02	0.03	0.17	0.14	0.05	0.01	8.52	

		Si	Ti	Al	Cr	V	Fe2+	Mn	Ni	Zn	Mg	Ca	Ba	Na	K	∑	F	Cl	Fe/FeMnMg	Al(IV)	Al(VI)	n =
Chlorite	avg	5.39	0.01	5.32	0.00	0.01	6.14	0.01	0.00	0.00	3.01	0.02	0.00	0.02	0.01	19.94	0.00	0.00	0.67	2.57	2.69	19
	SD	0.35	0.01	0.59	0.01	0.01	0.89	0.01	0.00	0.00	0.85	0.02	0.00	0.02	0.01	0.10	0.01	0.01	0.09	0.38	0.30	

		Si	Ti	Al	Cr	V	Fe	Mn	Ni	Zn	Mg	Ca	Na	K	∑	Fe/FeMnMg	Mg-#	n =
Hedenbergite	avg	1.98	0.00	0.02	0.00	0.00	0.80	0.02	0.00	0.00	0.24	0.93	0.01	0.00	4.01	0.75	23.36	8
	SD	0.02	0.00	0.01	0.00	0.00	0.10	0.01	0.00	0.00	0.09	0.03	0.01	0.01	0.01	0.08	8.67	

		Fe	Mn	Zn	Mg	Ca	Sr	Ba	n =
ankerite	avg	0.31	0.01	0.00	0.18	0.49	0.00	0.00	6
	SD	0.04	0.01	0.00	0.05	0.02	0.00	0.00	
calcite	avg	0.03	0.01	0.00	0.01	0.95	0.00	0.00	18
	SD	0.02	0.01	0.00	0.01	0.03	0.00	0.00	

		Si	Ti	Al	Fe2+	Mn	Mg	Ca	Ba	Na	K	∑	an	ab	or	n =
Plagioclase feldspar	avg	2.64	0.00	1.36	0.00	0.00	0.00	0.35	0.00	0.63	0.00	4.99	0.36	0.64	0.00	3
	SD	0.22	0.00	0.23	0.00	0.00	0.00	0.21	0.00	0.23	0.00	0.01	0.22	0.22	0.00	

		Si	Al	Ti	Cr	V	Fe+2	Fe+3	Mn	Ni	Zn	Mg	Ca	Σ	n =
Ilmenite	avg	0.00	0.21	0.77	0.00	0.00	0.98	0.03	0.01	0.00	0.00	0.00	0.00	2.00	14
	SD	0.00	0.42	0.42	0.00	0.00	0.02	0.02	0.01	0.00	0.00	0.00	0.00	0.01	
Magnetite	avg	0.01	0.06	0.05	0.08	0.18	8.02	15.58	0.00	0.00	0.00	0.00	0.01	24.00	9
	SD	0.01	0.06	0.05	0.15	0.31	0.03	0.47	0.01	0.00	0.00	0.00	0.01	0.00	

Garnet porphyroblasts may be absent or, alternatively, represent up to 75 vol.% of the rock. Pale red to locally pale orange, garnet range in size and shape from medium-grained subhedral poikiloblasts to coarse (5-10 mm) anhedral to subhedral masses or porphyroblasts (Figures 7-7A; 7-8; 7-9; 7-10A, B; 7-11). Irregular subhedral poikiloblasts are commonly intergrown with grunerite. Coarse, locally ribbon-like, porphyroblasts are intergrown with hornblende, biotite, chlorite, sulphides, quartz, and minor calcite. Coarse garnets are frequently fragmented with sulphides, mainly pyrrhotite, filling in fractures and pressure shadows. Inclusions in garnet include: chlorite, grunerite, hornblende, biotite, ilmenite, magnetite, pyrrhotite (-chalcopyrite), and gold. Garnet poikiloblasts in biotite-rich layers tend to have euhedral rims around inclusion-rich cores (where most chlorite inclusions are found), while garnet intergrown with grunerite is very ragged due to abundant disseminated grunerite inclusions. Most garnets also contain fine-grained ilmenite, pyrrhotite, and occasionally abundant magnetite inclusions. Gold in garnet occurs as inclusions in rims of large porphyroblasts with pyrrhotite, amphibole, and carbonate.

In general, garnets are Fe-rich almandine (Table 7-2) with 27-39 wt.% FeO, 0.28 to 7.32 wt.% MnO, fairly consistent MgO around 1 ± 0.3 wt.%, while CaO varies widely from 0.34 to 16.80 wt.%. When present, cores of zoned garnet grains are generally more Mn-rich than rims, which are Fe-rich. Zonation trends for Ca vary, in many cases: They are higher in rims than in cores, but in a few samples, it is the other way around or apparently random.

Some poikilitic garnet cores, showing zonation, solely contain anhedral magnetite and chlorite inclusions (Figure 7-8). Pyrrhotite is very rarely present in garnet cores. This suggests they formed prior to gold mineralization (no pyrrhotite or gold inclusions), or at an early stage, under upper greenschist to lower amphibolite metamorphic conditions. Some coarse garnet grains contain ilmenite, pyrrhotite ± magnetite inclusions (Figure 7-9A) and are therefore interpreted to have crystallized syn- to late gold mineralization. Inclusion-free rims are commonly euhedral and apparently undeformed (e.g., Figure 7-9D).

Biotite ranges from trace to 25 vol.% and occurs as fine- to medium-grained, pale to medium brown, subhedral grains intergrown with hornblende and pyrrhotite (Figures 7-7A, C; 7-8A; 7-9B, D), or as inclusions in garnet. Unusual green biotite is locally present near quartz veins and garnet-grunerite-plagioclase assemblage (Figure 7-10). Microprobe analyses (Table 7-2) do not show distinctive composition differences between green and brown biotite.

At least two distinct habitus of chlorite are documented. The first occurs as traces of fine-grained anhedral, pale to grassy green inclusion grains in garnet (Figure 7-11A, B). The second consists in chlorite present in the matrix. It occurs mostly as homogeneous masses in pressure shadows of garnet porphyroblasts, intergrown with ilmenite and/or magnetite and forming an apparently stable assemblage with biotite (Figure 7-11C to F). This chlorite is mainly Fe-rich (Fe-# 0.67; Table 7-2). Matrix chlorite is locally intergrown with grunerite and biotite interstitial to garnet. Interstitial, very fine-grained, anhedral green hercynite ($Fe^{2+}Al_2O_4$) is locally present in green biotite or chlorite.

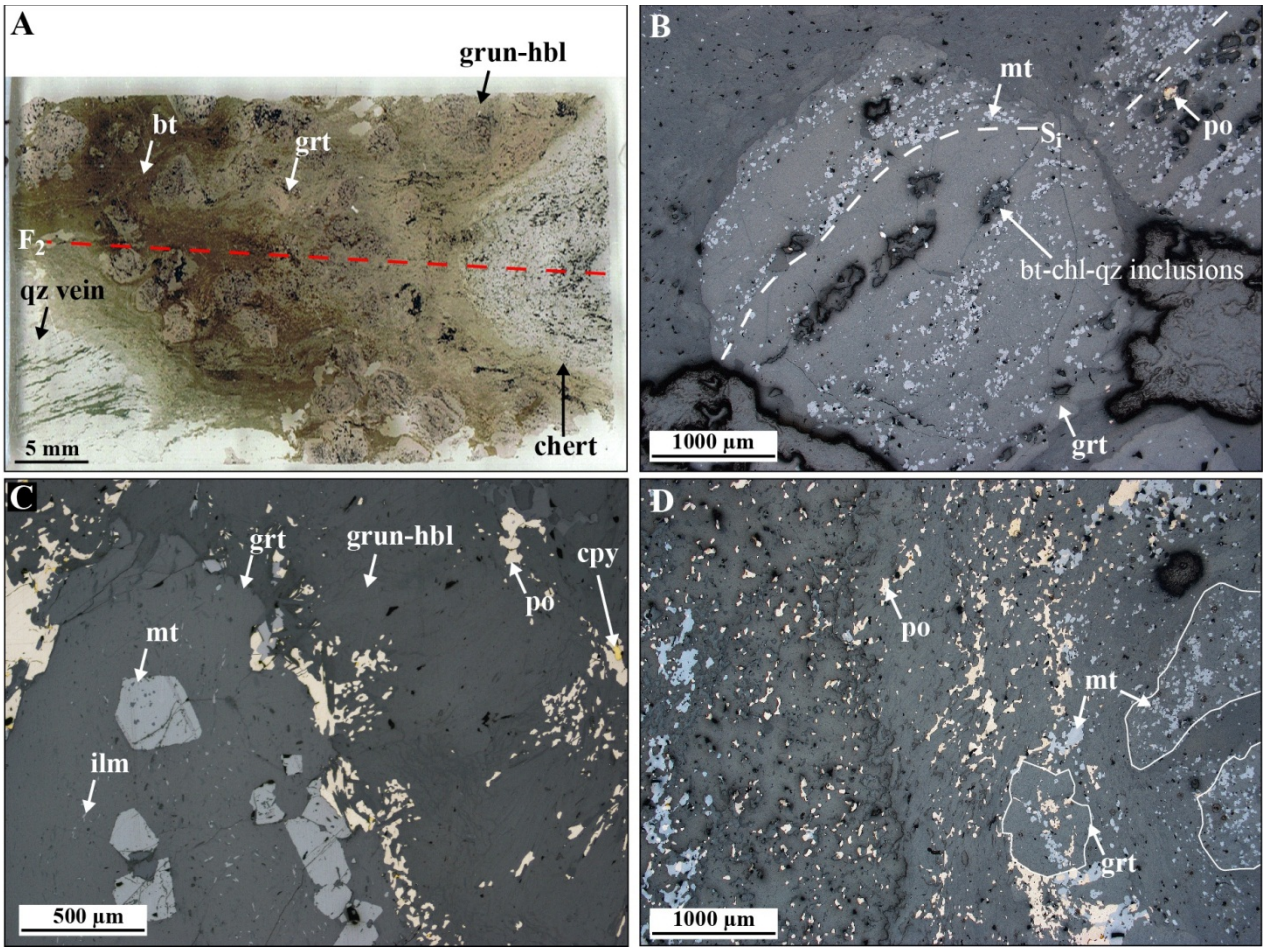

Figure 7-8: Garnet porphyroblasts in 4EA ore. A. Thin section scan of sample MW-12-242, DDH 06-PQE-013, 16 ppm Au showing a chert band and garnet-biotite-grunerite-pyrrhotite band affected by an F_2 fold. The lower left corner shows a quartz vein with hornblende-actinolite. B. Microphotograph in reflected light of a garnet porphyroblast containing trails of small, anhedral magnetite inclusions, as well as biotite and chlorite. C. Microphotograph in reflected light of garnet porphyroblast and grunerite-(hornblende)-pyrrhotite matrix, sample MW-12-153, DDH 06-PQE-091, 104 ppm Au. Magnetite in the matrix is almost completely replaced by pyrrhotite, while coarse, euhedral magnetite grains are preserved as inclusions in garnet, along with small ilmenite inclusions. D. Microphotograph in reflected light of pyrrhotite replacing magnetite in the matrix and subhedral garnets with magnetite and pyrrhotite inclusions, sample MW-12-242, DDH 06-PQE-013.

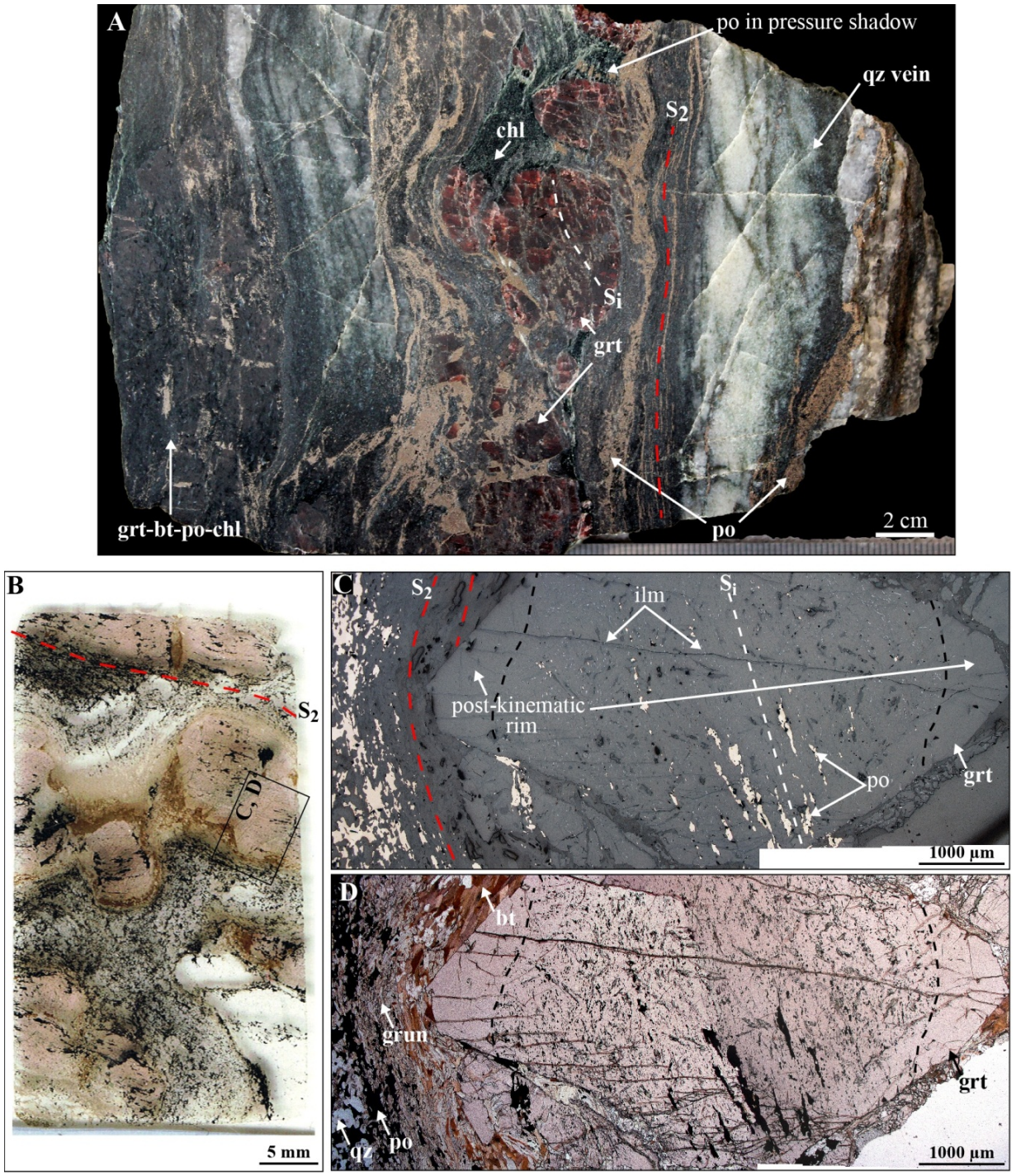

Figure 7-9: Garnet porphyroblasts in 4EA-hosted ore. A. Polished slab of 4EA ore from the Lynx zone showing typical coarse almandine garnet with pyrrhotite inclusions delineating an internal fabric. Garnets are intergrown with chlorite, amphibole, and pyrrhotite. Pyrrhotite is distributed along the main (S_2) fabric and in garnet pressure shadows. B. Thin section scan of sample MW-12-289, DDH 06-PQE-095 showing garnet-biotite-grunerite portions and pyrrhotite-grunerite-quartz portions. C. and D. Reflected light and plain polarized light microphotographs of a garnet porphyroblast at high-angle to the main foliation (S_2). The core contains an internal fabric marked by pyrrhotite and ilmenite inclusions sub-parallel to the external fabric (S_2). Inclusion-free rims of garnet overgrow biotite and the external fabric. The boudinaged aspect of garnet-rich bands in A. and B. is an indicator of post-garnet growth deformation.

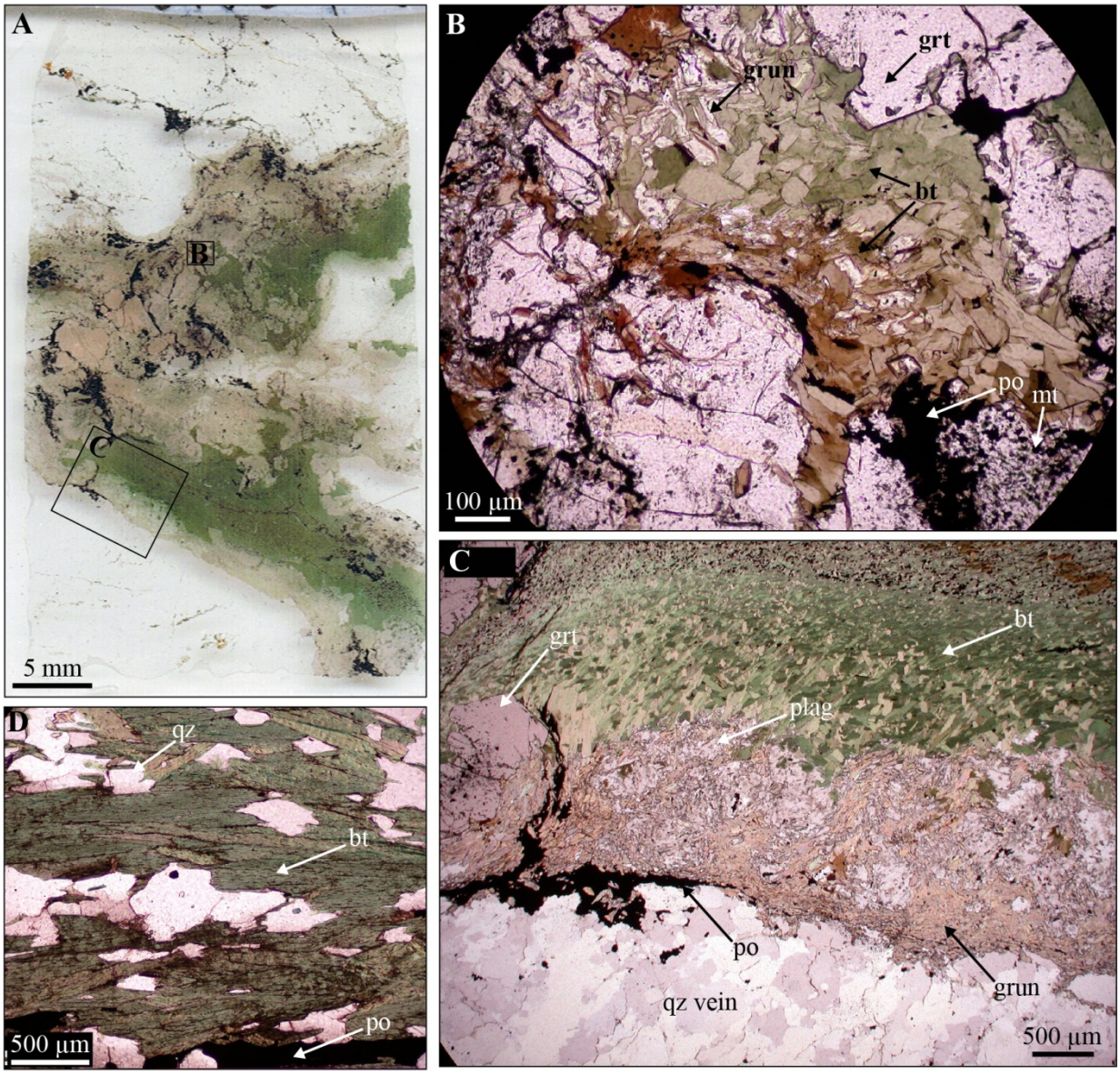

Figure 7-10: Biotite in 4EA ore. A. Thin section scan of sample MW-12-310, DDH 10-PQE-095, 22.2 ppm Au. Pyrrhotite is concentrated in garnet-grunerite-biotite assemblage. B. Close-up in plain polarized light of green to brown biotite adjacent to garnet porphyroblasts. C. Microphotograph in plain polarized light showing elongated green biotite adjacent to grunerite-plagioclase feldspar near a quartz vein. D. Microphotograph in plain polarized light of a green biotite-rich layer intergrown with quartz and pyrrhotite, underground sample MW-12-UG-024A, Lynx zone, 5.1 ppm Au.

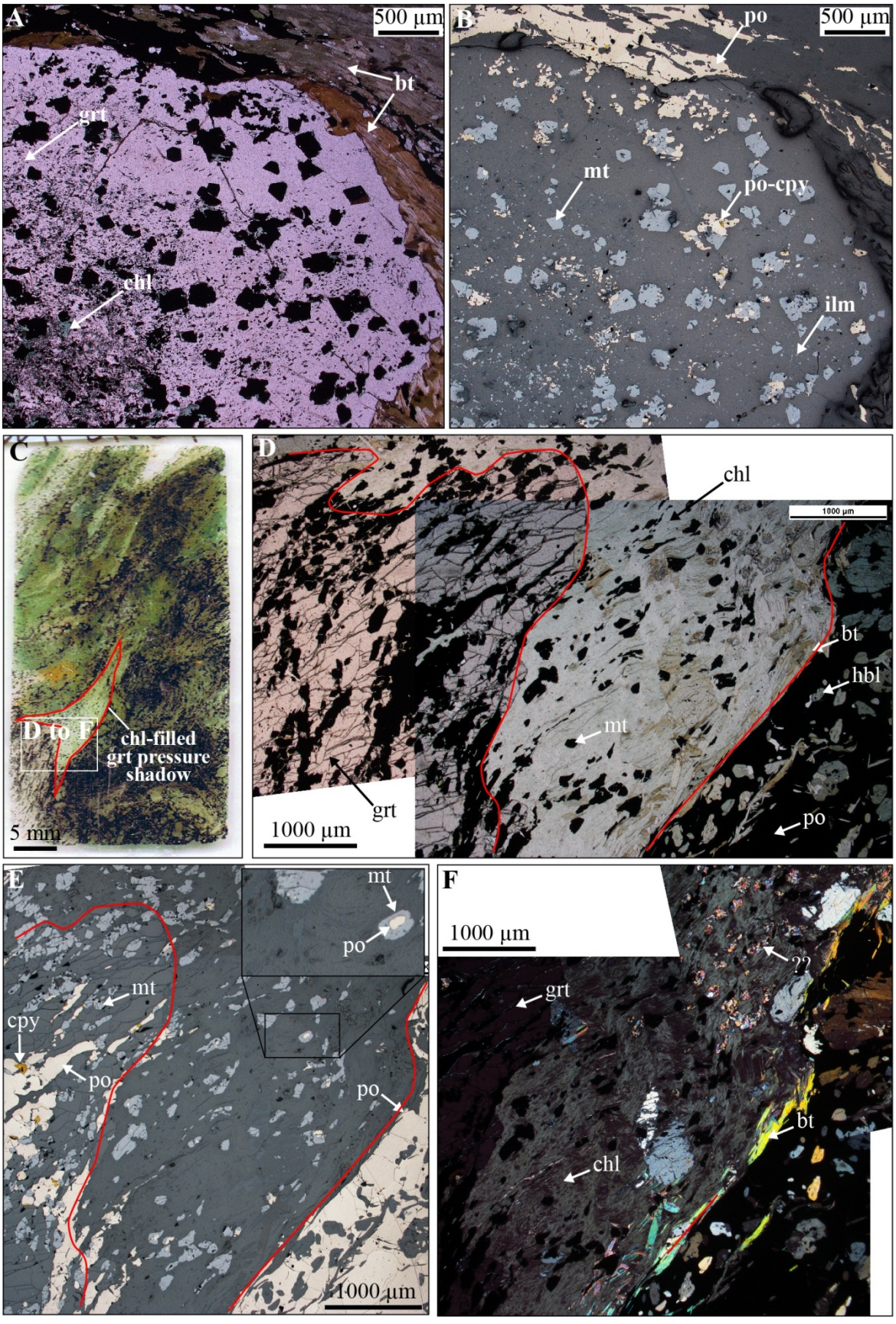
A
500 µm
bt
grt
chl
B
po
500 µm
mt
po-cpy
ilm
C
D to F
chl-filled
grt pressure
shadow
5 mm
D
chl
1000 µm
bt
hbl
mt
grt
1000 µm
po
E
mt
po
mt
cpy
po
po
1000 µm
F
1000 µm
??
grt
bt
chl

Figure 7-11: Chlorite in 4EA ore. A. Microphotograph of chlorite and opaque mineral inclusions in a garnet porphyroblast surrounded by brown and green biotite and pyrrhotite; plain polarized light. Sample MW-12-023, 18.6 ppm Au, DDH 10-PQE-115. B. Same as A. in reflected light, showing euhedral magnetite inclusions in a garnet porphyroblast. Note the increasing amount of pyrrhotite and ilmenite inclusions towards the rim. No magnetite is preserved in the matrix. C. Thin section scan of sample MW-12-475, DDH 10-PQE-014, 20.7 ppm Au. D., E., and F. Microphotograph collages in plain polarized, reflected, and cross-polarized light, respectively, of chlorite-magnetite assemblage in the pressure shadow of a coarse garnet porphyroblast with magnetite and pyrrhotite-chalcopyrite inclusions.

Clinopyroxene (hedenbergite, $CaFeSi_4O_8$; Table 7-2) represents trace to, very locally, up to 20 vol.% of the rock. It occurs as fine- to medium-grained pale green, locally greyish, anhedral grains intergrown in the matrix with hornblende, carbonate, and quartz. Pyrrhotite ± magnetite is also intergrown locally. Hedenbergite is most abundant when intergrown with garnet-hornblende ± pyrrhotite, near quartz veins.

Carbonates commonly form trace to 2-3% of the mineralogy and comprise calcite and ankerite (Table 7-2). Fine- to medium-grained anhedral calcite is the dominant carbonate species (Figure 7-7B), intergrown with grunerite, hornblende, quartz, and locally hedenbergite. It is preferentially distributed near quartz veins, where hedenbergite is also commonly present. Traces of fine-grained ankerite and dolomite are rare.

Feldspar is present in trace quantity, up to 2%. It is mostly fine-grained and anhedral, intergrown with hornblende, grunerite, and quartz ± garnet and pyrrhotite (Figure 7-10C). It is mostly of albitic composition (Table 7-2).

Magnetite and ilmenite are the major oxides present in the ore and mainly occur as inclusions in garnet porphyroblasts. Magnetite (Fe_3O_4) may be present in trace amount to a few volume percent. Fine-grained anhedral, partially resorbed magnetite grains are found in the matrix, adjacent to pyrrhotite or intergrown with grunerite and hornblende, and fine- to medium-grained, subhedral to euhedral inclusions are documented in garnet porphyroblasts. Ilmenite ($Fe^{2+}Ti^{4+}O_3$) is mainly present as very fine elongated inclusions in garnet. Inclusions in grunerite, hornblende, and biotite are occasional, and rare remnants of ilmenite are found in pyrrhotite. Ilmenite inclusions in garnet often delineate an internal fabric (Figure 7-9C, D).

Pyrrhotite (Fe_7S_8) typically represents 1 to 15 vol.% of the rock, but 95% of sulphides; chalcopyrite forming most of the remaining 5% (Figures 7-8C, D; 7-9A, C; 7-11B, E). Pyrrhotite occurs as fine- to medium-grained anhedral, bronze grains interstitial to matrix minerals and infiltrating garnet fractures, intergrown with chalcopyrite mainly, locally adjacent to magnetite. Pyrrhotite is also found as inclusions in garnet in small anhedral grains or elongated aggregates. Pyrrhotite is often marked by flame-textured exsolutions of troilite (FeS). Chalcopyrite ($CuFeS_2$) is present in trace amount, as fine-grained anhedral, yellow inclusions in or against pyrrhotite. On rare occurrences, trace pentlandite ($(Ni,Fe)_9S_8$) is present as

flame-shaped inclusions in pyrrhotite, as well as micrometric inclusions of galena (PbS), arsenopyrite (FeAsS), sphalerite (ZnS), sperrylite (PtAs), and altaite (PbTe; Table 7-3).

Gold usually occurs in association with pyrrhotite and chalcopyrite, as very fine-grained anhedral inclusions in matrix minerals (e.g., biotite, hornblende, grunerite, hedenbergite; Figure 7-12A to D) and in garnet (Figure 7-13). Gold locally occurs at the tip of pyrrhotite-filled fractures in garnet, indicating garnet growth during active D_2 deformation and prior to gold mineralization and/or gold remobilization. Electrum usually contains 10-15% silver and trace amounts of Cu, Se, Te, and Bi (Table 7-3). Trace Fe, S, Co, and Ni are interpreted as contaminants from adjacent sulphides.

Table 7-3: Average chemical composition and standard deviation of sulphide minerals and electrum in unit 4EA ore.

		S	Mn	Fe	Co	Ni	Cu	Zn	As	Se	Ag	Sn	Sb	Te	Au	Hg	Pb	Bi	Pd	Pt
Electrum	Average	0.17	0.00	0.92	0.01	0.01	0.04	0.00	0.01	0.01	**11.95**	0.01	0.01	0.01	**86.75**	0.02	0.00	0.10	0.00	0.00
n = 13	SD	0.17	0.00	0.57	0.01	0.01	0.03	0.00	0.02	0.01	1.95	0.01	0.01	0.01	3.15	0.06	0.00	0.11	0.00	0.00
Pyrrhotite	Average	**38.47**	0.00	**61.10**	0.02	0.07	0.02	0.02	0.01	0.01	0.02	0.02	0.00	0.01	0.03	0.01	0.01	0.09	0.00	0.00
n = 45	SD	0.40	0.01	0.51	0.02	0.07	0.04	0.03	0.01	0.01	0.02	0.02	0.00	0.01	0.05	0.02	0.02	0.06	0.00	0.00
Troilite		36.53	0.00	63.49	0.00	0.05	0.00	0.00	0.03	0.02	0.00	0.06	0.00	0.00	0.20	0.17	0.00	0.14	0.00	0.00
n = 1																				
Pentlandite	Average	**33.61**	0.00	**34.27**	**4.22**	**27.52**	0.02	0.01	0.03	0.01	0.02	0.02	0.00	0.01	0.07	0.00	0.00	0.09	0.00	0.00
n = 3	SD	0.85	0.00	5.23	5.22	4.10	0.02	0.01	0.02	0.01	0.04	0.01	0.00	0.02	0.10	0.00	0.00	0.08	0.00	0.00
Chalcopyrite	Average	**34.15**	0.01	**31.11**	0.01	0.02	**34.13**	0.02	0.01	0.03	0.02	0.02	0.00	0.02	0.05	0.02	0.00	0.10	0.00	0.00
n = 22	SD	0.33	0.02	0.94	0.01	0.02	0.78	0.03	0.01	0.04	0.02	0.01	0.00	0.02	0.08	0.03	0.01	0.06	0.00	0.00
Arsenopyrite	Average	**18.45**	0.02	**30.42**	**3.60**	0.55	0.00	0.02	**47.09**	0.27	0.02	0.02	0.01	0.02	0.07	0.05	0.00	0.02	0.00	0.00
n = 3	SD	1.76	0.02	2.30	1.73	0.56	0.00	0.03	2.42	0.04	0.03	0.03	0.02	0.02	0.09	0.07	0.00	0.04	0.00	0.00
Loellingite	Average	0.66	0.02	**15.72**	**5.01**	**7.93**	0.02	0.01	**70.09**	0.17	0.01	0.01	0.02	0.00	0.00	0.00	0.00	0.02	0.00	0.00
n = 2	SD	0.11	0.03	0.38	0.26	1.58	0.02	0.01	0.10	0.24	0.01	0.01	0.03	0.00	0.00	0.00	0.00	0.03	0.00	0.00
Altaite	Average	0.43	0.00	**10.60**	0.01	0.00	0.01	0.02	0.00	0.35	0.01	0.01	0.12	**25.65**	0.01	0.00	**44.47**	0.21	0.00	0.00
n = 2	SD	0.49	0.00	12.51	0.00	0.00	0.02	0.03	0.00	0.16	0.01	0.01	0.10	15.55	0.01	0.00	24.81	0.11	0.00	0.00
Sperrylite	Average	0.11	0.02	0.76	0.02	0.01	0.02	0.02	**42.67**	0.18	0.02	0.00	0.05	0.05	0.00	0.00	0.00	0.04	0.00	**55.42**
n = 2	SD	0.00	0.02	0.27	0.00	0.01	0.02	0.03	0.45	0.02	0.02	0.00	0.03	0.04	0.00	0.00	0.00	0.06	0.00	1.09

Other minor silicate minerals in the matrix include riebeckite, sericite, tourmaline, apatite and zoisite. Riebeckite ($Na_2Fe_5Si_8O_{22}(OH)_2$) is present in some samples as traces, deep inky blue alteration of amphibole (e.g., rims on grunerite) or subhedral grains near veinlets crosscutting the S_2 fabric. It is thus not considered to be related to gold mineralization and linked to subsequent alteration (chapter 8). Rare sericite-altered feldspar co-occurs with sodic amphibole or zoisite. Tourmaline is rare and occurs as fine-grained subhedral, dark olive green to brown or inky blue to pale blue grains intergrown with amphibole and garnet ± pyrrhotite. Apatite occurs as trace fine-grained subhedral grains intergrown with pyrrhotite, hornblende, or quartz.

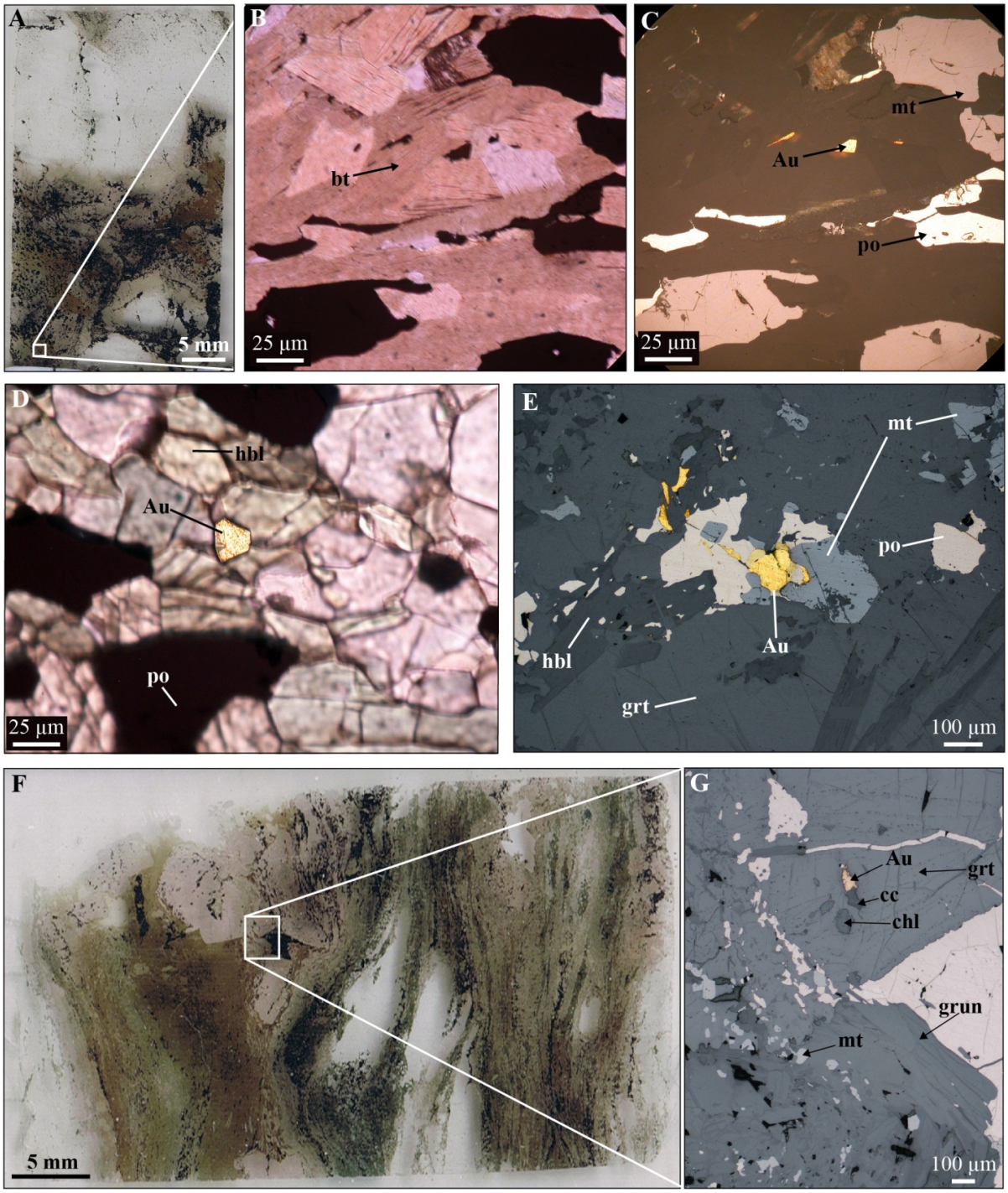

Figure 7-12: Gold in 4EA ore. A. Thin section scan of sample MW-12-111, DDH 10-PQE-053, 26.7 ppm Au. It shows the typical pyrrhotite-rich garnet-grunerite-biotite band adjacent to quartz band. B. and C. Close-up of matrix biotite intergrown with pyrrhotite, magnetite, and gold in plain polarized light and reflected light. D. Gold and pyrrhotite intergrown with hornblende, plain polarized light, sample MW-12-341, DDH 09-TAN-014, 35.5 ppm Au. E. Microphotograph in reflected light of gold intergrown with pyrrhotite, magnetite, and hornblende adjacent to garnet, sample MW-12-153, DDH 06-PQE-091, 104 ppm Au. F. Thin section scan of sample MW-12-346, DDH 09-TAN-014, 10.4 ppm. It shows the intense deformation of biotite-amphiboles and quartz bands. G. Close-up in reflected light of gold inclusion in garnet associated with calcite, near a chlorite inclusion.

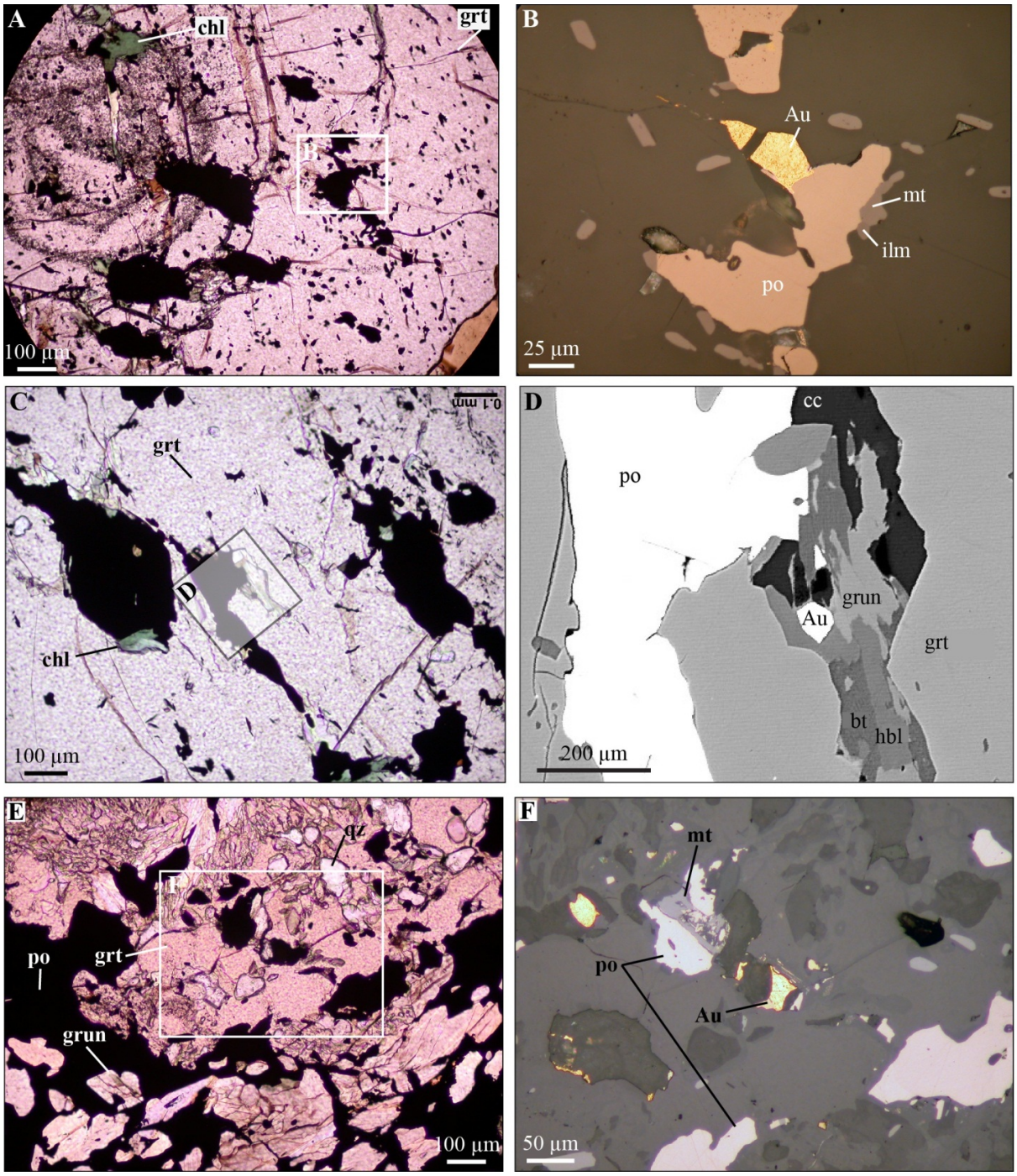

Figure 7-13: Gold in 4EA ore. A. Microphotograph in plain polarized light of garnet porphyroblast showing a zoned core with chlorite inclusions and intermediate and outer zones with pyrrhotite, magnetite and ilmenite inclusions. Sample MW-12-514, DDH 10-PQE-025, 18.2 ppm Au. B. Close-up in reflected light of gold-pyrrhotite-magnetite-ilmenite inclusion in garnet. C. Microphotograph in plain polarized light of chlorite-opaque minerals inclusions in garnet porphyroblast. Sample MW-11-105, DDH 10-PQE-053, 43.9 ppm Au. D. SEM close-up on gold inclusion in garnet, intergrown with biotite, hornblende, grunerite, calcite and pyrrhotite. E. Microphotograph in plain polarized light of poikilitic garnet with anhedral quartz and pyrrhotite inclusions in a grunerite-pyrrhotite matrix. Sample MW-12-154, DDH 06-PQE-091, 56.6 ppm Au. F. Close-up in reflected light on gold inclusions in garnet, intergrown with pyrrhotite, magnetite, and grunerite.

7.2.2 LA-ICP-MS 2D elemental mapping

Petrographic observations and microprobe data show there are multiple, distinct garnet phases. Some garnet porphyroblasts that are specifically associated to well-endowed gold-mineralized zones, are typically coarse, anhedral to subhedral and inclusion-poor (e.g., Figure 7-9A). 2D LA-ICP-MS quantitative elemental mapping was carried out on these porphyroblasts and compared to the more common medium-grained, subhedral, poikilitic garnet. The targets include porphyroblasts from high-grade 4EA-hosted ore (sample MW-12-UG-015, @76.9 ppm Au; Appendix V), and poikilitic garnet from a low-grade gold-bearing sample (MW-12-UG-023, 5.97 ppm Au; Appendix VI).

The logarithmic element distribution maps of garnet from the high-grade gold sample show a fairly homogeneous composition in terms of major components (e.g., CaO, Al_2O_3, MgO, MnO, and FeO; Figure 7-14). The dominant range of values for CaO is 22500 to 39200 ppm, MgO ranges between 18700 and 36800 ppm, MnO varies between 2800 and 5500 ppm, and FeO between 267000 and 511000 ppm. These values correspond to 7% CaO, 6% MgO, 0.9% MnO, and 86% FeO. Percentile distribution maps confirm an homogeneous composition (Figure 7-14), which also applies for elements such as P_2O_5, Y, and Zr (Figure 7-15). Y and Zr are locally enriched in garnet rims. Gold is present within surrounding sulphide phases.

In the low-grade sample (MW-12-UG-023), medium-grained subhedral garnet display chemical zonations with the core and rim enriched in Mn relatively to the intermediate zone (Figure 7-16). Ca content is also variable; Fe is largely homogeneous, whereas Mg steadily increases from core to rim. This is comparable to the microprobe map of garnet in barren pelitic rock (Figure 6-6).

Petrographic observations (7.2.1) and LA-ICP-MS maps show that sulphides occur adjacent to garnet porphyroblasts (e.g., Figure 7-15). They mostly consist of pyrrhotite with minor chalcopyrite, as documented in other samples. Pyrrhotite shows preferential enrichment in Ag, Cu, Se, Te, and Pb (Figure 7-17). Arsenic content is very low and distributed in the silicate matrix rather than in sulphide phases.

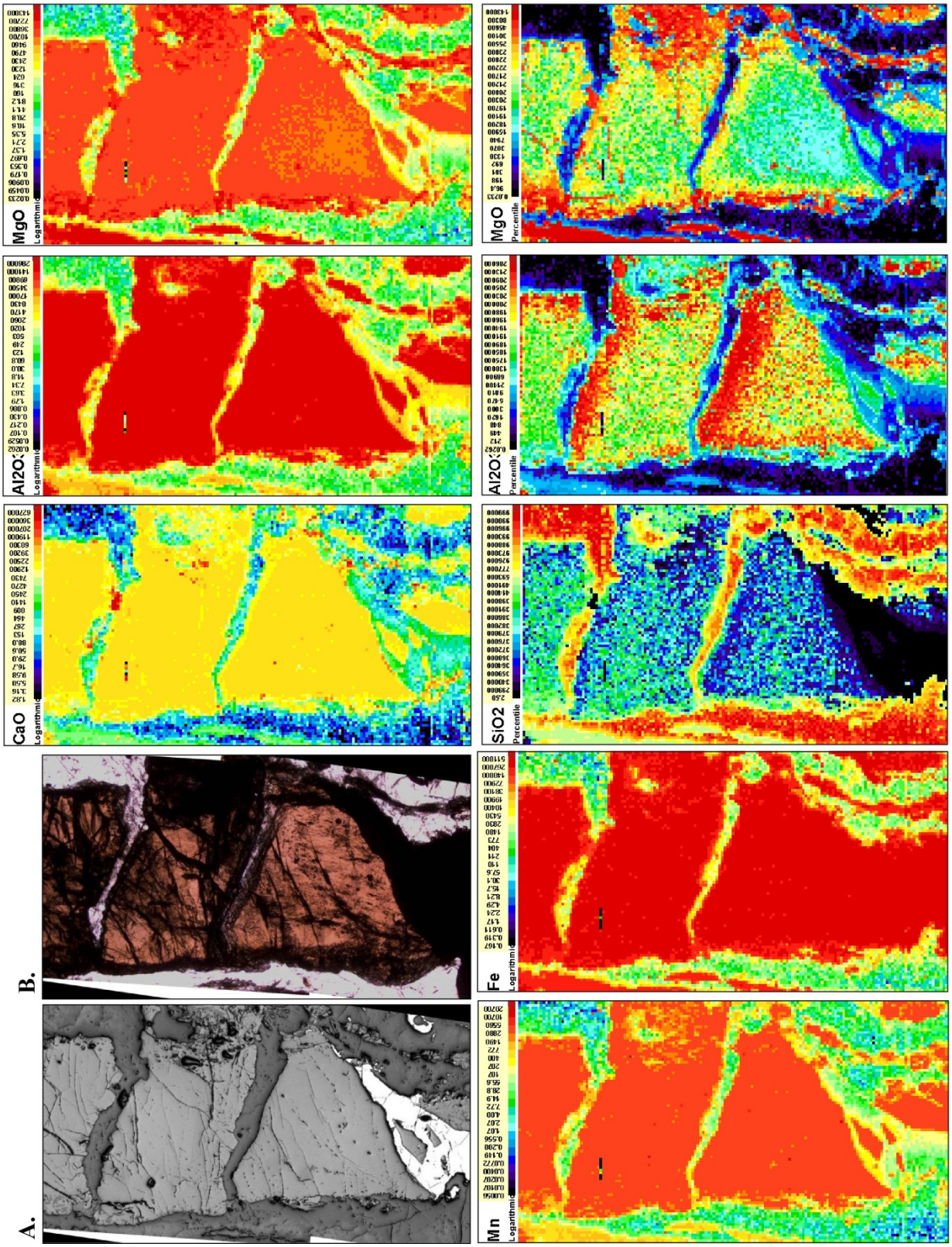

Figure 7-14: 2D LA-ICP-MS elemental maps of garnets associated with high-grade gold-mineralized unit 4EA sample (MW-12-UG-015A, 76.9 ppm Au). A. Microphotograph of map area in reflected light. B. Same as A. in plain polarized light, and, in order: calcium, aluminum, magnesium, manganese, and iron (logarithmic distribution map), and silica, aluminum, and magnesium (percentile distribution map).

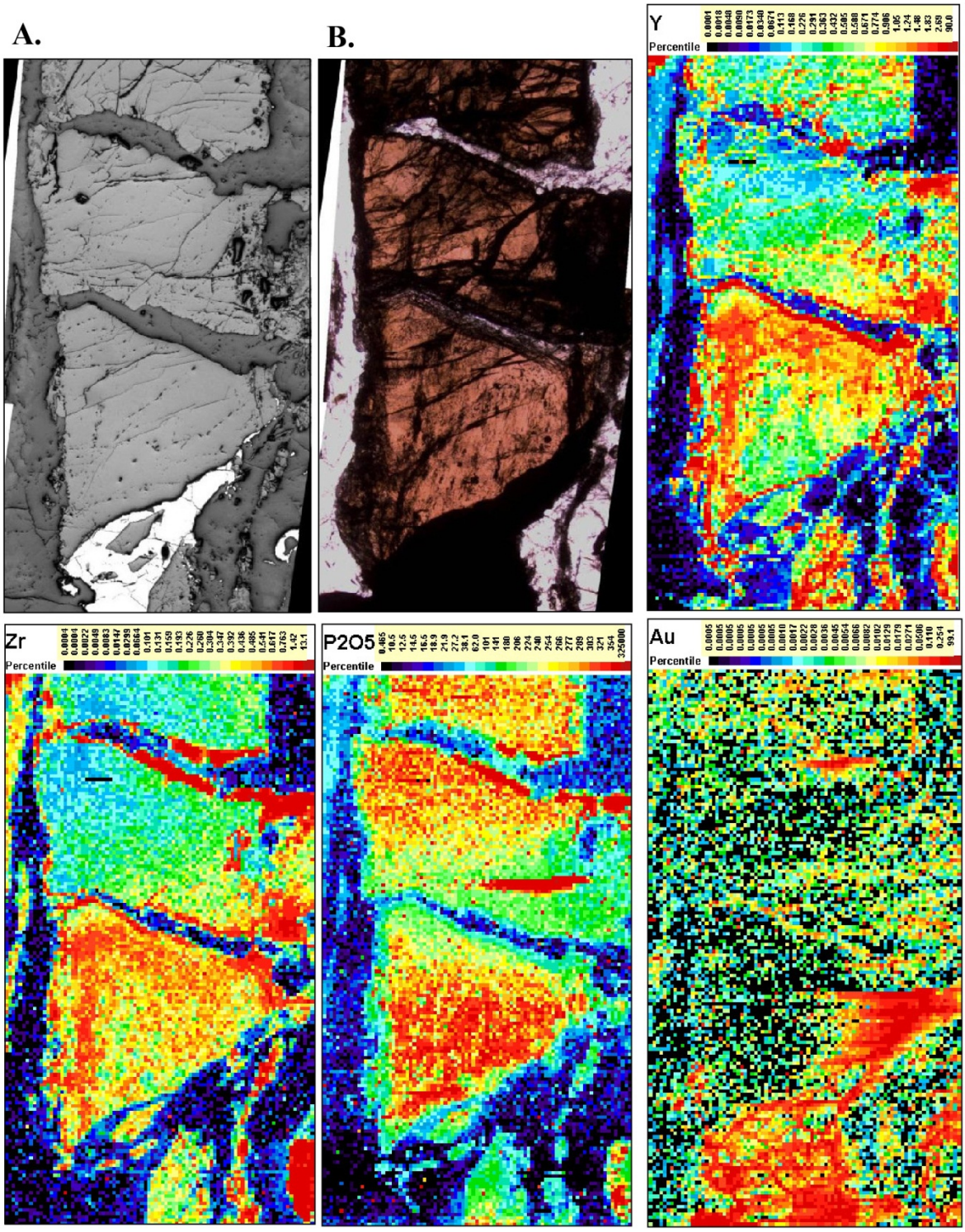

Figure 7-15: 2D LA-ICP-MS elemental maps of garnets associated with high-grade gold-mineralized unit 4EA sample (MW-12-UG-015A, 76.9 ppm Au). A. Microphotograph of map area in reflected light. B. Same as A. in plain polarized light, and, in order (percentile distribution map): yttrium, zirconium, phosphate, and gold.

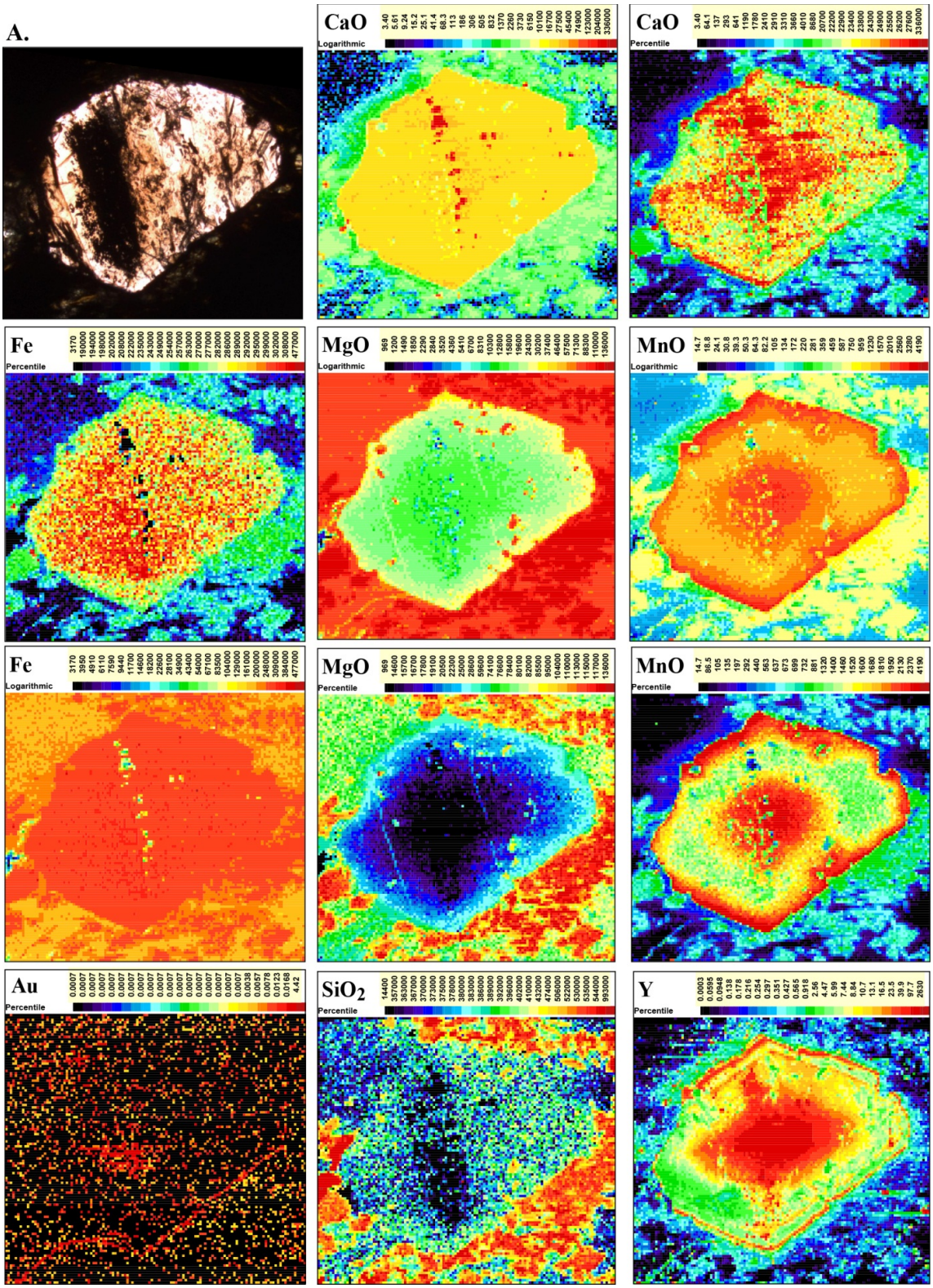

Figure 7-16: 2D LA-ICP-MS elemental map of garnet associated with low-grade gold-mineralized unit 4EA, sample MW-12-UG-023, 5.9 ppm Au. A. Microphotograph of map area in plain polarized light, and in order: CaO, MgO, Mn, and Fe maps in logarithmic and percentile distribution maps. Bottom row: Au, SiO_2, and Y percentile distribution maps.

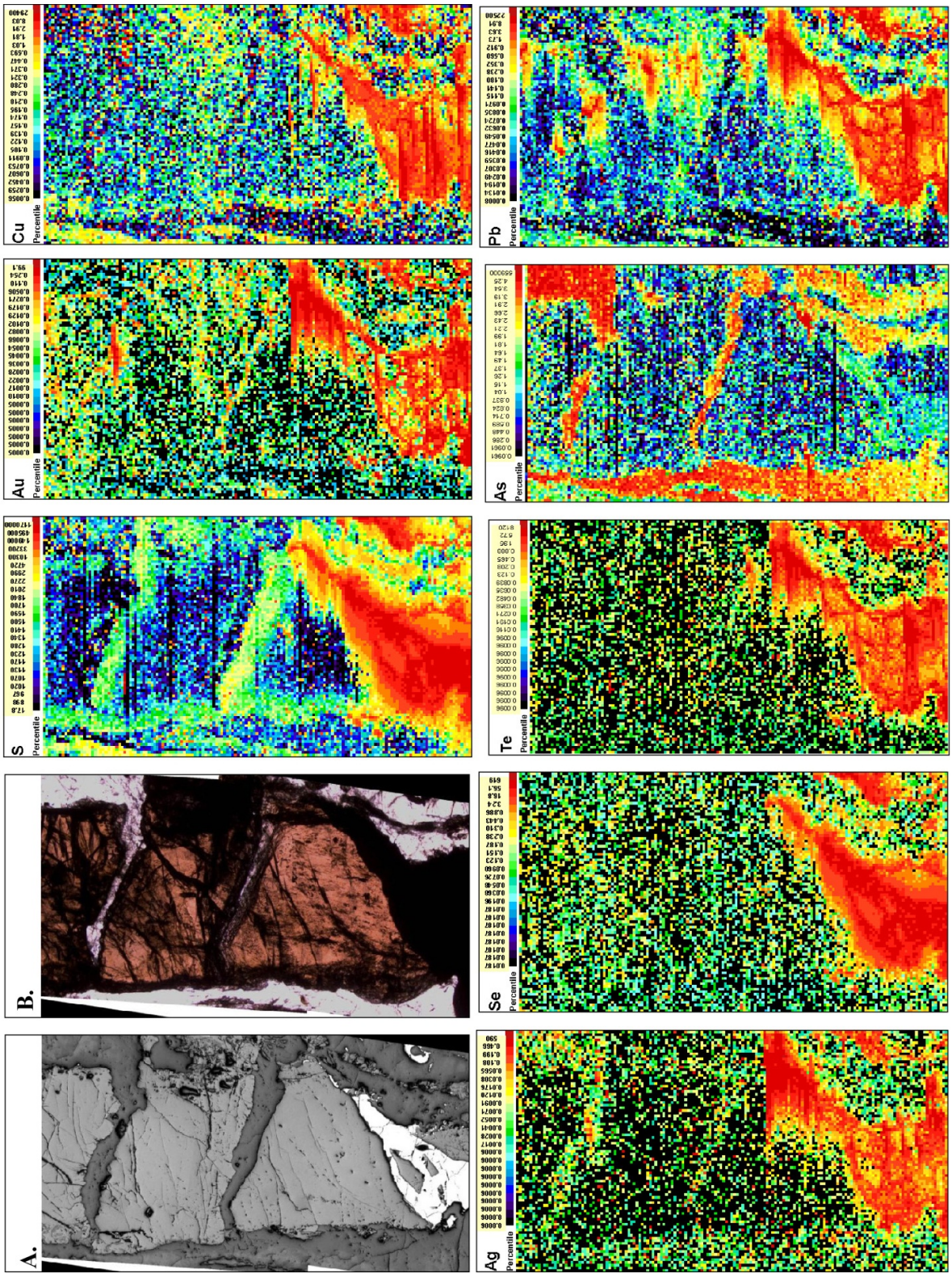

Figure 7-17: 2D LA-ICP-MS elemental map of sulphides associated with high-grade gold-mineralized unit 4EA sample (MW-12-UG-015A, 76.9 ppm Au). A. Microphotograph of map area in reflected light. B. Same as A. in plain polarized light, and, in order: sulphur, gold, copper, silver, selenium, tellurium, arsenic, and lead content maps.

7.2.3 Whole-rock geochemistry of 4EA-hosted ore

Whole-rock geochemical data of gold-mineralized samples are used hereafter to characterize gold ore and associated hydrothermal alteration (chapter 8). Focus is made on the replacement-type ore hosted in unit 4EA, as it has historically constituted 90% of the mined material at Musselwhite (McLeod, chief production geologist – personal communication, 2012). The use of geochemical data comprises some intrinsic challenges, one of which is the "closure effect" (Butler, 1982). This phenomenon stems from the fact that geochemical analyses theoretically provide data for the various elements or oxides that should add up to 1 or 100%, which inducing a statistical interdependence between the various variables (Verma et al., 2006). A way to tackle the issue is to perform a log transformation of the data, particularly major elements, involving the geometric mean for each sample, where $Y_n = \log(X_n / (\text{root}^{N-1}(X_1 \text{ x } X_2 \text{ x } X_3 \ldots X_N)))$. The result is a centered-log ratio (CLR) dataset that is no longer submitted to the interdependence issue within a given sample, and thus better-suited for statistical analysis using correlation coefficients and principal component analysis (see hereafter).

Average raw data composition and standard deviation for major and trace elements of the ore in BIF units is presented in Table 7-4. Major element data of unit 4EA samples containing over 1 ppm of gold is projected in a box plot as raw data and CLR data (Figure 7-18; 133 samples with 1 to 125 ppm Au). Raw data shows that SiO_2 content is relatively stable around 50 wt.%; Al_2O_3 content weakly varies around 7.5 wt.%; and approximately 36 wt.% total iron is distributed with a FeO/Fe_2O_3 ratio of 2.5. Beside sulphur, which can constitute up to 10 wt.% of a sample (median at 2.48 wt.%), MgO and CaO are the only other major oxides above 2 wt.% (2.87 and 2.48 median values, respectively). MnO median is around 0.44 wt.%; and K_2O and CO_2 at 0.48 and 0.24 wt.%, respectively, with highest values reaching 1.5-2 wt.% (Figure 7-18A). The CLR transformation allows comparing all major elements on a similar scale of values (between -3 and +3) and produces a distribution of data in which strongly variable elements are more easily identified (Figure 7-18B). The CLR box plot shows that Fe_2O_3, Na_2O, K_2O, CO_2, and total S have the most dispersed distribution, with widespread first and fourth quartiles. Such observations are consistent with the petrographic data of alteration minerals, including iron-bearing sulphides, carbonates, and micas.

Table 7-4: Average major and trace element composition of gold-mineralized samples of the various BIF units. Au is in ppb, major elements in wt.% and trace elements in ppm. Fe(T) means Fe_2O_3 total.

		Au	SiO_2	Al_2O_3	Fe_2O_3	FeO	Fe (T)	MnO	MgO	CaO	Na_2O	K_2O	TiO_2	P_2O_5	CO_2	Total S
Unit 4A	Average	8989.6	58.26	0.48	3.85	19.62	25.67	0.32	2.12	7.07	0.09	0.05	0.01	0.11	4.65	8.59
All > 1 ppm Au, n = 27	SD	9645.4	22.96	0.33	7.50	7.46	13.85	0.11	1.21	4.41	0.08	0.03	0.01	0.14	3.83	7.42
Unit 4A	Average	13766.7	50.93	0.50	5.98	22.27	30.74	0.32	2.43	7.64	0.09	0.05	0.01	0.10	5.18	11.13
All > 5 ppm Au, n = 15	SD	10829.4	24.66	0.36	9.83	6.65	14.99	0.11	1.34	4.61	0.10	0.04	0.01	0.07	4.41	8.32
Unit 4B	Average	7499.4	47.30	3.80	11.68	23.21	37.49	0.66	2.47	3.83	0.30	0.83	0.17	0.13	2.23	3.52
All > 1 ppm Au, n = 32	SD	9002.1	8.44	2.37	6.47	3.29	7.96	0.31	0.75	2.16	0.30	0.60	0.14	0.05	1.59	4.02
Unit 4B	Average	13223.3	46.40	3.31	12.53	23.20	38.33	0.69	2.38	3.98	0.28	0.76	0.15	0.13	2.56	4.35
All > 5 ppm Au, n = 15	SD	10584.3	10.78	2.40	7.80	3.94	9.37	0.41	1.00	2.58	0.24	0.67	0.16	0.05	2.05	5.40
Unit 4B, facies 4Bc	Average	12614.5	47.90	5.77	12.21	22.34	37.05	0.52	2.55	2.69	0.38	1.20	0.31	0.12	1.33	3.15
All > 1 ppm Au, n = 20	SD	13719.1	6.80	2.14	4.40	4.48	5.24	0.20	0.63	1.56	0.47	0.70	0.15	0.03	1.07	2.61
Unit 4B, facies 4Bc	Average	18196.2	48.20	5.23	12.38	22.50	37.40	0.52	2.36	2.77	0.31	0.85	0.27	0.12	1.49	4.27
All > 5 ppm Au, n = 13	SD	14188.5	8.13	2.18	4.91	4.94	4.83	0.18	0.63	1.78	0.48	0.49	0.15	0.02	1.15	2.59
Unit 4EA	Average	17714.9	49.29	7.45	8.54	23.93	35.16	0.44	2.94	2.66	0.26	0.58	0.36	0.14	0.40	3.42
All > 1 ppm Au, n = 133	SD	25648.5	7.92	1.84	4.62	4.29	6.39	0.17	0.59	1.10	0.24	0.45	0.14	0.03	0.43	3.07
Unit 4EA	Average	27374.6	49.21	7.05	7.17	25.27	35.26	0.42	2.85	2.68	0.26	0.56	0.33	0.13	0.38	4.59
All > 5 ppm Au, n = 79	SD	5609.9	29.26	3.97	2.77	13.89	20.34	0.19	1.66	1.10	0.01	0.09	0.15	0.07	0.02	0.25
Unit 4EA	Average	34993.0	48.90	6.79	6.77	25.91	35.59	0.42	2.84	2.73	0.26	0.51	0.32	0.13	0.37	5.19
All > 10 ppm Au, n = 57	SD	9920.5	19.73	2.66	2.58	9.79	13.84	0.14	1.11	0.91	0.12	0.23	0.12	0.05	0.19	1.84
Unit 4F	Average	6676.6	49.28	15.19	4.38	15.75	21.90	0.60	3.28	3.78	0.70	2.80	0.84	0.09	0.32	1.92
All > 1 ppm Au, n = 35	SD	9106.5	5.06	3.06	3.41	4.07	6.24	0.26	0.81	2.08	0.76	1.33	0.20	0.05	0.54	1.22
Unit 4F	Average	15385.0	47.58	15.30	2.83	16.24	20.89	0.51	3.46	5.25	0.77	2.78	0.88	0.08	0.56	3.09
All > 5 ppm Au, n = 12	SD	1718.2	31.27	8.58	0.68	8.26	11.07	0.24	1.75	1.20	0.04	1.04	0.45	0.03	0.15	0.50
Unit 4E	Average	7341.6	50.24	8.69	4.76	20.46	27.52	0.51	3.87	6.12	0.43	0.49	0.41	0.13	1.10	3.15
All > 1 ppm Au, n = 32	SD	6888.9	4.66	2.79	3.34	5.20	4.66	0.26	0.78	1.90	0.30	0.52	0.18	0.05	0.91	2.08
Unit 4E	Average	12601.3	49.45	7.40	3.47	23.55	29.66	0.44	3.95	6.03	0.43	0.37	0.32	0.15	1.25	4.46
All > 5 ppm Au, n = 16	SD	320.1	32.23	4.18	1.00	10.79	16.16	0.17	2.19	2.99	0.09	0.02	0.16	0.06	0.13	0.76

		Au	B	Be	Cr	Co	Ni	Sc	V	Cu	Pb	Zn	Ag	As	Ge
Unit 4A	Average	8989.6	1.04	0.52	52.85	4.36	17.89	2.06	24.19	111.96	7.11	21.24	0.30	109.07	0.86
All > 1 ppm Au, n = 27	SD	9645.4	1.11	0.10	27.71	2.59	13.11	2.37	11.88	74.96	5.45	8.68	0.15	200.19	0.43
Unit 4A	Average	13766.7	0.90	0.50	48.27	4.87	22.53	2.17	26.60	142.77	8.87	20.82	0.30	152.87	0.80
All > 5 ppm Au, n = 15	SD	10829.4	0.83	0.00	14.76	2.74	14.51	1.97	13.03	84.11	6.35	9.47	0.15	266.10	0.55
Unit 4B	Average	7499.4	1.98	1.55	56.85	13.14	51.90	6.03	56.28	105.21	5.80	49.11	0.60	131.96	1.96
All > 1 ppm Au, n = 32	SD	9002.1	2.26	0.67	33.78	10.22	90.87	4.41	34.39	82.42	3.76	17.19	0.92	269.58	0.90
Unit 4B	Average	13223.3	1.04	1.46	59.77	14.00	63.54	5.35	54.27	106.24	5.54	47.96	0.78	105.26	1.97
All > 5 ppm Au, n = 15	SD	10584.3	0.20	0.62	16.32	2.06	27.56	1.14	15.47	16.12	1.44	22.57	0.23	195.27	0.75
Unit 4B, facies 4Bc	Average	12614.5	2.25	1.55	89.55	16.56	43.45	10.80	90.70	85.36	6.35	66.29	0.44	36.63	2.63
All > 1 ppm Au, n = 20	SD	13719.1	3.92	0.60	22.48	4.92	12.71	4.57	38.72	45.65	2.54	41.02	0.43	83.43	0.96
Unit 4B, facies 4Bc	Average	18196.2	1.38	1.38	87.54	16.91	42.77	9.46	81.85	103.28	7.08	65.28	0.43	45.94	2.66
All > 5 ppm Au, n = 13	SD	14188.5	1.79	0.51	24.85	4.99	13.33	4.41	38.42	46.15	2.63	50.50	0.50	103.14	0.99
Unit 4EA	Average	17714.9	3.23	1.03	88.15	19.56	52.50	12.95	113.53	122.36	5.28	88.24	0.82	35.17	3.06
All > 1 ppm Au, n = 133	SD	25648.5	5.46	0.65	34.08	7.94	22.72	4.61	39.51	68.76	3.37	35.71	1.42	96.71	0.98
Unit 4EA	Average	27374.6	2.89	0.90	83.96	19.57	53.18	12.00	109.91	141.20	5.48	86.03	1.10	29.87	2.83
All > 5 ppm Au, n = 79	SD	5609.9	5.45	0.62	36.86	8.22	26.27	4.09	35.86	73.11	2.53	35.69	1.74	90.30	0.82
Unit 4EA	Average	34993.0	3.35	0.87	75.67	19.05	49.95	11.47	108.28	148.60	5.70	81.75	1.37	18.33	2.80
All > 10 ppm Au, n = 57	SD	9920.5	1.39	0.20	29.28	6.63	16.43	4.71	42.80	36.00	1.45	29.71	0.40	35.37	1.18
Unit 4F	Average	6676.6	48.84	1.49	218.14	45.19	125.92	34.31	266.34	160.88	6.12	141.22	0.61	69.67	2.88
All > 1 ppm Au, n = 35	SD	9106.5	70.17	0.92	73.04	16.47	40.06	9.83	71.68	128.78	3.12	59.07	0.55	156.08	0.89
Unit 4F	Average	15385.0	76.27	2.38	267.17	57.68	142.17	35.00	298.17	319.64	5.50	128.95	0.74	109.75	2.22
All > 5 ppm Au, n = 12	SD	1718.2	15.08	0.40	102.60	20.31	60.71	17.31	137.65	22.70	2.12	58.09	0.05	61.10	1.40
Unit 4E	Average	7341.6	9.70	0.78	125.66	28.67	87.91	16.13	132.09	222.79	4.94	187.86	0.58	64.05	2.28
All > 1 ppm Au, n = 32	SD	6888.9	13.90	0.46	75.11	11.69	52.51	7.99	53.29	132.67	3.31	151.48	1.54	106.55	0.95
Unit 4E	Average	12601.3	4.91	0.78	100.50	25.04	71.69	12.56	111.31	274.31	4.94	151.91	0.83	56.12	1.91
All > 5 ppm Au, n = 16	SD	320.1	2.97	0.23	35.74	12.01	25.03	5.75	55.72	63.73	1.15	25.73	0.68	30.05	0.94

Table 7-4 (cont'd): Average major and trace element composition of gold-mineralized samples of the various BIF units. Au is in ppb and trace elements in ppm.

		Au	Sb	Se	Te	Tl	Bi	Sn	W	Mo	Li	Ga	Cs	Ba	Rb	Sr
Unit 4A	Average	8989.6	0.70	13.38	1.45	0.04	0.57	0.50	0.89	2.80	1.63	1.52	0.06	14.57	1.20	67.56
All > 1 ppm Au, n = 27	SD	9645.4	0.44	8.81	1.02	0.06	0.80	0.00	0.56	1.24	1.27	1.00	0.05	9.81	0.80	45.40
Unit 4A	Average	13766.7	0.84	16.35	1.78	0.03	0.74	0.50	1.01	2.57	1.73	1.63	0.07	14.77	1.27	71.80
All > 5 ppm Au, n = 15	SD	10829.4	0.52	7.49	1.17	0.02	1.07	0.00	0.67	1.32	1.21	0.97	0.07	8.78	0.77	47.80
Unit 4B	Average	7499.4	2.17	9.93	4.00	0.11	0.32	0.53	2.28	1.30	8.98	6.88	3.22	126.75	35.58	59.85
All > 1 ppm Au, n = 32	SD	9002.1	8.05	13.32	12.49	0.09	0.92	0.11	1.30	1.08	8.35	3.66	5.36	107.01	26.85	24.09
Unit 4B	Average	13223.3	3.29	11.45	5.50	0.10	0.13	0.54	2.47	1.58	8.73	6.58	3.01	107.46	32.50	53.31
All > 5 ppm Au, n = 15	SD	10584.3	4.15	2.40	6.00	0.02	0.43	0.29	0.69	0.15	0.44	2.28	1.51	13.96	6.17	25.29
Unit 4B, facies 4Bc	Average	12614.5	0.40	6.72	1.44	0.15	0.12	0.50	3.23	1.68	14.00	10.75	5.73	178.60	54.10	52.30
All > 1 ppm Au, n = 20	SD	13719.1	0.40	5.55	1.29	0.14	0.16	0.00	3.15	1.03	9.73	5.17	8.02	109.14	32.88	20.79
Unit 4B, facies 4Bc	Average	18196.2	0.48	8.48	1.89	0.10	0.15	0.50	3.69	1.88	9.77	10.92	3.05	140.08	38.46	52.69
All > 5 ppm Au, n = 13	SD	14188.5	0.38	5.54	1.40	0.07	0.20	0.00	3.85	1.14	5.13	6.10	2.01	91.86	21.29	23.73
Unit 4EA	Average	17714.9	0.11	7.26	0.97	0.11	0.12	0.52	2.14	1.10	16.06	12.84	1.72	122.75	26.07	50.23
All > 1 ppm Au, n = 133	SD	25648.5	0.20	5.71	0.76	0.10	0.26	0.19	2.56	0.76	8.08	3.42	1.96	102.16	20.73	21.32
Unit 4EA	Average	27374.6	0.09	9.37	1.15	0.12	0.10	0.54	2.24	1.03	15.42	13.67	1.88	114.19	26.32	53.01
All > 5 ppm Au, n = 79	SD	5609.9	0.20	5.81	0.84	0.11	0.08	0.24	2.98	0.77	8.36	3.48	2.35	101.91	22.30	20.09
Unit 4EA	Average	34993.0	0.06	10.35	1.18	0.12	0.10	0.50	2.10	0.87	13.88	14.09	1.92	111.02	24.89	53.02
All > 10 ppm Au, n = 57	SD	9920.5	0.06	1.71	0.17	0.01	0.08	0.19	0.38	0.18	4.35	5.67	0.27	10.11	2.78	17.89
Unit 4F	Average	6676.6	0.07	2.63	0.56	0.31	0.10	0.66	2.89	1.09	52.98	18.64	3.06	301.58	98.37	49.96
All > 1 ppm Au, n = 35	SD	9106.5	0.15	3.49	0.68	0.15	0.16	0.48	3.29	0.78	34.81	3.36	1.27	163.10	47.62	28.14
Unit 4F	Average	15385.0	0.13	7.53	1.43	0.35	0.19	0.96	8.02	2.04	38.55	21.08	2.41	370.58	90.33	79.42
All > 5 ppm Au, n = 12	SD	1718.2	0.05	0.61	0.08	0.12	0.04	0.12	0.28	0.22	12.85	10.81	1.27	97.92	35.89	15.43
Unit 4E	Average	7341.6	0.16	5.97	1.29	0.06	0.11	0.50	3.91	1.31	17.78	11.94	0.68	57.84	15.33	55.91
All > 1 ppm Au, n = 32	SD	6888.9	0.21	4.15	0.90	0.06	0.09	0.00	4.71	0.80	9.96	2.66	0.66	64.11	17.82	20.05
Unit 4E	Average	12601.3	0.20	8.55	1.65	0.06	0.10	0.50	3.17	1.47	17.13	11.38	0.64	48.06	12.63	57.00
All > 5 ppm Au, n = 16	SD	320.1	0.04	1.28	0.28	0.00	0.02	0.35	0.57	0.36	5.53	6.56	0.01	4.43	1.76	25.36

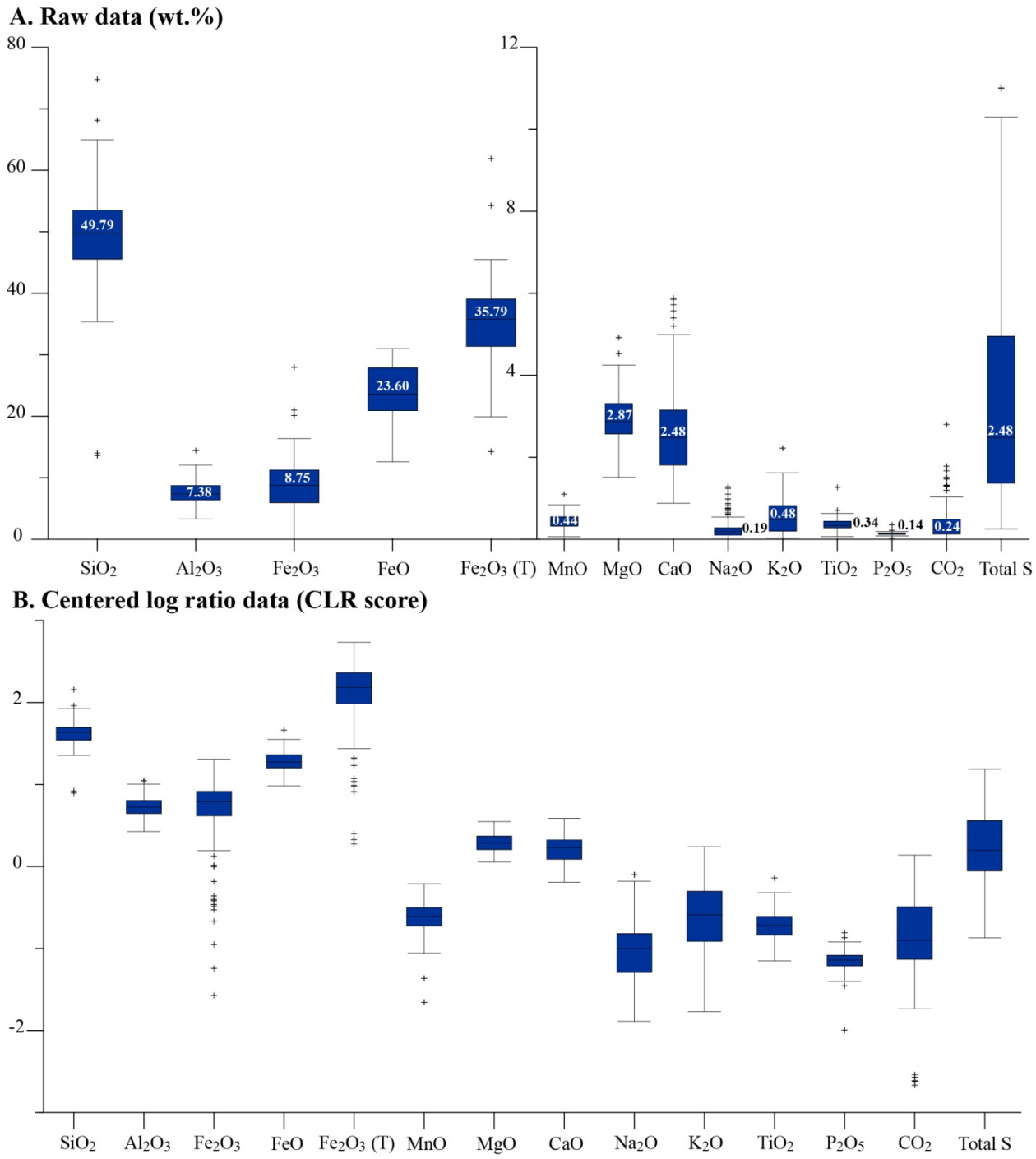

Figure 7-18: Box plot of major elements composition for 4EA samples with gold grade over 1000 ppb (133 samples), using: A. raw data, displaying median values, and B. log centered ratio data (CLR). Box = first to third quartile, black line = median, whiskers = interquartile range (IQR)*1.5 (Upton and Cook, 1996). Total Fe_2O_3 is calculated from CLR values of Fe_2O_3 and FeO. The CLR transformation of data mitigates the closure effects of geochemical analyses.

The relationships of correlation between gold and major elements, and amongst major elements, were subsequently examined using Pearson and Spearman correlation coefficients (PCC, SCC, respectively). The former provides a quantification of the quality of a linear correlation between two variables. The latter express whether one variable can be described as a monotonous function of another using the ranks of values (Fieller et al., 1957), which is helpful if the correlation between two variables is not linear (e.g., logarithmic). This is well illustrated by the correlation between gold and sulphur contents (Figure 7-19; Table 7-5): the 0.55 PCC is notable but does not show a strong positive correlation. However, the SCC of 0.88 shows that there is a reliable link between gold and sulphur (Table 7-5). Correlation coefficients were calculated for both datasets: raw data and centered-log ratio data. Despite the fact that loss on ignition (LOI) and total iron were not included, centered-log ratio data provides overall better results (i.e., higher correlation coefficients).

The main relationships derived from PCCs show the positive correlation between: 1) Al_2O_3 and TiO_2 with MgO (0.70 and 0.57), 2) MgO with FeO and MnO (0.55 and 0.47), 3) MnO with Fe_2O_3 and FeO (0.41 and 0.33), 4) FeO with total S (0.37), 5) P_2O_5 with SiO_2 and FeO (0.50 and 0.47), and 6) CaO and CO_2 (0.56). MnO, Fe_2O_3, and FeO also show weak positive correlation with Al_2O_3 and TiO_2 (around 0.25). Negative correlations include: 1) Na_2O with respect to MnO and MgO (-0.35 and -0.23), 2) K_2O to CaO, CO_2, and total S (-0.32, -0.20, and -0.29), 3) CO_2 with Al_2O_3 and TiO_2 (-0.43 and -0.31), 4) Fe_2O_3 with total S and Au (-0.38 and -0.40), and 5) MnO with Au (-0.31). PCC calculations on non-CLR data, which include LOI data, show LOI positively correlates with CO_2, total S and Au (0.45, 0.70, and 0.43, respectively). The negative correlation between Fe_2O_3 and total S and gold is interesting, as it shows magnetite was preferentially consumed during sulphidation of unit 4EA (grunerite contains iron as FeO only), and petrographic observations show magnetite is only preserved when included in garnet porphyroblasts (7.2.1).

Results of SCC calculations globally corroborate and frequently exceed results of PCC calculations. The most notable case is the correlation coefficient between total S and gold that changes from 0.55 to 0.88. Most negative PCC have better corresponding SCC (i.e., closer to -1). For example, Na_2O with respect to MgO and MnO (-0.23 to -0.42 and -0.35 to -0.53, respectively), or Fe_2O_3 in relation to total S and Au (-0.38 to -0.54 and -0.40 to -0.60, respectively). In some cases, positive correlations actually emerge from the data. Such relationships include the 0.34 SCC between SiO_2 and MgO or 0.29 SCC between SiO_2 and Al_2O_3.

Overall, these correlations are consistent with the mineral assemblages of analysed rock samples and the processes they reflect (e.g., magnetite replaced by pyrrhotite). For instance, MgO, which is present in garnet as well as amphiboles, biotite, or feldspar, is positively correlated to Al_2O_3 , Fe_2O_3, FeO, and MnO.

Negative correlations are also interesting, as they may represent the replacement process (e.g., Fe_2O_3 with respect to total S and Au) or mass changes (e.g., CO_2 with respect to Al_2O_3 and TiO_2; chapter 8). The specific positive correlation of CaO and CO_2 is notable, as one could expect CaO to be also positively correlated to other amphibole-forming elements. This supports the observation of calcite as the main carbonate species.

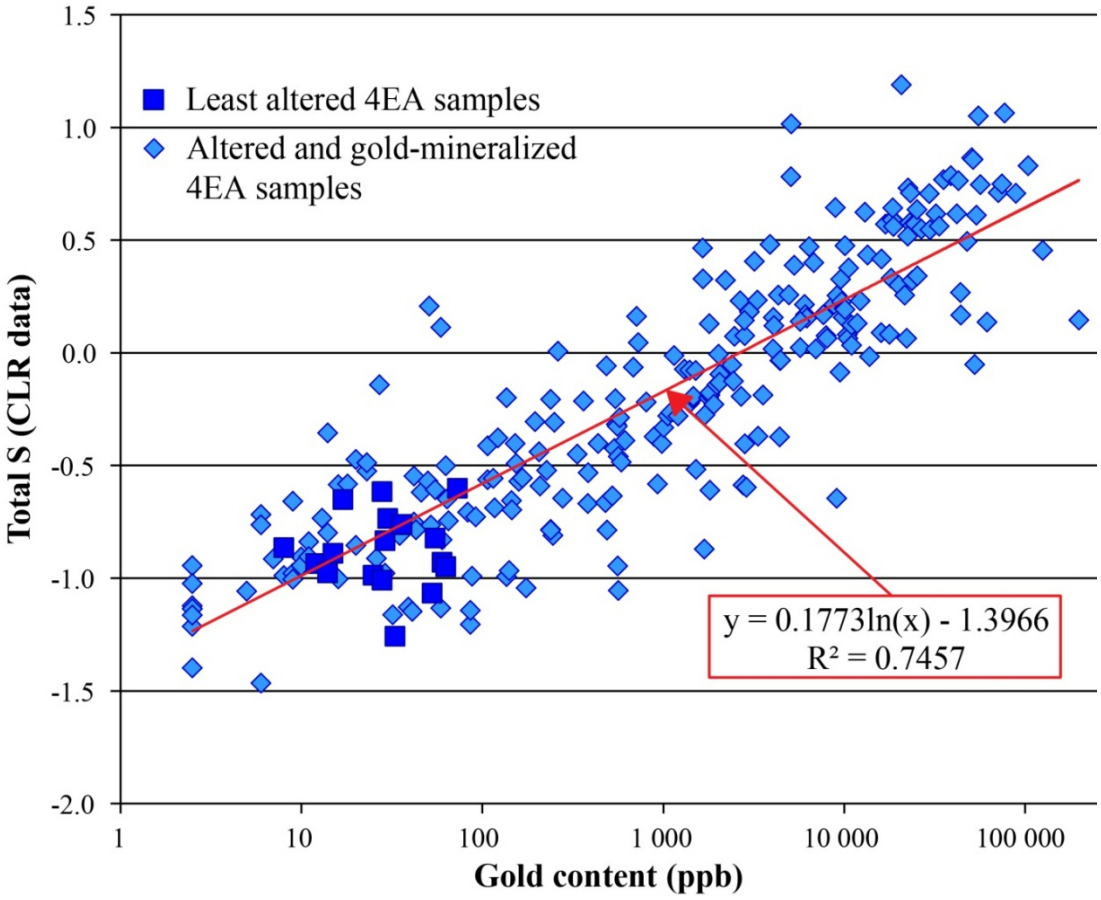

Figure 7-19: Binary plot of gold content and total sulphur content (CLR data) for least altered (blue squares) and altered to gold-mineralized (light blue diamonds) 4EA samples. The red line illustrates the logarithmic positive correlation between sulphur and gold in altered samples, with a fairly good R factor.

Table 7-5: Pearson and Spearman correlation coefficients for major elements of 4EA samples, after centered log ratio (CLR) transformation. Loss on ignition (LOI) was not included in the CLR operation due to negative values, which result from the Fe oxidation during ignition (chapter 1; Dahéron et al., 2015).

Pearson correlation coefficient

	Au	SiO_2	Al_2O_3	Fe_2O_3	FeO	Fe_2O_3 (T)	MnO	MgO	CaO	Na_2O	K_2O	TiO_2	P_2O_5	CO_2	Total S
Au	1	0.05	**-0.24**	**-0.40**	**0.15**		**-0.23**	**-0.17**	0.02	0.00	-0.03	**-0.22**	**-0.13**	-0.02	**0.55**
SiO_2	0.05	1	-0.01	-0.12	**0.13**		-0.07	-0.01	**0.13**	-0.02	0.02	**-0.17**	**0.50**	0.05	0.01
Al_2O_3	**-0.24**	-0.01	1	**0.28**	**0.24**		**0.24**	**0.70**	**-0.15**	-0.02	0.10	**0.84**	**0.14**	**-0.43**	**-0.25**
Fe_2O_3	**-0.40**	-0.12	**0.28**	1	**0.13**		**0.41**	**0.32**	**-0.24**	**-0.18**	-0.08	**0.26**	**0.33**	-0.09	**-0.38**
FeO	**0.15**	**0.13**	**0.24**	**0.13**	1		**0.33**	**0.55**	0.06	**-0.24**	**-0.24**	0.06	**0.47**	**-0.22**	**0.37**
Fe_2O_3 (T)															
MnO	**-0.23**	-0.07	**0.24**	**0.41**	**0.33**		1	**0.42**	**-0.13**	**-0.35**	-0.11	**0.15**	**0.23**	-0.09	**-0.31**
MgO	**-0.17**	-0.01	**0.70**	**0.32**	**0.55**		**0.42**	1	**0.13**	**-0.23**	**-0.20**	**0.57**	**0.35**	**-0.24**	**-0.13**
CaO	0.02	**0.13**	**-0.15**	**-0.24**	0.06		**-0.13**	**0.13**	1	-0.11	**-0.32**	**-0.15**	0.06	**0.56**	**0.14**
Na_2O	0.00	-0.02	-0.02	**-0.18**	**-0.24**		**-0.35**	**-0.23**	-0.11	1	0.03	0.07	**-0.16**	**-0.15**	-0.03
K_2O	-0.03	0.02	0.10	-0.08	**-0.24**		-0.11	**-0.20**	**-0.32**	0.03	1	0.05	**-0.13**	**-0.20**	**-0.26**
TiO_2	**-0.22**	**-0.17**	**0.84**	**0.26**	0.06		**0.15**	**0.57**	**-0.15**	0.07	0.05	1	-0.04	**-0.31**	**-0.27**
P_2O_5	**-0.13**	**0.50**	**0.14**	**0.33**	**0.47**		**0.23**	**0.35**	0.06	**-0.16**	**-0.13**	-0.04	1	**-0.12**	**-0.13**
CO_2	-0.02	0.05	**-0.43**	-0.09	**-0.22**		-0.09	**-0.24**	**0.56**	**-0.15**	**-0.20**	**-0.31**	**-0.12**	1	0.02
Total S	**0.55**	0.01	**-0.25**	**-0.38**	**0.37**		**-0.31**	**-0.13**	**0.14**	-0.03	**-0.26**	**-0.27**	**-0.13**	0.02	1

Spearman correlation coefficient

	Au	SiO_2	Al_2O_3	Fe_2O_3	FeO	Fe_2O_3 (T)	MnO	MgO	CaO	Na_2O	K_2O	TiO_2	P_2O_5	CO_2	Total S
Au	1	-0.12	**-0.34**	**-0.60**	0.01		**-0.46**	**-0.31**	-0.01	**0.14**	**-0.16**	**-0.38**	**-0.27**	-0.06	**0.88**
SiO_2	-0.12	1	**0.29**	0.07	**0.39**		0.06	**0.34**	0.11	-0.10	**-0.13**	0.09	**0.46**	**-0.16**	-0.07
Al_2O_3	**-0.34**	**0.29**	1	**0.28**	**0.21**		**0.26**	**0.66**	**-0.16**	**-0.21**	0.03	**0.86**	**0.16**	**-0.54**	**-0.27**
Fe_2O_3	**-0.60**	0.07	**0.28**	1	**0.18**		**0.49**	**0.34**	**-0.21**	**-0.32**	-0.10	**0.30**	**0.40**	**-0.12**	**-0.54**
FeO	0.01	**0.39**	**0.21**	**0.18**	1		**0.34**	**0.54**	-0.02	**-0.32**	**-0.33**	0.08	**0.52**	**-0.26**	**0.15**
Fe_2O_3 (T)															
MnO	**-0.46**	0.06	**0.26**	**0.49**	**0.34**		1	**0.41**	**-0.12**	**-0.53**	**-0.15**	**0.21**	**0.24**	-0.04	**-0.36**
MgO	**-0.31**	**0.34**	**0.66**	**0.34**	**0.54**		**0.41**	1	0.12	**-0.42**	**-0.30**	**0.55**	**0.40**	**-0.36**	**-0.16**
CaO	-0.01	0.11	**-0.16**	**-0.21**	-0.02		**-0.12**	0.12	1	-0.03	**-0.36**	**-0.18**	0.07	**0.41**	0.03
Na_2O	**0.14**	-0.10	**-0.21**	**-0.32**	**-0.32**		**-0.53**	**-0.42**	-0.03	1	**0.20**	**-0.13**	**-0.20**	**-0.17**	-0.01
K_2O	**-0.16**	**-0.13**	0.03	-0.10	**-0.33**		**-0.15**	**-0.30**	**-0.36**	**0.20**	1	0.03	**-0.20**	**-0.24**	**-0.29**
TiO_2	**-0.38**	0.09	**0.86**	**0.30**	0.08		**0.21**	**0.55**	**-0.18**	**-0.13**	0.03	1	0.02	**-0.41**	**-0.34**
P_2O_5	**-0.27**	**0.46**	**0.16**	**0.40**	**0.52**		**0.24**	**0.40**	0.07	**-0.20**	**-0.20**	0.02	1	**-0.19**	**-0.19**
CO_2	-0.06	**-0.16**	**-0.54**	**-0.12**	**-0.26**		-0.04	**-0.36**	**0.41**	**-0.17**	**-0.24**	**-0.41**	**-0.19**	1	-0.08
Total S	**0.88**	-0.07	**-0.27**	**-0.54**	**0.15**		**-0.36**	**-0.16**	0.03	-0.01	**-0.29**	**-0.34**	**-0.19**	-0.08	1

The closure effect is much less significant on trace elements (Aitchison, 1986; Aitchison and Egozcue, 2005), so the centered log ratio transformation is not necessary. Trace element data (including REE data) and major elements data was processed through principal component analysis (PCA), using Pearson correlation coefficient. This method uses matrix calculations to define vectors (or principal components, F_x), along which data variance is highest. Plotting the selected variables in the 2D space defined by principals components with the highest variance score allow visualizing variables that are positively correlated with each other (e.g., Au and total S).

The combination of trace elements data and CLR data for major elements produces the highest F1 variance score (42%), and F2 to F6 components have variance scores between 7 and 3% (Figure 7-20). This shows that, while interpretations on the geological processes responsible for the various trace element associations can be drawn from F1-F2 and F1-F3 projections, some relationships are not shown by this analysis. The PCA is accompanied by PCC calculations (Figure 7-21) showing that total S and Cu, Pb, Ag, Te, Se, and Ga positively correlate with gold.

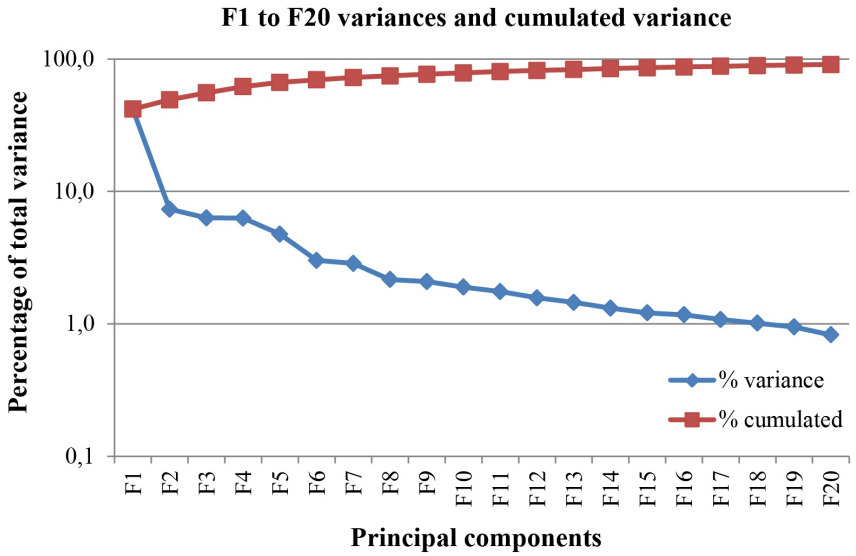

Figure 7-20: Binary plot showing the variance of components F1 to F20 (blue line) and cumulative variance (red line) associated with the Principal Component Analysis of geochemical data from 4EA samples (using non-centered log ratio data for major elements, trace elements, including REE).

With the exception of Ga, the Cu-Pb-Ag-Te-Se metallic association with gold is confirmed on the F1-F2 plane, where main clusters of variables include: 1) Au, Ag, Cu, Se, Te ± Pb, and total S lie at the top of the plot; 2) REE tightly cluster to the right; 3) Fe_2O_3, K_2O, MnO, and P_2O_5 are grouped with Ge, Be, Rb, Ba, Cs, and Tl; and 4) elements such as Co, Ni, and V or Zn, Cr, Sc, and Ti are spread within the top right quarter of the plot (Figure 7-22A). The central mass of elements includes CaO, CO_2, Na_2O, and FeO with Sr, B, Sb, and Mo, as well as As, and Bi nearby. SiO_2 shows a singular position with respect to other

elements, which is consistent with correlation coefficients. Previous work with PCA on non-CLR data, which includes LOI data, has shown that LOI clustered tightly with total S (Oswald et al., 2015a).

On F1-F3 plane (Figure 7-22B), SiO_2 is closer to mineralization-related trace metals (Au, Se, Te, Cu, Ag), showing the input of silica during gold mineralization as suggested by the silica flooding in some ore zones (see below). The cluster includes CO_2 and CaO, and FeO loosely associated. The association of K_2O and Rb is clearer, and Na_2O is clustered with B, Be, Sr, Cs, Tl, and Sb. Fe_2O_3, Al_2O_3, and TiO_2 are spread within the upper right quarter with Sc, V, Ni, Co, Nb, Li, Ge, Ga, and Ta. REE are divided into two clusters, one of which includes most LREE along with Th and U. Pb, As, Bi, and Sb are close to the center, not far from the gold related cluster but not specifically associated with it.

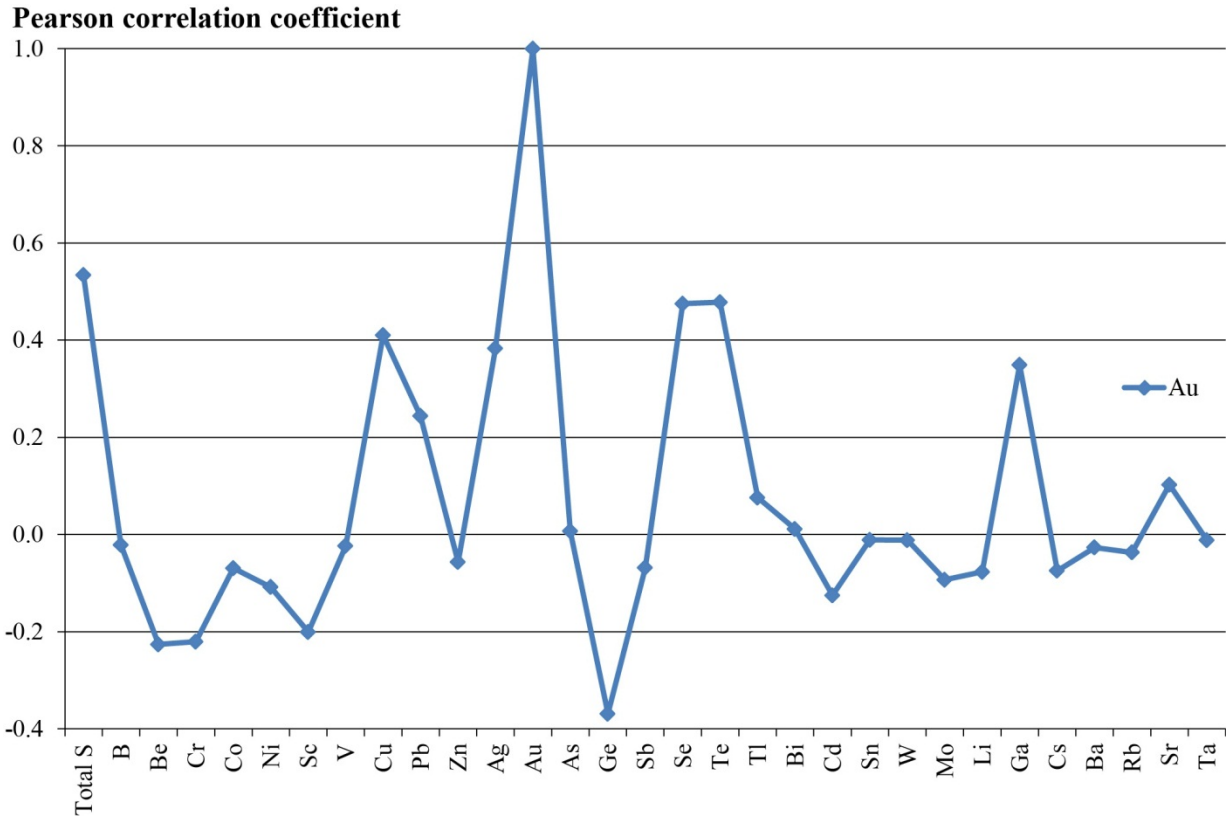

Figure 7-21: Pearson correlation coefficients of trace metals with gold associated with the Principal Component Analysis of geochemical data from 4EA samples (using non-centered log ratio data for major elements, trace elements, including REE).

Lithogeochemical data show that there is no significant silica addition during gold mineralization. Sulphur is the only major element that is clearly enriched and positively correlates with gold content. Also, Au is associated with Cu, Ag, Se, and Te (Pb and Ga to a lesser extent), which argues for a metamorphic origin of gold mineralization. The limited number of trace metals strongly positively correlated to Au in unit 4EA may indicate that gold mineralization resulted from a single, specific ore-

forming event. CaO and CO_2 are not strongly enriched in the ore. While their PCC and SCC with gold are close to 0 (Table 7-5), CaO and CO_2 contents seem to moderately correlate with gold and sulphur on the F1-F3 plot of the principal component analysis (Figure 7-22B). This apparent contradiction may be related to geological process, such as additional alteration and/or metamorphism og the gold-mineralized rocks.

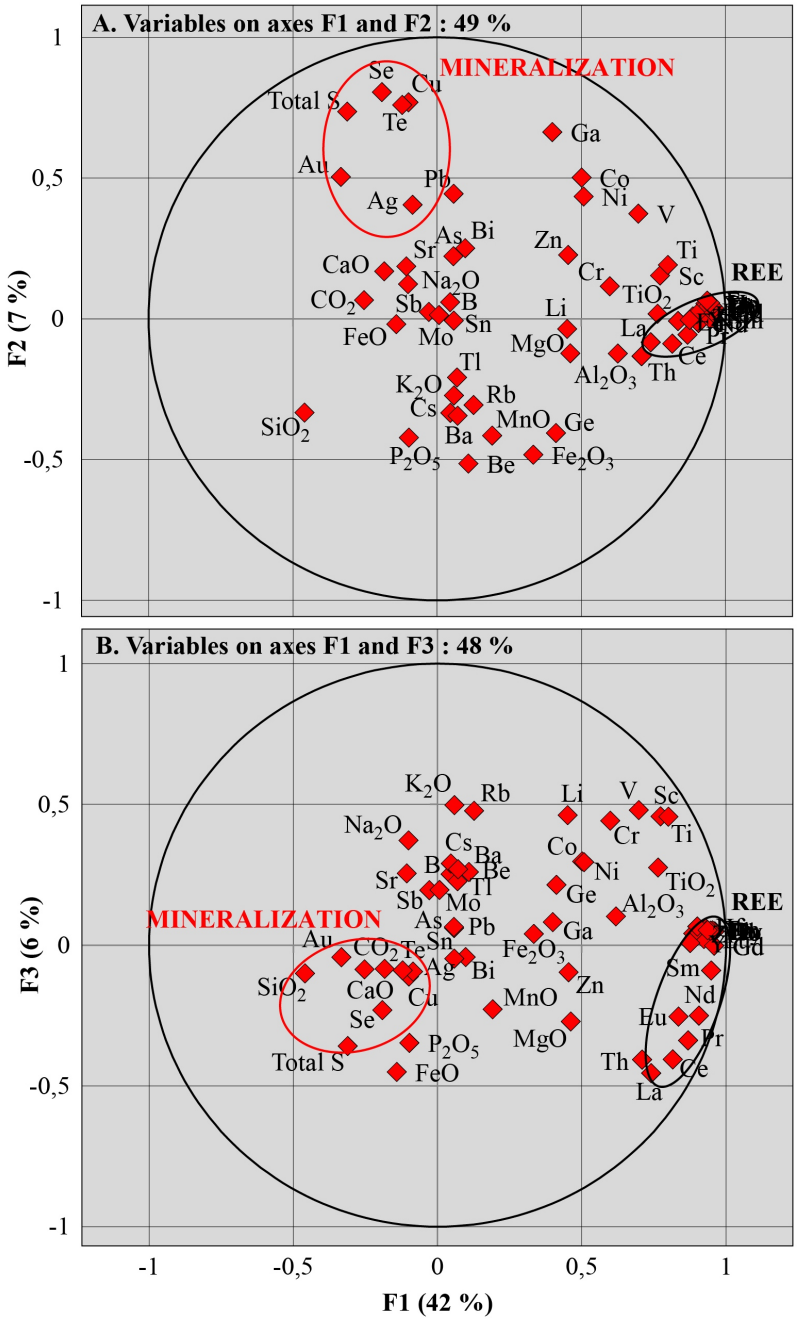

Figure 7-22: Principal Component Analysis of geochemical data from 4EA samples (using non-centered log ratio data for major elements, trace elements, including REE). A. Projection of variables on an F1-F2 components plane. B. Projection of variables on an F1-F3 components plane.

7.3 Variations of replacement-style mineralization

Although they share many features, lithologies of the NIF have slight compositional and rheological differences, which influence the product of replacement-style gold mineralization. Consequently, this section briefly exposes the characteristics of some unusual 4EA ore and other gold-mineralized BIF units. The term "variations" here covers differences in macroscopic textures, mineral proportions, and whole-rock chemical composition.

7.3.1 4EA – silica-flooding end-member

While there is apparently no significant increase in SiO_2 content between ore-grade and barren unit 4EA (Tables Table 3-4, Table 7-2), 4EA-hosted ore locally displays intense silica concentration or "silica flooding". This is interpreted to be the result of silica mobilization as chert is recrystallized. This produces portions of ore constituted by over 50% quartz (Figure 7-23), up to 70 wt.% SiO_2 (Table 7-2), notably in the Lynx zone. In such occurrence, the ore commonly shows a mechanical segregation of minerals into bands of coarse garnet with pyrrhotite and amphiboles and quartz-dominated bands, which form a new compositional layering sub-parallel to S_2 (Figure 7-23A). Gold grades are not proportional to the amount of silica in a given sample.

7.3.1 4EA – Pyrrhotite-rich end-member

Pyrrhotite-replacement of the iron formation is locally intense, forming semi-massive pyrrhotite. This is best illustrated in the C-block ore zone, where several drill sections and underground mine levels intersect a semi-massive pyrrhotite lens (Figure 7-24). In such occurrence, the garnet-grunerite-chert BIF is replaced by an amphibolitic matrix including ferro-tschermakite, hornblende, and actinolite with minor quartz and calcite (Figure 7-25A, B). Centimetre-scale garnet porphyroblasts can also be present, locally displaying a ribbon texture (Figure 7-25C). The boudinaged texture of garnet-rich bands and the presence of pyrrhotite inclusions indicate that garnet post-date pyrrhotite introduction. Quartz-calcite-hedenbergite ± garnet aggregates (Figure 7-25A) are interpreted to result from the metamorphic breakdown of amphiboles to pyroxene and of iron-bearing carbonate to calcite. The absence of grunerite also suggests metamorphic reactions with carbonates to form tschermakite, hornblende, and actinolite. The occurrence of matrix fragments within pyrrhotite (Figure 7-25A, C) and S_2-parallel boudinaged amphibolitic matrix layers (Figure 7-25B) suggest that introduction of such massive pyrrhotite is syn-D_2. However, randomly oriented, euhedral amphibole crystals included in the pyrrhotite matrix suggest the pyrrhotite lens is

located in a zone of low D_2 strain (Figure 7-25B). This is consistent with the oblique orientation (i.e., shallower dip) of the pyrrhotite lens, between two major high strain zones (Figure 7-24A).

Figure 7-23: Silica-rich replacement 4EA-hosted ore. A. Polished slab of underground sample MW-12-UG-133 from the Lynx zone. B. Drill core sample MW-12-310, DDH 06-PQE-095, PQD area. This sample contains 71.68 wt.% SiO_2 and 22.2 ppm Au.

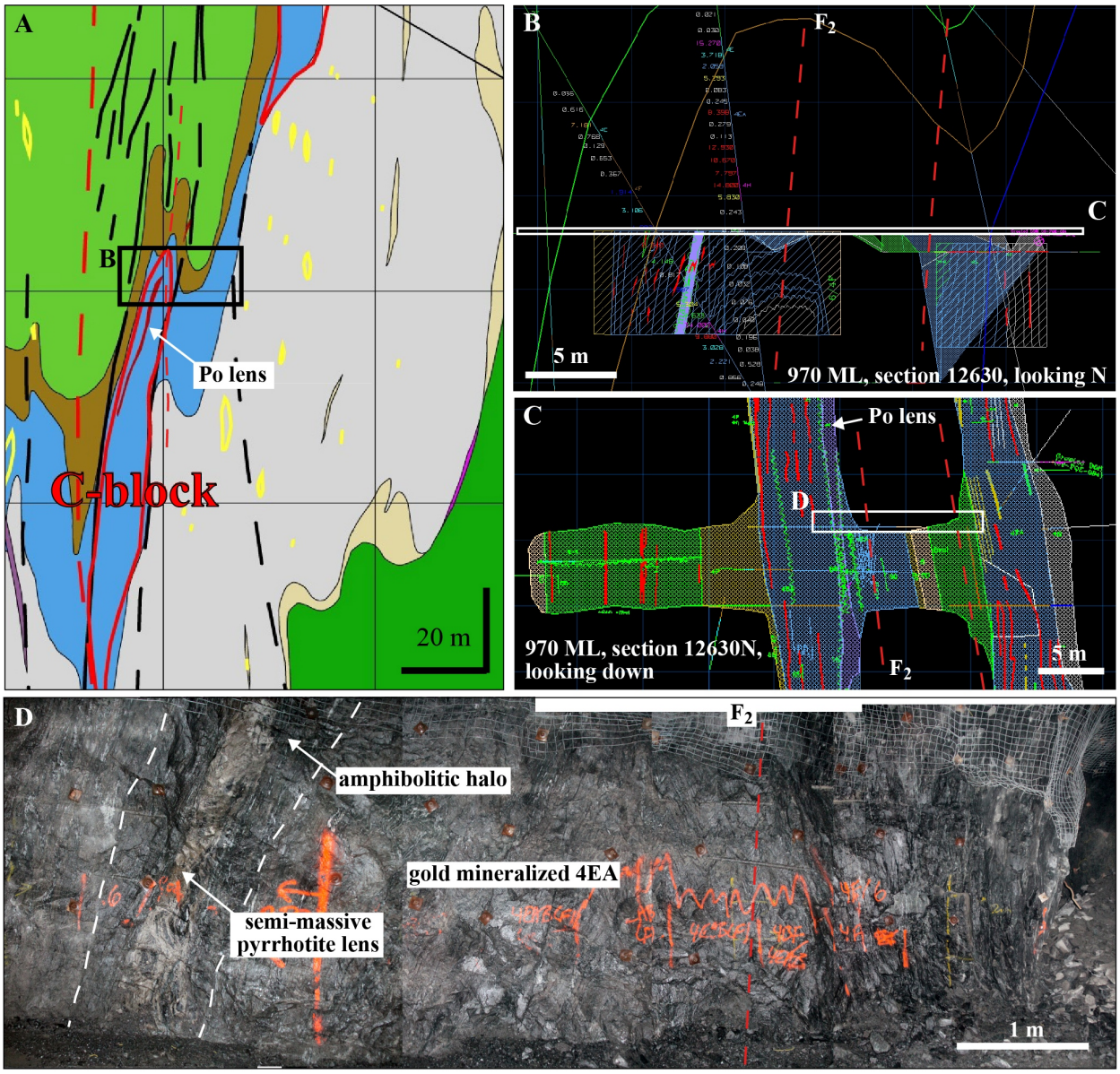

Figure 7-24: Massive pyrrhotite lens in C-block ore zone A. Location of the C-block ore zone and mine level 970 on section 12675 N. B. Section view of mine level 970 face map looking north (from Goldcorp's Musselwhite database); see Figure 7-1 for colour legend of units. Note the parasitic fold structure containing the C-block ore zone in the PDQ area (gold content figures along the drill holes traces, red and purple labels are for drill core segments over 10 ppm Au). C. Underground geological back map of the same area shown in B. showing the continuity of the pyrrhotite lens. D. Photograph of the underground face on mine level 970, section 12630 N. The semi-massive pyrrhotite lens is located along the long limb of the parasitic fold structure and surrounded by a halo of green amphibolite (Figure 7-25).

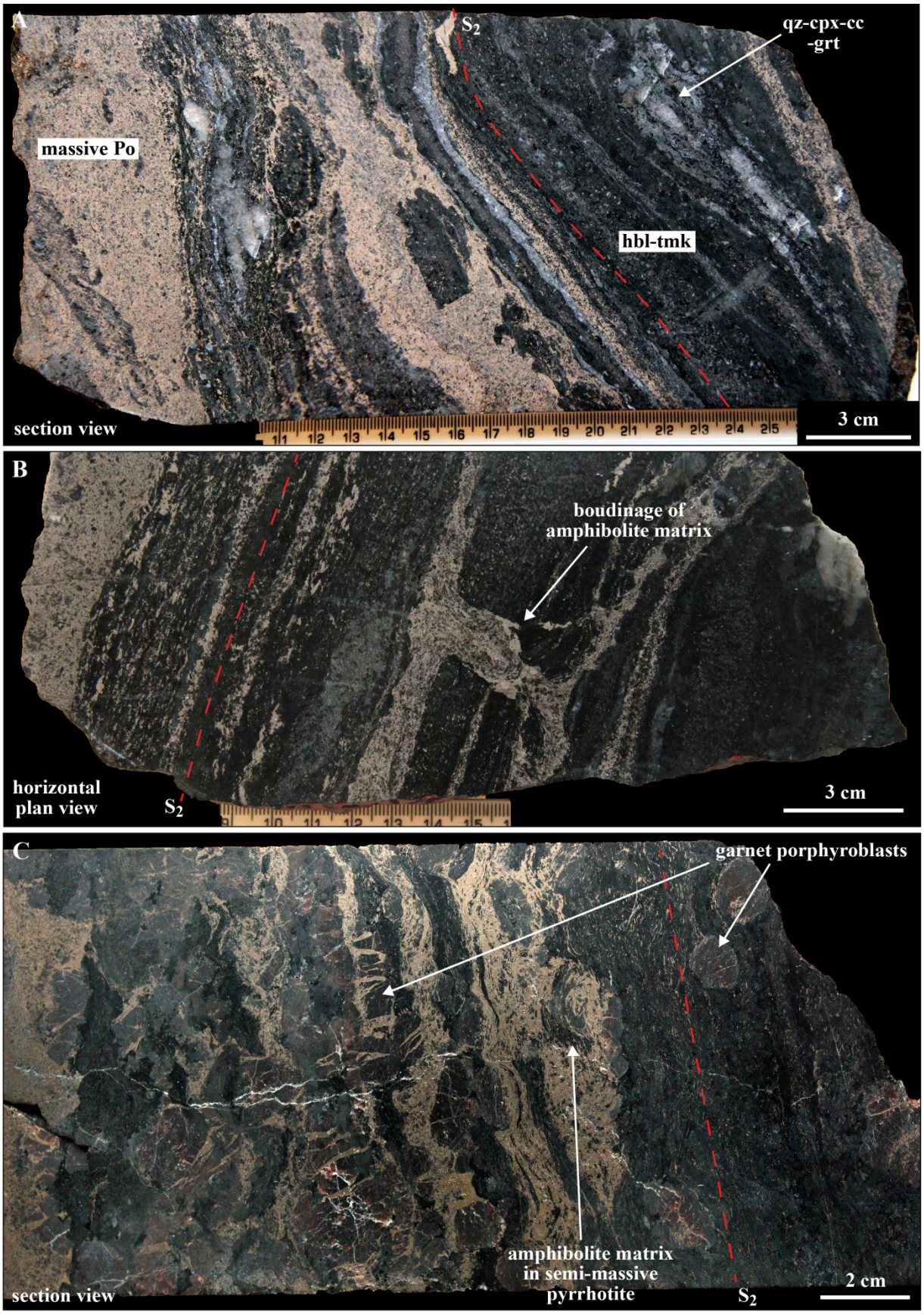
A
S_2
qz-cpx-cc
-grt
massive Po
hbl-tmk
section view
3 cm
B
boudinage of
amphibolite matrix
horizontal
plan view
S_2
3 cm
C
garnet porphyroblasts
amphibolite matrix
in semi-massive
pyrrhotite
section view
S_2
2 cm

Figure 7-25: Polished slabs of pyrrhotite-rich ore samples from mine level 970, section 12630 N. A. Section view of sample MW-12-UG-045. The semi-massive pyrrhotite vein (to the left of the sample) includes amphibolite matrix fragments. The matrix consists of medium-grained tschermakite and hornblende and local quartz-calcite-hedenbergite aggregates. The S_2 foliation is penetrative. B. Plan view of sample MW-12-UG-045. It shows the pyrrhotite vein and its amphibolitic selvage as well as boudinaged amphibolitic layers of host rock and flow of pyrrhotite in the neck of boudins. C. Vertical section of oriented sample MW-13-UG-056. The pyrrhotite-rich zones also include coarse, euhedral, or ribbon-like almandine garnet. Fractures in ribbon-textured garnets are filled with pyrrhotite. Some garnets are mostly inclusion-free and some display an internal fabric clearly defined by pyrrhotite inclusion trails sub-parallel to the external S_2 foliation.

7.3.2 Unit 4E "intraformational"

The garnet-amphibolite (unit 4E) is locally mineralized in the vicinity of gold-mineralized garnet-grunerite BIF as well as within some "intraformational" lenses in unit Bvol. Similarly to unit 4EA, gold mineralization in unit 4E is characterized by pyrrhotite-replacement of amphiboles (Figure 7-26A). Due to strain partitioning related to its location within or at the contact with mafic volcanic rocks, unit 4E usually displays a higher deformation intensity than unit 4EA. Chert bands are typically intensely folded, faulted, and/or boudinaged (Figure 7-26B).

Occasional garnet grains in unit 4E are pale pink to purplish, subhedral porphyroblasts that are associated with fine- to medium-grained, beige grunerite and pyrrhotite (Figure 7-27A, B). Garnet-grunerite-pyrrhotite bands commonly alternate with hornblende-actinolite-dominated bands and deformed quartz bands (i.e., remnants of chert layers or quartz veins; Figure 7-27B, C, D). Strongly mineralized 4E samples (Figures 7-26A; 7-27E, F) commonly include pale green hedenbergite intergrown with green hornblende, beige grunerite, and calcite. Preserved chert and quartz vein fragments are commonly surrounded by a thin layer of near pure grunerite oriented parallel to the S_2 foliation (Figure 7-27F), and locally associated with altered hedenbergite. This grunerite appears to replace some of the adjacent assemblage (i.e., cpx-grun/hbl-cc-po).

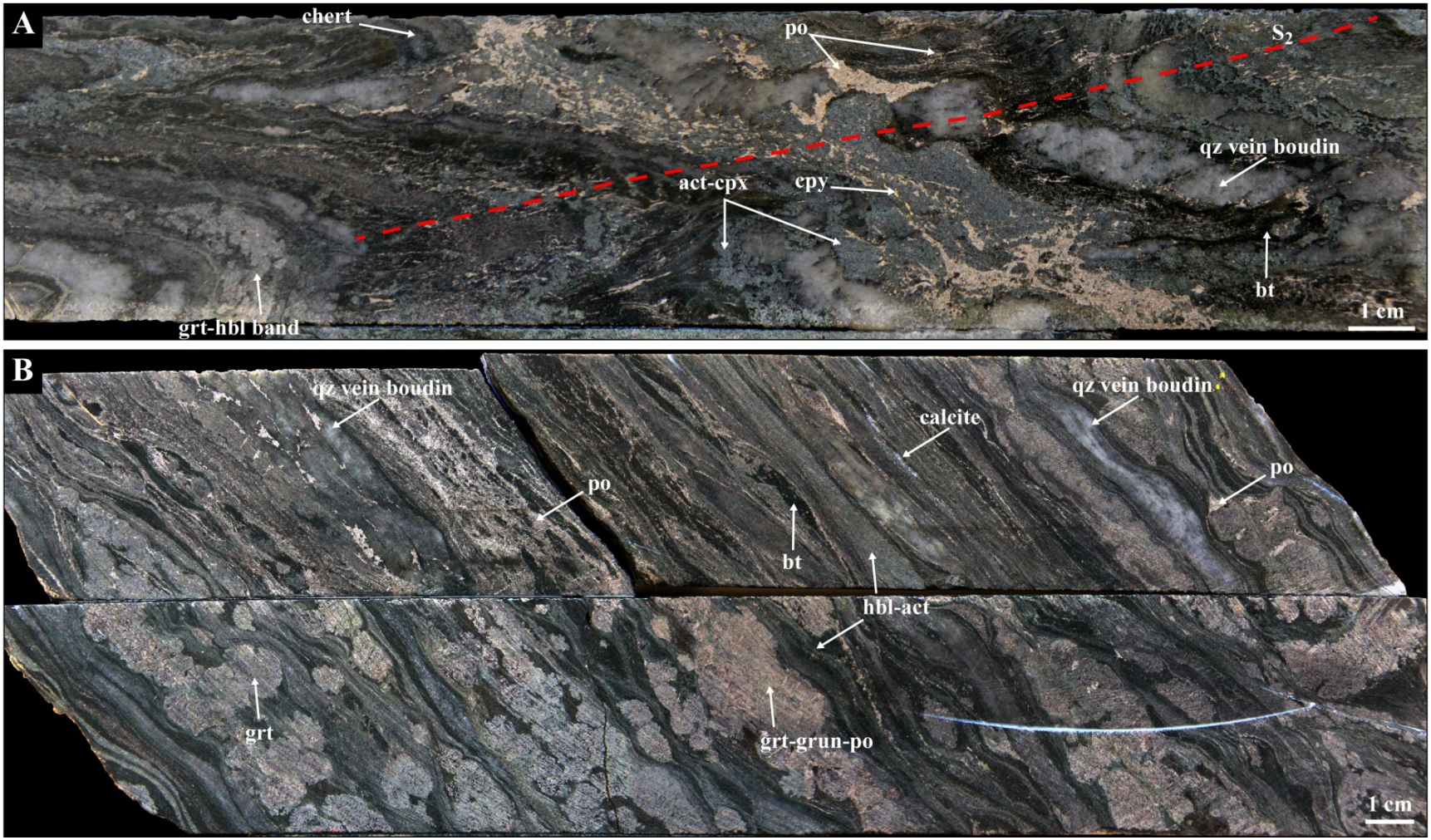

Figure 7-26: Gold-mineralized unit 4E. A. Drill core segment of gold-mineralized unit 4E, MW-12-217, DDH 06-PQE-013, 9 ppm Au. Gold mineralization is characterized by the development of the pyrrhotite-actinolite-biotite assemblage, where pyrrhotite is affected by the main fabric (axial planar S_2 foliation). The weakly deformed pyrrhotite-hedenbergite-actinolite assemblage suggests deformation and metamorphism of the gold-bearing rock. B. Drill core segment of gold-mineralized unit 4E, MW-13-364, DDH 12-PIL-002, 5.7 ppm Au, mine level 280, Esker area. The rock is strongly foliated, garnet-rich bands show evidence of boudinage, and pyrrhotite is locally distributed along foliation planes and pressure shadows.

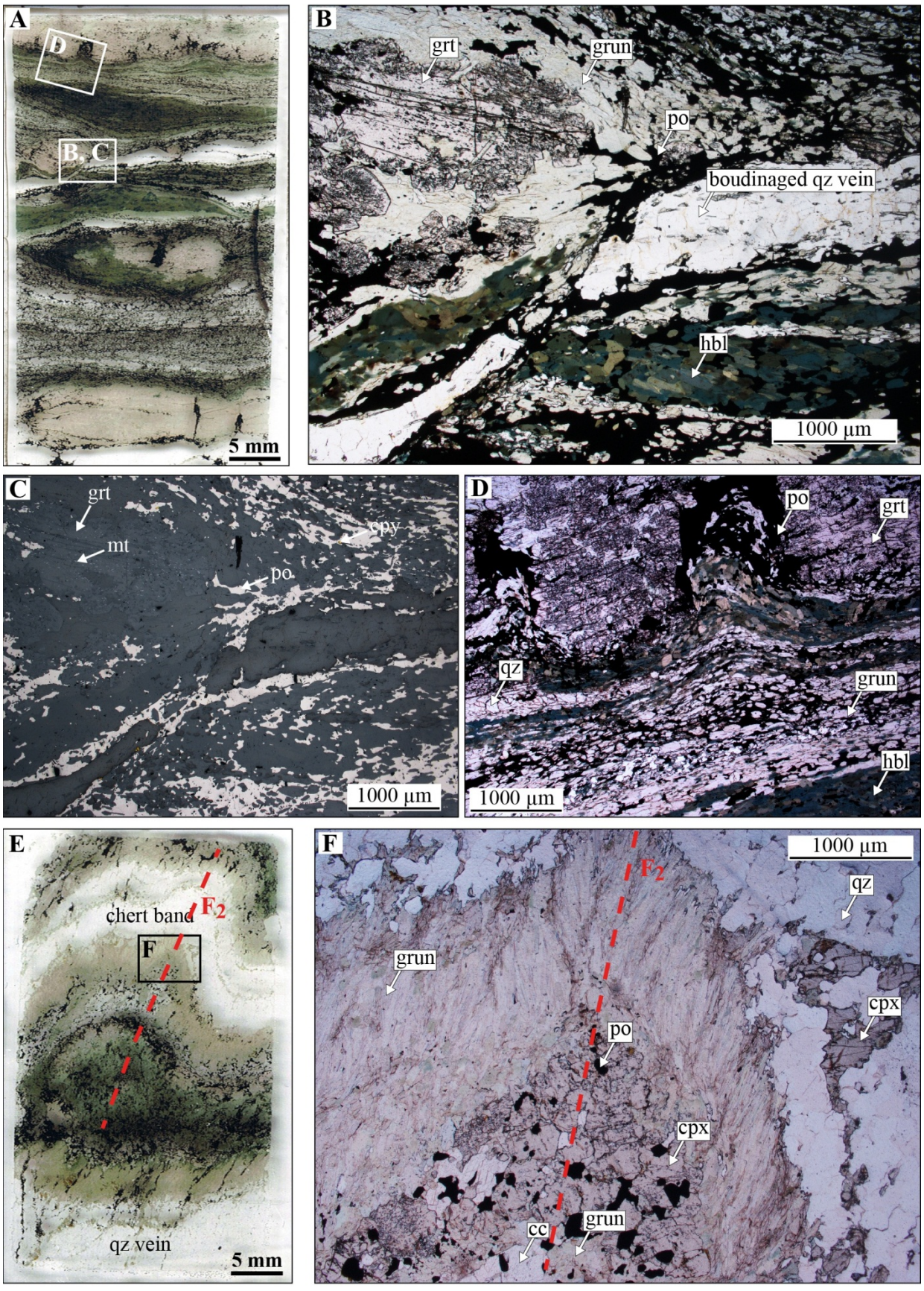
A
D
B, C
5 mm
B
grt
grun
po
boudinaged qz vein
hbl
1000 µm
C
grt
mt
cpy
po
1000 µm
D
po
grt
qz
grun
hbl
1000 µm
E
chert band
F2
F
qz vein
5 mm
F
1000 µm
F2
qz
grun
cpx
po
cpx
cc
grun

Figure 7-27: Mineral paragenesis of gold-mineralized unit 4E. A. Thin section scan of sample MW-13-364, DDH 12-PIL-001, 5.7 ppm Au. B. Microphotograph in plain polarized light of C. Same as B. in reflected light, showing the distribution of pyrrhotite. D. Microphotograph in plain polarized light of boudinaged garnet-grunerite band. Pyrrhotite and the adjacent hornblende-rich band accommodate the deformation. E. Thin section scan of sample MW-12-220, DDH 06-PQE-013, 22.7 ppm Au. F. Microphotograph in plain polarized light of a F_2 fold with axial planar grunerite, oriented parallel to S_2 foliation, gold-mineralized sample of unit 4E.

Gold-mineralized unit 4E (32 samples at 1 to 23.7 ppm Au) is mainly constituted of around 50 wt.% SiO_2, 9 wt.% Al_2O_3, and nearly 28 wt.% iron (with FeO/Fe_2O_3 ratio of 5; Figure 7-28; Table 7-4). CaO is the most abundant of minor oxides (5.74 wt.% median value), MgO makes up 3.71 wt.%, total S 2.61 wt.% and CO_2 0.63 wt.%. Other oxides are all under 0.5 wt.% median value abundance. Some samples have up to 2 wt.% K_2O. Principal component analysis of CLR major elements data from unit 4E (Figure 7-29) shows a positive correlation between Au and CaO, CO_2, and total S contents. SiO_2, MgO, MnO, P_2O_5, and FeO are also positively correlated, reflecting their association in the composition of amphiboles. Al_2O_3, TiO_2, and K_2O are positively correlated, and Na_2O has a distinct, isolated position.

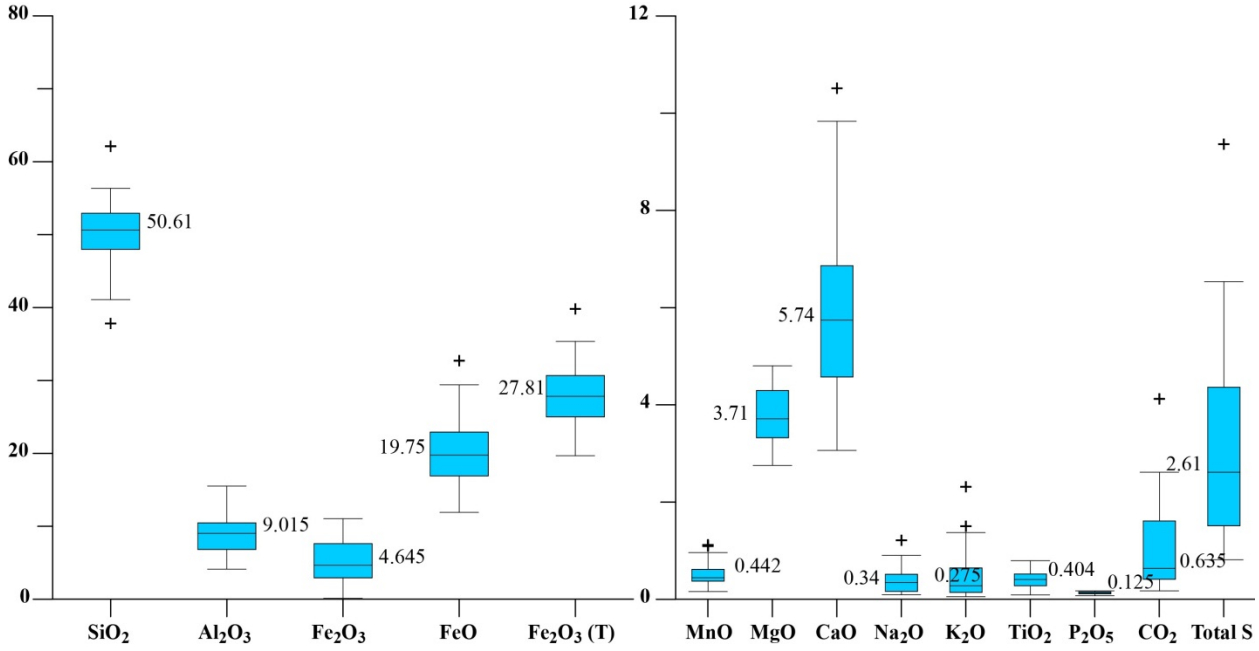

Figure 7-28: Major element whole-rock composition for samples with over 1 ppm Au of unit 4E (n = 32). Box = first to third quartile, black line = median, whiskers = interquartile range (IQR)*1.5, black cross = outliers (Upton and Cook, 1996).

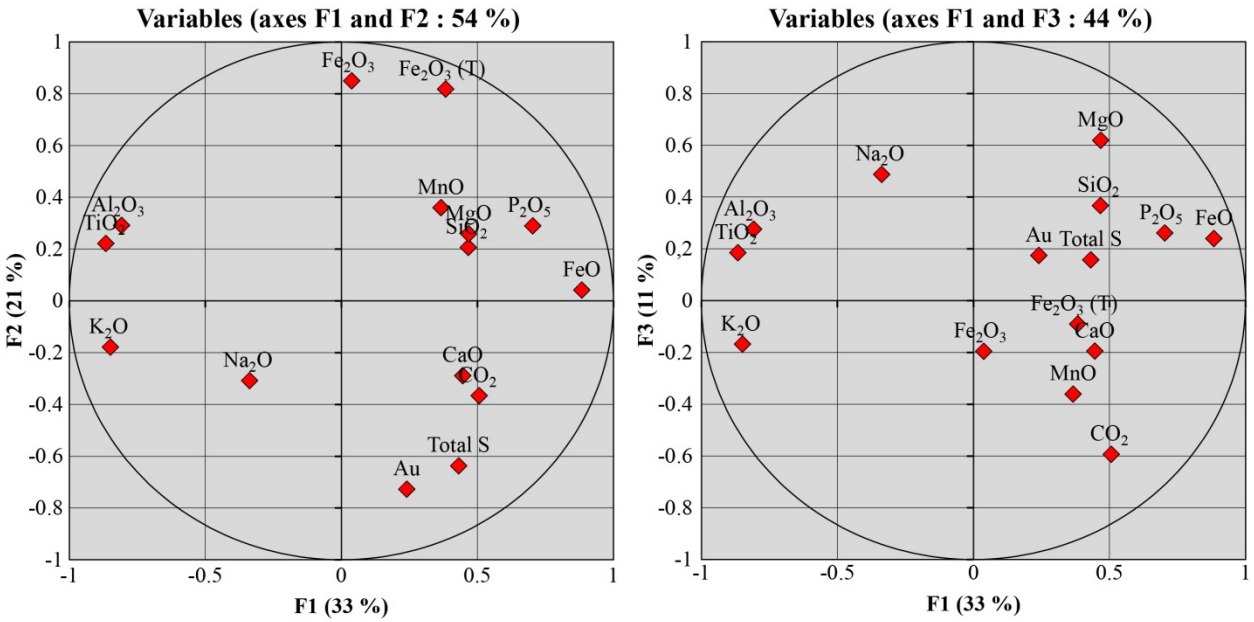

Figure 7-29: F1-F2 and F1-F3 projections of PCA on CLR data, major elements, unit 4E samples with over 1 ppm Au. The projections explain 58 and 48%, respectively, of data variation.

7.3.3 Unit 4A

In the NIF, no notable gold mineralization is present in the chert-grunerite BIF unit (unit 4A), which forms a discontinuous horizon of lenses between unit 4B and the "Basement basalts". Gold-mineralized unit 4A occurs in a tight Z-fold structure of the SIF sequence along the east limb of the East Bay synform. Gold mineralization is characterized by the replacement of grunerite and subordinate amphiboles by pyrrhotite (Figure 7-30). There is a strong disruption of the initial compositional layering and some quartz veining.

Typical mineralogy, besides quartz from chert and/or silica flooding, consists in coarse, pale green, subhedral hedenbergite intergrown with a mixture of fine- to medium-grained, beige grunerite, green hornblende, and actinolite (Figures 7-30; 7-31A, B). Pyrrhotite is found in and around this mineral assemblage, as well as intergrown with a fine-grained assemblage of calcite and grunerite (Figure 7-31B, C). Gold occurs as round grains associated with pyrrhotite and chalcopyrite (Figure 7-31D, E), as inclusions in hedenbergite or adjacent to it, in association with grunerite and calcite (Figure 7-31F, G).

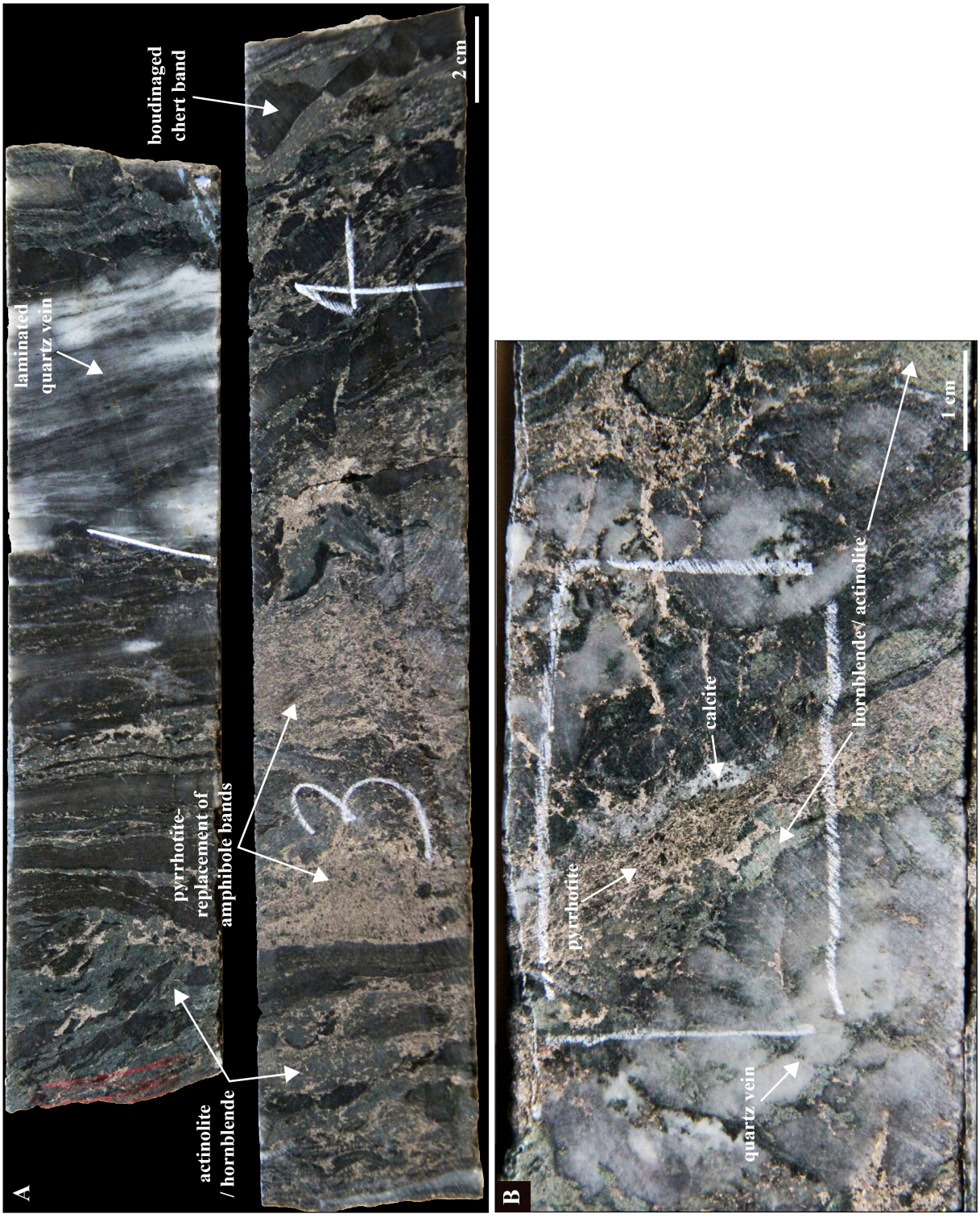

Figure 7-30: Gold-mineralized samples of unit 4A. A. 20 ppm gold, sample MW-13-305, DDH 08-THE-001, showing quartz veining associated with disrupted compositional layering and strong pyrrhotite-replacement of amphibole-rich bands. B. 9.3 ppm gold, sample MW-13-319, DDH 08-THE-004, showing the typical assemblage of deformed quartz vein or recrystallized chert layers and interstitial actinolite-hornblende-pyrrhotite-calcite assemblage.

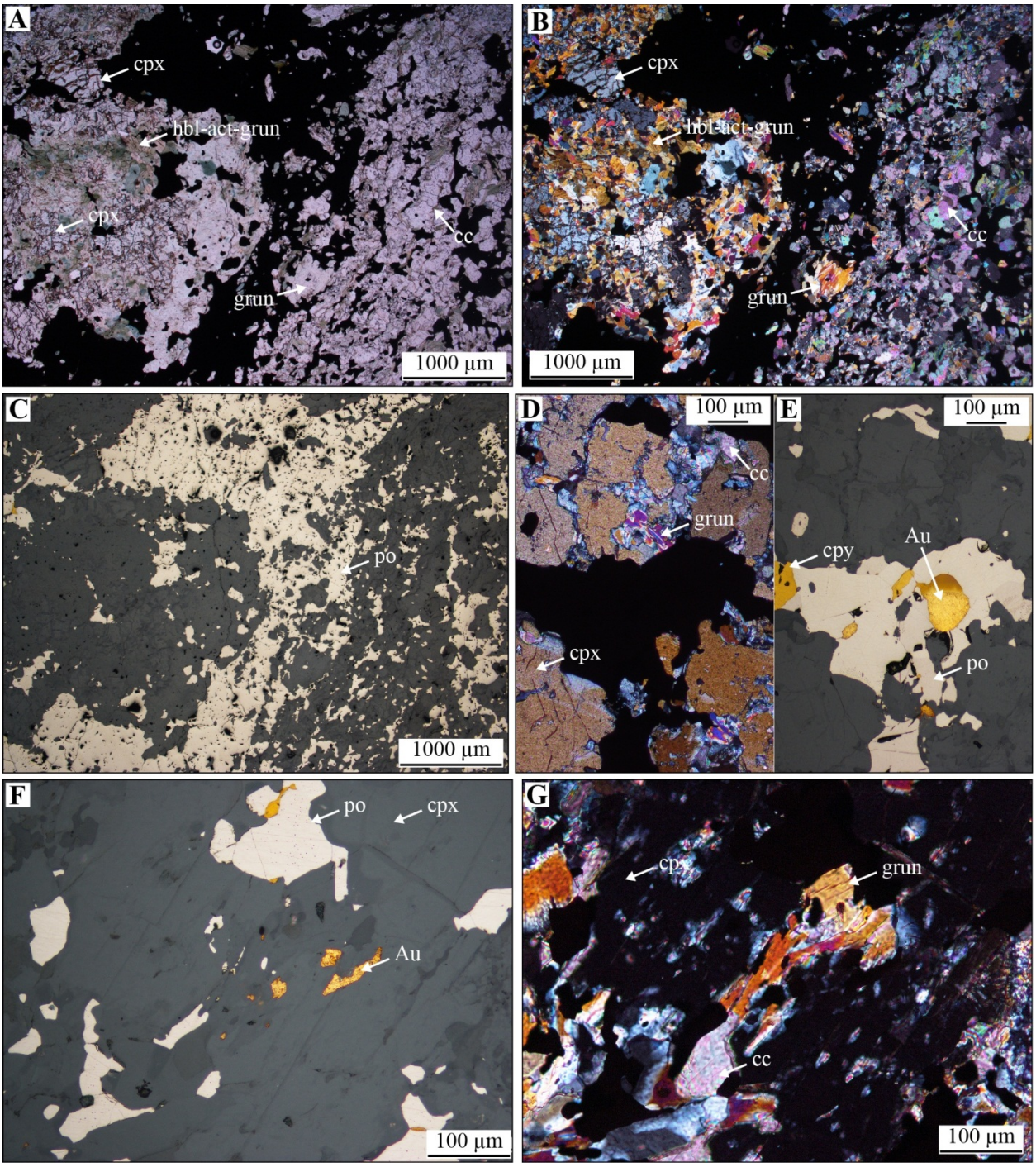

Figure 7-31: Mineral paragenesis of gold-bearing 4A. A. Microphotograph in plain polarized light of grunerite-hornblende-actinolite-hedenbergite assemblage and grunerite-calcite assemblage intergrown with pyrrhotite, sample MW-13-319, DDH 08-THE-004, 9.3 ppm Au. B. Same as A. in cross-polarized light. C. Same as A. and B. in reflected light. Pyrrhotite is the dominant sulphide phase. D. and E. Microphotographs in cross-polarized and reflected light of gold associated with pyrrhotite and chalcopyrite between hedenbergite crystals and minor calcite and grunerite, sample MW-13-365, DDH 10-RDW-005, 46.7 ppm Au. F. and G. Microphotograph in reflected light and cross-polarized light showing gold and pyrrhotite-chalcopyrite intergrown with grunerite, hedenbergite (cpx), and calcite. Sample MW-13-365, DDH 10-RDW-005, 46.7 ppm Au.

Geochemical data of gold-bearing unit 4A (27 samples at 1 to 46.7 ppm Au) reveals higher SiO_2 content than other units with median value of 70 wt.% (Figure 7-32; Table 7-4). Aluminum content is extremely low, which is consistent with the observed predominance of grunerite and actinolite over hornblende and tschermakite. Most of the iron content is FeO, with few occurrences of elevated Fe_2O_3, related to the presence of magnetite. MgO constitutes around 1.69 wt.% (median value), up to 4 wt.% of the rock. CaO, CO_2, and total S have median abundance of 5.80 wt.%, 2.37 wt.%, and 4.68 wt.%, respectively. CaO can reach 18 wt.%, CO_2 10 wt.%, and total S 24 wt.% in the most pyrrhotite-rich samples. PCA processing of CLR major element data (Figure 7-33) shows a positive correlation of gold with sulphur, CO_2, and CaO contents. K_2O is tightly associated with Al_2O_3 and TiO_2 and negatively correlated with Au, suggesting K_2O content variations are due to primary detrital input.

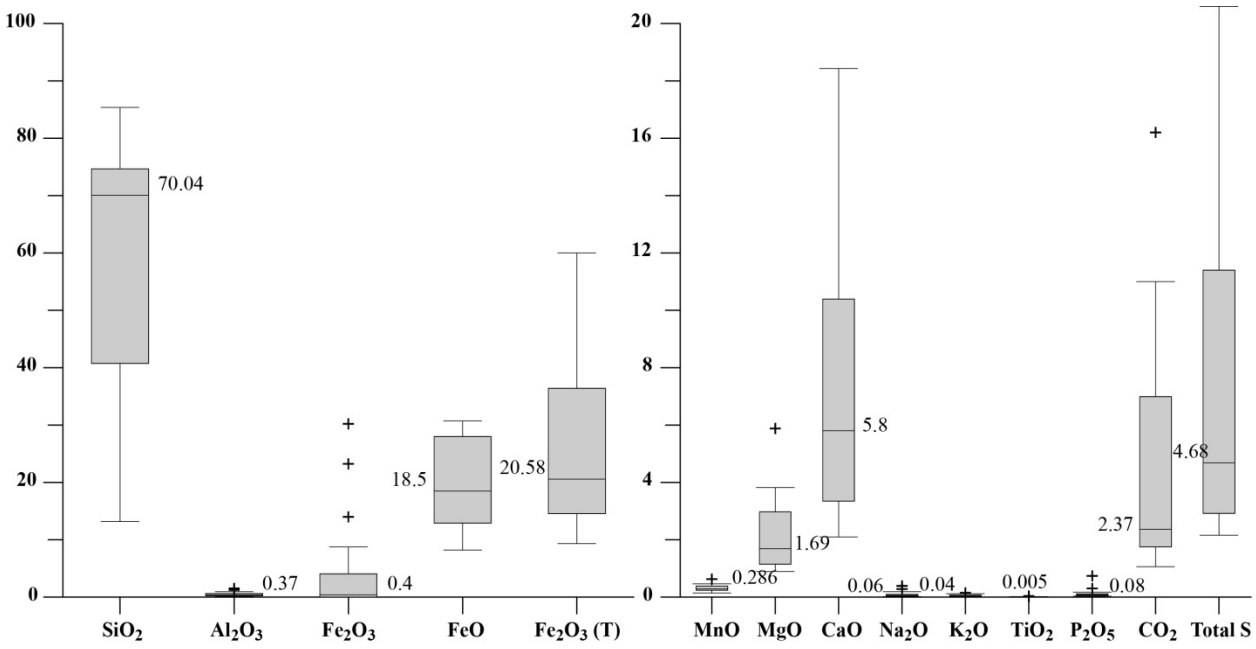

Figure 7-32: Major element whole-rock composition for samples with over 1 ppm Au of unit 4A (n = 27). Box = first to third quartile, black line = median, whiskers = interquartile range (IQR)*1.5, black cross = outliers (Upton and Cook, 1996).

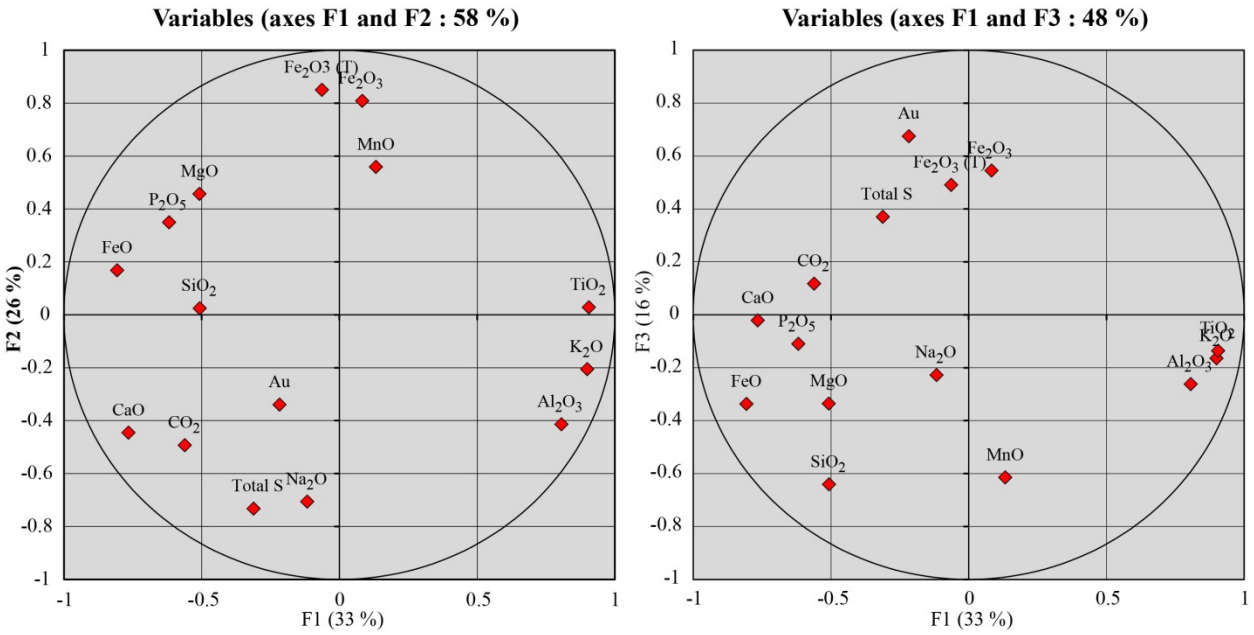

Figure 7-33: F1-F2 and F1-F3 projections of PCA on CLR data, major elements, unit 4A samples with over 1 ppm Au (n = 27). The projections explain 58 and 48%, respectively, of data variation.

7.3.4 Clastic 4B and typical 4B mineralized rocks

Gold mineralization in the clastic-rich (4Bc) and typical oxide BIF (4B) units is characterized by pyrrhotite-replacement of magnetite bands along quartz vein selvages (Figure 7-34). Veins are folded and, locally, transposed sub-parallel to the S_2 foliation (Figures 5-25, 7-34B). Any trace of clear pyrrhotite-replacement front usually encountered in BIF (Figure 1-16) has been obliterated.

Microscopic petrography of strongly mineralized samples of clastic 4B (Figures 7-35, 7-36) shows that silicate-rich bands comprise a fine-grained matrix of grunerite-biotite-hornblende with pyrrhotite replacing magnetite (Figure 7-36C). Magnetite is preserved where included in poikilitic, pink, medium-grained, subhedral garnet porphyroblasts (Figure 7-36B, C). Two garnet phases are clearly distinguished: poikilitic, magnetite-rich, and inclusion-free garnet. Some garnet porphyroblasts are elongated parallel to S_2 and comprise an S-shape internal fabric, which is in continuity, and therefore correlate, with the external S_2 fabric (Figure 7-36C), indicating syn-D_2 crystallization. Inclusion-free garnet occurs in the necks of boudinaged poikilitic garnet aggregates (Figure 7-36A) indicating a younger and syn-D_2 crystallization. In the vicinity of quartz veins, the silicate matrix locally includes an assemblage of hedenbergite-grunerite ± hornblende-actinolite (Figure 7-36D).

In mineralized 4B, the chert-magnetite layering is replaced by a fine-grained greyish calcite, beige grunerite, and green hornblende (Figure 7-37A, B, C), and comprises medium- to coarse-grained, pale

green hedenbergite and pink, subhedral, inclusion-poor to inclusion-free garnet porphyroblasts, similar to that of the clastic 4B. Quartz veins in “classic” chert-magnetite 4B unit are commonly short, a few centimetres-thick; there is a sharp transition from poorly to strongly mineralized 4B (i.e., from F_2 fold hinge to transposed high strain zone; Figure 7-37A), similar to facies 4Bc (Figure 7-34C). The typical pyrrhotite-chalcopyrite assemblage (Figure 7-37D) locally includes magnetite. Gold is found in association with pyrrhotite and chalcopyrite, as well as adjacent to garnet and grunerite. In strongly mineralized zones, quartz surrounded by grunerite (Figure 7-37E) appear to be remnants from the reaction quartz + magnetite + water = grunerite, where magnetite was a limiting reactant, as seen in 0. Magnetite is also the primary source of iron for the precipitation of pyrrhotite.

Whole-rock geochemical data for major elements shows that both facies of unit 4B (4Bc, 20 samples at 1 to 52 ppm Au; and 4B, 32 samples at 1 to 45 ppm Au; Figure 7-38; Table 7-4) have slightly less than 50 wt.% SiO_2 (48.6 and 47.1, respectively), which is similar to other BIF units (Figures 7-18, 7-28). Consistent with its clastic-rich character, 4Bc has a higher Al_2O_3 content than typical 4B (5.5 wt.% median value vs. 3.8, respectively), which may explain the absence of the magnetite-rich garnet phase in typical 4B. Total iron content is similar in 4Bc and 4B, with a FeO/Fe_2O_3 ratio of 2. MgO and CaO contents are within the same 2-3-wt.% range. CO_2 and total S contents are the most variable: While having median values of 2.5 and 1.6 wt.% in 4Bc and 4B, respectively, sulphur content has standard deviations of 2.6 and 4.0 and can reach 10 wt.%.

PCA processing of major element data of unit 4B shows similar results than other facies (Figure 7-39): Gold is positively correlated, but to a lesser degree, with total S, as well as CO_2 and CaO. The strong link between CaO and CO_2 is consistent with the presence of calcite. On the F1-F2 projection, with the exception of K_2O, TiO_2, and Al_2O_3, all other major oxides are well correlated. This is consistent with the presence of Fe- and Mg-bearing amphiboles. On the F1-F3 projection, the proximity of SiO_2 with total S and gold attests of the link between quartz veins and gold mineralization, which is not the case for other BIF facies.

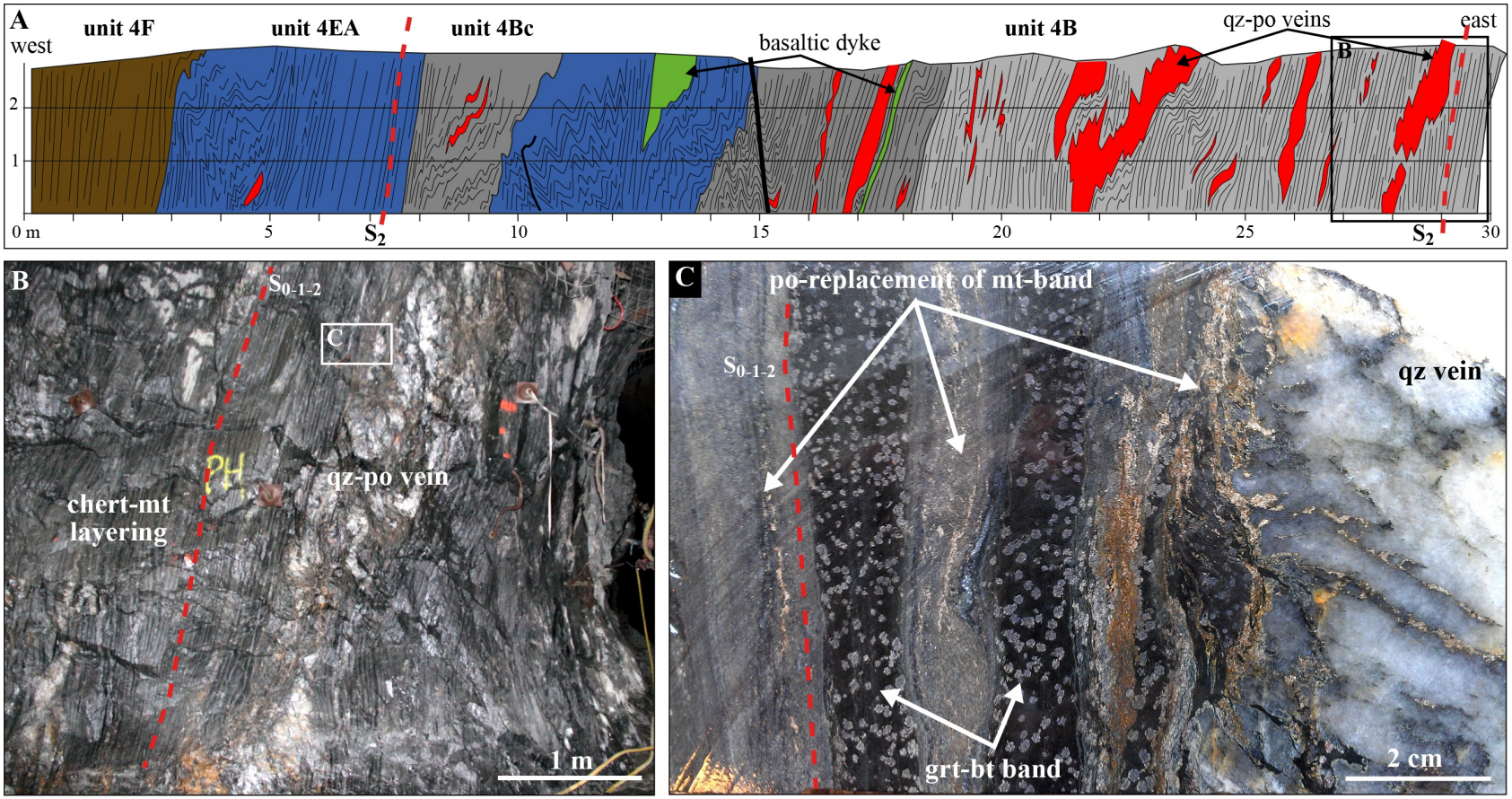

Figure 7-34: Gold-mineralized clastic 4B unit. A. Geological face map facing north on 12025 section, mine level 870. This section is located near the upper termination of the C-block ore zone. Gold mineralization is associated with thick quartz veins and pyrrhotite-replacement in the surrounding magnetite band. B. Photography of auriferous quartz-pyrrhotite vein in unit 4B. C. Close up photography of pyrrhotite-replacement of magnetite bands near a quartz vein. Clastic-rich bands are marked by biotite alteration.

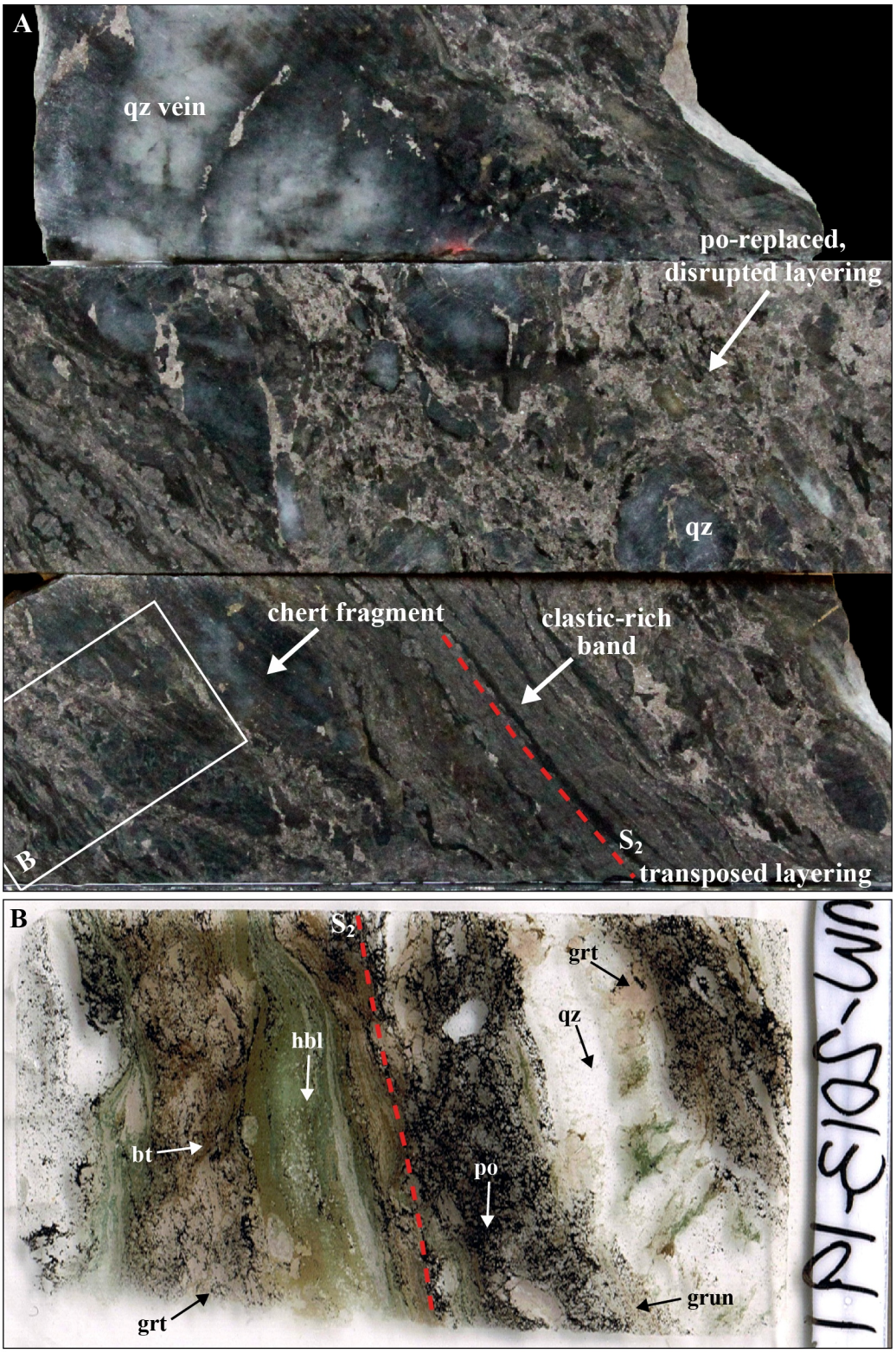

Figure 7-35: Gold-mineralized clastic-rich unit 4B. A. Drill core segment at 38 ppm gold, MW-13-191, DDH 11-LNX-126. B. Thin section scan of sample MW-13-191, DDH 11-LNX-126, 22.3 ppm Au. It shows a quartz vein with proximal garnet-hornblende-grunerite assemblage, pyrrhotite concentrated in its vicinity and garnet intergrown with hornblende and biotite away from the vein.

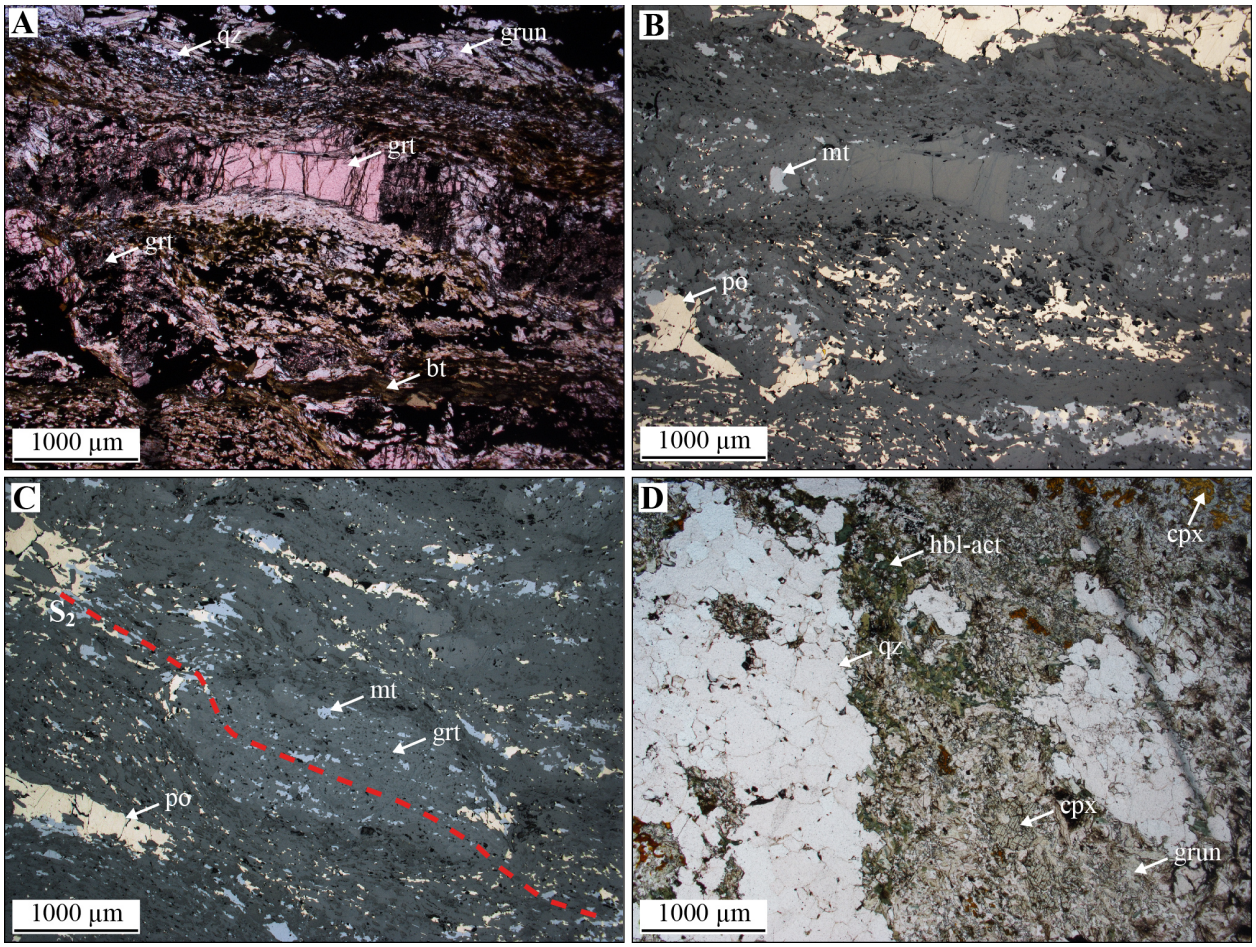

Figure 7-36: Mineral paragenesis of gold-bearing 4Bc. A. Microphotograph in plain polarized light of gold-mineralized unit 4B, MW-13-022, DDH 09-TAN-029, 17.7 ppm Au. B. Microphotograph at the same location as A. in reflected light, showing pyrrhotite replacing magnetite in the matrix. Magnetite included in garnet is preserved. C. Microphotograph in reflected light, sample MW-13-022, showing pyrrhotite replacing magnetite in the matrix. Garnet grains are elongated sub-parallel to S_2 and show an internal fabric defined by magnetite inclusions, continuous with the external fabric (garnet growth is syn-D_2). D. Microphotograph in plain polarized light showing the amphibole (grun, hbl, act)-pyroxene (cpx) assemblage proximal to quartz veins in gold-bearing unit 4B.

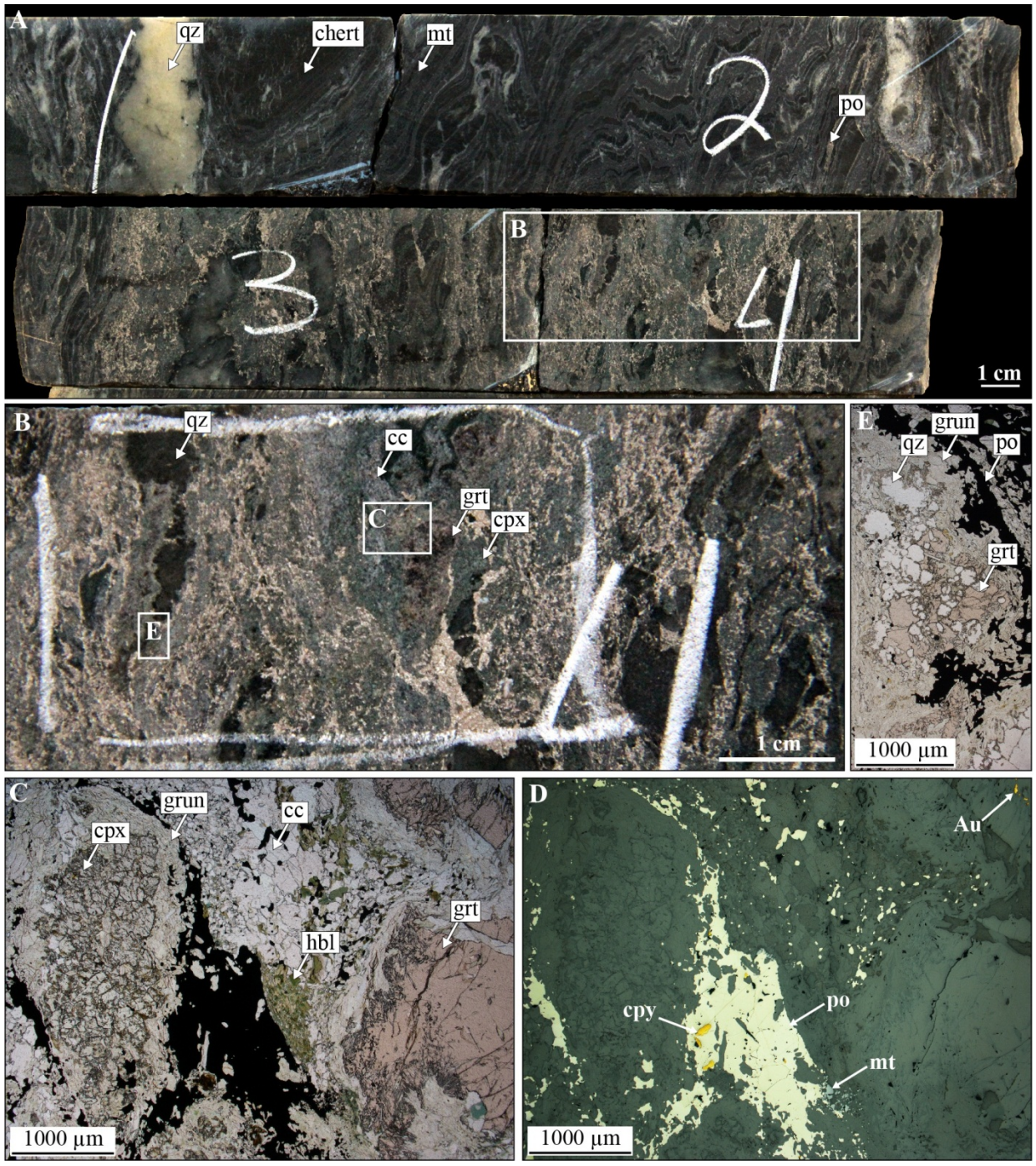

Figure 7-37: Petrography of gold-mineralized unit 4B. A. Drill core segment of unit 4B sample MW-13-311, DDH 08-THE-001, 14.2 ppm Au. It shows the sharp transition between altered 4B and strongly pyrrhotite-replaced 4B in the vicinity of quartz veins. B. Close-up photograph of pyrrhotite-rich 4B, including dark red, almandine garnet (grt), grey calcite (cc), pale green hedenbergite (cpx), and matrix amphiboles, as seen in: C. Microphotograph in plain polarized light of the garnet-hedenbergite-grunerite-hornblende-calcite assemblage associated with pyrrhotite. D. Microphotograph in reflected light showing the pyrrhotite-chalcopyrite±magnetite assemblage in gold-mineralized samples. Gold inclusions are present in association with grunerite and inclusion-free, syn-D_2 garnet. E. Microphotograph in plain polarized light of the grt-grun assemblage apparently replacing quartz.

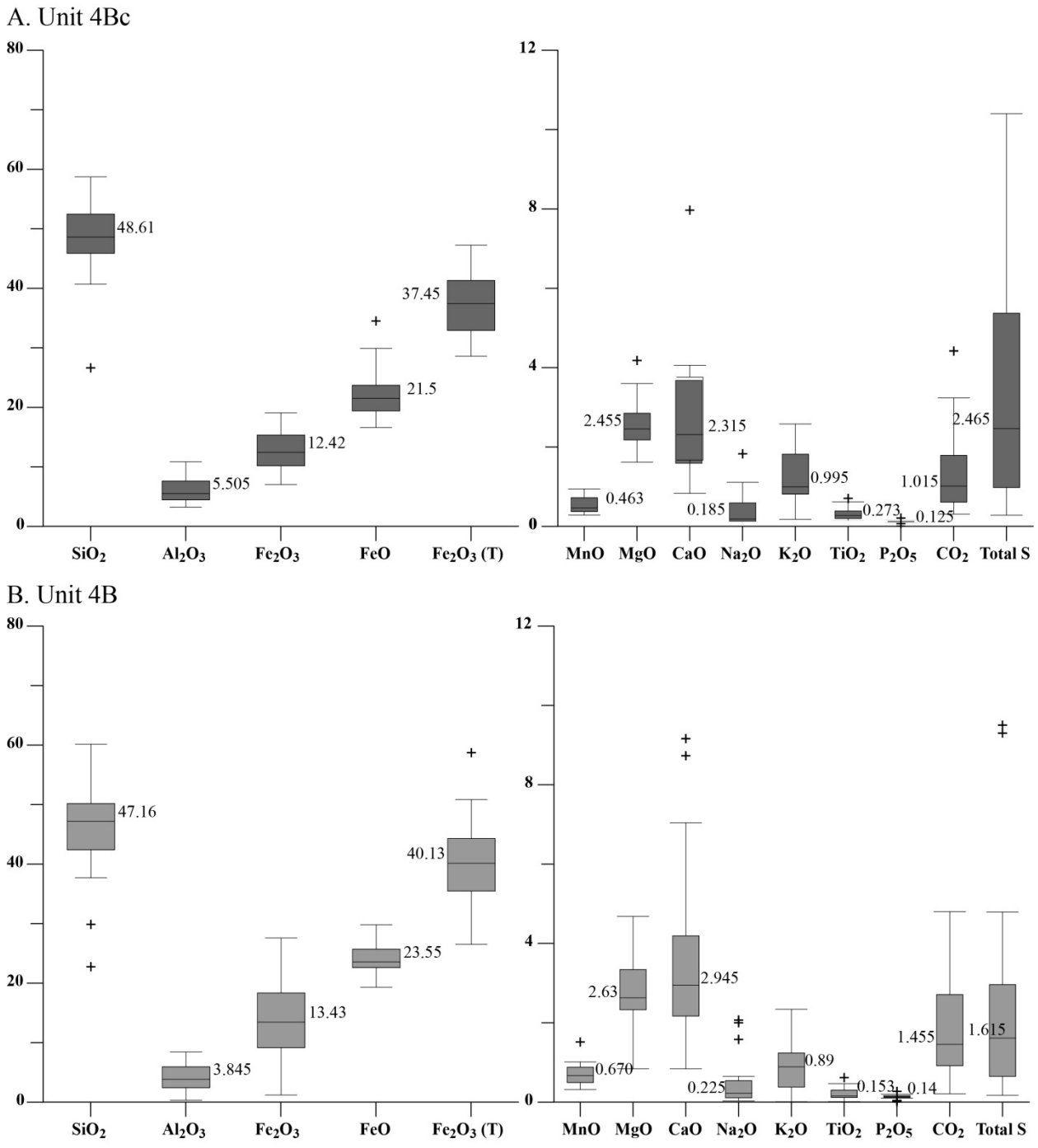

Figure 7-38: Major element whole-rock composition for samples with over 1 ppm Au of A. unit 4Bc and B. unit 4B. Box = first to third quartile, black line = median, whiskers = interquartile range (IQR)*1.5, black cross = outliers (Upton and Cook, 1996).

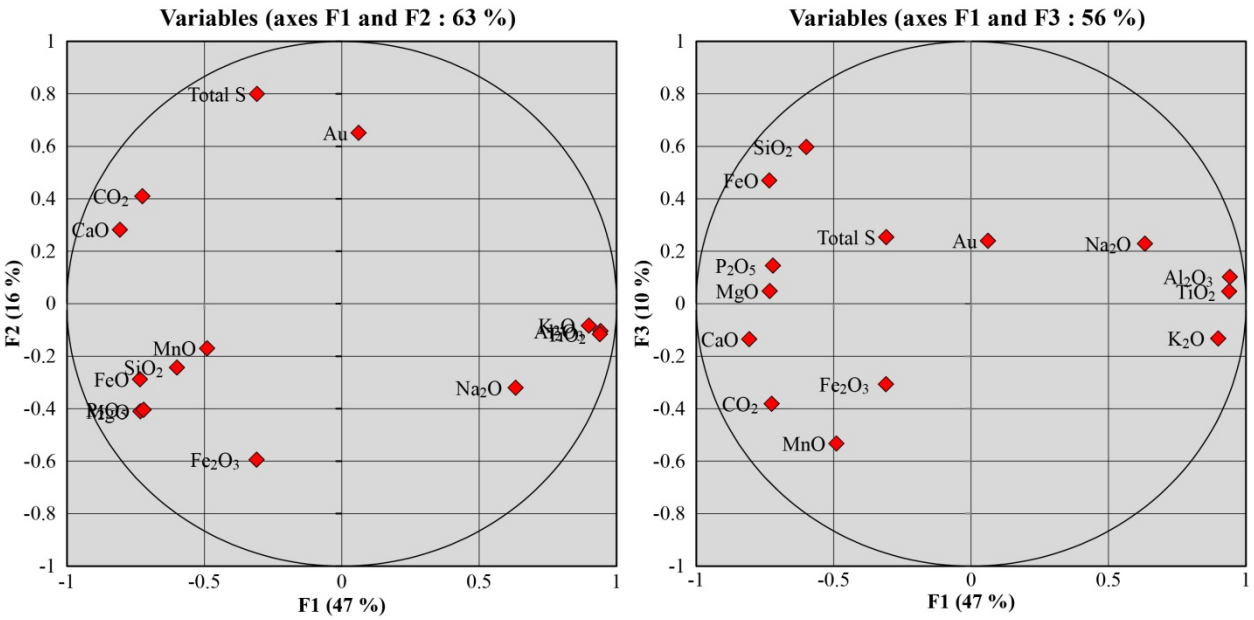

Figure 7-39: F1-F2 and F1-F3 projections of PCA on CLR data, major elements, all oxide-dominant BIF samples. The projections explain 63 and 56%, respectively, of data variation.

7.4 Main quartz-vein mineralization style

Although quartz veins associated with pyrrhotite-replacement ore are documented in other BIF facies, the mineralization style predominantly characterized by quartz veins mainly occur in pelitic rocks (garnet-biotite schist, unit 4F; Figure 7-40) and mafic volcanic rocks (unit Bvol; section 7.5). Before the discovery of abundant gold mineralization hosted by unit 4F in the West limb area (WEL; Figure 7-1), 4F-type ore mostly came from gold-bearing portions of the unit adjacent to 4EA-type ore (e.g., Lynx zone). There are two types of gold mineralization in unit 4F.

In type 1, tightly-folded quartz-pyrrhotite veins are hosted by a garnet-biotite schist that displays fine- to medium-grained purplish garnet porphyroblasts with no evidence of grain coarsening in the vicinity of veins (Figures 7-40A, B; 7-41A; 7-42A). The brown to dark brown biotite-feldspar-quartz matrix is strongly foliated and pyrrhotite is preferentially distributed along foliation planes and in low-pressure zones, such as garnet porphyroblast pressure shadows (Figure 7-41A, B, C, D). Fine-grained, euhedral, brown biotite is also concentrated in garnet pressure shadows as well as near veins. Garnet porphyroblasts display an internal zonation with a poikilitic core and inclusion-free rim (Figure 7-41D). The former includes quartz, magnetite, ilmenite, and pyrrhotite inclusions that form an internal fabric (Figure 7-41E, F). The latter appears to grow over the foliated, biotite-rich matrix and locally includes anhedral pyrrhotite-chalcopyrite.

Type 2 is distinguished by a proximal alteration halo near quartz-pyrrhotite veins that is composed of fine-grained subhedral green hornblende, medium-grained anhedral hedenbergite, traces of calcite and grunerite, and local green biotite (Figures 7-40C; 7-42D, E, F). Calcite is also found as elongated aggregates in the biotite-feldspar-quartz matrix. In some portions of type 2, gold-mineralized unit 4F, coarse, euhedral garnet porphyroblasts are documented in a matrix of fine-grained brown biotite and green chlorite (Figure 7-43A). Garnet porphyroblasts appear to preserve pyrrhotite as inclusions or in pressure shadows (Figure 7-43B, C, D). Biotite and chlorite appear to form a stable assemblage with a gradational transition from biotite to chlorite; the latter including homogeneously distributed oxides (magnetite and ilmenite).

Gold-mineralized garnet-biotite schist comprises around 50 wt.% SiO_2, which is similar to BIF units 4EA, 4E, and 4B (35 samples at 1 to 36.9 ppm Au; Figure 7-44; Table 7-4). Al_2O_3 constitutes 16 ± 4 wt.% and iron oxides around 20 wt.% (FeO/Fe_2O_3 ratio of 5). Other oxides include: 3 wt.% K_2O, 3 wt.% MgO, and 2.6 wt.% CaO. Total S content has a median value of 1.28 wt.% but is strongly variable. MnO content median value is close to 0.5 wt.%, as other BIF units, while P_2O_5 and CO_2 are almost absent, except for a few outliers with up to 1 wt.% CO_2.

Principal component analysis of CLR major element data shows that total S, CaO, and CO_2 are positively correlated with gold content (Figure 7-45), which also explains their greater variability (Figure 7-44). This is consistent with petrographic observations of carbonates and sulphides associated with gold mineralization (Figure 7-40). MnO and Na_2O are fairly isolated on both PCA projections, suggesting their content is probably influenced by specific factors: MnO could be concentrated in garnet cores and thus isolated from subsequent remobilization events; Na_2O could be related to a separate alteration event. MgO correlated with FeO, which is consistent with the importance of biotite (annite-phlogopite series) in the mineral assemblage.

Figure 7-40: Gold-mineralized samples of garnet-biotite schist (unit 4F). A. Drill core segment of type 1 4F, sample MW-14-014, DDH 14-WEL-006, 38.5 ppm Au. Besides the presence of quartz veins and pyrrhotite, this auriferous 4F is very similar to barren 4F. B. Drill core segment of type 1 4F, DDH 14-WEL-005, 6.4 ppm Au. C. Drill core segment of type 2 4F, DDH 14-WEL-005, 39.5 ppm Au, showing the hornblende-actinolite±hedenbergite mineral assemblage locally associated with auriferous quartz-pyrrhotite veins.

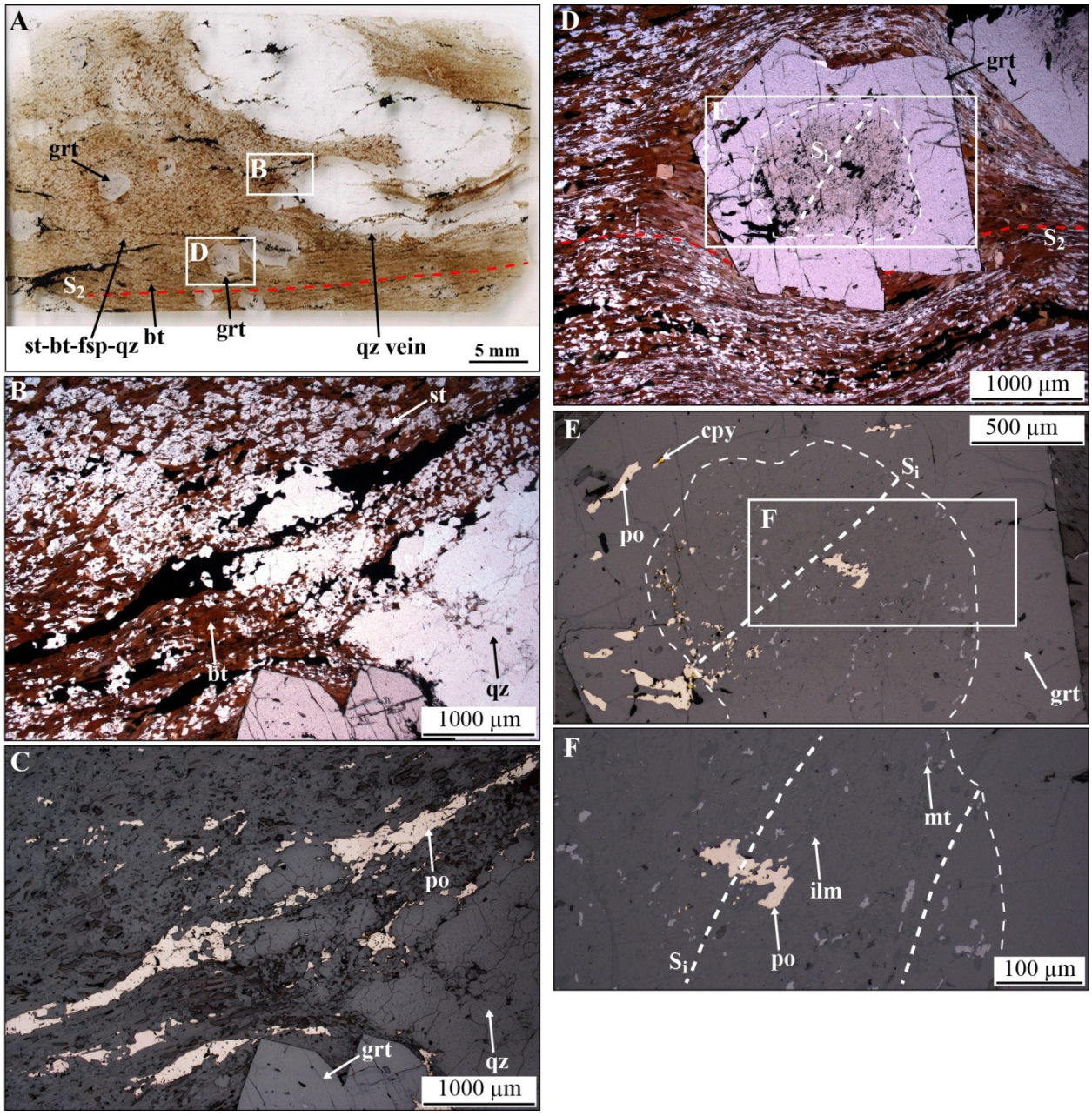

Figure 7-41: Mineral paragenesis of gold-mineralized 4F, sample MW-14-014, DDH 14-WEL-006, 38 ppm Au. A. Thin section scan of the sample. It shows a folded quartz vein in a biotite-feldspar-quartz-staurolite assemblage, which shows a more penetrative S_2 in its bottom portion. B. and C. Microphotographs in plain polarized and reflected light, respectively, showing garnet porphyroblasts in a biotite-feldspar-quartz-staurolite matrix with pyrrhotite in the vicinity of a quartz vein. D. Microphotograph in plain polarized light of a zoned garnet porphyroblast. The inclusion-free rim overgrows the external fabric, indicating a late- to post-D_2 kinematic growth. E. and F. Close-ups of microphotographs in reflected light of pyrrhotite, magnetite, and ilmenite inclusions in the core of a garnet porphyroblast and the inclusion-free rim.

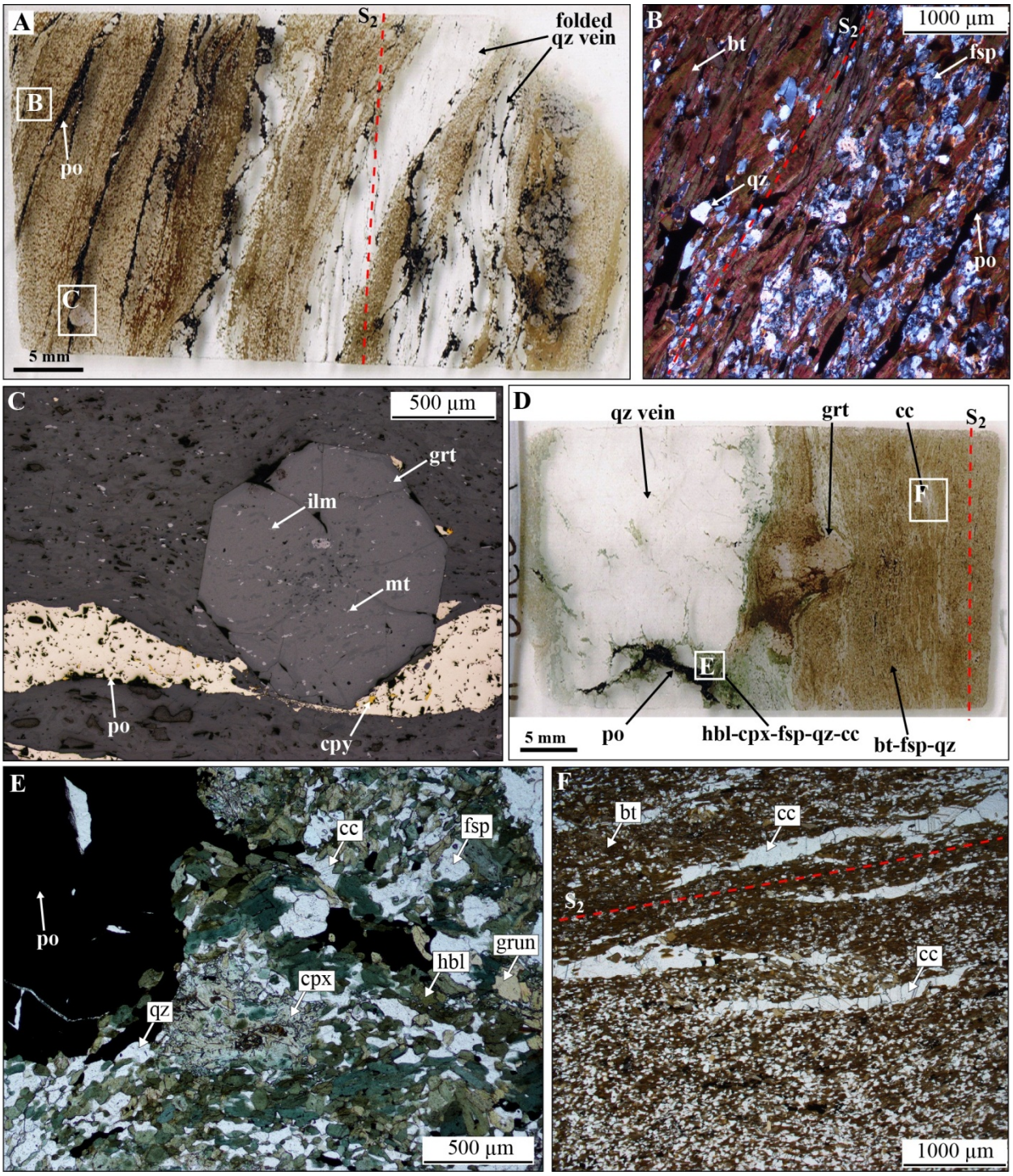

Figure 7-42: Petrography of gold-mineralized unit 4F. A. Thin section scan of gold-mineralized sample MW-14-003, DDH 14-WEL-002, 8 ppm Au. Tightly-folded quartz veins are similar to those of unit 4B. Pyrrhotite is preferentially distributed along foliation planes and in low-pressure zones, such as boudinaged quartz vein necks. B. Microphotograph in cross-polarized light of the biotite-feldspar-quartz-pyrrhotite matrix in sample MW-14-003. C. Microphotograph in reflected light of garnet porphyroblasts with magnetite and ilmenite inclusions. D. Thin section scan of gold-mineralized sample MW-12-165, DDH 06-PQE-095, 6.6 ppm Au. It shows a quartz-pyrrhotite vein with proximal hornblende alteration halo. E. Microphotograph in plain polarized light showing the hedenbergite (cpx)-hornblende (hbl)-feldspar (fsp)-quartz (qz)-calcite (cc)

assemblage proximal to the quartz-pyrrhotite vein. F. Microphotograph in plain polarized light of calcite aggregates in the bt-fsp-qz matrix, which may be remnants of strained and folded carbonate veins.

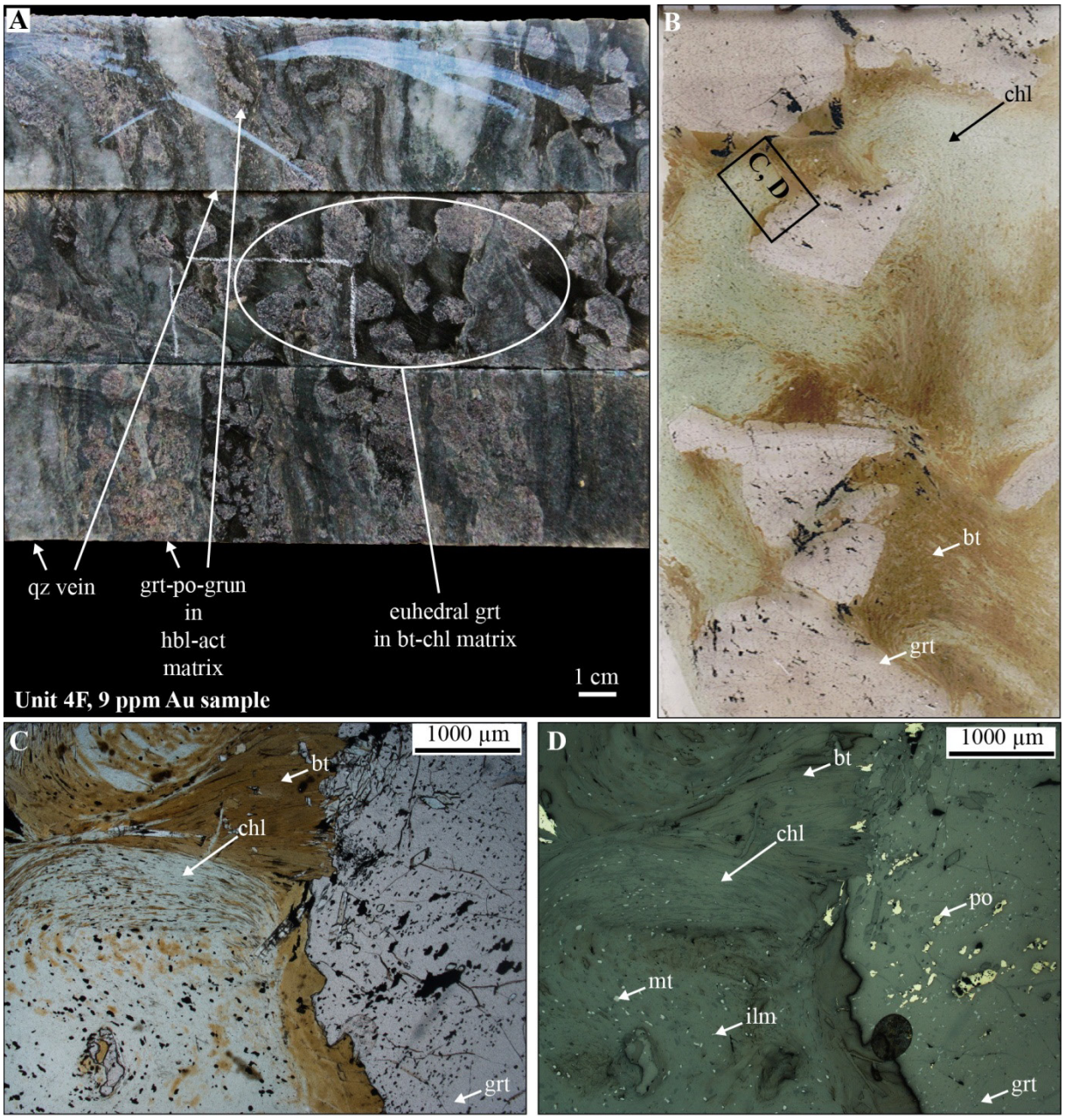

Figure 7-43: Garnet-biotite-chlorite assemblage in auriferous unit 4F. A. Drill core segment of unit 4F sample MW-13-116, DDH 09-TAN-060, 9.1 ppm Au. This sample includes two segments with intense quartz veining in a garnet-pyrrhotite-hornblende-hedenbergite assemblage (top and bottom core), separated by central portion with coarse, euhedral garnet in a chlorite-biotite matrix with minor quartz vein fragments. B. Thin section scan of sample MW-13-116, showing the transition between brown biotite and pale green chlorite with coarse, euhedral, pink garnets. The fabric in the bt-chl matrix wraps around garnet porphyroblasts. Opaque minerals are mainly present as inclusions in garnet and in their pressure shadows. C. and D. Microphotographs in plain polarized and reflected light of garnet porphyroblasts with pyrrhotite, magnetite, and ilmenite inclusions, adjacent to brown biotite. The transition from biotite to chlorite is gradational. Chlorite contains homogeneously distributed magnetite and ilmenite grains.

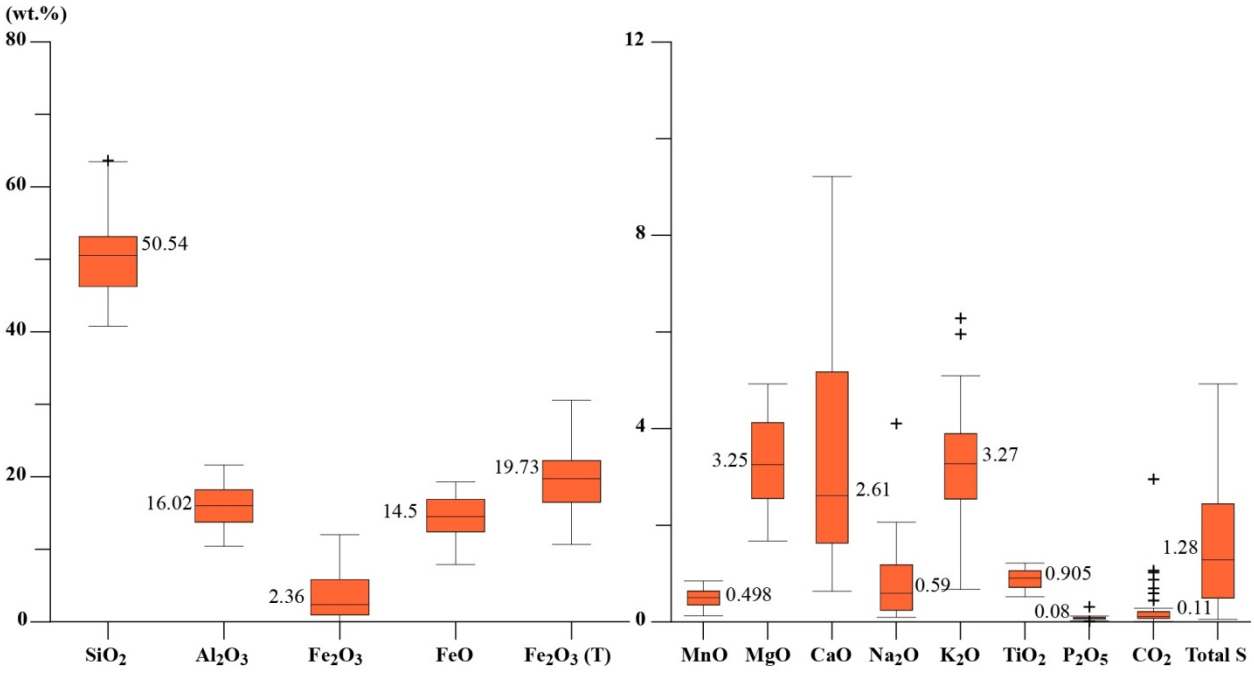

Figure 7-44: Major element whole-rock composition for samples with over 1 ppm Au of unit 4F (n = 35). Box = first to third quartile, black line = median, whiskers = interquartile range (IQR)*1.5, black cross = outliers (Upton and Cook, 1996).

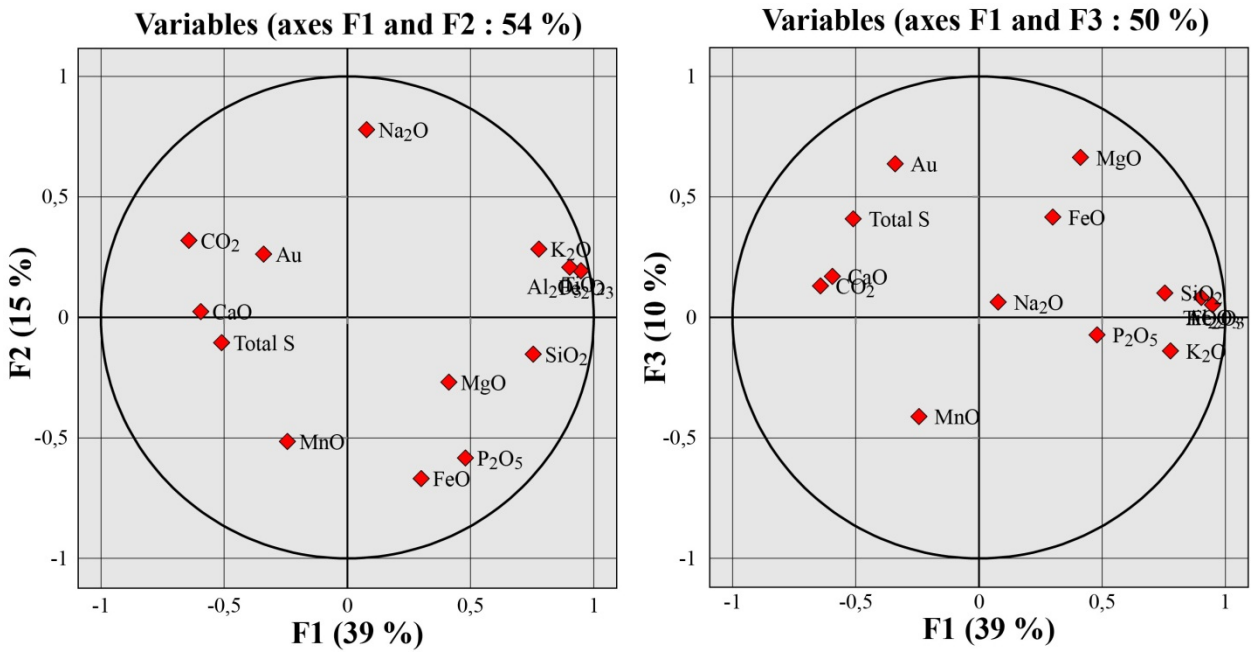

Figure 7-45: F1-F2 and F1-F3 projections of PCA on CLR data, major elements, all garnet-biotite schist samples. The projections explain 54 and 49%, respectively, of data variance.

7.5 Other quartz-vein mineralization styles

7.5.1 Auriferous quartz veins in mafic volcanic rocks

Limited occurrences of gold mineralization hosted in mafic volcanic rocks is present at Musselwhite. A typical example is the set of gold-bearing quartz veins intersected by drill holes in the upper Lynx area (i.e., parts of NIF and unit Bvol situated above the Lynx ore zone, on the east limb of the mine synform; Figures 7-1, 7-4). There, 1-3 m-long intersections of quartz veins have gold grades between 3 and 20 ppm, with one occurrence of 113 ppm (DDH 12-LNX-007; Figure 7-46). Sulphide content is remarkably low. The intensely D_2-deformed mafic host rock displays a proximal, 0.1-1.5 m-wide carbonate alteration halo (calcite enrichment), and a distal, 0.5-3 m-wide, potassic alteration halo (intense biotitization) around laminated veins (Figure 7-46).

Other occurrences of gold-bearing mafic volcanic rocks are located in the first few meters of unit Bvol overlying the NIF (Figure 5-26A). In such cases, gold mineralization consists of narrow quartz-pyrrhotite-carbonate veins and shear zones of variable grade (i.e., commonly low grade, Figure 7-47A, locally over 10 ppm, Figure 7-47B). In such cases, matrix minerals include hornblende-actinolite, grunerite, hedenbergite, magnetite, and calcite, with trace sericite replacing plagioclase feldspar (Figure 7-48A, B). Garnet porphyroblasts are locally present. Sulphides mainly occur as pyrrhotite with minor chalcopyrite and trace sphalerite and arfvedsonite (Figure 7-48C). Gold is associated with sulphides but also found as inclusions in actinolite and hedenbergite (Figure 7-48D). In the West limb area, these calc-silicate minerals are also found in close association to visible gold-bearing quartz veins hosted by unit Bvol (Figure 7-49). Mafic-hosted gold mineralization in the West limb area is fairly limited, usually restricted to the area immediately overlying unit 4F and spatially associated with a barren ultramafic dyke.

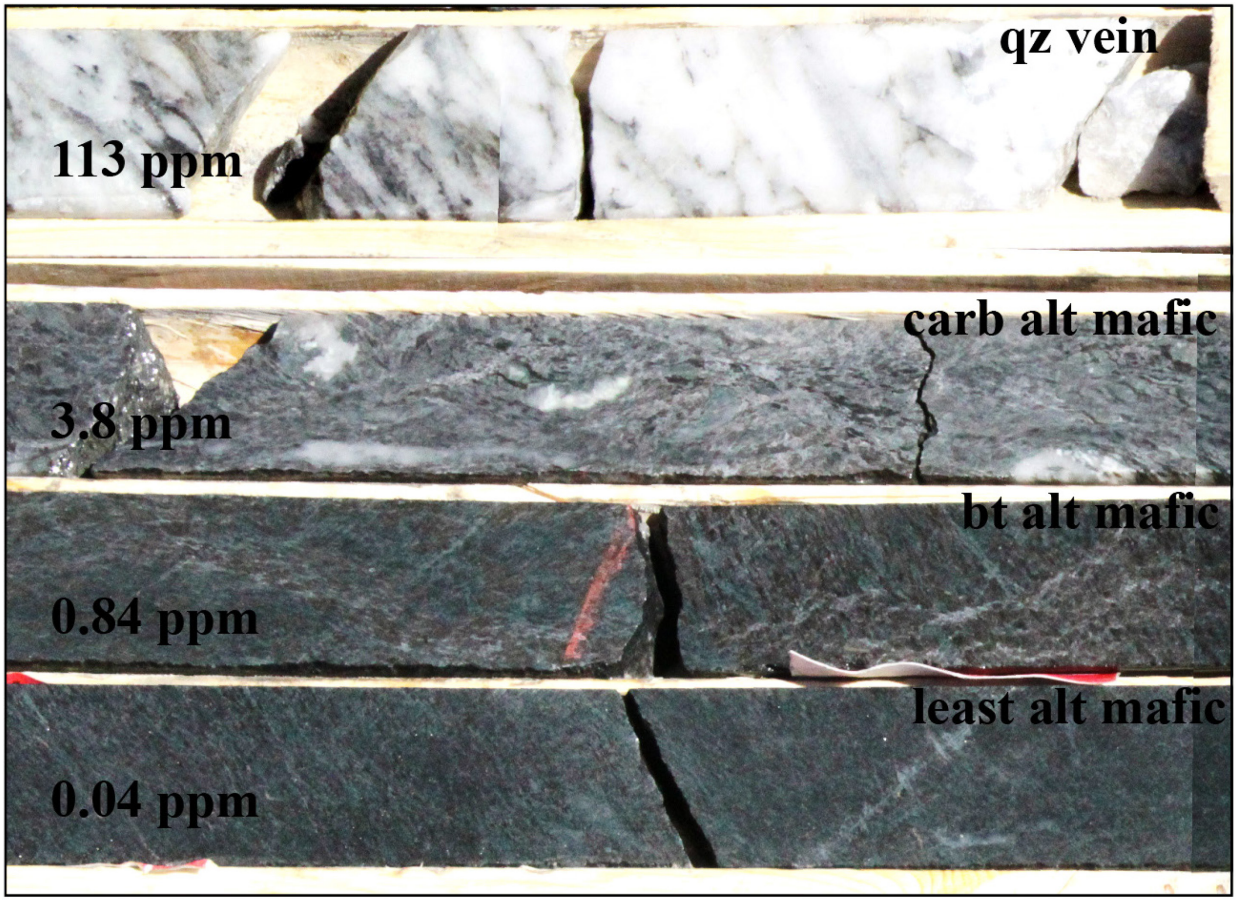

Figure 7-46: Auriferous quartz-calcite vein in unit Bvol. The mafic volcanic rocks hosting the vein show the typical proximal carbonate alteration and distal potassic alteration. The trace amount of sulphide is notable. DDH 12-LNX-007 @108-114 m.

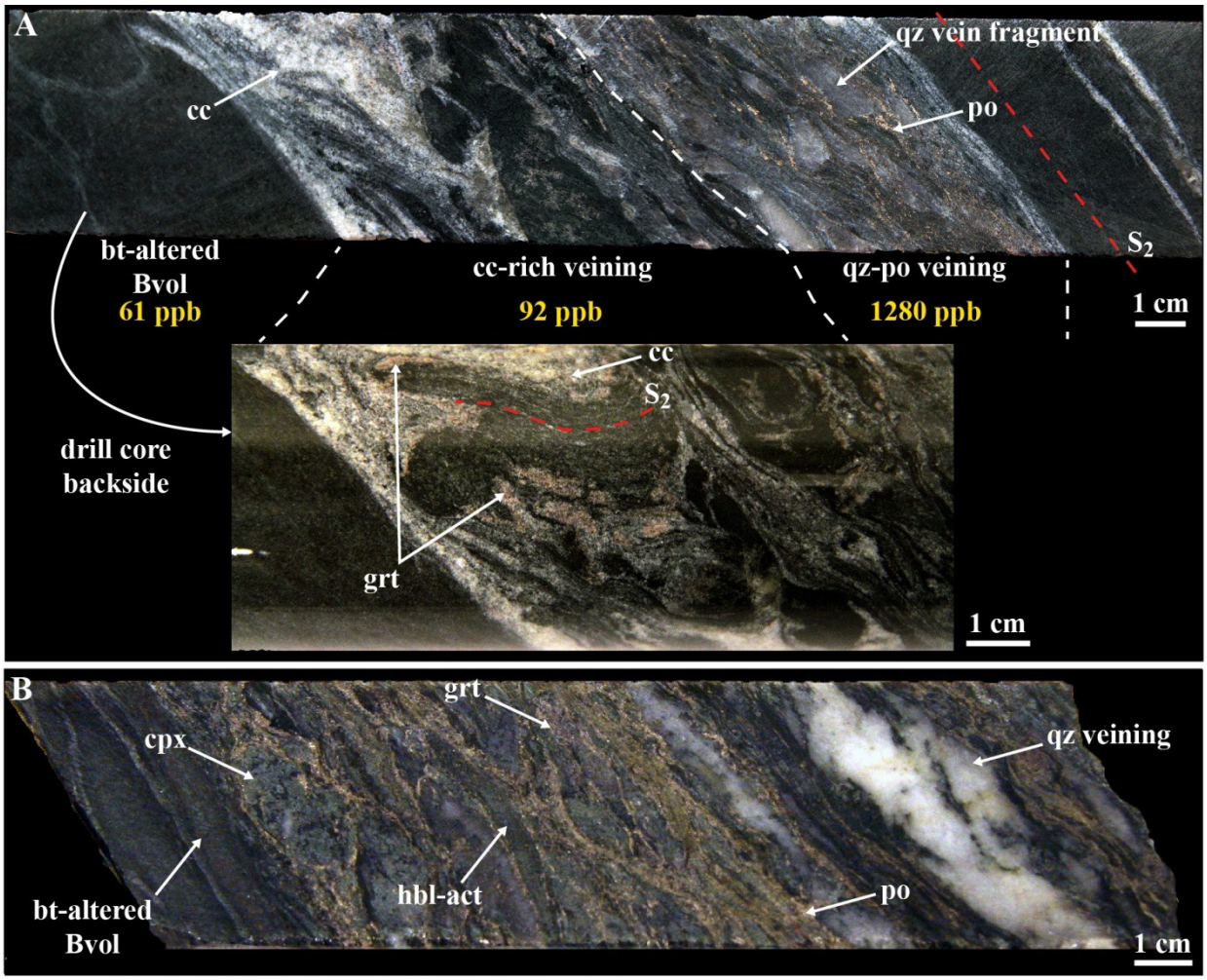

Figure 7-47: A. Quartz-pyrrhotite and calcite-rich veining in mafic volcanic rocks (unit Bvol), sample MW-12-273, DDH 06-PQE-095. Gold content is significantly higher in the qz-po veining (1280 ppb vs. 92 ppb in the calcite-rich portion). The presence of a foliated fragment of matrix in the calcite-rich portion and the sharp contact with the quartz-pyrrhotite part suggest that the calcite-rich veining is late-D_2. B. Sheared, quartz-pyrrhotite veining in mafic volcanic rocks containing 16 ppm gold, sample MW-11-015, DDH 10-PQE-054. Alteration minerals notably include: diopside (cpx), hornblende-actinolite, garnet, and trace calcite.

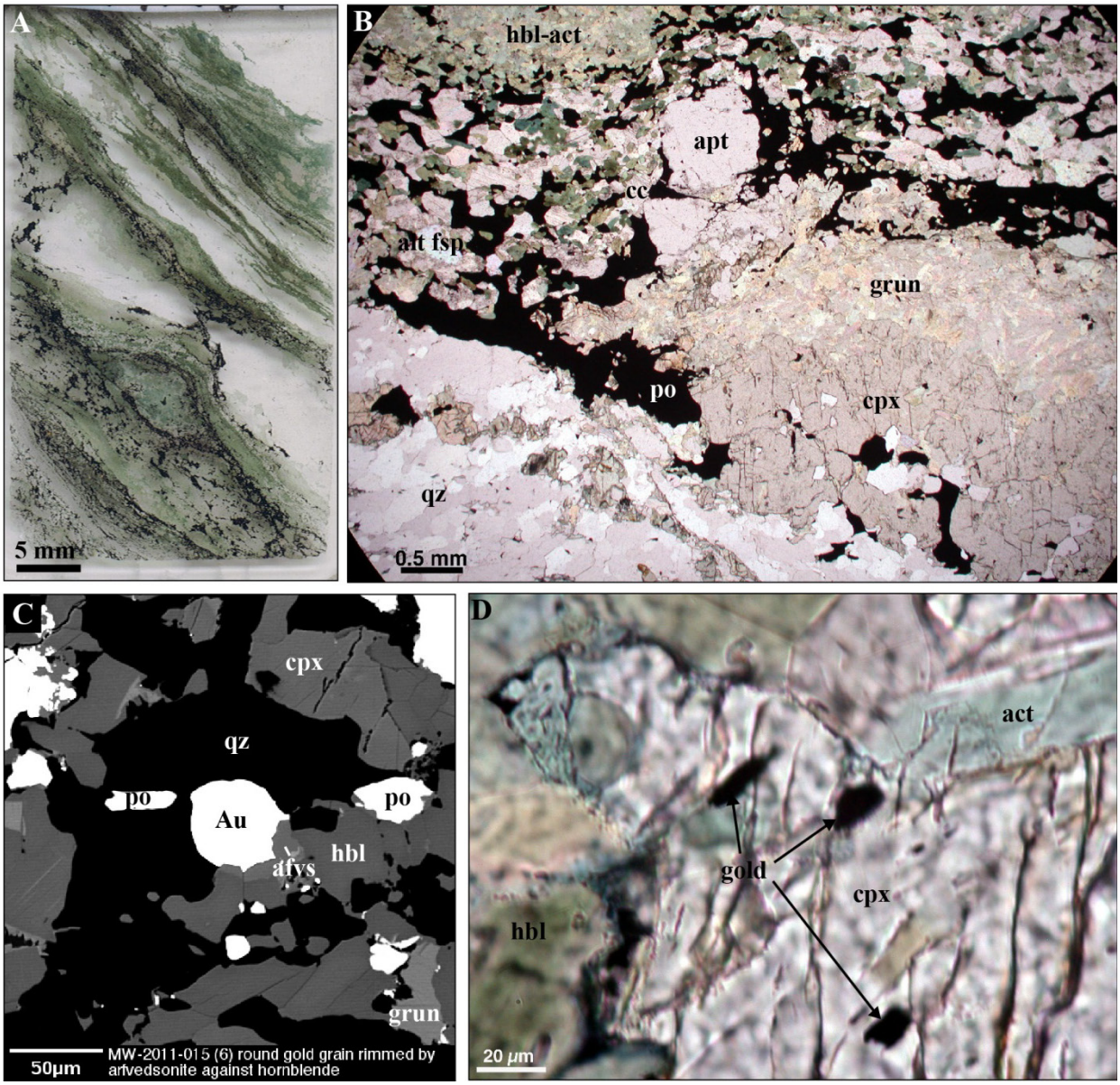

Figure 7-48: Gold in mafic rocks, sample MW-11-015, DDH 10-PQE-054. A. Strongly foliated, pyrrhotite-mineralized mafic rock showing quartz veins with clinopyroxene-bearing alteration assemblage. B. Microphotograph of hedenbergite intergrown with grunerite adjacent to a quartz vein (lower right), with sericite-altered plagioclase feldspar intergrown with calcite, pyrrhotite, hornblende, and apatite. The hornblende-actinolite matrix is visible at the top of the photo. C. SEM image of gold associated with pyrrhotite, quartz, and hornblende. D. Gold inclusions in hedenbergite intergrown with hornblende and actinolite.

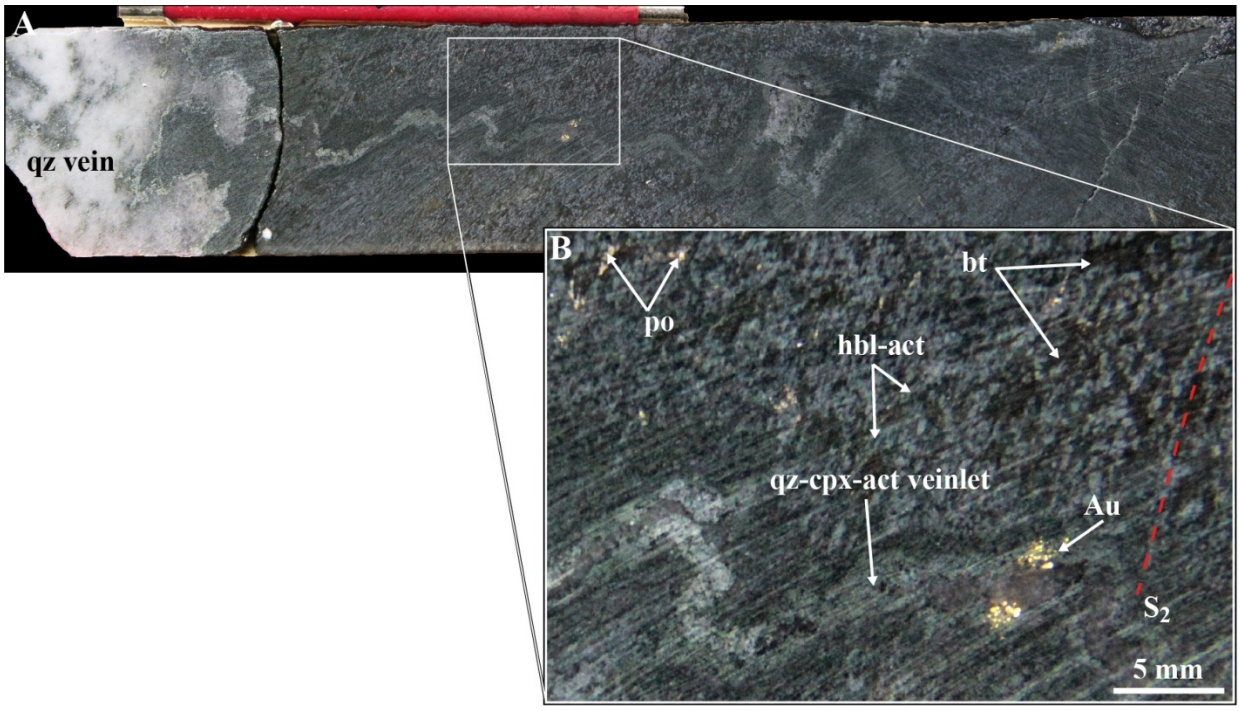

Figure 7-49: A. and B. Visible gold occurrence in the selvage of a D_2-deformed quartz vein hosted by mafic volcanic rock (unit Bvol). DDH 14-WEL-017, 357 ppm Au section. Note the calc-silicate alteration halo around the vein. The deformed vein is oblique to the S_2 fabric defined by intense biotite alteration of the host rock, and is itself folded, suggesting a syn- to late-D_2 timing for veining.

7.5.2 Visible gold occurrences

Besides the common millimetre-scale visible gold grains in strongly mineralized rocks of all types, major visible gold occurrences were documented in two main rock types: spectacular quartz-gold-sulphides veins in the 4EA and 4B ore (Figure 7-50), and minor quartz-gold veins hosted in mafic rocks overlying BIF-hosted gold-mineralized zones (Figure 7-51). The visible gold in BIF is comprised in 5-20 cm-thick light grey quartz veins, sub-parallel to the BIF compositional layering. The locally abundant visible gold is associated with minor sulphides, including pyrrhotite and, more rarely, arsenopyrite (Figure 7-50). The visible gold mineralization hosted in mafic rocks consists of minor tightly-folded and strained quartz-gold veins (Figure 7-51A, B, C). The lack of sulphide minerals and evidence of alteration around the vein suggest this represents local remobilization of gold in quartz veins due to intense D_2-strain and tightening of F_2 folds (Figure 7-51D).

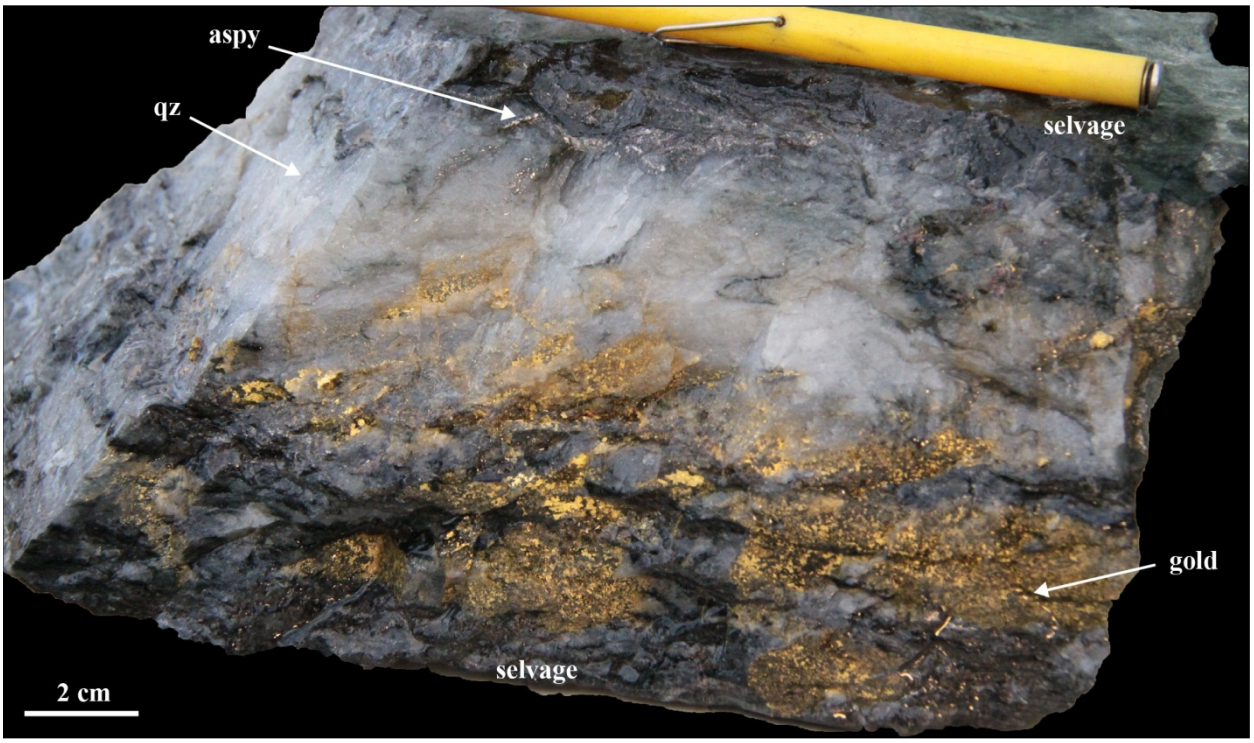

Figure 7-50: Visible gold occurrence associated with a quartz-pyrrhotite-arsenopyrite vein (photo B. Dubé).

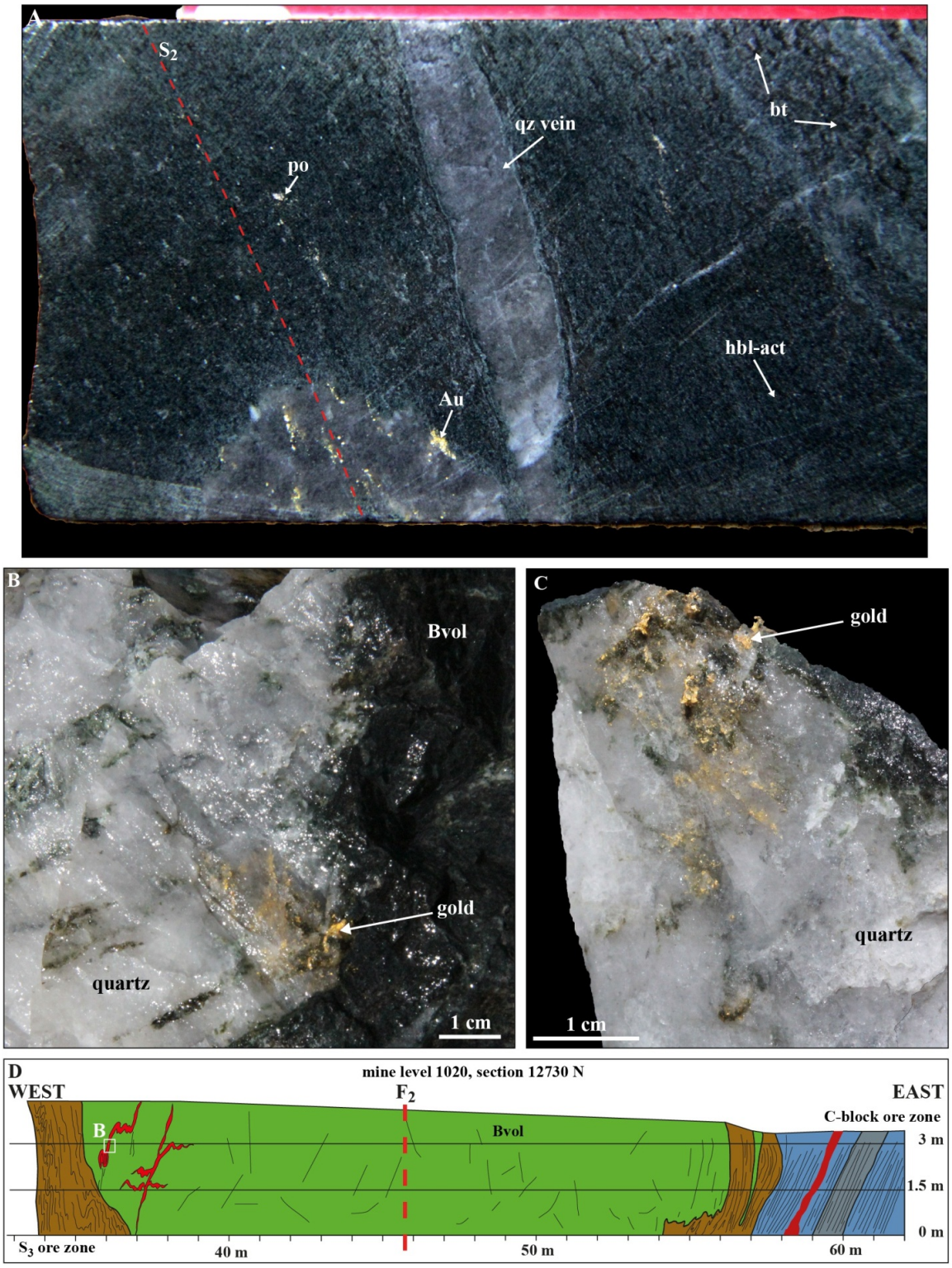

Figure 7-51: A. Visible gold occurrence in an F_2-folded quartz vein hosted by mafic volcanic rock (unit Bvol). Note that gold is in an axial-planar position, indicating syn-D_2 emplacement. This is similar to auriferous quartz vein observed in: B. and C. Quartz-gold vein hosted by mafic volcanic rock overlying the NIF on mine level 1020, main ramp. D. Geological face map of mine level 1020, main ramp, showing the portion of unit Bvol in the core of the East Bay synform between ore zones S3 and C-block.

7.6 Summary on gold mineralization

7.6.1 Main characteristics of gold-mineralized rocks

Two mineralization styles are documented: the first is dominated by pyrrhotite-replacement of the iron formation and local silica remobilization (7.2), the second is marked by the systematic presence of quartz veins at the core of mineralized zones (7.4). The former style is typical of BIF units (4EA, 4E, 4A, 4B), whereas the latter occurs in pelitic rocks (unit 4F) and mafic volcanic rocks. Gold mineralization in oxide BIF (unit 4B) is somewhat hybrid and consists in pyrrhotite-replacement systematically associated with quartz veins.

Unit 4EA is the better host for ore. High-grade gold mineralization in unit 4EA is characterized by the presence of coarse red, subhedral almandine garnet porphyroblasts in a matrix of grunerite, hornblende, ferro-tschermakite, hedenbergite, quartz, biotite, calcite, and, locally, magnetite. Opaque minerals inclusions in garnet porphyroblasts can be sorted into: magnetite-only, magnetite-ilmenite, magnetite-ilmenite-pyrrhotite, and pyrrhotite-ilmenite. Pyrrhotite is the major sulphide phase, constituting up to 95% of metallic minerals, with the remainder 5% consisting mainly of chalcopyrite.

Other gold-mineralized BIF lithologies typically show some mineralogic variations, based on their initial bulk chemical composition: The garnet amphibolite (unit 4E) is richer in Ca-amphiboles and hedenbergite, and commonly less garnet; oxide BIF (unit 4B) and silicate BIF (unit 4A) contain more grunerite and actinolite, as well as calcite, and rare garnets.

Lithogeochemical data shows that sulphur is the only major element that can be reliably used as a proxy for gold content, and that Au is consistently associated with Cu, Ag, Se, and Te. CaO and CO_2 also moderately correlate with gold mineralization. The negative correlation between Fe_2O_3 and gold indicate that magnetite is the primary source of iron for pyrrhotite.

7.6.2 Preliminary interpretations for the timing of gold mineralization

Previous studies of the Musselwhite deposit have all reported that gold is associated with D_2 structures (Breaks et al., 1985; Hall and Rigg, 1986; Breaks et al., 2001; Blower and Kiernan, 2003; Biczok et al., 2012; Kolb et al., 2012). Data from this study supports such an interpretation. Gold mineralization is systematically spatially associated with high strain zones related to F_2 folds (Figures 7-2, 7-3, 7-4). This aspect is further discussed in chapter 10.

The timing of gold introduction with respect to metamorphism is more difficult to establish. Garnet porphyroblasts show diverse, and locally contradictory relationships with gold and sulphides. While a majority of garnet porphyroblasts grew during D_2, some Mn-rich phases may have formed earlier (chapter 6), possibly under greenschist facies metamorphic conditions due to high Mn content (Paulick and Franz, 2001). The occurrence of pyroxene in the ore is compatible with amphibolite facies conditions. The presence of gold inclusions in pyroxene suggest that gold was introduced before the crystallization of the porphyroblasts. This is further discussed in 10.

8 HYDROTHERMAL ALTERATION

8.1 Introduction

This chapter focuses on the nature and spatial distribution of hydrothermal alteration associated with gold mineralization at the Musselwhite mine. Geological mapping and structural and petrographic analyses (chapters 5 and 6) show that while gold mineralization is synchronous to D_2 deformation and related regional metamorphism, both likely outlasted the emplacement of gold mineralization and related hydrothermal alteration (chapter 7). It occurred under approximate PT conditions of 540-650°C and 3 kbar (Hall and Rigg, 1986; Otto, 2002; this study). At amphibolite facies metamorphism, epigenetic, sulphide-replacement, gold mineralization is associated with the development of several types of alteration (chapter 1; Phillips et al., 1984; Mueller and Groves, 1991; Bullis et al., 1994; Mueller, 1997; Eilu et al., 1999; Goldfarb et al., 2005), including: 1) distal potassic alteration characterized by the presence of biotite, 2) proximal carbonate/calcic alteration characterized by calcite and/or Ca-bearing amphiboles, and 3) sulphidation of the iron formation. The footprint of hydrothermal alteration is a key vector in mineral exploration. Consequently, various scales of alteration are considered herein: From ore zones to mine-scale, using drillhole profiles, and at unit–scale, through mineralogical and chemical characteristics of specific units (Bvol, 4EA, 4B, 4F).

The identification of geochemical variations due to gold-related hydrothermal alteration of the iron formation is challenging. This is mainly due to three factors: 1) primary compositional variations, 2) contrasts in chemical reactivity with mineralizing fluids, and 3) rheological contrasts leading to strong permeability variations during deformation.

Due to changes in detrital and chemical inputs during BIF deposition (chapter 1), chemical elements show considerable primary compositional variations (chapter 3). This is the case for both mobile (e.g., K_2O) or immobile (e.g., Al_2O_3) elements. In the case of a BIF facies with a simple mineral assemblage, such as the chert-magnetite BIF, variations in the thickness of bands also result in compositional discrepancies within a group of least altered samples (section 3.10; Janvier, 2016).

Variations of BIF facies reactivity to hydrothermal fluids may lead to differences in mineralogical assemblages and intensity of alteration. This is notably illustrated by clastic chert-magnetite BIF (unit 4B, facies 4Bc; section 7.3.4), which shows that potassium-bearing minerals (here, biotite) are concentrated in amphibole-bearing bands while carbonate minerals are preferentially distributed in chert and magnetite

bands. Regional metamorphism can also modify the initial geochemical signature of hydrothermal alteration, as in the case of volcanogenic massive sulphides (Galley et al., 2007).

Lastly, iron formations are finely layered and thus more anisotropic than mafic volcanic rocks (considering pillows or flow top breccias as negligible) or other relatively homogeneous rock types (sections 1.4 and 5.1.2). Boundary surfaces between bands of different compositions are a primary locus for fluid flow. Likewise, permeability is drastically different in chert bands than in garnet-grunerite bands or magnetite bands, etc. (Oliver, 1996; Zhang, 1997). This may produce strong alteration gradients, from centimetre to decimetre-scale. Rapid transitions from barren or very low grade rocks to high-grade mineralized rocks are numerous throughout the mine. This is illustrated from the Thunderwolves and Redwing zones (unit 4A, Southern iron formation, East limb) to the WEL zones (unit 4F, West limb), regardless of host rocks (Figures 7-42 and 8-1).

Sampling methods, such as taking larger samples (e.g., a minimum length of 30 cm for sawed core pieces), can partly mitigate centimetre-scale compositional variations. Primary variations, especially those of immobile elements used for comparing samples (Grant, 1986), complicate the study of geochemical changes as they may obscure the effect of hydrothermal alteration.

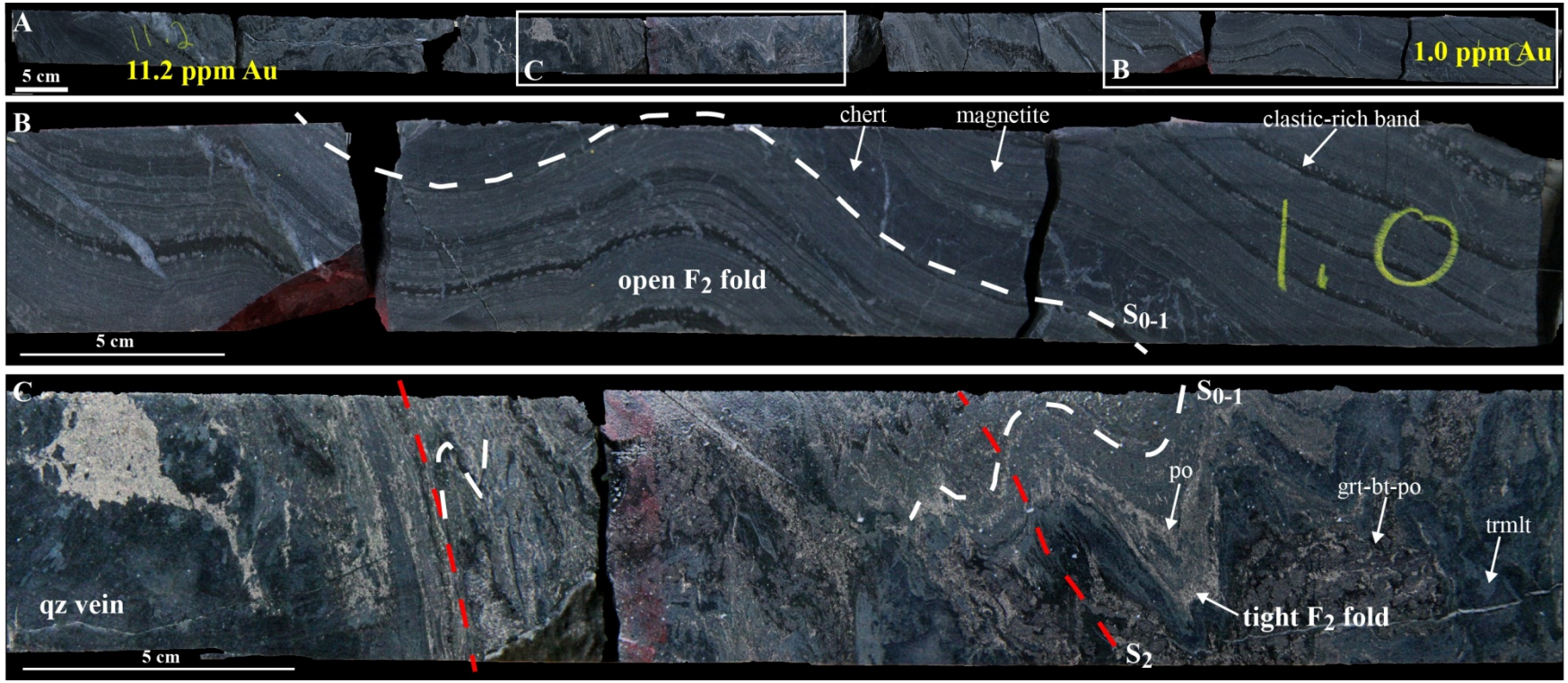

Figure 8-1: Variations in D_2 strain and gold mineralization gradients. A. Drill core segment of drill hole 14-WEL-002, from 552 to 553 m, showing 11.2 to 1.0 ppm quartz-vein-style gold mineralization in unit 4B (chert-magnetite BIF). B. Close-up of A. showing open-folded BIF with little evidence of alteration. C. Close-up of A. showing the strongly pyrrhotite-replaced and strongly altered chert-magnetite BIF. Deformation is most intense proximal to the quartz vein (left side), where minerals are aligned parallel to S_2. Alteration is characterized by amphibole-pyrrhotite layers and garnet-biotite ± pyrrhotite masses.

8.2 Spatial distribution of hydrothermal alteration

8.2.1 Methodology

The delineation of hydrothermal alteration zones is hindered by lithological diversity of host units and deformation overprint. Profiles of sampled/analysed drillholes are used to plot major element composition against the lithological and assay logs (Figure 8-2). Raw data profiles show that major element variations, with the exception of sulphur, are largely obscured by the overwhelming influence of lithology. To compensate, the average composition of "least altered" samples of each rock type was used to normalize raw data (i.e., dividing the altered sample value for a given element X_A by that of the average of least altered samples X_{LA}). "Least altered" sample groups, as defined in chapter 3 (Table 3-4), were established by excluding samples with major element values (e.g., total S, CO_2, K_2O, Na_2O, and SiO_2) exceeding specific thresholds and by retaining a minimum of 8-10 samples, which were then compared with those of the scientific literature (chapter 1) to ensure their reliability. The result of such normalization is shown on a series of profiles on which a red line marks the value 1, indicating a similar element quantity between "least altered" average and specific sample compositions (Figures 8-3 to 8-9). Values above or below the red line respectively indicate an increase or decrease of the specific element in the analyzed sample compared the "least altered" average composition. Overall, chemical variations related to potassic, carbonate, and sulphide alterations are much better constrained than on raw data profiles. The profiles produced by this method were plotted on mine section N11775 and zones of potassic, carbonate, and sulphide alteration were extrapolated across drill holes (Figure 8-10). Alteration zones are portrayed with opaque colour, whereas unalterated zones are shown with some transparency.

Table 8-1: Average major element composition and standard deviation for units 4F, 4EA, 4B, and 4A (data from this study). Negative LOI is due to iron oxidation during ignition (section 1.2.4; Dahéron et al., 2015). All numbers in wt.%, n = number of samples.

	SiO_2	Al_2O_3	Fe_2O_3	FeO	Total Fe_2O_3	MnO	MgO	CaO	Na_2O	K_2O	TiO_2	P_2O_5	CO_2	Total S	LOI	Au (ppb)	n =
Unit 4F																	19
Average	51.82	17.9	4.07	13.38	18.94	0.62	2.8	1.93	0.32	3.72	0.96	0.09	0.05	0.46	-1.09	22.15	
SD	2.62	2.07	1.91	2.34	2.57	0.38	0.56	1.02	0.43	0.56	0.13	0.02	0.06	0.19	0.41	15.72	
Unit 4EA																	18
Average	48.3	8.11	12.24	23.59	38.47	0.66	3.04	2.03	0.1	0.45	0.38	0.14	0.16	0.21	-4.5	34.17	
SD	3.59	1.08	2.22	2.56	3.46	0.25	0.39	0.4	0.06	0.26	0.07	0.02	0.08	0.07	0.48	19.18	
Unit 4Bc																	26
Average	48.72	5.94	15.04	21.2	38.61	0.58	2.4	1.4	1.11	1.43	0.3	0.13	0.42	0.18	-3.17	20.02	
SD	2.16	0.97	2.67	1.39	2.48	0.16	0.21	0.5	0.63	0.67	0.06	0.02	0.24	0.06	0.45	21.89	
Unit 4B																	36
Average	46.00	1.81	19.78	22.25	44.53	0.67	2.69	3.14	0.175	0.35	0.087	0.16	1.79	0.24	-2.11	25.39	
SD	2.15	1.07	3.81	1.71	2.86	0.23	0.56	0.95	0.14	0.23	0.06	0.02	0.77	0.1	0.92	26.90	
Unit 4A																	25
Average	63.53	1.002	5.13	18.92	26.17	0.84	2.69	3.60	0.054	0.236	0.038	0.123	2.05	0.98	-0.662	29.23	
SD	11.06	1.02	3.23	4.88	7.14	0.45	1.08	1.59	0.04	0.28	0.04	0.05	1.15	1.44	0.96	25.22	

SD = standard deviation

8.2.2 Results

The primary variability of a given element in the "least altered" group must be considered when examining the results of this normalization of geochemical data on DDH profiles (Table 3-4). For example, standard deviation on Fe_2O_3 content in unit 4B is close to 4 for an average content of 20 wt.%. This means that a 20% increase or depletion on the normalized DDH profiles (0.8 to 1.2 values) is not significant with respect to alteration. Data from unit 4A is particularly challenging in this regard, as some major elements show a standard deviation equal to 100% of the average content (e.g., Al_2O_3; Table 3-4).

Overall, SiO_2 is fairly stable and close to the value of 1 (Figures 8-3 to 8-9). This indicates that the common silica flooding in gold-bearing zones is not the result of significant addition of silica, but rather of its redistribution. Al_2O_3 is not as close to the value of 1 as expected, given its "immobile" nature. This is probably caused by primary variations in the iron formation due to the detrital origin of aluminum. Fe_2O_3 and FeO mostly show small variations. Peak values of Fe_2O_3 mostly occur in unit 4F and unit 4A; due to primary variations in the former (i.e., "least altered" samples have a standard deviation equal to 60% of the average composition; Table 3-4) and to magnetite-rich samples for the latter. MnO and MgO are a similar (Figures 8-3 to 8-9): variations within the "least altered" group are such that most enrichments and depletions on DDH profile cannot be considered as significant anomalies. This is especially relevant for MnO, which has an average content between 0.5 and 0.8 wt.% in most units.

CaO is positively correlated with CO_2 and, in units 4E, 4B, 4A, and 4F, positively correlated with gold (cf chapter 7). In DDH profiles, CaO content is mainly marked by peaks related to zones of strong CO_2 enrichment, in agreement with the presence of calcite observed in drill core and underground (e.g., within strongly carbonate-altered, mafic-hosted high strain zones; chapter 5). Na_2O show no correlation with other major elements nor gold (Figures 7-22, 7-29, 7-33, 7-39, 7-45; Table 7-5). In "least altered" samples, primary variations are strong in all major units (Table 3-4). Significant features in DDH profiles consist in strong depletion extending across multiple adjacent samples (e.g., weakly altered mafic rocks and oxide-BIF; Figure 8-9), or large enrichment peaks (Figure 8-8). These peaks typically occur for K_2O, CO_2, or total S content, regardless of the host rock. While enrichments in total S content in normalized data are largely similar to that of raw data, enrichments in normalized K_2O and CO_2 are better defined in all rock types (Figure 8-7), particularly in mafic volcanic rocks. Contrastingly, K_2O and CO_2 are fairly weak in unit 4EA (Figure 8-4).

Profiles of drill holes 10-PQE-056 and 10-PQE-066, located in the mine synform east limb on section 12675 N (Figure 7-4 and 8-10), provide a fairly simple setting to assess the benefit of this DDH profile normalization method (Figures 8-3 and 8-4). They show a well-defined potassic alteration, usually accompanied by moderate to strong carbonate alteration, associated with the high strain zones affecting mafic volcanic rocks (unit Bvol), above the NIF. Local gold-bearing lenses within unit 4E are identified by combined K_2O, CO_2, and total S peaks (Figure 8-4). The "conveyor shear" is marked by sharp K_2O and CO_2 peaks.

In the PQD area, located in the eastern portion of the mine synform hinge zone (Figure 7-2 and 8-10), potassic and carbonate alteration in high strain zones can be followed from drill hole 06-PQE-013 (Figure 8-5) to drill hole 06-PQE-095 (Figure 8-6) and drill hole 06-PQE-083 (Figure 8-7). In 06-PQE-013, alteration within the C-block ore zone is quite discrete. However, overlying mafic rocks show well-developed potassic and carbonate alteration. The underlying unit 4B displays carbonate and sulphide alterations related to the B-block and A-block ore zone, located above. Alterations related with the C-block, B-block, and A-block ore zones are conspicuous in drill hole 06-PQE-095 (Figure 8-6). The presence of strongly altered mafic rocks between the B- and A-blocks ("B-block shear") is shown by large peaks in K_2O and CO_2, and high strain zones in unit Bvol are shown by moderate K_2O enrichment. Similarly, drill hole 06-PQE-083 (Figure 8-7), located at the top of the 11775 N PQD drill hole fan, shows three distinct K_2O peaks associated with mafic-hosted high strain zones. It also intersects a small gold-bearing lense hosted in unit 4E. The trace of the B-block ore zone in the duplication lense of the NIF (Figures 5-21, 5-22, 7-2, 7-3) is marked by CO_2, total S, and gold peaks in unit 4B.

In the T-antiform area (Figure 7-2 and 8-10), profiles of drill holes show similar features (09-TAN-014, Figure 8-8; 09-TAN-029, Figure 8-9). In the former, sub-economic gold mineralization in the east limb of the T-antiform is evidenced by total sulphur enrichment, proximal carbonate and distal potassic alteration zones. On the east limb, the Moose ore zone is marked by sulphur enrichment, but alteration is asymmetrical, focused along its eastern side. CO_2 and K_2O enrichment is focused in mafic rocks adjacent to the ore zone, which are affected by a major high strain zone (Figure 7-2). The presence of significant mineralization in the BIF intercept following the high strain zone (locally referred to as the Eagle zone) suggests that the structure is the main pathway for gold-bearing fluids and that the Moose ore zone exemplifies the lithological control of unit 4EA on mineralization. Drill hole 09-TAN-029, located slightly above, shows similar features but in a more distal manner (i.e., potassic alteration and weak carbonate alteration, instead of strong carbonate alteration and sulphide alteration; Figure 8-9). Gold mineralization on the east limb of the T-antiform is visible but lacks significant sulphide. The Moose ore zone is not evidenced by a significant total S enrichment. Unit Bvol includes two peaks of potassium enrichment, and the last segment of the NIF sequence in the drill hole shows a distinct CO_2 enrichment.

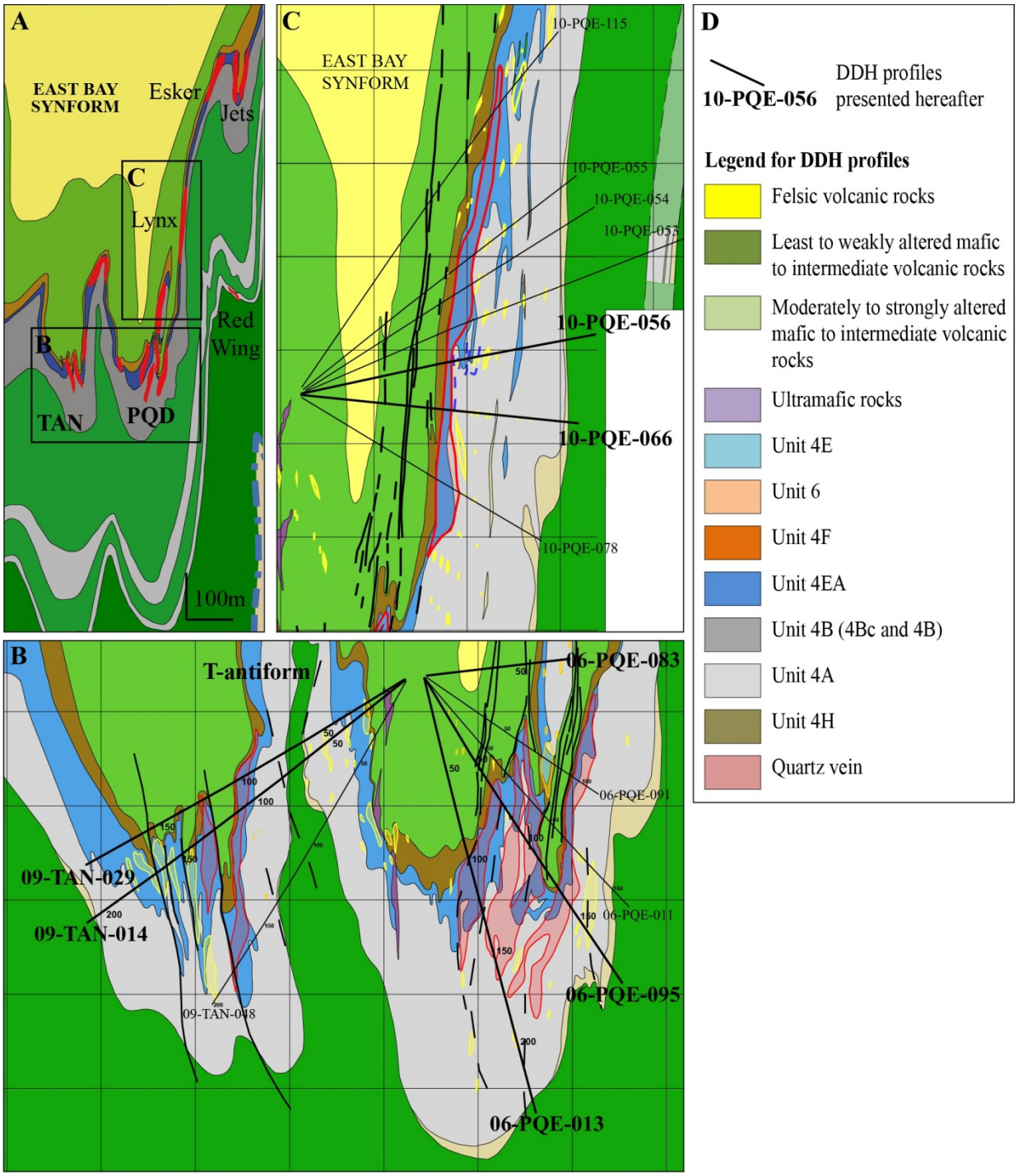

Figure 8-2: Sections of DDH profiles presented in this chapter. A. Close-up of Figure 7-1 showing a schematic mine section at 11775 N. See Figure 7-1 for rock type legend. B. Close-up of Figure 7-2 showing the TAN and PQD zones of the mine on section 11775 N. C. Close-up of Figure 7-4 showing the East limb and the Lynx ore zone. D. Legend for rock types in Figures 8-3 to 8-9.

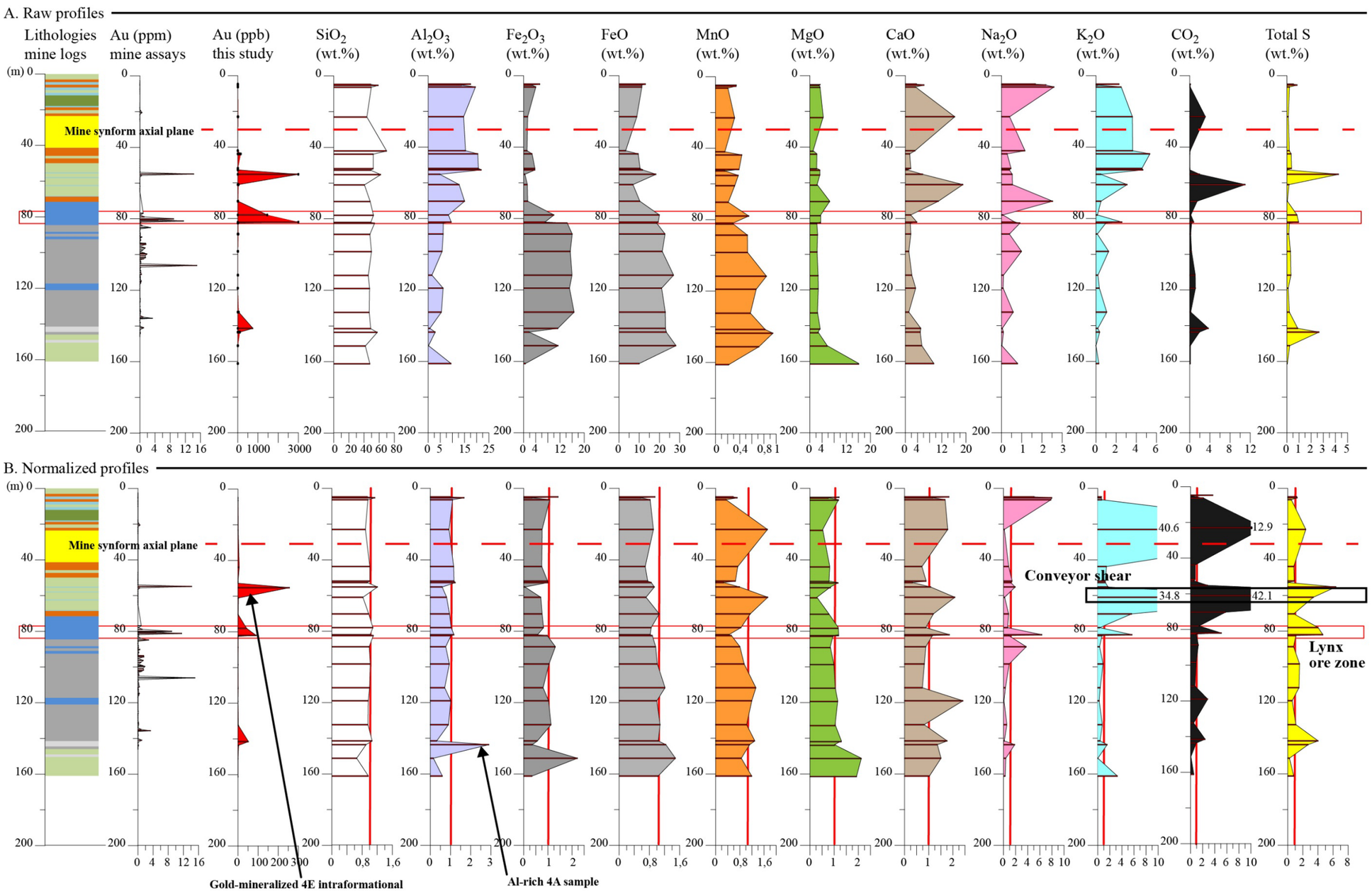

Figure 8-3: Gold and major elements profiles of drill hole 10-PQE-056, East limb area, section 12675 N. A. Profiles using raw whole-rock geochemical data. Geochemistry mainly reflects lithological variations in the mine stratigraphy. B. Profiles using data normalized with average "least altered" composition for each rock type. X-axis values correspond to the factor "y" in the operation $X_A = y\ (X_{LA})$ relating the altered sample value X_A to the least altered average value X_{LA}. Potassic, carbonate, and sulphide alteration zones in BIF and mafic volcanic rocks are better defined. See Figure 8-2 for rock type legend.

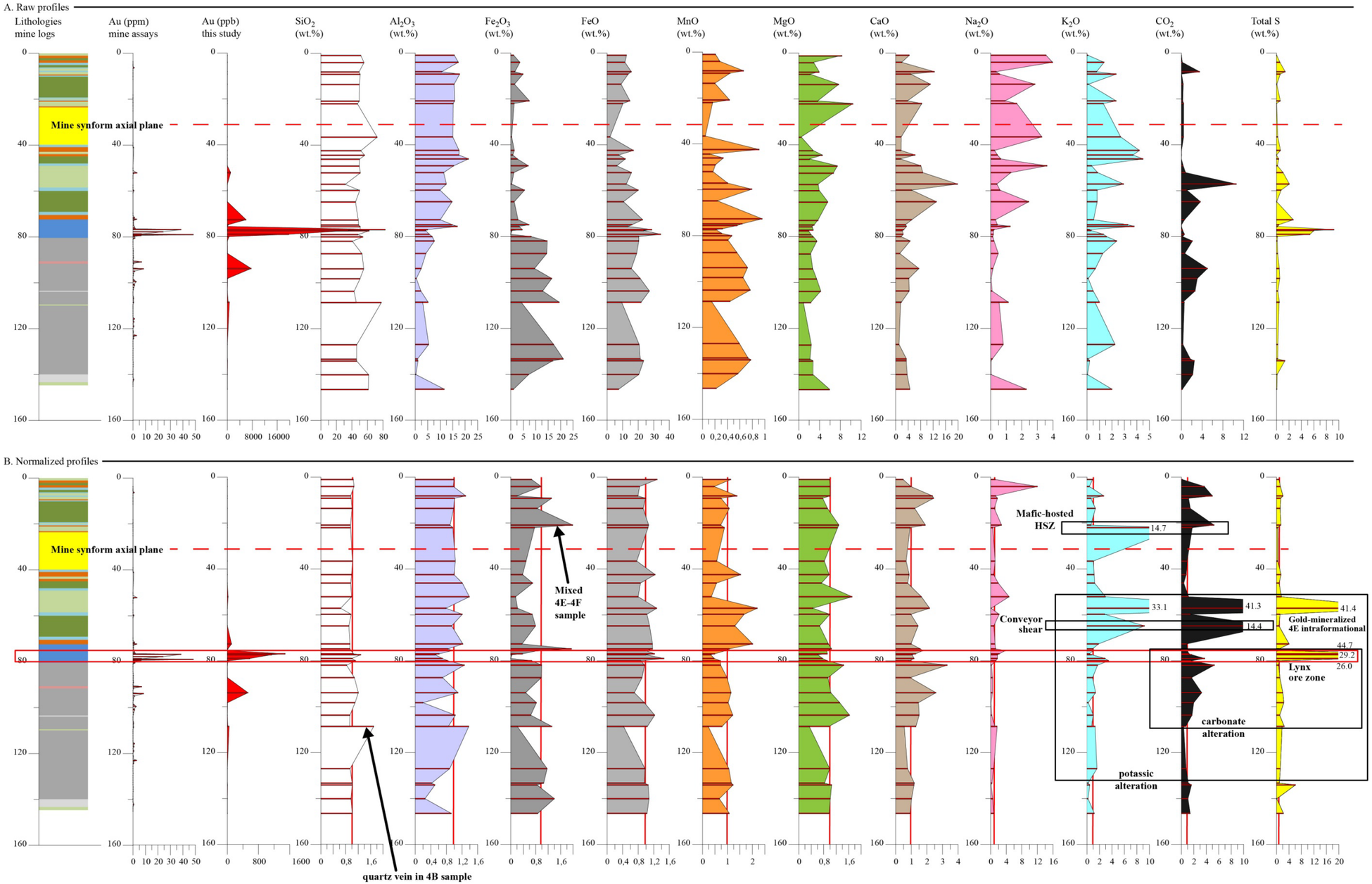

Figure 8-4: Gold and major elements profiles of drill hole 10-PQE-066, East limb area, section 12675 N. A. Profiles using raw whole-rock geochemical data. Geochemistry mainly reflects lithological variations in the mine stratigraphy. B. Profiles using data normalized with average "least altered" composition for each rock type. X-axis values correspond to the factor "y" in the operation $X_A = y\ (X_{LA})$ relating the altered sample value X_A to the least altered average value X_{LA}. Potassic, carbonate, and sulphide alteration zones in BIF and mafic volcanic rocks are better defined. See Figure 8-2 for rock type legend.

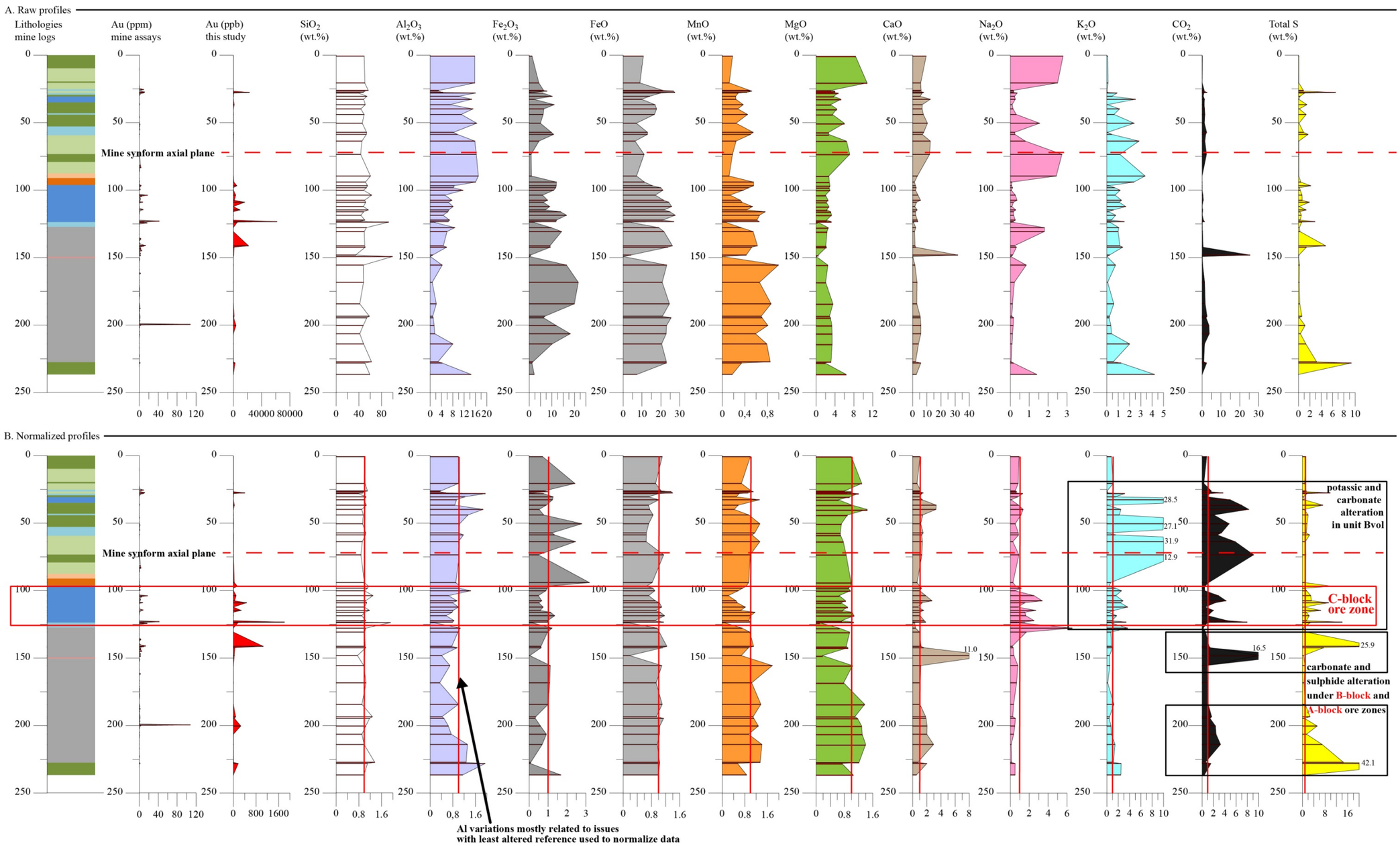

Figure 8-5: Gold and major elements profiles of drill hole 06-PQE-013, PQD area, section 11775 N. A. Profiles using raw whole-rock geochemical data. Geochemistry mainly reflects lithological variations in the mine stratigraphy. B. Profiles using data normalized with average "least altered" composition for each rock type. X-axis values correspond to the factor "y" in the operation $X_A = y\ (X_{LA})$ relating the altered sample value X_A to the least altered average value X_{LA}. Potassic, carbonate, and sulphide alteration zones in BIF and mafic volcanic rocks are better defined. See Figure 8-2 for rock type legend.

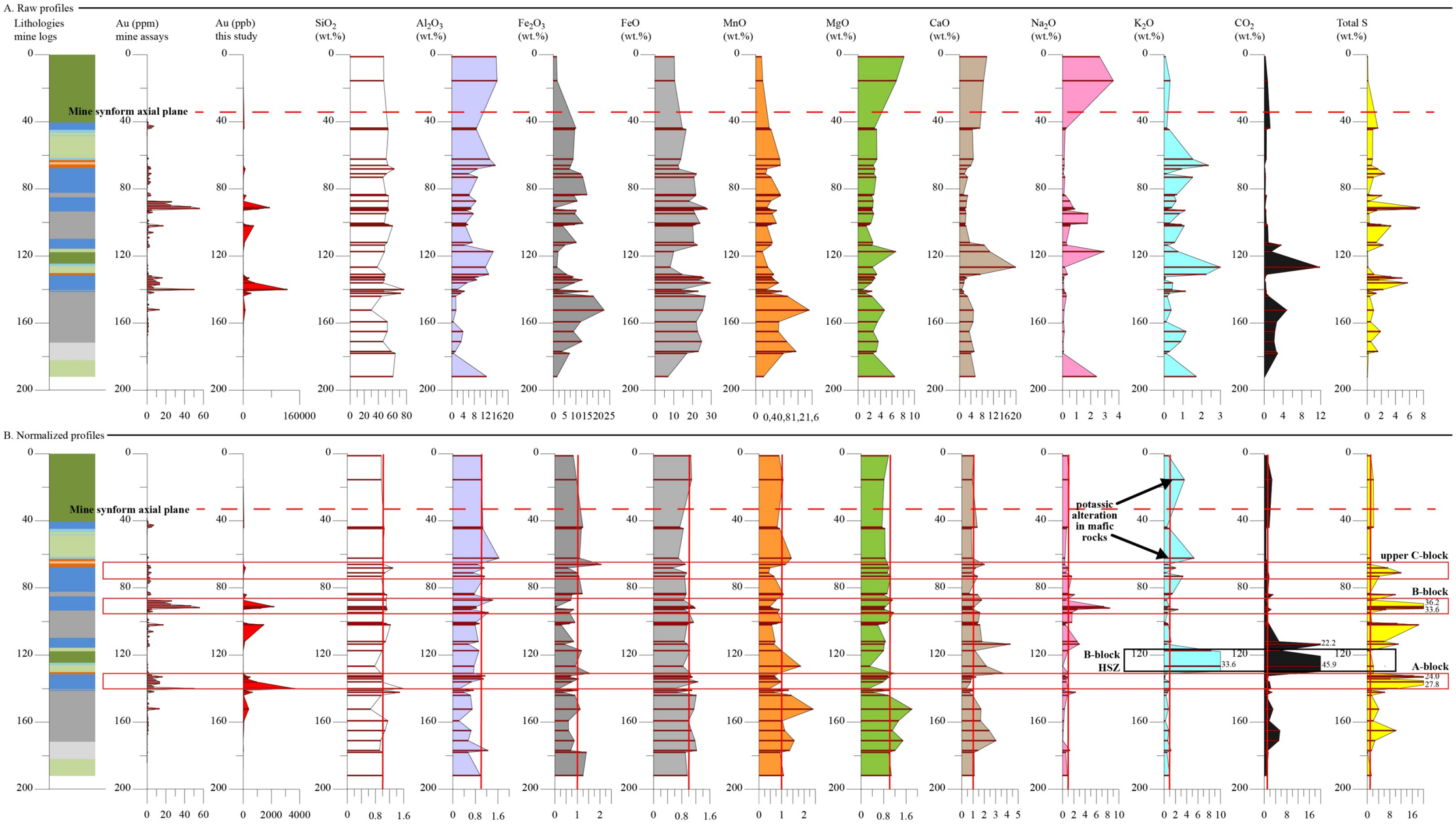

Figure 8-6: Gold and major elements profiles of drill hole 06-PQE-095, PQD area, section 11775 N. A. Profiles using raw whole-rock geochemical data. Geochemistry mainly reflects lithological variations in the mine stratigraphy. B. Profiles using data normalized with average "least altered" composition for each rock type. X-axis values correspond to the factor "y" in the operation $X_A = y\ (X_{LA})$ relating the altered sample value X_A to the least altered average value X_{LA}. Potassic, carbonate, and sulphide alteration zones in BIF and mafic volcanic rocks are better defined. See Figure 8-2 for rock type legend.

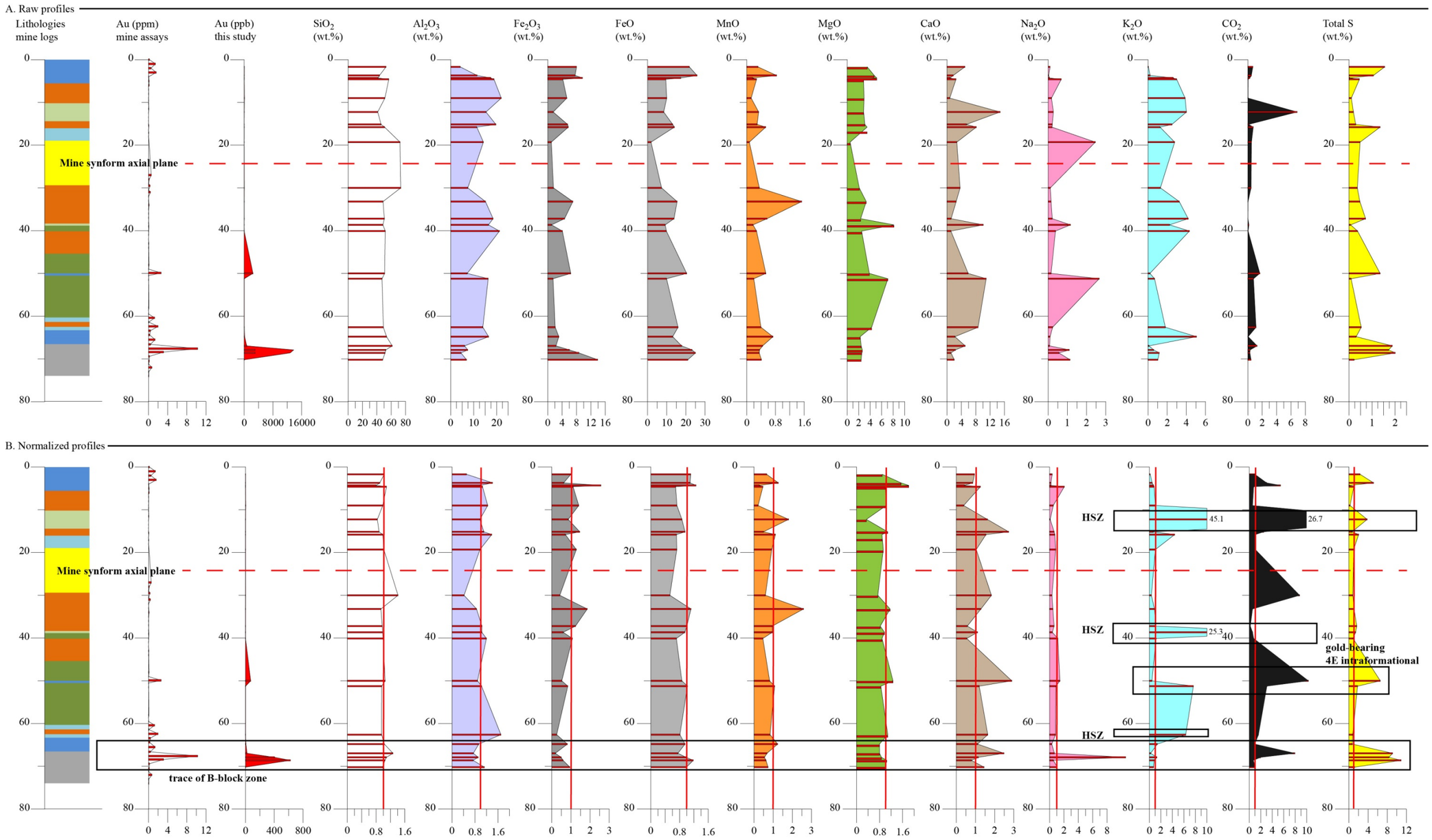

Figure 8-7: Gold and major elements profiles of drill hole 06-PQE-083, PQD area, section 11775 N. A. Profiles using raw whole-rock geochemical data. Geochemistry mainly reflects lithological variations in the mine stratigraphy. B. Profiles using data normalized with average "least altered" composition for each rock type. X-axis values correspond to the factor "y" in the operation $X_A = y\ (X_{LA})$ relating the altered sample value X_A to the least altered average value X_{LA}. Potassic, carbonate, and sulphide alteration zones in BIF and mafic volcanic rocks are better defined. See Figure 8-2 for rock type legend.

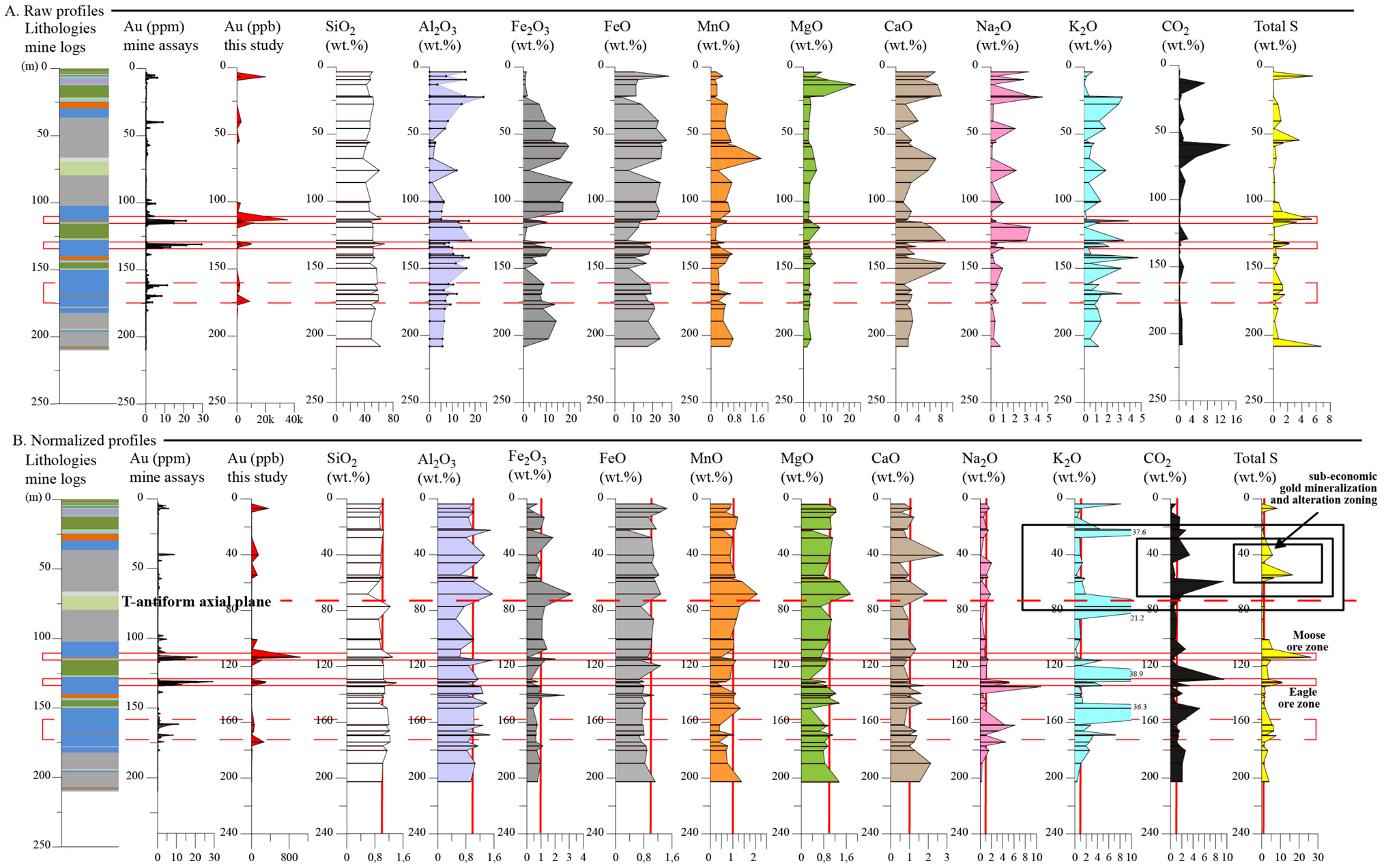

Figure 8-8: Gold and major elements profiles of drill hole 09-TAN-014, T-antiform west limb, section 11775 N. A. Profiles using raw whole-rock geochemical data. Geochemistry mainly reflects lithological variations in the mine stratigraphy. B. Profiles using data normalized with average "least altered" composition for each rock type. X-axis values correspond to the factor "y" in the operation $X_A = y\ (X_{LA})$ relating the altered sample value X_A to the least altered average value X_{LA}. Potassic, carbonate, and sulphide alteration zones in BIF and mafic volcanic rocks are better defined. See Figure 8-2 for rock type legend.

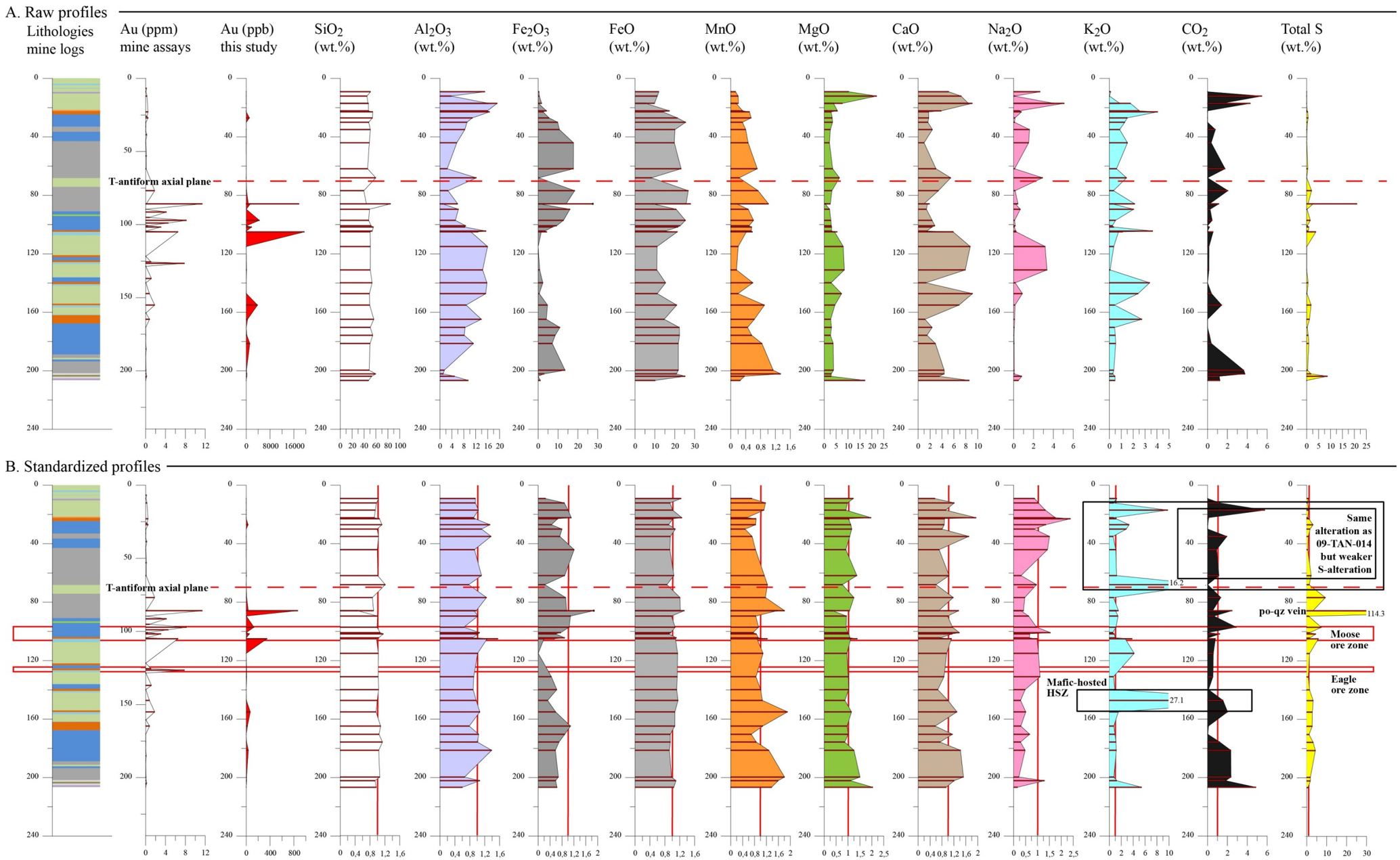

Figure 8-9: Gold and major elements profiles of drill hole 09-TAN-029, T-antiform west limb, section 11775 N. A. Profiles using raw whole-rock geochemical data. Geochemistry mainly reflects lithological variations in the mine stratigraphy. B. Profiles using data normalized with average "least altered" composition for each rock type. X-axis values correspond to the factor "y" in the operation $X_A = y\ (X_{LA})$ relating the altered sample value X_A to the least altered average value X_{LA}. Potassic, carbonate, and sulphide alteration zones in BIF and mafic volcanic rocks are better defined. See Figure 8-2 for rock type legend.

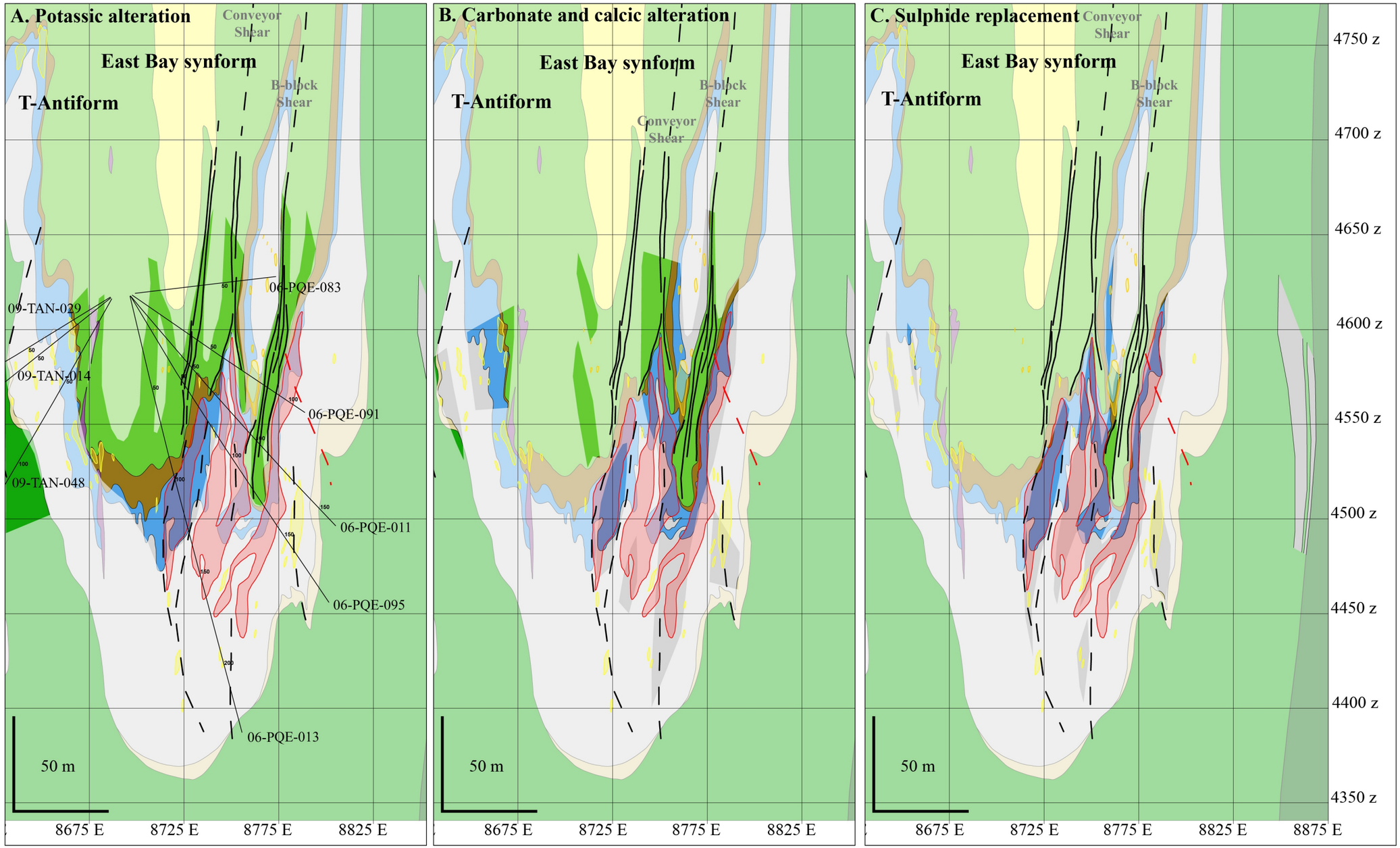

Figure 8-10: Distribution of alteration zones over the PQD area (section 11775N) of the Musselwhite deposit. Each zone is shown using opacity of the geological background: altered rocks are at full opacity, while unaltered rocks are at 50%. A. Potassic alteration. It is mainly developed in mafic volcanic rocks overlying the NIF. Although present in rocks under the NIF, it is difficult to delineate due to DDH length. B. Carbonate and/or calcic alteration. It is particularly well-developed in mafic volcanic rocks and the oxide-rich BIF (unit 4B). C. Sulphide-replacement. Consistent with geological and geochemical data, it has a distribution similar to that of gold mineralization.

Regardless of the variability in the "least altered" sample group, this normalization method reasonably illustrates the various hydrothermal alteration zones. Primary geochemical variations due to lithological diversity have been strongly attenuated, allowing a better documentation of the hydrothermal alteration. Some variation remains, especially in the case of units 4E and 4F that can be locally interlayered, or for unit 4B, the Al_2O_3 content of which is very different between the clastic facies (4Bc) and the "pure" oxide-BIF (4B). Nevertheless, "distal" potassic and proximal carbonate alteration are well constrained and show the contrast of reactivity between the different rock types (BIF vs. mafic volcanic). Potassic alteration is much better developed in mafic volcanic rocks (unit Bvol) than most sedimentary lithologies (4E, 4EA, 4B, 4A). Carbonate alteration is better expressed by mafic volcanic rocks and "pure" oxide-BIF (units Bvol and 4B). The alteration zones also show a strong spatial relationship with high strain zones (chapter 5), which acted as major fluid pathways. It may also explain the typical Na_2O enrichment along these high strain zones, despite the lack of correlation with gold or potassic/carbonate alteration. The distribution of alteration zones illustrates the influence of the NIF, while the distribution of gold exemplifies the role of unit 4EA as a chemical trap.

The use of DDH geochemical profiles constitute a deposit-scale approach to study the distribution hydrothermal alteration at Musselwhite. It outlines that iron formation lithologies have inherent variability that will impact the study of alteration at sample scale, and that each unit has a slightly different alteration signature. Drill core observations have also shown that great variations in alteration intensity, deformation intensity, and gold grade can take place within decametres (Figure 8-1). Consequently, the next sections of the chapter focus on hydrothermal alteration of mafic volcanic rocks and of BIF units.

8.3 Alteration characteristics of mafic volcanic rocks (unit Bvol)

Samples from unit Bvol have been taken on sections 11775 N, 12000 N, and 12675 N, from drill holes that targeted the ore zones of the NIF.

8.3.1 Alteration mineral assemblages

Overall, biotite alteration is widespread in unit Bvol. It is strongest near major, carbonate-altered high strain zones, such as the "conveyor shear" (chapter5; Figure 5-30). In addition, mafic rocks are typically weakly to moderately altered close to or at the contact with units 4E and 4F "intraformational" lenses and with the NIF.

Biotite and carbonate alteration is developed in rocks exposed at PQ trench and in mined-out open pits in the mine area (Figures 3-9B, 8-10A, B and 8-11). Relative timing relationships suggest that alteration is largely syn-deformation. Boudins of altered mafic rock and quartz-carbonate veins suggest deformation slightly outlasts alteration (Figure 8-11B). Potassic alteration is marked by the progressive development of light-brown biotite in green amphibolitic mafic rock (Figure 8-12A, B, C). Plagioclase feldspar is preferentially and commonly completely altered to sericite. As alteration increases, hornblende is replaced by biotite, and patches of deep brown biotite are formed.

Carbonate alteration commonly affects rocks that are biotite alterated (Figure 8-12D, E, F). Calcite is present as discrete wisps and veinlets in weakly altered rocks and as a pervasive, anastomosed network in the most strongly altered rocks (Figures 5-30 and 8-12D). In carbonate-altered rocks, elongated garnet porphyroblasts are locally present (Figure 8-12D). In some occurrences, carbonate alteration comprise an assemblage of hornblende-diopside/hedenbergite-quartz-calcite (Figure 8-12E, F, G). The presence of clinopyroxene either relates to an alteration under amphibolite facies metamorphic conditions or to a metamorphosed carbonate alteration, similar to that observed in the iron formation (chapter 6).

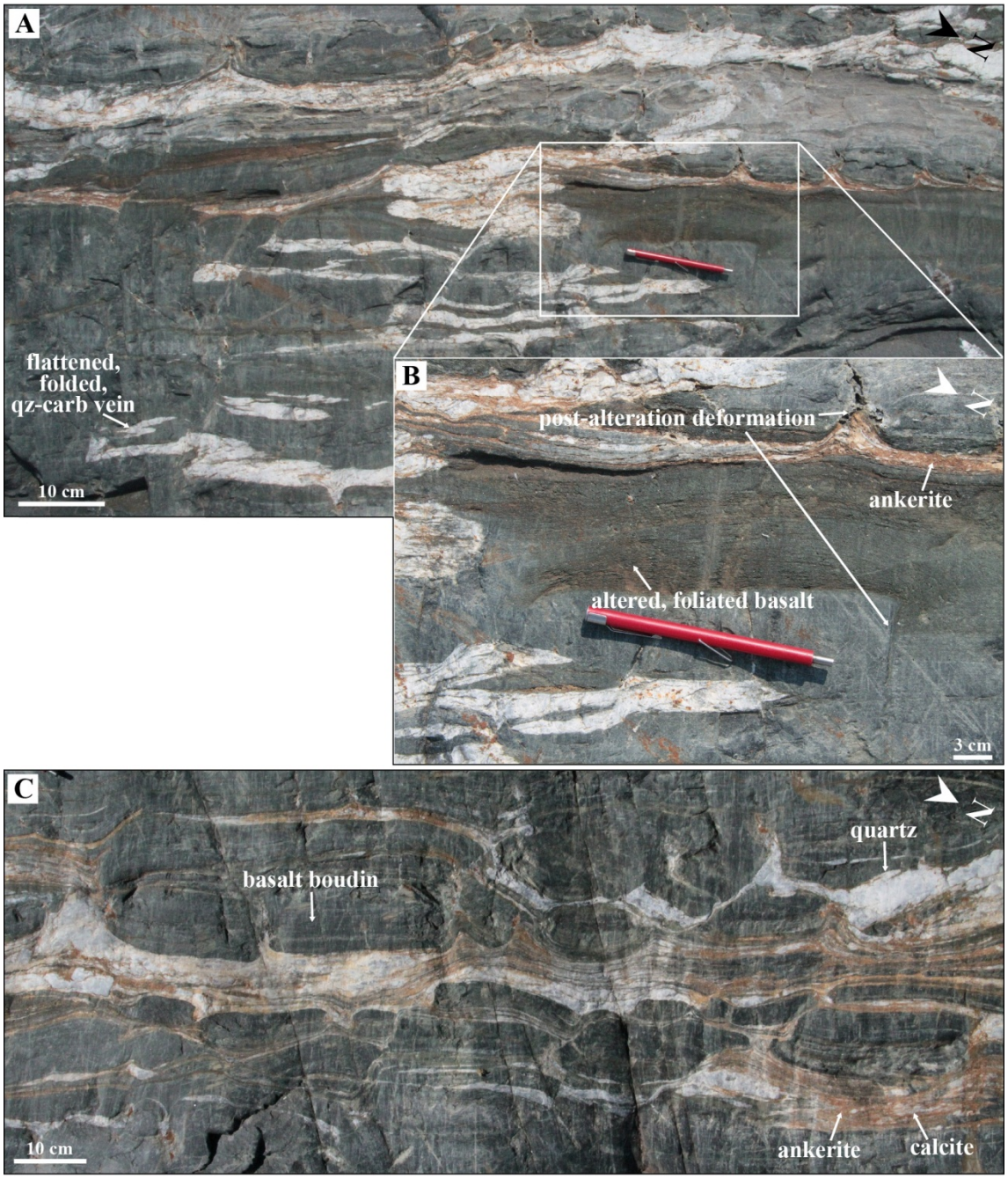

Figure 8-11: Biotite and carbonate alteration in unit Bvol, PQ trench, mine area. A. Quartz veins with ankerite-calcite proximal alteration halo in Bvol basalt. Veins are affected by D_2-folding, and D_2-flattening is evidenced by strong boudinage. B. Close-up on proximal alteration near the veins. The difference in foliation intensity as well as the development of boudinage show deformation outlasted veining and alteration. C. Intense deformation of quartz-carbonate veins in Bvol basalt.

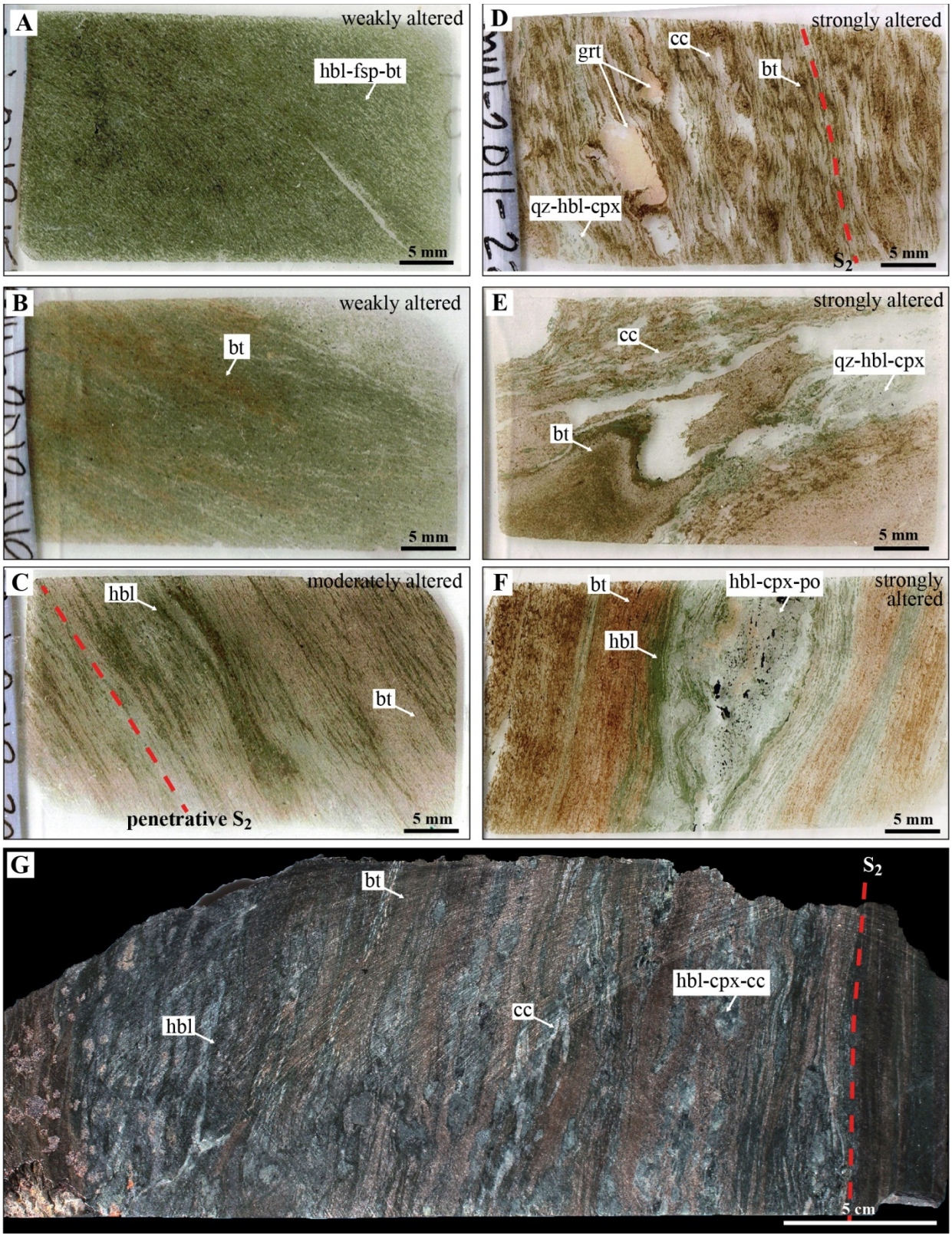

Figure 8-12: Altered mafic volcanic rocks. A. Thin section scan of sample MW-12-156, DDH 06-PQE-091. Biotite alteration is weak and hardly visible on hand-scale sample. B. Thin section scan of sample MW-12-

149, DDH 06-PQE-091. Brown biotite is more abundant. C. Thin section scan of sample MW-12-321, DDH 06-PQE-095. The sample is strongly foliated and shows well-developed biotite alteration. D. Thin section scan of sample MW-11-221, DDH 10-PQE-055. This sample is located within an intersection of the "conveyor shear", as illustrated by the intense biotite and carbonate alteration as well as the intense S_2 fabric. Alteration intensity is also evident from the presence of garnet porphyroblast elongated parallel to S_2. The sample appears to have experienced a strong flattening. E. Thin section scan of sample MW-12-301, DDH 06-PQE-095. Strongly biotite-altered mafic rock includes a deformed quartz-calcite vein and adjacent hornblende-diopside assemblage. F. Thin section scan of sample MW-13-363, DDH 12-PIL-001, mine level 280, Esker area. The strongly biotite-altered mafic rock displays overprinting hornblende-diopside-quartz-pyrrhotite-calcite alteration. Within a few metres of the mafic rock, unit 4EA of the NIF is gold-mineralized. G. Slab of underground sample MW-13-UG-044, mine level 620, showing hornblende-diopside-calcite alteration in mafic rocks overlying the NIF.

8.3.2 Geochemical variations

Geochemical data of unit Bvol includes 106 samples. The "least altered" samples (n = 36) were selected through macroscopic examination and then using Na_2O vs. K_2O binary plot as a first indicator of alteration (Figure 8-13A). Na_2O leaching is characteristic in this type of geological setting (Dubé and Gosselin, 2007). Samples outside the 2.5-3.9 wt.% Na_2O range were excluded; remaining samples were all under 0.6 wt.% K_2O. Samples with excessive values of CO_2 (<1.5 wt.%) and total S (<0.2 wt.%) were also excluded. The average composition of least altered Bvol samples is given in Table 8-2, with standard deviation. Altered samples (n = 70) show a clear trend of K_2O enrichment and Na_2O leaching (Figure 8-13A).

As shown in Figure 8-13, CO_2 enrichment is an indicator of increased alteration. Geochemical data show that CO_2 enrichment causes a relative decrease in Al_2O_3 content (Figure 8-13B). As Al is a relatively "immobile" element in most contexts of alteration (Rollinson, 1994), this "dilution" reflects rock volume change during alteration (Groves and Foster, 1993), as well as the "closure" effect inherent to geochemical analyses. CO_2 enrichment can be monitored in whole-rock data using the Calcite Index (CC index; Figure 8-13C). CC index values represent the ratio of the molar proportions of CO_2 over CaO. Values increase with alteration, yet are almost exclusively under 1. This is interpreted as showing that calcite is the only carbonate mineral present in the rock. It is consistent with petrographic observations on drill core samples, although ankerite is locally present on surface exposures (Figure 8-11). The projection of data between the CC index and the ratio K_2O/Al_2O_3, which relates to potassium-bearing silicates (Davies et al., 1982), shows the alteration trends start with an increase in the K_2O/Al_2O_3 ratio, followed by that of the CC index, as carbonate alteration intensifies (Figure 8-13D).

Altered samples (n = 70) can be redistributed into CO_2-poor and CO_2-rich groups. The threshold value was arbitrarily chosen at 5 wt.%, putting 45 samples in the former group and 25 in the latter. 5 wt.% is also roughly the value around which CO_2 enrichment causes a relative decrease in Al_2O_3 content. To

study trace element variations, the issue of "immobile" element variations can be mitigated using an isocon diagram (Grant, 1986). Two diagrams were made, using the average composition of each group of altered samples and the average composition of least altered samples (Table 8-2; Figures 8-14, 8-15).

The equation of the isocon was determined using the average of Al_2O_3, TiO_2, and Zr ratios between least altered composition and altered composition (i.e., $((Al_2O_{3A}/Al_2O_{3LA}) + (TiO_{2A}/TiO_{2LA}) + (Zr_A/Zr_{LA}))/3$). For the altered group 1 (moderate alteration; Figure 8-14), K_2O shows the highest enrichment. Other enrichments include: CO_2, total S, B, Tl, Se, As, Pb, and Sb. Na_2O is the main depleted element. Stronger alteration (altered group 2) results in markedly high Au, K_2O, CO_2, and total S enrichments (Figure 8-15). Other enriched elements include: CaO, Zn, B, Pb, Ag, Se, Tl ± Te, and MnO. Depletion in Na_2O is increased relatively to altered group 1, and MgO, Sb, and Ge are also depleted.

Table 8-2: Average major element composition and standard deviation of least altered and altered samples of unit Bvol. Least altered samples, n = 36; altered group 1, n = 45; altered group 2, n = 25.

	Au	SiO_2	Al_2O_3	Fe_2O_3	FeO	Fe_2O_3 (T)	MnO	MgO
Least altered Average	14.6	49.12	15.62	1.53	10.13	12.79	0.19	8.31
Standard deviation	13.4	1.25	0.56	1.27	1.28	1.04	0.03	1.03
Altered group 1 Average	75.8	49.2	15.5	1.6	9.6	12.2	0.2	6.2
Standard deviation	287.8	4.2	2.1	1.2	2.4	2.7	0.1	2.3
Altered group 2 Average	122.5	41.1	12.3	1.3	8.5	10.8	0.4	3.0
Standard deviation	428.0	4.7	2.6	0.8	3.3	4.0	0.1	1.6

	CaO	Na_2O	K_2O	TiO_2	P_2O_5	CO_2	Total S	LOI
Least altered Average	8.31	3.17	0.25	0.81	0.06	0.43	0.05	0.95
Standard deviation	1.74	0.37	0.17	0.13	0.01	0.40	0.04	0.43
Altered group 1 Average	9.6	1.7	2.0	0.8	0.1	1.3	0.1	2.1
Standard deviation	2.8	1.3	1.2	0.2	0.0	1.2	0.1	1.2
Altered group 2 Average	17.5	0.5	2.6	0.7	0.1	10.2	0.8	9.6
Standard deviation	4.7	0.6	0.8	0.2	0.0	4.5	1.9	4.0

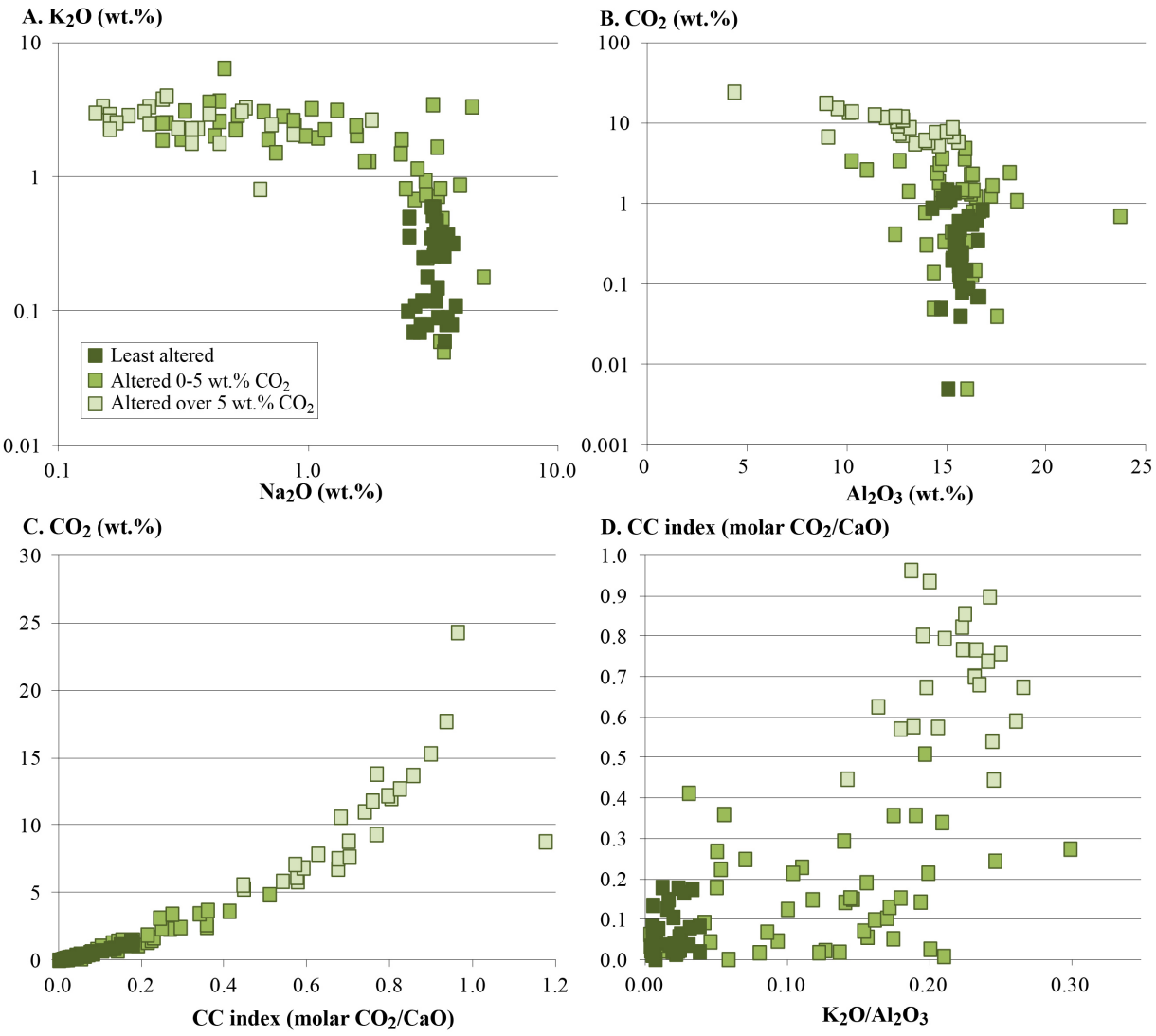

Figure 8-13: Geochemical footprint of alteration in unit Bvol. A. Binary plot of Na_2O vs. K_2O showing the sharp contrast between least altered mafic rocks and Na_2O-depleted, K_2O-enriched altered rocks. B. Binary plot of CO_2 vs. Al_2O_3. It shows the relative decrease of aluminum in samples due to the closure effect of geochemical analyses as well as the potential rock volume change during alteration (Groves and Foster, 1993). C. Binary plot of the Calcite Index (molar CO_2/CaO) vs. CO_2 in wt.%. CO_2 can reach 25 wt.% of the rock. Values of calcite index under 1 mean that only calcite is present; values over 1 mean dolomite-ankerite is present. D. Binary plot of Calcite Index vs. K_2O/Al_2O_3. The trend of alteration shows initial potassium enrichment followed by an increase of the calcite index, as carbonate alteration intensifies.

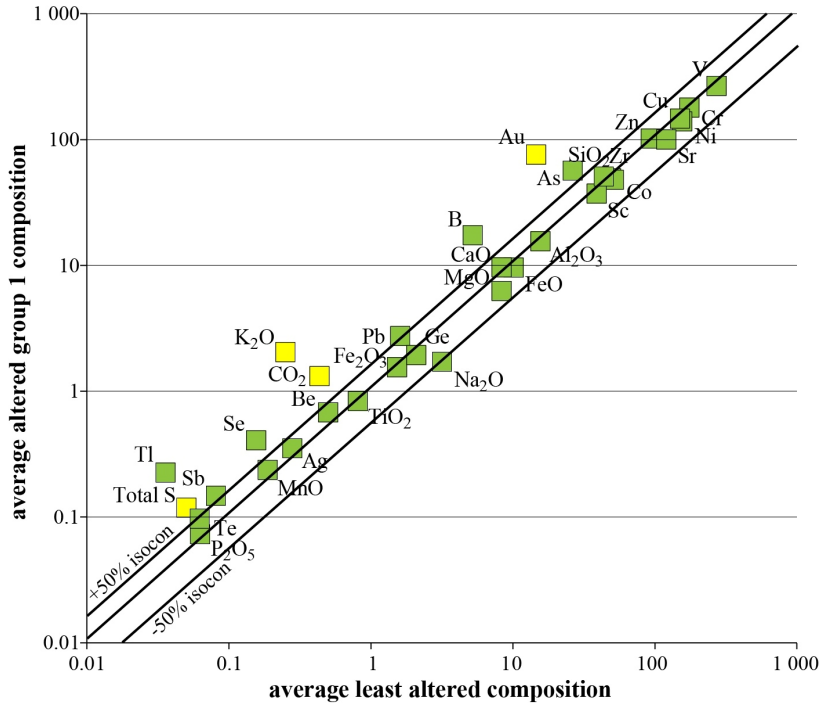

Figure 8-14: Isocon diagram between "least altered" and moderate alteration (altered group 1) average compositions (Table 8-2). Isocons were traced using Al_2O_3, TiO_2, and Zr ratios.

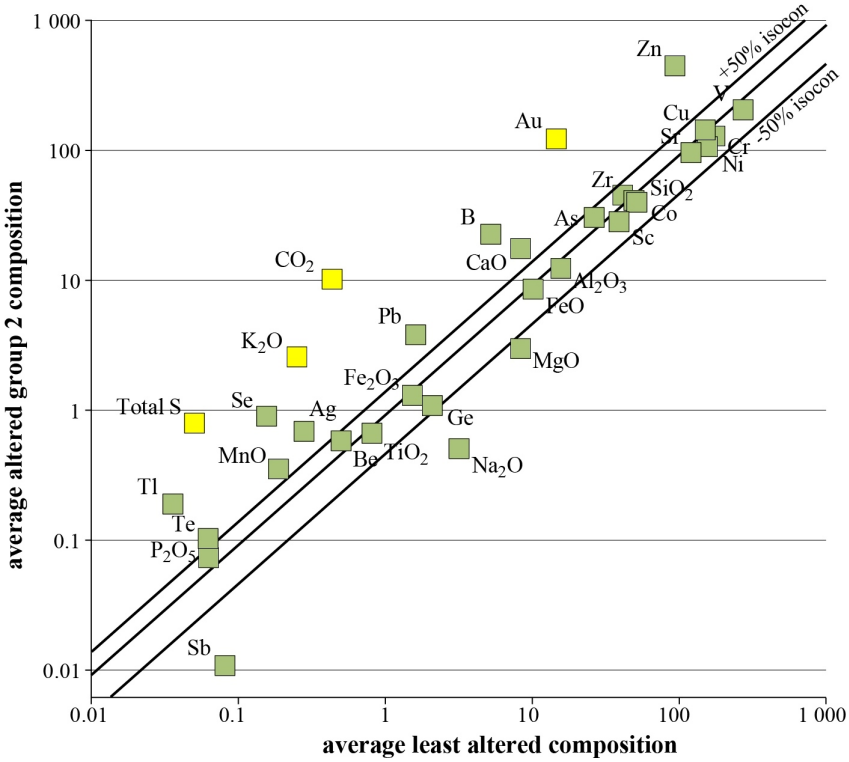

Figure 8-15: Isocon diagram between "least altered" and strong alteration (altered group 2) average compositions (Table 8-2). Isocons were traced using Al_2O_3, TiO_2, and Zr ratios.

8.4 Alteration characteristics of unit 4EA

Gold-related alteration of the iron formation at Musselwhite include biotite, magnetite conversion to grunerite, carbonate (especially in oxide facies), sulphidation, silica flooding, and garnet size/shape/colour variations (Hall and Rigg, 1986; Couture, 1995; Blower and Kiernan, 2003; Moran, 2008). Some garnet in chert-magnetite BIF was also attribute to alteration (Couture, 1995). Petrographic data from barren and gold-mineralized rocks shows that minerals such as biotite, grunerite, hornblende, and garnet are present in both metamorphic and hydrothermal and/or ore mineral assemblages (chapters 6 and 7). Finally, as ore zones mostly occur at contacts between different rock types (e.g., unit 4F vs. unit 4B; Figures 7-2, 7-3, 7-4), the development and type of alteration are affected by their distinct chemical composition and reactivity.

8.4.1 Alteration mineral assemblages

8.4.1.1 Garnet-grunerite-quartz-biotite mineral assemblage

Evidence of hydrothermal alteration of unit 4EA mainly consists in the presence of an assemblage of garnet, grunerite, quartz, and biotite (Figure 8-16). Biotite can be of metamorphic or hydrothermal origin. Metamorphic biotite, stemming from the detrital component of unit 4EA, is commonly characterized by a diffuse distribution of biotite in silicate bands (Figure 8-16A, B). In such cases, biotite is fine-grained and medium brown. Contrastingly, hydrothermal biotite is usually concentrated in specific layers (Figure 8-16C, D, E), coarser and of a darker brown. However, colour is an unreliable criterion, as biotite is locally green (Figure 7-10). Garnet porphyroblasts in biotite-rich layers tend to be coarser than in grunerite bands, as well as more euhedral (Figure 8-16C, D).

Another feature of alteration of unit 4EA is that magnetite in the matrix tends to be replaced by secondary grunerite (Figure 8-17). This process is enhanced by hydrothermal fluid flow, especially near chert bands, which provide the silica required for the reaction. Such hydrothermal grunerite is coarser and contains scattered, fine-grained pyrrhotite and chalcopyrite inclusions (Figure 8-17B). This phenomenon is also observed in unit 4B (section 8.6).

8.4.1.2 Garnet-grunerite-quartz-hornblende/actinolite-quartz mineral assemblage

In addition to biotitisation, the development of a garnet-grunerite-hornblende/actinolite/tschermakite-quartz mineral assemblage represents another major mineralogical change in unit 4EA (Figure 8-18).

Matrix composition progressively evolves from fine-grained beige grunerite to fine-grained, green hornblende and ferro-tschermakite. In weakly deformed samples, grunerite is preferentially distributed near garnet porphyroblasts (Figures 8-18A, C; 8-19A, B). In strongly deformed samples, grunerite is concentrated in silica-rich bands and near garnet porphyroblasts (Figure 8-18B, D). Garnet porphyroblasts are pink to pale red, fine- to coarse-grained almandine. Iron-bearing carbonate minerals are rare, and calcite occurs locally. Calcite commonly occurs in association with hedenbergite (cpx) and grunerite (Figure 8-19C), possibly through alteration of Ca-amphiboles to hedenbergite-grunerite ± calcite.

The progressive replacement of grunerite by ca-bearing amphiboles such as hornblende and ferro-tschermakite requires a source of Ca, as grunerite only contains Fe and Si. Ca can be locally sourced from adjacent phases such as carbonates (of metamorphic or hydrothermal origin) or garnet porphyroblasts, or externally sourced via Ca-bearing hydrothermal fluids. The former means that altered and “least altered” 4EA samples should contain similar amounts of CaO; while the latter implies Ca-enrichment during alteration.

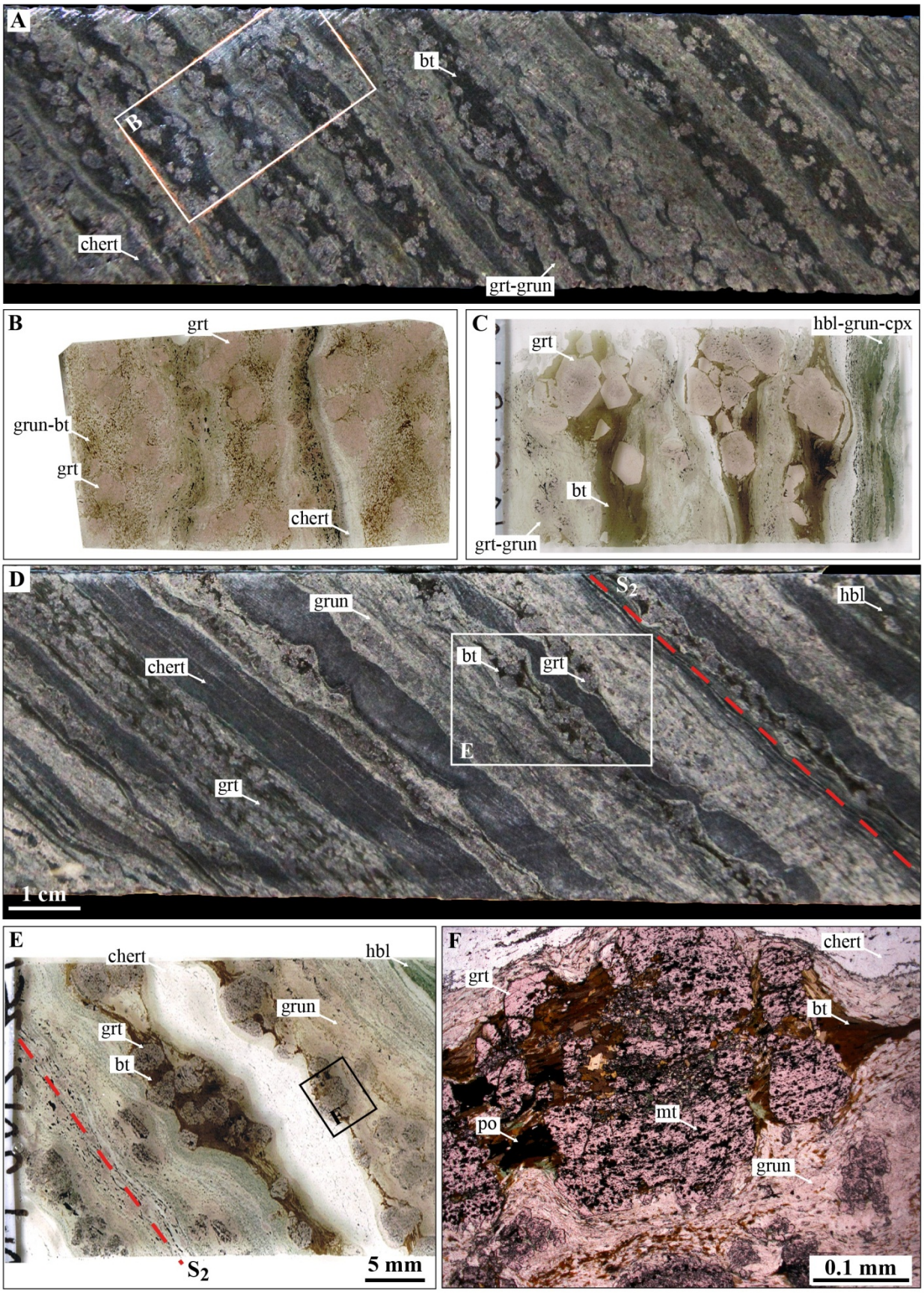
A
B
bt
chert
grt-grun
B
grt
grun-bt
grt
chert
C
grt
hbl-grun-cpx
bt
grt-grun
D
grun
S_2
hbl
chert
bt
grt
E
grt
1 cm
E
chert
hbl
grun
grt
bt
F
S_2
5 mm
F
chert
grt
bt
mt
po
grun
0.1 mm

Figure 8-16: Garnet-grunerite-biotite-quartz mineral assemblage in unit 4EA. A. Drill core section of unit 4EA, sample MW-12-349, DDH 09-TAN-014. The initial chert-garnet-grunerite compositional layering has been altered and includes biotite-rich bands. White box represents location of thin section. B. Thin section scan of sample MW-12-349. Biotite is quite homogeneously distributed in the matrix. C. Thin section scan of unit 4EA, sample MW-13-011, DDH 09-TAN-029. Biotite is preferentially distributed in semi-massive biotite bands including zoned, euhedral garnet porphyroblasts. D. Drill core section of sample MW-13-356, DDH 12-PIL-001. The transposed layering of unit 4EA contains garnet-biotite layers. E. Thin section scan of sample MW-13-356. Biotite is preferentially distributed on either sides of the chert band, underlining the role of band boundaries for fluid flow. Garnet in or near biotite is coarser and more euhedral. F. Close-up of E. in plain polarized light showing biotite surrounding garnet and to a lesser extent in the grunerite matrix. Some pyrrhotite-chalcopyrite is present between garnet grains. Opaque inclusions in garnet solely contain magnetite.

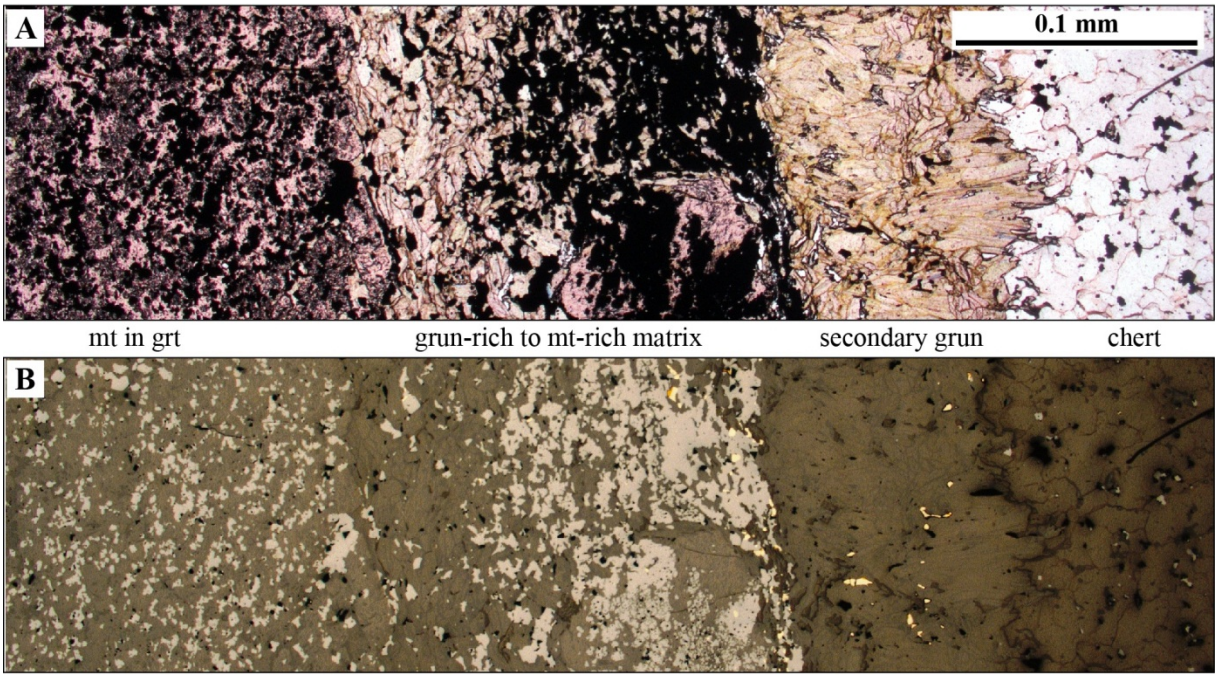

Figure 8-17: Secondary grunerite in unit 4EA. A. Primary and secondary grunerite at the boundary between a silicate band and a chert band, plain polarized light. Primary grunerite is intergrown with magnetite. Secondary grunerite is coarser grained and contains scattered sulphide grains. B. Same as A. in reflected light.

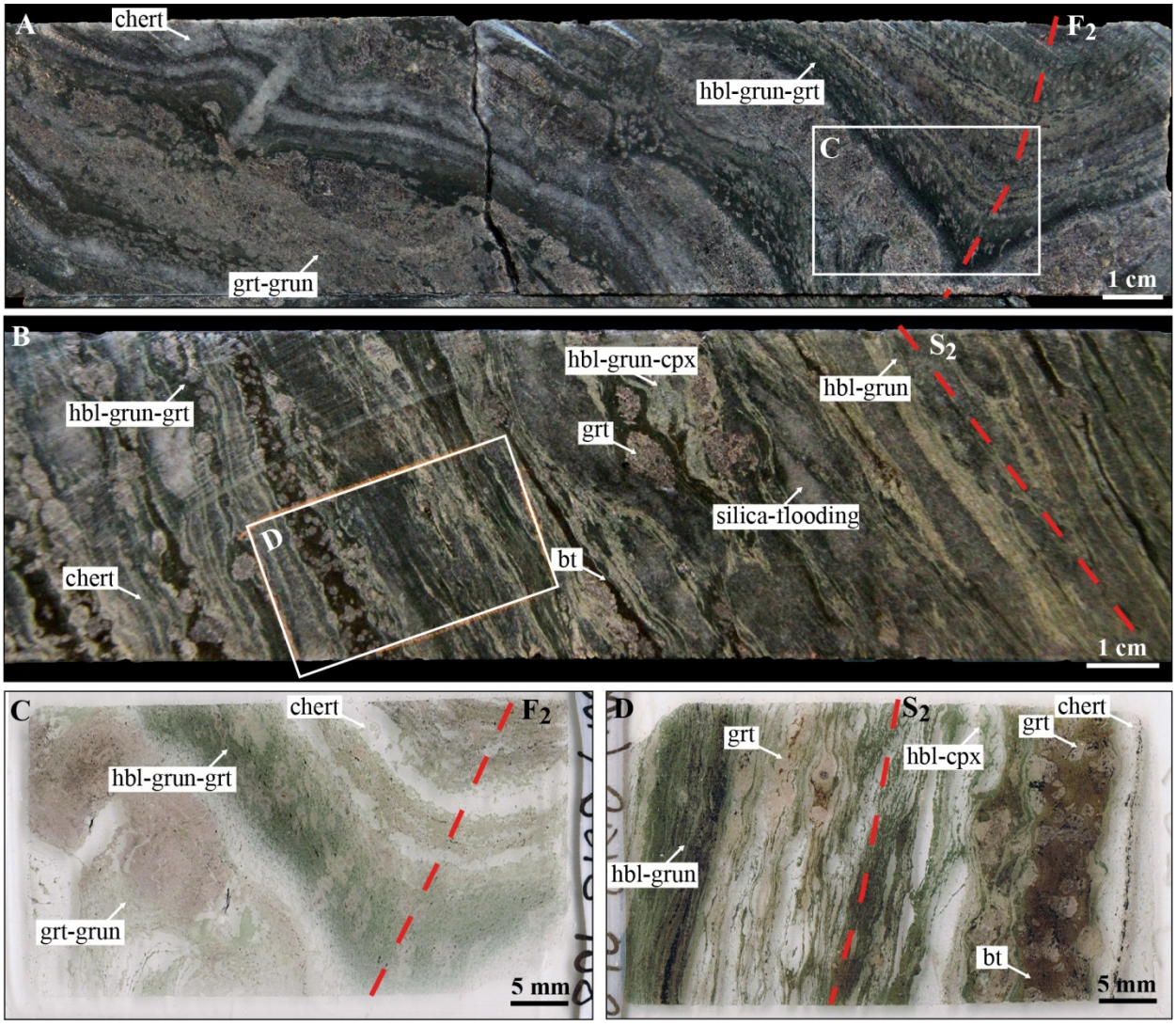

Figure 8-18: Proximal, Ca-amphibole-bearing alteration in unit 4EA. A. Drill core segment of sample MW-13-128, DDH 09-TAN-060, 136 ppb Au. The iron formation is affected by an open F_2 fold. B. Drill core segment of sample MW-12-362, DDH 09-TAN-014, 437 ppb Au. The iron formation is strongly disrupted and partially transposed, with silica flooding. C. Thin section of sample MW-13-128. Coarse, centimetre-size garnets are in grunerite-rich bands. Hornblende-rich bands contain sub-millimetre-size garnets surrounded by a halo of grunerite. D. Thin section scan of sample MW-12-362. Mechanical segregation of minerals is producing a new metasomatic/metamorphic layering, notably a garnet-biotite band.

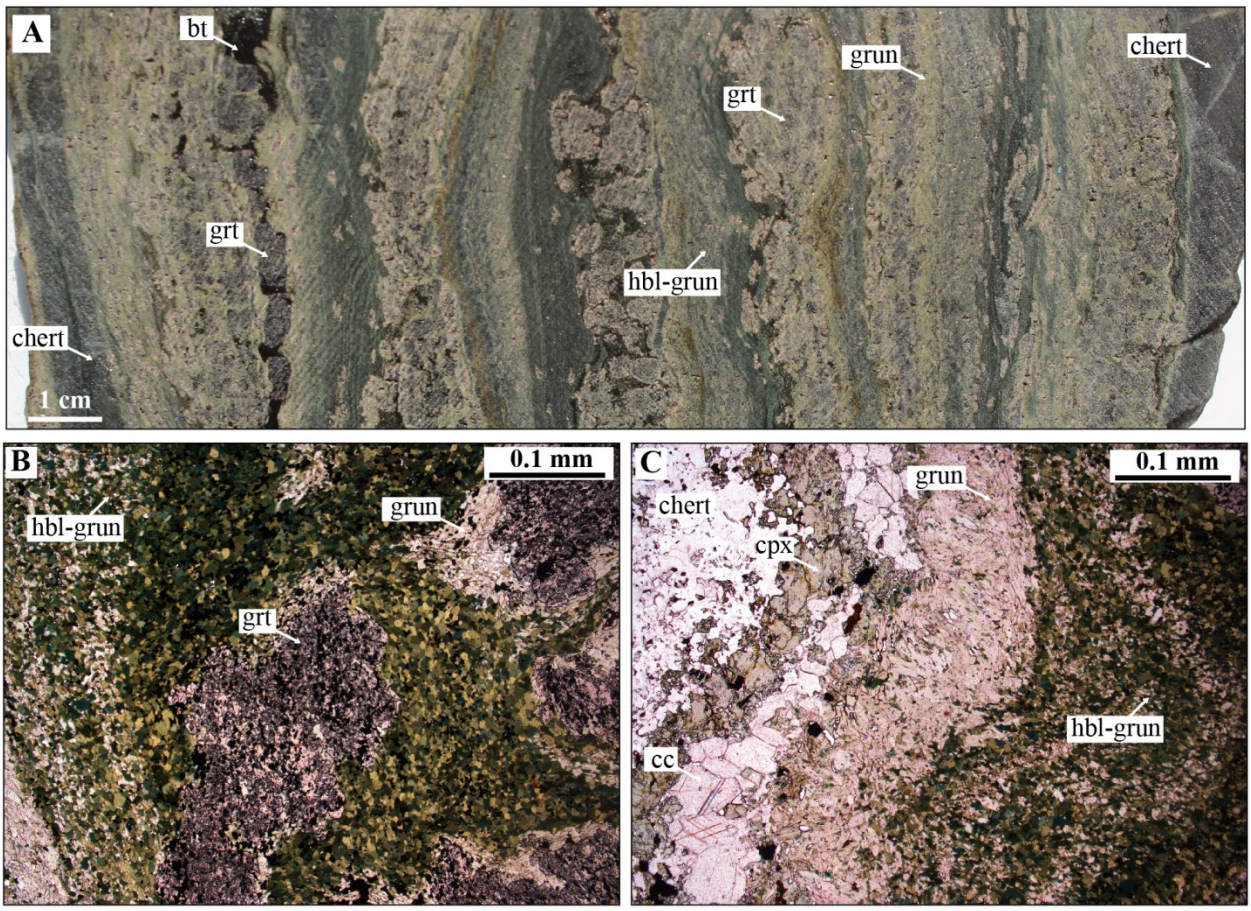

Figure 8-19: Garnet-grunerite-hornblende-quartz assemblage in unit 4EA. A. Slab of underground sample MW-12-UG-077, mine level 770, section 12780 N. It shows a thin layer of dark brown biotite produced by potassic alteration, progressive replacement of grunerite by Ca-amphibole due to calcic alteration, and a little iron staining indicating the presence of sulphide. B. Hornblende-rich matrix containing poikiloblastic garnet porphyroblasts with grunerite corona and/or pressure shadows. Plain polarized light, sample MW-12-248, DDH 06-PQE-013. C. Hedenbergite (cpx)-calcite-grunerite assemblage at the boundary between chert and silicate bands. Plain polarized light, sample MW-12-248, DDH 06-PQE-013.

8.4.2 Geochemical variations

Due to primary variations of unit 4EA (section 8.2.2; Table 3-4), geochemical data was projected in a ternary SiO_2-Al_2O_3-total Fe_2O_3 diagram (Figure 8-20A). It allows assessing component variations of BIF samples, which are, excluding high-grade samples, fairly stable. SiO_2 and Al_2O_3 are used on ternary plots to monitor chemical and detrital inputs of the BIF.

Relating alteration mineral assemblages with geochemical variations is confronted with the scale of observations and sampling. For example, stongly altered 4EA samples show replacement of grunerite by Ca-amphiboles, but still contain biotite-rich layers (Figures 8-18 and 8-19). This relates to the sampling method: longer drill core segments allow for an averaging of primary variations; however, they also

average the alteration signature. As a result, geochemical variations are partly obscured. The most practical way of sorting samples was to use gold content to define six groups, as follows: “least altered” samples, samples with 2.5-100 ppb Au, 101-1000 ppb Au, 1-5 ppm Au, 5-15 ppm Au, and over 15 ppm Au.

K_2O content does not significantly corrolate with gold content (Figure 8-20B). CaO appears slightly enriched in samples of intermediate to high gold grade (Figure 8-20C); and total S displays the clear positive correlation with gold content (Figure 8-20D). Separately examining Fe_2O_3 and FeO (Figure 8-21A, B) shows that variations of iron are due to loss of Fe_2O_3 in high-grade samples (i.e., due to sulphide-replacement of the BIF). CO_2 is enriched overall in altered samples, but the relation with gold content is not clear (Figure 8-21C). Lastly, Na_2O shows some enrichment, but there is no apparent link with gold content (Figure 8-21D). Projections with a selection of trace elements confirm correlations identified previously (chapter 7): Ag, Cu, Se, and Te are positively correlated with Au content (Figure 8-22A, B, C, D). Pb and Ga also show weakly developed trend (Figure 8-22E, F). Contrastingly, As, Bi, Sb, and Tl do not show any association with gold (Figure 8-22G, H, I, J).

These observations are confirmed by Pearson correlation coefficient (PCC) calculations using all altered and gold-rich samples of unit 4EA (n = 237; Table 8-3). These PCC were calculated for all major elements as well as an extended selection of trace elements, and show that K_2O correlates positively with Be (0.40), Tl (0.71), Cs (0.43), Ba (0.65), and Rb (0.95). This association is particularly outlined with the average composition of samples with 2.5 to 100 ppb gold, which has the highest enrichment in K_2O, Be, Tl, Cs, Ba and Rb (Figure 8-23).

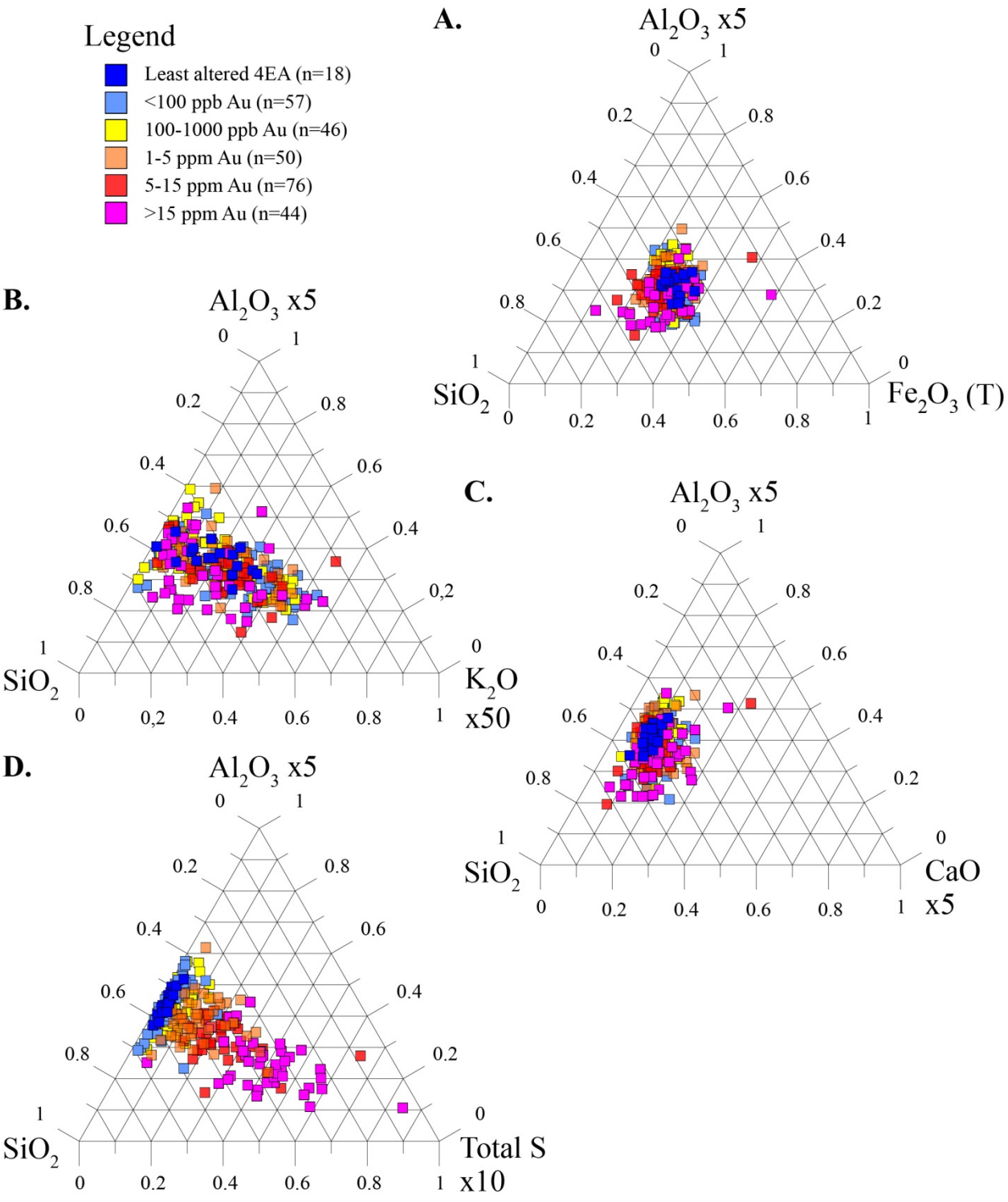

Figure 8-20: SiO_2-Al_2O_3-X ternary diagrams of major elements in unit 4EA. SiO_2 and Al_2O_3 are used to monitor primary compositional variations, combined with: A. total iron content, showing that the main components of unit 4EA retain quite stable proportions regardless of alteration; B. K_2O, showing the absence of clear trend; C. CaO, showing a slight enrichment in CaO with increasing gold values; and D. total S, showing the strong relation between gold content and sulphur.

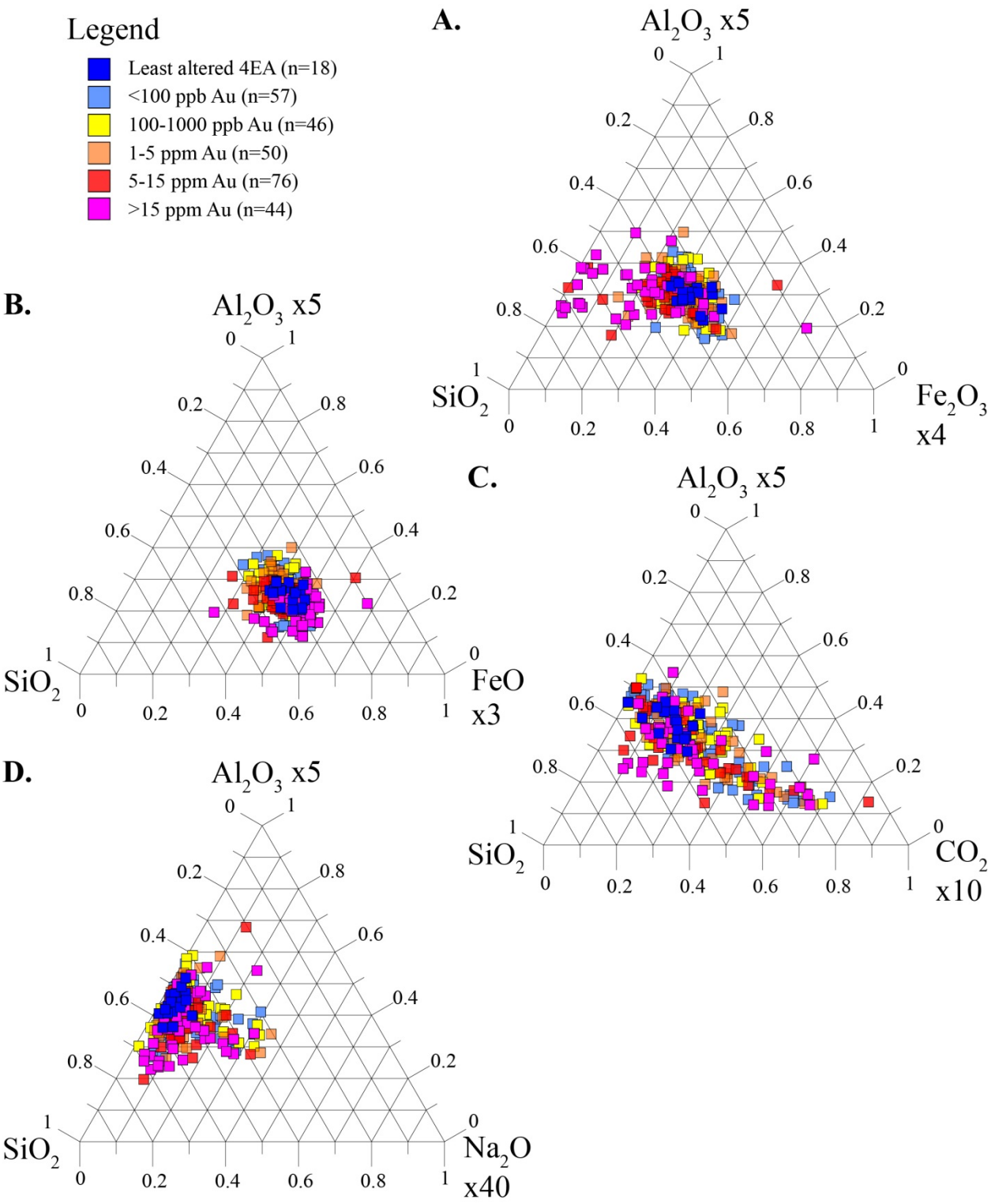

Figure 8-21: SiO_2-Al_2O_3-X ternary diagrams of major elements in unit 4EA. SiO_2 and Al_2O_3 are used to monitor primary compositional variations, combined with: A. Fe_2O_3 content, showing a decrease for strongly altered/mineralized samples; B. FeO, showing overall stable content through alteration; C. CO_2, showing no specific trend; and D. Na_2O, showing the variable content but no clear trend relative to gold content.

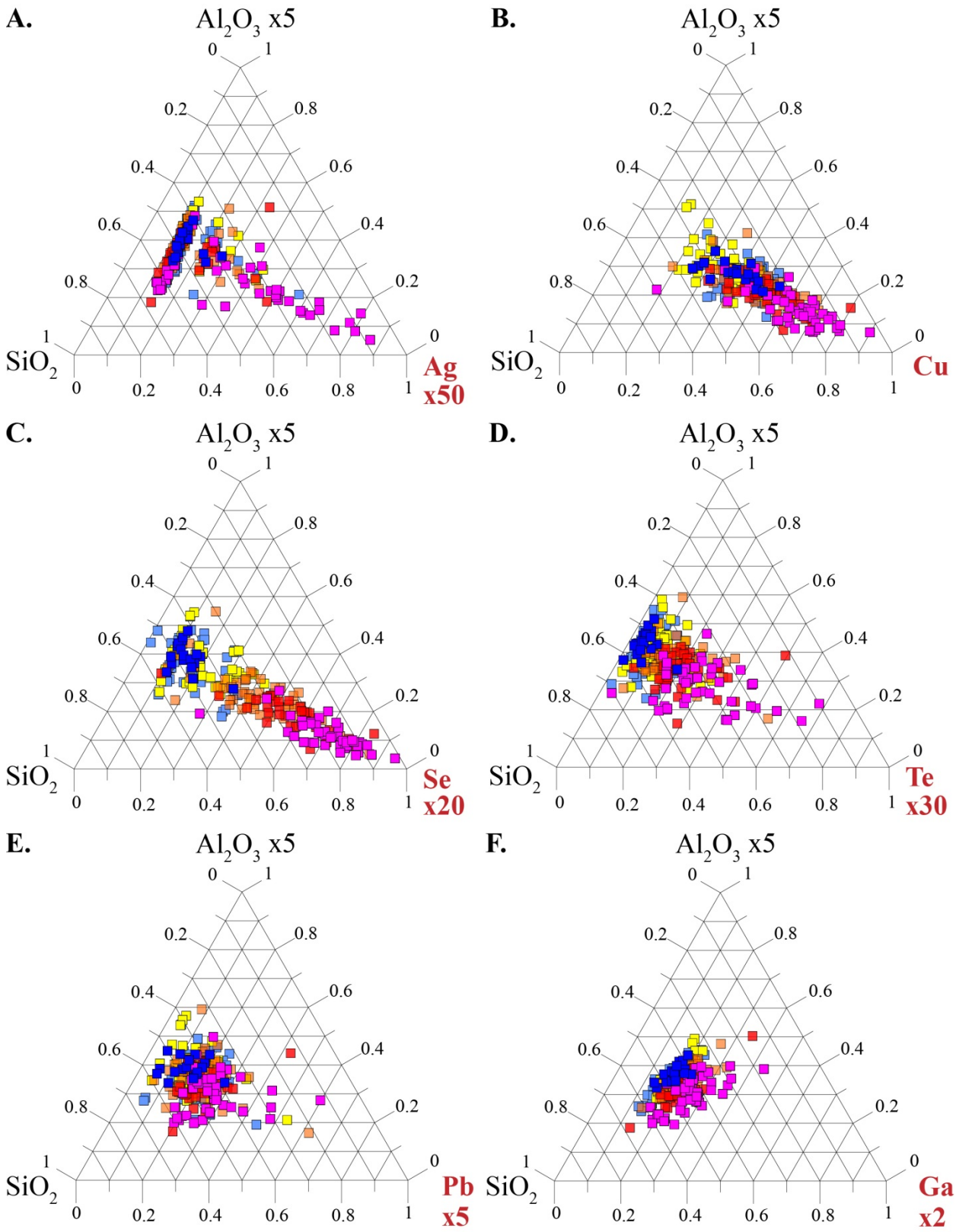
A.
Al_2O_3 x5
SiO_2
Ag x50
B.
Al_2O_3 x5
SiO_2
Cu
C.
Al_2O_3 x5
SiO_2
Se x20
D.
Al_2O_3 x5
SiO_2
Te x30
E.
Al_2O_3 x5
SiO_2
Pb x5
F.
Al_2O_3 x5
SiO_2
Ga x2

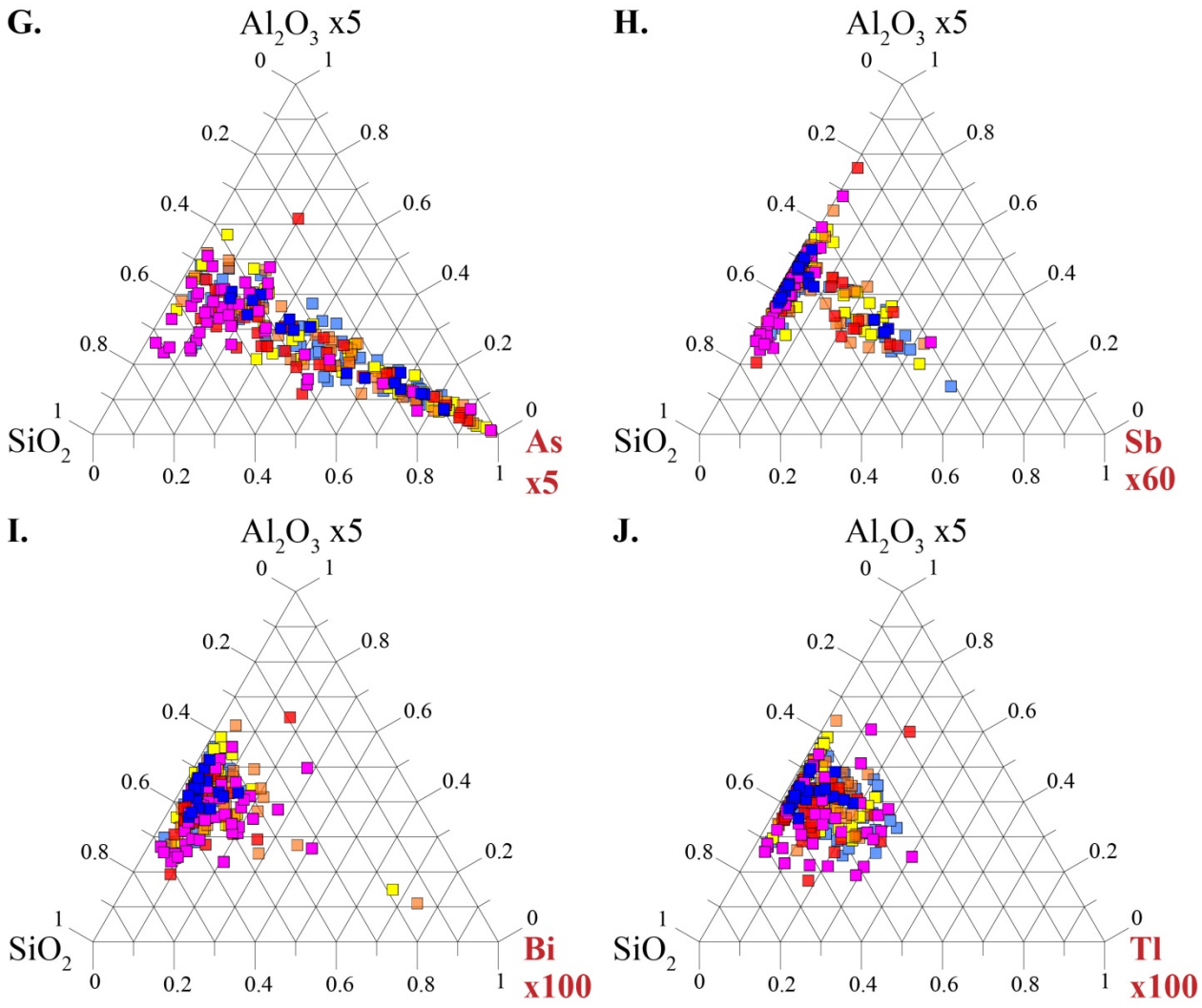

Figure 8-22: SiO_2-Al_2O_3-X ternary diagrams of trace elements in unit 4EA. SiO_2 and Al_2O_3 are used to monitor primary compositional variations, combined with: A. to F., trace elements positively correlated with gold content (as shown in chapter 7); G. to J., trace elements with no correlation with gold.

Table 8-3: Pearson correlation coefficients of major and trace elements of unit 4EA altered and mineralized samples (n = 237). Calculations were made using geochemical data of all samples excluded during the selection of the "least altered" samples.

	SiO_2	Al_2O_3	Fe_2O_3	FeO	MnO	MgO	CaO	Na_2O	K_2O	TiO_2	P_2O_5	CO_2	Total S	B	Be	Cr	Co	Ni	Sc	V	Cu	Pb	Zn	Ag	Au	As	Ge
SiO_2	1	**-0.38**	**-0.58**	**-0.69**	**-0.34**	**-0.60**	**-0.13**	0.02	-0.07	**-0.39**	**-0.20**	**-0.13**	**-0.27**	0.00	**-0.14**	**-0.23**	**-0.32**	**-0.30**	**-0.41**	**-0.43**	**-0.18**	-0.07	**-0.23**	-0.04	0.03	0.02	**-0.19**
Al_2O_3	**-0.38**	1	**0.18**	-0.03	**0.17**	**0.63**	-0.06	**0.15**	**0.21**	**0.85**	-0.09	**-0.22**	**-0.22**	**0.14**	0.00	**0.76**	**0.53**	**0.58**	**0.91**	**0.82**	-0.11	0.04	**0.43**	-0.04	**-0.22**	0.10	**0.40**
Fe_2O_3	**-0.58**	**0.18**	1	0.00	**0.36**	**0.21**	**-0.15**	-0.06	0.06	**0.21**	**0.27**	0.09	**-0.24**	0.01	**0.33**	**0.13**	0.04	0.05	**0.22**	**0.14**	**-0.29**	**-0.18**	-0.02	**-0.19**	**-0.38**	-0.05	**0.39**
FeO	**-0.69**	-0.03	0.00	1	**0.21**	**0.33**	0.00	-0.11	-0.10	-0.04	**0.17**	-0.06	**0.49**	-0.09	-0.08	-0.09	0.08	0.04	-0.03	0.05	**0.35**	0.08	0.07	**0.18**	**0.26**	-0.08	-0.08
MnO	**-0.34**	**0.17**	**0.36**	**0.21**	1	**0.33**	-0.07	**-0.25**	-0.01	0.12	**0.14**	0.04	**-0.29**	0.01	**0.14**	**0.19**	-0.02	-0.01	**0.16**	0.06	**-0.20**	**-0.18**	**0.23**	**-0.14**	**-0.22**	0.06	**0.35**
MgO	**-0.60**	**0.63**	**0.21**	**0.33**	**0.33**	1	**0.21**	-0.09	-0.04	**0.59**	0.11	-0.03	-0.06	-0.05	0.03	**0.49**	**0.41**	**0.43**	**0.62**	**0.59**	0.01	0.05	**0.52**	-0.04	-0.12	0.06	**0.26**
CaO	**-0.13**	-0.06	**-0.15**	0.00	-0.07	**0.21**	1	0.01	**-0.13**	0.06	0.06	**0.66**	**0.19**	0.02	**0.14**	-0.05	**0.13**	**0.12**	0.02	0.11	**0.28**	0.09	**0.18**	0.01	0.05	0.05	**-0.20**
Na_2O	0.02	**0.15**	-0.06	-0.11	**-0.25**	-0.09	0.01	1	0.10	**0.21**	-0.03	-0.04	-0.01	0.03	**0.15**	0.07	**0.15**	0.11	**0.16**	**0.21**	-0.01	**0.27**	-0.09	**0.24**	-0.01	-0.05	0.09
K_2O	-0.07	**0.21**	0.06	-0.10	-0.01	-0.04	**-0.13**	0.10	1	**0.17**	-0.03	-0.05	**-0.20**	0.10	**0.40**	**0.15**	0.05	0.05	**0.18**	0.12	**-0.14**	0.11	-0.05	-0.08	-0.02	0.03	0.00
TiO_2	**-0.39**	**0.85**	**0.21**	-0.04	0.12	**0.59**	0.06	**0.21**	**0.17**	1	-0.08	-0.04	**-0.19**	**0.12**	0.02	**0.73**	**0.60**	**0.58**	**0.94**	**0.94**	-0.06	0.07	**0.38**	-0.02	**-0.16**	**0.12**	**0.37**
P_2O_5	**-0.20**	-0.09	**0.27**	**0.17**	**0.14**	0.11	0.06	-0.03	-0.03	-0.08	1	-0.04	**-0.18**	-0.11	**0.29**	-0.11	-0.10	-0.11	**-0.13**	**-0.13**	**-0.18**	-0.08	-0.04	**-0.13**	**-0.13**	0.01	0.03
CO_2	**-0.13**	**-0.22**	0.09	-0.06	0.04	-0.03	**0.66**	-0.04	-0.05	-0.04	-0.04	1	0.11	-0.03	**0.17**	**-0.13**	-0.05	-0.08	-0.09	-0.04	**0.15**	0.06	0.09	-0.05	-0.02	0.03	**-0.16**
Total S	**-0.27**	**-0.22**	**-0.24**	**0.49**	**-0.29**	-0.06	**0.19**	-0.01	**-0.20**	**-0.19**	**-0.18**	0.11	1	-0.04	**-0.41**	**-0.23**	**0.24**	**0.20**	**-0.21**	0.02	**0.76**	**0.34**	0.00	**0.40**	**0.54**	0.01	**-0.48**
B	0.00	**0.14**	0.01	-0.09	0.01	-0.05	0.02	0.03	0.10	**0.12**	-0.11	-0.03	-0.04	1	-0.02	**0.13**	**0.20**	**0.18**	**0.20**	**0.17**	0.00	-0.03	0.01	-0.01	-0.02	-0.01	0.03
Be	**-0.14**	0.00	**0.33**	-0.08	**0.14**	0.03	**0.14**	**0.15**	**0.40**	0.02	**0.29**	**0.17**	**-0.41**	-0.02	1	-0.02	-0.12	-0.11	0.03	-0.04	**-0.34**	0.00	-0.09	**-0.19**	**-0.23**	-0.10	**0.26**
Cr	**-0.23**	**0.76**	**0.13**	-0.09	**0.19**	**0.49**	-0.05	0.07	**0.15**	**0.73**	-0.11	**-0.13**	**-0.23**	**0.13**	-0.02	1	**0.55**	**0.69**	**0.79**	**0.71**	-0.05	-0.01	**0.35**	**-0.13**	**-0.22**	**0.15**	**0.40**
Co	**-0.32**	**0.53**	0.04	0.08	-0.02	**0.41**	**0.13**	**0.15**	0.05	**0.60**	-0.10	-0.05	**0.24**	**0.20**	-0.12	**0.55**	1	**0.89**	**0.60**	**0.66**	**0.39**	**0.33**	**0.34**	0.05	-0.07	**0.37**	**0.21**
Ni	**-0.30**	**0.58**	0.05	0.04	-0.01	**0.43**	**0.12**	0.11	0.05	**0.58**	-0.11	-0.08	**0.20**	**0.18**	-0.11	**0.69**	**0.89**	1	**0.63**	**0.65**	**0.33**	**0.17**	**0.36**	0.01	-0.11	**0.24**	**0.22**
Sc	**-0.41**	**0.91**	**0.22**	-0.03	**0.16**	**0.62**	0.02	**0.16**	**0.18**	**0.94**	**-0.13**	-0.09	**-0.21**	**0.20**	0.03	**0.79**	**0.60**	**0.63**	1	**0.92**	-0.08	0.02	**0.41**	-0.06	**-0.20**	0.12	**0.40**
V	**-0.43**	**0.82**	**0.14**	0.05	0.06	**0.59**	0.11	**0.21**	0.12	**0.94**	**-0.13**	-0.04	0.02	**0.17**	-0.04	**0.71**	**0.66**	**0.65**	**0.92**	1	0.11	**0.15**	**0.39**	0.09	-0.02	0.11	**0.30**
Cu	**-0.18**	-0.11	**-0.29**	**0.35**	**-0.20**	0.01	**0.28**	-0.01	**-0.14**	-0.06	**-0.18**	**0.15**	**0.76**	0.00	**-0.34**	-0.05	**0.39**	**0.33**	-0.08	0.11	1	**0.33**	0.12	**0.26**	**0.41**	0.04	**-0.31**
Pb	-0.07	0.04	**-0.18**	0.08	**-0.18**	0.05	0.09	**0.27**	0.11	0.07	-0.08	0.06	**0.34**	-0.03	0.00	-0.01	**0.33**	**0.17**	0.02	**0.15**	**0.33**	1	0.08	**0.23**	**0.24**	**0.14**	**-0.14**
Zn	**-0.23**	**0.43**	-0.02	0.07	**0.23**	**0.52**	**0.18**	-0.09	-0.05	**0.38**	-0.04	0.09	0.00	0.01	-0.09	**0.35**	**0.34**	**0.36**	**0.41**	**0.39**	0.12	0.08	1	-0.05	-0.06	0.12	0.11
Ag	-0.04	-0.04	**-0.19**	**0.18**	**-0.14**	-0.04	0.01	**0.24**	-0.08	-0.02	**-0.13**	-0.05	**0.40**	-0.01	**-0.19**	**-0.13**	0.05	0.01	-0.06	0.09	**0.26**	**0.23**	-0.05	1	**0.38**	-0.03	**-0.16**
Au	0.03	**-0.22**	**-0.38**	**0.26**	**-0.22**	-0.12	0.05	-0.01	-0.02	**-0.16**	**-0.13**	-0.02	**0.54**	-0.02	**-0.23**	**-0.22**	-0.07	-0.11	**-0.20**	-0.02	**0.41**	**0.24**	-0.06	**0.38**	1	0.01	**-0.37**
As	0.02	0.10	-0.05	-0.08	0.06	0.06	0.05	-0.05	0.03	**0.12**	0.01	0.03	0.01	-0.01	-0.10	**0.15**	**0.37**	**0.24**	0.12	0.11	0.04	**0.14**	0.12	-0.03	0.01	1	-0.09
Ge	**-0.19**	**0.40**	**0.39**	-0.08	**0.35**	**0.26**	**-0.20**	0.09	0.00	**0.37**	0.03	**-0.16**	**-0.48**	0.03	**0.26**	**0.40**	**0.21**	**0.22**	**0.40**	**0.30**	**-0.31**	**-0.14**	0.11	**-0.16**	**-0.37**	-0.09	1
Sb	0.04	-0.04	-0.01	0.00	**0.21**	0.00	0.02	-0.01	-0.09	0.03	0.05	**0.12**	-0.09	-0.04	0.03	**0.33**	0.09	**0.13**	0.00	0.03	0.01	0.08	0.08	-0.12	-0.07	0.05	**0.17**
Se	**-0.24**	**-0.19**	**-0.25**	**0.47**	**-0.23**	-0.05	**0.16**	-0.02	**-0.21**	**-0.16**	**-0.12**	0.07	**0.93**	-0.03	**-0.46**	**-0.17**	**0.26**	**0.22**	**-0.18**	0.02	**0.75**	**0.27**	0.01	**0.38**	**0.48**	**0.16**	**-0.47**
Te	**-0.13**	-0.09	**-0.29**	**0.29**	**-0.18**	0.02	**0.19**	-0.04	**-0.13**	-0.03	**-0.15**	**0.13**	**0.67**	-0.05	**-0.36**	0.01	**0.27**	**0.24**	-0.07	0.10	**0.60**	**0.39**	**0.16**	**0.19**	**0.48**	**0.25**	**-0.39**
Tl	-0.04	0.05	-0.05	0.03	**-0.13**	-0.06	**-0.13**	**0.14**	**0.71**	0.02	0.07	-0.08	-0.05	-0.02	**0.29**	-0.08	-0.07	-0.10	0.00	-0.03	-0.07	**0.14**	-0.11	0.03	0.08	-0.08	-0.09
Bi	0.00	0.01	-0.05	0.01	-0.04	0.03	-0.02	**0.16**	-0.06	0.07	0.03	-0.01	0.06	-0.02	-0.05	-0.04	**0.31**	0.06	0.01	0.06	**0.16**	**0.69**	0.07	**0.14**	0.01	**0.16**	-0.01
W	0.00	**0.15**	0.00	-0.12	0.00	-0.01	0.11	0.00	0.09	0.10	-0.10	0.07	0.00	0.11	-0.03	**0.15**	-0.01	0.04	**0.13**	0.11	-0.02	-0.02	0.06	0.09	-0.01	0.06	-0.05
Mo	0.06	0.06	0.01	-0.12	0.08	0.01	-0.03	**-0.14**	0.08	0.06	-0.02	0.03	-0.05	0.00	-0.02	**0.40**	**0.14**	**0.25**	0.06	0.04	0.09	-0.05	0.10	**-0.16**	-0.09	0.04	0.07
Li	**-0.17**	**0.59**	0.06	-0.12	-0.07	**0.28**	**-0.13**	**0.13**	**0.67**	**0.49**	-0.11	**-0.21**	**-0.16**	0.06	**0.16**	**0.47**	**0.30**	**0.32**	**0.51**	**0.47**	-0.06	**0.13**	**0.12**	-0.08	-0.08	0.08	0.10
Ga	**-0.36**	**0.54**	**-0.19**	**0.29**	-0.06	**0.36**	0.11	**0.13**	0.09	**0.50**	**-0.16**	-0.09	**0.48**	0.08	**-0.33**	**0.37**	**0.41**	**0.39**	**0.48**	**0.63**	**0.45**	**0.33**	**0.27**	**0.34**	**0.35**	0.05	-0.10
Cs	-0.04	0.02	0.08	0.00	0.11	-0.02	**-0.12**	**0.14**	**0.43**	0.02	0.08	-0.04	**-0.19**	-0.01	**0.35**	0.01	-0.06	-0.06	0.01	-0.02	**-0.17**	0.09	-0.09	-0.08	-0.07	-0.07	**0.24**
Ba	-0.01	0.07	0.07	-0.09	-0.11	-0.07	-0.11	**0.12**	**0.65**	0.00	0.07	-0.11	**-0.20**	-0.02	**0.38**	-0.02	**-0.15**	**-0.13**	0.01	-0.05	**-0.23**	0.09	**-0.17**	-0.05	-0.03	-0.11	-0.08
Rb	-0.07	**0.18**	0.08	-0.09	0.02	-0.06	**-0.15**	**0.14**	**0.95**	**0.14**	0.00	-0.09	**-0.22**	0.08	**0.43**	0.12	0.01	0.01	**0.15**	0.09	**-0.17**	0.09	-0.08	-0.06	-0.04	-0.02	0.09
Sr	-0.04	-0.08	**-0.12**	-0.01	**-0.21**	-0.05	**0.50**	**0.49**	0.09	-0.01	0.07	**0.27**	**0.15**	-0.03	**0.22**	-0.09	0.01	-0.01	-0.04	0.05	**0.12**	**0.25**	**-0.14**	0.07	0.10	-0.06	-0.09

Table 8-3 (cont'd): Pearson correlation coefficients of major and trace elements of altered and mineralized unit 4EA samples.

	Sb	Se	Te	Tl	Bi	W	Mo	Li	Ga	Cs	Ba	Rb	Sr
SiO_2	0.04	**-0.24**	**-0.13**	-0.04	0.00	0.00	0.06	**-0.17**	**-0.36**	-0.04	-0.01	-0.07	-0.04
Al_2O_3	-0.04	**-0.19**	-0.09	0.05	0.01	**0.15**	0.06	**0.59**	**0.54**	0.02	0.07	**0.18**	-0.08
Fe_2O_3	-0.01	**-0.25**	**-0.29**	-0.05	-0.05	0.00	0.01	0.06	**-0.19**	0.08	0.07	0.08	**-0.12**
FeO	0.00	**0.47**	**0.29**	0.03	0.01	-0.12	-0.12	-0.12	**0.29**	0.00	-0.09	-0.09	-0.01
MnO	**0.21**	**-0.23**	**-0.18**	**-0.13**	-0.04	0.00	0.08	-0.07	-0.06	0.11	-0.11	0.02	**-0.21**
MgO	0.00	-0.05	0.02	-0.06	0.03	-0.01	0.01	**0.28**	**0.36**	-0.02	-0.07	-0.06	-0.05
CaO	0.02	**0.16**	**0.19**	**-0.13**	-0.02	0.11	-0.03	**-0.13**	0.11	**-0.12**	-0.11	**-0.15**	**0.50**
Na_2O	-0.01	-0.02	-0.04	**0.14**	**0.16**	0.00	**-0.14**	**0.13**	**0.13**	**0.14**	**0.12**	**0.14**	**0.49**
K_2O	-0.09	**-0.21**	**-0.13**	**0.71**	-0.06	0.09	0.08	**0.67**	0.09	**0.43**	**0.65**	**0.95**	0.09
TiO_2	0.03	**-0.16**	-0.03	0.02	0.07	0.10	0.06	**0.49**	**0.50**	0.02	0.00	**0.14**	-0.01
P_2O_5	0.05	**-0.12**	**-0.15**	0.07	0.03	-0.10	-0.02	-0.11	**-0.16**	0.08	0.07	0.00	0.07
CO_2	**0.12**	0.07	**0.13**	-0.08	-0.01	0.07	0.03	**-0.21**	-0.09	-0.04	-0.11	-0.09	**0.27**
Total S	-0.09	**0.93**	**0.67**	-0.05	0.06	0.00	-0.05	**-0.16**	**0.48**	**-0.19**	**-0.20**	**-0.22**	**0.15**
B	-0.04	-0.03	-0.05	-0.02	-0.02	0.11	0.00	0.06	0.08	-0.01	-0.02	0.08	-0.03
Be	0.03	**-0.46**	**-0.36**	**0.29**	-0.05	-0.03	-0.02	**0.16**	**-0.33**	**0.35**	**0.38**	**0.43**	**0.22**
Cr	**0.33**	**-0.17**	0.01	-0.08	-0.04	**0.15**	**0.40**	**0.47**	**0.37**	0.01	-0.02	0.12	-0.09
Co	0.09	**0.26**	**0.27**	-0.07	**0.31**	-0.01	**0.14**	**0.30**	**0.41**	-0.06	**-0.15**	0.01	0.01
Ni	**0.13**	**0.22**	**0.24**	-0.10	0.06	0.04	**0.25**	**0.32**	**0.39**	-0.06	**-0.13**	0.01	-0.01
Sc	0.00	**-0.18**	-0.07	0.00	0.01	**0.13**	0.06	**0.51**	**0.48**	0.01	0.01	**0.15**	-0.04
V	0.03	0.02	0.10	-0.03	0.06	0.11	0.04	**0.47**	**0.63**	-0.02	-0.05	0.09	0.05
Cu	0.01	**0.75**	**0.60**	-0.07	**0.16**	-0.02	0.09	-0.06	**0.45**	**-0.17**	**-0.23**	**-0.17**	**0.12**
Pb	0.08	**0.27**	**0.39**	**0.14**	**0.69**	-0.02	-0.05	**0.13**	**0.33**	0.09	0.09	0.09	**0.25**
Zn	0.08	0.01	**0.16**	-0.11	0.07	0.06	0.10	**0.12**	**0.27**	-0.09	**-0.17**	-0.08	**-0.14**
Ag	-0.12	**0.38**	**0.19**	0.03	**0.14**	0.09	**-0.16**	-0.08	**0.34**	-0.08	-0.05	-0.06	0.07
Au	-0.07	**0.48**	**0.48**	0.08	0.01	-0.01	-0.09	-0.08	**0.35**	-0.07	-0.03	-0.04	0.10
As	0.05	**0.16**	**0.25**	-0.08	**0.16**	0.06	0.04	0.08	0.05	-0.07	-0.11	-0.02	-0.06
Ge	**0.17**	**-0.47**	**-0.39**	-0.09	-0.01	-0.05	0.07	0.10	-0.10	**0.24**	-0.08	0.09	-0.09
Sb	1	-0.05	0.11	**-0.16**	**0.12**	0.10	**0.44**	-0.05	-0.06	0.07	-0.10	-0.06	0.01
Se	-0.05	1	**0.68**	-0.09	0.07	0.02	-0.03	**-0.15**	**0.49**	**-0.18**	**-0.22**	**-0.23**	**0.12**
Te	0.11	**0.68**	1	-0.10	**0.17**	0.08	0.07	-0.04	**0.45**	**-0.17**	**-0.19**	**-0.17**	0.12
Tl	**-0.16**	-0.09	-0.10	1	-0.03	-0.02	-0.05	**0.40**	0.09	**0.47**	**0.63**	**0.75**	**0.14**
Bi	**0.12**	0.07	**0.17**	-0.03	1	-0.02	-0.01	-0.06	0.08	-0.06	-0.06	-0.07	0.00
W	0.10	0.02	0.08	-0.02	-0.02	1	0.06	0.09	**0.13**	-0.06	0.00	0.07	-0.04
Mo	**0.44**	-0.03	0.07	-0.05	-0.01	0.06	1	0.11	-0.02	0.01	-0.02	0.09	**-0.13**
Li	-0.05	**-0.15**	-0.04	**0.40**	-0.06	0.09	0.11	1	**0.36**	**0.23**	**0.43**	**0.63**	0.07
Ga	-0.06	**0.49**	**0.45**	0.09	0.08	**0.13**	-0.02	**0.36**	1	-0.09	-0.02	0.06	0.12
Cs	0.07	**-0.18**	**-0.17**	**0.47**	-0.06	-0.06	0.01	**0.23**	-0.09	1	**0.35**	**0.57**	**0.16**
Ba	-0.10	**-0.22**	**-0.19**	**0.63**	-0.06	0.00	-0.02	**0.43**	-0.02	**0.35**	1	**0.67**	**0.15**
Rb	-0.06	**-0.23**	**-0.17**	**0.75**	-0.07	0.07	0.09	**0.63**	0.06	**0.57**	**0.67**	1	**0.13**
Sr	0.01	**0.12**	0.12	**0.14**	0.00	-0.04	**-0.13**	0.07	0.12	**0.16**	**0.15**	**0.13**	1

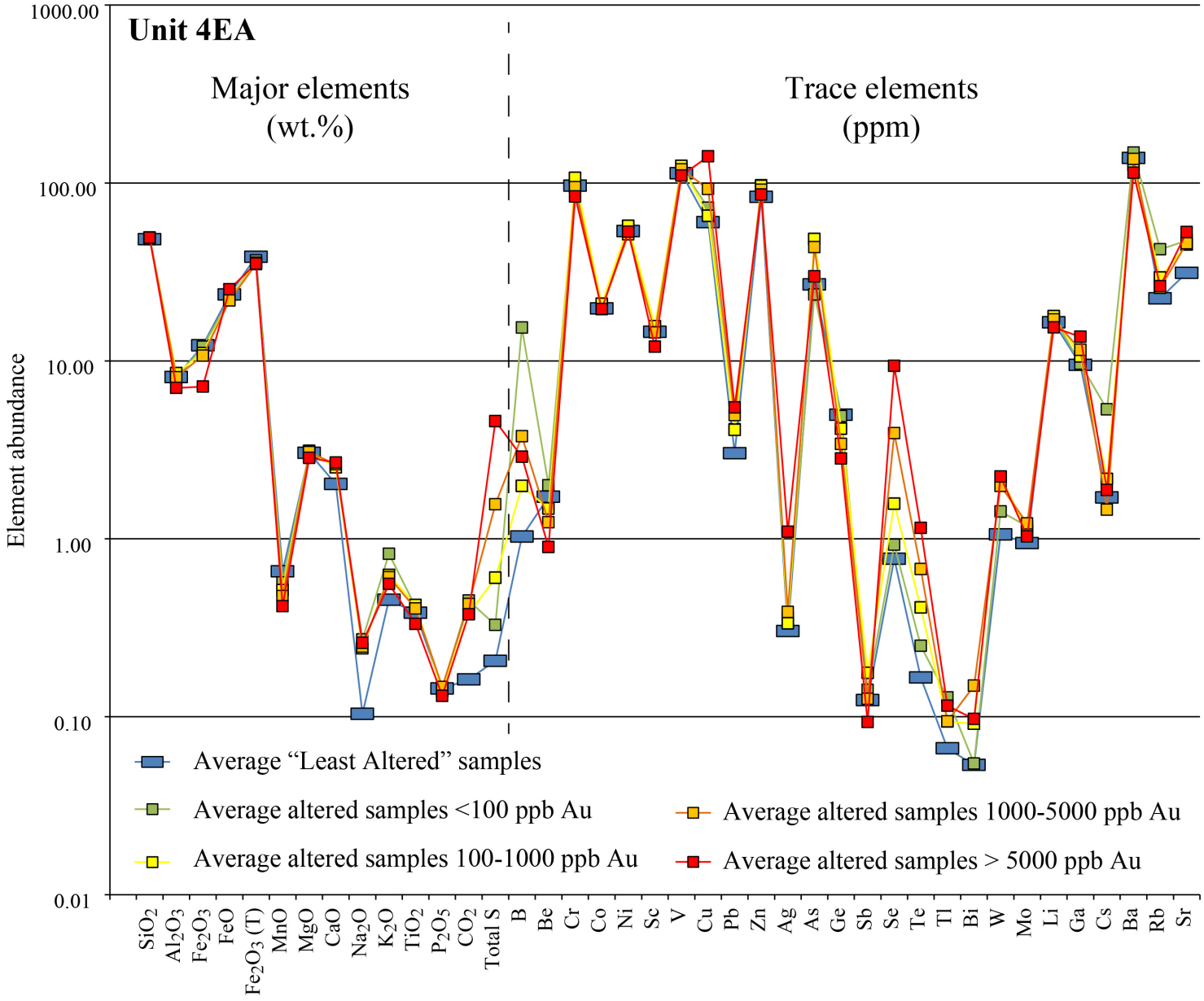

Figure 8-23: Major and trace element average values of 4EA unit, per gold assays value classes. Samples with <100 ppb Au show the highest enrichment in K_2O, B, Be, Rb, Tl, and Cs. CO_2 and CaO are enriched in all altered samples. The most gold-rich samples show the most elevated total S, Ag, Cu, Se, Te, Pb, and Ga, consistent with ternary diagrams.

8.5 Alteration characteristics of unit 4F

Before the 2014 discovery of gold mineralization hosted in unit 4F in the West limb area (WEL; Figure 7-1; Figure 8-24A, B, C), low-grade gold in that unit was only documented adjacent to 4EA ore zones (e.g., Lynx zone), ranging from a few hundreds ppb to a few ppm (Figure 8-24D), rarely exceeding 5 ppm. Nevertheless, evidence of hydrothermal alteration in unit 4F is common and a useful vector for exploration.

8.5.1 Alteration mineral assemblages

Although there are some primary variations, unaltered unit 4F typically comprises a biotite-quartz matrix with pale purple, millimetric garnet porphyroblasts (chapter 3). Alteration is characterized by textural changes of mineral species. Some hydrothermal alteration mineral assemblage are also found in the regional metamorphic mineral assemblage (i.e., biotite, garnet). This is shown by the occurrence of coarser and darker pink garnet, as well as zones of massive, dark brown biotite (Figure 8-25A, B). The fine-grained biotite-quartz matrix is progressively replaced by massive biotite and quartz-rich zones, with local quartz veins (Figure 8-25C, D). Stronger alteration is characterized by the presence of Ca-amphiboles and grunerite, with local calcite (Figures 8-24D and 8-25E). Highly altered 4F samples are constituted of quartz-rich zones with hornblende-grunerite, and biotite forms distinct masses with 0.5-1-cm, euhedral garnet porphyroblasts with local grunerite (Figure 8-25E). Scattered pyrrhotite is common in strongly altered samples. Comparisons of macroscopic evidence of alteration and gold content in drill cores show there is no clear correlation between alteration intensity and gold grade (Figure 8-25A, B).

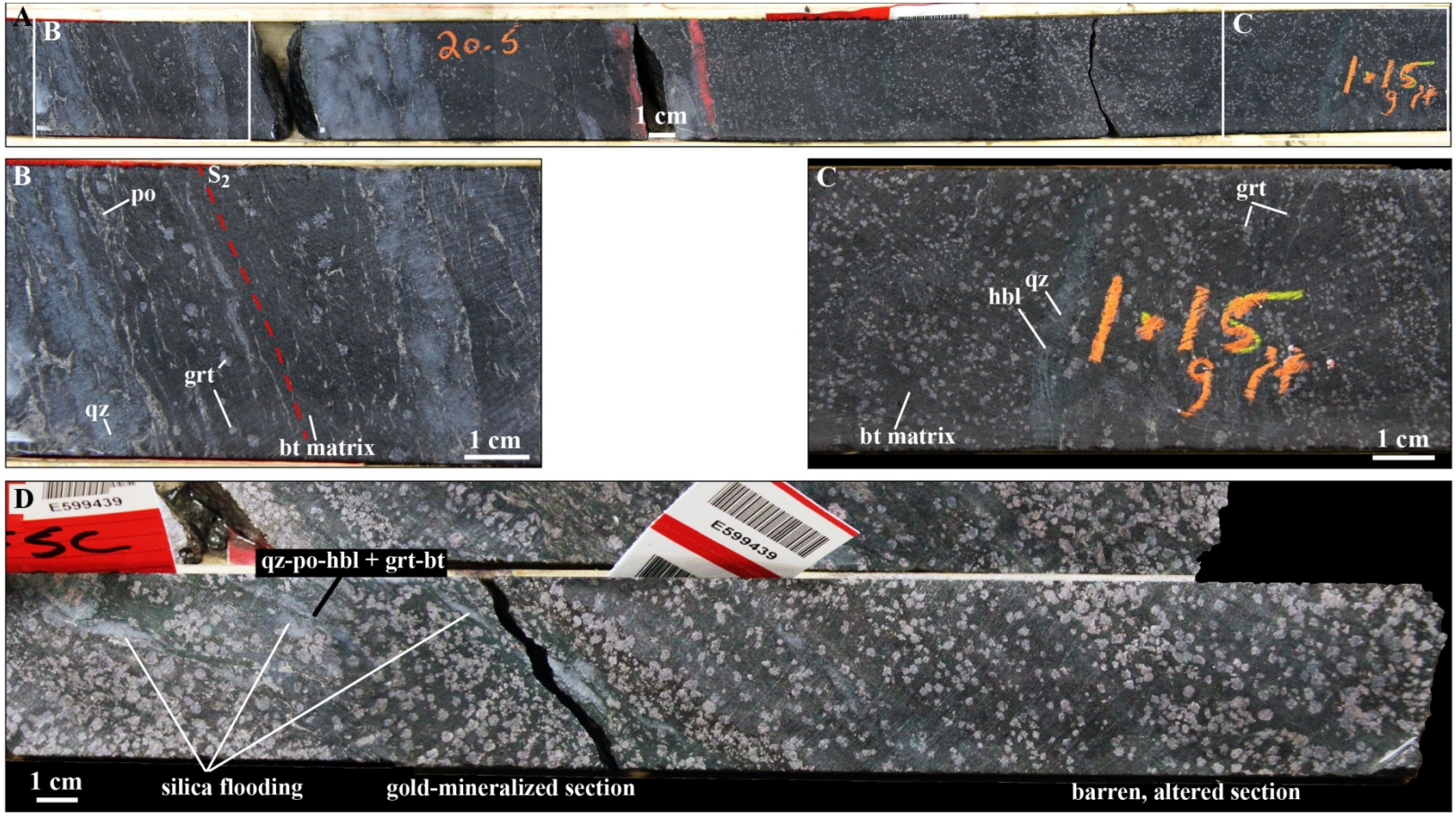

Figure 8-24: Drill core sections of altered unit 4F. A. Drill core section of gold-bearing garnet-biotite schist, WEL area. B. Close-up photograph of 20-ppm gold drill core section. Note the strong development of S_2 fabric, the presence of quartz vein and pyrrhotite aligned to S_2. Garnet porphyroblasts are notably less numerous than in the adjacent low-grade portion. C. Close-up photograph of 1.15-ppm gold drill core section. Note the weak deformation intensity and alteration. D. 2-ppm gold drill core sample of garnet-biotite schist, MW-12-539, DDH 09-PQE-052. The sample was taken in a larger 8-ppm gold interval (mine assay). Gold is concentrated in the silica-flooded, pyrrhotite-hornblende-bearing portion of the drill core.

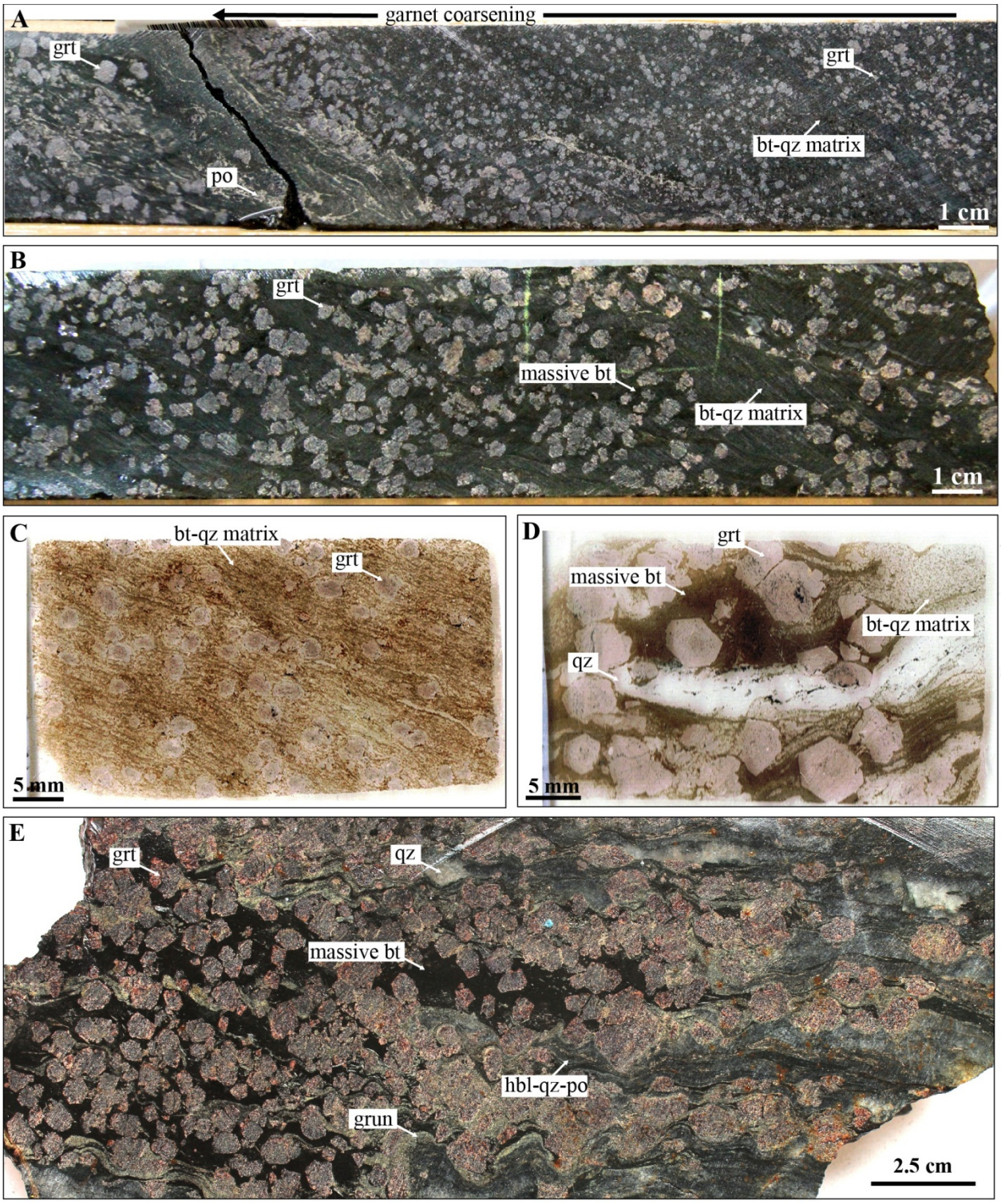

Figure 8-25: Alteration of unit 4F. A. Drill core section of sample MW-12-544, containing 17.7 ppm Au. Alteration is marked by garnet coarsening toward the zone of highest strain and highest pyrrhotite content. B. Drill core section of sample MW-12-328, containing 66 ppb Au. It shows the formation of massive biotite zones within the biotite-quartz matrix and the coarsening of garnet relative to "least altered" samples such as: C. Thin section scan of sample MW-12-146. This "least altered" sample shows the typical fine-grained biotite-quartz matrix with millimetre-size garnets. D. Thin section scan of sample MW-12-328. It shows

coarse, euhedral garnets, massive biotite, and a deformed quartz vein. E. Slab of underground sample MW-12-UG-009, Lynx zone. Alteration is marked by the presence of quartz veins with hornblende-grunerite selvages, as well as the presence of massive, deep brown biotite, and coarse euhedral garnet porphyroblasts rimmed by grunerite.

8.5.2 Geochemical variations

Ternary diagrams of geochemical data of unit 4F show SiO_2, Al_2O_3, and total Fe_2O_3 contents are stable in all samples groups (i.e., least altered, 1-100 ppb, 101-1000 ppb, 1-5 ppm, and over 5 ppm Au; Figure 8-26). Variations in total Fe_2O_3 are mostly due to Fe_2O_3, as variations in FeO content are minor. CO_2 shows some significant enrichment in altered samples, but not in a specific sample group. Contrastingly, CaO is enriched preferentially in samples with over 5 ppm gold. Potassium content shows a somewhat unexpected trend, as some altered samples are depleted in K_2O, possibly due to mobilization of K during crystallization of secondary biotite, which would be slightly less abundant than primary biotite. This shows that unit 4F is not reactive to potassic alteration, contrary to the overlying mafic volcanic rocks, and that biotite alteration in these rocks could be related to alteration in the underlying politic unit. Total S content shows the same positive enrichment correlation relative to gold as in unit 4EA. Finally, altered and gold-rich samples show variable enrichment in Na_2O, but no correlation with gold content.

The aforementioned relationships between gold and major elements are supported by the average composition of each sample group (Figure 8-27), which shows that progressive increase in alteration and gold content is notably marked by increasing CaO, CO_2, and total S content. The fact that CO_2 content is very low (i.e., <1 wt.% even in high-grade samples) suggests the prevalence of calcic alteration over that of carbonate. In contrast to unit Bvol and unit 4EA, altered 4F samples do not show significant K_2O increase. Trace elements showing a clear enrichment with increasing gold content include: Se, Te, Sr, W, and Mo (Figure 8-27). Cu, Ag, As, B, and Be also show enrichment to a lesser extent.

8.6 Alteration characteristics of unit 4B

Unit 4B lies on the opposite of side of ore zones compared to unit 4F (Figure 8-2). The compositional layering of unit 4B changes between the clastic, garnet-amphibole-chert-magnetite facies (4Bc) and the "purer" chert-magnetite ± amphibole facies (4B; chapter 3).

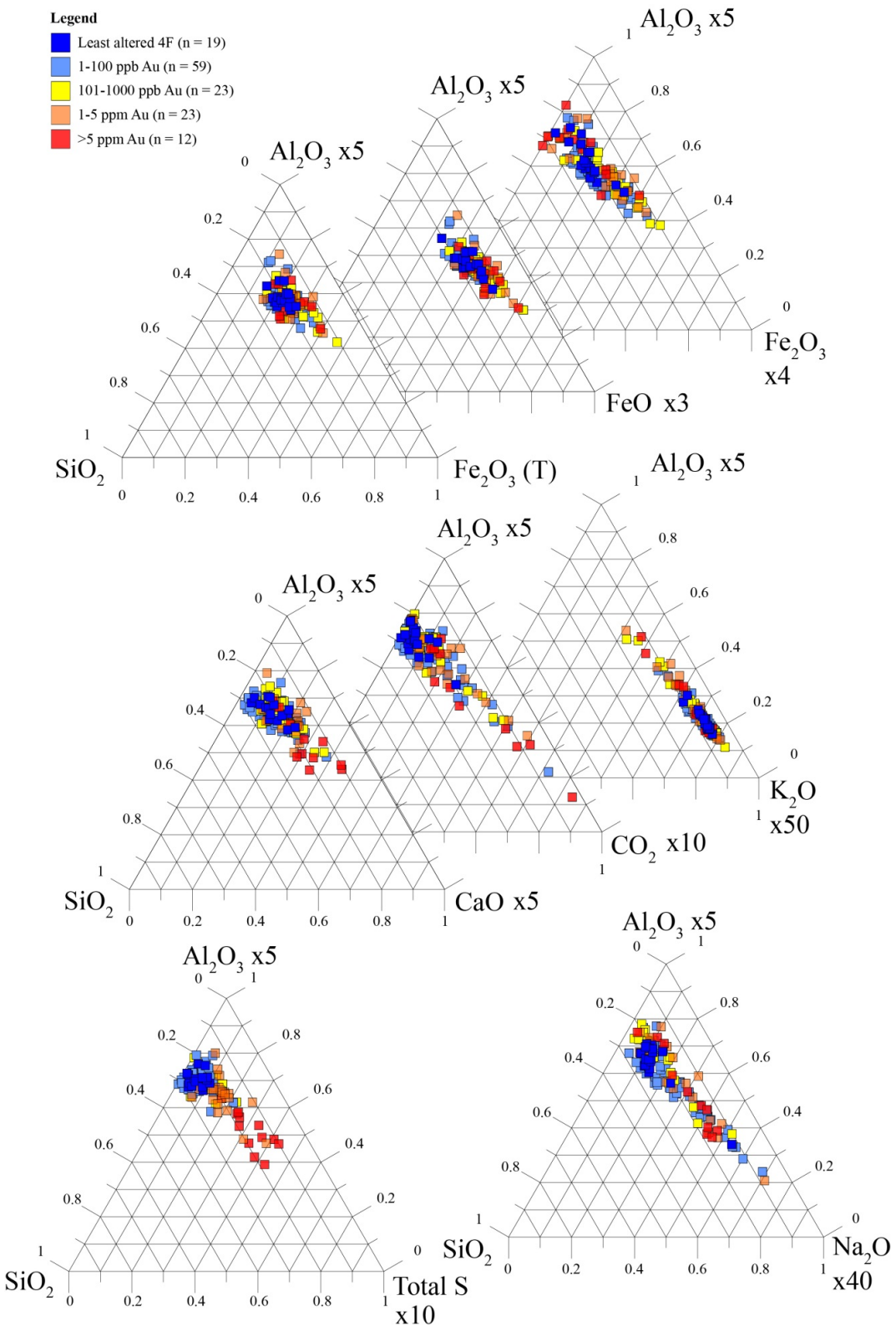

Figure 8-26: Ternary diagrams for major elements in unit 4F. SiO_2 and Al_2O_3 are used to monitor primary compositional variations, combined with: total iron content, FeO, and Fe_2O_3; CaO, CO_2, and K_2O; total S; and Na_2O.

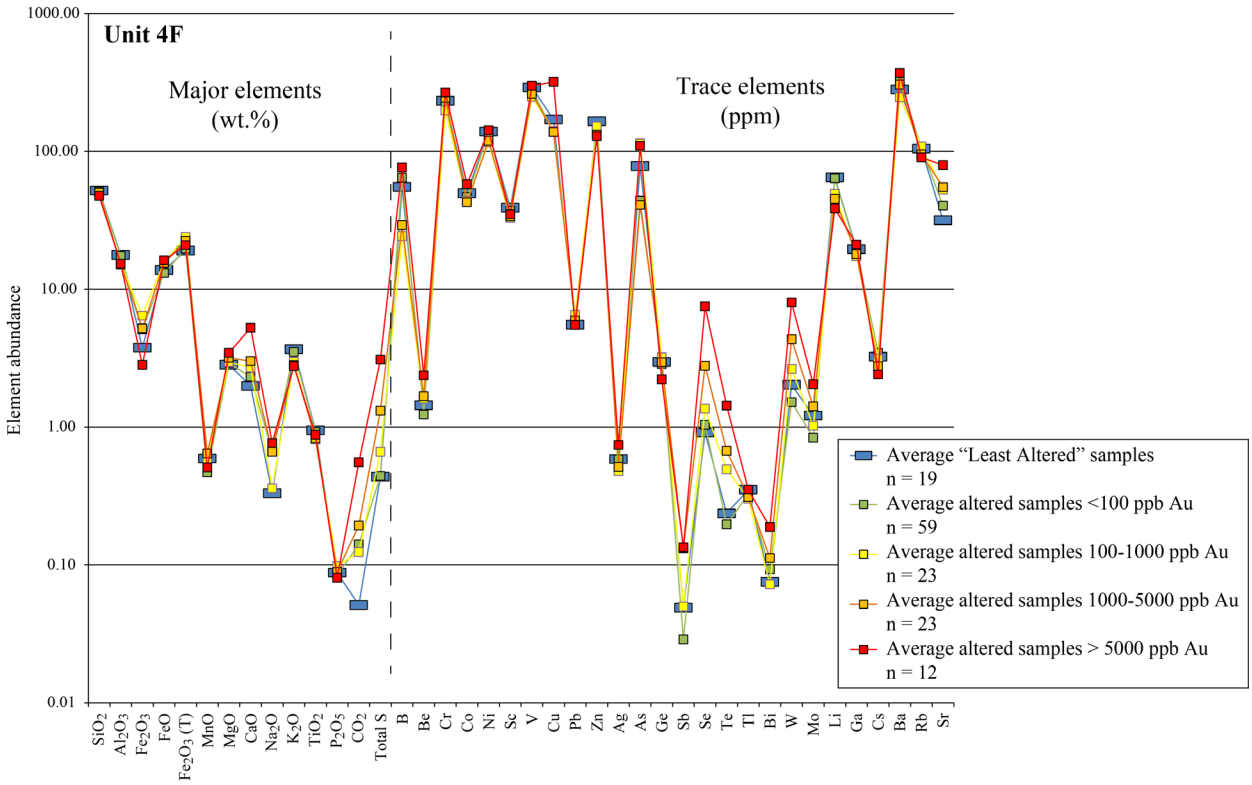

Figure 8-27: Average major and trace element content in unit 4F for sample groups of increasing gold content.

8.6.1 Alteration mineral assemblages

In the facies 4Bc, clastic bands constituted of garnet in an amphibole matrix have an overall chemical composition similar to mafic volcanic rocks and are reactive to potassic alteration. Altered 4Bc typically includes fine-grained biotite in clastic bands, and garnets are commonly coarser and more euhedral (Figure 8-28A). In biotite-altered samples, alteration is also characterized by syn-D_2 grunerite in and adjacent to magnetite-rich bands (Figure 8-28A, B, D; quartz + magnetite = grunerite; chapter 10).

Garnet porphyroblasts in clastic bands (Figure 8-28A, B, C) show a zonation similar to that observed in the least altered samples (chapter 3). The internal fabric (S_i) is Z-shaped and apparently discontinuous with the external S_2 foliation. This indicates that S_i is likely pre-D_2. Similarly to units 4EA and 4F, garnet porphyroblasts are typically coarser in altered samples. In 4B samples devoid of garnet-amphibole bands, alteration of amphibole included in the magnetite-quartz matrix may lead to garnet crystallization. Evidence of alteration also includes the presence of carbonates (Figure 8-29). This is well illustrated on surface, at PQ trench, where fine-grained calcite and brown, sugar-textured ankerite are present as a semi-continuous layer between chert and magnetite bands.

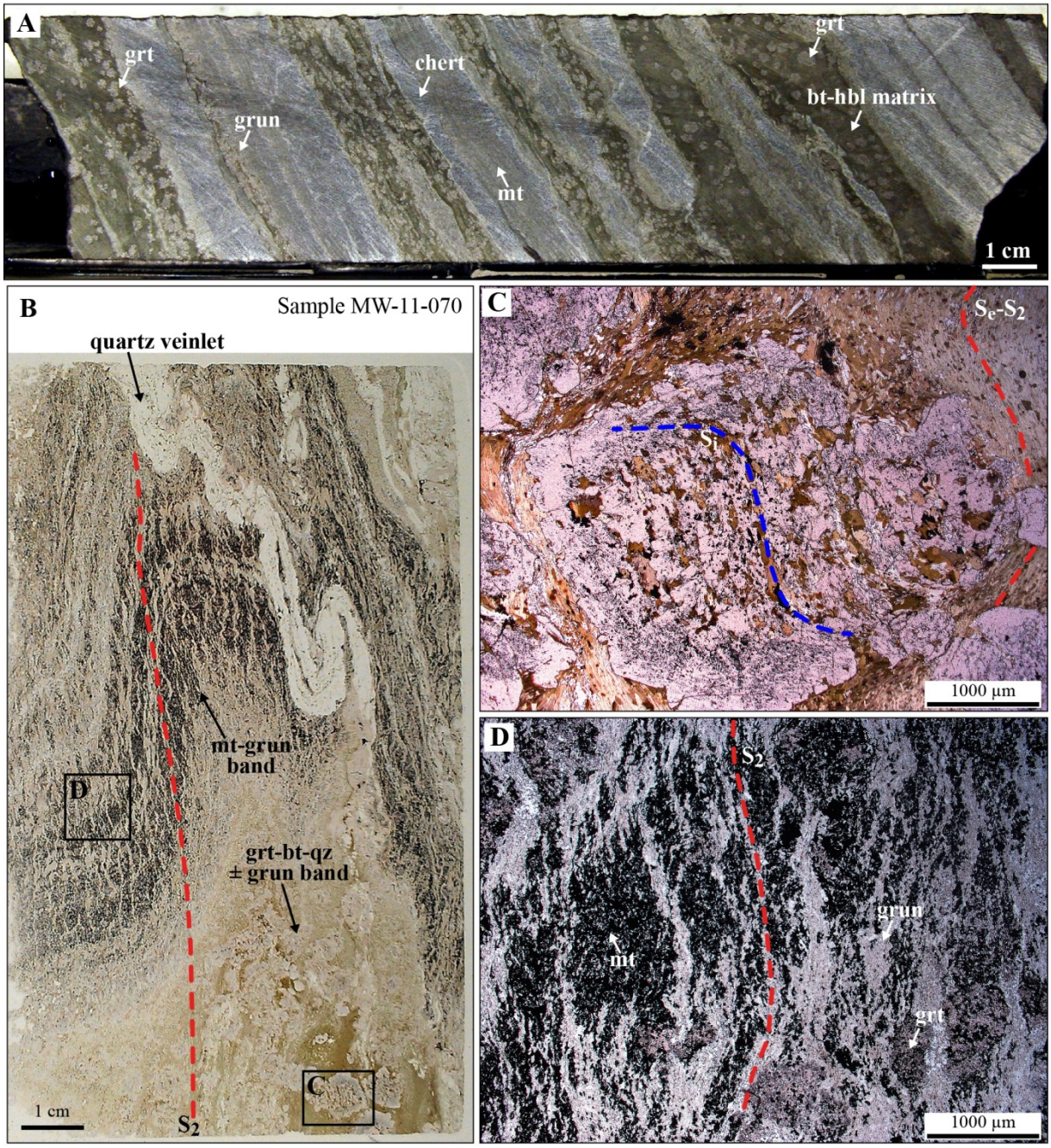

Figure 8-28: Alterated clastic facies of unit 4B. A. Drill core segment of sample MW-11-033, DDH 10-PQE-054. Note biotite alteration in clastic bands and coarsening of garnets. B. Thin section scan of sample MW-11-070, DDH 08-ITF-001, showing F_2-folded, magnetite-grunerite and garnet-biotite-quartz bands. The quartz veinlet displays a weak, proximal sulphide-replacement halo. C. Close-up microphotograph of garnet porphyroblast in biotite matrix. The porphyroblast displays rough Z-shaped internal fabric that appears to be distinct from the S_2 external fabric. D. Close-up microphotograph of the magnetite-grunerite band showing S_2-parallel grunerite.

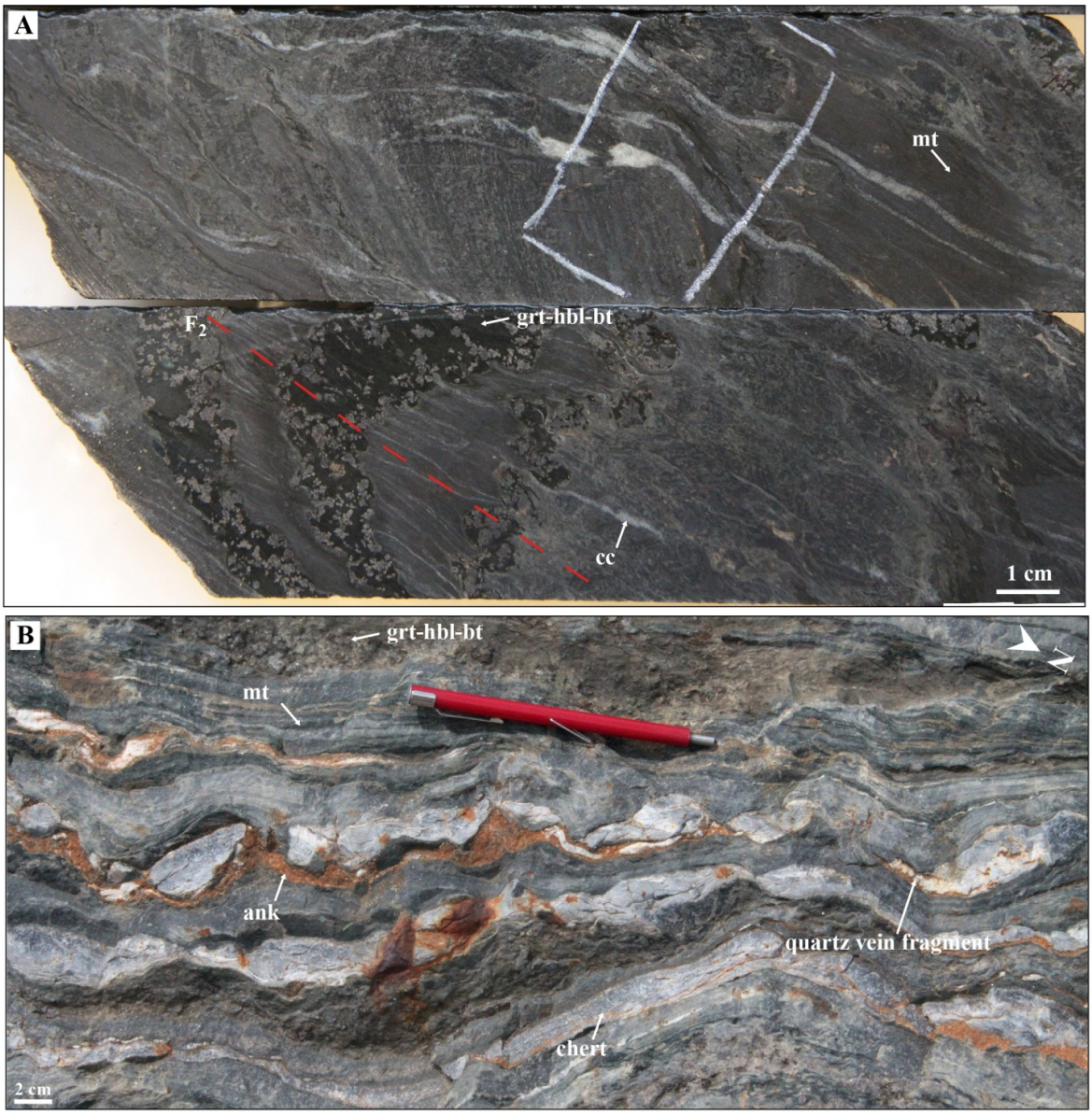

Figure 8-29: Carbonate alteration of unit 4B. A. Drill core segments of sample MW-13-450, DDH 07-JET-013. Axial planar calcite veinlets in chert-magnetite BIF with minor garnet-hornblende-biotite bands. B. At PQ trench, mine area; strongly boudinaged chert-magnetite BIF. Carbonate alteration consists in sugar-textured, iron-bearing carbonates preferentially distributed along boudinaged chert and near quartz-vein fragments.

8.6.2 Geochemical variations

Due to primary compositional variations (cf chapter 3), alteration of unit 4B can be difficult to identify and/or quantify using geochemical data. In "least altered" samples, the 4Bc to 4B transition is notably illustrated by the decrease in clastic-derived Al_2O_3 and K_2O contents (Figure 8-30A; Peter, 2003; Moran, 2008), and in the simultaneous increase in chemically-derived CO_2 content (Figure 8-30B; Table 3-4).

This means that the increase of CO_2 content in unit 4B samples that lacks macroscopic evidence of alteration (e.g., Figure 8-29) may be of primary origin and not related to alteration.

Geochemical data from all 4Bc and 4B samples in ternary diagrams shows that some gold-rich samples are depleted in Fe_2O_3 (Figure 8-31). K_2O shows a trend caused by primary composition with only few altered samples lying outside the area defined by "least altered" samples. This is consistent with DDH profiles (section 8.2) showing that, overall, there is no significant K_2O enrichment in unit 4B (using two separate average "least altered" compositions for 4Bc and 4B; Table 3-4). The situation is quite similar for CaO and CO_2, for which enrichment due to alteration is clearer. However, it is not as well-defined as that of total S content relative to gold content, regardless of unit 4B facies. Lastly, "least altered" samples appear to define two groups in the ternary Na_2O diagram. Altered samples are distributed within and between these poles, but there is no distinct link with gold content. These relationships are also illustrated by the evolution of major elements in average composition of sample groups of increasing gold content (Figure 8-32). Trace element content evolution shows approximately the same Cu-Se-Te-Pb association as other lithologies, and to a lesser extent, with Bi, Cs, Sr, and As. However, altered 4B samples appear to be distinctively enriched in Co, Ni, Sc, and V (Figure 8-32).

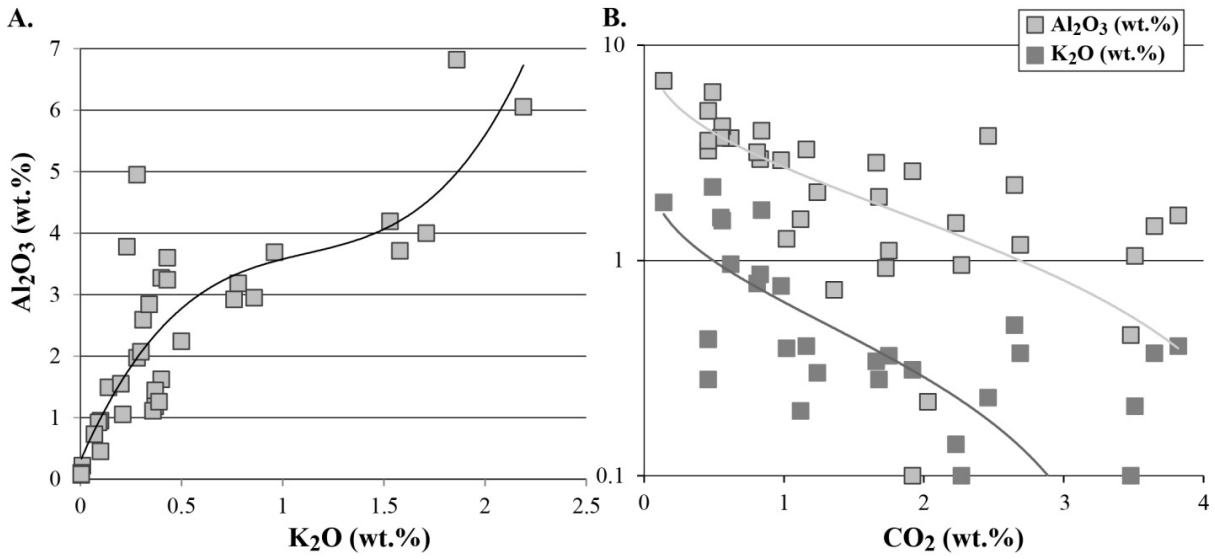

Figure 8-30: Relationships between primary Al_2O_3, K_2O, and CO_2 contents in least altered unit 4B. A. Al_2O_3 against K_2O content (wt.%) with polynomial regression line for the data set. B. Al_2O_3 and K_2O against CO_2 and respective logarithmic regression lines.

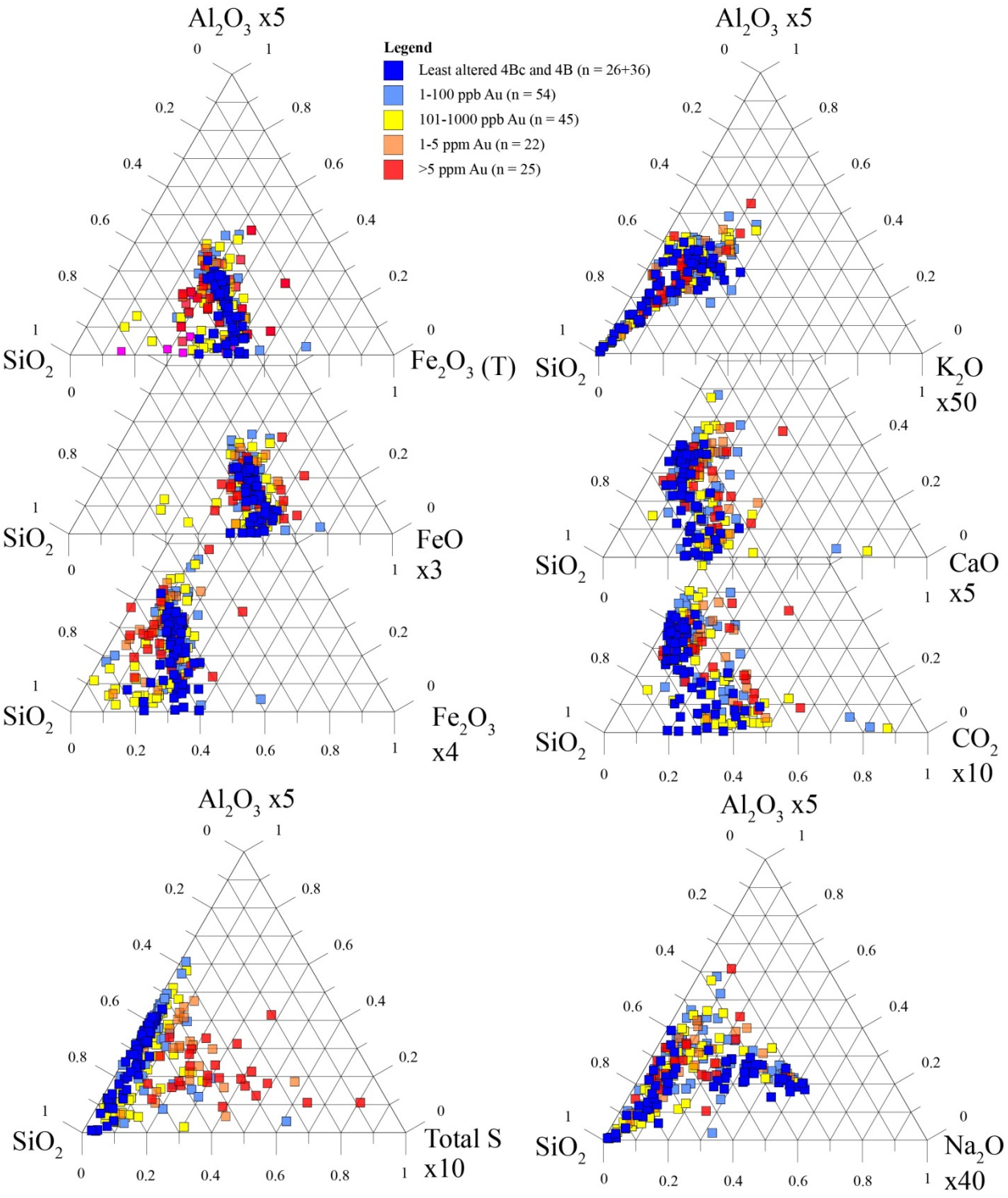

Figure 8-31: SiO_2-Al_2O_3-X ternary diagrams for unit 4B. Total iron shows small variations that can be attributed to Fe_2O_3 more than FeO, due to magnetite-replacement by pyrrhotite. K_2O shows a trend caused by primary composition, only a limited number of altered 4B samples show K_2O enrichment. CaO and CO_2 produce a complex trend controlled by primary composition with some poorly-defined influence of alteration. Total S content shows the same positive correlation with gold content as for other units. Samples are quite widely spread on the Na_2O diagram, but no link relative to gold is apparent.

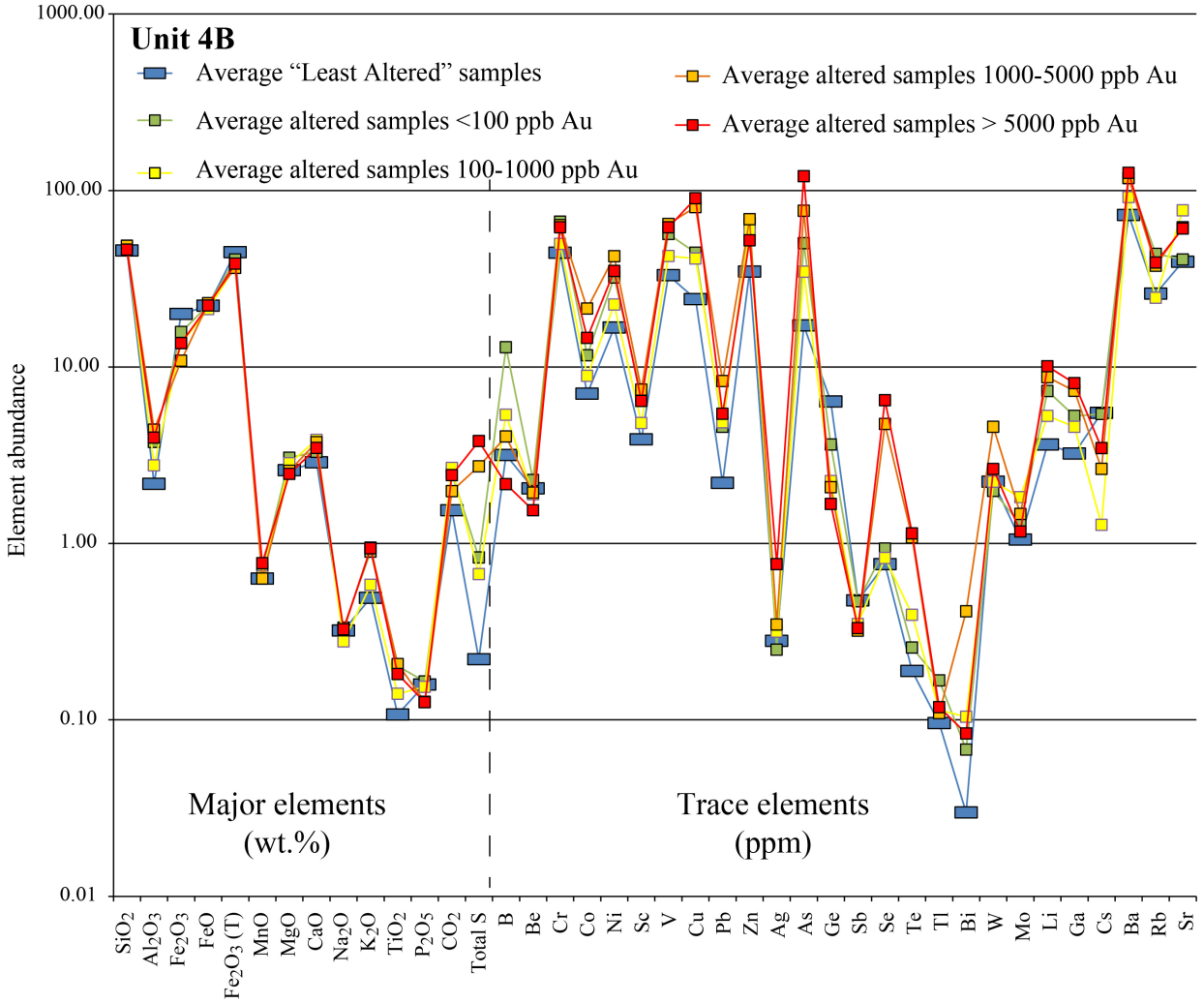

Figure 8-32: Average major and trace element content in unit 4B for sample groups of increasing gold content.

8.7 Na-bearing alteration mineral assemblages

Macroscopic and petrographic observations identified mineral phases interpreted as evidence of Na alteration. Na alteration can be associated with intrusion-related gold mineralization (Witt and Hammond, 2008; Witt et al., 2009). Its characterization is thus important to the genetic model of the Musselwhite gold deposit (chapter 10).

Here, evidence of sodic alteration consists mainly in calcite-aegirine veinlets crosscutting the iron formation compositional layering and S_2 fabric, and in more diffuse, Na-rich rims on hornblende-actinolite and replacement of grunerite by riebeckite (Figure 6-14B). Such evidence of Na alteration is fairly sporadic, and crosscutting relationships indicate this phenomenon is late to post-D_2. Moreover, whole-rock geochemical data of gold-rich samples of all units (chapters 7 and 8) shows that, although

locally enriched, Na_2O does not correlate with gold content or with any major element oxides (Table 7-5; Figures 7-22 and 8-33). Furthermore, Na_2O content in unit 4EA and 4F typically remains under 0.5 wt.%.

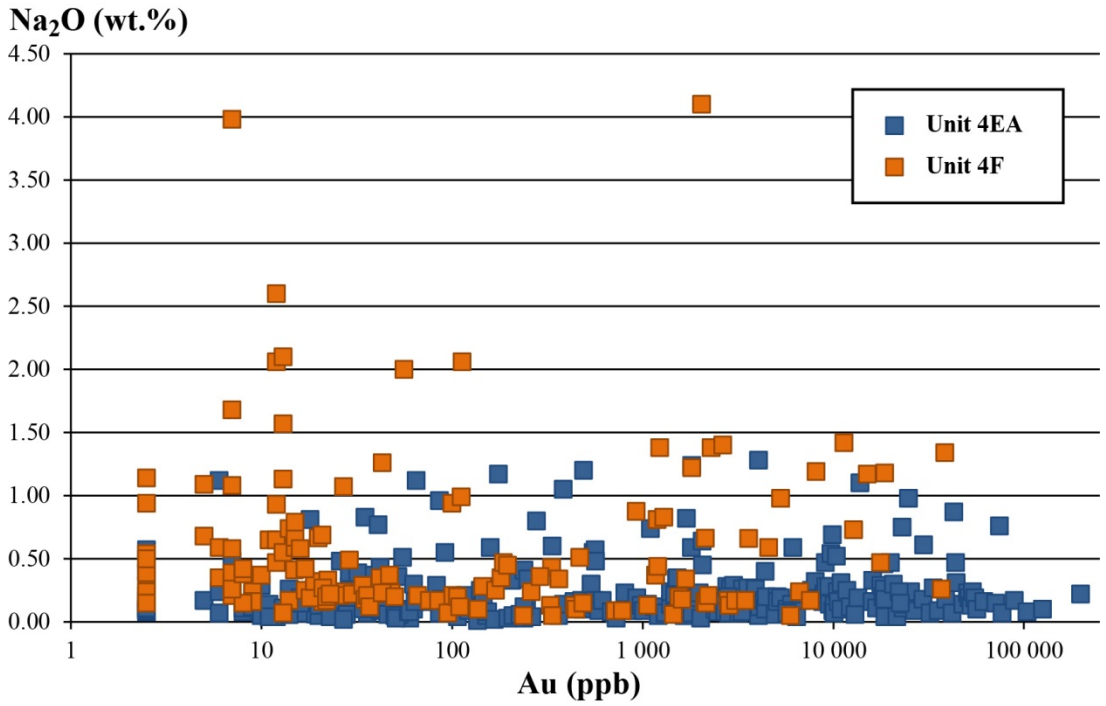

Figure 8-33: Na_2O content of all altered and gold-rich samples in units 4EA (n = 291) and 4F (n = 133); raw whole-rock geochemical data. It is generally under 0.5 wt.% and shows no correlation with gold values.

8.8 Summary

Alteration associated with mineralized zones at Musselwhite is consistent with typical orogenic gold deposits including potassic, carbonate/calcic, and sulphide zones (Eilu et al., 1999; Goldfarb et al., 2005; Dubé and Gosselin, 2007). However, the geological setting and the specific composition of the NIF sequence result in the heterogeneous development of alteration assemblages in the different rock types.

Drillhole profiles have allowed the delineation of broad alteration envelopes (Figure 8-10). Distal biotite alteration extends laterally over a few meters and vertically over tens to hundreds of meters, depending on host rock reactivity. Proximal calcic/carbonate alteration is more restricted, typically less than 5 meters laterally, and tens of meters vertical (hundreds in major high strain zones). Mafic volcanic rocks show the typical development of potassic/biotite and carbonate/calcite alteration, with associated K_2O and CO_2 enrichments. In the structurally underlying unit 4F, potassic alteration is expressed by secondary biotite crystallization, whereas calcic alteration is characterized by the presence of hornblende.These features are accompanied by garnet coarsening and local quartz flooding. Unit 4EA is weakly sensitive to potassic alteration, and replacement of grunerite by Ca-amphiboles is a more prominent feature of alteration, along

with pyrrhotite-replacement of the iron formation. Unit 4B shows little to no evidence of potassic alteration (only in the clastic facies, 4Bc) and is more reactive to carbonate alteration. Contrastingly, sulphidation is a consistent feature in all lithologies.

The primary variations in "least altered" samples, as well as the averaging effect of the sampling method, hinder to distinguish geochemical variations due to alteration. Sulphur enrichment is the most consistent evidence of alteration in whole-rock geochemical data. Fe_2O_3 depletion (due to magnetite replacement by pyrrhotite) in strongly altered samples is also common. K_2O, CaO, and CO_2 enrichments are variable. SiO_2 is fairly stable, indicating redistribution of silica rather than enrichment. Local concentration of silica was documented (chapter 7), but it is not positively correlated with gold. Trace element enrichments such as B, Be, Cs, and Rb are common, notably in K_2O-rich samples. Cu, Ag, Se, Te, and Pb enrichments are more typical of sulphide/gold-rich samples. Other trace elements, such as Tl, Ga, or As, show some enrichment in specific lithologies.

9 FLUIDS PATHWAYS AND METAL SOURCES

In continuity with the study of the controls on gold mineralization and alteration, the next step is to investigate for the potential source(s) and pathways of mineralizing fluids. Gold mineralization at Musselwhite is epigenetic (Hall and Rigg, 1986; Breaks et al., 1986; Breaks et al., 2001; Biczok et al., 2012; Oswald et al., 2015b, 2017). A metamorphic origin for gold-bearing fluids is largely suggested by structural, petrographic, and geochemical data as well as by the geological setting and the style of mineralization (Hall and Rigg, 1986; Breaks et al., 1986; Breaks et al., 2001; Duff, 2014). However, some studies suggest that magmatism had an influence (Isaac, 2008; Stott and Biczok, 2010). This chapter presents geological and structural data from drill core descriptions, petrography, and LA-ICP-MS 2D elemental mapping of sulphides (Appendix VII and VIII). The aim is to investigate the fluid pathways under the mine, and the potential sources for fluids and metals in the Opapimiskan Lake area. Although additional data and analyses are required, preliminary results contribute to elaborate a geological and genetic model for the Musselwhite deposit (chapter 10).

9.1 Potential fluid pathways

As previously described, most of the gold-mineralized zones at Musselwhite occur at the intersection of folded NIF and second-order high-strain zones, which also crosscut the structurally underlying “Basement basalts”, the SIF and “Lower basalts” units. The presence of gold-mineralized zones in the SIF (e.g., Red Wing zone) at the same depth level as NIF-hosted ore zones (Figure 7-1) is interpreted to suggest that mineralization could also occur in the East Bay synform hinge zone, below the well-endowed NIF (J. Biczok, personal comm, 2013). A few exploration drill holes have targeted the SIF in this projected hinge zone but did not intersect significant gold mineralization (Figure 9-1A). However, they enable the investigation of geological, structural, and alteration-related features under the mineralized zones in order to identify evidence of structures that could have channeled hydrothermal fluid flow toward NIF-hosted ore zone locations.

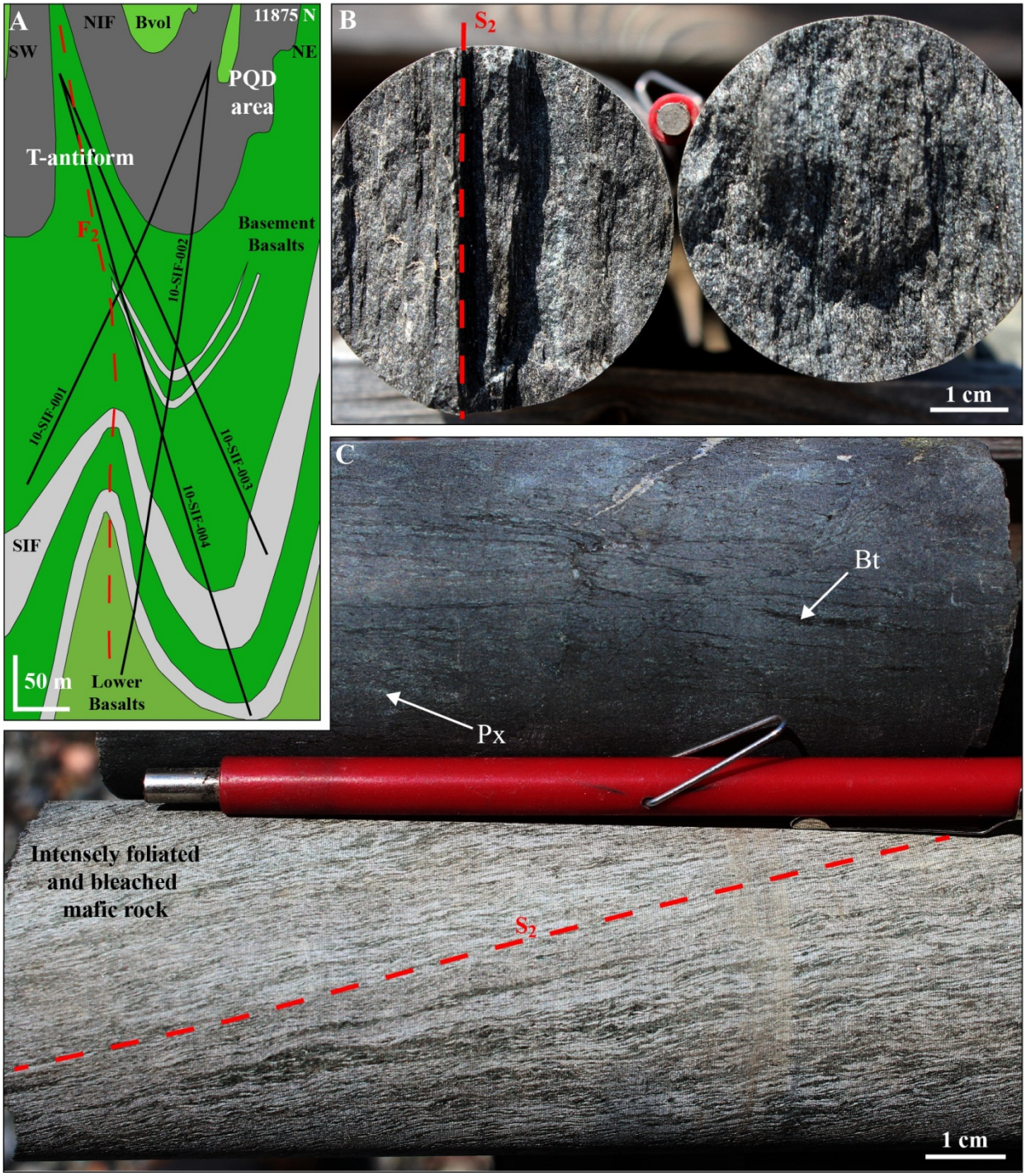

Figure 9-1: Alteration in "Basement basalts" unit. A. Close-up of mine section 11875 N showing the trace of four 10-SIF-xxx drill holes. B. Section view of drill core segment of strongly strained and altered mafic volcanic rock, "Basement basalts" unit, DDH 10-SIF-003, @136.5-139 m. C. Same drill core segments as B. The intense bleaching in some sections of the "Basement basalts" unit attests of hydrothermal fluid flow and alteration.

9.1.1 "Basement basalts" unit

Drill core segments from DDH 10-SIF-001 to -004 (Figure 9-1A) attest that the "Basement basalts" unit locally shows strongly developed S_2 fabric under the NIF (Figure 9-1B). Biotite alteration is common and pyroxene is locally present (Figure 9-1C). Some intervals of the "Basement basalts" unit is characterized by an intense bleaching (Figure 9-1C), highlighting the very strong S_2 fabric. This suggests that fluids may have used the structurally-induced secondary permeability as fluid pathways toward the NIF sequence (Oliver, 1996; Cox et al., 2001).

Samples of the "Basement basalts" unit were taken adjacent to the NIF, along the east limb of the mine synform (Figures 7-2, 7-3, 7-4), from drill holes that end below the NIF. They comprise altered andesite and basalt (section 3.4). Compared to unit Bvol (Figure 9-2A; section 8.3), basalt samples of the "Basement basalts" unit show moderate K_2O enrichment consistent with drill core observations (Figure 9-2B). However, they display very limited Na_2O depletion. Andesites also show a slight K_2O enrichment. The lack of Na_2O depletion suggests that those samples are located outside or at the edge of the envelope of major fluid flow.

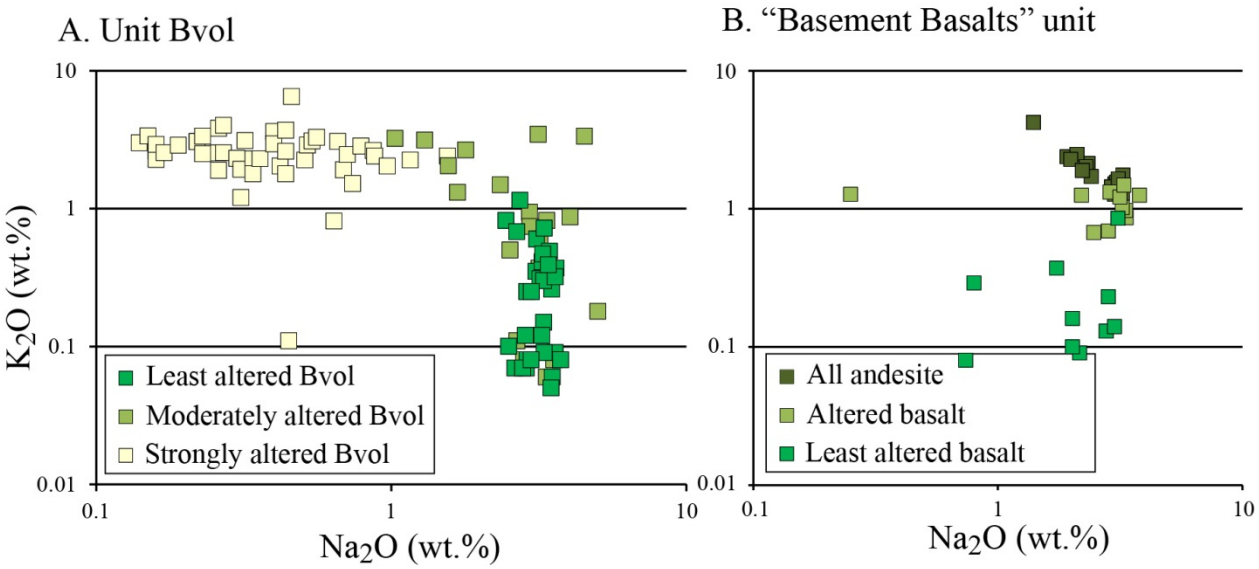

Figure 9-2: K_2O vs. Na_2O in units Bvol (A) and "Basement basalts" (B).

9.1.2 Southern iron formation (SIF)

The SIF horizons structurally underlie the "Basement basalts" unit (Figure 9-1A and 9-3A). Evidence of fluid flow are also present in the SIF. The contact between volcanic rocks and BIF is marked by a mineral assemblage of qz-hbl-cpx-po ± grt (Figure 9-3B), indicating strong hydrothermal alteration. The BIF consists of millimetre- to centimetre-scale bands/layers of chert and fine- to medium-grained magnetite (Figure 9-3C). Magnetite-rich bands are affected by amphibole- (grunerite and hornblende) and pyroxene-replacement (likely hedenbergite). Local quartz veins, axial planar to open F_2 folds, include red, centimetre-size, almandine garnet porphyroblasts (Figure 9-3C). Brown staining near quartz veins and disseminated pyrrhotite at the contact suggests that sulphur-bearing fluids flowed through the SIF, mainly filling D_2-related fractures, faults, and high strain zones. However, a well-defined high strain zone that would have focused fluid flow and induced stronger pyrrhotite-replacement of the BIF seems to be lacking. Abundance of pyroxene and presence of garnet suggest a higher metamorphic grade than in the NIF (Klein, 1983; chapter 1), which is consistent with their occurrence several hundred metres deeper than the NIF (Figure 9-1A). This also suggests the SIF could have contributed to the production of metamorphic fluids during the late stage of metamorphism, through the conversion of amphibole to pyroxene (Miyano and Klein, 1986).

9.1.3 Preliminary interpretations

Although additional data is needed to characterize mineralizing fluids and to establish their pathways, the intense bleaching in the "Basement basalts" unit and the alteration mineral assemblage of the SIF are good indicators of hydrothermal fluid flow. Fluids appear to have migrated along foliation planes and were focused in high strain zones. The geological and structural models developed in this study predict that such structures cut volcanic and sedimentary rocks underlying the mine (chapters 3 and 5). These rocks may have partly contributed to the volume of migrating fluids. In addition, the presence of S-type granite pegmatitic dykes in the vicinity of the mine (Biczok et al., 2012; Fry, 2013) suggests that partial melting of sedimentary rocks may have occurred at depth, potentially contributing to the fluid and metal budget.

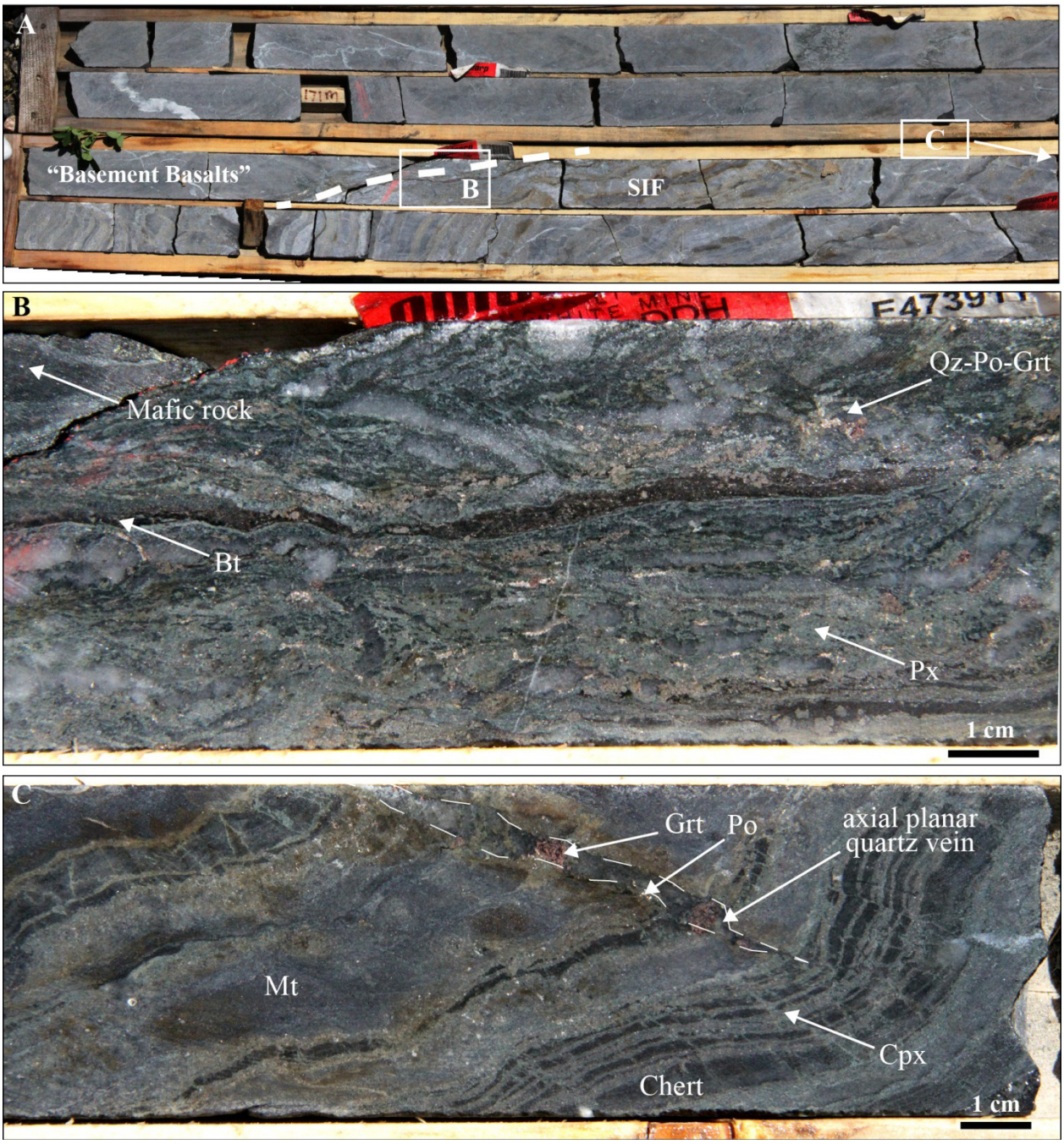

Figure 9-3: SIF. A. Drill core from DDH 10-SIF-003, 170 to 175 m, showing the contact between mafic rocks of the "Basement basalts" unit and one horizon of SIF chert-magnetite-pyroxene BIF. B. Close-up of the mafic rocks showing strong qz-hbl-px-po alteration near the contact zone. C. Close-up of the SIF. Replacement of magnetite by amphiboles and pyroxenes suggest higher-grade metamorphism (Klein, 1983).

9.2 Potential gold and metals sources

Many studies have focused on the potential sources of gold and trace metals in orogenic gold deposits (e.g., Pitcairn et al., 2006; Su et al., 2007; Large et al., 2011, 2012; Lisitsin and Pitcairn, 2016; Pitcairn et al., 2017). Sulphide-rich argillite horizons are potential contributors to the metal budget of gold deposits (Large et al., 2011, 2012). Metamorphosed argillite horizons are present at various stratigraphic levels in the Opapimiskan Lake area, such as unit 4H in the NIF and SIF sequences, and argillites with pyrite nodules in the Wilberforce area (West antiform area; Figure 3-1). Sulphide-rich, siliciclastic rocks of the ZHA are interpreted to occur at depth under the mine area (chapter 5) and are also thought to have a potential role as metal sources (Gao et al., 2015). To investigate the potential of such rocks to have acted as a source of precious and base metals at Musselwhite, LA-ICP-MS 2D elemental mapping of sulphides (chapter 1; Cabri and Jackson, 2011) was done on selected samples, in collaboration with Simon Jackson and colleagues at the Geological Survey of Canada in Ottawa.

9.2.1 Argillite horizons of the Wilberforce area

The discontinuous and extremely deformed nature of unit 4H in the mine area rendered it unfit for analysis. However, argillaceous units from the Wilberforce area (Figure 3-1) are similar to unit 4H in the NIF and SIF (chapter 3). Their bulk chemical composition is dominated by SiO_2, total iron, and total sulphur (Figure 9-4A). Al_2O_3 can constitute up to 10 wt.% and CaO up to 6 wt.% of the rock. All other major oxides make up less than 5 wt.%. REE profiles normalized to the Mudstone of Queensland (MUQ) standard show a fairly flat pattern with a moderate positive Eu* anomaly (Figure 9-4B). Such data indicates a detrital component consistent with a mafic-dominated basin source (Kamber et al., 2005) and a minor contribution from hydrothermal chemical sedimentation (Alexander et al., 2008).

Some argillaceous units of the Wilberforce area contain diagenetic sulphide nodules partially recrystallized to pyrite and pyrrhotite (Figure 9-5). Preliminary analyses of these nodules depicted intense metal zoning with strong gold enrichment (up to over 1000 ppb) along with that of As, Se, Ag, Sb, Te, Tl, Pb, and Bi (Jackson et al., 2013, 2015). Subsequent mapping of pyrite nodules and surrounding pyrite and pyrrhotite has corroborated such findings (Figures 9-6 and 9-7), highlighting four distinct phases. A typical nodule includes a core that is strongly enriched in Au, Ag, As, Sb, Te, Pb, Bi, and Ni and moderately enriched in Se, Co, and Tl (pyrite 1). It is rimmed by a second pyrite phase characterized by moderate enrichment in Au, Ag, As, Sb, Te, Pb, Bi, and Ni, and no Se or Co (pyrite 2). The surrounding silicate matrix is relatively enriched in Tl (Figure 9-6). An additional pyrite phase (pyrite 3), present in the matrix, is specifically Co-enriched (Figure 9-6L). In contrast, pyrrhotite is distinctively rich in Ni and

Se. In some cases, the two pyrite phases of the nodule can form oscillatory zoning (Figure 9-7). Interestingly, gold is either present in the pyrite nodule (Figure 9-6), or it is located in the adjacent silicate matrix (Figure 9-7; Jackson et al., 2013). One possible interpretation is that the metamorphism grade of these samples was sufficient to recrystallize pyrite and release gold in the matrix, but deformation intensity was insufficient to promote fluid and metal migration. Alternatively, gold present in the silicate matrix and pyrite 3 could be hydrothermal in origin, extraneous to the rock and introduced during syn-D_2 structurally controlled gold mineralization. Currently the first interpretation is favoured as these nodules were sampled in a zone of low D_2-strain intensity.

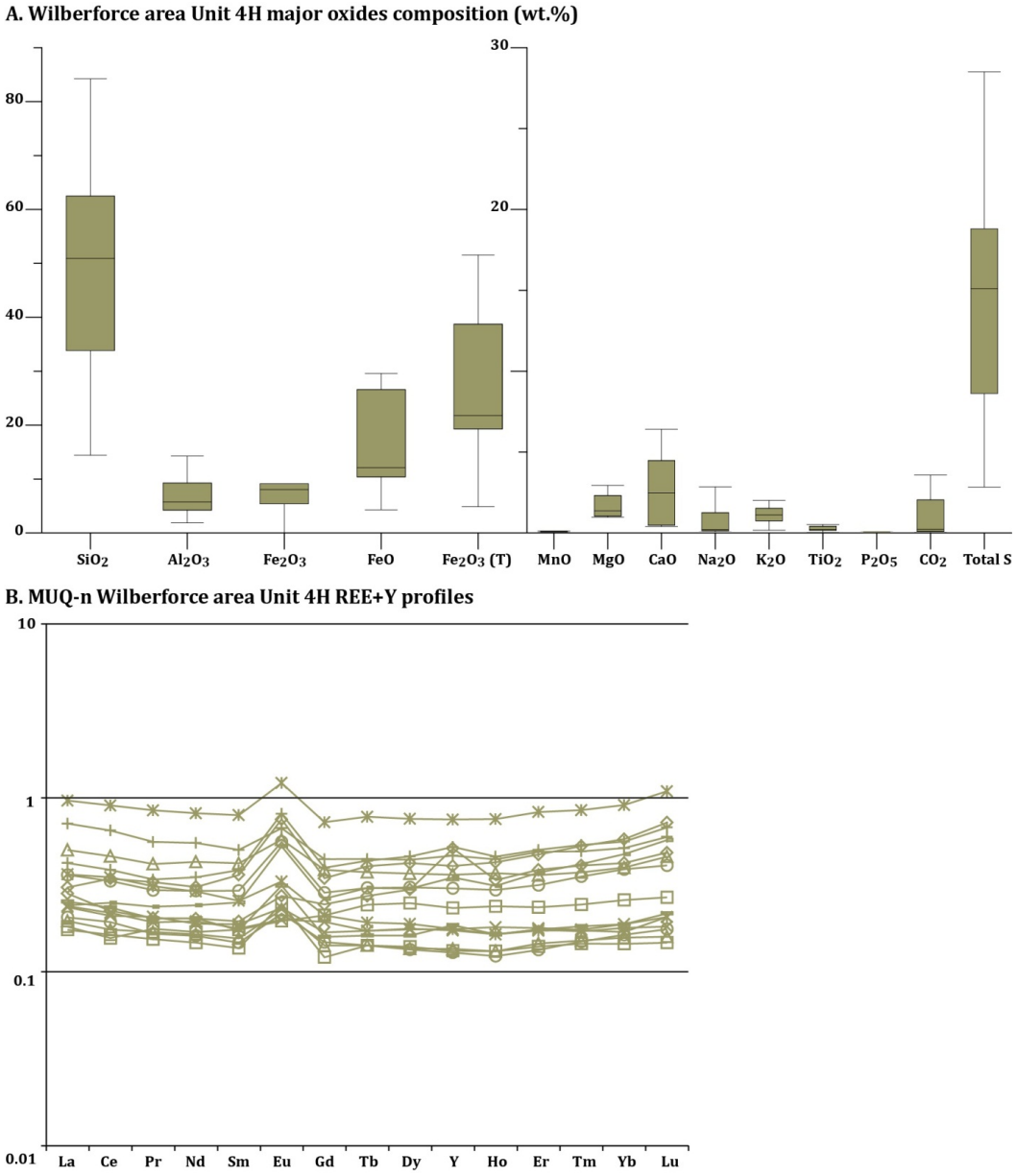

Figure 9-4: Wilberforce unit 4H, 16 samples. A. Box plot of major oxides composition of least altered 4H samples from the Wilberforce area. Box = first to third quartile, black line = median, whiskers = interquartile

range (IQR)*1.5 (Upton and Cook, 1996). B. REE+Y profiles of least altered Wilberforce 4H samples normalized to the MUQ standard (Kamber et al., 2005).

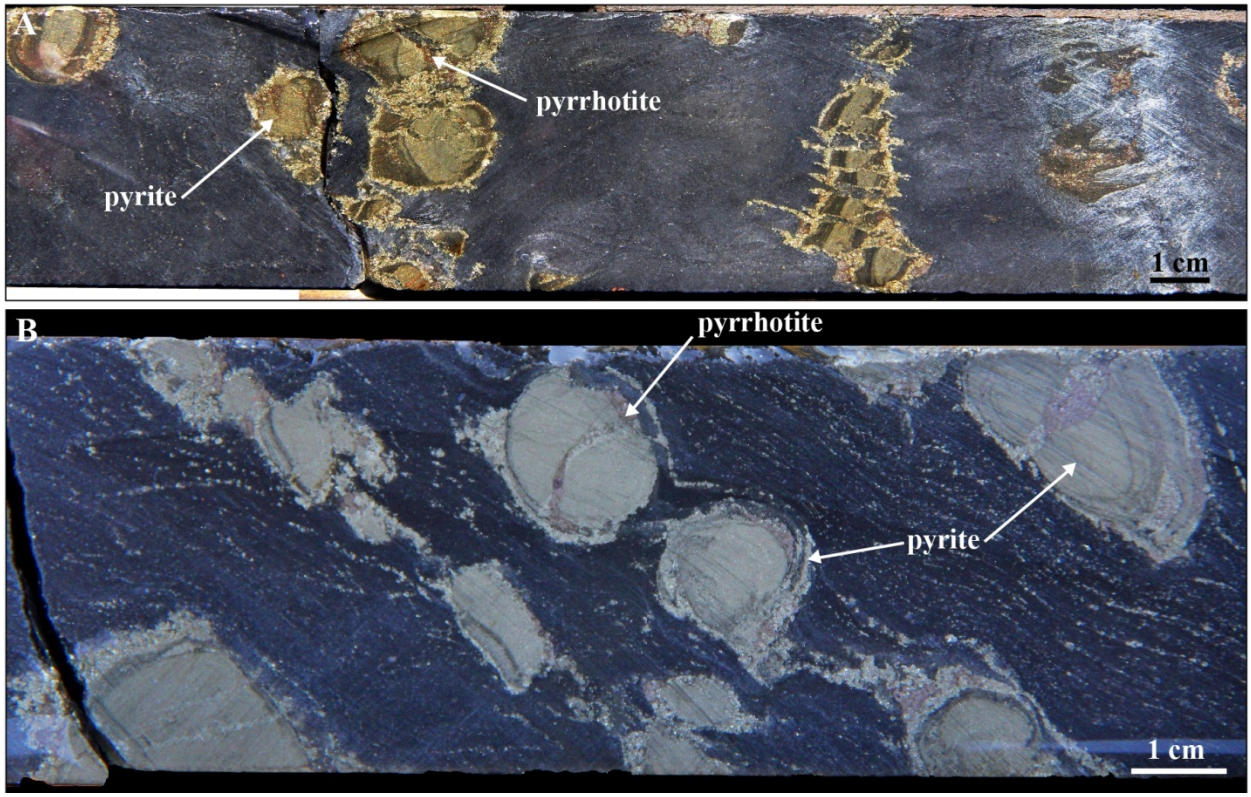

Figure 9-5: Pyrite nodules in argillaceous rock, Wilberforce area, West antiform area. A. Drill core segment from DDH 01-009, near 190 m depth. B. Drill core segment from DDH 12-WIL-001, near 417 m.

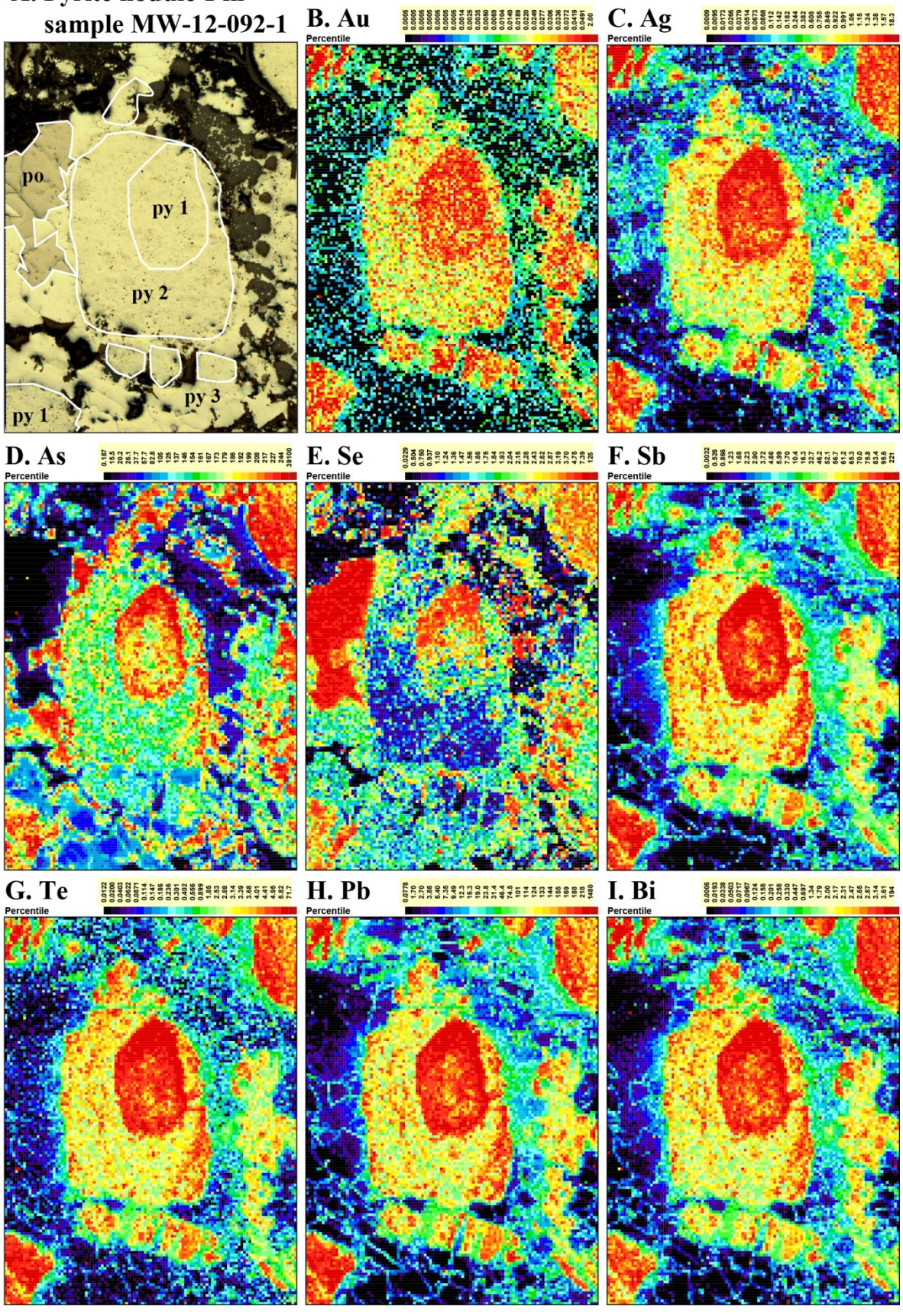
A. Pyrite nodule 1 in sample MW-12-092-1
po
py 1
py 2
py 3
py 1
B. Au
Percentile
C. Ag
Percentile
D. As
Percentile
E. Se
Percentile
F. Sb
Percentile
G. Te
Percentile
H. Pb
Percentile
I. Bi
Percentile

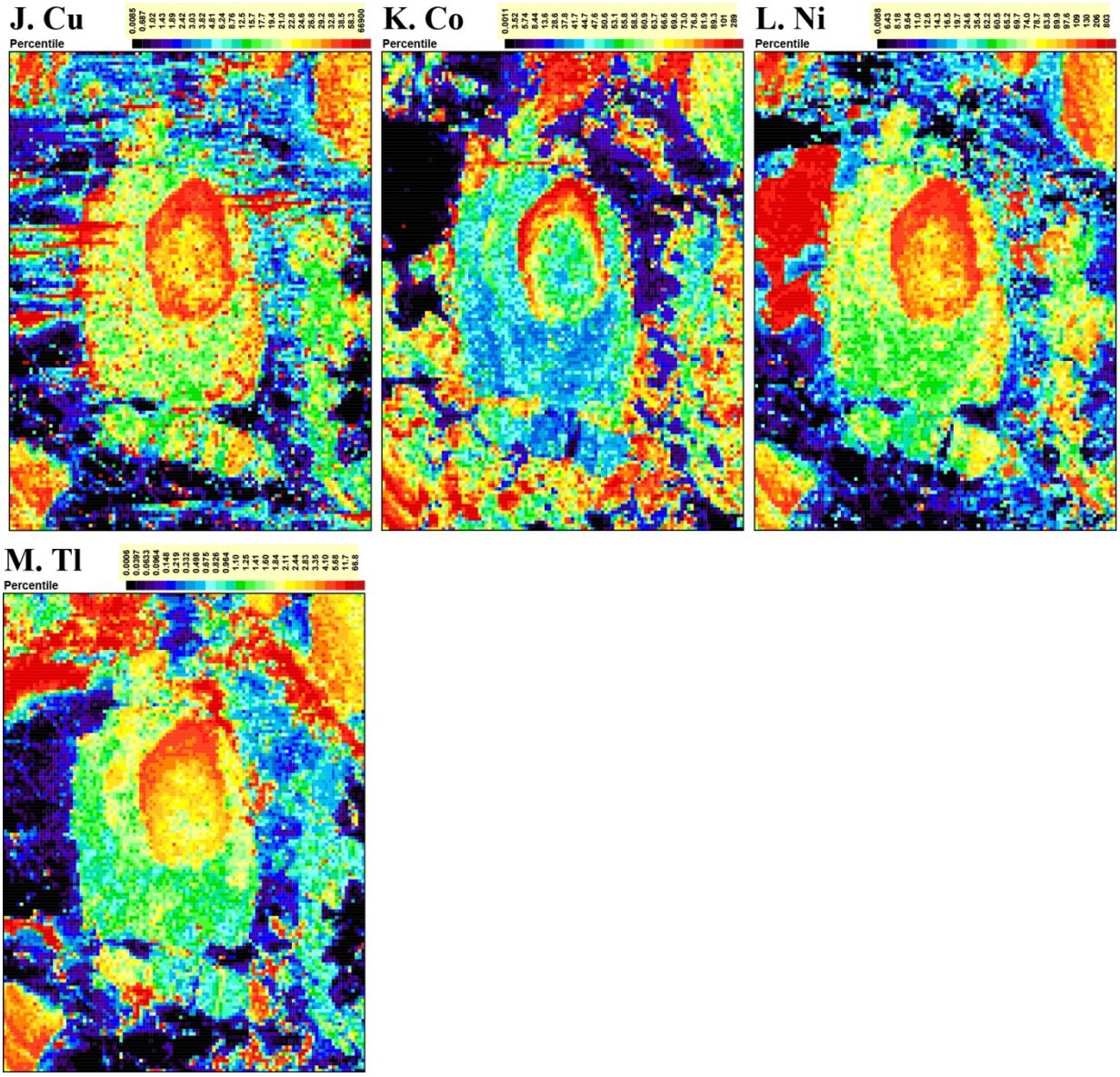

Figure 9-6: LA-ICP-MS 2D elemental maps of pyrite nodule #1 in sample MW-12-092-1. A. Microphotograph in reflected light of the pyrite nodule (pyrite 1 and 2) in the silicate matrix with pyrrhotite and secondary pyrite (pyrite 3). B. to M. Elemental maps.

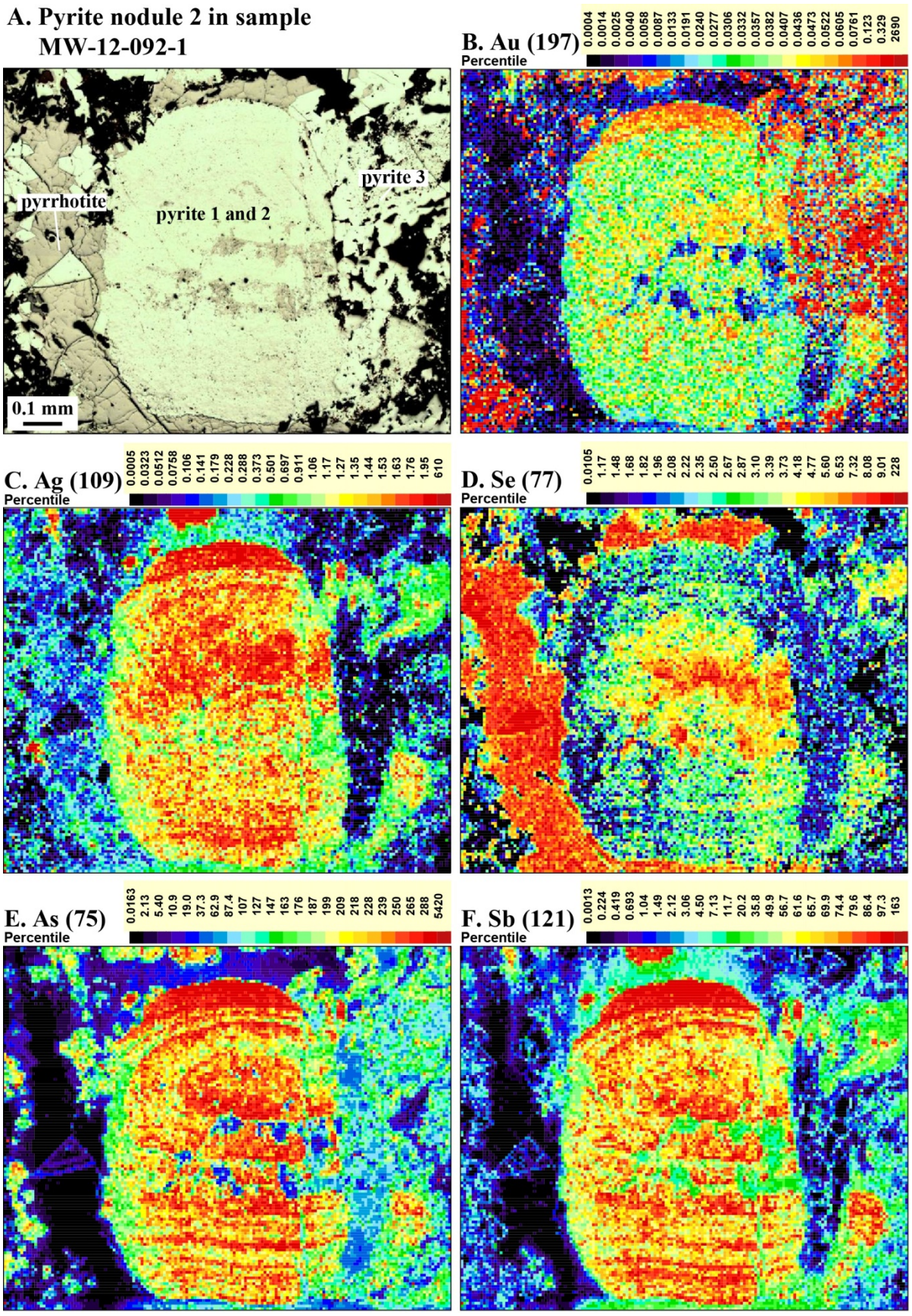
A. Pyrite nodule 2 in sample MW-12-092-1
pyrrhotite
pyrite 1 and 2
pyrite 3
0.1 mm
B. Au (197)
Percentile
0.0004 0.0014 0.0025 0.0040 0.0058 0.0087 0.0133 0.0191 0.0240 0.0277 0.0306 0.0332 0.0357 0.0382 0.0407 0.0436 0.0473 0.0522 0.0605 0.0761 0.123 0.329 2690
C. Ag (109)
Percentile
0.0005 0.0323 0.0512 0.0758 0.106 0.141 0.179 0.228 0.288 0.373 0.501 0.697 0.911 1.06 1.17 1.27 1.35 1.44 1.53 1.63 1.76 1.95 610
D. Se (77)
Percentile
0.0105 1.17 1.48 1.68 1.82 1.96 2.08 2.22 2.35 2.50 2.67 2.87 3.10 3.39 3.73 4.18 4.77 5.60 6.53 7.32 8.08 9.01 228
E. As (75)
Percentile
0.0163 2.13 5.40 10.9 19.0 37.3 62.9 87.4 107 127 147 163 176 187 199 209 218 228 239 250 265 288 5420
F. Sb (121)
Percentile
0.0013 0.224 0.419 0.693 1.04 1.49 2.12 3.06 4.50 7.13 11.7 20.2 35.8 49.9 56.7 61.6 65.7 69.9 74.4 79.6 86.4 97.3 163

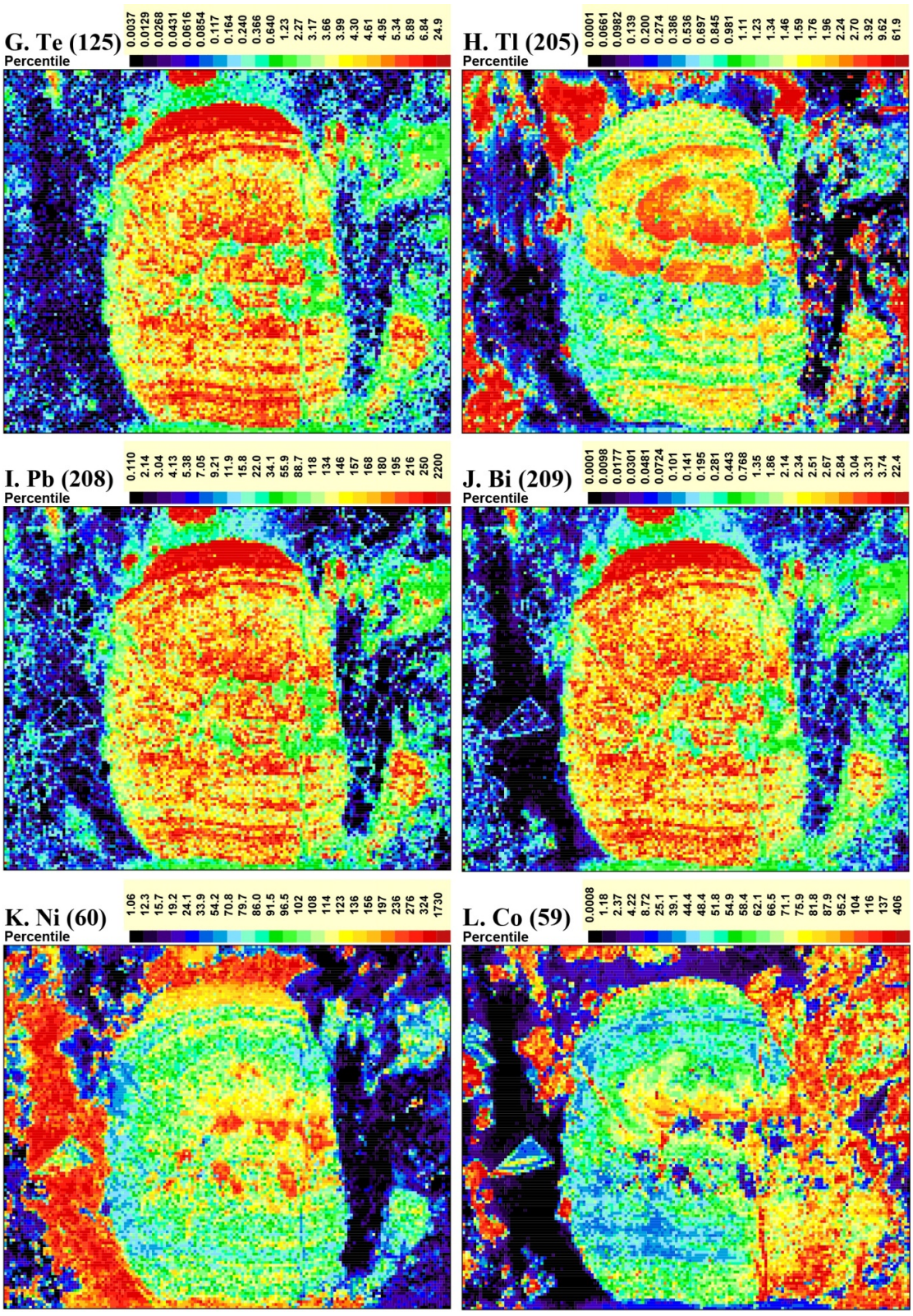

Figure 9-7: LA-ICP-MS 2D elemental maps of pyrite nodule #2 in sample MW-12-092-1. A. Microphotograph in reflected light of the pyrite nodule (pyrite 1 and 2) in the silicate matrix with pyrrhotite and secondary pyrite (pyrite 3). B. to L. Elemental maps.

9.2.2 Pyrite-rich sedimentary rocks of the ZHA

Pyrite-rich sedimentary rocks of the ZHA (Figures 3-42 and 3-43) occur near the contact with the OMA (Figure 5-12A). The pyrite of these sedimentary units are either diagenetic, similar to that of argillites in the Wilberforce area, or metamorphic/hydrothermal, and originating from sulphur-bearing fluids. The asymmetrical shape of pyrite grains suggests they experienced at least some D_2 deformation (Figure 9-8), and evidence of pyrite breakdown to pyrrhotite suggests they were affected by M_2 amphibolite facies metamorphism (Figure 9-8). The structural model presented in chapter 5 implies that the ZHA is present at depth under the mine site. Any pre-existing pyrite, whether metamorphic or diagenetic in origin, could therefore be considered as a potential contributor to some of the metal budget of the Musselwhite ore. Whole-rock geochemical data from these samples show they have a fairly low gold content varying between 7 and 63 ppb, with an average of 24.14 ppb and standard deviation of 14.13. Arsenic is low as well, averaging 16.24 ± 9.22 ppm (Table 9-1).

Microscopic observations in reflected light show that pyrite has a fairly homogeneous net-texture. However, 2D LA-ICP-MS elemental mapping of these pyrite grains shows internal compositional zoning. The pyrite core is very rich in As and Co, with moderate Se content (Figure 9-9). The intermediate zone has much lower As content and similar Co content as the core, with variable Se. The rim is completely devoid of As and has a distinct Se-rich signature. Ag, Sb, Bi, and Te show a common preferential distribution in pyrite fractures and at the pyrite-pyrrhotite contact. Pb partly shares this pattern but is mainly concentrated in the silicate matrix. Cu distribution highlights the presence of chalcopyrite grains that are preferentially located in pyrrhotite or along fractures. Au content is very low and Au appears to be concentrated in the silicate matrix, as well as along fractures in pyrite.

The microscopic texture, zoning, and composition of pyrite (in particular, its high As content at the core) suggest this pyrite formed during metamorphism, by replacing/overgrowing earlier framboid or nodule (Scott et al., 2009; Pitcairn et al., 2010). It is unclear if surrounding pyrrhotite is solely formed from pyrite breakdown in this rock. Ag, Sb, Bi, and Te appear to have been preferentially exsolved from pyrite during metamorphism, yet were not remobilized outside the grains (Figure 9-9). Some fractures delineated by elemental mapping appear to have been subsequently partially “healed” and are invisible on the polished grain surface. This phenomenon is interpreted to be caused by metamorphic recrystallization, which would have repaired the crystal structure but preserve the local concentration of Ag, Sb, Bi, and Te. Interstitial chalcopyrite in pyrrhotite suggests that it could represent a residual phase after pyrrhotite crystallization.

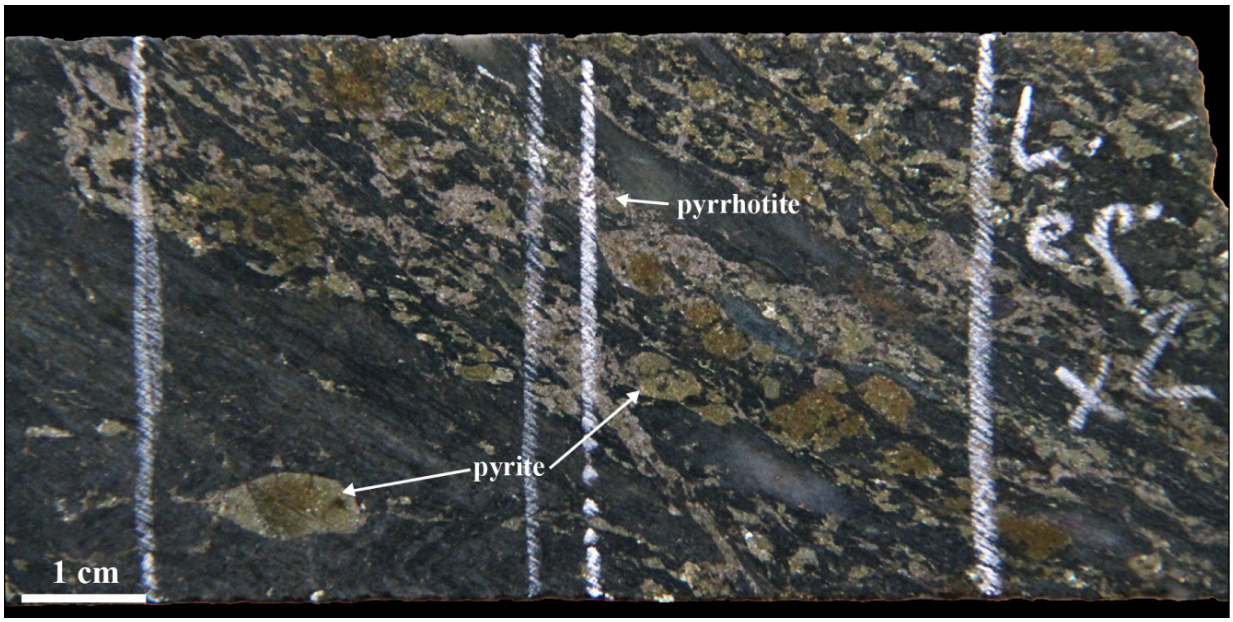

Figure 9-8: Drill core segment of sedimentary rock of the ZHA, sample MW-13-460, DDH 05-PQU-107. D2-deformed pyrite grains are in part converted to pyrrhotite.

Table 9-1: Trace element content of pyrite-rich sediment of the ZHA.

n = 14	**Au**	**Cr**	**Co**	**Ni**	**Sc**	**Cu**	**Pb**	**Zn**
average	24.14	369.71	93.16	291.86	12.50	115.94	10.14	250.21
SD	14.13	396.14	79.51	240.06	7.63	71.48	2.85	374.80
	Ag	**As**	**Ge**	**Sb**	**Se**	**Te**	**Tl**	**Bi**
average	ND	16.24	0.78	0.15	0.90	0.08	0.50	1.09
SD	ND	9.22	0.32	0.06	1.22	0.14	0.24	0.92

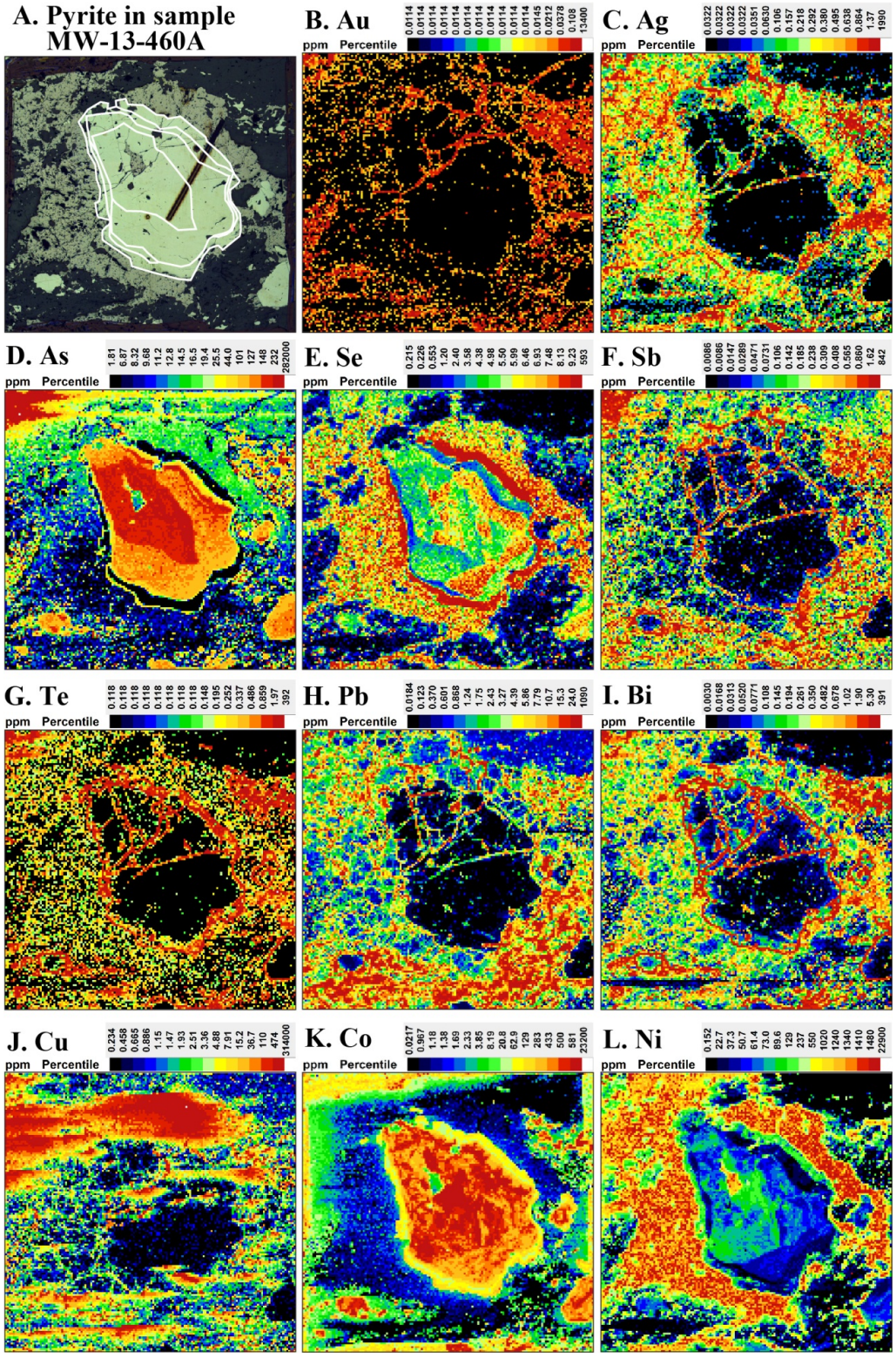

Figure 9-9: LA-ICP-MS 2D elemental maps of pyrite grain in sample MW-13-460A. A. Microphotograph in reflected light of the pyrite grain and surrounding pyrrhotite and silicate matrix. White lines are zonations derived from the arsenic map. B. to L. Elemental maps. Note: Co-rich zones in the periphery of the map are artefacts due to Co-rich pen ink.

9.2.3 Summary

Analyzed sulphides of the Wilberforce and mine areas are hosted in different rock types and tectonometamorphic domains, which may have influenced their growth and compositions. The sulphide phases display key textural differences. The Wilberforce pyrite nodules have a "spotted" texture, framboidal shape, and local oscillatory internal zoning. They display very irregular boundary between "spotted" pyrite and probable secondary "plain" pyrite (Figure 9-10A). Pyrrhotite in these samples is fairly plain. Contrastingly, pyrite grains in samples of the ZHA show a consistently smooth surface, with few inclusions and fractures (Figure 9-10B). The surrounding pyrrhotite is strongly poikilitic and chalcopyrite is commonly found as inclusions in pyrrhotite or in fractures (Figure 9-10B).

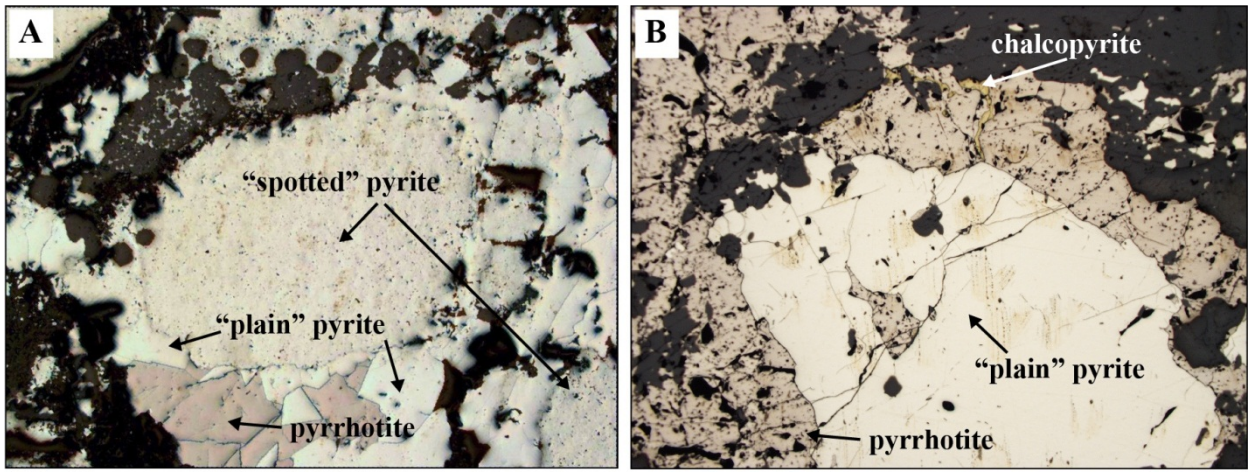

Figure 9-10: Wilberforce and ZHA pyrite A. Microphotograph in reflected light of pyrite nodule 1 in sample MW-12-092-1, Wilberforce area. Two phases of pyrite can be distinguished: a "spotted" pyrite, constituting the nodule, and a "plain" pyrite, with a smooth surface. B. Microphotograph of a pyrite grain surrounded by pyrrhotite in a silicate matrix, sample MW-13-460, DDH 05-PQU-107, mine area. Pyrite displays a very smooth surface.

The combination of textural and elemental pattern differences suggests that pyrite in the Wilberforce nodules is diagenetic, while that of the ZHA sediments is of metamorphic origin (Scott et al., 2009; Pitcairn et al., 2010; Thomas et al., 2011; Large et al., 2011). Pyrite in ZHA sediments is deformed by D_2 (Figure 9-8) and seems to pre-date the peak of M_2 metamorphism. The deposition age of the ZHA sedimentary rocks in the mine area is less than 2846 Ma (chapter 4).

Argillites of the Wilberforce area are a potential source of the metal content found in the ore at Musselwhite (Jackson et al., 2013, 2015). However, they were apparently not sufficiently metamorphosed and deformed to drive fluids and metals out of the matrix surrounding pyrite nodules. It could be the case for similar units located in a more suitable area, such as to the east in the OMA stratigraphy under the mine. This can apply to unit 4H in the NIF and SIF sequence, or any similar unit if present further at

depth. However, such units represent a fairly small volume with respect to other rock types, and are unlikely to have been the main source of metal of the Musselwhite mine.

Pyrite in the ZHA does not appear as a primary potential contributor to the metal budget of the Musselwhite deposit, mainly due to its metamorphic origin. Metasedimentary rocks of the ZHA appear to have played a potential role of fluid source. If metamorphism reached conditions sufficient for pyrite breakdown, then its metal content could have been released. Given the high arsenic content of these pyrite grains, it could probably be linked to arsenopyrite-rich veins, documented underground (mine level 1120, section 12900 N; mine level 845, A-block North, section 12160 N), which crosscut most D_2 structures and thus show a late-D_2-M_2 timing. This remains speculative and additional work is required.

10 SYNTHESIS, DISCUSSION, AND CONCLUSIONS

The previous chapters focused on providing key information stemming from the diverse sources of data examined during this study. Interpretations of the geological, structural, petrographic, geochronological, geochemical, and metallogenic data are integrated to address, fully or partially, the main objectives of this study (1). (1) Improve the understanding of the local and sub-regional geological and structural settings; (2) document the parameters that controlled the formation, distribution, and geometry of gold mineralization; (3) document the geochemical characteristics of gold mineralization and the alteration footprint of the auriferous hydrothermal system; (4) document the relative chronology between gold mineralization and the various tectono-metamorphic events including the timing of gold introduction in the main host unit, the Northern Iron Formation; (5) define exploration criteria for future exploration in the deposit area as well as the North Caribou greenstone belt and in other Archean terranes.

Data, interpretations and implications of this study are summarized in section 10.1. Regional-scale setting and evolution are discussed in section 10.2 to 10.4. Sections 10.2 and 10.3 focus on the implications of new data on the stratigraphic and tectonometamorphic settings of the North Caribou greenstone belt. Section 10.4 integrates this new knowledge to propose a revised model for the evolution of the NCG. Section 10.5 discusses the timing of the hydrothermal event and the controls on gold mineralization to present a genetic model for the Musselwhite gold deposit. Section 10.6 compares main characteristics of the Musselwhite deposit with those of relevant gold deposits in order to present, in section 10.7, the key parameters to improve exploration for BIF-hosted gold deposits in metamorphic terranes. Finally, section 10.8 reviews the conclusions of this study and the outstanding questions to be addressed.

The key elements of chapters 3 to 6, essential for the discussion, are summarized in Figure 10-1Figure 10-2Figure 10-3.

10.1 Synthesis of observations in the study area

10.1.1 Regional geological context and geology of the Opapimiskan Lake area

The Musselwhite deposit is located at a triple point of the North Caribou greenstone belt (Figure 10-1), where rocks of the South Rim (SRA), Opapimiskan-Markop (OMA), Eyapamikama (ELS), North Rim (NRA), and Zeemel-Heaton (ZHA) assemblages are complexly structurally intertwined (Figure 10-1A). The greenstone belt is surrounded by three major TTG-type intrusions: the ca. 2860 Ma North Caribou pluton to the west, the ca. 2850 Ma Schade Lake gneissic complex to the northeast, and the 2730-2710 Ma Southern batholith to the south.

East of the study area, the SRA consists of a volcanic sequence dominated by tholeiitic mafic rocks, with interlayered calc-alkaline intermediate to felsic rocks. N-S-trending horizon of banded iron formation separates the 3.05 Ga lower SRA sequence to the west, from the 2.98 Ga upper SRA sequence. The uppermost unit of the SRA, unit Avol, is constituted of calc-alkaline felsic rocks dated at 2978 Ma and is part of the mine sequence (Figure 10-2).

Covering a large portion of the study area, 2967-2909 Ma ultramafic to mafic rocks of the OMA dominantly have tholeiitic affinities. Transitional to calc-alkaline affinities are documented locally at the base of volcanic sequences. Algoma-type BIF sequences are intercalated within the OMA and are host to gold mineralization. The main BIF sequences are termed the Northern IF and Southern IF (Figure 10-2). The base of the NIF represent an episode of sedimentation dominated by fine-grained detrital mafic material (pelitic rocks, unit 4F). A progressive increase chemical input resulted in the deposition of Al-rich silicate-BIF (unit 4EA), followed by oxide-BIF (unit 4B), Al-poor silicate-BIF (unit 4A) and sulphur-rich argillite (unit 4H). The SIF is constituted by units equivalents to facies B, 4A and 4H, which represent different episodes of sedimentation. The combination of geochronological data from the OMA and the SRA coupled with geological stratigraphic (top indicators) and structural (F_1-F_2 fold interference pattern) data indicate that the mine sequence is overturned. Geochronological analyses show that felsic intrusions in the OMA were emplaced during three episodes: ca. 2890 Ma, ca. 2860 Ma, and ca. 2735 Ma; consistent with regional phases of magmatism.

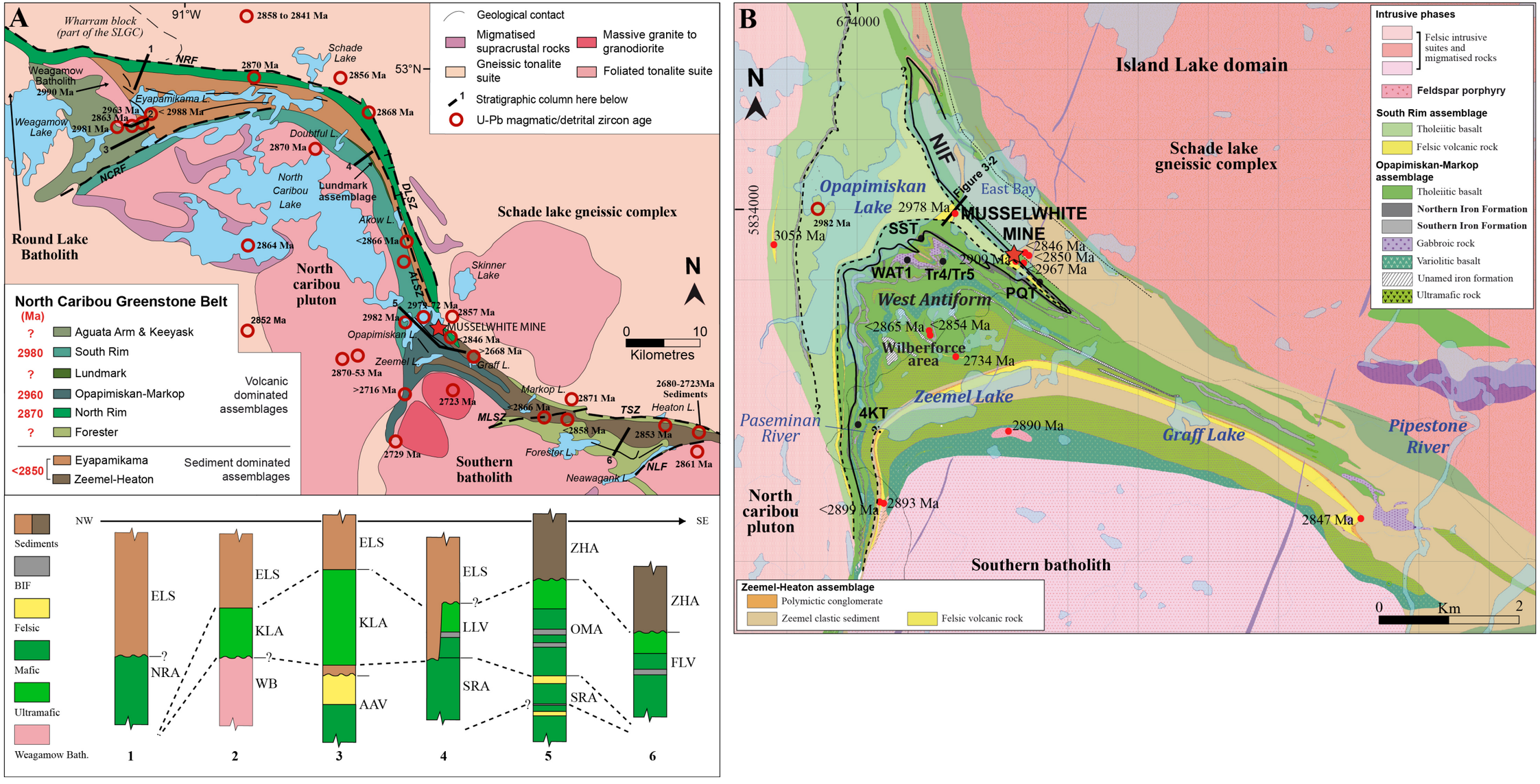

Figure 10-1: A. Simplified tectonostratigraphic map of the North Caribou greenstone belt and surrounding area (modified from McNicoll et al., 2016, after Biczok et al., 2012); geochronological data from Breaks (2001), McNicoll et al. (2013, 2016), Van Lankvelt (2013). Major fault zones from Breaks et al. (2001) and Gagnon et al. (2016): NRF: North Rim Fault, NCRF: North Caribou River Fault, DLSZ: Dinnick Lake Shear Zone, ALSZ: Akow Lake Shear Zone, MLSZ: Markop Lake Shear Zone, TSZ: Totogan Shear Zone, NLF: Neawagank Lake Fault. Revised schematic stratigraphic columns (not to scale) of the lithostratigraphic assemblages of the North Caribou greenstone belt. Columns 1 to 6 are located on the map. Question marks indicate the uncertain nature of the contact. Dash lines represent probable correlation across the NCG. B. Geological map of the Opapimiskan Lake area, with new geochronological data from McNicoll et al. (2016) and this study.

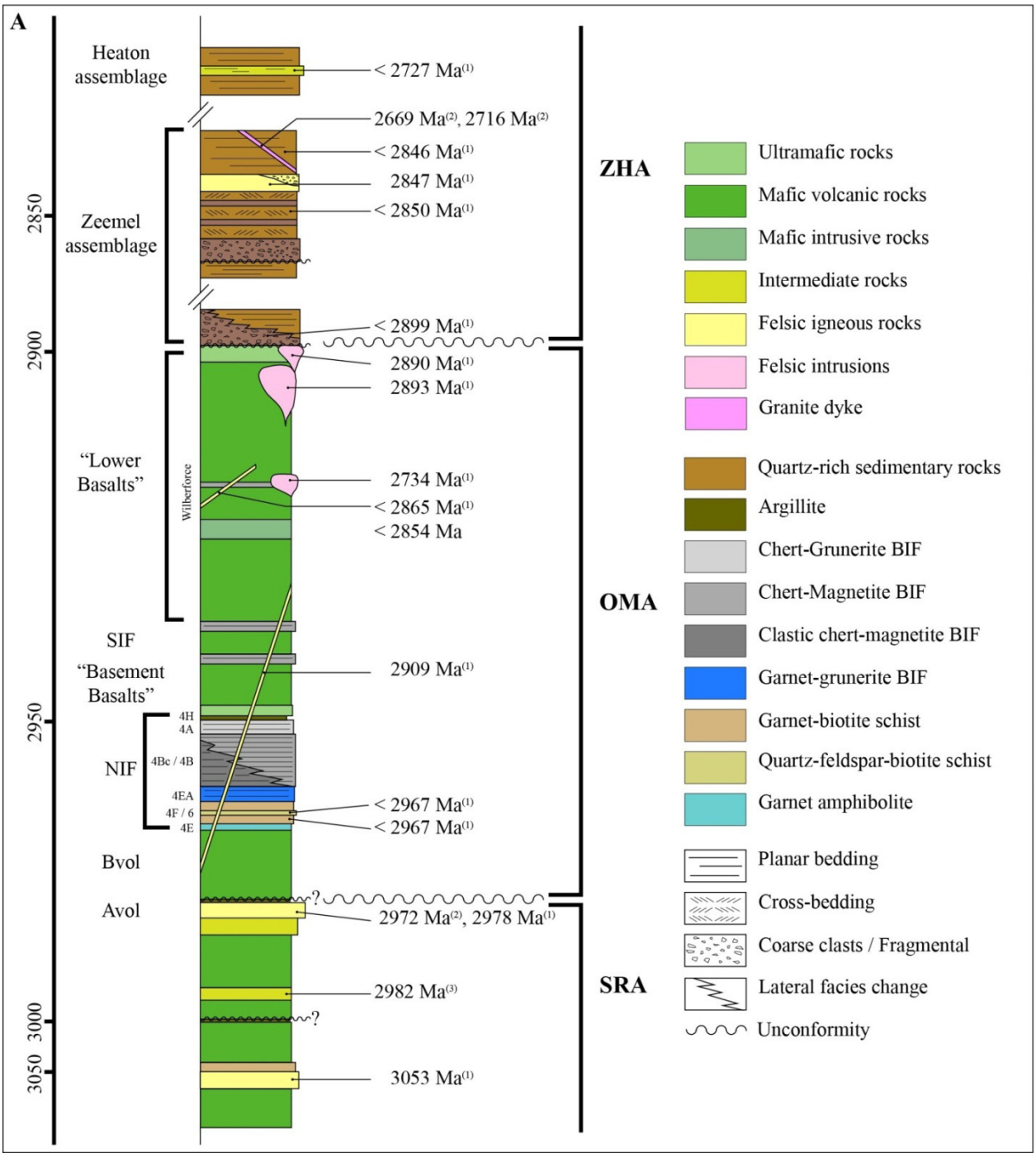

Figure 10-2: Synthetic lithological column of the NCG in the study area (not to scale; idealized stratigraphic relationships). Geochronological data from (1) this study, McNicoll et al. (2016), (2) Biczok et al. (2012), and (3) Davis and Stott (2001).

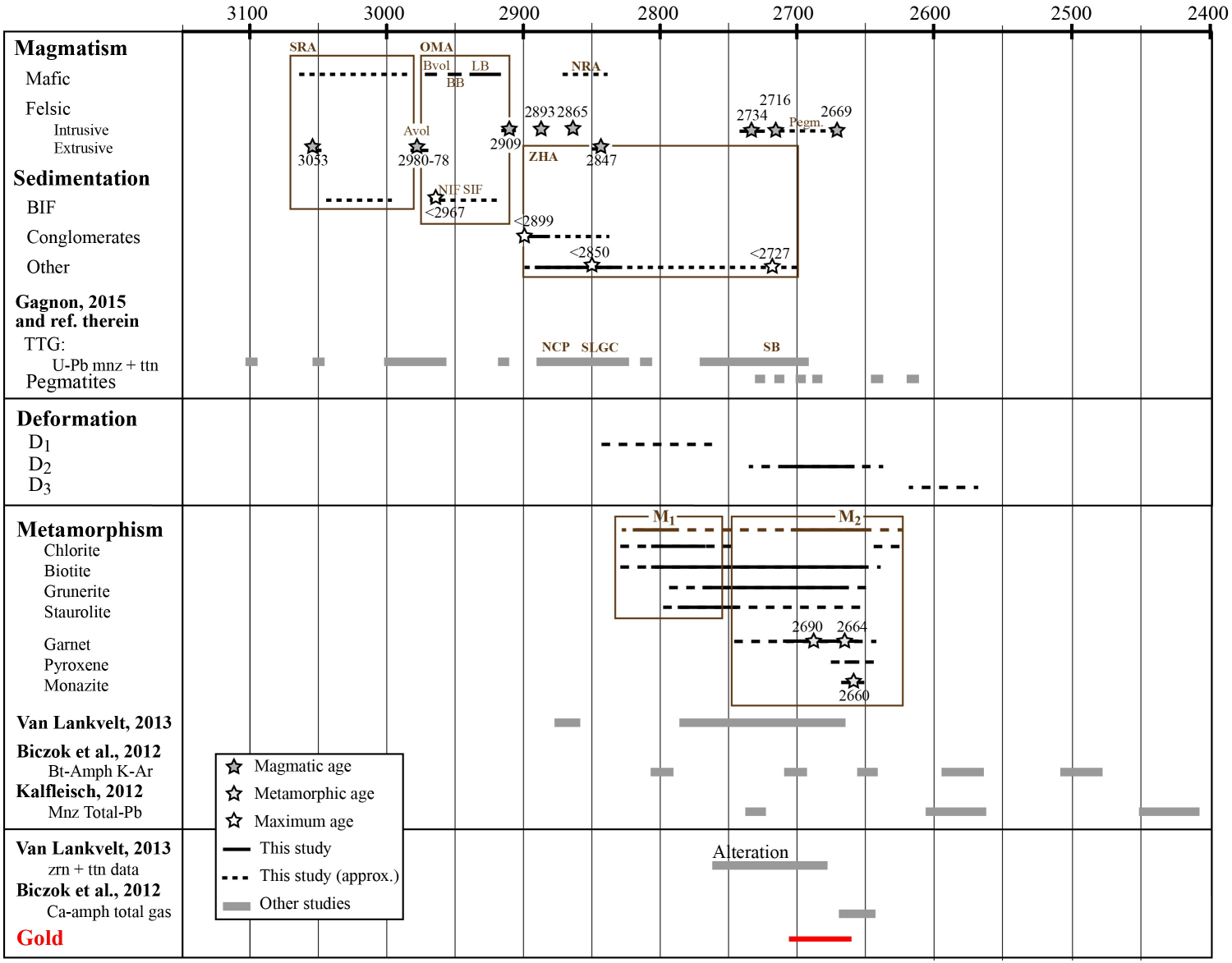

Figure 10-3: Synthetic chart of the tectonometamorphic evolution of the NCG in the Opapimiskan Lake area.

The Zeemel Lake area and easternmost part of the study area are dominated by sedimentary rocks of the ZHA, which comprises conglomerate and breccia, greywacke, sandstone, and argillite. Some intermediate to felsic volcaniclastic rocks and felsic volcanic rocks are also present. Conglomerate deposition occurred after 2899 Ma; sedimentary units of the ZHA in the mine area are younger than 2850 Ma and the felsic volcanic rocks are dated at 2847 Ma (Figure 10-2). The tectonostratigraphy of the ZHA is not fully constrained; however, a potential internal unconformity was mapped. The ZHA is interpreted to correlate with the ELS to the north.

10.1.2 Structure and metamorphism

Rocks in the study area are affected by three distinct tectonometamorphic events (D_1, D_2, and D_3). Evidence of D_1 folding is mostly found at metre- to decimetre-scale, in the iron formation where F_1-F_2 folds form type 3 interference fold pattern. The S_1 foliation is a penetrative fabric documented in the western and southern portions of the study area (Figure 10-5). To the west, S_1 is NNE-SSW trending and steeply dipping. It progressively changes to an E-W trend south of Zeemel Lake. The overturned OMA sequence and sediments of the ZHA in the Zeemel Lake area define the inverted limb of an F_1 syncline, which is itself folded by major F_2 folds. D_1 fabrics become increasingly penetrative to the east approaching the OMA-ZHA boundary, and the truncation of OMA units, suggest that the contact is tectonic and probably represents a D_1 thrust fault. M_1 metamorphism reached the upper greenschist facies in the study area, as evidenced by post D_1 staurolite porphyroblasts in pelitic rocks.

The D_2 deformation mainly consists in large, shallowly NW-plunging, upright antiforms and synforms (i.e., West antiform and East Bay synform; Figure 10-5) associated with regional-scale ductile fault zones. The Opapimiskan Lake area is characterized by a NE-increasing D_2 strain gradient: The low to medium strain area (West antiform) is typified by open folds with an axial planar S_2 spaced cleavage. The high strain zone (mine area) comprises of tight folds with axial planar shear zones, and a penetrative S_2 axial planar foliation. Strain keeps increasing to the NE, where sedimentary rocks of the ZHA show evidence of mylonitisation, and culminates along the North Caribou shear zone (i.e., SLGC-NCG boundary). Late Reorientation of matrix minerals and porphyroblasts (e.g., Ramsay and Huber, 1987), local inversion of the east limb of the East Bay synform, and changes in F_2 fold orientations in the northern Opapimiskan Lake area indicate late D_2 strain. D_2-deformed 2734 Ma felsic rocks (chapter 4) and 2730-2710 Ma Southern Batholith (chapter 2) provide a maximum age for D_2 (Figure 5-46).

The M_2 amphibolite facies metamorphism is reflected by ubiquitous presence of garnet porphyroblasts in pelitic rocks and Al-rich BIF units, as well as the presence of pyroxene in the iron formation. Textural

relationships including boudinaged garnet-rich layers in units 4E and 4EA attest for the syn-kinematic (D_2) growth of garnet porphyroblasts. Peak metamorphism is late-D_2 and dated at 2660 Ma using U-Th-Pb geochronology on monazite, providing a lower age constraint for D_2 (chapter 6). Garnet-biotite geothermometry yielded temperature estimates average 624 °C, which is significantly higher than previous intepretations but still consistent with observed metamorphic paragenesis. Retrograde metamorphism is evidenced by local chlorite-replacement of biotite in pelitic rocks and Al-rich BIF units, and grunerite-replacement of hedenbergite in unit 4A. Weak to moderate deformation of these mineral assemblages suggest late-D_2 timing for the start of retrograde metamorphism.

The D_3 deformation event is characterized by E-W dextral shearing that produced two conjugate sets of folds. A dominant set of ENE-WSW-trending, moderately W- to SW-plunging, Z-shaped folds, and a secondary set of N-S-trending folds. D_3 strain increases to the southeast and culminates along the Markop Lake shear zone (Figure 10-1A). There is little evidence of metamorphism associated with D_3 deformation in the study area.

10.1.3 Mineralization and alteration

Gold occurrences are documented throughout the study area; however, they are largely concentrated in the East Bay synform area. Mineralized and ore zones at Musselwhite are distributed over a 4 km-trend parallel to the fold axial plane. They form narrow (5-15 m) envelopes of 50 to 250 m height and 200 to 1 000 m length. They show a strong spatial association with D_2 high strain zones, which typically occur in the thickened hinge zone of major F_2 folds (e.g., T-antiform, PQD area), parasitic folds (e.g., Esker and Jets zones, Red wing-Thunder wolves zones), or along attenuated fold limbs (e.g., Lynx zone). These high strain zones are characterized by transposition of the BIF layering into an axial planar orientation. Ore is mainly constituted by pyrrhotite-replacement of the garnet-grunerite-chert BIF unit (unit 4EA), and to a lesser extent, in the clastic chert-magnetite BIF (facies 4Bc) and grunerite-chert BIF (unit 4A). Pyrrhotite-replacement is associated with local silica remobilization and minor deformed/fragmented sheeted veins. Vein-dominated mineralization style is documented in the garnet-biotite schist (unit 4F) and “pure” chert-magnetite BIF (unit 4B).

The main gangue mineral assemblage includes green hornblende/ferro-tschermakite, red almandine garnet, brown biotite, and smoky grey quartz. Pyrrhotite is the dominant ore mineral (95%), preferentially distributed along foliation planes and accumulated in pressure shadows of garnet porphyroblasts and inter-boudin spaces. Chalcopyrite is a systematically present but minor phase (5%), and trace minerals

include pentlandite, galena, and arsenopyrite. Gold content is positively correlated with total S, CaO, CO_2, Cu, Ag, Se, Te, and to a lesser extent Pb and Ga.

The distribution and type of alteration are controlled by axial planar D_2 high strain zones and constrating reactivity between rock types, notably in the iron formation. Two major alteration zones have been identified and delineated based on potassium enrichment ± sodium depletion, and calcium and/or carbonate enrichment. Distal alteration is best developed in mafic volcanic rocks and amphibole-bearing sedimentary rocks, and is mainly characterized by the occurrence of biotite. Distal alteration is poorly developed in rocks of the NIF sequence as they have a limited reactivity to hydrothermal fluids. Notable changes include local (re)crystallization of biotite, garnet coarsening (units 4F, 4EA), and crystallization of secondary grunerite (unit 4B). Proximal alteration in mafic volcanic rocks is characterized by abundant carbonates (mainly calcite), with local garnet and or pyroxene crystallization. In the NIF sequence, the nature of proximal alteration varies between calcic and carbonate. In unit 4F, it is characterized by hornblende crystallization and quartz veining. In unit 4EA, there is a progressive replacement of grunerite by Ca-amphiboles and traces of calcite. The proximal alteration involves mineral reactions leading to the coarsening but lesser amount of garnet porphyroblasts. In unit 4B, the proximal alteration is characterized by calcite and iron-carbonates.

10.1.4 Fluid and metal sources

The preferential distribution of alteration minerals along S_2 foliation planes suggest that fluid migration occurred during D_2. Both volcanic and sedimentary rocks under the mine appear as potential source for metamorphic devolatilization-derived mineralizing fluids. Metals may have been sourced in situ during fluids production, or leached from rocks during migration. LA-ICP-MS mapping of sulphides (pyrite and pyrrhotite) from the West antiform area show diagenetic pyrite nodules in argillite horizons were recrystallized during metamorphism and released part or all of their trace metal content in the surrounding matrix. In the West Antiform area, lower D_2 strain may have been insufficient to mobilize the released metals and fluids out of the rock. However, in areas of greater strain and metamorphic grade (e.g., closer to the mine), they may have been remobilized into mineralized high strain zones. Sulphide-bearing sedimentary rocks of the ZHA east of the mine show the breakdown of pyrite into pyrrhotite. LA-ICP-MS mapping of these sulphides shows a complex trace element distribution in and around pyrite indicating partial release of metals. Complete pyrite breakdown in sedimentary rocks at greater depth may have provided sulphur and metals to migrating mineralized fluids.

10.2 Revised tectonostratigraphy of the North Caribou greenstone belt

Geological, geochronological and geochemical data collected during this study complement previous work on the tectonostratigraphy of the NCG, notably in the Opapimiskan Lake area (Breaks et al., 1986, 2001 and reference therein; Hollings and Kerrich, 1999; Moran, 2008; Biczok et al., 2012; Smyk, 2013). Implications of this new data improve the understanding of tectonometamorphic evolution of the NCG, but are also critical to elaborate a genetic model for the Musselwhite deposit and to provide regional exploration guidelines. The following sub-sections propose a complete review of the tectonostratigraphy, plutonic phases and tectonometamorphic events that characterize the NCG.

10.2.1 Early volcanism and sedimentation (3.1-2.97 Ga)

The oldest preserved constituent of the NCG is the lower portion of the SRA, which hosts a 3053 Ma rhyolite unit (Figure 10-1; McNicoll et al., 2016). It is also the oldest felsic volcanic rock unit in the North Caribou terrane, which ranges in age from 3.0–2.7 Ga (Corfu et al., 1998; Percival et al., 2006, 2012). Evidence of older components is reflected by ca. 3.1 Ga detrital zircons in the ELS and ZHA (Duff, 2014; Bath, 2017). A hiatus in volcanic activity is evidenced by the deposition of BIF and argillite beds that are outlined by a linear electromagnetic anomaly, and intersected in exploration drilling (unpublished data, Goldcorp Musselwhite Ltd.).

The 2990 Ma Weagamow batholith (Figure 10-1A; de Kemp, 1987) intruded the belt before widespread volcanic activity resumed from 2982 Ma to 2972 Ma (Davis and Stott, 2001; Biczok et al., 2012), forming the upper SRA. Syn-volcanic intrusions of that age range comprise the Wharram Lake block (WLB, granodioritic batholith NW of the NCG) that yielded zircon core ages of ca. 2976 and ca. 2928 Ma (Van Lankvelt, 2013). Geological and geochemical data from this study (chapter 3) supports the hypothesis that the SRA is the product of a mantle plume-type source, as first proposed by Hollings and Kerrich (1999), similar to ocean plateau basalts (Sun and McDonough, 1989). In this hypothesis, initial mafic magmas slowly evolved to intermediate and felsic composition through assimilation-fractionation-contamination processes (Perring et al., 1996; Shervais, 2001; Dickin, 2005; Pearce, 2008; Smyk, 2013).

Age constraints on the Agutua Arm volcanic rocks (AAV; 2981 ± 1.8 Ma; de Kemp, 1987) suggest it is coeval with the upper SRA (unit Avol dated at 2972.4 ± 1.6 Ma; Biczok et al., 2012), although volcanic activity may have lasted longer in the southern NCG. In the northern part of the NCG, the AAV is overlain by sediments in the Keeyask assemblage (KLA; Breaks et al., 2001) that contain detrital zircons dated at 2978.1 ± 3 Ma (de Kemp, 1987), suggesting that volcanism had ceased by that time. Sediments

of the KLA include a basal conglomerate and mature quartz arenite, overlain by mudstone and siltstone units, some of which contain stromatolites attesting of a shallow-water shelf environment (Arias, 1986; Beukes and Gutzmer, 2008). Overlying chert-magnetite BIF, comprising breccia and laminated chert, is indicative of a transgressive regime with higher water level in the northern part of the belt. Lateral transition from BIF to dolomite-rich calcarenite (de Kemp, 1987) suggests shallower waters with detrital input (Beukes and Gutzmer, 2008). To the south-east, away from detrital sediment sources and in a deep-water environment, the top of the SRA is marked by argillitic units (between unit Avol and unit Bvol).

10.2.2 Mantle plume-related volcanism and iron formation deposition (2.97-2.91 Ga)

Based on similar volcanic lithologies and BIF occurrences, Breaks et al. (2001) correlate parts of the KLA with the Lundmark Lake assemblage (LLV), the OMA in the study area, and the Forester Lake assemblage (FLV; Figure 10-1A). Together, these assemblages represent a major pulse of volcanism between 2.97 and 2.91 Ga, interpreted as the product of a mantle plume (Hollings and Kerrich, 1999; this study). A breakdown of this period is presented here below, using the data acquired on the OMA during this study.

In the Opapimiskan Lake area, the OMA structurally overlays the SRA. Geochronological data on pelitic rocks of the OMA (units 4F and 6) and stratigraphic polarity indicators however show that the stratigraphy is inverted (chapter 4; McNicoll et al., 2016). Dating of the unit Avol and felsic dykes constrains the age of the OMA to between 2972 and 2909 Ma (chapter 4; Biczok et al., 2012; McNicoll et al., 2016). The OMA can be divided in two parts: the lower portion constituted by the Musselwhite mine sequence (unit Avol to Southern iron formation, SIF; Figure 10-2A), and the upper part that mainly includes the “Lower basalts” unit, with an intercalated horizon of iron formation, and the Wilberforce felsic volcanic rocks and associated massive sulphides.

The Musselwhite mine sequence represents three main episodes of underwater volcanism, separated by periods of detrital, chemical and hydrogenous sedimentation (chapter 3). The stratigraphically lowest, and structurally highest, part of the lower OMA is constituted of unit Bvol and intercalated horizons of unit 4F and unit 4E. Unit Bvol represents a period of tholeiitic, mafic volcanic activity (Figure 3-10). Geochemical data shows a few samples have transitional magmatic affinity, and their extended trace element profiles normalized to the Primitive Mantle display LREE enrichment, strongly negative Nb-Ta anomaly and weakly negative Ti anomaly (Figure 3-11). This is consistent with previous work (Hollings and Kerrich, 1999) and suggest the contamination of tholeiitic magma by calc-alkaline felsic crustal rocks, such as those of the underlying SRA. Geochronological data from units 4F and 6, which overlay

unit Bvol, constrain this magmatic episode between 2978 and 2967 Ma (chapter 4). Unit 4F is interpreted as a pelitic unit, dominantly composed of distal mafic detrital sediments and minor hydrothermally-derived chemical sediments (this study; Moran, 2008). Unit 4E is interpreted as locally-sourced epiclastic sediments mixed with chemical sediments, marking a strong hydrothermal activity and a short pause in volcanism.

The base of the NIF is generally marked by a horizon of unit 4E, indicating the interruption of volcanic activity and onset of hydrothermal activity with minor remobilization of flow top breccia and sediments. Then, unit 4F attests of abundant mafic pelitic sedimentation, whereas the more felsic unit 6 (chapter 3) suggests a temporary change in the source of sediments or to the hydrologic system. Progressively, the combination of hydrothermal activity and decrease in detrital input led to the deposition of a silicate-BIF (unit 4EA).

Unit 4EA may represent a primary facies of the iron formation sequence or the product of hydrothermal alteration. Moran (2008) interpreted this unit as a primary sedimentary facies, and geological and geochemical data from this study supports such interpretation. MUQ-normalized REE+Y profiles show a distinct geochemical signature with Eu* and Y* anomalies consistent with contributions of seawater and hydrothermal fluid to BIF deposition, with some detrital input (chapters 1 and 3; Bau and Dulski, 1996; Alexander et al., 2008; Moran, 2008; Gourcerol et al., 2016). The distribution of gold mineralization (chapter 7) and associated hydrothermal alteration (chapter 8) are discordant to lithological layering and cannot account for the distribution of unit 4EA and its lithological variations.

Geological and petrographic data (chapter 6) coupled with genetic models of Algoma-type iron formations (Figure 1-6; Rudnicki, 1995; Spry et al., 2000; Peter, 2003; Gross, 2009) and studies on the metamorphic paragenesis of iron formations (chapter 1; Tables Table 1-1, Table 1-2; French, 1968; Frost, 1979a; Haase, 1982; Klein, 1983, 2005; Peter, 2003) can be used to determine the nature of the unit 4EA protolith. Peter (2003) reported a mineralogical zonation in Algoma-type BIF of the Broken Hill and Pegmont areas in Australia, where the hydrothermal vent is surrounded by carbonate facies BIF, grading into oxide facies and, further away, into silicate facies. Such zonation may vary in nature and extent depending on the intensity and the thermal history of the hydrothermal system (Peter, 2003). Here, unit 4EA is distributed from the northern Opapimiskan Lake area to the West antiform area (Figure 10-1B), while overlying oxide BIF (unit 4B) and silicate BIF (unit 4A) appear to be much more extensive. In addition, mine geologists report that unit 4EA laterally grade into unit 4F or unit 4B (N. Guest, personal communication, 2013). Metamorphic reactions producing the garnet-grunerite mineral assemblage notably involve consumption of carbonate phases (Haase, 1982). Such reactions also require a silicate, aluminum-rich component, which, in the case of the NIF, was provided by detrital sedimentation mixing

with the product of hydrothermal activity. Unit 4EA can thus be interpreted as the metamorphic product of a protolith formed by carbonate particles derived from hydrothermal activity and detrital sediments.

The transition from unit 4EA to unit 4B is marked by the development of magnetite-rich beds, with detrital material restricted to specific bands (e.g., garnet-hornblende bands in the metamorphosed unit), suggestive of episodic detrital input. In addition, the transition from an inferred carbonate facies to oxide facies BIF suggests a decreasing hydrothermal input. Units 4B and 4A are more typical units of iron formation sequences (Klein, 2005). Lithological and mineralogical changes in these units, leading from chert-magnetite layering (unit 4B) to chert-grunerite (unit 4A), and capped by sulphide-rich argillite (unit 4H), show the slow decrease in hydrothermal activity, both in terms of input and fluid temperature (Moran, 2008). The sulphide-rich argillite unit marks the end of hydrothermal activity. The sulphide and graphite content indicates strongly anoxic ambient water conditions (Moran, 2008).

The sedimentation of the NIF is interpreted to have occurred in a probably deep basin, with little connection to open seawater (Gourcerol et al., 2016). The size of the basin is unknown, as it depends on whether iron formations of the Lundmark assemblage correlate with those of the OMA. Detrital sedimentation in the basin decreased over time, and chemical sediments from a well-developed and long-lived hydrothermal system took over (Moran, 2008; Baldwin, 2011). In contrast with clastic-dominated units (units 4F and 6), all BIF units show evidence of some hydrogenous input of chemical sediments (i.e., positive Y anomaly; Bau and Dulski, 1996; Oswald et al., 2015b).

The “Basement basalts” unit separates the NIF and SIF sequences. Its base is characterized by a thin calc-alkaline dacitic layer (Figure 3-13), and overlying mafic and ultramafic rocks show transitional and tholeiitic magmatic affinities. Some basaltic and komatiitic samples show moderate LREE enrichment and negative Nb-Ta and Ti anomalies (Figure 3-14), which are consistent with crustal contamination (Hollings and Kerrich, 1999). The considerable time period required for the deposition of tens of metres of iron formation (Pickard, 2002, 2003; Baldwin, 2011) allows the fractionation and/or crustal contamination of magma(s) during ascent. Contamination by thermal erosion during komatiites emplacement (Perring et al., 1996) is ruled out due to inconsistency between observed geochemical anomalies and those predicted in such setting (Nesbitt and Sun, 1976; Jochum et al., 1991; Hollings and Kerrich, 1999).

The Southern iron formation sequence comprises several BIF horizons separated by thin volcanic packages (Figure 10-2B; Moran, 2008). The SIF horizons typically comprise a basal magnetite-rich 4B layer, indicative of strong hydrothermal activity, followed by a progressively chert-rich and grunerite-rich layer (unit 4A), topped by a sulphide-rich argillite (unit 4H). These lithologies display similar geochemical characteristics than those of the NIF (REE+Y MUQ-n profiles, Eu* and Y* anomalies, etc.),

but with much lower to no detrital content. The multiple horizons of the SIF represent shorter-lived hydrothermal systems relative to the NIF. Local slump features in unit 4B and gravel-size beds in unit 4A portions of the SIF suggest briefs periods of instability (chapter 5).

The upper OMA in the mine area is only a few tens of metre-thick and solely constituted of the "Lower basalts" unit, which include mafic and ultramafic volcanic rocks of tholeiitic to slightly transitional magmatic affinity (Figure 3-17). In the West antiform area, it is much thicker, representing roughly twice the thickness of the lower OMA (Figure 10-1B), and includes thick packages of mafic to ultramafic flows with gabbro. It also comprises a BIF horizon and felsic and intermediate volcanic rocks that are contain VMS-type mineralization (Wilberforce area; Guest, 2013).

There is little geochemical data on mafic and ultramafic rocks of the upper OMA. Data on intermediate and felsic rocks of the Wilberforce area show a calc-alkaline magmatic affinity, strongly negative Nb-Ta anomalies and moderately negative Ti anomalies (Guest, 2013). These features are similar to that of intermediate and felsic rocks of the SRA (Hollings and Kerrich, 1999; Smyk, 2013), as well as intermediate rocks of the "Basement basalts" unit (Hollings and Kerrich, 1999; this study). It has been suggested that the 3053 Ma felsic rocks of the SRA (Smyk, 2013), and the felsic rocks of the Wilberforce area (Guest, 2013) evolved from a basaltic melt produced in a subduction-type tectonic setting. Such a geodynamic interpretation should be reconsidered in light of the petrological characteristics and geochronological data from all volcanic rocks in the Opapimiskan Lake area.

The rock units at the base of volcanic sequences of the OMA show a slightly evolved signature and evidence of contamination, while overlying volcanic rocks show transitional to tholeiitic signature. Later magmas appear to have benefited from well-established feeder systems ensuring little to no crustal contamination (Naldrett, 1999), leading to eruption of typical tholeiitic komatiites and basalts in an environment similar to modern ocean plateau (Pearce, 2008). In addition, basal volcanic rocks overlie argillites and/or iron formations that require significant amount of time for deposition (Altermann and Nelson, 1998; Pickard, 2003; Baldwin, 2011), suggesting that magmas had time to interact with the crust and acquire a mixed geochemical signature prior to eruption.

The mixing and contamination models show that felsic rocks of the SRA may have contaminated the magmas that produced rocks of the OMA (Hollings and Kerrich, 1999). On a Th/Yb vs. Nb/Yb plot (Pearce, 2008), least altered volcanic rocks of the OMA form a well-defined trend between the N-MORB field and the vicinity of the Archean crust composition (Figure 10-4). The OMA is thought to result from a period of plume-related volcanic activity, during which tholeiitic ultramafic to mafic magmas ascended through and interacted with an older crust of mixed mafic and felsic material. Between periods of intense volcanism, sedimentation took place in stratified-water basins (section 1.4; Veizer, 1983; Eriksson et al.,

2005), in which detrital and chemical inputs provided the sediments of pelitic and quartzo-feldspathic rocks (unit 4F, unit 6), iron formations (units 4E, 4EA, 4B, 4A), and argillites (unit 4H).

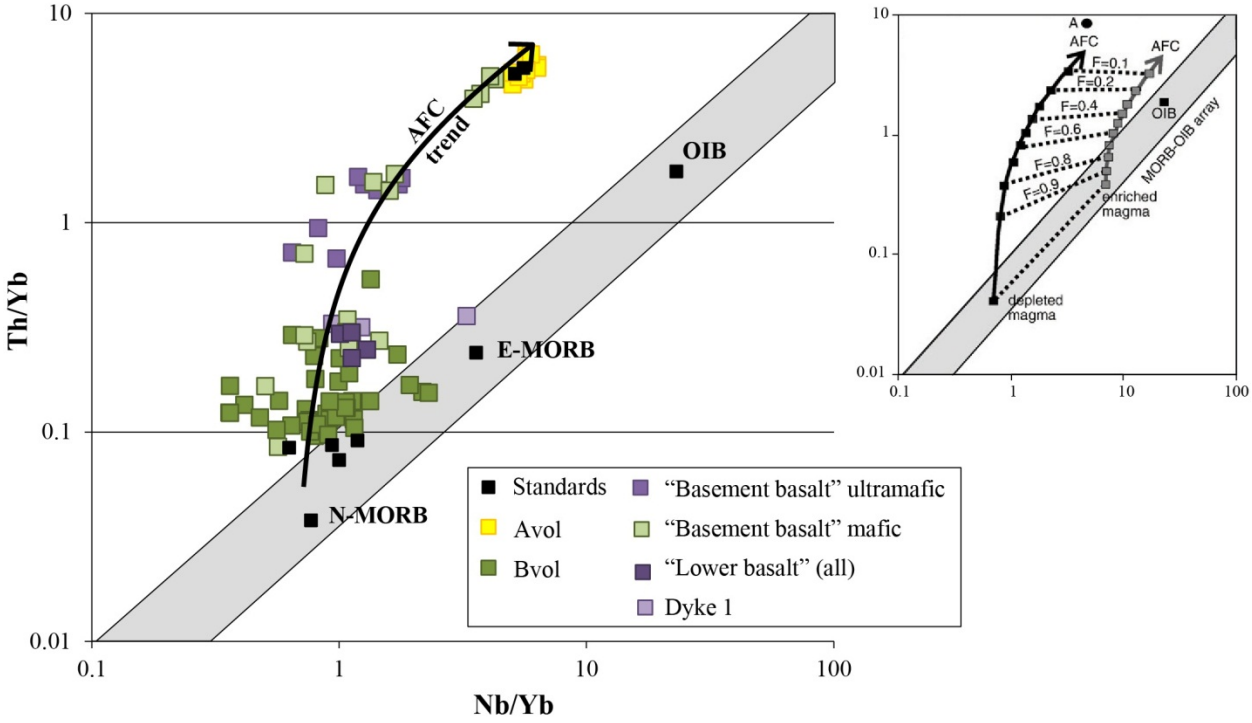

Figure 10-4: Th/Yb vs. Nb/Yb plot of "least altered" volcanic rocks from the Musselwhite mine stratigraphy. Inset: original plot from Pearce (2008) showing modelled AFC trends. Felsic rocks of unit Avol and standards for felsic volcanic rocks plot close to the composition of felsic Archean crust (inset: A). Most tholeiitic mafic rocks of unit Bvol plot slightly above the N-MORB field, while most mafic rocks and all ultramafic rocks of the "Basement basalts" unit are much higher, forming an average trend (black line) that is typical of AFC processes (Pearce, 2008).

10.2.3 Voluminous magmatism and crustal growth (2.90-2.82 Ga and 2.73-2.71 Ga)

10.2.3.1 From 2.90 to 2.82 Ga

The 3.05-2.9 Ga volcano-sedimentary succession of the NCG (SRA, KLA, and OMA) is intruded by several felsic bodies. The oldest, 2893 and 2890 Ma intrusions within the OMA occur in the southern part of study area (chapter 4). In the Wilberforce area, intermediate and intrusive felsic rocks are dated at <2865 and <2854 Ma. These rocks contained ca. 2982, 2910 and 2900 Ma inherited zircon grains comparable with age constraints on the deposition of the OMA. Such ages are also compatible with the 2863 ± 1 Ma age obtained for the Keeyask Lake porphyry that intrudes komatiites overlying sediments of the KLA (Figure 10-1; Davis and Stott, 2001). Slightly younger, a rhyolitic unit located within the ZHA is dated at 2847 Ma (chapter 4). Such age constrast, in combination with the 2870 Ma age obtained on

rocks of the North Rim assemblage (NRA; Davis and Stott, 2001) attests for the continued growth of the NCG.

The NCG is surrounded by the 2890-2830 Ma Schade Lake gneissic complex and North Caribou pluton (de Kemp, 1987; Davis and Stott, 2001; Biczok et al., 2012; Van Lankvelt, 2013). Both are composed of multiple intrusive phases (Van Lankvelt, 2013). The intrusion of NCP caused a metamorphic contact aureole in the neighbouring NCG, while the northwestern contact with the SLGC has been reworked and is clearly tectonic (Breaks et al., 2001; Kalbfleisch, 2012; Van Lankvelt, 2013).

The combination of geological data and geochronological constraints show a major episode (2.90 to 2.82 Ga) of crustal growth resulting from the emplacement of multi-phase TTG-type batholiths and extensive mafic volcanism. This is consistent with the evolution of the northwestern Superior province (Percival et al., 2012, and references therein), notably with those of the Oxford-Stull and Island Lake domains.

10.2.3.2 From 2.73 to 2.71 Ga

The poly-phase Southern batholith (SB; Figure 10-1; Biczok et al., 2012) marks a younger period of magmatism (2.73-2.71 Ga; Percival et al., 2006, 2012). The emplacement of 2734 Ma felsic sub-volcanic intrusive unit in the Wilberforce area (chapter 4) is coeval with the SB. Evidence of magmatism from this period is also found in sedimentary rocks of the ZHA, which contain detrital zircon populations dated at 2727.8±2.4 Ma (this study), 2696 ± 39 Ma (Bath, 2017) and 2674±29 Ma (Duff, 2014).

10.2.4 Detrital sedimentation (2.90-2.72 Ga)

The Eyapamikama Lake assemblage (ELS) and Zeemel-Heaton assemblage (ZHA) represent a major shift in the evolution of the NCG, from environments previously dominated by volcanism to a period of clastic sedimentation. In the northern NCG, samples of conglomerates to greywacke and slate from the ELS contain variable populations of detrital zircon age (de Kemp, 1987; Breaks and Bartlett, 1991). In the western part of the ELS, near the contact with the SRA and KLA, a sample of conglomerate provided a maximum age of deposition of <2962.6 ± 13 Ma (Davis and Stott, 2001), compatible with a sample of sandstone in the same area that yielded a detrital zircon population between 2989 and 2981 Ma with the youngest zircon at 2951 ± 12 Ma (Duff, 2014). Elsewhere, the maximum age deposition of the ELS is closer to <2850 Ma (de Kemp, 1987) or <2856 Ma (Duff, 2014). Rock types of the western ELS comprise proximal coarse-grained units and evolve into fine-grained sediments to the east and in the central NCG, reflecting changing depositional environments such as those of alluvial fans (de Kemp, 1987; Breaks and Bartlett, 1991; Breaks et al., 1991; Duff, 2014). Overall, the ELS is interpreted to have been deposited in

an shallow marine environment, such as those commonly found in Mesoarchean greenstone belts in syn-orogenic settings (Eriksson et al., 1994, 1997, 2005).

In the Musselwhite Mine area and southern NCG, the base of the ZHA includes conglomerate (<2899 Ma; chapter 4), greywacke, local argillite and interbedded volcaniclastic rocks (chapter 3). Such lithologies suggest a similar depositional environment than that of the ELS (Eriksson et al., 2005). Geochronological constraints in the Opapimiskan Lake area show that the first stage of basin development covers the 2899 to 2850 Ma period. This timeframe overlaps with a period of major felsic magmatism in the area, comprising 2893-2890 Ma feldspar porphyry plutons (Figure 10-1B), and regional batholiths such as the 2870-2830 Ma North Caribou pluton and the 2880-2830 Ma Schade Lake gneissic complex (de Kemp, 1987; Thurston et al., 1991; Biczok et al., 2012; Van Lankvelt, 2013).

The upper part of the ZHA (section 3.16.1.2) consists of poorly-sorted, polymictic to monomictic breccias interpreted to represent proximal alluvial fans, and cross-bedded sandstones reflecting braided fluvial systems (Long, 2004; Eriksson et al., 2005). A 2846 Ma felsic volcanic unit is interlayered in these sandstones. An internal unconformity (1km west of the Pipestone River; Figure 10-1B) separates a polydeformed greywacke affected by the S_1 and S_2 regional foliations from a poorly-sorted breccia and/or conglomerate, which is apparently unaffected by the earlier fabric. These observations suggest a more complex, probably multi-stage and partly syn-orogenic, deposition evolution of the ZHA.

Rocks from the 2850 to 2900 Ma period represent a major source of sedimentary material, as illustrated by the abundance of detrital zircon of this age range in samples of the ZHA (Duff, 2014; Bath, 2017). East of the Pipestone River, along the boundary with mafic rocks of the North Rim assemblage, arkosic sandstone samples have yielded detrital zircon ages between 2730 and 2710 Ma (Duff, 2014; Bath, 2017), showing that sedimentation persisted for an extended period. This process is coeval with batholith emplacement such as the Southern Batholith (Biczok et al., 2012; Van Lankvelt, 2013) and smaller intrusions emplaced at higher crustal levels, such as the 2734 Ma intrusion from the Wilberforce area (this study), suggesting that coeval felsic volcanic and/or plutonic rocks may have been exposed, eroded and deposited in the sedimentary basin.

Duff (2014) reports detrital zircon U-Pb ages as young as 2674 Ma in sedimentary rocks samples from the eastern NCG; however, these ages have large uncertainties (commonly 25-30 Ma), which prevent an accurate timing for basin closure and burial of these rocks. Detrital zircon ages from rocks sampled in the same area during this study give a maximum constraint for sediment deposition of <2727.8±2.4 Ma. Overall, the ZHA show typical characteristics of syn- to late orogenic, elongate sedimentary basins of Archean greenstone belts (Eriksson et al., 1994; Mueller and Corcoran, 1998; Eriksson et al., 2005).

Previous studies correlate the ELS and ZHA based on their similar rock types (Thurston et al., 1991; Breaks et al., 2001; Moran, 2008; Biczok et al., 2012). Geochronological analyses of samples from the ELS and ZHA suggest that the 2730-2710 Ma zircon population is typical of the ZHA (Duff, 2014). However, there is little evidence to argue against the correlation of the ELS and ZHA. The basin architecture and sedimentary depositional environment of the ELS and ZHA are uncertain. Duff (2014) argues ELS and ZHA were deposited from ca. 2900 Ma in a single, elongate basin. Bath (2017) rather interprets the different age constraints (i.e., absence of the 2730-2710 Ma zircon population) as a hiatus in sedimentation in the ZHA, which does not occur in the ELS. However, this difference can be caused by other parameters, such as sediment source rocks and basin drainage architecture (Eriksson et al., 2005), or position in the stratigraphic sequence. The preferred interpretation here is that the ELS and ZHA were deposited in a single elongate basin that had a protracted depositional history and accumulated sediments from multiple sources of different ages.

10.3 Revised tectonometamorphic evolution of the NCG

10.3.1 D_1-M_1 event

D_1 deformation and folding have been recognized throughout the NCG (Breaks and Bartlett, 1991; Breaks et al., 1991; Hall and Rigg, 1986). However, the nature, timing and significance of D_1 deformation have not been addressed in details.

10.3.1.1 Characteristics of D_1-M_1

Previous study coupled with geological data from this study show that D_1 event consisted in large-scale folding and thrusting that involved the SRA, OMA and, at least, parts of the ZHA. In the mine area, it resulted in the overturning of parts of the OMA sequence along a kilometre-scale F_1 synform, and the fault juxtaposition of 2.9 Ga volcanic rocks of the OMA over the younger sedimentary rocks of the ZHA. In the study area, F_1-F_2 "type 3" interference pattern and preserved S_1 foliation suggest that D_1 originally produced predominantly NW-SE-trending F_1 folds, with shallowly SW-dipping axial planes and most likely shallow-plunging fold axes (Figure 10-2B and 10-5). In the northern NCG, overturned E-W-trending, and presumably F_1 folds affect the ELS (Breaks and Bartlett, 1991).

The northward increasing metamorphic pattern of the northern NCG is interpreted to relate to metamorphism (M_1) that has locally reached the amphibolite facies (Breaks et al., 1991; Breaks and Bartlett, 1991). This is notably evidenced by the presence and internal structure of staurolite-cordierite-

andalusite porphyroblasts in metapelites of the ELS. Temperature estimates based on these mineral assemblages suggest 540-590°C, for 3 kbars pressure (Breaks et al., 1991, using Carmichael, 1978). Pressure may have been above 3 kbars in some area, as indicated by the presence of kyanite (Breaks and Bartlett, 1991). In the study area, post-S_1 pre-S_2 staurolite porphyroblasts in Fe- and Al-rich pelitic rocks show that M_1 reached at least the greenschist facies.

10.3.1.2 Timing of D_1 and M_1

Timing constraints on D_1 are scarce. With the current geological and structural data, there is no evidence that any major deformation event occurred over the 150 Ma, during the deposition of the SRA and OMA. Basal conglomerates of the ZHA are younger than 2899 Ma. The presence of a single zircon population in such rocks suggests that they represent an early, locally-sourced sedimentary unit, and that older rocks were probably not exposed. Higher in the stratigraphy of the ZHA, finer-grained sedimentary units (i.e., presumably with more distal source rocks) include older age populations of zircon (e.g., 2980 Ma). This suggests older crustal rocks were exposed at ca. 2850 Ma. This timeframe corresponds to the onset of a major episode of felsic magmatism, with the emplacement of the NCP and SLGC that may be have contributed to the uplift that exposed parts of the greenstone belt. Sedimentary rocks interpreted as part of the lower portion of the ZHA display evidence of deformation predating D_2 (near the 2847 Ma felsic rocks and ZHA internal unconformity; Figure 3-46). D_1 may have been driven, at least in part, by the emplacement of the NCP that destabilized the long-standing stratigraphic pile constituted by the SRA and OMA. Constraining the end of the D_1 event is equally difficult. The crosscutting relationship between the 2730-2710 Ma Southern batholith and the F_1 folded rocks of the OMA suggests that its intrusion post-dated D_1. The highly strained margins and unfoliated core of the complex (Biczok et al., 2012) suggest that it predates the D_2 event. Consequently, the timing of D_1 deformation is therefore loosely bracketed between 2850 and 2730 Ma (Figure 10-3).

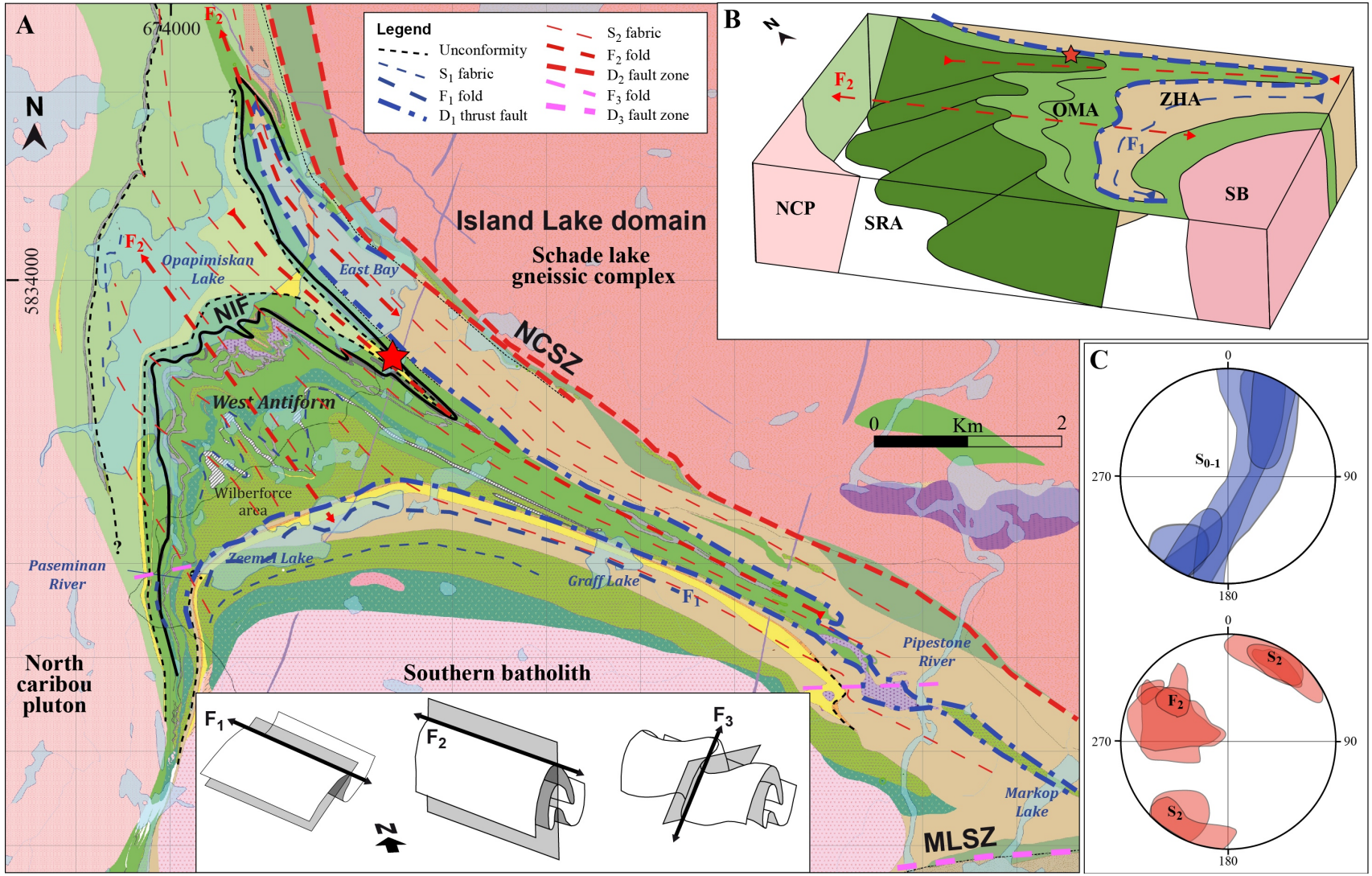

Figure 10-5: A. Structural map of the Opapimiskan Lake area with general orientation of the S_1 (thin blue dash line), S_2 (thin red dash line) and S_3 (thin purple dash line) fabrics, D_1 thrust fault, and D_2 high strain zone. B. Schematic block diagram of the study area. C. Stereographic projection of compiled S_{0-1} measurements (blue) and F_2 (plunge and axial plane) and S_2 measurements (red) from surface exposures. D. Schematic diagrams of the successive F_1-F_2 and F_1-F_2-F_3 fold interference patterns.

The interpretation that the NCP emplacement may have been synchronous with D_1 deformation resonates with other studies advocating for some vertical tectonism comprising diapirism and sagduction in the northwestern Superior province (Lin, 2005; Parmenter et al., 2006; Lin et al., 2006, 2013). Bath (2017) argues that patterns of detrital zircon age populations in the NCG partly support such an interpretation, based on similar data interpretations and model proposed elsewhere in the Superior Province (Lin et al., 2013). While structural characteristics of the northern NCG clearly bear evidence of horizontal tectonism, early stages involving sagduction and burial of the greenstone belt may have contributed to M_1 metamorphism. The northward-increasing M_1 metamorphic pattern could be related to an asymmetry in the burial, or the interplay with horizontal tectonism. The topic is beyond the scope of the study, but relates to the debate on the influence of vertical tectonism during the Archean (e.g., Bédard et al., 2003; Percival, 2006, 2012; Bédard and Harris, 2014; Harris and Bédard, 2014; Bédard, 2017).

10.3.2 D_2-M_2 event

10.3.2.1 Characteristics of D_2 structures

D_2 represents a complex, progressive ductile deformation event (Hall and Rigg, 1986; Zhang, 1997; Breaks et al., 2001; Gagnon, 2015; this study). In the Opapimiskan Lake area (sections 5.3 and 5.4; Figure 10-5), D_2 is characterized by upright, shallowly NW-plunging folds with thickened hinge zones, axial planar S_2, and local development of axial planar high strain zones. There is a NE-increasing strain gradient characterized by tightening of folds and development of axial planar high strain zones. In the mine area, structures such as the "conveyor shear", intense boudinage, and attenuated fold limbs attest of a strong flattening component during D_2. The intense deformation is illustrated by the local overturning of the east limb of the East bay synform, as documented during late stages in other long-lived tectonic environment (Bleeker, 2015). Petrographic data also shows the high intensity of D_2 deformation, as illustrated by the complex structures and textures of garnet porphyroblasts in barren, altered and mineralized rocks of the mine area (Figures 6-4, 6-5, 6-6, 7-8, 7-9).

North of the study area, D_2 folds and fault zones are oriented to the NNW (Breaks et al., 2001). The D_2 Akow Lake and Dinnick Lake shear zones (ALSZ, DLSZ; Figure 10-1) are dominated by dextral shear sense indicators (e.g., boudinaged veins) and sub-horizontal lineations, which support interpretations of dextral transpressive deformation made by Gagnon et al. (2016). Petrogenetic data from the SLGC suggests it represents a lower crustal level than the NCG and the NCP (Van Lankvelt, 2013; Vanlankvelt et al., 2016), implying that the DLSZ had a vertical component of displacement at some stage of its development. In the northern NCG, open to gentle, NW-trending F_2 folds have shallow to moderately

plunging axes (Breaks and Bartlett, 1991). D_2 structures in the southeastern NCG are well-developed, and kilometre-scale F_2 folds are evidenced on aeromagnetic maps (Ontario Geological Survey 1985). Folds and fabric appear to have a slightly different orientation than in the study area (i.e., trending WNW instead of NW).

The boundary between the NCG and the Island Lake domain (ILD) is a first-order structure characterized by intense D_2 deformation (Breaks et al., 2001; Kalbfleisch, 2012; Van Lankvelt, 2013; Gagnon et al., 2016; this study). The North Rim fault (NRF), Dinnick Lake shear zone, and Totogan shear zone (TSZ) constitute different segments of the boundary, which may have different kinematic evolution and/or timing. However, in the study area the wide fault zone in the ZHA rocks (over 700m; Figure 5-36) suggests that these segments are part of a single continuous structure, hereafter referred to as the North Caribou shear zone (NCSZ; Figure 10-5).

10.3.2.2 Timing of D_2 and M_2

The 2734 Ma felsic rocks of the OMA (chapter 4) and 2730-2710 Ma Southern Batholith (chapter 2) are affected by D_2 fabrics thus providing a maximum age for the deformation event. The lower constraint on timing results from the relationship between metamorphic minerals and D_2-related microstructures: 2660 Ma monazite grains (U-Th-Pb data; chapter 6) interpreted as dating the timing of peak M_2 metamorphism in the study area, are aligned in the S_2 fabric and suggest that D_2 deformation lasted until 2660 Ma, possibly slightly later.

Sm-Nd geochronology on garnet from Musselwhite ore samples by Maas (2006, unpublished data reported by Biczok et al., 2012) yielded a preferred age of 2690±9 Ma. This age is calculated with software from Ludwig (2001), using the average of three analyses on "whole rock" (i.e., powdered garnet-poor matrix) and one of two analyses of garnet separates. Garnet separates were constituted of pure (<1% impurities) and less pure (approx. 20% impurities) handpicked garnets. This type of garnet most likely corresponds to the inclusion-poor garnets typically associated with gold ore, similar to those analyzed by LA-ICP-MS elemental mapping (section 7.2.2). These garnets yielded an age of 2664±19 Ma (Maas, 2006, unpublished data; Isaac, 2008), which, with its uncertainty, overlaps monazite growth. This is in agreement with petrographic observations showing that monazite occurs in garnet rim. It is also in agreement with other petrographic data showing that garnet growth predates monazite growth, while some garnet rims grew after monazite, after 2660 Ma. The 2690 Ma Sm-Nd garnet age is interpreted as dating the main metamorphic growth of garnet, such as the inclusion-rich cores, whereas the 2664 Ma is interpreted as a late stage, syn- to post-gold mineralization growth of garnet. It is worth stressing that

given the multi-stage growth of garnet and the influence of host-rock on the timing of garnet growth, age interpretations are to be considered with caution. Lastly, $^{39}Ar/^{40}Ar$ geochronology on calcic amphiboles from a sample of gold-bearing unit 4EA provided a total gas age of 2658±13 Ma, which is interpreted to record the timing of cooling through the 500 °C isotherm (Biczok et al., 2012). Such amphiboles are part of the alteration mineral assemblage and locally contain gold inclusions (chapters 7 and 8), indicating that they are part of the mineralizing event. The margins of the Southern Batholith are affected by D_2 deformation (Biczok et al., 2012). Geochronological data on the SB (Van Lankvelt, 2013; Van Lankvelt et al., 2016) provides a maximum age constraint for D_2 and associated metamorphism ca. 2720 Ma, and peak amphibolite grade metamorphism is dated at 2660 Ma; thus providing some constraint on the timing of gold mineralization at Musselwhite (section 10.5.1.2).

10.3.2.3 P/T conditions of M_2 metamorphism

Previous thermobarometric data on M_2 metamorphism in the mine area (Hall and Rigg, 1986; Otto, 2002; section 6.4.1.1) reported temperature estimates of around 550 to 600°C and pressures of 0.3 GPa. Garnet-biotite geothermometry from this study using calibrations from Holdaway (2000) gave higher temperature estimates at 624±8°C. However, a study by Paulick and Franz (2001) pointed out the tendency of Holdaway's geothermeter to give high temperature estimates (i.e., in the 550-850°C range). The current data shows that M_2 has reached the middle amphibolite facies.

Constraints on M_2 metamorphic conditions are also provided by petrographic data from rocks a few kilometres north of Musselwhite mine (Gagnon, 2015; Gagnon et al., 2016), and from sedimentary units to the southeast (Bath, 2017). Gagnon et al. (2016) report ductile and plastic deformation features of quartz, feldspar, and hornblende in rocks of the DLSZ interpreted to represent syn-tectonic temperatures above 500°C. The occurrence of S-type granite intrusions in several localities, including further north within the ELS (Biczok et al., 2012; Fry, 2013; Kelly and Schneider, 2015) and pegmatitic dykes at the Musselwhite mine suggest that temperatures needed for partial melting were reached at depth during M_2 metamorphism.

10.3.3 D_3-M_3 event

In the study area, D_3 has mainly resulted in heterogeneously distributed S_3 crenulation cleavage and moderately WSW-plunging Z-folds. Locally, a south-plunging conjugate set of F_3 is documented (chapter 5). D_3 strain intensity increases to the south-west of the study area and culminates along the dextral MLSZ which merges eastward with the Totogan shear zone and overprints D_2 fabrics.

Constraints on the timing of D_3 are lacking due to the absence of crosscutting relationships with younger geological features. Geochronological data on metamorphic zircon (U-Pb, Van Lankvelt, 2013; Kelly and Schneider, 2015), monazite (total Pb, Kalbfleisch, 2012), titanite (Van Lankvelt, 2013), biotite, and amphiboles ($^{39}Ar/^{40}Ar$, Biczok et al., 2012; Gagnon, 2015) have defined three age groups, one of which could correspond to M_3. These include (Figure 10-3): 2600-2560 Ma, 2510-2480 Ma, and 2450-2410 Ma. M_3 appears to be one of multiple stages on the retrograde path of regional metamorphism.

10.4 Geological evolution of the NCG

The new insights on the tectonostratigraphy and on tectonometamorphic events of Musselwhite Mine area allows us to propose a refined model for the geological evolution of the NCG, which is summarized below (Figures 10-3 and 10-6). Prior to 2900 Ma volcanic rocks and BIF sequences were deposited in a relatively stable marine environment, with apparently no major tectonic event. Between 2900 and 2850 Ma, major crustal growth takes place, characterized by emplacement of large volumes of TTG-type intrusions (NCP, SLGC) and abundant volcanism. It appears to destabilize the greenstone belt structure, leading to the development of a large sedimentary basin, and commencing earlier in the northwestern part of the NCG. Between 2850 and 2750 Ma, D_1 compression, probably related to the collision of the Oxford-Stull and the Island Lake domains to the north (Percival et al., 2012), led to folding and thrusting across the NCG (Figure 10-6A, B).

Around 2730-2710 Ma, additional crustal growth is reflected by the emplacement of the SB. D_2-M_2 strong ductile deformation and regional metamorphism result from crustal thickening triggered by the ca. 2700 Ma collision of the Island Lake domain with the North Caribou terrane. Early D_2 sagduction and compression (Figure 10-6C) lead to thrusting of the SLGC over the NCG and burial of the NRA, OMA and parts of the ELS and ZHA (Figure 10-6D, E). Continued horizontal deformation is especially intense in the central NCG, where major ductile fault zones are formed in an apparently transpressive regime (Figure 10-6D; Gagnon et al., 2016). Transpression implies contemporaneous and partitioned dip-slip and strike-slip motions (Sanderson and Marcini, 1984). Geothermobarometric data (Van Lankvelt, 2013) suggests that the Schade Lake gneissic complex originated from a deeper crustal level than the North Caribou pluton and thus was juxtaposed (thrusted?) against the NCG and the North Caribou pluton during D_2. Dextral strike-slip strain is documented along the NCSZ (Gagnon et al., 2016). This evolution bears similarities with that of greenstone belts further to the west and northwest, such as the Cross Lake greenstone belt or the Gods Lake Narrows area (Lin, 2005; Parmeter et al., 2006; Lin et al., 2006; 2013).

In the Opapimiskan Lake area, the NCG separates into three branchs forming a triple-point (Figures 10-1, 10-6D). This geometry likely originated during D_2 deformation. The orientation of the first-order NCSZ changes from north-northwest-trending in the central part of the belt to northwest-trending south of the Opapimiskan Lake area. This bend induces complex structural characteristics, similar to those described in the southern Knee Lake area, Manitoba (Lin and Jiang, 2001). The north-northwest trending segment of the NCG likely accomodated a higher component of strike-slip motion (Figure 10-6D), while flattening dominated in the mine area (Figure 10-6D, E). Such features are highly prospective for gold mineralization (Hagemann and Cassidy, 2000; Goldfarb et al., 2005; Dubé and Gosselin, 2007; Groves et al., 2018), as will be discussed hereafter.

The southern NCG is later affected by E-W-trending D_3 dextral shearing during retrograde metamorphism.

10.5 Discussion

The following discussion focuses on the distribution, controls, and timing of gold mineralization at Musselwhite, the processes of hydrothermal alteration, the structural and lithological controls of gold precipitation, and the nature, sources, and migration pathways of mineralizing fluids and metals.

10.5.1 Distribution, controls, and timing of gold mineralization at Musselwhite

10.5.1.1 Previous constraints and geological models

Various genetic models have been proposed for the Musselwhite gold deposit. Following the regional-sclae mapping of Breaks et al. (1985, 1986), Hall and Rigg (1986) conducted a multidisciplinary study and concluded that the gold mineralization at Musselwhite was related to an epigenetic, syn-D_2, syn-metamorphic event. Subsequent research further contributed to this interpretation (Zhang, 1997; Otto, 2002; Blower and Kiernan, 2003; Snow, 2004, unpublished; Hill et al., 2006; Isaac, 2008; Moran, 2008; Kolb, 2010; Stott and Biczok, 2010; Biczok et al., 2012). A few studies have proposes that gold mineralization was partially (Kerswill, 1996; Otto, 2002) or entirely (Couture, 1995) of syngenetic origin. Some of these studies examined whether gold mineralization could be related to the emplacement of regional batholiths (Hall and Rigg, 1986; Stott et al., 1989; Isaac, 2008).

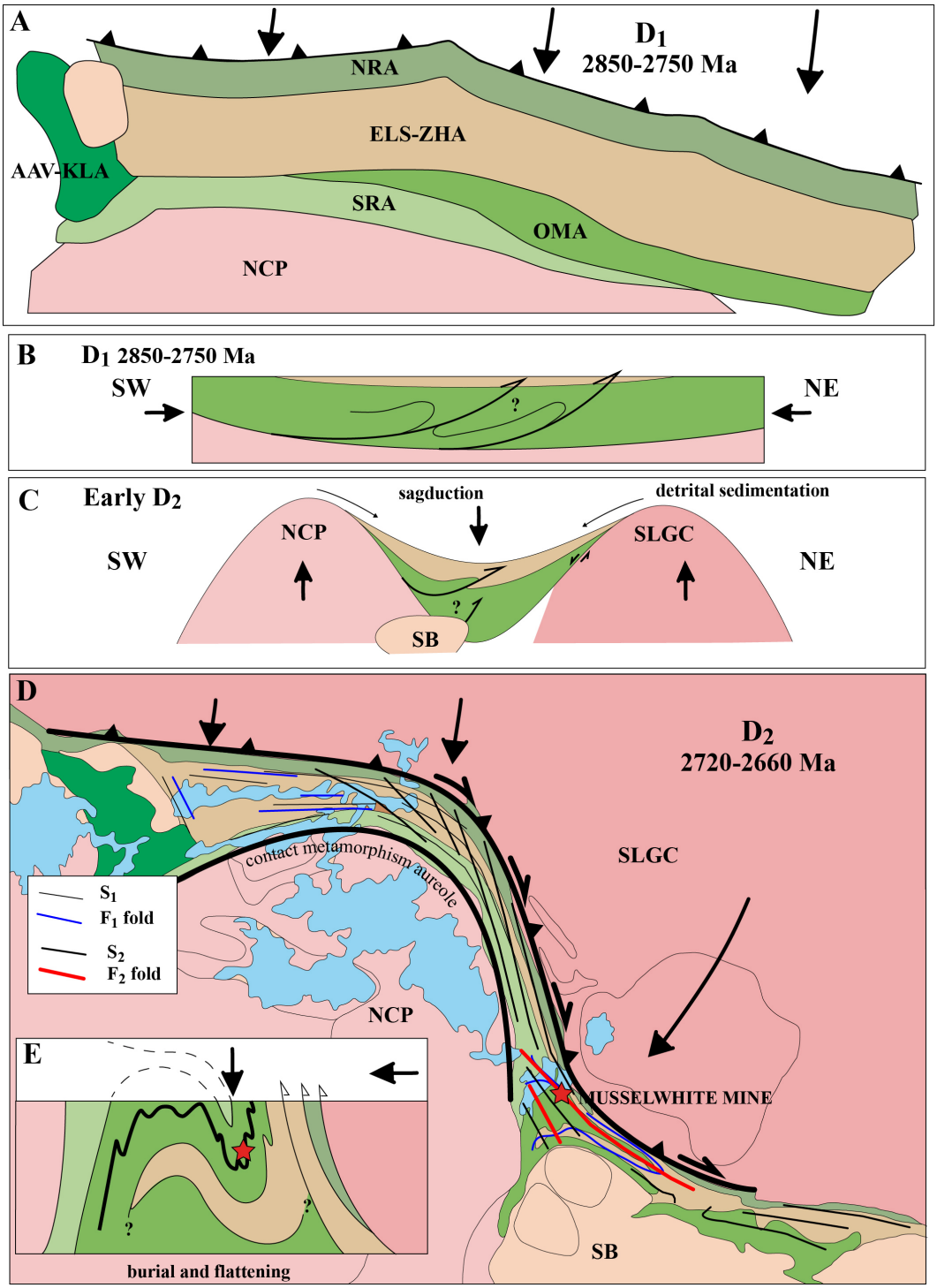

Figure 10-6: Schematic synthesis of tectonometamorphic events in the NCG. A. Plan view of D_1 deformation and associated greenschist metamorphism. B. NE-SW section view showing the initiation of D_1 thrusting and folding. B. Early D_2 sagduction and detrital sedimentation in the NCG, adapted from Parmenter et al., 2006 and Lin et al., 2013. D. D_2 horizontal shearing and flattening, synchronous with or following burial producing mid-amphibolite metamorphism. E. Schematic section view of D_2 flattening and burial in the Musselwhite mine area.

In parallel, exploration and mining activities at Musselwhite continuously improved the geological model of the ore zones. The earliest model, proposed in 1990, regarded the deposit as principally related to the fold closure of the T-antiform, where most of gold ore was mined at that time (Figure 10-7A). In 2002, additional data led geologists to propose a model in which faults principally controlled ore zones (Figure 10-7B, C). The limited displacement interpreted along the structures led, in 2006, to the development of a model involving shear zones affecting the folded BIF sequence (Figure 10-7D). Data collected since then from mining development and exploration has mostly resulted in more refined and detailed versions of the latter model (Figure 10-7E).

10.5.1.2 New constraints on gold mineralization

In line with previous research, this study show that gold distribution is strongly controlled by D_2 deformation. Mineralized zones of the NIF are spatially related to second order folds (e.g., such as the parasitic fold mapped on mine level 1045; chapter 5) along high strain zones, where the BIF layering is intensely transposed into the orientation of the axial planar S_2 foliation. Sulphides are concentrated within these high strain zones or in adjacent auriferous lower strain zones (e.g., Moose zone; C-block; Figure 7-6). The geometry, distribution, and abundant deformation features (e.g., rootless F_2 folds) of the Esker and Lynx zones suggest prolonged/progressive D_2 deformation during and after gold mineralization (Figures 5-34C and 7-26B). They were most likely emplaced during the formation of a parasitic fold that was subsequently flattened and vertically stretched. In the case of the Lynx zone, this is particularly apparent due to the thickened portion of the ore zone (Figure 7-4). The structural control of D_2 high strain zones and F_2 folds, and strong strain gradient are locally clearly illustrated in drill core (Figure 8-1). Over 1 metre interval of drill core, open F_2 folds with weak alteration and trace pyrrhotite grading 1 ppm Au evolve into a 10-ppm Au high strain zone with 10-15% pyrrhotite. The sharp transition zone includes a partially preserved pyrrhotite-replacement front of iron-rich bands between folded chert bands.

Gold and associated sulphides (po, cpy) are found intergrown and/or in inclusions in most minerals of alteration and ore mineral assemblages: coarse red, subhedral almandine garnet porphyroblasts, and matrix minerals such as beige grunerite, green hornblende, green ferro-tschermakite, brown biotite, pale green hedenbergite, and quartz. All of these minerals show textural evidence of syn-D_2 crystallization, and were progressively transposed and recrystallized by late-D_2 strain. Some occurrences of gold consist in rounded droplets, which can be interpreted as indicating late remobilization (Tomkins and Grundy, 2009).

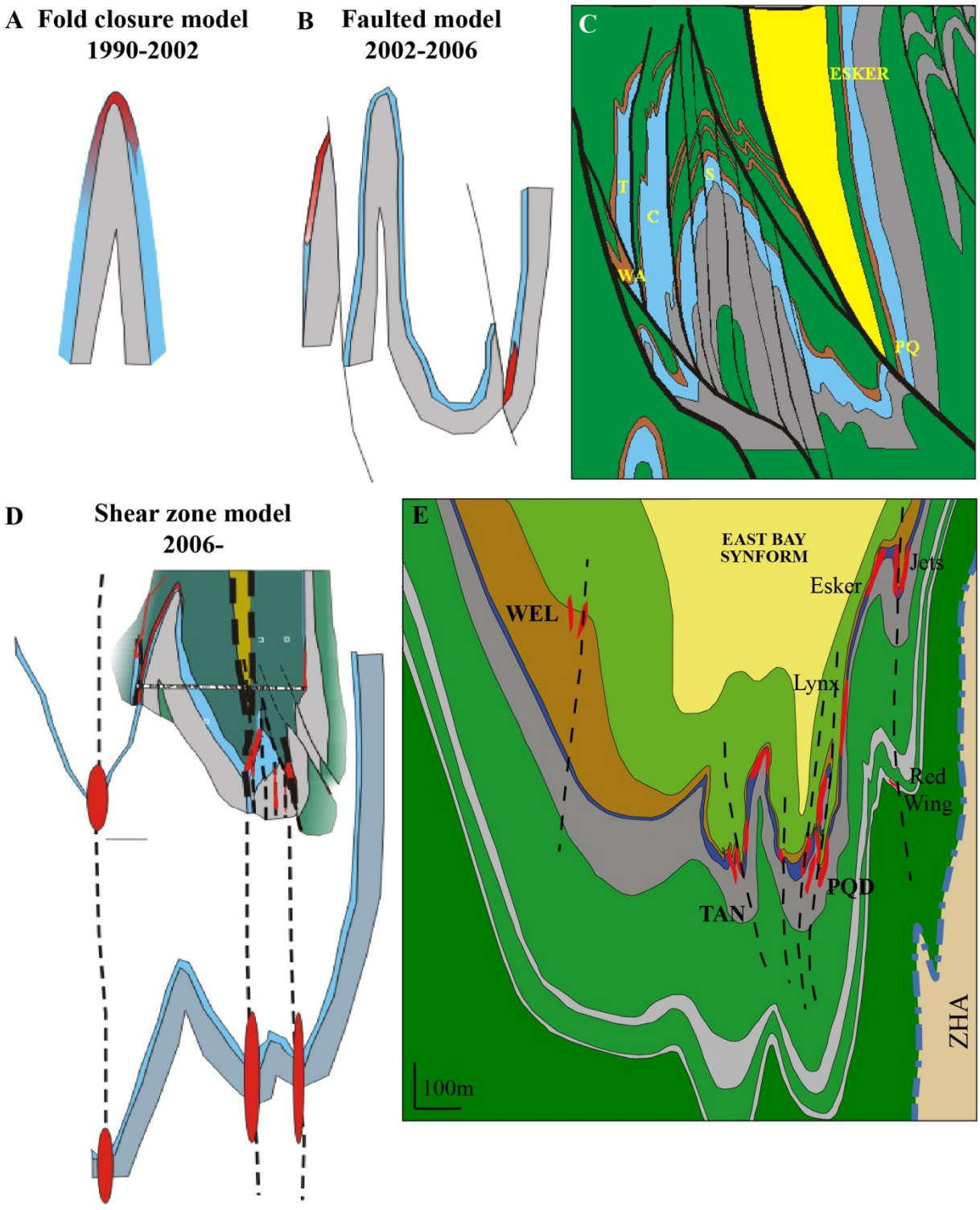

Figure 10-7: Evolution of the geological model for the Musselwhite deposit, from Biczok (2009, unpublished), Blower and Kiernan (2003). A. Fold closure model, from 1990 to 2002. B. Faulted model, 2002 to 2006. C. Faulted model, detailed version in Blower and Kiernan (2003) from Goldcorp (2002, unpublished). D. Shear zone model, from 2006 to current day, with predicted mineralized zones in the SIF (Hill et al., 2006). E. Simplified geological model, with addition of the approximate location of WEL zone mineralization.

The relationship between gold and garnet illustrates the contemporaneity of gold mineralization and the D_2-M_2 event. Zoned garnet crystals in ore samples typically have a core containing inclusions of magnetite and ilmenite. Inclusions in the intermediate zones and rims are more diverse including magnetite-only, to magnetite-ilmenite-pyrrhotite or pyrrhotite-ilmenite, to pyrrhotite-only. In the case of the inclusion-poor to inclusion-free garnets that are specifically found close to or within mineralized zones, pyrrhotite is commonly found in fractures, locally with gold. Pyrrhotite is also found in garnet pressure shadows and in the interspace of boudinaged quartz bands. These observations corroborate those of Kolb (2010) and represent additional evidence for the syn- D_2-M_2 timing of gold mineralization.

Evidence of deformation and metamorphism of mineralized zones include the local concentration of pyrrhotite into a semi-massive vein with a halo consisting of an amphibolite matrix, with local coarse red almandine garnets (e.g., C-block). Such matrix comprises aggregates of pyroxene-quartz-calcite resulting from the metamorphic conversion of Ca-amphiboles at higher temperature. The ore zones are locally affected by D_2 deformation such as late upright F_2 folds in the A-block, or by faulting of the B-block ore zone, located in the isolated duplication lens of the NIF, which is detached above the main PQD area (e.g., mine section 11775 N).

Local occurrence of weakly-deformed gold-bearing quartz veins (e.g., mine level 1020) hosted in mafic volcanic rocks and crosscutting the main S_2 fabric attests of minor remobilization from the NIF into the overlying unit Bvol, likely during the late stage of D_2 deformation. These veins form a typical network of fault-fill and associated extension veins (e.g., Robert et al., 2001), which are compatible with the horizontal shortening documented in the mine area. The presence of gold inclusions in hedenbergite attests that gold was introduced prior to or during peak metamorphic conditions, and evidence of deformation of pyroxene-bearing mineralized zones and altered haloes, as well as in the overlying high strain zones in the mafic rocks shows that parts of the D_2 deformation outlasted the peak of M_2 metamorphism.

In summary, structural, petrographic, and geochronological data from this study indicates that gold mineralization globally occurred during D_2 deformation and M_2 metamorphism. Garnet and amphibole geochronology contributes to a body of elements constraining the gold mineralization event at around 2720-2660 Ma (section 0). The characteristics of gold mineralization at Musselwhite are consistent with those of typical epigenetic gold deposits formed at the amphibolite facies (chapter 1, Figure 1-14; Groves, 1993; Goldfarb et al., 2005; Robert et al., 2005; Dubé and Gosselin, 2007): syn-kinematic and syn-metamorphism timing, little carbonate (calcite where present), virtual absence of muscovite (except in felsic rocks), ubiquity of biotite and calcic amphiboles with local clinopyroxene, presence of ilmenite (notably preserved in garnet porphyroblasts), predominance of pyrrhotite as the main ore mineral (and

exsolutions of troilite), and finally, the preferential occurrence of gold with boudins of laminated veins in shear zones, and disseminated lodes.

10.5.1.3 Alternative hypotheses

Alternative interpretations for the timing of gold mineralization at Musselwhite include mainly three possibilities: syngenetic gold introduction; D_1-related gold mineralization; and post-D_2 gold mineralization.

Syngenetic gold mineralization in iron formations has certain key characteristics (Phillips et al., 1984; section 1.5.3.2): laterally extensive sulphide-facies BIF with gradational transition to other facies, alteration halo restricted to the footwall of the iron formation (much like VMS deposits), the trace metal association found in the ore presents high base metal content and low Au/Ag values, and fluid inclusions reflect at least some involvement of Cl-rich brines. Logically, such deposits were formed prior to tectonometamorphic activity. Consequently, mineralization should not be controlled by a specific fault or fold generation, and gold grades should not be positively correlated with structural features crosscutting the primary layering or bedding.

On the bases of this study and the literature (e.g., Hall and Rigg, 1986), these criteria clearly do not apply to the Musselwhite deposit. The "sulphide facies" BIF at Musselwhite is not laterally extensive, and transition to other facies are typically sharp. Alteration is also evident in the stratigraphic hanging wall of the iron formation ("Basement basalts" unit), and the ore typically has low base metal content and high Au/Ag values. The strong control of D_2 structures on gold distribution also contradicts the hypothesis of syngenetic mineralization, even if considering remobilization may have occurred.

An additional alternative would involve syngenetic enrichment of the iron formation and subsequent concentration/remobilization of gold during D_2. Background values of oxide and silicate BIF at Musselwhite are within the range of typical values for Algoma-type iron formation (Gross, 1988): 1 to 100 ppb with average around 30 ppb. So the NIF is not enriched in gold relative to other Algoma-type BIF in Canada. It is enriched relative to mafic volcanic rocks, which contain 10-12 ppb Au on average. However, this would imply that any 30-60m-thick Algoma-type BIF would have the potential to form a Musselwhite-size gold deposit, and there should be many more known such gold deposits, which is not the case. Considering the hypothesis of concentration/remobilization of gold, such a process would leave evidence of lateral/vertical migration and very progressive enrichment of gold in the BIF, which is not observed. Lastly, the volume of BIF rock required to form the Musselwhite gold deposit through

remobilization of gold from the BIF is largely insufficient. Consequently, this hypothesis is not considered viable.

Regional M_1 metamorphism has reached greenschist facies in the Musselwhite deposit area. Although this represent the ideal tectonometamorphic level for epigenetic gold mineralization in Archean greenstone belts (e.g., Groves and Foster, 1993; Robert and Poulsen, 2001; Goldfarb et al., 2005; Dubé and Gosselin, 2007), there is no evidence that any gold was introduced during D_1/M_1 tectonism at Musselwhite. M_1-cores of garnet porphyroblasts in the ore zones do not contain gold-pyrite-pyrrhotite inclusions. Likewise, garnet porphyroblasts in proximal alteration zone do not contain inclusions of iron carbonates typical of greenschist grade mineralization. Hypothetical D_1 structurally-controlled ore zones would have formed tabular envelopes and would show discontinuous, crosscutting relationships with the overprinting D_2 structures, similar to that of folded F_1 as seen on outcrops. Such relationships have not been documented and there is no evidence of D_1 structural control on gold-mineralized zones, nor of F_2 folded ore zones, even in low D_2 strain area.

Gold mineralization during retrograde metamorphism is typical in low to medium grade metamorphic terranes (Goldfarb et al., 2005). It has been proposed for deposits in high grade terranes (Phillips and Powell, 2009; Tomkins and Grundy, 2009; Tomkins, 2010; Kolb et al., 2015), such as the Renco deposit in Zimbabwe (Kolb et al., 2000). In such case, gold should be specifically associated with retrograde minerals. At Musselwhite, this would result in an association of gold with chlorite, which is not recognized. For this reason, and others including structural and petrographic relative timing relationships, the main gold mineralization at Musselwhite cannot have occurred after D_2-M_2 tectonometamorphism.

10.5.1.4 Relationships between gold and magmatic events

A potential magmatic origin for gold mineralization at Musselwhite has been evoked (Hall and Rigg, 1986; Isaac, 2008; Stott and Biczok, 2010). However, recent geochronological constraints on the emplacement of regional batholiths and on deformation events render this hypothesis highly unlikely.

The age of emplacement of regional TTG-type intrusions such as the NCP and the SLGC is 100 to 150 Ma older than current constraints on the timing of D_2 deformation. Likewise, the main phase of emplacement of the Southern batholith is around 20 Ma older than the timeframe for gold mineralization at Musselwhite. While the batholith could have contributed to the regional heat flow, there is no evidence of a genetic link with gold mineralization.

An alternative relates to the felsic, pegmatitic dykes locally occurring in the mine area (Biczok et al., 2012; Fry, 2013), but also present as swarms or small intrusive bodies in areas of higher temperature

metamorphism in the greenstone belt (Breaks and Bartlett, 1991; Van Lankvelt, 2013, Kelly et al., 2013; Gagnon, 2015). These occurrences have been interpreted as S-type granite related to partial melting of sediments at depth (ELS or ZHA). There is no occurrence of auriferous pegmatitic dykes and no evidence that gold mineralization is linked to such feature. However, isotopic geochemistry studies (Otto, 2002; Isaac, 2008) suggested there could be a magmatic contribution to mineralization at Musselwhite. The late-D_2/M_2 sodic alteration documented in this study (sections 8.2.2 and 8.7) is interpreted to be related to partial melting at depth, resulting in a weak yet pervasive flow of Na-rich fluids, migrating via D_2-structures. Such phenomenon would alter the overall isotopic signature of minerals in the mine area and lead to invalid interpretations of isotopic data.

The only plausible magmatic link to gold mineralization occurs in the West antiform area, as reported by Hall and Rigg (1986). There, some gold is associated with Na-rich alteration and partly hosted by albite pegmatite dykes. However, subsequent attempts to find such occurrences have failed (Biczok J., personal communication, 2012; this study). It is possible that such pegmatitic dykes relate to the aforementioned late-M_2 S-type granites, and would have intercepted and remobilized pre-existing gold mineralization.

10.5.2 Alteration zonation and gold precipitation mechanisms

10.5.2.1 Alteration mineral paragenesis

The geochemical data (chapter 8) show that each rock type of the mine sequence has a specific reactivity to hydrothermal fluids. The resulting alteration zonation is not as regular as that encountered in a homogeneous medium (e.g., unit Bvol). Deformation and metamorphism synchronous with hydrothermal alteration, possibly affecting fluid flow and flow mechanisms (Ferry, 1988; Cox et al., 2001), lead to further blurring of the zonation, especially in the very competent BIF sequences. Nevertheless, two distinct alteration zones are identified and delineated (excluding the core sulphidation of the iron formation), which are analogous with those of orogenic gold deposits (Eilu et al., 1999). Studies on the mineralogy of BIF typically focus on metamorphic mineral assemblages and avoid zones of alteration (section 1.4.3; Haase, 1982; Klein, 1983, 2005). In BIF-hosted gold deposits (section 0; Bullis et al., 1994; Smith, 1996; Mueller, 1997) garnet-rich silicate BIF is usually a subordinate unit and studies of alteration focus on the grunerite-chert silicate BIF. The following section thus investigates the detail of reactions occurring during alteration and the interactions between fluids and mineral phases necessary to form the observed paragenesis.

In unit 4EA, the main features of alteration include biotite crystallization and conversion of grunerite to Ca-amphiboles, such as hornblende, ferro-tschermakite and actinolite (Figures 10-8 and 10-9). The

metamorphic mineral assemblage of unit 4EA includes quartz (chert)-grunerite-garnet ± magnetite ± biotite ± hornblende. The biotite alteration reaction occurs with the following reaction (Figure 10-8):

grun (+ grt) + K^{+}_{fluids} = bt + excess Fe-Si

In this reaction, the aluminum needed for biotite crystallization can be sourced from the surrounding partial recrystallization of garnet during alteration and mineralization. Alternatively, Al could originate from detrital biotite, if present, or from Al-bearing amphiboles. Any excess Si and Fe can be used to form secondary grunerite, along with hydrous hydrothermal fluid, similarly to the metamorphic reaction magnetite + quartz = grunerite (chapter 6). The reaction of conversion of grunerite to Ca-amphibole can be summarized as follows (Figure 10-8):

grun (+ grt) + Ca^{2+} = hbl + excess Fe

In this reaction, the calcium can be sourced from the hydrothermal fluids, as indicated by the enrichment of Ca in altered unit 4EA. It can also be taken from garnet as it contains a small grossular fraction. As hornblende and ferro-tschermakite require Al, some garnet involvement in the reaction is needed, therefore releasing Ca. Proof of the involvement of garnet in mineralogical reaction is evidenced by Ostwald ripening (Winter, 2001). This process, defined by the dissolution of small crystals to feed the growth of large ones, is one of the textural changes affecting garnet. This is best illustrated by pyrrhotite-rich zones in the mine (e.g., C-block ore zone and its massive pyrrhotite vein). There, garnet porphyroblasts are typically less abundant but much coarser (2-4 cm in diameter) than elsewhere. Also, the surrounding amphibolitic matrix tends toward a monomineralic composition of ferrotschermakite. The effect of Ostwald ripening on garnet porphyroblasts is interpreted to contribute to the availability of Ca, Mg, Al, and Si for the crystallization of biotite and Ca-amphiboles.

The weakness of the potassic alteration and the apparent low involvement of CO_2 can be attributed to the low reactivity of unit 4EA to these elements of hydrothermal fluids. Alternatively, it could be due to alteration during amphibolitic facies metamorphism. Geothermometry data has provided temperature calculations of 530°C-550°C in the West Antiform area (Hall and Rigg, 1986) to 570°C-620°C (Otto, 2002; this study) in the mine area. The presence of metamorphic monazite in the garnet-biotite schist, which usually crystallizes above 525°C ± 25°C (Smith and Barreiro, 1990), supports these values. Under such conditions, carbonate minerals in BIF react with other phases to form amphiboles (section 1.4; French, 1968; Frost, 1979a; Haase, 1982; Klein, 2005). Consequently, Ca-amphiboles preferentially crystallised over carbonates during alteration. The high intensity of carbonate alteration in the mafic volcanic rocks overlying the NIF may be attributed to the relative lack of CO_2 sink in the iron formation, except for the underlying oxide-facies.

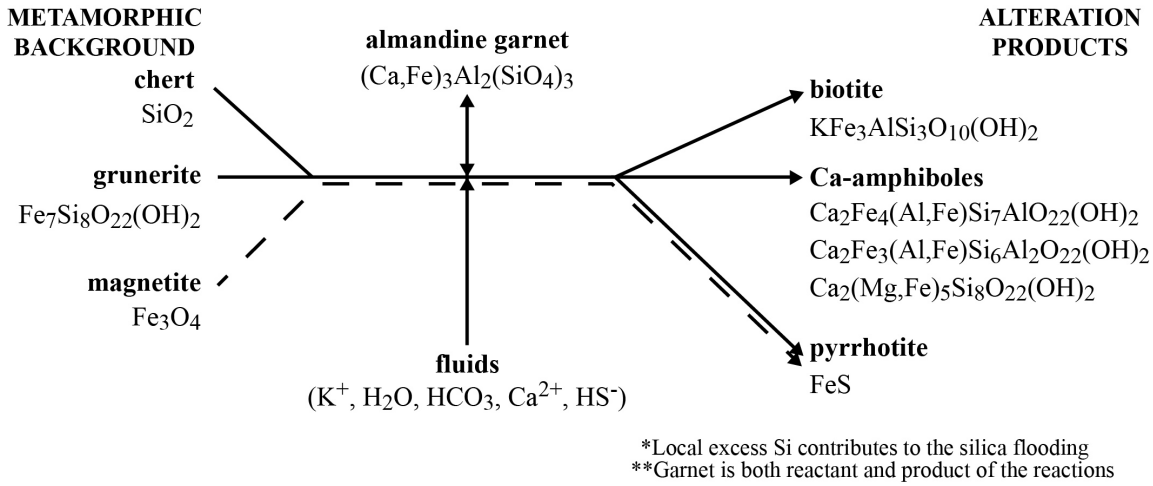

Figure 10-8: Summary of alteration mineralogical reactions in unit 4EA.

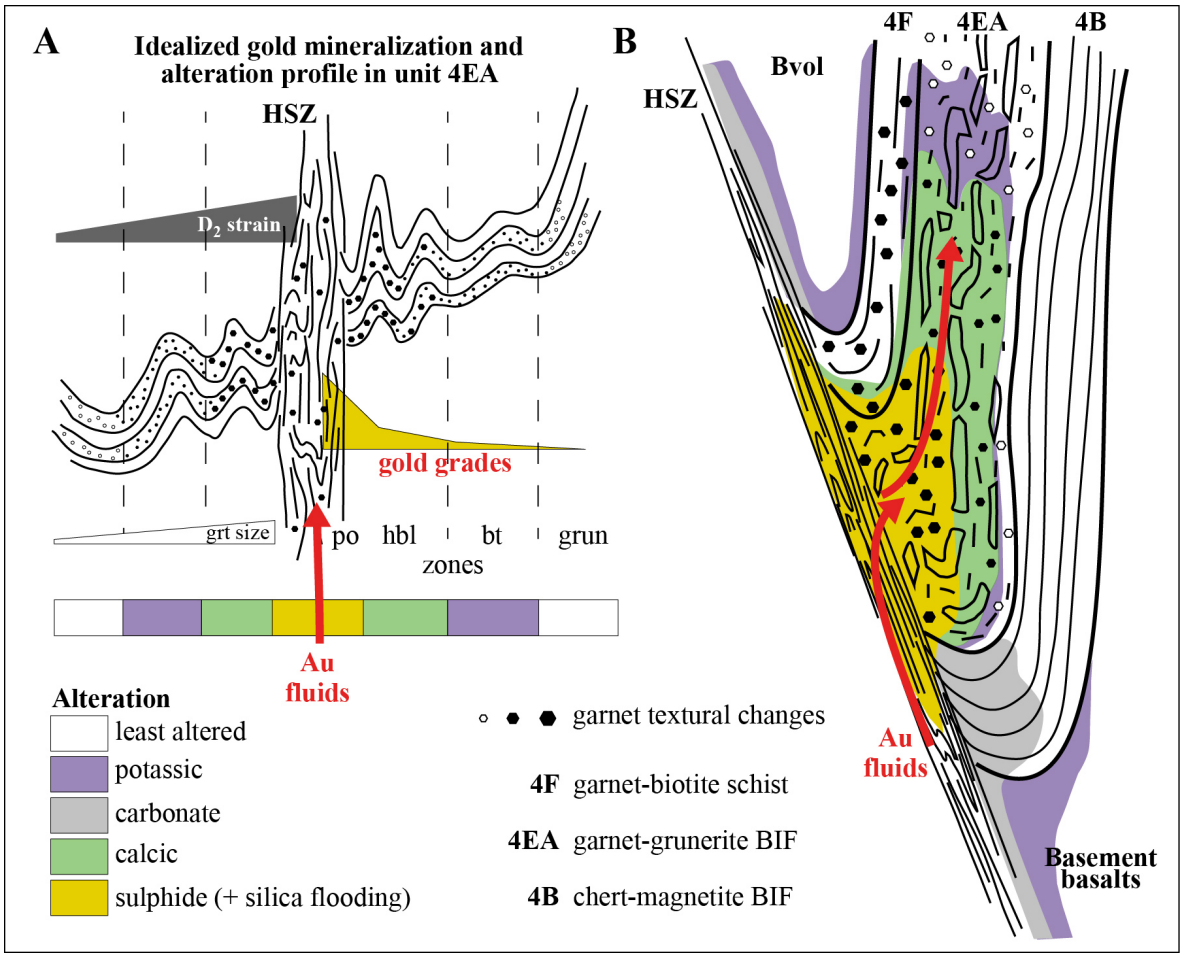

Figure 10-9: Gold mineralization and alteration in the iron formation. A. Idealized profile with a D_2 high strain zone crosscutting garnet-grunerite BIF (unit 4EA). B. Schematic diagram of an auriferous D_2 high strain zone affecting the NIF sequence (simplified to three main units). Pressurized fluids are released in unit 4EA, where high permeability enables fluid flow and fluid-rock interaction causing the pyrrhotite-replacement of the BIF. Lithological control leads to progression of mineralization and alteration along the

horizon. Hydrothermal alteration progressively and partially overprints itself. Note the lithological control on alteration zoning.

10.5.2.2 Sulphidation of the iron formation: Bvol-NIF comparison

The potency of Fe-rich rocks, particularly BIF, to act as a chemical trap for gold carried in mineralizing fluids as $Au(HS)_2$ bi-sulphide complex is well established (Hagemann and Cassidy, 2000; Phillips and Powell, 2010, and references therein). Sulphidation of the iron formation is typically the main process forming the core of BIF-hosted gold mineralization (Kerswill, 1996; Eilu et al., 1999). The specificity of Musselwhite lies in the distribution of gold: the specific endowments of the BIF compared to the mafic volcanic rocks, of the NIF compared to the SIF and of the silicate facies BIF (unit 4EA ± unit 4A) compared to the oxide facies (unit 4B). Preferential endowment of the silicate facies BIF over the oxide facies is documented in other deposits (e.g., Mineral Hill, Montana, USA; Smith, 1996). This lithological control is intrinsically linked to the structural control that plays a key role at Musselwhite (section 10.1.3). Both controls ultimately relate to the composition of the iron formation and its rheology during deformation and metamorphism.

At mine scale, the contrast of gold endowment between iron formations and mafic volcanic rocks, notably unit Bvol, appears to be partly related to the relatively homogeneous strain distribution in mafic rocks, limiting the likelihood of forming structural traps. Mafic rocks accommodated deformation by developing a penetrative foliation and, later, localized shear zones, ductile deformation hampering major variations in pressure (Cox et al., 2001). To some extent, this contrast is shown at centimetre scale in the clastic facies of the oxide BIF (Figure 10-10). Lower reactivity to mineralizing fluids due to lower iron content may also have contributed to the contrast. A hypothesis option would be to consider that the NIF may have trapped all the available gold. However, the occurrence of gold-bearing lenses of garnet-amphibolite (unit 4E) in unit Bvol shows that it is not the case.

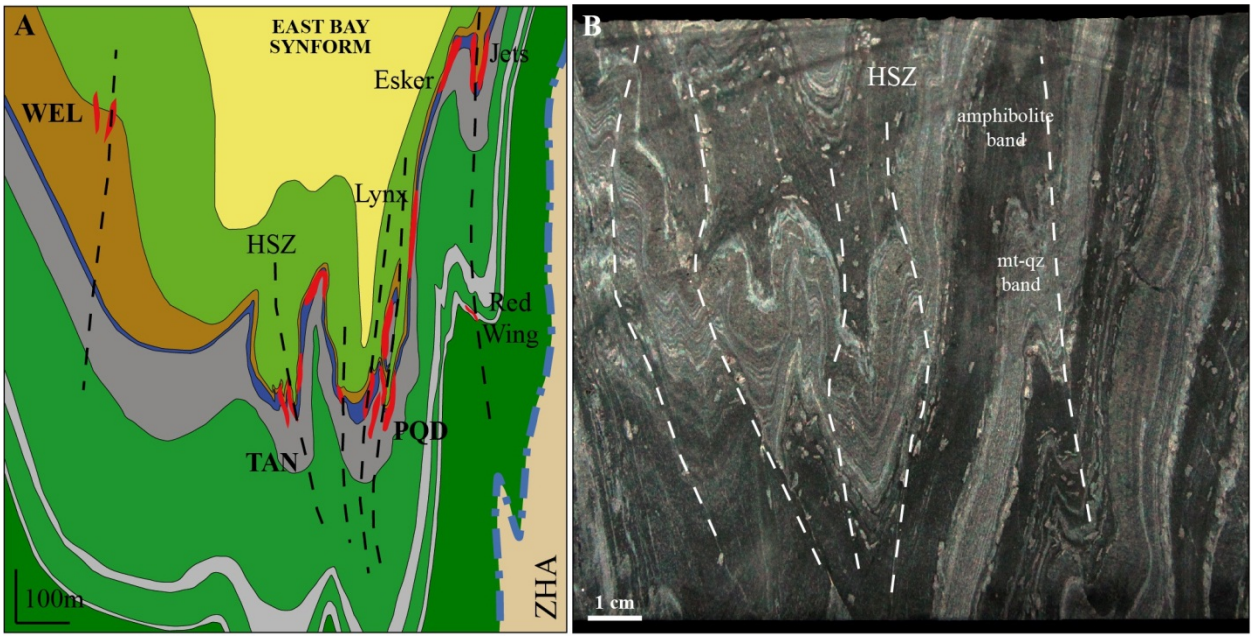

Figure 10-10: A. Simplified geological section of Musselwhite mine at 11775 N. B. Slab of clastic chert-magnetite BIF sample adjacent to the Moose ore zone, mine level 920. Clastic bands and magnetite-quartz bands form fold geometry and structures similar to mafic volcanic rocks and BIF sequences in A.

In contrast to mafic volcanic rocks, the NIF and SIF are extremely competent and are characterized by a strong layered anisotropy. This rheological contrast between the NIF and the mafic volcanic rocks leads to thickening of the NIF in F_2 fold hinges (PQD, T-antiform area). There, the heterogeneity of the BIF sequence leads to complex fold patterns and the development of axial planar high strain zones, which focused hydrothermal fluids (Figure 10-11). Furthermore, geological and structural mapping shows that each unit comprising the NIF and SIF sequences has a specific deformation style (sections 5.3 and 5.4). The garnet-biotite schist (unit 4F) is the most competent unit and is deformed by folds with extremely thick hinge zones and thin limbs. The garnet-grunerite BIF (unit 4EA) typically displays open to tight folds, where garnet porphyroblasts disrupt chert bands. The clastic facies of unit 4B partly shares this folding style. In the "pure" oxide facies, chert and magnetite accommodate ductile deformation (Figures 5-18 and 5-33), including local ductile high strain zones and associated drag folds. Lastly, unit 4A, the chert-grunerite BIF, displays a more brittle behaviour due to the thickness of chert bands. This rheological diversity can be directly related to BIF mineralogy.

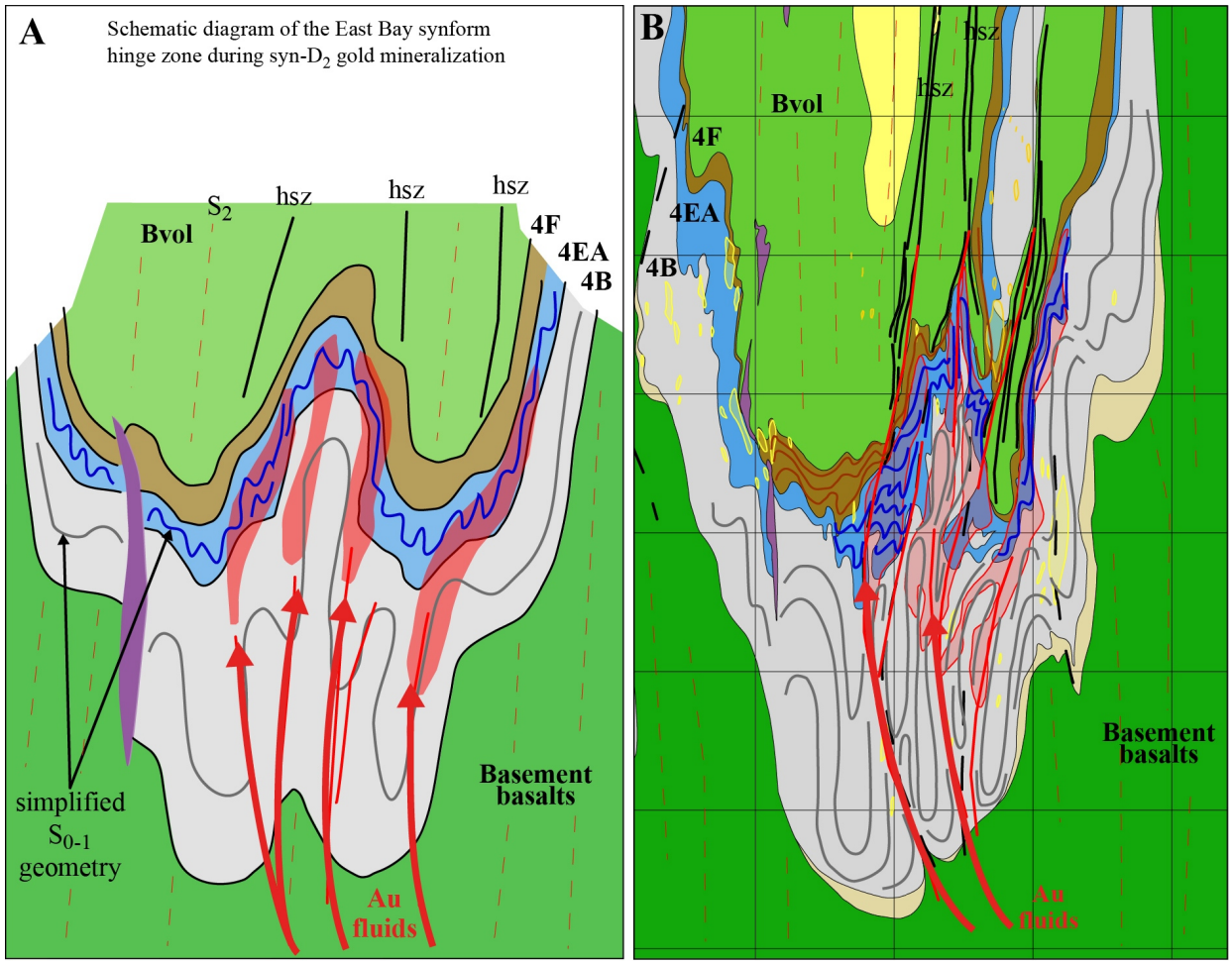

Figure 10-11: Schematic diagrams of the geometrical evolution of the East Bay synform hinge zone during syn-D_2 gold mineralization (based on section 11775 N). Emphasis is on the distinctive folding style of unit 4EA and unit 4B, which influence their final gold endowment. A. Hypothetical early structure and preferential emplacement of mineralized zones in the PQD area. Note the duplication lens of the NIF is omitted for clarity. B. Schematic fold pattern in units 4B, 4EA and 4F of the PQD area.

10.5.2.3 Sulphidation of the iron formation: 4B-4EA comparison

During deformation, local strain, foliation development, and fluid pressure conditions dictate the efficiency of secondary permeability, along with rock anisotropy (Cox et al., 2001). The permeability of a lithology may also evolve during metamorphism (Ferry, 1988). Mineralogical differences, through heterogeneous strain distribution, lead to the formation of pressure gradient driving fluid flow, which can lead to drastically different fluid flow pattern and permeability depending on the lithology, resulting in contrasting potential for fluid-rock interaction (Figure 10-9B). At Musselwhite, this is illustrated by units 4F, 4B, and 4EA. In the former, although garnet porphyroblasts are present, the biotite matrix is prone to plastic deformation, so that strain is diffused quite uniformly. Nearly monomineralic chert and magnetite

bands in unit 4B also promote a homogenous distribution of strain resulting in a style of deformation that includes similar folds and boudins (e.g., Figures 5-18, 5-25 and 5-27). As magnetite deforms plastically, quartz is submitted to diffuse strain that favours plastic deformation. Consequently, deformation in unit 4B likely involves a fairly low strain gradient; and very fine-grained magnetite and chert bands have a low secondary permeability. In opposition, the polymineralic nature of unit 4EA produces a much different environment for fluid flow. Amphiboles are a highly rigid silicate phase, displaying a brittle behaviour at higher temperature than quartz (Gagnon et al., 2016; Baratoux et al., 2005). Garnet remains relatively undeformed (Gagnon et al., 2016); petrographic observations show garnet accommodates high strain by fractures and locally by flattening with respect to the S_2 fabric. In this context, folding of such assemblage of rigid minerals with variable grain-sizes results in grain-scale strain gradients between low strain in pressure shadows and high strain in grain surfaces normal to local strain (Figure 7-9). Interlayered chert bands are typically more deformed, displaying fractures and boudinage (Figures 3-26 and 3-27). As a result, syn-kinematic secondary permeability is interpreted to have been much higher in unit 4EA than in other facies. Such interpretation is supported by observations on microstructures and gold made by Kolb (2010) on mineralized rocks at Musselwhite.

At mine-scale, gold distribution in unit 4B is fairly scattered, with high grades typically associated with isolated quartz veins (Figures 7-2, 7-3, 7-4). This suggests that mineralizing fluids have migrated through the unit (Figure 10-11) but only precipitated a limited amount of gold and sulphides. Difference in reactivity of magnetite and grunerite with mineralizing fluids may require further investigation; however, considering equal reactivity, the relative low gold endowment of unit 4B suggests fluids had limited interaction with oxide-rich layers. Moreover, ductile deformation and weak strain gradients likely minimized the creation of auriferous quartz veins. Generally, ductile deformation has preserved the lateral continuity of chert bands, which hampers fluids from migrating across layers. Thus, the sulphidation of the oxide BIF is laterally limited (e.g., mine level 770, section 11480 N; Figure 5-25A), making these occurrences uneconomic.

Contrastingly, gold mineralization in unit 4EA is much more abundant, and occurs over wider intervals with more homogeneous gold grades (DDH gold assay database, Goldcorp Musselwhite Ltd.). This illustrated by the pervasive distribution of pyrrhotite in hand samples (Figures 7-5 and 7-6), and in thin sections (Figure 7-7A). Nevertheless, pyrrhotite is typically more abundant along the contacts of iron-rich bands than in their centres, illustrating the importance of layer boundaries as preferential fluid pathways. In addition, silicate bands preserve the polymineralic character and the heterogeneous strain distribution during alteration, as grunerite is replaced by Ca-amphiboles, which behave similarly. Finally, this mode of strain distribution may partly explain the predominance of silica flooding over quartz veins in the ore.

In the 4EA unit, strain is distributed more homogeneously, while retaining high permeability that allows silica to precipitate throughout the rock volume, instead of being focused in a specific area such as contacts or fractures. Overall, unit 4EA represents a medium that enabled a more pervasive fluid flow and subsequent fluid-rock interaction. This led to highly efficient sulphur release from the fluids and deposition.

10.5.2.4 Sulphidation of the iron formation: SIF-NIF contrast and 4B-4A comparison

The contrast of gold endowment between the SIF and the NIF relates to two aspects. First, these two BIF comprise different proportions and types of facies and have different stratigraphic sequences (e.g., absence of 4EA in the SIF). Second, there is a difference in endowments between the chert-grunerite facies (unit 4A) and the chert-magnetite facies (unit 4B).

The structural setting and the characteristics of the folded multilayer sequences (i.e., mafic volcanic rocks + BIF horizon(s)) are interpreted to play a major role in the difference in gold endowment. The NIF constitutes a single, thick layer with a rheology different from surrounding mafic layers. On the other hand, the SIF comprises several thin layers intercalated with mafic layers of variable thickness. Multilayer sequences with different characteristics produce different fold structures (Ramsay and Huber, 1987). The NIF is deformed by tight to isoclinal folds with thickened hinge zone and complex internal structures including auriferous high strain zones, whereas the SIF affected by open to locally tight folds (Figure 10-7E). Gold mineralization in the SIF occurs along the East Bay synform east limb, within a parasitic set of much tighter folds (e.g., Red wing and Thunder wolves mineralized zones), a structural style that resembles that of the NIF.

Unit 4EA does not occur in the SIF. However, unit 4A plays a similar role, favouring gold mineralization, in contrast with unit 4B. Gold mineralization in the SIF is mainly related to strong lithological control of unit 4A via its rheological characteristics, and chemical reactivity. The abundance of chert in unit 4A led to a more incompetent nature and thus more brittle behaviour. This is illustrated by the presence of laminated quartz veins and dislocated chert bands (Figure 7-30). Contrastingly, the overlying unit 4B show ductile deformation behaviour. As discussed above (section 10.5.2.3), a grunerite-rich matrix was more efficient, under amphibolite grade, to react with mineralizing fluids and precipitate sulphur and gold. Ore mineral assemblages show that sulphidation of unit 4A probably took place following the reaction (Figure 10-12A):

grun ± qz + $(S, CO_2, Ca)_{fluids}$ = act + po + cc ± cpx

Some gold mineralization is also hosted in the oxide facies (4B) of the SIF (Figure 7-37). Mineral assemblages from the mineralized rocks suggest the following sulphidation reaction (Figure 10-12B):

$mt + qz + (S, CO_2, Ca)_{fluids} = grun + po + act + cpx$

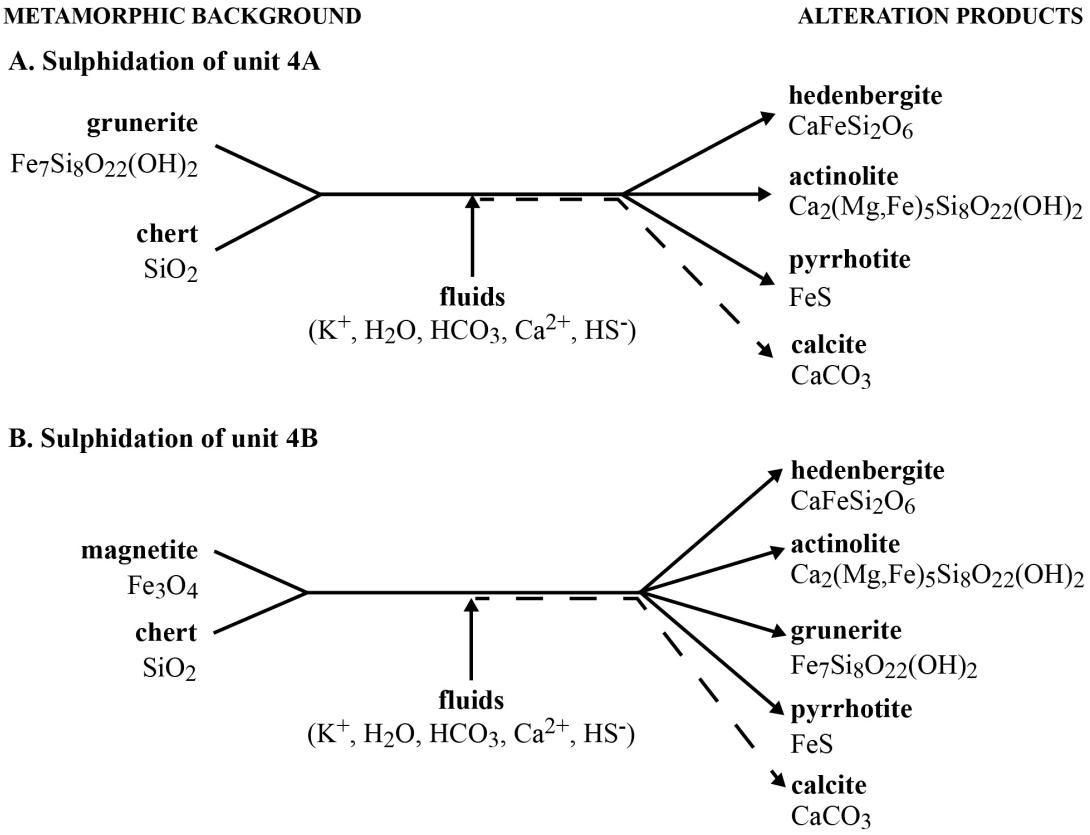

Figure 10-12: Summary of alteration mineralogical reactions in units 4A and 4B.

10.5.3 Potential influence of dykes on gold mineralization

Two types of dykes intrude the NIF: numerous thin mafic dykes scattered across the NIF and mapped in units 4B and 4EA; and fewer and thicker ultramafic dykes crosscutting the entire mine sequence. Both types are interpreted herein as syn-volcanic with the OMA. The mafic dykes have introduced an additional heterogeneity and competency contrast in the NIF sequence. There is no evidence that they influenced the distribution of gold.

The presence of serpentinized ultramafic dykes had a greater impact. They are deformed by F_2 folds, boudinaged, and some ore zones are locally spatially associated with them (e.g., T-antiform area, S3 ore zone; West Limb area). However, the dyke contain little to no gold, suggesting they were poorly reactive to mineralizing fluids and poorly permeable. These dykes rheologically contrasted with the BIF and acted

as planes of weakness, focusing strain and locally gold-bearing fluids. Their extent may have favoured mineralizing fluid flow throughout the entire mine sequence. In particular, these dikes may have allowed less interaction between the migrating fluids and the reactive oxide and silicate BIF units, thus facilitating the formation of mineralized zones in overlying pelitic rocks and mafic volcanic rocks the BIF, such as the WEL zones.

10.5.4 Origin of fluids and metals, and migration routes

10.5.4.1 Sources of hydrothermal fluids

Age relationships do not support a magmatic origin for gold at Musselwhite. The orogenic metamorphic model best explains the genesis of the deposit (Colvine, 1989; Powell et al., 1991; Groves et al., 1995; Phillips and Powell, 2010). In that model, fluids stem from metamorphic devolatilization and have a fairly consistent chemical composition (McCuaig and Kerrich, 1998; Mikucki, 1998; Ridley and Diamond, 2000; Hagemann and Cassidy, 2000; Goldfarb et al., 2005; Dubé and Gosselin, 2007; Ridley et al., 2000; Goldfarb and Groves, 2015): They are dominantly aqueous and CO_2-rich, with low salinity, variable CH_4 and N_2, and they transport gold as a reduced sulphur complex (Groves et al., 2003; Stefansson and Seward, 2004; Moran, 2008), which is consistent with available data at Musselwhite (Hall and Rigg, 1986; this study).

Some studies have proposed sedimentary rocks as the main providers for sulphur and metals in metamorphic fluids (Pitcairn et al., 2006; Tomkins, 2010; Large et al., 2011). In the study area, sediments of the ZHA represent a potential source for fluids and metals involved in the formation of the Musselwhite deposit. The various metamorphic reactions taking place in iron formation sequences intercalated in the OMA under the mine probably contributed to the overall volume of metamorphic fluids, notably of CO_2 (chapter 6; French, 1968; Haase, 1982; Klein, 2005). Mafic volcanic rocks are also potential contributors of fluids (Elmer et al., 2006; Phillips and Powell, 2010). However, their lower sulphur content requires a rock volume one or two orders of magnitude greater to produce the same amount of sulphur as carbonaceous shales (Tomkins, 2010). Sedimentary rocks of the ZHA do not include voluminous shale units. Available data (chapter 3) shows they consist of abundant coarse- to medium-grained siliciclastic sediments. Consequently, the proportion of fluids produced by mafic volcanic rocks with respect to sedimentary rocks may have been relatively significant.

10.5.4.2 Metal sources

The metallic association in the Musselwhite ore (Au, Ag, Cu, Se, Te) is not diagnostic of a particular deposit type, and it lacks trace metals such as As, Bi, Mo, Sn, and W, frequently found in orogenic gold deposits (Groves et al., 2003). Metals are typically leached from rocks from which fluids are generated, as well as from rocks located along the path of fluid migration. In the study area, fluids were likely produced by ZHA sedimentary rocks and volcanic rocks structurally underlying the deposit.

The trace metal association of the ore is the result of the hydrothermal fluids metal content, as well as the influence of physical and chemical conditions during deposition (Mikucki, 1998). Here, the positive correlation of Cu with Au is slightly atypical (chapters 7 and 8; Groves et al., 2003). Given the high Cu content of mafic volcanic rocks than sediments of the ZHA (i.e., in average twice as much based on the present study), this positive correlation could imply that mafic volcanic rocks could have contributed significantly to mineralizing fluids (and Cu was leached from the fluid source rock), or that migrating fluids leached out Cu content from mafic rocks. Alternatively, physico-chemical conditions during precipitations favoured Cu over other trace metals, for instance As, which has a very low content in the Musselwhtie ore.

The near absence of As in the Musselwhite ore and the lack of positive correlation with gold is also atypical for orogenic gold deposits (Groves et al., 2003). It is plausible that due to the particular nature of the host rock, precipitation conditions were outside the field of As-bearing sulphides. However this seems unlikely as deposits similar to Musselwhite do contain As-bearing minerals (see below, section 10.6). Also, As is present at Musselwhite as arsenopyrite-rich veins that crosscut most D_2 structures and thus are late- to post-D_2. More work is needed but the sulphides data fro the ZHA sedimentary rocks (chapter 9) may provide an explanation for the contrast between Au and As distribution.

Based on LA-ICP-MS elemental mapping data, pyrite occurrence in the ZHA is interpreted here as epigenetic in origin. It implies the passage of sulphur-bearing metamorphic fluids pre- to syn-D_2 deformation.The internal chemical zoning of pyrite grains reveals As-rich cores and intermediate zones, contrasting with margins devoid of As. Some Bi, Sb, and Pb is concentrated in the matrix around pyrite, suggesting that they were released from pyrite, but not remobilized by fluids. This also suggests a relative chronology in metal release from pyrite, with As released later than other metals. Sediments of the ZHA are interpreted to occur at depth under the mine, whereas local S-type granite intrusions attest of partial melting, possibly of the sediments. Pyrrhotite replacing pyrite at depth may have released As during the late stage of M_2 metamorphism. Consequently, As may not have been present in ore-forming fluids during the formation of the the Musselwhite deposit.

Lastly, argillites of the Wilberforce area (West antiform) were investigated to assess their for metal sources potential, using a method similar to Large et al. (2011). Results show that such argillites could have provided some of the metal content found in the ore at Musselwhite (chapter 9; Jackson et al., 2013, 2015). However, they were not sufficiently metamorphosed and deformed to drive fluids and metals out of the matrix surrounding pyrite nodules, contrary to similar more tectonized units, such as those east of the OMA under the mine, including unit 4H in the NIF and SIF sequence. Furthermore, such argillites represent a relatively fairly small and most probably insufficient volume to provide a significant part of the metal budget of the Musselwhite mine.

10.5.4.3 Migration mechanisms

In orogenic gold deposits, fluid migration is primarily achieved through major faults and shear zones that generate pressure gradients and focus fluid flow (Eisenlohr et al., 1989; McCuaig and Kerrich, 1998; Cox et al., 2001; Goldfarb et al., 2005). Fluid migration mechanisms in the study area can be considered at various scales, from microscopic scale to regional scale.

At mine scale, the sub-vertical high strain zones that largely control gold distribution are interpreted to represent the upper extension of deep-seated structures along which fluids migrated. Observations on drill core intersections from under the mine (chapter 9) show these shear zones are better developed in Bvol unit than in the "Basement basalt" unit. The distribution of alteration minerals in drill core suggests that foliation planes played a key role in enhancing a more diffuse permeability and as the main pathway for fluids.

The high strain zones of the mine area are 1 to 10 m-wide, which is one to two orders of magnitude thinner than the NCSZ and are thus interpreted as second-order structures. The Musselwhite gold deposit is located at a triple point of the NCG (Figure 10-1A), an area comparable to a flexure or dilatational jog (Cox et al., 2001). The central NCG north of Opapimiskan Lake is interpreted to have recorded intense transpressive deformation (Gagnon et al., 2016). Likewise, the southern NCG in the Graff to Markop lakes area is affected by strong D_2 compression. It is therefore possible to speculate that fluids expelled from deforming rocks of the central and southern parts of the NCG may have migrated vertically and laterally to contribute to gold mineralization in the Opapimiskan Lake area (Figure 10-13). A similar model, involving large-scale lateral fluid flow, has been proposed for gold mineralization in the Archean southern Kalgoorlie and Norseman terranes, Western Australia (Witt et al., 1997).

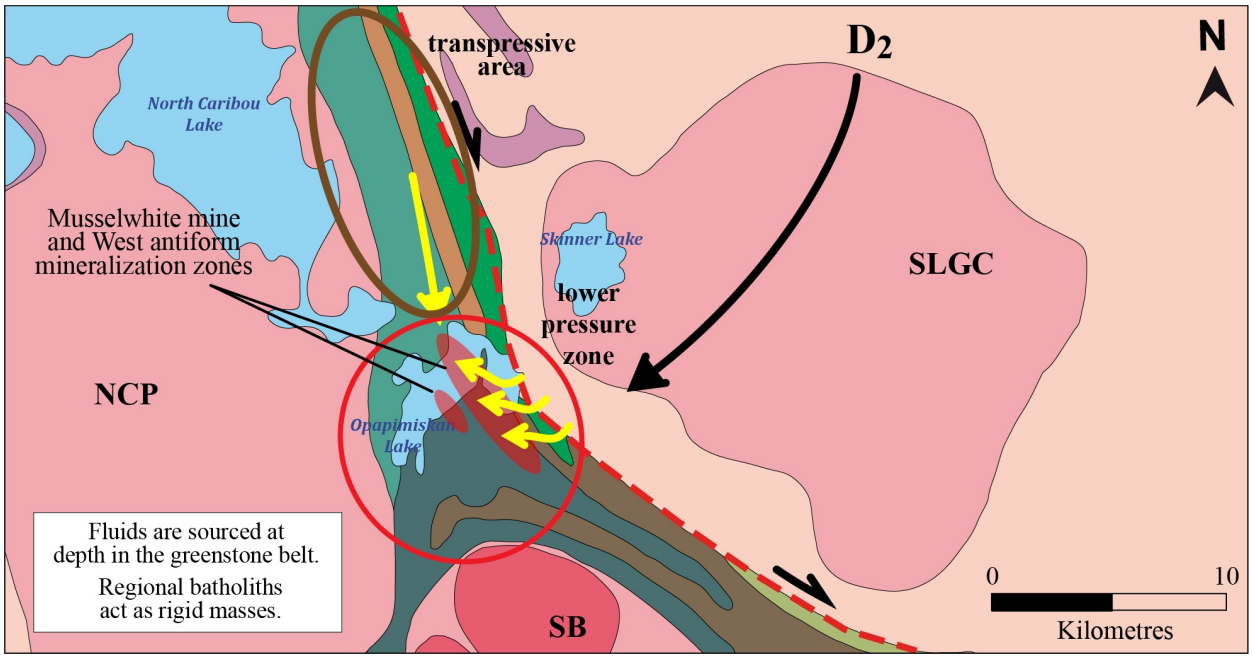

Figure 10-13: Schematic representation of possible fluid migration pathways at sub-regional scale in the study area. The different domains of stress regimes in the greenstone belt create a pressure gradient that favours fluid migration toward the Opapimiskan Lake area.

10.5.5 New genetic model for the Musselwhite gold deposit

The various datasets and interpretations from this study corroborate that of previous studies (Hall and Rigg, 1986; Zhang, 1997; Breaks et al., 2001, and references therein; Otto, 2002; Snow, 2004, unpublished; Hill et al., 2006; Isaac, 2008; Moran, 2008; Kolb, 2010; Biczok et al., 2012) indicating that gold mineralization at Musselwhite is epigenetic and orogenic in nature and was derived from metamorphic devolatilization during the main D_2-M_2 tectonometamorphic event (Figure 10-6). The main key aspects of this study presented and discussed above in this chapter constitute the foundations of a genetic model for the Musselwhite gold deposit, and are briefly synthesized below.

The first deformation event involved horizontal shortening that produced thrusting and folding in parts of the NCG. It occurred between 2850 and 2750 Ma, following emplacement of regional batholiths (NCP, SLGC). In the Opapimiskan Lake area, D_1 is interpreted to have isoclinally-folded and inverted the host sequence of the Musselwhite mine (this study; Figure 10-6). Metamorphic conditions reached upper greenschist facies following D_1 deformation.

Continued southward shortening, between 2710 and 2650 Ma, provoked intense ductile D_2 deformation in the central and southern NCG under lower to middle amphibolite facies metamorphism (M_2). The 2730-2710 Ma emplacement of the Southern Batholith contributed to the regional heat flow. Shortening was

accommodated along the regional first order NCSZ, which display a dextral ductile faulting component (Gagnon et al., 2016). Regional batholiths acted as rigid masses during deformation and induced a bend in the geometry of the the NCSZ and a triple point in the greenstone belt. Dextral transpressive strain dominated in the central NCG, whereas the Opapimiskan Lake area mostly experienced flattening, which produced second order high strain zones that host gold mineralization (Figures 10-6, 10-10A, 10-11). The triple point resulting from the greenstone belt-batholiths interaction during D_2 deformation constituted a lower pressure zone and likely favoured better preservation of the gold deposit.

The age of peak M_2 metamorphism is constrained by U-Th-Pb dating at 2660 Ma, which constitutes the minimum age for gold mineralization (Figure 10-3). Deformation and the resulting strain and pressure gradients have mobilized metamorphic fluids, and likely liberated additional fluids via syn-metamorphic recrystallization (e.g., Wheeler, 1987, 2014). Under amphibolite facies conditions, fluids migrated upward and laterally using the secondary permeability produced by the S_2 fabric and micro-fractures (e.g., Cox et al., 2001). Rheological contrasts between mafic volcanic rocks and the iron formation, as well as the strong layered anisotropy of the BIF, played a key role in the development of high strain zones that focused mineralizing fluids into the NIF (Figure 10-11). Lack of gold mineralization in the SIF directly underlying the deposit is interpreted to result from inefficient/inexistent structural and chemical traps.

Ore-forming fluids are interpreted to come from metamorphic devolatilization of rocks under the mine (Figure 10-11). The proportion of fluids and sulphur coming from sedimentary rocks versus that produced by mafic volcanic rocks is subject to debate (Phillips and Powell, 2009; Tomkins, 2010). In the case of the Musselwhite deposit, the available data does not permit any assessment. Argillite horizons may significantly contribute to the metal budget of certain gold deposits (Large et al., 2011, 2012; Steadman and Large, 2016). However, it is apparently not the case at Musselwhite as the volume of pyrite nodule-bearing argillite horizons in the study area is clearly insufficient (chapter 9).

Mineralizing fluids and their metal content migrated upward and reached the NIF. Gold precipitated during D_2 deformation, mainly in the tightly F_2-folded BIF, and in transposed NIF affected by axial planar D_2 high strain zones (Figure 10-7 and 10-10). The structural control exerted by fault zones on fluid flow is coupled with a lithological control derived from rheological contrasts. They result in deformation style differences between the various BIF facies (section 10.5.2). For instance, the oxide BIF deforms in a more ductile manner than the silicate BIF (Figure 10-11), especially at microscopic scale (i.e., competent magnetite band vs. rigid garnet-grunerite band). These rheological differences also produce contrasts in permeability between mineral assemblages that have an impact on the reactivity of each lithology (Figure 10-9), as fluids can react with a larger volume of rock.

The main host lithology, the one most highly reactive with mineralizing fluids, is characterized by a garnet-grunerite-chert assemblage. Gold-bearing fluids interacted with the grunerite (and local magnetite) to form pyrrhotite-rich ore that are surrounded by a proximal calcic alteration halo where grunerite is converted to Ca-amphiboles, and by a distal potassic alteration halo marked by secondary biotite. Alteration zoning is asymmetrical due to reactivity contrasts of the different host rocks (Figure 10-9). In mafic rocks, a distal alteration characterized by K-enrichment and Na-leaching is better developed, and a proximal alteration is marked by intense CO_2-CaO-enrichment. Gold-mineralized rocks typically show a strong S-enrichment, along with strong gains in Ag, Cu, Se, and Te. Gold mineralization occurred before peak metamorphism as illustrated by the presence of hedenbergite in alteration mineral assemblages. Gold-mineralized rocks were affected by some D_2 deformation, and ore zones were progressively deformed by late D_2 strain. Strain variations induced local, intra-BIF, remobilization of sulphides and gold (e.g., semi-massive pyrrhotite vein in the C-block), as well as some very minor injections in overlying mafic volcanic rocks (e.g., quartz-gold veins, mine level 1020).

Certain characteristics of the Musselwhite gold deposit suggest it represents a hypozonal orogenic gold deposit (Groves, 1993; Groves et al., 1998; 2003; Golfarb et al., 2005; Kolb et al., 2015), including: syn-metamorphic gold mineralization, amphibolite grade P/T conditions (550-650ºC at 3 kbar, eqvlt. to 10 km depth), alteration zoning including biotite over muscovite and Ca-amphiboles over carbonates, ore petrographic characteristics (pyrrhotite ± ilmenite-domianted opaque minerals, garnet, pyroxene), and shear-zone deposit style. Two models have been proposed for hypozonal gold deposits (Kolb et al., 2015): 1) syn- to post-peak metamorphic hydrothermal mineralization, and 2) overprinted pre-peak metamorphic mesothermal mineralization. Kolb et al. (2015) argues that hypozonal gold deposits are formed in more tectonically dynamic systems than those of the deep-later metamorphic devolatilization model (Stüwe, 1998) and typical mesothermal gold deposits (Elmer et al., 2006; Phillips and Powell, 2010). Episodes of thrusting and/or extensional shearing create and invert tectonometamorphic gradients that are interpreted to drive the migration of auriferous fluids expelled from buried lower metamorphic grade units into syn- to late-metamorphic structures of high grade rocks, where gold precipitates (Kolb et al., 2015). Synchronous emplacement of crustally derived pegmatites and granites is either thought to contribute directly to gold mineralization, or to increase heat flow and enhance metamorphic devolatilization.

Hypozonal gold deposits appear to be restricted to Precambrian terranes (Kolb et al., 2015). Geodynamic regimes during the Precambrian may have have been significantly different from Phanerozoic accretionary orogens, such as the North American Cordillera (Goldfarb et al., 1998). Non uniformitarian geodynamic regimes may have led to more complex tectonometamorphic evolutions (Harris and Bédard, 2014; Sizova et al., 2017), notably given the higher geotherm during the Archean (Kolb et al., 2015 and

reference therein). This is relevant to the case of the Musselwhite deposit as the northwestern Superior province is interpreted to have experienced synchronous vertical and horizontal tectonics (Lin, 2005; Parmenter et al., 2006).

10.6 Comparisons with other BIF-hosted gold deposits

10.6.1 Contwoyto-Point lakes area: the Lupin gold mine and regional gold occurrences

The Contwoyto-Point lakes area (CPL) is located in the Slave Province, Northwest Territories, Canada. It comprises Neoarchean plutonic rocks and supracrustal rock assemblages, notably the Yellowknife supergroup including the Contwoyto formation, which hosts the 3.5 Moz Lupin gold mine (Lhotka and Nesbitt 1989). The geology, structure and gold metallogeny of the area have been the subject of a number of studies (Bostock, 1980; King et al., 1988; Lhotka and Nesbitt 1989; and references therein), some of which focusing on the Lupin deposit (Gardiner, 1986; Kerswill, 1993; Bullis et al., 1994; Kerswill et al., 1996; Bullis et al., 1996; Geusebroek and Duke, 2004). Although distinct in some ways, the Lupin and Musselwhite mines show common features that deserve attention as they illustrate similar ore-forming processes.

The host stratigraphy of the Lupin deposit is dominated by metasedimentary rocks representing a turbidite sequence (Bullis et al., 1994), which differ from that of Musselwhite that is mostly constituted of mafic volcanic rocks. Barren iron formation at Lupin is mainly constituted of chert and grunerite with occasional magnetite and/or garnet porphyroblasts, similar to units 4A and 4EA at Musselwhite. Variations in garnet abundance reflect primary variations in Al-content. A pelitic iron formation made of an assemblage of garnet-grunerite-chlorite-quartz (Lhotka and Nesbitt 1989) compares well with unit 4F (garnet-biotite schist) and with some components of unit 4E (garnet amphibolite) at Musselwhite. Similarly to unit 4F at Musselwhite, this pelitic iron formation shows systematically low gold grades, except when it is the only host rock in a mineralized zone (i.e., West limb zones at Musselwhite, McPherson M1 and M2 zones at Lupin; Geusebroek and Duke, 2004), illustrating a lithological control on mineralization.

The bedrock of the CPL area is metamorphosed to the mid-greenschist to mid-amphibolite facies, where up to seven mineral isograds have been mapped (Lhotka and Nesbitt 1989). Contrastingly, the area surrounding Musselwhite mine is mainly metamorphosed to the amphibolite facies. The progression from low to medium metamorphism the CPL area shows the transition from chlorite to grunerite-garnet (Haase,

1982), similarly to what is inferred from chlorite inclusions in garnet porphyroblasts from unit 4EA at Musselwhite.

The origin of gold mineralization at Lupin was interpreted to be syngenetic (Kerswill, 1993; Kerswill et al., 1996) or epigenetic (Bullis et al., 1994, 1996; Geusebroek and Duke, 2004). The distribution of gold associated with sulphidized iron formation near quartz veins in Lupin mine area (Lhotka and Nesbitt, 1989) supports the latter interpretation. Gold mineralization is concentrated in or near the hinge zone of tight folds, spatially associated to second-order shear zone(s), and BIF units played a strong lithological control. Quartz veins have typically lower gold grade than their surrounding sulphide-rich halos. Sulphide content and gold grades are highest adjacent to the vein and decrease away from the vein. Hydrothermal alteration around the veins is mainly characterized by the replacement of grunerite by hornblende, similarly to Musselwhite. Two sets of auriferous veins have been identified, an early set associated with pyrrhotite-replacement of the iron formation, and a later set controlling the spatial distribution of arsenopyrite-rimmed löllingite grains. While resulting in a much higher gold endowment, this late stage of As-rich mineralization appears comparable to the late stage of arsenopyrite-rich veins documented at Musselwhite. The contrast in gold content may be partly explained by the contrast abundance of sedimentary rocks in the both host sequences, which are known to represent the primary source for As in greenstone belt (notably black shales, Large et al., 2011; Steadman et al., 2014).

Lupin ore bodies are also locally characterized by coarse-grained hedenbergite and quartz, with minor epidote, and local grossular garnet (Lhotka and Nesbitt, 1989), which are similar to that documented at Musselwhite. These are interpreted to represent a metamorphosed alteration mineral assemblage. Lupin's calc-silicate assemblages are cut by hornblende-actinolite-pyrrhotite-arsenopyrite microveinlets that indicate retrogression of mineral assemblages. This metamorphic retrogression is also illustrated by local pyrite-replacement of pyrrhotite, as well as chlorite replacing biotite in zones outside the mine. At Musselwhite, retrograde metamorphism is shown by replacement of hedenbergite by grunerite and biotite by chlorite.

Deformation history in the CPL area is more complex than that of NCG, as it is also affected by Proterozoic deformation, which has fairly limited impact of the local geology of Lupin. Archean deformation include rare F_1 folds with no apparent associated fabric (King et al., 1988). Subsequent ductile D_2 folding and brittle-ductile D_3 folding and shearing have produced a fold interference pattern. Timing of first gold introduction is interpreted to have occurred during latest-D_2 to earliest-D_3 deformation and hosted in F_2 fold structures (Geusebroek and Duke, 2004). D_2 and D_3 deformation at Lupin have a comparable structural significance to that of the D_1 and D_2 events at Musselwhite. Gold mineralization occurred approximately at the same relative tectonometamorphic timing in both cases,

during peak amphibolite facies metamorphism. At Lupin, magmatism has contributed to the regional heat flow during gold mineralization (Geusebroek and Duke, 2004), which is apparently not the case at Musselwhite.

10.6.2 Mineral Hill, Jardine, Montana, USA

The Mineral Hill mine is a lode gold deposit hosted in upper-greenschist to lower-amphibolite facies BIF of the Archean Wyoming craton (Smith, 1996). The rock sequence also comprises 3.0-3.2Ga metaturbidites and metapelites (Hallager, 1984; Smith, 1996), a lithological setting which is similar to that of the Lupin deposit.

The iron formation is dominantly Al-poor silicate facies BIF constituted by chert and grunerite, with local garnet-bearing pelitic lenses. This mineralogy is equivalent to units 4A and 4EA at Musselwhite. The tectonometamorphic evolution of the Mineral Hill deposit area also includes three major phases of deformation (Smith, 1996, and references therein): D_1, large-scale isoclinal folds, locally recumbent, with strong axial planar S_1 foliation; followed by D_2 upright close folds, and well-developed S_2 crenulation cleavage; and D_3 open folds and weak axial planar fabric. Habitus and textures of garnet and alumino-silicates porphyroblasts suggest that peak metamorphism occurred during M_1. Estimates of peak P/T conditions range between 530 and 560°C and 3 kbar. Local occurrences of sillimanite suggest that metamorphic conditions were locally higher, similar to that of Musselwhite.

Gold mineralization at Mineral Hill consists in arsenopyrite-pyrrhotite sulphidation of the BIF and spatially associated quartz veins crosscutting the iron formation layering. Hydrothermal alteration is mainly characterized by the conversion of grunerite into hornblende, with local masses of clinozoisite (Smith, 1996). Overall alteration and ore mineral assemblages are very similar to that of Musselwhite and Lupin. Likewise, carbonate alteration is conspicuously absent. In addition to Au, trace metal enrichments included As, Ag, Cu, Zn, Pb and Bi.

Proposed genetic models at Mineral Hill include a remobilized syngenetic origin for gold mineralization (Hallager, 1984) or more recently, a syn-metamorphic epigenetic origin (Smith, 1996, and references therein). Gold mineralization was tentatively attributed to prograde lower-amphibolite M_1 metamorphism based on textural relationships between garnet and alteration minerals, arsenopyrite growth, and deformed veins crosscutting the S_1 foliation. While garnet at Mineral Hill does not show coarsening with proximity with the ore, internal chemical zoning, inclusion size and abundance variations, and syn-kinematic growth are quite similar to that of garnet porphyroblasts at Musselwhite (chapter 7). Mineral Hill lacks the coarse,

angular, inclusion-free almandine garnet typically associated with mineralized zones at Musselwhite. Garnet at Mineral Hill contains inclusions of biotite and hornblende but no clinozoisite. This is interpreted as evidence that alteration associated with mineralization outlasted garnet growth. Chlorite-filled fractures in garnet suggest that some retrograde metamorphism was associated with later deformation events.

10.6.3 Homestake mine, South Dakota, USA

The Homestake mine is located in the Black Hills of South Dakota. It has produced over 40 Moz of gold and is the largest known BIF-hosted gold deposit (Caddey et al., 1991). The Paleoproterozoic host sequence of the Homestake deposit (2.012-1.974 Ga; Frei et al., 2009) consists of the carbonaceous black shale of the Poorman Formation, the carbonate facies BIF of the Homestake Formation, and turbidites and mudstones of the Ellison Formation, They are exposed in an erosional window through the Phanerozoic cover (Caddey et al., 1991; Steadman and Large, 2016).

Regional tectonometamorphism occurred at ca. 1.84 Ga, prior to the emplacement of 1.72 Ga Crook Mountain Granite. The Homestake iron formation mainly consists of a chert-siderite carbonate facies, and a minor chert-grunerite silicate facies. Subordinates biotite and chlorite are common, and garnet is locally present. Gold mineralization is interpreted to postdate metamorphism because the alteration mineral assemblage overprints the peak metamorphic paragenesis (Caddey et al., 1991; Bell, 2013). Geological contrainsts on gold mineralization include lead stepwise leaching analyses monazite inclusions in garnet at 1746-1713 Ma (Frei et al., 2009), and Re-Os data on arsenopyrite of 1736 ± 8 Ma (Bell, 2013).

The Homestake deposit is located along a folded garnet isograd (Caddey et al., 1991). Gold mineralization is nearly exclusively hosted in the carbonate facies BIF, and the ore consists in an assemblage of pyrrhotite, arsenopyrite, and minor pyrite, in a gangue of quartz-siderite-chlorite (Caddey et al., 1991). Siderite locally occurs as alteration-related porphyroblasts (Steadman and Large, 2016). The ore has a 5:1 Ag/Au ratio and base metals content is negligible. The distribution of the ore is controlled by the hinge zone of folds where dilatational segments developed during late stage ductile-brittle shearing. Such controls, and the presence of a well-developed shear zone at the contact between the sedimentary host and the BIF, emphasize the influence of BIF rheology on fluid flow.

Caddey et al. (1991) report three alteration mineral assemblages: the first two are interpreted as syn-metamorphic, and the third is associated with gold mineralization. After carbon remobilization, and potassic and carbonate alterations, retrogressive chlorite, siderite and sericite developed in and around the ore zones. As for other BIF-hosted deposits, the genesis of the Homestake deposit has been widely

debated, with proponents of a syngenetic origin (Rye and Rye, 1974; Kerswill, 1996), of a epigenetic origin (Caddey et al., 1991; Frei et al., 2009; Bell, 2013), or a mixture of both involving the underlying rocks of the Poorman Formation as sulphur and metal source (Steadman and Large, 2016).

The Homestake deposit differs from Musselwhite as it bears resemblances to the more typical late- post-metamorphic gold deposits occurring near the greenschist-amphibolite transition zones (Dubé and Gosselin, 2007). The nature of the iron formation sequence that hosts gold mineralization is also different (carbonate vs. silicate), but both share the same strong lithological (BIF rheology) and structural (thickened/tight fold hinges) controls on gold mineralization. Although alteration mineral assemblages of both deposits are dissimilar because they formed at different P/T conditions, they reflect a similar potassic and carbonate/calcic zoning.

10.6.4 Nevoria mine, Southern Cross belt, Yilgarn craton, Western Australia

The Nevoria mine was a major gold producer of the Southern Cross greenstone belt (Mueller, 1997). The overall stratigraphy of the 3.1-3.0 Ga greenstone belt is similar to that of the NCG: a lower portion constituted of tholeiitic basalt and komatiite, separated by three BIF sequences, and an upper portion consisting of greywackes and turbidites (Mueller, 1997). The greenstone belt was affected by ductile deformation and isoclinal folding, prior to the emplacement of batholiths between 2775 and 2724 Ma (Mueller et al., 2004) and concomitant greenschist to amphibolite facies metamorphism, and a second phase of folding, which produced crescent-shaped dome structures. A second phase of plutonism occurred at ca. 2634 Ma, , generating amphibolite grade contact metamorphism (600°C, 0.4 GPa; Mueller et al., 2004). U-Pb and Pb-Pb geochronological constraints and crosscutting relationships with dykes show that the Nevoria orebodies are coeval with ca. 2634 Ma granite emplacement. Mineralization is 90 m.y. younger than regional metamorphism and 20 m.y. younger than late-orogenic transpressional deformation related to the evolution of the Noreman-Wiluna belt (Mueller et al., 2004).

The Nevoria gold mineralization differs significantly from that of the Musselwhite deposit (Mueller, 1997), although ore and alteration mineralogy, as well as some ore-forming processes are remarkably similar. Ore at Nevoria is mostly hosted in chert-grunerite BIF (Mueller, 1997), including some Al-rich garnet-bearing lenses and a minor chert-magnetite BIF, which are similar to unit 4A, to units 4EA/4F, and to unit 4B at Musselwhite, respectively. Although some mineralization is present in the surrounding amphibolitic rocks, the reactivity of folded BIF sequences had a strong lithological control on mineralization that was concentrated along fold hinges. Concentration of high grade gold at the upper and

lower contact of the BIF also highlights the higher permeability of lithological boundaries and its impact on mineralizing fluid flow.

Gold mineralization at Nevoria is typically divided into reduced and oxidized types, the latter of which is absent from the BIF. The former has a minor early Mg-rich component, and a major Ca-rich component. Similarly to Musselwhite, calcic alteration at Nevoria is reflected by the replacement of grunerite by actinolite and hedenbergite. Sulphidation of the BIF is dominantly characterized by pyrrhotite (po-py 20:1 ratio), with minor chalcopyrite, trace arsenopyrite-löllingite (rim-core), Bi-tellurides, and scheelite. The hydrothermal system is marked by an outer potassic alteration zone with early biotite-microcline, and late-stage stilpnomelane-chlorite mineral assemblage (Mueller, 1997). Lastly, the deposit area is characterized by strike-slip faults that are marked by barren muscovite-chlorite-calcite alteration zones (Mueller, 1997).

Overall, the characteristics of the Nevoria deposit, and similar type of deposits in the Southern Cross belt, emphasize the potential of BIF sequences to host gold mineralization in Archean greenstone belts metamorphosed at amphibolite facies, especially in the vicinity of syntectonic intrusions. They comprise structural controls and alteration zoning that are fairly similar to that of purely metamorphic epigenetic orogenic gold mineralization.

10.6.5 Lac Lilois prospect, Ashuanipi complex, northeastern Superior province, Canada

The Lac Lilois prospect is located in the Ashuannipi gneissic complex, in the northeastern-most area of the Superior Province (Lapointe and Chown, 1993). Metamorphism at the Lac Lilois prospect reached granulite facies conditions, which is much higher than that of Musselwhite. Metamorphism of the iron formation at Lac Lilois resulted in recrystallization and the coarsening of grains, similarly to what is observed in the SIF under Musselwhite mine. Gold is associated with gangue minerals such as quartz and clinopyroxene ± orthopyroxene, biotite and plagioclase, and opaque minerals pyrrhotite, arsenopyrite and löllingite (Lapointe and Chown, 1993). The sulphides/arsenide occurs in fractures in garnet and ferrosilite and as semi-massive pods, illustrating post-gold mineralization local remobilization of sulphides induced by deformation. This is very similar to the massive pyrrhotite vein spatially associated with the two sub-vertical high strain zones in the C-block ore zone at Musselwhite.

Retrograde metamorphism at the Lac Lilois prospect induced grunerite-replacement of pyroxene and chlorite replacing biotite, which are also documented at Musselwhite. Lastly, geochronological constraints on the timing of the Lac Lilois mineralization suggest gold was emplaced between 2700 Ma and 2650 Ma (Percival et al., 1988; Moritz and Chevé, 1992), which is similar to that of Musselwhite.

10.6.6 Summary

The comparison of various BIF-hosted gold deposits allows to draw some similarities and differences, which may translate into potential exploration vectors. Under medium to high metamorphic conditions, tightly folded silicate-BIF and crosscutting ductile fault zones are critical features of gold mineralization. Pyrrhotite-replacement and replacement of grunerite ± garnet by Ca-amphibole ± garnet are typical of the alteration halo associated with the hydrothermal system (Mineral Hill). Gold mineralization is typically syn-metamorphic and structurally-controlled, with, in some cases, a fluid + metal (Nevoria) or heat (Lupin) contribution from syn-tectonic intrusions. Deformation may outlast gold mineralization, causing local remobilization of sulphides ± gold in low pressure zones (Lac Lilois).

The proposed models for hypozonal gold deposits (Kolb et al., 2015) include 1) syn- to post-peak metamorphic hydrothermal mineralization (hypozonal), and 2) overprinted pre-peak metamorphic mesothermal mineralization. The petrographic data and textural relationships show that the Musselwhite is not a mesothermal gold deposit. It is clearly syn-metamorphic, and does not show the post-peak metamorphism charateristics of typical hypozonal deposits (e.g. Renco; Kolb et al., 2015). Also, gold mineralization at Musselwhite is not linked to magmatism, in contrast with deposits such as Nevoria (Mueller, 1997). It apparently originates from fluids exclusively derived from metamorphic devolatilization (Elmer et al., 2006; Phillips and Powell, 2009; 2010), which were driven from their sources to the BIF host by major structures.

10.7 Implications for exploration

10.7.1 Exploration in the North Caribou greenstone belt

D_2 strain gradient, tight F_2 folds with thickened hinge zones and attenuated limbs, and associated high strain zones are the key structural exploration vectors outlined in this study. The thick, detrital-rich NIF sequence is the most prospective horizon; however, the SIF can be locally mineralized, provided sufficient strain. Data collected from the various mineralized zones has shown that while the silicate facies of the iron formation (both Al-rich and Al-poor) are the most viable host for gold mineralization, other lithologies such as the garnet-biotite schist may be attractive targets to host ore zones. In such occasion, other favorable structural and geological parameters should be present (e.g., tight folds, shear zones, dykes).

Macroscopic mineralogical and textural changes related to the hydrothermal alteration are additional vectors. Within the silicate BIF, secondary grunerite and biotite and coarser garnet porphyroblasts, and closer to mineralisation, Ca-amphibole replacement of grunerite associated with pyrrhotite are key indications of mineralized body. This is most helpful along strike of the silicate BIF unit. In adjacent pelitic rocks, proximity with mineralized rocks is mainly shown by biotite recrystallization and coarser garnet porphyroblasts. In the oxide BIF, abundant grunerite, secondary Ca-amphiboles, and calcite reflect alteration intensity.

Some features in mafic rocks and associated garnet-amphibolite lenses (unit 4E) overlying the BIF sequences can be used as indirect vectors to mineralized rocks. Biotite-altered and intensely carbonatized high strain zones are typically developed in the vicinity of mineralized zones. Garnet-amphibolite lenses can be locally mineralized to economic proportions; more frequently, they may be weakly mineralized, suggesting better potential at depth.

The previously underestimated presence of regional F_1 folds as documented in this study has large implications for the distribution of BIF sequences (NIF and SIF) in the study area. The mine is located on the inverted limb of a F_1 fold, the opposite limb of which is predicted to occur at depth under the deposit. The intersection between BIF sequences and D_2 high strain zones, notably extending from the central NCG, have the potential for significant new gold resources. Additional exploration drilling could therefore target the stratigraphy under the mine to improve local geological knowledge. It would yield critical information on the potential for gold mineralization further at depth.

Gold mineralization in the West antiform (Hall and Rigg, 1986) may extend further to the NW under Opapimiskan Lake. Moreover, the West antiform area includes several tight F_2 folds where the underlying oxide facies BIF has been shown to contain low grade gold mineralization over long drill core intervals, which could be economic (Biczok J., oral communication, 2013). Overall, many elements suggest there is still significant gold potential in the Opapimiskan Lake area.

Gold occurrences such as Arseno Lake, Castor-Pollux lakes, and McGruer Lake (i.e., north of Eyapamikama Lake; Figure 10-14) show the potential for gold in the northern NCG. In the central NCG, the LLV and SRA include some BIF horizons that are intensely deformed by the D_2 strain (Figure 10-6). Potential gold-mineralized zones would probably occur as shallowly-plunging, flat, elongated, cigar-shaped bodies. Exploration for such target requires careful identification of F_2-folded prospective BIF horizons neighbouring D_2 shear zones, preferably near or at lithological boundaries.

The Wesley-Neawagank lakes occurrence, hosted in the FLV, is the only known gold occurrence in the southern NCG (Figure 10-14; Piroshco et al., 1989). It is located in the transition zone between the greenschist and amphibolite facies (Gagnon et al., 2015) that is known to be a prospective tectonometamorphic level (Phillips and Powell, 2009 and references therein), and which could be an exploration vector in that area. Timiskaming-like metasediments along the northern tectonic boundary of the ZHA suggest that this structure could be a major basin-scale fault, which could have a potential similar to well–endowed major breaks of the southern Abitibi (e.g., Bleeker, 2015). D_3 deformation overprint is considerable in the southern NCG, and its impact on potential mineralization has to be considered.

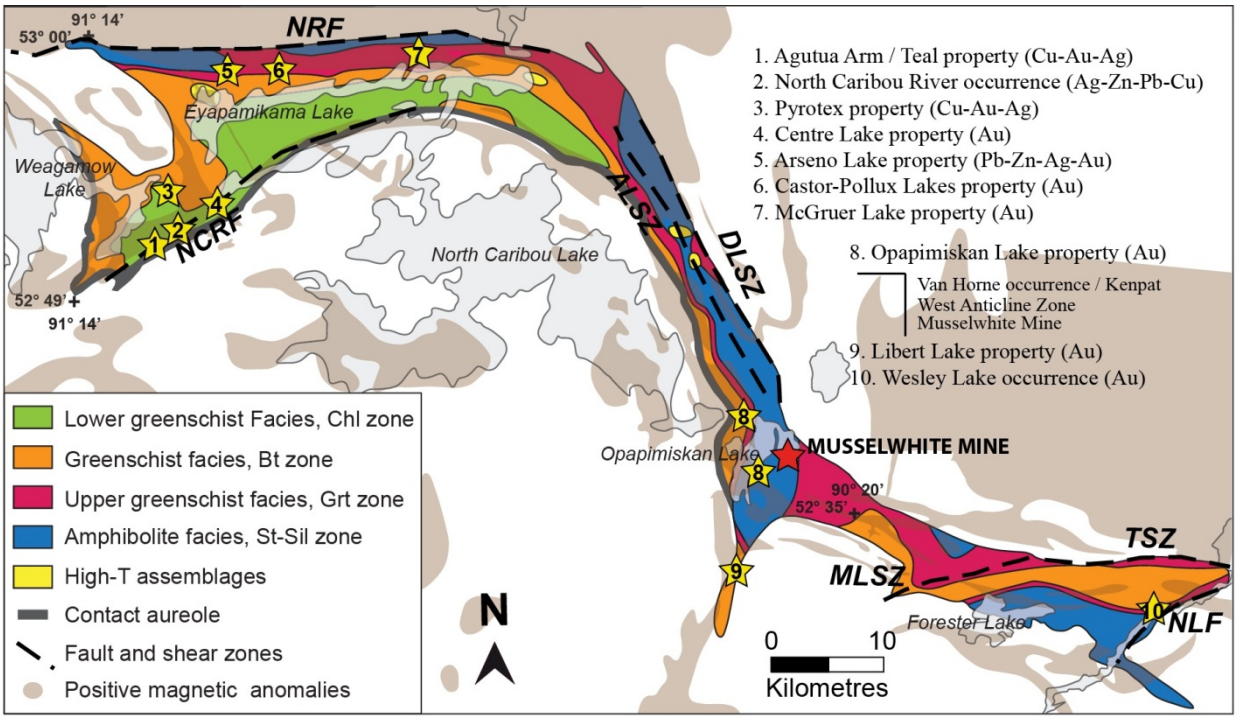

Figure 10-14: Metamorphic facies of the NCG (modified from Gagnon et al., 2015, after Breaks et al., 2001, and Kelly et al., 2013), with location of major mineral occurrences in the North Caribou greenstone belt. Data from Breaks et al., 2001, and reference therein. NRF: North Rim fault zone, NCR: North Caribou River fault zone, DLSZ: Dinnick Lake shear zone, ALSZ: Akow Lake shear zone, MLSZ: Markop Lake shear zone, TSZ: Totogan shear zone, NLF: Neawagank Lake fault zone.

Gold occurrences throughout the NCG show that there is a potential outside the Musselwhite-Opapimiskan Lake area. The specificity of the Musselwhite deposit stems from the set of parameters that contributed to focusing gold-bearing fluid flow during the D_2-M_2 event. Currently, Musselwhite is a single-standing world-class deposit, similar to Homestake or Lupin, but it has a great potential for continued gold mineralization northwestward at depth where the folded BIF sequences are likely intersected by high strain zones. In addition, the F_1 fold limb opposite to that of the Musselwhite mine

sequence represent a key target at greater depth in the mine area, but also closer to surface in the Graff Lake area (Figure 10-1B).

10.7.2 Exploration in other Precambrian terranes

This study of the Musselwhite gold deposit has produced a detailed geological model for gold mineralization, and as improved the understanding of its regional geological setting. Numerous key exploration vectors have been identified that may be useful for exploration in other Precambrian terranes.

The Musselwhite deposit is located in a key area of the greenstone belt at the meeting point of two sections with different orientations and having experienced transpressive strain regime (Gagnon et al., 2016), creating a favorable structural context, comparable to a flexure or dilatational jog along a major strike-slip fault zone (Cox et al., 2001). The deposit is located near a first order structure, and mineralized zones are dominantly hosted by folded silicate facies BIF affected by second order high strain zones. The thickened hinge zone of folds is a preferential locus for the development of ore zones.

The timing of gold mineralization is globally syn-D_2 deformation, under amphibolite grade conditions. Al-rich and Al-poor silicate facies BIF are the most favorable hosts for gold mineralization, due to their response to deformation and reactivity to mineralizing fluids at such metamorphic grade. Oxide facies BIF, iron-rich pelites, and mafic volcanic rocks are locally mineralized, especially in zones of greater strain where specific geological features such as dykes can help focus auriferous fluids. Reactivity to hydrothermal fluids drives the development of alteration zones around mineralized bodies. Macroscopic alteration features described in the previous section may represent exploration vectors in other analogous terranes.

Mineral exploration frequently involves soil geochemistry, where positive anomalies in gold and its associated trace metals are looked for. At Musselwhite, gold is notably associated with Ag, Cu, Se, and Te. The low As content at Musselwhite can be partly related to the moderate abundance of metasedimentary rocks in the local stratigraphy. In cases where the iron formation sequences are hosted by sediment-dominated stratigraphy (e.g., Lupin), arsenic is more abundant and typically associated to gold mineralization.

Determining the relative timing between regional batholiths and tectonometamorphic events appear critical. In the NCG, regional batholiths largely play a passive role, acting as rigid masses during geodynamic events. In the case of Lupin, intrusions appear to have contributed to the regional heat flow driving metamorphism and mineralization, while at Nevoria they are intimately linked to gold

mineralization. Timing relationships have major implications for establishing exploration models and prospective areas, regardless of whether they relate to epigenetic orogenic gold or skarn-type mineralization.

Lastly, deformation and metamorphic features of BIF-hosted gold mineralization at Musselwhite suggest the rheology of BIF limits remobilization of gold and sulphides outside the envelope of the BIF sequence, and even may concentrate it. This is likely partly due to the propensity of BIF to deform in a ductile manner, notably at medium to high metamorphic grade. While additional work is required, the Lac Lilois prospect would support such interpretations (Lapointe and Chown, 1993). Consequently, the understanding of the evolution of BIF-hosted gold mineralization in upper-amphibolite and granulite grade metamorphic terranes may help exploration in these areas, such as Grenville Province in Canada.

10.8 Conclusions

10.8.1 Main contributions

Geological and structural mapping, geochemical data processing, and high-precision geochronology has significantly enriched the geological knowledge of the North Caribou greenstone belt. This contribution notably includes: 1) better constrained tectonostratigraphic setting of the greenstone belt, 2) additional insights on the depositional environment of main rocks assemblages, 3) adding numerous absolute age constraints of rock assemblages of the NCG, 4) refining the understanding of the regional structural evolution, 5) providing a strongly reliable age for peak M_2 metamorphism in the Opapimiskan Lake area, and 6) producing a revised model for the tectonometamorphic evolution of the North Caribou greenstone belt, during which a major gold mineralizing event took place.

The stratigraphy of the Opapimiskan Lake area was produced by volcanism likely resulting from the interaction of a mantle plume with older crustal rocks (from 3.05 to 2.90 Ga), with interruptions allowing the deposition of multiple sequences of Algoma-type BIF. It was followed by a major shift toward basin development and detrital sedimentation (from 2.90 to 2.70 Ga). The SRA and OMA stratigraphy has been overturned during the D_1 event and refolded during the D_2 major ductile deformation event, which occurred between 2720 and 2660 Ma. Peak amphibolite facies metamorphism in the Opapimiskan Lake area occurred ca. 2660 Ma.

Musselwhite is an epigenetic, amphibolite-facies orogenic gold deposit mainly hosted in the Al-rich silicate facies of a folded Algoma-type BIF sequence, which is intersected by axial planar high strain zones. Gold mineralization is associated with pyrrhotite-replacement and local silica flooding of the

garnet-grunerite-chert metamorphic mineral assemblage of the iron formation. Pyrrhotite is the dominant sulphide phase, with minor chalcopyrite and trace galena, pentlandite, and arsenopyrite. Distal potassic alteration is characterized by secondary biotite crystallization and proximal calcic alteration by the replacement of grunerite by Ca-amphiboles. Almandine garnet porphyroblasts have recorded chemical variations and coarsening through the alteration and mineralization process. Au is mainly associated with Ag, Cu, Se, and Te.

Gold mineralization is controlled by D_2 sub-vertical high strain zones that crosscut BIF horizons. Gold is concentrated in these high strain zones and in adjacent lower pressure zones (e.g., F_2 fold hinge zone). D_2 strain gradients are a key vector toward gold mineralization. The layered anisotropy and chemical reactivity of the BIF facies also exert a lithological control on the distribution of gold, favouring its precipitation in the silicate facies. A minor proportion of gold mineralization is hosted by oxide facies BIF and metapelitic rocks. Gold was introduced during D_2 deformation and M_2 metamorphism. Timing constraints on D_2 and M_2 imply that gold mineralization occurred between 2720 and 2660 Ma. Pyrrhotite and gold distribution and textural relationships indicate that mineralized and altered rocks were metamorphosed and significantly flattened.

Geological data and LA-ICP-MS elemental mapping support the interpretation that mineralizing fluids were derived from metamorphic devolatilization and that regional horizons of sulphide-bearing argillite may have contributed to parts of the deposit's metal budget. The remainder is interpreted to originate from underlying mafic volcanic rocks and ZHA sedimentary rocks, similar to classic orogenic gold mineralization.

Exploration for similar gold mineralization should focus on areas with including major BIF sequences affected by large-scale polyphase folding in the vicinity of a first order fault zone. Hinge zone of tight folds intersected by secondary structures are highly prospective. Occurrence of intrusive rocks such as dykes can locally focus strain and gold-bearing fluids.

10.8.2 Outstanding questions

The multidisciplinary nature of this study has generated of a large amount of data, which still has potential for scientific research. Many questions remain to be addressed.

More research should be conducted in the Opapimiskan Lake area to better characterize and constrain the various stages of volcanism (timing, petrology, geochemistry, etc.) and sedimentation (stratigraphy, depositional environment, etc.), and their implications on the geological history of the NCG.

There are important knowledge gaps on the timing and condition of regional metamorphism in the NCG, and the implications for gold mineralization. For instance, petrographic data and available garnet Sm-Nd geochronology shows a complex, multi-stage growth of porphyroblasts that is not yet fully constrained. Lu-Hf garnet geochronology, as well as geothermobarometry would contribute to bridge those gaps.

Data from this study suggests there is little chemical difference between mineral phases, such as grunerite or biotite, present in the metamorphic and the alteration-related parageneses. More research is needed to distinguish the signature of metamorphic and hydrothermal mineral species.

This study has shown that mineralizing fluids are mostly metamorphic in origin. Consequently, the study of the isotopic composition of sulphur and metals such as Cu or Pb, with comparison of the various reservoirs and of the ore, could further investigate and characterize this model of gold mineralization.

Some singular features of the Musselwhite deposit remain to be studied in detail. This includes small occurrences of pyrrhotite-carbonate-gold veins (Liferovitch, 2007, unpublished), which could be related to remobilization of mineralization at greater depth. In addition, there are local occurrences of arsenopyrite, notably: disseminated arsenopyrite porphyroblasts in D_2 high strain zones, arsenopyrite-pyrrhotite massive veinlets crosscutting $S_{0\text{-}1}$ layering and S_2 fabric, and visible gold-bearing arsenopyrite veins. The study of these occurrences would likely bear insights on the late-stage evolution of the Musselwhite deposit.

Structure and lithological controls have a strong impact on gold mineralization. The mineralogy of BIF is identified as a key control of the secondary permeability. Further investigation and modelling of grain-scale strain gradients and fluid flow under various P/T conditions would help quantify the effect. It could lead to define the P/T conditions of the transition zone at which silicate BIF becomes a more favourable host than oxide BIF.

The geochemical characterisation of hydrothermal alteration of BIF is difficult. Investigating additional sampling and/or analytical techniques, as well as possible geochemical data processing methods for BIF would be beneficial to exploration.

REFERENCES

Aitchison J. & Egozcue J.J. (2005) Compositional data analysis: Where are we and where should we be heading? Mathematical Geology, 37(7):829-849.

Aitchison J. (1986) The statistical analysis of compositional data. In: Cox D.R., Hinkley D.V., Rubin D. & Silverman B.W. (Eds.) Monographs on Statistics and Applied Probability, 430 p.

Alexander B.W., Bau M., Andersson P. & Dulski P. (2008) Continentally-derived solutes in shallow Archean seawater: Rare earth element and Nd isotope evidence in iron formation from the 2.9 Ga Pongola Supergroup, South Africa. Geochimica et Cosmochimica Acta, 72:378-394.

Allmendinger R.W., Cardozo N.C. & Fisher D. (2013) Structural Geology Algorithms: Vectors & Tensors. Cambridge University Press, Cambridge, England, 289 p.

Altermann W. & Nelson D.R. (1998) Sedimentation rates, basin analysis and regional correlations of three Neoarchaean and Palaeoproterozoic sub-basins of the Kaapvaal craton as inferred from precise U–Pb zircon ages from volcanoclastic sediments. Sedimentary Geology, 120:225-256.

Arias Z. (1986) Archean stromatolites from the North Caribou Lake greenstone belt, Eyapamikama Lake area, northwestern Ontario. Unpublished BSc thesis, Carleton University, Ottawa, Ontario, 80 p.

Atherton M.P. & Brotherton M.S. (1982) Major element composition of the pelites of the Scottish Dalradian. Geological Journal, 17:185-221.

Baldwin G.J. (2011) The sedimentology and geochemistry of banded iron formations of the Deloro assemblage, Barlett Dome area, Abitibi greenstone belt, Ontario, Canada: Implications for BIF deposition and greenstone belt formation. M.Sc. thesis, Laurentian University, Sudbury, Ontario, 121 p.

Barclay W.A. (2003) Surface structural geology at recently exposed trenches, West Anticline Area, Musselwhite Property, Northwestern Ontario. W.A. Barclay Exploration Services Ltd report for Placer Dome Canada Limited, 67 p. and appendices.

Bard J.-P. (1980) Microtextures des roches magmatiques et métamorphiques. Masson, Paris, 192 p.

Baratoux L., Schulmann K., Ulrich S. & Lexa O. (2005) Contrasting microstructures and deformation mechanisms in metagabbro mylonites contemporaneously deformed under different temperatures (c. 650 °C and c. 750 °C). In: Pankhurst R.J. (Ed.) Deformation Mechanisms, Rheology and Tectonics: From Minerals to the Lithosphere. Geological Society, London, Special Publications 243, pp. 97-125.

Bateman R. & Hagemann S. (2004) Gold mineralisation throughout about 45 Ma of Archean orogenesis: Protracted flux of gold in the Golden Mile, Yilgarn craton, Western Australia. Mineralium Deposita, 39:536-559.

Bath O. (2017) Provenance of siliclastic sedimentary rocks in the eastern portion of the North Caribou greenstone belt. M.Sc. thesis, University of Ottawa, 142 p.

Bath O., Hattori K. & Biczok J. (2015) A provenance and metamorphic history of the sedimentary rocks in the eastern part of the North Caribou greenstone belt, host of the Musselwhite Gold Deposit. 2015 GAC-MAC joint conference, May 3-7, Montreal, QC, Canada, 1 poster.

Bau M. & Dulski P. (1996) Distribution of yttrium and rare-earth elements in the Penge and Kuruman iron-formations, Transvaal Supergroup, South Africa. Precambrian Research, 79:37-55.

Bédard J.H. (2017) Stagnant lids and mantle overturns: Implications for Archaean tectonics, magma genesis, crustal growth, mantle evolution, and the start of plate tectonics. Geoscience Frontiers, in press.

Bédard J.H. & Harris L.B. (2014) Neoarchean disaggregation and reassembly of the Superior craton. Geological Society of America, Geology, 42(11):951-954.

Bédard J.H., Brouillette P., Madore L. & Berclaz A. (2003) Archaean cratonization and deformation in the northern Superior Province, Canada: An evaluation of plate tectonic versus vertical tectonic models. Precambrian Research, 127(1):61-87.

Bekker A., Slack J.F., Planavsky N., Krapez B., Hofmann A., Konhauser K.O. & Rouxel J. (2010) Iron formations: The sedimentary product of a complex interplay among mantle, tectonic, oceanic, and biospheric processes. Economic Geology, 105:467-508.

Bell C. (2013) Structural controls on gold mineralization at the Homestake Mine and their implications for the geology of the Black Hills. Ph.D. thesis, James Cook University, 232 p.

Bethune K. & Scammel R.J. (1997) Precambrian geology, Koch Island area (part of NTS 37C, District of Franklin, Northwestern Territories). Geological Survey of Canada, Open File 3391.

Beukes N.J. & Gutzmer J. (2008) Origin and paleoenvironmental significance of major iron formations at the Archean-Paleoproterozoic boundary. Hagemann S., Rosière C., Gutzmer J. & Beukes N.J. (Eds.) Banded iron formation-related high-grade iron ore. Reviews in Economic Geology, 15:5-47.

Biczok J., Hollings P., Klipfel P., Heaman L., Maas R., Hamilton M., Kamo S. & Friedman R. (2012) Geochronology of the North Caribou greenstone belt, Superior Province Canada: Implications for tectonic history and gold mineralization at the Musselwhite mine. Precambrian Research, 192-195:209-230.

Bleeker W. (2015) Synorogenic gold mineralization in granite-greenstone terranes: The deep connection between extension, major faults, synorogenic clastic basins, magmatism, thrust inversion, and long-term preservation. In: Targeted Geoscience Initiative 4: Contributions to the Understanding of Precambrian Lode Gold Deposits and Implications for Exploration, B. Dubé and P. Mercier-Langevin (Eds.). Geological Survey of Canada, Open File 7852, pp. 25-47.

Bloem E.J.M. (1994) Structural controls, alteration history and genesis of Archaean gold deposits near Southern Cross, Yilgarn block, Western Australia. Unpublished PhD thesis, Department of Geology and Geophysics, The University of Western Australia, 181 p.

Blower S. & Kiernan J. (2003) Review of Musselwhite Mine operations, Ontario. AMEC Technical report for Kinross Gold Corp., 129 p.

Bolhar R., Kamber B.S., Moorbath S., Fedo C.M. & Whitehouse M.J. (2004) Characterization of early Archaean chemical sediments by trace element signatures. Earth and Planetary Science Letters, 222:43-60.

Borg G. (1993) Epigenetic, BIF-hosted Au mineralization at Geita, Tanzania, evidence from structural geology, ore petrography and geochemistry. Current Research in Geology Applied to Ore Deposit, Granada, pp. 415-418.

Bostock H.H. (1980) Geology of the Itchen Lake area, District of Mackenzie. Geological Survey of Canada, Memoir 391, 101 p.

Boström K. (1973) The origin and fate of ferromanganoan active ridge sediments. Stockholm Contributions to Geology, 27:147-243.

Breaks F.W., Osmani I.A. & de Kemp E.A. (2001) Geology of the North Caribou Lake area, northwestern Ontario. Ontario Geological Survey, Open File Report 6023, 80 p.

Breaks F.W., Bartlett J.R., de Kemp E.A. & Osmani I.A. (1991) Geology of the Doubtful-Akow lakes area, District of Kenora. Ontario Geological Survey, Open File Report 5795, 131 p.

Breaks F.W. & Bartlett J.R. (1991) Geology of the Eyapamikama Lake Area. Ontario Geological Survey, Open File Report 5792, 132 p.

Breaks F.W., Osmani I.A. & de Kemp E.A. (1987) Precambrian geology of the Opapimiskan-Neawagank lakes area, Opapimiskan Lake project, Kenora District (Patricia Portion). Ontario Geological Survey, 1 map.

Breaks F.W., Bartlett J.R., de Kemp E.A. & Osmani I.A. (1986) Precambrian geology of the Doubtful-Akow lakes area, Opapimiskan Lake project, Kenora District (Patricia Portion). Ontario Geological Survey, 1 map.

Breaks F.W., Bartlett J.R., Osmani I.A., Finamore P.F. & Wallace H. (1985) Opapimiskan lake project: Precambrian and Quaternary geology of the North Caribou Lake area, District of Kenora, Patricia Portion. In: John W., Owen L.W., Barlow R.B. & Colvine, A.C. (Eds.) Summary of Field Work and Other Activities 1985. Ontario Geological Survey, Miscellaneous Paper 126, pp. 268-276.

Bullis H.R, Hureau R.A. & Penner B.D. (1996) Distribution of gold and sulfides at Lupin, Northwest Territories – A reply. Economic Geology, 91:964-965.

Bullis H.R, Hureau R.A. & Penner B.D. (1994) Distribution of gold and sulfides at Lupin, Northwest Territories. Economic Geology, 89:1217-1227.

Bullis H.R. (1990) Geology of the Lupin Deposit, N.W.T. In: Padgham W.A. & Atkinson D. (Eds.) Mineral Deposits of the Slave Province, Northwest Territories, 8th International Association on the Genesis of Ore Deposits Symposium, Field Trip Guidebook, Field Trip 13, Geological Survey of Canada, Open File 2168, pp. 115-125.

Butler J.C. (1982) The closure problem as reflected in discriminant function analysis. Chemical Geology, 37:367-375.

Cabri L.J. & Jackson S.E. (2011) New developments in characterization of sulphide refractory gold ores. In: Deschênes G., Dimitrakopoulos R. & Bouchard J. (Eds.) World Gold 2011, Proceedings of the 50th Conference of Metallurgists, Montreal, Quebec, Canada, pp. 51-62.

Caddey S.W., Bachman R.L., Campbell T.J., Reid R.R. & Otto R.P. (1991) The Homestake Gold Mine, an early Proterozoic iron-formation-hosted gold deposit, Lawrence county, South Dakota. In: Shawe D.R., Ashley R.P. & Carter L.M.H. (Eds.) Geology and resources of gold in the United States, U.S. Geological Survey Bulletin 1857, pp. J1-J67.

Cardozo N. & Allmendinger R.W. (2013) Spherical projections with OSXStereonet. Computers & Geosciences, 51:193-205.

Carmichael D.M. (1978) Metamorphic bathozones and bathograds: A measure of the depth of post-metamorphic uplift and erosion on the regional scale. American Journal of Science, 278(6):769-797.

Catlos E.J., Gilley L.D. & Harrison M.T. (2002) Interpretation of monazite ages obtained via in situ analysis. Chemical Geology, 188:193-215.

Chadwick T. (2014) The lithological, geochemical and mineralogical analysis of the Cigar Lake Shear Zone, Northwestern Ontario, and its potential to host gold mineralization. B.Sc. thesis, Carleton University, 85 p.

Clout J.M.F. & Simonson B.M. (2005) Precambrian iron formations and iron formation-hosted iron ore deposits. In: Hedenquist J.W., Thompson J.F.H., Goldfarb R.J. & Richards J.P. (Eds.) Economic Geology 100th Anniversary Volume, pp. 643-680.

Colombi A. (1988) Métamorphisme et géochimie des roches mafiques des Alpes ouest-centrales (géoprofil Viège-Domodossola-Locarno). Ph.D. thesis, University Lausanne, 432 p.

Colvine A.C. (1989) An empirical model for the formation of Archean gold deposits: Products of final cratonization of the Superior Province, Canada. In: Keys R.R., Ramsay W.R.H. & Groves D.I. (Eds.) The Geology of Gold Deposits: The Perspective in 1988: Economic Geology, Monograph, 6:37-53.

Colvine A.C., Fyon J.A., Heather K.B., Marmont S., Smith P.M. & Troop D.G. (1988) Archean lode gold deposits in Ontario. Ontario Geological Survey, Miscellaneous Paper 139, 136 p.

Corfu F., Davis D.W., Stone D. & Moore M.L. (1998) Chronostratigraphic constraints on the genesis of Archean greenstone belts, northwestern Superior Province, Ontario, Canada. Precambrian Research, 92:277-295.

Corfu F. & Stone D. (1998) Age structure and orogenic significance of the Berens River composite batholiths, western Superior Province. Canadian Journal of Earth Sciences, 35:1089-1109.

Couture G. (1995) Stratigraphy, lithology, structural history and grade distribution of the Musselwhite gold prospect. Placer Dome Canada Ltd., internal report, 102 p.

Cox S.F., Knackstedt M.A. & Braun J. (2001) Principles of structural control on permeability and fluid flow in hydrothermal systems. Reviews in Economic Geology 14: 1-24.

Dahéron L., Jacques-Beyssen S., Pommez P. & Reutenauer F. (2015) Loss on Ignition for oxidizable iron ores with C/H analyzer. Progress in Analytical Chemistry & Materials characterisation in the Steel and Metals Industries, CETAS 2015, May 19-21, Düsseldorf, Germany.

Davis D.W. & Stott G.M. (2001) Geochronology of several greenstone belts in the Sachigo Subprovince, northwestern Ontario, #18 Project Unit 89-7. In: Baker C.L., Kelly R.I. & Parker J.R. (Eds.) Summary of Field Work and Other Activities 2001, Ontario Geological Survey, Open File Report 6070, pp. 18-1–18-13.

Davies J.F., Whitehead R.E.S., Cameron R.A. & Duff D. (1982) Regional and local pattern of CO_2-K-Rb-As alteration: A guide to gold in the Timmins area. In Hodder, R.W. & Petruk, W. (Eds.) Geology of Canadian gold deposits. The Canadian Institute of Mining and Metallurgy, 24:130-143.

de Kemp E.A. (1987) Stratigraphy, provenance and geochronology of Archean supracrustal rocks of western Eyapamikama Lake area, northwestern Ontario. M.Sc. thesis, Carleton University, Ottawa, Ontario, 98 p.

Dickin A.P. (2005) Radiogenic Isotope Geology: 2nd edition. Cambridge University Press, New York, 492 p.

Dubé B. & Mercier-Langevin P. (2015) Targeted Geoscience Initiative 4: Contributions to the Understanding of Precambrian Lode Gold Deposits and Implications for Exploration. Geological Survey of Canada, Open File 7852, 297 pp.

Dubé B., Mercier-Langevin P., Castonguay S., McNicoll V.J., Pehrsson S.J., Bleeker W., Schetselaar E.M. & Jackson S. (2011) Targeted Geoscience Initiative 4. Lode Gold deposits in ancient deformed and metamorphosed terranes – footprints and exploration implications: a preliminary overview of themes, objectives and targeted areas. In: Summary of Field Work and Other Activities 2011, Ontario Geological Survey, Open File Report 6270, pp. 38-1–38-10.

Dubé B., Gosselin P., Mercier-Langevin P., Hannington M. & Galley A. (2007) Gold-rich volcanogenic massive sulphide deposits. In: Goodfellow W.D. (Ed.) Mineral Deposits of Canada: A Synthesis of Major Deposit-Types, District Metallogeny, the Evolution of Geological Provinces, and Exploration Methods. Geological Association of Canada, Mineral Deposits Division, Special Publication No. 5, pp. 75-94.

Dubé B. & Gosselin P. (2007) Greenstone-hosted quartz-carbonate vein deposits. In: Goodfellow W.D. (Ed.) Mineral Deposits of Canada: A Synthesis of Major Deposit-Types, District Metallogeny, the Evolution of Geological Provinces, and Exploration Methods. Geological Association of Canada, Mineral Deposits Division, Special Publication No. 5, pp. 49-73.

Duff J. (2014) A Geochemical and Isotopic Investigation of Metasedimentary Rocks from the North Caribou greenstone belt, Western Superior Province, Canada. M.Sc. thesis, University of Ottawa, 189 p.

Duff J., Hattori K., Schneider D., Biczok J. & McFarlane C. (2013) Timiskaming-type sedimentary rocks near the Musselwhite gold mine in the North Caribou greenstone belt, Western Superior Province of Canada. Geological Association of Canada – Mineralogical Association of Canada joint annual meeting, May 22-24, 2013, Winnipeg, Manitoba, 36:88.

Easton R.M. (2000) Metamorphism of the Canadian Shield, Ontario, Canada. I. The Superior Province. The Canadian Mineralogist, 38:287-317.

Eilu P.K., Mathison C.L., Groves D.L. & Allardyce W.J. (1999) Atlas of alteration assemblages, styles and zoning in orogenic lode gold deposits in a variety of host rock and metamorphic settings. Geology and Geophysics Department (Centre for Strategic Mineral Deposits) & UWA Extension, The University of Western Australia, Publication 30, 50 p.

Eilu P.K. & Mikucki E.J. (1996) Geochemical and isotopic dispersion haloes in Archean lode-gold systems: Assessment of alteration indices for use in district-scale and mine-scale exploration. Minerals and Energy Research Institute of Western Australia, Report, 176(I):64.

Eisenlohr B.N., Groves D. & Partington G.A. (1989) Crustal-scale shear zones and their significance to Archaean gold mineralization in Western Australia. Mineralium Deposita, 24:1-8.

Elmer F.L., White R.W. & Powell R. (2006) Devolatilization of metabasic rocks during greenschist-amphibolite facies metamorphism. Journal of Metamorphic Geology, 24:497-513.

Eriksson P.G., Catuneanu O., Sarkar S. & Tirsgaard H. (2005) Patterns of sedimentation in the Precambrian. Sedimentary Geology, 176:17-42.

Eriksson K.A., Krapez B. & Fralick P.W. (1997) Sedimentological aspects. In: de Wit M.J. & Ashwal L.D. (Eds.) Greenstone belts. Oxford Monographs on Geology and Geophysics, 35(1):33-54.

Eriksson K.A., Krapez B. & Fralick P.W. (1994) Sedimentology of Archean greenstone belts: Signatures of tectonic evolution. Earth Science Reviews, 34:1-88.

Ewers W.E. (1983) Chemical factors in the deposition and diagenesis of banded iron-formation. In: Trendall A.F. & Morris R.C. (Eds.) Iron-formation: Facts and Problems. Elsevier, Amsterdam, pp. 491-512.

Ferry J.M. (1988) Contrasting mechanisms of fluid flow through adjacent stratigraphic units during regional metamorphism, south-central Main, USA. Contributions to Mineral Petrology, 98:1-12.

Ferry J.M. & Spear F.S. (1978) Experimental calibration of the partitioning of Fe and Mg between biotite and garnet. Contribution to Mineral Petrology, 66:113-117.

Fieller E.C., Hartley H.O. & Pearson E.S. (1957) Tests for rank correlation coefficients I. Biometrika, 44:470-481.

Findlay J.M., Parrish R.R., Birkett T.C. & Watanabe D.H. (1995) U-Pb ages from the Nimish Formation and Montagnais glomeroporphyritic gabbro of the central New Quebec orogen, Canada. Canadian Journal of Earth Sciences, 32:1207−1220.

Fischer W.W. & Knoll A.H. (2009) An iron shuttle for deep-water silica in Late Archean and early Paleoproterozoic iron formation. Geological Society of America Bulletin, 121:222−235.

Fitzsimons I.C.W., Kinny P.D., Wetherley S. & Hollingsworth D.A. (2005) Bulk chemical control on metamorphic monazite growth in pelitic schists and implications for U-Pb age data. Journal of Metamorphic Geology, 23:261-277.

Ford R.C. & Duke N.A. (1993) Concentration of gold during retrograde metamorphism of Archean banded iron formations, Slave Province, Canada. Canadian Journal of Earth Science, 30:1566-1581.

Fossen H. (2010) Structural Geology. Cambridge University Press, 463 p.

Franklin J.M., Gibson H.L., Jonasson I.R. & Galley A.G. (2005) Volcanogenic Massive Sulfide Deposits. In: Hedenquist J.W., Thompson J.F.H., Goldfarb R.J. & Richards J.P. (Eds.) Society of Economic Geologists, Economic Geology 100th Anniversary Volume, pp. 523-560.

Frei R., Dahl P.S., Frandsson M.M., Jensen L.A., Hansen T.R., Terry M.P. & Frei K.M. (2009) Lead-isotope and trace-element geochemistry of Paleoproterozoic metasedimentary rocks in the Lead and Rochefort basins (Black Hills, South Dakota, USA): Implications for genetic models, mineralization ages, and sources of leads in the Homestake gold deposit. Precambrian Research, 172:1-24.

French B.M. (1973) Mineral assemblages in diagenetic and low-grade metamorphic iron-formation. Economic Geology, 68:1063-1074.

French B.M. (1968) Progressive contact metamorphism of the Biwabik iron-formation, Mesabi Range, Minnesota. Minnesota Geological Survey Bulletin 45, 103 p.

Fripp R.E.P. (1976) Stratabound gold deposit in Archean banded iron-formation, Rhodesia. Economic Geology, 71:58-75.

Frost B.R. (1979a) Metamorphism of iron-formation: Parageneses in the system Fe-Si-C-O-H. Economic Geology, 74:775-785.

Frost B.R. (1979b) Mineral equilibria involving mixed volatiles in a C-O-H fluid phase: The stabilities of graphite and siderite. American Journal of Science, 279:1033-1059.

Fry K. (2013) A geochemical and petrogenetic study of three granitic dyke swarms within the southern North Caribou terrane. B.Sc. honours thesis, Lakehead University, 172 p.

Gagnon E., Schneider D.A., Kalbfleisch T., Habler G. & Biczok J. (2016) Characterization of transpressive deformation in shear zones of the Archean North Caribou greenstone belt (NW Superior province) and the relationship with regional metamorphism. Tectonophysics, 693:261-276.

Gagnon E. (2015) Investigation of transpressive deformation zones in the North Caribou greenstone belt (NW Superior) and relationships with regional metamorphism: Implications for the tectonothermal evolution during Archean cratonization. M.Sc. thesis, University of Ottawa, 205 p.

Gagnon E., Schneider D.A., Kalbfleisch T., Biczok J., Habler G. & Camacho A. (2015) Structural geology, geochemistry and geochronology of transpressive deformation zones in the North Caribou greenstone belt, NW Superior: Insights into the tectonothermal evolution of the belt in

Archean tectonics context. Geological Association of Canada – Mineralogical Association of Canada joint annual meeting, May 5-7, 2015, Montreal, Quebec, 1 poster.

Galley A.G., Syme R. & Bailes A.H. (2007) Metallogeny of the Paleoproterozoic Flin Flon Belt, Manitoba and Saskatchewan. In: Goodfellow W.D. (Ed.) Mineral Deposits of Canada: A Synthesis of Major Deposit-Types, District Metallogeny, the Evolution of Geological Provinces, and Exploration Methods. Geological Association of Canada, Mineral Deposits Division, Special Publication No. 5, pp. 509-531.

Gao J.-F., Jackson S.E., Dubé B., Kontak D.J. & De Souza S. (2015) Genesis of the Canadian Malartic, Côté Gold, and Musselwhite gold deposits: Insights from LA-ICP-MS element mapping of pyrite. In: B. Dubé and P. Mercier-Langevin (Eds.) Targeted Geoscience Initiative 4: Contributions to the Understanding of Precambrian Lode Gold Deposits and Implications for Exploration. Geological Survey of Canada, Open File 7852, pp. 157-175.

Gardiner J.J. (1986) Structural geology of the Lupin gold mine, Northwestern Territories. M.Sc. thesis, Acadia University, 206 p.

Geusebroek P.A. & Duke N.A. (2004) An update on the geology of the Lupin Gold Mine, Nunavut, Canada. Canadian Institute of Mining, Metallurgy and Petroleum, Exploration Mining Geology, 13(1-4):1-13.

Gibson H.L., Schwarz-Schampera U., DeWolfe M., Engelbert M. & Freitag R. (2015) Contrasting the settings of seafloor massive sulfide deposits on the South Central Indian Mid-Ocean Ridge: Results of the Bundesanstalt für Geowissenschaften und Rohstoffe (BGR) INDEX 2013 cruise. In: Program with Abstracts, GAC/MAC/AGU Joint-Annual Meeting, Montreal.

Gifkins C., Herrmann W. & Large R.R. (2005) Altered volcanic rocks: A guide to description and interpretation. University of Tasmania, CODES Special Publication, Hobart.

Goldberg I. (1964) Notes on the relationship between gold deposits and structure in southern Rhodesia. In: Houghton S.H. (Ed.) The geology of some ore deposits in southern Africa. Johannesburg, Geological Society of South Africa, 2:9-13.

Goldfarb R.J. & Groves D.I. (2015) Orogenic gold: Common or evolving fluid and metal sources through time. Lithos, 233:2-26.

Goldfarb R.J., Bradley D. & Leach D. (2010) Secular variation in economic geology. Economic Geology, 105:459-465.

Goldfarb R.J., Baker T., Dubé B., Groves D.I., Hart C.J.R. & Gosselin P. (2005) Distribution, character, and genesis of gold deposits in metamorphic terranes. In: Hedenquist J.W., Thompson J.F.H., Goldfarb R.J. & Richards J.P. (Eds.) Economic Geology 100th Anniversary Volume, pp. 407-450.

Goldfarb R.J., Groves D.I. & Gardoll S. (2001) Orogenic gold and geologic time: A global synthesis. Ore Geology Reviews, 18:1-75.

Gole M.J. & Klein C. (1981a) Banded iron-formation through much of Precambrian time. Journal of Geology, 89:169-183.

Gole M.J. & Klein C. (1981b) High-grade metamorphic Archean banded iron-formations, Western Australia: assemblages with coexisting pyroxenes ± fayalite. American Mineralogist, 66:87-99.

Goodwin A.M. (1962) Structure, stratigraphy and origin of iron formation, Michipicoten area, Algoma district, Ontario, Canada. Geological Society of America Bulletin, 73:561-585.

Goodwin A.M. (2000) Principles of Precambrian geology. San Diego, Academic Press, 327 p.

Govindaraju K. (1994) Compilation of working values and sample description for 383 geostandards. The Journal of Geostandards and Geoanalysis, Geostandards Newsletter, 18:158.

Gosselin P. & Dubé B. (2005) Gold deposits and gold districts of the world. Geological Survey of Canada, Open File 4893, 1 map.

Gourcerol B., Thurston P.C., Kontak D.J., Côté-Mantha O. & Biczok J. (2016) Depositional setting of Algoma-type banded iron formation. Precambrian Research, 281:47-79.

Graham C.M. & Powell R. (1984) A garnet-hornblende geothermometer: calibration, testing, and application to the Pelona Schist, Southern California. Journal of Metamorphic Geology, 2:13-31.

Grant J.A. (1986) The isocon diagram – A simple solution to Gresens' equation for metasomatic alteration. Economic Geology, 81:1976-1982.

Gromet L.P., Dymek R.F., Haskin L.A. & Korotev R.L. (1984) The "North American shale composite": Its compilation, major and trace element characteristics. Geochimica et Cosmochimica Acta, 48:2469-2482.

Gross G.A. (2009) Iron formation in Canada, genesis and geochemistry. Geological Survey of Canada, Open File 5987, 164 p.

Gross G.A. (1996) Stratiform iron. In: Eckstrand O.R., Sinclair W.D. & Thorpe R.I. (Eds.) Geology of Canadian Mineral Deposit Types. The Geology of North America, Geological Society of America (also Geological Survey of Canada, Geology of Canada, No. 8), P1:41-80.

Gross G.A. (1988) Gold content and geochemistry of iron-formation in Canada. Geological Survey of Canada, Paper 86-19, 59 p.

Gross G.A. (1983) Tectonic systems and the deposition of iron-formation. Precambrian Research, 20:171-187.

Gross G.A. (1980) A classification of iron formations based on depositional environments. The Canadian Mineralogist, 18(2):215-222.

Gross G.A. (1965) General geology and evaluation of iron deposits. In: Geology of Iron Deposits in Canada. Geological Survey of Canada, Economic Geology Report, 22(I):181.

Gross G.A. (1959) A classification for iron deposits in Canada. Canadian Mining Journal, October, pp. 87-91.

Groves D.I., Condie K.C., Hronsky J.M.A. & Vielreicher R.M. (2005) Secular changes in global tectonic processes and their influence on the temporal distribution of gold-bearing mineral deposits. In: Hedenquist J.W., Thompson J.F.H., Goldfarb R.J. & Richards J.P. (Eds.) Economic Geology 100th Anniversary Volume, pp. 407-450.

Groves D.I., Goldfarb R.J., Robert F. & Hart C.J.R. (2003) Gold deposits in metamorphic belts: Overview of current understanding, outstanding problems, future research, and exploration significance. Economic Geology, 98:1-29.

Groves D.I., Ridley J.R., Bloem E.J.M., Gebre-Mariam M., Hronsky J.M.A., Knight J.T., McCuaig, T.C., McNaughton N.J. & Ojala J. (1995) Lode-gold deposits of the Yilgarn Block: Products of late-Archaean crustal-scale over-pressured hydrothermal systems. In: Coward R.P. & Ries A.C. (Eds.) Early Precambrian Processes. Geological Society of London, Special Publication 95, pp. 155-172.

Groves D.I. & Foster R.P. (1993) Archaean lode gold deposits. In: Foster R.P. (Ed.) Gold Metallogeny and Exploration, pp. 63-103.

Groves D.I. (1993) The crustal continuum model for late Archean lode-gold deposits of the Yilgarn Block, Western Australia. Mineralium Deposita, 28:366-374.

Guest N. (2013) A geochemical study of the volcanogenic massive sulfide potential of the Wilberforce Lake area, Musselwhite gold mine, Northwestern Ontario. Pro. M.Sc. thesis, Laurentian University, 35 p.

Haase C.S. (1982) Metamorphic petrology of the Negaunee iron formation, Marquette District, Northern Michigan: Mineralogy, metamorphic reactions, and phase equilibria. Economic Geology, 77:60-81.

Hagemann S.G. & Cassidy K.F. (2000) Archean orogenic lode gold deposits. In: Hagemann S.G. & Brown P.E. (Eds.) Gold in 2000. Society of Economic Geologists, Reviews in Economic Geology, 13:9-68.

Hagemann S.G. & Brown P.E. (2000) Gold in 2000. Society of Economic Geologists, Reviews in Economic Geology 13, 559 p.

Hall R.S. & Rigg D.M. (1986) Geology of the West Anticline Zone, Musselwhite Prospect, Opapimiskan Lake, Ontario, Canada. In: Proceedings of Gold '86 Symposium, Toronto, pp. 124-136.

Hallager W.S. (1984) Geology of gold-bearing metasediments near Jardine, Montana. In: Foster R.P. (Ed.) Gold '82. Rotterdam, A.A. Balkema, pp. 191-218.

Harris L.B. & Bédard J.H. (2014) Crustal evolution and deformation in a non-plate-tectonic Archaean Earth: Comparisons with Venus, Chapter 9. In: Dilek Y. & Furnes H. (Eds.) Evolution of Archean Crust and Early Life. Modern Approach in Solid Earth Sciences, 7:215-291.

Hartigan J.A. (1975) Clustering Algorithms. John Wiley & Sons Inc., New York, 185 p.

Hashizume K., Pinti D.L., Orberger B., Cloquet C., Jayananda M. & Soyama H. (2016) A biological switch at the ocean surface as a cause of laminations in a Precambrian iron formation. Earth and Planetary Science Letters, 446:27-36.

Haskin M.A. & Haskin L.A. (1966) Rare earths in European shales: A redetermination. Science, 154:507-509.

Haugaard R., Frei R., Stendal H. & Konhauser K. (2013) Petrology and geochemistry of the ~2.9 Ga Itilliarsuk banded iron formation and associated supracrustal rocks, West Greenland: Source characteristics and depositional environment. Precambrian Research, 229:150-176.

Hill M.-L., Cheatle A.M. & Liferovich R. (2006) Musselwhite mine: An orogenic gold deposit in the western Superior province. Geological Association of Canada – Mineralogical Association of Canada joint annual meeting, May 14-17, Montreal, Program with Abstracts, 31:67.

Hobbs B.E., Means W.D. & Williams P.E. (1976) An outline of structural geology. John Wiley & Sons, Inc., 571 p.

Hodgson C.J. (1993) Mesothermal lode-gold deposits. In: Kirkham R.V., Sinclair W.D., Thorpe R.I. & Duke J.M. (Eds.) Mineral Deposits Modeling. Geological Association of Canada, Special Paper 40, pp. 635-678.

Hoisch T.H. (1990) Empirical calibration of six geobarometers for the mineral assemblage quartz + muscovite + biotite + plagioclase + garnet. Contributions to Mineralogy and Petrology, 104:225-234.

Holdaway M.J. (2000) Application of new experimental and garnet Margules data to the garnet-biotite geothermometer. American Mineralogist, 85:881-892.

Hollings P. & Kerrich R. (1999) Trace element systematics of ultramafic and mafic volcanic rocks from the 3 Ga North Caribou greenstone belt, northwestern Superior Province. Precambrian Research, 93:257-279.

Huston D.L. & Logan G.A. (2004) Barite, BIFs and bugs: Evidence for the evolution of the Earth's early hydrosphere. Earth and Planetary Science Letters, 220:41-55.

Hutchinson R.W. (1976) Lode gold deposits: The case for volcanogenic distribution. In: Proceedings of the Pacific Northwest Mining and Metals Conference, Portland, Oregon, Salem, Oregon Dept. Geology Mineral Industries, pp. 64-105.

Hutchinson R.W., Ridler R.H. & Surfel G.G. (1971) Metallogenic relationships in the Abitibi belt, Canada: A model for Archean metallogeny. Canadian Institute of Mining Metallurgy Transcripts, 74:106-115.

Immega I.P. & Klein C. (1976) Mineralogy and petrology of some metamorphic Precambrian iron-formations in southwestern Montana. American Mineralogist, 61:1117-1144.

Indares A. & Martignole J. (1985) Biotite-garnet geothermometry in the granulite facies: the influence of Ti and AI in biotite. American Mineralogist, 70:272-278.

Isaac C. (2008) Stable Isotope (N, O, H) Geochemistry, Petrology and Compositions of Biotite of the Musselwhite Mine, Ontario: Implications for Mineralization. Unpublished M.Sc. thesis, Lakehead University, 136 p.

Jackson S., Dubé B., Oswald W. & Yang Z. (2015) Quantitative LA-ICP-MS mapping of diagenetic pyrite at two major Canadian Archean Au deposits. Abstract for the 2015 Goldschmidt conference, August 16-21, Prague, Czech Republic, p. 1408.

Jackson S.E., Gao J. & Dubé B. (2013) Nouveaux développements applicables à l'analyse des éléments en traces dans les dépôts de minéraux et à la cartographie utilisée pour la recherche et l'exploration des gisements de minerai : exemples de gisements d'or du Québec et de l'Ontario. Proceedings of the 2013 Quebec Mines Conference, Quebec City, Quebec, Canada, p. 16.

Jackson S.E., Shuttleworth S. & Cabri L.J. (2009) Quantitative determination and mapping of trace element concentrations in geochemistry.

James H.L. (1954) Sedimentary facies of iron-formation. Economic Geology 49:235-293.

Janes D.A., Seim G.W. & Storey C.C. (1990) Sioux Lookout Resident Geologist's district – 1989. Ontario Geological Survey, Miscellaneous Paper 147, pp. 69-100.

Janvier V. (2016) Géologie du gisement d'or Meadowbank encaissé dans des formations de fer rubanées, Nunavut, Canada. Ph.D. thesis, Institut National de la Recherche Scientifique – Centre Eau-Terre-Environnement, 501 p.

Jébrak M. & Marcoux E. (2008) Géologie des ressources minérales. Ressources Minérales et Faunes du Québec, 667 p.

Jensen L.S. (1976) A new cation plot for classifying subalkalic volcanic rocks. Ontario Ministry of Natural Resources, Miscellaneous Paper 66, 22 p.

Jochum K.P., Arndt N.T. & Hofmann A.W. (1991) Nb-Th-La in komatiites and basalts: Constraints on komatiite petrogenesis and mantle evolution. Earth and Planetary Science Letters, 107:272-289.

Kalbfleisch N. (2012) Crustal-scale Shear Zones Recording 400 m.y. of Tectonic Activity in the North Caribou greenstone belt, Western Superior Province of Canada. M.Sc. thesis, University of Ottawa, 162 p.

Kamber B.S. (2010) Archean mafic-ultramafic volcanic landmasses and their effect on ocean-atmosphere chemistry. Chemical Geology, 274:19-28.

Kamber B.S., Greig A. & Collerson K.D. (2005) A new estimate for the composition of weathered young upper continental crust from alluvial sediments, Queensland, Australia. Geochimica et Cosmochimica Acta, 69:1041-1058.

Katsuta N., Shimizu I., Helmstaedt H., Takano M., Kawakami S. & Kumazawa M. (2012) Major element distribution in Archean banded iron formation (BIF): Influence of metamorphic differentiation. Journal of Metamorphic Geology, 30:457-472.

Kelly C.J. & Schneider D.A. (2015) Insights into the timing of mineralization and metamorphism in the North Caribou greenstone belt, western Superior Province, In: B. Dubé & P. Mercier-Langevin (Eds.) Targeted Geoscience Initiative 4: Contributions to the Understanding of Precambrian Lode Gold Deposits and Implications for Exploration; Geological Survey of Canada, Open File 7852, pp. 245-253.

Kelly C.J., Gagnon E. & Schneider D.A. (2013) Redefining the pattern and timing of metamorphism in the North Caribou greenstone belt. Ontario Geological Survey, Open File 6290, pp. 59.1-59.8.

Kerswill J.A., Henderson J.R. & Henderson M.N. (1996) Distribution of gold and sulfides at Lupin, Northwest Territories – A discussion. Economic Geology, 91:957-966

Kerswill J.A. (1996) Iron-formation-hosted stratabound gold. In: Eckstrand O.R., Sinclair W.D. & Thorpe R.I. (Eds.) Geology of Canadian Mineral Deposit Types. Geological Survey of Canada, Geology of Canada No. 8, pp. 367-382.

Kerswill J.A. (1993) Models for iron-formation-hosted gold deposits. In: Kirkham R.V., Sinclair W.D., Thorpe R.I. & Duke J.M. (Eds.) Mineral Deposit Modeling. Geological Association of Canada, Special Paper 40, pp. 171-199.

King J.E., Davis W.J., Relf C. & Avery R.W. (1988) Deformation and plutonism in the western Contwoyto Lake map area, central Slave Province, District of Mackenzie, N.W.T. In: Current Research, part C. Geological Survey of Canada, Paper 88-1C, pp. 161-176.

Kleeman U. & Reinhardt J. (1994) Garnet-biotite thermometry revisited: The effects of Al[VI] and Ti in biotite. European Journal of Mineralogy, 6:925-941.

Klein C. (2005) Some Precambrian banded iron-formations (BIFs) from around the world: Their age, geologic setting, mineralogy, metamorphism, geochemistry, and origin. American Mineralogist, 90:1473-1499.

Klein C. & Beukes N.J. (1993) Sedimentology and geochemistry of the glaciogenic Late Proterozoic Rapitan iron-formation in Canada. Economic Geology, 88:542-565.

Klein C. & Beukes N.J. (1989) Geochemistry and sedimentology of a facies transition from limestone to iron-formation deposition in the Early Proterozoic Transvaal Supergroup, South Africa. Economic Geology, 84:1733-1774.

Klein C. (1983) Diagenesis and metamorphism of Precambrian banded iron formations, In: Trendall A.F. & Morris R.C. (Eds.) Iron formation: Facts and Problems. Elsevier, Amsterdam, pp. 417-469.

Klein C. & Fink R.F. (1976) Petrology of the Sokoman Iron Formation in the Howells River Area, at the Western Edge of the Labrador Trough. Economic Geology, 71:453-487.

Klein C. (1973) Changes in Mineral Assemblage with Metamorphism of Some Banded Precambrian Iron-Formations. Economic Geology, 68:1075-1088.

Klein E.M. (2004) Geochemistry of the Igneous Oceanic Crust. In: Holland, H.D. & Turekian, K.K. (Eds.) Treatise on Geochemistry. Elsevier, Amsterdam, 3:433-463.

Klein T.L. & Day W.C. (1994) Descriptive and grade-tonnage models of Archean low-sulfide Au-quartz veins and a revised grade-tonnage model of Homestake Au. US Geological Survey, Open File Report, 94-250, 26 p.

Klipfel P. (2002) Musselwhite U-Pb zircon and Ar-Ar dates: Synthesis and interpretation. Internal report prepared for Placer Dome, 23 p.

Knight J.T. (1994) The geology and genesis of Archaean amphibolite-facies lode-gold deposits in the Coolgardie goldfield. Western Australia. with special emphasis on the role of granitoids. Unpublished PhD thesis, Department of Geology and Geophysics, The University of Western Australia, 239 p.

Kohn M.J. & Spear F.S. (1990) Two new geobarometers for garnet amphibolites, with applications to southeastern Vermont. American Mineralogist, 75:89-96.

Kolb M. (2010) A microstructural study of Musselwhite Mine and Hammond Reef shear-zone-hosted gold deposits. M.Sc. thesis, Lakehead University, Thunder Bay, Ontario, 204 p.

Kolb J., Dziggel A. & Bagas L. (2015) Hypozonal lode gold deposits: A genetic concept based on a review of the New Consort, Renco, Hutti, Hira Buddini, Navachab, Nevoria and The Granites deposits. Precambrian Research, 262:20-44.

Kolb J., Hellmann A., Rogers A., Sindern N., Vennemann T., Böttcher M.E. & Meyer F.M. (2012) The role of a transcrustal shear zone in orogenic gold mineralization at the Ajjanahalli Mine, Dharwar Craton, South India. Economic Geology, 99:743-759.

Kolb J., Kisters A.F.M., Hoernes S. & Meyer F.M. (2000) The origin of fluids and nature of fluid-rock interaction in midcrustal auriferous mylonites of the Renco mine, southern Zimbabwe. Mineralium Deposita, 35:109-125.

Krogh T.E. (1982) Improved accuracy of U-Pb zircon ages by the creation of more concordant systems using an air abrasion technique. Geochimica et Cosmochimica Acta, 46:637-649.

Kruskal T.B. (1978) Multidimensional Scaling. Sage Publications Ltd., 93 p.

LaBerge G.L., Robins E.I. & Han T.-M. (1987) A model for the biological precipitation of Precambrian iron-formations. A: Geological evidence. In: Appel P.W.U. & LaBerge G.L. (Eds.) Precambrian iron-formations, Athens, Greece. Theophrastus Publications, pp. 69-96.

Lapointe B. & Chown E.H. (1993) Gold-bearing iron-formation in a granulite terrane of the Canadian Shield: A possible deep-level expression of an Archean gold-mineralizing system. Mineralium Deposita, 28:191-197.

Large R. R., Thomas H., Craw D., Henne A. & Henderson S. (2012) Diagenetic pyrite as a source for metals in orogenic gold deposits, Otago Schist, New Zealand. New Zealand Journal of Geology and Geophysics, 55(2):137-149.

Large R. R., Bull S.W. & Maslennikov V.V. (2011) A carbonaceous sedimentary source-rock model for Carlin-type and orogenic gold deposits. Economic Geology, 106:331-358.

Lawley C.J.M., Dubé B., Mercier-Langevin P., McNicoll V.J., Creaser R.A., Pehrsson S.J., Castonguay S., Blais J.-C., Simard M., Davis W.J. & Jackson S.E. (2015) Setting, age, and hydrothermal footprint of the emerging Meliadine gold district, Nunavut. In: Dubé B. & Mercier-Langevin P. (Eds.) Targeted Geoscience Initiative 4: Contributions to the Understanding of Precambrian Lode Gold Deposits and Implications for Exploration. Geological Survey of Canada, Open File 7852, pp. 99-112.

Lawrence M.G. & Kamber B.S. (2006) The behaviour of the rare earth elements during estuarine mixing – revisited. Marine Chemistry, 100:147-161.

Lewis B.R. (1965) Gold deposit of Hill 50 mine. Proceedings of the 8th Commonwealth Mining Metallurgy Congress, Australia and New Zealand, pp. 98-100.

Lhotka P.G. & Nesbitt B.E. (1989) Geology of unmineralized and gold-bearing iron formation, Contwoyto Lake-Point Lake region, Northwest Territories, Canada. Canadian Journal of Earth Sciences, 26(1):46-64.

Liferovitch R. (2007) Detailed petrographic and mineralogical study of high-grade pyrrhotite-carbonate vein from the drill hole 03-PQU-062. Report for Goldcorp Canada Ltd., Musselwhite Mine, 20 p. and appendices.

Lin S., Parks J., Heaman L.M., Simonetti A. & Corkery M.T. (2013) Diapirism and sagduction as a mechanism for deposition and burial of "Timiskaming-type" sedimentary sequences, Superior Province: Evidence from detrital zircon geochronology and implications for the Borden Lake conglomerate in the exposed middle to lower crust in the Kapuskasing uplift. Precambrian Research, 238:148-157.

Lin S., Davis D.W., Rotenberg E., Corkery M.T. & Bailes A.H. (2006) Geological evolution of the northwestern Superior province: Clues from geology, kinematics and geochronology in the Gods Lake Narrows area, Oxford-Stull terrane, Manitoba. Canadian Journal of Earth Sciences, 43:749-765.

Lin S. (2005) Synchronous vertical and horizontal tectonism in the Neoarchean: Kinematic evidence from a synclinal keel in the northwestern Superior craton, Canada. Precambrian Research, 139:181-194.

Liou J.G., Kuniyoshi S. & Ito K. (1974) Experimental study of the phase relations between greenschist and amphibolite in a basalt system. American Journal of Science, 274:613-632.

Lisitsin V.A. & Pitcairn I.K. (2016) Orogenic gold minerals systems of the Western Lachlan Orogen (Victoria) and the Hudgkinson Province (Queensland): Crustal metal sources and cryptic zones of regional fluid flow. Ore Geology Reviews, 76:280-295.

Long D.G.F. (2004) Precambrian rivers. In: Eriksson P.G., Altermann W., Nelson D.R., Mueller W.U. & Catuneanu O. (Eds.) The Precambrian Earth: Tempos and Events, pp. 660-663.

Ludwig K.R. (2003) Mathematical-statistical treatment of data and errors for Th-230/U geochronology. Uranium-Series Geochemistry. Reviews in Mineralogy and Geochemistry, 52:631-656.

Ludwig K.R. (2001). SQUID 1.02 A user's manual: A Geochronological Toolkit for Microsoft Excel. Berkeley Geochronological Center.

Lydon J.W. (2007) An overview of the economic and geological contexts of Canada's major mineral deposit types. In: Goodfellow W.D. (Ed.) Mineral Deposits of Canada: A Synthesis of Major Deposit-Types, District Metallogeny, the Evolution of Geological Provinces, and Exploration Methods. Geological Association of Canada, Mineral Deposits Division, Special Publication No. 5, pp. 3-48.

Lydon J.W. (1984) Volcanogenic massive sulphide deposits. Part 1: A descriptive model. Geoscience Canada, 11:195-202.

Mahar E.M., Baker J.M., Powell R., Holland T.J.B. & Howell N. (1997) The effect of Mn on mineral stability in metapelites. Journal of Metamorphic Geology, 15(2):223-238.

Mattinson J.M. (2005) Zircon U-Pb chemical abrasion ("CA-TIMS") method: Combined annealing and multi-step partial dissolution analysis for improved precision and accuracy of zircon ages. Chemical Geology, 220:47-66.

MacLean T.J. & Barrett W.H. (1993) Lithogeochemical techniques using immobile elements. Journal of Geochemical Exploration, 48:109-133.

McClay K. (1987) The mapping of geological structures. Geological Society of London Handbook series, Open University Press, 161 p.

McCuaig T.C. & Kerrich R. (1998) P-T-t-deformation-fluid characteristics of lode gold deposits: Evidence from alteration systematics. Ore Geology Reviews, 12:381-453.

McMillan N. (1996) Late Archaean, syn-amphibolite facies, lode-gold deposits overprinted by Palaeoproterozoic deformation, metamorphism and hydrothermal activity at Marymia, Western Australia. Unpublished PhD thesis. Department of Geology and Geophysics, The University of Western Australia, 261 p.

McNicoll V., Dubé B., Castonguay S., Oswald W., Biczok J., Mercier-Langevin P., Skulski T. & Malo M. (2016) The world-class Musselwhite BIF-hosted gold deposit, Superior Province, Canada: New high-precision U-Pb geochronology and implications for the geological setting of the deposit and gold exploration. Precambrian Research, 272:133-149.

McNicoll V., Dubé B., Biczok J., Castonguay S., Oswald W., Mercier-Langevin P., Skulski T. & Malo M. (2013) The Musselwhite gold deposit, North Caribou greenstone belt, Ontario: new high-precision U-Pb ages and their impact on the geological and structural setting of the deposit, In: Program with Abstracts. Geological Association of Canada-Mineralogical Association of Canada joint annual meeting, May 22-24, 2013, Winnipeg, Manitoba, 36:142.

McPhie J. (1993) Volcanic textures: a guide to the interpretation of textures in volcanic rocks.

Mikucki E.J. (1998) Hydrothermal transport and depositional processes in Archean lode-gold systems: A review. Ore Geology Review, 13:307-321.

Miyano T. & Klein C. (1986) Fluid behavior and phase relations in the system Fe-Mg-Si-C-O-H: Application to high grade metamorphism of iron-formations. American Journal of Science, 286:540-575.

Miyano T. & Klein C. (1983) Conditions of riebeckite formation in the iron-formation of the Dales Gorge Member, Hamersley Group, Western Australia. American Mineralogist, 68:517-529.

Miyano T. & Miyano S. (1982) Ferri-annite from the Dales Gorge Member iron-formation, Wittenoom area, Western Australia. American Mineralogist, 67:1179-1195.

Montel J.-M., Kornprobst J. & Vielzeuf D. (2000) Preservation of old U-Th-Pb ages in shielded monazite: Example from the Beni Bousera Hercynian kinzigites (Morocco). Journal of Metamorphic Geology, 18:335-342.

Moran P. (2008) Lithogeochemistry of the sedimentary stratigraphy and metosomatic alteration in the Musselwhite Gold Deposit, North Caribou Lake belt, Superior Province, Canada: Implications for Deposition and Mineralization. M.Sc. Thesis, Lakehead University, 411 p.

Morelli R.M., Bell C.C., Creaser R.A. & Simonetti A. (2010) Constraints on the genesis of gold mineralization at the Homestake Gold Deposit, Black Hills, South Dakota from rhenium-osmium sulfide geochronology. Mineralium Deposita, 45:461-480.

Morfin S., Sawyer E.W. & Bandyayera D. (2013) Large volumes of anatectic melt retained in granulite facies migmatites: An injection complex in northern Quebec. Lithos, 168-169:200-218.

Moritz R.P. & Chevé S. (1992) Fluid-inclusion studies of high-grade metamorphic rocks of the Ashuanipi complex, eastern Superior Province: Constraints on the retrograde P-T path and implications for gold metallogeny. Canadian Journal of Earth Sciences, 29:2309-2321.

Morris R.C. (1993) Genetic modelling for banded iron formation of the Hamersley Group, Pilbara Craton, Western Australia. Precambrian Research, 60:243-286.

Mueller A.G., Nemchin A.A. & Frei R. (2004) The Nevoria gold skarn deposit, Southern Cross greenstone belt, Western Australia: II. Pressure-temperature-time path and relationship to postorogenic granites. Economic Geology, 99:453-478.

Mueller A.G. (1997) The Nevoria gold skarn deposit in Archean iron-formation, Southern Cross greenstone belt, Western Australia: I. Tectonic setting, petrography, and classification. Economic Geology, 92:181-209.

Mueller A.G. & Groves D.I. (1991) The classification of Western Australian greenstone-hosted gold deposits according to wallrock-alteration mineral assemblages. Ore Geology Reviews, 6:291-331.

Mueller W.U. & Corcoran P.L. (1998) Late-orogenic basins in the Archaean Superior Province, Canada: Characteristics and inferences. Sedimentary Geology, 120:177-203.

Müller S.G., Krapez B., Barley M.E. & Fletcher I.R. (2005) Giant iron-ore deposits of the Hamersley province related to breakup of Paleoproterozoic Australia: New insights from in situ SHRIMP dating of baddeleyite from mafic intrusions. Geological Society of America, Geology, 33:577-580.

Naldrett A. (1999) World-class Ni-Cu-PGE deposits: Key factors in their genesis. Mineralium Deposita, 34(3):227-240.

Nance W.B. & Taylor S.R. (1976) Rare earth element patterns and crustal evolution: I. Australian post-Archean sedimentary rocks. Geochimica et Cosmochimica Acta, 40:1539-1551.

Nesbitt R.W. & Sun S.S. (1976) Geochemistry of Archaean spinifex-textured peridotites and magnesian and low-magnesian tholeiites. Earth and Planetary Science Letters, 31(3):433-453.

Newton P.G. (1991) Structure and genesis of gold mineralization in the Prohibition BIF-hosted deposit, Meekatharra, Western Australia. Unpublished BSc (honours) thesis, Department of Geology, The University of Western Australia, 72 p.

Oberthür T., Saager R. & Tomschi H.-P. (1990) Geological, mineralogical and geochemical aspects of Archean banded iron-formation-hosted gold deposits: Some examples from southern Africa. Mineralium Deposita, 25:S125-S135.

Oliver N.H.S. (1996) Review and classification of structural controls on fluid flow during regional metamorphism. Journal of Metamorphic Geology, 14:477-492.

Ord A. & Oliver N.H.S. (1997) Mechanical controls on fluid flow during regional metamorphism: some numerical models. Journal of Metamorphic Geology, 14:477-492.

Oswald W., Castonguay, S., Dubé B., Malo M., Mercier-Langevin P., Bécu V. & Lauzièere K. (in prep) Whole-rock lithogeochemistry of the Archean Musselwhite BIF-hosted gold deposit, northwestern Superior Province, Ontario. Geological Survey of Canada, Open File 8388.

Oswald W., Castonguay, S., Dubé B., Malo M., McNicoll V., Mercier-Langevin P. & Lucas K. (2017) Controls of BIF-hosted gold mineralization, Musselwhite mine, Superior Province, Ontario, Canada. In: Proceeding of the 14th Biennial SGA Meeting, 20-23 August, Quebec City, Canada, 1:79-82.

Oswald W., Castonguay S., Dubé B., McNicoll V., Biczok J., Malo M. & Mercier-Langevin P. (2015a) Geological setting of the world-class Musselwhite gold mine, Superior Province, northwestern Ontario: Implications for exploration. In: Dubé B. & Mercier-Langevin P. (Eds.) Targeted Geoscience Initiative 4: Contributions to the Understanding of Precambrian Lode Gold Deposits and Implications for Exploration. Geological Survey of Canada, Open File 7852, pp. 69-84.

Oswald W., Castonguay S., Dubé B., McNicoll V., Biczok J., Malo M. & Mercier-Langevin P. (2015b) New insights on the geological and structural settings of the Musselwhite banded iron-formation hosted gold deposit, North Caribou green-stone belt, Superior Province, Ontario. Geological Survey of Canada, Current Research 2015-3, 19 p.

Oswald W., Castonguay S., Dubé B., McNicoll V., Biczok J., Malo M. & Mercier-Langevin P. (2015c) Geological setting of the world-class Musselwhite BIF-hosted gold deposit, Ontario, Canada. In: Proceeding of the 13th Biennial SGA Meeting, 24-27 August 2015, Nancy, France, pp. 1115-1119.

Oswald W., Dubé B., Castonguay S., McNicoll V., Biczok J., Mercier-Langevin P., Malo M. & Skulski T. (2014a) New insights on the structural and geological setting of the world-class Musselwhite gold deposit, Superior Province, Northwestern Ontario. Geological Survey of Canada, OF-DP7633, 1 poster.

Oswald W., Castonguay S., Dubé B., Mercier-Langevin P., Malo M., Biczok J. & McNicoll V. (2014b) Targeted Geoscience Initiative 4. Lode gold deposits in ancient deformed and metamorphosed terranes: Detailed mapping of key stripped out-crops in the Musselwhite Mine area, Northwestern Ontario and implications for the geological and structural setting of the gold mineralization. In: Summary of Field Work and Other Activities 2014. Ontario Geological Survey, Open File Report 6300, pp. 42-1–42-15.

Otto A. (2002) Ore forming processes in the BIF-hosted gold deposit Musselwhite Mine, Ontario, Canada. M.Sc. thesis, Freiberg Institute of Mining and Technology, 86 p. and appendices.

Parmenter A.C., Lin S. & Corkery M.T. (2006) Structural evolution of the Cross Lake greenstone belt in the northwestern Superior Province, Manitoba: Implications for relationship between vertical and horizontal tectonism. Canadian Journal of Earth Science, 43:767-787.

Parr J.M. & Plimer I.R. (1993) Models for Broken Hill-type lead-zinc-silver deposits. In: Kirkham R.V., Sinclair W.D., Thorpe R.I. & Duke J.M. (Eds.) Mineral Deposit Modelling: Geological Association of Canada, Special Paper 40, pp. 253-288.

Parrish R.R. & Noble S.R. (2003) Zircon U-Th-Pb geochronology by isotope dilution – thermal ionization mass spectrometry (ID-TIMS). In: Reviews in Mineralogy and Geochemistry, 53(1):183-213.

Parrish R.R. (1990) U-Pb dating of monazite and its application to geological problems. Canadian Journal of Earth Science, 27:1431-1450.

Parrish R.R., Roddick J.C., Loveridge W.D. & Sullivan, R.W. (1987) Uranium-lead analytical techniques at the Geochronology Laboratory, Geological Survey of Canada. In: Radiogenic age and isotopic studies. Report: Geological Survey of Canada, Paper 87-2, pp. 3-7.

Paulick H. & Franz G. (2001) Greenschist facies regional and contact metamorphism of the Thalanga volcanic-hosted massive sulfide deposit (northern Queensland, Australia). Mineralium Deposita, 36:786-793.

Pearce J.A. (2008) Geochemical fingerprinting of oceanic basalts with applications to ophiolites classification and the search of Archean oceanic crust. Lithos, 100:14-48.

Percival J.A., Skulski T., Sanborn-Barrie M., Stott G.M., Leclair A.D., Corkery M.T. & Boily M. (2012) Geology and tectonic evolution of the Superior Province, Canada. In: Percival J.A., Cook F.A. & Clowes R.M. (Eds.) Tectonic Styles in Canada: The LITHOPROBE Perspective. Geological Association of Canada, Special Paper 49, pp. 321-378.

Percival J.A. (2007) Geology and metallogeny of the Superior Province, Canada. In: Mineral Deposits of Canada: A Synthesis of Major Deposit-Types, District Metallogeny, the Evolution of Geological Provinces, and Exploration Methods. Geological Association of Canada, Mineral Deposits Division, Special Publication, 5:903-928.

Percival J.A., Sanborn-Barrie M., Skulski T., Stott G.M., Helmstaedt H. & White D.J. (2006) Tectonic evolution of the western Superior Province from NATMAP and Lithoprobe studies. Canadian Journal of Earth Sciences, 43:1085-1117.

Percival J.A., Mortensen J.K. & Roddick J.C.M. (1988) Evolution of the Ashuanipi complex: Conventional and ion probe U-Pb data. Geological Association of Canada, Program with Abstracts, 13:A97.

Perring C.S., Barnes S.J. & Hill R.E.T. (1996) Geochemistry of komatiites from Forrestania, Southern Cross Province, Western Australia: Evidence for crustal contamination. Lithos, 37:181-197.

Peter J.M. (2003) Ancient iron formations: their genesis and use in the exploration for stratiform base metal sulphide deposits with examples from the Bathurst Mining Camp. In: Lentz D.R. (Ed.) Geochemistry of Sediments and Sedimentary Rocks: Evolutionary Considerations to Mineral Deposit-Forming Environments. Geological Association of Canada, GeoText, 4:145-176.

Peter J.M. & Goodfellow W.D. (1996) Mineralogy, bulk and rare earth element geochemistry of massive sulphide-associated hydrothermal sediments of the Brunswick Horizon, Bathurst Mining Camp, New Brunswick. Canadian Journal of Earth Sciences, 33:252-283.

Phillips G.N. & Powell R. (2010) Formation of gold deposits: A metamorphic devolatilization model. Journal of Metamorphic Geology, 28:689-718.

Phillips G.N. & Powell R. (2009) Formation of gold deposits: Review and evaluation of the continuum model. Earth Science Reviews, 94:1-21.

Phillips G.N., Groves D.T. & Martyn J.E. (1984) An epigenetic origin for Archean banded iron-formation-hosted gold deposits. Economic Geology, 79:162-171.

Pickard A.L., Barley M.E. & Krapez B. (2004) Deep-marine depositional setting of banded iron formation: Sedimentological evidence from interbedded clastic sedimentary rocks in the early Palaeoproterozoic Dales Gorge Member of Western Australia. Sedimentary Geology, 170:37-62.

Pickard A.L. (2003) SHRIMP U-Pb zircon ages for the Palaeoproterozoic Kuruman Iron Formation, Northern Cape Province, South Africa: Evidence for simultaneous BIF deposition on Kaapvaal and Pilbara cratons. Precambrian Research, 125:275-315.

Pickard A.L. (2002) SHRIMP U-Pb zircon ages of tuffaceous mudrocks in the Brockman Iron Formation of the Hamersley Range, Western Australia. Australian Journal of Earth Sciences, 49:491-507.

Piroshco D.W., Breaks F.W. & Osmani I.A. (1989) The geology of gold prospects in the North Caribou Lake greenstone belt, District of Kenora, Northwestern Ontario. Ontario Geological Survey, Open File Report 5698, 94 p., 18 figures, 6 tables, 8 photos, and 4 maps in back pocket.

Piroshco D. & Shields H. (1985) Geology and gold mineralization of the Eyapamikama Lake area of the North Caribou Lake greenstone belt, District of Kenora. In: Ontario Geological Survey, Miscellaneous Paper 126, pp. 277-286.

Pitcairn I.K., Leventis N.-G., Beaudoin G. & Dubé B. (2017) A metasedimentary source for orogenic gold in the Abitibi belt? Abstract in Proceedings for the 14th Biennial SGA Meeting, Quebec City, August 20-23, 1:91-94.

Pitcairn I.K., Olivo G.R., Teagle D.A.H. & Craw D. (2010) Sulfide evolution during prograde metamorphism of the Otago and Alpine schists, New Zealand. The Canadian Mineralogist, 48:1267-1295.

Pitcairn I.K., Teagle D.A.H., Craw D., Olivo G.R., Kerrich R. & Brewer T.S. (2006) Sources of metals and fluids in orogenic gold deposits: Insights from the Otago and Alpine Schists, New Zealand. Economic Geology, 101:1525-1546.

Planavsky N., Bekker A., Rouxel O.J., Kamber B., Hofmann A., Knudsen A. & Lyons T.W. (2010) Rare Earth element and yttrium compositions of Archean and Paleoproterozoic Fe formations revisited: New perspectives on the significance and mechanisms of deposition. Geochimica et Cosmochimica Acta, 74:6387-6405.

Poulsen K.H., Robert F. & Dubé B. (2000) Geological classification of Canadian gold deposits. Geological Survey of Canada, Bulletin 540, 106 p.

Powell R., Will T.M. & Phillips G.N. (1991) Metamorphism in Archean greenstone belts: Calculated fluid compositions and implications for gold mineralization. Journal of Metamorphic Geology, 9:141-150.

Quinn J. (2014) Lithogeochemical and petrological analysis of a mafic metavolcanic sequence south of Musselwhite Mine, North Caribou greenstone belt. Lakehead University, B.Sc. honours thesis, xx pp.

Ramsay J.G. & Huber M. (1987) The Techniques of Modern Structural Geology. Volume 2: Folds and Fractures. Academic Press, London.

Ramsay J.G. (1967) Folding and Fracturing of Rocks. McGraw Hill, New York, 568 p.

Rayner N. & Stott G.M. (2005) Discrimination of Archean domains in the Sachigo Subprovince: A progress report on the geochronology. In: Summary of Field Work and Other Activities 2005, Ontario Geological Survey, Open File Report 6172, pp. 10-1–10-21

Rayner N.M. & Stern R.A. (2002) Improved sample preparation method for SHRIMP analysis of delicate mineral grains exposed in thin sections. Geological Survey of Canada, Current Research 2002-F10, pp. 1-3.

Ribeiro-Rodrigues L.C., Gouveia de Oliveira C. & Friedrich G. (2007) The Archean BIF-hosted Cuiabá gold deposit, Quadrilátero Ferrífero, Minas Gerais, Brazil. Ore Geology Reviews, 32:543-579.

Ridler R.H. (1970) Relationship of mineralization to volcanic stratigraphy in the Kirkland-Larder Lake Area, Ontario. Proceedings of Geological Association of Canada, 21:33-42.

Ridley J.R. & Diamond L.W. (2000) Fluid chemistry of orogenic lode gold deposits and implications for genetic models. Society of Economic Geologists Reviews, 13:141-162.

Ridley J. Groves D.I. & Knight J.T. (2000) Gold deposits in amphibolite and granulite facies terranes of the Archean Yilgarn craton, Western Australia: Evidence and implications of synmetamorphic mineralization. Reviews in Ore Geology, 11:1-25.

Robert F., Brommecker R., Bourne B.T., Dobak P.J., McEwan C.J., Rowe R.R. & Zhou X. (2007) Models and exploration methods for major gold deposit types. In: Milkereit B. (Ed.) Proceedings of Exploration 07: Fifth Decennial International Conference on Mineral Exploration, pp. 691-711.

Robert F., Poulsen K.H., Cassidy K.F. & Hodgson C.J. (2005) Gold metallogeny of the Superior and Yilgarn cratons. In: Hedenquist J.W., Thompson J.F.H., Goldfarb R.J. & Richards J.P. (Eds.) Society of Economic Geology, Economic Geology 100th Anniversary Volume, pp. 1001-1033.

Robert F. & Poulsen K.H. (2001) Vein formation and deformation in greenstone gold deposits. Reviews in Economic Geology 14:111-155.

Robert F., Poulsen K.H. & Dubé B. (1997) Gold deposits and their geological classification. In: Gubins A.G. (Ed.) Proceedings of Exploration 97: Fourth Decennial International Conference on Mineral Exploration, pp. 209-220.

Robert F., Poulsen K.H. & Dubé B. (1994) Structural analysis of lode gold deposits in deformed terranes and its application. Short course notes, Geological Survey of Canada, Open File Report 2850, 140 p.

Robert F. (1990) Structural setting and control of the gold-quartz veins of the Val d'Or area, southeastern Abitibi Subprovince. In: Ho S.E., Robert F. & Groves D.I. (Eds.) Gold and base-metal mineralization in the Abitibi Subprovince, Canada, with emphasis on the Quebec Segment. Short Course Notes, University of Western Australia, Publication No. 24, pp. 167-209.

Roberts R.G. (1987) Ore deposit models #11: Archean lode gold deposits. Geoscience Canada, 14(1):37-52.

Roddick J.C. (1987) Generalized numerical error analysis with applications to geochronology and thermodynamics. Geochimica et Cosmochimica Acta, 51:2129-2135.

Rollinson H.R. (1994) Using Geochemical Data: Evaluation, Presentation, Interpretation. Longman Geochemistry Series, Taylor & Francis, 352 p.

Ross P.-S. & Bédard J.H. (2009) Magmatic affinity of modern and ancient subalkaline volcanic rocks determined from trace-element discriminant diagrams. Canadian Journal of Earth Science, 46:823-839.

Rudnicki M.D. (1995) Particle formation, fallout and cycling within the buoyant and non-buoyant plume above the TAG vent field. In: Parson L.M., Walker C.L. & Dixon D.R. (Eds.) Hydrothermal Vents and Processes. Geological Society, Special Publication No. 87, pp. 387-396.

Rutherford R.A. (1993) Bounty Gold mine: Deformation history and the development of ore fluid pathways within an iron formation host, Western Australia. M.Sc. thesis, University of Tasmania, 95 p.

Rye D.M. & Rye R.O. (1974) Homestake Gold Mine, South Dakota: I. Stable Isotope Studies. Economic Geology, 69:293-317.

Satterly J. (1941) Geology of the Windigo-North Caribou lakes area. Ontario Department of Mines, Annual Report, 48(9):32. Accompanied by Map 48h, 1:63,360 scale or 1" to 1 mile; and Map 48j, 1:126,720 scale or 1 inch to 2 miles.

Scott R.J., Meffre S., Woodhead J., Gilbert S.E., Berry R.F. & Emsbo P. (2009) Development of framboidal pyrite during diagenesis, low-grade regional metamorphism, and hydrothermal alteration. Economic Geology, 104:1143-1168.

Sharp Z.D., Essene E.J. & Kelly W.C. (1985) A re-examination of the arsenopyrite geothermometer: Pressure considerations and applications to natural assemblages. Canadian Mineralogist, 23:517-534.

Shervais J. W. (2001) Birth, death, and resurrection: The life cycle of suprasubduction zone ophiolites. Geochemistry Geophysics Geosystems, 2:1.

Sibson R.H. (2001) Seismogenic framework for hydrothermal transport and ore deposition. Society of Economic Geologists Reviews, 14:25-50.

Simonson B.M. & Hassler S.W. (1996) Was the deposition of large Precambrian iron formations linked to major marine transgression? Journal of Geology, 104:665-676.

Sizova E., Gerya T., Brown M. & Stüwe K. (2017) What drives metamorphism in early Archean greenstone belts? Insights from numerical modeling. Tectonophysics, in press.

Skirrow R.G. & Franklin J.M. (1994) Silicification and metal leaching in semiconformable alteration beneath the Chisel Lake Massive Sulfide Deposit, Snow Lake, Manitoba. Economic Geology, 89:31-50.

Slack J.F., Grenne T., Bekker A., Rouxel O.J. & Lindberg P.A. (2007) Suboxic deep seawater in the late Paleoproterozoic: Evidence from hematitic chert and iron formation related to seafloor-hydrothermal sulfide deposits, central Arizona, USA. Earth and Planetary Science Letters, 255:243-256.

Smith D.S. (1996) Hydrothermal alteration at the Mineral Hill mine, Jardine, Montana: A lower amphibolite facies Archean lode gold deposit of probable syn-metamorphic origin. Economic Geology 91:723-750.

Smith H.A. & Barreiro B. (1990) Monazite U-Pb dating of staurolite grade metamorphism in pelitic schists. Contribution to Mineralogy and Petrology, 105:602-615.

Smyk E. (2013) Geochemistry and petrography study of a Mesoarchean felsic metavolcanic unit near Musselwhite Mine, North Caribou greenstone belt. Lakehead University, B.Sc. honours thesis, 108 p.

Spear F.S. (1993) Metamorphic phase equilibria and pressure-temperature-time paths. Mineralogical Society of America, Monograph, 821 p.

Spry P.G., Peter J.M. & Slack J.F. (2000) Meta-exhalites as exploration guides to ore. In: Spry P.G., Marshall B. & Yokes F.M. (Eds.) Metamorphosed and metamorphogenic ore deposits. Society of Economic Geologists, Reviews in Economic Geology, 11:163-201.

Steadman J.A. & Large R.R. (2016) Synsedimentary, diagenetic, and metamorphic pyrite, pyrrhotite, and marcasite at the Homestake BIF-hosted gold deposit, South Dakota, USA: Insights on Au-As ore genesis from textural and LA-ICP-MS trace element studies. Economic Geology, 111:1731-1752.

Steadman J.A., Large R.R., Davidson G.J., Bull S.W., Thompson J., Ireland T.R. & Holden P. (2014) Paragenesis and composition of the ore in the Randalls BIF-hosted deposits, Yilgarn Craton, Western Australia: Implications for the timing of deposit formation and constraints on gold sources. Precambrian Research, 423:110-132.

Stefansson A. & Seward T.M. (2004) Gold(I) complexing in aqueous sulphide solutions to 500°C at 500 bar. Geochimica et Cosmochimica Acta, 68:4121-4143.

Stern R.A. & Berman, R.G. (2000) Monazite U-Pb and Th-Pb geochronology by ion microprobe with an application to in situ dating of an Archean metasedimentary rock. Chemical Geology, 172:113-130.

Stern R.A. & Sanborn N. (1998) Monazite U-Pb and Th-Pb geochronology by high-resolution secondary ion mass spectrometry. Radiogenic Age and Isotopic Studies: Report 11. Geological Survey of Canada, Current Research 1998-F, pp. 1-18.

Stern R.A. (1997) The GSC sensitive high-resolution ion microprobe (SHRIMP): Analytical techniques of zircon U-Th-Pb age determinations and performance evaluation. In: Radiogenic Age and Isotopic Studies: Report 10. Geological Survey of Canada, Current Research 1997-F, pp. 1-31.

Stott G.M. & Biczok J. (2010) North Caribou greenstone belt: Gold and its possible relation to the North Caribou pluton emplacement – a beltwide contact-strain aureole? In: Summary of Field Work and Other Activities 2010, Ontario Geological Survey, Open File Report 6260, pp. 22-1–22-12.

Stott G.M., Corkery M.T., Percival J.A., Simard M. & Goutier J. (2010) A revised terrane subdivision of the Superior Province. In: Summary of Field Work and Other Activities 2010, Ontario Geological Survey, Open File Report 6260, pp. 20-1–20-10.

Stott G.M. (1997) The Superior Province, Canada. Oxford Monographs on Geology and Geophysics, 35(1):480-507.

Stott G.M., Corfu F., Breaks F.W. & Thurston P.C. (1989) Multiple orogenesis in northwestern Superior Province. Geological Association of Canada – Mineralogical Association of Canada, joint annual meeting, Program with Abstracts, 14:A56.

Stüwe K. (1998) Tectonic constraints on the timing relationships of metamorphism, fluid production and gold-bearing quartz vein emplacement. Ore Geology Reviews, 13:219-228.

Su W., Bin X., Zhang H., Zhang X. & Hu R. (2007) Visible gold in arsenian pyrite at the Shuiyindong Carlin-type gold deposit, Guizhou, China: Implications for the environment and processes of ore formation. Ore Geology Reviews, 33:667-679.

Sun S.-S. & McDonough W.F. (1995) The composition of the Earth. Chemical Geology, 120:223-253.

Sun S.-S. & McDonough W.F. (1989) Chemical and isotopic systematics of oceanic basalts, implications for mantle composition and processes. In: Sanders A.D. & Norry M.J. (Eds.) Magmatism in the Ocean Basins. Geological Society Special Publication, pp. 313-345.

Symmes G.H. & Ferry J.M. (1991) Evidence from mineral assemblages for infiltration of pelitic schists by aqueous fluids during metamorphism. Contributions to Mineralogy and Petrology, 108(4):419-438.

Taylor S.R. & McLennan S.M. (1985) The continental crust: Its composition and evolution. Blackwell Scientific Publication, Carlton, 312 p.

Thomas H.V., Large R.R., Bull S.W., Maslennikov V., Berry R.F., Fraser R., Froud S. & Moye R. (2011) Pyrite and pyrrhotite textures and composition in sediments, laminated quartz veins, and reefs at Bendigo Gold Mine, Australia: Insights for ore genesis. Economic Geology, 106:1-31.

Thompson M.J., Watchorn R.B., Bonwick C.M., Frewin M.O., Goodgame V.R., Pyle M.J. & MacGeehan P.J. (1990) Gold deposits of Hill 50 Gold Mine at Mount Magnet. In: Hughes F.E. (Ed.) Geology of the Mineral Deposits of Australia and Papua New Guinea, Vol. 1. The Australasian Institute of Mining and Metallurgy, Monograph, 14:221-241.

Thurston P., Osmani I.A. & Stone D. (1991) Northwestern Superior Province: Review and terrane analysis. In: Thurston P.C., Williams H.R., Sutcliffe R.H. & Stott G.M. (Eds.) Geology of Ontario. Ontario Geological Survey, Special Volume, 4(1):80-142.

Tinkham D.K., Zuluaga C.A. & Stowell H.H. (2011) Metapelite phase equilibria modeling in MnNCKFMASH: The effect of variable Al_2O_3 and MgO/(MgO+FeO) on mineral stability. Mineralogical Society of America, Geological Materials Research, 3-1:1-42.

Tomkins A.G. (2010) Windows of metamorphic sulfur liberation in the crust: Implications for gold deposit genesis. Geochimica et Cosmochimica Acta, 74:3246-3259.

Tomkins A.G. & Grundy C. (2009) Upper temperature limits of orogenic gold deposit formation: Constraints from the granulite-hosted Griffin's Find Deposit, Yilgarn Craton. Economic Geology, 104:669-685.

Tomlinson K.Y., Stone D., Stott G.M. & Percival J.A. (2004) Basement terranes and crustal recycling in the western Superior Province: Nd isotopic character of granitoid and felsic volcanic rocks in the Wabigoon subprovince, N. Ontario, Canada. Precambrian Research, 132:245-274.

Tóth Z., Lafrance B., Dubé B., McNicoll V.J., Mercier-Langevin P. & Creaser R.A. (2015) Banded iron formation-hosted gold mineralization in the Geraldton area, northwestern Ontario : Structural setting, mineralogical characteristics, and geochronology. In: Dubé B. & Mercier-Langevin P. (Eds.) Targeted Geoscience Initiative 4: Contributions to the Understanding of Precambrian Lode Gold Deposits and Implications for Exploration. Geological Survey of Canada, Open File 7852, pp. 85-98.

Trendall A.F., Compston W., Nelson D.R., De Laeter J.R. & Bennett V.C. (2004) SHRIMP zircon ages constraining the depositional chronology of the Hamersley Group, Western Australia. Australian Journal of Earth Sciences, 51:621-644.

Trendall A.F. (1983) The Hamersley basin. In: Trendall A.F. & Morris R.C. (Eds.) Iron Formation: Facts and Problems. Elsevier, Amsterdam, pp. 69-129.

Trendall A.F. (1973) Precambrian iron formations of Australia. Economic Geology, 68:1023-1034.

Trendall A.F. & Blockley J.G. (1970) The iron formations of the Precambrian Hamersley Group, Western Australia, with special reference to the crocidolite. Geological Survey of Western Australia Bulletin, 119:366.

Trendall A.F. (1968) Three great basins of Precambrian iron formation deposition: A systematic comparison. Geological Society of America Bulletin, 79:1527-1544.

Turner F.J. & Weiss L.E. (1963) Structural Analysis of Metamorphic Tectonites. McGraw-Hill, New York, 545 p.

Upton G. & Cook I. (1996) Understanding Statistics. Oxford University Press, 657 p.

Van Lankvelt A., Schneider D.A., Biczok J., McFarlane C.R.M. & Hattori K. (2016) Decoding Zircon Geochronology of Igneous and Alteration Events Based on Chemical and Microstructural Features: a Study from the Western Superior Province, Canada. Journal of Petrology, 57(7):1309-1334.

Van Lankvelt A. (2013) Protracted magmatism within the North Caribou terrane, Superior Province: Petrology, geochronology, and geochemistry of meso- to neoarchean TTG suites. M.Sc. thesis, University of Ottawa, 208 p.

Van Lankvelt A., Schneider D.A. & Hattori K. (2011) External Granitoids of the Mesoarchean North Caribou Terrane. Abstract for Advances in Earth Science Research Conference 2011.

Veizer J. (1983) Geologic evolution of the Archean-early Proterozoic Earth. In: Schopf J.W. (Ed.) Earth's earliest biosphere: Its origin and evolution. Princeton University Press, pp. 240-259.

Verma S.P., Guevara M. & Agrawal S. (2006) Discriminating four tectonic settings: Five new geochemical diagrams for basic and ultrabasic volcanic rocks based on log-ratio transformation of major-element data. Canadian Journal of Earth Science, 115(5):485-528.

Vernon R.H. (2004) A Practical Guide to Microstructure. Cambridge University Press, 594 p.

Vial D.S., DeWitt E., Lobato L.M., Ahorman C.H. (2007) The geology of the Morro Velho gold deposit in the Archean Rio das Velhas greenstone belt, Quadrilátero Ferrífero, Brazil. Ore Geology Reviews, 32:511-542.

Vielreicher R.M. (1994) The Mt. Morgans BIF-hosted gold deposit: Physical and chemical controls on mesothermal gold mineralization in a greenschist facies terrane. Unpublished PhD thesis, Department of Geology and Geophysics, The University of Western Australia, 233 p.

Villeneuve M., Hutton C., Bjerkelund C. & Paradis S. (2011) Overview of Targeted Geoscience Initiative 4 (TGI-4) Ore System Projects: A National, Thematic Program to Enhance Effectiveness of Deep Exploration.

Vos I.M.A., Bierlein F.P., Standing J.S. & Davidson G. (2009) The geology and mineralisation at the Golden Pride gold deposit, Nzega greenstone belt, Tanzania. Mineralium Deposita, 44:751-764.

Walker J.C.G. & Zahnle K.J. (1986) Lunar nodal tide and distance to the Moon during the Precambrian. Letters to Nature, Nature, 320:600-602.

Walker J.C.G., Klein C., Schidlowski M., Schopf J.W., Stevenson D.J. & Walter M.R. (1983) Environmental evolution of the Archean-early Proterozoic Earth. In: Schopf J.W. (Ed.) Earth's Earliest Biosphere, its Origin and Evolution. Princeton University Press, New Jersey, pp. 260-290.

Walshe J.L. (1986) A six-component chlorite solid solution model and the conditions of chlorite formation in hydrothermal and geothermal systems. Economic Geology, 81:681-703.

Weedon P. & Stallman M. (1995) Bounty gold mine. In: Schwebel P.J. (Ed.) Southern Cross greenstone belt, geology and gold mines. Nedlands, Western Australia, Geoconferences Inc., pp. 113-117.

Wheeler J. (2014) Dramatic effects of stress on metamorphic reactions. Geology, 42(80):647-650.

Wheeler J. (1987) The significance of grain-scale stresses in kinetics of metamorphism. Contributions to Mineral Petrology, 97:397-404.

Wheeler J.O., Hoffman P.F., Card K.D., Davidson A., Sanford B.V., Okulitch A.V. & Roest W.R. (1996) Geological map of Canada. 1:5,000,000 scale, Natural Resources Canada, 1 map.

White R.W., Powell R. & Johnson T.E. (2014) The effect of Mn on mineral stability in metapelites revisited: new a-x relations for manganese-bearing minerals. Journal of Metamorphic Geology, 32:809-828.

Williams G.E., Schmidt P.W. & Clark D.A. (2004) Paleomagnetism of iron-formation from the late Palaeoproterozoic Frere Formation, Earaheedy Basin, Western Australia: Paleogeographic and tectonic implications. Precambrian Research, 128:367-383.

Williams G.E. (2000) Geological constraints on the Precambrian history of Earth's rotation and the Moon's orbit. Reviews of Geophysics, 38:37-59.

Winchester J.A. & Floyd P.A. (1977) Geochemical discrimination of different magma series and their differentiation products using immobile elements. Chemical Geology, 20:325-343.

Winter J.D. (2001) An Introduction to Igneous and Metamorphic Petrology. Prentice Hall Inc., New Jersey, 697 p.

Witt W.K., Mason D.R. & Hammond D.P. (2009) Archean Karari gold deposit, Eastern Goldfields Province, Western Australia: A monzonite-associated disseminated gold deposit. Australian Journal of Earth Sciences, 56:1061-1086.

Witt W.K. & Hammond D.P. (2008) Archean gold mineralization. In: An Intrusion-Related, Geochemically Zoned District-Scale Alteration System in the Carosue Basin, Western Australia. Economic Geology, 103:445-454.

Witt W.K., Knight J.T. & Mikucki E.J. (1997) A syn-metamorphic lateral fluid flow model for gold mineralization in the Archean southern Kalgoorlie and Norseman terranes, Western Australia. Economic Geology: 92:407-437.

Witt W.K., Groves D.I. & Ho S.E. (1994) Ore deposits of the Eastern Goldfields, Western Australia. Geological Society of Australia (WA Division), Excursion Guidebook 8, 82 p.

Witt W. K. (1993) Lithological and structural controls on gold mineralization in the Archaean Menzies-Kambalda area, Western Australia. Australian Journal of Earth Sciences, 40:1, 65-86.

Witt W.K. (1991) Regional metamorphic controls on alteration associated with gold mineralization in the Eastern Goldfields province, Western Australia: Implications for the timing and origin of Archean lode-gold deposits. Geology, 19:982-98.5.

Woad G.M. (1981) Nature and genesis of banded iron-formation hosted gold deposits at Water Tank Hill, Mount Magnet, Western Australia. Unpublished BSc (honours) thesis, Department of Geology, The University of Western Australia, 99 p.

Wyman D.A., Hollings P. & Biczok J. (2011) Crustal evolution in a cratonic nucleus: Granitoids and felsic volcanic rocks of the North Caribou Terrane, Superior Province Canada. Lithos, 123:37-49.

Yardley B.W.D. (1989) An Introduction to Metamorphic Petrology. John Wiley, 248 p.

York D. (1969) Least squares fitting of a straight line with correlated errors. Earth and Planetary Science Letters, 5:320-324.

Zhang G. (1997) Structural characteristics and mechanical controls on fluid flow of gold deposit at the Musselwhite mine, Weagamow-North Caribou Lake greenstone belt, northwestern Ontario. Internal report for Placer Dome Ltd., 82 p.

Zhu X.K., O'Nions R.K., Belshaw N.S. & Gibb A.J. (1997) Significance of in situ SIMS chronometry of zoned monazite from the Lewisian granulites, Northwest Scotland. Chemical Geology, 135:35-53.

Zhu X.K. & O'Nions R.K. (1999) Zonation of monazite in metamorphic rocks and its implications for high temperature thermochronology: A case study from the Lewisian terrain. Earth and Planetary Science Letters, 171:209-220.

APPENDICES

Appendices I to XIII in separate file.